Mnaouar Chouchane
Tahar Fakhfakh
Hachmi Ben Daly
Nizar Aifaoui
Fakher Chaari *Editors*

Design and Modeling of Mechanical Systems - II

Proceedings of the Sixth Conference on Design and Modeling of Mechanical Systems, CMSM'2015, March 23–25, Hammamet, Tunisia

Springer

Lecture Notes in Mechanical Engineering

Mnaouar Chouchane · Tahar Fakhfakh
Hachmi Ben Daly · Nizar Aifaoui
Fakher Chaari

Editors

Design and Modeling
of Mechanical Systems - II

Proceedings of the Sixth Conference
on Design and Modeling
of Mechanical Systems, CMSM 2015
March 23–25, Hammamet, Tunisia

 Springer

Editors
Mnaouar Chouchane
National School of Engineers of Monastir
Monastir
Tunisia

Tahar Fakhfakh
National School of Engineers of Sfax
Sfax
Tunisia

Hachmi Ben Daly
National School of Engineers of Sousse
Sousse Erriadh
Tunisia

Nizar Aifaoui
Preparatory Institute for Engineering
   Studies
Monastir
Tunisia

Fakher Chaari
National School of Engineers of Sfax
Sfax
Tunisia

Preface

This book contains a compilation of 83 papers presented in the 6th International Congress on Design and Modeling of Mechanical System (CMSM'2015) held in Hammamet, Tunisia, from the 23rd to the 25th of March 2015. Since its first edition in 2005, the CMSM Congress has been held every two years to bring together specialists from universities and industrial companies to present state of the art researches, discuss recent findings and exchange research experiences in the field of Design and Modeling of Mechanical Systems. In each edition, the CMSM congress bring together about 300 participants who participate actively in the congress plenary sessions and in the sessions devoted to specialized topics. The CMSM Congress is organized by three Tunisian research laboratories: the Mechanical Engineering Laboratory (LGM) of the National Engineering School of Monastir, The Mechanical Laboratory of Sousse (LMS) of the National Engineering School of Sousse and the Mechanical, Modeling and Manufacturing Laboratory (LA2MP) of the National Engineering School of Sfax. The papers included in this book present recent research findings in the field of design and modeling of mechanical systems. The papers have been classified into the five following parts:

1. Design and manufacturing of mechanical systems
2. Modeling and analysis of structures and materials
3. Robotics and mechatronics
4. Dynamics and vibration of mechanical systems
5. Fluid structure interaction.

All the papers included in this book have undergone a rigorous reviewing. The contributions of the organizing committee, the scientific committee and the referees are greatly appreciated. The editors would also like to express their sincere thanks to

all authors who have submitted their most recent research work and considered the comments of the reviewers during the preparation of their revised papers. Special thanks are also due to the editing team of Springer publication for supporting this project.

Contents

Part II: Modeling and Analysis of Structures and Materials

Part III: Robotics and Mechatronics

Part IV: Dynamics and Vibration of Mechanical Systems

Part V: Fluid Structure Interaction

Part I
Design and Manufacturing
of Mechanical Systems

Conceptual Design of an Intelligent Welding Cell Using SysML and Holonic Paradigm

Abdelmonaam Abid[1], Maher Barkallah[1], Moncef Hammadi[2], Jean-Yves Choley[2], Jamel Louati[1], Alain Rivière[2], and Mohamed Haddar[1]

[1] National School of Engineers of Sfax (ENIS), B.P, 1173, 3038 Sfax, Tunisia
`abidmonom@gmail.com, louati.ttg@gnet.tn,`
`{bark_maher,mohamed_haddar}@yahoo.fr`
[2] High Institute of Mechanics of Paris (SUPMECA), 3 rue Fernand Hainaut 93407, Saint-Ouen Cedex, France
`{moncef.hammadi,jean-yves.choley,alain.riviere}@supmeca.fr`

Abstract. Manufacturing companies are more and more required to implement intelligent infrastructures to handle the dynamic nature of demands and make quick decisions. Very limited research has been reported on holonic control in a flow-line type manufacturing systems such as welding cells.

In this paper we present a conceptual design of an intelligent welding cell using SysML (Systems Modeling Language). The holonic paradigm has been adopted to check the different configurations desired by the customers, which allows users to pre-define and pre-design the different configurations of the welding cell. The top-down modeling method based on SysML and the holonic control paradigm allows designers to define the different requirements of the manufacturing system and generate the appropriate dynamic configurations without complicating the design process. The approach has been applied to the case of a welding cell of the remedial parts of scaffolding systems. The objective in this case is to adapt the manufacturing system to the client needs for using either cylindrical or oval cross sectional traverse parts, and therefore to respond to the manufacturing company needs in terms of flexibility and productivity.

Keywords: Reconfigurable manufacturing systems, Holonic paradigm, SysML, Welding cell.

1   Introduction

Manufacturing systems need to handle the dynamic nature of demands. For this purpose companies must implement an intelligent infrastructure to make quick decisions in order to adapt in real time to internal and external variability production. As a result, companies require assuring a product with high quality at lower costs and with short life cycles.

In this paper, we aim to provide a holonic paradigm for controlling and designing of a welding cell and to adapt the production with the client trends in which System Modeling Language (SysML), is adopted as a means to integrate

and organize the hierarchy of models necessary to describe all the aspects of the system and describe the requirements of the client.

There are many publications on designing manufacturing systems but only few concentrate on adopting the design phase with the client trends. In one of the first papers on the subject (Dazhong Wu et al. 2011) proposed to support variety management decisions, by implementing the SysML-based information models as a variety coding information system in a case study of switchgear wich enclosure production reconfiguration system .A second paper proposes an approach to verify complex systems using SysML as a language which describes the system structure and requirements. Authors demonstrate this methodology be using a factory automation system (Marcos V. Linhares et al. 2007).

We will show how it is possible to exploit SysML for establishing clear relationships among different configurations, consequently, for obtaining a comprehensive and coherent representation of a manufacturing system. In order to show the effectiveness of the holonic approach proposed in the paper.

This paper is structured as follows. Section 2 presents The case-study of a welding cell. Then, a SysML model for production reconfiguration is proposed in section 3. A holonic paradigm is detailed in section 4. Finally, section 5 presents our conclusion.

2   Case-Study of a Welding Cell

2.1   Definition of Shoring Tower

The shoring tower system as represented the (figure. 1) has been developed to meet the requirements of the modern construction industry in terms of speed, safety and profitability.

Fig. 1 Shoring tower-configuration

   The remedial article is a part in the shoring tower, in our case the welding cell should produces this article with integrating the re-configuration and the flexibility while introducing a controlling concept to validate the different configurations.

2.2   The Remedial Article

The final product shown in (Figure 2) of the welding cell is the remedial article. Two configurations of the remedial articles are considered, with traverse (3) either with cylindrical cross section or with oval cross section, depending on the customer needs. For this reason the welding cell process should be adapted with these two configurations.

Table 1 Shows the characteristics of both configurations

Reference	Form	Diameter	Thickness	Length
1	Cylindrical	40mm	2mm	135mm
2	Cylindrical	48.3mm	2.5mm	125mm
3	Cylindrical	33.7mm	2mm	1452mm
	Oval	30mm		
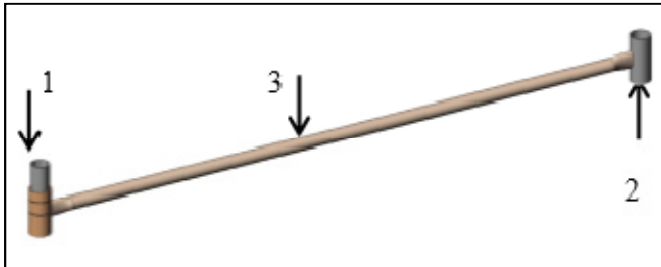
Fig. 2 3-D layout of the remedial article

   (Figure. 2) shows the 3-D geometry and the three parts to be welded to make the remedial article. The welding machine should therefore weld these three components which have the different characteristics cited in (table 1) with respect to the specifications imposed.

3   A SysML Model for Production Reconfiguration

The development of the information model for the production reconfiguration system poses many challenges. Modeling requirements and structure can provide a

robust system description. Therefore, the SysML (Tim Weilkiens 2007) based information model for production reconfiguration consists of requirements analysis and structural analysis.

Requirements analysis defines the hierarchy of requirements and interrelationships among requirements. Concerning the structural analysis it represents the elements of the production reconfiguration.

3.1 Requirements Analysis

The requirements diagram indicates all the capabilities or conditions that a system must satisfy. A requirement can be decomposed into sub-requirements, so that multiple requirements can be organized as a tree of composite entities. Each requirement is supposed to have an id (unique) and a text parameter, which contains its description. Requirements are essential in the validation step, so particular care must be taken in handling them.
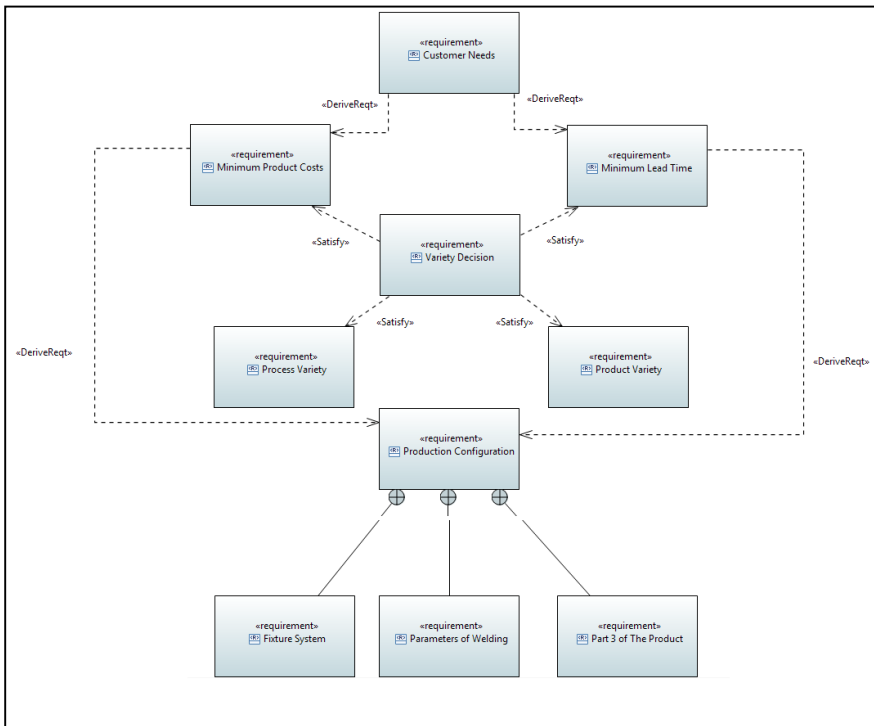
Fig. 3 SysML requirements diagram for production re-configuration

A requirement specifies a condition that must be satisfied, a function that a system must perform, or a performance level that a system must achieve. Requirements come from many sources, such as customers, designers, process

engineers, or organizations; (Figure 3) shows a requirement diagram of production reconfiguration system. This example highlights a number of different requirements relationships, including satisfy, derive and containment. For example, the satisfy relationship is used to assert that variety decisions satisfy the requirements of minimum production costs and minimum lead time. The derive relationship between a source requirement, customer needs, and the derived requirements, minimum production costs and minimum lead time, is established based on marketing analysis. Similarly, the requirement of production reconfiguration is derived from the requirements of minimum production costs and minimum lead time, based on production reconfiguration principle. The containment relationship represents how complex production reconfiguration requirements can be partitioned into a set of lower-level requirements. For instance, the requirements of production reconfiguration contain three requirements associated with fixture system and parameters of welding and part 3 of the product.

3.2   Structural Analysis

In software systems, the taxonomy that generates the division of the system into modules is contained in the class diagram, which contains the "building blocks" that implement the system functionality and whose interaction will determine the system architecture. SysML extends the concept of class to that of block, which is a composite structure endowed with an interface suitable to describe the architecture of a physical system. Structural information about blocks is contained in the block-definition diagram; for our validation procedure, we shall take into account only a limited number of relationships among the possible associations defined in the standard, namely the UML composition, aggregation, and association.

   (Figure 4) shows the structure analysis of the welding cell using a block definition diagram. In the context of production system, a block in SysML can represent any entity (e.g., part, function or operation). By including a number of blocks, a block definition diagram can define the hierarchy of the system of interest in terms of its structural feature and the relationships between the blocks. The welding cell structure consists of conveyor A, conveyor B, conveyor C part, Robot, welding machine, and conveyor D. To explain the BDD, the conveyor A, B and C are associated with a robot in order to load the different parts transported via the conveyors into the welding cell. After the welding operation made by the welding machine the Robot unload the final product, in this case the product with oval section cross or with cylindrical section cross, into the conveyor D to the stock.
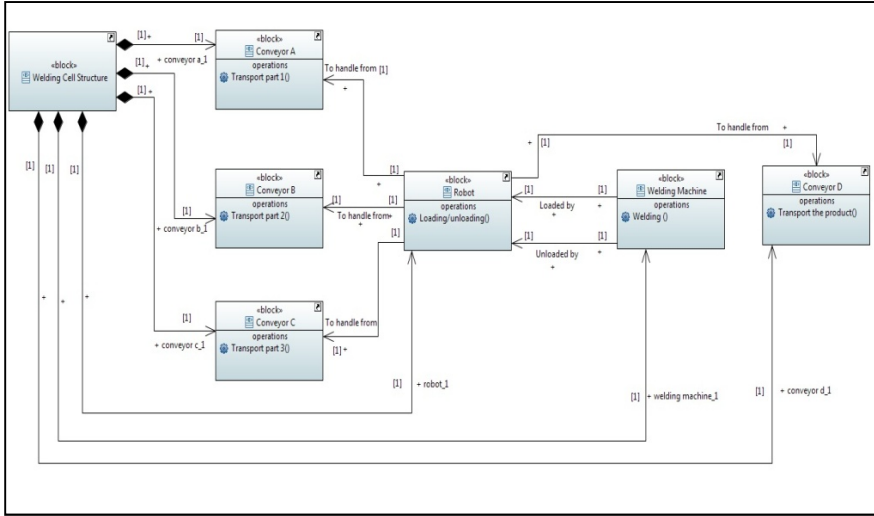
Fig. 4 SysML block definition diagram for welding cell structural model

3.3 Results

A SysML model is developed to formally represent the requirements and structure of the welding cell including production reconfiguration. It enables the system to share and exchange information among multiple domains in a multi-disciplinary team by ensuring semantic coherence along the entire design chain, keeping the traceability across levels of abstraction, and improving the interoperability among tools. Moreover, it supports trade-off analysis to evaluate production performance and costs by combining with other execution environments.

For controlling the SysML model during the pre-design phase, we propose the holonic paradigm for controlling and organizing the welding cell modeled by SysML in order to validate our model.

4   Holonic Paradigm

Holonic paradigm support the use of autonomous and cooperative manufacturing units called holons, organized in a flexible hierarchy in order to increase the agility and re-configurability of the manufacturing process. Manufacturing systems are becoming more and more complex and the development of many researchers are working for finding new paradigm solutions for managing and controlling this complexity which was modeled by different language in order to include re-configurability and flexibility of the production system.

The holonic paradigm (Jo Wyns 1998) can identify the types of holons necessary for any manufacturing system, its responsibilities, and the interaction structure in which they cooperate. The holonic architecture is made up of three

basic holons, order holon, product holon, and resource holon, extended with the concept of staff holon. These holons are specified using object-oriented concepts such as aggregation and specialization. Each of the basic holons is responsible for one of the following manufacturing controlling aspects: internal logistic, manufacturing scheduling, and resource management. A resource holon has a physical part and an information processing part that controls the resource; it combines the information of a physical device and the ability to control this device. The resource holon resembles the concept of class in Object-Oriented technology. A product holon stores the process and product knowledge needed to insure the correct manufacture of the product. It acts as an information server for the other holons in the HMS (P. Valckenaers et al. 1996). An order holon represents a task in a manufacturing system. It is responsible for doing the work assigned on time and in the right way. It manages the physical products that are being produced, the product status models, and all the logistic processing information related to the task. Order holon is in charge of production scheduling and control. It schedules the task progress after synthesizing the knowledge of process and configuration supplied by product holon and configuration holon respectively, triggers process execution properly according to the type of products, monitors the whole progress to find system deadlock and handle it in. With the interactions between them, all the holons generate mutually acceptable scheme and accomplish it in order to fulfill system goal because autonomy is one of its main characteristics, which means each holon is able to create a plan and execute it independently.
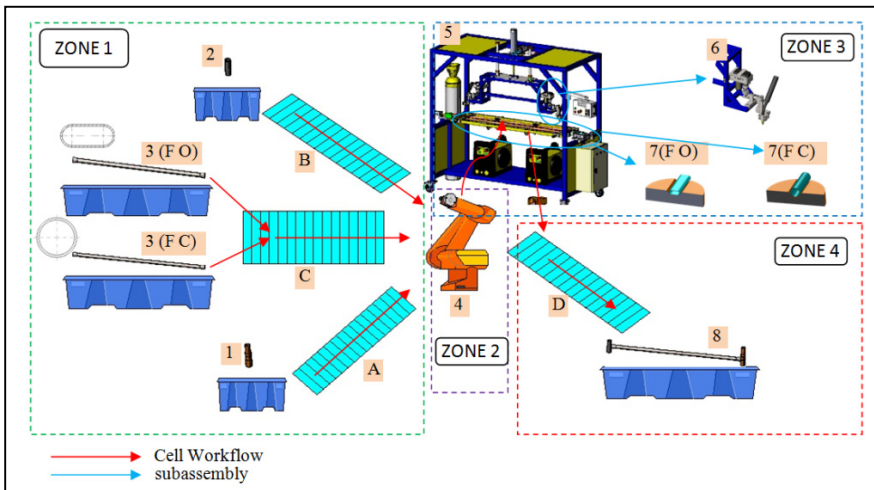
Fig. 5 Structure of the welding cell describing the holonic paradigm

The welding cell as shown in (figure 5) is composed of the three base holons

– Resource holons represent the physical devices. In our cases resource holons are the conveyors systems (A, B, C and D), the welding machine (5), the fixing systems (7FO and 7FC) and the gantry robot (4).
– Product holons represent the product to weld (8). In our case they are containers for information about the remedial article to be welded.
– Order holons are generated for each request. They are the driven agenda of the holonic system. They compete or collaborate with each other to configure the welding cell and ensure the appropriate parameters.

4.1   Results

A "top-down" technique used to decompose the welding cell from a design specification to basic levels. The holonic approach allows to model at different levels of abstraction system. The hierarchical organizational decomposition of a system can be refined up to the level where the designer considers the complexity of the behavior is sufficiently low for immediate implantation.

5   Conclusion

In this paper, we proposed an approach to design a welding cell based on SysML language to formally represent the requirements and structure of the welding cell including production reconfiguration while this design was controlled by the holonic paradigm in order to decompose the welding cell from a design specification to basic levels. The presented approach allows designers to integrate client trends and helps them in validating the design and making decisions efficiently.

References

Wu, D., Zhang, L.L., Jiao, R.J., Lu, R.F.: SysML-based design chain information modeling for variety management in production reconfiguration. J. Intell. Manuf. 24, 575–596 (2011), doi:10.1007/s10845-011-0585-6

Linhares, M.V., de Oliveira, R.S., Farines, J.-M.: Introducing the Modeling and Verification process in SysML. 1-4244-0826-1/07/$20.00 © 2007 IEEE (2007)

Weilkiens, T.: Systems Engineering with SysML/UML: Modeling, Analysis, Design (2011) ISBN 0080558313, 9780080558318

Wyns, J., Valckenaers, P., Bongaerts, L., Peeters, P.: Reference architecture for holonic manufacturing systems: Prosa. Computers in Industry 37(3), 255274 (1998)

Valckenaers, P., Van Brussel, H., Bongaerts, L., Wyns, J.: Holonic Manufacturing Systems (1996), doi:10.3233/ICA-1997-4304

Knowledge Versioning Dynamics during the Design Process in a Concurrent Engineering Environment

Alaeddine Zouari[*]

Research Unit LOGIQ « Logistique, Gestion Industrielle et de la Qualité »
ISGI Sfax – technopôle, Route de Tunis km 10 BP 1164 – 3021 Sfax
`ala.zouari@gmial.com`

Abstract. In an environment of concurrent engineering, design process sees various choices and decisions generated by actors involved in the design project. That results multiple interactions and disagreement between them. Besides, many product data and knowledge are modified and changed throughout this dynamic process. To capitalize and have traceability of knowledge modifications, we need to versioning those pieces of knowledge. This paper aims firstly to illustrate the dynamic structure of the design process. On the other hand, to explain our model of knowledge versioning dynamics, through annotations and changes generated throughout a collaborative design process. The model aims to dynamically build a project library that traces the history of engineering process and capitalizes knowledge related to the product, in order to re-use this informational inheritance.

Keywords: Design process dynamics, collaborative design, knowledge capitalization, knowledge versioning dynamics, Rules of versions evolution.

1   Introduction

The design process is part of a logical framework and both, scientific, social and economic (Poveda 2001). On the scientific level, knowledge is continuously increasing, what giving designers new ways to solving technical problems and new technological solutions. The knowledge increasing can lead to a partitioning of knowledge shared between several actors involved in the physical product development and the optimization of its quality and performance. On the social level, designers have to collaborate all along the design process. They have to share, to annotate and to evaluate product knowledge and data. Then a strong social relationship must associate them as a team. However, while performing their work, conflict can appears through both, shared knowledge annotations, urgent tasks, waiting time, tasks rework, etc. Indeed, in the economic field, it is now recognized that the issues and the most significant gains in terms of product

---

[*] Corresponding author.

quality, cost of investment and development time, are engaged in the early stages of product development, and mainly in the design phase (Clautrier 1991).

Versioning consists in studying the capacity to control modifications and their consequences, moreover having the design process traceability (in versions form). It is a critical functionality within this framework to treat versioning and multiple knowledge management. In fact, versioning requires a complete analysis of available knowledge, which is based on modifications presented by the transformation of a knowledge version into another different.   Such analysis leads to specifying the traceability of knowledge versions evolution that allows capitalizing them, by avoiding possible redundancies, with an aim of re-using them in other projects. To overcome these problems, we propose mechanism allowing expressing evolution rules, to define and to manage evolution strategies. Evolution rules suggested permit to express checks and propagations update to carry out before and after an operation making knowledge versions evolve.

2   Knowledge Dynamics in Design Tools

2.1   Design Dynamic Nature

One of the principal problems that must be addressed by defining knowledge models for design is caused by the dynamic nature of products design. During a design process, knowledge is not processed as static data but it is prone invariably to the change. It is due to the character of design problems resolution that implies information research then their analysis, structuring, interpretation and evaluation by repeating cycles. The most significant, is that it includes the information generation during this cyclic process and the combination of this new information with known one. This defines new information structures which lead to solutions of design. We conclude that the definition and the structure of information during the cyclic design process are a key question in design process support tasks. This requires knowledge models as well as knowledge management systems.

2.2   Knowledge Engineering in Collaborative Design

Knowledge capitalization aims at the same time to safeguard, share and especially re-use the know-how generated with the wire of the design projects (Chandrasegaran et al. 2013). The capitalization effort passes more concretely through modeling and having as objective to decrease the design time, while re-using what is already validated, to focus only on the new choices to manage for a new solution.

In literature we find many ways to model the product, such as structure-oriented product model, geometry-oriented product model, feature oriented

product model, knowledge-based product model, integrated product model, IDEF model, UML model, etc (Hong-Zhong et al. 2006). Many authors proposed models based on knowledge, aiming the collaborative design: Product model (Menand et al. 2001), (Tichkiewitch 1996), (Yvars 2001), etc. and design process Model (Dupinet 1991), (Harani 1997), (Ouazzani 1999), etc.

Several projects are used as support to the work called "in phase advance" in knowledge engineering domain such as DEKLARE (Design Knowledge Acquisition and Redesign Environment), MOKA (Methodology and tools Oriented to Knowledge Base Engineering Application project), IPPOP (Information sharing Product - Process - Organization Project.), etc. DEKLARE project, (Vargas 1995), allows defining a representation model of design knowledge in mechanical systems engineering, interesting more particularly in modeling of problems concerned with the routine design. It describes product in several manners (physical, functional, geometrical and constraint points of view). The design process model is described as succession of tasks to carry out to design a given object.

The advent of information technologies opens new prospects for information and experiments sharing between various actors in a company particularly designers working on the same project. In an environment of collaborative design, knowledge can be capitalized in a knowledge repository (group memory or project memory) (Ribière et al. 1998). This knowledge repository makes it possible to share knowledge between actors implied in the design process, and can be used with the entries or the exit of tasks process. According to Matta (Matta et al. 1999), the project memory is a possible materialization of company's memory: The project memory is a memory of knowledge and information acquired as well as product during the projects realization.

2.3   *Information Exchange Dynamics During a Design Process*

Project evolution illustrates the need for defining strict rules of exchange to maintain the agreement of system studied. These rules concern mainly the exchange of knowledge shared during a design process where actors manipulate knowledge to produce concepts, figure 1. Thus, it is inevitable that knowledge will change in order to correct errors, to adapt new information, or to adjust the representation of a particular domain. However, versioning mechanism can be carried out by knowledge annotations and validations done by other actors implied in the design process.
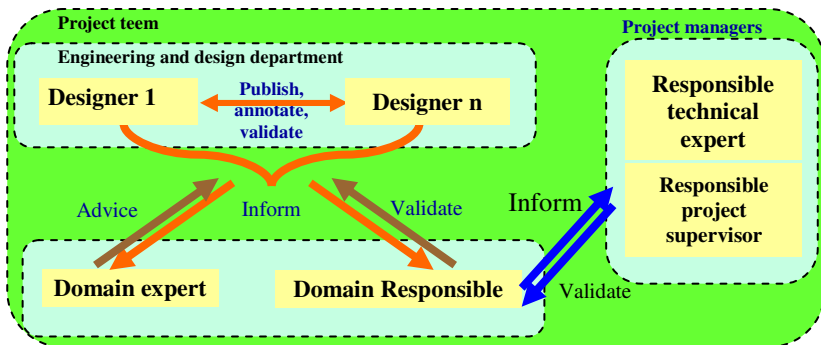
Fig. 1 Knowledge exchange within a project team

Each actor has a specific task in a project according to engagements' defined in the contracts, the quality management plan and domain laws. Each actor's task is employed during the project planning to define his role during the activities. The relational model (figure 2) employs actor's roles in an activity to determine relations that actors will have with pieces of knowledge. These roles can be: author, adviser, responsible, reader, etc.

Project actors take part in the tasks synchronization according to the project implementation conditions. Moreover a project actor can annotate the result of another actor because of non agreement of this result with a requirement or a project constraint. These annotations oblige the second actor to make modifications and to correct the parameter in question. In the event of conflict the actors must refer to experts who can also annotate or validate the results. The final validation of results is ensured by project managers who are the first responsible for project team. We modeled the various activities of designers implied in the design process by an UML class diagram (Zouari 2007), see figure 2.

This diagram represents the structure of our relational model. In this model we identify the following information types:

- Project: is formed by tasks,
- Tasks: where actors handle and produce knowledge,
- Participants (actors): it can be a simple person or a group of persons,
- Roles: that each actor has in an activity,
- Relations between the actors and knowledge: that determines the right of access on knowledge versions,
- Knowledge versions: that can be a simple parameter instance or a group of parameters instance version.
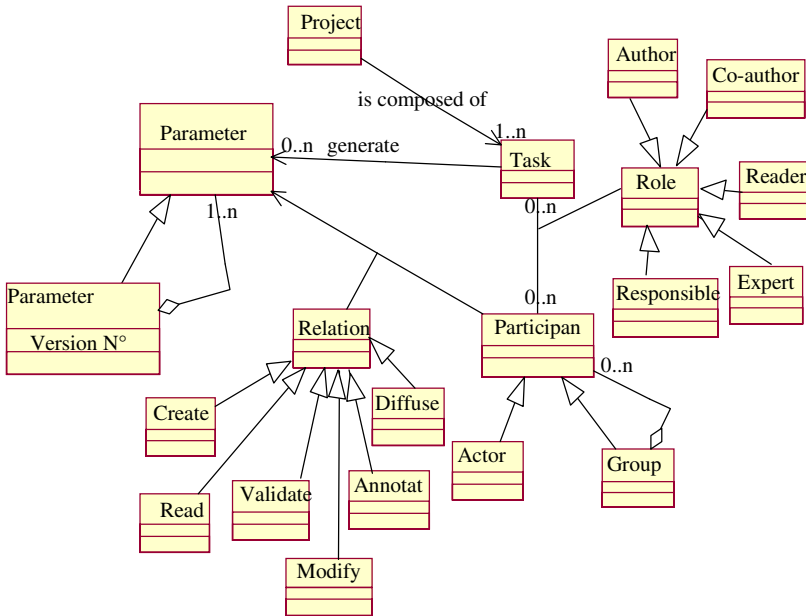
Fig. 2 Relational model

3   Evolution of Knowledge Mechanism

3.1   *Knowledge Versioning Dynamics During a Design Process*

During the design process, pieces of knowledge are frequently modified by actors who handle them, particularly parameters (Jarratt et al. 2011). We have classified entry parameters according to their appearance on tasks execution sheets as:

   • Individual external entry (IEE): this parameter is used as entry for only one task.
   • Shared external entry (SEE): this parameter is used as entry for several tasks.
   • Individual internal entry (IIE): this parameter is a result of one of the design process tasks, and can be used as entry only for one other task.
   • Shared internal entry (SIE): this parameter is a result of one of the design process tasks, and can be used as entry for several other tasks.

   To start the design process we need to know all project tasks and their necessary resources. Entry parameters are one of most important task resources. So we have to know them and their origin (external or internal to the design process). For internal parameter, we need to know, to which task each exit parameter belongs, and which tasks use it as entry parameter. Thus we can classify parameters as internal or external and if it is shared or not.

The classification will help us to prioritize all project tasks using an anteriority matrix. This step enables us to define and draw the design process workflow according to parameters that designers share and to define scheduling conditions of each task (Zouari et al. 2007).

Example: a design process formed by seven tasks carried out by various actors working in collaboration; see figure 3.
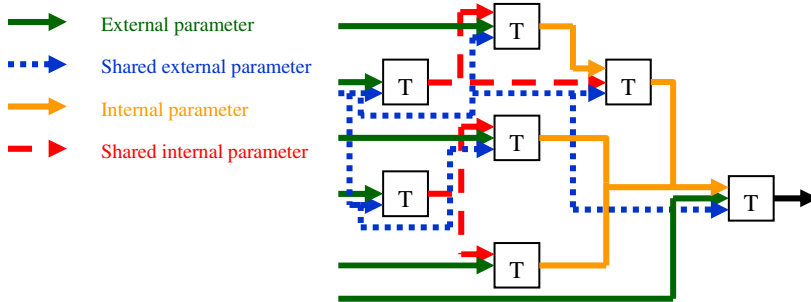
Fig. 3 Example of parameters types and of tasks succession defining a design process

3.2   *Knowledge Versions Management*

A significant question in collaboration activities is how to control knowledge versions. Maintaining knowledge versions has three objectives:

• Recording the knowledge history in order to avoid operations repetition.
• Allowing knowledge changes without compromising references to preceding knowledge versions.
• Allowing inspection and comparison of versions.

The FBM framework (Feature Based Modeling) (Jae Yeol et al. 2001) and RFBPs (Requirement– Function–Behavior–Principle solutions) model (Ma et al. 2013), have strong support for versions control, both for the type of characteristics and their instances.

In our model, knowledge characteristics edition (types and instances) will take place by means of a mechanism of control and execution, through which users obtain provisional privilege of edition. When knowledge is checked for edition, anterior versions can continue to be employed. After edition, knowledge can be subjected like a new version, or be employed as a revision (temporary version). Knowledge revisions are hierarchically lower than versions in the sense that they cannot be employed actively in a modeling operation yet, but only for a future edition (modification). This reduces versions number and allows the distinction between those whose submission has a true interest and those having only an intermediate statute. Example: if an actor creates knowledge while carrying out his design task. This knowledge will be temporarily recorded throughout design

process execution as being a revision likely to be modified through time. From this fact we obtain a new revision after each modification; figure 4.

Knowledge domain is continuously created and always modified by actors. The effective management of this knowledge needs its continuous checking, annotation and validation (V&V). Within this framework revisions created during the dynamic evolution of the design process through modifications and annotations will be validated at the end of the process. At this time revision will be definitive and it is transformed into a version and can be recorded in the project library.
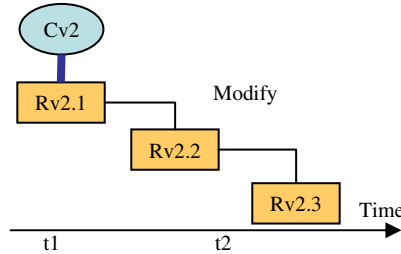
Fig. 4 Dynamic creation of revisions starting from a knowledge version

When a project actor creates a knowledge revision (task result), during a design process, it will be recorded in a temporary knowledge repostory while waiting for the reaction of actors who employ it in their tasks. Those actors can annotate this revision according to their tasks requirements. In this case, knowledge revision author (creator) must modify it by taking into account his colleagues' annotations. In the event of conflict the responsible of domain has to intervene and annotate or validate this knowledge revision. Knowledge revision cannot be recorded in the project library as being a knowledge version only if the whole of actors who share it as well as the responsible of domain validate it. Figure 5 gives an idea on this mechanism.
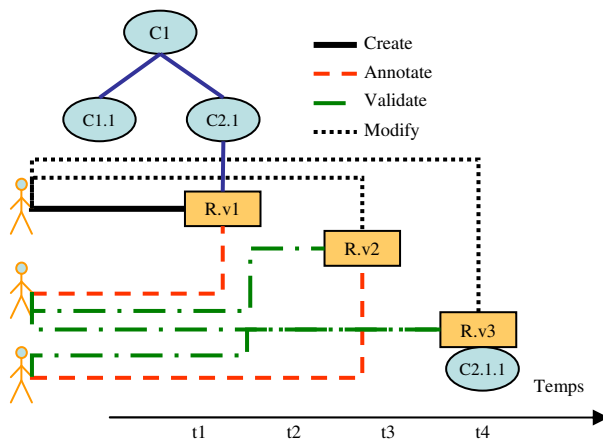
Fig. 5 Example of transformation mechanism from a revision into a knowledge version

4   DISKOVER Implementation

The study led to the development of a prototype of knowledge processing called "DISKOVER" (DesIgn Software with KnOwledge VERsioning). DISKOVER proposes a structure permitting the collection of knowledge related to a multi-actors design and the associated products.

For the consultation of knowledge, the software allows actors to:

• Consult design process tasks and their state: an actor will be able to consult design process tasks which concerns him (input data, output data, knowledge associated....) and their states (ready, non feasible…)

• Consult the product parameters: each actor can access parameters for which he is responsible, those that are necessary to carry out his tasks and getting their results. For knowledge dynamics, the traditional methods obliged designers to refer to a design guides, internal notes, knowledge books, Intranet etc. To help them to carry out a task and to take into account the experience feedback of previous projects, we propose to associate necessary knowledge for its realization to each task and to provide knowledge on a simple click.

• Assist the actors in the course of the design process: DISKOVER distributes to concerned actors their tasks and their associated knowledge (with constraints and experience feedback) depending on the progress of the design process. Thus, DISKOVER will warn user of his available tasks (task push); the actor opens this task, carries out it, launches its execution and save it.

Once identified, actor can consult tasks on which he will work. He must choose those whose conditions for implementation and scheduling are ready, at this time the button "execute" be highlighted.

While clicking on the execute button, the card of task appears. Internal parameters appearing on the card cannot be modified, but annotated.

The actor has the possibility of seizing the values of external parameters and consulting the task resources (tables, curves…). Once the card is filled, the actor clicks on the button execute to launch the computing process. Thereafter the actor can consult the results and save them before closing the card.

While clicking the save button, the designer gives the order to the system to save the results as a revision and to send output parameters values to the actors who need them. If the values are already stored in the data base, the software sends a message to the concerned actor indicating him that these values exist in a defined version.

5   Conclusion

Knowledge versioning during the design process allows us to have an auto expansion of the knowledge space, in other words the design process knowledge repository. During a design process, if an actor creates knowledge while carrying out his design task, it will be temporarily recorded throughout the design process

as being a revision likely to be modified. Revisions created during the dynamic evolution of the design process through modifications and annotations made by actors, will be validated at the end of the process. At this time revision will be final and can be transformed into a version to be recorded in the library of project. To validate this mechanism we proposed a scenario of the dynamic evolution of the design process through the interactive relations between actors implied in this design process. This scenario allows seeing constraints of knowledge sharing and versioning requirements.

References

Chandrasegaran, K., Ramania, K., Sriram, R., Horváth, I., Bernard, A., Harik, R., Gao, W.: The evolution, challenges, and future of knowledge representation in product design systems. Computer-Aided Design 45(2), 204–228 (2013)

Clautrier, M.: Difficultés de nouvelles approches de conception dans le spatial, Séminaire GSIP La conduite de projet pour méthodes et outils, Grenoble (1991)

Dupinet, E.: Contribution à l'étude d'un système informatique d'aide à la conception de produits mécaniques par la prise en compte des relations fonctionnelles, PhD Thesis, Central School of paris, France (1991)

Harani, Y.: Une approche multi-modèles pour la capitalisation des connaissances dans le domaine de la conception. PhD Thesis, National Polytechnic Institute of Grenoble, France (1997)

Huang, H.-Z., Gu, Y.-K.: Development Mode Based on Integration of Product Models and Process Models. CERA Journal 14(1), 27–34 (2006)

Lee, J.Y., Kim, H., Kim, K.: A Web-Enabled Approach to Feature-Based Modeling in a Distributed and Collaborative Design Environment. CERA Journal 9(1), 74–87 (2001)

Jarratt, T.A.W., Eckert, C.M., Caldwell, N.H.M., Clarkson, P.J.: Engineering change: an overview and perspective on the literature. Research in Engineering Design 22(2), 103–124 (2011)

Ma, J., Hu, J., Zheng, K., Peng, Y.H.: Knowledge-based functional conceptual design: Model, representation, and implementation. CERA Journal 21(2), 103–120 (2013)

Matta, N., Corby, O., Ribière, M.: Définition d'un modèle de mémoire de projet. Rapport de recherche INRIA N° 3720 Juin 1999 (1999)

Menand, S., Tollenaere, M., Canella, C.: Multi: a tool and a method to support collaborative functional design. In: 13th ICED Conference, Glasgow, UK (August 2001)

Ouazzani, A.: Représentation dynamique du processus de conception: une perspective de capitalisation de l'historique de conception. PhD Thesis, Central School of paris - France (1999)

Poveda, O.: Pilotage technique des projets d'ingénierie simultanée, modélisation des processus, analyse et instrumentation. Thèse de doctorat INP, Grenoble (2001)

Ribière, M., Matta, N., Cointe, C.: A proposition for managing project memory in concurrent engineering. In: Proceedings of International Conference on Computational Intelligence and Multimedia Applications (ICCIMA 1998), Churchill, Australia (1998)

Tichkiewitch, S.: Specifications on integrated design methodology using a multi-view product model. In: Engineering System Design and Analysis Conference, ASME 1996, Montpellier, France (1996)

Vargas, C.: Modélisation du processus de conception en ingénierie des systèmes mécaniques: Application à la conception d'une culasse automobile. PhD thesis, Normal Higher School of Cachan, France (1995)

Yvars, P.A.: Contribution à la représentation des connaissances en ingénierie intégrée de produits et de systèmes automatisés de production. HDR, National Polytechnic Institute of Grenoble, France (2001)

Zouari, A., Tollenaere, M., Maalej, A., Ben Bacha, H.: Etude d'un mécanisme de versionnement de connaissances dans une démarche de conception collaborative. In: International Conference: Design and Mechanical System Modelling, CMSM 2007, Monastir, Tunisia, Mars 19-21 (2007)

Zouari, A.: Proposition de mécanismes de versionnement et d'agrégation des connaissances de domaine en conception collaborative de produits industriels. PhD thesis, National Polytechnic Institute of Grenoble, France (2007)

An Environmental Impact/Cost Model for Evaluating Multiple Feature-Based Machining Methods

Raoudha Gaha[1], Abdelmajid Benamara[1], and Bernard Yannou[2]

[1] Laboratoire Genie Mecanique, Ecole Nationale d'Ingenieurs de Monastir,
Universite de Monastir, Rue Ibn Aljazzar 5019 Monastir, Tunisia
raoudha.gaha@gmail.com, abdel.benamara@enim.rnu.tn

[2] Laboratoire Genie Industriel, Ecole Centra Paris, Grande Voie des Vignes
92290 Chatenay-Malabry, France
bernard.yannou@ecp.fr

Abstract. For a designed part, if different sets of features are used for machining, the manufacturing Environmental impacts (EIs) as well as cost may vary. In this research, a new methodology based on feature technology is proposed in order to help designer till detail design phase to choose the most optimal compromise Environmental Impact/Cost in manufacturing process. Hence an Environmental impact/Cost model is presented. This model follows the activities required for machining a set of features which are tool set-ups, fixturing set-ups and machining tool paths. The paper starts by presenting features based models which are the base of the methodology proposed. Then, a state of the art about using Feature technology in reducing on one side manufacturing cost and on the other side manufacturing environmental impacts is presented. Finally an environmental impact/cost methodology for evaluating multiple feature-base machining methods is proposed.

Keywords: Environmental evaluation, cost estimation, features technology, detail design, CAD, LCA.

1   Introduction

Today, energy, resources and environmental problems become more and more serious. That's why they are highlighted in regulations frameworks such as WEEE (European Union,, 2003a), RoHS (European Union,, 2003b), EuP (European Union,, 2005) directives and the REACH regulation (European Union,, 2006), which are pushing industrials to adopt sustainable strategies to develop their products.

The eco-design approach, presents, firstly, as a multi-criteria approach taking into account all environmental impacts and secondly, it is also an approach multi-step that takes into account all stages of the life cycle. Hence it is largely studied,

this last decade, in order to be used in industries. The most studies realized tried to integrate environment constraint in the early design stages such as conceptual design phase which decides about 70%-80% property of the product (Song et al., 2003). However, choices done in detailed design phase are responsible on about 80% of both environmental impacts and costs. How to eco-design in CAD phase with a low cost, if it is possible, is the key for a successful green and less expensive design. After a state of the art on works based on FT to reduce manufacturing cost or EI or both and based on the work of Tseng and Jiang (2000), firstly, in this paper, we put forward the concept of "eco-feature", and then it is used for environmental and cost evaluation in order to choose the most acceptable compromise Environmental impacts/cost. Secondly, a methodology is proposed based on the eco-feature concept. Finally the application of the proposed methodology on a case study is realized.

2   Features Based Models

A feature is a local shape of a product directly related to the manufacturing process. Smith and Dagli (1995) define features as high-level design primitives with their attributes, their qualifiers and restrictions which affect the functionality and/or the ability for the product to be manufactured.

There are different types of features: Shape Features, Constraint Features, Precision Features (or tolerance), Assembly Features, Functional Features, Material Features and Primitive Features.

In combination with surface representation, geometric representation of features shape is oriented to volume representation (3D) such as the representation based on B-REP (Boundary Representation), on CSG (Constructive Solid Geometry), as well as hybrid representation as shown in Wang and Ozsoy (1991).

Techniques developed to create models based on features are divided into two main approaches according to Allada and Anand (1995) and Shah and Mantyla (1995):

- Features recognition: features are recognized from a geometric model applying rules of recognition. More features models, describing the same product, can therefore be derived.
- Design features: a product model is developed based on predefined features. In this case, a product's explicit geometry is created from the features model.

To evaluate a part environmentally, non-geometric data has to be attached to the geometric model for eco-designing products in the detail design phase.

3   State of the Art

Current product development activities in manufacturing companies are still predominantly driven by quality/cost concerns. This does not prevent the existence of some works coupling cost and sustainability. Feature technology (FT) is used in cost estimation of a manufacturing process plan such as cost estimation models of product based on CAD/CAPP integration based on features-based modeling presented in (Tseng and Jiang, 2000),(Shuangxia et al., 2002) (Jinks et al., 2010). In the side of sustainability FT is used to evaluate environmental impacts of manufacturing processes, it is oriented to reducing or avoiding processes which have an impact on ecosystems, human health, etc. Sheng et al. (1995) developed a hierarchical part planning strategy for environmentally conscious machining in order to choose the least impact set of machining sequences order because a feature can be machined with different scenarios. Features are not only used for EE but also for green process planning selection, such as methods developed by Cao et al. (2002) and Tan et al. (2006) for green CAPP selection have to be developed in order to be used as numerical methods integrated in CAD systems and also a method for environmentally conscious process planning proposed by Zhao et al. (2012). Finally FT is also explored in the side of environmental evaluation and cost. In fact, we can find works integrating Life cycle assessment (LCA) to life cycle costing (LCC) such as the novel redesign approach propose by Bovea and Wang (2007) that integrates Quality Function Deployment (QFD) , LCA, life cycle cost (LCC), and contingent valuation (CV). Bevilacqua et al. (2007) also evaluated the environmental impact of circuit board design based on both LCA technique and economic aspects, Kloepffer (2008) proposed a new direction which summarizes environmental LCA, LCC, and Social LCA and the eco-design tool prototype "CAST-tool" developed by Morbidoni et al. (2011). However many disadvantages are detected as high dependence on data accuracy, less intuition of evaluation result, lack of special software and databases and long evaluation cycle, etc. (Xin et al., 2012). Hence, it is necessary to consider environmental and cost constraints of a manufacturing process till feature attribution in detail design phase.

4   Proposed Methodology

Our methodology consists in exploring features technology to evaluate the environmental impact (EI) as well as cost of a part manufacturing process till the detail design phase. In fact the influence of geometrical characteristics of a product on reducing the EI was proved on previous works (Gaha et al., 2011) (Gaha et al., 2014). For the cost reducing it is proved by Tseng and Jiang (2000).

According to Tseng and Jiang (2000) there are three activities in manufacturing process that are related to manufacturing costs and can be evaluated:

1. Tool set-ups.
2. Fixturing set-ups.
3. Machining tool paths.

We adopt these activities which can be also evaluated in terms of environmental impacts. Evaluating manufacturing costs and environmental impacts for Multiple Sets of features is a way to localize, the set of features that can be machined with the lowest manufacturing compromise cost Cmin /Environmental impact EImin which is considered a "good" set of features.
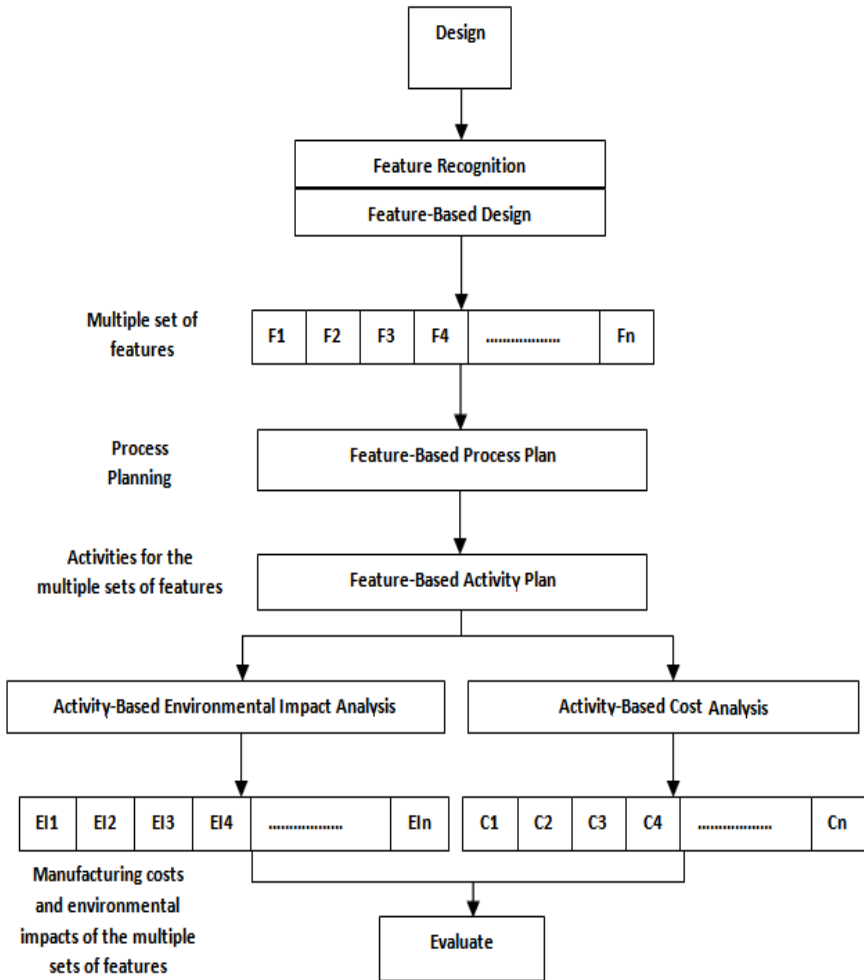
Fig. 1 Proposed methodology based on features technology for cost estimation and environmental evaluations of possible process plans

Given feature set Fi, i=1, %, n, performs the following steps:

1. Calculate tool set-up cost CFSi and environmental impact EIFSi.
2. Calculate fixturing set-up cost CFXi and environmental impact EIFXi .
3. Calculate cost of machining tool paths CFTi and environmental impact EIFTi.
4. The manufacturing cost and Environmental impacts for machining feature set Fi are:

Ci = CFSi + CFXi + CFTi.

EIi= EIFSi + EIFXi + EIFTi.

5. Find the smallest in *Ci* as *Cmin = Min {Ci, i = 1, %, n}*

Find the smallest in *EIi* as *EImin = Min {EIi, i = 1, %, n}*

6. *CFmin* is the feature set with the lowest manufacturing cost and *EIFmin* is the feature set with the lowest manufacturing environmental impact.

So it gives both indications about the cost and about the environmental impact. If we are more interested in eco-design, the best environmental profiles set features is then selected if they are superimposed and we cannot decide then the least expensive set of features is selected

The feature set that can be machined with the lowest activity-based cost/Environmental impact is considered the most suitable method for producing the part.

5   Conclusion

This paper is developed base on the work of Tseng and Jiang. It presents and discusses the need for integrating cost and environmental performances into manufacturing process based on feature technology in order to optimize the manufacturing part process in terms of cost as well as environmental impact till detail design phase. In fact, for a given design, different machining scenarios are possible based on different sets of features. Hence manufacturing costs and environmental impacts may vary. A methodology for analyzing different manufacturing costs and environmental impacts for machining using different sets of features were proposed using an activity-based cost/environmental impact model. The activities used in cost and environmental impact analysis were tool set-ups, fixturing set-ups and machining tool paths.

References

Tseng, Y.-J., Jiang, B.C.: Evaluating multiple feature-based machining methods using an activity-based cost analysis model. The International Journal of Advanced Manufacturing Technology 16(9), 617–623 (2000)
Wang, N., Ozsoy, T.M.: A scheme to represent features, dimensions, and tolerances in geometric modeling. Journal of Manufacturing Systems 10, 233–240 (1991)

Allada, V., Anand, S.: Feature-based modelling approaches for integrated manufacturing: state-of-theart survey and future research directions. International Journal of Computer Integrated Manufacturing 8, 411–440 (1995)

Sheng, P., Srinivasan, M., Kobayashi, S.: Multi-objective process planning in environmentally conscious manufacturing: a feature-based approach. CIRP Annals-Manufacturing Technology 44(1), 433–437 (1995)

Zhao, F., Murray, V.R., Ramani, K., Sutherland, J.W.: Toward the development of process plans with reduced environmental impacts. Frontiers of Mechanical Engineering, 1–16 (2012)

Bovea, M.D., Wang, B.: Redesign methodology for developing environmentally conscious Products. Journal of Production Research 45(18), 4057–4072 (2007)

Bevilacqua, M., Ciarapica, F.E., Giacchetta, G.: Development of a sustainable product life-cycle in manufacturing firms: a case study. International Journal of Production Research 45(18-19), 4073–4098 (2007)

Kloepffer, W.: State-of-the-Art in Life Cycle Sustainability Assessment (LCSA) Life cycle sustainability assessment of products. The International Journal of Life Cycle Assessment 13(2), 89–95 (2008)

Xin, L.-L., Jia, X.-J., Li, F.-Y., et al.: Green feature modeling for mechanical and electrical product conceptual design. Computer Integrated Manufacturing Systems 18(4), 713–718 (2012)

Song, H.J., Liu, Z.H.: Expression of scheme case and scheme generation in product's conceptual design. Journal of Machine Design 20(4), 9–11 (2003)

Smith, A.E., Dagli, C.H.: Manufacturing feature identification for intelligent design. In: Intelligent Systems in Design and Manufacturing, Boston, MA, USA, pp. 213–230 (1995)

Cao, H.J., Liu, F., He, Y., Zhang, H.: Study on model set based process planning strategy for green manufacturing. Jisuanji Jicheng Zhizao Xitong/Computer Integrated Manufacturing System (China) 8(12), 978–982 (2002)

Tan, X., Liu, F., Dacheng, L., Li, Z., Wang, H., Zhang, Y.: Improved methods for process routing in enterprise production processes in terms of sustainable development II. Tsinghua Science and Technology 11(6), 693–700 (2006)

Gaha, R., Benamara, A., Yannou, B.: Eco-design of a basin mixer in geometric modeling phase. Key Engineering Materials 572, 7–11 (2014)

Shah, J.J., Mantyla, M.: Parametric and Feature Based CAD/Cam: Concepts, Techniques, and Applications. John Wiley and Sons, Inc., New York (1995)

European Union, Directive 2002/95/EC of the 27 January 2003 on the restriction of the use of certain hazardous substances in electrical and electronic equipment (European Directive), Official Journal of the European Union (2003a)

European Union, Directive 2002/96/EC of the 27 January 2003 on waste electrical and electronic equipment (WEEE) (European Directive), Official Journal of the European Union (2003b)

European Union, Directive 2005/32/EC of 6 July 2005 establishing a framework for the setting of ecodesign requirements for energy-using products (European Directive), Official Journal of the European Union (2005)

European Union, Regulation (EC) n° 1907/2006 of the European Parliament and of the Council of 18 December 2006 concerning the Registration, Evaluation, Authorisation and Restriction of Chemicals (REACH) (European Regulation), Official Journal of the European Union (2006)

Shuangxia, P., Shaofei, J., Youzhong, X.: A cost estimation model of product based on CAD/CAPP integration. In: Proceedings of the 4th World Congress on Intelligent Control and Automation, vol. 4, pp. 2650–2654. IEEE (2002)

Jinks, S., Scanlan, J., Reed, P., Wiseall, S.: Utilising dynamic factory simulation to improve unit cost estimation and aid design decisions. In: Proceedings of the 2010 Winter Simulation Conference (WSC), December 2010, pp. 1758–1766. IEEE (2010)

Gaha, R., Benamara, A., Yannou, B.: Influence of geometrical characteristics on eco-designed products. In: Proc. of the Int. Conf. on Innovation Methods in Product Design 2011, pp. 242–247 (2011)

Morbidoni, A., Favi, C., Germani, M.: CAD-Integrated LCA Tool: Comparison with dedicated LCA Software and Guidelines for the improvement. In: Glocalized Solutions for Sustainability in Manufacturing, pp. 569–574. Springer, Heidelberg (2011)

Multi-objective and Multi-physics Optimization of Fully Coupled Complex Structures

Hamda Chagraoui[1], Samir Ghanmi[2], Mohamed Guedri[3],
Mohamed Soula[4], and Noureddine Bouhaddi[5]

[1] Research Unit in Structural Dynamics, Modeling and Engineering of Multi-physics
Systems
hmdchagraoui@gmail.com
[2] Tabuk College of Technology, Department of Mechanical Kingdom of Saudia Arabia
samir.ghanmi@ipein.rnu.tn
[3] Makkah College of Technology, Department of Mechanical Kingdom of Saudia Arabia
mohamed.guedri@isetn.rnu.tn
[4] Laboratory of applied mechanics and engineering, ENIT, High Institute of Sciences and
Techniques of Tunis (ENSIT), Tunis University–Tunisia
Soulamed2003@Yahoo.fr
[5] FEMTO-ST Institute UMR6174-Applied Mechanics Department, University of Franche-
Comté, Besançon, France
noureddine.bouhaddi@univ-fcomte.fr

Abstract. This work presents an improved approach for multi-objective and mul-ti-physics optimization based on the hierarchical optimization approach of the typ-ical MOCO ("Multi-objective Collaborative Optimization") whose objective is to solve multi-objective multi-physics optimization problem. In this document, we propose a new hierarchical optimization approach named Improved Multi-objective Collaborative Optimization (IMOCO) whose goal is to decompose the optimization problems of the complex systems hierarchically in two levels (system and disciplinary level) according to the disciplines. In other words, according to the different physical (mechanical-electrical-acoustical) involved in the mechani-cal structures design. The presented approach uses a NSGA-II "Non-dominated Sorting Genetic Algorithm II" as an optimizer, and uses a coordinator between the system optimizer and the disciplinary optimizer, which has the role, is to ensure consistency between the various disciplines of the complex system. For the pur-poses of validation of the proposed method, we chose two examples: (i) numerical problem and (ii) engineering problem. These examples are solved using the pro-posed IMOCO method and the previous approaches. The obtained results are compared well with those obtained from the previous approaches: (i) non-hierarchically based AAO optimization approach and (ii) hierarchically based MOCO optimization approach, which show the good performance of our proposed IMOCO method.

Keywords: multi-objective optimization, multi-physics optimization, hierarchical optimization, MOCO, IMOCO, NSGA-II, disciplines.

1   Introduction

The complex engineering systems in the real world often involve several physical (mechanical, electrical, acoustic and thermal, etc.), subsystems and components. Many examples of advanced engineering systems may be find in the industry, such as the design of aircraft systems, automotive and nano, micro-electro-mechanical systems (NEMS, MEMS), which are intrinsically linked them by interdisciplinary interactions. The classical optimization approaches that ignore the interactions between the different disciplines are unable to give the desired optimal solutions. The use of advanced optimization techniques are required for these types of problems in order to achieve practical solutions. Multi-disciplinary Design Optimization (MDO) is a relatively field recent to engineering science which is based on the decomposition of these complex systems based on the different specialties where disciplines whose aim is to respond more effectively to design problems integrating different disciplines. The decomposition of these complex systems can be done in a number of different ways according to different criteria. The most frequent decomposition methods are: (i) decomposition by disciplines, (ii) decomposition according to the structural components. Typical MDO approaches of such large systems is characterized by the interdisciplinary couplings, the multiple objectives, a large design variable space and a significant number of design constraints   (Tappeta and al 1997). The MDO approaches can be classified into two groups: Single level optimization approaches e.g. AAO ("All At Once") and multilevel optimization approaches (Aute and Azarm 2006). Due to the multiple criteria of multi-disciplinary optimization problems, recent work has focused on the formulation of the optimization problem of a multi-objective and multidisciplinary manner. For example, (Aute and Azarm 2006) proposed a new genetic algorithm based approach for Multi-objective Collaborative Optimization (MOCO) to handle the multi-objective and multi-disciplinary optimization problems. (Ghanmi and al 2011) developed an algorithm for multi-objective and multi-level optimization to solve the optimization problems of complex structures with low Multi-physics coupling.

  This paper is organized as follows: Section 2 gives a brief description of the strategy IMOCO (Improved Multi-Objective Collaborative Optimization). Sections 3.1 and 3.2 show the application of our proposed approach in the cases of a numerical problem and an engineering problem of capacitive Micomachined Ultrasonic Transducers (cMUT). The obtained solutions from the IMOCO approach compare well with those obtained from a non-hierarchically based AAO optimization approach and from a hierarchically based MOCO optimization approach.

2   Improved Multi-objective Collaborative Optimization

The presented multi-disciplinary optimization approach called IMOCO, which uses NSGA-II, is suitable for multi-physics problematic whose objective is to divide the optimization problem of widely multi-physics structures according to

different disciplines involved in the design. For simplicity, a multi-physical system is considered in the present document that involves two disciplines (mechanical and electrical) in order to illustrate the optimization procedure of the IMOCO method as shown by the Figure 1. As illustrated in Fig.1, the system level optimizer has objectives functions f_G and constraints g_G. The vector X_G includes the share variables x_{sh}^G between the two disciplines previously mentioned and the system auxiliary variables (t_{me}^G, t_{em}^G), with the super script 'G' referring to a system level. The mechanical optimizer has a set of disciplinary objectives functions f_m, disciplinary constraints g_m and a vector of disciplinary design variable X_m includes the local design variables x_m, the local shared variables x_{sh}^m, and the local auxiliary variable t_{em}^m. The write y_{me} represents the coupling variable, which is calculated by the disciplinary state equation (represented by Y_{me}) depending of X_m. Likewise, the electrical optimizer has a set of disciplinary objectives functions f_e, disciplinary constraints g_e and a vector of design variable X_e, which includes the local design variables x_e, the local shared variables x_{sh}^e, and the local auxiliary variable t_{me}^e. The write y_{em} represents the coupling variable: the output of the electrical optimizer used as an input variable in the mechanical optimizer. In addition, each discipline requires shared variables x_{sh}^G and inputs from other disciplines indicated by (y_{me}, y_{em}). The coordination problem $C(X)$ is introduced between the two optimizers (mechanical and electrical). The aim of the coordinator (coordination problem) is to minimize the difference between the shared parameters (x_{sh}^m, x_{sh}^e) transferred from the disciplinary level and the coordination shared variables x_{sh}. On the other hand, the coordination problem aims to minimize the difference between the auxiliary variables (t_{me}, t_{em}) and the auxiliary parameters (t_{me}^m, t_{em}^e) transferred from the disciplinary level. In addition, it reduces the difference between the auxiliary variables (t_{me}, t_{em}) and the coupling variables (y_{me}, y_{em}) transferred from the disciplinary level.

After the optimization of coordination problem and the optimal solutions with the smallest value of the penalty function we chose the optimal variables (x_m^*, x_e^*) at disciplinary level which are then transferred towards the system optimizer. Note that, the optimal variables (x_m^*, x_e^*) are transferred from the disciplinary optimizer and temporarily stored in the coordination problem. In the literature there are many methods aimed at addressing the coupling variables. In our proposed

approach IMOCO, we use the auxiliary variables ((Aute and Azarm 2006) (Tappeta and al.1997)) to decouple all disciplines and add a constraint of consistency, which aims to ensure compatibility interdisciplinary. New form defines the constraint of consistency of the mechanical discipline such as

$$\left\|1-\left(x_{sh}^{m}\,/\,x_{sh}^{G}\right)\right\|_{2}+\left\|1-\left(y_{me}\,/\,t_{me}^{G}\right)\right\|_{2}+\left\|1-(t_{em}^{m}\,/\,t_{em}^{G})\right\|_{2}$$ and to integrate in the objective

functions of the optimization problem of the mechanical discipline. In addition, the constraint of consistency of the electrical discipline is defined by

$$\left\|1-\left(x_{sh}^{e}\,/\,x_{sh}^{G}\right)\right\|_{2}+\left\|1-\left(y_{em}\,/\,t_{em}^{G}\right)\right\|_{2}+\left\|1-(t_{me}^{e}\,/\,t_{me}^{G})\right\|_{2}$$ and to integrate in the objective

functions of the optimization problem of the electrical discipline
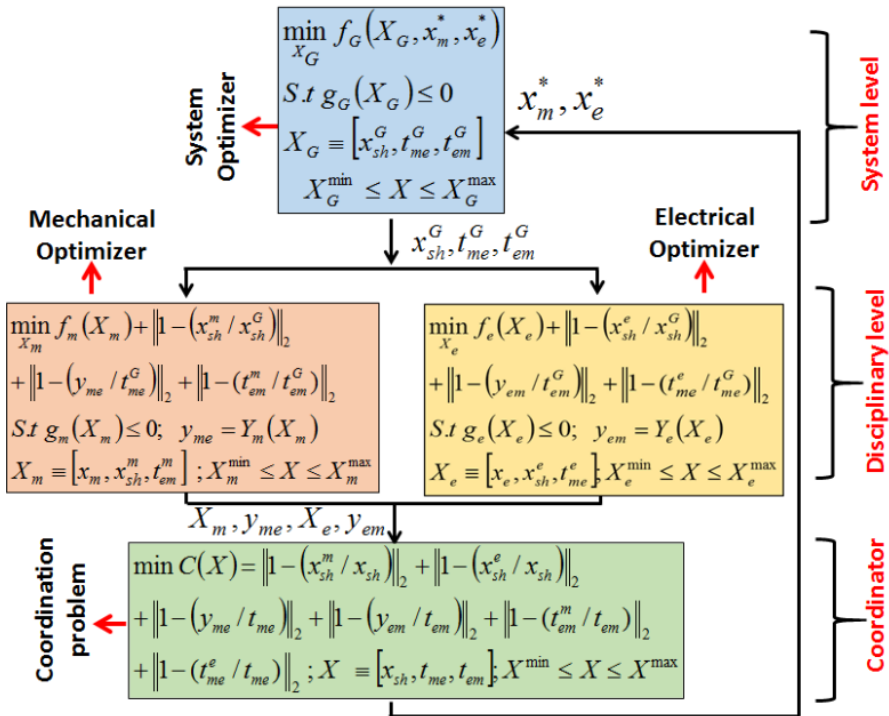
Fig. 1 Procedure of the IMOCO

3 Numerical Simulations

3.1 Numerical Problem

This first bi-objective numerical problem taken from a test case is used by (Aute and Azarm 2006). The two-objective optimization formulation for this problem, in the non-hierarchical AAO method is given in Equation (1). The problem with two

cost functions f_1 and f_2 as to minimize admits six design variables and six inequality constraints. To decompose the problem, we use the proposed method, which is illustrated in Fig.1. The non-hierarchical optimization problem is decomposed into two-optimization level : (i) optimization problem at the system level is given by Equation (2) and (ii) two optimization problems at the disciplinary level is given by Equation (3-4). The formulation of typical MOCO approach is omitted here can be found in (Aute and Azarm 2006).

$$\text{minimize } f_1(x) = -\left[25\left(x_1 - 2\right)^2 + \left(x_2 - 2\right)^2 + \left(x_3 - 1\right)^2 + \left(x_4 - 4\right)^2 + \left(x_5 - 1\right)^2 \right]$$

$$\text{minimize } f_2(x) = x_1^2 + x_2^2 + x_3^2 + x_4^2 + x_5^2 + x_6^2$$

$$\text{subject.to } g_1 = 2 - x_1 - x_2 \le 0; \quad g_2 = x_1 + x_2 - 6 \le 0$$

$$g_3 = x_2 - x_1 - 2 \le 0; \quad g_4 = x_1 - 3x_2 - 2 \le 0$$

$$g_5 = \left(x_3 - 3\right)^2 + x_4 - 4 \le 0; \quad g_6 = 4 - \left(x_5 - 3\right)^2 + x_6 \le 0$$

$$0 \le x_1, x_2, x_6 \le 10; \quad 1 \le x_3, x_5 \le 5; \quad 0 \le x_4 \le 6$$

(1)

❖ **Decomposition according to the proposed approach IMOCO:**
System level Optimization

$$\text{minimize} f_1(X_G, \overset{*}{X}_{D1}) = f_{11} + f_{21}$$

$$\text{minimize } f_2(X_G, \overset{*}{X}_{D1}, \overset{*}{X}_{D2}) = f_{12} + f_{22}$$

$$\text{subject.to } g_1, g_2, g_3, g_4 \ge 0$$

$$x_{sh} = \left[x_1, x_2\right], \ X_G \equiv \left[x_{sh}, t_{21}^G\right]$$

(2)

Discipline level optimization 1

$$\text{minimize} f_{1.1}\left(X_1\right) = -\left[12.5\left(x_1 - 2\right)^2 + 0.5\left(x_2 - 2\right)^2 + \left(x_3 - 1\right)^2 + \left(x_4 - 4\right)^2\right]$$

$$+ \left\|1 - (x_{sh}^1 / x_{sh}^G)\right\|_2 + \left\|1 - (t_{21}^1 / t_{21}^G)\right\|_2$$

$$\text{minimize} f_{1.2}\left(X_1\right) = 0.5\left(x_1^2 + x_2^2 + x_3^2 + x_4^2 + x_5^2\right) + \left\|1 - (x_{sh}^1 / x_{sh}^G)\right\|_2 + \left\|1 - (t_{21}^1 / t_{21}^G)\right\|_2$$

$$\text{subject.to } g_5 \ge 0 \ ; \ x_{sh}^1 \equiv \left[x_1, x_2\right]; \ X_{D1} \equiv \left[x_3, x_4\right]; \ t_{21}^1 \equiv x_5 \ X_1 \equiv \left[X_{D1}, x_{sh}^1, t_{21}^1\right]$$

(3)

Discipline level optimization 2

$$\text{minimize} f_{2.1}\left(X_2\right) = -\left[12.5\left(x_1 - 2\right)^2 + 0.5\left(x_2 - 2\right)^2 + \left(x_5 - 1\right)^2\right]$$

$$+ \left\|1 - (x_{sh}^2 / x_{sh}^G)\right\|_2 + \left\|1 - (y_{21} / t_{21}^G)\right\|_2$$

$$\text{minimize} f_{2.2}\left(X_2\right) = 0.5\left(x_1^2 + x_2^2\right) + x_6^2 + \left\|1 - (x_{sh}^2 / x_{sh}^G)\right\|_2 + \left\|1 - (y_{21} / t_{21}^G)\right\|_2 \qquad (4)$$

$$subject.to\ g_6 \geq 0$$

$$x_{sh}^2 \equiv \left[x_1, x_2\right];\ X_{D2} \equiv \left[x_6\right];\ y_{21} \equiv x_5;\ X_2 \equiv \left[X_{D2}, x_{sh}^2, y_{21}\right]$$

After the optimization of coordination problem in Equation (5) and the optimal solutions with the smallest value of the penalty function we chose the optimal variable at disciplinary level (x_{D1}^*, x_{D2}^*) which are then transferred towards the system optimizer (Equation (2)).

Coordination problem

$$\text{minimize}\ C\left(X\right) = \left\|1 - (x_{sh}^1 / x_{sh})\right\|_2 + \left\|1 - (x_{sh}^2 / x_{sh})\right\|_2 + \left\|1 - (y_{21} / t_{21})\right\|_2$$

$$+ \left\|1 - (t_{21}^1 / t_{21})\right\|_2\ ;\ X \equiv \left[x_{sh}, t_{21}\right];\ X^{min} \leq X \leq X^{max} \qquad (5)$$

The constrained Pareto optimal front for numerical example generated by AAO, MOCO and IMOCO approaches using NSGA-II (Deb 2001) are plotted in the objective space as in Fig.2. The Pareto solutions obtained by MOCO and IMOCO approaches are compared well to those from AAO approach, which is considered as a reference. Figure 2 shows that the Pareto optimal solutions of the IMOCO method are in good concordance than those from the MOCO. This is also was confirmed by the Mahalanobis distance (D_M^2) used by (Ghanmi and al 2011) between AAO and MOCO on the one hand, and AAO and IMOCO on the other hand. To better compare the performance (precision and convergence time) of the IMOCO and the MOCO methods we used (i) the OS metrics (Overall Spread metric) (Wu and Azarm 2001) aims to measure the precision and (ii) the CPU time to measure the speed of convergence. The results in Table 1 show the advantage of our proposed IMOCO method.
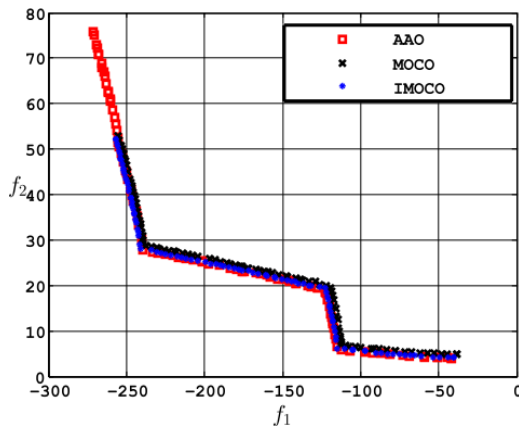
Fig. 2 Feasible objective space for numerical example. Generated by AAO, MOCO and IMOCO

Table 1 Performance of the proposed IMOCO method.

Approach	CPU (%)	D^2_M	OS
AAO	100		
MOCO	82	0.2633	0.3456
IMOCO	74	0.2748	0.3461

3.2   Engineering Problem : cMUT

The Capacitive Micomachined Ultrasonic Transducers (cMUT) is a complex system that involve the coupling between three physical: electrical, mechanical (mechanical structures) and acoustical. The cMUT device manufactured according to the technologies of micro-electro-mechanical systems (MEMS) and that generates or detects acoustic waves. As it is sketched in Fig.3 (a), the geometry of the mobile part of a cMUT cell is composed of a Silicon Nitride membrane of e_{mbr} thickness, partially covered with aluminum electrode of e_{elec} thickness, and a vacuum cavity h_{Gap}.
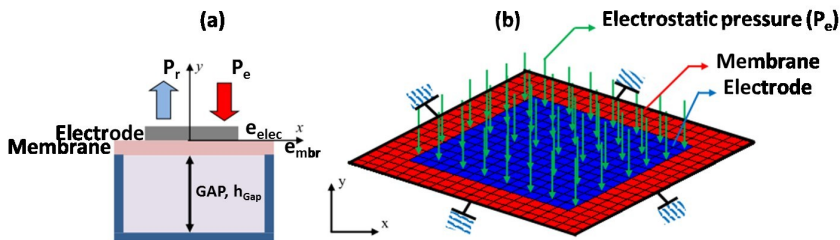
Fig. 3 (a) Representation of cMUT cell and definition of the geometric parameters, (b) a finite element model of cMUT cell.

The cMUT cell is biased with a constant voltage value (V_{dc}) thus creating an electrostatic pressure (P_e) which goes cause a displacement of the membrane. This movement himself generate a radiated pressure in fluid (P_r) in front face of the membrane. The boundary conditions considered in the numerical simulation model are illustrated in detail in fig.3 (b). The details of material and the geometric properties of the cMUT cell can be found in (Meynier and al 2010).

The multi-objective optimization problem of the cMUT cell is given by Equation (6) to solve following the non-hierarchical approach AAO using NSGA-II admits two cost functions, eight design variables and four inequality constraints:

(1) Minimize the mechanical resonance frequency of a cMUT ($f_{rm}(MHZ)$);

(2) Maximize the electromechanical coupling coefficient (K_T^2).

The multi-objective optimization problem to solve is then:

$$
\begin{cases}
\text{minimize}\left(f_{rm}(x), -K_T^2(x)\right) \\
subject.to \ \ g_1 = e_{mbr} + e_{elec} - 700\,e^{-9} \geq 0 \\
\qquad\qquad g_2 = u_{dc} - \dfrac{2}{3}h_{eqv} \leq 0 \ ; h_{eqv} = h_{Gap} + \dfrac{e_{mbr}}{\varepsilon_{mb}} \\
\qquad\qquad g_3 = V_{dc} - 105 \leq 0; g_4 = V - 105 \leq 0 \\
\qquad\qquad x \in (E_{mbr}, E_{elec}, e_{mbr}, e_{elec}, \rho_{mbr}, \rho_{elec}, V_{dc}, V)
\end{cases} \tag{6}
$$

Where, u_{dc} and h_{eqv} represent the static deflection of the membrane and the effective height between the two electrodes respectively. The electromechanical coupling coefficient of CMUT is calculated in (Yaralioglu and al 2003) as follows:

$$
K_T^2 = 1 - \frac{C^S}{C^T} \tag{7}
$$

The fixed capacitance C^S of a single membrane can be calculated as follows:

$$
C^S = \frac{Q}{V_{dc}} = \frac{\varepsilon_0\,S}{2\left(h_{eqv} + u_{dc}\right)} \ \ ; \ avec \ \ Q = \frac{\varepsilon_0\,V_{dc}}{2\left(h_{eqv} + u_{dc}\right)} \tag{8}
$$

The free capacitance C^T is defined as the slope of the voltage-voltage curve:

$$
C^T = \frac{dQ(V)}{dV}\bigg|_{u_{dc}, V_{DC}} = V\frac{d\left(C^S\right)}{dV}\bigg|_{u_{dc}, V_{DC}} = \frac{C_V^{\,S}\left(V - V_{dc}\right) - C^S \times V_{dc}}{\left(V - V_{dc}\right)} \tag{9}
$$

$$
with \ V = V_{dc} + \Delta V_{dc}
$$

In the present work, the cMUT cell operates in a vacuum, therefore two physical are considered in our optimization problem. The objective function for this problem in Equation (6) can be decomposed into two levels of optimization (system and disciplinary level) Using the proposed IMOCO approach.

Equation (10) represents the system level optimization problem. Although each discipline has its own design variables, four variables are shared between the optimization problem at the system level and at the disciplinary level and are the Young's modulus (E_{mbr}), the thickness of the membrane (e_{mbr}), the Young's modulus (E_{elec}), and the thickness of the electrode (e_{elec}).

System level optimization problem

$$\begin{cases} \text{minimize} \left(f_{rm}(X_G, x_m^*), -K_T^2(X_G, x_e^*) \right) \\[2mm] subject.to \; g_1, g_3 \geq 0 \\[2mm] x_{sh} = \left[E_{mbr}, E_{elec}, e_{mbr}, e_{elec} \right], \; X_G \equiv \left[x_{sh}, t_{em}^G \right] \end{cases} \tag{10}$$

In the system level optimization problem, $X_G \equiv [\, x_{sh}, t_{em}^G \,]$ includes the four shared design variables [$E_{mbr}, E_{elec}, e_{mbr}, e_{elec}$]; and the auxiliary variable t_{em}^G corresponds to the coupling variable y_{em}.

The system level optimization problem aims the minimization of the mechanical resonance frequency (f_{rm}) and the maximization of the electromechanical coupling coefficient (K_T^2). The super script (*) indicates that the design parameters are optimized at the disciplinary level.

Mechanical Optimizer	**Electrical Optimizer**
minimize $f_{rm}\left(X_m \right) +$	maximize $C^T \left(X_e \right)$
$\left\| 1 - (x_{sh}^m / x_{sh}^G) \right\|_2 + \left\| 1 - (t_{em}^m / t_{em}^G) \right\|_2$	$+ \left\| 1 - (x_{sh}^e / x_{sh}^G) \right\|_2 + \left\| 1 - (y_{em} / t_{em}^G) \right\|_2$
$subject.to \; g_2 \geq 0$	$subject.to \; g_4 \geq 0$
$x_{sh}^m \equiv \left[E_{mbr}, E_{elec}, e_{mbr}, e_{elec} \right]$	$x_{sh}^e \equiv \left[E_{mbr}, E_{elec}, e_{mbr}, e_{elec} \right]$
$x_m \equiv \left[\rho_{mbr}, \rho_{elec} \right]; t_{em}^m \equiv \left[V_{dc} \right]$	$x_e \equiv \left[V \right]; y_{em} \equiv \left[V_{dc} \right]$
$X_m \equiv \left[x_m, x_{sh}^m, t_{em}^m \right]$	$X_e \equiv \left[x_e, x_{sh}^e, y_{em} \right]$

$$\tag{11}$$

At the disciplinary level in Equation (11), we find two disciplinary optimizers: (i) mechanical optimizer and (ii) the electrical optimizer. The mechanical optimizer has his own design variables; the two variables also include the density of the membrane (ρ_{mbr}), the density of the electrode (ρ_{elec}), and the local copy of the

auxiliary variable for t_{em}^{G} i.e., t_{em}^{e} which allows minimizing the mechanical re-
sonance frequency (f_{rm}) of the mechanical discipline. Equally, the electrical op-
timizer includes local design variable is the bias voltage (**V**), and the interdiscipli-
nary coupling variable y_{em}, whose value is evaluated in electrical optimizer and is
used in Mechanical optimizer. This optimizer aims to maximize the free capacit-
ance C^{T}.

After the optimization of coordination problem in Equation (12) and the optim-
al solutions with the smallest value of the penalty function we chose the optimal
variables (x_{m}^{*}, x_{e}^{*}) at disciplinary level which are then transferred towards the sys-
tem optimizer (Equation (10)).

Coordination problem

$$
\text{minimize } C\left(X\right) = \left\|1 - (x_{sh}^{m} \, / \, x_{sh})\right\|_{2} + \left\|1 - (x_{sh}^{e} \, / \, x_{sh})\right\|_{2} + \left\|1 - (y_{em} \, / \, t_{em})\right\|_{2}
$$
$$
+ \left\|1 - (t_{em}^{m} \, / \, t_{em})\right\|_{2} \; ; \; X \equiv \left[x_{sh}, t_{em}\right] \; ; \; X^{\min} \leq X \leq X^{\max} \tag{12}
$$

The Feasible optimal solutions obtained by IMOCO method are compared with
those generated by MOCO as shown in Fig.4. In terms of proximity to the refer-
ence (AAO) cloud of the optimal solutions, the spread in the objective space and
the CPU time, the IMOCO solutions are better than the MOCO solutions. We can
observed in the Table 2 that the CPU time, the values for Mahalanobis distance
(D^{2}_{M}) and Overall spread (OS) from the IMOCO are better than MOCO.
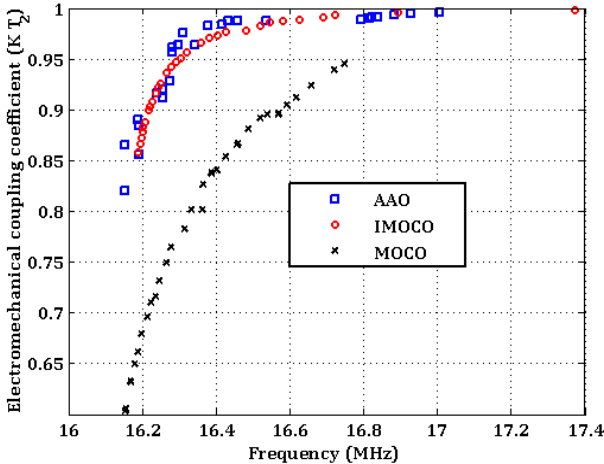
Fig. 4 Feasible objective space for cMUT cell obtained using AAO, MOCO and IMOCO

Table 2 Performance of the proposed IMOCO method

Approach	CPU (%)	D^2_M	OS
AAO	100		
MOCO	75	5.7348	0.4221
IMOCO	72	0.0632	0.3455

4   Conclusion

In this work, we have presented the IMOCO method using NSGA-II for the design of fully coupled complex systems. The IMOCO enhances the convergence by adding a coordination problem between the system level and the discipline level optimizer. This improvement allows the IMOCO to achieve convergence more efficiently than the previous MOCO method. Based on the results from the numerical example and the engineering example we can be concluded that the optimal solutions obtained by IMOCO are better than the MOCO solutions. First, in terms of proximity to the reference (AAO) cloud of Pareto optimum solutions and the spread in the feasible objective space. Secondly, in terms of the CPU time to measure the speed of convergence. Consequently, we conclude that the proposed IMOCO method is able to solve a fully coupled Multi-objective Multi-physics Optimization Problem more efficiently than the MOCO approach. Finally, in our future research we propose to apply our method on complex systems involve several disciplines (mechanical-electrical-acoustical…) fully coupled.

References

Aute, V., Azarm, S.: Genetic Algorithms Based Approach for Multidisciplinary Multiobjective Collaborative Optimization. In: Proceedings of the 11th AIAA/ISSMO Multidisciplinary Analysis and Optimization Conference, Portsmouth, VA (2006)

Deb, K.: Multi-Objective Optimization Using Evolutionary Algorithms. John Wiley & Sons, Chichester (2001)

Ghanmi, S., Guedri, M., Bouazizi, M.-L., Bouhaddi, N.: Robust Multi-Objective and Multi-Level Optimization of Complex Mechanical Structures. Mechanical Systems and Signal Processing 25(7), 2444–2461 (2011)

Meynier, C., Teston, F., Certon, D.: A Multiscale Model for Array of Capacitive Micromachined Ultrasonic Transducers. The Journal of the Acoustical Society of America 128(5), 2549–2561 (2010)

Tappeta, R.V., Renaud, J.E.: Multiobjective Collaborative Optimization. Journal of Mechanical Design 119(3), 403–411 (1997)

Wu, J., Azarm, S.: Metrics for quality assessment of a multi-objective design optimization solution set. J. Mech. Des. 123(1), 18–25 (2001)

Yaralioglu, G.G., Ergun, A.S., Bayram, B., Haeggstrom, E., Khuri-Yakub, B.T.: Calculation and Measurement of Electromechanical Coupling Coefficient of Capacitive Micromachined Ultrasonic Transducers. IEEE Transactions on Ultrasonics, Ferroelectrics and Frequency Control 50(4), 449–456 (2003)

Design and Fabrication of an Automatic Sprinkler Fire Fighting System

Abdalsalam Ahmed, Abdulsalam Mansor, and Abdulgani Albagul

Faculty of Electronic Technology Baniwald, Tripoli Road, Baniwalid, Libya
{abci7854,abci1987ncir}@gmail.com, albagoul@yahoo.com

Abstract. This paper attempts to integrate microcontrollers into smoke detector circuitry and other components for safety purpose. This can be achieved by placing some sensors and devices in the building. In the proposed system, a smoke detector upon senses smoke activates its alarm, sends a low voltage signal to microcontrollers. The microcontroller will activate the relays which are connected to other components to alert residents that one of the smoke detectors has sensed smoke by means of voice and flashing lights. At the same time, it will send signals to valves, air suckers and the water pump. The solenoid valve will operate the water pump which delivers water to the room through pipes installed inside the building to attack the fire. Meanwhile, the air sucker will suck the smoke from the room to prevent suffocation. The proposed design is aiming to have cost efficient system, compact design, easily expandable, simple to install and replaceable components.

Keywords: safety systems, smoke detection, microcontrollers, mechatronics system.

1   Introduction

Fire is a phenomenon which is familiar to everyone, It is used daily to cook our meals and heat our homes during the cold season, when harnessed, the power and energy from fire serve us as well. Meanwhile when it is uncontrolled, a fire can quickly consume and destroy whatever lies in its path. Fires are classified into four classes; Class A which involves solid material, such as wood, clothes, papers, rubbers and plastics. Class B involves inflammable liquids, oil, tars and flammable gases. Class C involves gases. Class D involves metals. Class K fires involve combustible cooking media such as oils and grease commonly found in commercial kitchens (Ted Boothroyd et al. 2005). All fire classes produce dangerous smokes which is a visible suspension of carbon or other particles in the air which emitted from a burning substance. Smoke inhalation is the primary cause of death in victims of indoor fires. Thus, awareness and consciousness of the importance of smoke detection system must be planted on people mind. In addition, fires are more dangerous at night. Therefore, smoke detector must be placed at the major

area inclusive every rooms. It is very important issue to take suitable measures and steps to prevent the fire from spreading and keep it under control until it is extinguished completely. There are two ways to fight fire; manually and automatically by different approaches. A fire sprinkler system is an active fire protection measure, consisting of a water supply system, providing adequate pressure and flow rate to a water distribution piping system, onto which fire sprinklers are connected. Although historically only used in factories and large commercial buildings, systems for homes and small buildings. Fire sprinkler systems are extensively used worldwide, with over 40 million sprinkler heads fitted each year. In buildings completely protected by fire sprinkler systems, over 99% of fires were controlled by fire sprinklers alone (Puchovsky, M 2003). This paper is devoted to design and implant an automatic way to extinguishing fire using water for class A

2   Related Work

Many works have been conducted in the area of fire fighting over years. There are many ways to fight fires ranging from conventional manual methods to more sophisticated ones. The cost of sophisticate system is very high but effective. Ambrose Godfrey created the first successful automated sprinkler system in 1723. He used gunpowder to release a tank of extinguishing fluid (Ted Boothroyd et al. 2005). In 1812, the first modern recognizable sprinkler system was installed in the Theatre Royal, Drury Lane in the United Kingdom. The system which was designed by William Congreve consisted of a cylindrical airtight fed by a (250 mm) water main which branched to all parts of the theatre. A series of smaller pipes fed from the distribution pipe were pierced with a series of (13 mm) holes which pour water in the event of a fire (Gelb, Michael J 1989). From 1852 to 1885, perforated pipe systems were used in textile mills throughout New England as a means of fire protection. However, they were not automatic systems; a person had to operate the system. Inventors first began experimenting with automatic sprinklers around 1860. The first automatic sprinkler system was patented by Philip W. Pratt in 1872. Henry S. Parmalee of New Haven, Connecticut is considered the inventor of the first automatic sprinkler head. Parmalee improved upon the Pratt patent and created a better sprinkler system (Bryan 1990). Bryan states that an Automatic sprinkler system is a system of pipes, tubes, or conduits provided with sprinklers or nozzles, which is automatically activated and (in some types) deactivated, utilizing the sensing of fire-induced stimuli consisting of light, heat, visible or invisible combustion products, and pressure generation, to distribute water and water-base extinguishing agents in the fire area. In 1874, he installed his fire sprinkler system into the piano factory that he owned. Frederick Grinnell improved Parmalee's design and in 1881 patented the automatic sprinkler that bears his name. He continued to improve the device and in 1890 invented the glass disc sprinkler, essentially the same as that in use today. Until the 1940s, sprinklers were installed almost exclusively for the protection of commercial buildings. Over the years, fire sprinklers have become mandatory safety equipment in some parts of North America, in certain occupancies, including, but not limited to newly constructed hospitals, schools, hotels and other public buildings, subject to the local

building codes and enforcement. Sprinkler systems are a reliable way to protect property from fire damage. Since their invention in the late 19th century, they have served as a method of managing fires until firefighters arrive at the scene (C.L. Beyler 1977). The earliest sprinkler systems consisted of steel pipe networks with drilled holes or perforations provided along the length of pipe. The concept of employing a heat-actuated device dates back to approximately 1860 (Puchovsk 2003). Automatic sprinkler systems are thermosensitive devices designed to react at predetermined temperatures by automatically releasing a stream of water and distributing it in specified patterns and quantities over designated areas (Z.G. Liu and A.K. Kim 2000).

3   Types of Sprinkler Systems

Sprinkler systems are a reliable way to protect property from fire damage. Since their invention in the late 19th century, they have served as a method of managing fires until firefighters arrive at the scene. The earliest sprinkler systems consisted of steel pipe networks with drilled holes or perforations provided along the length of pipe. Today, there are different types of sprinkler styles which serve many different purposes. The four most common styles of sprinkler systems are a standard spray upright, standard spray pendent, sidewall sprinkler, and the extended coverage sprinkler.

3.1   Wet Pipe System

It consists of some pipes containing water under pressure. It is used in normal ambient conditions and the sprinkler pipes are always filled with water. The sprinklers on this system are heat sensitive and will only activate after reaching a designated temperature. With this system, each individual sprinkler can react to heat from a fire, operating to distribute water over the source of that heat (Fleming 2003). The heat from the fire will break a glass bulb, fusible link, or chemical pellet that is under pressure, releasing a spring which allows water to dispense out of the sprinkler (Wieder and Smith 1998). In 2007, 89% of reported fires involved only one or two sprinklers when wet pipe sprinklers operated (Hall 2010).

3.2   Dry Pipe System

It uses heat sensitive sprinklers. It is commonly found in colder environments where there is the possibility of the wet pipe system freezing. Rather than being filled with water like the wet pipe system, this system is filled with air and is under pressure. When the heat sensitive sprinkler activates, the air is released and water flows to the open sprinkler where it is dispersed. Similar to the wet pipe system, only the sprinkler that reaches the designated temperature will discharge water. The water is held back in piping at a climate controlled environment to prevent freezing. According to (Gagnon 1997), this should take no longer than sixty

seconds, in accordance with NFPA 13. In 2007 when dry pipe sprinklers operated, 74% reported fires involved only one or two sprinklers (Hall 2010).

3.3 Preaction System

It is a type of dry system that employs a deluge-type valve, fire detection devices, and closed sprinklers. This system only discharges water into the piping in response to a signal from the detection system. Once the detection system signals the preaction system, water will be discharged into the piping system like a wet pipe sprinkler system. The system will not disperse water onto the fire until each sprinkler head is activated. Preaction systems are typically found in spaces containing computer or communications equipment, museums, and other facilities where inadvertent water leakage from system piping is of major concern and it is critical that there are not accidental discharges of water in these areas (Puchovsky 2003).

3.4 Deluge System

It is also like the dry pipe sprinkler system, but is equipped with open sprinklers and a deluge valve. This has all open sprinklers and allows the flow of water to be evenly spread throughout all of the sprinklers. This is activated by an alarm system that triggers the system and disperses the water. A concern of businesses looking into installing sprinkler systems is the fear that they will discharge accidentally, causing unnecessary water damage. However, sprinkler systems are designed in such a way that this accidental discharge rarely occurs. Sprinkler systems that accidentally discharge have typically been exposed to extreme heat or have been damaged (Tremblay and McCarthy 2002).

3.5 Foam Water System

It is a special application system, discharging a mixture of water and low expansion foam concentrate, resulting in a foam spray from the sprinkler. These systems are usually used with special hazards occupancies associated with high challenge fires, such as flammable liquids, and airport hangars. Operation is as described above, depending on the system type into which the foam is injected.

3.6 Water Spray System

It is operationally identical to a deluge system, but the piping and discharge nozzle spray patterns are designed to protect a uniquely configured hazard, usually being three-dimensional components or equipment (i.e., as opposed to a deluge system, which is designed to cover the horizontal floor area of a room). The nozzles used may not be listed fire sprinklers, and are usually selected for a specific spray pattern to conform to the three-dimensional nature of the hazard (e.g., typical spray

patterns being oval, fan, full circle, narrow jet). Examples of hazards protected by water spray systems are electrical transformers containing oil for cooling or turbo-generator bearings. Water spray systems can also be used externally on the surfaces of tanks containing flammable liquids or gases (such as hydrogen). Here the water spray is intended to cool the tank and its contents to prevent tank r upture/explosion (BLEVE) and fire spread.

3.7 Water Spray System

It is used for special applications in which it is decided that creating a heat absorbent vapor is the primary objective. This type of system is typically used where water damage may be a concern, or where water supplies are limited. Water mist is defined as a water spray with a droplet size of less than 1000 microns at the minimum operation pressure of the discharge nozzle. The droplet size can be controlled by the adjusting discharge pressure through a nozzle of a fixed orifice size. By creating a mist, and equal volume of water will create a larger total surface area exposed to the fire. The larger total surface area better facilitates the transfer of heat, thus allowing more water droplets to turn to steam more quickly. A water mist, which absorbs more heat than water per unit time, will more effectively cool the room, thus reducing the temperature of the flame. Water mist systems can operate with the same functionality as deluge, wet pipe, dry pipe, or pre-action systems. The difference is that a water mist system uses a compressed gas as an atomizing medium, which is pumped through the sprinkler pipe.

4 Sprinkler System Design and Components

A fire sprinkler system is an active fire protection measure, consisting of a water supply system, providing adequate pressure and flow rate to a water distribution piping system, onto which fire sprinklers are connected. In this paper the system is designed for a small prototype for pilot scale building. The system consists of hardware and software systems.

4.1 Hardware Design and Construction

The hardware system consists of a small home with three rooms where smoke and heat sensors, fans and sprinkler nozzle are installed in each room as shown in figure 1. The sensors and other components are connected to the microcontroller through some circuitry as shown in figure 2.

Fig. 1 The prototype of a small home

Fig. 2 The circuit diagram for the system

The overall system consists of a PIC microcontroller, LM35 series are precision integrated circuit temperature sensors, relays, light-emitting diodes, booster pump, solenoid valve, smoke detectors, air fans, push buttons, sprinkler nozzles and an emergency key.

4.2   The Operation Procedures

The system starts by reading the status of heat and smoke sensors. If anyone the smoke detectors is triggered or heat sensors provided a reading above 60° C, then the microcontrollers will send signals to turn on room lamp, triggers the alarm, flashing light and on the air fans to suck smokes outside the building. The system then will take some time delay for few seconds before it triggers the pump and solenoid valve to pump the water to fight the fire through the sprinkler nozzle. Once the smoking alarm goes off and temperature goes dawn, the system will take delay fore few seconds before it switches off the water pump and the alarm. Figure 3 shows the flowchart of the proposed technique.
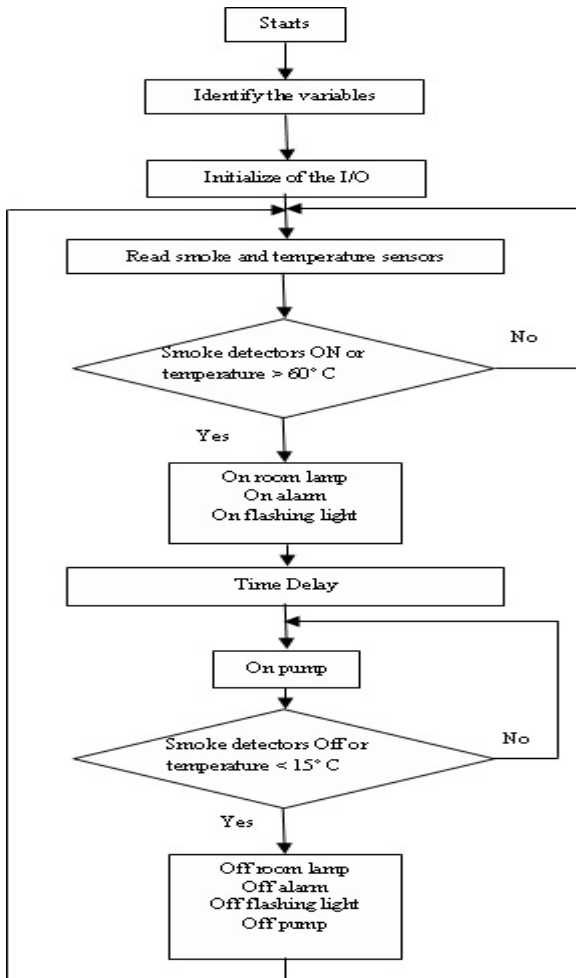
Fig. 3 The flowchart of the proposed technique

5   Conclusion

The automatic window cleaning robot has been successfully designed and fabricated. The system works automatically and manually. However, if the sensor didn't work or was late in reaction, the manual emergency switch which is usually installed inside the building and is used to operate the fire system manually. The system consists of a number of devices, which are interconnected to perform the required task. The components used in this work are simple and cheap. The software programming is simple and can be modified and implemented easily. The automatic sprinkler system is an effective means to control fires in enclosed areas. In general the system works adequately as anticipated in the design process. The idea of mechatronics engineering can be seen where some of engineering display were encompassed in the system

References

Boothroyd, T., Ruane, T., Murnane, L.: Fire Detection and Suppression Systems, 3rd edn. Paperback (2005)

Puchovsky, M.: Automatic sprinklers. In: Cote, A. (ed.) Fire Protection Handbook, 19th edn., vol. 2, Section 10, pp. 185–212. National Fire Protection Association, Quincy (2003)

Mawhinney, J.R., Solomon, R.: Water mist fire suppression systems. In: Fire Protection Handbook. National Fire Protection Association, Quincy (1997)

Gelb, M.J.: How to Think Like Leonardo da Vinci. Dell Publishing, New York (1998)

Bryan, J.: Automatic sprinkler and standpipe systems, 2nd edn. National Fire Protection Association, Quincy (1990)

Beyler, C.L.: The Interaction of Fire and Sprinklers, NBS GCR 77-105. National Bureau of Standards, Washington, DC (1977)

Liu, Z.G., Kim, A.K.: A review of water mist fire suppression systems - Fundamental studies. Journal of Fire Protection Engineering 10(3), 32–50 (2000)

Hall Jr., J.R.: U.S. Experience with sprinklers and other automatic fire extinguishing equipment. National Fire Protection Association, Quincy (2010)

Chow, W.K.: On the Evaporation Effect of a Sprinkler Water Spray. Fire Tech., pp. 364–373 (1989)

Evans, D.D.: Sprinkler Fire Suppression Algorithm for HAZARD, NISTIR 5254. National Institute of Standards and Technology, Gaithersburg (1993)

Fleming, R.: Principles of automatic sprinkler system performance. In: Cote, A. (ed.) Fire Protection Handbook, 19th edn., vol. 2, Section 10, pp. 159–170. National Fire Protection Association, Quincy (2003)

Bukowski, R.: Household fire warning equipment. In: Cote, A. (ed.) Fire Protection Handbook, 19th edn., vol. 2, Section 9, pp. 79–88. National Fire Protection Association, Quincy (2003)

Gagnon, R.: Design of water-based fire protection systems. Delmar Publishers, Boston (1997)

Roberts, J.: Automatic fire detectors. In: Cote, A. (ed.) Fire Protection Handbook, 19th edn., vol. 2, Section 9, pp. 17–34. National Fire Protection Association, Quincy (2003)

Hall Jr., J.R.: An analysis of automatic sprinkler system reliability using current data. National Fire Protection Association, Quincy (2006)

Grant, G., Brenton, J., Drysdale, D.: Fire Supression by Water Sprays. Progress in Energy and Combustion Science (2000)

Liu, Z., Kim, A.K.: A Review of water mist fire suppression systems fundamental studies. Journal of fire Protection Engineering 10(3), 32–50 (2000)

Wigus, R.: Engineering relations for water mist fire suppression systems. In: Proceedings of Halon Options Technical Working Conference, Albuquerque, NM, pp. 397–409 (1995)

Verle, M.: PIC Microcontrollers, 1st edn. mikroElektronika (2008)

Bates, M.: PIC Microcontrollers: An Introduction to Microelectronics, 3rd edn. Newnes (2011)

Boothroyd, T., Ruane, T., Murnane, L.: Fire Detection and Suppression Systems, 3rd edn. Paperback (2005)

A New Design of an Adjustable Length Container with a New Lighter Material in the Field of Intermodal Transport

Cont'able project a vision for the future

Anis Abdallah[1], Mohamed Sahbi Miled[2], Taoufik Nasri[3], and Jalel Briki[4]

[1] LR-MAI, ENIT, université Tunis Elmanar, Campus universitaire, Tunisie
  anis.abdallah.enim@hotmail.fr
[2] ISET Sup SAS, Marseille, France
  sahbimiled@gmail.com
[3] LR-MAI, ENIT, université Tunis Elmanar, Campus universitaire, Tunisie
  nasri.taoufik@gmail.com
[4] LR-MAI, ENIT, université Tunis Elmanar, Campus universitaire, Tunisie
  Jalel.Briki@enit.rnu.tn

Abstract. To solve the problems of empty return and storage of empty containers (cost, safety) and for economic and environmental benefit, the new adjustable length container is the solution which should be able to increase or reduce its volume autonomously and in a few minutes. This will reduce the cost of transporting empty containers while respecting the standards containers in force size, strength, and devices used for handling and securing the means of road or rail shipping.

This container will be the feature of reconfigurable and compactable in length so as to reduce its volume vacuum and thus to optimize its size, storage, transport (land and sea).

Study the behavior of a lightweight material selected under monotonic loading in different environments and service (high and low temperatures, humidity, shock ...) containers in their new form.

Keywords: container, adjustable, son container, mother container, lightweight material, monotonic loading, intermodal transport.

1   Introduction

Since 1956 the year of the container invention we are living a revolution in our life. The container made shipping very cheap, and by doing so changed the shape of the world economy.

The total cost of a container multimodal transport includes land transport and also the transport of the empty container[1]. Cost transport depends on volume of goods and this rule is available for container transport. Transporting a full container seems cost-efficient, while moving and storing an empty one certainly is

not. Cont'able presents solution for this. A certified adjustable container made with composite material is currently being developed. The new container made of composite material with corrosion resistance weighs 25 % less than a steel container and can be transformed from a 20 feet to a 40 feet container in few minutes. Many advantages results from the new design of the container. It will be adapted to the needs of transporter. Secondly when the container is empty so we can reduce the volume to became a 20 feet container and for land transport, it well be carried by a middle size truck and we don't need a trailer. Thirdly loading of the new container will be easier. in fact we can reduce time of loading empty container in ships.

As a result all stakeholders in the international transport chain will find interest and in particular:

-         Chargers: exporters, importers, manufactures, distributors
-         Shipping companies; maritime carriers: "deep sea"; "Short sea" carriers.
-         Road carriers
-         Intermodal operators.
-         Port authority with less space for storing.
-         Control authority such as customs administration with non intrusive control (scan).

2   Scientific Context

The innovative project called "Cont'able" and which is the subject of our research is to design and manufacture a new type or model container ISO-compliant standards used for multimodal transport of goods.
This container will be the feature of reconfigurable and compactable in length so as to reduce its volume vacuum and thus to optimize its size, storage, transport (land and sea).

The PhD project aims to study the behavior of a lightweight material selected under monotonic loading in different environments and service environments (high and low temperatures, humidity, shock ...) containers in their new form (Fig 1).

The use of a composite material we will firstly a reduction in weight of the vacuum container [2,5] and also facilitates the movement of these two removable compartments.

So we will have a lighter container (up to 25% weight gain) and the loading capacity of container ships increased in terms number of containers that transport.
An important aspect to note is made that the new container helps preserve the environment by reducing the number of empty trips thereby reducing CO_2 emissions into the atmosphere. (Divide by at least two empty journeys).
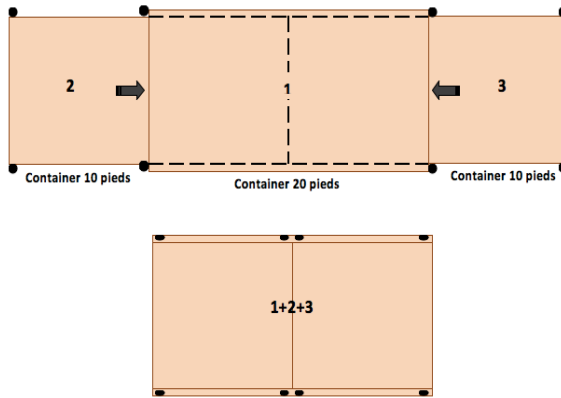
Fig. 1 Technical solution

1 :fixed block length of 20 feet.
2: left mobile compartment
3: right mobile compartment

The curb weight of a conventional 40-feet container varies between 3.5 and 4.5 tones and that depending on the year of construction and the manufacturer [6]. For our model we hope does not exceed 4.5 tones for the first phase and 3.5 tons for the second phase , that is to say after using components and lighter composite materials. The use of other materials must reflect a different stress resistance of the roof of the container and which is equal to 300 kg on a surface of 60 cm * 30 cm .

Indeed, in practice the containers are stacked on top of each other and may have a situation where the container will have to bear the weight of other 4 or 5 containers.

The lifetime of a conventional container is 15 years. From our model would be made with mechanisms and mechanical equipment, is provided for a service life of 10 years this model .

The average loading capacity of conventional containers of 20 feet or 40 feet by weight are respectively 27 and 30 tones and maximum values were 29 and 32 tons.

3   Steel Adjustable Container Design

3.1   Design of Different Parts

The innovative container consists of a central element, characterized in that said central member comprises a fixed central portion (mother container) corresponding to an ISO container of 20 feet dimension and two integral parts

(son containers) of the fixed central part, movable in the lengthwise and deployable on either side of the central fixed part, and allowing the processing dimension of the container 20 feet container 40 feet in dimension. Fig 2
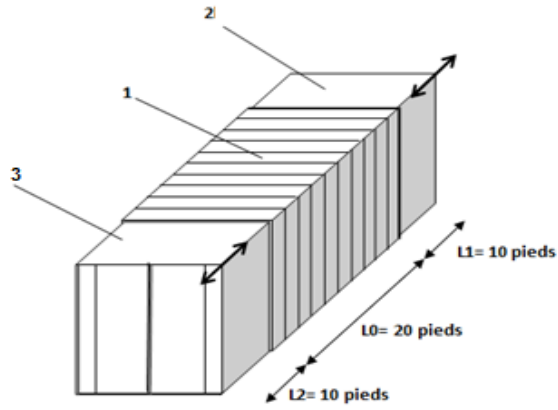
Fig. 2 Sketch of the technical solution

1 :fixed block length of 20 feet.
2: left mobile compartment
3: right mobile compartment

A solution is proposed for this system variable structure. The following images show the different views for a 3D model.Fig 3
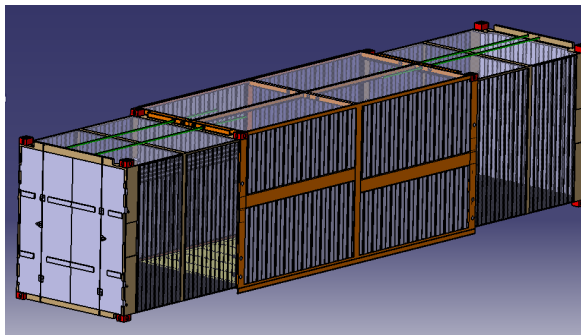
Fig. 3 3D view of adjustable container

In the following two cases, the adjustable container has external   standardized dimensions ISO 668:

• The closed cases (20 feet container) 6058 x 2438 x 2591 mm,(Fig 4)
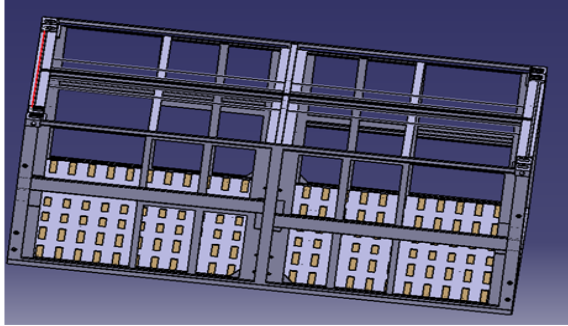
Fig. 4 Adjustable closed container case (20 feet)

• The open cases (40 feet container) 12192 x 2438 x 2591 mm.(Fig 5)

The lengths of the adjustable container consider a real challenge as the standard length of the   40 feet container larger than the 20 feet container. So we had to design an appropriate solution find all the dimensions in both cases.
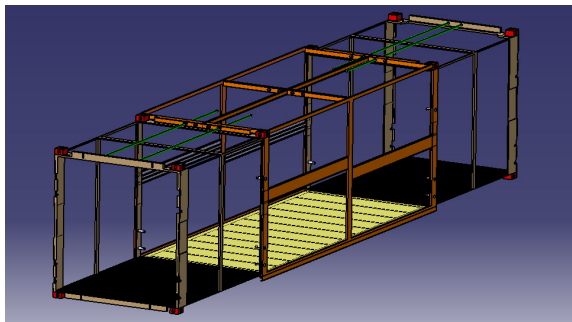
Fig. 5 Adjustable opened container case (40 feet)

a. Mother Container:

The fixed central container called mother container, has dimensions 6058 x 2438 x 2591 mm and has a wooden floor which treated and resistant (eg Mahogany). A guide-spring system is used to position the floor on two different levels. The mother container is steel S355MC and the eight corners are made of carbon steel alloy. Fig 6
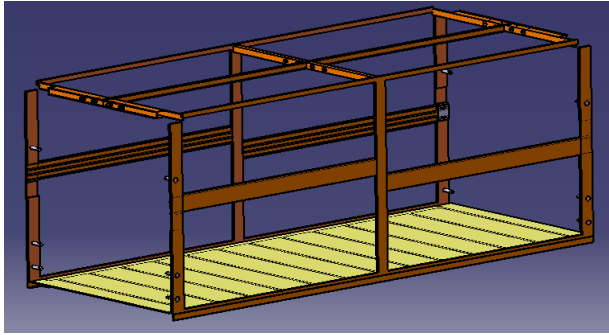
Fig. 6 Mother container

b. Son Container:

A 145 mm long portion of each son container remains inside the mother container to improve the strength, insulation, sealing and weaken the vibration.(Fig 7)

To improve the sealing is provided the use of the rubber seals and small pipes to drain water from the rooftops. Each son container must bear a load of 7 tons of goods.
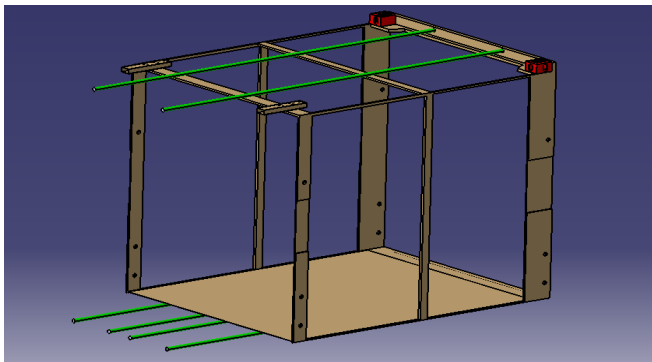
Fig. 7 Son container

4   Choice of Materials

The framework and the plates of adjustable container are in stainless steel X30Cr13.

In order to maintain son container, six guide tube in steel X30Cr13 are added (4 down and 2 in the roof).

Conventional doors and corners of containers son are in Aluminum Alloy AlMn1Mg1 3.0526 (EN-AW 3004) because we want to get the lightest possible of container son.

The following table describes the choice of material for each component of adjustable container (Tab 1).

Table 1 Summary table for choice of material

Component	Material
mother container	Steel S355MC
Son container	Stainless steel X30Cr13
The mother floor	treated wood
The son floor	Aluminum Alloy 3004
Coins	Carbon Steel AISI 4340

The corners of the container mother are in carbon-steel alloy. The AISI 4340 material are chosen with a high yield because the handling is carried out at these corners**.**

5   Numerical Validation of Model: Strength of Materials

Son Container in Storage

The container must withstand a load of 4 containers above for shipping.
The maximum unit load container is 24T
The forces applied are as follows:
- The force applied on the corners: (24T*4)/2=56 Tons.
- The force applied on the son floor: 6 Tons
- limit conditions: 4 lower tubes and the son floor are fixed

Von Mises Result: The maximum value of the Von Mises criterion is 5.05 E +08 N /m (Fig. 8) which is below the yield strength of the steel selected (7.85 E +08 N / m²).
The son container is resistant against the maximum load during storage.
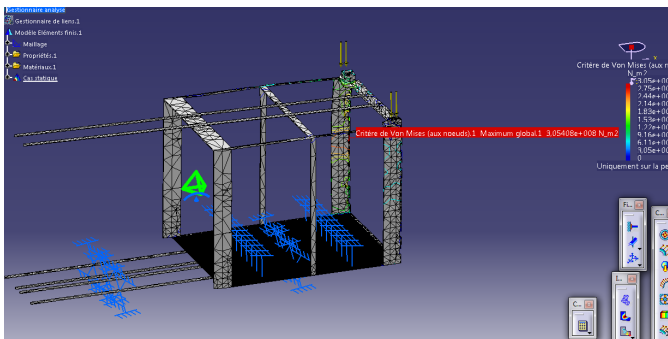
Fig. 8 Von Mises criterion for storage

The displacement at the nodes of the container is as shown in the following picture Fig 9. This maximum displacement is 4.62mm and is located at coins level. This deformation is obviously still in the elastic range according to the Von Mises criterion.
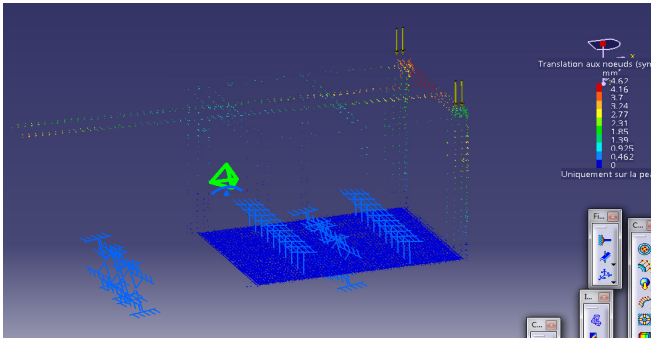
Fig. 9 Translation nodes for storage

Son container in handling

-    The force applied is 6 tons on the floor.
-    limit conditions: 6 guide tubes are fixed

Von Mises Result: The deformations of container son in handling are distributed over the entire structure with a maximum value of 1.15 E +08 N/m in the lower tubes (Fig 10). Deformations remain in the elastic range and structure withstands the load handling.
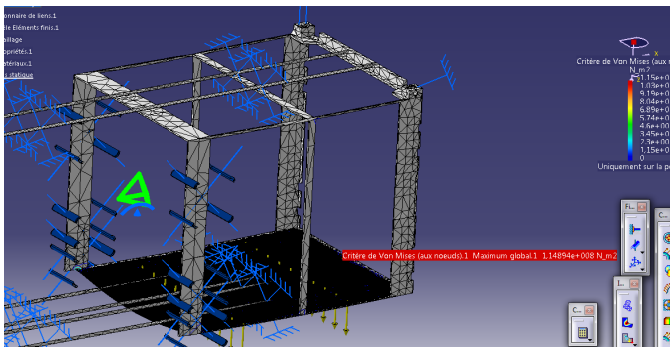
Fig. 10 Von Mises criterion for handling

The displacement at the nodes of the container is as shown in the following picture Fig 11. This maximum displacement is 0.608mm due to the bending and is located at floor level. This deformation is obviously still in the elastic range according to the Von Mises criterion.
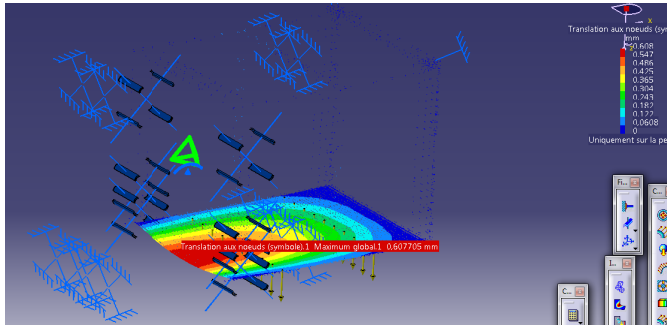
Fig. 11 Translation nodes for handling

Mother Container in Storage

The container must withstand a load of 4 containers above for shipping. The maximum unit load container is 24T.

The forces applied are as follows:
- The force applied on the corners: (24T*4)=46 Tons.
- limit conditions: mother floor is fixed

Von Mises Result: The maximum value of the Von Mises criterion is 2.04 E +08 N /m (Fig. 12) which is below the yield strength of the steel selected (3.55 E +08 N / m²) of the Steel S355MC. (Fig 12).
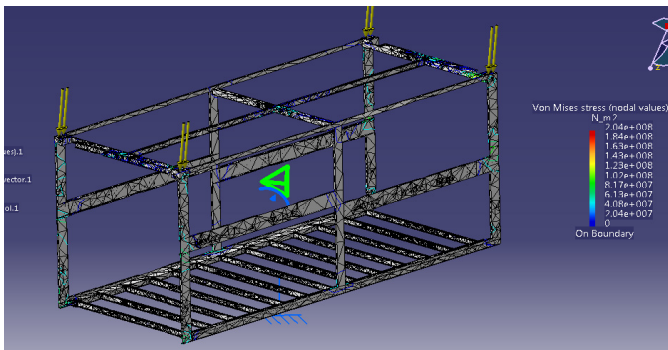
Fig. 12 Von Mises criterion for mother container

6   Mobility of Two Son Container

The mobility of tow son container for the case retractable containers on both sides can be done with a single shot manually or with the assistance of a vehicle [3,4] (truck, forklift ...)Fig 13
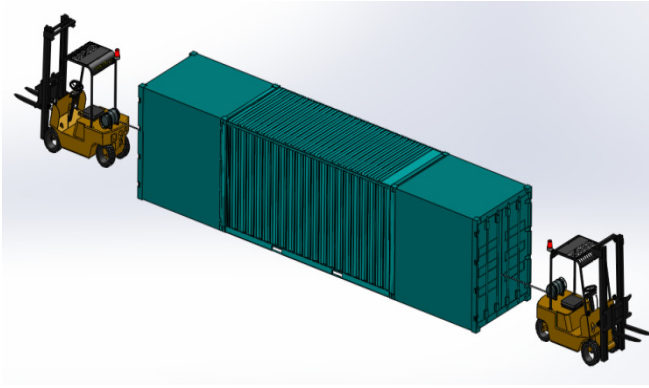
Fig. 13 Technical solution of mobility

7   Problem and Work Objectives of the Phd Subject to Come

Specifically the invention is to design a 40-feet container consists of a fixed and solid core with the same properties , characteristics and load capacity than current container 20 feet and on the market (or a container 20 and feet of height equal to that of a High Cube container) .

Thus, for our topic and thesis , the first phase of work will keep on steel as constituent material and then after scientific validation (analytical modeling) and experimental including the construction of a functional prototype , we will develop a material composite lighter construction for the two moving parts . This is our second stage of labor. This weight gain on the one hand allow a weight reduction of the vacuum container and also facilitates the movement of these two removable compartments . This is the principle of optimization or optimal allocation of resources need to use the same constituent material for parts whose mechanical properties and resistance requirements (mechanical, thermal , shock, corrosion has) are different , the central portion will bear most of the weight . So we will have a lighter container (up to 25% weight gain) but with the same weight capacity and volume than a conventional container.

8   Expected Value (Socio-Economic Impact, ...)

The new container is designed that the chargers would not change their habits or invests in new equipments or material. With a potential price tag three times that a traditional container investor on the green label container well have a return on investment after 18 months approximately. The new container will stimulate the intermodal - multimodal transport in by so we will reduce logistic costs, environment impacts, decrease using trucks and land transport in general.

The use of a composite material we will firstly a reduction in weight of the vacuum container and also facilitates the movement of these two removable compartments.

So we will have a lighter container (up to 25% weight gain) and the loading capacity of container ships increased in terms number of containers that transport.

An important aspect to note is made that the new container helps preserve the environment by reducing the number of empty trips thereby reducing CO_2 emissions into the atmosphere. (Divide by at least two empty journeys).

9   Conclusion

The proposed solution of adjustable container (20 feet and 40 feet) respects the external dimensions of the ISO 668 standard. It supports a total load of 24 tones and the additional mass of the system.

The proposed work in this container is 100% manufacturable. Certainly, working with the expertise of the manufacturer optimizes the final version of this adjustable container.

References

Montreuil, B.: Transforming the way physical objects are moved, stored, realized, supplied and used, aiming towards greater efficiency and sustainability. Physical Internet Manifesto, Laval University, Québec, Canada, version. 1.11.1 (November 2012)

Gargoshell. Cargoshell – The first CSC-certified composite shipping container in the world, `http://www.cargoshell.com/` (page viewed on December 20, 2013)

Staxxon: Vertical Floding container, How Staxxon's ISO Container Technology Works [video en ligne], `http://www.youtube.com/watch?v=QTdgZ2YuAM8` (viewed on December 20, 2013)

Staxxon, Folding a 20 ISO Container with Staxxon vertical Folding/Nesting Technology. [video en ligne], `http://www.youtube.com/watch?v=1rRPX79mWPg` (viewed on December 14, 2013)

Gargoshell, Werkendams bedrijf introduceert opvouwbare zeecontainer. [video en ligne], `http://www.youtube.com/watch?v=vHlTrOVv9gs` (viewed on December 26, 2013)

Juntai, Producteur et Fournisseur de conteneurs neufs, [en ligne], `http://www.container-in-china.com/` (viewed on December 22, 2013)

Integrated CAD Approach for Generating Assembly Sequence Plans Based on Collision Study Results

Riadh Ben Hadj, Moez Trigui, and Nizar Aifaoui

Mechanical Engineering Laboratory, National Engineering School of Monastir,
University of Monastir, Av. Ibn Eljazzar 5019 Monastir, Tunisia
{riadh.bhadj,moez.trigui,nizar.aifaoui}@gmail.com

Abstract. Given its economical and technical benefits, the assembly sequence planning remains an indispensable process during the life-cycle of a mechanical product. Many approaches and methods had been proposed to design and optimize the assembly sequences of a mechanical product. Moreover and in order to be more efficient, many researchers adopted integrated solutions to the CAD systems. In this paper an approach using a collision study and permitting the generation of the assembly sequences planning of a mechanism is proposed. The collision test is performed by the use of both the API and the interference test tool of the CAD software. Driven by the obtained results and the collected data from the CAD assembly file, the developed algorithm determines only feasible sequences.

Keywords: ASP, assembly model, integrated design, collision study.

1   Introduction

The assembly sequence planning (ASP) is an innovative concept which allows the improvement of the assembly design. The ASP offers many economical and technical advantages such as the control of the production costs and the improvement of the maintenance processes. Given its advantages, the ASP problem has taken its place into the life-cycle of mechanical products and it has been the subject of many research works.

In the literature, several works have been proposed to generate and/or to optimize the assembly plans using various methods such as graphs, questions, heuristics and geometric reasoning based approaches. The methods based on geometric reasoning, employ generally an interference analysis to carry out or to check the feasibility of the assembly plans. Some relevant examples of contributions about this object are as follows: Dini and Santochi are the firsts to propose an approach which uses interference matrices (Dini and Santochi 1992). This method, allows the detection of subassemblies based on the product's interference, contact, and connection matrices. Dini and Santochi modelled the interferences through six

matrices according to ±X, ±Y and ±Z axes. Huang et al. proposed an improved method to generate disassembly sequences based on the interference matrices (Huang et al. 2002). Ciszak proposed an approach which combines the theory of graphs, heuristics algorithms and collision matrix to generate and simulate ASP (Ciszak 2012). Liu et al. developed an integrated approach to CAD system which carries out the disassembly sequences using the interference matrix and calculation of the disassembly constraint degree of components (Liu et al. 2013). The proposed method allows the inspection of the manoeuvrability of the assembly tool, however, it's limited to X,Y and Z axes. Viganò and Gómez proposed an automatic method based on the contacts and interferences data acquired from the assembly model (Viganò and Gómez 2013). The proposed approach generates at least a feasible solution. The cited contributions above are based on Dini and Santochi interference matrices which are restricted to the three axes of the coordinate system. Hu et al. proposed an integrated method which determines the disassembly paths by using the information extracted from the mating features of components (Hu et al. 2002). This method uses an interference test to check the non-presence of collision during the disassembly of components.

In this work, an automatic approach integrated to CAD system which generates feasible assembly sequences based on collision study is presented. The different stages of the developed approach are explained through an illustrative example.

2 Collision Study

The collision study is performed in order to describe spatial relations between components by identifying any obstacles which may be present in the assembly path. In this work, each component of the mechanical assembly is moved by a translational displacement to simulate its disassembly. During this movement, the analyzed component may collide with other elements of the mechanism. In this case, the names of the interfering elements are retrieved and saved. When the component arrives at the final point of displacement, it returned to its initial position in order to be analyzed in another direction. This procedure is repeated with all components of mechanism.

Figure 1 shows an illustrative example used to explain the developed algorithm. The considered mechanism is an air starting valve composed of ten components.
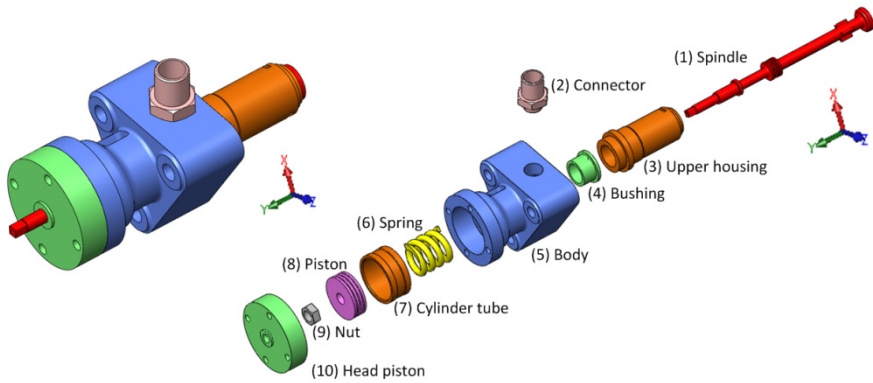
Fig. 1 Illustrative example: Air starting valve

2.1 Assembly Directions

The collision study is performed according to defined directions which are specifics to each component. In the literature, approaches based on interference study use interference matrices in which the components are tested along the ±X, ±Y, and ±Z axis of the coordinate system of the mechanical product. However, this method may constitute a limitation to generate ASP especially with the complex geometry mechanism. As an example, the component "Connector" of the illustrative mechanism, can be assembled along the Δ axis which is an inclined axis specified by the director vector $\vec{U}$ (Fig. 2).

Where

$$\vec{U} = 0,92\vec{x} + 0,39\vec{z}$$
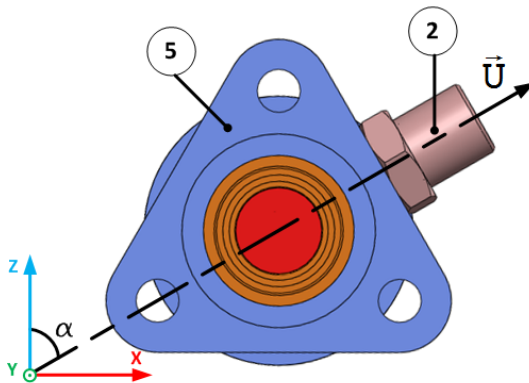
Fig. 2 Example of inclined assembly direction

To ensure accurate results and to be compatible with any component having specific shapes, the collision test is carried out along directions deduced from the assembly constraints "mates" of the CAD model. The algorithm of identification of assembly directions is illustrated by the flowchart in the figure 3. The main idea of the proposed algorithm is the analysis of the contact type and the director vector of assembly constraints.
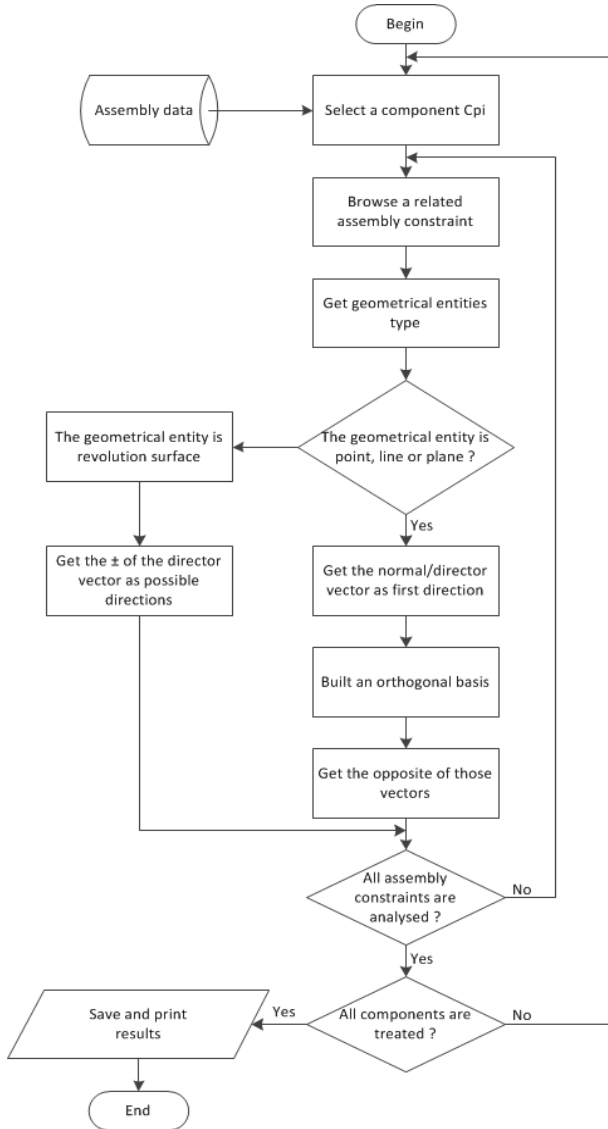
Fig. 3 Flowchart of directions identification algorithm

2.2 Collision Results

Given the diversity, each component can have a different set of possible assembly directions according to its geometric position. The results of the approaches based on Dini and Santochi method, are presented in six interference matrices. Differently to the previous cited approaches, the developed approach presents the results as tables. Each table, representing the collisions results for a specific component, contains the interfering elements according to directions of the analysed component. Table 1 presents an example of the connector collision study of illustrative example. As it can be noticed, the connector collides with body, spindle, bushing and upper housing according to Δ axis.

Table 1 Collision results of component "Connector"

Component name	Connector	
Direction [i, j, k]	[0,92, 0, 0,39]	[-0,92, 0, -0,39]
Interfering components names		Body
		Spindle
		Bushing
		Upper housing

3 Assembly Sequence Generation Process

To generate ASP, the developed algorithm begins by the calculation of a score to each component. These scores will be used for identification of the base element and to rank components. Subsequently, the algorithm searches the sequences based on geometric reasoning which uses the contact relationship between components and the collision results.

3.1 Scores Components Calculation

Given the lack of information about the precedence relationships, a score calculation for each component was proposed. The component score is calculated via the volume, area and the number of relationships.

The calculated scores serve in the first step to define the base component on which most elements will be assembled. In fact, the base component must have the higher score and can't be a fastener element. In a second stage, those scores will be used by the ASP algorithm for the components' ordering. The algorithm of scores calculation and base component identification is presented by the flowchart in figure 4.

For a component Cp_i, the score Sc_i is calculated according to formula (1)

$$Sc_i = 0,35.\frac{V_i}{V_a} + 0,35.\frac{A_i}{A_a} + 0,3.Nb \tag{1}$$

where
- V_i and A_i are respectively the volume and area of the component Cp_i,
- V_a and A_a are respectively the average volume and area of components constituting the assembly,
- Nb represents the number of relationships of component Cp_i
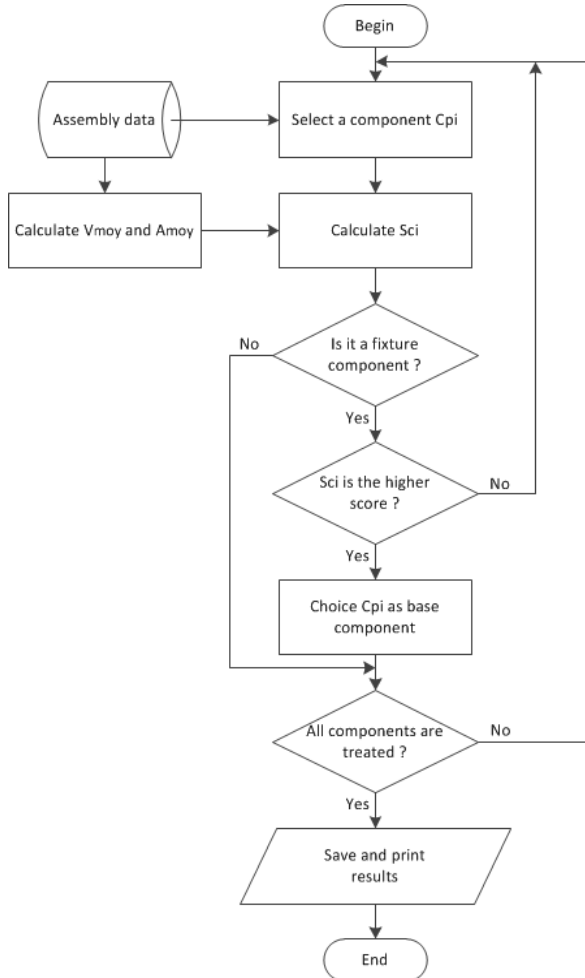
Fig. 4 Algorithm of scores components **calculation and base identification**

3.2   Assembly Sequences

Once the collision study is accomplished the ASP algorithm, presented by the flowchart in figure 5, begins by the scores calculation process. Thereby, all components are sorted in decreasing order according to their scores then the base component is identified. Therefore, the algorithm selects the related components

with the base component respecting the score order. For each related component, the algorithm analyses the possible assembly directions (presented in section 2.1). If the checked direction doesn't present an assembled element, then, it's considered as an assembly direction for the present component. Once all component related to the base are assembled, the algorithm denotes an assembled component as a new base component by respecting the descending order of scores. This procedure is repeated until all components are processed.

In some cases, a component with lower score must be assembled before another having a higher one. When the algorithm detects the impossibility of assembling a component, it changes the order of the concerned element and re-executes the procedure until solving the problem.

On the illustrative example, the calculated scores are presented in table 2. The base component is the body (5). The algorithm begins by assembling components related to this element by respecting the descending order of scores. During this process, a case of impossible assembly was detected. A demonstration to solve this problem is explained as follows:

Step1: (5)

Step2: (5) → (3)

Step3: (5) → (3) → (10)

Step4: (5) → (3) → (10) → (7): Component (7) can't be assembled ⇒ Impossible sequence ⇒ Permutation of (7) with (10) and re-execute the ASP algorithm.

Step5: (5) → (3) → (7) → (10) → (6): Component (6) can't be assembled ⇒ Impossible sequence ⇒ Permutation of (6) with (10) and re-execute the ASP algorithm.

Step6: (5) → (3) → (7) → (6) → (10) → (4) Component (4) can't be assembled ⇒ Impossible sequence ⇒ Permutation of (4) with (10) and re-execute the ASP algorithm.

Step7: (5) → (3) → (7) → (6) → (4): Component (4) can't be assembled ⇒ Impossible sequence ⇒ Permutation of (4) with (6) and re-execute the ASP algorithm.

Step8: (5) → (3) → (7) → (4): Component (4) can't be assembled ⇒ Impossible sequence ⇒ Permutation of (4) with (7) and re-execute the ASP algorithm.

Step9: (5) → (3) → (4): Component (4) can't be assembled ⇒ Impossible sequence ⇒ Permutation of (4) with (3) and re-execute the ASP algorithm.

Step10: (5) → (4) → (3) → (7)

After a few iterations, the final result of the air starting valve is presented by figure 6.
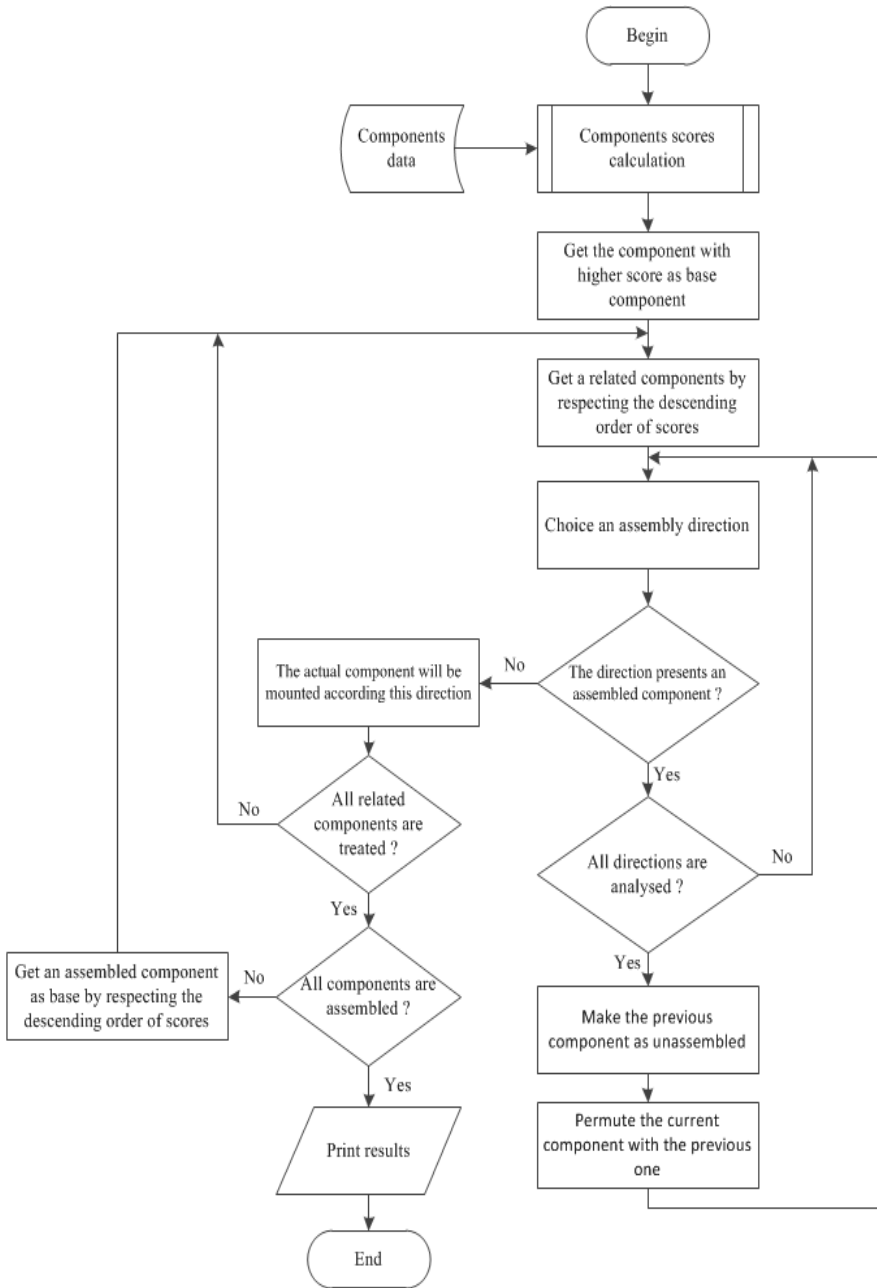
Fig. 5 General algorithm of assembly sequence generation

Table 2 Calculated scores of the illustrative example

	Component	Score Sc
1	(5) Body	4,981901535
2	(1) Spindle	1,941839493
3	(8) Piston	1,518659854
4	(3) Upper housing	1,403503685
5	(10) Head piston	1,298692677
6	(7) Cylinder tube	0,864483507
7	(6) Spring	0,861620095
8	(4) Bushing	0,735552781
9	(9) Nut	0,638321465
10	(2) Connector	0,555424907

	Component	Direction	Score
	(5) Body		4,98190153
1	(4) Bushing	[0, 1, 0]	0,73555278
2	(3) Upper housing	[0, 1, 0]	1,40350369
3	(7) Cylinder tube	[0, -1, 0]	0,86448351
4	(6) Spring	[0, -1, 0]	0,86162009
5	(2) Connector	[-0,92, 0, -0,39]	0,55542491
6	(1) Spindle	[0, 1, 0]	1,94183949
7	(8) Piston	[0, -1, 0]	1,51865985
8	(9) Nut	[0, -1, 0]	0,63832147
9	(10) Head piston	[0, -1, 0]	1,29869268

Fig. 6 ASP results of the air starting valve example

4 Conclusion

In this work, an automatic approach for generating assembly sequences based on collision study and relationships between components was presented. The collision study permits the detection of any eventual interference during the assembly of components. Then, an algorithm of ranking components and determining the assembly directions was performed. Finally, the presented approach does not need prior precedence knowledge and it offers the advantage of generating only possible sequences.

References

Dini, G., Santochi, M.: Automated sequencing and subassembly detection in assembly planning. Annals CIRP 41(1), 1–4 (1992)

Huang, Y.M., Huang, C.T.: Disassembly matrix for disassembly processes of products. International Journal of Production Research 40(2), 255–273 (2002)

Ciszak, O.: Computer aided determination of the assembly sequence of machine parts and sets. Advances in Engineering Software 48, 17–26 (2012)

Liu, X., Liu, Y., Xu, B.: A converse method-based approach for assembly sequence planning with assembly tool. The International Journal of Advanced Manufacturing Technology 69(1), 1359–1371 (2013)

Viganò, R., Gómez, O.G.: Automatic assembly sequence exploration without precedence definition. Int. J. Interact. Des. Manuf. 7, 79–89 (2013)

Hu, D., Hu, Y., Li, C.: Mechanical Product Disassembly Sequence and Path Planning Based on Knowledge and Geometric Reasoning. International Journal of Advanced Manufacturing Technology 19, 688–696 (2002)

Optimisation of Machining Parameters in Hard Turning by Desirability Function Analysis Using Response Surface Methodology

Nabil Kribes[2], Zahia Hessainia[1], and Mohamed Athmane Yallese[1]

[1] Mechanics and Structures Research Laboratory (LMS), May 8th 1945 University,
   P.O. Box 401, Guelma 24000, Algeria
   `normila1@yahoo.fr`
[2] Laboratory (LMANM) May 8th 1945 University, P.O. Box 401, Guelma 24000, Algeria
   `normila1@yahoo.fr`

Abstract. In this study, the effects of cutting speed, feed rate and depth of cut on surface roughness in the hard turning were experimentally investigated. AISI 4140 steel was hardened to (56 HRC) .The cutting tool used was an uncoated AL_2O_3/TiC mixed ceramics which is approximately composed of 70% of AL_2O_3 and 30% of TiC. Three factor (cutting speed, feed rate and depth of cut) and three-level factorial experiment designs completed with a statistical analysis of variance (ANOVA) were performed. Mathematical model for surface roughness was developed using the response surface methodology (RSM) associated with response optimization technique and composite desirability was used to find optimum values of machining parameters with respect to objectives surface roughness. The results have revealed that the effect of feed is more pronounced than the effects of cutting speed and depth of cut, on the surface roughness. However, a higher cutting speed improves the surface finish. In addition, a good agreement between the predicted and measured surface roughness was observed. Therefore, the developed model can be effectively used to predict the surface roughness on the machining of AISI 4140 steel with in 95% confidence intervals ranges of conditions studied.

Keywords: Hard turning, Surface roughness prediction, Response surface methodology (RSM), Ceramic tool, ANOVA, desirability.

1   Introduction

The surface roughness of machined parts is a significant design specification that is known to have considerable influence on properties such as wear resistance and fatigue strength. The quality of the surface is a factor of importance in the evaluation of machine tool productivity. Hence it is important to achieve a consistent tolerance and surface finish. When surface finish becomes the main criteria in the quality control department, the productivity of the metal cutting operation is limited by the surface quality. According to (Palanikumar.k et al 2008) and

(Thomas TR 1981), surface finish can be characterised by various parameters. The various roughness height parameters such as arithmetic average roughness average (Ra), maximum height of peaks (Rp), root mean square (Rq), maximum height of the profile (Rt) and mean of the third point height (R3z) can be closely correlated. The present study uses average roughness (Ra) for the characterisation of surface roughness, being that used most widely in the industry for specifying surface roughness. Response Surface Method (RSM) is an empirical modeling approach for determining the relation ship between various process parameters and the responses with the various desired criteria, by means of which we can further search the significance of these process parameters on the coupled responses. It is a sequential experimentation strategy for building and optimizing the empirical model. Therefore, RSM is a collection of mathematical and statistical procedures that are useful for the modeling and the analysis of problems in which response of demand is affected by several variables and the objective is to optimize this response (Montgomery D C 2001). Through using the design of experiments and applying regression analysis, the modeling of the desiring response to several independent input variables can be gained. Consequentially, the RSM is utilized to describe and identify with a great accuracy, the influence of the interactions of different independent variables on the response when they are varied simultaneously. In addition, it is one of the most widely used methods to solve the optimization problem in the manufacturing environments as studied by (York Puri A B et al 2005), (Ozcelik B et al 2005)] Most of the previous investigators have studied the effect of cutting variables such as speed, feed and depth of cut using response surface methodology has been widely reported in literature ((Choudhury L A 1997), (Arbizu I P et al 2003), (Dabnun M A 2003), (Sahin Y et al 2003), (Cakir M C et al 2009), (Hessainia Z et al 2013), (Kribes N et al 2012)). In this paper, an experimental contribution that focuses on prediction and optimization of surface roughness during hard turning of AISI 4140 steel with **Al_2O_3 + TiC mixed** ceramic tool, using response surface methodology is presented. The ANOVA involve the effects of cutting parameters (cutting speed, feed rate and depth of cut).

2   Experimental Procedure

2.1   Equipment and Materials

The goal of this experimental work was to investigate the effects of cutting parameters on surface roughness, and to establish a correlation between them. In order for this cutting speed, feed rate and depth of cut were chosen as process parameters.

The work material was AISI 4140 steel in the form of round bars with 74mm in diameter and 380mm in length. The work material was hardened and tempered to 56 HRC. Chemical composition of work material is as follows: 0.42% C; 0.25% Si, 0.08% Mn; 0.018% S; 0.013% P; 0.021% Ni; 0.022% Cu; 1.08% Cr; 0.004% V; 0.209% Mo; 96.95% Fe.

The cutting tests were conducted in dry conditions using a universal lathe type SN40 with 6,6KW spindle power.

The cutting tool used was uncoated AL2O3 + TiC mixed ceramic which is approximately composed of 70% of AL2O3 and 30% of TiC. Mixed ceramic tool, type SNGA120408T01020 was clamped onto a tool holder with a designation of PSBNR 25×25K12, its geometry is as follows -6° rake angle, 6°clearance angle, -6° inclination angle and 75° approach angle, nose radius of 0.8mm.

Surface roughness measurements were performed by using a Surftest 201 Mitutoyo with a cut-off length of 0,8mm and sampling length of 5mm. (Fig 1)

Fig. 1 (a) Surftest 201 Mitutoyo, (b) Expérimental configuration for measuring surface roughness

Three levels were specified for each of the factors as indicated in Table 1. A randomized schedule of runs was created using the design of experiment shown in Table 2.

Table 1 Attribution of the levels to the factors

Level	Cuttingspeed, Vc (m/min)	Feed rate, f (mm/rev)	Depth of cut, ap (mm)
1 (low)	90	0.08	0.15
2 (medium)	120	0.12	0.30
3 (high)	180	0.16	0.45

2.2 Design of Experiments

The response surface methodology (RSM) is a procedure for determining the relationship between the independent process parameters with the desired response and exploring the effect of these parameters on responses, including six steps (Gained V N et al 2009).

These are, (1) define the independent input variables and the desired responses with the design constants, (2) adopt an experimental design plan, (3) perform regression analysis with the quadratic model of RSM, (4) calculate the statistical analysis of variance (ANOVA) for the independent input variables in order to find which parameter significantly affects the desired response, then, (5) determine the situation of the quadratic model of RSM and decide whether the model of RSM needs screening variables or not and finally, (6) optimize and conduct confirmation experiment and verify thes predicted performance characteristics.

In the current study, the relationship between the inputs, called the cutting conditions such as cutting speed (Vc), feed rate (f) and depth of cut (ap) and the out put Y define as a machinability aspect for cutting forces and surface roughness is given as:

$$Y = F(Vc, f, ap) + e_{ij} \tag{1}$$

Where Y is the desired machinability aspect and F is proposed by using a nonlinear quadratic mathematical model, which is suitable for studying the interaction effects of process parameters on machinability characteristics.

In the present work, the RMS based second order mathematical model is given by [15]:

$$Y = a_o + \sum_{i=1}^{3} a_i X_i + \sum_{i=1}^{3} a_{ii} X_i^2 + \sum_{i \angle j}^{3} a_{ij} X_i X_J \tag{2}$$

Table 2 Design layout and experimental results(Hessainia Z 2014)

Run	Coded factors			Actual factors			Surface roughness (μm)		
	X_1	X_2	X_3	Vc	f	ap	Observed	Predicted	%
				(m/min)	(mm/rev)	(mm)	Value	Value	Error
01	-1	-1	1	90	0.08	0.45	0.43	0.44	-2.32
02	1	0	1	180	0.12	0.45	0.49	0.49	0.00
03	1	0	0	90	0.12	0.30	0.66	0.64	3.03
04	-1	0	-1	90	0.12	0.15	0.64	0.62	3.12
05	-1	-1	-1	90	0.08	0.15	0.39	0.39	0.00
06	1	1	0	180	0.16	0.30	0.53	0.52	1.88
07	1	-1	0	180	0.08	0.30	0.32	0.31	3.12
08	0	-1	0	120	0.08	0.30	0.35	0.34	2.85
09	-1	1	1	90	0.16	0.45	0.78	0.77	1.28
10	0	-1	1	120	0.08	0.45	0.37	0.36	2.70
11	-1	1	-1	90	0.16	0.15	0.72	0.72	0.00
12	0	1	0	120	0.16	0.30	0.63	0.62	1.58
13	1	-1	1	180	0.08	0.45	0.34	0.33	2.94
14	1	-1	-1	180	0.08	0.15	0.30	0.30	0.00
15	1	1	-1	180	0.16	0.15	0.51	0.50	1.96
16	1	0	-1	180	0.12	0.15	0.46	0.46	0.00

Table 3 (*continued*)

17	-1	0	1	90	0.12	0.45	0.68	0.66	2.94
18	0	0	0	120	0.12	0.30	0.54	0.54	0.00
19	0	-1	-1	120	0.08	0.15	0.33	0.32	3.03
20	1	0	0	180	0.12	0.30	0.47	0.47	0.00
21	1	1	1	180	0.16	0.45	0.55	0.54	1.81
22	0	0	1	120	0.12	0.45	0.56	0.56	0.00
23	0	1	-1	120	0.16	0.15	0.62	0.61	1.61
24	-1	-1	0	90	0.08	0.30	0.41	0.41	0.00
25	0	0	-1	120	0.12	0.15	0.51	0.52	-1.96
26	0	1	1	120	0.16	0.45	0.64	0.65	-1.56
27	-1	1	0	90	0.16	0.30	0.74	0.75	-1.35

Where ao is constant, ai, aii, and aij represent the coefficients of linear, quadratic and cross product terms, respectively. Xi reveals the coded variables that correspond to the studied machining parameters. The coded variables Xi,i = 1,2,3 are obtained from the following transformation equations.

$$X_1 = \frac{Vc - Vco}{\Delta Vc} \tag{3}$$

$$X_2 = \frac{f - fo}{\Delta f} \tag{4}$$

$$X_3 = \frac{ap - apo}{\Delta ap} \tag{5}$$

Where X1, X2 and X3 are the coded values of parameters Vc, f and ap respectively. Vco, fo and apo at zero level. ΔVc, Δf and Δap are the values of Vc, f, and ap, respectively.

3 Data Analysis Results and Discussion

The plan of the experiment was developed for assessing the influence of the cutting speed (*Vc*), feed rate (*f*) and depth of cut (*ap*) on the surface roughness (*Ra*). Table 2 illustrates the experimental results for *Ra*.

The ANOVA table in this study shows that all these five factors are significant well with p-value equal to zero. The variance ratio, denoted by F in ANOVA tables, is the ratio of the mean square due to a factor and the error mean square. In robust design F ratio can be used for qualitative understanding of the relative factor effects. A large value of F means that the effect of that factor is large compared to the error variance. So, the larger value of F, the more important that factor i influencing the response. In present study, the most significant factor was feed rate with 353.27 F ratio and importance most of other factors based on the F was quadratic effect of feed rate, interaction effect of cutting speed and feed rate,

quadratic and effect of cutting speed, respectively. The percentage of each factor contribution (P) on the total variation thus indicating the degree of influence on the result. After analyzing, it may be observed that the *f* factors (P ≈ 67.32%), the *Vc* (P ≈ 22.02 %) and the interaction *Vc×Vc* (P ≈ 2.32%), *f×f* (P ≈ 4.09%) also have considerable influence on the surface roughness, especially the feed rate factor this is a good agreement with the previous researchers' works ((Choudhury L A 1997), (Arbizu I P et al 2003), (Dabnun M A 2003), (Sahin Y et al 2003), (Cakir M C et al 2009)). The *ap* factor, the interactions of *ap×ap* and *Vc×ap* do not present significative percentages of contribution on the obtained surface roughness (*Ra*).

Design of Experiments

Estimated regression coefficients for surface roughness using data in uncoded units are shown in Table 4. The quadratic model of response equation in terms of actual factors for surface roughness (*Ra*) is given below in Eq. (6).

$$Ra = -0.0438 - 6.4 \times 10^{-4} Vc + 14.508\, f + 1.44 \times 10^{-1} ap$$
$$+ 2.51 \times 10^{-5} Vc^2 - 36.805\, f^2 - 1.71 \times 10^{-2} Vc \times f \tag{6}$$

R^2 value of the model is 99.5%, which shows that the model can explain 99.5% of total variations in surface roughness.

The percentage error for each experimental run was calculated by the following relation

$$\% error = \frac{\exp erimental value - predicted value}{\exp erimental value} \times 100 \tag{7}$$

It is evident from the Table 2 that the error between the experimental value and predicted value is less than 5%.

Table 4 Pearson correlation coefficient of parameters with (Ra)

Parameter	Pearson correlation coefficient
Constant	-0.04382
Vc	-0.00645
f	14.5089
ap	0.14497
Vc×Vc	0.00002
f×f	-36,8056
Vc×f	-0.01716

4 Optimization of Response

One of the most important aims of experiments related to manufacturing is to achieve the desired surface roughness of the optimal cutting parameters (Palanikumar K et al 2006), (Hessainia Z et al 2013). To this end, the response surface optimization is an ideal technique for determination of the best cutting parameters combination in turning.

Here, the goal is to minimize surface roughness (Ra). To resolve this type of parameter design problem, an objective function, F(x), is defined as follows:

$$DF = \left(\prod_{i=1}^{n} d_i^{wi} \right)^{\frac{1}{\sum_{j=1}^{n} wi}} F(x) = -DF \tag{8}$$

$$F(x) = -DF$$

Where di is the desirability defined for the i th targeted output and wi is the weighting of di.

For a goal to search for a minimum, the desirability can be defined by the following formulas:

$$di = 1 \quad \text{if} \quad Y_i \leq Low_i$$

$$di = \left[\frac{High_i - Y_i}{High_i - Low_i} \right] \quad \text{if} \quad Low_i \leq Y_i \leq High_i \tag{9}$$

$$di = 0 \quad \text{if} \quad Y_i \geq High_i$$

Where the Yi is the found value of the i th output during optimization processes; the Lowi and the Highi are, respectively, the minimum and the maximum values of the experimental data for the i th output. In Eq. (9), wi is set to one since the di is equally important in this study. The DF is a combined desirability function (Myers R H et al 2002), and the objective is to choose an optimal setting that maximizes a combined desirability function DF, i.e., minimizes F(x).

RSM optimization result for surface roughness parameter (Ra) is shown in Figure 2 and Table 5 are found to be cutting speed of 156.36 (m/min), feed rate of 0.08 (mm/rev) and depth of cut of 0.15 (mm). The optimized surface roughness parameter is Ra = 0.28 µm.

Table 5 Response optimization for surface roughness parameters

Paramaters	Goal	Optimum combination			Lower	Target	Upper	Predicted reponse
		Vc (m/mm)	f (mm/rev)	ap (mm)				
Ra (µm)	Minimum	156.36	0.08	0.15	0.30	0.30	0.78	0.28

Desirability = 1

Composite desirability = 1
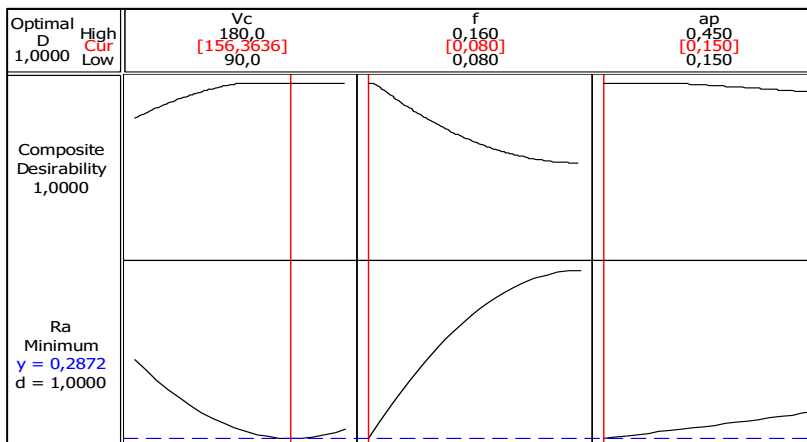
Fig. 2 Response optimization plot for surface roughness parameter components

5   Conclusion

In this paper, the application of RSM on the hard turning of AISI 4140 steel with
Al2O3/TiC mixed ceramic tool had carried out the mathematical model of the sur-
face roughness (Ra) so as to investigate the influences of machining parameters,
for finding optimum value the following conclusions of research are as follows.

The analysis of machining parameters using RSM technique has the advantage
of investigating the influence of each machining parameter on the value of surface
roughness.

The surface roughness increases with the increase of feed rate and almost de-
creases with the increase of cutting speed.

The best surface roughness was achieved at the lower feed rate and the highest
cutting speed.

Surface roughness model: the feed rate provides primary contribution and in-
fluence most significantly on the surface roughness with 67.32% contribution in
the total variability of model whereas cutting speed has a secondary contribution
of 22.02% in the model. Quadratic effect of feed rate, interaction effect of cutting
speed and feed rate, quadratic effect of cutting speed provide secondary contribu-
tion and account for 4.09%, 2.34% and 2.32%, respectively. in the total variability
of model.

The results of ANOVA and the conducting confirmation experiments have
proved that the mathematical model and predict value of surface roughness which
is close to those readings recorded experimentally with a 95% confident interval.

Using response optimization show that the optimal combination of machining
parameters are cutting speed of 156.36 m/min, feed rate of 0.08 mm/rev, depth of
cut of 0.15 mm. The optimized surface roughness parameter is Ra = 0.28 μm.

References

Palanikumar, K., Mata, F., Davim, J.P.: Analysis of surface roughness parameters in turning of FRP tubes by PCD tool 204, 469–474 (2008)

Thomas, T.R.: Characterisation of surface roughness parameters. Precis. Eng. 3, 2 (1981)

Montgomery, D.C.: Design and Analysis of Experiments. John Wiley & Sons, New York (2001)

York Puri, A.B., Bhattacharya, B.: Modeling and analysis of white layer depth in a wire – cut, EMD process through response surface methodology. Int. J. Mach Manuf. 25, 301–307 (2005)

Ozcelik, B., Erzurmlu, T.: Determination of effecting dimensional parameters on war-page of thin shell plastic parts using integrated response surface method and genetic algorithm. Int. Commun. Heat Mass Transfer 32, 1085–1094 (2005)

Choudhury, L.A., El-Baradie, M.A.: Surface roughness prediction in the turning of high-strength steel by factorial design of experiments. J. Mater. Process. Technol. 67(1-3), 55–61 (1997)

Arbizu, I.P., Perez, C.J.L.: Surface roughness prediction by factorial design of experiments in turning processes. J. Mater. Process. Technol. 143, 390–396 (2003)

Dabnun, M.A., Hashmi, M.S.J., El-Baradie, M.A.: Surface roughness prediction model by design of experiments for turning machinable glass-ceramic (Macor). J. Mater. Proc-ess. Technol. 164-165, 1289–1293 (2003)

Sahin, Y., Motorcu, A.R.: Surface roughness model for machining mild steel with coated car-bide tool. Mater. Des. 26(4), 321–326 (2003)

Cakir, M.C., Ensarioglu, C., Demirayak, I.: Mathematical modeling of surface roughness for evaluating the effects of cutting parameters and coating material. J. Mater. Process. Technol. 209(1), 102–109 (2009)

Hessainia, Z., Belbah, A., Yallese, M.A., Mabrouki, T., Rigal, J.F.: On the prediction of surface roughness in the hard turning based on cutting parameters and tool vibrations. Measurement 46, 1671–1681 (2013)

Kribes, N., Hessainia, Z., Yallese, M.A., Ouelaa, N.: Statistical analysis of surface roughness by design of experiments in hard turning. Mechanika 18(5), 605–611 (2012) ISSN 1392-1207

Hessainia, Z.: Thèse de doctorat, Etude de l'impact des paramètres affectant la rugosité des surfaces et les efforts de coupe en usinage des pièces traitées thermiquement, Université de 08 Mai 1945 Guelma (2014)

Gained, V.N., Karnik, S.R., Faustino, M., Davim, J.P.: Machinability analysis in turning tung-sten-copper composite for application in EDM electrodes. Int. J. Refract. Metals Hard Mater. 27, 754–763 (2009)

Palanikumar, K., Karthikeyan, R.: Optimal machining conditions for turning of particulate metal matrix composites using Taguchi and response surface methodologies. Mach. Sci.Technol. 10, 417–433 (2006)

Myers, R.H., Montgomery, D.C.: Response surface methodology: process and product optimization using designed experiments, 2nd edn. John Wiley and Sons, Inc., New York (2002)

Surface Roughness Model and Parametric Welding Optimization in Friction Stir Welded AA2017 Using Taguchi Method and Response Surface Methodology

Khaled Boulahem[1,3], Sahbi Ben Salem[2,3], and Jamel Bessrour[3]

[1] ISET Jendouba, Jendouba University Campus, 8100 Jendouba, Tunisie
`khaboulahem@yahoo.fr`
[2] *IPEI Nabeul*, Mrazka University Campus, 8000 Nabeul, Tunisia
`sahbi_bensalem@yahoo.fr`
[3] Labo MAI, National Engineering School of Tunis, UTM, Tunisia
`jamel.bessrour@enit.rnu.tn`

Abstract. This paper focuses on the development of a mathematical model of arithmetic mean heights of surface (Sa) in friction stir welded AA2017 aluminium alloy using Taguchi L_8 orthogonal design of experiments and response surface methodology. Machining variables such as rotation speed, traverse speed and tool shoulder diameter are considered in building the model. 3D surface topographies are used to characterize the surface roughness. The analysis of variance results showed that all the welding parameters are statistically significant at 95 % confidence level. According to Main Factor Plots, an increase in the rotation speed decreases the surface roughness while any increase in the traverse speed or the tool diameter shoulder increases it.

Keywords: Friction Stir Welding, Surface roughness state, Taguchi method, ANOVA, Response Surface Method.

1   Introduction

Friction-stir-welding (FSW) is a solid-state joining process without using filler metal developed by the Welding Institute in 1991. Compared to other welding processes, FSW is a more economical method that produces better mechanical properties of joints aluminium alloy and fewer weld defects such as cracks and porosity and lower residual stress. Therefore, this technique is useful to join aluminium alloys especially 2xxx and 7xxx series that are difficult to weld by traditional fusion processes. Among the 2xxx series aluminum alloy, AA2017 is most widely used in various industrial sectors; including in the construction, aerospace, aircraft and automotive industries due to its high strength, excellent fatigue and corrosion resistance. Thus, it has been selected as the workpiece

material in this study. In the manufacturing industry, the surface must be within certain limits of roughness to improve corrosion resistance and to reduce life cycle cost. This theory has been studied by (Hatamleh et al. 2009). In addition, (Jolu et al. 2011) also suggested that surface roughness is a kind of irregularity in welding operation responsible of many cases of fatigue crack initiation due to generated stress concentrations.

Therefore, in the case of improving quality of surface roughness joints, many researchers are devoted to define the welding parameters and tool geometry leading to welded joints with optimum surface roughness. Recently, (Shigematsu et al. 2009) found that the rotation speed tool and traverse speed tool are very important parameters in controlling the surface morphology of the joint. Also, (Nejah 2011) suggested that surface roughness is a result of the geometry of the tool and feed rate. The results indicated that an increase in the ratio (transverse speed/rotational speed) improves the surface state.

A number of studies were carried out to develop a mathematical relationship between the welding variables and mechanical properties of the joint by theoretical models and experimental design methodology. The optimal welding conditions were also determined. Nevertheless, (Palanivel et al. 2009) used response surface methodology and Taguchi method in order to estimate ultimate tensile strength of aluminium alloy AA6351 depending on rotation speed, traverse speed and axial force. Thus, (Aydin et al. 2010) studied the multi-response optimization of friction stir welding process for an optimal parametric combination to yield favorable tensile strength and elongation in terms of rotating speed, welding speed and tool shoulder diameter using the Taguchi based Grey relational analysis. Moreover, (Jung et al. 2007) developed mathematical models using response surface methodology and center composite design method to study the effects of parameters (welding speed, rotational speed and tilting angle of the tool tip) on the fatigue strength of the joints of AA6005-T5 alloy sheets.

At last, through our search for works applying Taguchi method in friction stir welding, it appears that optimization of surface roughness in FSW of AA2017 aluminium alloy using Taguchi Method and Response Surface Methodology have not been reported yet in literature.

The overall aim of this research is to predict a mathematical model of arithmetic mean heights of surface (Sa) in friction stir welding of AA2017 Aluminum alloy in terms of rotation speed tool, transverse speed, and tool shoulder diameter using Taguchi method and Response Surface Methodology.

2 Experimental Work and Conditions

2.1 Materials

This study carried out using MOMAC milling machine, which had 7 kw spindle motor. The workpieces materials used were AA2017-T351 aluminum alloy plates in the form of 25x80x6 clamped on the machine milling table as shown in (fig.1.a). The chemical composition and mechanical properties of the base

material are presented in (Tables 1 and 2). The longitudinal direction of the FSW was perpendicular to the rolling direction of AA 2017 aluminium alloy. Butt welding configuration was followed to fabricate the joints (fig. 1.b).

A rolling tool welding made of high carbon steel with conical threaded pin profile and concave shoulder was used in this work (fig. 1.c). The dimensions of the tool are shown in (Table 3). Tow specimens were prepared from each joint to evaluate the surface roughness.

Table 1 Chemical compositions and mechanical proprieties of AA2017-T351

Si	Fe	Cu	Mn	Mg	Cr	Zn	Al
0.20 à 0.80	0.7	3.5 à 4.5	0.40 à 1.0	0.40 à 1.0	0.1	0.25	Balance

Table 2 Mechanical properties of the base plate AA2017-T351 alloy

Yield strength (MPa)	Tensile strength (MPa)	Elongation (%)	Vickers Hardness (HV)
380	450	12	125

Table 3 Tools dimension

Process parameters	Values
Tool shoulder diameter D(mm)	18 ; 22
Pin diameter , d (mm)	6
Angle of taper pin(◦)	$\beta = 2°$
Pin length (mm), L (mm)	5.7
Tool inclined angle (◦)	3°
Pitch of threaded pin (mm)	1.1
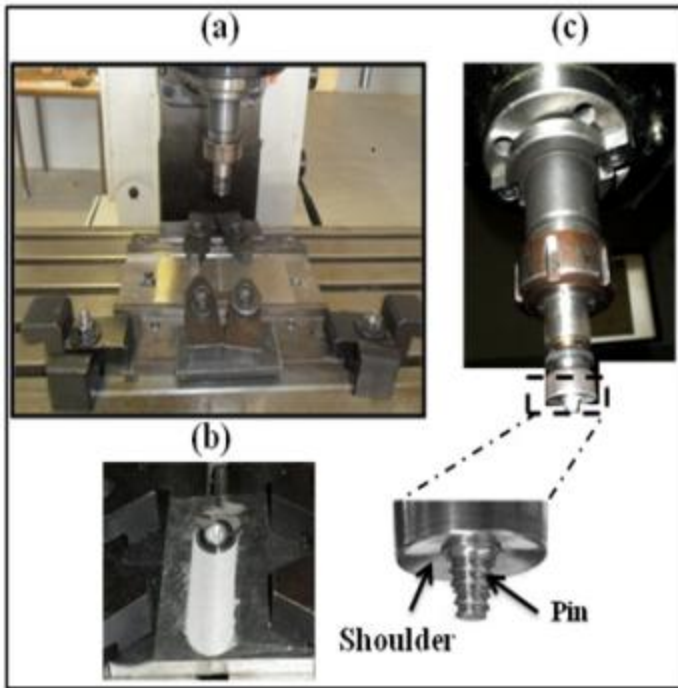
Fig. 1 Friction stir welding machine (a) The clamping devices, (b) Butt welding configuration and (c) welding tool shape

2.2   Surfaces Roughness Measurements

Surface roughness of welded joint is defined as the inherent irregularities of the work piece form circular holes affected by interaction tool/workpiece. The parameter used in this study to characterize surface roughness is the arithmetic mean heights of surface (Sa), which is given in (Eq. 1). In addition, the output process parameters were obtained using a 3D optical profilometer surface treated by software program MountainsMap. The layout of

$$Sa = \frac{1}{a} \iint_a |Z(x, y)| dx \, dy \tag{1}$$

Where "a" is the surface taken for observation and "z" the ordinate of the surface roughness.

2.3   Parameters Process

The parameters selected for experimentation are tool rotational speed (N), traverse speed (T) and tool shoulder diameter (D) (Table 4).

Table 4 Friction stir welding parameters and their levels

No.	Parameters	Notation	Unit	Levels	
				Min	Max
1	Rotation speed	N	rpm	1280	1700
2	Traverse speed	T	mm/min	67	86
3	Tool Shoulder diameter	D	mm	18	22

3 Analysis of Experimental Data

3.1 Taguchi Method

The Taguchi method is an experimental method used in to minimize the number of test compared with traditional techniques. It provides a predictive model for finding optimal configurations and the possibility to suggest quickly experimental results. The steps of Taguchi method as follows:

1. Identification input and output parameters of study
2. Selection of proper orthogonal array
3. Analysis of variance (ANOVA) and S/N ratio
4. Development of the mathematical model
5. Identification of the influence of welding parameters on arithmetic mean heights of surface (Sa)
6. Optimization of welding parameters
7. Conclusion

3.1.1 Orthogonal Arrays

Three factors were studied in this research (rotational speed, traverse speed and shoulder diameter). Two levels of each factor were considered for optimum roughness surface of friction stir welded joints of AA2017 aluminium alloy. Therefore, an L_8 Orthogonal Array was selected for this study (Table 5).

Table 5 Experimental conditions and result

Trial number	Welding parameters			Coding			Surface roughness	S/N ratio
	N(rpm)	T(mm/min)	D(mm)	X_1	X_2	X_3	Sa(μm)	
1	1280	67	18	-1	-1	-1	6.64	-16.44
2	1280	67	22	-1	-1	1	12.30	-21.79
3	1280	86	18	-1	1	-1	11.25	-20.90
4	1280	86	22	-1	1	1	21.10	-26.48
5	1700	67	18	1	-1	-1	3.61	-11.15
6	1700	67	22	1	-1	1	6.91	-16.78
7	1700	86	18	1	1	-1	5.81	-15.28
8	1700	86	22	1	1	1	11.70	-21.36

3.1.2   Signal to Noise Ratio

The goal of this research was to produce minimum arithmetic mean heights of surface (Sa) of the friction stir welded joint. A smaller (Sa) values represent the best surface roughness.

In order to evaluate influence of input parameters (N,T and D) on response (Sa); the performance indicator correspondent for this study is the S/N ratio with a lower-the-better characteristic developed by Taguchi (Table 5).The ratio is given by the following equation:

$$\frac{S}{N} = -10 \log_{10}\left(\frac{1}{n}\sum_{j=1}^{n} y_i{}^2\right) \tag{2}$$

y_i is the value of surface roughness for the ith test and n is the total number of the tests.

3.1.3   Analysis of Variation ANOVA

The Analysis of Variance(ANOVA) is a statistical method employed to determine the most significant FSW process parameter on output response characteristics (Sa) using Fisher Ratio test and P-value test with a significance level of P-value<0.05. The ANOVA is calculated by using the statistical software, MINITAB 16.

According to Table 6, rotation speed (N), traverse speed (T) and shoulder diameter (D) have a significantly affect the quality characteristic (Sa). The value of the F-ratio of the shoulder diameter is 18.82, followed respectively by rotation speed F-ratio=16.69 and traverse speed F-ratio=12.84. In addition, the P-value is less than 0.05. These factors have a statistically significant effect on (Sa) at the 95% confidence level (Table 6).

Table 6 ANOVA results for roughness surface

Source	Sum of Squares	Df	Mean Square	F-Ratio	P-Value
N	67.6285	1	67.628	16.69	0.0150
T	52.02	1	52.02	12.84	0.0231
D	76.2613	1	76.2613	18.82	0.0123
RESIDUAL	16.2109	4	4.0527		
TOTAL	212.121	7			

R^2= 92.3577 % Standard Error of Est = 2.03
Adjusted R^2 = 86.626 % Mean absolute error = 1.22
Df :Degrees of freedom, Mean squares :Fisher ratio, P :probability that exceeds the 95 % confidence level.

The R-Squared statistic indicates that the model as fitted explains 92.35% of the variability in (Sa). The adjusted R-squared statistic, which is more suitable for comparing models with different numbers of independent variables, is 86.62%.

The standard error of the estimate shows the standard deviation of the residuals to be 2.03. The mean absolute error of 1.22 is the average value of the residuals.

These results suggest that the developed model best fits to find the (Sa) of friction stir welded AA 2017 aluminium alloy (Table 6).

4   Results and Discussion

4.1   Surface Roughness Model

The empirical model used to describe the output welding parameters (rotational speed, traverse speed and shoulder diameter) to the output process variable (Sa) is expressed as:

$$Sa \ = \ K.N^n.T^m.D^p \tag{3}$$

Whereas (Sa) is the predicted surface roughness (µm) and N, T, D are the input parameters. Application of logarithmic transformation linearizes the above nonlinear equation (Eq. 3).

$$\ln(Rm) \ = \ \ln(k) \ + n \ \ln(N) \ + \ m \ \ln(T) \ + \ p \ \ln(D) \tag{4}$$

Similarly, this model can be represented by this equation:

$$y = \ \beta_0 \ + \beta_1 \ x_1 + \beta_2 \ x_2 + \ \beta_3 \ x_3 \tag{5}$$

Where, y= ln(Sa), x_1=ln(N), x_2=ln(T) and x_3=ln(D)are the logarithms of the output and input parameters, respectively; β_1, β_2 and β_3 are the corresponding coefficients.

The empirical model of arithmetic mean heights of surface (Sa) is:

$$Sa \ (\mu m) \ = \ 0{,}423 \ . N^{-2{,}14} . T^{2{,}07} . D^{3{,}24} \tag{6}$$

Table 7 Levels matrix

Level	Coding	N(rpm)	T(mm/min)	D(mm)
Min	-1	1280	67	18
Max	1	1700	86	22

4.2   Influence of Welding Parameters on Surface Roughness (Sa)

4.2.1 Surface Topography

The visual inspection of the weld seam clearly shows the presence of circular holes on the surface (Fig. 2). These streaks are surface roots of a periodic action of the tool shoulder on the work pieces to weld.

The 3D average surface roughness (Sa) is significantly lower for test number 5. The lower value of arithmetic mean deviation of the surface is Sa=3.61µm and higher value is Sa=21.10 µm (Table 5).The spacing of grooves on the surface of the work piece is based on the traverse and rotation speed of the shoulder that determine the surface state of the weld bead. The ratio traverse/rotation speed

represents the feed rate of the tool which is also the distance traveled by the axis of the tool during one complete rotation.
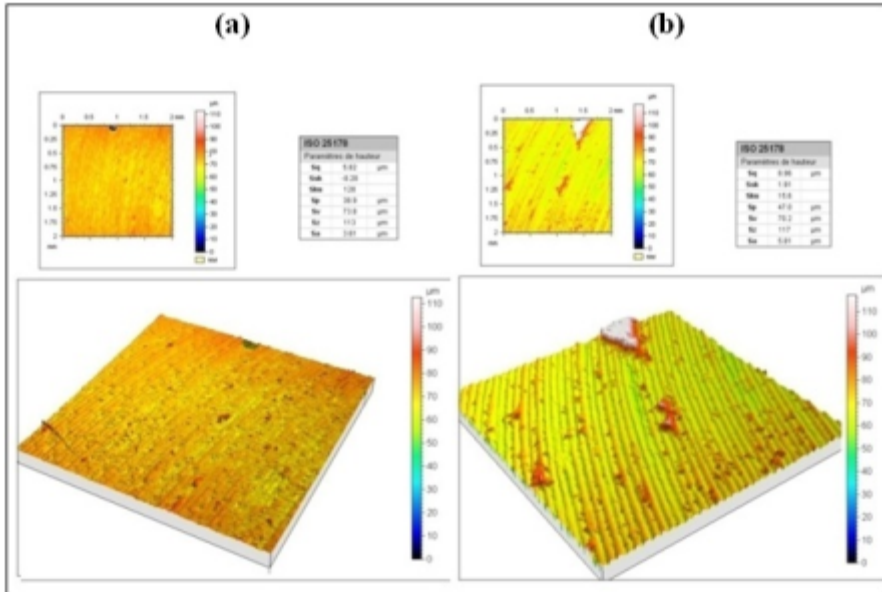
Fig. 2 3D surface topographies for workpieces: (a) (Sa=3.61 μm); (b) (Sa=5.81 μm)

4.2.2 Effects Plot

Fig. 3 shows the effects of the three parameters tested upon the surface roughness parameter (Sa). This graphics contains a curve representing the mean and a curve representing the S/N ratio. According to Main Factor Plots, an increase in the rotation speed decreases the surface roughness while any increase of the traverse speed or the tool diameter shoulder increases it (Fig. 3.a).

The S/N ratio can be used for performance analysis. Moreover, a higher S/N ratio yields the optimal performance and minimal variance. The level that has a higher value determines the optimum level of each factor. For example, in (Fig. 3.b), level one for tool rotation speed (N2= 1700 rpm) has the highest S/N ratio value, which indicated that the machining performance at such level produced minimum variation of the surface roughness. Furthermore, level two of tool transverse speed (T1= 67 mm/min) has indicated the optimum situation in terms of mean value. Similarly, the level three of tool shoulder diameter (D1=18 mm) has also indicated the optimum situation in terms of S/N ratio and mean value.
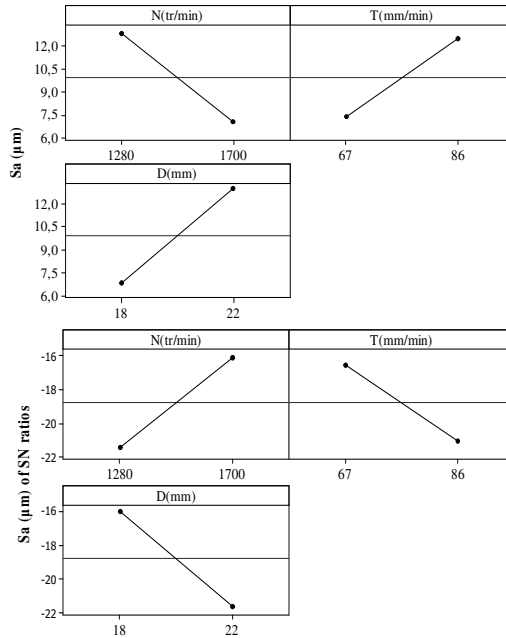
Fig. 3 Effect of process parameters on surface roughness: (a) response mean; (b) S/N ratio

4.3 Optimization of Welding Parameters

4.3.1 Contour Plots and Response Surfaces

Contour plots play a very important role in the study of the response surface analysis. Through the layout of contour plots and Response plots, you can found all the operating conditions that give the same value of the answer. It was a mean for optimizing the parameters of friction stir welding.

One can observe that the best surface roughness values of the objective function are in the dark blue colored areas in the different curves contour plots (Fig. 4). For example, the optimum surface roughness is exhibited for values of (N) around 1470/1700 rpm and for values of (T) around 67/79 mm/min.
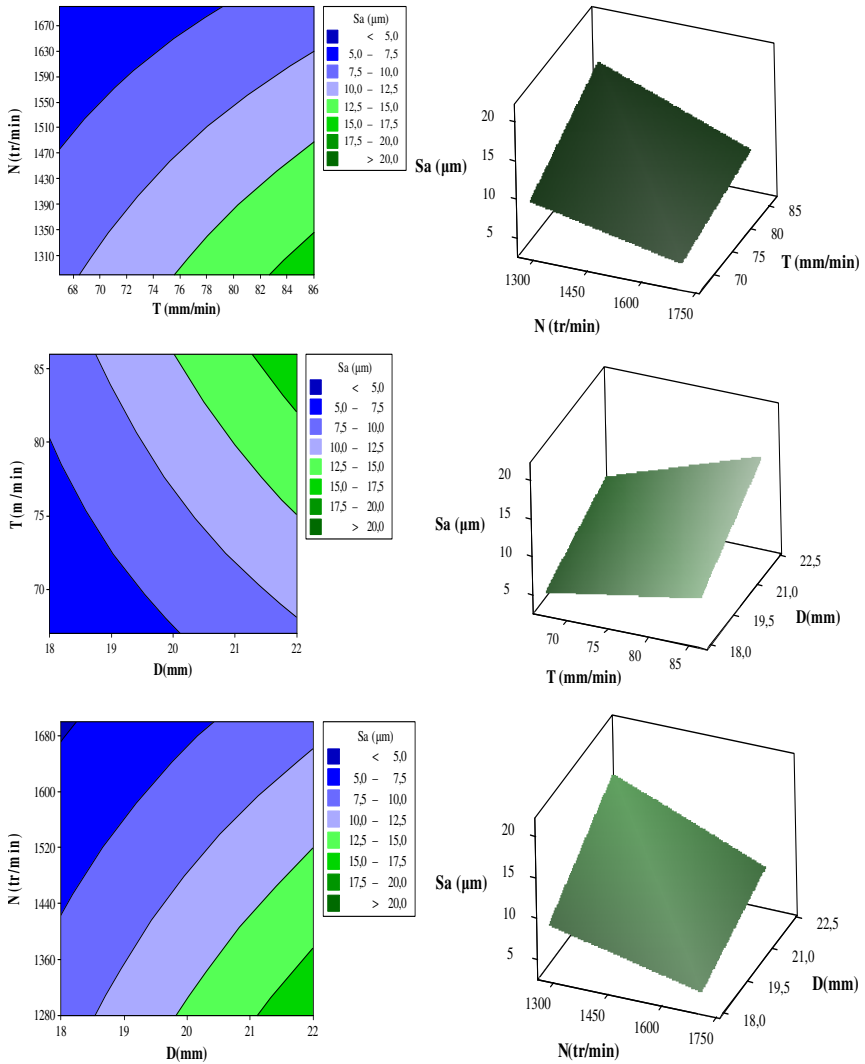
Fig. 4 Contour Plots and Response plots of Sa (μm) for AA 2017

5   Conclusion

This paper has described the use of a design of experiments for conducting experiments. Our model was developed for predicting the arithmetic mean heights of surface (Sa) of friction stir welded AA2017 aluminum alloy using Taguchi method and Response Surface Methodology. The following conclusions were reached:

(1) The optimum levels of the rotational speed, traverse speed and tool shoulder diameter are 1700 rpm, 67 mm/min and 18 mm respectively.

(2) According to the variance analysis results, rotational speed, traverse speed and tool shoulder diameter significantly affect the quality characteristic of the surface roughness (Sa) of the friction stir welded joint.

(3) The surface roughness of the friction stir welded joint decreases with increasing in tool rotation speed but increases with increasing traverse and tool shoulder diameter, respectively.

(4) Contour plots and response surfaces are drawn to study the interaction effect of the welding parameters under study on FSW surface roughness of welded joints of the AA2017 aluminium alloy.

References

Hatamleh, O., Smith, J., Cohen, D., Bradley, R.: Surface roughness and friction coefficient in peened friction stir welded 2195 aluminum alloy. Applied Surface Science 255, 7414–7426 (2009)

Shigematsu, I., Kwon, Y.J., Saito, N.: Dissimilar Friction Stir Welding for Tailor- Welded Blanks of Aluminum and Magnesium Alloys. Materials Transactions 50, 197–203 (2009)

Palanivel, R., Koshy Mathews, P., Murugan, N.: Development of mathematical model to predict the mechanical properties of friction stir welded AA6351 aluminum alloy. Journal of Engineering Science and Technology Review 4, 25–31 (2011)

Aydin, H., Bayram, A., Esme, U., Kazancoglu, Y., Guven, O.: Application of grey relation analysis and taguchi method for the parametric optimization of friction stir welding process. Materials and Technology 44, 205–211 (2010)

Jung, S.P., Park, T.W., Kim, Y.G.: Fatigue strength optimization of friction stir welded A6005-T5 alloy sheets. Science and Technology of Welding and Joining 15, 473–478 (2010)

Le Jolu, T.: Étude de l'influence des défauts de soudage sur le comportement plastique et la durée de vie en fatigue de soudures par friction-malaxage d'un alliage Al-Cu-Li. Dissertation, École nationale supérieure des mines de Paris (2011)

Nejah, J.: Qualification du domaine de soudabilité en soudage par friction malaxage. Dissertation, École Nationale Supérieure d'Arts et Métiers (2011)

Numerical and Experimental Approach in Assisted Cryogenic Machining

Sabrine Trabelsi[1], Zoubeir Bouaziz[1], Guenael Germain[2], and Anne Morel[2]

[1] ENIS
trabelsi4sabrine@gmail.com,
Zoubeir.Bouaziz@enis.rnu.tn
[2] ENSAM Angers
{Guenael.germain,Anne.morel}@ensam.eu

Abstract. Understanding of local mechanisms chip forming during machining by removal of material is difficult, to this end; a cutting finite element modelling is required. This study aims initially to model orthogonal cutting of Ti17 titanium alloy in dry and cryogenic machining and in a second time to study the influence of the application of cryogen during machining on temperature fields and cutting forces in numerical simulation. An experimental study was also conducted to determine the mode of tool wear and the evolution of flank wear.

Keywords: Ti17, cryogenic assistance, numerical simulation, flank wear, cutting forces.

1   Introduction

The use of titanium alloys in the field of aeronautics increases with time having regard to its compatibility with the composite reinforced with carbon fibers (CFRP), but the mechanical characteristics of the material such as its hardness machining, its low conductivity make it difficult to machine [1]. To this end, the cryogenic machining assistance is one of the solutions to reduce the temperature at the tool / chip interface [2-3].

2   Experimental Approach

The machining tests were carried out by a CNC turning machine LEADWELL LTC25iL (2500 rev / min and 24 kW maximum). The acquisition system is composed of a Kistler dynamometer (9257B), the forces exerted on the quartz crystals are transformed into piezoelectric signals as a result of efforts to acquire the three components of the cutting force. The analog signals derived are amplified by a charge amplifier (Kistler 5019B). Thereafter, they are passed to an analog / digital converter. The evolution of the effort over time is provided by the software (Catman Easy).

The uutting parameters for machining Ti17 are: depth of cut ap=1.5mm, feed f=0.3 mm/rev and cutting speed is 0.83 m/s.

Fig. 1 Presentation of the cryogen's flow and the cutting tool

The cutting tool used is Seco PCLNR JetStream 2525 M12 and a plate CNMG 120412-23 shade of H13A, the cutting edge $\alpha = 7\,°$ and the draft angle $\beta = 6\,°$, the radius of curvature of 30 µm.

The liquid cryogen is stored in a ranger equipped with a 15 bar pressure imitator and is then injected on the rake face of the tool by two microbuses of 1.7 mm of diameter.

Cutting tests were performed for both lubrificated and cryogenic cutting of Ti17 to get cutting forces and flank wear.

The criterion of end of life of the tool is set at a flank wear VB=0.3mm and which was measured on constant time using a binocular microscope.
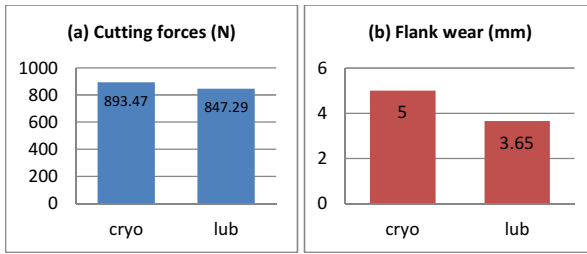
Fig. 2 Cutting forces and flank wear in both cryogenic assistance and wet machining (Vc=50m/min, f=0.3mm/rev, ap=1.5mm)

It is noted that with the cryogenic support there was no reduction in cutting forces, but, on the other hand, the life of the tool has increased 3.65min lubrication 5min which may approximated by an increase of 27%. This may be explained by the decrease of the temperature.

A study was done to determine the mode of tool wear.

- **Degradation Mode of the Tool:**

At first sight of the flank face, we think that the materiel of the tool is being removed by abrasion, to determine the mode of degradation; the cutting insert was examined under scanning electron microscope (SEM)SEM views of worn tools while turning Ti17 under VC = 50 m/min and f= 0.3 mm/rev.
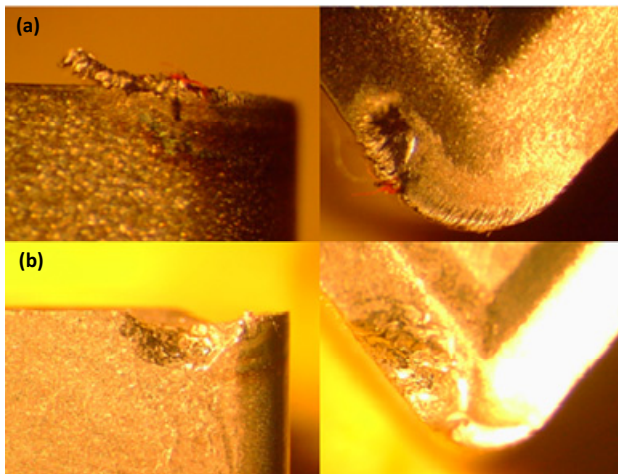
Fig. 3 Microscopic observation of the tool in cryogenic machining at (a) 1min and (b) 4min(f0.3mm/rev;ap1.5)

We found that the percentage of titanium that is the material of the machined piece increases over the time, so we conclude that the principal degradation mode of tool wear is adhesion.
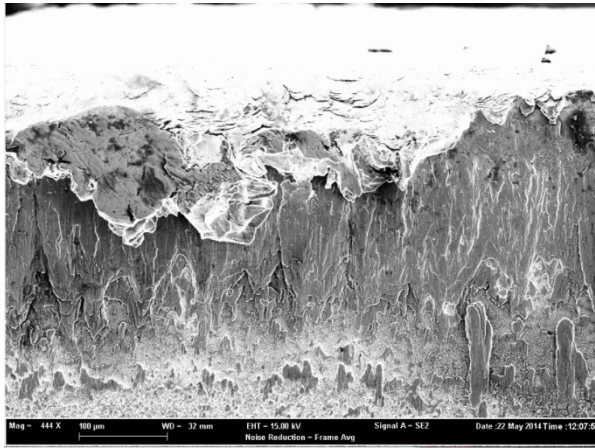
Fig. 4 SEM views of worn tools while turning Ti17 under f=0.3mm/rev and VC = 50 m/min

It is noted that there is a deposition of titanium on the flank face, this shows, that the tool wear is by adhesion, the material accumulated on the surface of the insert is removed after that.

3   Numerical Study

3.1   Model Description

2D model was developed on ABAQUS / explicit 6.11 to model orthogonal cutting. A lagrangian formalism was adopted. The boundary conditions are the embedding of the tool; the lower surface of the part has zero displacement Uy = 0, and the cutting speed is imposed on the left surface of the work piece V1=0.83m/s (Figure5).

The cutting tool is made of tungsten carbide which the parameters are presented in paragraph (2).

CPE4RT elements were used for a coupled temperature-displacement problem.
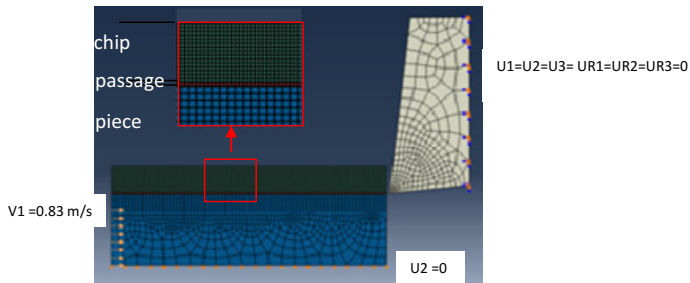
Fig. 5 Boundary conditions

3.2 Law of Material Behavior

The behavior of the material was introduced by Johnson Cook constitutive law [4]. The equation generally used to describe the behaviour of the material is the BC law represents the yield stress of the material [Johnson 1983].

$$\sigma = (A + B\ \varepsilon^n)\ (1 + C\ \ln\frac{\dot{\varepsilon}}{\varepsilon 0})\ [1 - (\frac{T - Tr}{Tm - Tr})^m] \tag{1}$$

σ: equivalent stress vonMises;
ε: equivalent plastic strain;
ε˙: The equivalent plastic strain rate;
ε˙0: The equivalent plastic strain reference rate;
T: work piece temperature.
Tm: Melting
Tr: Room temperature

A, B, C, n and m are material constants determined from tests. The main advantage of this law is the decoupling of the terms of hardening and dependence on strain rate and temperature.

Table 1 The parameters of material behavior Law [5]

A(MPa)	B(MPa)	n	C	m	Tr (°C)	Tm (°C)
1012	399	0.22	0.035	0.85	50	1650

3.3 Damage Law

The use of Lagrangian formalism requires the use of a criterion of separation between the work piece and the chip which is expressed by a deterioration law Johnson and Cook [3] (Johnson et al, 1985). The damage variable is:

$$D = \sum \left(\frac{\Delta \varepsilon_{eq}^p}{\varepsilon_{eq}^{p\ f}} \right) \tag{2}$$

Where ε_{eq}^p is the increment of plastic deformation in a no integration and $\varepsilon_{eq}^{p\ f}$ current equivalent plastic strain at break:

$$\varepsilon_{eq}^{p\ f} = [D1 + D2\ \exp (D3\ \sigma^*)]\ (1 + D4\ \ln \dot{\varepsilon}^{p\ *})\ [1 + D5\ T^*] \tag{3}$$

D1, D2, D3, D4 and D5 are constants for the material σ *: The stress triaxiality rate defined by the P / σ_{vm} where P is the hydrostatic pressure and σ_{vm} rupture is reached when the damage variable D = 1. The corresponding element is deacti-

vated. The variables and $\dot{\varepsilon}p$ and $T * = (T-Tr) / (Tm-Tr)$ are identical to those defined in the constitutive law (1).

Table 2 The parameters of the damage law [5]

D1	D2	D3	D4	D5	$\dot{\varepsilon} 0$
-0.2	0.34	-0.5	-0.035	2.7	0.1

3.4 Modelling of Cryogenic Support

In our simulation, the elements of the damaged portion are removed after the passage of the tool, it is the lower surface of the chip which rubs on the tool. To simulate the application of the cryogenic jet on the rake face and in the lower surface of the chip detached from the tool, we use the programming software Python. The approach is as follows (fig7)

The tool rake face is a right which can determine the equation:

$$y_{tool} = a * x_{tool} + b$$
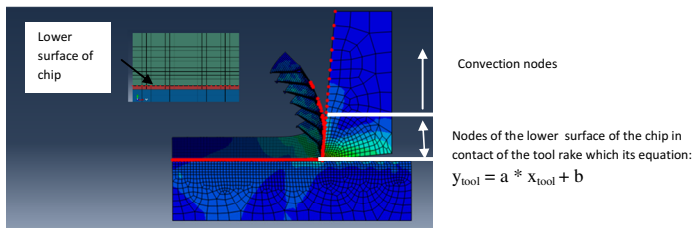
Fig. 6 Determination of convection nodes

dx is the distance of remoteness of the nodes with respect to the cutting face from which convection is applied.

The nodes of the lower surface of the chip which are more in contact with the face of the tool ie if $[x_{chip} <((y_{chip}-b) / a) -dx]$ then applied convection at this node.

In those nodes, convection is applied with a temperature sink of -196°C. (figure 6)
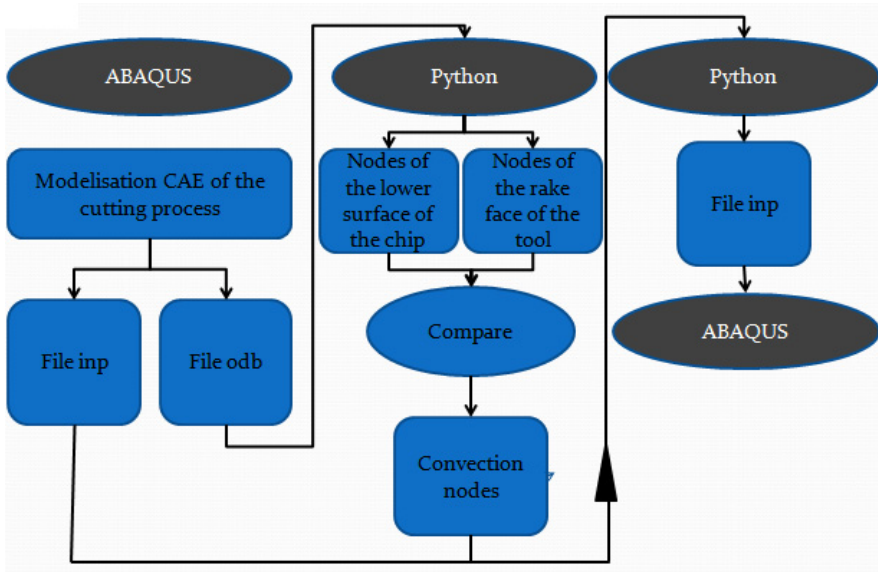
Fig. 7 Steps of modeling the convection on the rake face

4   Results and Discussion

4.1   Temperature Fields

Ti17 titanium alloys generates segmented chip at the cutting speed of Vc=50m/min and the feed rate f = 0.3mm / rev.

The maximum temperature is 861.4° C in dry machining, while in cryogenic support it decreases to 659°C in the secondary shear zone, that's cooled the tool avoiding degradation modes at high temperatures and increases its life and provides
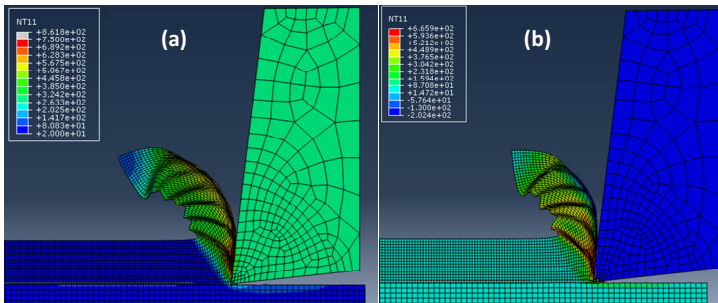
Fig. 8 Temperature fields in (a) dry and (b) cryogenic assisted machining

4.2 *Cutting Forces*

We note that with the cryogenic assistance, the fluctuation of the effort has decreased, that's decreases tool's vibration, provides stable conditions machining and increases the tool life.
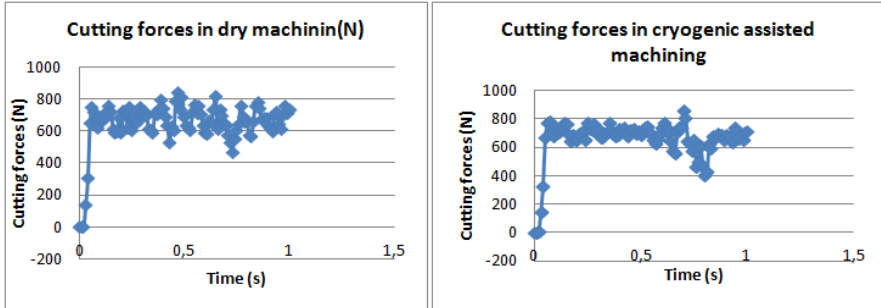
Fig. 9 Evolution dry cutting efforts, in cryogenic assistance on the rake face

Cutting efforts in cryogenic assisted machining in numerical model is 641.95N (f0.3; ap1) while in practice 595.3 N for the same conditions.$Fc_{exp} = Fc_{num} \pm 50N$.

Cutting forces in cryogenic cooling are very close to dry machining efforts. This can be explained by the temperature of the primary shear zone that cryogen has not cooled.

5   Conclusion

• Cryogenic assistance on the rake face had no influence on the cutting forces, for against it decreases the temperature on the secondary shear zone during machining
• The wear pattern observed is the adhesive wear
• The cryogenic support decreases flank wear and preserve a longer life time. This gain was quantified at 27% for f0.3 and p1,5.

References

[1] Dudzinski, D., Devillez, A., Moufki, A., Larrouquère, D., Zerrouki, V., Vigneau, J.: A review of developments towards dry and high speed machining of inconel 718 alloy. International Journal of Machine Tools and Manufacture 44(4), 439–456 (2004)
[2] Uehara, K., Kumagai, S.: Chip formation, surface roughness and cutting force in cryogenic machining. Ann. CIRP 17(1), 68–74 (1968)
[3] Wang, Z.Y., Rajurkar, K.P., Fan, J.: Turning Ti–6Al–4V with cryogenic cooling. Trans. NAMRI/SME 24, 3–8 (1996)
[4] Johnson, G.R., Cook, W.H.: A constitutive model and data for metals subjected to large strains, strain rates and high temperatures. In: 7th Int. Symp. Ballistics, pp. 541–547 (1983)
[5] Ayed, Y.: Approches expérimentales et numériques de l'usinage assisté jet d'eau haute pression: étude des mécanismes d'usure et contribution à la modélisation multi-physiques de la coupe (Décembre 5, 2013)

Intelligent Generation of a STEP-NC Program for Machining Prismatic Workpiece

Ezzeddine Haddad, Romdhane Ben Khalifa,
Noureddine Ben Yahia, and Ali Zghal

Unité de recherche en mécanique des solides, des structures et de développement technologique, ENSIT, 5 Av Taha hussein, BP. 56 Bab Mnara Tunis, Tunisia
haddad.ezzeddine2012@gmail.com

Abstract. Advances in CNC technology, coupled with improvements in computer systems provided the basis to review how computer-based systems can be used to allow universal fabrication. The G code no longer meets the current expectations of the program ever modern and complex machines. Indeed, the standard STEP-NC (STEP-Numerical Control) offers new solutions and integration of manufacturing in the full numerical chain. In this paper, we propose a new numerical control based on a standard high conceptual level STEP-NC machining process for prismatic parts, which aims to develop intelligent and powerful tools for sharing and data integration in CAD/CAM systems.

Keywords: STEP-NC, ISO-14649, G-code, CAD/CAM, CNC.

1   Introduction

Currently, a large number of developments have affected the field of mechanical production, the emergence of new CNC machines to the most advanced flexible machining cells, through the representation of new manufacturing processes. Indeed, machine tools and CNC will face new challenges of productivity, flexibility, interoperability, scalability and portability. The evolution of technology is in all components of the manufacturing cell and the CNC to the tool, but also by its full integration in CAD/CAM systems. Today, a new data standard known as STEP-NC [ISO 14649-10, 2004], which is to define non-complex way all the data of a product during its life cycle. In addition, it provides full interoperability and portability of this data to be interpreted by any type of computer system. The objective of this research is the development of a new digital channel based on a standard high conceptual level STEP-NC, used in the machining process for prismatic parts. The aim of this subject is to develop intelligent and powerful tools for sharing and integrating data into numerical chain of CAD-CAMCNC [Laguionie et al, 2009]. This work begins with the presentation of the STEP-NC program and the benefits over the conventional program code G. Then a proposal of the architecture of the model developed of generation of STEP-NC. The implementation of

this model in the integrated design environment is developed by object-oriented programming, using the VBA CATIA interface. However, the validation of the results of the model developed is through case studies of prismatic work piece, and the compilation and verification of data programs of STEP-NC generated for all cases by STEPTOOLS, simulation of machining was performed with CATIA V5.

2   Programming STEP-NC

2.1   STEP-NC

The STEP-NC is a standard for data exchange for the G-code [Shin et al, 2007]. It is based on the STEP standard (Standard for the Exchange of Product data). It includes both the properties of STEP; integration of the design process, development, manufacture and maintenance during all life stages of the object and high level information for the manufacture of product. The standard STEP-NC is standardized through ISO 14649 (MRA: Application Reference Model) and the 10303 -AP238 application protocol (AIM: Application Interpreted Model). The ARM to define the data model corresponding to advanced users formalization of data to the user vocabulary. This modeling can be performed by EXPRESS-G (Fig. 1). STEP-NC is a new standard that has emerged in order to overcome the shortcomings of the current digital channel with regard to the production of CNC machine tool.
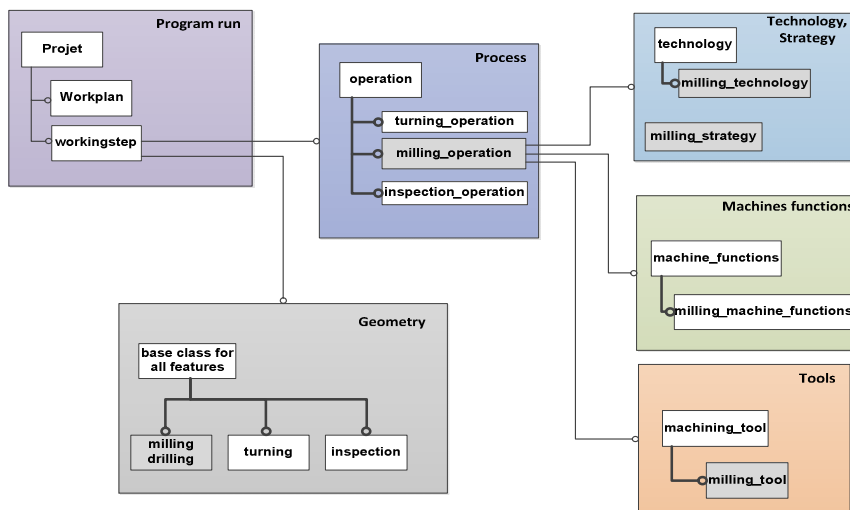
Fig. 1 EXPRESS-G model for STEP-NC

2.2 Comparison of G-code and STEP-NC

The increased productivity on CNC machine involves improving programming thereof. The language which is currently based programming that dates from the early 80s with the 6983 standard, which defines the principles of the G code programming this program joins a path in accordance with the movement of machine tool axes, rather than to focus on the needs of the machining in accordance with the workpiece. It is programmed by auxiliary functions (M-type) and technological (F, S, etc.). But it has certain inconvenience to the views of the new machining strategies and creates a break in the numerical chain at the manufacture. Among these drawbacks, the semantics can sometimes be blurred and manufacturers sometimes add language extensions to fill the gaps and adapt to changing technologies and the portability of a program then proves not between different manufacturers. There are also the flow of information is unidirectional: the lack of feedback (Feedback) possible production design causes difficulties of communication and correction [Xu, 2006]. Similarly, the preservation and capitalization of experiences prove complicated (Fig. 2).
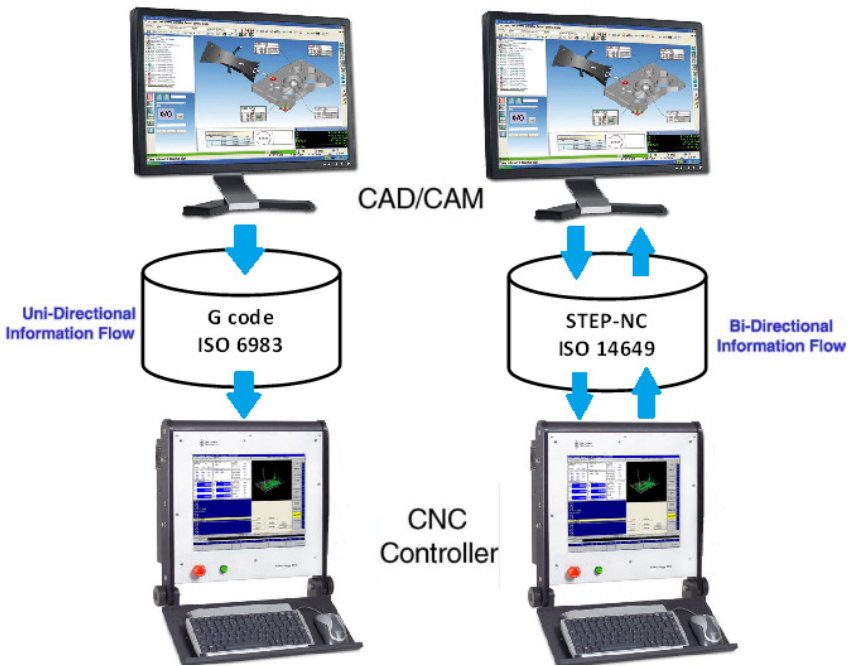
Fig. 2 Bi-directional information flow with STEP-NC

The STEP-NC [Rauch, 2007] [Rauch et al, 2012] reduces machining time for parts small and medium series due to intelligent optimization, also, it can be integrated into the controllers. Indeed, in this new programming, the post-processor

will be eliminated as the interface requires no information specific to the machine, so the STEP-NC file is transportable from one machine to another without the need for adaptation, because it predominantly contains generic information treatable by all interpreters.

2.3 Structure of STEP-NC

The contents of the ISO 14649 [ISO 14649 Part 11, 2004] information consist of: task description, description of the technology, a description of the tool, and description of the geometry. The job description describes the logical sequence of executable tasks and data types. Details of each "working step" are covered in the description of the technology in reference to the description of the tool and the description of the geometry. A graphical summary of the information available in the STEP-NC program Express-G [Newmen et al, 2009] is shown in Fig. 3 below:
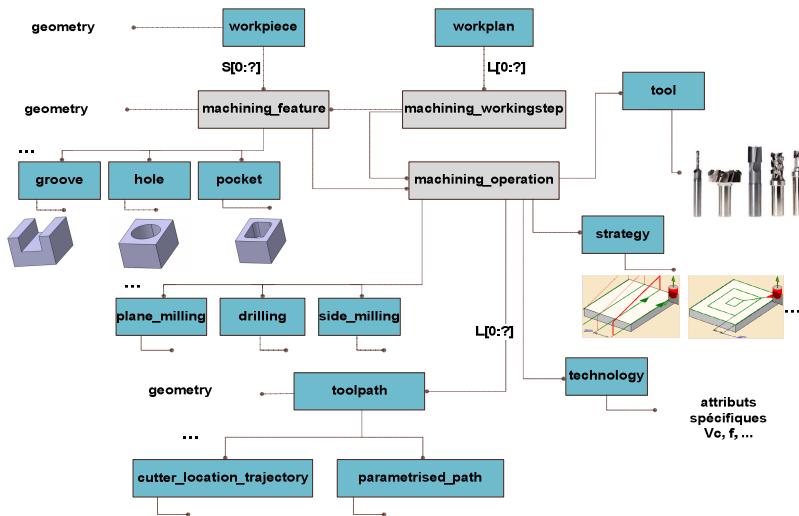
Fig. 3 Geometry, technology and process information in STEP-NC

All of these part data is broken down into three parts:

- ✓ A header section (Header) on general program presentation information (author, date, my tumble... etc.).
- ✓ Information of geometry, which concern the machining features.
- ✓ Information for machining: for each operation on a processing entity, the STEP-NC file defines the set of information such as the type of operation, the tools, the cutting parameters and machining strategies.

Fig. 3 shows part of the internal structure of STEP-NC data. The exert from a STEP-NC file **[ISO10303-21]** is shown as follows:

```
ISO-10303-21;
HEADER;
FILE DESCRIPTION(('A STEP-NC testing file'),'1');
FILE NAME('sample part1.stp',$,('AUMS'),(''), 'Prototype Mill','','');
FILE SCHEMA(('STEP-NC milling schema'));
ENDSEC;
DATA;
// Project and workplan
#1=PROJECT('Contour',#2,(#3));
#2=WORKPLAN('Work plan',(#4),$,#5);
#3=WORKPIECE('Workpiece',#6,0.01,$,$,#8,());
// Working steps
#4=MACHINING WORKINGSTEP('Rough Contour',#13,#16,#17);
#5=SETUP('main setup',#44,#48,(#51));
#6=MATERIAL('ST-50','Steel',(#7));
#7=PROPERTY PARAMETER('E=200000 N/mm^2');
#8=BLOCK('Block',#9,260.000,210.000,110.000);
// Geometric data
#9=AXIS2 PLACEMENT 3D ('BLOCK',#10,#11,#12);
----
// Manufacturing features
#16=GENERAL OUTSIDE PROFILE ('Profile',#3,(#17),#18,#22,$,$,$,$,#23,$,$);
// Operation data
#17=SIDE ROUGH MILLING($,$,'Contour profile',#38,10.000,#39,#40,#43,$,$,$,20.000,5.000,0.000);
#18=AXIS2 PLACEMENT 3D('Position of contour',
#19,#20,#21);
#19=CARTESIAN POINT('Position of contour',(40.000,90.000,100.000));
#20=DIRECTION ('',(0.0,0.0,1.0));
#21=DIRECTION ('',(1.0,0.0,0.0));
#22=TOLERANCED LENGTH MEASURE(20.000,$,$,$);
#23=COMPOSITE CURVE ('Contour Profile',(#24,#25,#56),,F.);
----
// Tool data
#40=CUTTING TOOL('End mill 10 mm',#41,(),(50.000),50.000);
#41=TAPERED ENDMILL(#42,3,.RIGHT.,F.,$,$);
#42=TOOL DIMENSION(10.000,$,$,$,$,$,$);
// Machining technology
#43=MILLING TECHNOLOGY($,.TCP.,$,3.3333,$,0.10,.T.,.F.,.F.);
#44=AXIS2 PLACEMENT 3D('Reference point to Machine zero,#45,#46,#47);
#45=CARTESIAN POINT ('',(20.000,30.000,10.000));
----
#56=COMPOSITE CURVE SEGMENT (.CONTINUOUS.,.T.,#57);
#57=POLYLINE('Second cut of the contour', (#29,#30,#31,#32,#33,#27));
ENDSEC;
END-ISO-10303-21;
```

Fig. 4 Example STEP-NC physical file

3   Creation of the Interface of STEP-NC Module and Validation

In programming STEP-NC manufacturing parameters such as cutting conditions (cutting speed, feed rate... etc.) [Cuenca et al, 2011] are given by the user in the program or on the machine to use, since the one of its advantages is compatible with all CNC machine tools that contain a STEP-NC processor. This programming is required of all production data for used and ordered according to the relationships

between machining features and raw part with the diagram STEP-NC. The flow of work in the generation system developed STEP-NC [Haddad et al, 2014] is followed by the process and the structure of the chart of Fig. 5:
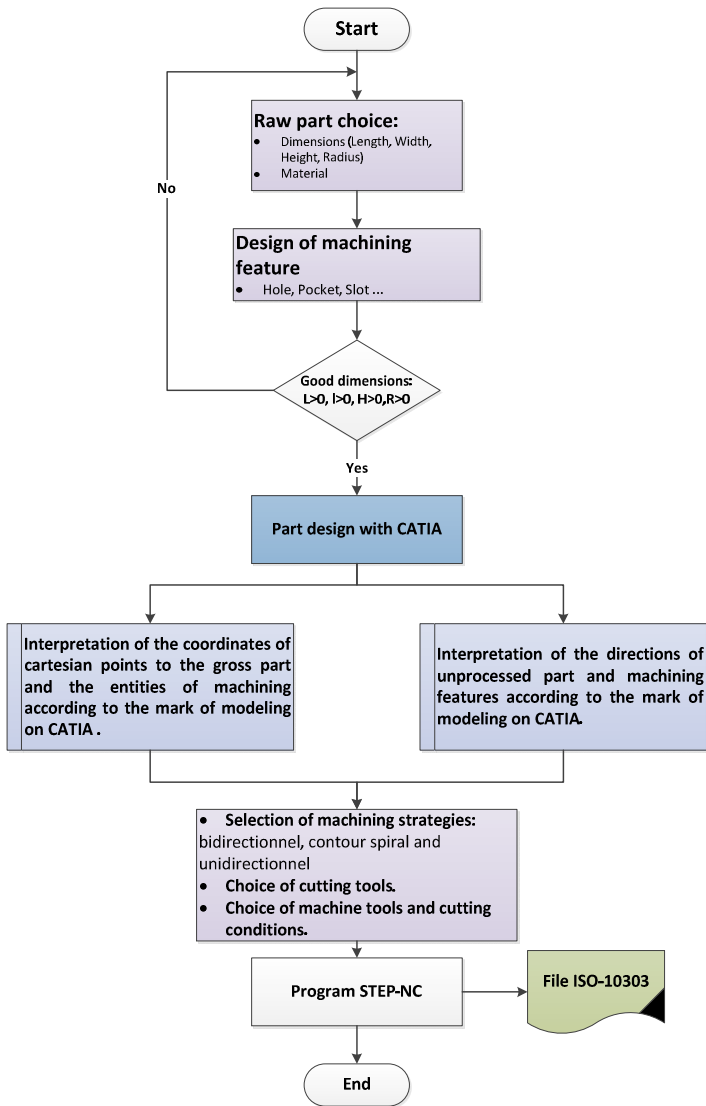
Fig. 5 Flowchart program for development STEP-NC from the part data

4   Steps of the Model Developed

The generation of the model developed STEP-NC consists of several modules to generate the STEP-NC program:

➢ A modeling module and rough material.
➢ A modeling module of machining features and automatic creation of finished part CATIA.
➢ A module to interpret the directions of orientation of the part in the same frame.
➢ A module to display the STEP-NC program.
➢ A simulation module and validation of STEP-NC CATIA.

The relationships between these modules are defined in Fig. 6. These modules are integrated in a database. Using these modules, the flow of work in the generation of the model developed STEP-NC is followed by the algorithm in Fig. 5.
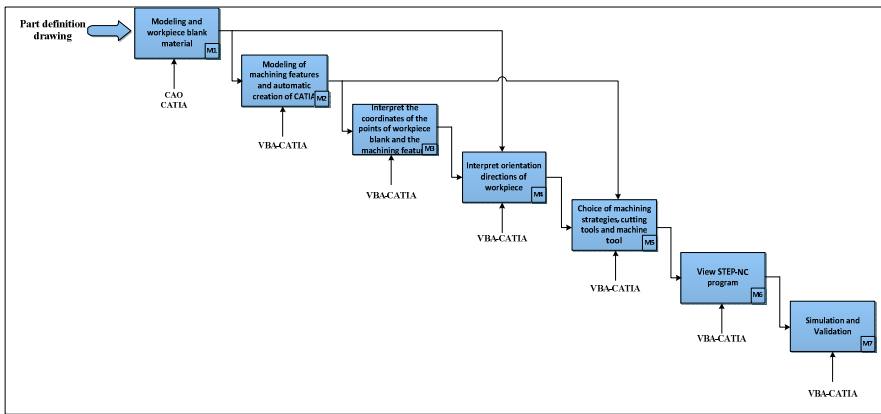
Fig. 6 Architectural Overview of the generation system of STEP-NC

5   Case Study

The application we have proposed to validate the developed generation computer system STEP-NC, is a workpiece containing single prismatic machining features of type " hole ", Pocket'' and " Slot '. The following table shows the characteristics of this feature and the associated blank.
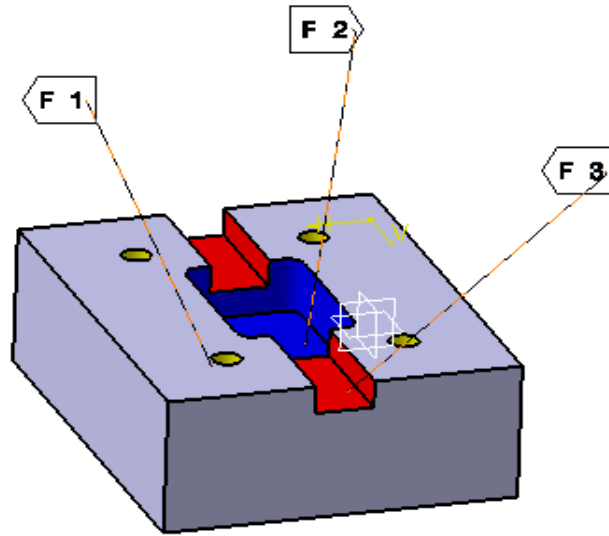
Fig. 7 Example of prismatic workpiece

Table 1 The characteristics of machining units and the blank

	Dimension	Tolerance	Cutting tool	Machine tool
F 1	Hole diameter 20 mm and 100 mm deep	±0.1	Drill (Ø20 mm)	3-axis milling machine
F 2	Pocket width 40 mm and 10 mm deep	±0.2	Pocket cutter (Ø10 mm)	3-axis milling machine
F 3	Slot width 80 mm and 30 mm deep	±0.2	Slot cutter ARS (Ø20 mm)	3-axis milling machine

When starting the computer application displays the menu in Fig. 8 for part modeling with the choice of its form (prismatic or cylindrical), its dimensions and material.

After the creation of the piece on CATIA in proceeds to the next step in the interpretation of the coordinates of the nodes and vertices of the blank and entities "Hole" "Pocket", and "Slot". And in the menu of Fig. 10, the position is interpreted by the workpiece origin and orientation according to the directions.

Fig. 8 Raw part modeling

Fig. 9 Interpretation of the coordinates of the nodes for raw part and machining features
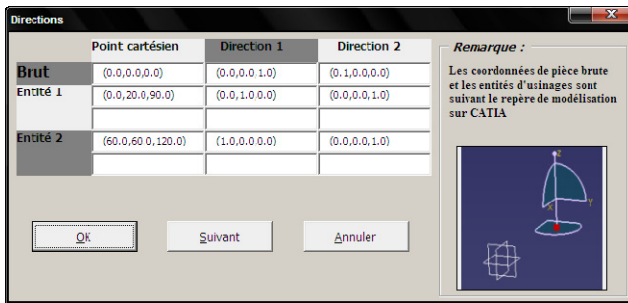
Fig. 10 Interpretation of the directions of orientation for raw part and machining features
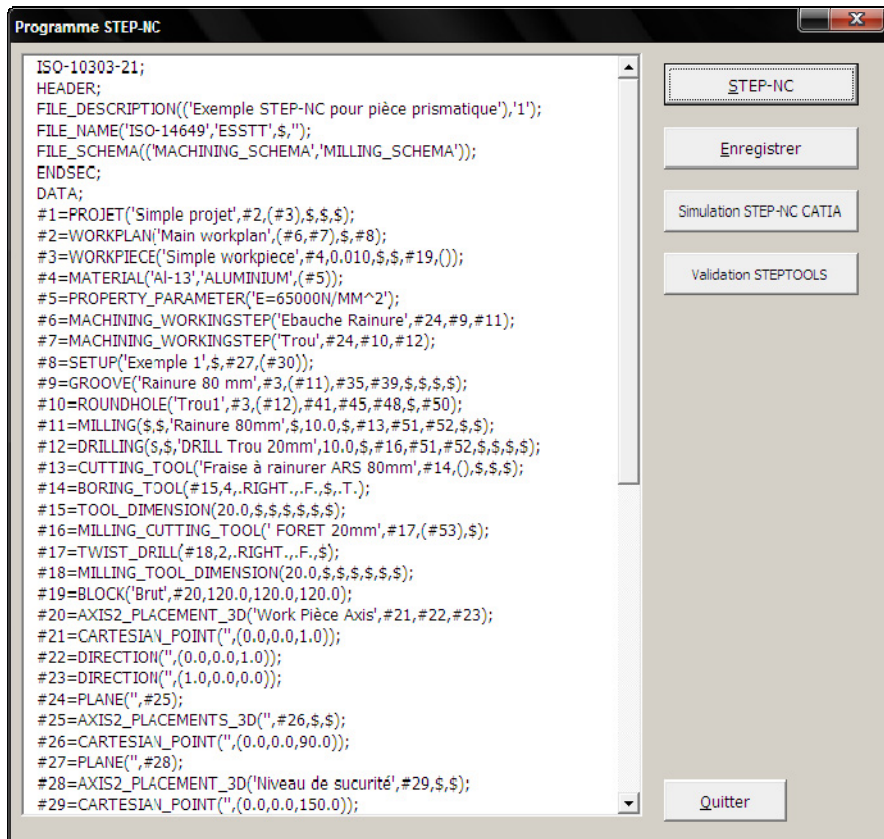
Fig. 11 Generated of STEP-NC (ISO 14649) part program

The application program result is displayed in a menu as shown in Fig. 11, which can be saved as a STEP file [ISO 10303-21]. Then we made the validation of our program by a compiler STEPTOOLS as shown in the following Fig. 12.
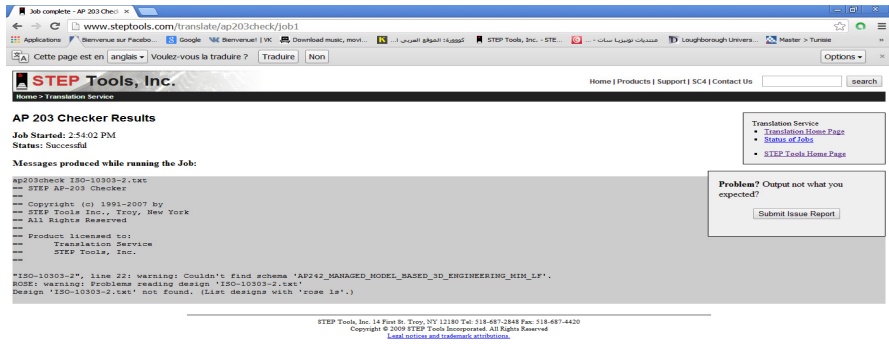
Fig. 12 Validation by STEPTOOLS compiler

6   Conclusion

This work is concerned with the integration of the entities based programming for processing on CNC machines in a context multi process. Programming STEP-NC can fill the skips of G-code and fully integrate CAD-CAM-CNC system. Indeed, in this paper we propose a development approach of STEP-NC allows manufacturers to use the new generation of machine tools based on STEP NC programming. The STEP-NC uses a high-level language and is based on the implementation of a single file. It allows two-way flow of data and the eradication of postprocessors and code-G. However, the programming method proposed STEP-NC is carried out with CATIA VBA module. This intelligent programming method allows using workpiece data and knowledge of machining experts. The implementation of this module was developed with programming VBA, EXPRESS-G and CATIA.

References

[Shin et al, 2007] Shin, S.-J., Suh, S.-H., Stroud, I.: Reincarnation of G-code based part programs into STEP-NC for turning applications. Computer-Aided Design 39(1), 1–16 (2007)

[ISO 14649-10, 2004] Internationnal Standard Organization.Industrial automation systems and integration - physical device control - data model for computerized numerical controllers - Part 10: general process data, ISO TC 184/SC1/WG7/FDIS (2004)

[Haddad et al, 2014] Haddad, E., Khalifa, R.B., Yahia, N.B., Zghal, A.: Développement du programme STEP-NC pour les pièces prismatiques. In: COTUM 2014, Sousse, Mars 24-26 (2014)

[Newmen et al, 2009] Newman, S.T., Nassehi, A.: Machine tool capability profile for intelligent process planning. CIRP Annals-Manufacturing Technology 58(1), 421–424 (2009)

[Xu, 2006] Xu, X.W., Newman, S.T.: Making CNC machine tools more open, interoperable and intelligent—a review of the technologies. Computers in Industry 57(2), 141–152 (2006)

[Laguionie et al, 2009] Laguionie, R., Hascoët, J.-Y., Rauch, M.: Une plate-forme STEP-NC pour la programmation avancée et intelligente des machines-outils. 11ème coll. Nat. AIP PRIMECA (2009)

[Rauch, 2007] Rauch, M.: Optimisation de la programmation des MOCN - Application aux machines à structure parallèle. Thèse de doctorat, Ecole Centrale de Nantes / Université de Nantes (2007)

[Cuenca et al, 2011] Cuenca, S., Jimeno-Morenilla, A., Martínez, A., Maestre, R.: Hardware approach to tool path computation for STEP-NC enabled CNC: A case study of turning operations. Computers in Industry 62, 509–518 (2011)

[Rauch et al, 2012] Rauch, M., Laguionie, R., Hascoet, J.-Y., Suh, S.-H.: An advanced STEP-NC controller for intelligent machining processes. Robotics and Computer- Integrated Manufacturing 28, 375–384 (2012)

[ISO 10303-21] Industrial automation systems and integration – product data representation and exchange – part 21: Implementation methods: Clear text encoding of the exchange structure (physical file). ISO/IEC, Geneva, Switzerland (1994)

[ISO 14649 Part 11, 2004] Industrial automation systems and integration – Physical device control – Data model for computerized numerical controllers – Part 11: Process data for milling, TC 184/SC 1 (2004)

Numerical Chain of Forging Railway Axle and Wheel Press Fitting Operation

Sofiane Saad[1,2], Vincent Magnier[1,2], Philippe Dufrenoy[1,2], Eric Charkaluk[2,3], and François Demilly[4]

[1] Univ. Lille Nord de France, F-59000 Lille, France
   `saad.sofiane1@gmail.com`
[2] Univ. Lille1, Laboratoire de Mecanique de Lille, F-59650 Villeneuve d'ascq, France
   `vincent.magnier@polytech-lille.fr`
[3] CNRS, UMR 8107, F-59650 Villeneuve d'Ascq, France
   `philippe.dufrenoy@polytech-lille.fr`
[4] MG-Valdunes SAS, F-59125 Trith Saint Leger, France
   `eric.charkaluk@ec-lille.fr, Francois.DEMILLY@valdunes.com`

Abstract. In today's competitive business environment, it has become increasingly important to reduce manufacturing and raw materials costs. For this purpose, an innovative process of design and manufacturing railway axles is developed. It is based on forging hollow axle which allows a significant reduction in steel consumption. In this work, we tried to analyse how these modifications induced by this new process and design impact on the residual stress field. For this particular study, a numerical chain has been developed going from the simulation of the hot upsetting manufacturing process of the railway axle with the explicit method, to the analysis of the cutting and the press fitting assembly operation. This study consists in modelling the forging process with the dynamic FEM in order to take into account the dynamic phenomena and predict the residual stress field and the initial plastic strain. Then the evaluation of the cutting operation of the upper axle surface and finally the simulation of assembling the wheel on the axle with a static model, to better estimate the stress relaxation and redistribution.

Keywords: Dynamic FE simulation, Hot upsetting, Press fitting, Residual stress.

1 Introduction

Railway axles were investigated at the very beginning of fatigue research and design. Regarding safety, this part is among the most important components in railway vehicles (Fig. 1). This work is part of the InnovAxles project, dedicated to the study of innovative solutions needed to reduce manufacturing costs and raw material of the axle. The purpose of this project is to develop a new method of manufacturing hollow axles based on the forging operation. This switch from machining manufacturing process to forging, reduces the amount of raw material used to produce the
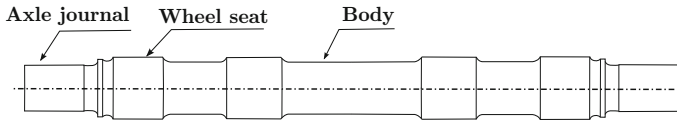
Fig. 1. Different section of the railway axle

railway axle. The weight saving is estimated between 20% and 30%, offering energy savings and a reduction in steel consumption of about 25% compared to current machining process. In the case of a freight axis where the finished full axis mass is 396 kg, it is necessary to use 604 kg of steel which induces a loss of 34% of the metal. The same axis, drilled at 65 mm provides a mass of 340 kg giving 44% of the initial metal loss. The objective of this work is to propose a comprehensive design method of the new common forged axle, which allows to take into account the residual stresses from each stage of forging, machining and assembling.

Due to the switch of the axle manufacturing process from the cutting operations to the forging process, a numerical investigation was required to understand, analyse and evaluate the impacts of this new industrial technique. In this numerical chain the explicit and the implicit integration schemes was used to solve respectively the dynamic and static problem. In addition, different behaviour laws was implemented to satisfy the needs and the particularities of the present phenomena. The difficulties of such numerical chain are to make a link between each model in terms of results transfer and to reduce the computation time since we model a full scale axis.

2   Hot Upset Forging

The purpose of this study is to provide a model which produces from a pipe the final axle shape in one step. This process of hot upsetting shown in Fig. 2a, was developed by *Barriol & Dallière Industries* in order to reduce steel consumption and manufacturing cost. The hot upsetting process proceed by the displacement of the middle parts of the axle (wheel seat) by applying with a press an axial force to the tube. So this process produces with a single push, preformed in a closed die, the final part (Fig. 2b). This technique has the advantage of reducing the amount of raw material used for the initial geometry of the axle, since the diameter D of the initial cylinder is equal to the diameter of the body of the finale axle shape. This operation decreased the number of manufacturing step and handling of the axle. It also has the advantage of having a fiber which is continuous over the entire piece unlike the axle produced with the cutting process.

Several studies have focused on simulating the forging process of railway wheel as in (Davey et al., 2001) where an iterative solution technique and structured remeshing strategies was used, and the rear axle shown in (Lei et al., 2000) based on rigid-plastic finite element program. Moreover, most of the papers, like in (Lin, 1998) focused on the static finite element method coupled with thermo-mechanical analysis. More recently in the work of (Debin and Lin, 2014) dynamic finite element method coupled with thermal effects model was developed for practical study.

(a) Initial upsetting configuration   (b) Final step of the upsetting axle
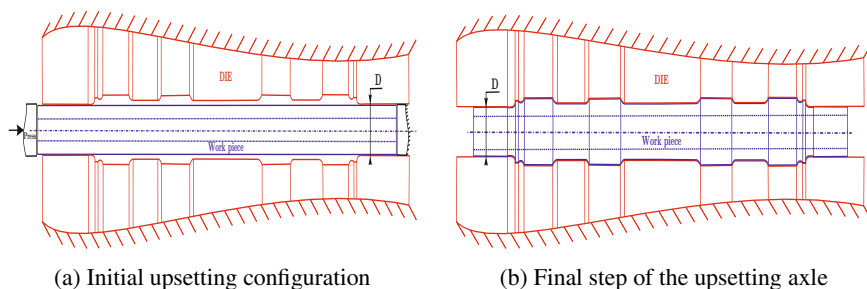
Fig. 2. Schematic drawing of the upsetting axle

In this paper we present the axisymmetric finite elements model developed to upset the axle with thermal-elastic-viscoplastic behaviour and the different approaches employed to reduce the computation time since a full scale model is developed.

2.1 Numerical Methods

In this section we describe the different numerical methods used to develop the finite element axisymmetric simulation of the upsetting and cooling step. Fig. 3 presents the upsetting configuration, where the tool is animated by a motion whereas the die and the right surface of the workpiece are fixed. In this simulation we opted to refine mesh in the wheel seat section, since we focused our investigation in this area. This mesh configuration was used throughout the numerical chain. Therefore in order to have a compromise between the results accuracy and a reasonable computing time we chose a mesh size of 1 mm. The tool and the die are assumed to be elastic whereas the material in the workpiece is modelled by thermal-elastic-viscoplastic behaviour. An explicit scheme was adopted to solve the coupled mechanical and thermal problem. The advantages of this method is to allow the simulation of the dynamic phenomena of the forging operation and to offer better contact manager as it was explained in (Lucia Garcia, 2004).

2.1.1 Material Law and Mesh Formulation

The XC38 material was chosen for manufacturing railway axles, which is widely known as EA1N (EN13261, 2003). A high strain, strain rate and temperature in upsetting process have strong influence on material's flow. To get better analysis results, a material model that combines all these aspects was necessary. Therefore in this simulation, the thermo-elastic-viscoplastic Johnson and Cook (Johnson and Cook, 1983) model was opted. Johnson and Cook model considers any kinematic hardening and expresses rather the equivalent stress as a function of plastic strain, strain rate and temperature. The parameters used are detailed in the work of (Öpöz and Chen, 2010). In order to avoid the mesh distortion, the Arbitrary Lagrangian-Eulerian (ALE) approach presented in (Boman, 2010) was used. This approach combines the
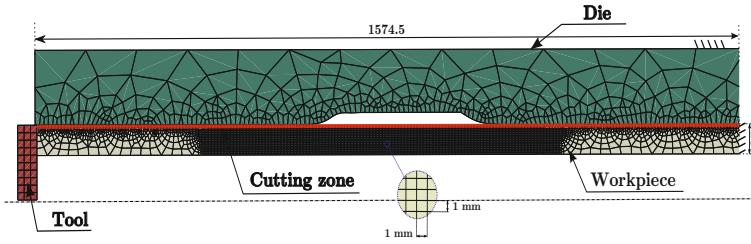
Fig. 3. The upsetting configuration and mesh details

advantages of the Lagrangian formulation which is summarized in a good definition of boundaries conditions and the advantages of the Eulerian formulation which tolerate large distortions. Thus, this method is presented as the most appropriate formulation for modeling large deformation simulation and the study of coupled problems.

2.1.2 Interface Conditions (Friction and Heat Transfer)

The friction and heat-transfer conditions at the interface between the die and the tube have a significant effect on the metal flow and the loads required to produce the part. A constant coulomb friction coefficient along with a penalty formulation as contact algorithm was used, as well as a heat transfer coefficient. Then, we proceeded by applying a film coefficient in the external shape of the forged axle to model the axle air convection process. A uniform value of the air convection was employed to model the axle cooling step with a value of 25 $W/m^{2\circ}C$. The friction

Table 1. Thermal parameters literature review

References	Material	Process	$\dot{\varepsilon}_p$ [s^{-1}]	T_{Tool} [°C]	T_{axle} [°C]	μ	h kW/m^2°C
(Lv, et al., 2008)	stainless steel	Upsetting	0.1	300	1160	0.3	11
(Jeong, et al., 2005)	Nimonic 80A	forging	0.5	450	1125		2
(Hyun and Lindgren, 2004)	stainless steel SS316L	forging	3.5	20	1000	0.3	25
(Liu, et al., 2008)	AISI 1015	Upsetting	10	20	160	0.2	0.022
(Brooks et al., 1998)	Ti–48Al– 2Nb–2Cr –1B	forging	10	20	1125	0.2	-
(Lin, 1998)	Acier doux	hydroforming	10	20	20	0.15	-

coefficient is assumed to be 0.1 and 90% of the work dissipated by friction as well as by plastic strain is assumed to become heat as in the work of (Hyun and Lindgren, 2004), where a forging process using an adaptive meshing approach was developed. The initial temperature of the tube and the tools were 1200°C and 25°C respectively. The simulation of cooling started by removing the tools at the end of the forging step. Thereafter the heat transfer occurred via air convection. Regarding the heat transfer coefficient, the value depending on the initial temperature of the part and tools and materials in contact as shown in (Tab.1). In this model a coefficient of 1 kW/m²°C was used based on geometric sensitivity study.

2.1.3 Mass Scaling

The explicit integration scheme was used to solve the thermo-mechanical problem. It allows the use of mass-scaling approach that reduce the simulation computing time. It is based on the artificial increase of the material density ρ. As a result an increase of the time increment $\Delta t = \frac{L_e}{C_d}$ and thus a decrease the computation time, where C_d is the speed of wave propagation $C_d = \sqrt{\frac{E}{\rho}}$ and L_e is the length of the smallest element edge. Many works like (Wisselink and Huétink, 2004), (Wang and Nakamura, 2004) where a comparison between static implicit and dynamic explicit procedures for the hydroforming process was presented and shows the advantages of the explicit FEM coupled with mass scaling approach, proved that to have a good calculation accuracy you must have the kinetic energy $< 5\%$ to the internal energy of the FE simulation. In the same reasoning, Abaqus reference manual presented two energy criteria to ensure the accuracy of the explicit results. The first criterion is the maintains of an artificial energy less than 10% of the internal energy and the kinetic energy $< 1\%$ of the internal energy. In this study we chose to apply these two criteria.

A Sensitivity analysis of the optimal mass scaling parameter was done by applying four different mass scaling. We chose to apply the mass scaling by fixing the increment time Δt. The sensitive mass scaling study was developed in full size model scale and each job was running with the following computing machine: 2 cpus Xeon E5-2670 2.6 GHz / 20 MB x 8 core (s) per cpu = 16 cores per node with 64 GB memory per node. The evolution of the kinetic and artificial energy as a function of the computation time progress can ensure the validity of the calculation accuracy criteria.

Case 1: The first case, detailed in Fig. 4a, is relative to a mass scaling equal to $\Delta t = 10^{-3}$s. We noted that the artificial energy was less than 10% of the internal energy throughout the simulation. Whereas the second criterion was not respected, we noticed that the kinetic energy exceeded 1% of the internal energy. So this mass scaling case was not taken into consideration.

Case 2: As the first case, the second one shown in Fig. 4b respected the first criterion relative to the artificial energy. As far as the kinetic energy, we noted that at the beginning of the forging simulation the kinetic energy exceeded 1% of the internal energy and thereafter stabilized at an acceptable value. This case is ruled out.

Case 3: This case is illustrated in the Fig. 4c. We noted that during one second at the beginning of the simulation the kinetic energy criterion was not respected. On the contrary, this area that didn't respect the kinetic criteria decreased drastically compared to previous cases and present a computation time of 35h. This value will be used in the hot upsetting model.

Case 4: The next mass scaling is $\Delta t = 10^{-5}$s. The Fig. 4d shows that the kinetic energy was less than 1% of the internal energy throughout the forging and cooling step. This case induced an important calculation time of about 221 h. For this reason this value was discarded.

(a) Case 1: $\Delta t = 10^{-3}$s

(b) Case 2: $\Delta t = 10^{-4}$s

(c) Case 3: $\Delta t = 5.10^{-5}$s

(d) Case 4: $\Delta t = 10^{-5}$s
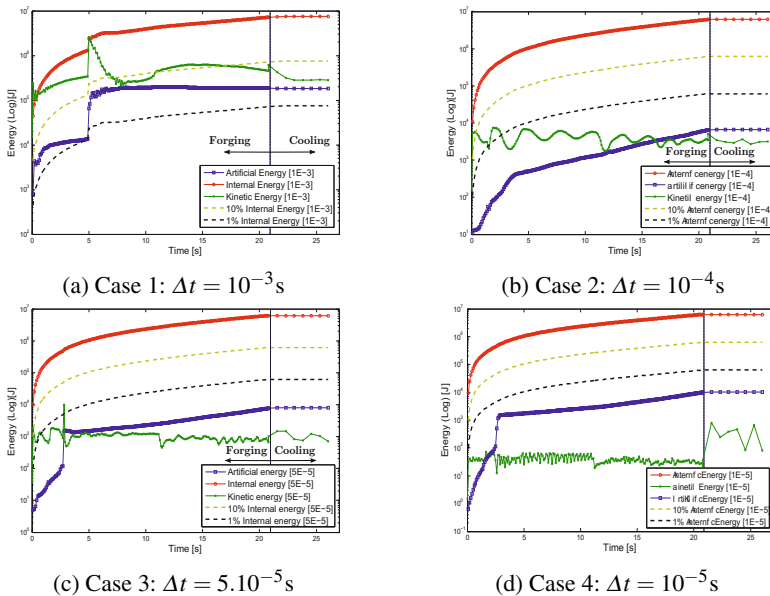
Fig. 4. Energies evolution throughout the forging and cooling step

2.2 Hot Upset Forge Results

In this section, we present numerical results of the upsetting operation. The first results from the forging simulation gave a good correlation in terms of the outer and internal shape of the experimental axle manufactured by *BDI* company shown in Fig. 5b. This comparison showed geometrical precisions to predict the external and internal numerical shapes of the axle. Fig. 5a represents the numerical results of the upsetting process in the end of cooling step. In accordance with the experimental
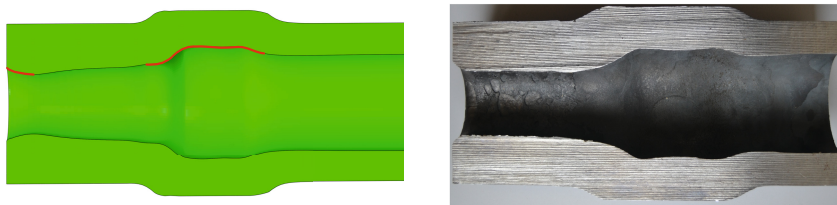
(a) Final numerical geometry of the forged axle   (b) Hollow axle hot upsetting test Result

Fig. 5. Schematic drawing of the upsetting axle

forging tests, we noticed that the simulation predicts an increased thickness of the axle journal and kept the same thickness for the axle body. Regarding the shape of the inner axle, we observed that within the wheel seat the numerical simulation succeeded to predict the same shape in form of **w** as the experimental test. The same as under the axle journal where we noticed the generation of a chamfer and the enlargement of the thickness of the part.

Fig. 6 shows the *Von Mises* stress distribution after the cooling stage. We can observe, at the external surface of the wheel seat, that the stress level reached a value of 235 MPa. This value decreased from the outer surface to the inner surface of the hollow axle to reach 135 MPa. In the core of the axis the stress level is almost zero. This distribution is the result of the cooling rates differences in function of depth. The equivalent plastic strain resulting from the forging process is very important (Fig. 7). It is noted that the most deformed area of the axle was the wheel seat. We noticed an increase of the plastic deformation in the inner area next to the axle journal fillet which reached 72%. However, the wheel seat surface plastic strain value was 30%.

3   Cutting and Press Fitting Operation

The cutting and the assembly operations of the wheel on the axle were made by *Valdunes* company. The first stage is relative to the cutting operation, where we proceeded by removing the machining allowance of $e = 1$ mm (Fig. 8), after the forging process. Then, we proceeded by the press fitting. This operation allowed the tightening of the wheel on the axle in order to ensure tightness between these two parts. The principle was to provide a diameter D_a of a portion of the axle, called wheel seat, greater than the diameter of the wheel hub D_w (Fig. 9). *Valdunes* company used different values of tightness ($s = D_w - D_a$) for each type of axle. However these parameters varied between 0.2 and 0.35mm. This operation is carried out in room temperature with a feed rate of 2 mm s^{-1}. To check a coaxiality between the wheel and the axle at the beginning of the operation, the axle was provided with a chamfer. The chamfer is characterized by its height h, calculated by $h = l \times tg(\alpha)$. In our case, we are interested by this configuration where the angle α is equal to 2° and with a chamfer length of $l = 10$ mm (Yameogo, 2004).
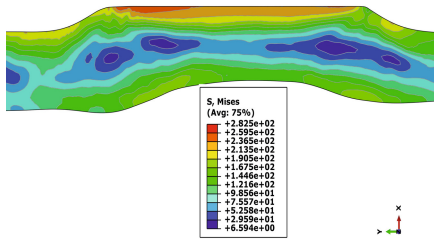
Fig. 6. *Von Mises* Stress distribution in the axle wheel seat
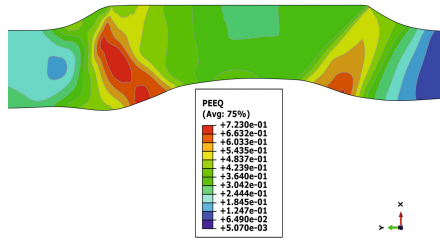
Fig. 7. Equivalent plastic strain distribution
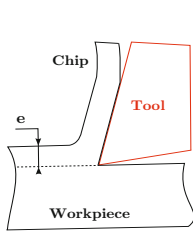
Fig. 8. Cutting operation
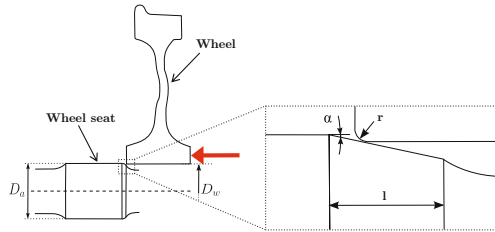
Fig. 9. Characteristics of the Press fitting operation

The company *Valdunes* validated this operation by comparing the experimental press force to the upper and the lower masters curves. The experimental force according to the distance must be between this two curves (Fig. 10a). This industrial method has been applied to validate the numerical model.

3.1   Numerical Methods and Tensile Properties

In this simulation two steps were developed. The first one was the simulation of cutting process and the second one was the press fitting. The results transfer was performed from the forging explicit model to the new implicit model with Abaqus. The aim of such a transfer was to keep the residual stress and plastic strain as an initial state of the cutting and assembly model. The cutting of the upper surface of the axle was done in a simplified way. The motion of the cutting tool was prescribed and some elements were automatically removed from the model. Thus the elements with some residual stresses were removed but the cutting was not simulated as in (Salvatore et al., 2013), where a damage area is modelled in order to simulate the chip removal. In this simulation the whole machining allowance was removed at once, knowing that there was no noticeable difference between removed elements neither one by one nor at once as shown in the work of (Hyun, 2001). The advantage of switching from the explicit scheme, used in the previous forging simulation, to the implicit was based on the fact that we did not model dynamic and thermal phenomena. Furthermore this method is known for its accuracy in spring back

prediction. In addition, during the assembly operation, the implicit method presented more accurate results with a lower computational time for non-dynamic phenomena.

The press fitting is a relatively severe operation for the first sub-layers of surface in contact. Indeed, despite the lubrication, the shear rate at the surface of the wheel seat still very important during the passage of the wheel. These results from a significant stretching, in the direction of fitting, of the grains in surface. In order to describe the plastic strain due to the impact of the friction of the wheel against the wheel seat axle, we chose to implement a tensile behaviour for the two parts.

3.2 Full and Hollow Axles Comparison

The press fitting simulation was validated by comparing the press fitting numerical forces to the upper and lower surface. Fig. 10b shows that the numerical forces were between the two curves throughout the simulation, and reached a force level of 0.32 MN and 0.27 MN at the end of the simulation respectively for hollow and full axle. This force level difference was explained by applying a scale factor of 500 to the structures, it was possible to show how the wheel seat deforms. In the case of a hollow axle, the axle seat is deformed by generating a conical geometry with a higher gradient than in the case of a solid axle. This cone induces additional resistance to fitting the wheel.

A comparison between a full and hollow axle is done in terms of stress and plastic strain distribution. This comparison allows us to focus on the differences generated by this geometrical modification between the two configurations. The surface residual stress distribution at the end of the cooling step is shown in Fig. 11 at the wheel seat area, the journal and body fillet where the study was focused. This distribution revealed that in three directions the stress fields are generally compressive at the surface of the wheel seat, where crack initiation problems are observed. We generally notice that the two operations of forging and press fitting directly affects the distribution of residual stress fields in the wheel seat. The hot upsetting operation induces compressive stresses on the surface of the wheel seat for both hollow and full axle in the three directions. The residual stress in the axial direction are on

(a) Experimental force for full axle   (b) Numerical force
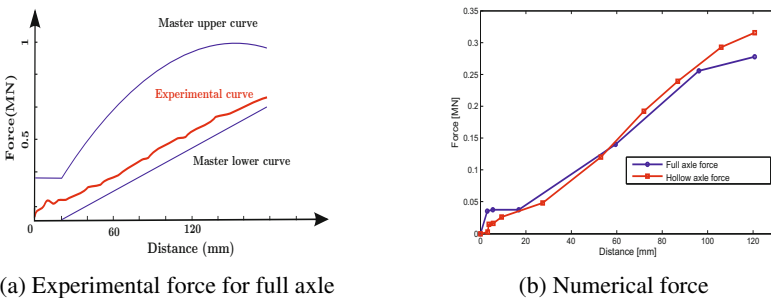
Fig. 10. Experimental and Numerical press fitting force

average equal to -150 MPa for a full axle (Fig.11b) and -200 MPa for a hollow axle (Fig.11e). This stress levels differences lies in the fact that we axially deformed more the hollow axle in order to embracing the internal die surface. In addition, the forging operation generates a compressive field distribution on the circumference in the fillets and the wheel seat. By against in the extremity of the wheel seat the stress level pass from -200 MPa to zero in the case of a full axle (Fig.11c), and it stabilizes at -50 MPa in the case of a hollow axle (Fig.11f). This is explained by both ends which have a relatively sharp geometries, which induces once deformed into the die, very close contact areas between the outer axle surface and the die inner surface where the contact pressure is insignificant. Regarding the radial direction of the axle, there are a compressive stress field localized in the chamfer and in the opposite side, with zero stress in wheel seat in both cases. After the press fitting operation, we noticed a redistribution of stress fields on the wheel seat surface. The first observation relates to the appearance of a radial compression peak in the end of the chamfer in the two cases. For the hollow axle this peak is greater and reaches -340 MPa (Fig.11a) and -265 MPa in the case of a full axle (Fig.11d). This stress level difference can be explained by the rigidity of the solid axle that induces a plastic deformation of the wheel unlike a radial flexibility of the hollow axle which induces an elastic deformation in the chamfer. In addition, a second pressure peak of -105 MPa is present at the end of the wheel seat in the case of a full axle. This does not occur in the other case, which means less grip between wheel and axle in this

(a) Full axle radial stress   (b) Full axle axial stress   (c) Full circumferential stress

(d) Hollow axle radial stress   (e) Hollow axle axial stress   (f) Circumferential stress
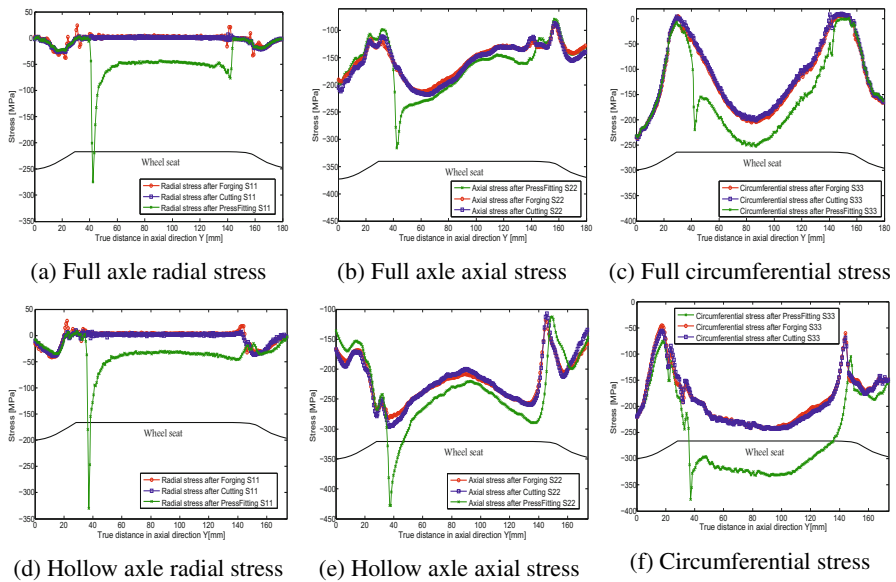
Fig. 11. Hollow and full axle stress distribution

area. This adhesion between the wheel and axle is represented by the radial stress that reaches a −55 MPa.

The plastic strain distribution is essentially induced by the forging operation. Globally, we noticed that the machining operation reduces the plastic strain magnitudes in the axle (Fillet) with a low values of about 0.02. The impact of the manufacturing process is noticeable in the circumferential plastic strain distribution, where in both cases, the shape follows the external axle geometry and reached a value of 16%. This distribution highlights the upsetting operation principle, that causes an expansion of the material in the die at the wheel seat area (Fig.12c). Regarding the axial direction the plastic deformation is the most important. We note a homogeneous compressive distribution under wheel seat for a full axle with an average value of 26% (Fig.12b). In the case of a hollow axle, this distribution is highly variable and present larger strain values that reaches 47% (Fig.12e). This curve has two compression peaks at the extremity of the wheel seat which is explained by a strong grip in the curved die region which results a localized plastic strain peaks. Radially, the upset effect resulting in a tensile strain at the wheel seat surface. This pulling is more pronounced in the case of a hollow axle where a maximum value about 35% is achieved (Fig.12d) against a value of 21% (Fig.12a).

(a) Full: Radial plastic strain   (b) Full :Axial plastic strain   (c) Full: Circumferential

(d) Hollow: Radial plastic strain (e) Hollow: Axial plastic strain (f) Hollow: Circumferential
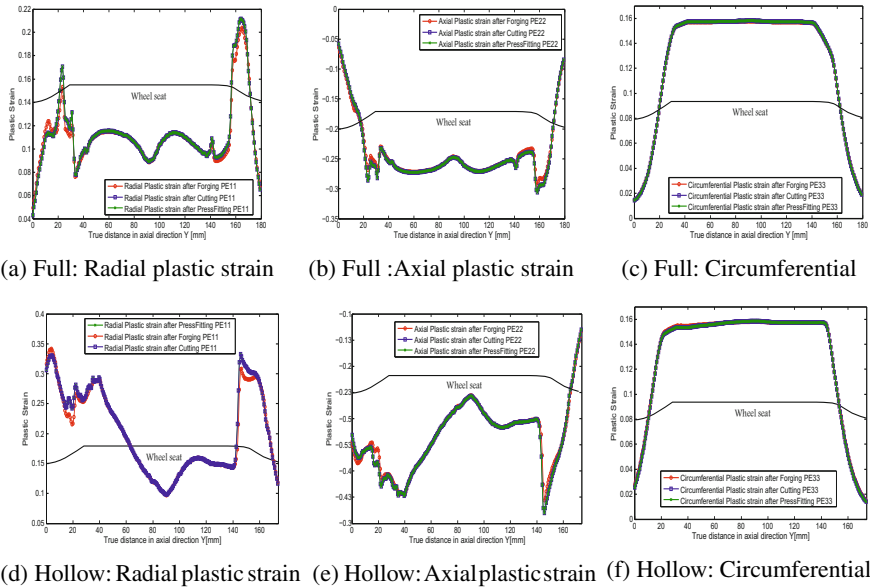
Fig. 12. Hollow and full axle plastic strain distribution

4 Conclusion

A numerical chain was developed to predict the residual stress and plastic strain throughout three simulations. In the first step, the upsetting operation was simulated with explicit scheme to take into account the hot forging dynamic phenomenon. In the second step, we proceed by transferring results in terms of the forging residual and plastic strain into the cutting and pressfitting simulation based on the implicit scheme, to predict the redistribution of stress and plastic strain under the wheel seat. The hydrostatic pressure is an indicator used by several fatigue criteria to estimate the crack initiation risk, like Dang Van (Dang Van et al., 1989) and Crossland criterion. It is observed that the distribution of the hydrostatic pressure level in the external hollow wheel seat surface is less important of about 50 MPa than the full axle. It is noted that the press fitting operation induces a pressure peaks in the chamfer end in both cases that reached -379 MPa and -296 MPa, respectively for a hollow and full axle. In these areas the risk of crack initiation is high. The difference between the two axle configurations is observed in the axle core. The inner surface of the hollow axle has positive hydrostatic pressures that reaches 115 MPa whereas the full axle distribution decrease to reach 40 MPa at the middle of the axle. Therefore in order to dimension the hollow axle under a fatigue load a criterion that can provide a fatigue limit for negative hydrostatic pressure like (Liu and Zenner, 2003) is needed.

References

Boman, R.: Développement d'un formalisme arbitraire lagrangien eulérien tridimensionnel en dynamique implicite. application aux opérations de mise à forme. Ph.D. thesis, Université de Liège (March 2010)

Brooks, J., Dean, T., Hu, Z., Wey, E.: Three-dimensional finite element modelling of a titanium aluminide aerofoil forging. Journal of Materials Processing Technology 80-81, 149–155 (1998)

Dang Van, K., Griveau, B., Message, O.: On a new multiaxial fatigue criterion: theory and application. biaxial and multiaxial fatigue. In: Brown, M.W., Miller, K.J. (eds.) EGF 3, pp. 479–496. Mechanical Engineering Publications (1989)

Davey, K., Miller, B., Ward, M.: Efficient strategies for the simulation of railway wheel forming. Journal of Materials Processing Technology 118(1-3), 389–396 (2001)

Debin, S., Lin, Y.: Hot forging. In: Yilbas, B., Hashmi, S., Batalha, G.F., Van TyneBekir, C.J. (eds.) Comprehensive Materials Processing, pp. 275–289. Elsevier, Oxford (2014)

EN13261, Railway applications - wheelsets and bodies - axles - production requirements (2003)

Hyun, S.: Simulating a sequence of manufacturing steps. In: Seventh International Conference on Numerical in Industrial Forming Processes, NUMIFORM 2001 (2001)

Hyun, S., Lindgren, L.-E.: Simulating a chain of manufacturing processes using a geometry-based finite element code with adaptive meshing. Finite Elements in Analysis and Design 40(5-6), 511–528 (2004)

Jeong, H.S., Cho, J.R., Park, H.C.: Microstructure prediction of nimonic 80a for large exhaust valve during hot closed die forging. Journal of Materials Processing Technology 162-163, 504–511 (2005)

Johnson, G.R., Cook, W.H.: A constitutive model and data for metals subjected to large strains, high strain rates and high temperatures. In: Proceedings of the 7th International Symposium on Ballistics, vol. 21 (1983)

Lei, L.-P., Kim, J., Kang, B.-S.: Analysis and design of hydroforming process for automobile rear axle housing by FEM 40(12), 1691–1708 (2000)

Lin, S.: Upsetting of a cylindrical specimen between elastic tools 86(1), 73–80 (February 1998)

Liu, C.-H., Wang, A.-C., Chen, Y.-S., Wang, C.-M.: The coupled thermomechanical analysis in the upsetting process by the dynamic FEM. Journal of Materials Processing Technology 201(1-3), 37–42 (2008)

Liu, J., Zenner, H.: Fatigue limit of ductile metals under multiaxial loading. In: de Freitas, M., Carpinteri, A.S.A. (eds.) European Structural Integrity Society. Biaxial/Multiaxial Fatigue and Fracture 6th International Conference on Biaxial/Multiaxial Fatigue and Fracture, vol. 31, pp. 147–164. Elsevier (2003)

Lucia Garcia, A.: Etude thermo-mécanique et modélisation numérique de l'emboutissage à chaud de l'usibor 1500. Ph.D. thesis, Ecole des mines de Paris (January 2004)

Lv, C., Zhang, L., Mu, Z., Tai, Q., Zheng, Q.: 3d FEM simulation of the multi-stage forging process of a gas turbine compressor blade. Journal of Materials Processing Technology 198(1-3), 463–470 (2008)

Öpöz, T., Chen, X.: Finite element simulation of chip formation. In: School of Computing and Engineering Researchers' Conference, pp. 166–171 (December 2010)

Salvatore, F., Saad, S., Hamdi, H.: Modeling and simulation of tool wear during the cutting process. Procedia CIRP 8, 305–310 (2013)

Wang, Z., Nakamura, T.: Simulations of crack propagation in elastic-plastic graded materials. Mechanics of Materials 36(7), 601–622 (2004)

Wisselink, H., Huétink, J.: 3d FEM simulation of stationary metal forming processes with applications to slitting and rolling. Journal of Materials Processing Technology 148(3), 328–341 (2004)

Yameogo, A.: Etude expérimentale et numérique de l'amorçage et de la propagation de fissures de fretting dans un assemblage roue/essieu ferroviaire. Ph.D. thesis, Ecole Centrale de Paris (2004)

A Genetic Algorithm and a Local Search Procedure for Workload Smoothing in Assembly Lines

Triki Hager[1], Mellouli Ahmed[2], and Masmoudi Faouzi[3]

[1] University of Sfax, Sfax Engineering School, ENIS, La2MP, BP 1173, 3038, Sfax, Tunisia
  hager_triki@yahoo.fr
[2] University of Sousse, Sousse Engineering School, ENISo, La2MP,
  BP 1173, 3038, Sfax,Tunisia
  ahmed.mellouli.eniso@gmail.com
[3] University of Sfax, Sfax Engineering School, ENIS, La2MP, BP 1173, 3038, Sfax, Tunisia
  faouzi.masmoudi@enis.rnu.tn

Abstract. In this paper, a genetic algorithm and a local search procedure are proposed to minimize workload smoothness index in an extension of Simple Assembly Balancing problem 2 (SALBP-2). The performance criteria considered are the cycle time and the smoothness index before local search procedure, and after local search procedure. The effectiveness of the proposed approach has been evaluated through a set of instances randomly generated.

Keywords: Balancing, Assembly line, Precedence and zoning constraints, Cycle time, Smoothness Index.

1   Introduction

The configuration of assembly line is used extensively in mass production systems to make the manufacture and control easier. One of the configuration problems is Assembly Line balancing Problem (ALBP). It is the way of getting an optimal assignment of tasks to the stations so as to achieve the desired level of performance.

The basic problem of the ALBP family is the Simple Assembly Line Balancing Problem (SALBP) (Baybars 1986). Table 1 illustrates the different versions of SALBP problems presented by Scholl and Becker (2006). For instance, SALBP-1 and SALBP-2 have a dual relationship (Scholl and Becker, 2006), because the first minimizes m (Number of stations) with a given C (Cycle time), while the second minimizes C (maximizes the production rate) for a given m (Baybars 1986). SALBP-E maximizes the line efficiency E to determine the quality of balance. Finally, the problem of getting a feasible balance F for a given m and a given C is called SALBP-F.

Table 1 The versions of SALBP

SALBP version		Cycle time C	
		Given	Minimize
Number of stations m	Given	SALBP-F	SALBP-2
	Minimize	SALBP-1	SALBP-E

The kinds of SALBP can be complemented by a secondary objective which is the smoothing station loads. It is an attempt to obtain equal amounts of work (tasks) to the various stations along the line. This objective guarantees a better flow of material (Mozdgir et al. 2013). Although there are many research works addressing this type of problem (Rachamadugu and Talbot 1991etc.), most of them treat the smoothing station loads as a primary objective. The Smoothness Index (SI) can be minimized providing that the combination (m, C) is optimal with respect to line efficiency (Kirkpatrick et al. 1983). The approach developed in this paper is to minimize workload smoothness index in an extension of SALBP-2. In the proposed problem, the number of stations is known and the objective is to minimize the cycle time at first time and the workload smoothness index at second time where both precedence and zoning constraints between tasks must be satisfied.

Different techniques have been developed in the literature to solve ALBPs using optimum seeking methods, such as branch-and-bound procedures (Miralles et al. 2008). Due to the combinatorial nature of the problem, these methods have a practical use limited for large sized problems. Therefore, some researchers are directed towards the development of heuristics (Chiang and Urban 2006) and metaheuristics for the solution of ALBPs such as simulated annealing (Kirkpatrick et al. 1983) and Genetic Algorithm GA (Holland 1975). The common characteristic of all the heuristic search methodologies is the use of problem-specific knowledge intelligently to reduce the search efforts (Sabuncuoglu et al. 2000). In fact, GAs mechanism is intelligent random search that received an increasing attention from the researchers in various combinatorial optimization problems such as ALB, supply chain, management and etc.

These studies indicated that GA method is able to pass from one solution set to another and to incorporate the specific characteristics of problem. The GA is a very effective search technique in solving difficult NP-hard problems. ALBPs belong to the NP-hard class of combinatorial optimization problem (Gutjahr and Nemhauser 1964) then the proposed problem is NP-hard. Due to the NP-hardness, a GA is proposed to solve the proposed extension of SALBP-2 to minimize the cycle time and a local search is proposed to minimize the SI.

The contribution of this paper is to show the useful of application the local search procedure in the GA solutions to improve the quality of the line balancing. The outline of the rest of this paper is as follows: Section 2 presents the steps of the proposed GA. Section 3 describes the local search procedure. Section 4 shows computational results. Finally, concluding remarks are presented in Section 5. In what follows, we describe solution procedures using the notations of Table 2.

Table 2 Notations

Symbol	Signification
n	Total numbers of assembly tasks; index $i, j=1, 2, …, n$
T	A set of n tasks; $T=\{1…n\}$
m	Total numbers of stations; index $s= 1, 2, …, m$
S	A set of m stations; $S=\{1...m\}$
SI	Smoothness Index
t_i	Processing time of Task i
t_s	Station time of station s
C	Cycle time
G	The precedence graph
IT	The set of incompatible pair tasks $(i, j) \in T$ which are incompatible (with $i<j$).
LT	The set of linked pair tasks $(i, j) \in T$ which are linked (with $i<j$).

2   Steps of Genetic Algorithm

To achieve the benefits of GA, its standard schema should be properly modified and adapted to the problem domain.
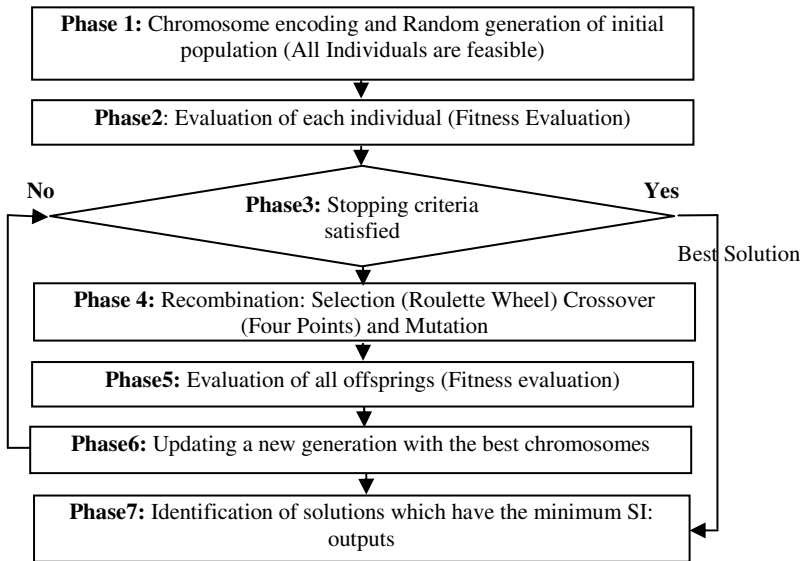
Fig. 1 Flowchart of the proposed GA

The genetic operators and the GA parameters are modified according to the proposed problem. The flow chart of the proposed GA is presented in Fig 1.

2.1 Chromosome Encoding and Random Generation of Initial Population (Phase 1)

The encoding scheme is task-oriented and it is similar to the scheme generated by (Leu et al. 1994).The length of the chromosome is equal to the number of tasks and each gene of the chromosome represents a task. The set by these chromosomes is the initial population which is randomly generated by assuring the feasibility of the precedence constraints among the tasks.

2.2 Fitness Evaluation (Phase 2)

The proposed GA employs the fitness of a chromosome (individual) as the inverse of the cycle time of the solution to be suitable with a minimisation problem. Therefore, the lowest cycle time the solution has, the more important its fitness is.

$f(j) = \dfrac{1}{C}$ denotes the fitness function value of chromosome j; $j = 1, \ldots, N$.

The cycle time of the chromosome is determined according to the following five steps:

Step 1: Determine the initial cycle time value which is Lower Bound (*LB*). It is calculated as shown in equation (1).

$$LB = \max\left(\max_{1 \leq i \leq n}\{t_i\}, \frac{\sum_{i=1}^{n} t_i}{m}\right) \qquad (1)$$

Step 2: Each pair of linked tasks is assigned the task-number to ensure the satisfaction of the zoning constrains of set *LT*

Step 3: Determine the number of stations by the following procedure as proposed by Akpinar and Bayhan (2011): Tasks are assigned to stations according to the task sequence in the chromosome as long as the predetermined cycle time is not overtaken. Once this cycle time is surpassed at least for a model, or the zoning constraints of set *IT* are not satisfied, a new station is opened for assignment and the procedure is repeated until the last task is assigned.

Step 4: If the obtained number of station is equal to a given *m* go to Step 5, or else the cycle time *C* will be incremented by 1 and go to Step 3.

Step 5: Terminate the procedure and present the cycle time of chromosome. Table 2 presents an example which illustrates the steps of assignment of tasks to stations.

To present all phases of the proposed approach, an illustrative example will be explained. Fig 2 presents the precedence graph *G*. *m*=6 stations (S), n=11 tasks, (4,5)∈ *IT*,   (6,7)∈ *LT*.
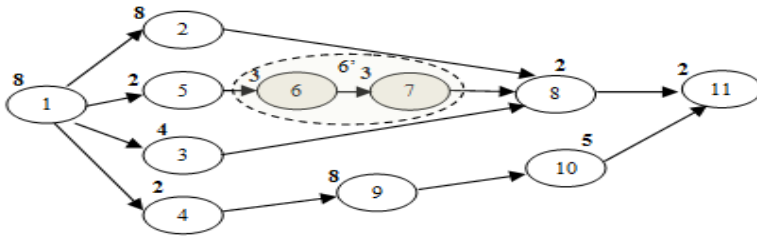
Fig. 2 Precedence graph G of the illustrative example

Table 3 The assignment of tasks to stations for the illustrative example

Step1					C=LB=8							
Chromosome associated to *G*	1	2	3	4	5	6	7	9	8	10	11
Step2	Task	1	2	3	4	5	6'		9	8	10	11
Step3	Task time	8	8	4	2	2	6		8	2	5	2
	Station	S1	S2	S3		S4			S5	S6		S7
Step4	*C=LB=8 => m =7>6 => C=C+1=9 go to step3*											
Step3	Task time	8	8	4	2	2	6		8	2	5	2
	Station	S1	S2	S3		S4			S5	S6		
Step4	*C=9 => m=6: The desired number of stations*											
Step5	End procedure : The cycle time of this chromosome is C=9											

2.3   Stopping Criteria (Phase 3)

After a simple convergence study, the GA procedure stops after 1000 iterations.

2.4   Selection, Crossover Operator and Mutation (Phase 4)

The parent chromosomes are selected by the ''Roulette Wheel strategy`` proposed by Holland (1975). The two parent chromosomes selected will be crossover and mutated by genetic operators:

   - A proposed Crossover Operator *(CO)* uses four crossover points, it works as follows:
• Four points generated randomly, cut each parent into five parts (0-1, 1-2, 2-3, 3-4, 4-5), as shown in the Fig 3.
• All elements from parts (0-1, 2-3, 4-5) of the first parent are copied to identical positions in the offspring 1.
• All the elements within the parts (1-2, 3-4) of the first parent are reordered according to the order of their appearance in the second parent vector   to generate the remaining parts of offspring 1.

   The second offspring is generated by the same steps, with the roles of its parents reversed.
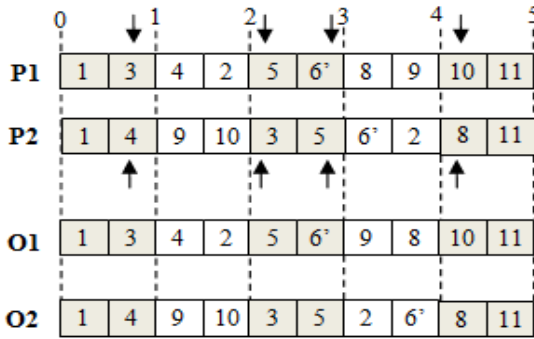
Fig. 3 The crossover operator (CO)

2.5   Evaluation of All Offsprings (Phase 5)

The evaluation of each offspring is identical to phase 4. In every crossover and
mutation, new candidate solutions are created. The new solutions may be better or
worse. This means that performing solutions are to be replaced using a
replacement strategy.

2.6   Updating a New Population (Phase 6)

The replacement strategy which is applied in Simaria and Vilarinho (2004) is used
to create the new population. This strategy takes into account the fitness value of
the individuals. The individuals of the new generation must have the best fitness
(higher fitness value= minimum cycle time) of all individual forms:

  i)   the current population
  ii)   offsprings produced by crossover
  iii) offsprings which underwent mutation

   The best solution of each generation is stored in order to avoid its loss over
generations.

2.7   Identification of Solutions Which Have the Minimum SI:
Outputs (Phase 7)

The best solutions obtained by the GA have different SI values. The chromo-
somes, which possess the minimum SI will be the outputs of the proposed GA.
These outputs will undergo a local search procedure to further reduce the SI that is
given below.

3   Local Search Procedure: Sequence Search of Moving Many Tasks

Many researchers have used the local search procedure for improving convergence speed towards the global optimum (Rubinovitz and Levitin 1995, Gao et al. 2009). In this setting, a local search procedure (Sequence search of moving many tasks) is employed to minimize the SI of each solution found by the GA. SI is calculated via formula (2).

$$SI = \sqrt{\sum_{s=1}^{m} (C - t_s)^2} \qquad (2)$$

The local search is developed based on the transfer the tasks from the bottleneck station to the smallest time station. The cycle time found by the GA will be considered as the Upper Bound (UB) in this procedure. The proposed local search is applied to every solution (outputs). Sequence search of moving many tasks consist in two sub-procedures (procedure of moving and exchange procedure). It is explained in five steps as follow:

Step1: Identification of the bottleneck station b.
Step2: Identification of the smallest time station st.
Step3: Execution of procedure of moving:
Let i the task which has the smallest execution time of b. i has to be moved from station b to station st without violating the existing constraints (the precedence and zoning constrains).
Let T_{st} is the station time of st, if $T_{st} <$ UB, $i = i+1$ and the procedure is repeated. Otherwise ($T_{st} >$ UB), we go to step 4.
Step 4: An exchange procedure (Rubinovitz and Levitin 1995) will be realized between the st and b:
Let j the task which has the smallest execution time of st, j has to be moved to station b.
Step 5: End of the procedure: Sequence search of moving many tasks
Tables 4 and 5 illustrate the application of sequence search of moving many tasks to the illustrative example which is shown in Fig 2.

Table 4 C and SI: before sequence search of moving many tasks

Chromosome associated to G	1	2	5	6'	3	4	9	8	10	11
Task time	8	8	2	6	4	2	8	2	5	2
Station	S1	S2	S3		S4		S5	S6		
Station time	8	8	8		6		8	9		
C-t_s	1	1	1		3		1	0		
SI	3,6									

Table 5 C and SI: after sequence search of moving many tasks

Chromosome associated to G		1	2	5	6'	3	4	9	8	10	11
	Task time	8	8	2	6	4	2	8	2	5	2
	Station	S1	S2	S3		S4			S5	S6	
	Station time	8	8	8		6			8	9	
Steps 1&2	Station					*st*			*B*		
Step 3	Task	1	2	5	6'	3	4	9	⑧	10	11
		1	2	5	6'	3	4	8	9	10	11
	Task time	8	8	2	6	4	2	2	8	5	2
Step5	Station	S1	S2	S3		S4			S5	S6	
	Station time	8	8	8		8			8	7	
C=8	C-t_s	0	0	0		0			0	1	
	SI	1									

The solution obtained after applying the local search procedure is given in Table 5. As can be seen in tables 4 and 5, the local search procedure has improved the quality of solutions by reducing the SI and the cycle time.

4   Results and Discussion

The effectiveness of the proposed method has been evaluated through a set of instances randomly generated (A, B, C, D, E, F). The data and the computational results of each instance are summarized in table 6.

n+: Number of linked task pairs; n-: Number of incompatible task pairs

According to table 6, the local search procedure has improved the quality of balancing of each instance by reducing the SI and the cycle time.

Table 6 Set of validation test problems (randomly generated)

	Instances	A	B	C	D	E	F
	n	30	30	30	35	35	35
	m	3	4	5	3	4	5
	n+	1	1	1	2	3	2
	n-	1	1	1	2	2	2
Before local search procedure	C	20	16	13	30	22	20
	SI	3,16	4,58	4,24	5	5,39	8,37
After local search procedure	C	18	15	12	28	20	18
	SI	1	3,16	1,73	1	1	3

5 Conclusion

A Genetic Algorithm (GA) is addressed in this paper to solve an extension of SALBP-2. To furthermore reduce the workload smoothness index (SI) of the line, a proposed local search procedure, called sequence search of moving many tasks, is applied to the solutions obtained by this GA. In this situation, the number of stations is known and the objective is to minimize cycle time at first time and the workload smoothness index at second time where both precedence and zoning constraints between tasks must be satisfied. The effectiveness of the proposed approach has been evaluated through a set of instances randomly generated. In fact, the application of local search procedure in all instances has improved the quality of solutions.

References

Akpına, S., MiracBayhan, G.: A hybrid genetic algorithm for mixed model assembly line balancing problem with parallel workstations and zoning constraints. Eng. Appl. of Artificial Intel. 24, 449–457 (2011)

Baybars, I.: A survey of exact algorithms for the simple assembly line balancing problem. Manag. Sci. 21, 909–932 (1986)

Scholl, A., Becker, C.: State-of-the-art exact and heuristic solution procedures for simple assembly line balancing. Eur. J. of Operat. Research 168, 666–693 (2006)

Mozdgir, A., Mahdavi, I., Seyedi Badeleh, S.I., Solimanpur, M.: Using the Taguchi method to optimize the differential evolution algorithm parameters for minimizing the workload smoothness index in simple assembly line balancing. Mathemati. and Comp. Model. 57, 137–151 (2013)

Rachamadugu, R., Talbot, B.: Improving three quality of workload assignments in assembly lines. Int. J. of Prod. Resear. 29, 619–633 (1991)

Kirkpatrick, S., Gelatt Jr., C.D., Vecchi, M.P.: Optimization by simulated annealing. Sci. 220, 671–680 (1983)

Miralles, C., Garcia-Sabater, J.P., Andres, C., Cardos, M.: Branch and bound procedures for solving the assembly line worker assignment and balancing problem. Application to sheltered work centres for disabled. Discr. Appl. Math. 156, 352–367 (2008)

Chiang, W., Urban, T.L.: The stochastic U-line balancing problem: A heuristic procedure. Eur. J. of Oper. Research 175, 1767–1781 (2006)

Holland, H.J.: Adaptation in natural and artificial systems. The University of Michigan Press, Ann Arbor (1975)

Sabuncuoglu, I., Erel, E., Tanyer, M.: Assembly line balancing using genetic algorithms. J. of Intel. Manufact. 11(3), 295–310 (2000)

Gutjahr, A.L., Nemhauser, G.L.: An algorithm for the line balancing problem. Managem. Sc. 11, 308–315 (1964)

Leu, Y.Y., Matheson, L.A., Rees, L.P.: Assembly line balancing using genetic algorithms with heuristic generated initial populations and multiple criteria. Dec. Sc. 15, 581–606 (1994)

Simaria, A.S., Vilarinho, P.M.: A genetic algorithm based approach to the mixed-model assembly line balancing problem of type II. Comput. & Industri. Engin. 47, 391–407 (2004)

Comparative Study for a Multi-objective MLCSP Problem Solved Using NSGA-II & E-Constraint

Wafa Ben Yahia[*], Houssem Felfel, Omar Ayadi, and Faouzi Masmoudi

Mechanics, Modeling and Production Research Laboratory,
National Engineering school of Sfax (ENIS), Sfax University, Tunisia
Route de Sokra B.P.1173 - 3038, Sfax, Tunisia
`wafa.benyahia@hotmail.fr`, `omar.ayadi@yahoo.fr`,
`faouzi.masmoudi@enis.rnu.tn`, `houssem.felfel@gmail.com`

Abstract. Operational production planning received much attention in the literature. In this paper, a multi-objective MLCLSP problem is proposed and two approaches "ε-constraint" and "NSGA-II" are compared when solving this problem. The multi-objective optimization model aims to minimize simultaneously the total production cost and the average inventory levels in a multi-period, multi-item environment. Several tests are developed to generate the Pareto optimal solution using the two optimization methods. The experimental results indicate that the ε-constraint is faster than NSGA-II and provides a better quality of the Pareto optimal solution.

Keywords: Multi-objective MLCLSP model, ε-constraint method, elitist genetic algorithm, NSGA-II.

1   Introduction

Developing a production plan fulfilling the requirements and constraints is one of the most important objectives of an enterprise taking part into a supply chain. For an efficient supply chain, coordination must exist between the partners in order to link local processes between partners and give the optimal solution for production planning through all the chain. Lot sizing is one of the most difficult and main problems in production planning. The problem to find production plan and to determine the suitable lot sizes for a multi-stage production system, assuming a limited capacities within a time period, corresponds, in the literature, to the multi-level capacitated lot sizing problem (MLCLSP). Ertogral and Wu (2000) define the MLCLSP in a multiple tier supply chain context as follows: given external demand for end items over a time horizon, a bill-of-material structure for each end

---

[*] Corresponding author.

item where the production of sub-assemblies may be spread across multiple facilities, find a production plan over multiple facilities that minimizes total inventory holding and setup costs.

Most of the researches deal with only one objective, like in Dudek & Stadtler (2005, 2007), Dudek (2004), Stadtler (1996, 2003), Maes et al. (1991), Sahling et al. (2009), Tempelmeier & Helber (1994), Almeder (2010), Chen & Chu (2003), Pitakaso et al. (2006), Clark & Armentano (1993), and Berretta et al.(2005)… All these works aim to minimize a cost function consisting of the sum of inventory holding cost, setup cost, overtime cost or operation cost.

In order to solve the MLCLSP problems, different approaches are used in the literature. A lot of works used meta-heuristics, such as genetic algorithms (Xie and Dong (2002), Kimms (1999)), or tabu research (Hung &Chien (2000), Gopalakrishnan et al. (2001), Hung et al. (2003)), or neural networks (Aarts et al. (2000), Gaafar & Choueiki (2000)), or simulated annealing (Kuik et al. (1993), Özdamar and Barbarosoglu (2000), Barbarosoglu and Özdamar (2000)), or memetic algorithms (Berretta and Rodrigues (2007)), and the local research (Almeder (2010)). Other researchers used the Lagrangean relaxation and decomposition (Chen & Chu (2003), Tempelmeier and Helber (1994), Boctor and Poulin (2005)). Also Mathematical programming approaches are used (Sahling et al. (2009), Stadtler (2003), Stadtler (1997), Akartunalı and Miller (2009)).

The purpose of this paper is to propose a multi-objective MLCLSP problem and solve it with ε-constraint method and the non-dominated Sorting Genetic Algorithm -II (NSGA-II), in order to compare the quality of optimal Pareto solutions proposed by each method.

The paper is organized as follows. In section 2 the MLCSP model is described and formulated. The resolution methodologies are presented in section 3, followed by the computational results in section 4. Finally, a conclusion and future research directions are drown in section 5.

2   Problem Statement and Model Formulation

The proposed optimisation MLCSP model aims to provide an optimal production plan for a multi-echelon manufacturing supply chain within a fixed time horizon facing a finite capacity of personnel and machines. The complexity of the problem can be viewed in the case of multi-level product structure, where products are related to each others by successor or predecessor items according to the bill of materials and the sequences of operations. The external demand of each finished product or semi-finished product is supposed to be known, and the due date requested by the customer corresponds to the end of the last planning period.

The developed model must satisfy the following assumptions:

- Many resources, with limited availabilities, can process several items.
- Raw materials are always available.
- No inventories at the first period.

- Items can be only produced if all their predecessor components are presented.
- Periodic external demand of each article is known.
- Overtime is allowed to extend the main available capacity.
- Backlogging is not authorized.
- The sequence of operations required to produce an item is fixed, and any alternative routing is prohibited.
- Inventory is calculated at the end of each planning period.
- Setup time is neglected.
- External demand has to be fully satisfied in time and quantity.

We consider a cooperative supply chain (SC), where different manufacturing plants cooperate together with the purpose of generating a global optimal production plan. These production sections share diverse information with each others, such as the external demand of customers, the production capacity and the production costs. Each manufacturing plant has eight working hours per day, but has different capacities and operations times. Products are transferred from a plant to the next one until reaching the last plant, where the finished products are stored to be delivered to the customer.

The purpose of the proposed model is to generate production plans that simultaneously minimize the total production cost of the SC and minimize the average of inventory levels.

Consider the following notations:

Indexes

t	planning period, $t = 1,..., T$.
j	operation, $j = 1,..., J$.
r	resource, $r = 1,..., R$.

Set Indexes

T	set of planning periods
J	set of operations
R	set of resources
S_j	set of direct successors of operation j

Parameters

cv_j	unit cost of operation j
cf_i	setup cost of operation j
co_r	unit cost of overtime (capacity expansion) at resource r
$D_{j,t}$	(external) demand for operation j in period t
$C_{r,t}$	Capacity of resource r in period t
$L_{j,t}$	Big constant
$a_{r,j}$	Unit requirement of resource r by operation j
$r_{j,k}$	Unit requirement of operation j by successor operation k
	(Depends on the manufacturing process)

Variables

C	total production cost
I_{moy}	average of inventory level for all operations
$x_{j,t}$	output level of operation j in period t (lot size)
$i_{j,t}$	inventory level of operation j at the end of period t
$y_{j,t}$	binary setup variable of operation j in period t

($y_{j,t}=1$ if product j is set up in period t; $y_{j,t}=0$ otherwise)

$o_{r,t}$	overtime at resource r in period t

Formulation

$$Min(C, \mathrm{I}_{m\,oy}) \tag{1}$$

$$St \quad C = \sum_{t=1}^{T}\sum_{j\in J}[(cv_j.x_{j,t})+(cf_j.y_{j,t})]+\sum_{t=1}^{T}\sum_{r\in R}co_r.o_{r,t} \tag{2}$$

$$\mathrm{I}_{m\,oy} = \frac{1}{T}\sum_{t=1}^{T}\sum_{j\in J}i_{j,t} \tag{3}$$

$$i_{j,t-1} + x_{j,t} = D_{j,t} + r_{j,k}x_{k,t} + i_{j,t} \qquad \forall j\in J\ ,\forall t \tag{4}$$

$$\sum_{j} a_{r,j}.x_{j,t} \le C_{r,t}+o_{r,t} \qquad \forall j\in J\ ,\forall t,\ \forall r\in R \tag{5}$$

$$x_{j,t} \le L_{j,t}.y_{j,t} \qquad \forall j\in J\ ,\forall t \tag{6}$$

$$x_{j,t} \ge 0, \qquad i_{j,t} \ge 0 \qquad \forall j\in J\ ,\forall t \tag{7}$$

$$o_{r,t} \ge 0 \qquad \forall t,\ \forall r\in R \tag{8}$$

$$y_{j,t} \in \{0,1\} \qquad \forall j\in J\ ,\forall t \tag{9}$$

The objective functions are presented by the two first equations (2) and (3). The first objective introduces the total production cost, which is the sum of the operations, setup and overtime costs. The second objective introduces the average level of inventory with respect to the number of planning periods. The decision variables are the operations levels ($x_{j,t}$), the inventory levels ($i_{j,t}$) for each considered operations, and the expansions of resource capacities through overtime ($o_{r,t}$). The Equation (4) provides the constraints capturing the flow balance between output, inventory and consumption by external demand and successor operations. The constraint (5) represents the capacity restrictions in using the different resources to produce the different items. Lot-sizing relationships and the choice of the items to be produced at each time period and at each plant location are expressed in (6). The constraints (7), (8) and (9) specify the domains of the different variables.

So formulation necessitates to satisfy (J*T) equality constraints and (2*R*T+4*J*T) inequality constraints.

Formulating the MLCLSP with such a bi-objective model presents the advantage of modelling the inventory level by a dissociated objective function. This allows giving the inventory level its necessary importance by considering it as a quantity to be minimized instead of converting it into a cost function integrated in a total cost formula.

3   Description of the Resolution Methods

3.1   NSGA-II Description

Evolutionary algorithms (EA) have become established as an alternative to classical methods and attracted a lot of research effort during the last 20 years (Zitzler 1999, A. Zhou et al. 2011). Moreover, GAs show good performances in finding near-optimal solutions for multi-level lot sizing, which is the basic problem in the considered work (Dellaert and Jeunet 2000, Dellaert et al. 2000, Xie and Dong 2002, Jung et al. 2006). We adapt here the popular elitist genetic algorithm NSGA-II, initially developed by Deb (2002), to solve our model containing integer variables. This algorithm is chosen for the many reasons, first the use of elitism, which shows its importance in the comparison made by Zitzler (2000) on a set of test problems. So only the best individuals keep alive during optimization. Second, according to Deb (2002), NSGA-II has a computational complexity equal to $O(MN^2)$ (M is the number of objectives and N is the population size), compared to other Multi-objective Evolutionary Algorithms (MOEAs), where the computational complexity is equal to $O(MN^3)$.

Like any genetic algorithm, NSGA-II deals simultaneously with a set of possible solutions called population and each solution is an individual of this population. This algorithm allows finding Pareto optimal fronts which consists on the set of optimal solutions with equal performances (non-dominated). Initially, a random parent population P_0 is created. The population is sorted in order to provide different fronts composed of feasible solutions having the same rank. In fact, individuals are ranked based on the concept of domination: an individual x_1 dominates another individual x_2 if the following two conditions are verified: first, all the objective functions of x_1 are not worse than *x2*, second, at least x_1 is strictly better than x_2 in one objective function. In addition, we define the parameter *crowding distance*, calculated for each individual. This parameter is calculated to estimate the density of solutions surrounding a particular individual in the population. The solution located in a lesser crowded region is selected. Selection is made using tournament between two individuals. From N parents, N new individuals (offspring) are generated in every generation by the use of the Simulated Binary Crossover (SBX) and Polynomial mutation (Deb et al., 2002 and 2001).

3.2   Epsilon-Constraint Description

The ε-constraint method has widely been used in the literature to generate exact Pareto-optimal solutions for multi-objective supply chain planning problem (You and Grossmann (2008), Franca et al. (2010) and Sabri and Beamon (2000)). The e-constraints approach is proposed by Chankong and Haimes (1983) is among the best known approach for solving multi-objective problems and finding a set of Pareto solution. In the e-constraint method, one of the objective functions is selected to be optimized and the other objectives are considered as constraints bounded by some allowable levels $ε_j$. Then, the level of $ε_j$ are altered to generate the set of Pareto. The modified problem can be represented as follows:

Minimize $f_1(x)$

Subject to $f_j(x) \le ε_j$ $\forall j = 2, ..., M$.

With M : number of objective functions $f(x)$.

$x \in X$.

4   Experimental Results

4.1   Tests Description

Two cases are studied here. In the first case, two plants are planning together (2R) over two periods (2T) to meet the external demand of three items (3I). The 3I .2R.2T case has 22 decision variables, 6 equality constraints and 32 inequality constraints. In the 4I.4R.4T case, four plants are planning together (4R) over four periods (4T) to meet the external demand of four items (4I). The 2R.3P.3I has 64 decision variables, 16 equality constraints and 96 inequality constraints.

The production plants must fulfill the given demand of products while facing finite capacities of personnel and machines. In the 3I.2R.2T case, where three kinds of items are produced: operation 3 requires one unit of operation 2, and operation 2 requires one unit of operation 1. But in the 4I.4R.4T case, operation 2 requires one unit of operation 1, and operation 4 requires one unit of operation 3. One period of the planning horizon corresponds to one month with four working weeks, each week with six working days and eight hours per day.

For all the cases we face an increasing external demand as it is shown in table 1. For the increasing demand, to minimize the total production cost it necessary to avoid the use of overtime. So to meet the demand of the last periods, production is done in advance. By consequence, the inventory level increases. But if the inventory level is minimized and the production of each period is done at that same period, the planner is obliged sometimes to use the overtime, which increases the total production cost. Thus, the evolution of the objective functions becomes contradictory.

Table 1 Customer demand features

	3I.2R.2T		4I.4R.4T			
Demand of	1st period	2nd period	1st period	2nd period	3rd period	4th period
Product 1	200	450	100	150	180	250
Product 2	150	350	150	200	230	300
Product 3	100	200	200	250	280	350
Product 4	-	-	100	150	180	250

4.2 Test Results

The development of NSGA-II and its implementation are done in C-language. The execution time does not exceed 2 minutes for all tests. And the ε-constraint method is implemented using Lingo 14.0 software package, which consits on exact method. But Lingo was faster than the meta-heuristic algorithm. This can be due to the integer decision variables and especially the presence of the equality constraint. As Coello et.al (2004) said, handling the equality constraints is nontrivial in the case of evolutionary approaches. The comparison between both Pareto of optimal solutions of the objective functions for both methods is shown in figure 1 and figure 2. Each Pareto consists of the non-dominated solutions generated during the optimization. The figures show that the ε-constraint method outperforms the NSGA-II in finding the optimal Pareto. Most of the solutions found by the NSGA-II are dominated by those found by the ε-constraint method. So the NSGA-II reached a local optimal solution front, however the ε-constraint method reached the Pareto optimal solution. Moreover, the divergence of the front of solution found by the NSGA-II is not too large from the optimal front. And the spread of solutions found by both optimization methods is comparable, but the research space of the ε-constraint method is larger than that of NSGA-II. In addition, the concave shape is observable only in the case of the ε-constraint method. The diversity of solutions gives multiple choices to the partners and allows them to choose according to their preference. In the set of the solution found by the ε-constraint method, one can notice that there are some solutions that are almost aligned. For example in the case of 4I.4R.4T to minimize the total production cost by 0.03%, the average of inventory level is decreased by 83.33%. And in the 3I.2R.2T case, the average of inventory level is maximized by 65% to decrease the total production cost by 0.01%. It is true that the ε-constraint gives wider range of solutions than NSGA-II, but this is by generating slightly different solutions of the total production cost and a significant difference between the averages of inventory level solutions. According to the Pareto generated by NSGA-II, this algorithm can propose close solutions to the Pareto optimal solutions by better compromise between both objective functions.

Finally, the quality of the solution is judged by the partners, who benefit from diverse productions plans to face different situations, such as supply interruption of some components, a breakdown, preventive maintenance or the absence of personnel.
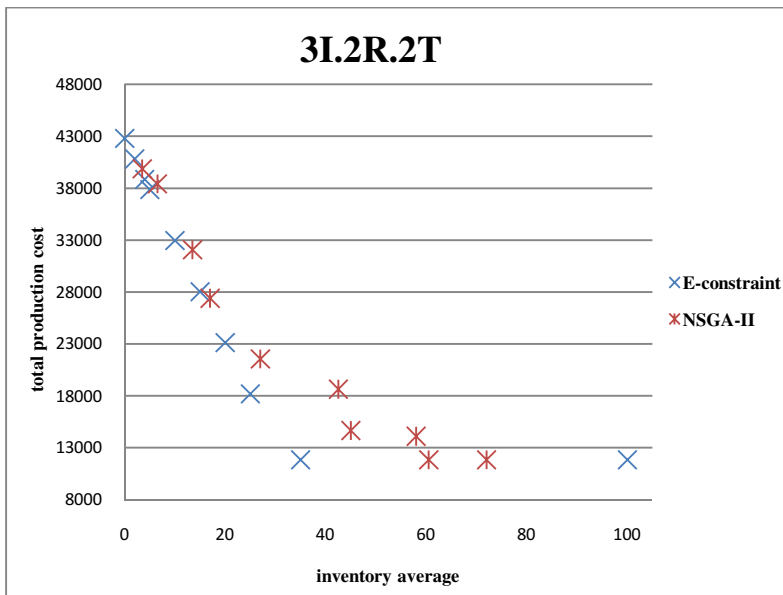
Fig. 1 The non-dominated front of objective functions for 3I.2R.2T case
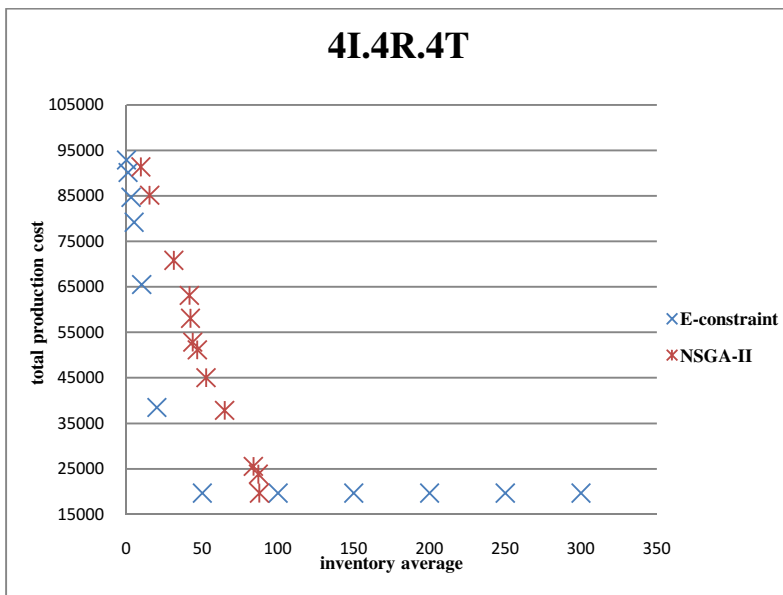
Fig. 2 The non-dominated front of objective functions for 4I.4R.4T case

5 Conclusion and Future Work

This paper is concerned with developing a cooperative planning framework for multi-tier and multi-item linear SC. The developed bi-objective MLCLS optimization model aims at minimizing the total production cost and the average inventory level of the SC partners, which foster the innovation of the proposed model. The inventory is not considered as a holding cost to be minimized but as a quantity to be minimized. A comparative study between the qualities of the optimal fronts was done, when solving the problem by NSGA-II algorithm and the ε-constraint method. Computational results for two problems with different sizes indicate that the ε-constraint method is more efficient in finding the Pareto optimal solution. The diversity of the proposed solutions allows partners to have larger range of negotiation on production plans to be considered by each of them in order to satisfy external demands. Proposing negotiation schemes based on generated optimal Pareto solutions represents an interesting future direction. In addition, more constraint can be added to the model, like using the main capacity before using the overtime or adding a storage capacity restriction.

References

Akartunalı, K., Miller, A.J.: A heuristic approach for big bucket multi-level production planning problems. European Journal of Operational Research 193(2), 396–411 (2009)

Almeder, C.: A hybrid optimization approach for multi-level capacitated lot-sizing problems. European Journal of Operational Research 200, 599–606 (2010)

Aarts, E.H.L., Reijnhoudt, M.F., Stehouwer, H.P., Wessels, J.: A novel decomposition approach for on-line lot sizing. European Journal of Operational Research 122, 339–353 (2000)

Barbarosoglu, G., Özdamar, L.: Analysis of solution space-dependent performance of simulated annealing: the case of the multi-level capacitated lot sizing problem. Computers and Operations Research 27, 895–903 (2000)

Berretta, R., Rodrigues, L.F.: A memetic algorithm for a multistage capacitated lot-sizing problem. International Journal of Production Economics 87, 67–81 (2007)

Berretta, R., Franca, P.M., Armentano, V.A.: Metaheuristic approaches for the multilevel resource-constrained lot-sizing problem with setup and lead times. Asia-Pacific Journal of Operational Research 22, 261–286 (2005)

Boctor, F.F., Poulin, P.: Heuristics for the n-product, m-stage, economic lot sizing and scheduling problem with dynamic demand. International Journal of Production Research 43, 2809–2828 (2005)

Chankong, V., Haimes, Y.: Multi-objective decision making theory and methodology. Elsevier Science, New York (1983)

Chen, H., Chu, C.: A Lagrangian relaxation approach for supply chain planning with order/setup costs and capacity constraints. Journal of Systems Science and Systems Engineering 12, 98–110 (2003)

Clark, A., Armentano, V.: Echelon stock formulation for multi-stage lot sizing with component lead times. International Journal of Systems Sciences 24(9), 1759–1775 (1993)

Coello, C.A., Lamont, G.B.: Application of mutli-objective evolutionary algorithms, 1st edn. World Scientific Pub. Co. Inc. (2004)

Deb, K., Pratap, A., Agarwal, S., Meyarivan, T.: A Fast and Elitist Multiobjective Genetic Algorithm: NSGA-II. IEEE Transactions on Evolutionary Computation 6(2), 182–197 (2002)

Deb, K.: Multi-objective optimization using Evolutionary Algorithms. John Wiley & Sons Ltd., Singapore (2001)

Dellaert, N., Jeunet, J.: Solving large unconstrained multi-level lot-sizing problems using a hybrid genetic algorithm. International Journal of Production Research 38(5), 1083–1099 (2000)

Dellaert, N., Jeunet, J., Jonard, N.: A genetic algorithm to solve the general multi-level lot-sizing problems with time varying costs. International Journal of Production Research 68(5), 241–257 (2000)

Dudek, G.: Collaborative planning in supply chains: a negotiation-based approach. Springer (2004)

Dudek, G., Stadtler, H.: Negotiations-based collaborative planning between supply chain partners. European Journal of Operational Research 163(3), 668–687 (2005)

Dudek, G., Stadtler, H.: Negotiation-based collaborative planning in divergent two-tier supply. International Journal of Production Research 45(2), 465–484 (2007)

Ertogral, K., Wu, S.D.: Auction-theoretic coordination of production planning in the supply chain. IIE Transactions 32(10), 931–940 (2000)

Franca, R.B., Jones, E.C., Richards, C.N., Carlson, J.: Multi-objective stochastic supply chain modeling to evaluate tradeoffs between profit and quality. International Jour. of Production Economics 127(2), 292–299 (2010)

Gaafar, L.K., Choueiki, M.H.: A neural network model for solving the lot-sizing problem. Omega 28, 175–184 (2000)

Gopalakrishnan, M., Ding, K., Bourjolly, J.-M., Mohan, S.: A tabu-search heuristic for the capacitated lot-sizing problem with set-up carryover. Management Science 47(6), 851–863 (2001)

Hung, Y.-F., Chien, K.L.: A multi-class multi-level capacitated lot sizing model. Journal of the Operational Research Society 51, 1309–1318 (2000)

Hung, Y.F., Chen, C.P., Shih, C.C., Hung, M.H.: Using tabu search with ranking candidate list to solve production planning problems with setups. Computers & Industrial Engineering 45, 615–634 (2003)

Jung, H., Song, I., Jeong, B.: Genetic algorithm based integrated production planning considering manufacturing partners. The International Journal of Advanced Manufacturing Technology 32(5-6), 547–556 (2006)

Kimms, A.: A genetic algorithm for multi-level, multi-machine lot sizing and scheduling. Computers & Operations Research 26, 829–848 (1999)

Maes, J., McClain, J., van Wassenhove, N.: Multilevel capacitated lotsizing complexity and LP-based heuristics. European Journal of Operational Research 53(2), 131–148 (1991)

Kuik, R., Solomon, M., Van Wassenhove, L., Maes, J.: Linear programming simulated annealing and tabu search heuristics for lotsizing in bottleneck assembly systems. IEE Transactions 25(1), 162–172 (1993)

Özdamar, L., Barbarosoglu, G.: An integrated Lagrangean relaxation-simulated annealing approach to the multi-level multi-item capacitated lot sizing problem. International Journal of Production Economics 68, 319–331 (2000)

Pitakaso, R., Almeder, C., Doerner, K.F., Hartl, R.F.: Combining population-based and exact methods for multi-level capacitated lot- sizing problems. International Journal of Production Research 44, 4755–4771 (2006)

Sabri, E.H., Beamon, B.: A multi-objective approach to simultaneous strategic and operational planning in supply chain design. Omega 28(5), 581–598 (2000)

Sahling, F., Buschkühl, L., Tempelmeier, H., Helber, S.: Solving a multi-level capacitated lot sizing problem with multi-period setup carry-over via a fix-and-optimize heuristic. Computers & Operations Research 36(2009), 2546–2553 (2009)

Stadtler, H.: Multilevel lot sizing with setup times and multiple constrained resources: Internally rolling schedules with lot-sizing windows. Operations Research 51(3), 487–502 (2003)

Stadtler, H.: Reformulations of the shortest route model for dynamic multi-item multi-level capacitated lotsizing. Operations Research Spektrum 19, 87–96 (1997)

Stadtler, H.: Mixed integer programming model formulations for dynamic multi-item multi level capacitated lotsizing. Eur. J. Oper. Res. 94, 561–581 (1996)

Tempelmeier, H., Helber, S.: A heuristic for dynamic multi-item multi-level capacitated lotsizing for general product structures. European Journal of Operational Research 75, 296–311 (1994)

Xie, J., Dong, J.: Heuristic genetic algorithms for general capacitated lot sizing problems. Computers Mathematics with Applications 44(1-2), 263–276 (2002)

You, F., Grossmann, I.: Design of responsive supply chains under demand uncertainty. Computers & Chemical Engineering 32(12), 3090–3111 (2008)

Zitzler, E., Deb, K., Thiele, L.: Comparison of multiobjective evolutionary algorithms: empirical results. Evolutionary Computation 8(2), 173–195 (2000)

A Multi-objective Multi-site Supply Chain Planning Problem under Risk and Uncertainty

Houssem Felfel, Omar Ayadi, and Faouzi Masmoudi

University of Sfax, National School of Engineers of Sfax,
Laboratory of Mechanics, Modeling and Production,
Road of Soukra km 3.5, BP1173 - 3038 Sfax, Tunisia
`houssem.felfel@gmail.com, omar.ayadi@yahoo.fr,`
`faouzi.masmoudi@enis.rnu.tn`

Abstract.   In this paper, we propose a multi-objective two-stage stochastic programming model for a multi-site supply chain planning problem under demand uncertainty. Decisions such as the amount of products to be produced, the inventory level, the quantity of lost demand and the amounts of product transported between plants and customer are considered. In order to develop a robust supply chain planning solution, a risk measure is incorporated into the stochastic programming model. The proposed multi-objective model aims simultaneously to minimize the expected total cost, to minimize the worst-case cost and to maximize the customer demand satisfaction level. A numerical example is illustrated in order to show the effectiveness of the proposed model.

Keywords: supply chain planning, multi-objective, risk management, stochastic programming.

1   Introduction

In the face of today's highly competitive markets, manufacturing environments have changed from traditional single-plant to multi-site structure. Recently, multi-site production planning problems have attracted many researchers 'attention (Lin and Chen 2006, Verderame and Floudas 2008, Shah and Ierapetritou 2012, Felfel et al. 2014). All these works are dealing with deterministic approaches. However, production planning problem are characterized by several sources of uncertainty such as customer demand, unit cost and processing time. Hence, the assumption that all these parameters are deterministic will lead to no-optimal or unrealistic results. Therefore, it is crucial to develop an optimization model in multi-site supply chain planning problem that considers existing uncertainties.

Several approaches were proposed in the literature to incorporate uncertainty in the mathematical model. These approaches can be classified into four main categories: stochastic programming approach, fuzzy programming approach, robust optimization approach, and stochastic dynamic programming approach

(Sahinidis, 2004). Stochastic programming technique (Birge and Louveaux, 1997) is widely used in the literature to solve optimization problem under uncertainty. In this approach, the decision variables are divided into two sets. The first set corresponds to the first-stage variables representing the decision to be made "here-and-now" before the realization of the random events. The second set corresponds to the second-stage variables that are made based on the first stage decisions in a "wait-and-see" mode after the realization of uncertainty.

The stochastic programming approach has been successfully applied to a wide variety for supply chain planning problem (Gupta and Maranas, 2003; Leung et al., 2006; Awudu and Zhang, 2013). Gupta and Maranas (2003) studied a midterm multi-product multi-site supply chain planning problem under demand uncertainty by means of a two-stage stochastic programming approach. The proposed model aims to minimize the total cost including production cost, raw material purchase cost and transportation cost. Awudu and Zhang (2013) proposed a production planning problem for a biofuel supply chain under uncertainty. A two-stage stochastic programming model is developed in order to maximize the expected profit. Leung et al. (2006) proposed a mid-term multi-site aggregate production planning problem under an uncertain environment. The authors developed a stochastic programming model in order to minimize the total cost. The total cost involves the labor cost, the hiring and laying-off cost, the production cost, the inventory cost and the penalty cost.

Face to the highly competition, the decision makers have to reduce the risk of high cost when managing their supply chains. Although the stochastic programming approach optimizes the expected value of the objective function, it does not provide any control on the variability of the objective function over different scenarios (Bonfill et al., 2004). To the best the authors' knowledge, the risk management has been rarely considered in multi-site supply chain planning problem.

In supply chain planning problem, most of the papers focused on minimizing the total cost or maximizing profit as a single objective function (Fahimnia et al. 2013). Furthermore, the customer demand satisfaction is one of the most important criteria that should be considered when formulating the supply chain planning model.

The objective of this paper is to propose a new mathematical model of a multi-product, multi-period, multi-site supply chain under demand uncertainty taking into account the risk management. The proposed model aims simultaneously to minimize the total cost as well as to maximize the customer demand satisfaction. A two-stage stochastic programming approach is proposed in order to incorporate uncertainty in the mathematical model. Risk management is introduced in the developed model by incorporating a risk metric associated with the total cost distribution in the stochastic programming model. This approach results in a multi-objective optimization problem where the total cost, the customer demand satisfaction and the risk measure are three objective functions to be optimized. A numerical example is illustrated to demonstrate the effectiveness of the proposed model.

The remainder of the paper is organized as follows. In section 2, the problem statement is described. The third section presents the two-stage stochastic programming model of the multi-site supply chain planning problem. Section 4 describes the solution approach of the multi-objective optimization problem. Section 5 presents an illustrative example and corresponding analyses. Finally, conclusions and perspectives are presented in section 6.

2   Problem Statement

In this paper, we consider a multi-plant supply network wherein the end product is produced through different stages. The manufacturing process consists of many production stages. Each stage may involve more than one plant forming a multi-site supply network manufacturing as shown in Fig. 1. A distribution lead time is taken into account in shipping finished and semi-finished products between the plants of the different stages.
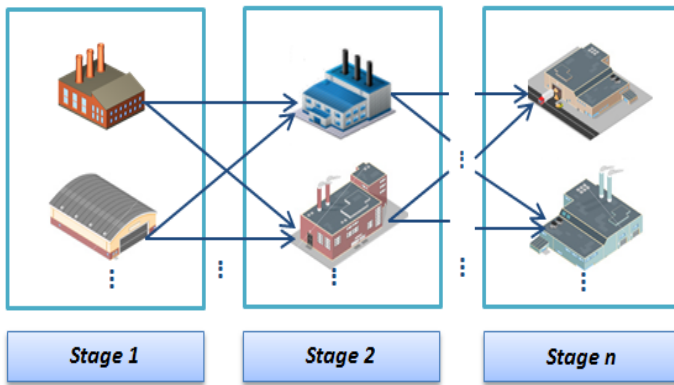
Fig. 1 The multi-stage and multi-site supply chain environment

On the other hand, products are characterized by volatile demand and short life cycle. The stochastic product demand could lead to excessive inventory and production costs or to loss of market share and unsatisfied customer demand.

The objective of the supply chain planning problem is to minimize the total expected costs, to minimize the worst-case cost and to maximize the customer demand satisfaction level. The total costs involve production costs, penalty costs, inventory costs as well as transportation costs. Model decision variables include the amount of production at each plant, the inventory level of finished or semi-finished products, the amount of lost demand as well as and the quantity of transportation between the different plants and customers considering demand uncertainty.

3   Proposed Stochastic Programming Model

In order to tackle the uncertainty of customer demand, a two-stage stochastic programming model is proposed. It is assumed that the uncertain demand is considered as a set of discrete scenarios associated with known probability in the stochastic programming formulation. It is worthwhile mentioning that the stages of the stochastic model are related to different steps of decision making and it does not correspond to time periods. The first-stage decisions include the amounts of products to be produced at each plant as well as the transportation amounts of products between upstream and downstream plants. Decisions such as the amount of products to be transported to the customer, inventory level and lost demand are considered as second-stage decisions. The indices, parameters and the decision variables used to formulate the mathematical model are introduced as follows:

Indices

L_i	Set of direct successor plant of plant i.
ST_j	Set of stages (j= 1,2, ..., N).
i, i'	Production plant index (i,i' = 1, 2 , ...,I) where i belongs to stage n and i' belongs to stage $n+1$.
k	Product index (k = 1,2, ..., K).
t	Period index (t = 1,2, ..., T).
s	Scenario index (s = 1,2,. . .,S).

Decision variables

P_{ikt}	Production amounts of product k at plant i in period t in regular-time.
S_{ikt}^s	Amounts of end of period inventory of product k for scenario s at plant i in period t.
JS_{ikt}^s	Amounts of end of period inventory of semi-finished product k for scenario s at plant i in period t.
$Dlost_{kt}^s$	Lost demand amounts of finished product k for scenario s in period t.
$TR_{i->i',kt}$	Amounts of product k transported from plant i to i' in period t.
$TR_{i->CUS,kt}^s$	Amounts of product k transported from the last plant i to customer for scenario s in period t.
$Q_{i,k}$	Amounts of product k received by plant i for scenario s in period t.

Parameters

cp_{ik}	Unit cost of production for product k in regular-time at plant i.
$ct_{i->i',k}$	Unit cost of transportation between plant i and i' of production for product k.

$ct_{i->CUS,k}$	Unit cost of transportation between the last plant i and the customer.
cs_{ik}	Unit cost of inventory of finished or semi-finished product k at plant i.
pe_k	Penalty cost of product k.
pr_{kt}^s	Unit sales price of finished product k for scenario s in period t.
$capp_{it}$	Production capacity at plant i in normal working hours in period t.
$caps_{it}$	Storage capacity at plant i in period t.
$capt_{i->i',t}$	Transportation capacity at plant i in period t.
D_{kt}^s	Demand of finished product k for scenario s in period t.
b_k	Time needed for the production of a product entity k [min].
DL	Delivery time of the transported quantity.
π^s	The occurrence probability of scenario s where $\sum_{s=1}^{S} \pi^s = 1$

Problem formulation

$$Min\ E[Cost] = \sum_{s=1}^{S} \pi^s \sum_{t=1}^{T} \sum_{k=1}^{K} \sum_{i=1}^{I} cs_{ik}(S_{ikt}^s + JS_{ikt}^s)$$

$$+ pe_k Dlost_{k,t}^s + ct_{i->CUS,k} TR_{i->CUS,kt}^s \tag{1}$$

$$+ \sum_{t=1}^{T} \sum_{k=1}^{K} \sum_{i=1}^{I} cp_{ik} P_{ikt} + ct_{i->i',k} TR_{i->i',kt}$$

$$Cost^s \le WC\ Cost \tag{2}$$

$$Max\ E[DS] = \sum_{s=1}^{S} \pi^s DS^s = \sum_{s=1}^{S} \pi^s \frac{\sum_{t=1}^{T} \sum_{k=1}^{K} D_{kt}^s - Dlost_{kt}^s}{\sum_{t=1}^{T} \sum_{k=1}^{K} D_{kt}^s} \tag{3}$$

$$DS^s \ge MDS \tag{4}$$

$$S_{ik,t}^s = S_{ik,t-1}^s + P_{ikt} - \sum_{i' \in L_i} TR_{i->i',kt}, \quad \forall i \in ST_{j<N}, \forall k,t,s \tag{5}$$

$$\sum_{i=1}^{I} S_{ik,t}^s = \sum_{i=1}^{I} S_{ik,t-1}^s + P_{ikt} - TR_{i->CUS,kt}^s, \quad \forall i \in ST_{j=N}, k,t,s \tag{6}$$

$$JS_{ik,t}^s = JS_{ik,t-1}^s + Q_{ikt} - P_{ikt}, \quad \forall i,k,t,s \tag{7}$$

$$Dlost_{kt}^{s} = D_{kt}^{s} - TR_{i->CUS,kt}^{s}, \quad \forall k,t,s \qquad (8)$$

$$Q_{i'k,t+DL} = \sum_{i' \in L_i} TR_{i->i',kt}, \qquad \forall i,k,t,s \qquad (9)$$

$$\sum_{k=1}^{K} b_k P_{ikt} \le capp_{it}, \qquad \forall i,t \qquad (10)$$

$$\sum_{k=1}^{K} S_{ikt}^{s} + JS_{ikt}^{s} \le caps_{it}, \qquad \forall i,t,s \qquad (11)$$

$$\sum_{k=1}^{K} TR_{i->i',kt} \le captr_{it}, \qquad \forall i,t,s \qquad (12)$$

$$P_{ikt}, S_{ikt}^{s}, JS_{ikt}^{s}, TR_{i->i',kt}, TR_{i->CUS,kt}^{s}, Q_{i,k}, Dlost_{kt}^{s} \ge 0, \quad \forall i,k,t,s \qquad (13)$$

The first objective function aims to minimize the expected total cost including production cost, inventory cost, penalty cost on lost demand and transportation cost as shown in Equation (1). In order to manage the risk of high cost, a risk measure (worst-case scenario) associated with the total cost distribution is included in the proposed stochastic model. This risk metric was shown to be a very effective approach in stochastic programming models (Bonfill et al. 2004). Both the expected total cost and the worst-case cost (*WC Cost*) are to be minimized. The worst-case cost is obtained from the maximum cost over all the scenarios as shown in Equation (2). Indeed, the total cost should not exceed the value of worst-case cost in all the scenarios. The second objective function shown in Equation (3) maximizes the customer demand satisfaction level. The customer demand satisfaction level is measured as the ratio of the covered demand. However, the mathematical formulation of the second objective function doesn't present a real operational policy and can lead to unrealistic results. Therefore, we consider a minimum target for the customer demand satisfaction (*MDS*) that must be attained in all the scenarios as detailed in Equation (4). Equation (5) provides the balance for the inventory level of products in each production stage expect the last stage considering the amounts of products to be transported between the different plants in every scenario s. Equation (6) represents the balance for inventory in the last production stage taking into account the products to be shipped to the customers in every scenario s. Equation (7) provides the inventory balance for the semi-finished products in every scenario s. Equation (8) provides the balance equation for lost products demand at time period t in every scenario s. The lost demand is equal to the end product demand minus the amounts of products transported to the customer. Constraint (9) represents the balance for transportation between the different production plants. Indeed, the quantity of products transported to one plant is received after a delivery time *DL* in every scenario s. The set of equation (10), (11) and (12) represents the production capacity constraint, storage capacity constraint and transportation capacity constraint respectively. Constraint (13) is the non-negativity restriction on the decision variables.

4 Solution Approach

The obtained mathematical formulation can be finally expressed as follows:

$$\min\{E[Cost], WC\,Cost, -MDS\}$$
$$s.t.\ Eqs\ (1)-(13) \tag{14}$$

The solution of the above problem is a front of Pareto optimal solutions. This front of Pareto optimal reveals the tradeoffs that exist between the considered objective functions. In order to obtain the front of Pareto optimal solutions, the e-constraint method developed by (Haimes et al. 1971) is applied. The e-constraint method has been widely applied in multi-objective supply chain planning problems (Guillén et al. 2005, You and Grossmann 2008, Franca et al. 2010). In this approach, one of the objective functions is selected to be optimized and the other objective functions are transformed into constraints with allowable bounds ε_i.

Subsequently, The level of ε_1 and ε_2 in Equation are altered in order to generate the entire front of Pareto optimal solutions as follows:

$$\min\{E[Cost]\}$$
$$s.t.\ Eqs\ (11)-(13)$$
$$WC\,Cost \le \varepsilon_1 \tag{15}$$
$$MDS \ge \varepsilon_2$$

5 Illustrative Example

The considered example involves is a multi-site manufacturing network which consists of 5 production stages with 8 plants and 2 finished products. The planning horizon contains 8 time periods and the length of a period is one week. According to the past sales records, the uncertain demand can be assumed to be one of four

Table 1 Uncertain end product demand

Scenario	T1 => T5, T7 &T9		T6			T8			T10		
	P1	P2	P2	P2	PROB	P1	P2	PROB	P1	P2	PROB
BOOM	0	0	3750	3330	0.25	3450	3110	0.2	3 250	3050	0.25
GOOD	0	0	2850	2610	0.35	2440	2370	0.35	2120	1980	0.3
FAIR	0	0	2060	1850	0.25	1830	1640	0.3	1650	1420	0.35
POOR	0	0	1410	1220	0.15	1280	1060	0.15	1020	830	0.1

scenarios: boom good, fair or poor. The stochastic products demand of the finished products P1 and P2 in periods T6, T8 and T10 for different scenario are detailed in Table1. The numerical example is solved using LINGO 14.0 and MS-Excel 2010 on a 32-bit Windows 7 based computer with an INTEL(R) Core (TM) 2Duo CPU,T5670@1.8 GHZ, 1.8 GHZ, 2 GB RAM.
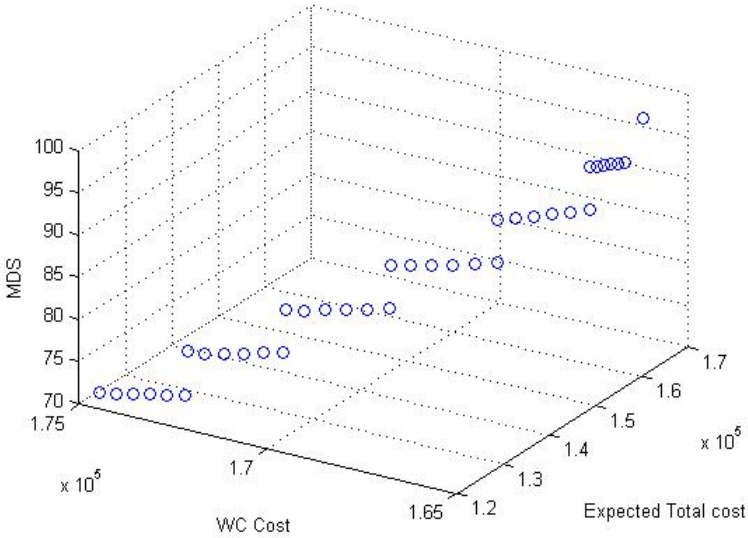
Fig. 2 Pareto optimal solutions distribution

In this section, the e-constraint method is applied to solve the multi-objective supply chain planning problem and to generate the front of Pareto-optimal solutions. The obtained front of Pareto is shown in Fig. 2. It is worth noting that every point of the front of Pareto in Fig. 2 represents a particular set of planning decisions.

The obtained front of Pareto optimal solutions is depicted for different customer demand satisfaction level (*MDS*=70%, 75%, 80%, 85%, 90%, 95% and 100%). For ease of understanding of the existing tradeoffs among the objective functions, the Pareto curve of the expected total cost and the worst-case cost is plotted for a fixed customer demand satisfaction level (*MDS*=90%) as shown in Fig. 3. It is clear from Fig. 3 that there is a significant conflict between these objective functions. Indeed, when the expected total cost decreases, the worst-case cost increases. It should be noted that point A represents the supply chain planning before risk management and point B represents the planning after risk management with minimum WC Cost. The WC Cost decreases from 167419 (Point A) to 165964 (Point B) which represents a reduction of 0.88%, whereas the total expected cost increases from 148493.9 (Point A) to 156394.4 (Point B) which represents an increase of 5.05%. In order to take in account the risk management in the supply chain planning and to reduce the high value of total cost, the decision maker could choose the point B from the set of Pareto optimal solutions.
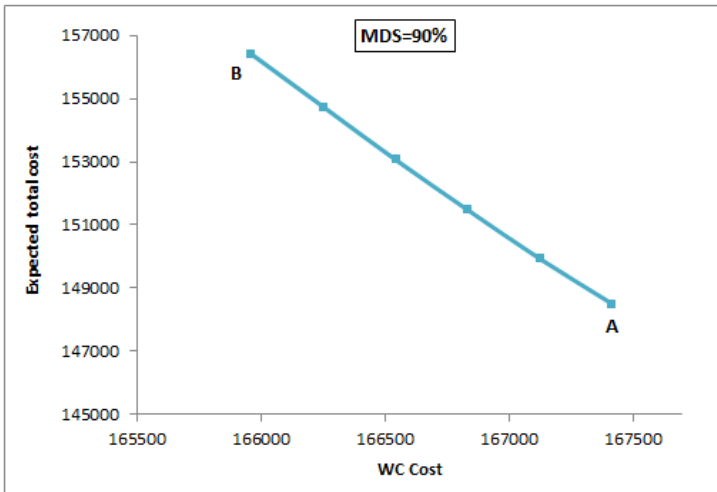
Fig. 3 Pareto curve for the expected total cost and the worst-case cost for different demand satisfaction level

6   Conclusion

In this work, a two-stage stochastic programming model is proposed to deal with a multi-period multi-site supply chain planning problem under demand uncertainty. The supply chain planning problem is modeled as a multi-objective optimization formulation accounting for the minimization of the expected total cost, the minimization of the worst-case cost as well as the maximization of customer demand satisfaction. The e-constraint method is applied in order to solve the proposed model. As the considered objective functions conflict with each other, the optimization problem yields to a front of Pareto-optimal solutions that reveals the trade-offs between the different objective functions. A risk management tool (the worst-case scenario) is explicitly considered as a mean to reduce the high cost risks. Computational results show that this risk measure can relatively reduce the risk of incurring in high total costs. Further research needs to be done in order to introduce and to compare other risk measures such as downside risk and conditional value-at-risk. Moreover, the effectiveness of the proposed strategy can be highlighted by a real industrial case study.

References

Awudu, I., Zhang, J.: Stochastic production planning for a biofuel supply chain under demand and price uncertainties. Applied Energy 103, 189–196 (2013)

Birge, J.R., Louveaux, F.: Introduction to stochastic programming. Springer, New York (1997)

Bonfill, A., Bagajewicz, M., Espuňa, A., Puigjaner, L.: Risk management in the scheduling of batch plants under uncertain market demand. Ind. Eng. Chem. Res. 43, 741–750 (2004)

Fahimnia, B., Farahani, R.Z., Marian, R., Luong, L.: A review and critique on integrated production–distribution planning models and techniques. Journal of Manufacturing Systems 32(1), 1–19 (2013)

Felfel, H., Ayadi, O., Masmoudi, F.: Multi-objective Optimization of a Multi-site Manufacturing Network. In: Abbes, M.S., Choley, J.-Y., Chaari, F., Jarraya, A., Haddar, M. (eds.) Mechatronic Systems: Theory and Applications. LNME, pp. 69–76. Springer, Switzerland (2014)

Franca, R.B., Jones, E.C., Richards, C.N., Carlson, J.P.: Multi-objective stochastic supply chain modeling to evaluate tradeoffs between profit and quality. International Jour. of Production Economics 127(2), 292–299 (2010)

Guillén, G., Mele, F.D., Bagajewicz, M.J., Espuña, A., Puigjaner, L.: Multiobjective supply chain design under uncertainty. Chemical Engineering Science 60(6), 1535–1553 (2005)

Gupta, A., Maranas, C.D.: Managing demand uncertainty in supply chain planning. Computers and Chemical Engineering 27, 1219–1227 (2003)

Haimes, Y.Y., Lasdon, L.S., Wismer, D.A.: On a bicriterion formulation of the problems of integrated system identification and system optimization. IEEE Transactions on Systems, Man and Cybernetics 1, 296–297 (1971)

Leung, S.C.H., Wu, Y., Lai, K.K.: A stochastic programming approach for multi-site aggregate production planning. Journal of the Operational Research Society 57, 123–132 (2006)

Lin, J.T., Chen, Y.Y.: A multi-site supply network planning problem considering variable time buckets– A TFT-LCD industry case. The International Journal of Advanced Manufacturing Technology 33(9-10), 1031–1044 (2006)

Shah, N.K., Ierapetritou, M.G.: Integrated production planning and scheduling optimization of multisite, multiproduct process industry. Computers and Chemical Engineering 37, 214–226 (2012)

Sahinidis, N.V.: Optimization under uncertainty: state-of-the-art and opportunities. Computers and Chemical Engineering 28(6-7), 971–983 (2004)

Verderame, P.M., Floudas, C.A.: Integrated operational planning and medium-term scheduling for large-scale industrial batch plants. Industrial & Engineering Chemistry Research 47(14), 4845–4860 (2008)

You, F., Grossmann, I.E.: Design of responsive supply chains under demand uncertainty. Computers & Chemical Engineering 32(12), 3090–3111 (2008)

Modelling Dependencies in Engineering Change Management (ECM)

Masmoudi Mahmoud[1,2], Leclaire Patrice[1], Zolghadri Marc[1],
and Mohamed Haddar[2]

[1] Laboratoire d'Ingénierie des Systèmes Mécaniques et des MAtériaux (LISMMA),
SUPMECA, 3 rue Fernand Hainaut, 93407, Saint-Ouen Cedex, France
`{mahmoud.masmoudi,patrice.leclaire,marc.zolghadri}@supmeca.fr`

[2] Ecole Nationale d'Ingénieurs de Sfax, Université de Sfax, Laboratoire de Mécanique,
Modélisation et Production, Route Soukra Km 3.5, BP 1173, 3038 Sfax, Tunisia
`mohamed.haddar@enis.rnu.tn`

Abstract. Products in engineering design are susceptible to be changed. A change in one product element can involve changes in other elements. While, in most cases, the change impact can be partly predictable, unexpected propagation of the change can occur. The main objective of this work is to characterise this change impact in order to predict as finely as possible the consequence of the product change on its structure and its functions. We develop a process to explain how to use regression analysis to identify the type of dependency existent between two dimensions. Findings show that, although qualitative dependency, already used in the literature, aids to predict either the increase or decrease of the affected dimension's value after a change in instigating dimension's value, functional dependency offers an effective way for characterising the relationship between two dimensions and translate it into a function which can be helpful in the further works of change propagation analysis.

Keywords: Regression, Engineering Change Management (ECM), Dependency, Least Squares Method (LSM).

1   Introduction

Products could be changed, modified or updated to answer new requirements. It is largely admitted that changes can be propagated within the product structure and functions. Predicting the possible product change propagation behaviour is an important task in Engineering Change Management (ECM), (Wynn, Caldwell, & Clarkson, 2010). This requires an appropriate method for characterising the change before analysing the propagation effect.

Research on the subject, such as (Kusiak & Wang, 1995), has been mostly restricted to provide qualitative and quantitative dependency values for characterising change. But authors think that a functional dependency procures a higher analysis capability. Qualitative dependency aids to predict either the

increase or decrease of the affected dimension's value after a change in instigating dimension's value. But, functional dependency offers an effective way for characterising the relationship between two dimensions and making regression, which is defined as the construction of a function from a given set of data points. Among interpolation methods, one of the most commonly used is the Lagrange. According to (Archer & Weisstein, 1999), the more data points that are used in an interpolation, the higher degree of the resulting Lagrange interpolating polynomial is found. Therefore, our purpose is to find the simplest polynomial function with the lowest possible degree that fit with the point cloud.

This paper describes the proposed process using the least squared method for regression. The identified function approximates the dependency between the product parameters. This approximation is obtained thanks to a trade-off between the function complexity and dependency computation.

The rest of this paper is organized as follows: Section 2 gives a brief review of the regression techniques; Section 3 provides details about the CAD-based approach for dependency identification for Engineering Change proposed in a previous paper. The last section is concerned with the methodology used for this study and how those techniques are implemented.

2   Regression and Statistics Review

In this section, we give a quick introduction to the basic elements of statistics needed for regressions dealing with function fit and regression analysis.

2.1   Lagrange Polynomial Interpolation

Given a set of $n+1$ data points $(x_0, y_0), (x_1, y_1), \ldots, (x_n, y_n)$, where each two x_j are different, the interpolation polynomial $P(x)$ in the Lagrange form is a linear combination of Lagrange basis polynomials (Jeffreys & Jeffreys, 1988), of degree $\leq n$ passes through all these points and is given by:

$$P(x) = y_0 L_0(x) + y_1 L_1(x) + \cdots + y_n L_n(x) \tag{1}$$

Where

$$L_i(x) = \frac{(x - x_0)(x - x_1) \cdots (x - x_{i-1})(x - x_{i+1}) \cdots (x - x_n)}{(x_i - x_0)(x_i - x_1) \cdots (x_i - x_{i-1})(x_i - x_{i+1}) \cdots (x_i - x_n)}$$

$$= \prod_{\substack{j=0 \\ j \neq i}}^{n} \frac{x - x_j}{x_i - x_j}, \forall i = 1 \cdots n \tag{2}$$

2.2   The Least Squares Method (LSM)

The least square method (LSM) is one of the most famous and oldest techniques in statistics analyses (Abdi, 2007). The method of Least Squares is a procedure, requiring just some calculus and linear algebra, to estimate the unknown parameters' values of a function that fit with a set of data points (Miller, 2006). The oldest and the most frequent of its use is the linear regression, which estimates the problem as finding a line that best fits a set of data points. In this case, the prediction is given by the following equation:

$$\hat{Y} = a + bX \tag{3}$$

Two parameters are estimated with LSM which specify the intercept (a) and the slope (b) of the regression line, given by:

$$a = \overline{Y} - b\overline{X} \tag{4}$$

$$b = \frac{\sum_{i=0}^{n}(Y_i - \overline{Y})(X_i - \overline{X})}{\sum_{i=0}^{n}(X_i - \overline{X})^2} \tag{5}$$

$$\text{Where } \overline{X} = \frac{1}{n}\sum_{i=0}^{n} X_i \tag{6}$$

Polynomial regresion is used to determine the parameters' values a_i, $\forall i \in \{0 \cdots n\}$ that make the curve best fit the data points. With three or more parameters, the equation describes a curve; more parameters create a more flexible curve.

The quality of the regression is computed by the coefficient R^2, which ranges from 0 to 1, is defined by the ratio of the residual sum of squares to the total sum of squares:

$$R^2 = 1 - \frac{SS_{res}}{SS_{tot}} \tag{7}$$

Where

$$SS_{res} = \sum_{i=0}^{n}\left(Y_i - \hat{Y}_i\right)^2 \text{ and } SS_{tot} = \sum_{i=0}^{n}\left(Y_i - \overline{Y}\right)^2 \tag{8}$$

If R^2 equals zero it means that the regression quality was unacceptable and on the contrary, R^2 equals 1 is the best quality.

3   CAD-Based Approach for Dependency Identification for Engineering Change

Characterising dependency is an important task in the EC field for evaluating the risk of a change and predicts its impact in and out of the system.

A CAD-based approach for dependency analysis was originated from our previous works (Zhang, 2013). The aim of this approach is to study change engineering passing through four steps: modelling the system, defining the change by selecting the instigating elements, characterising the dependency between elements and interpreting the results, cf. Fig. 1.

The modelling step consists in a construction of an initial model for the studied system. In this model, we present all the necessary information about the system structure/architecture and formalise the constraints associated with parameters. In the second step, the identification of the change causes and the selection of the instigating element are essential. According to (Clarkson, Simons, & Eckert, 2004), instigating element represents the sub-system or the component corresponding to changes dealing with new product requirements and needs. At the third stage, a characterisation of the dependency between every couple of elements of the system's model quantitatively, qualitatively and by a function linking them. At the last level of the method, all the obtained results about the dependency of parameters and/or components are analysed.
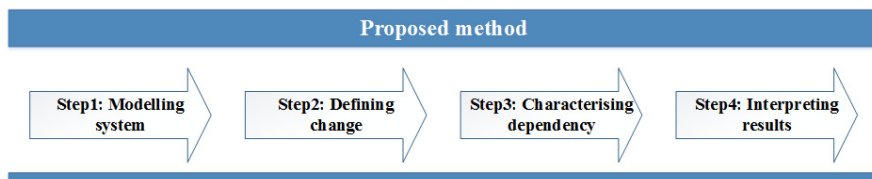
Fig. 1 Engineering Change proposed approach

In the following, we focus only on the third step of the method.

4   The Proposed Process for Regression

In the third step of the Engineering Change proposed approach presented in the previous section, and once we have finished testing all the possibilities of change on different dimensions, we have to identify the type of dependency between the dimensions pairwise.

We denote by $(x_1, y_1), (x_2, y_2), \ldots, (x_m, y_m)$ the series of observations within two geometric dimensions D_i and D_j of the built CAD-model change.

Assume that X_i represents the instigating element or the dimension to change and Y_i constitutes the affected dimension after the change.

Each dimension in the CAD-model has a definition interval. We denoted $\underline{X_i}, \overline{X_i}, \underline{Y_i}, \overline{Y_i}$ by the lower and the upper limit of the dimension X and Y respectively.

Where

$$X_i \in [\underline{X_i}, \overline{X_i}] \text{ and } Y_i \in \left[\underline{Y_i}, \overline{Y_i}\right], \forall i \in \{1 \ldots m\} \tag{9}$$

We define also the sampling step σ_X between a change and another on X-values,

$$\sigma_X = X_{i+1} - X_i \tag{10}$$

The point cloud associated with statistical series of two different dimensions can have different forms (as shown in Fig. 2). Some of the structures are easily known, such as cloud (a) where points are almost aligned and a linear function exist, while others requires a deeper analysis, cloud (c) for example.
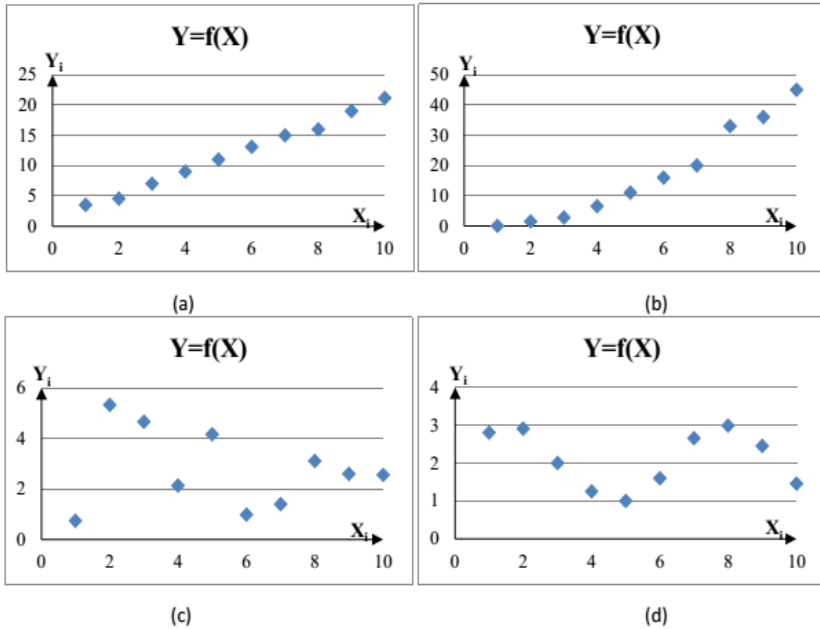
Fig. 2 Point cloud examples

We propose to find the closest function f, such as, $Y = f(X)$, that represents better the dependency between X and Y, when varying X-values.

Given all the series of observations as input, the point cloud is plotted at a first time, and then a number of hypotheses are set up until finding this polynomial function, as presented in Fig. 3.

The first hypothesis is $(n = 0)$. The variance of Y, which is one of several descriptors of a probability distribution, is calculated.

$$V(Y) = \frac{1}{m}\sum_{k=1}^{m}(y_i - \overline{Y}) \; \forall i \in \{1 \cdots m\} \tag{11}$$

If this variance is null, it means that all the values are identical and there is no dependency between the two dimensions. If it is not the case, we suppose another hypothesis $(n = 1)$ where a linear dependency exists between the two studied dimensions. This hypothesis is validated if the value of the linear regression
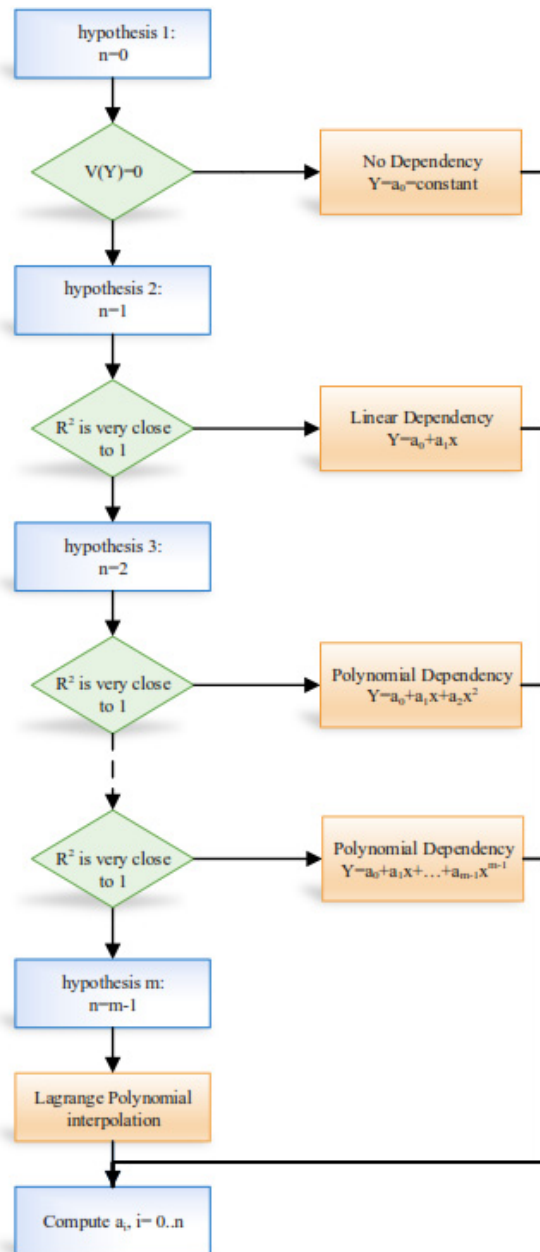
Fig. 3 Functional fit process

coefficient R^2 is very close to 1. Else, the dimensions are linked with a polynomial regression. Every time we check if the polynomial regression coefficient R^2 is very close to 1, or n will be increased until finding a k degree $(k < m)$ polynomial, using the Least Squares Method, that fit better to point cloud data. And if we aren't able to find it, we use the Lagrange Polynomial interpolation, since the Lagrange form is unique and exist for all cases.

In contrast of some reports in the literature that used the quantitative and qualitative results as characterisation of the change impact, we proposed the process (presented before) to generate an equation that describes the statistical relationship between two different dimensions D_i and D_j using some statics techniques.

To our knowledge, this is the first study to deal with regression analysis in engineering change management.

Let us suppose that we have a dependency between two dimensions denoted by D_1 and D_2. The cloud points describing the variation of the affected dimension D_2 due to a change on D_1, is represented in Fig. 4 Regression plot. (25; 50) are the initial values of $(D_1; D_2)$.

Following the process presented in Fig. 3, we validate hypothesis 3, so a polynomial dependency exist between D_1 and D_2. Qualitative result, equal to (-), defined by the sign of the variation of D_2, shows that D_2 is decreasing while D_1 increase. Quantitative dependency which is defined by the slope of the tangent line passing throw the initial point ((25; 50) in our example), give us only an idea about the variation of D_2 next to the initial point. However, functional dependency provides a function describing the variation trend of D_2 in the definition domain of D_1.
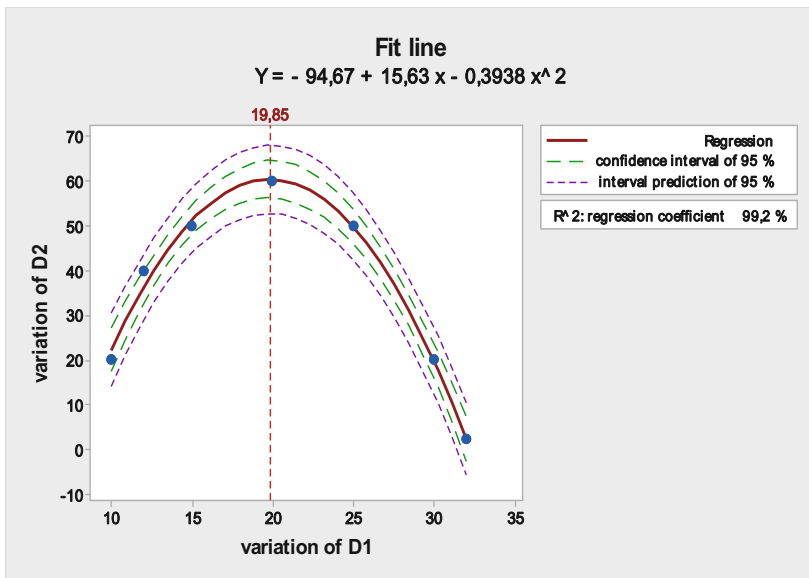
Fig. 4 Regression plot

If we compare the qualitative, quantitative results with the polynomial dependency founded, we could conclude that functional dependency is the most detailed. It shows that there are two behaviours of the D_2 variation, at a first time, it increase until reaching a maximum value, and then begin to decrease. With the functional dependency we are able to evaluate the change impact from one dimension to another.

5   Conclusion

The present study was designed to characterise the dependency of one system element on another in an Engineering Change Management approach. A process was proposed to find the polynomial function that fits better the data set points, using the mathematical theorems and statistics methods. As presented in section two, Lagrange Polynomial interpolation guarantees the existence of a k degree polynomial function that pass through all the m points, where $k < m$. However, there is a trade-off between finding a better fit and having a simpler function when constructing interpolating polynomials. The contribution of this study has been to find a k' degree polynomial function ($k' < k$) that pass through the majority of points with a correlation coefficient R^2 very close to 1.

Further research might explore the selection of the sampling step chosen between two changes (or two points) and investigate the optimal number of data points which allow a better and more detailed interpolation study.

References

Abdi, H.: The Method of Least Squares. In: Encyclopedia of Measurement and Statistics, pp. 530–532. Sage Publications, Thousand Oaks (2007)

Archer, B., Weisstein, E.W.: Lagrange Interpolating Polynomial. (1999), http://mathworld.wolfram.com/LagrangeInterpolatingPolynomial (retrieved December 24, 2014)

Clarkson, P.J., Simons, C., Eckert, C.: Predicting change propagation in complex design. Journal of Mechanical Design 126(5), 788–797 (2004)

Jeffreys, H., Jeffreys, B.S.: Methods of Mathematical Physics, 3rd edn. Cambridge University Press, Cambridge (1988)

Kusiak, A., Wang, J.: Dependency analysis in constraint negotiation. IEEE Transactions on Systems, Man, and Cybernetics 25(9), 1301–1313 (1995)

Miller, S.J.: The Method of Least Squares. Mathematics Department Brown University Providence, 2912, 1–7 (2006)

Wynn, D.C., Caldwell, N.H., Clarkson, P.J.: Can change prediction help prioritise redesign work in future engineering systems? In: International Design Conference, Design 2010, Dubrovnik, Croatia (2010)

Zhang, X.: Contribution to engineering change management in product development projects: reference models and multi-based simulation, Bordeaux (November 19, 2013)

Optimization of a Maintenance Policy in Industrial Field: Case Study

Abderrazek Djebala, Nouredine Ouelaa, and Mohamed Khemissi Babouri

Mechanics and Structures Laboratory, University of Guelma, Algeria
{djebala_abderrazek,n_ouelaa,babouri_bmk}@yahoo.fr

Abstract. This article concerns the optimization of the maintenance policy existing in the biggest fertilizer products company in Algeria. The work comprises in the first part an assessment of the current policy using an audit of the maintenance function performed on the basis of the Lavina questionnaire. Improvement suggestions were presented. Secondly, one proposes the application of the "Optimization of the Maintenance by Reliability" approach as an effective tool for the optimization of the production equipment's dependability (safe of operation). An application of this approach is carried out, for example, on a steam-turbine generator; a vital machine in the production process. Reliability study using Weibull's model and a Failure Modes Effects Criticality Analysis (FMECA) have been carried out. This application has allowed, for the studied machine, selecting the optimal maintenance management method based on vibration analysis using appropriate tools. The same approach developed for the steam-turbine generator can then be applied for the other production equipment.

Keywords: Maintenance policy, Optimization of the Maintenance by Reliability, Reliability analysis, Failure Modes Effects Criticality Analysis.

1   Introduction

In a competitive context, companies must satisfy the demand of their customers, ensuring quality and quantity of desired product at a lower cost and within the required time. Depending on the specific industry, maintenance costs can represent between 15 and 60 percent of the cost of goods produced. For example, in food-related industries, average maintenance costs represent about 15 percent of the cost of goods produced, whereas maintenance costs for iron and steel, pulp and paper, and other heavy industries represent up to 60 percent of the total production costs (Belmahdi, 2006). Moreover, the result of ineffective maintenance management represents a loss of more than $60 billion each year (Belmahdi, 2006). A reliable and efficiency policy should then be adopted.

The maintenance policy is defined as the technical and economic objectives related to the equipment handling by the maintenance crew (service). It is in the context of this policy that the maintenance service "boss" implements the means

appropriate to the fixed objectives; we then speak about the strategy for medium term and tactic for the short term. Maintenance management mainly takes into account the technical, economic and financial aspects of the different methods used (curative, conditional preventive, and systematic preventive maintenance) to optimize the equipment's availability (Meziani), (Zille, 2009).

The traditional maintenance techniques are based on the curative maintenance (still called run-to-failure), and on the preventive maintenance that includes the systematic and the conditional types. The development of the analysis and the monitoring methods used in the conditional maintenance (vibration and acoustic advanced analysis tools, lubrication oil analysis techniques, and thermography, etc.), allowed creating a new maintenance technique called predictive maintenance, we then speak about the early detection.

A variety of a specific maintenance management methods have been developed these last years, such as the Japanese concept called Total Productive Maintenance (TPM), the Maintenance Steering Group developed in 1960s for the preventive maintenance of the Boeing 747 airplanes, the Reliability Centered Maintenance (RCM) developed in 1970s in USA, and the Optimization of the Maintenance by Reliability developed by EDF (Electricité De France) in 1990s under the French abbreviation OMF (Optimisation de la Maintenance par la Fiabilité).

The Optimization of the Maintenance by Reliability was developed by EDF since 1990 on the base of MSG-3 and RCM methods. Pilot studies carried out on different nuclear systems have established the foundations of the method. It was then generalized on the totality of the nuclear power plants and implemented since 1993 on fifty systems considered as most important on the view-point of safety, availability, and operational costs criteria. The method was adapted in 1995 for use on other types of plants (coal power plants, combustion turbines, transmission lines, wind ...). Maintenance service companies have transferred this method to other industries (automotive, offshore ...). A second generation method was developed in 2003 to allow including the revision of preventive maintenance programs established with the initial method, and the analysis of smaller systems (Mortureux).

In this paper an optimization of the maintenance policy existing in the biggest fertilizer products company in Algeria using the concept (OMF) is proposed. First an evaluation of the existing maintenance policy is carried out using the Lavina questionnaire (Lavina, 1994). The application of the Optimization of the Maintenance by Reliability approach is then proposed to improve the dependability of the production equipment. This method is applied on a steam-turbine generator which is a vital machine in the production process. Reliability study using Weibull's model and a Failure Modes Effects Criticality Analysis (FMECA) have been carried out.

2   Evaluation of the Actual Maintenance Policy

The essential step in this case is to assess the actual maintenance policy, to target the eventual weaknesses, and to make necessary changes. We propose the following questionnaire based on the work of Lavina (Lavina, 1994). This questionnaire is

prepared in 12 categories. For each item, a series of questions is asked. For each question, five answer choices are offered. For each response, a score is assigned. At the end of each section, the total points are added. As the questionnaires are very long, it is impossible for us to show all of them, it is for this reason that we show in table 1 just an extract relating to the first category (general organization). The final result of this analysis is shown by table 2. It identifies six areas of weaknesses where improvement's action is a priority. These are the areas for which the percentage indicated in the fourth column of the table 2 is less than that of the total score: (general organization, organization of the workshop, tools, technical documentation, subcontracting, and control of activity). Weaknesses are identified, suggestions for improvement were made (table 3). Figure 1 shows the diagram of Kiviat showing the state of the current maintenance method and the desired state after the proposed improvements.

Table 1 Extract of the item related to the general organization

A – General organization	No	Rather no	Neither yes nor no	Rather yes	Yes
1. Have you defined in writing and approved the organization of the maintenance function?	0	7.5	15	22.5	30
2. Is the function's sheets of each of running positions exist?	0	5	10	15	20
3. Have you periodical meetings with your staff to review the work to be performed?	0	2.5	5	7.5	10
-	-	-	-	-	
-	-	-	-	-	

Table 2 Results of the Lavina questionnaire

Analysis domain	Obtained score	Max. possible	%
General organization	155	250	**62%**
Work method	245	250	98%
Equipment's technical follow-up	235	250	94%
Activity coast management	295	300	98.33%
Spare part stock	175	200	87.5%
Spare part purchasing and supplying	155	200	77.5%
Organization of the workshop	127.5	200	**63.75%**
Tools	110	200	**55%**
Technical documentation	132.5	200	**66.25%**
Personnel and training	350	400	87.5%
Subcontracting	102.5	250	**41%**
Control of activity	170	300	**56.66%**
Total score	**2252.5**	**3000**	**75.08%**

Table 3 Suggestions of improvement

General organization	- Define the tasks and responsibilities in the organization and check them periodically - Strengthen the management staff - Appointment of a responsible for coordinating the work, supplies, installation and training
Organization of the workshop	- Moving the workshop near equipment to maintain
Tools	- Update inventory regularly - Provide special tools and test equipment - Perform a reliable calibration of measuring equipment
Technical documentation	- Update drawings and diagrams of equipment - Record the equipment's modification and classify the corresponding repair files - Strengthening of reprographic means
Subcontracting	- Carefully elaborate descriptions of the work and the specifications - Evaluate and engage subcontractors according to technical and skill criteria
Control of activity	- Follow service performance - Make regular activity report - Make regular reports tracking hours, consumed parts, and labor costs
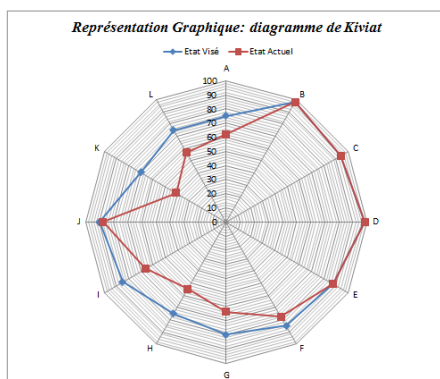
Fig. 1 Diagram of Kiviat (in red the current state, and in blue the desired state)

3   Application of the "Optimization of the Maintenance by Reliability" Approach (OMF)

Dependability is defined as "the set of properties that describe the availability and its influencing factors: reliability, maintainability and maintenance support." Three main approaches of the dependability exist: The MSG-3 method developed

in the 1960s by Boeing, Reliability Centered Maintenance (RCM) developed in the 1970s in USA, and finally the OMF (as developed in French language: Optimisation de la Maintenance par la Fiabilité)) approach developed in the 1990s by EDF (Electricité De France).

The OMF approach includes, among others, reliability analysis, and a risk assessment by applying the FMECA method (Failure Modes Effects Criticality Analysis), and finally an optimization of the maintenance actions. Figure 2 represents the steps of the OMF. An application of this approach was performed on a turbo-generator which is one of the most important equipment of the company. Figure 3 shows a photo of the turbo-generator.

Risk evaluation
1. Functional analysis of the system
2. FMECA analysis

Maintenance history
1. Factual and economic analyses of the experience feedback
2. Evaluation of the reliability indicators

Maintenance optimization
1. Analysis and selection of the maintenance tasks
2. Final choice and tasks grouping
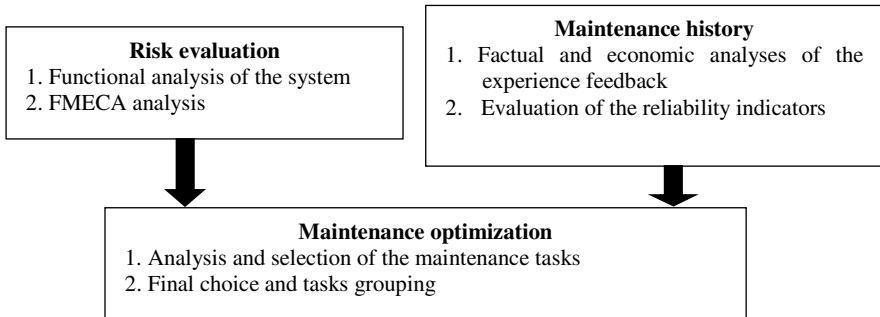
Fig. 2 Steps of the OMF approach

Reducer

Alternator

Steam-turbine
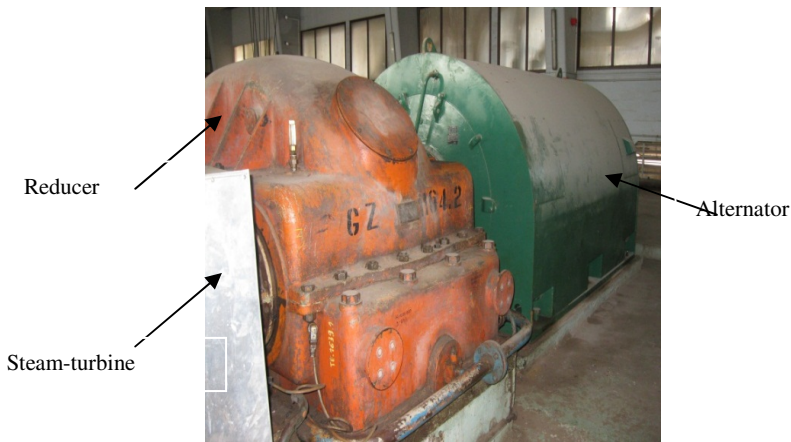
Fig. 3 Photo **of the** turbo-generator

3.1 Reliability Analysis Using Weibull's Model

Figure 3 shows the adjustment of the TBF (Time Between Failure) obtained by the Weibull's model, and the figure 4 shows the reliability function of the machine. Two main points are to note:

1. The machine has a Mean Time Between Failure (MTBF) equal to 814 hours, which is used to estimate the frequencies of preventive visits;

2. The machine is not reliable because its reliability for t=MTBF is equal to 35.85%, which is a very low rate. This leads us to seek to make improvements or adjustments to the maintenance strategy applied to this machine.
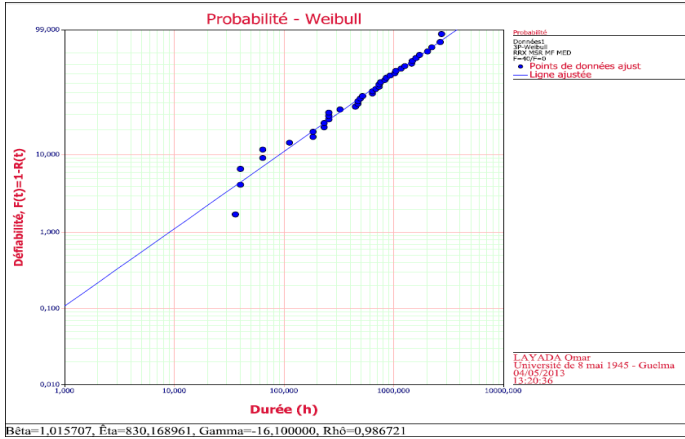
Fig. 4 TBF distribution and Weibull's model adjustment
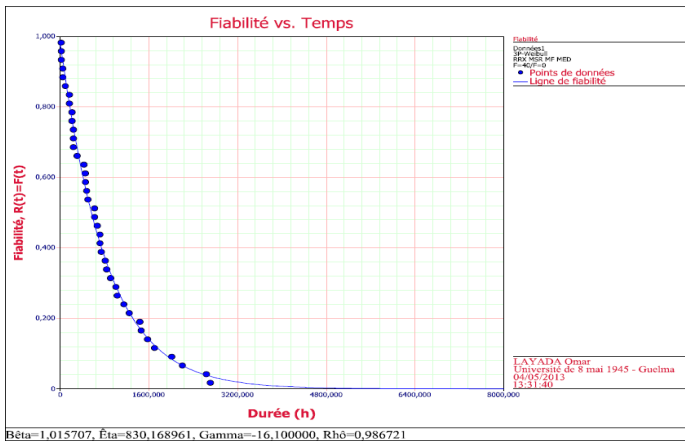
Fig. 5 Reliability vs. time of the turbo-generator obtained by Weibull's model

3.2   *Failure Modes Effects Criticality Analysis*

The FMECA method consists in decomposing a system into several subsystems, to identify all the failure modes of each component as well as its corresponding cause(s). Criticality (C) is then assigned to each mode and which is the product of three criteria: (O) criterion like occurrence, the criterion (D) like detection, and

finally the criterion (G) like gravity. Tables to assess the three criteria are used. Before the application of the FMECA method the machine is decomposed into four components: the steam-turbine, the reducer, the alternator, and the coupling system (see the functional analysis in figure 5). For each component the possible failure modes and the corresponding cause(s) are evaluated. A criticality (C) is then assigned to each cause starting from the three criteria (O, D, and G). Table 4 shows an extract of the FMECA method of the turbo-generator concerning just the reducer, because the whole analysis is very long.

Table 4 Extract of the FMECA method concerning the reducer

Element	Function	Failures			Criticality			
		Modes	Causes	Effects	O	D	G	C
Speed reducer	Reduce the rotation speed from 9000 RPM to 1500 RPM	Abnormal noise	- Bearings failure	- Bearings overheating.	1	4	4	16
		High vibration	- Misalignment of the reducer's rotor	- Abnormal noise and vibration	1	2	4	8
			- Reducer gear's teeth wear	- Abnormal noise and vibration	2	4	4	**32**
			- Loosening or shearing of anchor bolts	- Axial displacement (emergency stop)	1	3	3	9
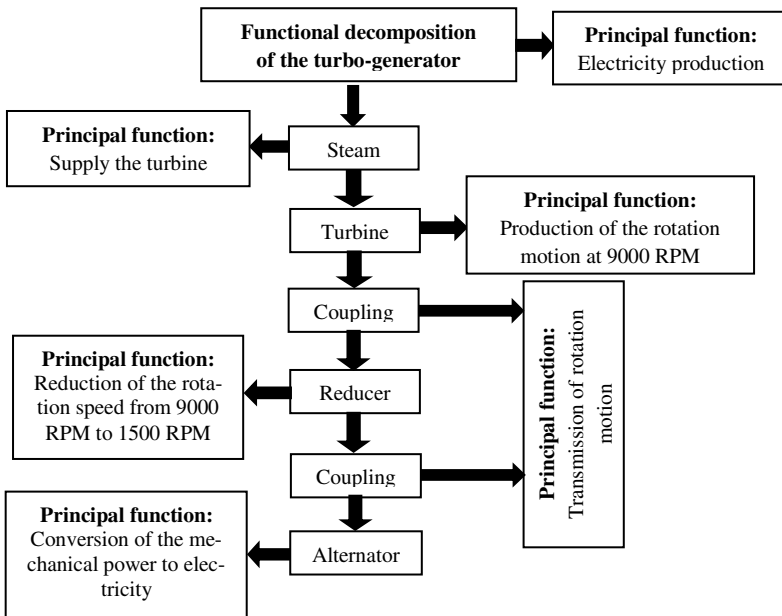
Fig. 6 Functional analysis of the turbo-generator

3.3   Proposition of a Special Maintenance Plan

Table 5 shows the proposed new maintenance plan based on the reliability analysis and the FMECA method. One can see that the usual maintenance operations are conserved (as lubrication, periodical checks, periodical replacements, etc.). The special maintenance plan concerns the failure modes having a criticality criterion upper than 16. The highest criticality is equal to 32, it concerns the failure mode "Reducer gear's teeth wear". In this context we propose the implementation of a maintenance plan based on the vibratory analysis using adapted analysis tools.

3.4   Application of the Vibratory Analysis for the Detection of a Gear Teeth Failure of the Reducer

During our investigations a critical problem has been observed; it is the high level of vibrations and an intense noise especially on the reducer. This leads to carry out a series of vibratory measurements and the signals' processing using spectral and cepstral analyses. Actually it is a real test of the proposed maintenance policy. Figure 6 shows two spectra around the meshing frequency, which is modulated by sidebands spaced with the rotation speed of the input and the output shafts.

Table 5 Proposed maintenance plan

		Periodicity
Usual maintenance operations: lubrication, periodical checks, periodical replacements, …etc.		The same periodicity adopted by the maintenance crew
Proposed special maintenance plan		
Operation (failure mode)	**Mode's criticality**	**Periodicity**
General visit of the whole machine including a vibratory monitoring by overall measures (especially reducer's bearings and wheels)	16 for reducer's bearings failure 32 for reducer's wheels wear	Every day using portable analyzer or by adopting an online monitoring system.
Check the global state of the coupling (coupling play)	16	Every week
Check the alignment of the turbine by spectral analysis	18	Every 15 days or if the overall measures are high than standards
Periodical check of the reducer's wheels wear: - Using specific scalar indicators (kurtosis, crest factor) - Using spectral analysis or advanced signal processing tools like cepstrum or envelope analysis	32 (the highest criticality)	Every week Every 15 days or if the overall measures are high than standards

This put in the mind the presence of a combined defect. The diagnosis is confirmed by the cepstrum of figure 7. The cepstrum highlights two quefrencies corresponding to the rotation frequency of the input and output shafts. The diagnosis is confirmed by the maintenance crew few times after the vibratory analysis.
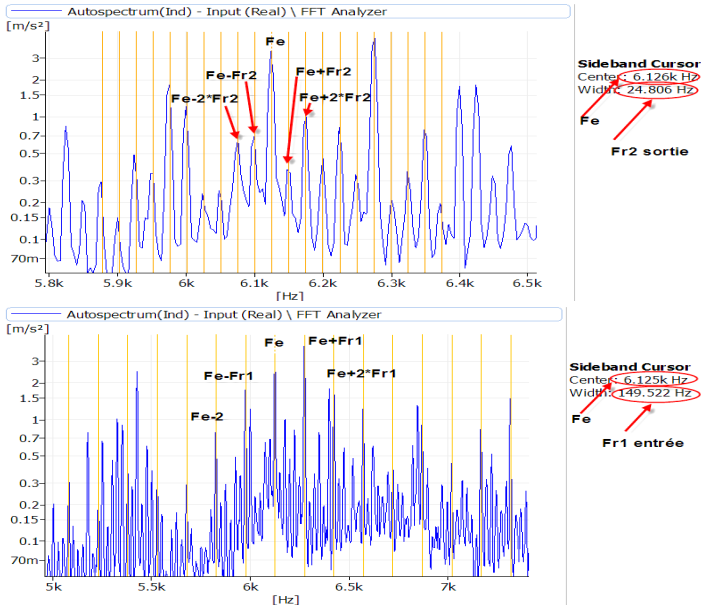
Fig. 7 Spectra around the meshing frequency
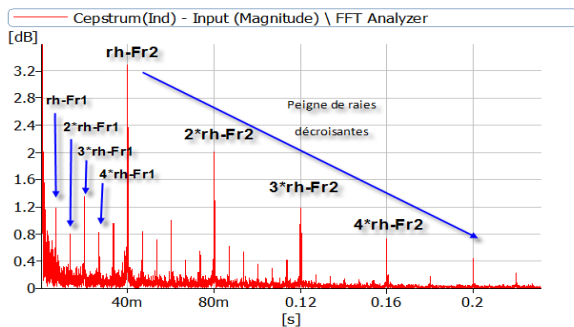
Fig. 8 Cepstrum showing two quefrencies

4   Conclusion

An approach is proposed in this paper for the optimization of the maintenance policy in the largest Algerian company of fertilizer products. The work includes an evaluation of the current policy by the method of Lavina, leading to target weaknesses and identify improvements to make. Secondly the "Optimization of the Maintenance by Reliability" approach is proposed as an effective tool for optimizing the dependability of the production equipment; the pillar of a good maintenance policy. An example of this approach has been applied on a turbo-generator, including functional and reliability analyses, and a FMECA approach. A new maintenance plan is proposed on the base of the results obtained by the (OMR) approach. The same analysis carried out on the turbo-generator can be applied on the other vital production equipment of the company.

References

Belmahdi, K.: Technic of maintenance. University of Pierre and Marie Curie, Paris VI, Paris, France (2006)

Meziani, S.: Concepts, objectifs et politiques de la maintenance,
    `http://www.umc.edu.dz`

Zille, V.: Modélisation et évaluation des stratégies de maintenance complexes sur des systèmes multi-composants. Thesis Université de Technologie de Troyes, France (2009)

Mortureux, Y.: La sûreté de fonctionnement: Des méthodes pour maitriser les risques. Techniques de l'ingénieur BM 5008

Lavina, Y.: Audit de la maintenance. Les éditions d'organisation, Paris (1994)

Pre-dimensioning of the Dynamic Properties of the Wind Turbine System Using Analytical Approach

Ghazoi Hamza[1,2], Jean-Yves Choley[2], Moncef Hammadi[2], Maher Barkallah[1], Jamel Louati[1], Alain Riviere[2], and Mohamed Haddar[1]

[1] Mechanics Modeling and Production Research Laboratory (LA2MP),
   National School of Engineers of Sfax (ENIS), B.P, 1173, 3038 Sfax, Tunisia
   `hamza.ghazoi@gmail.com`, `bark_maher@yahoo.fr`,
   `louati.ttg@gnet.tn`, `mohamed.haddar@enis.rnu.tn`
[2] Laboratory of Engineering of the Mechanical Structures and Materials (LISMMA),
   High Institute of Mechanic of Paris (SUPMECA) 3 rue Fernand Hainaut 93407,
   Saint -Ouen Cedex, France
   `{jean-yves.choley,moncef.hammadi,alain.riviere}@supmeca.fr`

Abstract. The higher complexity of the mechatronical wind turbine system requires taking a great effort from the early stage of the design process. Wind turbine power trains are subjected to a very diverse spectrum of dynamic loads. In order to obtain preliminary information about the dynamic behavior of the wind turbine system and its operating environment, the drive system model is developed in this paper. This model contains flexible and rigid structural components in order to predict the dynamic characteristics of the torsional vibration. All these structural components are systematically coupled in one analysis model, through a simple modeling process in Modelica/Dymola environment. Making the right technology and architectural choices early in the development program, will substantially decrease rework and related costs.

Keywords: Wind turbine, Flexible, Preliminary design, Torsional vibration, Modelica/ Dymola.

1   Introduction

Mechatronic is the synergistic integration of mechanical system, electronics components, actuators and sensors. The mechanical system can be seen as a multi physic system coupling the mechanical structure with other multi-physic subsystems such as electrical, thermal and electromagnetic (Hammadi et al. 2014). Integrated mechatronic design aims to analyze the behavior of the mechatronic system, taking into consideration the tight coupling between control and multiphysics system (Hammadi 2012).

The wind turbine can be considered as a typical mechatronic system which is consisting of mechanical, electrical and control subsystems interacting among

each other. It became an important choice for renewable electrical energy production throughout the world. Because of this, Investigation of wind turbines using numerical simulation becomes more and more significant.

Similar to all projects, the one of wind turbines is divided, with well-defined target, into successive phases. In every phase, operations have to be carried out and decisions must to be taken by various actors, taking into consideration the technical, environmental, economical and political issues.

In the past few decades, wind turbine technology has been substantially developed. Latest technology enables wind turbines to generate large electrical power in order to meet the energy demand. In fact, the aim of the modern wind turbine research is to maximise the output electrical power and to have stable power output with the minimum possible cost and with the instability of wind speed. To achieve this, specific information on the environmental loading and structure response is needed form the early phase of the design cycle of the wind turbine.

For instance, (Arbaoui and Aski 2010) developed a support tool for the preliminary design of a wind turbine. This approach is based on the development of a set of constraints derived from engineering knowledge, in order to support the different actors in making decisions about choices inherent to their activities in the field of wind energy. It targets to maximize the performance and to reduce the cost of the produced energy.

In the preliminary design phase, a quick overview on the environmental load of the wind turbine on its structure may be very useful. Moreover, in this phase a very few detail about the environmental parameters and the wind turbine structure is known. Therefore, to simulate the wind turbine requires just the most principal input data. In the last few years a lot of attention has been given to model the mechanical structure of wind turbine. For example, (Zhaoa et al. 2007) developed a new multi-rigid-body model for a wind turbine structure. In this approach, the flexible bodies like shafts, rotors blades and tower are modelled by a set of rigid bodies connected by cardanic joints geometrically and constrained by spring forces elastically. This methodology is adapted for the analysis of global vibration. (Chantharasenawong et al. 2011) proposed a preliminary design of the modular tower of 1.5-MW onshore wind turbine. This method is based on studying the increased tower base diameter effects on its tower mass and wall thickness.

(Lee et al. 2002) presented a new methodology to study the dynamic behavior of the wind turbine. This method is based on representing the wind turbine as a multi-flexible-body system. In fact, it is based on separating the complete system into rigid body (nacelle, hub) and flexible subsystems (blades, tower). The rigid bodies are modeled using Kans' method. This method allows reducing the complexity of the equations of motions for the multi-rigid body part. The tower and the blades are considered to be flexible in bending and torsion in two directions.

Extreme fatigue and structural loads are important issues in turbine design; the reduction of these loads might create a significant diminution in turbine cost by reducing required materials, decreasing maintenance, and improving global turbine reliability. Thus, applying new and innovative load control techniques can decrease excessive loads, which affect the mechanical structure of the system.

This engineering challenge pushes researchers to ameliorate the techniques of controlling rotors power and loads. Many published literature is available regarding wind turbine control. For examples, PID (proportional integral derivative controller) was used to control the rotor speed in order to regulate the output frequency of induction generator (Paret 2014). PID controller can also eliminate system error, adjust overshoot of the system and regulate rotor speed in order to capture the maximum rotor power (Hou 2014).

The objective of this paper is to propose a pre-dimensioning approach to study the influence of various parameters on the dynamic response of the wind turbine system driven in order to produce a suitable compromise between the viability, the cost as well as the quality of the energy produced. A proportional derivative integral Controller (PID) is used to control the aerodynamic power of the wind turbine. The organization of this paper is as following: the first section deals with this introduction. In Section 2, the wind turbine description is presented. In section 3, we introduce the modelling of the system using the modelling language Modelica. The results of simulation are shown in section 4. The conclusion of our paper is given in section 5.

2   Wind Turbine Description

The current wind power generation system is adapted to transform the slow rotation speed of the rotor side to a fast rotational speed of the generator side. It consists of a rotor, a low speed of the rotor shaft, a gearbox and a high-speed shaft of the generator rotor. The slow shaft is considered as flexible while the fast shaft is infinitely rigid. The flexible modes of blades are supposed high enough to be neglected and all the flexible modes are located in the flexible element of the slow shaft. We consider that the mechanical system is characterized by the sum of all the mechanical characteristics. We used then, the mechanical model of the drive system having two-mass which is very used in the literature as shown in Fig. 1.
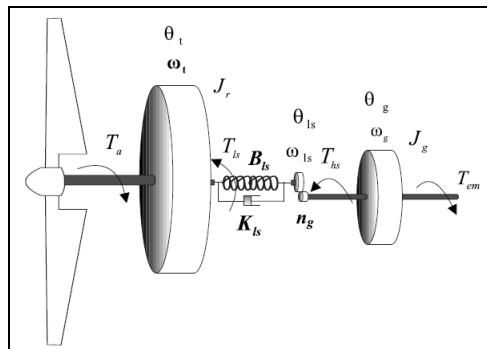
Fig. 1 Schema of the drive system with two masses

The masse inertia of the rotor side is represented by J_r, the slow shaft is characterized by a torsion coefficient B_{ls} and an elasticity K_{ls}, the fast shaft is rigid; the inertia of the fast shaft associated with the generator is represented by J_g.

The power available from the wind through a surface s is defined by:

$$P_V = \rho.s.v^3 \tag{1}$$

where, ρ is the air density and v is the wind speed.

The mechanical power of the wind turbine is then:

$$P_{tur} = C_p \frac{\rho.s.v^3}{2} \tag{2}$$

The power coefficient is defined by the ratio of the power received by the turbine on the wind power:

$$C_p = \frac{P_{tur}}{P_V} \tag{3}$$

The aerodynamic torque is given by this relation:

$$T_a = \frac{P_{tur}}{\omega_t} = \frac{1}{\omega_t} C_p \frac{\rho.s.v^3}{2} \tag{4}$$

Where, ω_t is the rotor speed.

The multiplier is the connection between the turbine and the generator in order to adjust the speed of the turbine with that of the generator. Friction, elasticity and wasted energy in the multiplier are neglected. For an ideal multiplier:

$$T_{lc} = n_g.T_{hc} \tag{5}$$

where, n_g is the transmission ratio of the multiplier, T_{lc} is the torque of the slow shaft, T_{hc} is the torque of the fast shaft.

The rotor dynamic is characterized by a differential equation of the first order:

$$J_r \dot{\omega}_t = T_a - T_{ls} \tag{6}$$

$$T_{ls} = B_{ls}\left(\theta_t - \theta_{ls}\right) + K_{ls}\left(\omega_t - \omega_{ls}\right) \tag{7}$$

where, ω_{ls} is the speed of the slow shaft, θ_t is the angular position of the rotor and θ_{ls} is the angular position of the slow shaft.

The speed and the angular position of the generator

$$\theta_g = n_g \theta_{ls}$$
$$\omega_g = n_g \omega_{ls} \tag{8}$$

3 Modelica Implementation

Exploiting the object-oriented features of the Modelica language, we implement the studied model in Modelica. The system may be composed of a connected set of objects using the standard Modelica library.
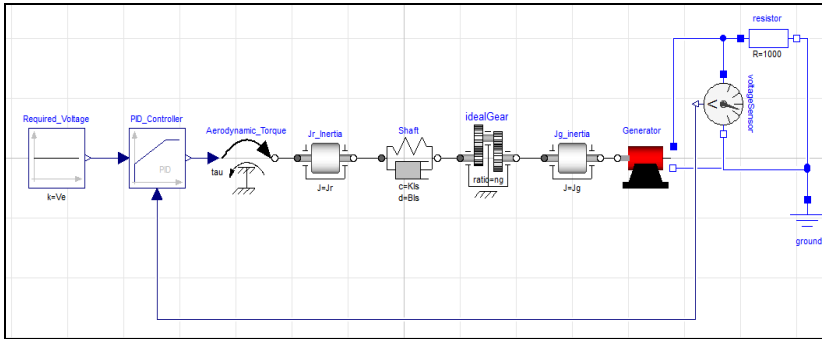
Fig. 2 Model of the system in Dymola/Modelica

The considered elements in the wind turbine modeling are: Control part (PID), torque, generator, inertias, spring, damper, ideal gear, voltage sensors, ground and resistor.

In order to control the output power, we used a control system. The PID controller checks the power output of the turbine. In fact, we used a voltage sensor to measure the voltage at the terminals of the generator. When the power output cross a threshold limit, it sends an actuating signal in order to adjust the input torque. We assume that the PID controller allows generating a maximum torque of 7000 N. m, and the desired generated voltage is about 700 V.

4 Parametric Study

After modelling the entire system, an analysis was carried out for different parameters. Figs.3 and 4 show the input torque and the measured voltage according to time.

Figs.3 and 4 show that when the measured voltage is very low, a maximum torque is needed (the rotor will rotate with a very quick speed) until the voltage reaches the value of 700V (the nominal value). After that, the rotor will run freely and the amplitude of torque tends to zero. Therefore, the PID controller tries to maintain the output voltage.
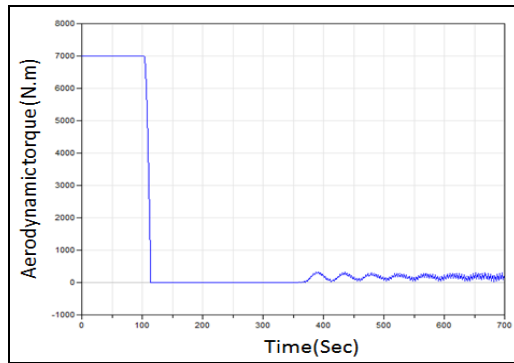
Fig. 3 Input torque (N.m)
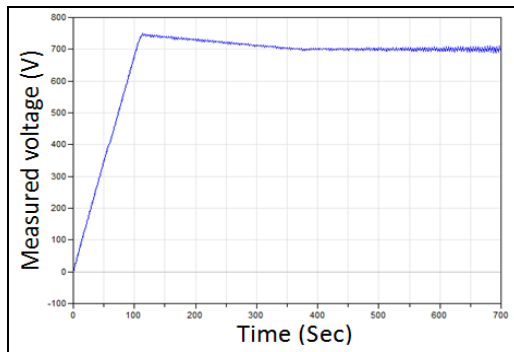
Fig. 4 Measured voltages (V)

To bring up the effect of the mechanical characteristic of the wind turbine on the output power, we observed the response of the system (the variation of the input torque and the measured voltage) for three values of the multiplier ratio ($n_g = 0.01$ $n_g = 0.02$ and $n_g = 0.03$) as shown in Figs. 5and 6.
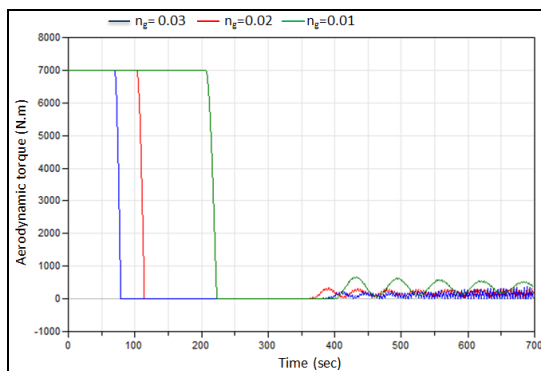
Fig. 5 Aerodynamic torque according to the multiplier ratio
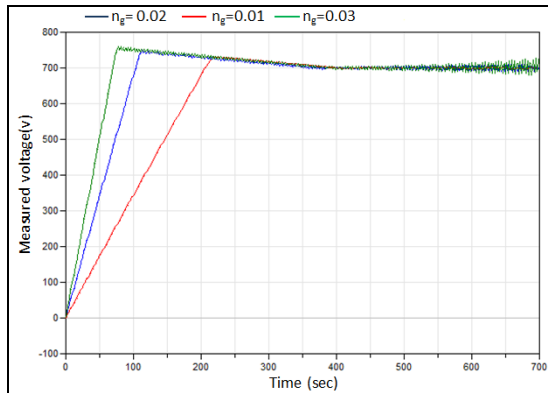
Fig. 6 Measured voltages according to the multiplier ratio

Figs. 5 and 6 illustrate that when $n_g = 0.03$, the measured voltage reached quickly the nominal value (700V) and the input torque lasts less time at the nominal value (7000 N.m). But we can notice also, that the fluctuation frequency on the two curves (torque and voltage) when $n_g = 0.01$ is the lower. We can deduced that the multiplier ratio has a great effect on the response time to generate electricity and that the right choice of the multiplier can reduce vibration and minimizing mechanical stresses in the wind turbine structure.

The mechanical properties have a great influence on the dynamic response of the wind turbine system. Fig. 7 shows the variation of the angular position of the generator according to the friction and the twist coefficients on the slow shaft. It can be seen that the angular position of the generator increases with the increasing of the two parameters (the twist and the friction coefficient) and then, the torsion vibration increases with the flexibility of the slow shaft. Therefore, we can deduce that the shaft characteristics have an important impact on reducing the torsional vibration of wind turbine components.
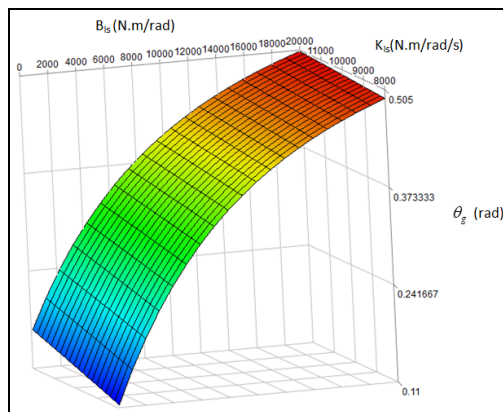
Fig. 7 Angular position of the slow shaft according to the twist and friction coefficient

Fig. 8 illustrates the variation of the angular position of the generator according to the multiplier ratio. As it can be seen, the angular position increases with the increasing of the multiplier ratio. So, despite the increase value of the multiplier ration has the advantage of quickly reach the value of the desired voltage, the increasing of this ratio has an important impact on the torsional vibration of the shafts.
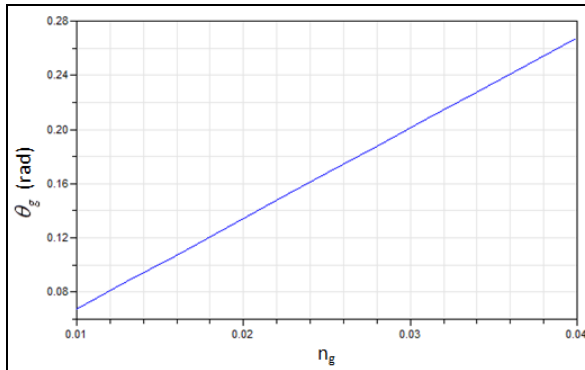
Fig. 8 Angular position of the generator according to multiplier ratio

Figs. 9 and 10 show the variation of the measured voltage according to diverse inertia values of inertia (mass inertia of the rotor side J_r and mass inertia of the generator side J_g)
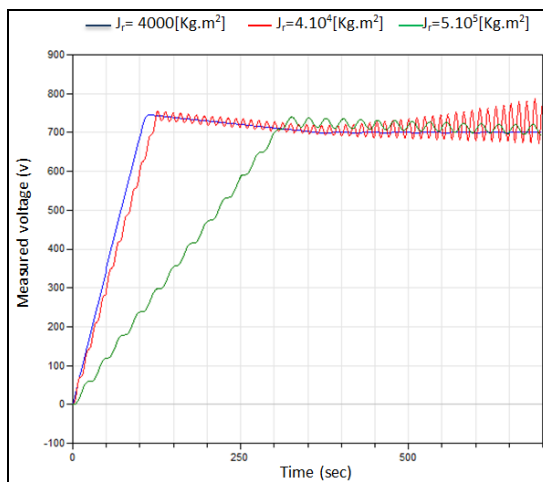
Fig. 9 Measured voltages according to different values of J_r
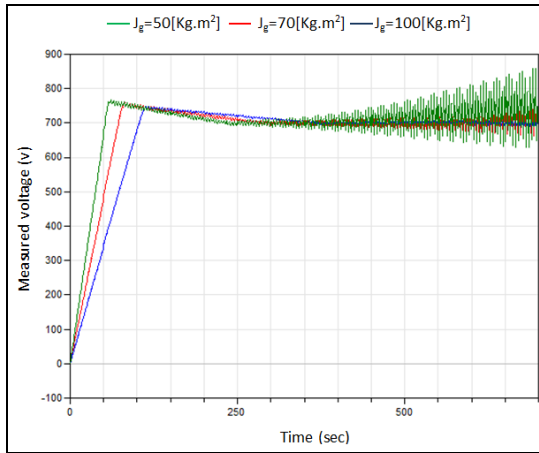
Fig. 10 Measured voltages according to different values of J_g

   These figures show clearly that the output generated power depends enormously on the mass inertia of the rotor side as well as the mass inertia of the generator side. So, the more the inertia value decreases the more the desired tension value reached very quickly. Inertias of the rotating components have an influence on the output voltage value.

5   Conclusion

In this paper, we proposed a method of the preliminary design. This method allows studying the dynamic behaviour of the wind turbine drive system. In order to capture the pertinent characteristics, a two mass model has been used. A Proportional Integral Derivative (PID) controller is used to control the voltage produced in order to adjust the input torque and therefore to maximize the generated electric power. The system was simulating using Modelica/Dymola. This method can be useful to study the influence of various parameters on the mechatronical system response in order to regulate the output power and to minimize the mechanical vibration on various parts of the wind turbine.

References

Arbaoui, A., Asbik, M.: Constraints Based Decision Support for Site-Specific Preliminary Design of Wind Turbines. Energy and Power Engineering 2, 161–170 (2010)

Chantharasenawong, C., Jongpradist, P., Laoharatchapruek, S.: Preliminary Design of 1.5-MW Modular Wind Turbine Tower. In: The 2nd TSME International Conference on Me-chanical Engineering (2011)

Hammadi, M.: Contribution à l'intégration de la modélisation et la simulation multi-physique pour conception des systèmes mécatroniques (Doctoral dissertation, Ecole centrale Paris) (2012)

Hammadi, M., Choley, J.-Y., Mhenni, F.: A multi-agent methodology for multi-level modeling of mechatronic systems. Advanced Engineering Informatics 28(3), 208–217 (2014)

Hou, Y.: Wind Turbine Control Systems Analysis Introduction to PID Controller Design, Spring E4511 Power Systems Analysis (2014)

Lee, D., Hodges, D.H., Patil, M.J.: Multi-flexible-body Dynamic Analysis of Horizontal Axis Wind Turbines. Wind Energy 5, 281–300 (2002), doi:10.1002/we.66.

Paret, A.A.: PID Controlled Frequency Regulation Of Wind Turbine. International Journal of Advanced Research in Electrical, Electronics and Instrumentation Engineering 3, 2320–3765 (2014)

Zhaoa, X., MaiXerb, P., Wu, J.: A new multibody modelling methodology for wind turbine structures using a cardanic joint beam element. Renewable Energy 32, 532–546 (2007)

Part II
Modeling and Analysis of Structures and Materials

Mechanical Response of a Pressurized Cylindrical Shell with a Hexagonal Stringer Grid

Maher Bouazizi[1], Tarek Lazghab[2], and Mohamed Soula[3]

[1] Mechanical Engineering Department, ENSIT, 5,
  Avenue Taha Hussein 1008 Tunis, Tunisia
  `bouazizi_maher@yahoo.fr`
[2] Applied Engineering Mechanics Lab, ENIT, P.O. Box 244, El Manar,
  Tunis 2092, Tunisia
  `lazghabt@yahoo.com`
[3] Applied Engineering Mechanics Lab, ENIT, ENSIT, 5,
  Avenue Taha Hussein 1008 Tunis, Tunisia
  `Soulamed2003@Yahoo.fr`

Abstract. In this work a new design for the geometrical configuration of the stringers in a pressurized cylindrical fuselage panel is proposed. This design seeks to improve the mechanical performance in terms natural frequencies, deformation, stress, strain, etc while keeping its mass less than or equal to the stringer design currently in use.

A quasi-hexagonal tessellation design is used for the stringers. A finite element model was built for two fuselage panel sections one with quasi-hexagonal stinger configuration and the other with a conventional stringer configuration. The performance of both panels in terms of natural frequencies their response typical fuselage loading conditions was compared. Results indicate that the quasi-hexagonal string configuration maybe superior in some respects.

Keywords: Tessellation, Fuselage, Eigenmodes, Stress analysis.

1 Introduction

The fuselage of most aircraft is a cylindrical shell stiffened by primary structural members known as stringers and frames; they run longitudinally and circumferentially respectively on the inner side of the cylindrical shell. Their primary purpose is to provide stiffness and bear most of the loads applied to the fuselage. The longitudinal configuration of the stringers has remained practically unchanged in most fuselage designs.

Fig. 1 shows the inner side of a typical fuselage structure where he primary and secondary structural stiffening members are indicated. The frames are supporting members that run along the circumference of the fuselage. The stringers are members that run along the axial direction of the fuselage. The roles of these members

is to support a major part of the loads experienced by the fuselage structure and at the same time provide support for the skin. The operating environment of the fuselage requires it to be stiff, fatigue resistant and light.

Other stiffening features are used in launch vehicles in aerospace applications. Space vehicles are subjected to compressive loading among other things and are prone to buckling failure. Their shells are stiffened using isogrids or anisogrids to prevent buckling as shown in Fig. 2. Several studies are conducted on the buckling of grid stiffened shells and their optimization. Vasiliev has conducted several experimental studies on the performance of composite materials anisogrids (Vasiliev et al. 2001; Vasiliev et al. 2012; Vasiliev and Razin 2006). Totaro has conducted a theoretical study on the buckling of anisogrids and their optimization (Totaro 2012, 2013; Totaro et al. 2013). Buragohain has also studied the buckling analysis of a hexagonal lattice stiffened cylindrical shell (Buragohain and Velmurugan 2009).

The motivation behind this work is to explore the possibility of using stringer configurations other than axially aligned linear stringers as shown in Fig. 3(b). There are many possible configurations such isogrids Fig. 2, regular hexagonal grid, isogonal periodic, semi-regular, Voronoi, Delaunay, etc. The tessellation of a non-plane surface is a subject of interest in disciplines such computer graphics, meshing algorithms and architectural design. Pottmann (Pottmann et al. 2015) presents and overview of architectural structures which are either composed of polyhedral cells or closely related shapes.

Among all possible tessellations, the honeycomb hexagonal regular grid is the most interesting. The honeycomb conjecture states that a regular hexagonal grid is the most optimal way to partition a surface into regions of equal area with the least amount of total perimeter. This is an ancient result by Marcus Terentius Varro dates back to 36 B.C and has been recently proven mathematically by Hales (Hales 2001). If we consider the stringers on a cylindrical fuselage panel as the partitioning element as shown in Fig. 3(a) and if these stringers are arranged in hexagonal grid configuration then according to the honeycomb conjecture we can be sure that the shortest total length of stringers is being used to stiffen the cylindrical fuselage panel. In fact, the honeycomb conjecture applies to plane surfaces only but Wenninger (Wenninger 1979) stated that applying it to a cylindrical surface is not a much different problem.

Knowing that the shortest total length of the stringers is guaranteed with a hexagonal grid it is interesting to explore the mechanical performance of a panel section with such a stringer configuration based and compare it to the baseline case of linear stringer configuration of Fig. 3(b). In particular, we interested in the natural vibration modes, displacements and stresses when the fuselage panel section is subjected to internal pressure, axial loading, etc. These are typical loading conditions experienced by commercial aircraft fuselage panel sections. A finite element study is conducted to evaluate the response of the structure to loading in terms of displacement, stress and natural frequencies. These results will be compared to those of an identical panel section but with a conventional rectangular stringer grid as shown in Fig. 3(b).
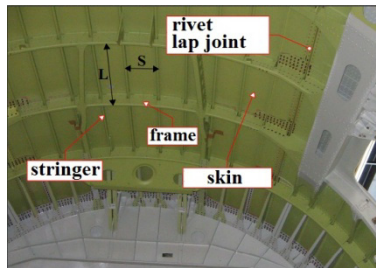
Fig. 1 Typical fuselage structure with stiffening members
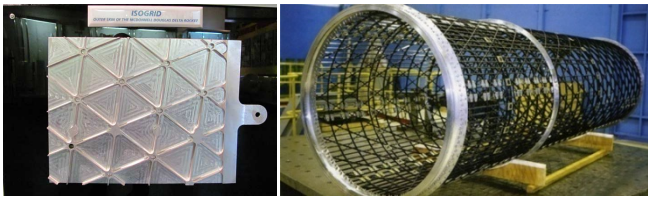
Fig. 2 (left) isogrid stiffening detail; (right) cylindrical anisogrid stiffening structure
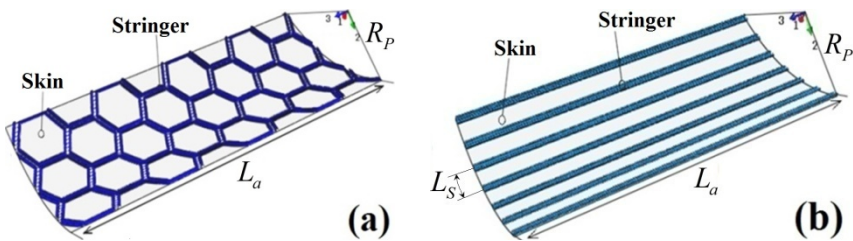
Fig. 3 (a) Cylindrical stiffened by a hexagonally tessellated grid; (b) cylindrical shell stiffened by a linear grid

2   Statement of the Problem

2.1   *Geometry and Parameters*

Fig. 3 shows both fuselage panel sections (hexagonal and linear grids) with the frames, the geometric parameters for the skin, frames and stringer grids are given in Fig. 3 and Fig. 4 for both structures and they are defined as follows:

Skin:

t_P : skin thickness

R_P : Radius of the panel section (skin)

L_a : axial length of the panel section.

L_θ : circumferential length of the panel (section)

Linear grid stringers:

A_S : cross-sectional area of the stringer.

L_S : inter-stringer distance

n_S : number of stringers in the panel.

Frame:

A_F : cross-sectional area of the frame.

L_F : inter-frame distance

n_F : number of frames in the panel.

Hexagonal grid stringers: (see Fig. 4)

n_a : number of hexagonal cells in the axial direction.

n_θ : number of hexagonal cells in the circumferential direction.

α, β : inscribed hexagonal cell angles.

a, b : lengths of the sides of the hexagonal cell
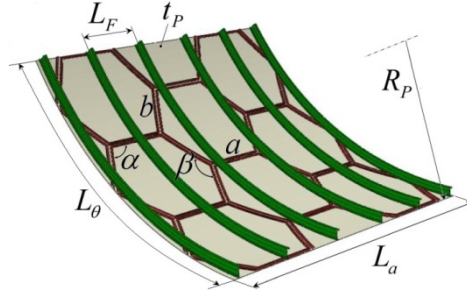
Fig. 4 geometric parameters for hexagonal grid panel

2.2 Total Stringer Length Equivalence

In both grids (hexagonal and linear) of Fig. 3 we wish to use the same total length of stringer elements that can tessellate the surface area of the fuselage panel of dimensions $L_a \times L_\theta$ as in Fig. 4. The total length of the stringer elements L_L in the linear configuration is defined as:

$$L_L = n_S L_a \tag{1}$$

The total length of stringer elements L_H in the hexagonal grid is a function of the geometric parameters as follows:

$$L_H = L_H\left(a, b, \alpha, \beta, n_a, n_\theta\right) \tag{2}$$

In the most general case the variables (a,b,α,β) of the geometry of the hexagonal grid in equation (2) can lead to shapes that do not tessellate the shell's surface. In order to avoid this, the following constraints are added:

$$a = b \text{ and } \alpha > 0 \tag{3}$$

This results in the relation $\beta = \frac{\pi}{2} - 2\alpha$. In light of this we can write:

$$L_H = L_H\left(a,\alpha,n_a,n_\theta\right) \tag{4}$$

The length equivalence between the hexagonal and linear grids requires that $L_H = L_L$. However, this is not always possible. Instead, we seek to minimize the difference between the two lengths while keeping $L_H \leq L_L$ by finding the optimal set of variables (a,α,n_a,n_θ). The problem is stated as:

$$\begin{cases} \min \left\|L_H\left(a,\alpha,n_a,n_\theta\right) - L_L\right\| \text{ such that } (n_a,n_\theta) \in \mathbb{N}^+; a > 0; \quad \alpha \in \left[0,\pi\right] \\ \text{subject to: } L_\theta = 2n_\theta a \sin\left(\frac{\alpha}{2}\right) \text{ and } L_a = n_a a + a\left(n_a + 1\right)\cos\left(\frac{\alpha}{2}\right) \end{cases} \tag{5}$$

L_H in equation (5) is given

$$L_H\left(a,\alpha,n_a,n_\theta\right) = aN_S$$

$$N_S = 3n_a n_\theta + 2n_\theta + \frac{n_a}{2} + p ; \quad \text{where } p = \begin{cases} \frac{1}{2} \text{ if } n_a \text{ is odd} \\ 0 \text{ otherwise} \end{cases} \tag{6}$$

N_S is the total number of hexagon sides in the grid assumed to be all of equal length a. Equations (5) and (6) constitute a mixed integer nonlinear programming optimization problem since the variables (n_a,n_θ) are constrained to be integers they represent the number of hexagonal cells along the axial and circumferential directions, respectively.

Fig. 5 Optimum hexagonal grid search using MS Excel solver capability

This problem is solved using the addin solver capability in the Microsoft-Excel spreadsheet software as shown in Fig. 5. Using values for $\left(L_\theta, L_a, n_s\right)$ given in Table 1 the optimal point solution to problem (5) and the associated constraint (6) is $\left(a^*, \alpha^*, n_a^*, n_\theta^*\right) = \left(216.1 \text{ mm}, 133.3^\circ, 8, 3\right)$; these values are used to build the finite element model of the structure with hexagonal grid stringer configuration.

3   Finite Element Analysis

Two analyses are conducted for each panel. The first is an eigenmodes extraction procedure in order to determine the natural frequencies and their associated modes. In the second, a uniform pressure is applied on the inner side of the panel section and displacement and stresses in both structures are analyzed and compared.

3.1   Geometry and Material Data

The geometries of the both panels (hexagonal, linear) are shown in Fig. 3 and Fig. 4; the numerical values for the parameters therein are given in Table 1.

The materials used for the fuselage section are AL2024T3 for the skin and AL7075T3 for the frames and stringers. There material data is provided in Table 2 along with their thicknesses.

3.2   Mesh, Boundary Conditions and Loading

The models of the fuselage panel sections (hexagonal, linear) were built using the ABAQUS finite element software. Thin shell elements of type S4R (4-noded reduced integration shell elements) were used to model all the components of the panel section. The assembly of the frames and stringers to the skin is modeled using multipoint constraints; nodes from different parts in contact with each other are constrained to have the same displacement vector. Table 3 provides some statistics about the finite element mesh for both models.

The boundary conditions applied are shown in Fig. 6 with respect to a cylindrical reference frame whose Z axis coincides with longitudinal axis of the fuselage panel. The boundary conditions are: θ Symmetry on edges A, B $\left(u_\theta = r_\theta = r_Z = 0\right)$ Z Symmetry on edges C, D $\left(u_Z = r_r = r_\theta = 0\right)$; where $\left(u_r, u_\theta, u_Z\right)$ and $\left(r_r, r_\theta, r_Z\right)$ are the components of the displacement and rotation vectors in the cylindrical reference frame $\left(r, \theta, Z\right)$, respectively.

The skin of the panel section is subjected to a uniform pressure $p = 0.06$ MPa as shown in Fig. 6

Table 1 Geometric parameters for the fuselage panel section

	Skin			Frame			Stringers	
	Unit	Value		Unit	Value		Unit	Value
t_P	mm	1.2	A_F	mm^2	443.2	A_S	mm^2	148.8
R_P	mm	1676	L_F	mm	482.6	L_S	mm	190.5
L_a	mm	2500	n_F	-	6	n_S	-	7
L_θ	mm	1190				n_a^*	-	8
						n_θ^*	-	3
						α^*	Deg	133.2
						a^*	mm	216.05

Table 2 Material data of the fuselage panel section

Component	Material	Young's modulus	Yield limit	Density	Poisson's Coefficient	Thickness
Unit		GPa	MPa	kg/m^3	-	mm
Skin	2024T3	71	276	2680	0.3	1.2
Frame Stringers	7075T3	71	540	2680	0.3	1.6

Table 3 Finite element model mesh statistics

Component	Element type	Number of elements	
		Linear grid	Hexagonal grid
Skin		6776	6776
Stringer	S4R	8280	143630
Frame		19080	19080
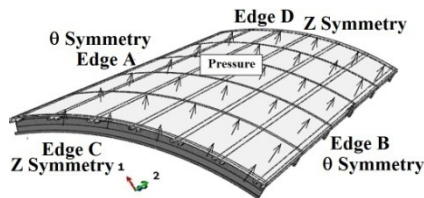
Fig. 6 loading and boundary conditions

4 Results and Discussion

Panel sections with hexagonal and linear grids were analyzed for eigenmode extraction and static analysis. The same analyses was repeated for the panel section

but with the frames removed in order single out the effect of the stringer grid on the skin. A total of eight analysis cases were conducted.

4.1   Eigenmode Extraction

Panels without Frames: The first 15 modes for the panels with hexagonal and linear stringer grids without frames are extracted the eigenvalues for each panel are shown in Fig. 7. Graphs show that over the first 15 modes the eigenvalues for the panel section with the hexagonal grid (PSHG) are greater than the eigenvalues of the panel section with a linear grid (PSLG). Keeping in mind that these to structure have the same mass we can conclude that the PSHG is stiffer than the PSLG under the current boundary conditions. At the 15th eigenmode the frequency of PSGH is 3 times as much as it counterpart in PSLG.

Panels with Frames: similarly the first 15 eigenmodes were extracted for the panel section with hexagonal grid and with frames (PSHGF) and the panel section with linear grid and with frames (PSLGF). The results are presented in Fig. 8; the stiffening effect of the frames on the PSLGF can clearly be seen in the first 3 modes; in subsequent modes the PSHGF remains stiffer than the PSLGF. However, this difference decays as the mode number increases.
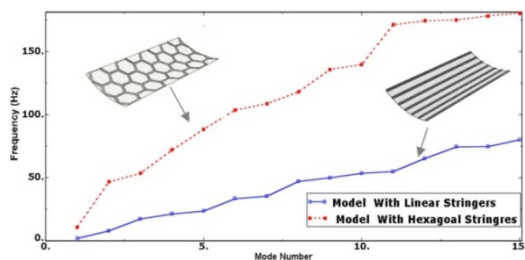
Fig. 7 Eigenvalues for PSHG and PSLG
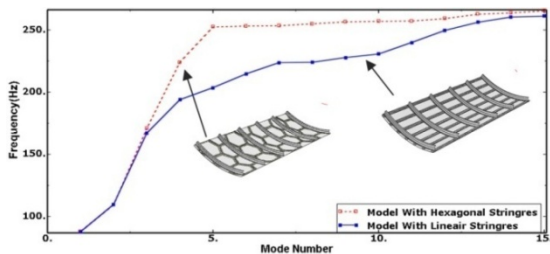
Fig. 8 Eigenvalues for PSHGF and PSLGF

4.2   Static Analysis

Panels without Frames: the PSHG and PSLG were analyzed in static analysis under a uniform pressure load $(p = 0.06 \text{ MPa})$. The Mises stress fields in the skin for both panels are presented in Fig. 9. The overall stress levels in the PSHG are about 7% higher than PSLG. It is clear that the skin in PSHG is experiencing severe stress conditions in comparison to PSLG.

Panels with Frames: the Mises stress for PSHGF and PSLGF are presented in Fig. 10, the average stress level in PSHGF is approximately 10% higher than in PSLGF. Again the skin is experiencing more severe stress states in PSHGF.
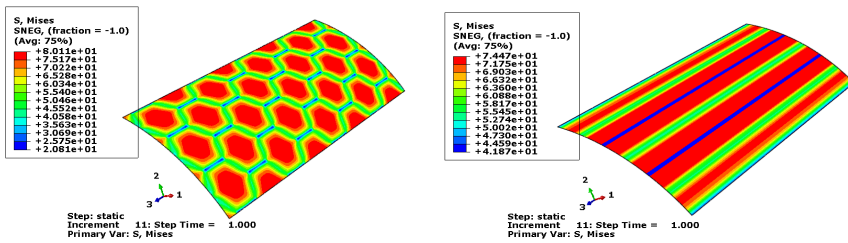
Fig. 9 Mises stress for PSHG and PSLG (no frames)
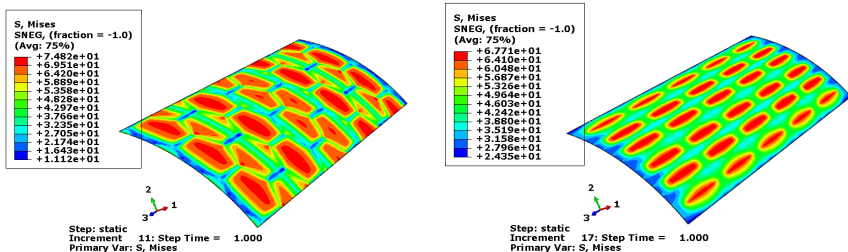
Fig. 10 Mises stress for PSHGF and PSLGF (with frames)

5   Conclusion

A fuselage panel with a hexagonal stringer grid was analyzed and compared to a conventional fuselage panel section with a linear stringer grid. The parameters of the hexagonal cell were determined from a mixed-integer programming optimization problem. The optimal design parameters are used to build finite element model of the panel section with a hexagonal grid; also a finite element model is built for the fuselage panel section with a linear stringer grid. The response of the two structure from an eigenmode extraction analysis and a static pressurization analysis show that the hexagonal grid structure is stiffer. However, under static analysis stress in the hexagonal structure are higher by as much as 10%.

The use of stringer tessellation (configurations) other than linear show promising results; there is room for improvement of the optimal configuration. It may even be possible to reduce the total length of stringer necessary to support the structure, further studies are needed.

References

Buragohain, M., Velmurugan, R.: Buckling analysis of composite hexagonal lattice cylindrical shell using smeared stiffener model. Defence Science Journal 59(3), 230–238 (2009)

Hales, T.C.: The Honeycomb Conjecture. Discrete & Computational Geometry 25(1), 1–22 (2001), doi:10.1007/s004540010071

Pottmann, H., Jiang, C., Höbinger, M., Wang, J., Bompas, P., Wallner, J.: Cell packing structures. Computer-Aided Design 60, 70–83 (2015),
http://dx.doi.org/10.1016/j.cad.2014.02.009

Totaro, G.: Local buckling modelling of isogrid and anisogrid lattice cylindrical shells with triangular cells. Composite Structures 94(2), 446–452 (2012),
http://dx.doi.org/10.1016/j.compstruct.2011.08.002

Totaro, G.: Local buckling modelling of isogrid and anisogrid lattice cylindrical shells with hexagonal cells. Composite Structures 95(0), 403–410 (2013),
http://dx.doi.org/10.1016/j.compstruct.2012.07.011

Totaro, G., De Nicola, F., Caramuta, P.: Local buckling modelling of anisogrid lattice structures with hexagonal cells: An experimental verification. Composite Structures 106(0), 734–741 (2013),
http://dx.doi.org/10.1016/j.compstruct.2013.07.031

Vasiliev, V.V., Barynin, V.A., Rasin, A.F.: Anisogrid lattice structures – survey of development and application. Composite Structures 54(2-3), 361–370 (2001),
doi: 10.1016/S0263-8223(01)00111-8,
http://dx.doi.org/10.1016/S0263-8223

Vasiliev, V.V., Barynin, V.A., Razin, A.F.: Anisogrid composite lattice structures – Development and aerospace applications. Composite Structures 94(3), 1117–1127 (2012),
http://dx.doi.org/10.1016/j.compstruct.2011.10.023

Vasiliev, V.V., Razin, A.F.: Anisogrid composite lattice structures for spacecraft and aircraft applications. Composite Structures 76(1-2), 182–189 (2006),
 http://dx.doi.org/10.1016/j.compstruct.2006.06.025

Wenninger, M.J.: Spherical Models. Dover (1979)

Element Free and Improved Element Free Galerkin Methods for One and Two-Dimensional Potential Problems

Imen Debbabi, Zohra Sendi, and Hédi Belhadj Salah

LGM, ENIM, Univercity of Monastir, Monastir, Tunisia
{imen.debbabi86,hedi.belhadjsalah1}@gmail.com,
zohrasendii@yahoo.fr

Abstract. Potential difficulties appears with various physical and engineering problems where functions satisfy a given partial differential equations and particular boundary conditions. From problems which are time independent and involve only space coordinates, one- dimensional examples and bidimensional diffusion equations are studied using two meshless methods: Element Free Galerkin (EFG) and Improved Element free Galerkin(IEFG).These two methods give good results when compared with analytical solution, but IEFG method based on IMLS approximation is in a higher computing speed and precision.

Keywords: meshless method, Element free Galerkin method, Improved Element Free Galerkin method, MLS approximation, IMLS approximation, diffusion equation.

1   Introduction

A potential problem is a very important engineering problems, because it occurs in connection with electrostatics filed, incompressible fluid flow, steady states heat conduction and many others. In case of complex boundary conditions it is difficult to find analytic solution and we use numeric methods. In case of some complicated figure such as large deformation or the modeling of crack propagation, traditional numerical methods such as MEF cannot be effectively applied and meshless methods which are based on nodes distributed in the domain can be used (T.Belytschko,Y.Krongauz 1996).

   In computational mechanic, meshless methods have attracted such attention in recent decades. They can solve many engineering problems when conventional methods are not able to give results especially problems with large deformation, dynamic fracturing and explosion's problem (K.M.Liew,T.Y.Ng.2002). The main objective of meshless method is to reduce the difficulty of meshing and remeshing the whole structure by adding nodes. The difference between meshless and conventional methods is how shape functions are formulated, when the shape function is formed, the final discrete equations are obtained by the same way.

Many meshless method have been developed such as MLPG (Atluri SN, Zhu TL.1998),EFG(Belytschko.T and Lu.1994),FPM(OnarteE.1996),MRKP(Liu WK, Chen Y.1996). Between all of these methods, EFG is the most famous and the most applied.

The EFG method is based on Moving Least Square approximation (MLS). The main disadvantage of this approximation is that the final discreet equation's system is ill- conditioned and sometimes it is impossible to get the correct numerical solution(Zhang.Z,Zhao.P,2009).To avoid this problem the improved moving least square approximation is presented. In the IMLS (Liew KM, Cheng Yumin, 2006) the orthogonal function system with a weight function is used as the basis function. The new equation system is not ill conditioned and the solution can be obtained without having to derive the inverse matrix.In addition there is fewer coefficient in the IMLS approximation which leads to a greater computational speed and efficiency.

In this paper MLS and IMLS approximations are presented, then the Improved Element Free Galerkin Method is discussed. To present a comparison between EFG and the IEFG methods one and two dimensional problems such as diffusion equation with different types of boundary conditions are introduced using the two meshless methods.

2 Moving Least Square (MLS) Approximation

2.1 MLS Interpolants Functions

In the EFG method, MLS approximation is used to construct the shape functions.

For a field variable u(x) defined in the domain Ω, the approximation of u(x) denoted u^h(x) is

$$u^h(x) = \sum_{i=1}^{m} p_i(x)a_i(x) = \boldsymbol{p}^T(x)\boldsymbol{a}(x) \tag{1}$$

Where $\boldsymbol{p}(x)$is a vector of monomial basis functions, m is the number of terms in the basis and $\boldsymbol{a}(x)$ is a vector of coefficients of the basis functions.

In general basis functions are as following:

- ▪ Linear basis:
  $\boldsymbol{p}^T(x) = (1, x_1)$ in 1D.
  $\boldsymbol{p}^T(x) = (1, x_1, x_2)$ in 2D.
- ▪ Quadratic basis
  $\boldsymbol{p}^T(x) = (1, x_1, x_1^2)$ in 1D.
  $\boldsymbol{p}^T(x) = (1, x_1, x_2, x_1^2, x_1 x_2, x_2^2)$ in 2D.

The local approximation of the function u(x) as given by Lancaster and Salkauskas (Lancaster P, Salkauskas K.1981.):

$$u^h(x, \bar{x}) = \sum_{i=1}^{m} p_i(\bar{x})a_i(x) = \boldsymbol{p}^T(\bar{x})\boldsymbol{a}(x) \tag{2}$$

Because it is a moving least square approximation $\bar{x}$ can be chosen arbitrary and it can be the node position x_I. To obtain the local approximation of u(x), the

difference between the local approximation $u^h(x)$ and $u(x)$ must be minimized by a weighted least square method.

Define a function:

$$J(a) = \sum_{I}^{n} w(x - x_I)[u^h(x, x_I) - u(x_I)]^2$$

$$= \sum_{I}^{n} w(x - x_I)[\sum_{i=1}^{m} p_i(x_I)a_i(x) - u(x_I)]^2 \tag{3}$$

where $w(x - x_I)$ is a weight function with a domain of influence, and $x_I,\ I = 1,2,\ldots n$ are the nodes in the domain of influence that cover x.

Equation (3) can be written as

$$J = (Pa - u)^T W(x)(Pa - u) \tag{4}$$

where

$$u^T = (u_1, u_2, \ldots\ldots, u_n) \tag{5}$$

$$P = \begin{bmatrix} p_1(x_1) & p_2(x_1) & \cdots & p_m(x_1) \\ p_1(x_2) & p_2(x_2) & & p_m(x_2) \\ \vdots & & \ddots & \vdots \\ p_1(x_n) & p_2(x_n) & \cdots & p_m(x_n) \end{bmatrix} \tag{6}$$

$$W = \begin{bmatrix} w(x - x_1) & 0 & \cdots & 0 \\ 0 & w(x - x_2) & & 0 \\ \vdots & & \ddots & \vdots \\ 0 & 0 & \cdots & w(x - x_n) \end{bmatrix} \tag{7}$$

The minimization condition requires

$$\frac{\partial J}{\partial a} = 0 \tag{8}$$

which gives the equation system

$$A(x)a(x) = B(x)u \tag{9}$$

Where matrices $A(x)$ and $B(x)$ are

$$A(x) = P^T W(x)P \tag{10}$$

$$B(x) = P^T W(x) \tag{11}$$

u is the vector that collects nodal parameters.

From equation (9) we can write

$$a(x) = A^{-1}B(x)u \tag{12}$$

The expression of $u^h(x)$ is then

$$u^h(x) = \Phi(x)u = \sum_{I}^{n} \Phi_I u_I \tag{13}$$

where $\Phi(x)$ is the vector of MLS shape functions.

$$\Phi(x) = P^T(x)A^{-1}(x)B(x) \tag{14}$$

2.2 The Orthogonal Basis Functions

In the IMLS approximation and to avoid the problem that the system equations (9) is sometimes ill-conditioned, the basis functions are chosen to be weighted orthogonal.

In the Hilbert space $span(p)$ for the set of point $\{x_i\}$ and the tions $\{w_i\}$ if the function s $p_1(x), p_2(x), \ldots, p_m(x)$ satisfy the condition

$$(p_k, p_j) = \sum_{i=1}^{n} w_i p_k(x_i) p_j(x_i) = \begin{cases} 0, & k \neq j \\ A_k, & k = j \end{cases} \quad (k, j = 1, 2 \ldots, m) \tag{15}$$

Then the functions set is called a weighted orthogonal set functions with a weight function $\{w_i\}$ about point $\{x_i\}$. In the case of $p_1(x), p_2(x), \ldots, p_m(x)$ are polynomials then the function set $p_1(x), p_2(x), \ldots, p_m(x)$ is called a weighted orthogonal polynomials set with the weight function $\{w_i\}$ about point $\{x_i\}$.

Using equation (15) equation (9) can be written as

$$\begin{bmatrix} (p_1, p_1) & (p_1, p_2) & \cdots & (p_1, p_m) \\ (p_2, p_1) & (p_2, p_2) & & (p_2, p_m) \\ \vdots & & \ddots & \vdots \\ (p_m, p_1) & (p_m, p_2) & \cdots & (p_m, p_m) \end{bmatrix} \begin{bmatrix} a_1(x) \\ a_2(x) \\ \vdots \\ a_m(x) \end{bmatrix} = \begin{bmatrix} (p_1, u_I) \\ (p_2, u_I) \\ \vdots \\ (p_m, u_I)) \end{bmatrix} \tag{16}$$

But the basis functions set is a weighted orthogonal functions set, then equation (16) has this expression

$$\begin{bmatrix} (p_1, p_1) & 0 & \cdots & 0 \\ 0 & (p_2, p_2) & & 0 \\ \vdots & & \ddots & \vdots \\ 0 & 0 & \cdots & (p_m, p_m) \end{bmatrix} \begin{bmatrix} a_1(x) \\ a_2(x) \\ \vdots \\ a_m(x) \end{bmatrix} = \begin{bmatrix} (p_1, u_I) \\ (p_2, u_I) \\ \vdots \\ (p_m, u_I)) \end{bmatrix} \tag{17}$$

$a_i(x)$ are then directly obtained as follows:

$$a_i(x) = \frac{(p_i, u_I)}{(p_i, p_i)}, \qquad (i=1,2,\ldots,m) \tag{18}$$

Then

$$a(x) = \bar{A}(x)B(x)u. \tag{19}$$

where

$$\bar{A}(x) = \begin{bmatrix} \frac{1}{(p_1, p_1)} & 0 & \cdots & 0 \\ 0 & \frac{1}{(p_2, p_2)} & & 0 \\ \vdots & & \ddots & \vdots \\ 0 & 0 & \cdots & \frac{1}{(p_m, p_m)} \end{bmatrix} \tag{20}$$

$\bar{A}(x)$ is a diagonal matrix, and it is impossible to get an ill-conditioned system equations. Coefficients a(x) are also directly and simply obtained. The approximation $u^h(x)$ has then the expression as follows

$$u^h(x) = \bar{\Phi}(x)u = \sum_{I=1}^{n} \overline{\Phi}_I u_I \tag{21}$$

$$\bar{\Phi}(x) = P^T(x)\bar{A}(x)B(x) \tag{22}$$

The Schmidt method can be used to have the orthogonal basis functions (p_i):

$$p_1 = 1;$$
$$p_i = r^{i-1} - \sum_{k=1}^{i-1} \frac{(r^{i-1}, p_k)}{(p_k, p_k)} p_k, \quad i = 2,3 \dots \tag{23}$$

Where r= x in 1D and r= $x_1 + x_2$ or $\sqrt{x_1^2 + x_2^2}$ in 2D problems.

In addition, the Schmidt method can be used to form a weighted orthogonal basis from a given monomial basis function, then if the monomial basis functions is, for example,

$$\bar{p} = (\bar{p}_i) = (1, x_1, x_2, x_1^2, x_1 x_2, x_2^2) \tag{24}$$

The weighted orthogonal basis function can be formed as

$$p_i = \bar{p}_i - \sum_{k=1}^{i-1} \frac{(\bar{p}_k, p_k)}{(p_k, p_k)} p_k, \quad i = 1,2,3, \dots \dots \tag{25}$$

In the IMLS approximation, compared with MLS approximation, there are fewer coefficients in the trial function; also fewer nodes are needed in the domain of influence. Thus the IEFG method which uses the IMLS approximation needs fewer nodes in the whole domain than in the EFG method which uses the MLS approximation (Zhang.Z,Zhao.P,2009).

2.3   Weight Function

The weight function is non-zero only over a small neighborhood of a node x_I. This neighborhood is called the domain of influence of node I. the common weight functions used in literature are cubic spline function , quadratic spline and the exponential weight function. In this paper we chose to use quadratic spline function:

$$w(s) = \begin{cases} 1 - 6s^2 + 8s^3 - 3s^4, & |s| \leq 1 \\ 0 & |s| \geq 1 \end{cases} \tag{26}$$

Where $s = \frac{\|x - x_I\|}{d}$ where $\|x - x_I\|$ is the distance from a sampling point x to a node x_I, and d is the size of the domain of influence of the Ith node.

In the case of a circular domain $d = a_c d_i$, where a_c is a scalar and d_i is the average distance between nodes. In literature $1.2 \leq a_c \leq 1.4$.

3   Improved Element Free Galerkin Method(IEFG) for Potential Problems

In this section we present the IEFG method for a 2D Poisson's equation:

$$\nabla^2 u + f(x) \; = 0, \; x \in \Omega \tag{27}$$

$$u(x) = \bar{u}(x), \qquad x \in \Gamma_u \tag{28}$$

$$\frac{\partial u(x)}{\partial n} = \bar{q}(x), \qquad x \in \Gamma_q \tag{29}$$

Where Ω is a 2D domain bounded by contour $\Gamma = \Gamma_u \cup \Gamma_q$, u(x) is an unknown function, $f(x)$ is a known function, $\bar{u}(x)$ is a dirichlet boundary condition and $\bar{q}(x)$ is a Neumann boundary condition.

The Galerkin weak form of equations (27)-(29) is

$$\int_\Omega \delta (Lu)^T (Lu) d\Omega - \int_\Omega \delta u. f d\Omega - \int_{\Gamma_q} \delta u. \bar{q} d\Gamma_q = 0; \tag{30}$$

Where δ is the variational operator and L is the differential operator.

From the approximation function (21) equation (30) can be written as follows:

$$K.U = F \tag{31}$$

Where

$$K_{IJ} = \int_\Omega \bar{\Phi}_{I,x_1} \bar{\Phi}_{J,x_1} + \bar{\Phi}_{I,x_2} \bar{\Phi}_{J,x_2} d\Omega \tag{32}$$

$$F_I = \int_\Omega \bar{\Phi}_I^T f d\Omega + \int_{\Gamma_q} \bar{\Phi}_I^T \bar{q} d\Gamma \tag{33}$$

In a steady state heat transfer problem, which is a typical Poisson's problem, U is the temperature field ,$\bar{q}$ is the heat flux function and f(x) is the internal heat generation.

3.1   *Enforcement of Essential Boundary Conditions*

The lacking of Kronecker delta property in IEFG and EFG shapefunctions makes the imposition of essential boundary condition difficult. For this reason essential boundary conditions cannot be imposed directly. Different methods are used to consider boundary conditions like Lagrangien multipliers, coupling with finite element and penalty method. The advantages of the penalty approach is that the size of the system of equations is constant and the modified stiffness matrix still positively defined. for these reasons we use the penalty method to enforce boundary conditions in this paper.

The new Galerkin week form using the penalty method to introduce essential boundary conditions becomes:

$$\int_{\Omega} \delta(Lu)^T (Lu)d\Omega - \int_{\Omega} \delta u.fd\Omega - \int_{\Gamma_q} \delta u.\overline{q}d\Gamma_q + \frac{\alpha}{2}\delta\int_{\Gamma_u} (u-\overline{u})^T (u-\overline{u})d\Gamma_u = 0; \quad (34)$$

where α is the penalty factor chosen between 10^3 and 10^{13}.
using Equation (21) , the final system matrix can be written

$$[K + K^{\alpha}]u = F + F^{\alpha} \quad (35)$$

where

$$K_{IJ}^{\alpha} = \int_{\Gamma_u} \overline{\Phi}_I^{T} \alpha \overline{\Phi}_J d\Gamma \quad (36)$$

$$F_I^{\alpha} = \int_{\Gamma_u} \overline{\Phi}_I \alpha \overline{u} d\Gamma \quad (37)$$

4   Numerical Examples

4.1   1-D Equation

The following equation is solved the EFG and IEFG methods. The number of nodes N used for this example is 51nodes, the size of the domain of influence is d= 0.021. The government equation and the boundary conditions are

$$-\frac{du}{dx^2} + u = \sin(\pi * x), \quad x \in [0,1] \quad (38)$$

$$u(0) = 0 \quad (39)$$

$$u(1) = 0 \quad (40)$$

with analytic solution

$$u(x) = \sin(\pi * x)/(1+\pi^2) \quad (41)$$

Fig.1 shows results evolution by both EFG and IEFG method plotted with analytic solution. The IEFG method has a faster computer time then the EFG method: about 80% of computation time is saved with the IEFG method(IEFG:0.27s, EFG:1.4s using a pc (ram 16Go,processeur Intel Core (TM) i7-3770,CPU@3.4Ghz).. The relative errors between results of EFG method and analytic solution and IEFG method and analytic solution are shown in Fig.2. IT is clear that the IEFG method and EFG method have a very close rate of precision.

The relative error is calculated as follows:

reltive error= $\left| \frac{u^{calc} - u^{analy}}{1 + u^{analy}} \right|$;
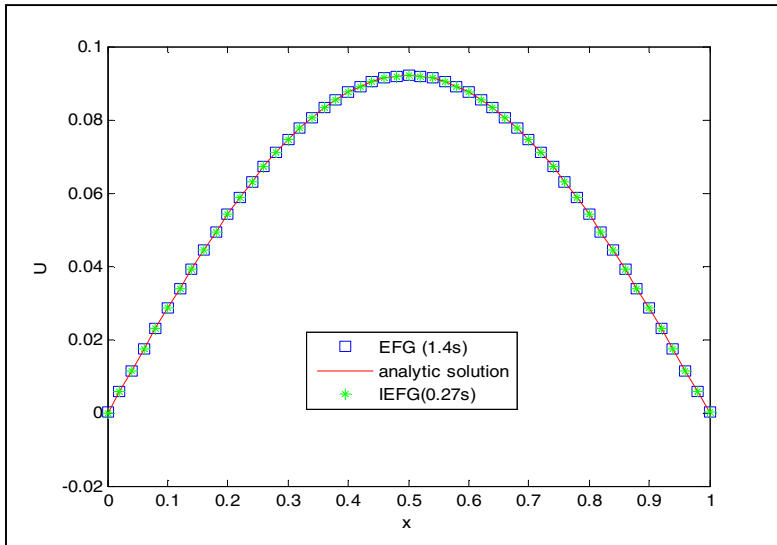
Fig. 1 Results computed with EFG and IEFG methods

4.2 *Diffusion Equations*

Two different examples are selected to demonstrate the precision and the speed of the IEFG method compared with EFG.The results of these examples are compared with the analytical solutions.

4.2.1 Laplace's Equation on a Rectangular Plate

A temperature field of a rectangular plate governed by Laplace's equation (Hong-pingRen and Ymin Cheng.2012)

$$\nabla^2 T = \frac{\partial^2 T}{\partial x_1^{\,2}} + \frac{\partial^2 T}{\partial x_2^{\,2}} = 0 \qquad x_1 \in [0,5], x_2 \in [0,10] \qquad (42)$$

the boundary conditions are

$$T(x_1, 0) = 0 \qquad\qquad 0 < x_1 < 5 \qquad\qquad (43)$$

$$T(x_1, 10) = 100 * \sin\left(\pi * \frac{x_1}{10}\right) \qquad 0 < x_1 < 5 \qquad (44)$$

$$T(0, x_2) = 0 \qquad\qquad 0 < x_2 < 10 \qquad (45)$$

$$\frac{\partial T(5, x_2)}{\partial x_1} = 0 \qquad\qquad 0 < x_2 < 10 \qquad (46)$$

with analytic solution

$$T(x_1, x_2) = \frac{100 * \sin(\pi * x_1 / 10) sh(\pi * x_2 / 10)}{sh(\pi)} \qquad (47)$$
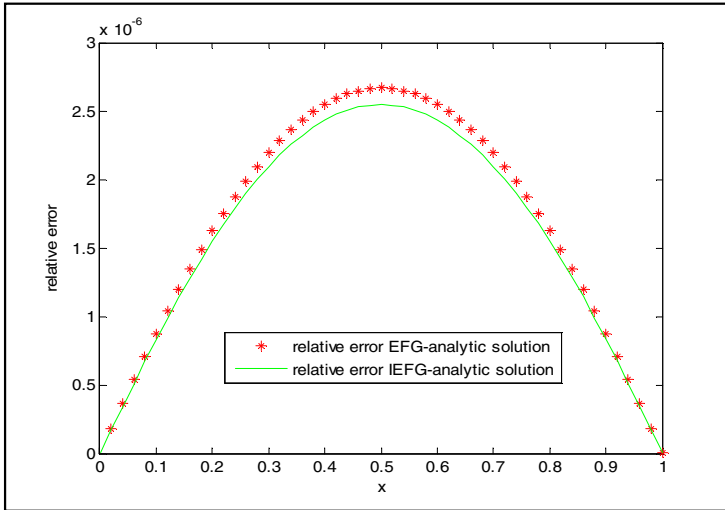
Fig. 2 Relative error between EFG, IEFG and analytic solution
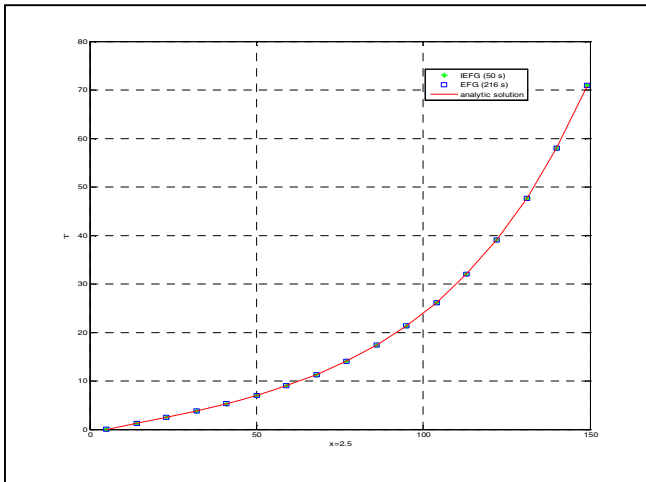
Fig. 3 Temperature at x1=2.5

The regular distribution of nodes is used, we employed 9*17 nodes .The linear basis functions and the weight function (26) are used. The size of the domain of influence is chosen to be d=0.9.

The IEFG's numerical results shown in Fig.3 agree well with analytic solution and EFG ones. When using the IEFG method we save more than 75% of the EFG's calculation time(IEFG:50s, EFG:216s using a pc(ram 16Go,processeur Intel Core (TM) i7-3770,CPU@3.4Ghz).Relative errors between IEFG, EFG and analytic solution   are presented in Fig.4. The IEFG method and EFG method have a close rate of error which is under 0.36%.
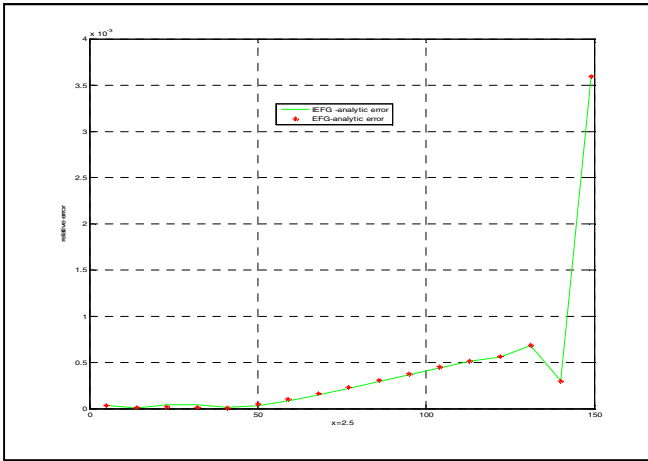
Fig. 4 Relative error at x1=2.5

4.2.2   Poisson's Equation on a Rectangular Plate

A temperature field of a rectangular plate governed by Poisson's equation

$$\nabla^2 T = -\sin(\pi * x_1) * \sin(\pi * x_2) \qquad x_1 \in [0,1], x_2 \in [0,1] \tag{48}$$

$$T(0, x_2) = 0; T(1, x_2) = 0; T(x_1, 0) = 0; T(x_1, 1) = 0; \tag{49}$$

the analytic solution is

$$T(x_1, x_2) = \frac{1}{2\pi^2} \sin(\pi * x_1) \sin(\pi * x_2) \tag{50}$$

We employed an 11*11 regular node distribution, The numerical results with the IEFG method are in excellent agreement with the analytical solution and the numerical results which are obtained with the EFG method.

From Fig.5 and Fig.6 we can see that the IEFG method gives the same precision with a good computational time.
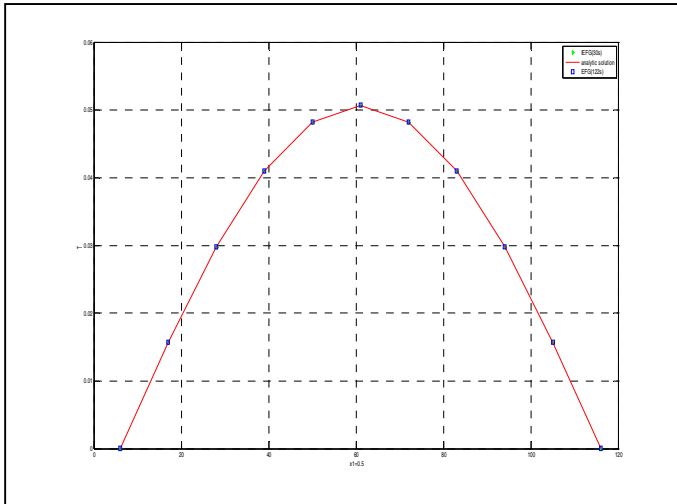
Fig. 5 Temperature at x1=0.5
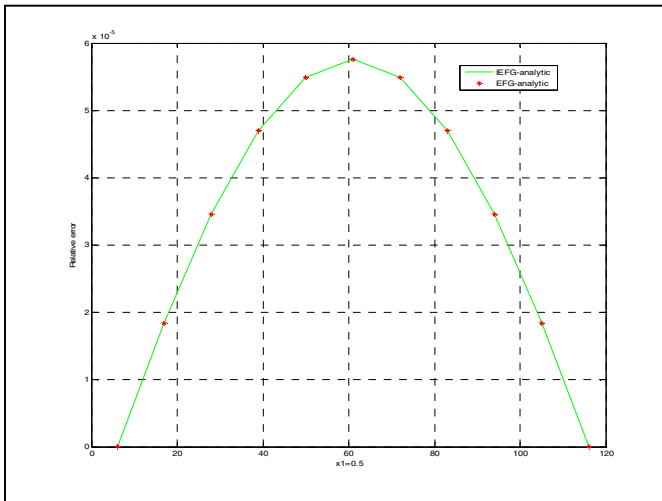
Fig. 6 Relative error at x1=0.5

5   Conclusion

This paper presents comparison between the Element Free Galerkin method using the MLS approximation and the Improved Element Free Galerkin method using the IMLS approximation. These two meshless methods are applied for one and two dimensional problems.When the IMLS approximation is used there is no ill-conditioned system's equation, this means that solution can be obtained without

matrix inversion which accelerate the computing speed. From numerical examples it is shown that, in case of the use of the IEFG method, about 75% of calculation time can be saved compared with the calculation time of the EFG method. The IEFG method gives the same or better precision than the EFG method.Thus for 1-D and 2-D potential problems, it is more suitable to use the IEFG method than the EFG method.

References

Belytschko, T., Krongauz, Y., Organ, D.: Meshless methods: An overview and recent developments. Computer Methods in Applied Mechanics and Engineering 139, 3–47 (1996)

Liew, K.M., Ng, T., Yand Wu, Y.C.: Meshfree method for large deformation analysis–a reproducing kernel particle approach. Engineering Structure 24, 543–551 (2002)

Atluri, S.N., Zhu, T.: A new meshless local Petrov–Galerkin (MLPG) approach in computational mechanics. Computational Mechanics 22, 117–127 (1998)

Belytschko, T., Lu, Y.Y., Gu, L.: Element-free Galerkin methods. International Journal for Numerical Methods in Engineering 37, 229–256 (1994)

Onarte, E.: A finite point method in computational mechanics. International Journal for Numerical Methods in Engineering 39, 3839–3866 (1996)

Liu, W.K., Chen, Y., Uras, R.A., Chang, C.T.: Generalized multiple scale reproducing kernel particle. Computer Methods in Applied Mechanics and Engineering 139, 91–158 (1996)

Zhang, Z.: Improved element-free Galerkin method for two-dimensional potential problems. Engineering Analysis with Boundary Elements 33, 547–554 (2009)

Liew, K.M., Yumin, C.: Boundary element-free method (BEFM) and its application to two-dimensional elasticity problems. International Journal for Numerical Methods in Engineering 65(8), 1310–1332 (2006)

Lancaster, P., Salkauskas, K.: Surface generated by moving least squares methods. Mathematics of Computation 37, 141–158 (1981)

Hongping Ren, Y.: Cheng The interpolating element-free Galerkin (IEFG) method for two-dimensional potential problems. Engineering Analysis with Boundary Elements 36, 873–880 (2012)

Finite Element Investigations of the Shrink-Fit Assembly with Radial Cyclic Load

Haykel Marouani[1] and Tarek Hassine[2]

[1] Mechanical Engineering Laboratory, National Engineering School of Monastir,
  University of Monastir, Tunisia
  `haykel.marouani@enim.rnu.tn`
[2] Mechanical Engineering Laboratory of Sousse,
  National Engineering School of Sousse, University of Sousse, Tunisia
  `t.hassine@gnet.tn`

Abstract. Fretting is a widely used process to assemble mechanical parts and its knowledge is based on simple calculation models applied for simple and symmetric geometries. In this paper we model this process for cylindrical parts in order to study the behavior of a modified assembly under a cyclic radial load through a rigid drive shaft. A tangential movement of the shrink relative to the hub is raised. When these movement are localized and do not present a global rotation of the shrink, the behavior of the assembly is ensured. However, under certain conditions, these tangential displacements accumulate from one cycle to another up to initiate a global relative movement of the shrink, which in some cases lead to the failure of the assembly. In this work, we highlight this phenomenon and other studies will follow to improve the knowledge of this behavior.

Keywords: fretting, cyclic load, cumulative slip.

1   Introduction

Fretting is an assembly operation between a hub and a shaft. The fit between the two assembled parts is clamped: The shaft diameter is greater than the diameter of the hub. Clamping is generally obtained by cooling the shaft. Its thermal contraction can be positioned freely in its bore. At room temperature, the clamping pressure which is induced through the friction between the contacting surfaces prevents relative movement. This process has been rarely used in industry due to its poor knowledge. Indeed, its modeling is mainly based on very simplified rules, valid only for simple shapes (NF E22-621 1984). Thanks to the development of numerical tools, the shaft-fit process is increasingly used because it is more economical than other methods of assembly, which requires additional mechanical parts to ensure the adhesion function. Moreover, the standards recommend the use of numerical simulation to design this process (PR NF E22-621 2014).

Several recent works have shown the interest of proposing models to optimize the shrink-fit assemblies. (Croccolo et al. 2010) was able to model the fatigue

behavior of the front motor bike suspension with the steering shaft press fitted into the fork whose complex shapes made the traditional approach unable to predict the fatigue behavior. (Sniezek et al. 2010) studied by finite elements the strengthening strength by Laser heat treatment for conical joints subjected to torsion. (Eyercioglu et al. 2009) used the finite element method to design and optimize a forging tool having shrunk parts. However, few studies have examined the relative tangential displacement of the shaft relative to the hub when excessive loads are applied or under cyclic loading. The accumulation of these displacements can damage the assembled structures. (Antoni et al. 2007) studied the tangential slip for crank mechanisms for the automotive industry. The existence of an asymmetry in the assembly appears to be a necessary condition for the phenomenon to occur. Furthermore, this phenomenon is sensitive to asymmetries of the friction laws and surface roughness (Antoni et al. 2007).

This work is intended to validate the numerical modeling of the fretting process. Then a geometrical asymmetry of the assembly is introduced to highlight the tangential slip phenomenon between a ring and a hub. The main goal is to understand the process in order to model later the assemblies of complex shapes and under complex loadings (conical shapes, asymmetric shapes, friction law, cyclic loading ...) and to study the tangential shaft displacements compared to the hub.

2   Shrink-Fit Assembly Modeling

For this study, we consider the shrinking of a hub and a circular shaft (Fig.1).
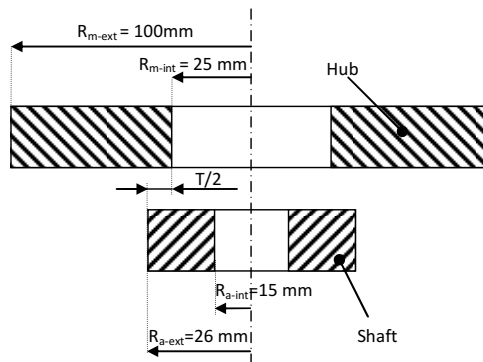
Fig. 1 Schematic diagram of the shrink-fit model

Both parts have the same mechanical properties (Young's modulus E= 210 GPa, Poisson's ratio υ= 0.3). The tightening T is defined as:

$$T = 2.(R_{a-ext} - R_{m-int})\qquad(1)$$

A proportional tightening variable A is defined by:

$$A = \frac{T}{2.R_{m-\mathrm{int}}} \tag{2}$$

The value of A should be between 0.1% and 5% (for our study case A = 4%).

2.1 Analytical Modeling

The theory of elasticity for the thick-walled tubes or cylinders (Timoshenko 1956) defines radial and tangential stress along the shaft and hub as follows:

$$
Shaft:
\begin{cases}
\sigma_{rr}(r) = -\dfrac{EA}{2}\dfrac{R_{m-ext}^2 - R_{m-\mathrm{int}}^2}{R_{m-ext}^2 - R_{a-\mathrm{int}}^2}\left(1 - \left(\dfrac{R_{a-\mathrm{int}}}{r}\right)^2\right)(<0) \\[3mm]
\sigma_{\theta\theta}(r) = -\dfrac{EA}{2}\dfrac{R_{m-ext}^2 - R_{m-\mathrm{int}}^2}{R_{m-ext}^2 - R_{a-\mathrm{int}}^2}\left(1 + \left(\dfrac{R_{a-\mathrm{int}}}{r}\right)^2\right)(<0)
\end{cases}
$$
$$
Hub:
\begin{cases}
\sigma_{rr}(r) = \dfrac{EA}{2}\dfrac{R_{m-\mathrm{int}}^2 - R_{a-\mathrm{int}}^2}{R_{m-ext}^2 - R_{a-\mathrm{int}}^2}\left(1 - \left(\dfrac{R_{m-ext}}{r}\right)^2\right)(<0) \\[3mm]
\sigma_{\theta\theta}(r) = \dfrac{EA}{2}\dfrac{R_{m-\mathrm{int}}^2 - R_{a-\mathrm{int}}^2}{R_{m-ext}^2 - R_{a-\mathrm{int}}^2}\left(1 + \left(\dfrac{R_{m-ext}}{r}\right)^2\right)(>0)
\end{cases}
\tag{3}
$$

These expressions are valid for the following assumptions: small perturbations, homogeneous and isotropic materials, uniforms solicitations, idealized surfaces. The shaft-hub interface pressure expression is:

$$P = \frac{E.A}{2.R_{m-\mathrm{int}}^2}\cdot\frac{\left(R_{m-ext}^2 - R_{m-\mathrm{int}}^2\right)\left(R_{m-\mathrm{int}}^2 - R_{a-\mathrm{int}}^2\right)}{\left(R_{m-ext}^2 - R_{a-\mathrm{int}}^2\right)} \tag{4}$$

2.2 Finite Element Modeling

The hub and the shaft are modeled as a 2D deformable body with Abaqus software. The fretting is performed by applying a pressure on the outer radius of the shaft that generates a radial compression of the external interface greater than T. The contact between the shaft and the hub is modeled without friction. Quadrilateral elements with quadratic interpolation and reduced integration (CPS8R element) are used. A fine mesh is used for simulations (147770 elements for the hub, 6977 for the shaft). Fig. 2 compares the analytical solution σ_{rr} and $\sigma_{\theta\theta}$ (Eq. 3) to that found by finite element simulation. We note a good agreement between them. These curves can be used to find the most stressed areas of the two parts.

For example, holding the Tresca criterion, we see that this is the bore shaft ($r=R_{a\text{-}int}$) which is the most requested – that for the hub – and it is also the most stressed bore ($r=R_{m\text{-}int}$).

The analytic pressure at interface P is equal to 2578 MPa (Eq. 4), found by the FE simulation which is equal to 2684 MPa.
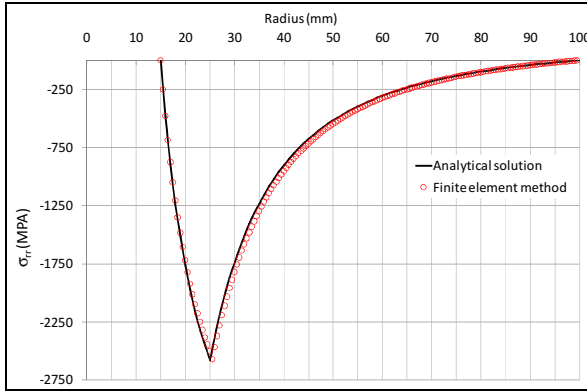
(a)
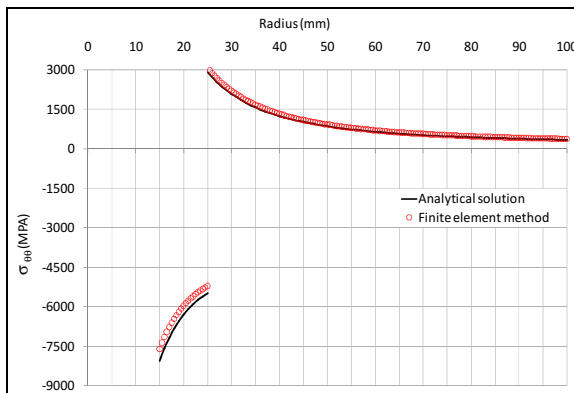
(b)

Fig. 2 Comparison between the analytical solution and the finite element method: (a) σ_{rr} ; (b) $\sigma_{\theta\theta}$

3   The Cyclic Load Application

During their real use, the boundary conditions of the shrink-fit assembly can be not symmetric. In some industrial cases, even the shape of the assembly is not symmetric. In addition to this, a third component can be used with the shrink and the hub to the power or motion transmission. Thus, we modify the already

validated shrink-fit model by adding a rigid drive shaft and by considering a dis-symmetry of the boundary conditions, as show in Fig. 3 (the top-right quarter of the outer radius of the hub is fixed). This rigid body is biased by a cyclic triangu-lar load (see Fig. 4). The problem dimensions are summarized in Tab. 1. The inter-face pressure between the shaft and the hub is equal to 14 MPa (according to Eq. 4). The contact between them is modelised with the Coulomb friction law ($\mu = 0.02$). The contact between the rigid drive shaft and the shaft is modeled as a normal contact.
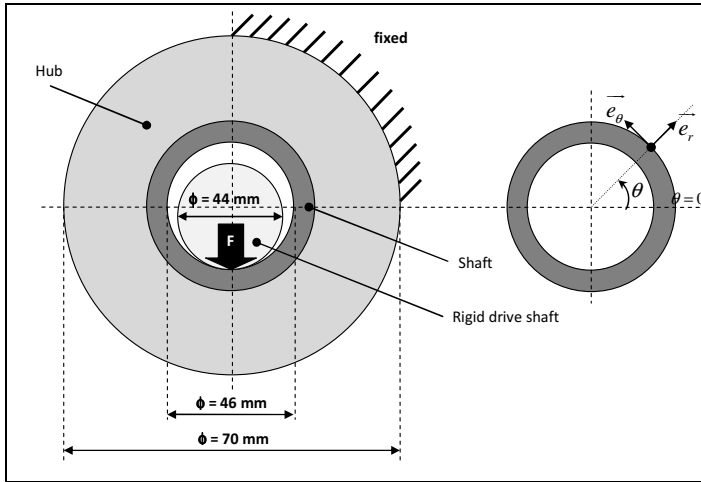
Fig. 3 Schematic diagram of the modified shrink-fit model

Table 1 Geometric dimensions

Component		Value (mm)
Hub	Inner radius	25
	Outer radius	35
Shaft	Inner radius	25.02
	Outer radius	23
Rigid drive shaft	radius	22

We note that before the application of the cyclic load, all points belonging to the outer radius of the shaft and the inner radius of the hub are subjects to tangen-tial displacements called respectively U_θ^{shaft} and U_θ^{hub}. Their tangential movements are shown in Fig. 5. We define the G variable as the difference of the tangential displacement of the shaft to the hub. G is called the relative tangential displace-ment of the shaft relatively to the hub.

$$G(mm) = U_\theta^{hub} - U_\theta^{shaft} \qquad (5)$$
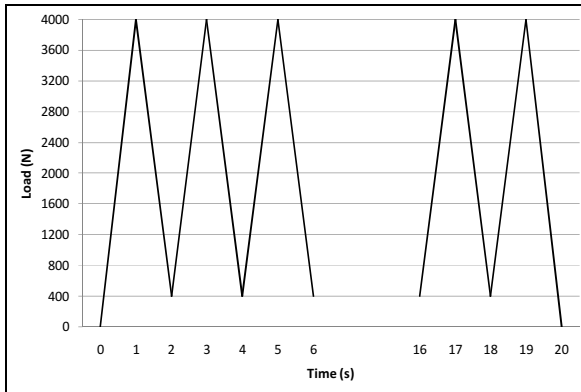
Fig. 4 Cyclic load applied to the shaft
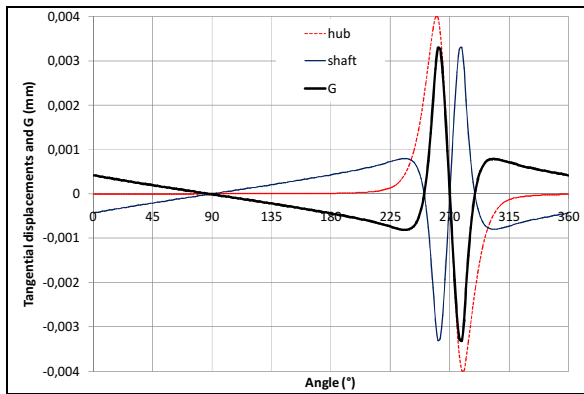
Fig. 5 Tangential displacements of the shaft U_θ^{shaft} and the hub U_θ^{hub} and relative tangential displacements of shaft to hub (G)

Thus, to study the tangential slip generated by the cyclic radial load, it is imperative to subtract the initial fitting slip to the global one calculated at each end of the cycle. Fig. 6 illustrates the relative slip of the shaft to the hub along the contact interface at the end of some cycles.

We note that for the first cycles, some points of the hub shaft interface rotate positively, some negatively and others do not move. No movement of the rigid body is denoted. However, starting from the 5th cycle, all the points move in the same direction (here in the sense $-\vec{e}_\theta$). We call 'Reptation', the minimum relative slip of the shaft to the hub.

$$\text{Reptation} = \min\left(|G|\right) \tag{6}$$

Fig. 7 shows the evolution of the 'reptation' with the number of cycles. At the beginning of this cyclic load, the relative tangential slip of the shaft does not generate a 'reptation'. Starting the 5th cycle, its evolution is linear: each additional cycle generates a shaft sliding of 2.6 μm (10^{-4} rad).
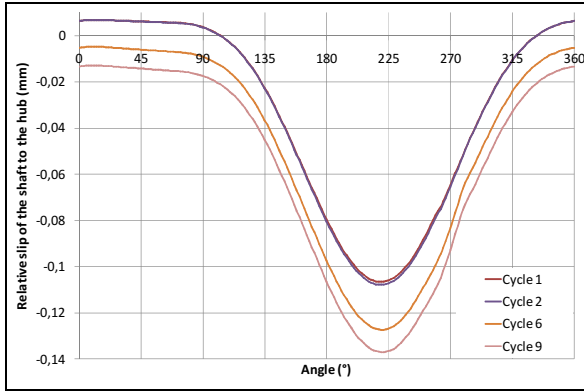
Fig. 6 Relative slip of the shaft to the hub along the contact interface for some cycles
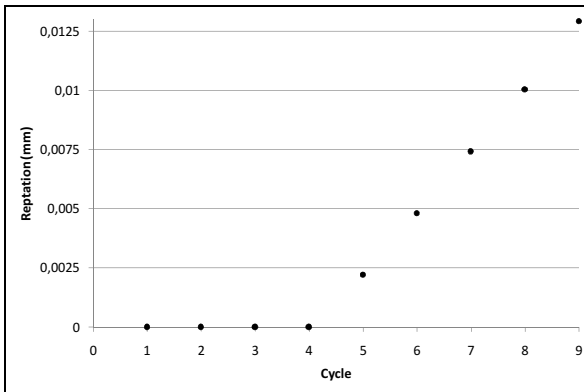
Fig. 7 Evolution of the 'Reptation' with the number of cycles

4   Conclusion

This work is an introductory study carried out to validate the analytical and numerical circular hub-shaft assembly models. In the presence of some dissymmetry, the shrink-fit process induces a very small tangential sliding of the shaft according to his hub. The radial cyclic load of the shrink, under certain conditions, adds some additional permanent sliding (with the number of cycles). These micro-slips could affect or damage the assembly function. The next studies must be focused on the sensitivity of this phenomenon to the hub-shaft friction law (static, dynamic, viscous, non-symmetric laws...), to the type of cyclic load (shape, maximum

and minimum level of charge...), to the materials properties (Young modulus, poisson's ratio...), and to the surface conditions (roughness...).

References

Antoni, N., Ligier, J.L., Saffré, P., Pastor, J.: Asymmetric friction: Modelling and experiments. Int. J. Eng. Sci. 45, 587–600 (2007)

Antoni, N., Nguyen, Q.S., Ligier, J.L., Saffré, P., Pastor, J.: On the cumulative microslip phenomenon. Eur. J. Mech. A-Solid 26, 626–646 (2007)

Croccolo, D., De Agostinis, M., Vincenzi, N.: Static and dynamic strength evaluation of interference fit and adhesively bonded cylindrical joints. Int. J. Adhes Adhes 30, 359–366 (2010)

Eyercioglu, O., Kutuk, M.A., Yilmaz, N.F.: Shrink fit design for precision gear forging dies. J. Mater Process Tech. 209, 2186–2194 (2009)

NF E22-621. Assemblages frettés sur portée cylindrique - Fonction, réalisation, calcul (1984)

PR NF E22-621. Transmissions mécaniques - Assemblages frettés sur portée cylindrique - Fonction, réalisation, calcul (2014)

Sniezek, L., Zimmerman, J., Zimmerman, A.: The carrying capacity of conical interference-fit joints with laser reinforcement zones. J. Mater Process Tech. 210, 914–925 (2010), doi:10.1016/j.jmatprotec.2010.02.004

Timoshenko, S.: Strength of materials part II: advanced theory and problems. In: Nostrand, D.V. (ed.), 3rd edn. (1956)

State Feedback Control of Ship Electric Propulsion System

Habib Dallagi and Bechir Sabri

Automatique et Robotique Marine (ARM), Naval Academy,
Menzel Bourguiba, BP 7050, Tunisia
`habib.dallagi@ept.rnu.tn, bechir.sabri@yahoo.fr`

Abstract. This article describes the synthesis of a state feedback control of an electric propulsion system of a ship propulsion using for such a synchronous motor. The highly nonlinear characteristics of the studied system make it difficult to control. A state feedback control is then necessary. The technique adopted control tested by computer simulation has shown the validity and usefulness of this approach to the pursuit of speed and stator current of the synchronous motor to control the ship speed.

Keywords: Ship electric propulsion system, Linear and non-linear model, State feedback control, Numerical simulation.

1   Introduction

Characterization of industrial processes conducted in most cases non-linear models, which are usually difficult to control. The study of such processes was generally conducted via a linearization leads to a linear model in which the arsenal of linear control can be applied.

   This work is structured around four parts: modeling of the various elements constituting the ship with its electric propulsion system with permanent magnet synchronous motor. The resulting overall model is highly non-linear and coupled. The linearization of the overall model around a nominal operating point and synthesis of state feedback control of the linear system to regulate the stator current and the motor speed is then performed and finally a study by numerical simulation of the studied system provided with the law control.

2   Summary of Electric Propulsion System of Vessel

The Electric ship generally comprises two main parts:

- The first part providing energy production includes several alternators driven by either diesel engines or by gas turbines. It supplies all users on board and propulsion equipment.

• A second part of electric propulsion generally includes one or two electric motors (may go to the following four vessel), each electric motor drives a propeller with fixed blades. Controls motor speeds are provided by frequency inverters. The figure 1 shows the block diagram of the propulsion system.
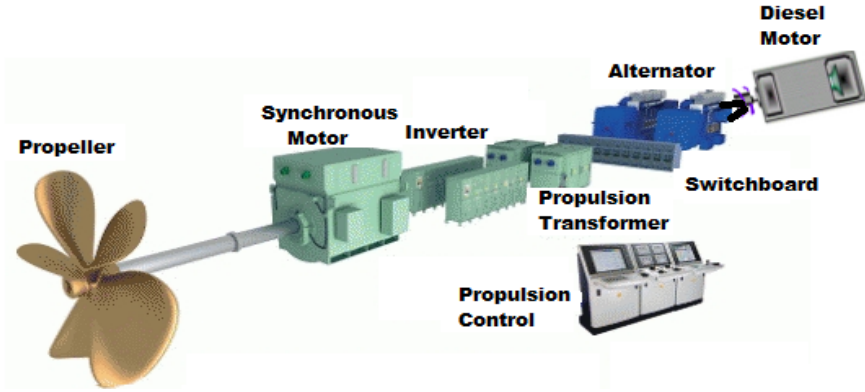
Fig. 1 Integrated electric propulsion

3 Modelling of the Power Electrical System

3.1 Modeling of Permanent Magnet Synchronous Motor

By Park transformation, the equations of the synchronous motor with permanent magnet voltages are written:

$$\begin{cases} v_d = R_s i_d + L_d \dfrac{di_d}{dt} - p\Omega L_q i_q \\ v_q = R_s i_q + L_q \dfrac{di_q}{dt} + p\Omega L_d i_d \end{cases} \tag{1}$$

The torque provided by the motor is:

$$C_e = p\Phi_f i_q + p\left(L_d - L_q\right) i_d i_q \tag{2}$$

The mechanical equation given by:

$$I_m \dot{\Omega} = C_e - Q_{prop} \tag{3}$$

with: φf: the inductive fl, Rs: stator phase resistance, vd: stator voltages longitudinal component, vq: stator voltages transverse component, id: stator currents

longitudinal component, iq: stator currents transverse Component, Ld: longitudinal inductance Lq: transverse inductance Im: shaft line inertia moment, p: pole pairs number, Ce: electromagnetic torque, Q_{prop}: propulsion couple, Ω: motor speed.

3.2   Modelling the Walking Resistance

The total resistance is given by:

$$R = R_f + R_w + R_{app} + R_{air} \tag{4}$$

with: R_f: frictional resistance, R_w: wave resistance; R_{app}: Appendices Resistance, R_{air}: air resistance.

   This model is based on the ship's resistance tests. The total resistance can be represented by the sum of four resistors (4). It is obtained by performing tensile tests on a model similar to the real ship. The running resistance can be modeled by a function of the following form:

$$R = aV^2 \tag{5}$$

   The figure 2 shows the values of the total resistance according to the speed:
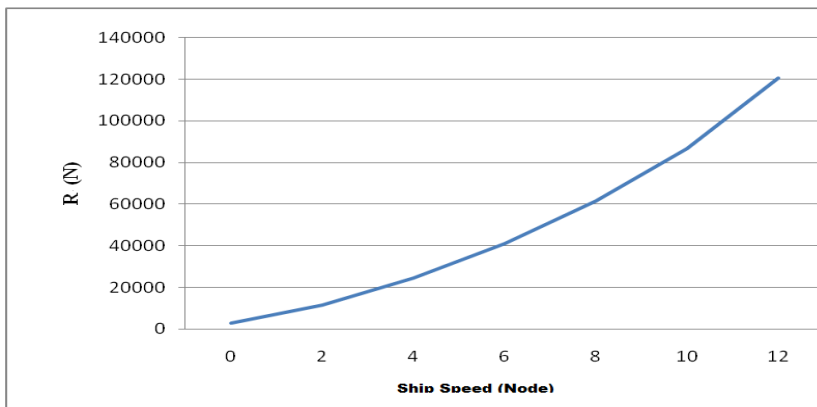
Fig. 2 Total resistance

3.3   Propeller Equations

The model of the propulsion thrust and torque of the propeller can be written as follows:

$$T_{prop} = \rho\, n^2 D^4 K_T \tag{6}$$

$$Q_{prop} = \rho\, n^2 D^5 K_Q \tag{7}$$

where: Q_{prop} is torque of the propeller, T_{prop} is the propeller thrust.

The coefficients K_T and K_Q are determined from tests on the ship, they are primarily a function of the advanced speed of the propeller (v_a), the helical pitch (z), the ship speed (v), the feed ratio of the helix (J) of the wake coefficient (w) and the fan speed (n).

$$J = \frac{Va}{nD} \tag{8}$$

and

$$Va = (1 - w)v \tag{9}$$

K_T and K_Q coefficients can be represented (approximated) by affine lines figure 3 with the following forms:
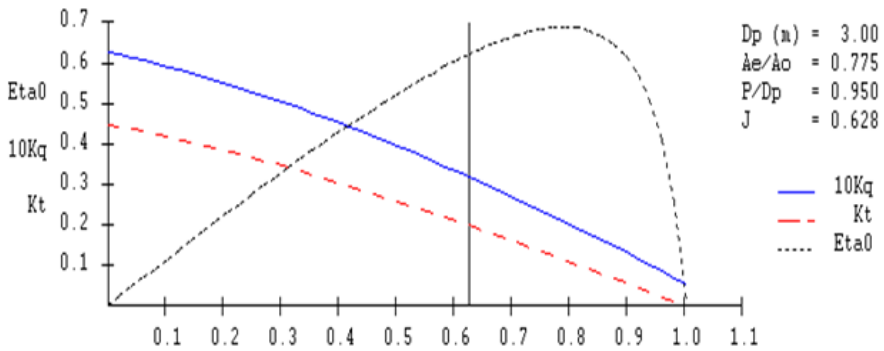
Fig. 3 Optimal characteristics of the selected propeller

$$K_T = r_1 + r_2 J \tag{10}$$

and

$$K_Q = s_1 + s_2 J \tag{11}$$

Substituting equations (8), (9), (10) into (6) gives:

$$T_{prop} = \rho n^2 D^4 (r_1 + r_2 \frac{(1 - w)v}{nD}) \tag{12}$$

Substituting equations (8), (9), (11) in (7), we get:

$$Q_{prop} = \rho n^2 D^5 (s_1 + s_2 \frac{(1 - w)V}{nD}) \tag{13}$$

We have:

$$I_m \dot{\Omega} = C_e - Q_{prop} \tag{14}$$

With: $\Omega = 2\pi n$ (n en tr/s) and:

$$C_e = p(L_d - L_q)i_d i_q + p\Phi_f i_q \tag{15}$$

$$\dot{\Omega} = \frac{p(L_d - L_q)i_d i_q + p\Phi_f i_q}{I_m} - \frac{Q_{prop}}{I_m} \tag{16}$$

The vessel motion equation is given by:

$$m\dot{V} = -R + (1-t)T_{prop} - T_{ext} \tag{17}$$

3.4 Global Model of Power-Driven Vessel

The global system of power-driven vessel is then:

$$\begin{cases} \dot{n} = \dfrac{2\Pi}{I_m}[p(L_d - L_q)i_d i_q + p\Phi_f i_q - \rho 2\Pi^2 n^2 D^5 s_1 - \rho 2\Pi n D^4 s_2(1-w)v] \\[2ex] \dot{v} = \dfrac{1}{m}[-av^2 + (1-t)\rho n^2 4\Pi^2 D^4 r_1 + (1-t)\rho n 2\Pi D^3(1-w)vr_2 - T_{ext}] \\[2ex] \dot{i}_d = \dfrac{-R_s}{L_d}i_d + pn\dfrac{L_q}{L_d}i_q + \dfrac{1}{L_d}V_d \\[2ex] \dot{i}_q = -pn\dfrac{L_d}{L_q}i_d - \dfrac{R_s}{L_q}i_q + \dfrac{1}{L_q}V_q - \dfrac{1}{L_q}pn\Phi_f \end{cases} \tag{18}$$

4   Linearisation Model Ship Propulsion System

The propulsion system is often designed to operate in control mode, ie that one wishes to maintain output as close as possible to the desired operating point, despite the various disturbances tending to depart. Under these conditions, the use of a non-linear representation overall condition, for control purposes it is not necessary. It is enough of a representation of local linear state.

The model (18) obtained from the propulsion system is a nonlinear model can be put in the form: $\begin{cases} \dot{x} = f(x) + g(x)u \\ y = h(x) \end{cases}$

By linearizing the system, one can obtain the linear model form (19):

$$\begin{cases} \dot{x} = Ax + Bu \\ y = Cx \end{cases} \tag{19}$$

with:

$x \in \mathfrak{R}^n$ the state vector , $u \in \mathfrak{R}^m$ the control vector, $y \in \mathfrak{R}^p$ the output vector and the matrices A, B and C of the constant matrices of suitable dimensions.

$$A = \frac{\partial f}{\partial x}\Big|_{x=x_0} ; \quad B = \frac{\partial f}{\partial u}\Big|_{u=u_0} \text{ et } \quad C = \frac{\partial h}{\partial x}\Big|_{x=x_0}$$

The matrices A, B and C are the Jacobians presented respectively as follows:

$$x = \left[n, v, i_d, i_q\right]^T, x_0 = \left[n_0, v_0, i_{d0}, i_{q0}\right]^T,$$
$$u_0{}^T = \left[v_{d0} \quad v_{q0}\right]^T, y_0 = \left[n_0, v_0, i_{d0}, i_{q0}\right]^T$$

Linearization of the system (17) around the nominal operating point characterized by the triplet (x_0, u_0, y_0), gives:

$$\begin{cases} \dot{n} = \dfrac{2\Pi}{I_m}(a_{id}i_d + a_{iq}i_q + a_n n + a_v v) \\ \dot{v} = \dfrac{1}{m}(b_n n + b_v v) \\ \dot{i}_d = c_{id}i_d + c_{iq}i_q + c_n n + \dfrac{1}{L_d}V_d \\ \dot{i}_q = d_{id}i_d + d_{iq}i_q + d_n n + \dfrac{1}{L_q}V_q \end{cases} \tag{20}$$

5   Study of the Control of the Power Electrical System

The state feedback control condition is to calculate the gain K of the matrix by a pole placement such that the eigenvalues of the matrix (A-BK) are placed in pre-fixed positions. To correct the error in the system output while maintaining system stability and changing the dynamics of the response. The state feedback control is to consider the model of the process in the form (19) and make a loop shape (Figure 4):

$$u(t) = -Kx(t) + Fe(t) \tag{21}$$

Where F and K are constant matrices of suitable dimensions and e (t) is the reference set of dimensional m.
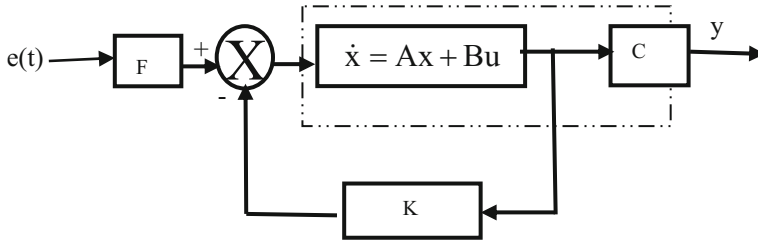
Fig. 4 State feedback control

The purpose of designing a state feedback control is to determine the F and K matrices to satisfy certain specifications. Indeed, for a gain K stabilizing the closed loop system, the loop leads to the following system:

$$\begin{cases} \dot{x}(t) = (A - BK)x(t) + BFe(t) \\ y(t) = Cx(t) \end{cases} \tag{22}$$

This for constant reference leads to static gain: $C(BK - A)^{-1}BF$

The dynamics of the closed loop system is determined by the eigenvalues of the matrix (A-BK); These eigenvalues are the roots of the characteristic equation: det(pI - (A - BK)) = 0

5.1 Controllability Theorem (Criterion Kalman)

The following system: dx (t)/dt=Ax(t)+Bu(t) which $A \in \mathbb{R}^{n.n}, B \in \mathbb{R}^{n.m}$ is controllable iff M controllability matrix has rank n:

$$M = \begin{bmatrix} B & AB & \ldots & A^{n-1}B \end{bmatrix} \quad \text{and rank (M)} = n$$

5.2 Calculation of the Pre-filter Matrix

The state equations and output under static conditions are written:

$$\begin{cases} 0 = (A - BK)x(t) + BFe(t) \\ y(t) = Cx(t) \end{cases} \tag{23}$$

$$\begin{cases} x(t) = (A - BK)^{-1}BFe(t) \\ y(t) = C(A - BK)^{-1}BFe(t) \end{cases} \tag{24}$$

From where

$$F = -[C(A - BK)^{-1}B]^{-1} \tag{25}$$

One way to determine F of imposing a static gain Γ, which gives:

$$F = [C(BK - A)^{-1}B]^{-1}\Gamma \qquad (26)$$

5.3 Using Closed Loop

Assuming that the entire state is accessible, the state feedback control that we want to implement is of the form:

$$u(t) = Fe(t) - Kx(t) \qquad (27)$$

Where e(t) is the new entry, and K is the state feedback gain that is defined by the desired structure for the closed loop system (A - BK), and gain F of prelooping which is generally calculated according to the desired static gain.

Figure 5 provides an overview of the system structure as well as the inputs and outputs of the various subsystems.
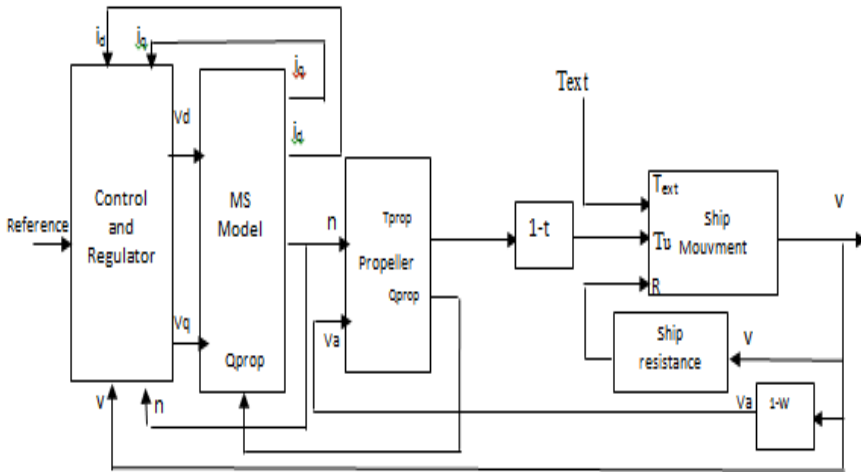
Fig. 5 Synoptic of ship propulsion system

6 Principle of Control of the Power System

The proposed control requires that the current i_q is in quadrature with respect to the rotor flux. A method of regulation, said dq, allows tracking of continuous magnitudes that are the amplitudes of id and iq. It is then transformed, from the position two sinusoidal quadrature references then by a two-phase/three-phase transformation, generating 3 references for control of the inverter. Accordingly, the current id should be collinear with the rotor flux. If one imposes the current reference id to zero (i_d=0), the electromagnetic torque becomes proportional to the stator quadrature axis current and therefore it becomes the main parameter setting.

Maintain the value of the id current zero, provides for given amplitude of statotrique currents, the maximum torque/current. To control the speed, it operates on the current iq that is to say on the torque developed by the motor.
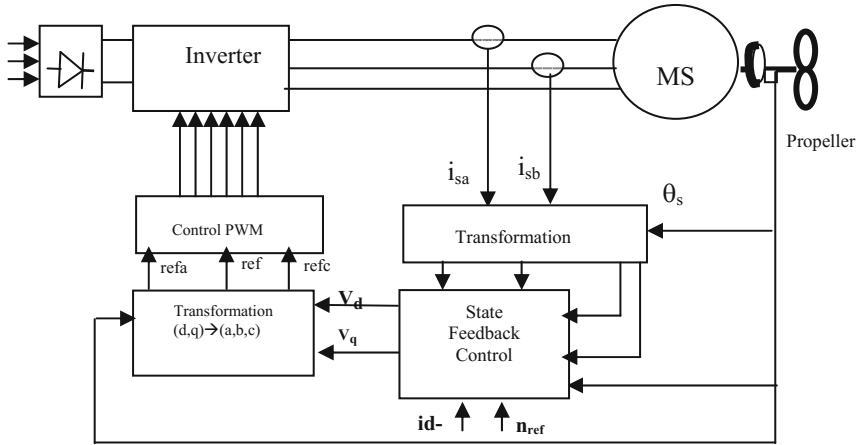
Fig. 6 Synoptic of ship propulsion system

7   Simulation Results

The model was validated by performing simulations using Matlab/Simulink. The digital simulation of the proposed control law has been carried out with on the ship electric propulsion system using the following characteristics:

$$A = \begin{bmatrix} -2.4688 & 157.1681 & 9.8230\text{e}+03 & 0 \\ -162.8829 & -2.5133 & -1.6982\text{e}+03 & 0 \\ 4.2441\text{e}-04 & 0.0040 & -203.9692 & 56.2285 \\ 0 & 0 & 0.0386 & -0.0265 \end{bmatrix} \quad C = \begin{bmatrix} 1 & 0 & 0 & 0 \\ 0 & 1 & 0 & 0 \\ 0 & 0 & 1 & 0 \\ 0 & 0 & 0 & 1 \end{bmatrix}$$

$$K = \begin{bmatrix} 1.4034 & -0.0057 & 0.0000 & 1.7183 \\ -0.0058 & 1.3957 & -0.0000 & 0.7666 \end{bmatrix} \quad B = \begin{bmatrix} 166.8102 & 0 \\ 0 & 169.8158 \\ 0 & 0 \\ 0 & 0 \end{bmatrix}$$

$$p = \begin{bmatrix} -5 & -4 & -2 & -1 \end{bmatrix}$$

Para.	Value		Par.	value
ρ	1025 Kg/m^3		s_1	0.0635
Dp	3 m		s_2	-0.0535
m	20690000 kg,		r_1	045
Lq	0.0059		r_2	-045
R_s	0.0148		t	0.178
Φ_f	1		w	0.2304
Ld	0.0060		a	937.5
p	4		I_m	25000 Kgm^2
P/Dp	0.950		Ae/Ao	0.775

Fig. 7 System parameters
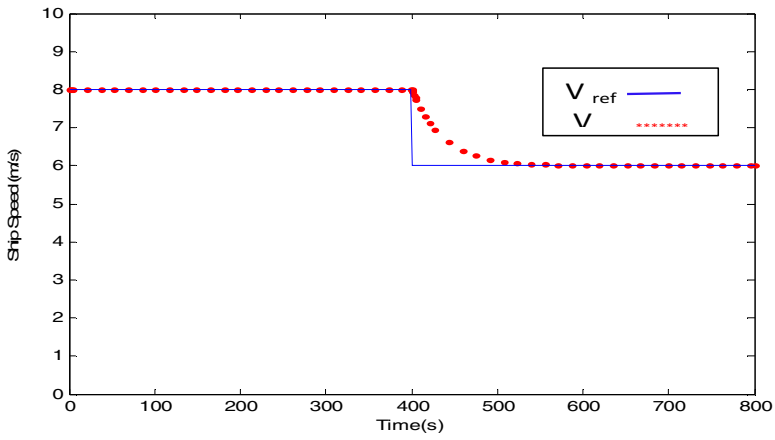
Fig. 8 Ship Speed
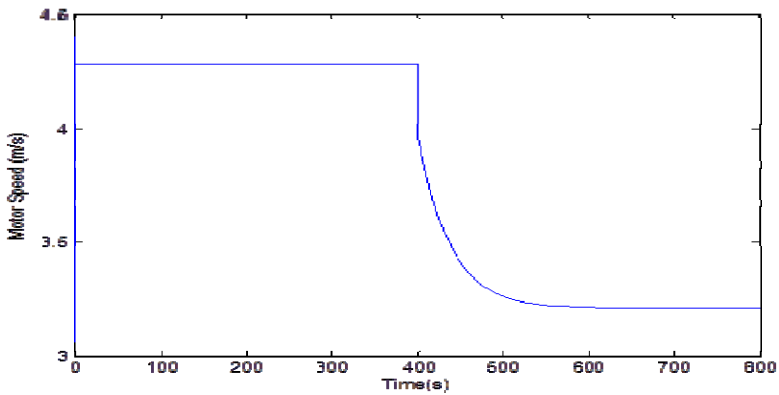
Fig. 9 Motor Speed
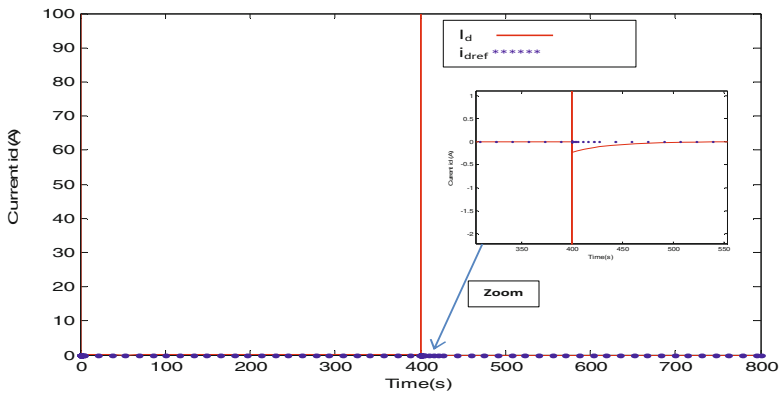
Fig. 10 Current Motor id
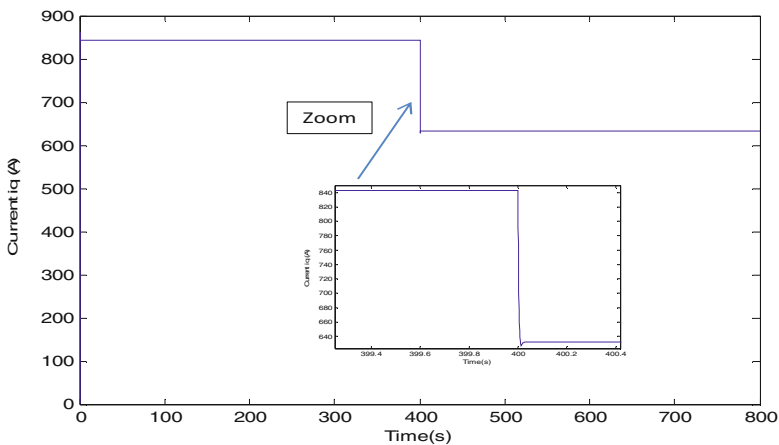
Fig. 11 Current Motor iq

The performances of the proposed strategy control law are depicted in the figures 8, 9, 10 and 11. Figures 8, 9, 10, 11 respectively show the curves of the ship speed, motor speed, current id and current iq. The ship speed is needed to reach the reference speed value Vref=8m/s in the interval [0 400s] and Vref =6 m/s in the interval [400 800s]. It appears from the curves figure 8 that the proposed control law allows a rapid convergence towards the component of the ship speed.

Furthermore, if we impose idref=0, then the electromagnetic torque becomes proportional to component of statoric current iq. In order to control the motor speed, on acts the statoric current component iq, on the developed torque by controlling the voltage component vq.

The figure 9 shows the behavior of the motor speed. It's clear that the motor speed changes where the variation of the propeller speed changes.

8   Conclusion

We proposed in this paper a nonlinear model of an electric propulsion system of a ship; the same model was linearized around a nominal operating point for the syntheses of a state feedback control for proper condition ensure the closed loop control. This control approach is mounted efficient in ensuring a good continuation of the stator current and rotor speed of the propulsion motor.

Numerical simulation results of the control approach, applied to the electric propulsion system, have demonstrated the effectiveness of this approach for further reference the speed of the stator current of the drive motor.

References

Chiasson, J.: A new approchoach to dynamic feedback linearization control of an-induction motor. IEEE Transactions an Automatic Control 43, 391–397 (1998)

Snitchler, G., Gambe, B.B., Ige, K.S.: The stats of HTS ship propulsio-motor developments. IEEE Transaction on Applied Superconductivity (2006)

Fossen, T.I.: Guidance and Control of Ocean vehicule. University of Trondhein, Norway (2000)

Rotella, F.: Commande des systèmes linéaires à plusieurs entrées, Ecole Nationale d'ingénieurs de Tarbes

Xhuvani, "Modélisation et identification des paramètres d'une machine synchrone destinée à être alimentée par un convertisseur statique", Thèse de doctorat, Institut National Polytechnique de Toulouse (1989)

Jebsen, G.: Podded Propulsion for Naval Warships, 'An Office of Naval Research Perspective Presented at the Podded Drives Industry Day (January 17, 2002)

Kalsi, S., Karon, S.: Compact Light Weight Ship Propulsion Motors. Presented at the Ship Propulsion Systems Conference, London, UK, October 21-22 (2002)

K.: boudriga, H. dallagi, B. Sabri, Estimation et optimisation de la résistance totale d'une carène et de la puissance propulsive des navires. In: 4th International Congress Conception Design and Modeling of Mechanical Systems (CMSM 2011) (2011)

Habib, D.: Fault Detection of Nonlinear Systems using Multi-Model Struture: Application to a Ship Propulsion System, 5th International Congress Conception Design and Modeling of Mechanical Systems (CMSM 2013) (2013)

The Design of Control Boost Air Temperature System on Marine Diesel Engine Based on Trials Curves

Bechir Sabri and Habib Dallagi

Automatique et Robotique Marine (ARM), Naval Academy,
Menzel Bourguiba, BP 7050, Tunisia
`bechir.sabri@yahoo.fr, habib.dallagi@ept.rnu.tn`

Abstract. The air boost temperature cause a change in the specific fuel oil consumption, the exhaust gas amount and gas temperature and (NOx) emissions of the diesel engine. Controlling emissions is becoming a more and more important task in the development of diesel engines. Today the International Maritime Organization (IMO) is close to completing regulations prescribing the upper limits for nitrogen oxides (NOx) emissions from engines running on ships. The charge air temperature is not constant but varies with the engine load. For the execution of this work we have taken as a model a marine diesel engine type Wartsila NSD 12 ZAV 40S installed a board car ferry. Engine manufacturers provide charts on relationships gas flow, power etc experiments on a dynamometers bench and some Trials aboard. This work is based on data curves and trials for modeling of the control system. The paper is divided into three parts

- · Relationship between the different parameters
- · Design of the control loop
- · Verify the   controller design through simulation

Keywords: Marine diesel engine, cooling system, simulation, modelling.

1   Introduction

The main aim of the approach is to predict the boost air temperature to optimising the efficiency of the engine. Air pressurized by turbochargers increases temperature which negatively effects engine durability, performance and emissions. After-cooling, inter-cooling or charge air cooling are interchangeable terms describing the system responsible for removing excess heat from the air charging the cylinders. Charge air cooling is an important technology for reducing N0x emission which also has a number of other benefits. Fuel economy, power output and the maximum injection rates an engine can sustain are improved through charge air cooling. The main aim of the approach is to predict and achieve the control of boost air temperature.

NB: The normal engine operation and between 60% and 100% of the rated power P_n and the study is conducted on this basis.

2   Air as a Function of the Power

2.1   Relationship Engine Power and Boost Air Temperature

The figure 1 showed the relationship between inlet cooling water temperature, engine power and boost air temperature done by the engine manufacture. The cooling water temperature is a constant which equals 32°C.
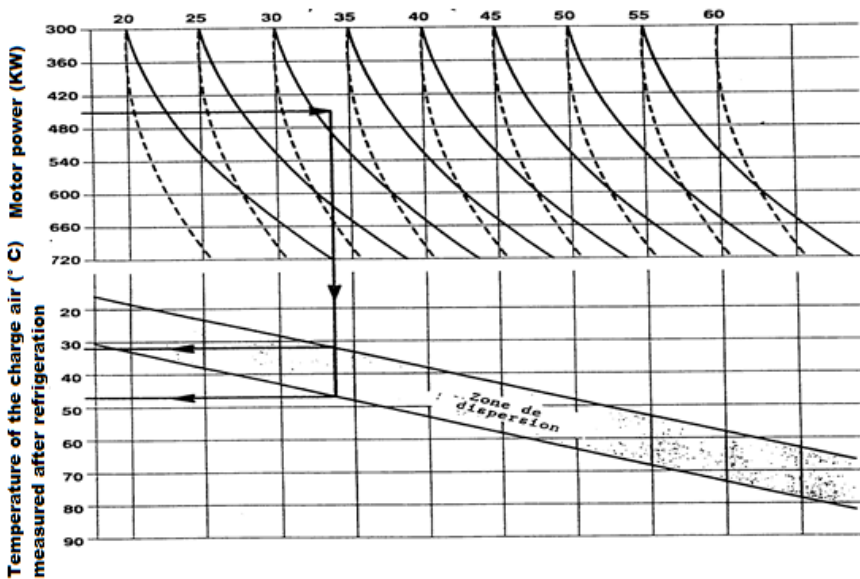
Fig. 1 Curves provide by engine manufacture (relationship engine power and boost air temperature)

The set temperature from figure 1:

$$T_S = 13 \ 10^{-4} \ (\% P_n)^2 - 219 \ 10^{-4} \ \% P_n + 39,11 \qquad (1)$$

Where T_S is the set point boost air temperature in °C and P_n is the nominal engine power (8200 Kw) and $\% P_n$ the percentage of rated power without unity.

2.2 Fuel Setting and Power

The characteristic function of the variation of power as a function of the fuel setting according to the Engine Performance curves can be expressed by the following equation (figure 13 annex).

$$\%P_n = 12.5.C_r - 15 \qquad (2)$$

Where Cr the fuel setting (0 to10)

3 A Relationship between the Various Operating Parameters

3.1 The Turbocharger

We recall that all formulas are applicable to the normal operation of the engine between 60% and 100%. Engine room temperature: 25°C

The turbocharger is characterized by a series of curves compressor air pressure, speed and flow. The following equations give the relationships between the different parameters of the system (from figure 13 and 15 annex).

- **Relation Turbocharger speed and volume flow**

$$V_{TC} = -1.79\left(\%\,P_n\right)^2 + 389.37\left(\%\,P_n\right) + 788.31 \qquad (3)$$

- **Air flow**

$$Q_{vair} = 1.4323(V_{TC}) - 10842 \qquad (4)$$

$$Q_{vair} = -2.56(\%P_n)^2 + 557.70(\%P_n) - 10055.67 \qquad (5)$$

- **Air temperature**

$$T_{aTC} = 210^{-7}V_{TC}^2 + 6.210^{-3}V_{TC} - 60.22 \qquad (6)$$

$$T = 10^{-7}6.41(\%P_n)^4 - 10^{-4}2.79(\%P_n)^3 + 10^{-3}18.94(\%P_n)^2 + 2.54(\%P_n) - 57.56 \qquad (7)$$

Where V_{TC}: the turbocharger speed in rev/min, Q_{vair}: volume air flow rate in m³/h, T_{air}: the boost air temperature in °C.

3.2   The Cooling Water

- **Regulating Valve**

Valve stroke 100 mm
Flow from 0 to 100 m³/h
Relationship stroke Vs flow
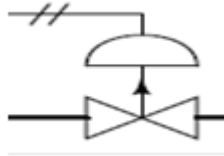
Fig. 2 Aautomatic valve

$$Q_{cw\,f} = 34.51\,LnV_{s} - 60.23 \tag{8}$$

Where Q_{cwf}: Low water temperature flow and V_s: Valve stroke in mm

- **Valve Command**

$$V_{s} = 6.25\,I_{v} - 25 \tag{9}$$

Where I_V: the valve control current ($I_v = I_c$)

- **The air cooler**

By varying different parameters, flow air and water at different engine powers.
Manual valve stroke 100 mm
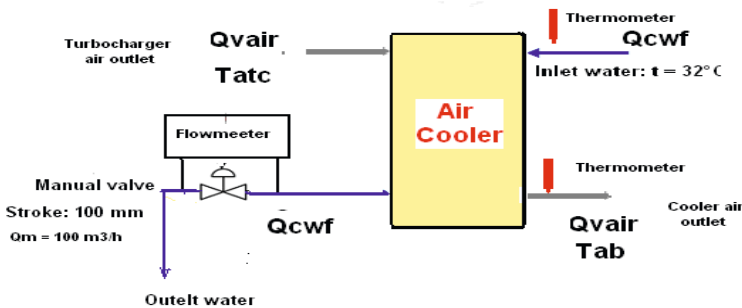
Fig. 3 Experience to determine the relationship of the various parameters of the heat exchanger

$$T_{ab} = -0.6 Q_{cwf} + ((T_{aTC} - 100)/2) + 63 \qquad (10)$$

Where $\mathbf{T_{ab}}$ the cooler outlet air temperature and $\mathbf{T_{aTC}}$ the cooler inlet air temperature   and $\mathbf{Q_w}$ the flow cooling water.

3.3   Temperature Transmitter

$$I_{as} = 0.16 T_{ab} + 4 \qquad\qquad (11)$$

4   The Controller

After several tests we chose the prametre of the PI controller. The PI controller can get the desired value of the parameter quickly and can hold the position with great accuracy.

   By choosing the proper constants for the controller (Tuning the PI), we can have a better control fig 4.
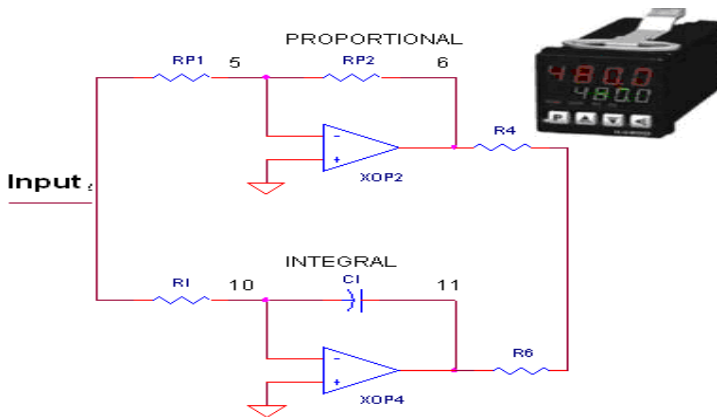
Fig. 4 The PI controller

5   Simulation

5.1   Figure Block

Acting on the lever fuel setting, the power varies; an electric signal according to T_s is the input controller figure 5. The controller is responsible for developing order according to away T_s / T_{ab}. The organ setting responsible to act on the method is a valve to regulate the water flow throw the air cooler;

Fig. 5 Block diagram of the control loop

5.2   *The Loop*

Each block presented in Figure 6 is a discretization of the main supplies and mathematical formulation has been used to develop the model.

Fig. 6 Model developed using MATLAB/Simulink

5.3   Numerical Simulation

The first simulation figure 7 improve the function (Variation of the output air temperature in the Turbocharger, T_{aTC} as a function of the power   according the power just for making sure that the model is working, figure 8 the air temperature set point according to the engine power   to verify the manufacturer's data figure 1.

In figure 9 we see the difference between temperatures T_s and T_{ab} for a given position of cooling water flow control valve without controller, figure 10 the variation of air temperature without controller in case of disturbance.
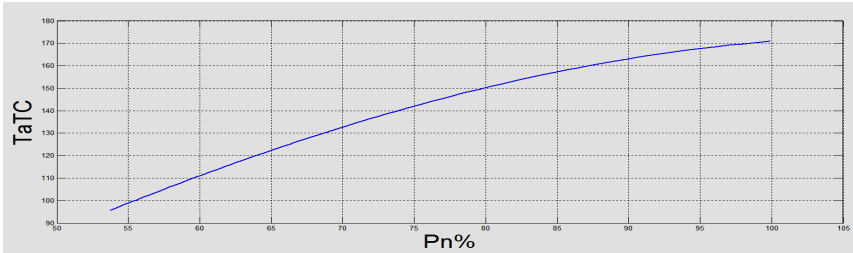
Fig. 7 Variation of the air temperature in the Turbocharger output as a function of the power
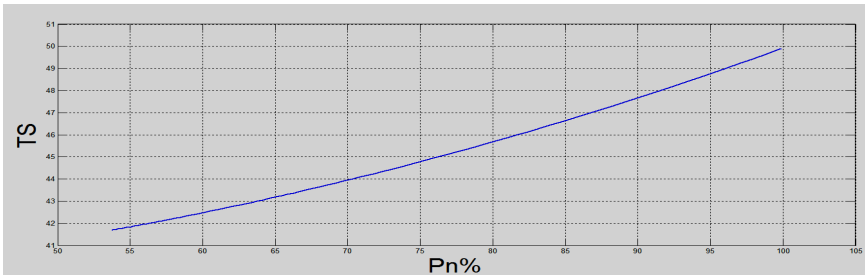
Fig. 8 Relationship power and boost air temperature
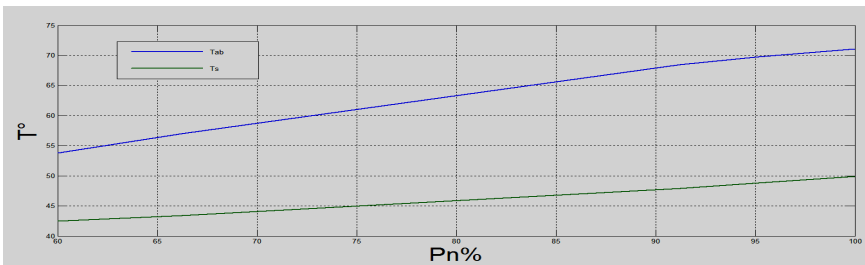
Fig. 9 Variation of air temperature without controller
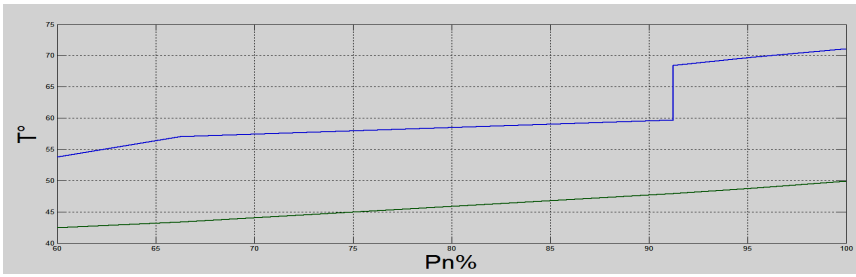
Fig. 10 Variation of boost air temperature without controller with disturbance
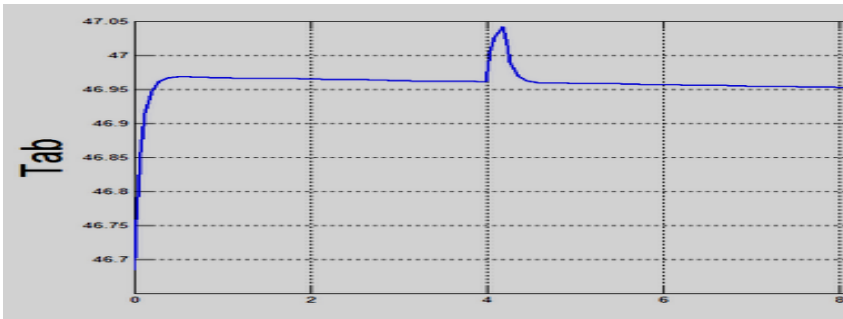
Fig. 11 Response of the system when suddenly disturbance with constant load $P_{n\%} = 85$
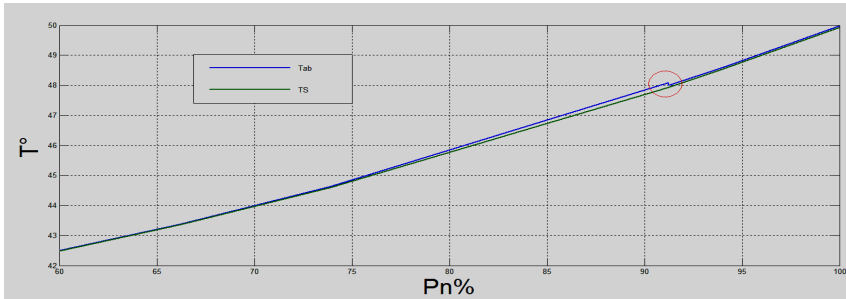
Fig. 12 Response of the system when suddenly disturbance with load variation

The figure 11 show that in the case where the engine is at steady state, a change in the temperature of the supercharging air for example due to clogging of the air cooler, the controller PI is responsive adjusts the temperature of the system to a value adequate. The figure 12 shows the responses of the system to a disturbance in the increasing pace at instant 4 seconds and the response of the system.

6   Conclusion

To obtain a correct supply of air for the main engine's combustion process, for the power, economy and emission of the marine diesel engine owner gives the relationship between the power and the inlet air temperature of the engine. The design of a control system capable of adjusting the boost air temperature of the engine 12 WARTSILA ZAV S 40 by controlling a valve mounted on the air cooling system.

Based on the performance curves provided by the manufacturers for the modelling of the system we took the data on test benches manufacturers on the one hand and on the other, based on tests on board, we implemented a control closed loop to follow the reference value of air boost temperature. We visualized our system by MATLAB SIMULINK tool.   By varying the fuel setting then the power output, the temperature set point changes and the response reach it and the system adjusts any disturbance like the cooler fooling. The optimization procedure provides the optimum air temperature in use and after several tests we conclude that the PI controller is best configuration. Finally we can use the system developed in this paper for the setting temperatures of the charge air with high precision.

References

Journal article

Peili, H.W., Jundong, Z.: Modelling and Simulation of Working Process of Marine Diesel Engine with a Comprehensive Method. International Journal of Computer Information Systems and Industrial Management Applications 5, 480–487 (2013) ISSN 2150-7988

Rakopoulos, C.D., et al.: Analysis of combustion and pollutants formation in a direct injection diesel engine using a multi-zone model, pp. 63-88 (1995)

Hountalas, D.T.: Prediction of marine diesel engine performance under fault conditions. Applied Thermal Engineering 20, 1753–1783 (2000)

Bechir, S.: Optimization of the Combustion in Large Marine Diesel Engine by controlling the exhaust gas. Springer (2013)

References Books

Engine Wartsila 12ZA 40S NSD (Technical Documents)
ABB Turbocharger Technical Documents
Test bench diesel Engine Wartsila 12ZA40S
Pt100 Spirax Sarco EL2270 AND EL 2271 Temperature probes
MEIRI 520 – PT100 et PT1000 pour Automatics valves fisher documentations
CLA - VAL FLUID Handling Solutions: Automatic Control Valves

Dissertation

Champoussin, J.C., Liazid, A.: Turbocharged diesel engine transient behaviour by know-
    ledge model. In: Younes, M.M.R.: LMT, Ecole Centrale de Lyon SIA N° 93051
Mosleh, M.: A simplified model of turbocharged marine power plant: Engine Wartsila
    12ZA 40S NSD (Technical Documents) (March 2003)
Test bench diesel Engine Wartsila 12ZA40S, Pt100 Spirax Sarco EL2270 and EL 2271
    Temperature probes, MEIRI 520 – PT100

Annex

Fig. 13 12 ZAV 40 S Engine Performance curves
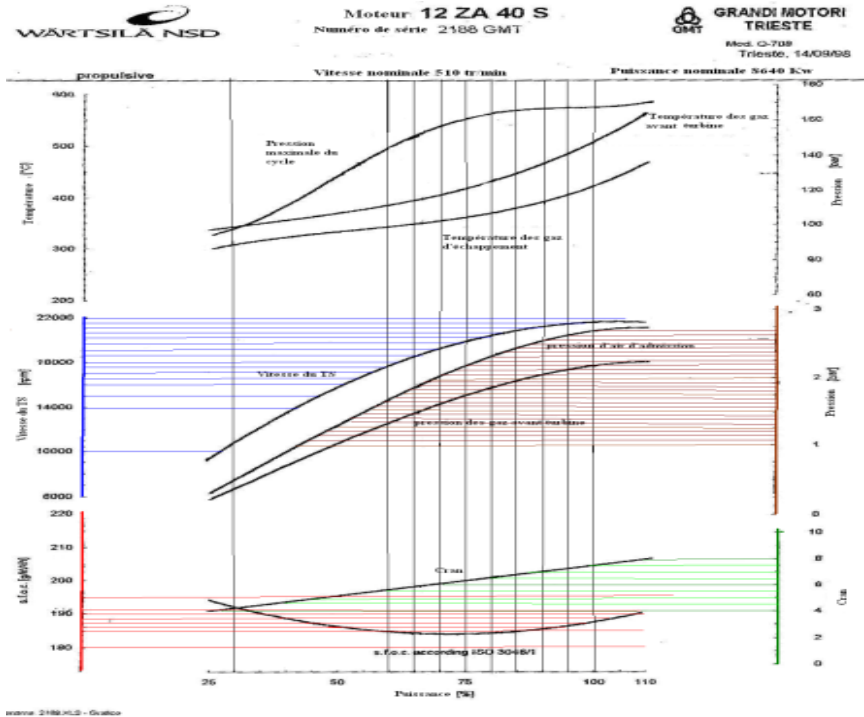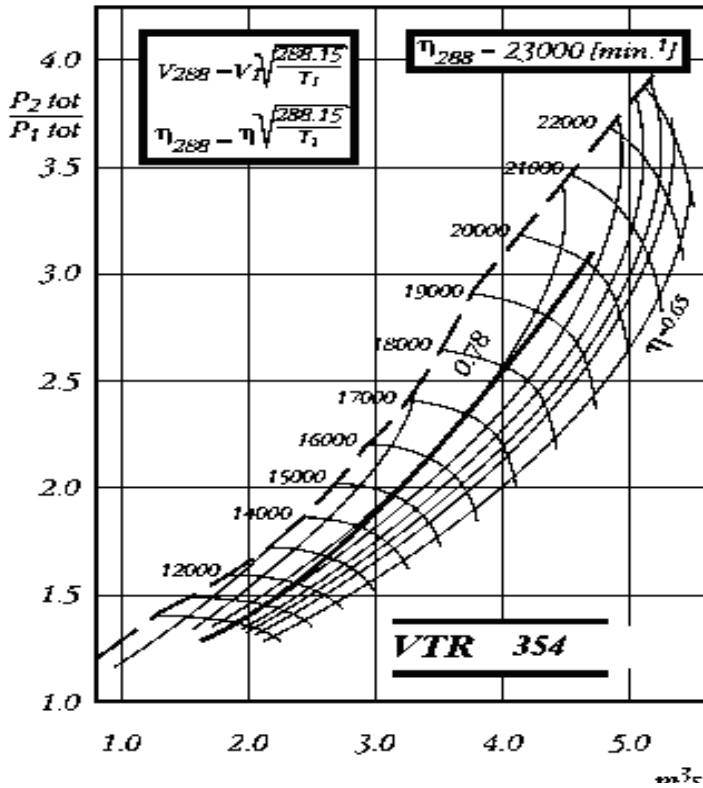
Fig. 14 VTR 354 Turbocharger
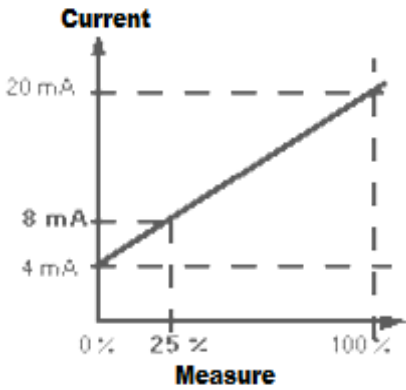
Fig. 15 Valve Stroke/ current
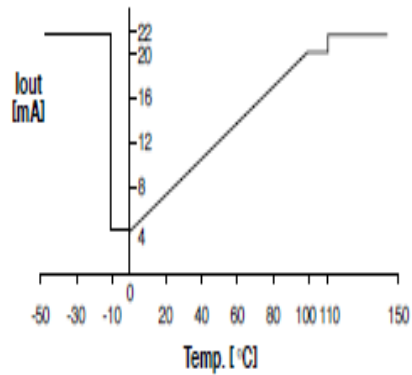
Fig. 16 Temperature transmitter From Del

The Effect of Fuel Additives on Spark Ignition, and Their Implications on Engine Performance: An Experimental Study

Nabil M. Muhaisen[1] and Rajab Abdullah Hokoma[2]

[1] Mechanical & Industrial Engineering Department,
   Faculty of Engineering, University of Tripoli, Libya
   `rhokoma@me.uot.edu.ly`
[2] Mechanical Engineering Department,
   High Institute for Engineering Science, Zliten, Libya
   `n_m203@yahoo.com`

Abstract. This paper is designed to present an experimental study being recently conducted for investigating the effect of some fuel additives on the performance of spark ignition within a benzene engine. Three types of additives were added separately (Gasoline Additive, Gasoline Booster, and Octane Booster) to pure gasoline with a volumetric ratio 1:6, 1:7, and 1:8 respectively. Four separate laboratory experiments being conducted using an internal combustion engine at rotational speed ranges from 600 to 3000 rpm, where the three mixtures and the pure gasoline itself were used.

   The findings showed that there was a positive effect on the engine performance as the brake power increases by 8%, 13% and 23% at the use of Gasoline Additive, Gasoline Booster, and Octane Booster respectively as compared with using only the pure gasoline. The brake thermal efficiency (η_{th}) was also affected positively showing its maximum value of about 8% for Octane Booster, and with a minimum value for using Gasoline Additive at about 4.7%. In addition, this study showed that the value changes in the brake specific fuel consumption for Gasoline Additive, Gasoline Booster, and Octane Booster was at the levels of 1%, 2%, and 5% respectively compared with using only the pure gasoline. Furthermore, the results also showed that the use of Octane Booster gave the highest level of air fuel ratio.

Keywords: Additives, Ignition, Performance, Spark.

1   Introduction

The assessment of performance levels of any engine depends on some key factors; among of them is to focus on the performance of brake power, brake specific fuel consumption, brake thermal efficiency, air to fuel ratio, engine speed, and the emission issues [1]. Most importantly is the type of the used fuel, which is considered to be one of the most important indicators that affect the engines' performance especially the combustion engines [2].

With the aim of improving the quality of the fuel in order to obtain its best performance levels, it must be a focus on the improvements of the Octane number which can be improved by Catalytic reforming, Isomerization, Alkylation, Cracking, and adding especial additives. The most important materials that could be added to the gasoline are organic compounds (organometallic) such as Tetra Methyl Lead or Tetra Methyl Lead, where both of them should be added by a certain percentage levels based on the Octane issues within the pure gasoline [2].

Many research have been conducted on the effect of the additives to the gasoline on performance of the engines' spark [3]-[7], stating that using additives improves the Octane number, thereby the engine performance positively affected. In this research, the focus is on investigating three commercial additives that available within the local market to show their effects on the pure gasoline based on the improvements on the engine performance and on any other related issues. The additives were added separately to the pure gasoline (collected directly from the refinery) in order to investigate the impact of these additives on the engine's performance based on the engine power, and the engine's thermal efficiency, the specific fuel consumption, and the ratio of fuel to air.

2   Experimental Study

Laboratory experiments for this study took place using an internal combustion engine model GR03061000/037A with a single-cylinder four-stroke, along with a compression ratio and spark timing. The engine was hitched to a hydraulic dynamometer fixed on a steel frame and linked to cooling, fuel systems. A dashboard includes gauges speed spin, plucks and inside and outside cooling water, compression ratio indicator and the pressure difference on both sides of intake air nozzle. In addition, Table 1 shows the related characteristics of the used engine [7].

Table 1 The specifications of the used engine

Engine Model	An internal combustion engine
Number Of Strokes	Four-Stroke
Number Of Cylinders	Single-cylinder
Diameter Of Piston	90 mm
Length Of Stroke	85 mm
Swept volume	541 mm^3
Compression Ratio	4.175
Cooling System	cooling water
Type Of dynamometer	Hydraulic

3 Samples Preparation

In order to achieve the main goal of this research, four different samples were laboratory prepared; the first was pure gasoline, where its specifications are shown in Table 2 [9].

Table 2 The pure gasoline specifications

Octane number	89
The composition	Aromatic of hydrocarbons
The beginning of the boiling degree	$176 \ C^0$
The degree of the end of the boiling	$36 \ C^0$
Vapor pressure	psi8
Specific Gravity	0.7531

The second sample was a mixture of fuel gasoline and Gasoline Booster by volumetric ratio of 1:7. The third one was a mixture of gasoline and Octane Booster at 1:8, whereas the last one was a mixture of gasoline and pure Gasoline additive by 1:6.

4 Experimental Testing and Investigations

The experimental part of this research included set of operations covering the four samples being previously prepared. As a starting point, the engine was started up and gradually increasing the speed, leaving a period of time for stability and warming up (15-20 minutes). At this time determinations of the engine's performance took place while the engine's speed ranges between 600-3000 rpm.

Table 3 Illustrates al the used symbols throughout the experimental study

Term	Symbol	Unit
Air fuel ratio	A/F	----
Brake specific fuel consumption	Bsfc	g/kw.hr
Volumetric flow rate of fuel	Qf	m^3/s
Calorific value of the fuel	QHV	KJ/kg
Mass flow rate of air	m°_a	Kg/sec
Mass flow rate of fuel	m°_f	Kg/sec
Rotating speed	N	rpm
Brake power	W_b	KW
Swept volume	v_d	m^3
Air density	ρ_a	Kg/m^3
Fuel density	ρ_f	Kg/m^3
Brake thermal efficiency	η_{bth}	%
Brake torque	T	N.m

This determination took place throughout a fixed compression ratio and using mixing fixed and fully open throttle valve using the four samples being prepared previously. This determination includes readings from the dashboard such as N (rpm), rotational speed, torque (N.m), total flow rate of the fuel, pressure drop at the clouds, and the inlet and outlet temperatures of the engine. The symbols related to the experimental study and calculations are illustrated in Table 3 [8], whereas key findings are shown in Tables 4-6.

Table 4 Value changes of t, m°a, m°f using sample I

m°f	m°a	T	N
10.48	92.2	4.7	600
147.7	1477	5.7	1000
195.5	2209.15	6.3	1500
277	3371.1	7.16	2000
482.9	6760.6	7.64	2500
652.5	10505.25	9.2	3000

Table 5 Value changes of t, m°a, m°f using sample II

m°f	m°a	T	N
136.2	1525.4	6.6	600
212.5	2635	6.9	1000
223.1	2833.37	7.4	1500
276.24	3563.5	7.8	2000
402.3	5712.6	8.1	2500
618.8	10210.2	8.72	3000

Table 6 Value changes of t, m°a, m°f using sample III

m°f	m°a	T	N
133.17	1438.2	6.6	600
148.75	1698.7	6.77	1000
209	2581.15	7.3	1500
283	3775.2	8.1	2000
481.6	6886.8	8.56	2500
628.6	9919.3	9.8	3000

Table 7 Value changes of t, m°a, m°f using sample IV

m°f	m°a	T	N
133.17	1438.2	6.6	600
148.75	1698.7	6.77	1000
209	2581.15	7.3	1500
283	3775.2	8.1	2000
481.6	6886.8	8.56	2500
628.6	9919.3	9.8	3000

5   Calculations of Parameters [10]-[14]

Brake power calculated as: $W_b = \dfrac{2\pi NT}{60000}$

The mass flow of fuel being calculated as: $m°_f = P_f * Q_f$

Consumption qualitative expanding brake fuel being found as: Bsfc $= 3.6 \ \dfrac{m°_f}{w_b}$

Brake thermal efficiency as: $_{th} = \dfrac{w_b}{m°_f \, Q_{HV} \, c}$, where c equals to 97%

Ratio of air to fuel calculated as: $A\big/_F = \dfrac{m°_a}{m°_f}$

6   Results and Discussing

Using the previous equations, the related performance indicators were calculated as shown in Tables 8-11. Each Table shows the performance indicators being calculated from each four samples (mentioned before).

Table 8 Values of WB, BSFC, ηTH throughout engine's speed changes using sample I

A/F	η$_{th}$	Bsfc	W$_b$	N
8.8	7.55	1116	0.34	600
10	9.44	886.3	0.6	1000
11.3	11.42	730.8	1	1500
12.17	11.6	718	1.3	2000
14	12.3	760	2.2	2500
16.1	12.8	810	2.9	3000

Table 9 Values of Wb, BsFc, η_th throughout engine's speed changes using sample II

A/F	η_{th}	Bsfc	W_b	N
11.2	7.6	1089.6	0.41	600
12.4	9.9	850	0.63	1000
12.7	12.14	730.2	1.1	1500
12.9	12.18	710	1.41	2000
14.2	12.6	763	2.3	2500
16.5	12.8	790	3	3000

Table 10 Values of Wb, BsFc, η_th throughout engine's speed changes using sample III

A/F	η_{th}	Bsfc	W_b	N
10.8	7.9	1088.2	0.45	600
11.42	10.2	840	0.68	1000
12.35	12.26	684	1.3	1500
13.34	12.3	703	1.5	2000
14.3	12.8	744	2.5	2500
15.78	13	730	3.2	3000

Table 11 Values of Wb, BsFc, η_th throughout engine's speed changes using sample IV

A/F	η_{th}	Bsfc	W_b	N
8.8	8.2	1059.8	0.5	600
10	10.6	810.4	0.8	1000
11.3	12.46	690	1.4	1500
12.17	12.6	680	1.7	2000
14	13	624	2.8	2500
16.1	13.4	683	3.4	3000

The findings from the previous four tables are illustrated on Fig. 1, showing the relations between the calculated brake powers with the rotating speed throughout the use of the four samples. The figure pointed out that the brake power was positively increased by using the three additives compared with using only the pure gasoline at rotational speed of 2000 rpm, whereas the highest level of these values
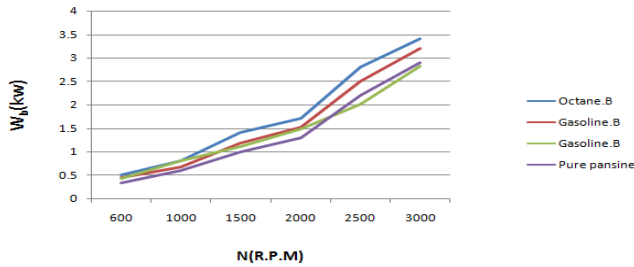
Fig. 1 Relationship between the brake powers with the rotational speed

was at 23% for the Octane booster mixed with the pure gasoline, founded as W_b for Octane Booster minus W_b for pure gasoline divided by W_b for Octane Booster.

The brake thermal efficiency was also calculated throughout using the three mixtures along with the use of only the pure gasoline at rotational speed of 2000 rpm. The improvement could be clearly seen on Fig. 2, showing that using the Octane booster gives the highest brake thermal efficiency value stands at   about 8%, whereas the gasoline additives stands at only   at 4.7% (calculated similar to the previous one).
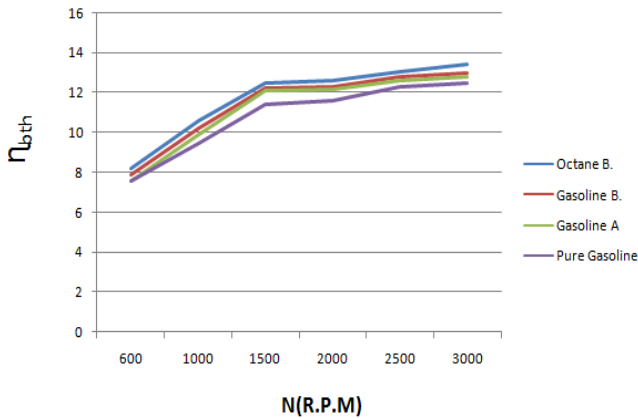
Fig. 2 The relationship of brake thermal efficiency with the rotational speed

The fuel saving that can be reached as seen on Fig. 3, showing that the Octane booster provides saving of about 5% compared with using the pure gasoline itself at rotational speed of 2000 rpm without using any additives.
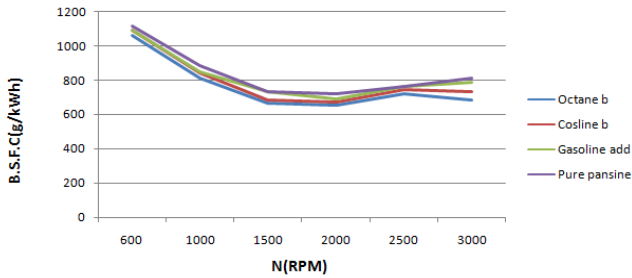
Fig. 3 The relationship between brake specific fuel consumption with the rotational speed

7   Conclusions

The paper has presented an investigation of using three different types of fuel additives that being separately added to the pure gasoline. These three different mixtures along with the pure gasoline itself have been used separately for the internal combustion engine model GR03061000/037A. Different rotational speeds being applied throughout all the four stages of the experimental work. The key findings can be summarized as follows:

- The brake power increased while using the three additives; in particular the Octane booster gave the highest level for about 23%, whereas the other two provides 12.6% and 18% respectively.
- The increase in the brake thermal efficiency pointed to its highest level by using the Octane booster with about 8%, whereas the lower result was seen while using the Gasoline additive of about 4.7% compared with the pure fuel.
- A significant improvement in the brake specific fuel consumption was found in its highest level (5%) by using Octane booster, whereas while using the Gasoline additive, the brake specific fuel consumption stands at only 1 % compared with using the pure gasoline.

References

[1] Alvydas, Saugirdas, Juozas: Influence of combustion of Gasoline-Ethanol Blends on parameters of Internal combustion engine. Journal of Koues Internal Combustion Engines 10, 3–4 (2003)
[2] Al-Omari, M.: Oil and petroleum industry, 1st part, Al-Qura University College of Applied Sciences (2002)
[3] Goodger, Hydrocarbon Fuels, Production, Properties and Performa of Liquids and Gases (1973)
[4] Jaseem, R.R.: An Experimental Investigation of the Effect of Enhancement on Spark Ignition Engine Performance. Kirkuk University Journal of Scientific Studies 6(2) (2011)

 [5] Abdulghani: Fuel consumption of a spark ignition engine blended with MTBE. In: The 6th Saudi Engineering Conference, Kfupm, phahran, vol. 5 (2002)
 [6] Tangamells, Linauish: Methanol as motor fuel or Gasoline Blending component, S.A.E, No. 750123 (1975)
 [7] Yusaf, Buttsworth, Najafi: Theoretical and experimental investigation of SI engine performance and exhaust emissions using ethanol-gasoline blended fuels. In: 3rd International Conference on Energy and Environment, ICEE 2009, pp. 195–201 (2009)
 [8] Instruction Manual, Variable compression Engine 'VARICOMP' Dual Diesel/petrol cycle with Dynamometric Test unit (2003)
 [9] Instruction Manual of the oil refining, pure gasoline specifications at Alzawia Company
[10] Mathur, Sharma: Internal combustion engine, 1st edn., pp. 62–80 (1984)
[11] Muhaisen, N., Hokoma, R.: Calculating the Efficiency of Steam Boilers Based on Its Most Effecting Factors: A Case Study. International Journal of Engineering and Applied Sciences 6 (2012)
[12] Muhaisen, N., Hokoma, R., Alshogi: Potential Saving For Steam Boilers Based on the Impact of Most Affecting Factors: A Case Study. In: Proceedings of the 2014 International Conference on Industrial Engineering and Operations Management, Bali, Indonesia (2014)
[13] Pulkrabek, W.: Eng. Fundamentals of the Internal Combustion Engine, 1st edn. (1997)
[14] Kirit, Muhesh: Performance and emission of natural gas fueled internal combustion engine. Journal of Scientific & Industrial Research 64, 333–338 (2005)

New Multiaxial Fatigue Limit Criterion for Defective Material: 1045 Steel

Hassine Wannes[1], Anouar Nasr[2], and Chokri Bouraoui[3]

[1] LGM, université de Monastir ENIM, Avenue Ibn Eljazzar, Monastir 5019
 `hassine.wannes@gmail.com`
[2] LGM, EPEIM, Avenue Ibn Eljazzar, Monastir 5019
 `anouar.nasr@hotmail.fr`
[3] LGM, université de Monastir ENIM, Avenue Ibn Eljazzar, Monastir 50190
 `chokri.bouraoui@enim.rnu.tn`

Abstract. The aim of this paper is to present a fatigue life criterion for defective material. Defects are simplified to spherical or elliptical pore at surface of specimen under cyclic loading. The Finite Element method was used to determine stress distribution around defect for different morphology and loading modes. It is that shown a relevant mechanical parameter governing the fatigue limit for defective material could be the affected depth, which is the depth from the tip of defect to the bulk of sample where Crossland criterion was violated. A multiaxial fatigue criterion for defective material is proposed and validated for different metallic materials and loading conditions.The proposed criterion was able to take into account the defect size, shape of defect and loading mode. Results are good and show that the affected depth is a good parameter to characterize the influence of a defect on the fatigue behaviour.

Keywords: Multiaxial high cycle fatigue, Defects, Affected depth, Kitagawa diagram.

1   Introduction

The fatigue limit of components containing inherent defect is of great importance for the industrial application and always depends on defect morphology and the loading mode. The designer needs to compromise between the fatigue resistance of the component and the allowable defect size due to the process. Consequently, the influence of the defect behaviour must be characterized to correlate the fatigue limit into size of defects. The objective of this paper is to study the stress gradient around defect and correlate fatigue limit of defective material with defect size.

Several ways are explored and different authors have proposed fatigue limit calculations based on the size of defect. Murakami [1] proposed an interesting approch based on experimental results. A geometrical parameter, $\sqrt{area}$, which is the square root of the projected area of defect on the plane perpendicular to the direction of the maximal principal stress, is used to model the defect size.

This approch suggests a practical relationship between the fatigue limit, hardness and this parameter of size. Endo [2] has extended Murakami's criterion to proportional biaxial loading. According to this criterion, the ratio between torsion and tension limits which is supposed constant whatever the size of the defect.

Using numerical tools other approaches have been proposed as The CDM (Critical Distance Method) criterion which is based on measurement of a criterion at a given distance from the surface of defect [3]. The last criterion leads to very good results in the case of small defects as shown by Leopold and Nadot [4].

Recently, Nadot and Billaudeau [5] have proposed an approch to determine the influence of defect size and geometry on fatigue behaviour .They use the gradient of the maximal hydrostatic stress, which was taken into account to propose the HCF criterion for defective material.

In the present paper we propose a new approch to correlate fatigue limit to defect size. Cracks initiate always at the tip of defect [6]. The variation of Crossland stress equivalent was studied along the axis starting from the tip of defect to the bulk. A definition of affected depth was given, which is the depth from the tip of defect to the bulk of sample where Crossland criterion was violated. The evolution of the affected depth, with load and defect size, allows us to determine fatigue limit for defective material. This approach has been applied for two materials under different loading conditions with different defect morphology. The obtained results are very coherent and treat well the problem of small defects in fully reversed tension and torsion. For elliptical pore, longitudinal or transverse ellipsoidal defects, simulation gives fair results (3% difference).

2   Simulation of Stress Gradient around Defect

2.1   FE Analysis

This study was carried on the 1045 steel and a cast aluminum alloy AS7G06-T6. Experimental databases containing Multiaxial fatigue results with induced defects have been previously published [6, 7]. Defects are always the preferential sites for crack initiation. So we need to characterise the stress distribution around the defect. Finite Element simulations have been conducted for each defect size under different loading mode. Considering the symmetry of the problem (geometry and loading), only one fourth parallelepiped is considered for the FE simulation Fig.1. The FE simulation is performed considering the material isotropic linear elastic. A tetrahedral mesh with a refinement close to defect is used as illustrated in Fig.4.The FE simulations are performed with ABAQUS® software.
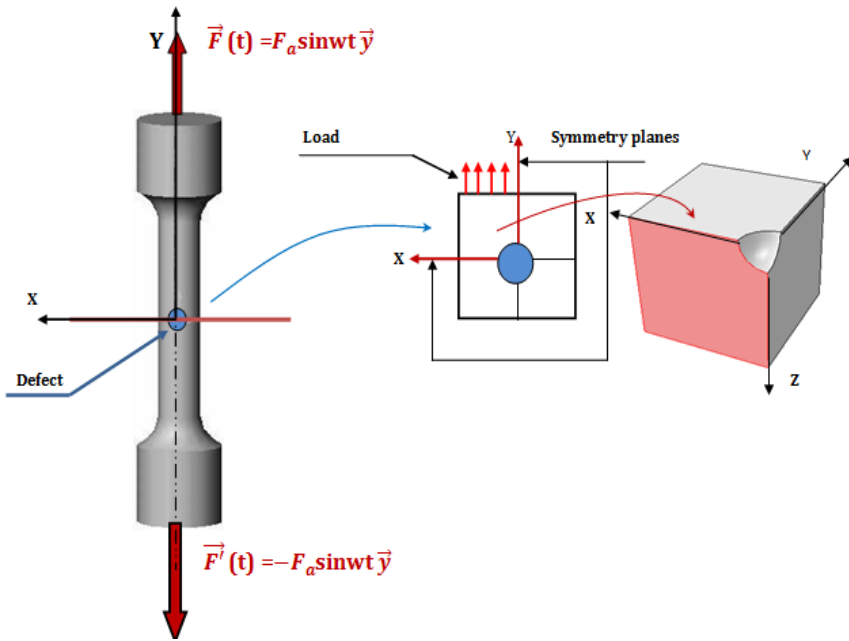
Fig. 1 Completed model and simplified model

2.2   FE Simulation

Based on FE calculation, it is observed that the plane perpendicular to maximum stress direction is the Highest Loaded Plane (HLP) Fig.2. In other hand experimental works provides that the crack initiated always at the tip of the defect in the maximum shear plane [6]. And the macroscopic crack that leads to failure of the sample propagates in HLP. Consequently we will be interested in the distribution of stress along axis Z starting from the tip of defect to the bulk (Fig.4).

For three defect sizes, that describe the defect size range, at fatigue limit load we plot Crossland equivalent stress σ_{cr} versus coordinate along axis Z from the tip of defect (A) to the bulk Fig.4.

Interpretation

(i) At fatigue limit, for the three defect sizes, the curves cross a pivot point H. This remark we'll be a starting point for our study.

(ii) Close to the tip of defect the crossland criterion was violated but not violated along far. Consequently we are lead to introduce the following definition:

Affected Depth

The affected depth by the gradient of stress for a given defect and an applied load is the depth from the tip of defect to the bulk where the Crossland equivalent stress is greater than or equal to **β** (Fig6)**.**

a) Tension loading   b) Torsion loading
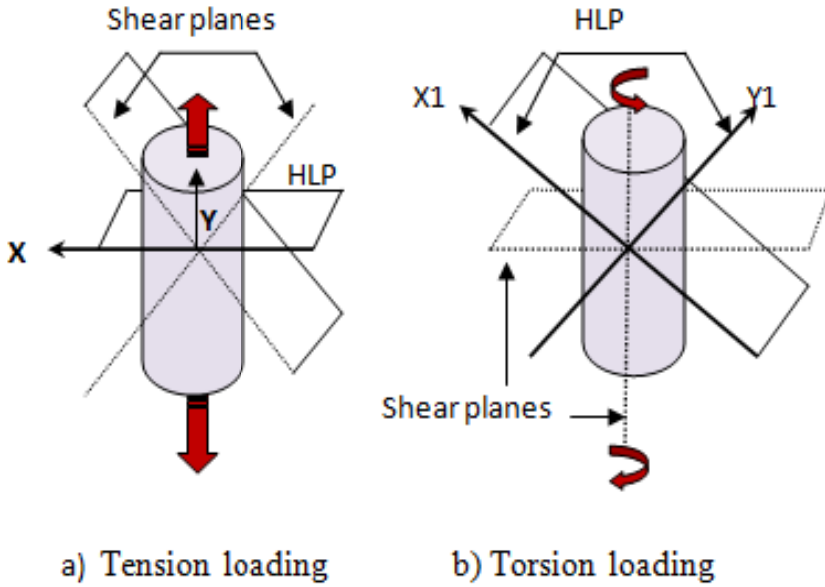
Fig. 2 Shear and Highest Load Planes: a) Tension loading b) Torsion loading
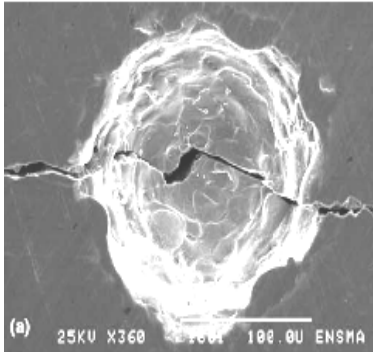
Fig. 3 Crack initiation [6]   **Fig. 4** Stress distribution around defect
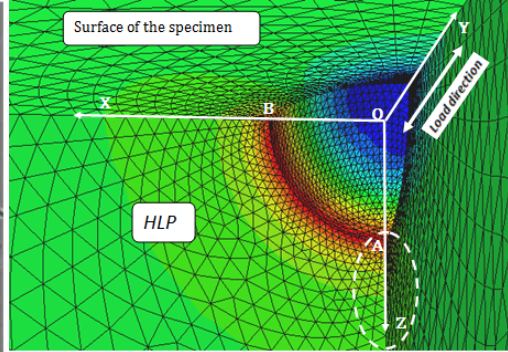
Table 1 Experimental data [6]

Defect size $\sqrt{area}$ μm	Fatigue limit on alternative tension : MPa
170	195
400	152
900	132
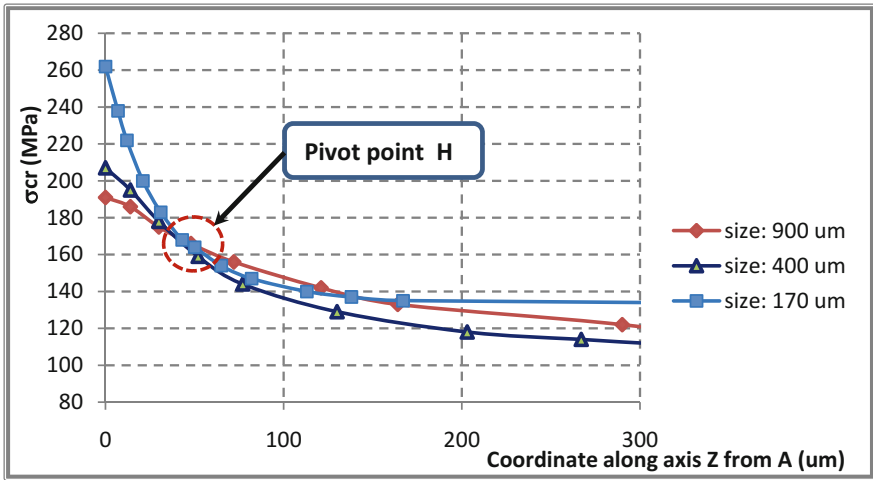
Fig. 5 Evolution of Crossland equivalent stress along axis Z for three defect sizes at fatigue limit. Tension loading
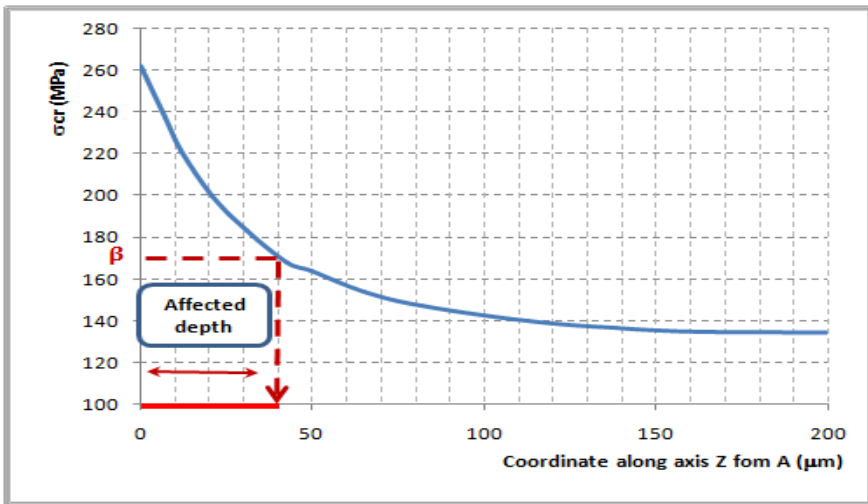
Fig. 6 Affected depth

2.3 FE Results Analysis

From results of numerical simulations, we can conclude that the affected depth at fatigue limit for each defect size is almost the same. At fatigue limit the affected depth was noted a_w . That means, for a given size, if affected depth is less than a_w there is no failure before 10^7 cycles. If affected depth is greater than a_w the sample can be broken before 10^7 cycles. Simulations are performed for two

materials: 1045 steel and cast aluminium AS7G06-T6 with two load ratio (ratio between minimum and maximum stress during one cycle loading) R_σ= -1 and 0.1.The applied load corresponds always at experimental fatigue limit for each mode loading: tension or torsion .We deduce that The parameter a_w depends only on material and load ratio R_σ.

In torsion loading, crack which leads to failure, initiates nearly on surface. The parameter a_w will be determinated on surface along X_1 axis   Fig.2

3 New Approach of High Cycle Fatigue Behaviour of Defective Material

3.1 Methodology

Our objective is to correlate fatigue limit into defect size for different loading conditions. For a given material to simulate Kitagawa diagram we need material property, loading conditions and an experimental fatigue limit of a given size, under the same loading conditions.
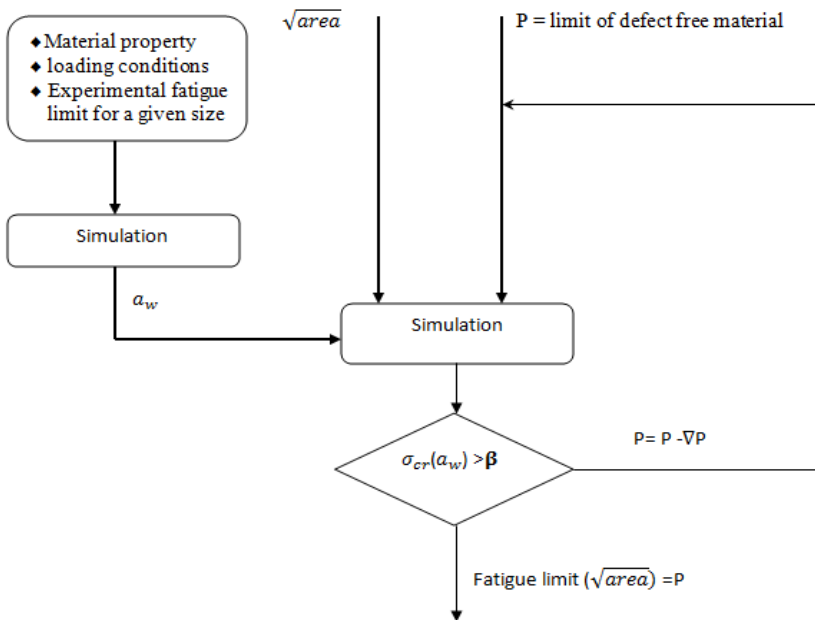
Fig. 7 Algorithm of the AD model

The experimental fatigue limit is used to determine the depth limit a_w. For each defect size the fatigue limit was determinate by modifying the loading amplitude until affected depth be equal to a_w.

Proposed Criteria for Defective Material

$$\sigma_{cr}(a_w) \leq \beta \tag{1}$$

Where**:**
$\beta = t_{-1}$: fatigue limit on fully reversed torsion for defect free material.
a_w : parameter deduced from an experimental fatigue limit of defective material
In the following, the new approch, using the proposed criterion for defective material (1) will be named AD model (**A**ffected **D**epth model). To summarize necessary steps for the proposed approach we can use the algorithm fig.7

3.2 Applications

In order to validate the proposed approach, we use the available results of an experimental investigation[6] carried out on 1045 carbon steel, corresponding to fully reversed torsion and bending limits of t_{-1} = 169 MPa and f_{-1} = 240 MPa, respectively. And to try the approach with other material we use an experimental data base containing Multiaxial fatigue results for cast aluminium AS7G06-T6 [7].The main properties of the cast aluminium are : Young modulus E= 73GPa, Poisson's ratio υ=0.3,fatigue limits under fully reversed torsion and tension are t_{-1} =80MPa and σ_{D-1} =91MPa respectively. For each material and loading condition, by simulation, we determinate the affected depth limit a_w for a medium defect size then the algorithm Fig.7 was applied to simulate Kitagawa diagram.

Table 2 Experimental data [6,7] and affected depth limit a_w

Material	R_σ	Solicitations	Defect size $\sqrt{area}$ (μm)	Fatigue limit (MPa)	Affected depth limit : a_w (μm)
1045 steel	- 1	Tension	400	152	45
		Torsion	400	145	135
AS7G06-T6	-1	Tension	700	80	360
	0.1	Tension	720	100	160

3.2.1   Spherical Pore
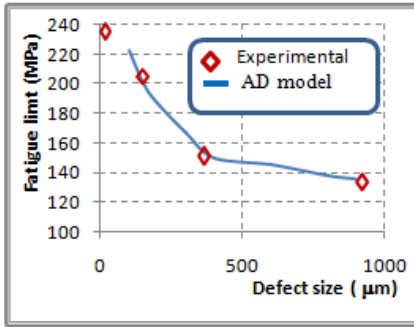
Fig. 8 Simulation of Kitagawa diagram using the new approach. 1045 steel, tension loading, $R_\sigma = -1$
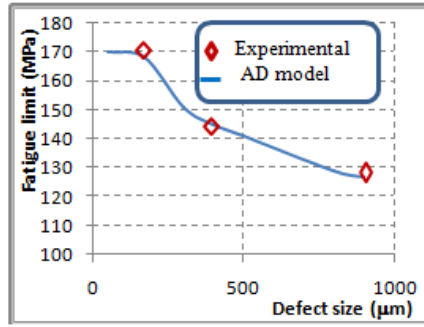
Fig. 9 Simulation of Kitagawa diagram using the new approach. 1045 steel, torsion loading, $R_\sigma = -1$
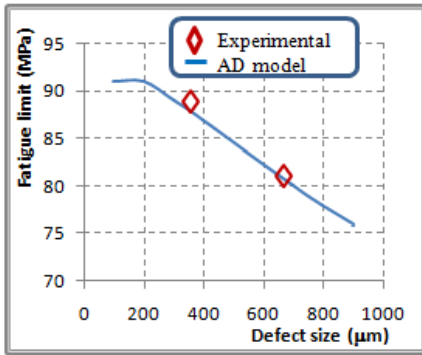
Fig. 10 Simulation of Kitagawa diagram using The new approach on cast aluminium, AS7G06-T6, tension loading, $R_\sigma = -1$
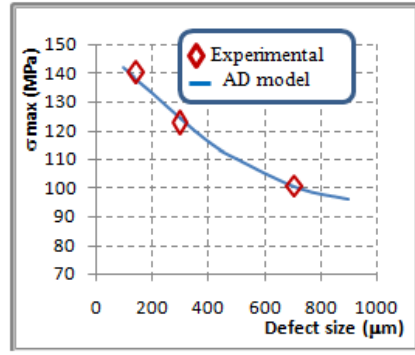
Fig. 11 Simulation of Kitagawa diagram using the new approach on cast aluminium AS7G06-T6, tension loading, $R_\sigma = 0.1$

For different defect sizes and loading conditions Fig.8, 9,10,11 show that the obtained results by AD model , as well as those from experimental work.

3.2.2   Ellipsoidal Pore

The same simplified model and boundary conditions, used for simulation in cases of spherical pore, are taken. To define exactly the shape of ellipsoidal we adopt a ratio, $\rho =10$, between the major axis and minor axis of the ellipsoidal pore. This aspect ratio has been chosen in accordance with the corresponding value considered in the experimental study[6] .This example was taken, to test the ability of AD model to describe the influence of defect morphology referring to experimental results.
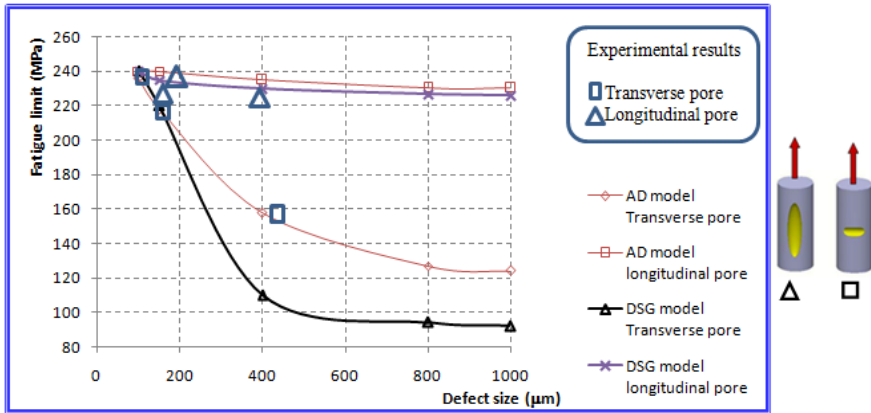
Fig. 12 Comparison between experimental results and simulation using DSG model and AD model for transverse and longitudinal ellipsoidal pore in tension loading $(R_\sigma = -1)$ with $\rho = 10$

4   Conclusions

The AD (Affected Depth) model, using the proposed criterion for defective material, is validated for different cases. Obtained results for all cases are on good agreement with experimental results (maximum 3% difference).

In other words, AD model is able to describe the evolution of the fatigue limit with defect size for different morphology and loading conditions. The mean stress effect is analyzed and results show that this effect can be described by the AD model.

Results for ellipsoidal defect improve that the parameter size $= \sqrt{area}$ alone is not able to describe the morphology influence in relation to the applied loading. AD model, depending on its simplicity, can be used as an interesting method for engineering design.

References

[1] Murakami, Y., Endo, M.: The $\sqrt{area}$ parameter model for Small defects and non metallic inclusion in fatigue strength: experimental vidences and application. Actes de. In: Blom, A.F., Beevers, C.J. (eds.) Theoretical Concepts and Numerical Analysis of Fatigue, EMAS, Birmingham, UK, pp. 51–71 (1992)

[2] Endo, M.: Effects of small defects on the fatigue strength of steel and ductile iron under combined axial/torsional loading. In: Ravichandran, K.S., Ritchie, R.O., Murakami, Y. (eds.) Proceeding of Small Fatigue Cracks: Mechanics, Echanisms and Applications, Hawaii 1999, pp. 375–387 (1999)

[3] Susmel, L., Taylor, D.: Two methods for predicting the Multiaxial fatigue limits of sharp notches. Frac. Eng. Mater. Struct. 26, 821–833 (2003)

[4] Leopold, G., Nadot, Y.: Fatigue from an induced defect: experiments and application of different Multiaxial fatigue approach. J. ASTM Int. 7 (2007)

[5] Nadot, Y. Billaudeau, T. Multiaxial fatigue limit criterion for defective materials. Engineering Fracture Mechanics 2005

[6] Billaudeau, T., Nadot, Y., Bezine, G.: Multiaxial fatigue limit for defective materials: mechanisms and experiments. Acta Mater 52, 3911–3920 (2004)

[7] Mu, P., Nadot, Y., Nadot–Martin, C., Habod, A.C., Serrano-Munoz, I., Verdu, C.: Influence of of casting defects on the behaviour of cast aluminium AS7G06-T6. Int.J of Fatigue 63, 97–109 (2014)

Optimization of Stress-Strain Curves of WC-Co Two-Phase Materials by Artificial Neural Networks Method

Rabah Taouche

Département des Sciences de la Matière, Faculté des Sciences, BP 26 Route d'El Hadaiek, Université du 20 août 1955 Skikda 21000, Algeria
taouche.rabah@yahoo.fr

Abstract. In this study, an artificial neural networks method was used to optimize and predict the stress-strain curves as a function of second phase volume fraction of WC-Co two-phase materials deformed in compression and in tension. In order to train the artificial neural network, a set of different volume fractions of Co having different stress-strain curves of the WC-Co two-phase materials was used. A maximum of stress corresponding to each curve was obtained and used as a base to predict the theoretical stress-strain curve for no corresponding second phase volume fractions. The results of this study show that there is a good agreement between experimental and optimized stress-strain curves and the artificial neural networks method created is capable of successfully predicting the evolution of the stress-strain curves of WC-Co two-phase materials as a function of second phase volume fraction.

Keywords: Artificial Neural Networks, Two-phase materials, Stress-strain, WC-Co.

1   Introduction

The WC-Co two-phase materials and material composites in general have received considerable attention because of their superior mechanical properties as compared to those of most conventional materials. These materials have a great interest in practice since they provide both high strength and good formability. Different types of models have been used to build the theoretical stress-strain curve of a two-phase material from the stress-strain of its corresponding single-phase materials: mixture laws (Mileiko 1969; Araki et al. 1977), finite element methods (Durand and Thomas de Montpreville 1990; Durand and Pastor 1992) and self-consistent models (Berveiller and Zaoui 1981; Durand and Altibelli 1993). The artificial neural networks method is a new approach to optimize and predict the mechanical behaviour of materials; it is actually widely used in materials science field and there are no studies were carried out in the field of mechanical behaviour of two-phase materials.

This paper presents the results of using an artificial neural networks method to predict the mechanical behaviour of two-phase materials based on the stress-strain experimental data.

2   The Artificial Neural Networks

Artificial Neural Network (ANN) is a network with nodes or neurons analogous to the biological ones. The nodes are interconnected to weighted links (Zhang and Friedrich 2003; Bahrami et al. 2005; Koker et al. 2007). The weights are usually adjustable and can be trained through a learning process and training examples. It has different layers, interconnected through a complex network. The Figure 1 shows the structure of an artificial neural network with various layers.
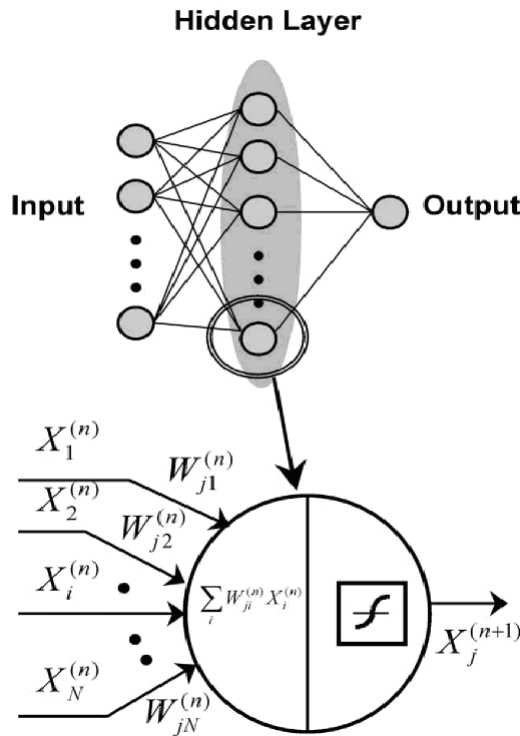
Fig. 1 A schematic description of an artificial neural network (Zhang and Friedrich 2003)

In this study, the feed-forward multilayer perceptron (MLP) was used and trained with back propagation algorithm. The strain and volume fraction are used as inputs of the artificial neural networks, the stress is the output of the latter.

All the variables were normalised (Yescas et al. 2001) between 0 and 1 as follows:
For the stress (Eq. 1):

$$x_N = \frac{x}{x_{max}} \tag{1}$$

For the strain and the volume fraction (Eq. 2):

$$x_N = \frac{x}{100} \tag{2}$$

Because the variables are in percentage.

In the learning process, a set of data that contains the inputs and their corresponding outputs was used to train the network. An iterative algorithm 'Levenberg-Marquardt algorithm' adjusts the weights that the outputs of the network (Eq. 3) be the most possible nearest to the desired outputs. This is attained by minimising the learning error, defined by the mean squared error (Eq. 4).

$$y_i = f\left(\sum_{j=1}^{n} w_{ij} x_j + b_i\right) \tag{3}$$

Where:

y_i is the output, x_j is the input, f is the activation function, w_{ij} are the weights and b_i is the bias.

$$MSE = \frac{1}{QN} \sum_{m=1}^{Q} \sum_{n=1}^{N} \left(d_n(m) - y_n(m)\right)^2 \tag{4}$$

Where:

d is the desired output, y is the output of the network, Q is the number of the learning sets and N is the number of the outputs.

3 The Network Architecture

The network used in this study presents the following characteristics:

- An input layer, in which the inputs are presented, that are the deformations and the volume fractions.
- An output layer, in which the outputs are presented, that are the stresses.
- The network training: to train the network, an iterative back propagation algorithm was used; four (04) volume fractions are used as training examples.
- A one hidden layer constituted of 16 neurons which is fixed after different tests (Tab. 1).

- The activation function is a logarithmic sigmoid for the hidden layer, it has the following form (Eq. 5):

$$f(x) = \frac{1}{1 + e^{-x}} \qquad (5)$$

- The activation function is linear for the output layer, it has the following form (Eq. 6):

$$g(x) = x \qquad (6)$$

4   Choice of the Number of Neurons in the Hidden Layer

The table 1 shows that the minimum of the mean squared error (MSE) corresponds to the number 16 neurons, what justifies the choice of the number 16 in the hidden layer.

Table 1 Mean squared error versus the number of neurons in the hidden layer

Number of neurons	Mean squared Error (MSE)
2	202.7287
4	0.2261
6	0.0013
8	0.0082
10	2.9047E-5
12	3.1902E-5
14	3.3057E-6
16	**2.8471E-6**
18	1.8146E-4
20	9.2306E-5
22	9.7610E-6

5   Application of the Artificial Neural Networks in the Mechanical Behaviour

In the mechanical area, a certain number of the experimental results are necessary to develop an effective neural network, including its architecture, training functions, training algorithm and the other network parameters, followed by a training process and an evaluation method. After the network is to be trained to resolve the problem based on this data, the new data of the same problem can be inputted in the trained network to output the real solutions. The process of the building the neural networks consists in the following four steps:

1. Collection of data: analyse and treatment of data.
2. Network training: this includes the choice of its architecture, the training functions, the training algorithm and the network parameters.
3. Test of the trained network: to evaluate the network performance.
4. Use of the trained network in the simulation and prediction.

6   Results

The neural networks method using a MATLAB platform is applied to optimize and predict the stress-strain curves of the WC-Co two-phase material deformed in compression (Doi et al. 1969) and in tension (Nishimatsu and Gurland 1960).

6.1   WC-Co in Compression

For the training of the stress-strain behaviour of the WC-Co material deformed in compression, the optimized experimental stress-strain curves were used for the following volume fractions of Co: 43%, 36%, 21% and 10%. The optimized curves obtained by using the neural networks are in good agreement with the experimental results (Figure 2). In order to test the validity of the network, the application of the trained network is interpolated to other volume fractions included between 43% and 10% of Co. It is proceeded with the following manner: another neural network with the same architecture was trained in order to determine the maximum of stress corresponding to each volume fraction (Figure 3), then the network is interpolated to the fractions of 40%, 30%, 25% and 15% of Co based on the predicted maximum stress corresponding to each volume fraction. The Figure 4 shows the position of the interpolated curves within the experimental ones; they are in good accord with the evolution of the experimental curves.

6.2   WC-Co in Tension

By following the same manner that in compression case, Figure 5 illustrates the comparison between optimized and experimental stress-strain curves for the volume fractions of 90%, 85%,75% and 65% of Co, it shows a good agreement. The trained and predicted maximum of stress corresponding to each volume fraction is visualised on the Figure 6. The Figure 7 shows the position of interpolated curves corresponding to the fractions of 88%, 80%, 72% and 70% of Co within the experimental curves, a good accord with the evolution of the experimental curves is found.
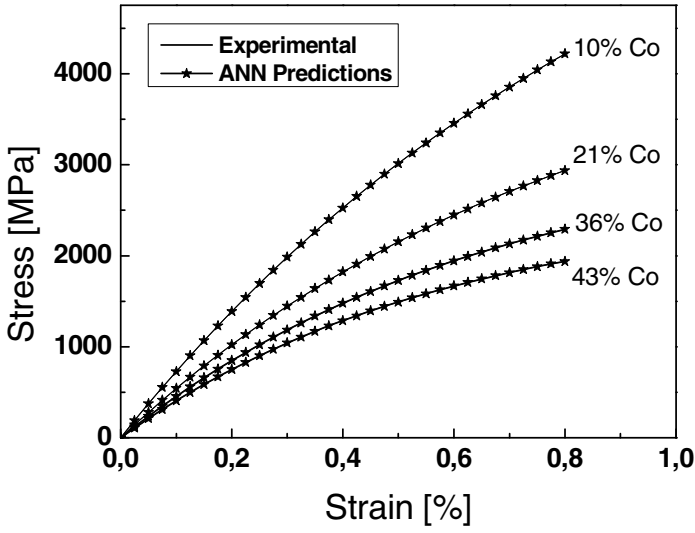
Fig. 2 Optimized stress-strain curves. WC-Co system in compression (experimental data (Doi et al. 1969))
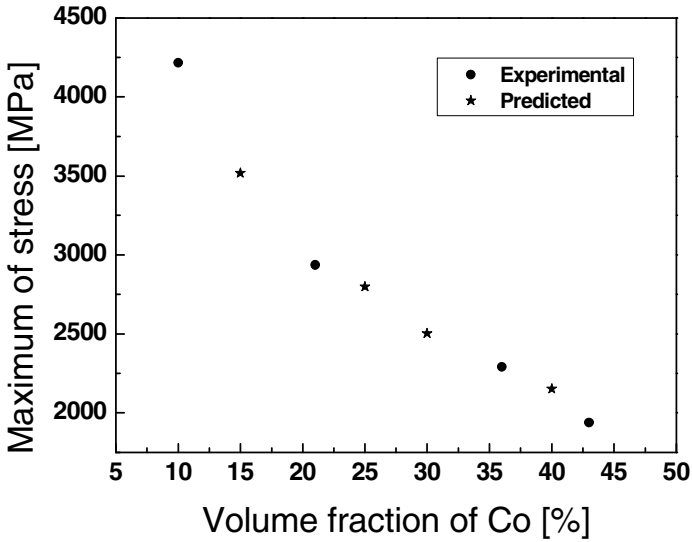
Fig. 3 The maximum of stress versus volume fraction of Co for the system WC-Co in compression
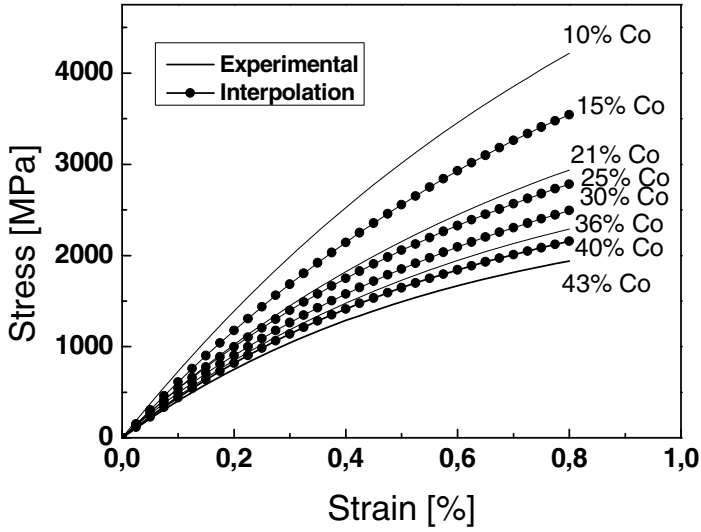
Fig. 4 Interpolated curves position in the evolution of the experimental behaviour of the WC-Co system in compression (experimental data (Doi et al. 1969))
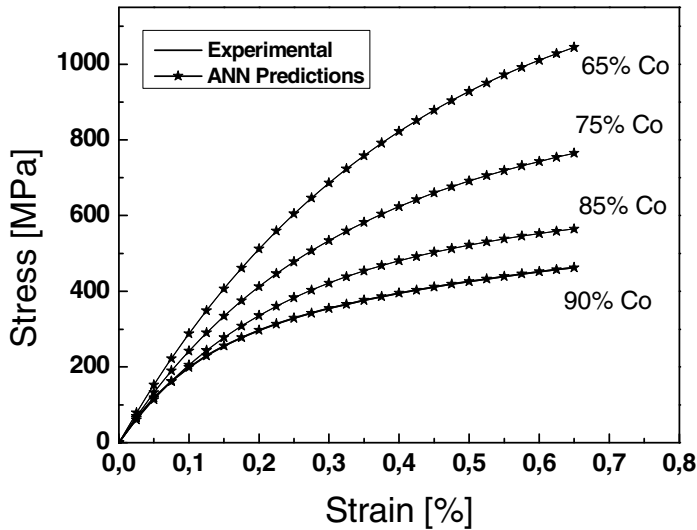
Fig. 5 Optimized stress-strain curves. WC-Co system in tension (experimental data (Nishimatsu and Gurland 1960))
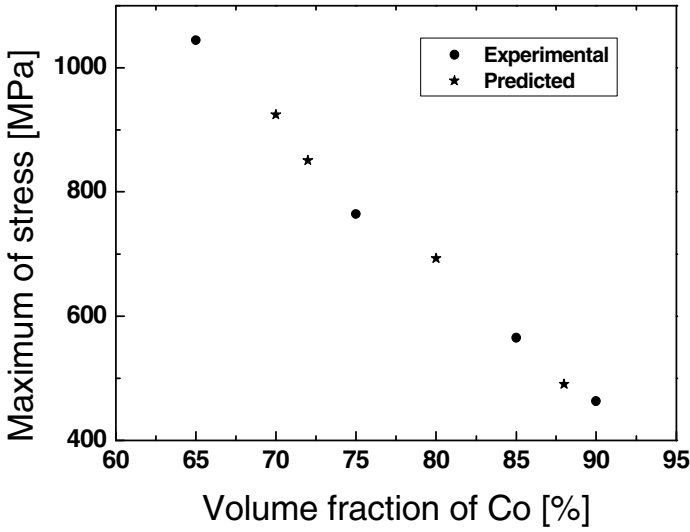
Fig. 6 The maximum of stress versus volume fraction of Co for the system WC-Co in tension
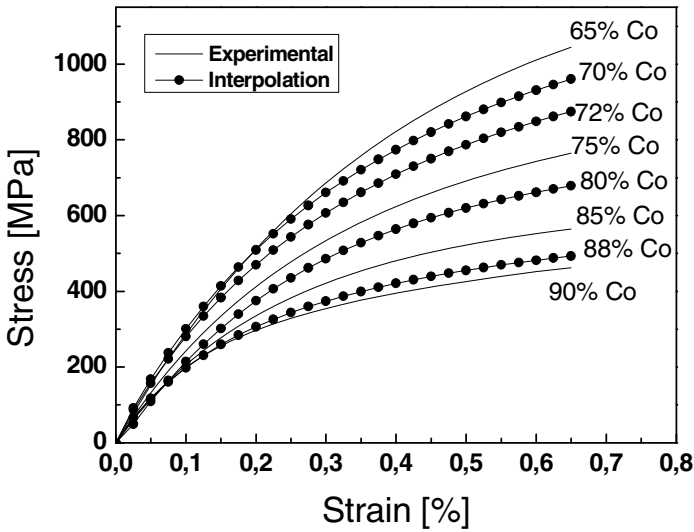
Fig. 7 Interpolated curves position in the evolution of the experimental behaviour of the WC-Co system in compression (experimental data (Nishimatsu and Gurland 1960))

7 Discussion

- The training is more effective that the number of experimental data is greater, after a set of tests, it is noticed that the minimum required for these two examples is four (04) volume fractions (i.e. four curves).
- The similarity evolution of the experimental behaviour of data used in the training phase has a great influence on the obtained results; this is more effective that the evolution of the experimental behaviour is similar.
- The maximum of stress of each volume fraction is a very important parameter to predict the theoretical stress-strain curve as a function of second phase volume fraction.

8 Conclusions

An artificial neural network method was used to optimize and predict the stress-strain curves of WC-Co two-phase materials from experimental stress-strain data. The method has allowed the stress-strain evolution of WC-Co two-phase materials as a function of Co volume fraction based on the predicted maximum of stress to be approximated. The agreement with the experimental behaviour is very satisfactory as long as the similarity of the behaviour is greater. The determination of the maximum of stress has allowed to predict the theoretical stress-strain curves with no corresponding experimental ones, it shows the predicting capacity of this parameter. This study of the mechanical behaviour of two-phase materials has shown the capacity of neural networks to predict the stress-strain behaviour of two-phase materials of WC-Co as a function of Co volume fraction.

References

1. Mileiko, S.T.: The tensile strength and ductility of continuous composites. J. Mater Sci. 4, 974–977 (1969)
2. Araki, K., Takada, Y., Nakoka, K.: Work hardening of continuously annealed dual phase steels. Trans. ISIJ 17, 710–717 (1977)
3. Durand, L., Thomas de Montpreville, C.: Etude du Comportement Mécanique des Matériaux Biphasés au moyen de la Méthode des Eléments Finis. Res Mechanica 29, 257–285 (1990)
4. Durand, L., Pastor, P.: Finite element method applied to tensile deformation of an equivolume two-phase alloy. Materials Characterization 29, 39–47 (1992)
5. Berveiller, M., Zaoui, A.: A simplified self-consistent scheme for the plasticity of two-phase metals. Res. Mech. Lett. 1(3), 119–124 (1981)
6. Durand, L., Altibelli, A.: Application d'un Modèle Autocohérent à la Traction de Matériaux Biphasés à Grains Allongés. Rev. Mét CIT/SGM 90(12), 1593–1600 (1993)
7. Zhang, Z., Friedrich, K.: Artificial neural networks applied to polymer composites: a review. Composites Science and Technology 63, 2029–2044 (2003)

8. Bahrami, A., Mousavi Anijdan, S.H., Ekrami, A.: Prediction of mechanical properties of DP steels using neural network model. Journal of Alloys and Compounds 392, 177–182 (2005)
9. Koker, R., Altinkok, N., Demir, A.: Neural network based prediction of mechanical properties of particulate reinforced metal matrix composites using various training algorithms. Materials and Design 28, 616–627 (2007)
10. Yescas, M.A.: Bhadeshia HKDH, Mackay DJ Estimation of the amount of retained austenite in austempered ductile irons using neural networks. Materials Science and Engineering A 311, 162–173 (2001)
11. Doi, H., Fujiwara, Y., Miyake, K.: Mechanism of plastic deformation and dislocation damping of cemented carbides. Trans. Metall Soc. A I M E 245, 1457 (1969)
12. Nishimatsu, C., Gurland, J.: Experimental survey of the deformation of hard-ductile two-phase alloy system WC-Co. Trans. Am. Soc. Metals 52, 469 (1960)

Numerical Study of Localized Necking in the Strain Path of Copper Hydroformed Tube: Effect of Friction

Abir Abdelkefi[1,2,3], Noamen Guermazi[1], Nathalie Boudeau[2,3], Pierrick Malécot[2,3], and Gerard Michel[2,3]

[1] Laboratoire de Génie des Matériaux et environnement (LGME),
  Ecole Nationale d'Ingénieurs de Sfax (ENIS), B.P 1173-3038, Sfax,
  Université de Sfax, Tunisie
[2] FEMTO-ST, Département Mécanique Appliquée,
  24 rue Epitaphe, 25000 Besançon, France
[3] ENSMM, 26 rue Epitaphe, 25030 Besançon Cedex, France
  {abdelkafi.abir,noamen.guermazi}@gmail.com,
  {nathalie.boudeau,pierrick.malecot,gerard.michel}@ens2m.fr

Abstract. The effect of the friction coefficient in the strain path of hydroformed tube is discussed in this paper. A finite element simulation with the LS-DYNA/Explicit software has been performed and experiments have been carried out. The localized thinning can be related to necking and then, the use of the Forming Limit Curve (FLC) and the analysis of the strain path can give some indications on the risk of fracture in the hydroformed part. FE simulations have been performed with different friction coefficients to study their effect on the resulting strain path and to predict the localized thinning during tube hydroforming in a square section die. Hydroforming experiments have been performed on deoxidized copper (Cu-DHP) tubes to validate the finite element results. When the pressure increases, the strain increases firstly in the transition zone, that next leads to severe thinning in the corner zone and finally, in the straight wall. The comparison between the results obtained with the finite element and experiments confirms that the thickness reduction is more important in the transition zone between the straight- wall and the corner radius and the localized necking occurs in the transition zone. It is then possible to define the limits of the process and enhance the necking prediction.

Keywords: Tube hydroforming, Friction effect, Strain path, Localized necking.

1   Introduction

In recent years, there is an increasing demand for hydroformed parts dedicated for aeronautical and automotive applications. This is because hydroforming offers various advantages such as weight reduction, part consolidation, lower tooling cost, improved structural strength and stiffness improvements, secondary operations bypass and scrap reduction (Ahmetoglu and Altan 2000). In this

context, great efforts have been focused on tube hydroforming using analytical models, numerical computations and experimental characterizations (Kridli et al. 2003; Hwang and Chen 2005). The success of such process depends on the knowledge of the material properties of the tube, the dies geometries and the friction conditions. The friction coefficient directly affects the flow of material in the die, thus the thickness repartition over the final part. In the literature, many researchers have been interested in the study of the strain path of the hydroformed tubes (Bihamta et al. 2013; Li et al. 2012 ; Xu et al. 2009-a; Xu et al. 2009-b). Indeed, to estimate if this thickness change is safe from fracture, the forming limit diagram or curve (FLD or FLC) was generally used. Consequently, in Ls-Dyna software the FLD for each section of the workpiece (after hydroforming) was drawn. Bihamta et al., (Bihamta et al. 2013) have used the FLC to control the hydroforming process and then to estimate the validity of this technique in the case of hydroforming in complex dies. Li et al. (Li et al. 2012) have also used this method to study the strain path and to predict the localization of defects in elliptical section. In addition, FE simulations have been performed with different friction coefficients to examine their effect on the resulting strain path. Xu et al. (Xu et al. 2009-a) have investigated the (FLC) in a squares section die to study the thickness variation for different points, indeed they have concluded that the thinnest element of the tube wall occurs at the transition zone, while the thickest element is located at the middle of the side wall. Xu et al., (Xu et al. 2009-b) have investigated the (FLC) in a trapezoidal sectional die and they have predicted the localized thinning.

2   Experimental Procedure

2.1   Material

In the present study the material used is deoxidized copper (Cu-DHP) tube with outer diameter of 35mm and nominal thickness of 1 mm, and 250 mm of length.
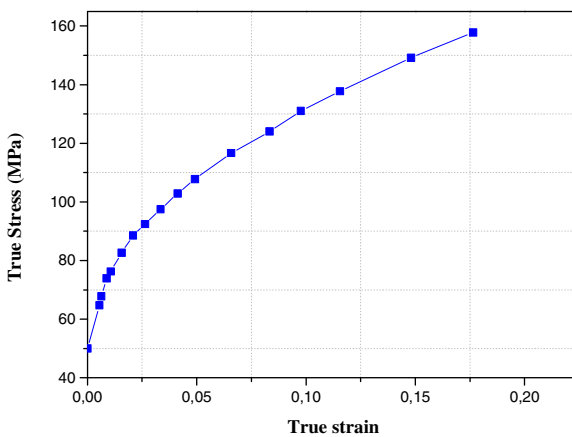
Fig. 1 Typical true stress-true strain curve for the tested material

In the meanwhile of bulging test, internal pressure and pole height of the tube (also named the bulge height) are continuously measured resulting in a pressure–bulge height curve. The previous curve with the analytical model proposed in the literature (Boudeau and Malécot 2012) leads to obtain the curve of the true stress-true strain curve as given in Fig.1.

The mechanical properties of the tested material are listed in Table1.

Table 1 Mechanical properties of the used copper

Density (tonne/mm^3)	8.49e-9
R_m (MPa)	440
$R_{p0.1}$ (MPa)	420
A_{10} (%)*	2
E (GPA)	132
Poisson coefficient υ	0.34
Strength coefficient K.(MPa)	263.63
Strain hardening coefficient n	0.287
Yield stress σ.(MPa)	50
Initial strain ε_0	0.0043

*A_{10}:-Elongation of drawn copper tubes on annealing temperature after cold work.

2.2   Hydroforming Procedure

In the present study, a modular tool has been designed to run tube bulging tests in an open die or tube hydroforming in closed shape dies. This tool is installed in a press. The experimental devices are illustrated in Fig.2. A multiplier pressure cylinder creates the high pressure to bulge the tube and two vertical cylinders clamp the tube at its two extremities by cone-cone contacts. The test proceeds as following: (1) conical plungers come in contact with the ends of the tube; (2) the hydraulic fluid is pumped into the specimen through the conical plungers resulting in a slow increasing pressure inside the tube. (3) the tube deforms and takes, little by little, the shape of the die. During the hydroforming process, the internal pressure inside the tube and the tube deformation are measured. In the present test, the maximal internal pressure was 28 MPa that allows a tube expansion without any risk of crack (Fig.3). This maximal pressure was estimated through numerical simulations and optimization procedure. The tests are conducted without specific lubricant, but the tools are oiled to avoid their degradation.

The copper tubes were hydroformed using a square cross-section die with 50 mm of length and 5 mm of corner radius .The geometry of a half tube is considered and it is shown in Fig.4.
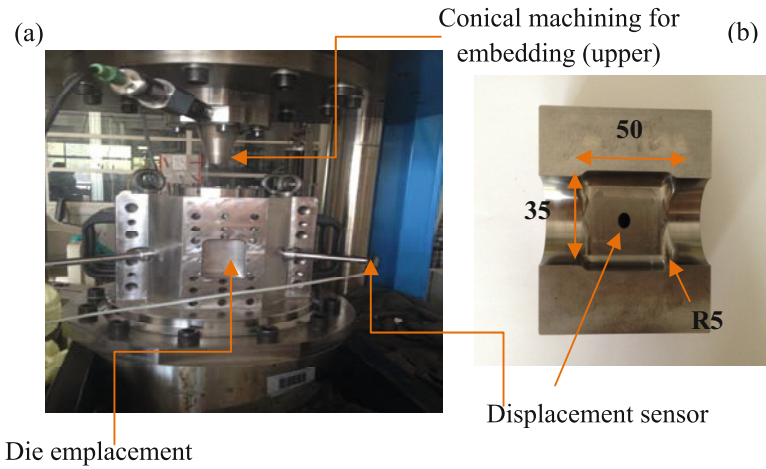
Fig. 2 The modular tool installed on the press at FEMTO-ST lab (a) and the main dimensions of the square section die (b)

Fig. 3 Tube after hydraulic expansion with various internal pressures: experimental result

3   The Finite Element Study

Because of the symmetry of the geometry, only a half tube is considered to simulate the tube hydroforming in a square die *via* LS-DYNA/Explicit© software (Hallquist 1989). The geometry is meshed with 51448 nodes and 51164 Belytschko-Tsay shell elements. The element size is based on the smaller detail in the model, meaning the die corner radius r = 5 mm. The die is assumed to be a rigid elastic material. The tube material is assumed as elastic-plastic and isotropic.

In the plastic range, the Swift law $\bar{\sigma}(MPa) = 263.63(0.0043 + \bar{\varepsilon})^{0.287}$ is

considered. The Swift parameters have been identified from experimental hardening curve obtained with the tube bulging test (Boudeau and Malécot 2012). The tube is clamped at its two ends. Finally, an internal pressure is applied on the inner surface of the tube. Based on the experimental measurements, the maximum pressure varies from 15 to 28 MPa, in a virtual period of 0.001s (Fig.4). We assume, for the simulation, a contact "automatic one way surface-to-surface" and we introduce various friction coefficients. Two friction coefficients (μ=0.05 and μ=0.1) between tube and die are considered and, then, the thickness distribution in the final part is studied. Post-processing the numerical results will consist in analyzing the evolution of thickness reduction, thickness spatial repartition and die radius evolution in relation with the different friction conditions.
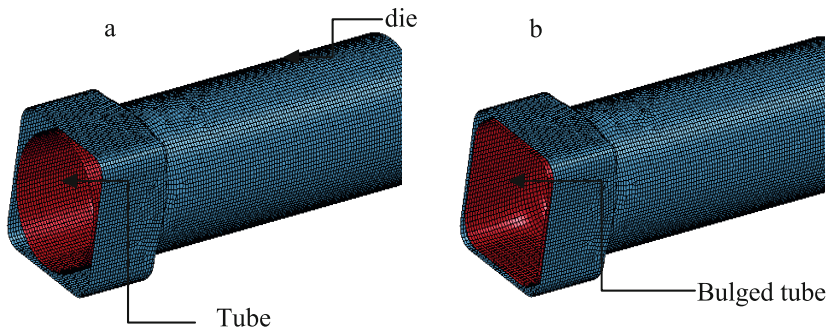
Fig. 4 FE model (a) and typical FE results (b)

The dimensions of the cooper tube and the main results are summarized Table.2.

Table 2 Dimensions of the tube and main results

External radius (mm)	Half model length (mm)	Tube thickness (mm)	Friction	Thickness reduction (%)	Final radius (mm)
17.5	125	1	0.05	20.5	5.32
17.5	125	1	0.1	21.5	5.23

4   Effect of Friction on Tube Hydroforming and Prediction of Thinning Location

In this section, we are interested in thinning and its location in the hydroformed tube (Fig.5). A quarter of the tube was considered due to the geometrical symmetry.
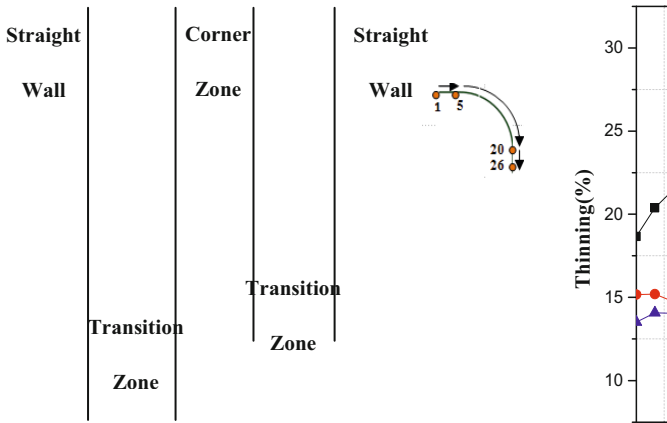
Fig. 5 Thickness reduction under different friction coefficient values and experimental result for several measurement points

A profile is defined in the centered cross section of the tube and the thickness reduction *versus* the points of measure defined along the transversal profile is also shown in Fig.5. The values for the friction coefficient have been chosen from experimental results obtained on pin-on-disk tribometer realized at the University of Sfax (LGME) with samples corresponding to the two materials in contact during tube hydroforming. The thickness reduction measured from experiments presents a maximum value of 30% while FEM results lead to exhibit 21.5% of reduction. Points 1 and 26 define the midline of the straight wall while points 5 and 20 define the beginning of the transition zone. A significant increase of the thickness reduction was obtained and this can be ascribed to the increase of the friction coefficient, especially in the transition zone. Whereas the friction coefficient was found to have a little effect on the thickness reduction in both straight wall and corner zone. This finding is consistent with that obtained in the literature (Orban and Hu 2007). Despite the 9% of difference between numerical and analytical results, the two approaches show similar evolutions. These differences can be linked to:*i)* the friction coefficient is not characteristic of the real friction conditions during tube hydroforming; *ii)* the 3D shell model is not sufficiently precise for thickness evaluation. In addition, the FE simulations are certainly more representative of the real process but, a model based on shell elements can lead to an over estimation of the thickness. A 3D model with solid finite elements would be more appropriate for the evaluation of the thickness reduction.
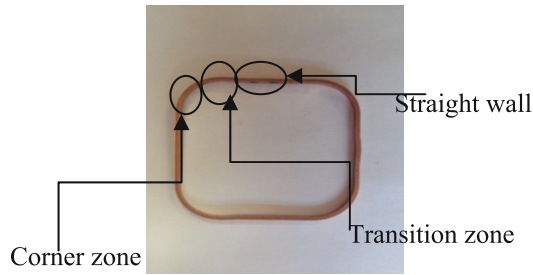
Fig. 6 Thinning localization in the hydroformed tube

In order to validate the numerical results, a real hydroformed tube profile is examined as shown in Fig.6. As it can be seen exactly the location of the thinning is in the transversal profile of the hydroformed tube. This confirms again that the severe thinning occurs in the transition zone and thus a good correlation was obtained between the numerical and experimental studies.

5 Effect of the Friction on the Strain Path and the Study of the Localized Necking

The localized thinning can be related to necking and then, the use of the Forming Limit Curve (FLC) and the analysis of the strain path can give some indications on the risk of fracture in the hydroformed part. Two friction coefficient values were used: $\mu=0.05$ and $\mu=0.1$. Three zones are considered: the straight wall (S343), the transition zone (S3790) and the corner area (S3787) illustrated in Figs.7 and 8 .The strain evolution on the FLC diagram reveals, in particular when the final pressure is 28MPa, that no risk of necking to be detected (Fig.7).

On the other hand, another simulation with a maximum pressure of 36 MPa, corresponding to crack formation during experiments, has been post-processed with the same way as previously described. As illustrated in Fig. 8, the main results indicated that a severe thinning takes place in the transition zone. In addition, when the pressure increases from 28 to 36 MPa, the strain increases firstly in the transition zone, that next leads to severe thinning in the corner zone and finally, in the straight wall. Therefore, both of experimental and numerical results (Figs.7 and 8) let us to believe that the localized necking occurs in the transition zone.
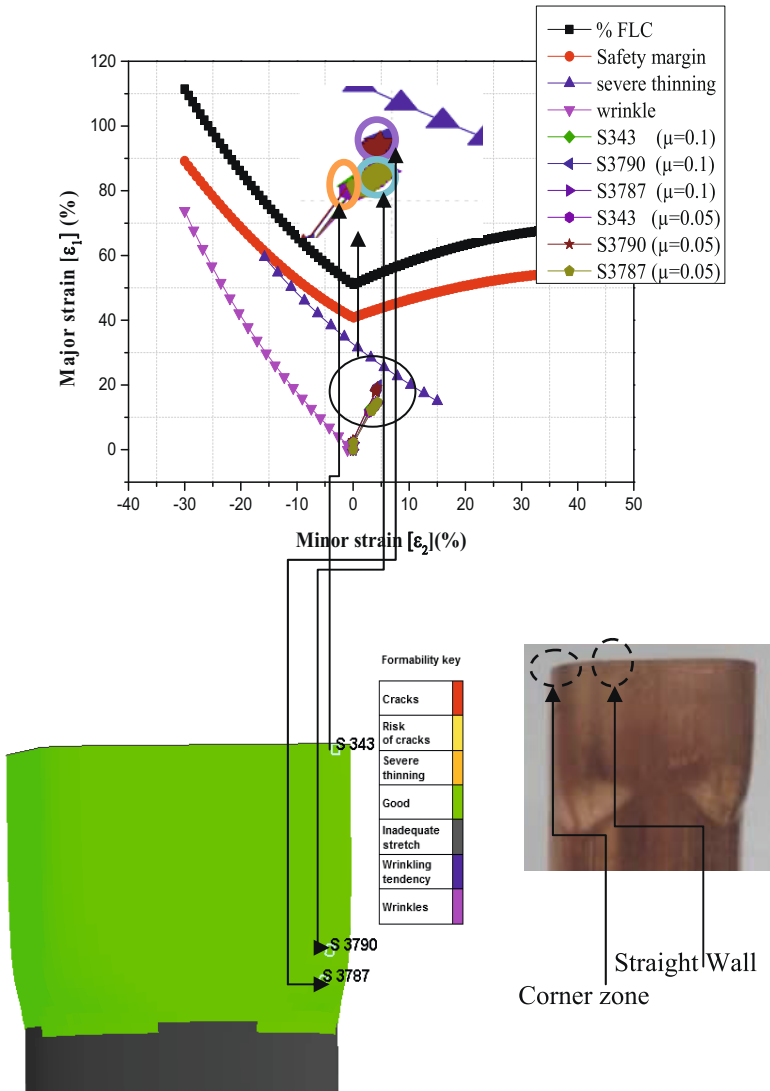
Fig. 7 Experimental/FE results obtained under different friction coefficients and a pressure value of 28 MPa
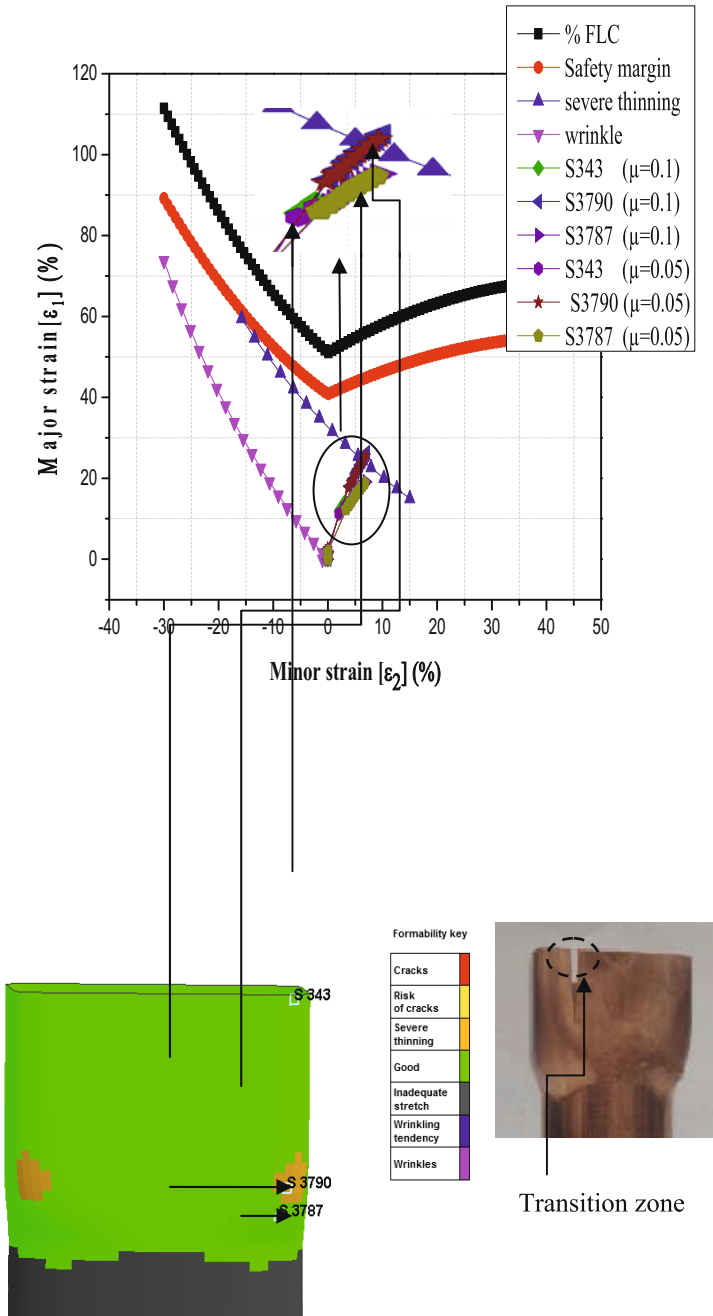
Fig. 8 Experimental / FE results obtained under different friction coefficients and a pressure value of 36 MPa

6   Conclusion

In this work, we have focused our attention on the study of the friction effect on the strain path using the forming limit curve (FLC). The prediction of the localized thinning for hydroformed tube was alos investigated. During tube hydroforming experiments a square die was used. Numerical simulations have been performed with LS-DYNA/Explicit software. The correlation between the numerical and experimental results was discussed. Through the finite element simulations, one can conclude that, the predicted FLC matches well with the obtained experimental data. Therefore, such correlation emphasizes the accuracy and the validity of our numerical approaches. Finally, it is equally important to note that the localized thinning occurs firstly in the transition zone, then in the corner zone and finally in the straight wall.

References

(Ahmetoglu and Altan 2000)
Ahmetoglu, M., Altan, T.: Tube hydroforming: state-of-the-art and future trends. Journal of materials Processing Technology 98(2000), 25–33 (2000)
(Kridli et al. 2003)
Kridli, G.T., Bao, L., Mallick, P.-K., Tian, Y.: Investigation of thickness variation and corner filling in tube hydroforming. Journal of Materials Processing Technology 33, 287–296 (2003)
(Hwang and Chen 2005)
Hwang, Y.M., Chen, W.-C.: Analysis of tube hydroforming in a square cross-sectional die. International Journal of Plasticity 21, 1815–1833 (2005)
(Bihamta et al. 2013)
Bihamta, R., D'Amours, G., Bui, Q.H., Guillot, M., Rahem, A., Fafard, M.: Numerical and experimental studies on the new design concept of hydroforming dies for complex tubes. Materials and Design 47, 766–778 (2013)
(Li et al. 2012)
Li, S., Chen, X., Kong, Q., Yu, Z., Lin, Z.: Study on formability of tube hydroforming through elliptical die inserts. Journal of Materials Processing Technology 212, 1916–1924 (2012)
(Xu et al. 2009-a)
 Xu, X., Li, S., Zhang, W., Lin, Z.: Analysis of thickness distribution of square-sectional hydroformed parts. Journal of Materials Processing Technology 209, 1397–1403 (2009)
(Xu et al. 2009-b)
 Xu, X., Lin, Z., Li, S., Zhang, W.: study of tube hydroforming in a trapezoid-section die. Journal of Materials Processing Technology 209, 158–164 (2009)
(Boudeau and Malécot 2012)
Boudeau, N., Malécot, P.: A simplified analytical model for post-processing experimental results from tube bulging test: Theory, experimentations, simulations. Journal of Mechanical Sciences 65, 1–11 (2012)
(Hallquist 1989)
Hallquist, J.O.: LS-DYNA3D User Manual v970, LSTC, Livermore (1989)
(Orban and Hu 2007)
Orban, H., Hu, S.J.: Analytical modeling of wall thinning during corner filling in structural tube hydroforming. Journal of Materials Processing Technology 194, 7–14 (2007)

Behavior Analysis of the Aluminum 2017A Sheet Using Vapor Bulge Test

Salah Aissa[1], Mahfoudh Ayadi[2], Mohamed-Ali Rezgui[3], and Mohamed Soula[4]

[1] ISET-Sousse, Cité Erriadh - B.P 135 - Sousse 4032, Tunisia
 salah_mel_aissa@yahoo.fr
[2] B.P N°65 Campus Universitaire Menzel Abderrahmane 7035, Bizerte, Tunisia
 mahfoudayadi@gmail.com
[3] UR-MSSDT (99-UR11-46), ENSIT, 5 Av Taha Hussein, Montfleury 1008, Tunis, Tunisia
 Mohamedali.rezgui@esstt.rnu.tn
[4] LR-MAI (11-ES19), ENIT, BP 37, 1002, Le Belvédère, Tunis, Tunisia
 soulamed2003@yahoo.fr

Abstract. The hot forming of thin structures (plates) uses the temperature as a factor that could increase the forming limits of the sheet metal. On top of the improving of forming limits, increasing temperature induces a decrease of spring- back and a clear reduction of limits loads necessary for the forming operation. The hot forming process is usually done in two independent phases: the first step is the blank heating and the second one is the load application. The present work shows a forming technique based on both temperature and pressure to make a sheet form. These parameters are linked to the water vaporization process into a cavity covered by the blank. This study will try to show:

(i)   Experimental aspects of sheets forming under the action of water vapor pressure.
(ii) Correlation between the blank geometry, level pressure and the forming temperatures.
(iii) Performances of the process expressed in terms of:
          - Surface creation
          - Decrease of the loads of making form
          - Increase of the forming limits

Keywords: Temperature, pressure, vaporization, forming, sheet.

1   Introduction

The reduction of the energy consumption in the transport sector constitutes a huge problem to the constructors. The slight materials such as aluminum and magnesium are among the best alternative solutions of this issue by the optimization of the design and the choice of the right process. In the last years, these kinds of materials are characterized by a growing demand especially in the car industries and aerospace (Toros et al. 2008, Yuan et al. 2011).

For that, all the studies were oriented to a new thermo-forming experimental approach to reach a plastic deformation. In fact, the forming limits at high temperatures increase significantly contrary to the forming loads which decrease. In this is context several investigations and analysis at high-temperature behavior of many sheets of lightweight alloy such as Al5052 and AL6061, are presented in (Mahabunphachai and Koc 2010). The present work shows a new possibility of free bulging of thin sheet metal (aluminum 2017A), by using heated vapor pressure. This new technology is based on coupling temperature and pressure.

2   Experimental Setup

2.1   Vapor Bulge Test Setup

The free bulging under steaming pressure is similar to the hydraulic forming. The loading system is made by a vapor generator. The forming pressure is generated by the vapor produced by the process of water vaporization. The vapor bulge test set up shown in figure 1 is designed and built at ISET Sousse. This dispositive can produce different levels of heating power by converting the electric energy into heat.
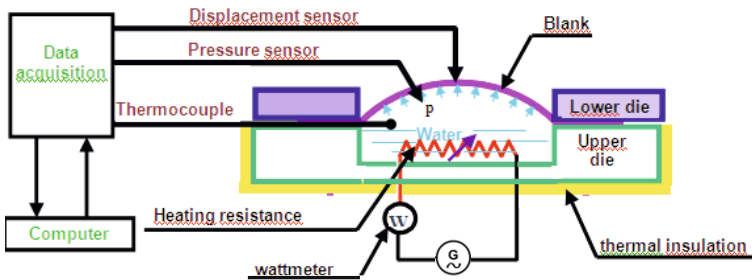
Fig. 1 Schematic setup for vapor bulging test

2.2   Blank Specifications

The type of piece materials chosen for these essays is aluminum alloys 2017A. The circular sheet metal subjected to the tests has 0.6mm of thickness and 275mm of diameter. The part of the blank submitted to the pressure has 160 mm of diameter and the time of test is a function of the calorific power generated by the heating source.

2.3   Acquisition of Measurements

During the forming process, the measures are taken every 1.67 s. The experimental results are exploited to observe the evolution of the following variables:

- The average equivalent stress according to the cumulated average of plastic deformation
- The surface creation developed according to the forming pressure.
- The work ratio of the pressure forces /creation surface according to the pressure

3   Experimental Results

In this paragraph, we present the experimental results related to:

- The hydraulic bulging at room temperature.
- The free bulging with vapor Tests are realized with three different thermal loads: 1KW, 1.5KW and 2KW.   To get the vapor water, we use the same amount of water injected initially for the whole experiences which is 630 cm^3.

   The tests of the vapor bulging show that the time of the experience depends on the power imposed by the thermal source. In these experiences, the deformation volume of the sheet metal increases under vapor pressure until the rapture of the sheet as shown in figure 2.

Fig. 2 Experimental setup for vapor bulging test

   Figure 3 presents the evolution of heating speed. It's necessary to observe a quick ascending phase between 90 and 120s corresponding respectively to 105°C/mn and 15°C/mn. This phase shows the effect of the amount of electric injected power to start our forming operation. It corresponds to the transitory thermal phase representing the heating volume of water enclosed in the die cavity and the rest of the device before the beginning of the vaporization.

Furthermore, figure 3 shows also a slow evolution of the internal temperature that has an asymptotic tendency of heating speed being able to attain 2°C/mn. This phase, representing the progressive vaporization of water obtained at different levels of pressure and temperature of the saturating vapor with variable volume, can be considered as a quasi stationary thermal regime
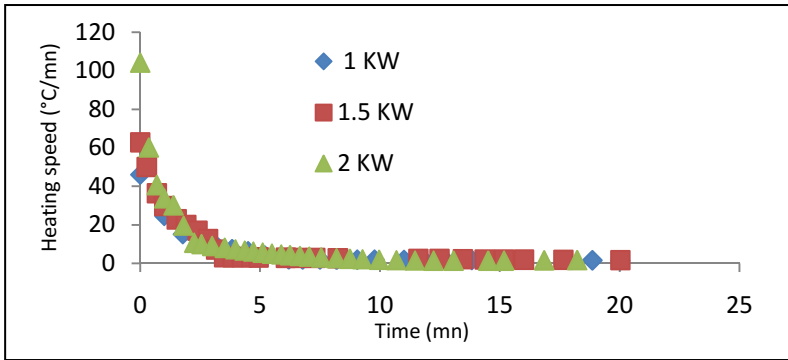
Fig. 3 Evolution of the heating speed

The mixture liquid water and water vapor at starting point (100°C and 1 bar) are in a state of equilibrium. The search of correlations between pressure and temperature of the saturating vapor has shown the existence of empirical models linking the thermodynamic variables explaining the vaporization of water to a variable volume. These models can be written as follows:

$$\frac{P}{P_{max}} = k\left(\frac{T - T_0}{100}\right)^n \tag{1}$$

where P(bar) represents the pressure, T (°C) is the vapor temperature, P_{max} (bar) is a reference pressure equal to 8 bars and T_0, K, n are the coefficients of the model. The identification of the results was obtained with a coefficient of correlation more than 0.98. Tables 1 and 2 present the relative results of the parameters of the different thermal powers applied to the forming process.

Table 1 Model coefficients at $T_0 = 0$°C

Power (KW)	1.0	1.5	2.0
k	0.044	0.038	0.059
n	5.197	5.447	4.583
R^2	0.980	0.980	0.985

Table 2 Model coefficients at n = 4

Power (KW)	1.0	1.5	2.0
k	0.190	0.228	0.127
T_0 (°C)	32.08	37.82	18.37
R^2	0.982	0.981	0.985

The objective fixed by the following study consists in showing:

- The feasibility of sheet metal forming under the action of the saturated vapor.
- The improvement of the sheet forming limits under the effect of vaporization.
- The reduction in the work of vaporization pressure forces compared to the expansion at room temperature.

Figure 4 represents a comparison of the dome height between the room bulging and the warm bulging realized with various thermal powers. We remark a significant increase in the dome height before the initiation of the bursting for the steam tests illustrating an improvement of the forming limits of the sheet metal. This improvement is associated with a significant decrease in the maximum pressure recorded at the bursting. The bursting pressure reaches approximately 11.7 bar at room temperature and 7.2 bar at steam bulging corresponding to relative decrease about 38%.
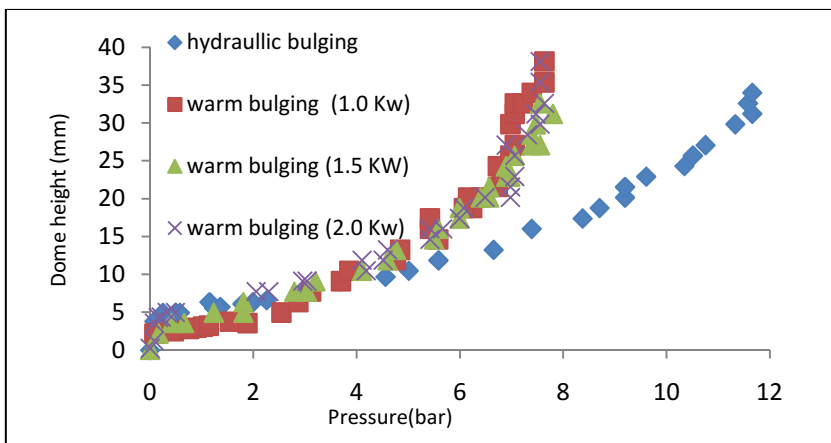
Fig. 4 Evolution dome height versus pressure

4   Interpretation and Discussion of the Results

In this paragraph, we will try to evaluate the performances of the steam bulging compared to the room bulging. Under the pressure the metal will start to bulge and the deformed surface it assumed to a hemispherical shape as shown in figure 5. This deformed surface is characterized by the bulge radius (R), the dome height (h), the die cavity radius (r_0) and the initial thickness of sheet metal (e_0).

Deformed surface
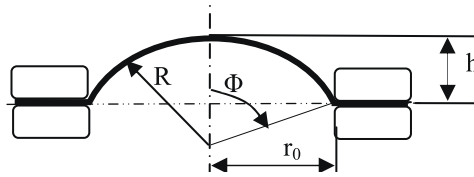
Fig. 5 Schematic diagram of bulge test

The geometrical data (h) and (r_0) allow respectively to evaluate the bulge radius (R), the angle (Φ_0), the surface creation (Sc), the volume (V_0) of the deformed surface, the average values of the circumferential deformation (ε_{mc}), the thickness (e) and the circumferential stress (σ_{mc}). For a bulging test, all these variables are calculated based on the following equations:

$$R = \frac{r_0^2 + h^2}{2h} \tag{2}$$

$$\Phi_0 = \text{arctg}\left(\frac{r_0}{R - h}\right) \tag{3}$$

$$S_c = \pi(2Rh - r_0^2) \tag{4}$$

$$\varepsilon_{mc} = \frac{R\Phi_0}{r_0} \tag{5}$$

$$e_m = e_0 \exp(-2\varepsilon_{mc}) \tag{6}$$

$$\sigma_{mc} = \frac{PR}{2e_m} \tag{7}$$

$$V_0 = \frac{\pi}{3}h^2(3R - h) \tag{8}$$

The bulging pressure (P) and the dome height (h) values at the room temperature and for the different thermal power (1KW, 1.5KW and 2KW) were used for the flow curve calculations. The flow curves in figure 6 represent the material behavior of the aluminum alloy 2017A.
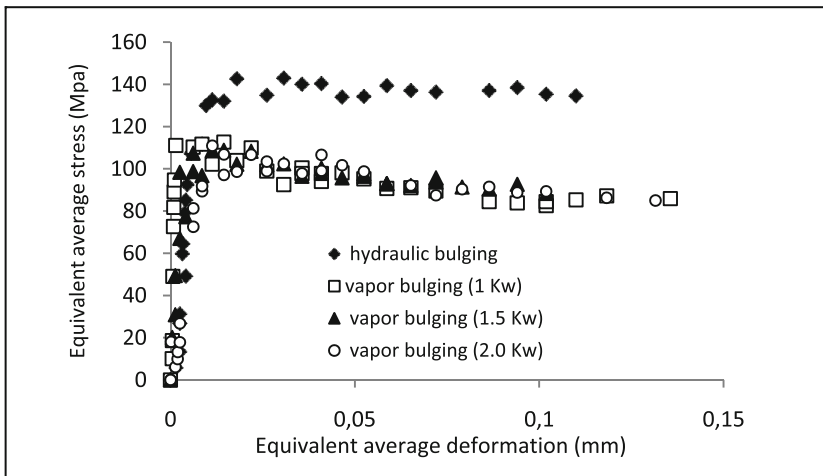
Fig. 6 Stress- strain curves at different testing conditions

The results obtained show:

- A significant decrease of the plastic flow stress. This decrease shows an alloy softening under the vaporization temperature effect.
- An increase in the limit deformations before bursting
- The heating speed has no effect on the alloy behavior at the range of the thermal powers used.

Figure 7 shows for different steam temperature levels, the profile of the circumferential deformations versus the angular positions taken along a median straight cut of the deformed. These deformations were deduced from the experimental thinning blank. We note that the experimental deformation profiles corresponding
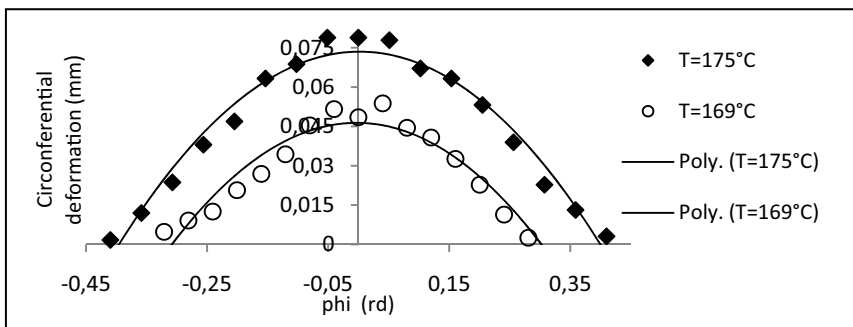
Fig. 7 Profiles of the angular deformations

to the different levels of the temperature can be approximated by parabolic aspects characterized by a maximum located at the dome. These aspects can be represented by the following equation:

$$\varepsilon_c = a\varphi^2 + b \qquad (9)$$

In addition, a comparative study between the proposed models of the prevision average deformation and the same experimental deformations deduced from the thinning measurements at different temperatures, shows coherence as in figure 8.
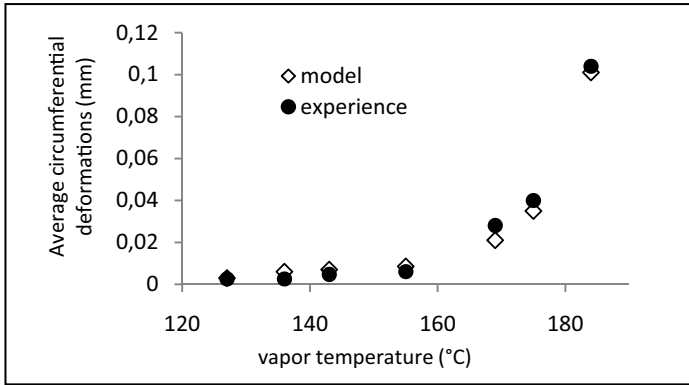
Fig. 8 Average circumferential deformations versus vapor temperature

According to the equation (9), it will be possible to express the circumferential deformation in function of its average value and its angular position as shown in the following equation:

$$\varepsilon_c = \frac{3}{2}\varepsilon_{mc}(1 - \frac{\varphi^2}{\Phi_0^2}) \qquad (10)$$

This expression provides a quick estimation of the maximum deformation after a measurement of the limit dome height. Table 3 summarizes the estimations of deformations and limits stress according to the rolling direction of the sheet.

Table 3 Experimental estimation of deformations and limit stresses from bulging tests

	Deformation (%)	Tress (Mpa)
Room temperature bulging	13.9 à 15.6	134.2
Steam bulging (1 Kw)	18.1 à 20.4	85.9
Steam bulging (1.5 Kw)	13.5 à 15.2	88.3
Steam bulging (2.0 Kw)	18.0 à 19.8	86.4

The estimations presented in table 3 show:

(i)   A little increase of the limit deformations for the steam bulging, with a variations extending between 11.7% and 18.4%.
(ii)   A significant decrease of the limit stresses for the steam bulging with a relative variation about 35%.

The result proves that the thermal power intensity has no direct influence on the forming limit. These limits depend more on the temperature reached during the vaporization phase. Furthermore these limits are controlled by the mechanical properties of the sheet, the dimensions of the active part of the blank (radius and thickness) and the final shape of the finished part.

Figure 9 shows the ratio of the working pressure forces by the surface creation for the bulging operations. The calculation of work was made by transforming the pressure/height curve at the dome into a pressure / volume curve of the spherical cap. The work of the pressure forces is obtained by the following expression:

$$W(P_0) = \int_0^{V_0} P(V)dV$$

(11)

P (V) is obtained by polynomial interpolation of the experimental curve pressure / volume of spherical cap. P_0 is the pressure associated to the volume V_0. In addition, the difference between the surface of the spherical cap and the initial surface of the active portion of the sheet metal defines the created surface. As a result, we can associate for each pressure P_0 a created surface S_C (P_0). So the work of the pressure forces per unit of area created can be   obtained by the ratio:

$$w(P_0) = \frac{W(P_0)}{S_c(P_0)}$$

(12)
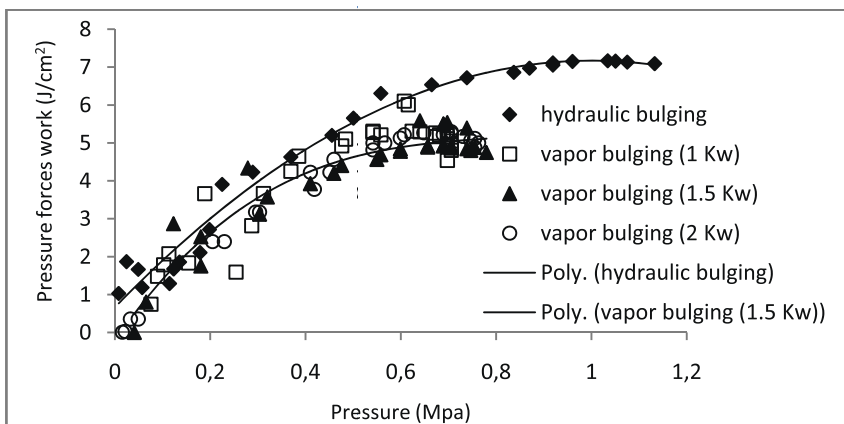
Fig. 9 Ratio of the working pressure forces for the bulging operations

After calculation we get a significant decrease of the pressure forces work for all steam tests. The energetic curves attain a maximum of almost 7.2 J/cm^2 for room test and 5.4 J/cm^2 for steam test. The maximum of the external forces work can be used to introduce the notion of plastic instability according to energetic measure.

5   Conclusion

The experimental study has demonstrated the feasibility of the sheet metal forming under the action of the pressure generated by the vaporization of water. According to the huge advantages offered by the steam forming, we believe that this process certainly can be viable. The forming process is auto-regulated in both pressure and temperature. These thermodynamic variables are controlled by the vaporization process. Their amount depends on the mechanical characteristics of the sheet material then on initial and final geometries of the metal parts. This whole study shows the forming process performance in different levels, particularly we distinguish:

1. The simplification of the loading system used for the forming tests.
2. The important reduction of the energy necessary to forming.
3. The gain of the surface creation and the forming limits, confirmed by the decrease of stress and an increase of deformations.

Finally, the existence of relation that associate the pressure evolution of the vapor and temperature rising could be useful to analyze the temperature influence on metal forming limits. In fact, with vapor forming, we can get a state of pressure and temperature loading by a simple modification of any of the geometrical parameters of the active metal part.

References

1. Toros, S., Ozturk, F., Kacar, I.: Review of warm forming of aluminum-magnesium alloys. Journal of Materials Processing Technology, 2008 207(1-3), 1–1 (2008)
2. Cui, J., Roven, H.J.: Recycling of automotive aluminum. Transactions of Nonferrous Metals Society of China 20(11), 2057–2063 (2010)
3. Yuan, S., He, Z., Liu, G., Wang, X., Han, C.: New developments in theory and processes of internal high pressureforming. The Chinese Journal of Nonferrous Metals 21(10), 2523–2533 (2011)
4. Mult, E.H., Geiger, M.: Sheet and tube hydroforming at elevated temperatures. In: International Conference on Hydroforming, Fellbach, Germany, pp. 259–278 (2003)
5. Lin, Y., He, Z., Yuan, S., Wu, J.: Formability determination of AZ31B tube for IHPF process at elevated temperature. Transactions of Nonferrous Metals Society of China 21(4), 851–856 (2011)

6. Jestwiet, J., Geiger, M., Engel, U.: Metal forming progress since 2000. Journal of Manufacturing Science and Technology, 2008 1(1), 2–17 (2008)
7. Wang, H., Luo, Y., Friedman, P., Chen, M., Gao, L.: Warm forming behavior of high strength aluminum alloy AA7075. Transactions of Nonferrous Metals Society of China 22(1), 1–7 (2012)
8. Mahabunphachai, S., Koc, M.: Investigations on forming of aluminum 5052 and 6061 sheet alloys at warm temperatures. Materials and Design 31(5), 2422–2434 (2010)

A Comparison between Numerical Simulation and Experimental Determination of Porosity

Badiâ Ait El Haj, Aboubakr Bouayad, and Mohammed Alami

Laboratory of Mechanics, Energetics and Materials, Ecole Nationale Supérieure d'Arts et Métiers (ENSAM), Moulay Ismaïl University (UMI), Meknes, Morocco
aitelhaj.badia@gmail.com, a.bouayad@ensam-umi.ac.ma,
alami_simed@hotmail.com

Abstract. Porosity is one of the major defects in aluminum castings, which is induced by several mechanisms (solidification shrinkage and gas segregation). One of the methods for complex evaluation of macro and micro porosity in Al-Si alloys is Tatur test technique. This article deals with evaluation of porosity with help of Tatur test for an Al-Si alloy. The simulation tests were conducted using commercial FEM based software. The simulation results obtained using ProCAST software will be compared with experimental measurement of porosity. Comparison has shown good agreement of simulation and experiment in predicting and localizing the major defects of shrinkage except for slump defect in top part of the casting which would mean, that the solidification modeling included in the tested software does not reflect phenomena responsible for the solidification processes in real castings properly. Further tests, with different types of software and more fundamental studies on the solidification process modeling would be desirable.

Keywords: Al9Si alloy, casting, Tatur test, porosity, simulation.

1 Introduction

Nowadays there is a great demand of lightweight parts with high mechanical performances. Over the past decades, aluminum components have been produced to substitute cast iron components. When the substitution is possible, low costs production and component weight reduction is obtained due to their great production rate and process control. (Dobrzanski et al. 2007; Mallapur et al., 2010; Hosseini et al., 2013)

In the past decades, the rapid development of numerical simulation methodology and the solidification simulation of castings have been introduced as an effective tool for modeling the casting process and improving the quality of castings. The use of simulation software saves time and reduces the costs of the casting-system design and of the materials used. The field of solidification modeling covers micro- and

macrosegregation, microstructure and defect formation, and thermomechanical aspects. Simulations are becoming increasingly more sophisticated and accurate as a result of refined physical models, improved thermodynamic, thermophysical and mechanical data, development of powerful numerical techniques and the availability of affordable and powerful computers. (Gandin ch.-A, Rappaz M, 1994 ; Rappaz M, Gandin ch.-A, 1993).

It is commonly accepted that the shrinkage and the gas inclusions are the two major causes of porosity. The shrinkage porosity is associated with the "hot spots" in the casting. The gas porosity is caused by entrapped air or gas in the liquid metal and the cavity, the gas generated from burned lubricants, the water in the cavity and hydrogen. The porosity of castings can be examined with destructive testing, with visual observation after machining and non-destructing testing, like X-ray microscopy and image-processing technology, which can provide more detailed information about the pores. It is also observed that the chemical composition of the alloy, the grain refinement and the modification affect the porosity of the cast components. (Dobrzanski et al., 2007; Gunasegaram et al., 2009; Jose Manuel ROZOT, 2005)

The paper focuses on tatur test as a porosity quantifier. It describes the comparison of an AlSi9 casting specimen in a steel die and the simulation of the test by ProCAST APM model (Pequet et al. 2002). The Tatur test, which is optimal for assuming complex macro and microporosity, will allow qualitative and quantitative porosity description.

2 Materials and Methods

2.1 Tatur Test

The Tatur test is a technique used to assess macro and micro porosity in Al-Si alloys. The test uses a permanent mold of standard geometry shown in Fig. 1.
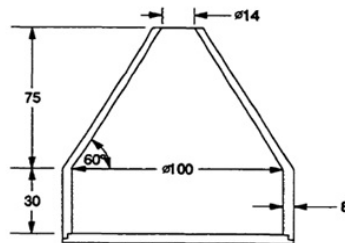
Fig. 1 Dimensions of Tatur test (mm)
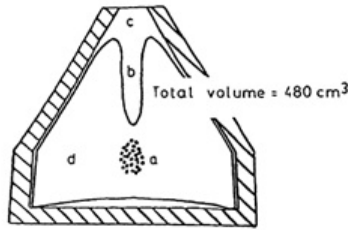
Fig. 2 a) microporosity, b) pipe volume, c) slumping and contraction volume, d) actual casting volume

Slumping and contraction, macroshrinkage (pipe) and microshrinkage can be assessed by density measurement (Fig. 2). (Brůna et al.2012)

2.2   Experimental Procedure

In this study we used a silicon aluminum alloy whose chemical composition corresponding to average values of three measurements in the sample is obtained by spectrometry, is shown in Table 1:

Table 1 Chemical composition of the casting alloy (wt.%)

Alloy	Si	Mg	Fe	Cu	Zn	Mn	Ti	Pb	Al
AS9	8.687	0.021	0.413	0.058	0.294	0.190	0.01	<0.001	Bal.

For these experiments, the alloy was melted in silicon carbide crucibles using a resistive furnace. The alloy was melted until the metal reached 700°C prior pouring the molten metal in Tatur mold. To be in similar configurations in each experiment, we measure the initial temperature of the mold. This latter will be preheated to 150 °C prior to casting.

2.3   Numerical Simulation

One of the most often-applied numerical methods for modeling of casting filling and solidification processes and predicting defaults in casting is the Finite elements method (FEM). Computer simulation software, such as ProCAST, is widely used to these purposes.

In this study, the comparative calculations were carried out by simulating the casting of aluminum alloy Al-9Si in an H13 steel die (Tatur mold) using ProCAST software in order to assess the quality of casting and location of shrinkable defects. The pouring temperature was 700 ° C, and the initial mold temperature was 150 ° C.

The simulation was performed for the shrinkage mold. A mesh composed of tetrahedral elements (17 664 nodes, 81 735 elements, the average characteristic size 2.2 mm) was used. Aluminum alloy AlSi9 thermomechanical properties were assigned to the specimen, Technology included casting in metal mold of aluminum alloy AS9 with chemical compound, %: Si - 9; Mn - 0.4; Mg - 0.15; Ti - 0.2; Ni - 0.1; Cu -0.25; Zn - 0.2. Liquidus temperature is 598 °C, solidus temperature is 546 °C.

3   Results and Discussion

The evolution of the liquid fraction in the specimen allows obtaining information on changes in the solidification with time.
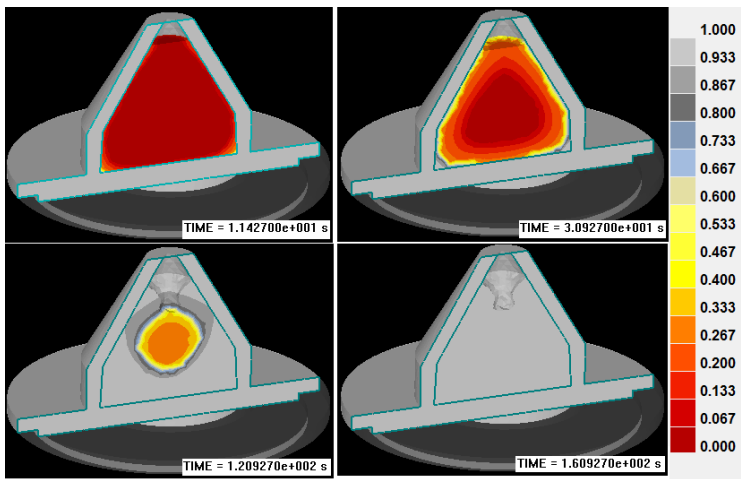
Fig. 3 Evolution of solid fraction of casting in function of time – PROCAST

The Tatur test utilizes a steel permanent mold of fixed geometry containing two parts kept in contact during the filling. Fig. 3 shows the evolution of solid fraction during solidification. Considering the geometry of the mold, the solidification occurs first at the extremities of the cast and propagated to the center of the specimen (hot spot) which will be subjected to tension. (Fig. 3), wherein the solid phase is represented in gray and the liquid phase in red, illustrates this principle. The solidification time is nearly 161 seconds.

These heat maps (Fig. 4) show the evolution of the temperature during solidification. It is observed that the last point to solidify in the center of the specimen which will ineluctably contain the shrinkage defect.

Moreover, It is observed that the shrinkage porosity (i.e. liquid regions completely surrounded by the solid) appeared in the area around the center and areas without porosity are most likely near the metal mold (Fig. 5).
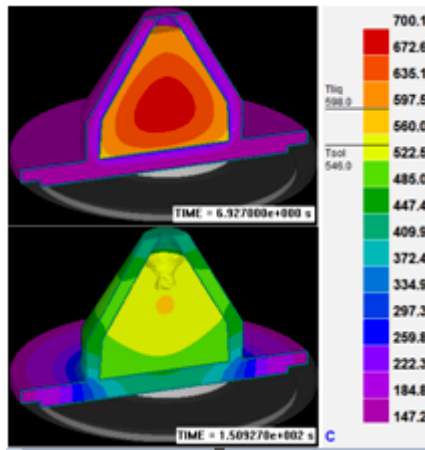
Fig. 4 Evolution of Temperature in function of time
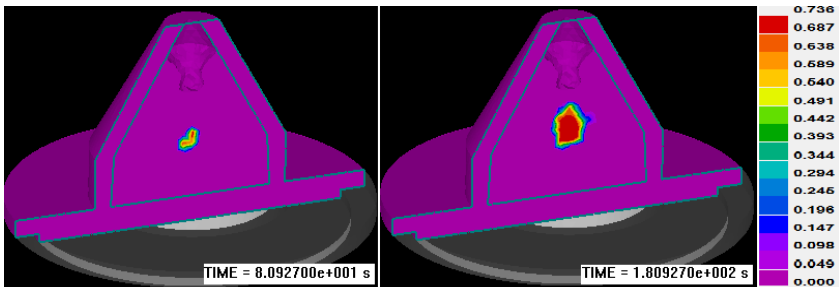
Fig. 5 Probability of formation of shrinkable defects (porosity) in casting alloy - ProCAST

Fig. 6 Shapes and positions of internal and external shrinkage cavities

In castings poured in Tatur mold we notice, as shown in Fig. 6, that various forms of internal and external porosities. The areas in contact with the metallic mold do not show any porosity. The shrinkage porosity is concentrated around the center line of the specimen. However, on the contrary of simulation, it is observed the absence of slump on the top of the specimen.

Noticeably, the final quality of the castings and the solidification shrinkage occurring in a closed pocket of liquid were predicted by ProCAST. However, the external macroporosity i.e. the solidification shrinkage occurring at the free surface are not taken into account by the used software.

4   Conclusion

In the present work, a comparison between porosity prediction in Tatur test was performed using ProCAST, a FEM-based software, and experiments. The simulation gives valuable information for the final quality of the castings. Moreover, we can assume that simulation is overall in good agreement with experiments in predicting and localizing the major defects of shrinkage. Nevertheless, solidification simulation results have shown the possibility of shrinkage defect appearance in the top part of casting (slumb) that is not completely in good agreement with the experimental results.

The assumption as the possible reason of inadequate modeling of solidification of casting can be inexact thermodynamic, thermophysical and mechanical data as a function of temperature. Obviously, comparisons between these input data and experimental ones would be beneficial. Another step would be to carry out simulations similar to those described in the present study, using other commercial software packages.

A practical conclusion resulting from the present study is that simulated solidification results, in the form of the shrinkage defects distribution, should be utilized with great care. The issues related to solidification modeling and shrinkage porosity formation in solidifying castings certainly require further studies.

References

Pequet, Ch., Gremaud, M., Rappaz, M.: Modelling of microporosity, macroporosity, and pipe-phrinkage formation during the solidification of alloys using a mushy-zone refinement method: applications to Aluminium alloys. Metallurgical and Materials Transactions 33A, 2095–2105 (2002)

Gandin, Ch.-A., Rappaz, M.: A coupled finite element-cellular automaton model for the prediction of dendritic grain structures in solidification processes. Acta Metal. Mater. 42(7), 2233–2246 (1994)

Rappaz, M., Gandin, Ch.-A.: Probabilistic modelling of microstructure formation in solidification processes. Acta Metal. Mater 41(2), 345–360 (1993)

Dobrzanski, L.A., Manaiara, R., Sokolowski, J.H.: The effect of cooling rate on microstructure and mechanical properties of AC AlSi9Cu alloy. Archives of Materials Science and Engineering 28, 105–112 (2007)

Gunasegaram, D.R., Farnsworth, D.J., Nguyen, T.T.: Identification of critical factors affecting shrinkage porosity in permanent mold casting using numerical simulations based on design of experiments. Journal of Materials Processing Technology 209, 1209–1219 (2009)

Rozot, J.M.: Modèle prédictif de l'apparition de la microporosité de retrait durant la solidification d'un alliage Aluminium-Silicium (Ph.D. thesis, Université de BORDEAUX 1) (2005)

Brůna, M., Sládek, A., Kucharčík, L.: Formation of porosity in Al-Si alloys. Archives of Foundry Engineering 12(1), 5–8 (2012), doi:10.2478/v10266-012-0001-5

Mallapur, D.G., Rajendra Udupa, K., Kori, S.: Influence of grain refiner and modifier on the microstructure and mechanical properties of a 356 alloy. International Journal of Engineering Science and Technology 2(9), 4487–4493 (2010) ISSN: 0975-54624487

Hosseini, V.A., Shabestari, S.G., Gholizadeh, R.: study on the effect of cooling rate on the solidification parameters, microstructure, and mechanical properties of lm13 alloy using cooling curve thermal analysis technique. Materials and Design 50, 7–14 (2013), `http://dx.doi.org/10.1016/j.matdes.2013.02.088`

Dobrzanski, L.A., Krupinski, M., Krupinska, B.: Structure analysis of Al cast alloy. Journal of achievements in Materials and Manufacturing Engineering 27(1), 23–26 (2007)

Efficient Layerwise Finite Element Model for Multilayer Sandwich Plates Analysis

Mohamed Ouejdi Belarbi[1], Abdelouahab Tati[2], and Abdelhak Khechai[3]

[1,2] Laboratory of Energy Engineering and Materials (LGEM),
University of Biskra, BP 145, 07000 Biskra, Algeria
`belarbi.m.w@gmail.com, abdeltati@yahoo.fr`
[3] Laboratory of Civil Engineering (LRGC), University of Biskra,
BP 145, 07000 Biskra, Algeria
`abdelhak_khechai@hotmail.fr`

Abstract. In this paper, a new 2D quadrilateral finite element model, based on the layerwise approach, is developed for bending and free vibration analysis of multilayer sandwich plates. Unlike any other layerwise theory, the number of degrees of freedom in this present model is independent of the number of layers. Both, high order and first order shear deformation theories are used in order to model the core and face-sheets respectively. This combined theory satisfies the compatibility conditions as well as continuity of displacements, at the interface. The numerical results obtained by our model are compared favorably with those obtained via analytical solution and numerical results obtained by other models.

Keywords: layerwise, finite element, sandwich plates, bending, free vibration.

1   Introduction

Due to their low weight, high stiffness and high strength properties, the composites sandwich structures are widely used in various industrial areas, e.g. civil constructions, marine industry. However, due to their rigidity and material properties variation between the core and the face sheets, the effect of shear deformation and stresses in sandwich structures can be a major reason for the material failures.

In the literature, several 2D theories have been proposed to study the behavior of composite sandwich structures. Two approaches can be distinguished: The Equivalent Single Layer approach (ESL) and The Layerwise approach (LW). The ESL approach can be divided into three major theories, namely: (1) the classical laminated plate theory (CLPT); (2) the first order shear deformation theory (FSDT); and (3) the higher order shear deformation theories (HSDT).

However, the ESL approach is unable to predict accurately the local behavior (e.g. interlaminar stresses) of sandwich structures. For that reason, many researchers developed more accurate theories such as the zig–zag theories (ZZT) (Pandit et al. 2008; Khandelwal et al. 2013) and the global-local higher order shear deformation

theories (GLHSDT) (Zhen,Wanji 2010). Recently, various works have adopted the LW approach (Linke et al. 2007; Oskooei,Hansen 2000; Maturi et al. 2014; Ćetković,Vuksanović 2009) to assume separate displacement field expansions within each material layer, thus providing a kinematically correct representation of the strain field in discrete laminated layer, and allowing accurate determination of ply level stresses (Reddy 1993).

In the finite elements development, many researchers have adopted the LW approach for the sake of a good description of sandwich structures. On this topic, we can distinguish the work of Oskooei,Hansen (2000) and Nabarrete et al. (2003), where a 3D layerwise finite element model is developed for the static and free vibration analysis of sandwich plates, respectively. They used the FSDT to model the face sheets, whereas the HSDT was adopted for the core. In addition, an 18-nodes 3D brick mixed finite element with 6 DOF per node, has been developed by Ramtekkar et al. (Ramtekkar et al. 2003) for an accurate evaluation of transverse stresses in laminated sandwich. Linke et al. (2007) developed a 3D layerwise finite element model containing 11 DOF at each node for static and stability analysis of sandwich plates. Later, Ćetković,Vuksanović (2009) used a LW displacement model of Reddy to study bending, free vibration and buckling of laminated composite and sandwich plates.

Unlike layerwise models, mentioned above, that the number of variables dramatically increases with the number of layers, which requires high computational effort, in this work a new 2D layerwise finite element model has been developed for the bending and free vibration analysis of laminated composite and sandwich plates, where the number of variables in this present model is independent of the number of layers. The results obtained from this investigation will be useful for a more understanding of the bending and free vibration behavior of sandwich laminates plates.

2   Mathematical Model

Sandwich plate is a structure composed of three principal layers as shown in Fig.1, two face sheets (top-bottom) of thicknesses (h_t), (h_b) respectively, and a central layer named core of thickness (h_c) which is thicker than the previous ones. Total thickness (h) of the plate is the sum of these thicknesses. The plane (x, y) coordinate system coincides with mi-plane plate.
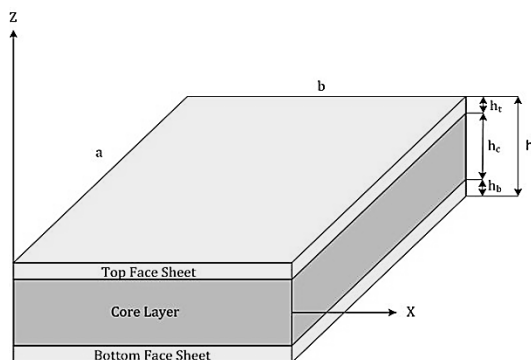
Fig. 1 Geometry and notations of a sandwich plate

2.1   Kinematic Assumptions for the Core

In the proposed model, the core is modeled using the HSDT. The through-thickness variation of in-plane displacements (u and v) and transverse displacement (w) may be expressed, respectively as follows:

$$
\begin{aligned}
u_c &= u_0 + z\psi_x^c + z^2\eta_x^c + z^3\zeta_x^c \\
v_c &= v_0 + z\psi_y^c + z^2\eta_y^c + z^3\zeta_y^c \\
w_c &= w_0
\end{aligned}
\tag{1}
$$

Where u_0, v_0 and w_0 are respectively, in-plane and transverse displacement components at the mid-plane of the sandwich plate. ψ_x^c, ψ_y^c represent normal rotations about the x and y axis respectively. The parameters η_x^c, η_y^c, ζ_x^c and ζ_y^c are higher order terms.

The strain-displacement relationships can be written in the following form:

$$
\begin{aligned}
\varepsilon_{xx} &= \varepsilon_x^{(0)} + z\chi_x^{(1)} + z^2\chi_x^{(2)} + z^3\chi_x^{(3)} \\
\varepsilon_{yy} &= \varepsilon_y^{(0)} + z\chi_y^{(1)} + z^2\chi_y^{(2)} + z^3\chi_y^{(3)} \\
\gamma_{xy} &= \gamma_{xy}^{(0)} + z\chi_{xy}^{(1)} + z^2\chi_{xy}^{(2)} + z^3\chi_{xy}^{(3)} \\
\gamma_{yz} &= \gamma_{yz}^{(0)} + z\chi_{yz}^{(1)} + z^2\chi_{yz}^{(2)} \\
\gamma_{xz} &= \gamma_{xz}^{(0)} + z\chi_{xz}^{(1)} + z^2\chi_{xz}^{(2)}
\end{aligned}
\tag{2}
$$

2.2 Kinematic Assumptions for the Face Sheets

The face sheets are modeled using the FSDT. The compatibility conditions as well as the displacement continuity at the interface (top face-sheet-core- bottom face-sheet), leads to the following improved displacement fields:

Top face sheet:

$$u_t = u_0 + \left(\frac{h_c}{2}\right)\psi_x^c + \left(\frac{h_c^2}{4}\right)\eta_x^c + \left(\frac{h_c^3}{8}\right)\zeta_x^c + \left(z - \frac{h_c}{2}\right)\psi_x^t$$

$$v_t = v_0 + \left(\frac{h_c}{2}\right)\psi_y^c + \left(\frac{h_c^2}{4}\right)\eta_y^c + \left(\frac{h_c^3}{8}\right)\zeta_y^c + \left(z - \frac{h_c}{2}\right)\psi_y^t \qquad (4)$$

$$w_t = w_0$$

Bottom face sheet:

$$u_b = u_0 - \left(\frac{h_c}{2}\right)\psi_x^c + \left(\frac{h_c^2}{4}\right)\eta_x^c - \left(\frac{h_c^3}{8}\right)\zeta_x^c + \left(z + \frac{h_c}{2}\right)\psi_x^b$$

$$v_b = v_0 - \left(\frac{h_c}{2}\right)\psi_y^c + \left(\frac{h_c^2}{4}\right)\eta_y^c - \left(\frac{h_c^3}{8}\right)\zeta_y^c + \left(z + \frac{h_c}{2}\right)\psi_y^b \qquad (5)$$

$$w_b = w_0$$

The strain-displacement relationships of the top face-sheet are given by:

$$\varepsilon_{xx}^t = \frac{\partial u_t}{\partial x} = \frac{\partial u_0}{\partial x} + \left(\frac{h_c}{2}\right)\frac{\partial \psi_x^c}{\partial x} + \left(\frac{h_c^2}{4}\right)\frac{\partial \eta_x^c}{\partial x} + \left(\frac{h_c^3}{8}\right)\frac{\partial \zeta_x^c}{\partial x} + (z - \frac{h_c}{2})\frac{\partial \psi_x^t}{\partial x}$$

$$\varepsilon_{yy}^t = \frac{\partial v_t}{\partial y} = \frac{\partial v_0}{\partial x} + \left(\frac{h_c}{2}\right)\frac{\partial \psi_y^c}{\partial y} + \left(\frac{h_c^2}{4}\right)\frac{\partial \eta_y^c}{\partial y} + \left(\frac{h_c^3}{8}\right)\frac{\partial \zeta_y^c}{\partial y} + (z - \frac{h_c}{2})\frac{\partial \psi_y^t}{\partial y}$$

$$\gamma_{xy}^t = \frac{\partial u_t}{\partial y} + \frac{\partial v_t}{\partial x} = \left(\frac{\partial u_0}{\partial y} + \frac{\partial v_0}{\partial x}\right) + \frac{h_c}{2}\left(\frac{\partial \psi_x^c}{\partial y} + \frac{\partial \psi_y^c}{\partial x}\right) + \frac{h_c^2}{4}\left(\frac{\partial \eta_x^c}{\partial y} + \frac{\partial \eta_y^c}{\partial x}\right) \qquad (6)$$

$$+ \frac{h_c^3}{8}\left(\frac{\partial \zeta_x^c}{\partial y} + \frac{\partial \zeta_y^c}{\partial x}\right) + (z - \frac{h_c}{2})\left(\frac{\partial \psi_x^t}{\partial y} + \frac{\partial \psi_y^t}{\partial x}\right)$$

$$\gamma_{yz}^t = \frac{\partial w_0}{\partial y} + \psi_y^t, \quad \gamma_{xz}^t = \frac{\partial w_0}{\partial x} + \psi_x^t$$

The same steps are followed to elaborate the strain-displacement relationships of the bottom face sheet.

2.3   Constitutive Relationships

In this work, the two face sheets (top and bottom) are considered as laminated composite, where the core is considered as an orthotropic composite material. So, the stress-strain relationship in the global coordinate system is given by:

$$\left[\sigma^{(k)}\right] = \left[Q^{(k)}\right]\left[\varepsilon^{(k)}\right] \tag{7}$$

The efforts resultants of the core are obtained by integration of the stresses through the thickness direction of laminated plate:

$$
\begin{Bmatrix} N \\ M \\ \overline{N} \\ \overline{M} \end{Bmatrix} =
\begin{bmatrix} [A] & [B] & [D] & [E] \\ [B] & [D] & [E] & [F] \\ [D] & [E] & [F] & [G] \\ [E] & [F] & [G] & [H] \end{bmatrix}
\begin{Bmatrix} \varepsilon^{(0)} \\ \chi^{(1)} \\ \chi^{(2)} \\ \chi^{(3)} \end{Bmatrix} ,\quad
\begin{Bmatrix} V \\ S \\ R \end{Bmatrix} =
\begin{bmatrix} [A^s] & [B^s] & [D^s] \\ [B^s] & [D^s] & [E^s] \\ [D^s] & [E^s] & [F^s] \end{bmatrix}
\begin{Bmatrix} \gamma_s^{(0)} \\ \chi_s^{(1)} \\ \chi_s^{(2)} \end{Bmatrix} \tag{8}
$$

3   Finite Element Formulation

The developed finite element, named QSFT52, is a C^0-continuous four-node quadrilateral isoparametric sandwich plate element with thirteen DOF per node. Each face-sheet has only two rotational DOF per node and the core has 9 DOF per node: six rotational degrees and three translation components which are common for the all sandwich layers (Fig.2).
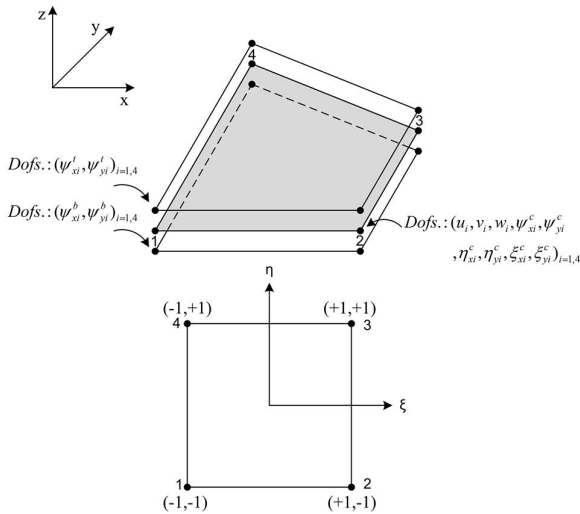
Fig. 2 Geometry and corresponding degrees of freedom of the QSFT52 element

The displacements vectors δ at any point of coordinates (x, y) of the plate are given by:

$$\delta(x, y) = \sum_{i=1}^{n} N_i(x, y)\,\delta_i \tag{9}$$

where N_i are the interpolation functions associated with the node i.

The nodal displacement vector of the present element is defined by:

$$\delta_i = \left\{ u_i\ \ v_i\ \ w_i\ \ \psi_{xi}^c\ \ \psi_{yi}^c\ \ \eta_{xi}^c\ \ \eta_{yi}^c\ \ \zeta_{xi}^c\ \ \zeta_{yi}^c\ \ \psi_{xi}^t\ \ \psi_{yi}^t\ \ \psi_{xi}^b\ \ \psi_{yi}^b \right\}^T$$

3.1   Equilibrium Equations

The governing differential equations of motion can be derived using Hamilton's principle

$$\delta\Pi = \delta\int_{t_1}^{t_2} \left(\delta U - \delta T + \delta W\right) dt = 0 \tag{10}$$

where t is the time, U is the total strain energy of the system, T is the total kinetic energy of the system and W is the work done by the external forces

Using the standard finite element procedure, the governing differential equations of motion, for free vibration, can be rewritten as

$$[M]\{\ddot{\delta}\} + [K]\{\delta\} = 0 \tag{11}$$

where the total element stiffness matrix:

$$[K] = \sum_e \int_{-1}^{1}\int_{-1}^{1} \left(\left[B^t\right]^T \left[D^t\right]\left[B^t\right] + \left[B^c\right]^T \left[D^c\right]\left[B^c\right] + \left[B^b\right]^T \left[D^b\right]\left[B^b\right] \right) \det(J)\, d\xi d\eta \tag{12}$$

and the element mass matrix:

$$[M] = \sum_e \int_{-1}^{1}\int_{-1}^{1} \left([N]^T \left[m^{(t)}\right][N] + [N]^T \left[m^{(c)}\right][N] + [N]^T \left[m^{(b)}\right][N] \right) \det(J)\, d\xi d\eta \tag{13}$$

Now, after evaluating the stiffness and mass matrices for all elements, the governing equations for free vibration analysis can be stated in the form of generalized eigenvalue problem.

$$[K_T]\{\chi\} - \omega^2 [M_T]\{\chi\} = 0 \tag{14}$$

4 Numerical Results and Discussions

4.1 Symmetric Square Sandwich Plate Subjected to a Sinusoidal Load

For static analysis, a simply supported square sandwich plate subjected to sinusoidal load is considered. The material properties of the sandwich plate are presented in table 1. The thickness of each face sheet is 0.1h and the thickness of the core is 0.8h, where h is the total thickness of the plate. The non-dimensional results of transverse displacement and transverse shear stress, for different mesh sizes and thickness ratios, are displayed on Table 2. It is found that the present results especially for the transverse shear stresses, are in excellent agreement with those obtained by the elasticity solution given by Pagano (1970) and other finite elements models based on higher order zig-zag theory (HOZT) (Khandelwal et al., 2013 and Pandit et al., 2008), which shows the performances, the accuracy and the convergence of the proposed finite element model.

Table 1 Material properties for sandwich plate

		Elastic properties					
	Location	E_{11}	E_{22}	G_{12}	G_{13}	G_{23}	ν_{12}
Sandwich plates	Core	0.04E	0.04E	0.016E	0.06E	0.06E	0.25
	Face	25E	E	0.500E	0.5E	0.20E	0.25

Table 2 Normalized maximum deflection and transverse shear stresses at the important points of a simple supported square sandwich plate under sinusoidal loading

$\dfrac{h}{a}$	Reference		$\bar{\tau}_{xz}\left(0,\dfrac{b}{2},0\right)$	$\bar{\tau}_{yz}\left(\dfrac{a}{2},0,0\right)$	$\bar{w}\left(\dfrac{a}{2},\dfrac{b}{2},0\right)$
0.05	Present (10×10)	QSFT52	0.3025	0.0407	1.1953
	Present (12×12)	QSFT52	0.3069	0.0393	1.2058
	Present (16×16)	QSFT52	0.3115	0.0379	1.2164
	(Pagano 1970)	Elasticity	0.3174	0.0361	1.2264
	(Pandit et al. 2008)	HOZT	0.3342	0.0392	1.2254
	(Khandelwal et al. 2013)	HOZT	0.3374	0.0415	1.2128
0.1	Present (10×10)	QSFT52	0.2880	0.0534	2.2036
	Present (12×12)	QSFT52	0.2916	0.0532	2.2075
	Present (16×16)	QSFT52	0.2952	0.0530	2.2115
	Pagano (1970)	Elasticity	0.3000	0.0530	2.2004
	Pandit et al. (2008)	HOZT	0.3158	0.0570	2.2002
	Khandelwal et al. (2013)	HOZT	0.3185	0.0598	2.1786
0.2	Present (10×10)	QSFT52	0.2476	0.0903	5.5599
	Present (12×12)	QSFT52	0.2505	0.0908	5.5571
	Present (16×16)	QSFT52	0.2535	0.0913	5.5554
	Pagano (1970)	Elasticity	0.2569	0.0918	5.4746
	Khandelwal et al. (2013)	HOZT	0.2530	0.1025	5.4464

4.2 Free Vibration Analysis of Un-Symmetric Laminated Sandwich Plate

To assess the performance of our model to the thin as well as thick plate, a simply supported square sandwich plate with un-symmetric laminated face sheets $(0/90/C/0/90)$ is considered. The mechanical properties of the sandwich plate are presented in table 3. The thickness ratio (a/h) is considered to vary from 2 to 100, where the ratio of thickness of core to thickness of face sheet (h_c/h_f) is considered as 10. The comparison of the non-dimensional results of natural frequencies $\overline{\omega} = \omega b^2/h \sqrt{\rho_c/E_{22f}}$, considering mesh size (12 × 12), are shown in figure 3, with those obtained by the 3D-elasticity solution (Rao et al. 2004), the FEM-Q8 solution based on GLHSDT (Zhen et al. 2010) and the analytical results (Kant,Swaminathan 2001).

Table 3 Material properties for laminated sandwich plate

Material	Elastic properties						
	E_{11}	E_{22}	G_{12}	G_{13}	G_{23}	ν_{12}	ρ (Kg/m^3)
Face	131	10.34	6.9	6.9	6.9	0.22	1627
Core	0.0069	0.0069	0.0034	0.0034	0.0034	10^{-5}	97
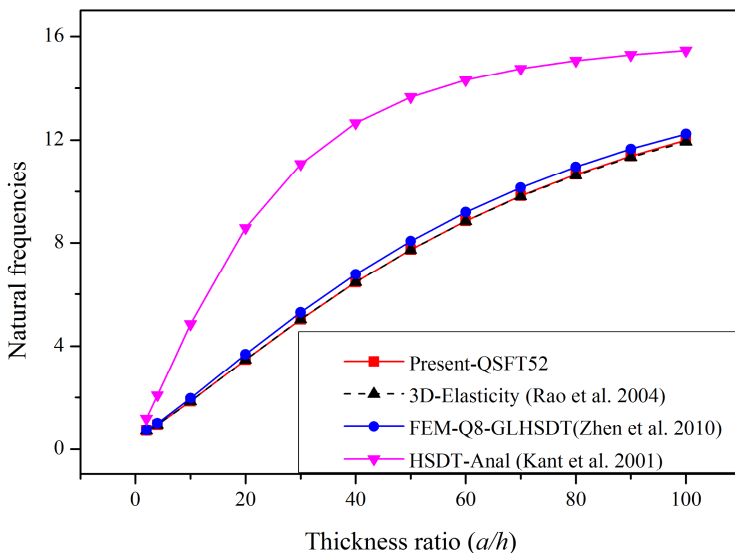
Fig. 3 Simply supported square sandwich plate with un-symmetric laminated face sheets for different thickness ratios (*a/h*). Comparison of natural frequencies
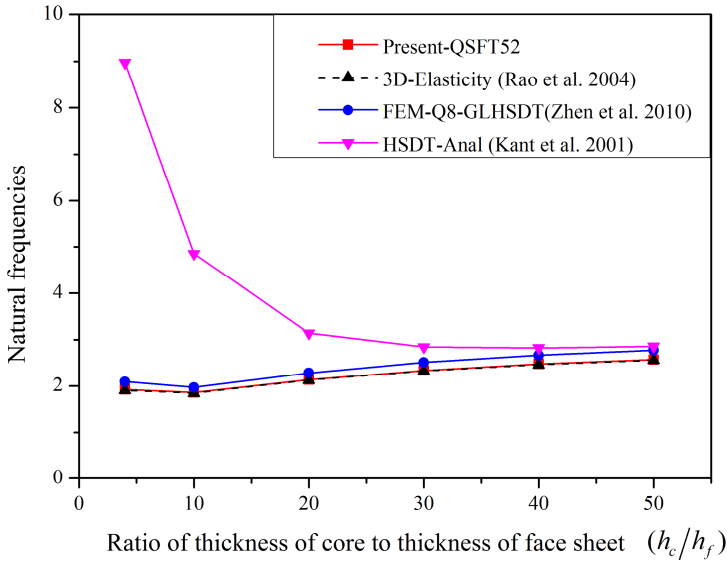
Fig. 4 Simply supported square sandwich plate with un-symmetric laminated face sheets for different ratios (h_c/h_f). Comparison of natural frequencies

Moreover, it was seen, from the figure 4 that the values of non-dimensional natural frequencies $(\bar{\omega})$ increase when increasing h_c/h_f ratio. This is due to the effect of the thickness of the core which has an important role in the sandwich plates. The results of our developed element are very good agreement, which confirm the good performance of the proposed formulation. It can be noticed that the present finite element model is applicable in both thick and thin sandwich plates.

5   Conclusion

In this work, a new isoparametric finite element model, based on the layerwise approach, has been developed for the bending and free vibration analysis of multilayer sandwich plates. The proposed model is based on a proper combination of higher-order and first-order, shear deformation theories. The results obtained by our model were compared with those obtained by the analytical results and other finite element models found in literature, which show that the element has excellent accuracy and a broad range of applicability. The use of the proposed finite element and the combination of the first order shear deformation theory and the higher-order plate theory, used respectively to modulate the face sheets and the core of sandwich, showed a good accuracy and convergence speed for both thin and thick plates.

References

Ćetković, M., Vuksanović, D.: Bending, free vibrations and buckling of laminated composite and sandwich plates using a layerwise displacement model. Composite Structures 88(2), 219–227 (2009)

Kant, T., Swaminathan, K.: Free Vibration Of Isotropic, Orthotropic, and Multilayer Plates Based on Higher Order Refined Theories. Journal of Sound and Vibration 241(2), 319–327 (2001)

Khandelwal, R., Chakrabarti, A., Bhargava, P.: An efficient FE model based on combined theory for the analysis of soft core sandwich plate. Computational Mechanics 51(5), 673–697 (2013)

Linke, M., Wohlers, W., Reimerdes, H.-G.: Finite element for the static and stability analysis of sandwich plates. Journal of Sandwich Structures and Materials 9(2), 123–142 (2007)

Maturi, D.A., Ferreira, A.J.M., Zenkour, A.M., Mashat, D.S.: Analysis of sandwich plates with a new layerwise formulation. Composites Part B: Engineering 56(0), 484–489 (2014)

Nabarrete, A., De Almeida, S.F.M.: Sandwich-plate vibration analysis: three-layer quasi-three-dimensional finite element model. AIAA Journal 41(8), 1547–1555 (2003)

Oskooei, S., Hansen, J.: Higher-order finite element for sandwich plates. AIAA Journal 38(3), 525–533 (2000)

Pagano, N.: Exact solutions for rectangular bidirectional composites and sandwich plates. Journal of Composite Materials 4(1), 20–34 (1970)

Pandit, M.K., Sheikh, A.H., Singh, B.N.: An improved higher order zigzag theory for the static analysis of laminated sandwich plate with soft core. Finite Elements in Analysis and Design 44(9), 602–610 (2008)

Ramtekkar, G., Desai, Y., Shah, A.: Application of a three-dimensional mixed finite element model to the flexure of sandwich plate. Computers & Structures 81(22), 2183–2198 (2003)

Rao, M., Scherbatiuk, K., Desai, Y., Shah, A.: Natural Vibrations of Laminated and Sandwich Plates. Journal of Engineering Mechanics 130(11), 1268–1278 (2004)

Reddy, J.N.: An evaluation of equivalent-single-layer and layerwise theories of composite laminates. Composite Structures 25(1-4), 21–35 (1993)

Zhen, W., Wanji, C.: A C0-type higher-order theory for bending analysis of laminated composite and sandwich plates. Composite Structures 92(3), 653–661 (2010)

Numerical Optimization Method to Model Crack Propagation

Hamdi Hentati[1], Radhi Abdelmoula[2], and Aref Maalej[1]

[1] LASEM, University of Sfax, Tunisia
 `hamdi.hentati@yahoo.fr`
[2] LSPM, University of Paris XIII, Villetaneuse, France

Abstract. In this work, we present numerical simulations of the quasi static crack propagation based on the variational approach. An alternate minimizations algorithm is used. Based on these numerical results, we show the importance of trying to optimize the time of numerical computation and we present the first attempt to develop a simple numerical method to optimize this time.

Keywords: Fracture mechanics, Optimization, variational approach.

1   Introduction

The main goal of fracture mechanics is to determine the crack propagation in a continuous medium as a function of the applied load. The developments related to the theory of brittle fracture are mainly based on the ideas of (Griffith 1921). In numerical level, the fracture mechanics has been revisited by proposing different models of quasi static growth of brittle fracture in linearly elastic bodies inspired from the classical Griffith's criterion. The variational theory (Francfort 1998) was developed by (Bourdin et al. 2000) aiming to model brittle fracture. The new functional, parameterized by ε, is defined by:

$$E(u,\alpha) = \frac{\mu}{2}\int_{\Omega}\left(\left\{(1-\alpha)^2 + \varepsilon(\eta)\right\}|\nabla u|^2 + G_c\left\{\frac{\alpha^2}{4\eta} + \eta|\nabla\alpha|^2\right\}\right)d\Omega \qquad (1)$$

Where u is the displacement field, α is the damage variable and ε and η are numerical parameters.

In order to simulate the crack propagation based on the variational theory, (Bourdin et al. 2008) employ a numerical method based on alternate minimization algorithm.

In this formulation, the regularized energy is made of two parts to a displacement modeled by u and a crack state of a material modeled by α. The first part is equal to the elastic energy, computed at the places where the material is not cracked, while the second one is proportional to the crack area.

Based on the research works (Hentati et al. 2012), the choice of the mesh size h is a compromise between the value of parameter η and the maximum capacity of

the processor to perform the calculation. We should ensure the following condition: that we must reduce the mesh size h as possible without increasing the computing time. Hence we need to find a solution to optimize ours algorithms. Different numerical simulations show that the $(\nabla\alpha\nabla\alpha)$ term requires a considerable time to build the matrix containing all its terms. So, we will show in the first step the importance of considering the $(\nabla\alpha\nabla\alpha)$ term in the regularized energy E(u,α) and in the second step, we will propose an optimized algorithm to reduce the time required to build the matrix containing all terms of E(U,α), especially, the $(\nabla\alpha\nabla\alpha)$ term. This method is based on the work of (Cuvelier 2012) in which, he developed different algorithms of a quasi static fracture problem.

2   Importance of $(\nabla\alpha\nabla\alpha)$ Term

In this section, we prove the emphasis of considering $(\nabla\alpha\nabla\alpha)$ term in the energy regularized function. We simulate the crack propagation based on the variational theory using an alternate minimizations algorithm. Two examples of anti-plane problem for which exact solution can be computed is presented below.
In the first example (Fig. 1), we consider a square structure.
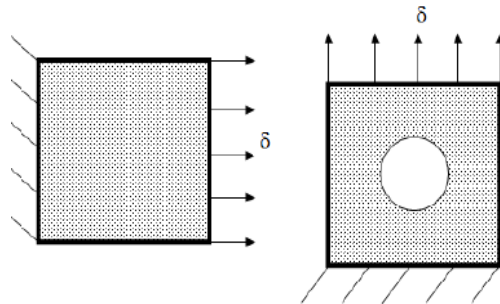
Fig. 1 Square structure and Square matrix containing a circular hole

We keep all numerical parameters only the mesh size h and we study the influence of the $(\nabla\alpha\nabla\alpha)$ term on the localization of crack. These structures are fixed at left edge and submitted at the right edge to a load-dependant boundary condition δ. The lower and upper edges are stress free.
We represent in the following figures (Fig.2a and Fig.2b) the effect of the existence of $(\nabla\alpha\nabla\alpha)$ term in the expression of the regularized energy E(u,α) on the location of crack in the square matrix when we modify the mesh size h.
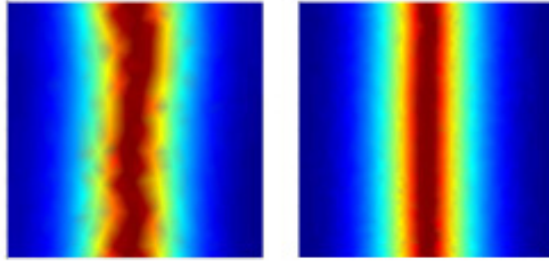
Fig. 2a Evolution of crack in square structure - regularized energy with $(\nabla\alpha\,\nabla\alpha)$ term
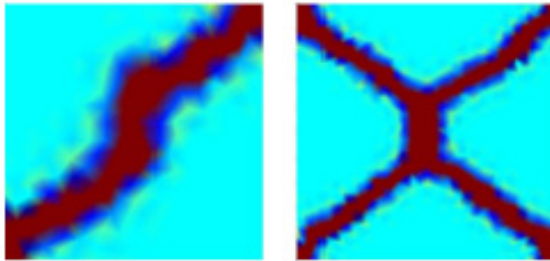
Fig. 2b Evolution of crack in square structure - regularized energy without $(\nabla\alpha\,\nabla\alpha)$ term

In the second example, we represent also in figures (Fig.3a and Fig.3b) the influence of the existence of $(\nabla\alpha\,\nabla\alpha)$ term on the location of crack in the square matrix containing a circular hole when we modify the mesh size h.

We show the mainly second result which is the localization of crack. So, it is the same when the $(\nabla\alpha\,\nabla\alpha)$ term is added in the expression of the regularized energy E(U,α) and the location of the crack is very sensitive to mesh size when the $(\nabla\alpha\,\nabla\alpha)$ term is removed from the expression of the regularized energy.
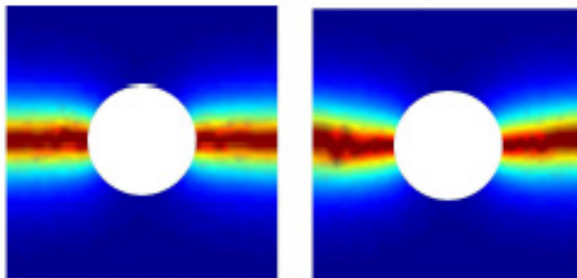
Fig. 3a A square matrix containing a circular hole - regularized energy with $(\nabla\alpha\,\nabla\alpha)$ term
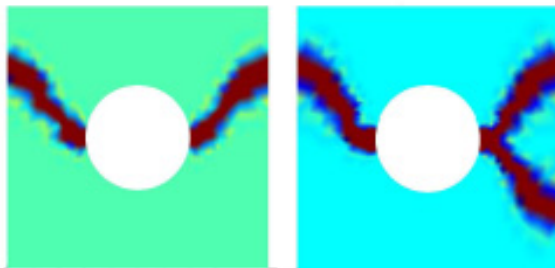
Fig. 3b A square matrix containing a circular hole - regularized energy without $(\nabla\alpha\,\nabla\alpha)$ term

3   Optimization of Numerical Computations

A function space with a given number of the base functions is used. Each function is defined as linear combination of the base functions φ_i. In general, the base functions fulfill some properties such as continuity, smoothness, etc., which is also preserved by the linear combination. When these functions are stored, a function space comprising a finite number of basis vectors is introduced. Each function of this function space can be described as weighted sum of base functions. Each of these base functions is non-zero on the given set (local support) whereas it is zero otherwise [8;16]. In the following figure, we represent the base functions φ_{12} and φ_{20}. We note $q^{\,j}$ is the node index j, we have $\varphi_i\left(q^{\,j}\right)=\delta_{ij}$. For our example, $\varphi_{12}=$ 1 in different nodes belonging to the elements 3, 8, 17, 19, 23 and 25 and $\varphi_{12}=0$ otherwise. $\varphi_{20}=1$ in different nodes belonging to the elements 1 and 6 and $\varphi_{20}=0$ otherwise. It should be noted that the method which has been shown for triangles archetypes.

   Based on this theory, we represent an example of optimized algorithm. In fact, to optimize the time of numerical computation, we present an example of assembling the stiffness matrix. The algorithm below will assemble the components of the matrix of the discretized domain.

   Algorithm: Assembly of the stiffness matrix not optimized:

   1. For i = 1 to N_s
   2. For j = 1 to N_s
   3. For k = 1 to N_t
   4. R_{ij} ⟵ $R_{ij} + R_{ij}(T_k)$
   5. End for

   N_s and N_t represent respectively the number of nodes and element of discretization. $R = R_{i\,j}$ is the square stiffness matrix N_s x N_s. We represent in the following algorithm, the optimized method for assembling the stiffness matrix.
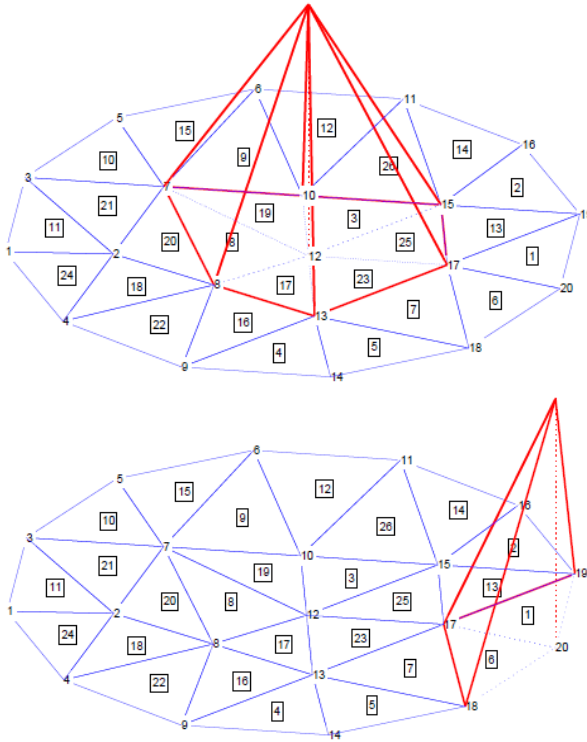
Fig. 4 Base function φ_{12} in the right and φ_{20} in the left [8]

Algorithm: Assembly of the stiffness matrix - optimized method version 1:

1. For k = 1 to N_t
2. For i = 1 to N_s
3. For j = 1 to N_s
4. R_{ij} ◄——— $R_{ij} + R_{ij}(T_k)$
5. End for

So with an optimized algorithm presented above, we only calculate the non-zero terms of the elementary stiffness matrix based on the following equation

$$R_{ij}(T_k) \neq 0 \quad \text{if} \quad i\,;j \in \{k,k+1\}$$

Then we assemble the stiffness matrix. This method is used for assembling different matrices. Using the two algorithms, we find the same numerical results but in a short time with the second algorithm. It is less than half the time simulation of the original algorithm. Other attempts to further reduce the simulation time.

4   Conclusion

The variational approach was applied to simulate the quasi static crack propagation. We used an alternate minimization algorithm to predict its evolution. In order to obtain validated numerical results, we should reduce the mesh size h as possible without increasing the computing time. We present the first attempt to develop a simple numerical method to optimize different algorithms. In this context, we proved the importance of considering $(\nabla\alpha\,\nabla\alpha)$ term in the energy regularized function $E(U,\alpha)$.

References

Griffith, A.: The phenomena of rupture and flow in solids. Philosophical Transactions of the Royal Society of London 221, 163–198 (1921)

Francfort, G.A.: Revisiting Brittle Fracture as an Energy Minimization problem. Int. J. Mech. Phy. 48(4), 797–826 (1998)

Bourdin, B., Francfort, G.A., Marigo, J.J.: Numerical experiments in revisited brittle fracture. J. Mech. Phys. Solids 48(4), 797–826 (2000)

Bourdin, B., Francfort, G.A., Marigo, J.J.: The variational approach to fracture. J. Elasticity 91(1-3), 5–148 (2008)

Cuvelier, F.: Méthode des éléments fins, de la théorie à la programmation (2012)

Hentati, H., Abdelmoula, R., Maalej, A., Maalej, K.: Quasi static fracture-global minimizer of the regularized energy. Applied and Materials Journal 32(13), 97–101 (2012)

Hentati, H., Abdelmoula, R., Maalej, A., Maalej, K.: Quasi static analysis of anti plane shear crack. Applied and Materials Journal 32(13), 92–96 (2012)

Effects and Sensitivity Analysis of Cracking Parameters on the Fatigue Crack Propagation

Ahmed Bahloul[1] and Chokri Bouraoui[2]

[1] Laboratoire de Génie Mécanique.LGM/ENIM,
  Ecole Nationale D'Ingénieurs de Sousse, BP 264 Sousse Erriadh 4023 Sousse, Tunisie
  `bahloulahmad@hotmail.fr`
[2] Laboratoire de Génie Mécanique.LGM/ENIM,
  Ecole Nationale D'Ingénieurs de Sousse, BP 264 Sousse Erriadh 4023 Sousse, Tunisie
  `chokri.bouraoui@enim.rnu.tn`

Abstract. For fracture mechanics, the crack propagation law is often modelled by the linear model usually known as Paris law. This law depends on two constants characteristic of the material. The existence of a correlation between the Paris-Erdogan model parameters was the focal point of several research studies since 1971. These studies suggest that there is a relationship between these two parameters. The aim of this work is to present a statistical study based on the confidence level approach by referring to the different test that were conducted on steel and aluminum alloys from the literature. This study has shown that the relationship between C and m is significant for a confidence level of 95%. In this context and according to many experimental studies, this correlation gives the so called, a pivot point (the intersection point of cracking curves). A probabilistic approach is used to prove the existence of this point and to predict the range scattering of the so called, pivot point, for steels and aluminum alloys. Finally, a study based on design of experiments approach was adopted to analyze the effects and the sensitivity of the Paris law parameters on the stress intensity factor amplitude of the pivot point.

Keywords: Paris-Erdogan law, probabilistic approach, Confidence level, Design of experiments, Taguchi method, Pivot point.

1   Introduction

The fracture mechanics was introduced by the British aeronautical engineer Griffith in 1920 in order to predict the failures which have occurred during the service life. It describes the crack growth evolution with a focus on the parameters affecting this cracking. Paris has been proposed an empirical relationship to predict crack evolution for structure subjected to mode I. He considered that the crack propagation is governed only by the stress intensity factor amplitude. This paper will attempt to show that the Paris model can be reformulated to a law that depend on only one parameter instead of two. The new expression of this model led to the existence of a pivot point. Moreover, an approach based on design of experiments

techniques will be applied to determine the effect and the sensitivity of external parameters on the pivot point.

2   The Relationship between Paris Law Parameters

The Paris-Erdogan law is the most popular model used to evaluate the process of the fatigue-crack propagation in a structure subjected to in-plane mode I loading until structural failure. This expression is given by the following equation:

$$\frac{da}{dN} = C(\Delta K)^m \tag{1a}$$

Where:

ΔK is the range of the stress intensity factor, N and a are respectively, the number of load cycles and the crack length. C and m are material constants.

Or even

$$\log\left(\frac{da}{dN}\right) = \log C + m\log(\Delta K) \tag{1b}$$

The existence of a correlation between the parameters C and m was the focal point of many research works [1, 2, 3, 4, 5, 6, 7, 8, 9]. All these studies agree that there is a relationship between these two parameters that can be defined as follows:

$$C = \frac{A}{B^m} \tag{2a}$$

Having A and B as two constants determined from experimental data, this correlation can be rewritten in an equivalent form as follows:

$$\log C = a + bm \tag{2b}$$

With

$$A = 10^a \quad and \quad B = 10^{-b} \tag{2c}$$

3   Significance of the Pivot Point

In fact, by replacing the expression (2b) which translates the linear relationship between logC and m in equation (1b), it gives the following expression:

$$\log\left(\frac{da}{dN}\right) = a + m(b + \log \Delta K) \tag{3}$$

Having the variation interval of m for a given material and taking for example three values of m (m1, m2 and m3) corresponding to different external conditions, the plot of the log-log curves leads to the existence of an intersection point. This point is called the pivot point (figure 1).
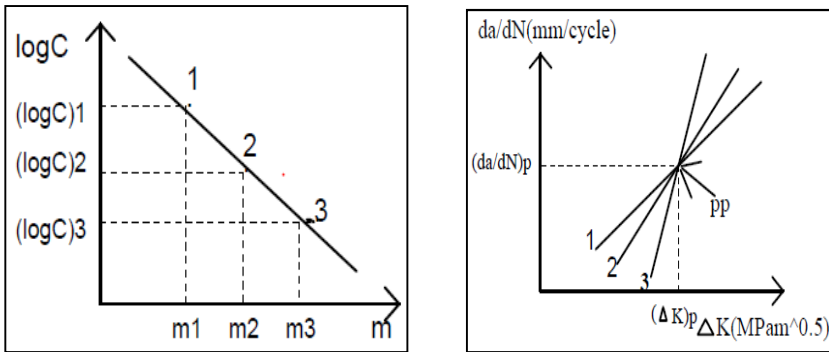
Fig. 1 Definition of pivot point

It is worth mentioning here that whenever the equation (3) is verified, the existence of the point pivot is obvious.

4   Probabilistic Analysis

4.1   Scattering Range of Cracking Parameters

According to the different correlations proposed by several researchers between logC and m for different types of steel, including, engineering steels, alloy steels, brittle steel, ductile steel, ... and the different types of aluminum alloys, a linear regression model is determined linking between logC and m in order to determine the confidence intervals for a given confidence level and to decide if the linear model is accepted or not for a threshold of significance. After the determination of the confidence intervals of the parameters a and b shown in equation 3, a simulation of the different correlations between the parameters C and m in the case of steel and aluminum alloys is carried. As a result, it seems that there is no overlap between the variation range of steels and aluminum alloys (figure 2), therefore, for a confidence level of 95%, there is a relationship between logC and m for each material family (case of steels and aluminum alloys). Within a confidence level of 95%, the existence of a significant relationship between C and m can be confirmed.

For a confidence level of 95%, the following values of a and b are used to generate the variation range between the Paris law parameters (C and m) shown in figure.2.

For Steel

$$-4.04 \leq a \leq -3.62$$
$$-1.46 \leq b \leq -1.34$$

And
For Aluminum alloys

$$-3.73 \leq a \leq -3.14$$
$$-1.24 \leq b \leq -1.06$$
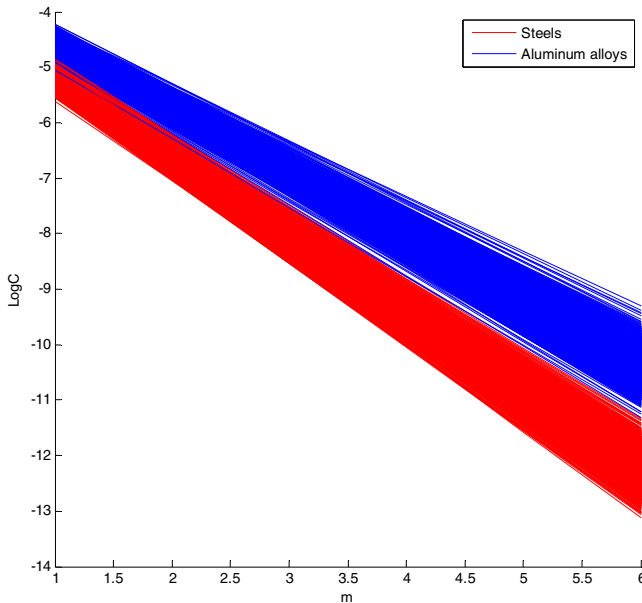
Fig. 2 Range of variation between logC and m

The approximate confidence intervals of the parameters a and b as noted before, was estimated according to the central limit theorem (CLT):

$$\Pr\left(A, B - Z\alpha_{/2}\frac{\sigma_{A,B}}{\sqrt{n}} \le a, b \le A, B + Z\alpha_{/2}\frac{\sigma_{A,B}}{\sqrt{n}}\right) = (1 - \alpha)\% \tag{4}$$

Where

$(1-\alpha)$ is the confidence level.

A, B are the regression parameters.

n is the number of experimental points for the couple (a, b).

$Z\alpha_{/2}$ is a constant determined from the statistical table of the normal distribution.

$\sigma_{A,B}$ is the standard deviation respectively of A and B.

4.2   Numerical Simulation of the Pivot Point Scattering

In order to predict the variation range of the coordinates of pivot points, a simulation of the bi-logarithmic curves of crack propagation for the family of steels and aluminum alloys was generated. The simulation of these curves requires knowing the laws of distributions and statistical characteristics of three cracking parameters a, b and m. The draw curve of cracking is done according to the assumption of the normal distribution where the means and the standard deviation were determined from experimental point. The numerical simulation which has been developed, in

order to estimate the intersection points (pivots points), is based in the random aspect. The following results can be drawn (figure.3):
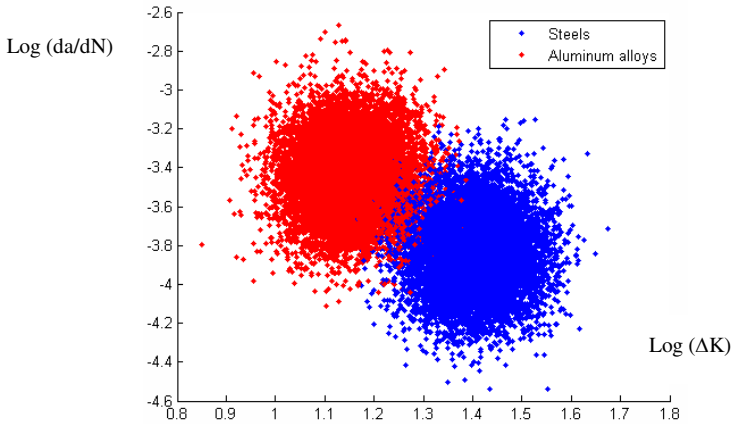
Fig. 3 Simulation of pivots points

It should be noted that the majority of the coordinates of pivot points extracted from the literature [2] [4] [3] and [9], in the case of steels or in the case of aluminum alloys are located in the scattered points, determined by the numerical simulation as indicated in figure 3, so at this level, the results obtained allow us to conclude that the developed numerical approach has given us results in good agreement with the experimental investigations. It must be noted that each material has its own coordinates of pivot points.

5 The Effects and Sensitivity of Cracking Parameters on the Pivot Point Scattering

In the recent paper, the effects of the Paris-Erdogan parameters dispersions on the stress intensity factor amplitude of pivot point are investigated. A methodology based on the design of experiments is implemented. The sensitivity of the different factors on the variability of pivot point in the presence of external perturbations is analyzed to optimize the performance of the behavior prediction system.

5.1 Effects of Cracking Parameters on the Pivot Point

According to the Paris law expression (eq.3), which reflects the existence of a pivot point for any variation of the parameter m, a study of the effects of different parameters on the variability of this point is implemented. A full factorial plan is implanted giving the response of each parameters levels combination. The approach adopted for each test is to generate a value of a, b and m according to their

respective distribution laws. As a result to each test, a beam of 1000 cracking curves was obtained. For each test, the mean and the standard deviation of the stress intensity factor amplitude of these points are determined. Since, we have three input factors a, b and m at three levels, which require 27 numerical experimental responses with fixed level parameters. For each response a 1000 random sample set of the a, b and m parameters according to their density probability law is generated. According to MINITAB software, figure 4 illustrates the effect of each parameter on the system response (the stress intensity factor amplitude of the pivot point).

(a) case of aluminum alloys   (b) case of steels
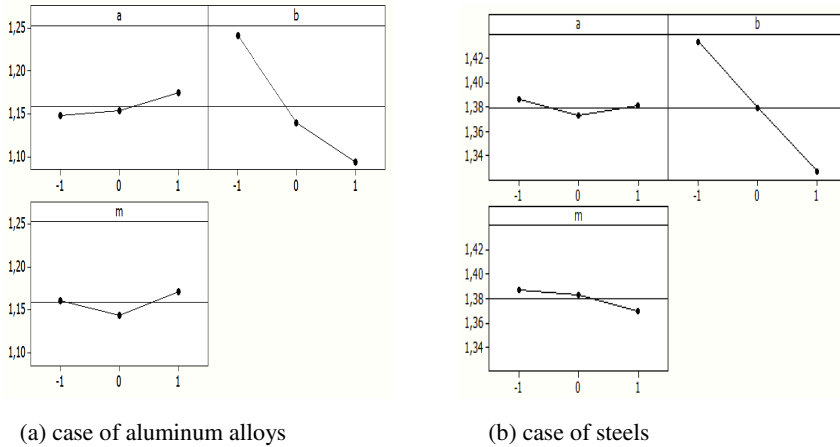
Fig. 4 The effects of cracking parameters on the stress intensity factor amplitude of pivot point

By treating the different results extracted from experimental design with Minitab software, for steels and aluminum alloys, the following results can be drawn:

The factor **a** has a low effect on the system response, the exponent **m** presents also a low effect on the stress intensity factor amplitude of the pivot point. The factor **b** is the most significant factor, it has a linear effect on the stress intensity factor amplitude of pivot point.

In fact, an increase in the value of **b** led to a decrease in the value of the stress intensity factor amplitude of pivot point.

However, the analysis of the effect of each parameter separately cannot explain how a system responds according to the parameters specially when the interaction between the different parameters exists. It is difficult to have a configuration in which all the factors are independent. So it seems interesting to study the effects of interactions between factors.

Figure 5 shows the degree of interactions between the different Paris law parameters on the variability of the pivot point.

It seems that for the interaction between **a**, **b** and **a**, **m**, all the lines crosses each other, which means that a change in one factor has a significant effect on the other factor, as a result , there is respectively a strong interaction between **a**, **b** and **a**, **m**. Concerning the degree of interaction between **b** and **m**, the lines which represent the different levels of **b** according to factor **m** do not intersect each other but they are also not parallel which implies that the degree of interaction between **b** and **m** is relatively low.

(a) case of aluminum alloys   (b) case of steels
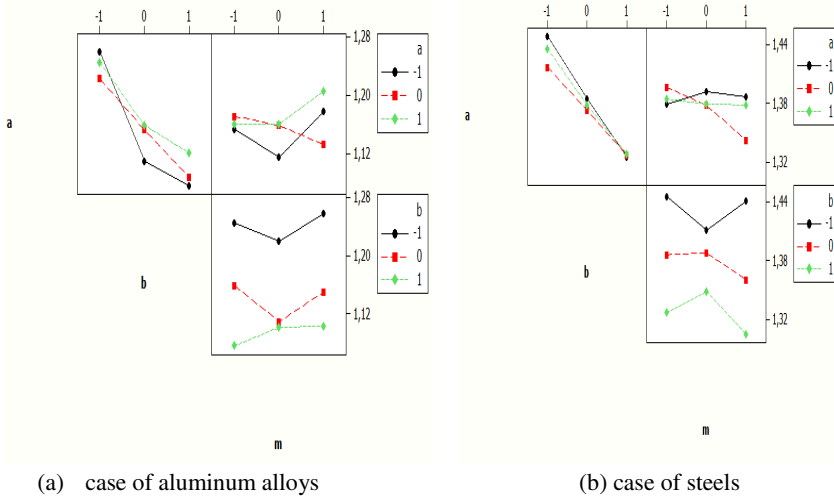
Fig. 5 The interaction between the cracking parameters on the stress intensity factor amplitude of pivot point

5.2   *Sensitivities of Cracking Parameters in the Presence of External Perturbations*

Generally, the main objective of the Taguchi method is to optimize system performance and to minimize the sensitivity of the response by taking into account the dispersions of factors. Genichi Taguchi proposed in this stage an expression called 'SNR'(Signal Noise ratio) which takes into account the standard deviation and the mean of the response. This expression can be written as follows:

$$SNR = 10log_{10}\left(\frac{Y^2}{\sigma^2}\right) \qquad (5)$$

Where Y and σ are respectively the mean and the standard deviation of the response. The Taguchi method was inspired by the fact that for several experimental tests were carried out , while maintaining the same input factors, we end up with a different results, and that due to the existence of external disturbances (noise) affecting response. In order to know the optimum value of each factor required to minimize the effect of external disturbances on the response of our system, the quality characteristics larger-the-better is used.

The approach consists to compute the value of signal-to-noise ratio for each test using the mean and the standard deviation of the stress intensity factor amplitude of the pivot point.

Figure 6 illustrates the sensitivity of cracking parameters on the variability of the pivot point. The following results can be deduced:

The exponent **m** is very sensitive in the presence of the noise, this sensitivity is reflected by the perfect linearity of this factor. The factor **b** presents a significant sensitivity and linear effect on the signal to noise ratio. The factor **a** has no detectable effect, it shows no sensitivity in the presence of external perturbations.
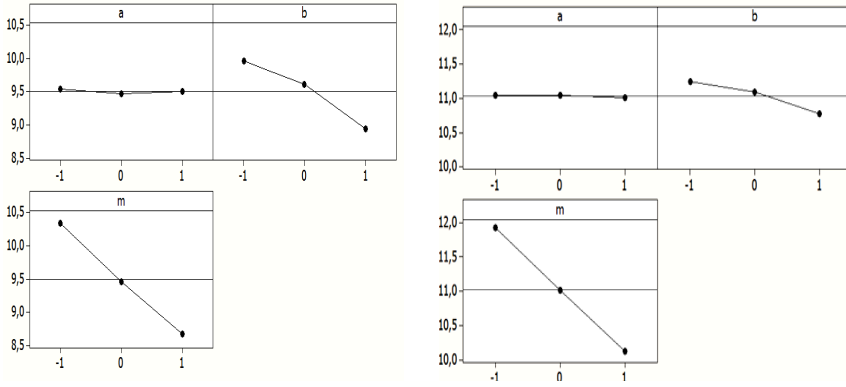
(a) case of aluminum alloys   (b) case of steels

Fig. 6 The sensitivity of the cracking parameters on the signal noise ratio
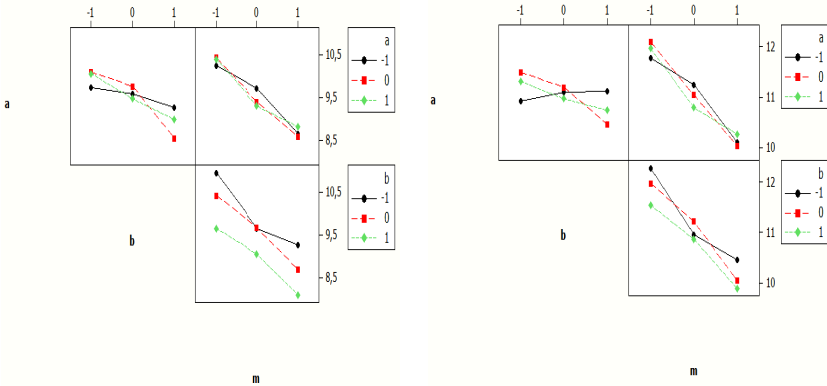
(a)   case of aluminum alloys   (b) case of steels

Fig. 7 The interaction between the cracking parameters on the signal noise ratio

Figure 7 show clearly the intensity of interaction of different factors as a function of signal to noise ratio.

It is found that in the presence of noise, the interaction between the different factors increases and becomes stronger and more significant and it appears clearly between **b** and **m.** In fact in normal conditions, there is a little interaction between these two parameters but via the presence of external disturbances, the sensitivity between **b** and **m** increases.

6   Conclusion

The existence of a correlation between **C** and **m** from the Paris-Erdogan law leads to the presence of a pivot point which give further informaton on the outbreak streaking mechanism. From the previous analysis results and discussion presented in this work, the following conclusions can be drawn.

- According to the different correlations proposed by several researchers between **C** and **m**, a numerical simulation based on the concept of confidence intervals, has shown that the relationship between **C** and **m** is significant for a confidence level of 95%.
- A probabilistic approach is proposed to determine the range of variation of the coordinates of the pivot point .This technique has confirmed that each material has its own pivot points. In coordinate point of view, this result is very important, only one parameters is needed for cracking analysis. It reduces clearly the experimental tests costs.
- A methodology based on the design of experiments has shown that the factor **b** has a significant and linear effect on the stress intensity factor amplitude of pivot point. However ,for the parameters **a** and **m** , they do not have a significant effect. The sensitivity analysis of these parameters in the presence of external disturbances provides that the factors **b** and **m** have an appreciable effect in terms of the signal to noise ratio, however, the factor **a** has no detectable effect, it shows no sensitivity in the presence of external perturbations.

References

[1] Cortie, M.B.: The irrepressible relationship between the Paris law parameters. Engineering Fracture Mechanics 3, 681–682 (1991), doi:10.1016/0013-7944

[2] Lost, A., Lesage, J.: On the existence of a pivot point for stage II fatigue crack growth. Engineering fracture mechanics, 585–596 (1990), doi:10.1016/0013-7944(90)90114-V

[3] Cavallini, M., Lacoviello, F.: Fatigue models for Al alloys. International Journal of Fatigue, 442-446 (1991), doi:10.1016/0142-1123(91)90477-G

[4] Tanaka, K., Matsuoka, S.: A tentative explanation for two parameters, C and m, in Paris equations of fatigue Crack growth. International Journal of Fatigue, 563–583 (1977), doi:10.1007/BF00017293

[5] Zilberstein, V.A.: On correlations between the power-law parameters. International Journal of Fracture, 57–59 (1992), doi:10.1007/BF00015624

[6] Cortie, M.B., Garrett On, G.G.: the correlation between the C and m in the Paris equation for fatigue crack propagation. Engineering Fracture Mechanics, 49–58 (1980), doi:10.1016/0013-7944(88)90254-8.

[7] Bailon, J.P., Masounave, J., Bathias, C.: On the relationship between the parameters of Paris law for fatigue crack growth in aluminum alloys. Scripta Metallurgica, 1101–1106 (1977), doi:10.1016/0036-9748(77)90315-5.

[8] Benson, J.P., Edmonds, D.V.: The relationship between the parameters C and m of Paris law for fatigue crack growth in a low-alloy steel. Scripta Metallurgica, 645–647 (1978), doi:10.1016/0036-9748(78)90278-8.

[9] Cavallini, M., Lacoviello, F.: A statistical analysis of fatigue crack growth in a 2091 alloy. International Journal of Fatigue, 135–139 (1995), doi:10.1016/0142-1123(95)95893-L.

Development of Bulge Test for Aluminum Sheet Metal

Mohamed Khlif, Moufida Mhadhbi, and Chedly Bradai

National School of Engineers of Sfax Tunisia (ENIS)
LASEM (Analysis Laboratory of the Electro-Mechanical Systems)
BP.1173. W. 3038 Sfax, Tunisia
khlifmohamed@yahoo.fr

Abstract. The bulge test is frequently used experiment to characterize the material stress-strain response at the highest possible strain levels. It consists of a metal sheet placed in a die with a circular opening. It is clamped in place and inflated with hydraulic pressure. This paper presents the development of a measuring system to be incorporated in a hydraulic bulge test machine, which allows stress-strain determination up to higher levels of plastic deformation. A continuous increasing of pressure produces a biaxial tension applied to a sheet metal specimen up to breaking point. By measuring the vertical displacement using a transducer and the strain variation with an extensometer, one can estimate the strain and stress being applied to the specimen. Preliminary results indicate the efficiency of the procedure to obtain real time data for stress-strain sheet metal characterization.

Keywords: bulge test, sheet metal, aluminum.

1   Introduction

Determining the mechanical behavior is one of the settings issues in analyzing materials. Many techniques are used to obtain the behavior curve of the materials such as tensile test, compression, torsion, hardness, plane strain compression and hydraulic bulge test. The determined strain stress curves using different tests do not replicate each other due to effects of stress state, yield criterion assumption, anisotropy, experimental inaccuracies, temperature and general weakness of the modeling. Hence, none of the test methods can be considered as the best or optimal [1], each one has its own specific field of application due to certain straining paths. Among those test system, the most widely used one is uni-axial tensile test. Limitations of uni-axial tensile test have been described by several researchers [2,3]. On the other hand, bi-axial stress state tests such as hydraulic bulge test provides flow curves for the materials with extended range of plastic strain levels up to 70% before bursting occurs [4,5]. Another benefit of using bi-axial state of stress test is that it is more appropriate for sheet metal forming operations in which the deformation mode is bi-axial rather than uni-axial.In this paper, a bulge testing

apparatus is presented it was designed, manufactured, calibrated to measure the stress-strain response of an aluminum sheet metal and establish its onset of failure. The custom design incorporates a draw-bead for clamping the plate. A controlled servo hydraulic pressurization system consisting of a pressure booster is used to pressurize the specimens. Deformations of the bulge are monitored with a displacement transducer and a pressure sensor. Relevant parameters, including the local strains and radius of curvature, will be extracted from the LabVIEW software to calculate the equivalent stress-true plastic strain response to be compared to tensile test responses.

2   Theory for Stress and Strain Measurement

The bulge test is a well described experimental set-up for biaxial loading, where pressure is used to deform a specimen. The set-up consists only of a pressure chamber and clamping mechanism. The bulge test is mostly used for testing thin films, as bending stresses can be neglected for that case. The pressure can be build up by a gas or a fluid. [6,7].
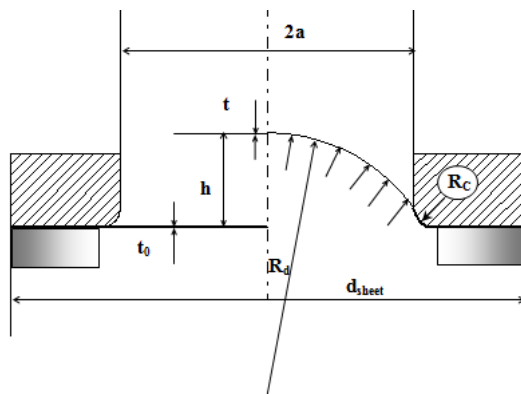
Fig. 1 Scheme of hydraulic bulge test

A simple bulge test set-up is shown in figure 1, with the most important properties visualized being t_0 and t_d, the initial and final thickness of the sheet, d: sheet diameter of the sheet, dc: diameter of the die cavity, h_d the height of the dome and R_C the radius of the die edge. R_d: radius of the bulge in a circular set-up. Rd is divided in two values R_1 and R_2 for an elliptic bulge, with the two radii relating to the bulge radius in the principle directions. For large apertures, the membrane theory can be used to compute stresses, strains and pressures, as will be discussed in the next section.

$$\frac{\sigma_1}{R_1} + \frac{\sigma_2}{R_2} = \frac{p}{t} \tag{1}$$

Where $\sigma 1$ and $\sigma 2$ are the principle stresses on the sheet surface, R1 and R2 the radii, perpendicular to each other, p the pressure applied to the sheet and t the thickness of the sheet. In the pure biaxial case where the bulge is a perfect bowl, $R_1 = R_2 = Rd$ and $\sigma = \sigma_1 = \sigma_2$, so the equations can be simplified to

$$\sigma = \frac{PR_d}{2t_d} \tag{2}$$

With t_d the thickness at the top of the dome. The effective stress can be written as

$$\bar{\sigma} = \frac{P}{2}\left(\frac{R_d}{t_d} + 1\right) \tag{3}$$

In the above relations the dome radius R_d is defined as

$$R_d = \frac{(a + R_c)^2 + h^2 - 2R_c h}{2h} \tag{4}$$

The radius of the die edge is very small compared to the radius of the dome

$$R_d = \frac{a^2 + h^2}{2h} \tag{5}$$

and the thickness at the top of the dome can be expressed by

$$t = t_0 \left(\frac{1}{1 + (2h/a)^2}\right)^2 \tag{6}$$

For the current sheet thickness t evaluation, measurement is done in terms of the initial sheet thickness t_0 and the current thickness strain ε_t, such as:

$$t = t_0 \exp(-\varepsilon_t) \tag{7}$$

The thickness strain ε_t is calculated taking into account the assumption of material incompressibility. If the volume remains constant during plastic deformation, the relation

$$\varepsilon_t = -(\varepsilon_1 + \varepsilon_2) \tag{8}$$

is verified, where ε_1 and ε_2 are the principle plastic strain components on sheet surface. As for stresses and curvature radius, the hypothesis of equal values for both surface strains near the pole is assumed and strain in thickness direction is given by:

$$\varepsilon_t = -(\varepsilon_1 + \varepsilon_2) = -2\varepsilon \qquad (9)$$

where ε is the membrane strain.

$$\varepsilon = \frac{2h^2}{3a^2} \qquad (10)$$

3   Design and Realization of the Bulge Test Apparatus

Following the theoretical analysis of the bulge test, a bulge test apparatus for thin films is designed and manufactured.

The plate is clamped using a draw-bead machined into the base plate. In particular, the detailed design of the draw-bead and the corresponding recess groove in the clamping ring were determined from these solutions. Figure 2.a shows the initial configuration before clamping; figure 2.b shows the final configuration after applying a force on the clamping ring.
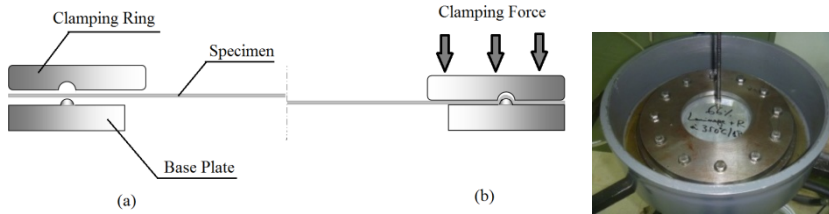
Fig. 2 Schematic of bulge tester including base plate, clamping ring, and closing plate

4   Experimental Methodology

A user interface has to be programmed for the bulge test apparatus that is compatible with the different sensors, which ensures the data acquisition, data processing and control.

4.1   Data Acquisition and Processing

For the data acquisition the visual programming language NI LabVIEW is used. The program reads in the voltage values that are transmitted from the three

pressure sensors. using conversion factors allows obtaining the different pressures. The deflection of the sample is measured using an optical surface profiler.

The starting times of the processes are known, which means that the times of both the pressure and deflection measurements are known. This is used to find the correct pressure data with the deflection data. The pressure-time, deflection profile of the centre of the membrane and the global stress-strain curves are plotted during the measurement and all data that is needed for the post-processing is saved to two data files. This data can be used to obtain stress-strain curves with the use of the different bulge equations or other conversion methods.
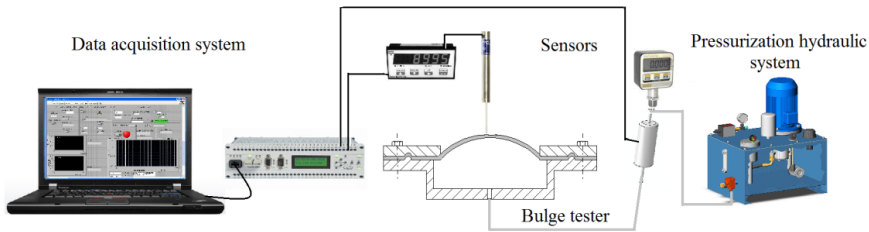
Fig. 3 Schematic of experimental setup consisting of the bulge tester, the pressurization system, and the data acquisition system

4.2 Experimental Results

One of the advantages of bulge testing is that it prolongs the onset of instability and failure, thereby allowing a more complete material model to be obtained when compared to a simple tensile test. This section presents the result of experimental bulging test performed on Al-1050 plates. A simple formulation is then used to obtain the material stress-strain response up to failure.

As mentioned above, specimen preparation is crucial for proper test results. It was also one of the most important reasons to choose the bulge test as a testing method. The working area of the apparatus is 160 mm in diameter (area of the specimen where pressure is applied). Specimen are made with a diameter of 200 mm, therefore the borders of the specimen do not influence the test, see Figure 4.

The aluminium alloy A1050 that was used in this study in 0.5 mm thick. The aluminium sheet was cut into bulge specimens and tested using the equipment described previously. Figure 5, shows the variation of pressure as a function of the dome height, it is noted that the pressure increases in proportion to the displacement. The maximum pressure to wait for the bursting of the specimen is the 19 bar approximately. Figure 6 shows the variation of stress versus strain, these results are obtained from the equations defined above. according to stress strain curve,we conclude that the behavior of A1050 material has two domains, an elastic field for small deformation and plastic large deformation field.

Fig. 4 Bulge tester for aluminum sheet metal
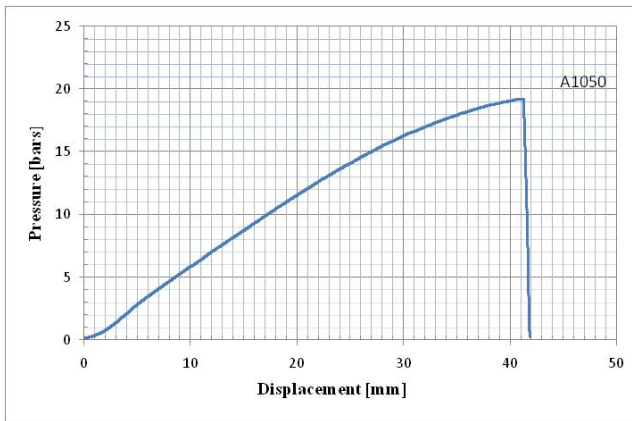
Fig. 5 Pressure displacement curve
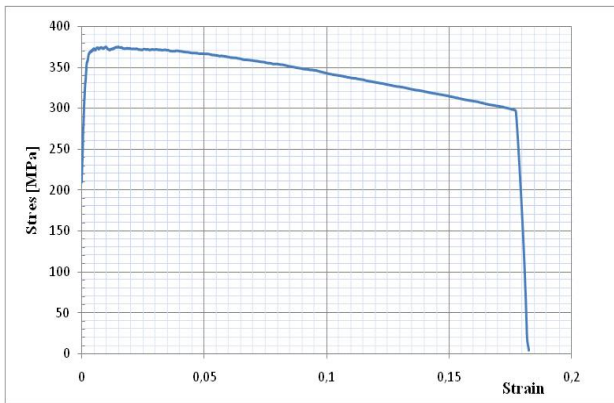
Fig. 6 Biaxial stress strain curve for A1050

5   Conclusion

In this paper, a bulge test apparatus for testing the aluminium sheet metal was developed. The apparatus uses a compressed oil to test a metallic material. The apparatus is instrumented by a displacement sensor for measuring the height of the dome and a pressure sensor. The signal are amplified and transmitted to the computer via a data acquisition card, processing the signals is provided by the Labview software. The results obtained with swelling tests allowed us to these results determined the material behaviour laws are reliable and compliant with bibliography. Further improvement of the methodology and testing will follow.

References

[1] Lange, K.: Handbook of metal forming. McGraw-Hill, New York (1985)
[2] Altan, T., Palaniswamy, H., Bortot, P., Mirtsch, M., Heidl, W., Bechtold, A.: Determination of sheet material properties using biaxial tests. In: Proceedings of the 2nd International Conference on Accuracy in Forming Technology, Chemnitz, Germany (2006)
[3] Keller, S., Hotz, W., Friebe, H.: Yield curve determination using the bulge test combined with optical measurement. In: International Conference on International Deep Drawing Research Group IDDRG 2009, Golden, CO, USA (2009)
[4] Kaya, S., Altan, T., Groche, P., Klöpsch, C.: Determination of the flow stress of magnesium AZ31-O sheet elevated temperatures using hydraulic bulge test. Int. J. Mach. Tools Manuf. 48, 550–557 (2008)
[5] Güner, A., Brosius, A., Tekkaya, A.: Analysis of the hydraulic bulge test with FEA concerning the accuracy of the determined flow curves. Key Eng. Mater 411, 439–447 (2009)
[6] Gutscher, G., Wu, H.-C., Ngaile, G., Altan, T.: Determination of flow stress for sheet metal forming using the viscous pressure bulge (VPB) test. J. Mat. Proc. Techn. 146, 1–7 (2004)

[7] Liu, J., Ahmetoglu, M., Altan, T.: Evaluation of sheet metal formability, viscous pressure forming (VPF) dome test. J. Mat. Proc. Techn. 98, 1–6 (2000)

[8] Marshall, T.G., Marshall, F.E.: New treatments emerge as sarcoidosis yields up its secrets. ClinMed NetPrints (2003),
`http://clinmed.netprints.org/cgi/content/full/2003010001v1`
(accessed June 24, 2004)

Characterisation of Polishing 316L Stainless Steel with Structured Abrasive Belts

François Goossens, Mehdi Cherif, and Olivier Cahuc

Univ. Bordeaux, I2M UMR 5295, F-33400 Talence, France
`{francois.goossens,mehdi.cherif,olivier.cahuc}@u-bordeaux.fr`

Abstract. Finishing process like polishing is usually used to obtain high quality mechanical surface characteristics such as texture and roughness. These operations are mainly handmade and need highly trained operators thus limiting their repeatability and profitability. To optimize the industrialization of the polishing process, it is therefore necessary to modelize the process to built efficient parameter database. The aim of this study is to characterise the polishing of 316L stainless steel with structured abrasive belts. The geometric data of the belts are given, and we then propose a model to determine material removal. An experimental test bench is set up to test this model and characterise the polishing process in terms of forces. It produces samples for different polishing conditions. The different polished surfaces are then analyzed thanks to the roughness and the wettability. Using experimental designs, we are able to validate the proposed model and identify the parameters that influence a polishing operation.

Keywords: polishing, structured abrasive, roughness, material removal rate, wettability.

1   Introduction

Polishing is the last stage in the manufacturing of industrial parts to give surfaces well-defined characteristics. These may be related to roughness for aesthetic or functional reasons, to surface stresses to ensure better fatigue behaviour or to corrosion and wettability when a protective coating is to be applied.

This process differs from other material removal processes as the thrust force exerted by the abrasive grains on the polished surface has to be controlled. Other factors can intervene, such as the morphology of the surface to be polished and the aggressiveness of the abrasive grains, which can change in the course of the polishing cycle. These operations must therefore be carried out by experienced operators in order to meet the most stringent level of requirements for the polished parts.

To derive the maximum from abrasive tools in terms of quality, productivity and repeatability, it is necessary first to identify and control the parameters that govern the polishing process and the operating range of each one.

Here we describe a study carried out to provide this information for structured abrasive belts polishing a 316L stainless steel. We give the geometric characteristics of the abrasive belts used in the experiment and propose a model to characterise the material removal rate. Next, we describe the equipment set up to test this model and provide data to characterise the polishing process in terms of stress, roughness and wettability of the polished surface.

2 State of the Art for the Study of Abrasive Polishing

Studies to date can be divided into three categories according to their scale. At microscopic level, (Felder 2009), (Klocke et al. 2008) have studied the action of an indenter on the material. They demonstrate the different metal cutting/pickup mechanisms. The macroscopic approach, the second level of study, considers the overall effect of an abrasive tool on a portion of material. Finally, some authors consider the polishing operation as a whole. (Pessoles and Tournier 2009) defined the trajectory to be applied to the abrasive tool in order to obtain similar results to those produced by skilled workers. (Nagata et al. 2007) studied mould polishing using a polyarticulated robot. They show that it is vital to use a trajectory-stress combination to finish skew surfaces successfully.

To date, the models that best characterise polishing at macroscopic level are empirical models. The model by (Preston 1927) is the one most often used to deal with the issue of material removal. (Wang et al. 2002), (Luo and Dornfeld 2001) and (Guiot et al. 2012) have attempted to complete this model for certain polishing processes and these models provide useful data for designing a polishing process. (Lacharnay et al. 2012) defined the operating procedure to achieve a mirror finish quality using rotating discs.

Here, we intend to validate Preston's model for polishing 316L stainless steel parts with structured abrasive belts and to characterise this process in terms of roughness and wettability of the polished surfaces.

3 Characterisation of the Abrasive Belts

The abrasive belts used in our study (reference TRIZACT 307EA, 3M) are structured abrasives. The aluminium oxide abrasive grains are arranged in the form of pyramids, with a synthetic resin ensuring cohesion between grains and the bond with the flexible cloth belt (Fig. 1).

Fig. 1 Portion of new TRIZACT 307EA belt

The grain sizes selected for our study cover the range offered by the manufacturer. They are given in Table 1.

Table 1 Average size of abrasive grains

3M Reference	FEPA Classification	Average grain size according to FEPA
A100	P180	82 μm
A30	P800	21.8 μm
A6	P2500	8.4 μm

The geometric characterisation of the belts is obtained by digitising the surface of the pyramids using a 3D ALTISURF 500 roughness meter with a conical 60° point. In order to take into account any variation in the dimension of the pyramids, each reading relates to an alignment of 10 pyramids. From each reading the profile of the pyramids is extracted in the plane normal to the belt and over their apex. Figure 2a shows the profile of an alignment of grade A100 pyramids as new and then at two stages of wear of the abrasive belt.

(a): Reading for alignment of pyramids   (b): Geometric parameters
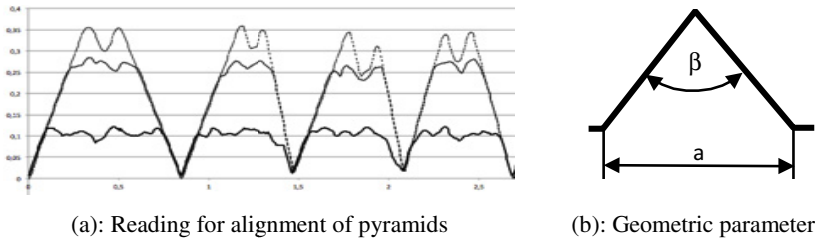
Fig. 2 Geometric characteristics of abrasive pyramids

Figure 2b shows the geometric parameters of a pyramid: the width of the base (a) and the angle at the apex (β). Table 2 gives the dimensions for the abrasive belts studied and their standard deviation, values for each belt reference derive from 100 pyramids: 10 alignments of 10 pyramids sampled from different belts.

Other parameters such as the concentration of grains, mechanical resistance and the adhesive strength of the synthetic resins also come into play when defining the process. However, these data are not usually provided by manufacturers and are rather difficult to determine experimentally.

Table 2 Width and angle at the apex of the pyramids and standard deviation

Parameters	unit	A100	A30	A6
Width of base (a)	mm	0.638	0.483	0.499
Standard deviation of (a)	mm	0.077	0.070	0.054
Angle at apex (β)	degree	75.68	78.82	75.90
Standard deviation of (β)	degree	6.96	11.49	5.53

4   Study Model

Using the model most often referred to in publications on abrasive machining, we put in the equations that govern material removal. From these we obtain valuable theoretical information for the designers of polishing processes based on the technology of structured abrasives.

Our study is based on Preston's model (equation 1). This defines the speed of indentation by the abrasive tool in the polished material (dz/dt). This speed is the product of a constant (Cp) specific to the polished material, the nature and size of the grains and the characteristics of the binder, and the pressure (p) exerted by the abrasive grains on the polished surface and the feed speed of the grains (V).

$$\frac{dz}{dt} = C_p \cdot p \cdot V \tag{1}$$

Taking into account the relative movement of the abrasive grains as they sweep a surface ($S_{projected}$), if pressure (p) is exerted at any point on the apex of the pyramid ($S_{contact}$) by the abrasive grains of which it is composed (see Fig. 3a), then the larger the abrasive-material contact area, the more material will be removed. To take account of changes in the geometry of the abrasives used according to the wear, an evolution of the Preston's model is given in equation (2).
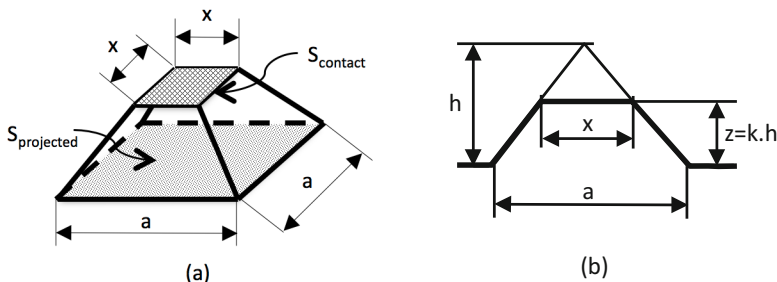
Fig. 3 Geometric parameters of pyramids when in use

$$\frac{dz}{dt} = \frac{S_{contact}}{S_{projected}} \cdot C_p \cdot p \cdot V \tag{2}$$

Considering the geometry of the pyramids when in use, as shown in Fig. 3b, the surface ratio is expressed in equation (3).

$$\frac{S_{contact}}{S_{projected}} = \left(\frac{x}{a}\right)^2 = \left(\frac{h-z}{h}\right)^2 = (1-k)^2 , \tag{3}$$

where k represents the rate of wear of the pyramids. The pyramids are new when k=1, and fully worn when k=0. Equation (2) then becomes:

$$\frac{dz}{dt} = (1-k)^2 \cdot C_p \cdot p \cdot V \tag{4}$$

From this, the material removal rate can be expressed:

$$\frac{dv}{dt} = S_{projected} \cdot \frac{dz}{dt} = S_{projected} \cdot (1 - k)^2 \cdot C_p \cdot p \cdot V \qquad (5)$$

Pressure (p) derives from the thrust force (Fz) applied to a pad with a constant cross-section pressing the abrasive grains downwards onto the material to be polished. Here too the ratio of the area of the pad to the area of the pyramid apices in contact with the part to be polished must be taken into account.

$$p = \frac{F_z}{S_{contact}} = \frac{F_z}{S_{projected} \cdot (1-k)^2} \qquad (6)$$

When the thrust force is constant, the pressure exerted at the apex of the pyramids decreases as the contact surface of the abrasives increases due to the effect of wear. The material removal rate can then be expressed as

$$\frac{dv}{dt} = C_p \cdot F_z \cdot V \qquad (7)$$

and the indentation speed of the abrasive belt in the material can also be written:

$$\frac{dz}{dt} = C_p \cdot \frac{F_z \cdot V}{S_{projected}} \qquad (8)$$

In the context of our study, designing a polishing process consists mainly of defining: the thrust force to be exerted by a polisher with a pad that has a constant cross-section and a feed speed for the belt. When these are determined, material removal is constant in theory, whatever the degree of wear on the structured abrasive belts.

Based on Preston's model, for pyramid-shaped structured abrasive belts we put in place models defining the forward speed of the polisher across the material and the material removal rate. We show that the material removal rate does not vary throughout the life cycle of the belts we studied, when the parameters of the process remain fixed. We shall see later to what extent this model is verified.

5   Experimental System

An experimental approach is used to characterise the polishing process of the pyramid abrasive belts. The aim is to characterise: the material removal rate, the tangential cutting coefficient, the ratio of the polishing force borne by the polished surface (Fx) to the thrust force (Fz) applied perpendicular to the polished surface (see Fig. 4.a), the roughness and the wettability of the polished surface. We devised a test bench to measure the thrust force (Fz), the tangential stress (Fx), the feed speed of the abrasive grains (V) in the course of a polishing operation and the position of the polisher which remained normal to the material.

(a): Polishing force → sample   (b): Layout of the polishing bench
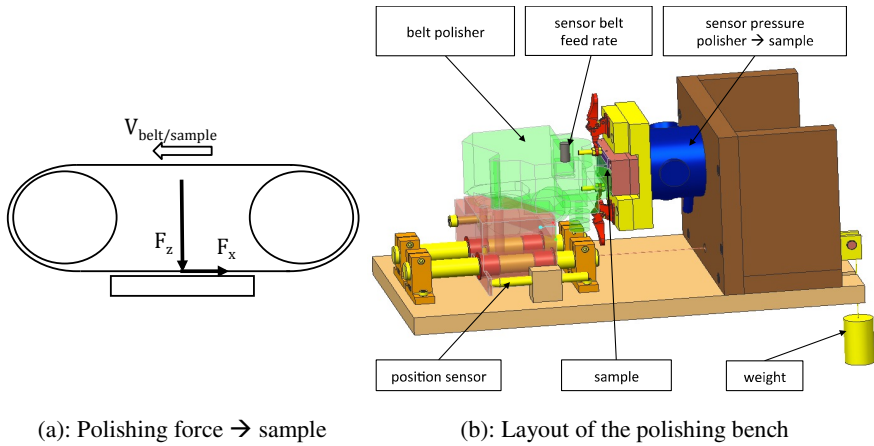
Fig. 4 Principal features of the polishing bench

Figure 4b shows the layout of the polishing bench. It consists of a pneumatic abrasive belt polisher (reference DINABRADE 14200 – speed without load = 30 m/s – belt width = 25.4 mm – belt length = 457 mm). To ensure that the polisher covers the sample correctly (maximum dimensions: 40 x 70 x 2 mm), it is guided in translation by sleeve bearings mounted on two rigid columns. The thrust force is obtained by a cable attached to a weight suspended in mid-air. The forces applied to the sample by the polisher are measured with a six-component dynamometric sensor. The feed rate of the belt is controlled by a flow regulator with a cone-point set screw. It is measured using an inductive sensor combined with a metal pad placed on the roller ahead of the polisher. Lastly, the position of the polisher in relation to the sample is measured with an LVDT sensor.

6   Characterisation of the Performance of the Abrasive Belts

6.1   Design of Experiments

An factorial design of experiments (DOE) is proposed to determine material removal (dz/dt), the tangential cutting coefficient (f) and roughness (Ra) for polishing operations with grade A100, A30 and A6 belts. The input parameters and their boundaries are given in Table 3. These boundaries of DOE are defined from preliminary tests and test bench limits.

Table 3 Input parameters of the experimental design

Parameters	Symbol	Unit	Min. boundary	Max. boundary
Abrasion pressure	p	N/cm^2	10	20
Speed	V	m/s	10	25
Wear rate	k		0.2	0.7

6.2 Polisher Indentation Speed

These tests will help to identify influent parameters on material consumption (dz/dt) and will be compared to the modified Preston's model results. Fig. 5a shows the average indentation speed (dz/dt) for the three types of belt considered. The productivity of a polishing operation is closely linked with the size of the grains, with a ratio of 1 to 10 for the two extreme grades studied (A100 and A6).

(a): Average values   (b): Coefficients of input parameters – A100 belt
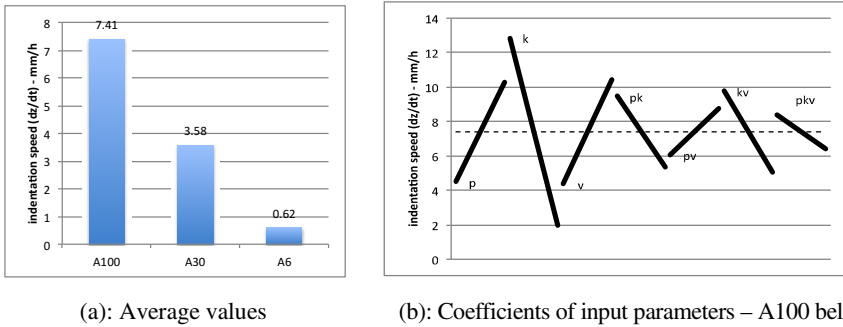
Fig. 5 Results for indentation speed (dz/dt)

Figure 5b shows the coefficients for the input variables for the A100 belt. It can be seen that the weight of the p, k and V coefficients is significant, as are all the interactions. The different tests carried out on the A30 and A6 belts show identical changes to those shown in Fig. 5b.

The tests established for this experimental design enable us to determine the Preston constant (Cp) using a least squares regression. We are therefore able to calculate the theoretical values for indentation (dz/dt) for each test in the experimental design.
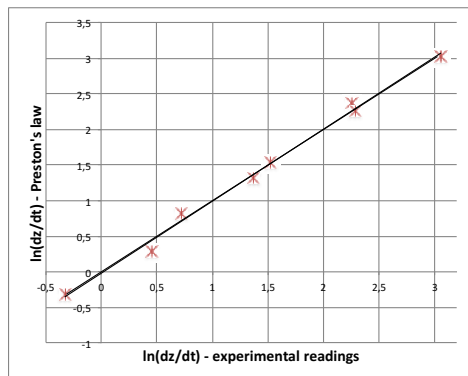
Fig. 6 Deviations between experimental readings and Preston's law –A100 belts

In Fig. 6 we show the comparison between these calculations and the values from the tests. An Ln-Ln scale is used for a better distribution of the points on the graph, revealing a good correlation between the model and the experimental values. Behaviour is similar for the A30 and A6 belts.

6.3   Tangential Cutting Coefficient

From the experimental design dealing with the tangential cutting coefficient the average of this parameter can be established for each type of belt (see Fig. 7a). It is greater the larger the size of the grains.

The coefficients of input parameter effect and interaction are less than 1/10 of the average standardised value. The pressure, speed and abrasive wear parameters therefore have only a very weak influence on the tangential cutting coefficient.

(a): Tangential cutting coefficient   (b): Arithmetic average deviation (Ra)
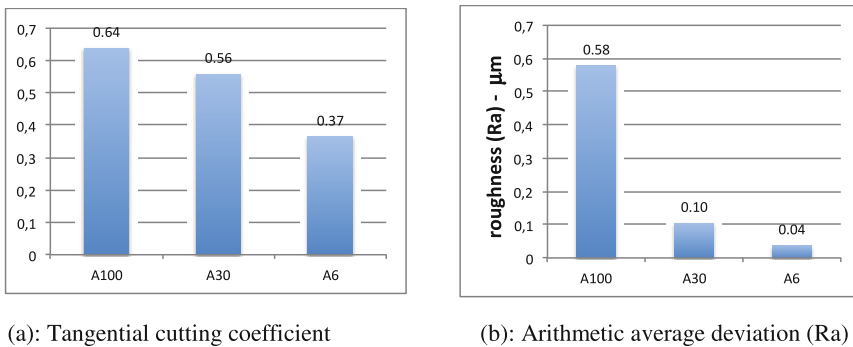
Fig. 7 Average values from experimental design

6.4   Roughness of the Polished Surface

Standard NF EN ISO 4287 (ISO 4287) suggests different parameters to characterise the roughness of a metal surface. For our work, we decided to use the arithmetic average deviation criterion of the profile (Ra). Readings were taken using a 3D ALTISURF 500 roughness meter equipped with a confocal white light sensor.

Figure 7b shows the average values of (Ra) for the three types of belt studied. In this instance too, average values are lower the smaller the grain size. For the interaction coefficients specific to each input parameter, values have little influence on output, with most being less than 10% and with a maximum at 20%. And here too the parameters of the process, with the exception of grain size, have no influence on the arithmetic average deviation of the profile of the polished surface.

6.5   Wettability

Wettability is the ability of a liquid to spread over a surface. It is defined by the angle (θ) between the tangent at the base of a drop of distilled water and the

surface on which the drop is placed. Based on Young's equation, the link can be established between surface tensions σ_{solid}, σ_{liquid}, interfacial tension $\gamma_{liquid/solid}$ and contact angle θ using the following equation:

$$\sigma_{solid} = \gamma_{liquid/solid} + \sigma_{liquid} * \cos(\theta) \tag{9}$$
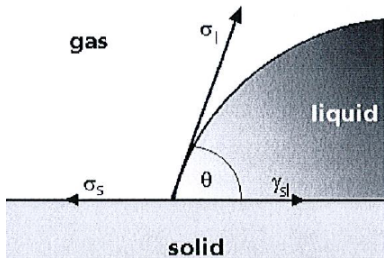
(a): Angle determining wettability
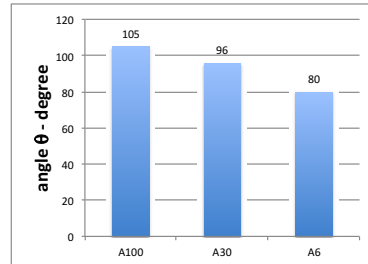
(b): Angle (θ) for 316L stainless steel

Fig. 8 Characterisation of wettability

This ability runs counter to the process whereby paint or adhesive sticks to a backing. The greater the angle (θ) the more difficult it will be to make a coating adhere to the surface. The results obtained here show the influence of particle size on the wettability of the surface obtained for 316L stainless steel.

7   Conclusion

The aim of this study was to characterise the polishing process for 316L stainless steel using structured abrasive belts. After describing their main geometric characteristics, we proposed a model based on Preston's law to determine material removal. We set up an experimental test bench in order to produce an experimental design and were thus able to validate the model suggested for different grain sizes. We were also able to specify the tangential cutting coefficient, roughness and wettability of the polished surface for three types of belt and show that only grain size has a bearing on these production goals.

References

Felder, E.: Usinage par abrasion - analyse expérimentale et théorique. Techniques de l'Ingénieur (2009)

Guiot, A., Tournier, C., Quinsat, Y.: Modélisation de l'usure des abrasifs pour garantir la qualité des surfaces polies. 13ème Colloque National AIP PRIMECA (2012)

ISO 4287. Geometrical Product Specifications (GPS) – Surface texture : Profile method – Terms, definitions and surface texture parameters (1998)

Klocke, F., Dambon, O., Zunke, R.: Modeling of contact behavior between polishing pad and workpiece surface. Prod. Eng. Res. Devel. 2, 9–14 (2008), doi:10.1007/s11740-007-0059-z

Lacharnay, V., Tournier, C., Poulachon, G.: Design of experiments to optimise automatic polishing on five–axis machine tool. International Journal of Machining and Machinability of Materials 12, 76–87 (2012)

Luo, J., Dornfeld, D.: Material removal mechanism in chemical mechanical polishing: theory and modeling. IEEE Transactions on Semiconductor Manufacturing 14, 112–133 (2001), doi:10.1109/66.920723

Nagata, F., Hase, T., Haga, Z., Omoto, M., Watanabe, K.: CAD/CAM-based position/force controller for a mold polishing robot. Mechatronics 17, 207–216 (2007), doi:10.1016/j.mechatronics.2007.01.003

Pessoles, X., Tournier, C.: Automatic polishing process of plastic injection molds on a 5-axis milling center. Journal of Materials Processing Technology 209, 3665–3673 (2009), doi:10.1016/j.jmatprotec.2008.08.034

Preston, F.W.: The Theory and Design of Plate Glass Polishing Machines. Journal of the Soc of Glass Technology, 214–256 (1927)

Wang, C.-C., Lin, S.-C., Hochen, H.: A material removal model for polishing glass–ceramic and aluminum magnesium storage disks. International Journal of Machine Tools and Manufacture 42, 979–984 (2002), doi:10.1016/S0890-6955(02)00004-4

Degradation of Mechanical Proprieties of TiN Coatings under Cyclic Nanoindentation

Kaouther Khlifi[1], Hafedh Dhifelaoui[1], Ahmed Ben Cheikh Larbi[1], and Ali Beskri[2]

[1] Ecole Nationale Supérieure des Ingénieurs de Tunis, Université de Tunis,
   5 Rue Taha Husein, 1008 Tunis, Tunisia
[2] Ecole Polytechnique de Tunisie, Université de Carthage, Tunisia
   khlifi.kaouther@yahoo.fr,
   {dhafedh,ahmed.cheikhlarbi}@gmail.com,
   beskri.ali@hotmail.fr

Abstract. TiN thin film was deposited on 100C6 steel (AISI 52100) substrate with the PVD technique using magnetron sputtering. Morphological examination showed the presence of domes and craters which are uniformly distributed over the entire surface. Mechanical properties, plastic and elastic deformation resistance of TiN coating were studied using conventional indentation method. Cyclic nanoindentation technique, with variation of loading rate, was used to analyze the failure modes and depth profile of mechanical proprieties of TiN thin film. Cyclic nanoindentation technique was performed with a Berkovich indenter at maximum loads of 100 mN, then unloaded to 100% of the maximum load and repeatedly reloaded. The indentation cycles were 200 cycles. When the loading rate was increased from 200mN/mn to 400mN/mn, the mechanical proprieties were decreased. For the highest loading rate (400 mN/mn), hardness and Young's modulus falling have reached to 50, 50 % and 71,28%   respectively.

Keywords: cyclic nanoindentation, thin film, depth profile, mechanical properties.

1   Introduction

TiN-based hard PVD coatings remain always coatings reference. They have been successfully applied to a wide range of tools, dies and mechanical parts to enhance the lifetime and performance due to their high hardness, wear resistance and chemical stability (S. PalDey and S.C. Deevi 2003) (F. Vaz 1999) (S. Sveen 2013) (Tobias Sprute 2014) because it has a potential applications in many fields such as high speed machining and hot forming [Yucel Birol and Duygu I˙sler 2011]. Therefore, the resistance of the coatings to repetitive impact is also of great importance especially when speaking of thin films with nanometer scale layers. Nanoindentation test shows the famous solution which allows the determination of mechanical properties of thin films (G.G. Fuentes et al 2010 (Li Chen et al 2008)

(S.V. Hainsworth and W.C. Soh 2003). However, conventional nanoindentation test cannot be used to study the fatigue resistance of hard coatings. A new variation of the conventional test is cyclic nanoindentation, where the sample is immediately reloaded to higher loads/depths than the previous loading cycle. Few efforts have been conducted on this type of test to study phase transformation in materials (K.-D. Bouzakis et al 2004) investigation of the effect of the applied load, loading/unloading rate and dwell time on the mechanical parameters of the plasma polymer film (T. Saraswati et al 2000) and penetration profile of the Young's modulus and hardness of monolayer coating as we studied in our previous study (R. Trivedi and V. Cech 2010).

In the current study, cyclic nanoindentation test has been applied by repeatedly indenting the same location with a Berckovich nano-indenter in an attempt to quantify the mechanical behavior of thin films under cyclic loading and to obtain information about their fatigue resistance .A comparative study of conventional nanoindentation and cyclic nanoindentation, which was carried out under the same measurement conditions, was discussed.

2   Experimental Procedures

2.1   Substrate Material and Coating Deposition

100C6 steel (AISI 52100) is used as substrate. The sample was ground with a series of emery papers of 600 grit and 800 grit to be   polished to mirror-like with 1 μm-diamond powder corresponding to a surface roughness (Ra) of approximately 0,1 μm. And finally, it was ultrasonically cleaned with acetone and ethanol in an ultrasonic bath for 10 min before being dried and placed into the PVD deposition chamber. TiN coating was deposited in a commercial PVD magnetron sputter unit from the company Balzers in France. For the preparation of TiN coating, target was pure Ti (99.9% in molar fraction) from which titanium plasma was generated. A N2 gas was introduced in the chamber to reach a work pressure of 4 Pa, the gas flow rate is 150 cm3/min and the arc current is 18 A; substrate temperature – 280 °C. The total thickness of the film was 3 μm. To improve adhesion, a metallic Ti layer of thickness 200 nm was deposited.

2.2   Microstructural and Mechanical Characterizations

The morphological characterization of the coatings like the topography, the grain size, and the average roughness of the surface were obtained using an atomic force microscopy (AFM) with a cantilever tip in contact mode. Nanoindentation measurements of the TiN thin film were carried out at room temperature using a CSM instruments Switzerland attached to an optic microscope and an atomic force microscope. The displacement and load resolutions of the instrument were 0.0004 nm and 1mN, respectively.   A triangular pyramid (Berkovich) diamond indenter with a radius of curvature of 50 was used.

Conventional nanoindentation test was performed using a diamond Berkovich tip with a loading/unloading rate of 400mN/mn and with 10s dwell time at maximum load to determine the mechanical properties such as hardness and modulus. The maximum load was 50 mN, at this load; the indentation depth was much less than 1/10th of the film thickness, thus minimizing the effect of substrate on the hardness measurements (K. KHLIFI and A. Ben CHEIKH LARBI 2014). Cyclic indentation were conducted at different loading rates ranging from 200 mN/mn to 400mN/mn. A Berkovich indenter was used at maximum load of 100 mN and a dwell time of 10s at maximum and minimum loads. Then unloaded to 100% of the maximum load and repeatedly re-loaded to 200 cycles.

3   Results and Discussion

3.1   Morphology

AFM observation allows the examination of the surface topography as well as the determination of surface roughness of the nanolayer coating.   The three-dimensional surface morphologie of TiN coatings are shown in Figure 1.   It exhibited domes and craters which are uniformly distributed over the entire surface. TiN coating has an average roughness surface value of 27 nm.
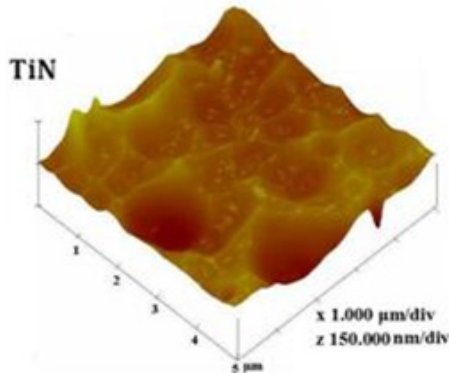
Fig. 1 Three-dimensional AFM images TiN/TiAlN nanolayer films along with their two-dimensional images

3.2   Conventional Nanoindentation

As we mentioned before, we have conducted nanoindentation measurements on TiN coating deposited in order to evaluate nano-mechanical film properties such as hardness and reduced elastic modulus values. The hardness to elastic modulus ratios (H/E and H^3/E^2) which have been proposed and consistently used to

evaluate the resistance to elastic and plastic deformation of thin film (Zenghu H et al 2004) (Ipaz L et al 2012). The load/unload vs. displacement curve (Figure 2) has a shape giving evidence of an elasto-plastic behavior of TiAlN/TiN coating. The Oliver–Pharr method (W. C. Oliver and G. M. Pharr 1992) was used to calculate mechanical properties, such as the modulus and hardness, using the upper portion of the unloading curve.
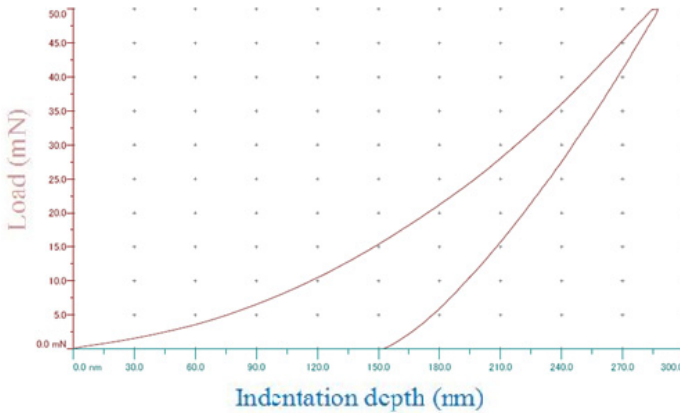
Fig. 2 A load–displacement curve of TiN thin film

Five indentations test were made and the result of hardness, elastic modulus, H/E and H^3/E^2 ratio values of the studied coating are given in table 1.

Table 1 Mechanical properties from the conventional nanoscale characterization of TiN and 100C6 steel

Mechanical proprieties	H(GPa)	E (GPa)	H/E	H^3/E^2
TiN	23	350	0,065	0,10
100C6 steel	9	200	0,045	0,018

The values of hardness and elastic modulus are significant when. This has influenced the mechanical behavior and increased resistance to plastic and elastic deformation of the film comparing to the substrate behavior.

3.3 Cyclic Nanoindentation

Furthermore, we have conducted cyclic nanoindentation tests in order to study the deformation behavior when reloading-unloading many times the TiN thin film. Indentation test with Berkovich indenter was used at maximum loads from 100 mN then unloaded to 100% of the maximum load and repeatedly re-loaded to 200 cycles as shown in figure 3.
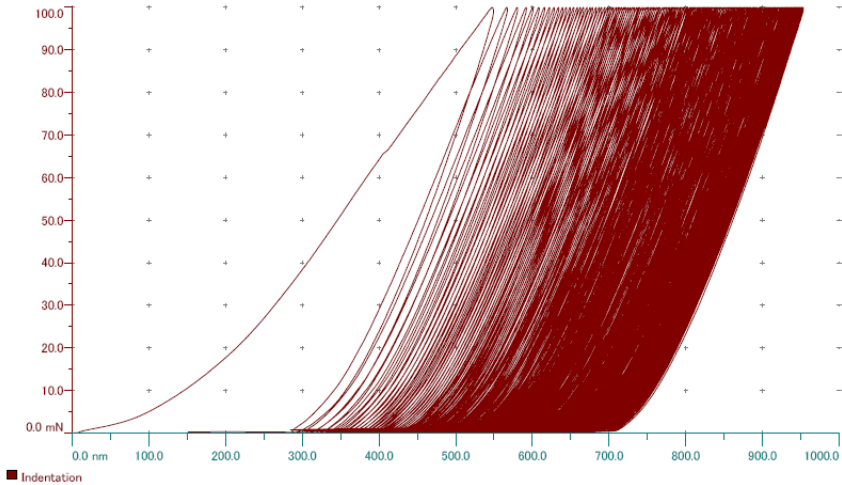
Fig. 3 Relationships between the applied load and impression depth of the investigated coating at 200 cycles

All unloading–reloading curves were found to superpose showing an elasto-plastic behavior when reloading again the TiN coating. A similar trend for load–displacement curves was also observed at the maximum loading rate of 400mN/mn. The influence of the number of applied cycles on the maximum impression depth under loading rate of 200 mN/mn and 400mN/mn is illustrated in Figure 4.
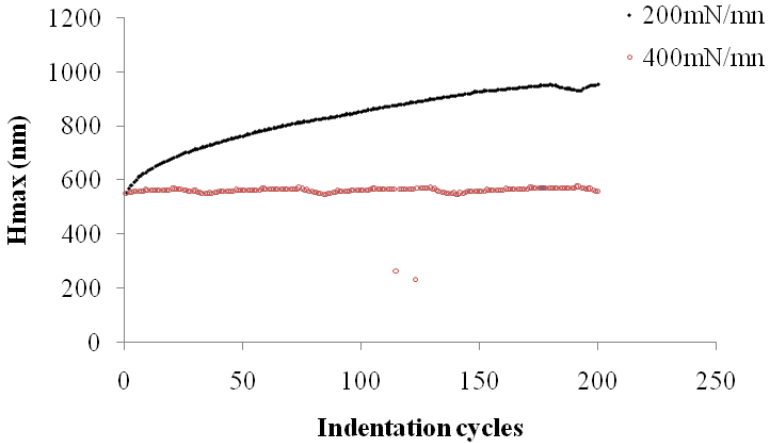
Fig. 4 Variation of maximum indentation depth with indentation cycles

A similar behavior has been found during indentation cyclic fatigue with a variation of loading rate. The increase of cycle number increases the maximum indentation depth. Nevertheless, it can be clearly seen that the maximum indentation depth increases very slowly with an increase of cycle number at low loading rate (200 mN/mn). When the loading rate was 400mN/mn, abrupt step increases in the maximum indentation depth appeared as illustrated by curve shown in Figure 4.

During the 200 cycles, the impression depth of the TiN coating increases slightly with the increase of number of cycles. For the higher loading rate of 400 mN/mn, the coating system was deformed more extensively and was exhibited an impression depth $\approx$ 954 nm. We noted that the maximum depth corresponding to the highest loading rate exceeded the 10% of the film thickness. Moreover, the influence of the number of cycles used in cyclic experiments on the mechanical properties such as hardness and Young's modulus measurements were plotted versus the loading rates, and are shown in Figures 5 and 6.
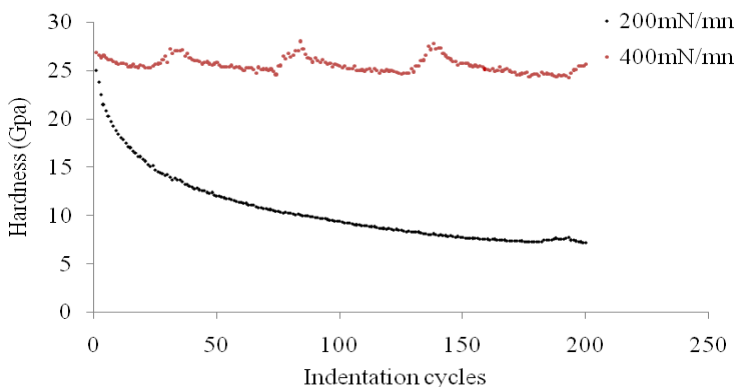
Fig. 5 Variation of hardness with the indentation cycles
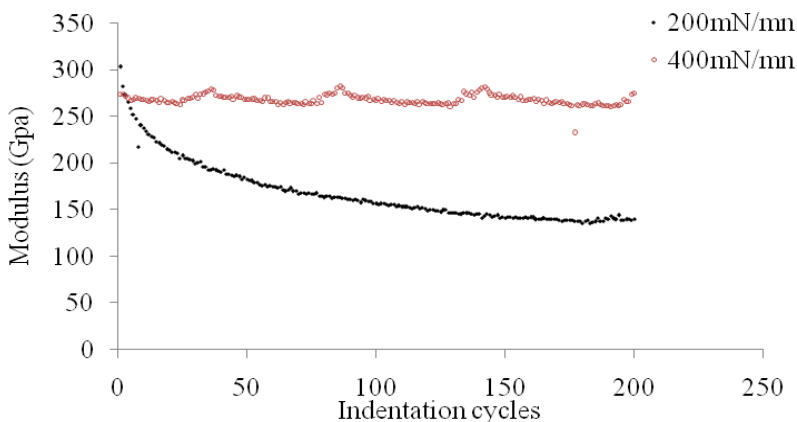
Fig. 6 Variation of Young's modulus with the indentation cycles

Figure 5 and 6 show the relationship between the mechanicals proprieties (hardness and Young's modulus) and the indentation cycles of TiN thin film for a different loading rate.

The results show two major ideas: the mechanicals proprieties decrease when the indentation cycles increase and it decrease also when the loading rate increase.

Therefore, the hardness and Young's modulus decrease when the indentation cycles increased regardless the loading rate value. The degradation of mechanical properties with the number of cycles is explained by the loss of rigidity of the film material during cyclic loading.

This result is proved when compared the results obtained by conventional nanoindentation and those achieved by cyclic nanoindentation. The values of mechanical properties (hardness and modulus) obtained by the conventional nanoindentation are higher than those obtained by cyclic nanoindentation. In the case of cyclic loading, degradation of mechanical properties of the coatings is more important. This is related to the increase of maximum depth as a function of the number of cycles (Figure 4) because the loading time is more important.

But it is clear that the fall in the hardness and Young's modulus values as a function of indentation cycles is not the same when moving from the lowest loading rate (200 mN/mn) to the highest loading rate (400 mN/mn). with increasing the indentation cycles from the first cycle to the 200 cycles and for a loading rate of 400 mN/mn, the hardness and the Young's modulus decreases respectively by 50,50% from 25 to 7,18 GPa and by 71,28% from 282 to   139 GPa, as the indentation cycles was increased from one cycle to 200 cycles. The degradation of mechanical properties is more significant in the case of high loading rate. Indeed, a high loading rate is linked to a low indentation time and a large accumulation of plastic deformation followed by chipping and damage of film/substrate interface. In this case, there will be a very rapid onset of substrate effect on the film behavior because the maximum depth corresponding to the highest loading rate was more than 954 nm. It exceeded the 10% of the film thickness showing the substrate effect.

4   Conclusion

TiN thin film was deposited on 100C6 steel (AISI 52100) substrate with the PVD technique using magnetron sputtering. The mechanical behavior of TiN coating was studied using both the conventional indentation method and cyclic indentation method, accelerating depth-profile analysis. The conventional method was used to in order to determine the mechanical proprieties (hardness and Young's modulus). Cyclic nanoindentation tests were performed over a wide range of indentation cycles from one cycle to 200 cycles at various loading rates in the range of 200 and 400mN/mn to characterize the effect of cyclic solicitation modes on mechanical behavior of TiN coating. Nanoindentation fatigue experiments can provide very useful informations on plastic deformation and mechanical proprieties in thin film coatings.

The results obtained from the two methods conventional and cyclic were followed the same trend. However, the prolonged time used for cyclic indentation resulted in a diminished value of the Young's modulus and hardness.

The variation of the hardness and the modulus as a function of cycle number for different loading rate was studied. After 200 cycles, the measured hardness is found to decrease rapidly for the highest loading rate of 400mN/mn comparing to 200mN/mn. The same behavior was be found for Young's modulus. The mechanisms related to the evolution of indentation fatigue depth at constant indentation load were then at the origin of the loss of mechanical properties of a coating.

References

PalDey, S., Deevi, S.C.: Mater. Sci. Eng. A-Struct. 342 58 (2003)

Vaz, F., Rebouta, L., Andritschky, M., da Silva, M.F., Soares, J.C.: J. Mater. Process. Technol. 169, 92–93 (1999)

Sveen, S., Andersson, J.M., M'Saoubi, R., Olsson, M.: Wear 308, 133–141 (2013)

Sprute, T., Tillmann, W., Grisales, D., Selvadurai, U., Fischer, G.: Surface & Coatings Technology, 369–379 (2014)

Birol, Y., I'sler, D.: Materials Science and Engineering A 528, 4703–4709 (2011)

Fuentes, G.G., Almandoz, E., Pierrugues, R., Martinez, R., Rodriguez, R.J., Caro, J., Vilaseca, M.: Surf. Coat. Technol. 205, 1368 (2010)

Chen, L., Wang, S.Q., Zhou, S.Z., Li, J., Zhang, Y.Z.: International Journal of Refractory Metals & Hard Materials 26, 456–460 (2008)

Hainsworth, S.V., Soh, W.C.: Surface and Coatings Technology, 163–164, 515–520 (2003)

Bouzakis, K.-D., Skordarisa, G., Hadjiyiannisa, S., Asimakopoulosa, A., Mirisidisa, J., Michailidisa, N., Erkensb, G., Cremerb, R., Klockec, F., Kleinjansc, M.: Thin Solid Films, 264–271, 447–448 (2004)

Saraswati, T., Sritharan, T., Mhaisalkar, S., Breach, C.D., Wulff, F.: J. Mater. Sci. Eng., Gogotsi, Y.G., Domnich, V., Dub, S.N., Kailer, A., Nickel, K.G.: J. Mater. Res. 15, 871 (2000)

Trivedi, R., Cech, V.: Surface & Coatings Technology 205, S286–S289 (2010)

Khlifi, K., Ben Cheikh Larbi, A.: Journal of Adhesion Science and Technology 1, 28 (2014)

A Study of the Plastic Deformation of CrN Coatings Deposited by RF Sputtering

Asma Jellad

Laboratoire de Génie Mécanique LGM-MA05, ENIM, Av. Ibn El Jazzar, 5019 Monastir, Tunisie
ja_asma@yahoo.fr

Abstract. Nanoindentation tests were conducted on chromium nitride thin films deposited on two different substrates: silicon and Zr-based metallic glass. The coatings have a thickness of 300 nm and are deposited by RF sputtering using a chromium target. The plastic deformation of the CrN coatings were investigated by cyclic indentation tests at various loading rates. The plastic behaviour was studied in the case of the two used substrates. It is shown that the films deposited on silicon substrate show higher values of hardness and reduced elastic modulus as well as an increase of the plastic and wear resistance with the indentation depth. Furthermore, we found that these CrN films deposited on silicon substrate exhibit higher irreversible plastic deformation compared to the films prepared on bulk metallic glass substrate under cyclic indentation tests conducted at low loading rate of 100µN/s.

Keywords: Cyclic nanoindentation tests, Thin films.

1   Introduction

Chromium nitride films deposited by physical vapour deposition technique are widely applied to protect the surface of the material because of their attractive properties. They show excellent properties in hardness, adhesion strength, ductility, wear and corrosion resistance. Due to these properties, they were used as hard protective films for forming and casting applications (Mitterer et al. 2000) (Gekonde et al. 2002) (Lin et al. 2008). Nanoindentation technique was used to evaluate the mechanical properties of thin coatings. Cyclic nanoindentation tests could be used to extract sensitive material information that could not reflected in the conventional indentation test. Several studies have shown that cyclic indentation tests could be used to study plastic deformation material and phase transformations under stress (Mann et al. 2002) (Dub et al. 2001). It was found that a hysteresis loop, ie when the reloading path may not overlap with the unloading path of the previous loading cycle, could occur for Ca-doped Au rods under cyclic indentation tests (Saraswati et al. 2006). This material behaviour was related to the Baushinger effect when a limited reversible plastic deformation on unloading occurs and a difference in unloading and reloading paths was observed. In this

paper, we conducted several cyclic nanoindentation in order to study the deformation mechanisms occurring in the CrN coatings deposited on silicon and Zr-based metallic glass ($Zr_{50}Cu_{40}Al_{10}$) substrates. We focused on the influence of the substrate on the mechanical properties such as hardness, reduced elastic modulus and plastic behaviour of these CrN thin films.

2 Experimental

The CrN coatings were deposited by RF sputtering technique on silicon and Zr-based metallic glass ($Zr_{50}Cu_{40}Al_{10}$) substrates using a chromium metallic target. The target-substrate distance was fixed at 7 cm. The CrN films were deposited at room temperature under nitrogen reactive gas and a pressure of 0.67 Pa. The samples were previously cleaned with acetone and alcohol ultrasonic baths before the deposition process. The investigated CrN films have a thickness of 300 nm.

Indentation tests were conducted on CrN coatings, silicon and $Zr_{50}Cu_{40}Al_{10}$ samples using a triboscope system (Hysitron Inc.) coupled with an atomic force microscope (S. Labdi et al. 2006). The displacement and the force resolutions of the system were 0.04 nm and 1 nN, respectively. Before indentation tests, a calibration of the system was done on a fused silica sample in order to correct machine compliance and establish the area function. A Berkovich indenter tip with an included angle of 142.3° and a final radius of 100 nm was used and five tests were repeated at each indentation test. The loads applied for the tests were ranged from 750 µN to 6000 µN. The tests were performed at various loading rates (100µN/s , 500 µN/s , 2500 µN/s).

The hardness H and the reduced elastic modulus E were determined from the experimental load-displacement curve using the Oliver and Pharr model (Oliver and Pharr 1992) (Chicot and Tricoteaux 2010). The indentation impression was observed with an atomic force microscope using the same indenter tip.

3 Results and Discussions

The Nanoindentation tests were conducted on four samples: silicon (Si), Zr-based metallic glass (BMG), chromium nitride films deposited on silicon (CrN/Si) and on Zr-based metallic glass (CrN/BMG). First, we have applied single loading-unloading indentation conventional tests. The residual impression of the indentation tests was captured using the same indenter. Figure 1 shows the AFM images obtained for the CrN samples when indenting at a normal load of 3750 µN at a loading rate of 100µN/s. As seen in Fig.1, the residual topography of the indentation impression was found to have almost the same size and the plastic deformation behaviour was not described by the pile-up phenomenon.
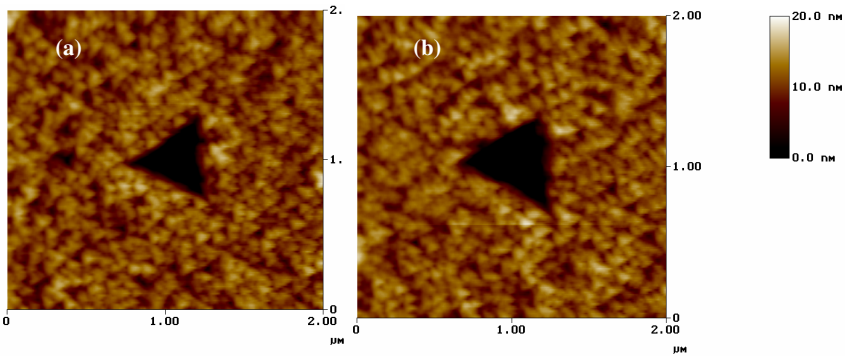
Fig. 1 AFM images of two indentations conducted on (a) CrN/Si and (b) CrN/BMG samples at a load of 3750 μN

The hardness *H*, elastic reduced modulus *E* and *H/E* ratio values of silicon and metallic glass substrates are given in table 1. The evolution of the average of the indentation hardness and elastic modulus as a function of the indentation depth are shown in Fig. 2. As shown in Fig.2, the highest values of hardness and elastic modulus were obtained for the CrN films deposited on silicon substrate. The evolution of *H/E* ratio values of the CrN samples as a function of the indentation depth is plotted in Fig. 2. As reported in (Jellad et al. 2008) (Rebholz et al. 1999) (Musil et al. 2002), the *H/E* ratio parameter could be used to evaluate the resistance of the film to plastic deformation and wear. As shown in Fig.2c, *H/E* ratio was found to increase with the indentation depth in the case of the CrN/Si films. This means that these films show the best resistance to plastic deformation. In addition, we have conducted cyclic nanoindentation tests in order to have more information about the plastic deformation behaviour of the CrN films. We have applied three indentation cycles (loading-unloading). The tests were done at three values of loading rate (100 μN/s , 500 μN/s , 2500 μN/s).

Table 1 Hardness, elastic reduced modulus and H/E ratio values of the silicon and Zr-based metallic glass substrates

Substrates	H(GPa)	E(GPa)	H/E
Silicon	10.78±1.36	150.2±7.00	0.072
$Zr_{50}Cu_{40}Al_{10}$	7.59±0.27	113.6±5.9	0.066

Fig. 3 shows the experimental load-displacement curves obtained for the CrN samples deposited on silicon and metallic glass at loadings rates of 100 μN/s , 500 μN/s and 2500 μN/s. We can notice that for CrN films deposited on both silicon and bulk metallic glass substrates, the unloading-reloading paths overlap and form a hysteresis loop, as shown in Fig.3a. This behaviour signifies that the material was harder on reloading compared to the previous unloading path. This phenomenon was observed only at a loading rate of 100 μN/s when conducting three cyclic indentation test and disparate at higher values of loading rate (500 μN/s and 2500 μN/s) where the unloading-reloading paths do not overlap, as shown in Fig. 3b and Fig. 3c.
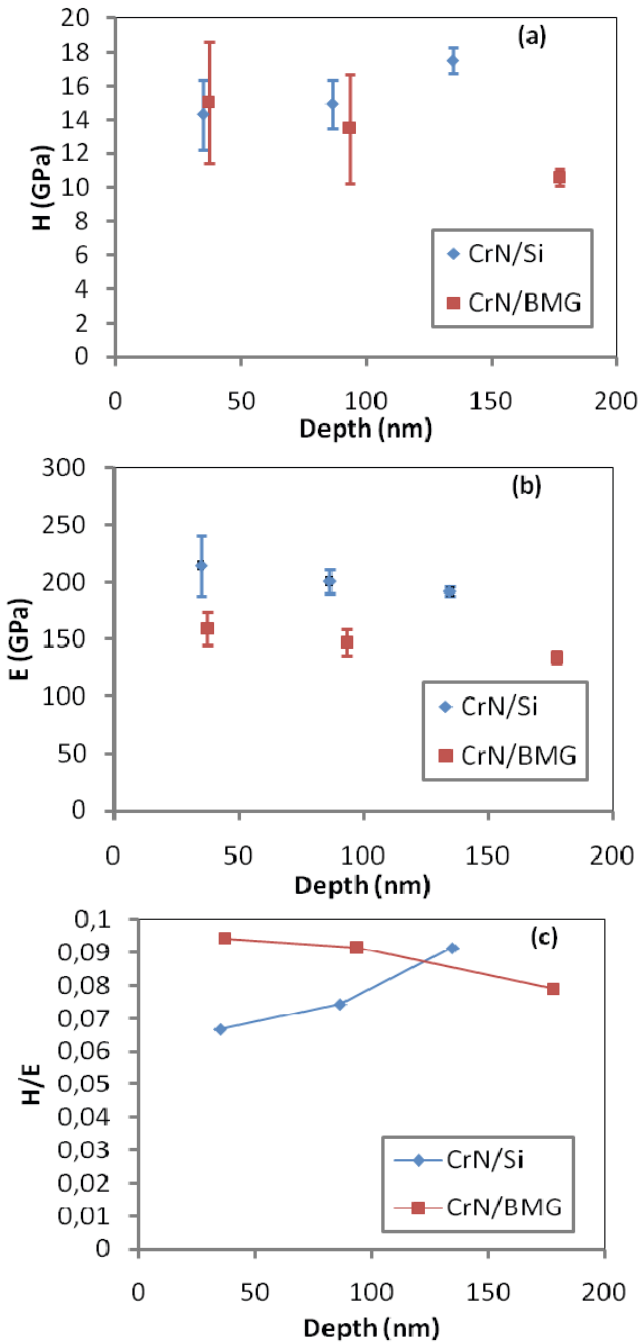
Fig. 2 (a) Hardness (b) elastic reduced modulus and (c) H/E ratio values obtained for the CrN films deposited on silicon (Si) and Zr-based metallic glass (BMG)
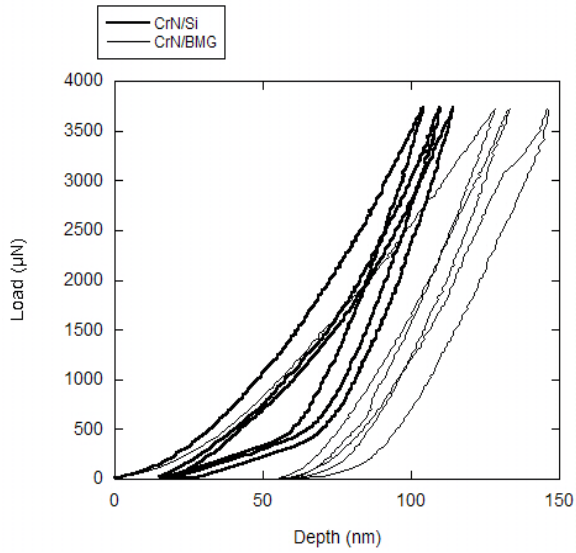
(a)
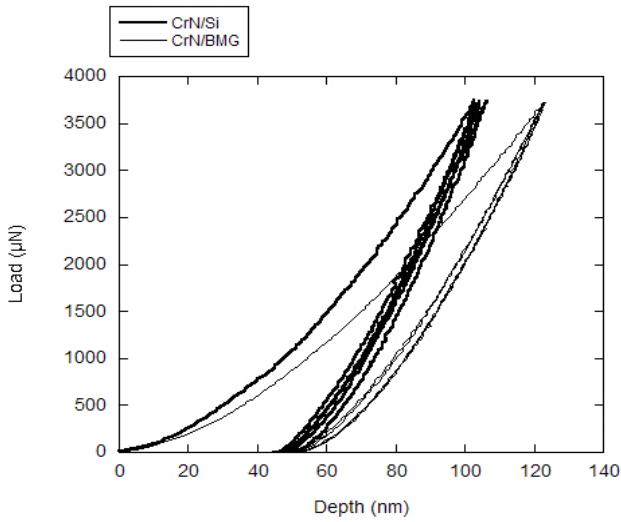
(b)

Fig. 3 Experimental load-displacement curves under cyclic indentation tests (three loading-reloading cycles) conducted on CrN/Si and CrN/BMG samples at various values of loading rate (a) 100 μN/s (b) 500 μN/s and (c) 2500 μN/s
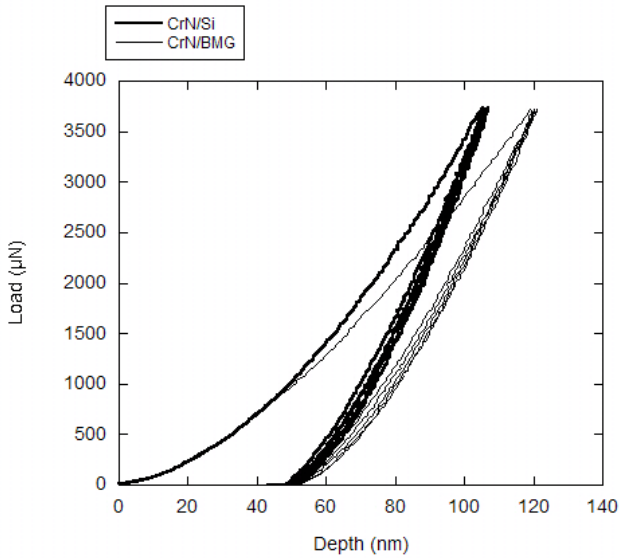
(c)

Fig. 3 (*continued*)

Some studies in the literature have noted this hysteresis behaviour in interrupted tensile tests of high-Si steels and Al alloys, as reported in (Brownrigg and Sitharan 1987) (Sitharan and Chandel 1997). This mechanism of the formation of hysteresis loops was explained, in the case of tensile or compressive tests, and related to micro-back stress resulting from inhomogeneous plastic deformation (Sritharan and Chandel 1997). As reported in (Sritharan and Chandel. 1997), the loop width may be a good indicator of the average residual micro back stress in the material. To quantify this material behaviour, other authors used the parameter "Full Width at Half Maximum" (FWHM), defined as the loop width at the average load between maximum and minimum load points in an unloading-reloading cycle (Saraswati 2006). This parameter measures the disparity between the reloading and unloading paths. An average FWHM value of 3 nm was computed for CrN films deposited on BMG substrate where a greater value of approximately 8nm was found for CrN deposited on silicon substrate. This means that the hardening behaviour was more important in the case of the CrN films deposited on silicon substrate (the reloading path has a higher gradient than the unloading path). So, it is clear that the CrN films deposited on silicon substrate shows the best resistance to penetration and ductility.

4   Conclusion

Cyclic indentation tests were carried out at various loading rate values on CrN samples deposited on Si and $Zr_{50}Cu_{40}Al_{10}$ in order to study the effect of the substrate on deformation mechanisms of these coatings. An enhanced increase of both hardness and reduced elastic modulus values have been obtained for the CrN coatings compared to the substrates values. The ratio H/E value was found to increase with the indentation depth for the CrN films deposited on silicon substrate, showing a better plastic resistance compared to the films deposited on BMG substrate. In addition, cyclic indentation tests show that an hysteresis behaviour was occurred for CrN films deposited on Si and BMG and this at the lower value of the loading rate of 100µN/s. This disparity between unloading and reloading paths was found to be dependent on the loading rate value. Both plastic energy and the FWHM observed from the unloading-reloading paths show a highest irreversible plastic deformation and a best wear resistance for CrN films deposited on silicon substrate.

References

Mitterer, C., Holler, F., Ustel, F., Heim, D.: Application of hard coatings in aluminium die casting soldering, erosion and thermal fatigue behaviour. Surf. Coat. Technol., 125–233 (2000)

Gekonde, H.O., Subramanian, S.V.: Tribology of tool–chip interface and tool wear mechanisms. Surf. Coat. Technol., 149–151 (2002)

Lin, J., Mishra, B., Moore, J.J., Sproul, W.W.A.: Study of the oxidation behavior of CrN and CrAlN thin films in air using DSC and TGA analyses. Surf. Coat. Technol., 3202–3271 (2008)

Mann, A.B., Dvan, H., Pethica, J.B., Bowes, P., Weighs, T.P.: Contact resistance and phase transformations during nanoindentation of silicon. Philos. Mag. A82, 1921 (2002)

Dub, S.N., Milman, Y.V., Lotsko, D.V., Belous, A.N.: The anomalous behavior of Al-Cu-Fe quasicrystal during nanoindentation. J. Mater. Sci. Lett. 20, 1043 (2001)

Saraswati, T., Sritharan, T., Mhaisalkar, S., Breach, C.D., Wulff, F.: Cyclic loading as an extended nanoindentation technique. Materials Science and Engineering A, 423–414 (2006)

Labdi, S., Jellad, A., Maciejack, O.: Loading rate effect on lateral force measurements on nanostructured Ti and TiN thin films. Surf. Coat. Technol. 201-113 (2006)

Oliver, W.C., Pharr, G.M.: Improved technique for determining hardness and elastic modulus using load and displacement sensing indentation experiments. J. Mater. Res. 7, 1564 (1992)

Chicot, D., Tricoteaux, A.: Mechanical properties of ceramics by indentation. Principle and applications, Ceramic Materials Chapter (2010)

Jellad, A., Labdi, S., Malibert, C., Renou, G.: Nanomechanical and nanowear properties of Cr3C2 thin films deposited by rf sputtering. Wear, 264–893 (2008)

Rebholz, C., Leyland, A., Schneider, J.M., Voevodin, A.A., Mattews, A.: Structure, hardness and mechanical properties of magnetron sputtered titanium aluminium boride films. Surf. Coat. Technol. 120, 121–412 (1999)

Musil, J., Kunc, F., Zeman, H., Polakova, H.: Relationships between hardness, Young's modulus and elastic recovery in hard nanocomposite coatings. Surf. Coat. Technol. 154–304 (2002)

Brownrigg, A., Sritharan, T.: Spring steel hysteresis. Mater. Forum 10, 58 (1997)

Sritharan, T., Chandel, R.S.: Phenomena in interrupted tensile tests of heat treated aluminium alloy 6061. Acta Mater 45, 3155 (1997)

Influence of Tribological Parameters on Single and Multi-indenter Scratch Behavior of Aluminum Alloy

Fatma Elwasli[1], Slah Mzali[1], Ali Mkaddem[2,3], Frahat Zemzemi[4], and Salah Mezlini[1]

[1] LGM, Ecole Nationale d'Ingénieurs de Monastir,
Avenue Ibn Aljazzar 5019 Monastir, Tunisie
`elwaslifatma@gmail.com`,
`mzalislah@laposte.net`
[2] University of Jeddah, Mechanical Engineering Dept. - P.O. Box 80200,
21589 Jeddah, Saudi Arabia
`amkaddem@uj.edu.sa`
[3] Arts et Metiers Paris Tech, Rue Saint Dominique, B.P.508,
51006 Châlons-en- Champagne, France
`ali.mkaddem@ensam.fr`
[4] LMS, Ecole Nationale d'Ingénieurs de Sousse,
BP 264 Sousse Erriadh 4023 Sousse, Tunisie
`{fzemzemi,salah.mezlini}@gmail.com`

Abstract. The aim of the present paper is to study aluminum alloy behavior against single and multi-indenter scratch tests. An experimental device was designed. Scratch test, using a steel conical indenter, was carried out at a constant sliding velocity of 210 mm/min. First of all, the influence of tribological parameters on apparent friction coefficient was investigated. Four attack angles of 10, 30, 45 and 60° are selected. The normal load was varied from 10 to 25N by increment of 5N. Moreover, the study of the wear mechanisms by microscopic observation has been conducted. It has shown that tribological parameters have an essential influence on the apparent friction coefficient and wear mechanism. Then correlation between tribological parameters and wear mechanisms has been highlighted. This correlation allowed elaborating a map wear for both single and multi-indenter scratch tests. Finally, comparison between single and multi-indenter scratch test has been performed in order to understand the effect of interaction between scratches.

Keywords: scratch test, tribological parameters, wear mechanisms, wear map.

1 Introduction

Thanks to its low density, the use of aluminum is introduced in several applications such as shipbuilding, trailers, tanks, etc... The operating conditions of these structures often require a good wear resistance. The abrasive wear is one of the predominant forms of wear in the industrial world. It occurs when there is friction between two surfaces in sliding movement and causes damage to the surface.

Experimental investigation is an interesting ways to analyze the wear mechanism. There are numerous methods for testing the abrasive wear (Khrushchev 1974). The scratch test is one of the most useful techniques to investigate the scratch behavior of materials. This test enables analysis of the elementary wear mechanisms. It allows to study the effect of each parameter separately.

Many previous experimental investigations have been performed on metallic and non-metallic material (Kayaba et al. 1986), (Hokkirigawa and K. Kato 1988) and (B. J. Briscoe 1996). Hokkirigawa and K. Kato (Hokkirigawa and K. Kato 1988) realized a pin on disc test on brass S45C and SUS304. They followed the evolution of friction coefficient and wear mode as a function of degree of penetration. Experimental investigation has shown the presence of three wear mechanisms for the brass S45C and SUS304): cutting, wedge formation and ploughing. The correlation between degree of penetration and wear mechanisms has been established by developing a wear mode diagram for lubricated and unlubricated sliding test. This diagram has revealed that the degree of penetration has an important effect on the transition of wear mechanism.

In order to study the effect of scratch parameter on material behavior, numerous researches have been carried out (Mezlini et al. 2005) (Woldman et al. 2013) (Kato 1990). They showed that the wear mechanism depends not only on the degree of penetration, but also on normal load, sliding velocity and abrasive particle geometry. Mezlini et al. (Mezlini et al. 2005) performed a scratch test on aluminum alloy using a conical indenter for different attack angles and normal loads. They showed that the wear mechanisms depend heavily on indenter shape. In fact, the increase of attack angle induces the transition of wear mechanism from ploughing to cutting. However, wear mechanism is independent of the normal load and neither is the friction coefficient.

The effect of indenter shape was also studied by Woldman et al (Woldman et al. 2013) using a pin on flat surface. For this experimental study a conical indenter with a hemispherical tip was used. The indenter has an attack angle of 60° and the tip radius was varied from 50 to 200 µm. Experimental results showed that wear rate increases with the decrease of the tip radius.

Extensive research has been undertaken to study the repeated sliding test. Kato (Kato 1990) and Kitswnai et al. (Kitswnai et al. 1990) extended the work of Kayaba et al. (Kayaba et al. 1986) by studying the effect of the number of friction cycles on the transition between wear modes during repeated sliding. They show that increasing the degree of penetration during repeated sliding test causes the transition of abrasive wear mode from ploughing to cutting. In contrast, the transition of wear mechanisms from cutting to ploughing occurs when the number of sliding increases.

Over the last decade, few researches have been interested on studying the interaction between scratches. Particularly, Mezlini et al. (Mezlini et al. 2004) studied the interacting between scratches by performing interacting scratches experiments for two aluminum alloys. For the 7xxx aluminum alloy, interaction between grooves induces the transition of wear mechanism from ploughing and wedge formation to cutting. However, for the 5xxx aluminum alloy the interaction between grooves has not a significant effect on the wear mechanisms.

Later, D.Silva et al. (D.Silva et al. 2011) investigated the scratch behavior of cooper by realizing a parallel scratches test. They studied the effect of the degree of superimposition. This parameter defines the ratio of the distance between the scratches to the width of a single scratch. They found that increasing the degree of superimposition causes the increase of mass removal and the wear mechanisms change from ploughing and wedge formation to micro-cutting.

Mapping is a suitable approach to illustrate the results obtained from the tribological characterization of materials. The scratch map presents an excellent description of the dependence of the material behavior on tribological parameter. Kato (Kato 1992) has established the scratch map that correlates between the wear mode and the degree of penetration.

Later, a scratch map for homogeneous and heterogeneous material was constructed by Mezlini et al. (Mezlini et al. 2009). Based on microscopic observation, they deducted the correlation between tribological parameters and wear mechanisms. The evolution of wear mechanism versus attack angle and normal load was followed. They found that the wear mechanism depends only on attack angle for the aluminum alloy, but for the nodular cast iron it depends on indenter shape and normal load.

This paper presents an experimental investigation of the scratch test. Single and multi-indenter scratch test have been conducted on aluminum alloy specimen. The effects of normal load and attack angle on friction coefficient and on wear mechanisms have been studied. Correlation between tribological parameters and wear mechanisms has been highlighted by establishing two wear maps for single and multi-indenters scratch test.

2   Single Indenter Scratch Test

2.1   Tests and Experimental Conditions

Experimental tests were carried out on an aluminum alloy sample using the scratch device (Fig. 1). The description of the scratch device was already detailed by Mzali et al (Mzali et al. 2013). This device is composed of a planning system, a sliding table, a motor and a piezoelectric transducer. The planning system adjusts the parallelism of the sample to the scratch direction. The motor assures the sliding of the table. Piezoelectric transducer controls the intensity of tangential load.

In order to understand the effect of tribological parameter on the friction coefficient and the wear mechanism, a series of tests was performed on aluminum alloy specimen. The scratch length was fixed at 20 mm and it was realized at a constant sliding velocity of 210 mm/min. A steel conical indenters with a hemispherical tip were used. According to previous work (Tkaya et al 2007) attack angle present an important parameter. Four attack angles of 10, 30, 45 and 60° were chosen to study their effects on friction coefficient and on wear mechanisms. The imposed normal load was varied from 10N to 25N. The tests were repeated at least three times for each sliding condition, and all experiments were realized without lubrication.
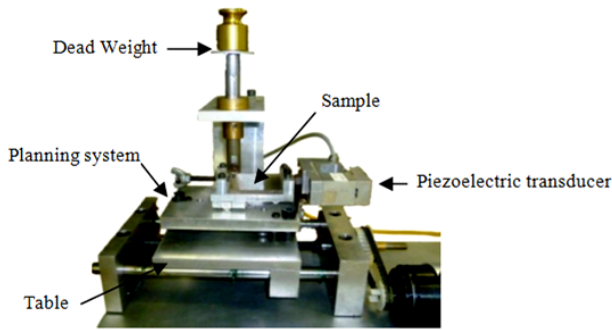
Fig. 1 Scratch device

2.2   Results and Discussion

Experimental tests were carried out for different attack angles and normal loads. During each test, tangential force was recorded. Fig. 2 illustrates an example of the evolution of tangential force and the apparent friction coefficient versus sliding distance for an attack angle of 10° at a normal load of 25N. The tangential force and friction coefficient remain almost constant during the sliding distance.
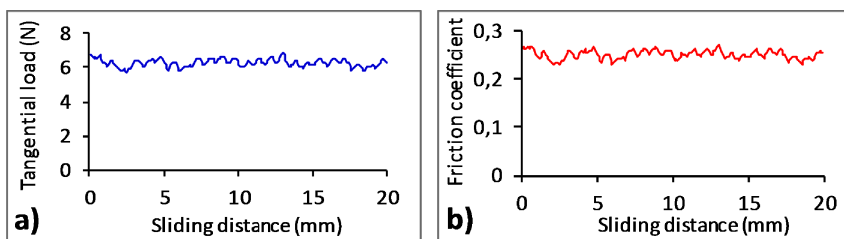
Fig. 2 a) Tangential force and b) Apparent friction coefficient versus sliding distance for an attack angle 10° and a normal load 25N

Firstly, the recorded results were used to calculate the average of friction coefficient for each configuration. Then, the apparent friction coefficient evolution was studied as function as the attack angle and normal load.

Fig. 3 shows the evolution of the apparent friction coefficient versus the attack angle for a normal load 10, 15, 20 and 25N. The apparent friction coefficient increases with the attack angle. Its value is multiplied by four from 10° to 60°. That is mainly due to the severe plastic deformation caused by a sharp indenter. The use of a sharp indenter induces a high dissipation of energy through plastic deformation. This suggests that the attack angle has an important influence on the apparent friction coefficient. By contrast, the effect of normal load is not significant and the friction coefficient remains almost constant.
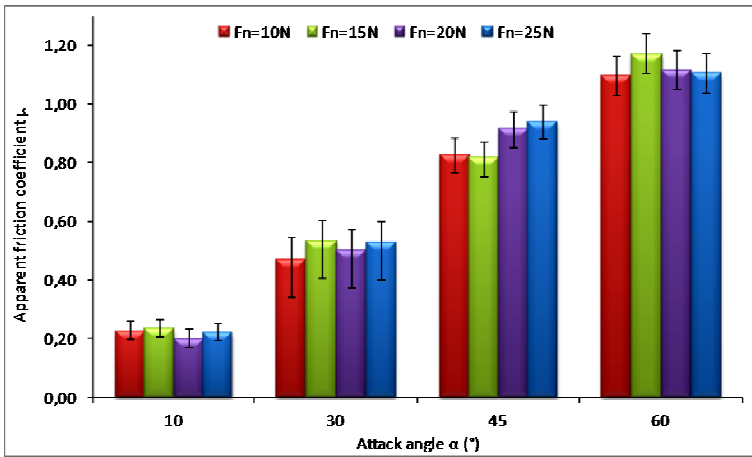
Fig. 3 Apparent friction coefficient versus attack angle for different normal load

In order to analyze the wear mechanisms, microscopic observations have been performed for different tribological conditions. Fig. 4 shows an example of microscopic observation made for two grooves using 10° and 60° attack angles at a normal load of 15N.

For an attack angle of 10° (Fig. 4.a), the material is pushed in the sides of the scratch without any material removal. In this case the dominant wear mechanism is the ploughing. However, an attack angle of 60° (Fig. 4.b) produces several debris and causes the material removal. Chip formation is generated in the sides and at the end of scratch because of the high contact pressure and the severe plastic deformation. So, for a high attack angle the cutting regime is established.

Microscopic observation has shown that the increase of the attack angle induces the transition of the wear mechanism from ploughing to cutting. Similar observation has been detected by Khellouki et al (Khellouki et al. 2013) for AISI 52100 steel.
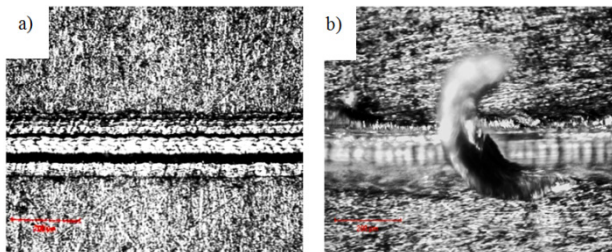
Fig. 4 Microscopic observation for attack angle: a) 10 and b) 30

Correlation between the wear mechanisms with tribological parameter was established through a wear map shown in Fig. 5. The analysis made on different attack angle and normal load has revolted the presence of three wear mechanisms: ploughing, transition and cutting.

The ploughing mechanism is the dominant wear mode essentially for an attack angle of 10° in addition to a 30° attack angle at low normal load (≥15N). In these conditions, material is pushed in the sides of the groove and there is no material removal. It was also noted that the apparent friction coefficient is the lowest.

The transition wear mechanism is dominant in two zones. The first one is at a large normal load (≥20N) and an attack angle of 30°. The second one is at a low normal load (≤15N) and an attack angle of 45°. Beyond these condition cutting phenomenon is dominant.

Cutting and wedge formation are the primary surface deformation processes which occur when the scratches were performed using a sharp attack angle. In this case, the scratch test was characterized by a high friction coefficient. This is due to the high energy dissipated through the plastic deformation. Microscopic observation has shown that, the chip formation is more severe with high normal load. This severe plastic deformation results from the high penetration of the sharp indenter.

The wear map shows the transition of wear mechanism from ploughing to cutting with the increase of attack angle and the normal load.
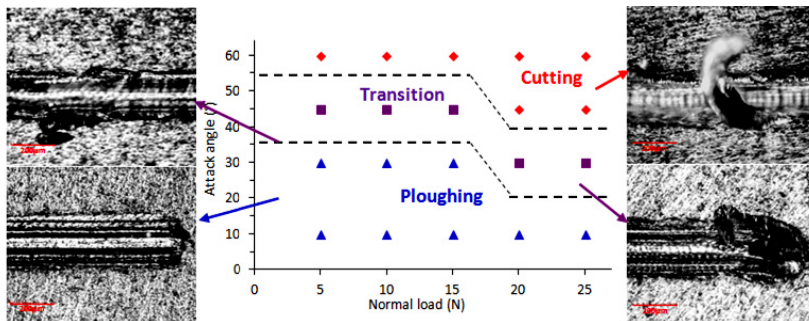
Fig. 5 Wear mechanism map for a single indenter scratch test

3   Multi-indenter Scratch Test

3.1   Tests and Experimental Conditions

In the first section, elementary analysis of the abrasive wear has allowed the comprehension of the abrasive wear mechanisms. Actually abrasive wear occurs due to a friction with several abrasive grains successively (Fig.6). In order to take into consideration the real phenomenon, the interaction between grooves will be taken into account. For that purpose, a multi-indenter scratch test was designed.

a)   b)
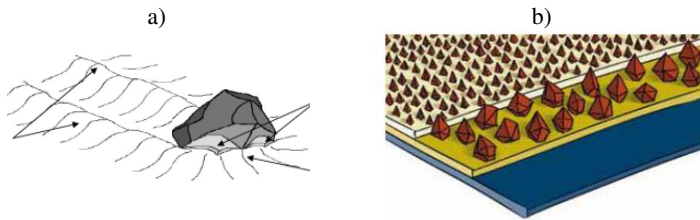
Fig. 6 a) Single abrasive grain, b) Structure of an abrasive tool

In this part, scratches are made on an aluminum specimen, without lubrication, using three indenters simultaneously. This device allows performing multi-indenter scratch test. The sliding distance and the sliding velocity were maintained at 30mm and 210mm/min, respectively. The scratches were realized using conical indenters with different attack angles varying from 10° to 60°. The normal load has been varied from 5 to 20N. It was applied using a dead weight for each indenter. The tangential force recorded by the piezoelectric transducer corresponds to the resultant force.

L and B are the distances between grains in the direction of the slide and the lateral direction respectively. These distances are fixed to ensure that B is equal to 100 μm (Fig. 7).
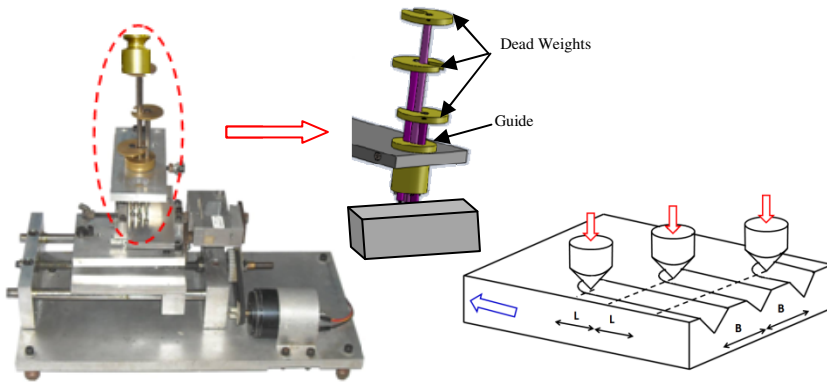
Fig. 7 Multi-indenter scratch test device

3.2   *Results and Discussion*

The tangential force recorded for the multi-indenter scratch test F_t is three times higher than that for the single indenter scratch test. The friction coefficient of multi-indenter scratch test μ is calculated according to the following equation:

$$\mu = \frac{F_t}{\sum F_n} \tag{1}$$

The effects of tribological parameter on friction coefficient have been investigated by varying the normal load and the attack angle. Fig. 8 illustrates the evolution of the apparent friction coefficient versus normal load and attack angle. It clearly shows the increasing trend of the apparent friction coefficient with the attack angle. That is due to the increase of the contact pressure with the attack angle. However, the normal load has not a significant effect on the friction coefficient.

Comparing the results found in single and multi-indenture scratch test, the use of several indenters induces the increase of the tangential force. However, a similar value of the friction coefficient evolution has been observed.
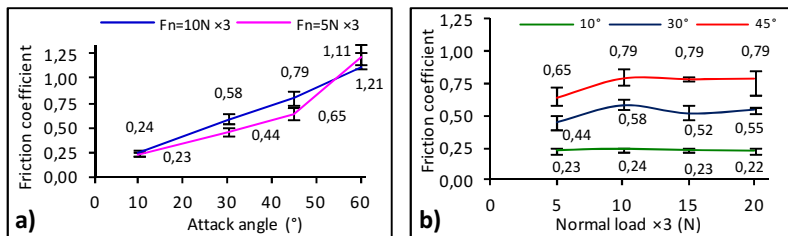
Fig. 8 Apparent friction coefficient versus a) attack angle for a normal load 15N and 30N, b) normal load with attack angles 10 and 45°

Microscopic observations have been performed to analyze the abrasive wear mode. Fig. 9 illustrates an example of microscopic observation of multi-indenter scratch test performed with indenters of 45° attack angle and three dead weight of 15N. The first indenter slides and causes the displacement of material on two sides of the groove without any loss of material (Fig. 9a). The second indenter passes on one of the two wedges generated by the first indenter (Fig. 9.b). This induces the loss of the wedge and the chip formation only on the left side where the interaction occurs. Then, a third indenter slides next to the two previous scratches and induces the chip formation on worn sides of the last scratch (Fig. 9.c). At first material is deformed plastically and wedges were formed. Then, the material removal and the chip formation were observed.
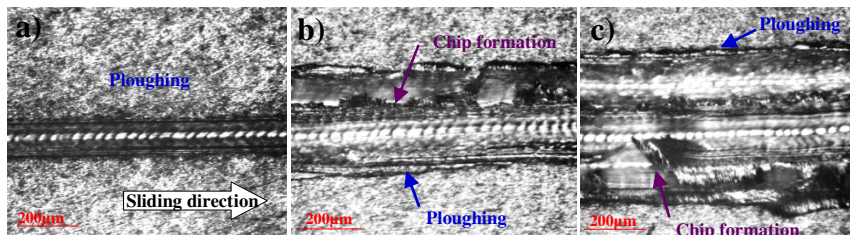
Fig. 9 Microscopic observation a) two parallel scratches and b) three parallel scratches

Fig. 10 illustrates a wear map for the multi-indenter scratch test. The correlation between wear mechanisms and tribological parameters allow differentiation between three wear mechanisms; the ploughing, the transition and the cutting. Ploughing is identified for low attack angle of 10°. In this case interactions have not any effect on the wear mechanisms. Material is pushed on the two sides of the groove without any material detachment. Whereas the attack angle of 45° at normal loads of 20N and attack angle of 60° cause the chip formation. In this region the dominant wear mechanism is the cutting. The interaction between scratches induces more material removal in comparison to the single indenter scratch test. In the intermediate zone, the ploughing and the cutting mechanisms both are present.
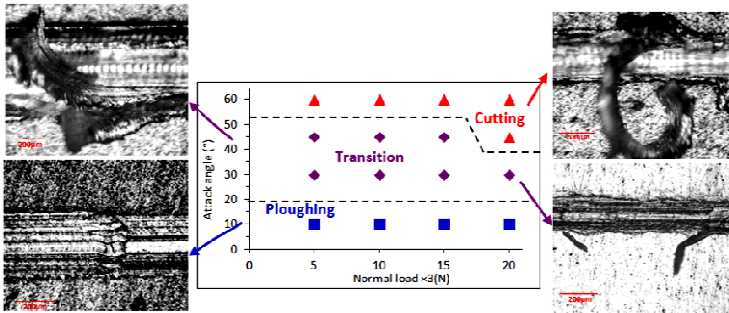
Fig. 10 Wear mechanism map

Wear map showed that, the dominant wear mechanisms are influenced by the interaction between scratches. In fact, for multi-indenter scratch test, the chip formation mechanism was observed even with a small attack angle which cannot cut material initially. In addition, the scratch superimposition enhances the material removal. Thus, the interaction between scratches causes the transition of wear mechanism from ploughing to wedge formation and accelerates the generation of material removal.

4   Conclusion

The main objective of this paper is to improve comprehension of wear mechanisms during single and multi-indenter scratch test. Single and multi-indenter scratch tests were performed to understand the effect of tribological parameter on friction coefficient and on wear mechanisms. The experimental results allowed to take into account the phenomenon of interaction between scratches. In addition, they permit the identification of the different wear mechanisms generated by scratching test.

Two wear maps were developed from the correlation between tribological parameters and microscopic observations. Three dominants regions are observed on the maps: ploughing, transition (wedge formation) and cutting.

For the single indenter scratch test, the variation of attack angle induces the transition of wear mechanisms. In fact, for a small attack angle of 10° the wear mechanism was the ploughing and for high attack angle of 45 or 60° the dominant wear mechanism was the cutting.

For multi-indenter scratch test transition region becomes larger. Wear mechanism passes from ploughing, for single indenter scratch test, to wedge formation for multi-indenter scratch test. Even with a small attack angle a material removal was observed.

References

Khruschov, M.M.: Principles of Abrasive Wear. Wear 28, 69–88 (1974)

Kayaba, T., Hokkirigawa, K., Kato, K.: Analysis of the abrasive wear mechanism by successive observations of wear processes in a scanning electron microscope. Wear 110, 419–430 (1986)

Hokkirigawa, K., Kato, K.: An experimental and theoretical investigation of ploughing, cutting and wedge formation during abrasive wear. Tribology International 21, 51–57 (1988)

Briscoe, B.J., Evans, P.D., Pelillo, E., Sinha, S.K.: Scratching maps for polymers. Wear 200, 137–147 (1996)

Mezlini, S., Zidi, M., Arfa, H., Ben Tkaya, M.: Kapsa, Ph.: Experimental, numerical and analytical studies of abrasive wear: correlation between wear mechanisms and friction coefficient. C. R. Mecanique 333, 830–837, doi:10.1016/j.crme, 09.005 (2005)

Woldman, M., VanDerHeide, E., Tinga, T., Masen, M.A.: The influence of abrasive body dimensions on single asperity wear. Wear 301, 76–81 (2013),
doi: http://dx.doi.org/10.1016/j.wear.2012.12.009

Kato, K.: Wear mode transitions. Scripta metallurgica et materialia 24, 815–820 (1990), doi:10.1016/0956-716X(90)90118-Z.

Kitswnai, H., Kato, K., Hokkirigawa, K., Inoue, H.: The transitions between microscopic wear modes during repeated sliding friction observed by a scanning electron microscope tribosystem. Wear 135, 237–249 (1990)

Mezlini, S., Kapsa, Ph., Henon, C., Guillemenet, J.: Abrasion of aluminium alloy: effect of subsurface hardness and scratch interaction simulation. Wear 257, 892–900, doi:10.1016/j.wear, 05.004 (2004)

Da Silva, W.M., Costa, H.L., de Mello, J.D.B.: Transitions in abrasive wear mechanisms: Effect of the superimposition of interactions. Wear 271, 977–986 (2011), doi:10.1016/j.wear.2011.04.010.

Kato, K.: Micro-mechanisms of wear - wear modes. Wear 153, 277–295 (1992)

Mezlini, S., Ben Tkaya, M., El Mansori, M., Zahouani, H., Kapsa, Ph.: Correlation Between Tribological Parameters and Wear Mechanisms of Homogeneous and Heterogeneous Material. Tribol. Lett. 33, 153–159, doi:10.1007/s11249-008-9403-5 (2009)

Mzali, S., Mezlini, S., Zidi, M.: Effect of tribological parameters on scratch behavior of a unidirectional E-glass fiber reinforced polyester composite. Tribology - Materials, Surfaces and Interfaces 7, 175–182 (2013), doi:10.1179/1751584X13Y.0000000048.

Ben Tkaya, M., Zahouani, H., Mezlini, S., et al.: The effect of damage in the numerical simulation of a scratch test. Wear 263, 1533–1539 (2007), doi:10.1016/j.wear.2007.01.083.

Khellouki, A., Rech, J., Zahouani, H.: Micro-scale investigation on belt finishing cutting mechanisms by scratch tests. Wear 308, 17–28 (2013), doi: http://dx.doi.org/10.1016/j.wear.2013.09.016

Effect of Skewness and Roughness Level on the Mechanical Behavior of a Rough Contact

Meriem Bel Hadj Amor, Saoussen Belghith, Salah Mezlini, and
Hedi Bel Hadj Salah

Mechanical Engineering Laboratory, National Engineering School of Monastir,
University of Monastir, 5000, Tunisia
{meriem.belhadjamor,belghith.saoussen}@gmail.com

Abstract. In this work, we investigate the effects of roughness level and asymmetry of profile on the mechanical behavior of an engineering surface. A numerical model was performed to simulate bi-dimensional surfaces with different roughness parameters (The arithmetic average height parameter R_a and skewness) values. This model predicts the contact load, real area and interfacial stiffness. It takes into account the elastic-plastic material behavior, asperities interactions and more realistic geometry than the analytical models. Both symmetric and asymmetric profiles were simulated. Symmetric (Gaussian) profiles were generated through experimentally measured surfaces. These profiles were artificially edited in order to put forward the effect of roughness parameters on the contact performances. The Pearson system of frequency curves is used to produce asymmetric profiles with the same roughness level. The effect of crushing and roughness level as well as the skewness parameter on the contact performance in terms of real area, contact load and interfacial stiffness was analyzed.

Keywords: Mechanical behavior, real contact area, Normal stiffness, Numerical simulation, Roughness parameters.

1   Introduction

The contact between two rough surfaces occurs particularly at discrete contact spots. Accordingly, the real contact area is a small fraction of the apparent area (Bowden and Tabor, 1950). The presence of roughness significantly affects the interfacial behavior in terms of load, real area of contact and interfacial stiffness. The prediction of these quantities is considered to be a necessary requirement to govern several tribological properties and processes such as lubrication, fretting, corrosion and contact vibrations (Sherif 1991). Several models have been proposed in order to describe the behavior of contacting rough surfaces (Greenwood and Williamson 1966, Whitehouse and Archard 1970, Robbe-Valloire et al 2001, Poulios and Klit 2013).

In the pioneering contact model of Greenwood and Williamson (GW) (Greenwood and Williamson 1966) asperities were modeled as elastic, identical and

independent hemispheres with the same curvature radius and Gaussian asperities height distribution. The real area of contact and the contact load were estimated and expressed in terms of the distance between the smooth surface and the mean line of the rough surface. Later, (Whitehouse and Archard 1970) extended the GW model by considering the asperities curvature distribution. Recently, a statistical model based on the standard procedure for roughness and waviness parameters (ISO12085) has been performed by (Robbe-Valloire et al 2001). This model estimate the load and the real area of an elastic, elasto-plastic and fully plastic contact. More recently, (Poulios and Klit 2013) investigate the elastic-plastic contact between rough surfaces. For this purpose, a finite-element model to simulate a real surface topography has been developed. Authors demonstrate that neglecting the plasticity have significant effect on the calculated real area and mean contact pressure.

(Sherif 1991) proposed a theoretical model to predict the normal stiffness of a contact between two different rough surfaces. Author showed that the normal contact stiffness increases with decreasing the standard deviation of asperities height distribution. Many other authors were studied the interfacial stiffness of a rough contact and determinated its dependence on the pressure and roughness level (Shi and Polycarpou 2005), the standard deviation of asperities slopes and standard deviation of curvatures (Buczkowski and Kleiber 2006).

It can be noted here that the rough interface was modeled based on several simplifying assumptions related to the geometry, asperities interaction and material behavior. The asperities heights distribution is assumed to be Gaussian, which is not appropriate in many engineering applications. Most of the common machining processes produce surfaces with asymmetric (non-Gaussian) profiles. For example, turning and shaping generate rough surfaces with positive skewness. Whereas grinding, honing and milling generate rough surfaces negative skewness and high kurtosis (Zhang et al. 2014). (Tayebi and Polycarpou 2004) perform an analytical model to investigate the effect of the asymmetry (skewness) and flatness (kurtosis) of the surface distribution on the static friction and friction coefficient. To do this, the distribution function was generated using the Pearson system of frequency curves to product probability density functions of different skewness and kurtosis values. The dimensionless area, force, mean pressure and the number of contacting asperities were determined for different skewness and kurtosis values. Authors show that these roughness parameters have a great effect on the static friction coefficient.

The objective of the present work is to analyze the effect of the arithmetic average height parameter (R_a) and the skewness parameter (R_{sk}) on the mechanical behavior of a rough contact under normal load. For this purpose, we performed a 2D finite element model in order to calculate the real area, load and normal stiffness of a rough contact. The elastic-plastic deformation, asperities interactions and the friction law were considered. Simulated profiles were generated using motif parameters (ISO 12085) obtained from an experimental measurement of an engineering surface. The Pearson system of frequency curves is also adopted for modeling asymmetric profiles for a given skewness and a fixed kurtosis value of a Gaussian distribution. Five different values of the parameter R_a and three values of skewness are considered. Contact characteristics such as contact area ratio, contact load and normal interfacial stiffness are specially analyzed.

2   Geometrical Characterization of the Studied Profiles

In this section, two sets of profiles were generated based on two different procedures. To study the effect of R_a, profiles of two engineering surfaces were experimentally measured. The geometrical specification of each profile was carried out by using the standard procedure for roughness and waviness parameters (ISO 12085) called 'motif' procedure. The contact between rough deformable surfaces was transformed into a contact between a smooth rigid flat and a rough deformable surface called sum surface. Micro-geometry characteristics of the latter were computed from each surface in contact as shown in Table 1.

Table 1 Motif parameters for the rough surfaces

Motif parameters (µm)	S1	S2	Sum surface
R (µm)	0.96	1.26	2.23
SR (µm)	0.21	0.39	0.45
AR (µm)	145.1	125.3	135.2
SAR (µm)	75.8	54.4	93.3
W (µm)	0.61	0.65	1.26
SW (µm)	0.13	0.19	0.23
AW (µm)	741.2	594.1	667.6
SAW (µm)	429.1	618.7	752.9

The sum surface profile, called 'profile1', was generated based on its roughness and waviness parameters (Belghith et al. 2010). The roughness parameter R_a of profile1 is about 1.14µm. A Matlab program was performed to generate four other profiles from 'profile1' by multiplying its R_a by 1.5, 2, 2.5 and 3. The obtained profiles are respectively 'profile2'; 'profile3', 'profile4', and 'profile5' (see Fig. 1). These five profiles were inserted in the numerical model using Python scripts. Indeed, the surface roughness was shaped by introduced these different profiles consecutively.
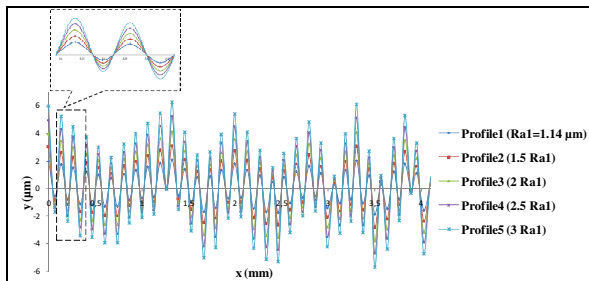
Fig. 1 Simulated profiles with different R_a (profiles 1-5)

In the second set, to study the effect of the profile asymmetry, a Matlab program was performed to generate asymmetric profiles by adopting the Pearson

system of frequency curves. The latter is a family of curves that can generate a density function of asperities heights distribution using its first four moments, i.e., the mean, standard deviation, skewness and kurtosis (Elderton and Johnson 1969). Generated profiles have the same parameters (mean, standard deviation, kurtosis and R_a) of profile1. However, the skewness parameter has varied values: 1, zero and -1 (Fig. 3). Profile with zero skewness is the profile1 generated previously.

(a)

(b)

(c)
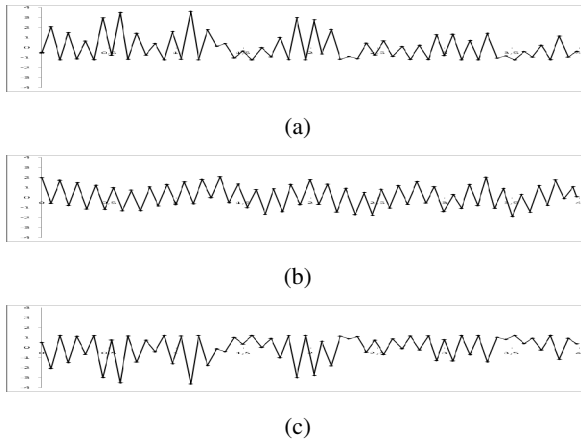
Fig. 2 Simulated profiles with different R_{sk}: (a) R_{sk}=1, (b) R_{sk}=0, (c) R_{sk}= -1

3   Numerical Study

3.1   Finite Element Contact Model

The rough contact was simulated using a commercial finite element solver ABAQUS/Standard. The model considered a 2D micro-geometry and was constituted of a smooth rigid and deformable rough body. To investigate the effect of R_a and R_{sk} on the contact stiffness, the surface roughness was modeled by introducing the profiles described previously. Schematic of the F.E.M, different parts, dimensions and boundary conditions are shown in Fig. 3.

The bottom surface of the deformable body was fixed and the two lateral surfaces of the same body were imposed to symmetry conditions. A normal displacement (u_n) was applied on the rigid flat to achieve the crushing of asperities. The deformable body was partitioned into three different density and shape mesh. Near the region of the surface roughness, the model sufficiently refined the element mesh which is triangular (CPE3), to allow the surface irregularities to be covered and accurately simulated. In the other two zones, quadratic elements (CPE4R), with a gradual coarser mesh upon distancing from the interface, were assigned. The material's properties of the rough deformable body were taken (Young modulus of 76 GPa, a Poisson ratio of 0.3 and a constant yield stress of 39 MPa). A hardening elastic-plastic behavior was used in the present simulations (Fig. 4).
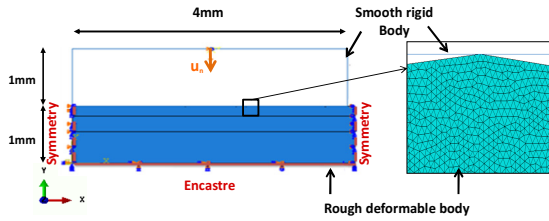
Fig. 3 Schematic representation of the F.E.M, boundary conditions, dimensions and mesh used in numerical simulation
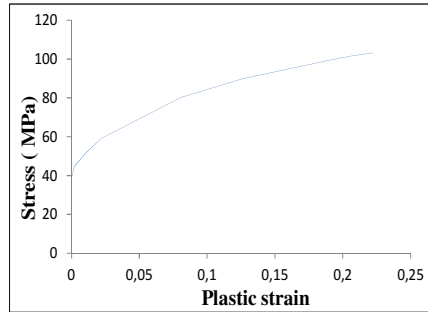
Fig. 4 Stress–strain hardening curve

3.2 Results and Discussion

3.2.1 Effect of R_a

To study the effect of the roughness parameter R_a on the mechanical behavior of the rough interface, five profiles with different values of R_a were simulated, $R_a=$ {1.14, 1.71, 2.28, 2.85 and 3.42 μm}. In this section, we present results obtained with the numerical model in terms of relevant quantities in the contact (real area (A_r), load and normal stiffness) as a function of normal displacement (u_n) and normal approach (w). The latter is the difference between the displacement (u_n) imposed on the rigid flat and the displacement of the mean line of the rough surface.
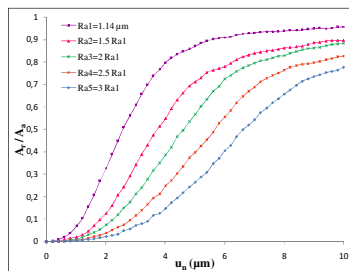
Fig. 5 Effect of Ra on the contact area ratio versus the normal displacement

Fig. 5 shows the evolution of the ratio of the real to the apparent contact area (A_r/A_a) as a function of the normal displacement for different values of R_a. It is seen that, as expected, the real area of contact increases with the normal displacement. This increase is due to the growth of the number of contact spots and their areas and governed by the surface topography and materiel properties. For a given normal load condition, with the increase of the roughness parameter R_a the contact area decreases. For example, for u_n= 5µm, when R_a increases from 1.14 µm to 3.42 µm, contact area ratio decreases from 86% to 26% of the apparent area. However, for u_n= 10µm the difference is less important. When R_a increases from 1.14 µm to 3.42 µm, contact area ratio decreases from 95% to 77% of the apparent area. Accordingly, the real area depends on the asperities crushing level and on the surface roughness parameter R_a.

Fig. 6(a) and (b) show respectively the effect of R_a on the evolution of the contact load with the normal displacement (u_n) and the normal approach (w). For each profile, with increasing u_n and w the contact load increases. This behavior was confirmed by the GW model which demonstrates that both real contact area and normal load increase with the normal approach of rigid flat (w). In Fig. 6(a), for higher normal displacement, the increase of the normal load was governed by the non-linear elastic-plastic behavior of the material. At this range of loading, the normal stress beyond the yield strength of the material therefore the piece into contact deforms plastically. Asperities are entirely crushed and the bulk deformation thereby dominates the interfacial deformation. Numerical results illustrated in Fig. 6(b) were used to calculate the normal contact stiffness by fitting the numerical data using exponential curves.

(a)   (b)
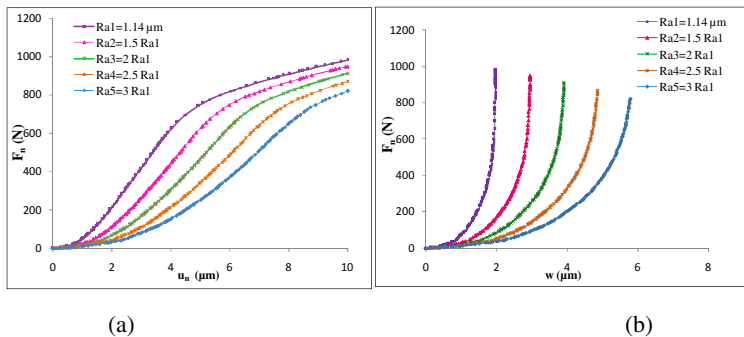
Fig. 6 Effect of R_a on the contact load versus: (a) the normal displacement (b) the normal approach

Fig. 7 shows the effect of roughness parameter R_a on the evolution of the normal contact stiffness K_n with the normal approach (w). Numerical results demonstrate that the normal contact stiffness increases as the normal approach (w) increases. The most notable increase was for the smoothest profile. For a fixed normal approach value, with increasing the roughness parameter R_a the normal contact stiffness decreases. For normal approach (w) about 1.4µm the normal contact stiffness decreases from 384 to 25 N/µm, with increasing R_a from 1.14 to 3.42 µm.
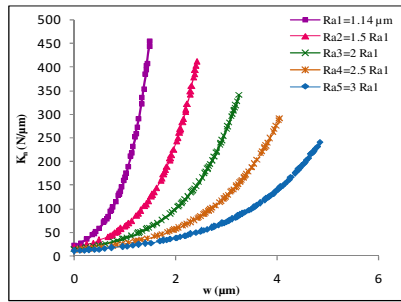
Fig. 7 Effect of R_a on the normal contact stiffness versus the normal approach

3.2.2   Effect of Skewness on the Normal Behavior

In addition to the effect of R_a, the effect of the skewness parameter (R_{sk}) on the contact stiffness was investigated in this section. The parameter R_{sk} is used to measure the symmetry of the profile about the mean line and can be used to differentiate between two profiles with the same R_a (Gadelmawlaa et al. 2002). Fig. 8 illustrates the evolution of the contact area ratio (A_r/A_a) with the normal imposed displacement for different values of skewness. The same trend is observed for different values of skewness. As for the Gaussian profile ($R_{sk}=0$), for the negative and positive skewness values, the real area of contact increases with the normal displacement. For a given crushing level, the profile with skewness value equal to -1 has the higher contact area ratio while the profile with skewness value equal to 1 has the lower one. For higher normal displacement, greater than 6.5µm, asperities were entirely crushed. Hence, the real area of contact for different skewness values reaches more than 90% of the apparent area. It can be seen that for lower crushing level, the difference between the three cases is more important. It can be explained by the fact that at this range the negative asymmetric profile, compared with the other profiles, has the most number of asperities into contact. For example, for $u_n = 0.75$µm, the profile with skewness value equal to -1 has 28 asperities into contact (Fig. 9(a)), the Gaussian profile has 10 asperities (Fig. 9(b)). Whereas the profile with skewness value equal to 1 has only 4 asperities into contact (Fig. 9(c)).
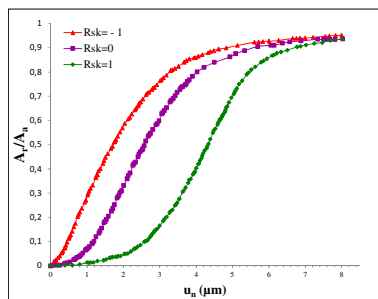
Fig. 8 Effect of R_{sk} on the contact area ratio versus the normal approach

(a)

(b)

(c)
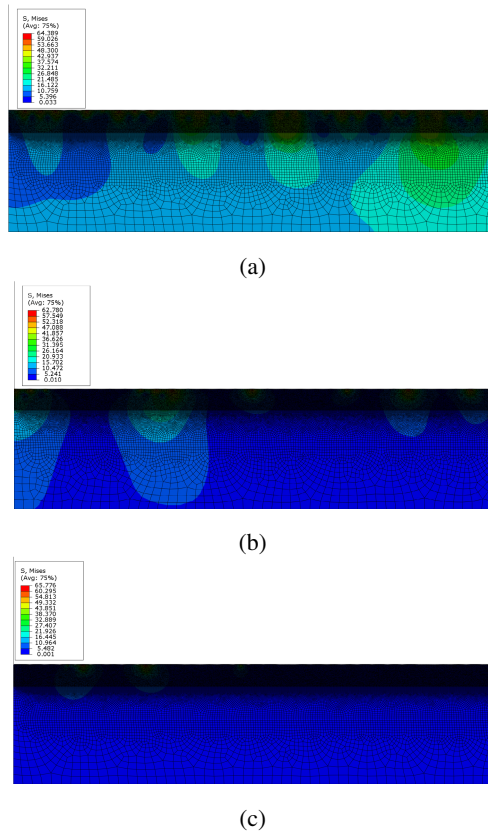
Fig. 9 Von Mises stress (MPa) distribution in the deformed part for u_n=0.75µm: (a) R_{sk}=-1, (b) R_{sk}=0, (c) R_{sk}= 1.

Fig. 10 (a) and (b) illustrate the evolution of the contact force versus, respectively, the normal imposed displacement and the normal approach for different values of skewness. Similar trends for all three skewness values are shown. For a fixed crushing level, the profile with skewness value equal to -1 has the higher contact load value whereas the profile with skewness value equal to 1 has the lower one. The symmetric profile has a contact load value included between these two extreme values. It can be explained by the fact that at a given normal displacement, the negative asymmetric profile has more asperities into contact. It is also seen that for a certain imposed displacement the difference between two consecutive skewness cases is much less between negative and zero than positive and zero skewness values. Simulation results presented in Fig. 10(b) was used to calculate the normal contact stiffness for each value of R_{sk} by fitting the numerical results using exponential curves.

(a)   (b)
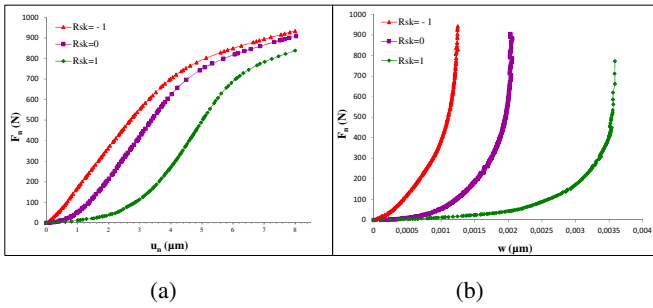
Fig. 10 Effect of R_{sk} on the contact load versus: (a) the normal displacement (b) the normal approach

Fig.11 shows the normal contact stiffness as a function of the nominal contact pressure for three skewness values, $R_{sk}=\{-1, 0, 1\}$. The normal contact stiffness decreases with the increase of skewness. For a fixed nominal pressure, the highest value of the normal contact stiffness was obtained for negative skewness ($R_{sk}= -1$) and the positive skewness has the lowest normal contact stiffness value. At low pressure, the negative skewness results predict larger deviation from the symmetric profile ($R_{sk}=0$).
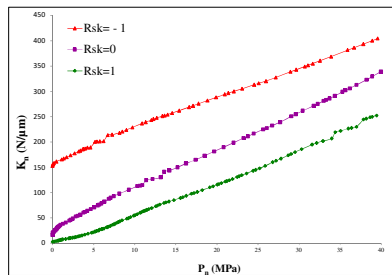
Fig. 11 Effect of R_{sk} on the normal contact stiffness versus the nominal pressure

4   Conclusion

In this paper, we have investigated the normal interfacial behavior of a rough contact. A bi-dimensional finite element model has been developed in the microscopic scale. The nonlinear elastic-plastic behavior of the contacting rough surfaces and the asperities interactions were considered. The surface roughness was also shaped using two different methods. Firstly, experimentally measured profile was used and then artificially modified in order to study the effect of roughness parameter R_a on the real area, load and normal stiffness of a rough contact. Secondly, asymmetric profiles were generated using the Pearson system of frequency curves in order to analyze the effect of skewness on these relevant proprieties. A significant effect of the arithmetic average height parameter R_a and skewness parameter R_{sk}

on the real area, contact load and normal contact stiffness has been deduced. The present study demonstrates that profiles with the same level of roughness (R_a, standard deviation) and different degree of asymmetry haven't the same contact properties. Accordingly, the Gaussian distribution, widely used in the analytical models, is not appropriate to study asymmetric surfaces. It is also clearly demonstrated that negative skewness and lower value of R_a are advisable in order to achieve high normal contact stiffness.

References

Belghith, S., Mezlini, S., BelHadjSalah, H., Ligier, J.L.: Modeling of contact between rough surfaces using homogenisation technique. Compte. Rendus Mécaniques 338, 48–61 (2010)

Bowden, F.P., Tabor, D.: The friction and lubrication of solids, pt. 1. Oxford University Press (1950)

Buczkowski, R., Kleiber, M.: Elasto-plastic statistical model of strongly anisotropic rough surfaces for finite element 3D-contact analysis. Comput. Methods Appl. Mech. Engrg. 195, 5141–5161 (2006)

Elderton, P.E., Johnson, L.: System of frequency curves. Cambridge University Press, London (1969)

Gadelmawlaa, E.S., Kourab, M.M., Maksoudc, T.M.A., Elewaa, I.M., Solimand, H.H.: Roughness parameters. Journal of Materials Processing Technology 123, 133–145 (2002)

Greenwood, J.A., Williamson, J.B.P.: Contact of nominally flat surfaces. Proc. R. Soc. Lond. Ser. A 295, 300–319 (1966)

International Organisation for Standardisation (ISO), NF EN ISO 12085, Spécifications géométriques des produits - Méthode du profil - Paramètres lies aux motifs (1988)

Poulios, K., Klit, P.: Implementation and applications of a finite-element model for the contact between rough surfaces. Wear 303, 1–8 (2013)

Robbe-Valloire, F., Paffoni, B., Progri, R.: Load transmission by elastic, elastoplastic or fully plastic deformation of rough interface asperities. Mechanics of Materials 33, 617–633 (2001)

Sherif, H.A.: Parameters affecting contact stiffness of nominally flat surfaces. Wear 145, 113–121 (1991)

Shi, X., Polycarpou, A.A.: Measurement and Modeling of Normal Contact Stiffness and Contact Damping at the Meso Scale. ASME 127, 52–60 (2005)

Tayebi, N., Polycarpou, A.: A Modeling the effect of skewness and kurtosis on the static friction coefficient of rough surfaces. Tribology International 37, 491–505 (2004)

Whitehouse, D.J., Archard, A.F.: The properties of random surfaces of significance in their contact. Proc. R. Sot. A 316, 97–121 (1970)

Zhang, S., Wang, W., Zhao, Z.: The effect of surface roughness characteristics on the elastic–plastic contact performance. Tribology International 79, 59–73 (2014)

Perforation of Aluminum Foam Core Sandwich Panels under Impact Loading: A Numerical Study

Ibrahim Elnasri[1,2] and Han Zhao[3]

[1] Laboratoire de Génie Mécanique, Ecole Nationale d'Ingénieurs de Monastir,
  Av. Ibn El   Jazzar, Monastir- 5019, Tunisia
[2] Institut Supérieur des Systèmes Industriels de Gabès,
  Rue Slaheddine Ayoubi 6011 Gabès, Tunisia
  `Ibrahim.nasri@issig.rnu.tn`
[3] Laboratoire de Mécanique et Technologie, ENS-Cachan/CNRS-UMR8535/
  Université de Paris Saclay, 61, avenue du président Wilson, 94235 Cachan cedex, France
  `zhao@lmt.ens-cachan.fr`

Abstract. This paper reports the numerical results of the inversed perforation test instrumented by Split Hopkinson Pressure Bar SHPB with an instrumented pressure bar on the AlSi7Mg 0.5 aluminum foam core sandwich panels with 0.8mm thick 2024 T3 aluminum top and bottom skin. The numerical models are developed, in order, to understand the origin of enhancement at the top skin loads found under impact loading (paper published by (Zhao et al. 2006)). The predicted numerical piercing force vs. the displacement curves are compared to the experimental measurements (tests at impact velocities at 27 and 44 m/s). The simulation catches all processes of the perforation of the sandwich panels (top skin, foam core, and bottom skin). Within this experimental scatter, there is a good agreement between the numerical predictions and the experimental measurements. Virtual tests with different impact velocities up to 200 m/s are presented and showed a significant enhancement of the piercing force under impact loading (top skin peak and foam core plateau loads). The results also demonstrate that the shock front effect is responsible for the enhancement of the piercing force under impact loading.

Keywords: Perforation, sandwich panel, foam, shock wave, impact, numerical simulation.

1   Introduction

Sandwich plates and shells are important elements in modern lightweight construction. The main advantage of the sandwich principle is the fact that structures with high bending stiffness and rather low specific weight are obtained. The impact behaviours (energy absorption, perforation limits) are the important design features for sandwich panels used in aeronautics structures. The core materials of

such panels (honeycombs, foams, hollow sphere agglomerates, etc.) play often dominant roles in the whole energy absorption as well as their penetration behaviour. (Hou et al 2005) conducted experimental and finite element studies on aluminium foam sandwich panels subjected to both quasi-static and impact loadings. Four deformation modes were summarised as global bending, localised indentation, localised indentation with global bending, and localised indentation with bending along clamping edge. However, key features of force–displacement curves, detailed deformation in face-sheets and foam core were not highlighted. (Hanssen et al 2006) carried out experimental tests and numerical simulations of the bird strike on sandwich panels made from aluminium foam core with aluminium face sheets. There is no perforation observed from the tests. (Cantwell and Kiratisaevee 2005) investigated the impact response of sandwich panels with Alporas foam cores and fibre-reinforced thermoplastic, and fibre-metal laminate (FML) face-sheets. The indentation resistance of these sandwich panels was found to be rate sensitive over the full range of conditions examined.

(Zhao et al. 2006) tested the perforation behaviour of AlSi7Mg0.5 aluminium foam core sandwich panels with 0.8mm thick 2024 T3 aluminium top and bottom skin using a SHPB, and recorded the piercing force displacement history. Quasi-static, impact tests (around 20 m/s and around 45 m/s) were performed. A significant enhancement of the top skin peak loads under impact loading was observed, although the skin sheet as well as foam cores are nearly rate insensitive. They suggested that a possible reason is the difference of compressive strain level of foam core reached before the perforation of top skin under static and impact loading because of different face-foam core interaction mechanism. Such localised foam core strength enhancement leads to the increase of the top skin peak loads. However, no detailed quantitative analysis has been presented in this work and there is no detailed local information due to experimental difficulties to better understand the original of the enhancement of the top skin peak loads observed under impact loading. Additionally, the explanation of the puzzling results have not convinced the scientists, meaning that they still need an in depth study. For this purpose, a numerical model is built and it is calibrated by testing the results to be sure that the main features of the perforation of the aluminium foam core sandwich panels are well represented. Numerical testing at various impact velocities up to 200 m/s is also performed and the local information, which are not experimentally available, (stress, strain, etc.) are analysed in order to understand the piercing process.

2   Dynamic Perforation

The numerical model is defined on the explicit code (Ls-Dyna 2007). Figure 1 shows the numerical model of the perforation of the sandwich panel which consists of 6 parts. The sandwich panel is integrated between two rigid parts. The aluminium hollow tube-like projectile (part 6) and aluminium clamping ring (part 2) are

modelling as the rigid body by the material type 20 * (MAT_RIGID) in LS-DYNA codes. The rigid parts are merged for one part 6 via the command *CONSTRAINED_RIGID_BODIES available in LS-Dyna code. This command can make the two parts in only part.   The perforator is represented as the elastic by the material type 1 * (MAT_ELASTIC, density =8050 Kg/m^3, Young moduli: 188 GPa, Poisson ratio =0.3). The aluminium 2024 T3 sheet are represented by shell elements with five integration points in the thickness. This model consists of 4800 2-D elements for the two sheets. The foam is modelled by using brick elements. This model consists of 90195 nodes, 76536-3D elements divided in 28416 for the part of the perforator, 120 for the two rigid parts and 48000 brick elements for the foam core. As the most important zone is the penetration area just under the perforator, the sandwich panels is modelled with a fine mesh along with the length (figure 2). The number of the elements on the thick is 21 elements for the foam core. The number of the elements on the transverse direction is 51 elements for the sheet and for the foam core. Tiebreak constraints were applied between the faceplate and the foam core. Here, the nodal tiebreak failure in the interface was given by the following quadratic failure criterion;

$$(\frac{\sigma_{tb}}{N_{tb}})^2 + (\frac{\tau_{tb}}{S_{tb}})^2 \geq 1 \tag{1}$$

Where σ_{tb} and τ_{tb} are the nodal normal and shear stress components and N_{tb} and S_{tb} are the strength of the adhesive in pure tension or pure shear, respectively. Here, $N_{tb} = S_{tb} = 5 MPa$ was used. Contact between SHPB perforator bar and sandwich plate was established using eroding surface to surface contact. To model contact between faceplate and the foam core after failure, eroding single surface contact was defined. Segment based contact option (SOFT=2) was used for simulating the sandwich plate impact. Frictionless contact was used in all simulations. All the parts in present work were modelled with single integration point (constant stress solid element, ElFORM=1) because the reduced integration elements are robust choices for nonlinear analysis to overcome negative volumes, which are prone to happen in full integration elements. In spite of the afore mentioned benefits, the reduced integration elements suffer from non-physical spurious/hourglass modes. Control hourglass type 1 control cart is used to overcome this non-physical behaviour.

The boundary conditions in the impact simulation are the following: the perforator is fixed in z-translation and z-rotation in degrees of freedom in the no-impact end. The contact between the sandwich panel and the two parts is defined as tied. The velocity of the sandwich panel and the projectile are modelled and put as initial velocity nodes for the sheets and for the foam and via the command INATIAL_RIGIG_BODY_VELOCITY for the projectile.

PERFORATION SANDWICH (MM,MS,KG,GPA,KN)
Time =   0
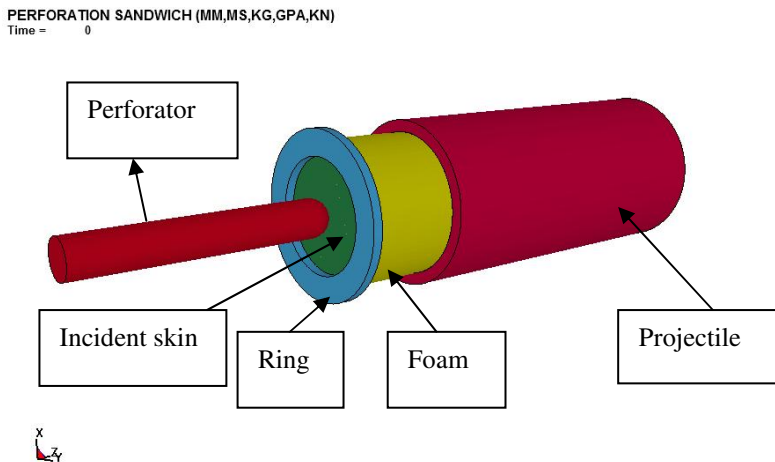
Fig. 1 Numerical model for the perforation of the sandwich panels

The behaviour of the skin sheet is modelled by a damageable isotropic harden-ing elastic-plastic constitutive law proposed by (Lemaitre 1996), available in (Ls-Dyna 2007) code as the model of type 104 (MAT_DAMAGE_1). The pa-rameters used for 2024 T3 aluminium sheet were identified from normalised ten-sion tests by (Pattofatto et al 2012). The foam core is modelled by a honeycomb constitutive model (MAT_26) available on the Ls-Dyna code with appropriate tensile failure strain. The normal stress vs. volumetric strain is obtained from quasi-static compression test (density= 235 kg/m^3, velocity= 0.01 mm/s). Due to the fact that they do not have a specific device to perform a shear test, the shear stress vs volumetric strain curve is deduced from the quasi-static compressive curve which is equal to the half. The fracture of the cell of the foam is achieved by using available tensile failure strain. Iteratively different values were used to achieve the appropriate failure strain value. The constitutive properties of the foam are: $\rho = 235\,kg/m^3$, E=70GPa, $\upsilon = 0.285$, SIGY=240MPa, Vf=0.23,TSEL=0.05

2.1   Results and Discussions

With appropriate selection of constitutive model of the foam core, Figure 2 shows the simulated piercing force-displacement curves at 44 m/s compared with the experimental result. The piercing force is obtained by using the so-called com-mand: *DATABASE_NODAL_FORCE_GROUP. All nodes on the perforated end were integrated in the group nodes which can be compared to the piercing force recorded by the strain gauge instrumented on the Split Hopkinson Pressure Bar. It was observed that the simulated piercing curve was in good agreement with experiments. One can note that the simulated peak piercing force for the incident

sheet is small lower than the experiment case but the difference was not significant to affect the final result and is apriority due to errors for the modelling. It can be seen the simulation catch ell the petalling failure mode observed on the experimental test (figure 3 for the bottom skin and figure 4 for the top skin).
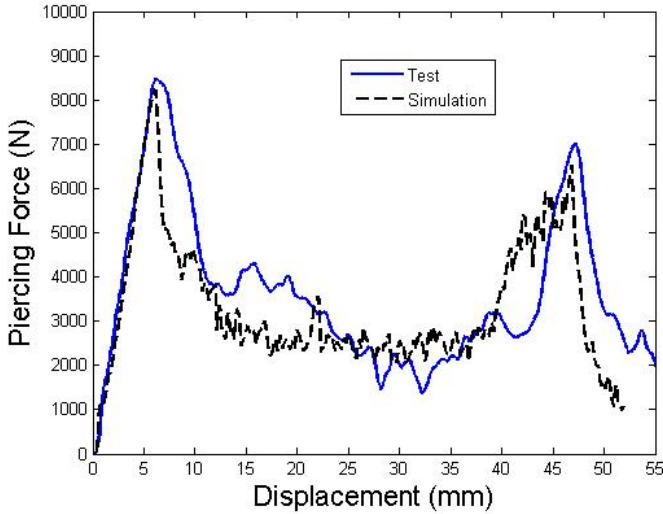
Fig. 2 Comparison between experimental and simulated piercing force vs displacement curves of the sandwich panel perforated at impact velocity44 m/s
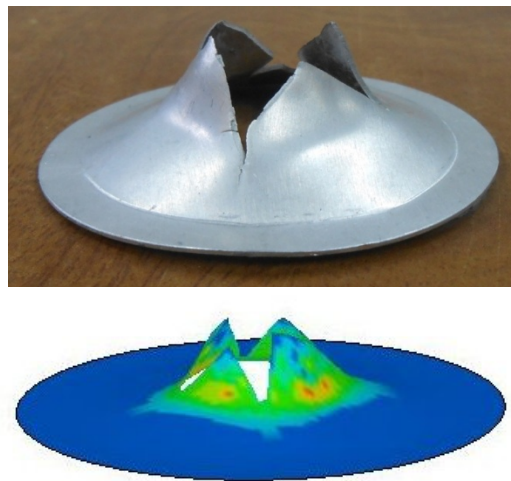
Fig. 3 Breaking "petal" shape by simulation and by post mortem observation (Bottom skin, v=44m/s)
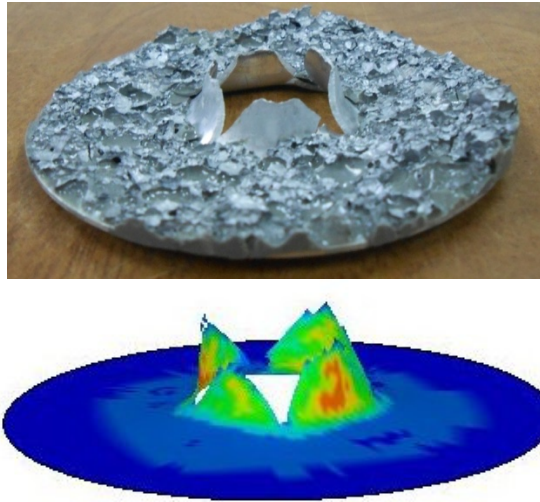
Fig. 4 Breaking "petal" shape by simulation and by post mortem observation (top skin, v=44 m/s)

3   Quasi-static Perforation

For quasi-static simulation, the configuration of impact simulation is conserved: the perforator is also fixed as the same boundary conditions. To ensure quasi-static loading when using en explicit code, we can use the prescribed velocity field given by (Hanssen et al 2002):

$$v(t) = \frac{\pi}{\pi - 2} \frac{d_{max}}{T} [1 - \cos(\frac{\pi}{2T} t) \qquad (2)$$

Here, T is the total duration of the loading, d_{max} is the final displacement. The termination time T was 0.14 s. The velocity of the projectile is modelling via the BOUNDARY_PRESCRIBED_MOTION_RIGID command. Figure 5 shows the simulated piercing force-displacement curves at quasi-static loading compared with the experimental result. The piercing force is also obtained by using the so-called command: *DATABASE_NODAL_FORCE_GROUP. One can be observed that the simulation peak piercing force curve for the incident top skin is a good agreement with the experimental curve and for that the bottom skin is lower than the experiment curve. This discrepancy is a prior due to not taking account on the numerical model of the cells of the foam which are stickled on the face sheet. It can conclude that simulation agrees with experiment quasi-static results.
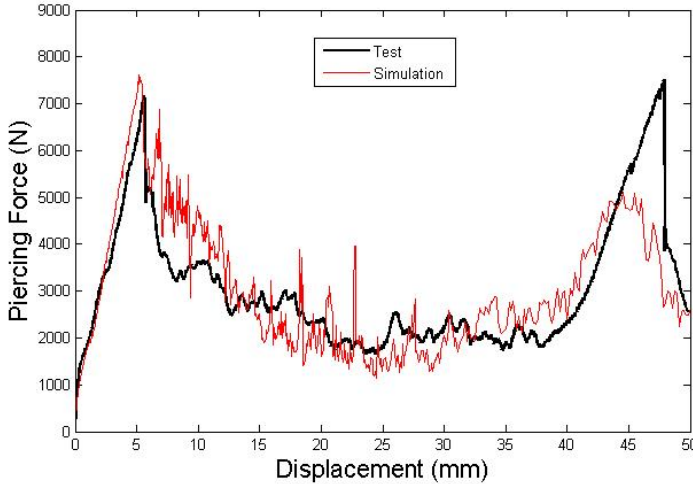
Fig. 5 Comparison between quasi-static experimental and simulated piercing force vs displacement curves of perforated sandwich panel

4   Analysis of Virtual Numerical Tests

The present numerical model provides the virtual tests where all the detailed information are not available in a real test (strain, stress, etc) is known. Five numerical tests are conducted in dynamic loading up to the impact velocity 200 m/s. Piercing impact force vs displacement curves for impact velocities 44, 100, 140 and 180 m/s are given in figure 6. It is observed that:

- The piercing top skin peak force and level of the plateau of the perforation of the foam core increases regularly with the impact speed. It indicates that this model contains probably the hints for the understanding of this force enhancement, which is probably due to the propagation of the shock front because the constitutive relation used for the foam cores as well as aluminium sheets are all rate insensitive.
- The maximum displacement of the top skin before breaking is unchanged with the impact velocity increase and the displacement of the bottom skin breaking is the same of all curves, these can prove that the foam core isn't sustained for a compression.
- The peak load of the piercing force of the bottom skin is nearly the same value for all curves; this is confirmed that the aluminium face sheet is rate insensitive.
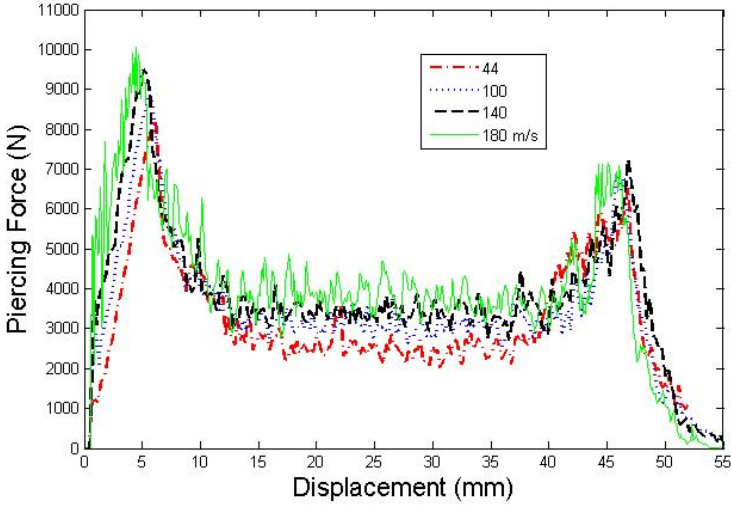
Fig. 6 Comparison of simulated piercing force vs displacement curves of the sandwich panel perforated at 44, 100, 140 and 180 m/s
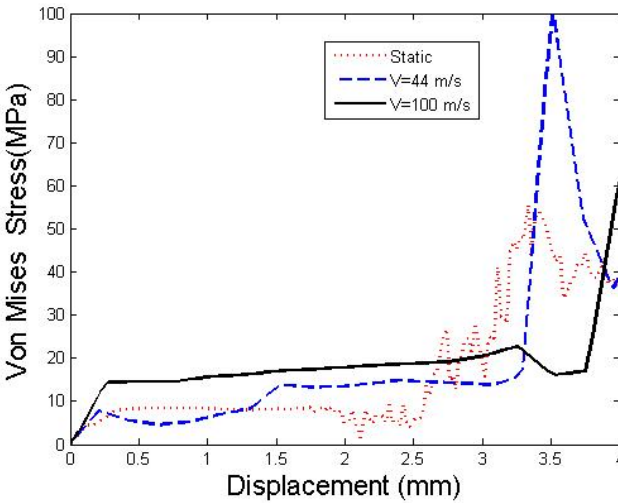
Fig. 7 Comparison of Von Mises Stress vs displacement curves for the element for three impact velocities (static, v=44 m/s, v=100 m/s). The coordinates of the element along the loading direction are (0,2mm)

In order to understand the origin of these force enhancements, any difference of detailed local information between static and dynamic loading is interesting. A noticeable difference is to study the stress level in the elements of the foam core in

the contact with the perforator. Figure 7 shows the equivalent Von Mises Stress vs displacement for one element located in the middle of the foam core.   The coordinates of the element along the loading are (0, 2 mm). A significant increase in stress amplitude is found for impact loading case and is in increase with impact velocity, the huge enhancement on the strength is prior due to the propagation of the shock front in the foam core, which is the possible reason, because the uncompressing of the foam core is confirmed by simulation, which leads to a higher local foam core strength under the perforator and can increase the top skin peak loads.

5   Conclusion

The numerical models of the inversed perforation test instrumented with SHPB with an instrumented pressure bar on the AlSi7Mg0.5 aluminium foam core sandwich panels with 0.8mm thick 2024 T3 aluminium top and bottom skin are developed in order to understand the origin of the enhancement of the top skin loads found under impact loading (paper published by Zhao et al 2006).The numerical simulation is done using 3D finite element models in Ls-Dyna. The behaviour of the skin sheet is modelled by a damageable isotropic hardening elastic-plastic constitutive law as the model of type 104 (MAT_DAMAGE_1), where the foam core is modelled by a honeycomb constitutive model (MAT_26) with appropriate tensile failure strain.

Numerical predicted piercing force vs displacement curves are compared with experimental measurements (tests at impact velocities at 27 and 44 m/s). The simulation catch all processes of the perforation of the sandwich panels (top skin, foam, and bottom skin). Within experimental scatter, there is a good agreement between numerical predictions and experimental measurements. Virtual tests with different impact velocities up 200 m/s are presented and showed:

- The piercing top skin peak force and level of the plateau of the perforation of the foam core increases regularly with the impact speed. It indicates that this model contains probably the hints for the understanding of this force enhancement, which is probably due to component interaction because the constitutive relation used for the foam cores as well as aluminium sheets are all rate insensitive.
- The maximum displacement of the top skin before breaking is unchanged with the impact velocity increase and the displacement of the bottom skin at breaking is the same of all simulated tests, these can prove that the foam core isn't sustained to a compression.
- The peak load of the piercing force of the bottom skin is nearly the same value for all curves; this is confirmed that the aluminium face sheet is rate insensitive.

In order to understand the origin of these force enhancements, a stress level in the element of the foam core on the contact with the perforator for three impact velocities (static, 40 m/s and 100 m/s) for three impact velocities (static, 40 m/s

and 100 m/s) is analysed. A significant increase in the stress amplitude is found for impact loading case and is in increase with impact velocity, the huge enhancement on the strength is prior due to propagation of shock front in the foam core and is the one possible reason, because the uncompressing of the foam core is confirmed by simulation, which leads to a higher local foam core strength under the perforator and can increase the top skin peak loads and the foam core loads.

References

Hou, W., Zhang, H., Lu, G., Huang, X.: Failure modes of circular aluminium sandwich panels with foam core under quasi-static loading. In: Conference on Shock and Impact Load on Structures, pp. 275–82 (2005)

Hanssen, A.G., Girard, Y., Olovsson, L., Berstad, T., Langseth, M.: A numerical model for bird strike of aluminium foam-based sandwich panels. Int. J. Impact Eng. 32(7), 1127–1147 (2006)

Cantwell, W.J., Kiratisaevee, H.: Low-velocity impact response of highperformance aluminum foam sandwich structures. J. Reinf Plast Compos 24(10), 1057–1072 (2005)

Zhao, H., Elnasri, I., Girard, Y.: Perforation of aluminium foam core sandwich panels under impact loading: an experimental study. Int. J. Impact Eng. 34(7), 1246–1257 (2007)

LS-DYNA keyword user's manual, Livermore Software Technology Corporation (2007)

Lemaitre, J.: A course on damage mechanics. 2nd ed. Springer, Berlin (1996) ISBN 3-540

Pattofatto, S., Zeng, H.B., Zhao, H.: On the piercing force enhancement of aluminium foam sandwich plates under impact loading. J. Sand. St. Mat. 2, 211–226 (2011)

Hanssen, A.G., Hopperstad, O.S., Langsethand, M., Ilstad, H.: Validation of constitutive modelsapplicable for aluminium foams. I. J. Mech. Sc. 44, 359–406 (2002)

Effect of the Environmental Conditions on the Ultimate Load of Damaged Unidirectional of Natural Fiber/Epoxy Composite

Sidi Mohammed Amine Khiat[1,*], Ramdane Zenasni[1], and Vina Oley Jaime[2]

[1] University of Mostaganem, Dept. of Mechanics, Laboratory LMNEPM, BP 265 Algeria
  `aminek@netcourrier.com`

[2] University of Oviedo, Dept. of Material Sciences, Campus de Viesques, 33204 Gijon, Spain

Abstract. The present paper proposes a strength reliability model for unidirectional composites with natural fibers in a hexagonal array. The model assumes that, a central core of broken fibers flanked by unbroken fibers which are subject to stress concentrations from the broken natural fibers. The approach of the model consists of using a modified shear lag model to calculate the ineffective lengths and stress concentrations around fiber breaks. In this paper, we attempt to incorporate in the proposed model the unidirectional composite property variation with temperature and moisture in order to predict even composite strength degradation. Strength degradation is often seen as a result of changes in ineffective lengths at natural fiber breaks and the corresponding stress concentrations in intact neighboring fibers.

Keywords: Unidirectional composite, fractured fibers, stress concentrations, temperature, moisture, unidirectional displacement.

1   Introduction

The composite materials are, and, will be used more and more in the industrial applications. They often come dethroner the metallic materials in many fields. Two crucial factors pushed the development and the use of composites. The first, was the high ratio strength/weight [1]. The second factor, having also pushed the development of the composites, is related to the specificity of these materials give, that it is from a mechanical, thermal view point,…. give an additional liberty for a designer: that to choose the material behaviour [1, 2] according to the type of fibers and resin, the rate of reinforcement, the fibers orientations and the process of manufacturing. Two of these properties are essential in the dimensioning of composite structures. It is about the on scale micromechanical and macromechanical characterization of elastic modulus and the mechanical resistance. A synthesis of

---

* Corresponding author.

these properties can be found in work of Christensen [3]. This work is based on the micromechanical homogenization models based on a representative elementary volume in order to carry out a homogenization of the composite. Many research have been conducted, Zweben and Rosen [4,5] which are considered among the oldest models for the prediction of the resistance of composites polymeric matrix. Foster [6] proposed a direct numerical simulation and an analytical model to predict the resistance of composites in traction and flexion. By using a regular square arrangement of intact fiber, it determined the resistance of a Ti matrix 6Al- 4V reinforced by fibers in SiC. It also showed that the fibers failure occurs in a random way when the load reaches the composite limit strength. Consequently, the statistical accumulation of this failure can lead to the total damage of the composite.

This model is based on Gao and Reifsnider [7] models which allow it possible to predict the resistance and the durability of unidirectional composite by using micromechanical techniques. The comparative study of the life cycle of a automotive part or in epoxy matrix reinforced by hemp fibers, and a part manufactured from polystyrene-butadiene acrylonitrile (ABS) according to various methods, revealed that not only the part reinforced with hemp fibers present an advantage from the view pointenvironment during the phase of manufacturing [8,9]. Finally, the use of natural hemp fibers as reinforcement can allow it possible to reach interesting mechanical properties, while reducing to significant degree composite costs. An analysis of the process of the longitudinal failure including the micromechanical interactions between natural fibers and the matrix is carried out by taking account of the effect of the environmental conditions on the degradation of the composite components.

2   Model of Longitudinal Fracture

The hygrothermal behaviour of the laminated composites Hemp/Epoxy is widely determined by the properties of the matrix at the interfaces, on the other hand the natural fibers in hemp are relatively sensitive to the increase in moisture and the temperature. The effect of moisture generates residual stresses, the plasticity of polymers as well as degradation at the interfaces [10, 11]. Moreover, plasticity can involve the reduction in glass transition temperature [12], which can affect the behaviour of the composite in high temperature environments. To introduce the effect of the temperature and the variation of moisture concentration on the mechanical properties, Tsai [12] proposed the non-dimensional temperature T*, which is the principal parameter to evaluate the hygrothermal characteristics of the composite.

$$T^* = \frac{T_g - T_{opr}}{T_g - T_{rm}}$$

(1)

$$T_g = T_g^{\,0} - g\,C \tag{2}$$

We can use the no dimensional temperature $T*$ in an empirical way to express the rigidity of the matrix and fiber (E_M, E_F). If Tg is the glass transition temperature of the matrix, Topr is the operating temperature and Trm is the reference room temperature, it is also supposed that moisture removes the glass transition temperature in a dry environment $T_g^{\,0}$ by a change from relative temperature for unit absorbed moisture "gC". We used the model of Gao and Reifsnider [7] to estimate the strength of unidirectional composite. This model allows introducing the variation of the mechanical characteristics of the matrix and natural fibers according to the temperature and of moisture in order to predict the strength of unidirectional composite. This strength generally varies as function, of the change ineffective lengths [δ] in the zone of faiure fiber and the stress concentrations corresponding to the intact neighbouring fibers. The ineffective length is generally defined as the length between the fracture zone of the fiber until the length for which the fiber renewal its capacity to bear the complete loading. This concept is illustrated on figure 1, where σ_f is the fiber stress.

According to Gao and Reifsnider [7], the properties due to the tensile of fiber reinforced composite, depend on the strength, the elastic modulus of fiber, the strength and the chemical stability of the matrix and also of the effectiveness adherence to the interface fiber/matrix during the transfer load. In the case of the hemps fibers and even as carbon fibers which we used in the preceding study, the elastic modulus and the mechanical resistance of fiber remain almost unchangeable with the variation in the temperature and moisture. Contrary, the epoxy matrix, receive changes of the properties. The crack at the interface will increase when the stress shear at the interface reached τ_0. The model of Gao and Reifsnider [7] is distinguished from the other models by the presence of the effect of shearing and the take in account the local damages in the form of a debonding at the interface and a plasticity. In this area, the shear stress of the matrix and interface was considered as constant with a value $\eta\tau_0$. Where η is a shear parameter defining the shear stress in the inelastic area. When η tend to zero, no transfer of shearing took place between broken fibers and their neighbours in this area. It would be the case in an area, completely detached or from a cracked matrix. Contrary when $\eta= 1$, the shear stress in the inelastic area is equal to τ_0. For the application of this model in this study, we used $\eta =1$.
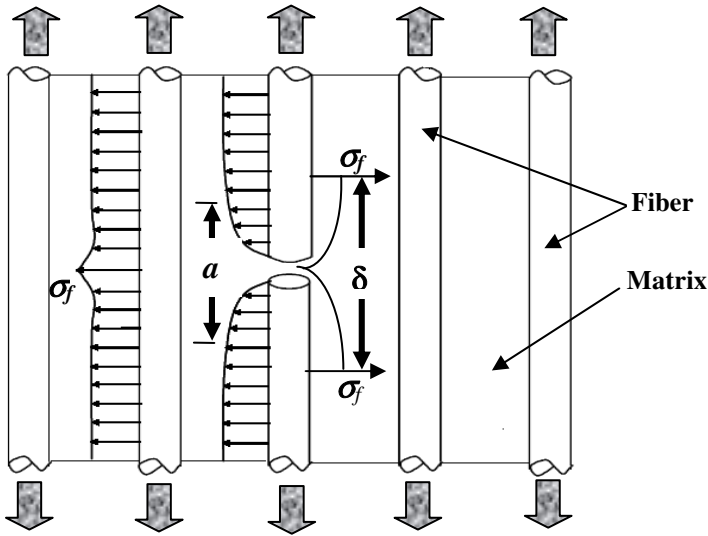
Fig. 1 Broken fibers with the elongation of the ineffective length

It is supposed that the broken cell can be assimilated to an homogeneous material with a transversal circular cross section whose Young modulus can be obtained by the rule of mixtures:

$$E = \frac{i A_f E_f + \left[i A_m - \pi \left(r_0^2 - (r_0 - d)^2 \right) \right] E_m}{\pi (r_0 - d)^2} \tag{3}$$

Local damages are included in the model by the introducing of an area of debonding and local plasticity, where the shear stress of the matrix and interface are considered as constant for the value $\eta \tau_0$. The equilibrium equations in this zone $(0 \leq x \leq a)$ are:

$$i A_f E_f \beta \frac{d^2 U_0}{dx^2} - 2 \pi r_0 \eta \tau_0 = 0 \tag{4}$$

$$i A_f E_f \frac{d^2 U_1}{dx^2} + 2\pi (r_0 + 2d + 2r_f) \frac{G_m}{2d} (U_2 - U_1) + 2\pi r_0 \eta \tau_0 = 0 \tag{5}$$

β was given as function of the geometrical modulus of fiber and the matrix respectively. A represent the half length of the debonding area locally plasticized. U_0, U_1 and U_2 represent the stresses and the displacements in the three zones, see fig.2.

The solution of equations 6 and 7:

$$U_0(x) = \frac{\eta \tau_0}{r_0 E_1} x^2 + C_0 \tag{6}$$

$$U_1(x) = C_1 \left(e^{\lambda_1 x} - e^{-\lambda_1 x} \right) + \frac{2r_0 \eta \tau_0}{(R_2^2 - r_0^2)E} \frac{1}{\lambda_1^2} \left(1 - e^{-\lambda_1 x} \right) + \frac{\sigma_C}{E_C} x \tag{7}$$

Also for the zone $a \leq x \leq \infty$ where there is no yield at the interface, the equilibrium equations are:

$$E\pi(r_0 - d)^2 \frac{d^2 U_0}{dx^2} + 2\pi r_0 \frac{G_m}{2d}(U_1 - U_0) = 0 \tag{8}$$

$$n_i A_f E_f \frac{d^2 U_1}{dx^2} + 2\pi(r_0 + 2d + 2r_f)\frac{G_m}{2d}(U_2 - U_1) - 2\pi r_0 \frac{Gm}{2d}(U_1 - U_0) = 0 \tag{9}$$

The solution of equations 8 and 9:

$$U_0(x) = C_2 e^{-\sqrt{\gamma_1} x} + C_3 e^{-\sqrt{\gamma_2} x} + \frac{\sigma_c}{Ec} x \tag{10}$$

$$U_1(x) = C_2(1 - \frac{\gamma_1}{A})e^{-\sqrt{\gamma_1} x} + C_3(1 - \frac{\gamma_1}{A})e^{-\sqrt{\gamma_2} x} + \frac{\sigma_c}{E_c} x \tag{11}$$

3   Model Validation

First, we carried out many applications on specimen of laminated plate graphite/epoxy. The mechanical and geometrical characteristics are given respectively in tables 1 [12, 13]. To appreciate the evolution of the damage at the zones locally plasticized; we carried out a progressive increase in the load external consequently an increase of the applied tensile stress to the samples edges. The increase in the load, has enabled to us to quantify the extension of the zone locally plasticized and the ineffective zone for which the fiber renewal with its capacity to bear the complete loading and that according to the number of broken fibers. Finally, we will determine the evolution of longitudinal displacement of broken and intact fiber according to the length of the sample.

Table 1 Mechanical and geometrical characteristics of composite Hemp/epoxy [12, 13]

Fiber Young modulus E_f	27.6 GPa
Matrix Young Modulus E_m	4.2 GPa
Fiber reference resistanceσ_0	3.10 GPa
Shear stress τ_0	25.20 MPa
Matrix Poisson coefficient ν_{12m}	0.43
Fiber volume fraction V_f	0.51
Shear parameterη	1.0
Specimen lenght$L$	200 mm
Fiber radiusr_f	120 μm
Maximal number of broken fibers n_i	40

The validation of our model was carried out by comparison with the Foster analysis method [6] for a square arrangement of unidirectional broken fibers and that for a hexagonal arrangement Graphite/epoxy[9]. The fig 2 shows that for the three methods, the stress concentration increases a ccording to the number of broken fibers.
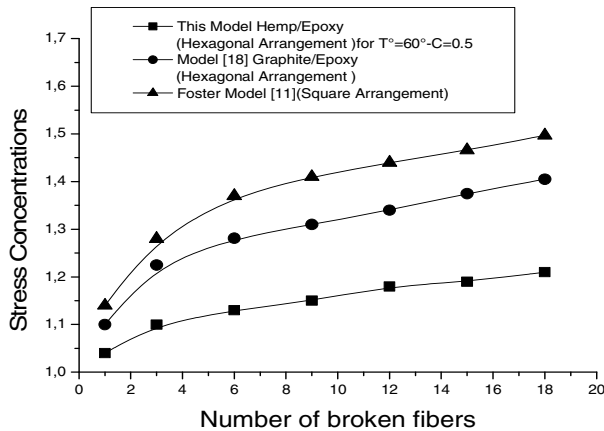
Fig. 2 Comparison of stress concentrations for normal environmental conditions, models validations [6 and 9]

The maximum difference between the Foster curves [6] and the results [9] is lower than 5%. This difference is due to the choice of the fiber arrangement which is hexagonal for the Hemp/Epoxy composite [9] and square arrangement in Foster models. On the other hand in model of Hemp/Epoxy composite and that of Graphite/Epoxy, the maximum difference was lower than 7% due to the arrangement and the nature fibers under the effect of the environmental conditions. We can

conclude that our results are in good agreement with those of Foster [6] and the preceding results [9].

4   Evolutions Ineffective Lengths

The ineffective length δ is defined as being the length ranging between the fractured zone fibers until the length for which the fiber renewal with its capacity to bear the complete loading, therefore it must include the locally plasticized zone locally a ($\delta \geq$ a) [Fig 3].
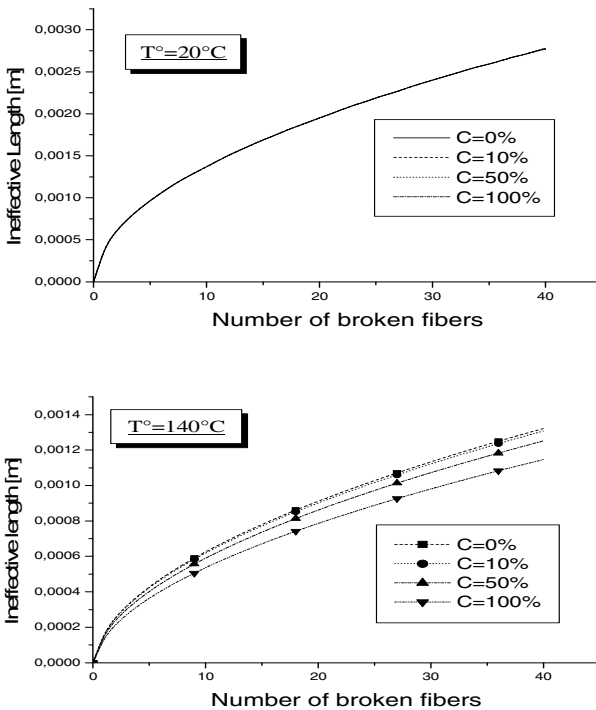
Fig. 3 Evolution of ineffective length under various moisture concentrations for temperatures T = 20°C and T=140°C (σ= 0.5σ_0)

According to behavior lawsand starting from the fractured zone, the natural broken fiber must pass by a locallyplasticizedzone a, then by a transitory zone before reaching the perfectly elastic zone delimited by a length δ called ineffective that under the effect of moisture and temperature.

For T°=20°C, a superposition of all representative curves the ineffective length. We can deduce that for low temperatures, the variation of moisture concentration have no effect on the ineffective length. With the increase in the temperature of

140 °C, the sensitivity of the ineffective length for a variation of moisture concentration becomes increasingly important. For T = 140 °C, the ineffective length for 40 broken fibers which is of 1.32 mm for C = 0% to become 1.15 mm (C = 100%). We can deduce that the temperature is an important factor for the determination of the ineffective length

5   Evolution of the Stress Concentrations

The estimation of length of the locally plasticized zone, ineffective length and longitudinal displacement, allows the determination of the stress concentration factor. This factor is of great importance because it offers to us the relationship between the stress calculated at the point of fibers fracture and external applied stress. What will enable us to determine the stress concentration at the zone of broken fibers, and to predict a probably of neighboring adjacent fracture fibers under the effect of moisture and temperature, it is well known that the matrix is very sensitive to the variation of temperature, and that the adhesion to the interface are between hemp fibers and the matrix becomes very weak; thus the debonding phenomenon appears, and leading to the fiber fracture. When it appear fracture fiber in the composite, an influence area generated around the end of the broken fiber where there exists a stress concentration. In addition, the load can be transferred in broken fiber with a shear stress to the interface fiber/matrix To illustrate the effect of the environmental conditions on the degradation of the ineffective area surrounding by broken hemp fibers, the stress concentrations becomes more important with the increase in the number of broken fibers. Thereafter, this stress concentration becomes relatively stable if the number of fibers is very high. For the low temperatures, the effect of the moisture concentration on the stress concentration is almost negligible as shown in the figure 5 for T°=20°C.

The rafter the effect of moisture concentration becomes increasingly important with the increase in temperature of 140°C. For T = 140°C, a clear distinction appears between all the curves, for example, for 40 broken fibers, the stress concentration varies from 1,065 for C = 0% to 1,074 for C = 100%.

The use of natural hemp fibers according to the results above we can deduce that in the neighboring area of intact fibers, the stress concentration is very high. But, when the number of broken fibers is very important, the concentration of the stress to the ineffective area is more important and the ineffective length is large. The neighboring area becomes less stiff, and the broken fiber reacted more easily and can communicate together to cause a complete failure.
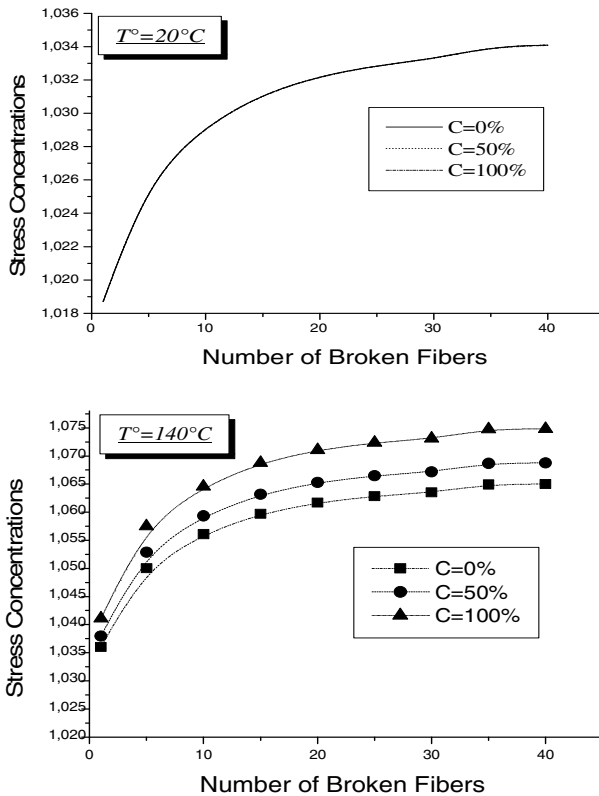
Fig. 4 Evolution of the stress concentration as function of broken fibers for a progressive variation of moisture concentration for $\sigma=0.5\sigma_0$

6   Conclusions

The main goal of the study was the analytical modeling of the behavior of hemp/epoxy unidirectional composite material under the effect of environmental. This behavior depends primarily on the arrangement, the orientation and the fraction volume fibers inside the matrix. The stress transmission from one fiber to another passes by the matrix in the presence of shear stresses at the interfaces. The determination of the stress concentration factor makes it possible to have a clearer idea on the evolution of the fibers failure and the probability of damage of adjacent neighbor fibers.The vicinity of the failure zone is characterized by a locally plasticized zone which will become elastic while moving. Under the effect of a simultaneous variation of the temperature and the moisture concentration, the plastic zone and the ineffective area become widely according to the number of broken fibers and thereafter they become critical under the extreme environmental conditions, in addition it increases longitudinal displacement in the plastic zone

which lead to fast passage of the damage from a broken fiber to another, which permit us to make the conformity with the micromechanical.

In other the fabric hemp composites has advantages and disadvantages. Indeed, the hemp/epoxy composite, presents a great stiffness flexion. They are more resistant to the damage introduced by flexion than the carbon fiber composites. The obtained results also showed that the fiber resistance and the Young modulus are relatively insensitive to the concentration of temperature and moisture, but the epoxy matrix is very influenced by the increase in the environmental conditions.

References

[1] Boyer, C.M.: Composites unidirectionnels : modèles probabilistes de rupture et évaluation de la fiabilité. Thèse d'université, Blaise Pascal (1997)

[2] Manne, P.M., Tsal, S.W.: Design optimization of composite plates: Design criteria for strength, stiffness, and manufacturing complexity composite plates. Journal of Materials Science 32, 544–571 (1998)

[3] Christensen, R.M.: Mechanics of composite materials. Krieger Publishing Company, Malabar (1991)

[4] Rosen, B.W.: Tensile failure of fibrous composites. AIAA J. 2, 1985–1991 (1964)

[5] Zweben, C.: Tensile failure of fiber composites. AIAA J. 6, 2325–2331 (1968)

[6] Foster, G.C.: Tensile and Flexure Strength of Unidirectional Fiber-Reinforced Composites: Direct Numerical Simulations and Analytic Models, Master of Science in Engineering Mechanics, Virginia Polytechnic Institute and State University (1998)

[7] Gao, Z., Reifsnider, K.L.: Micromechanics of Tensile Strength in Composite Systems. In: Composite Materials: Fatigue and Fracture, Fourth Volume, ASTM STP 1156, pp. 453–470 (1993)

[8] Scrivener, K., Van Damme, H.: Construction Materials: From Innovation to Conservation. MRS Bulletin, 308–312 (May 2004)

[9] Khiat, M.A., Sereir, Z., Chateauneuf, A.: Uncertainties of unidirectional composite strength under tensile loading and variation of environmental conditio. Theoretical and Applied Fracture Mechanics 56, 169–179 (2011)

[10] Camata, G., Corotis, R., Spacone, E.: Simplified stochastic modeling and simulation of unidirectional fiber reinforced composites. Probabilistic Engineering Mechanics 19, 33–40 (2004)

[11] Raman, M.R., Wisnom, M.R.: Three-dimensional Finite Element Analysis of the Strss Concentration at a Single Fiber Break. Composites Science and Technology 51, 517–524 (1994)

[12] Cox, H.L.: The elasticity and strength of paper and other fibrous materials. British Journal of Applied Physics, 72–79 (1952)

[13] Curtin, W.A., Takeda, N.: Tensile strength of fiber-reinforced composites: II. Application to polymer matrix composites. Journal of Composite Materials 32, 2060–2081 (1998)

Failure Analysis of HDPE Pipe for Drinking Water Distribution and Transmission

Mohamed Ali Bouaziz[1,2], Mohamed Amine Guidara[1,2], Christian Schmitt[2],
Julien Capelle[2], Ezzdine Haj Taieb[1], Zitounie Azari[2], and Said Hariri[3]

[1] Laboratoire de Mécanique des Fluides Appliqués, Génie des Procédés et Environnement,
Ecole Nationale d'Ingénieurs de Sfax, Université de Sfax, BP 1173, 3038, Sfax, Tunisie
[2] Laboratoire de Biomécanique, Polymères et Structures (LaBPS), Ecole Nationale
d'Ingénieurs de Metz, 57070 Metz, France
[3] Département Technologie des Polymères et Composites and Ingénierie Mécanique,
Ecole des Mines de Douai, 59508 Douai, France
mohamedali.bouaziz@gmail.com,
mohamed-amine.guidara@univ-lorraine.fr

Abstract. Pipes and elbows are important components in any piping systems for transportation of water. These structures are subjected to complex loads taking into account their geometrical configuration and the multiplicity of the loading conditions in service. The origin of failure of these mechanical components is directly related to the presence of defects. The principal objective of this work is to analyze the severity of defects on high density poly-ethylene pipe widely used for water piping networks.

An experimental program, including longitudinally notched (125 mm) PE100 pipe specimens with 11.4 mm thickness containing an external notch with four different notch depths (a), was developed. The three dimensional finite element method based on the computation of the J integral was used to analyze the fracture behaviour of these structures.

The numerical proposed method permit to calculate the crack initiation pressure in PE 100 pipes with a longitudinal external defect. Numerical results were experimentally validated by PE100 notched pipes bursting tests.

The predicted crack initiation pressure agrees well with the test results.

Keywords: J integral, burst test, 3D-FEM model, HDPE PE100 pipe.

1   Introduction

PE pipe due to its chemical inertness, non-corrosive nature and long term durability offers outstanding service life, with conservative estimates standing at 100+ years (Lang et al 1997) and (Janson 1999). Today PE is the material of choice for pipeline transportation of water and gas (AWWA research foundation 2004) where pressure containment and structural integrity is considered critical for the lifetime of the pipeline since system failure can result in flood, explosion, fire and

loss of life resulting in costly litigation and damages. In addition, this can cause service interruption, safety concerns and loss of brand credibility.

The accurate prediction of the failure pressure in damaged pipelines remains a critical issue for the safety assessment of high-pressure piping systems, including onshore and offshore facilities.

Several authors (Ainsworth 1984), (Miller 1988), (Zahoor 1991), (Rahman 1998), (Kim 2003) and (Kim2004) have studied pipe fracture problems by means of experimentation and numerical simulation in order to assess the mechanical integrity, taking into account different crack shapes

In the present work the 3D-FEM based on the computation of the J integral (Rice 1968) at the notch front was used to analyze the defect severity in order to study the evolution of damage degree in the equipment (HDPE pipe) under internal pressure during its propagation. Longitudinally notched PE100 pipe specimens subjected to internal pressure were numerically studied. A series of full scale burst tests were performed on the same end-capped pipe specimens. In this paper, experimental and numerical results were compared and analyzed.

2   Geometrical and Material Models

High Density Polyethylene (HDPE) is a thermoplastic material which is supplied by the manufacturer in a 'ready to use' pelletized form. The grades suitable for pipe manufacture are PE 63, PE 80 and PE100. The pipe manufacturer converts this material into pressure pipe.

For drinking water application HDPE strength class PE100 is widely used. The properties of this material, which is described as the third generation of polyethylene types, are given below in table 1.

In this study experimental and numerical study were made on PE100 pipe specimens. The dimensions of the pipe pieces, showed in Figure 1, are 400 mm length, of thickness t = 11.4 mm and external diameter De = 125 mm with different external notches.

Notches are machined by disc cutter that has a plate thickness of 0.5 mm and an outer diameter (r) of 80 mm. The depth of the notch (a) is due to the disc cutters penetration depth into the pipe wall. Figure 1 shows the geometries of defected test specimen.

Table 1 Mechanical properties of PE 100

Proportional limit (MPa)	Tensile strength(MPa)	Elongation at fracture (%)	Young's modulus (MPa)	Tenacity (KJ/m^2)
σ_y = 22-26	σ_u = 21-25	>600	E = 900-1100	J_{IC} =7.69
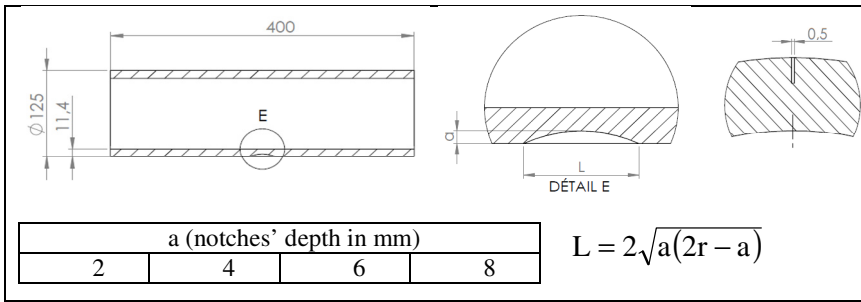
Fig. 1 Notched pipe geometry

3 Finite Element Modeling

Finite element simulation was performed using the code Warp3D (non-mechanical linear Out). The numerical simulation of crack propagation in three dimensions is known tricky for reasons related to the mesh near the notch front, especially when it comes to polymer materials.

Figure 2 shows a three dimensional representation (3-D FE) of the finite element mesh. Symmetric conditions were fully utilized. Only a quarter of the model is studied in order to reduce the computation time. The mesh was created using HyperMesh in three dimensions with quadratic elements C3D20. The second order, reduced integration elements were used for efficient computation. It has been sufficiently refined in the vicinity of the notch with special elements to increase the accuracy in local area and predict correctly the energy release rate into the notch root. Overall, the nodes number in typical FE meshes is ranged between 200000 and 320000 nodes. The normal to the notch front is used to specify the crack extension direction, as shown in Figure 2. Six rings elements surrounding the crack tip are used to evaluate the contour integrals. To incorporate the large geometry change effect, the calculations are made with the geometrically nonlinear ABAQUS software (large displacements) by taking into account of the variation of the strain rate.
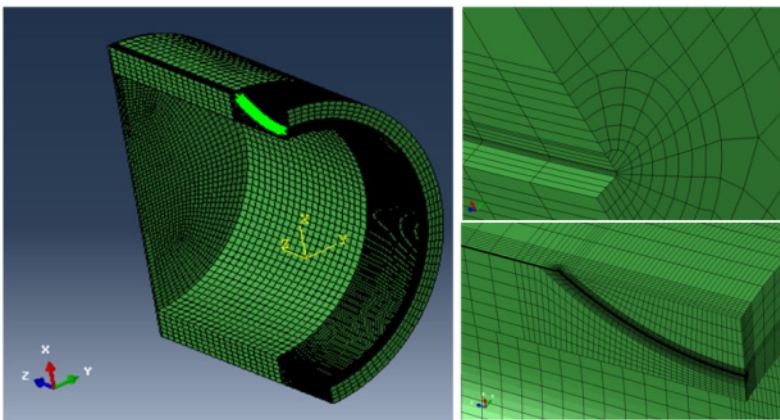
Fig. 2 3D Crack Mesh

Thermoplastic materials such as PE 100 have a viscoelastic behavior and a high degree of ductility. Normally, the fracture behavior (the initiation and propagation of cracks) must be analyzed using the concept of viscoelastic-plastic fracture mechanics (Brostow et al. 1991) and (Favier et al. 2002). However, it has been shown (Benhamena et al. 2010, 2011) that elastic–plastic approaches can approximate with acceptable accuracy the critical J integral of the polyethylene.

4   Burst Tests

To validate the theoretical method, burst tests were conducted under various temperatures. The structural parameters of the PSP specimen are listed in figure 1. All specimens were made from the same material and production batch. Test temperature was set at 20C, and three specimens were used for each group of tests.

PE100 specimens were exposed to closed-end internal pressure tests using the testing apparatus shown in Fig 3. Fig 4 shows the details of the clamp, with a flange 3 and chucking parts 2 and 7 forming the main structure of the clamp by the clumping nut 8.

The outer surface of the compressing part 6 bears a tooth system that runs in the hoop direction. The compressing part 6 is pressed on the inner surface of PE100 1, such that the loads exerted on compressing part 6, particularly those in the axial direction, can be transmitted reliably to the PE100 to limit the axial displacement of the pipe. A compressing part 5 is next to the compressing part 6. Compressing part 5 is pressed against a gasket 4, which efficiently prevents water leakage.

A controlled burst test machine was employed, and the pressure controlling precision reached up to 0.01 MPa. The test process for determining the PE100 burst pressure was based on ISO1167-1:2006.

All specimens have been loaded with a continuous pressure rate of 10 bar per minute until failure (figures 5). The measurement results have been presented as a curve of pressure versus volume of added water.
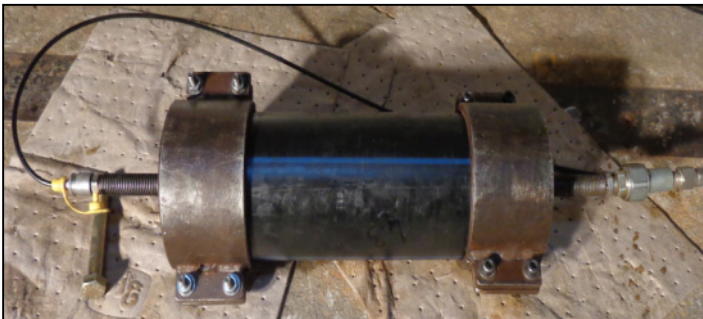
Fig. 3 A photograph of the clamp general assembly
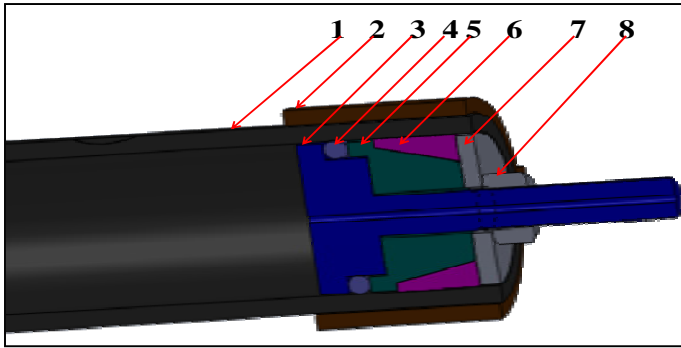
Fig. 4 Details of the test apparatus. 1: PE100; 2: chucking; 3: flange; 5, 6: compressing parts; 4: gasket; 7: chucking; 8: clamping nut.

Fig. 5 Typical specimen failure of short-term burst tests

5 Results and Discussions

The figure 6 shows the variation of the internal pressure as a function of volume of water added to each specimen during burst test. It is independent of the notch depth. The ultimate pressure is greatly affected by the size of the notch depth. The numerical prediction of pressure variation vs added volume is similar to the value measured experimentally.
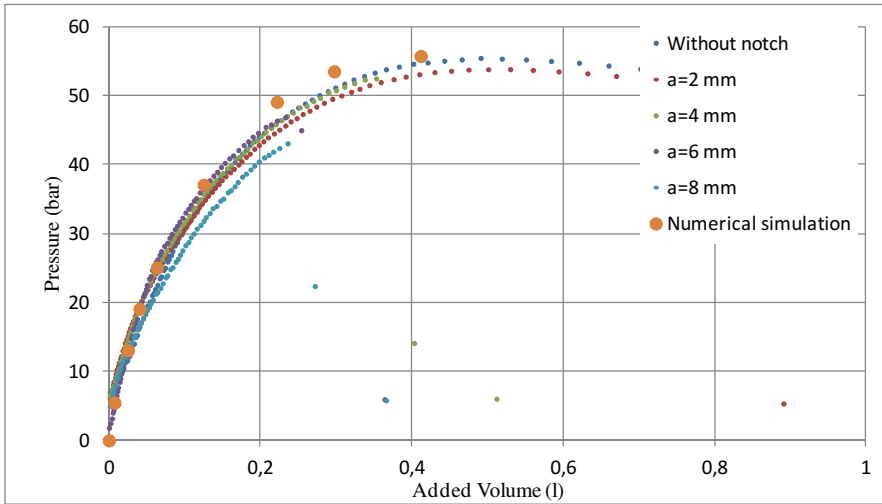
Fig. 6 Internal pressure vs added volume (Burst test)

The figure 7 shows the evolution of the energy release rate in different contours in the normal plane to the notch front. The curve of the energy release rate versus pressure and the value of the critical fracture resistance (JIC=7.69 KJ/m2) allow to determine the internal pressure which lead to the crack initiation. These pressures are represented in figure 8 as a function of the notch depth.

The PE 100 critical fracture resistance JIC was experimentally determined in previous studies using pre-cracked CT specimens.
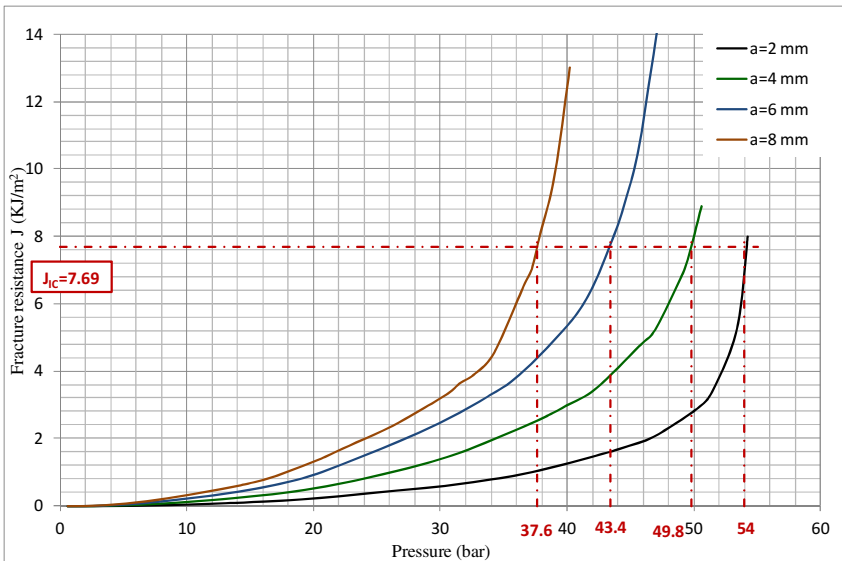
Fig. 7 Variation of the fracture toughness J versus Pressure

Burst pressures are deduced from figure 6 and represented on figure 8. These results show a sharp drop in the burst pressure (experimentally determined) and the internal pressure which leads to the crack initiation (numerically determined) when the notch's depth is more than 4mm.

The result is quite logic because the pressure which leads to the crack initiation is less than the burst pressure.
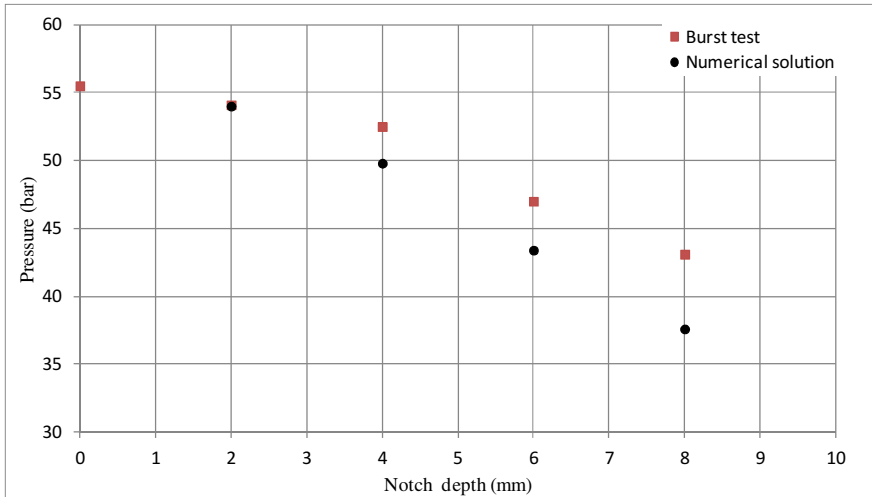
Fig. 8 Burst pressure variation vs notch depth

6   Conclusion and Perspectives

A numerical method is proposed to calculate the crack initiation pressure in a PE 100 pipes with a longitudinal external defect. Numerical results were experimentally validated by PE100 notched pipes bursting tests.

The predicted crack initiation pressure agrees well with the test results with a relative error ranging from 6.72% to 13.82%. This is quite logic because the pressure which leads to the crack initiation is usually less than the burst pressure.

Results show a proportional increase in the error with the notch's depth. It could be due to the fact that the crack initiation pressure is closely related to the JIC that is intrinsic to PE100 material in case of cracks, and it can be different for notches. It also depends on the notch size (even if we have the same notch root geometry).

In the upcoming study some improvement will be made like:
- Use a concept of visco elastic-plastic fracture mechanics to analyze the fraction behavior
- Effects of the notch radius on the fracture toughness JIC of a High Density Polyethylene (PE100)
- Introduce a damage criterion in the numerical simulation
- Perform a dynamic testing to study the effect of transient flow in cracked pipes

References

Lang, R.W., Stern, A., Doerner, G.: Applicability and limitations of current lifetime prediction models for thermoplastics pipes under internal pressure. Die Angewandte Makromolekulare Chemie 247, 131–137 (1997)

Janson, L.E.: Plastics pipes for water supply and sewage disposal. Borealis, Stockholm (1999)

American Water Works Association/Water Environment Federation (AWWA/WEF) research foundation, Techniques for Monitoring Structural Behaviour of Pipeline Systems, infrastructure reliability, New York (2004)

Ainsworth, R.A.: The assessment of defects in structures of strain hardening materials. Eng. Fract. Mech. 19, 633–642 (1984)

Miller, A.G.: Review of limit loads of structures containing defects. Int. J. Pres. Ves. Pip. 32, 197–327 (1988)

Zahoor, A.: Ductile fracture handbook. EPRI/NP-6301 (1991)

Rahman, S.: Net-section-collapse analysis of circumferentially cracked cylinders – part II: idealized cracks and closed-form solutions. Eng. Fract. Mech. 61, 213–230 (1998)

Kim, Y.J., Shim, D.J., Nikbin, K., Kim, Y.J., Hwang, S.S., Kim, J.S.: Finite element based plastic limit loads for cylinders with part-through surface cracks under combined loading. Int. J. Pres. Ves. Pip. 80, 527–540 (2003)

Kim, Y.J., Shim, D.J., Nikbin, K., Kim, Y.J., Hwang, S.S.: Kim JS Elastic–plastic fracture mechanics assessment of test data circumferential cracked pipe. Eng. Fract. Mech. 71, 173–191 (2004)

CSIRO, Life Cycle Analysis of Water Networks, presented at Plastics Pipe XIV, Budapest (2008)

Rice, J.R.: A Path Independent Integral and the Approximate Analysis of Strain Concentration by Notches and Cracks. Journal of Applied Mechanics 35, 379–386 (1968)

ASTM D 6068 Standard Test Method for Determining J-R Curves of Plastic Materials

WARP3D. Release 15.0 manual, civil engineering, reports no UILU-ENG-95-2012, University of Illinois, Urbana (2004)

Benhamena, A., Bouiadjra, B., Amrouche, A., Mesmacque, G., Benseddiq, N., Benguediab, M.: Three finite element analysis of semi-elliptical crack in high density poly-ethylene pipe subjected to internal pressure. Materials and Design 31, 3038–3043 (2010)

Benhamena, A., Aminallah, L., Bouiadjra, B., Benguediab, M., Amrouche, A., Benseddiq, N.: J integral solution for semi-elliptical surface crack in high density poly-ethylene pipe under bending. Materials and Design 32, 2561–2569 (2011)

Favier, V., Giroud, T., Strijko, E., Hiver, J.M., G'Sell, C., Hellinckx, S., et al.: Slow crack propagation in polyethylene under fatigue at controlled stress intensity. Polymer 43, 1375–1382 (2002)

Brostow, W., Fleissner, M., Müller, W.: Slow crack propagation in polyethylene: determination and prediction. Polymer 3, 419–425 (1999)

A Finite Element Model for Orthogonal Cutting of Unidirectional [(0,90)₂]S Composite Laminate

Mohamed Ali Chebbi[1], Frédéric Lachaud[2], and Florent Blanchet[2]

[1] Ecole de l'Aviation de Borj El Amri, Rue de Medjez El Bab 1142 Borj El Amri, Tunisia
med_chebbi@yahoo.com
[2] Institut Supérieur de l'Aéronautique et de l'Espace, Toulouse, France
{frederic.lachaud,Florent.BLANCHET}@isae.fr

Abstract. The orthogonal cutting of composite T800/M21 is simulated using a dynamic explicit analysis. To simulate the cavity behavior in the inner ninety-degree plies, a three-dimensional model with an elastic homogenous damage-evolving material is used. Modified Matzenmiller failure criteria are applied to predict damage initiation and evolution in the studied structure. The used approach consists on combining a parametric modeling, based on an adequate prediction strategy, with a damage delaying procedure. A significant qualitative match between experimental results and numerical calculations is found. The outlined cavity aspect has been successfully retraced. Transverse shear damage and breakage in fiber direction are responsible of the failure of elements in the zero-degree plies. Each damage mode contribution to the collapse of the composite is discussed.

Keywords: Composites, Finite element model, Orthogonal cutting, Matzenmiller failure criteria.

1 Introduction

Composite materials have high strength to weight ratio which makes them frequently used in aeronautical industry. Assembling and manufacturing processes in general and drilling process in particular are responsible of the appearing of damage affecting the material integrity and therefore lowering its efficiency.

Several studies (Wang and al. 1995, Chen 1997, Ramulu and al. 2001, Eshetu and Ramulu 2014) have been conducted to investigate the drilling process and to define the optimal cutting conditions. Faced to costly and time consuming experimental tasks, modeling the problem using numerical platforms is the final relief.

Zitoune (Zitoune and al. 2004) uses the virtual crack extension (VCE) of Samcef® to describe the chip formation mechanism. A good agreement between the numerically-evaluated cutting forces and the experimental results was found. Nevertheless, this approach is based on a pre-existing crack in the work piece.

Thus, the failure location is beforehand known. Recent implementations consist on modeling the material separation using whether element erosion or node splitting to overcome this problem. The node splitting approach constraints crack growth along element edges. The results are therefore mesh-dependent. The erosion method is applied in several models (Mahdi and Zhang 2006), Venu Gopala Rao and al. [2006,2007,2008]) and is undergoing outstanding results.

This approach is based on multi-scale analysis; it generates reliable approaches for a better understanding of the manufacturing process. Heterogeneous fields (separation between the different components) are mainly used to study the interfacial debonding and micro-cracks propagation. Macro-mechanical models are suited for chip formation mechanism and cutting force studies.

The aim of this work is to introduce a three-dimensional model which uses a two-phase material (0°, 90°). It aims to confirm the ability of the modified Matzenmiller failure criteria (Matzenmiller and al. 1995, Xiao and al. 2007, Lachaud 2011) to model damage growth in composite T800/M21. A user-defined behavioral law is introduced to model the damage evolution in the material.

2   Finite Element Model Formulation

Model dimensions are optimized to reduce computation time. A 60 mm length, 20 mm height and 2 mm width sample is considered (Fig.1). The finite element model is split into two zones where different material behaviors are addressed. An 8-node linear brick element (C3D8R) is used.   Damage is calculated only in the 5 mm depth finely-meshed first zone (Element size= $0.1^2*0.0625$ mm^3).The second zone is coarsely meshed and considered as an elastic homogenous material (EHM). A six-degree rake angle rigid tool, with a zero-edge radius, is moving at a 10 m/s cutting speed. A reference point is modeled to control the tool movement.

The cutting is simulated using a hard contact model. Therefore, the piece undergoes stress at zero distance from the tool. The displacements of the button of the work material are restrained in all directions. The extreme right is restrained in the cutting direction. Temperature variations are not taken into account. As experiments are conducted at a very high speed, speed effects are covered by the model. The depth of cut equals 1 mm.
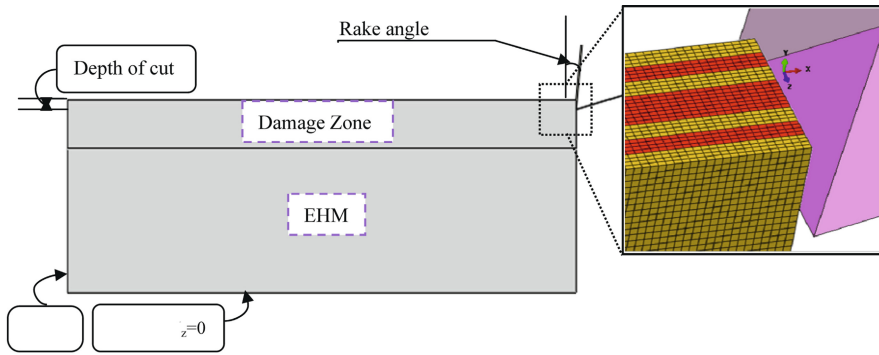
Fig. 1 Schematic view of the model. Yellow color stands for 0° plies (The ply master direction coincide with the X direction). Red color illustrates the 90° plies (The ply master direction coincide with the Y direction).

The behavioral law is applied in the local material axis of each ply. It is defined using the following set of mechanical properties.

Table 1 Mechanical properties of the material used in FEM simulation

Properties	Values
Elastic constants	E_{11}^{0}=165 GPa, E_{22}^{0}=E_{33}^{0}= 8.5 GPa,, v_{12}=v_{13}=0.3, v_{23}=0.45, G_{12}^{0}=G_{13}^{0}= 4.8 GPa, G_{23}^{0}=3.5 GPa
Tensile strengths	$\sigma_{11}^{RT,stat}$=250 MPa, $\sigma_{22}^{RT,stat}$= $\sigma_{33}^{RT,stat}$=60 MPa
Compressive strengths	$\sigma_{11}^{RC,stat}$=1400 MPa, $\sigma_{22}^{RC,stat}$= $\sigma_{33}^{RC,stat}$=300 MPa
Shear strengths	$\sigma_{12}^{S,stat}$=$\sigma_{13}^{S,stat}$=95 MPa, $\sigma_{23}^{S,stat}$=60 MPa
Release strength	σ_{11}^{R}=1000 MPa

2.1   Damage Initiation and Evolution in the Material

Several models assign elastic behavioral laws to composite materials. Failure can be modeled by different criteria (Hinton and al. 2004). To study the evolution of structural composite response, it is important to model the loss of mechanical properties. This passes through the use of a damage based model. Crack, initiation phase, and propagation can be taken into account.

The present work assumes that micro-cracks initiation and propagation depends on ply master direction. Damage is orthotropic and is modeled by stiffness degradation as:

$$E_{ii} = E_{ii}^{0}(1 - d_{i}); i = 1..3 \tag{1}$$

$$G_{ij} = G_{ij}^{0}(1 - d_{k}); i \neq j \in \{1, 2, 3\}, k = 4..6 \tag{2}$$

E_{ii}^0 and G_{ij}^0 are respectively the initial Young's and Coulomb's Modules.

The softened softness matrix can be written as follows:

$$S = \begin{bmatrix} \dfrac{1}{E_{11}^0(1-d_1)} & \dfrac{-v_{12}}{E_{11}^0} & \dfrac{-v_{13}}{E_{11}^0} & 0 & 0 & 0 \\[2mm] \dfrac{-v_{12}}{E_{11}^0} & \dfrac{1}{E_{22}^0(1-d_2)} & \dfrac{-v_{23}}{E_{22}^0} & 0 & 0 & 0 \\[2mm] \dfrac{-v_{13}}{E_{11}^0} & \dfrac{-v_{23}}{E_{22}^0} & \dfrac{1}{E_{33}^0(1-d_3)} & 0 & 0 & 0 \\[2mm] 0 & 0 & 0 & \dfrac{1}{2G_{12}^0(1-d_4)} & 0 & 0 \\[2mm] 0 & 0 & 0 & 0 & \dfrac{1}{2G_{23}^0(1-d_5)} & 0 \\[2mm] 0 & 0 & 0 & 0 & 0 & \dfrac{1}{2G_{13}^0(1-d_6)} \end{bmatrix} \tag{3}$$

The model assumes that one damage mode is necessary generated by a full combination of different failure occurrences. The damage modes can be described by the relationship below:

$$\begin{Bmatrix} d_1 \\ d_2 \\ d_3 \\ d_4 \\ d_5 \\ d_6 \end{Bmatrix} = \begin{bmatrix} 1 & 1 & 1 & 0 & 0 \\ 0 & 0 & 1 & 1 & 0 \\ 0 & 0 & 1 & 1 & 1 \\ 1 & 1 & 1 & 1 & 1 \\ 0 & 0 & 1 & 1 & 1 \\ 1 & 1 & 1 & 1 & 1 \end{bmatrix} \times \begin{Bmatrix} \phi_1 \\ \phi_2 \\ \phi_3 \\ \phi_4 \\ \phi_5 \end{Bmatrix} \tag{4}$$

where ϕ_i are the damage functions obtained directly from the failure criteria via the following formula:

$$\phi_i = 1 - \exp(\frac{1 - r_i^{m_i}}{m_i}) \tag{5}$$

r_i; $i=1..5$ are the evaluated failure criteria, m_i are parameters that govern the damage evolution.

2.2 Modified Matzenmiller Failure Criteria

Failure criteria are calculated using a linear elastic effective behavioral law. The failure by tensile in fiber direction is given by:

$$r_1^2 = \left(\frac{\sigma_{11}}{\sigma_{11}^{RT}}\right)^2 + \left(\frac{\sigma_{12}^2 + \sigma_{13}^2}{\left(\sigma_{12}^R\right)^2}\right) \tag{6}$$

σ_{11}^{RT} is the tensile failure strength in fiber direction. σ_{11}^{R} is the failure strength that describes the fiber-interface debonding. It is defined as the strength needed
to free the fiber from the composite structure. Failure by compression is formulated as:

$$r_1^2 = \left(\frac{\langle -\sigma_{11}\rangle}{\sigma_{11}^{RC}}\right)^2 + \left[\frac{\sigma_{12}^2 + \sigma_{13}^2}{\left(\sigma_{12}^R\right)^2}\right] \tag{7}$$

σ_{11}^{RC} is the compressive failure strength. Failure by squishing can occur when the directional strengths summation is compressive. It is given by the relationship below:

$$r_3^2 = (\frac{\langle -\sigma_{11}-\sigma_{22}-\sigma_{33}\rangle}{3\sigma_{33}{}^{RC}})^2 \tag{8}$$

σ_{33}^{RC} is the squishing failure strength. Since the fiber is highly resistant to squishing especially when transverse and out-of-plane directional stresses (σ_{22} and σ_{33} respectively) are dominant, fiber-direction elements hardly fail by squishing. The outlined failure strength is augmented when dealing with this situation. The matrix failure criterion is formulated as follows:

$$r_4^2 = (\frac{\langle \sigma_{22}\rangle}{\sigma_{22}{}^{RT}})^2 + (\frac{\langle -\sigma_{22}\rangle}{\sigma_{22}{}^{RC}})^2 + (\frac{\sigma_{12}}{\sigma_{12}{}^S + \langle -\sigma_{22}\rangle tan\varphi})^2 + (\frac{\sigma_{23}}{\sigma_{23}{}^S + \langle -\sigma_{22}\rangle tan\varphi})^2 \tag{9}$$

$\tan\varphi$ accounts for friction generated after the fiber-matrix debonding when the directional stress σ_{22} is compressive. The delamination failure describes the inter-laminar debonding. Friction effects have been considered so that the criterion could take the following form:

$$r_5^2 = A^2 \cdot [(\frac{\langle \sigma_{33}\rangle}{\sigma_{33}{}^{RT}})^2 + (\frac{\langle -\sigma_{33}\rangle}{\sigma_{33}{}^{RC}})^2 + (\frac{\sigma_{13}}{\sigma_{13}{}^S + \langle -\sigma_{33}\rangle tan\varphi})^2 + (\frac{\sigma_{23}}{\sigma_{23}{}^S + \langle -\sigma_{33}\rangle tan\varphi})^2] \tag{10}$$

A quantifies the extent of damage between plies. This parameter is not considered for the present work. High speed effects are incorporated in the model and are presented by the augmentation of failure thresholds. The new expression of the different elastic-limit stresses is given by:

$$\sigma_{ii}^{RT/C} = \sigma_{ii}{}^{RT/C,stat}\left(1 + C_{ii}\ln\left(\frac{\dot{\varepsilon}}{\dot{\varepsilon}_c}\right)\right); i=1..3 \tag{11}$$

$$\sigma_{ij}^S = \sigma_{ij}{}^{S,stat}\left(1 + C_{ij}\ln\left(\frac{\dot{\varepsilon}}{\dot{\varepsilon}_c}\right)\right); i\neq j; i,j \in \{1,2,3\}) \tag{12}$$

$\dot{\varepsilon}$ is the equivalent strain rate defined as the quadratic summation of the individual strain rates (Eq. 13). Each increment Δt, the strain rate is calculated and compared to the critical strain rate $\dot{\varepsilon}_c$. If the resultant ratio is higher than 1, speed effects are considered and failure thresholds increased. C_{ii} and C_{ij} govern the different failure strengths' correction.

$$\dot{\varepsilon} = \sqrt{\frac{1}{2}\sum_{i=1}^{3}(\frac{\Delta\varepsilon_{ii}}{\Delta t})^2 + (\frac{\Delta\varepsilon_{12}}{\Delta t})^2 + (\frac{\Delta\varepsilon_{23}}{\Delta t})^2 + (\frac{\Delta\varepsilon_{13}}{\Delta t})^2} \qquad (13)$$

2.3   Calculation Algorithm

During the simulation, the stress tensor is periodically evaluated by multiplying the updated stiffness matrix to the actual strain tensor. At time t, the stress and strain tensors are respectively $\overline{\overline{\sigma}}_t$ and $\overline{\overline{\varepsilon}}_t$. At time $t + \Delta t$, the new strain tensor is given by:

$$\overline{\overline{\varepsilon}}_{t+\Delta t} = \overline{\overline{\varepsilon}}_t + \overline{\overline{\Delta\varepsilon}} \qquad (14)$$

After evaluating the damage functions using equation (5), Damage is calculated by equation (4). Using the following set of parameters (m_1, m_2, m_3, m_4, m_5)=(0.05, 0.05, 0.05, 0.04, 0.03), the resulting damage distributions in one element of the damage zone (Fig.1) are shown in figure 2. Damage rate is so high that elements undergo very fast softening. To solve the localized aspect problem, spatial regularization should be applied.
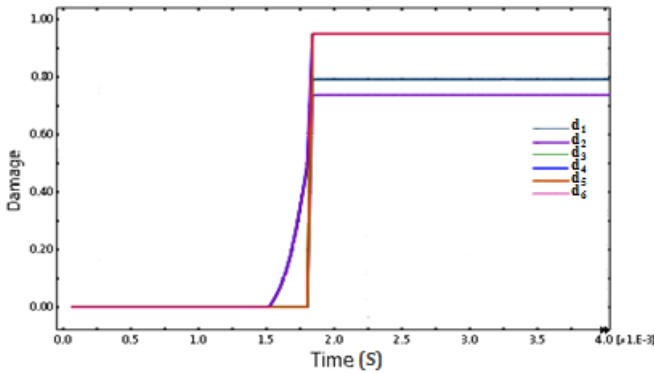
Fig. 2 Evolution of different damage modes without spatial regularization

Spatial regularization is simulated using this assumption; One element should diffuse damage to adjacent elements. To meet the outlined assumption, damage increment Δd_i is adjusted using the following formula:

$$\Delta d_i = \frac{\Delta t}{\tau}(1 - \exp^{-a(d_{i,t+\Delta t} - d_{i,t})})$$ (15)

where a and τ are user-defined scalars allowing to spread damage over the whole work piece. The new delocalized damage variable is given by:

$$d_{i,t+\Delta t_{delayed}} = d_{i,t} + \Delta d_i$$ (16)

Equations (15 and 16) were implemented in the model. By maintaining the same set of parameters   (m_1, m_2, m_3, m_4, m_5)=(0.05, 0.05, 0.05, 0.04, 0.03) and using : $\frac{\Delta t}{\tau} = 10^{-4}$; a=1, Damage is distributed over the whole meshed area. All damage rates have decreased significantly (Fig.3). As a result, elements exhibit relaxed softening before getting removed from the structure.
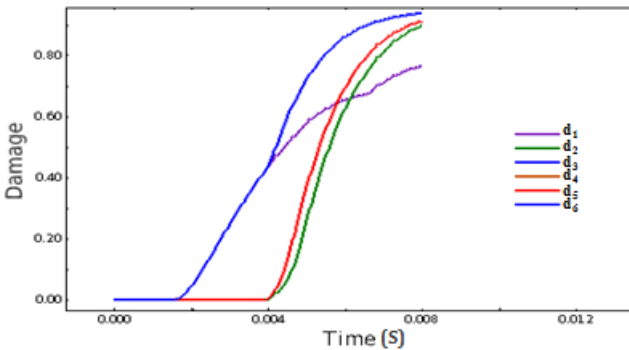
Fig. 3 Shows the spatial regularization effect on different damage modes

The softness matrix is updated using the delayed damage variables so that the new stress tensor could be written as follows:

$$\overline{\overline{\sigma_{t+\Delta t}}} = S^{-1}\overline{\overline{\varepsilon_{t+\Delta t}}}$$ (17)

The following diagram (Fig. 4) demonstrates the implemented calculation method for the used behavioral law. The same algorithm is repeated each time increment.

$$t + \Delta t : \overline{\overline{\sigma_{eff}}}, \ \overline{\overline{\Delta \varepsilon}}$$

Evaluating the new strain rate (Eq. 13)

False

$$\dot{\varepsilon} > \dot{\varepsilon}_c$$

True

Adjusting failure thresholds (Eqs. 11&12)

Evaluating failure criteria (Eqs. 6-10)

Calculation of damage functions (Eq. 5)

Calculation of damage variables (Eq. 4)

Applying spatial regularization (Eqs.15&16)

Updating the softness matrix (Eq. 3)

New stress tensor $\overline{\overline{\sigma_{t+\Delta t}}}$ (Eq. 17)
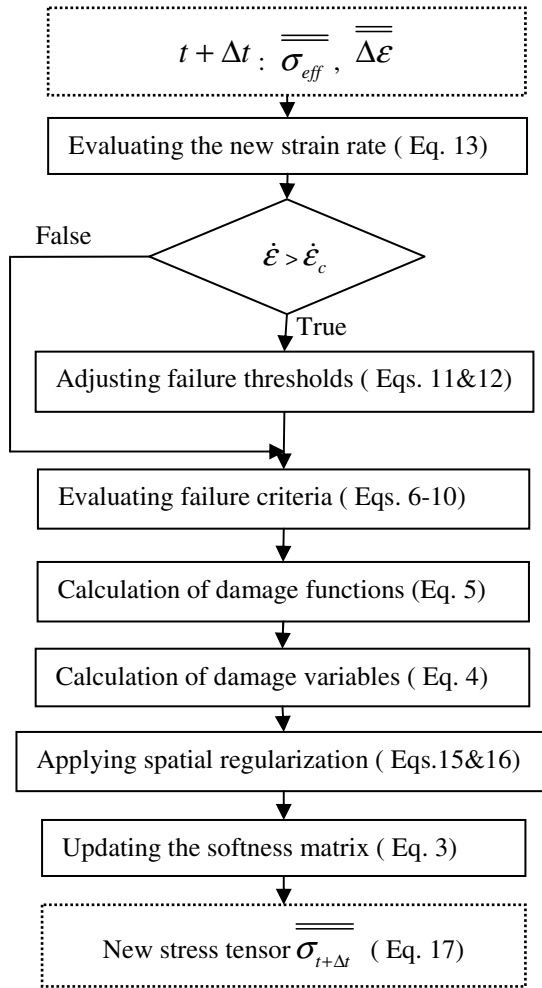
Fig. 4 User-defined behavioral law proceeding diagram

2.4 Results and Discussion

For the numerical model based on equations (15 and 16), two sets of parameters were used.

The first set of parameters is : $\dfrac{\Delta t}{\tau} = 10^{-4}$, a=1 and (m_1, m_2, m_3, m_4, m_5)= (0.05, 0.05, 0.05, 0.04, 0.03).

Figure 5 shows a highly delayed damage which causes the removal of significant chunks in the material (around 2 mm radius) and results in very poor cut surface quality.
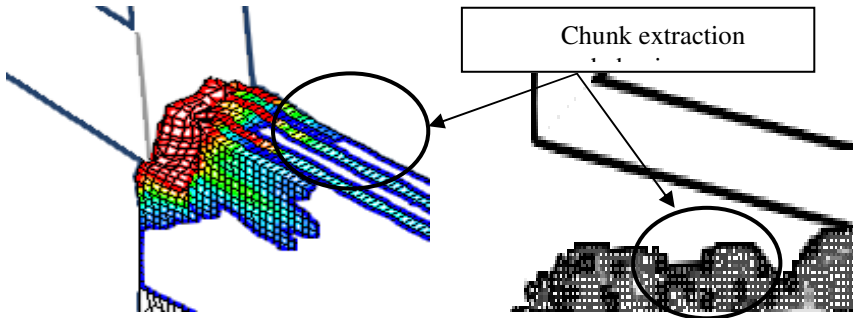
Fig. 5 Schematic view of transverse shear damage (d$_4$) localized aspect prior to material removal
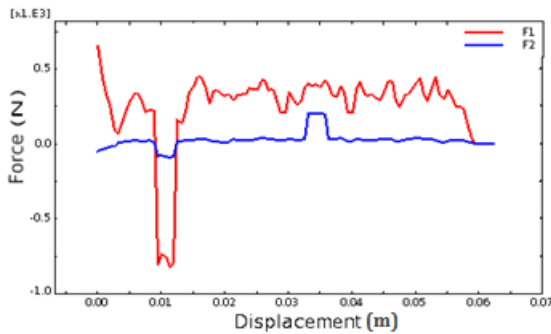
Fig. 6 Resultant cutting forces

Figure 6 shows negative values of the cutting forces at the beginning of simulation. As the tool moves forward, the elements resist the tool advance before getting massively extracted. After the first contact shock, the cutting forces stabilize. The prescribed parameters do not offer a realistic approach. Damage is over-delayed which generates oscillation problems. Therefore, a compromise is to be adopted when choosing values of the delaying parameters.

Using $\dfrac{\Delta t}{\tau} = 10^{-3}$, a=1 and (m$_1$,m$_2$,m$_3$,m$_4$, m$_5$)=(0.5, 0.4, 0.5, 0.5, 0.2), the cavity aspect occurring in the middle 90° plies and commonly noticed during experimental tasks, is obtained by the numerical model as shown in figure 3.

The formation of chips is not clearly noticed during this analysis due to the different material phases encountered by the cutting tool. Considering the 90° orientations, the cutting plane does not follow a regular pattern due to fiber excessive bending before failure. At the beginning of simulation, the 0° plies exhibit breakage in fiber, cracking in transverse and out-of-plane directions (respectively d$_1$,d$_2$,d$_3$) as represented in figure 8. The 0° orientation elements fail by local compression after bending around the Z axis (Fig. 8 d$_1$). The 90° orientation elements have not exhibited yet any damage mode.
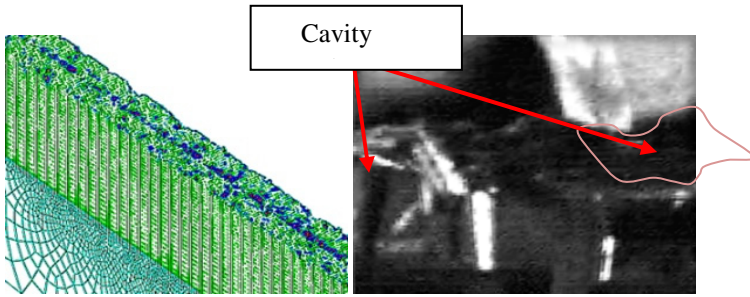
Fig. 7 Shows the 90° inner plies cavity aspect noticed in both numerical and experimental results
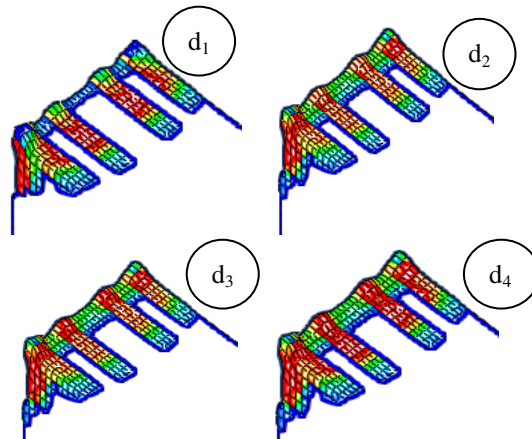
Fig. 8 Extent of damage by breakage in fiber direction, cracking in transverse and out-of-plane directions and transverse shear damage (d_1, d_2, d_3, d_4 respectively)

The adjusted parameters have moderated the resulting cutting forces (Fig. 9) which become qualitatively similar to the experimental ones. Compared to figure 6, the horizontal force has dropped to around 100 N average. In fact, elements' resistance has decreased significantly.
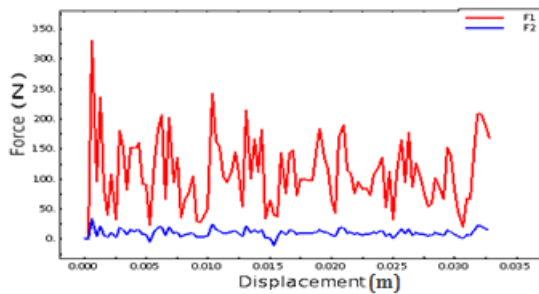
Fig. 9 Schematic view of the resultant cutting forces for the adjusted parameters

3   Conclusions and Future Work

An explicit dynamic analysis is conducted in the present work. To make the model describe the damage diffusion in the material, a damage-delaying procedure is introduced. The trend study has succeeded to retrace the cavity aspect in the 90° inner plies. In the 0° plies, failure is mainly caused by breakage in fiber direction, cracking in transverse and out-of plane directions and transverse shear damage. Thus, Modified Matzenmiller failure criteria show ability to describe composite failure. As a future work, the coefficient coupling matrix can be reconsidered using an energetically based approach.

References

Wang, D.H., Ramulu, M., Arola, D.: Orthogonal cutting mechanisms of graphite/epoxy composite. Part I. Unidirectional laminate. Int. J. Mach. Tool Manuf. 35(12), 1623–1638 (1995), doi:10.1016/0890-6955(95)00014-O

Chen, W.-C.: Some experimental investigations in the drilling of carbon fiber-reinforced plastics (CFRP) composite laminates. Int. J. Mach. Tool Manuf. 8, 1097–1108 (1997), doi:10.1016/S0890-6955(96)00095-8

Ramulu, M., Branson, T., Kim, D.: A study on the drilling of composite and titanium stacks. Compos. Struct. 54, 67–77 (2001), doi:10.1016/S0263-8223(01)00071-X

Eneyew Eshetu, D., Ramulu, M.: Experimental study of surface quality and damage when drilling Unidirectional CFRP composites. Brazilian Metallurgical, Materials and Mining Association (2014), doi:10.1016/j.jmrt.2014.10.003

Zitoune, R., Collombet, F., Lachaud, F., Piquet, R., Pasquet, P.: Experiment-calculation comparison of the cutting conditions representative of the long fiber composite drilling phase, IUT Paul Sabatier, 31077 Toulouse Cedex4, France (2004), doi:10.1016/j.compscitech.2004.09.028

Mahdi, M., Zhang, L.: A finite element model for the orthogonal cutting of fiber-reinforced composite materials. The University of Sydney, Australia (2006), doi:10.1016/S0924-0136(01)00675-6

Venu Gopala Rao, G., Mahajan, P., Batnagar, N.: Micro-mechanical modeling of machining of FRP composites cutting force analysis. Indian Institute of Techology Delhi, India (2006)

Venu Gopala Rao, G., Mahajan, P., Batnagar, N.: Machining of UD-GFRP composites chip formation mechanism. Indian Institute of Technology Delhi, India (2007), doi:10.1016/j.compscitech.2007.01.025

Venu Gopala Rao, G., Mahajan, P., Batnagar, N.: Three-dimensional macro-mechanical finite element model for machining of unidirectional fiber reinforced polymer composites. Indian Institute of Technology Delhi, India (2008), doi:10.1016/j.msea.2007.11.157

Matzenmiller, A., Lubliner, R.L., Taylor, A.: A constitutive model for anisotropic damage in fiber composites (1995), doi:10.1016/0167-6636(94)00053-0

Xiao, J.R., Gamma, B.A., Gillespie Jr., J.W.: Progressive damage and delamination in plain weave S-2 glass/SC-15 composites under quasi-static punch-shear loading (2007), doi:10.1016/j.compstruct.2005.09.001

Hinton, M.J., Kaddour, A.S., Soden, P.D.: Failure criteria in Fibre Reinforced polymer composites. The Worldwide Failure Exercise (2004)

Lachaud F.: Contribution à l'analyse multi-échelle du comportement mécanique non linéaire matériau des structures composites, Habilitation à Diriger des Recherches, Université de Toulouse, France (2011)

Finite Element Analysis of Stress Concentrations in Isotropic and Composite Plates with Elliptical Holes

Abdelhak Khechai[1], Abdelouahab Tati[2],
Mohamed Ouejdi Belarbi[2], and Abdelhamid Guettala[1]

[1] Laboratory of Civil Engineering, University of Biskra, BP 145, 07000 Biskra, Algeria
 abdelhak_khechai@hotmail.fr, guettalas@yahoo.fr
[2] Laboratory of Energy Engineering and Materials, University of Biskra, BP 145, 07000
 Biskra, Algeria
 abdeltati@yahoo.fr, belarbi.m.w@gmail.com

Abstract. Panels and shells with variously shaped cutout are often used in both modern and classical aerospace, mechanical and civil engineering structures. The understanding of the effects of cutout on the load bearing capacity and stress concentration of such plates/shells is very important in designing of structures. Finite element investigation is undertaken to study the stress analysis of plates with central elliptical holes. In this study, the stress concentration factors (SCF) in cross-and-angle-ply composite plates as well as in isotropic plates subjected to uniaxial loading is studied. The main objective of this study is to demonstrate the accuracy of present element for stress analysis of plates with central cutout. The varying parameters, such as cutout shape (circular or elliptical), hole sizes (*a/b*) or cutout orientations, which affect the stress distributions and SCF in the perforated plates, are considered. The numerical results obtained by the present element are compared favorably with the analytic findings published in literature, which demonstrates the accuracy of the present element.

Keywords: finite element analysis, laminated composite plates, stress concentration, geometric singularity.

1 Introduction

Superior mechanical properties of composite materials such as high stiffness and strength to weight ratios caused it to be used increasingly in many areas of technology including marine, aerospace, automotive and others. In recent years, researchers have put enormous efforts in order to analyze the stress distribution around circular and elliptical holes. Numerous investigators have attempted to calculate the SCF for different kinds of geometric discontinuity under different types of loads by using various methods (Wang and Qin 2012).

Circular, elliptical, and rectangular cutouts are two-dimensional holes usually. For circular hole problems in finite field, there are some research results using approximate analytical methods (Louhghalam, A., et al 2011). However, research achievements about elliptical hole are relatively few in comparison with circular holes.

One of the most powerful methods for the analytical calculation of stress distribution and in particular SCFs around holes in an infinite elastic plate is the Muskhelishvili conformal mapping complex variable method. The method is presented in detail in Muskhelishvili's monograph (Muskhelishvili 1977) as well as in classical books on the theory of elasticity. Moreover, (Sharma 2012) obtained the general stress functions for determining the SCF around circular, elliptical and triangular cutouts in laminated composite infinite plate subjected to arbitrary biaxial loading at infinity by use of the Muskhelisvili's complex variable method.

While the complex variable method is very powerful in solving a wide variety of elasticity problems, it is complicated and must be reformulated for each type of far-field load. The other main class of methods for evaluating SCFs in plates is based on the finite element method. Many researchers have recently attempted to study the stress distribution around various shapes holes by using special finite elements (Nishioka and Atluri 1982), (Piltner 1985), (Chen 1993), (Pan and Yang 2001), and (Wang and Qin 2012). (Khechai et al 2014) pointed out the effect of fiber orientation on the stress concentration around circular holes of single layered anisotropic plates and their failures by comparing the layer without a hole.

The main purpose of this paper is to calculate the SCFs around circular and elliptical holes in thin isotropic, cross-and-angle-play laminated composite plates, subjected to uni-axial loading by using a quadrilateral finite element, previously developed by (Tati and Abibsi 2007) for the bending and mechanical buckling of laminated composite plates. To evaluate the performance of the proposed element, some numerical examples are considered in this study. The numerical obtained results are compared favorably with analytical results which demonstrate the accuracy of the present element.

2   Finite Element Formulations

The displacement field (Khechai et al 2014) according to the classical laminated plate theory, based on the Kirchhoff assumptions, is given by the followings

$$
\begin{aligned}
U(x,y,z) &= u_0(x,y) - z\frac{\partial w}{\partial x} \\
V(x,y,z) &= v_0(x,y) - z\frac{\partial w}{\partial y} \\
W(x,y,z) &= w_0(x,y)
\end{aligned}
\tag{1}
$$

where u_0, v_0 and w_0 are the mid-plane displacement components of the plate. The strain-displacement relations, including the large deformations, can be determined as

$$
\begin{Bmatrix} \varepsilon_x \\ \varepsilon_y \\ \gamma_{xy} \end{Bmatrix} = \begin{Bmatrix} \dfrac{\partial u}{\partial x} + \dfrac{1}{2}\left(\dfrac{\partial w}{\partial x}\right)^2 \\[2mm] \dfrac{\partial v}{\partial y} + \dfrac{1}{2}\left(\dfrac{\partial w}{\partial y}\right)^2 \\[2mm] \dfrac{\partial v}{\partial x} + \dfrac{\partial u}{\partial y} + \dfrac{\partial w}{\partial x}\dfrac{\partial w}{\partial y} \end{Bmatrix} + z \begin{Bmatrix} -\dfrac{\partial^2 w}{\partial x^2} \\[2mm] -\dfrac{\partial^2 w}{\partial y^2} \\[2mm] -2\dfrac{\partial^2 w}{\partial x \partial y} \end{Bmatrix} = \underbrace{\left\{ \varepsilon_L^0 + \varepsilon_{NL}^0 \right\} + z\{k\}}_{\{\varepsilon\}} \qquad (2)
$$

By adopting the classical laminate theory, the forces N and moments resultants M are related to the mid-surface strains ε^0 and to the curvatures k by

$$
\begin{bmatrix} N \\ M \end{bmatrix} = \begin{bmatrix} [A] & [B] \\ [B] & [D] \end{bmatrix} \begin{Bmatrix} \varepsilon^0 \\ k \end{Bmatrix} \qquad (3)
$$

where $[A]$, $[B]$ and $[D]$ is the extensional, coupling and bending rigidity matrix, respectively, which can be defined by

$$
\{A, B, D\}^{\mathrm{T}} = \int_{-\frac{h}{2}}^{\frac{h}{2}} \left[\overline{Q}_{ij}\right]_k (1, z, z^2)\,dz \qquad (4)
$$

with $\overline{Q}_{ij}$ are the coefficients of elasticity of a layer in the global coordinate system (x, y, z) of the laminate forming an angle θ with the local coordinate system (1,2,3). The proposed element is a combination of an isoperimetric membrane quadrilateral element and a first order Hermitian rectangular plate element of high degree of accuracy. The element has 4 nodes of 8 degrees of freedom each. The displacements state leads to 32 degrees of freedom by element with 8 degrees of freedom by node and the resulting displacement vector $\{q\}$ is

$$
\{q\} = \left\{ u_i, v_i, w_i, \frac{\partial w_i}{\partial x}, \frac{\partial w_i}{\partial y}, \frac{\partial^2 w_i}{\partial x \partial y}, \frac{\partial^2 w_i}{\partial x^2}, \frac{\partial^2 w_i}{\partial y^2} \right\}_{i=1,4} \qquad (6)
$$

The strain energy U of the element is

$$
U = \frac{1}{2} \int_{-1}^{1}\int_{-1}^{1} \{q\}^T \left(\begin{array}{l} [S_\varepsilon]^T [A][S_\varepsilon] + [S_\varepsilon]^T [B][S_k] \\ + [S_k]^T [B][S_\varepsilon] + [S_k]^T [D][S_k] \end{array} \right) \{q\}|J|\,d\xi d\eta \qquad (7)
$$

where

$$\{\varepsilon_L^0\} = [S_\varepsilon]\{q\}, \quad \{k\} = [S_k]\{q\} \tag{8}$$

In which, $\{q\}$, $[S_\varepsilon]$, and $[S_k]$ are the resulting displacement vector of the element, the strain displacement matrix for membrane, bending, respectively. $|J|$ is the determinant of the Jacobian matrix. Based on the principle of minimum potential energy, the first variation provides the expression of the elementary stiffness matrix $[K_e]$

$$[K_e] = \int\limits_{-1}^{1}\int\limits_{-1}^{1} \left(\begin{array}{l} \{S_\varepsilon\}^T [A]\{S_\varepsilon\} + \{S_\varepsilon\}^T [B]\{S_k\} \\ + \{S_k\}^T [B]\{S_\varepsilon\} + \{S_k\}^T [D]\{S_\varepsilon\} \end{array} \right) |J| d\xi d\eta \tag{9}$$

We would like to note here that more details on the finite element formulation are given in the work of (Khechai et al 2014).

3   Numerical Results

3.1   Infinite Isotropic Plate with a Centered Elliptical Hole under Arbitrary Uniaxial Tension

In this study, an infinite domain is idealized by a large square domain with the side length 100 *cm*. The major axis of the elliptical hole is taken to be 2*a* and the minor axis is taken to be 2*b*. The laminated plate is selected as symmetrical about mid-plane. The thickness of each layer is 0.01*cm*. All of the thicknesses of the laminate are equal.

The first study, for which exact solutions are available, is chosen to demonstrate the accuracy of the present element. In this example, we analyze an infinite isotropic plate ($E = 200\ MPa$, $G = 80\ MPa$ and $v = 0.25$) with a centered elliptical hole subjected to arbitrary unidirectional tension, and the plane stress state is assumed. The exact analytical solution given by (Forest and Amestoy 2004) for the circumferential stress around elliptical hole in isotropic plate subjected to uniaxial loading inclined at angle ϕ with the *x*-direction Fig. 1, could be calculated as

$$\sigma_\alpha = \frac{1 - m^2 + 2m\cos 2\phi - 2\cos 2(\alpha - \phi)}{1 - 2m\cos 2\alpha + m^2}\sigma, \quad m = \frac{a - b}{a + b}, \quad 0 \leq m \leq 1 \tag{10}$$
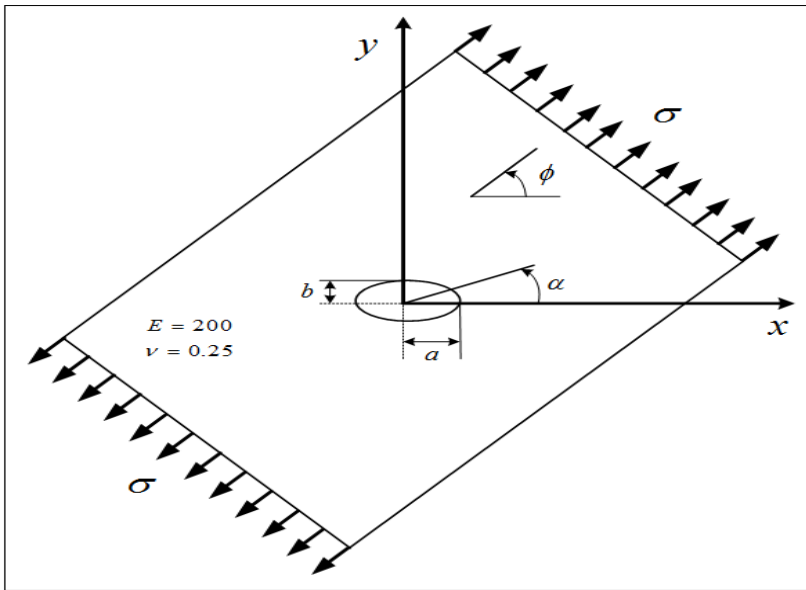
Fig. 1 Square isotropic plate with a centered elliptical hole under inclined tension

In the computation, a computer program was prepared for studying the stress distributions in isotropic plate with circular or elliptical holes by using the stress functions given by Eq. (10). In the first example, isotropic plates with various aspect ratios a/b are chosen for validating the present element by comparing numerical results with available numerical and analytical solutions. The plates are loaded parallel to the y-direction. For different aspect ratio a/b, the maximum SCFs found by the present element, exact analytical findings given by Eqs. (10) and the numerical results, obtained by (Wang and Qin 2012) are tabulated in Table 1.

Table 1 SCFs for different ratios of a/b

Material	Isotrope									
a/b	1		2		3		4		5	
	Max	Min	Max	Min	Max	Min	Max	Min	Max	Min
Exact	3.00	-1.00	5.00	-1.00	7.00	-1.00	9.00	-1.0	11.00	-1.0
Ref. [1]	3.01	-	5.01	-	7.01	-	9.02	-	11.02	-
PE	3.00	-1.01	5.01	-0.99	7.05	-0.99	9.05	-1.0	11.11	-1.0
Percentage error (%)	0.00	0.60	0.12	0.50	0.67	0.30	0.53	0.30	1.00	1.10

As presented in Table 1, it is found that the maximum relative error is just 1.10 %, indicating that the present element can precisely capture the dramatic variation

of stress on the elliptical hole boundary and the accurately of the element is verified.

3.2   Effect of Hole Sizes and Elliptical Hole Orientations on SCF

After verifying the accuracy and efficiency of the element against the known cases in the literature, we study now the effect of the varying parameters, such as cut-out shape (circular or elliptical) holes, aspect ratio *a/b* and cut-out orientations, which affect the stress distributions and SCF in the perforated plates, the second example is an infinite isotropic plate, containing an inclined elliptical hole, subjected to uniform tension parallel to *x*-direction. The elliptical hole can have arbitrary orientation such that the major axis of the cut-out is directed at angle β with the *x*-direction Fig.2.
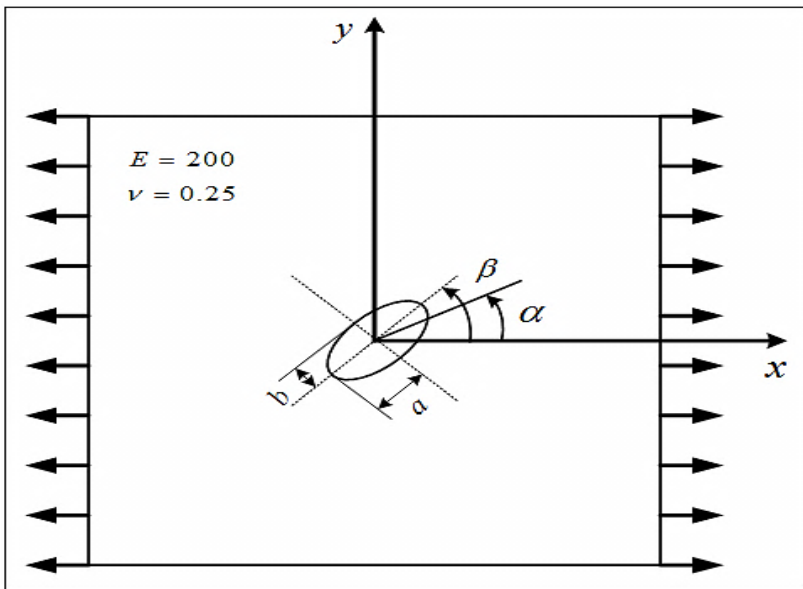
Fig. 2 Square isotropic plate with an inclined elliptical hole under tension

Since the plate is isotropic, the rotation of the elliptical hole and load angle has exactly the same effect on SCF (Rezaeepazhand, J. and M. Jafari 2010), consequently, the analytical solutions can be obtained using the Eq. (10). The size of the solution domain is selected to be the same as the square plate used in Example 1. For each plate, the varying parameters such as the elliptical orientations $\beta = 0°$, 30°, 45°, 60° and 90°, or the hole sizes *a/b*=1, 2, 3, 4, 5, 9,which affect the stress distributions and the SCFs in the perforated plates, are considered.

In order to compare the results found for different inclination angle β and for various aspect ratio *a/b*, the stress concentration coefficients, obtained by the

present element, are presented in Fig. 3. As shown in Fig. 3, it can be seen that the SCF is affected considerably by the inclination angle β. It is observed that, for different aspect ratio of a/b, the value of the SCF increases with the increasing of the inclination angle β. Also, the SCFs increase with the increasing of the aspect ratio a/b.
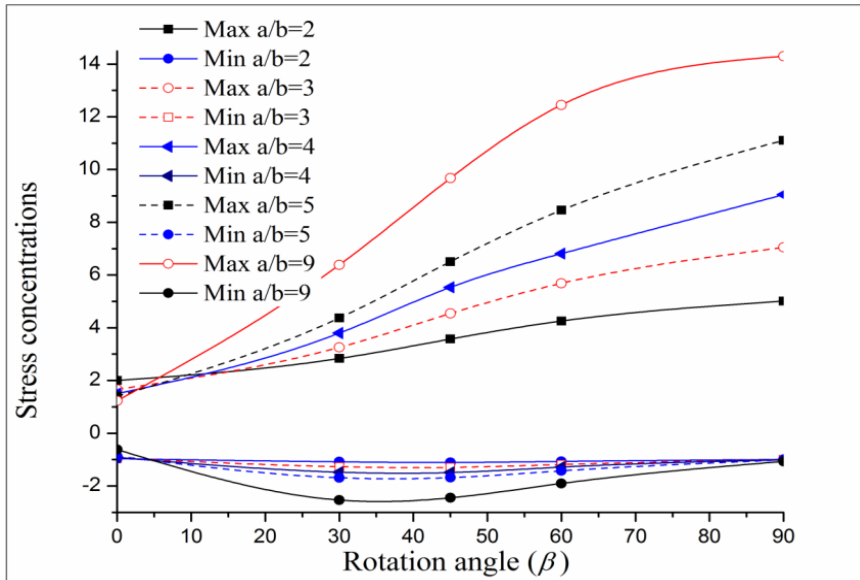
Fig. 3 Variation of SCFs for different rotation angles of the elliptical hole

For the maximum compressive stress, we can see that, for various aspect ratio a/b, the SCFs are not affected too much by the changes in β and the SCFs are quite close. It is noticed that, the aspect ratio $a/b=9$ gives a maximum compressive stress equal to 2.53.

3.3 *Infinite Anisotropic Plate with a Centered Elliptical Hole*

The third numerical experiment is used to assess the ability of the present element for analyzing the stress concentration in cross-ply laminated plates containing circular and elliptical holes. In this example, isotropic, Glass-Epoxy ($E_1 = 47.4\ MPa$, $E_2 = 16.2\ MPa$, $G_{12} = 7.0\ MPa$ and $v_{12} = 0.26$) and Graphite-Epoxy ($E_1 = 181.0\ MPa$, $E_2 = 10.3\ MPa$, $G_{12} = 7.17\ MPa$ and $v_{12} = 0.28$) composite laminated are considered. The stacking sequence of the laminates is [0°/90°]s. The laminates are loaded parallel to the y-direction. The size of the solution domain is selected to be the same as the square plate used in Example 1.

For different ratio *a/b*=1, 2, 3, 4, and 5, the maximum SCFs obtained by the present element are presented in Fig.4.
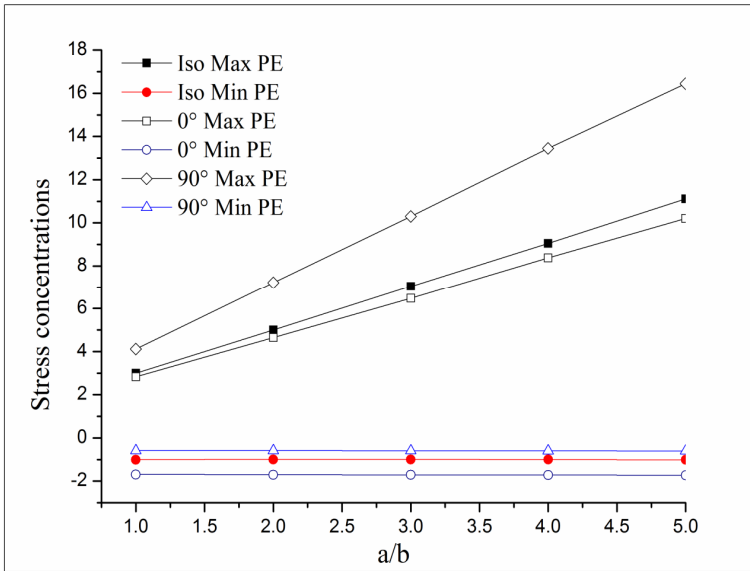
(a)
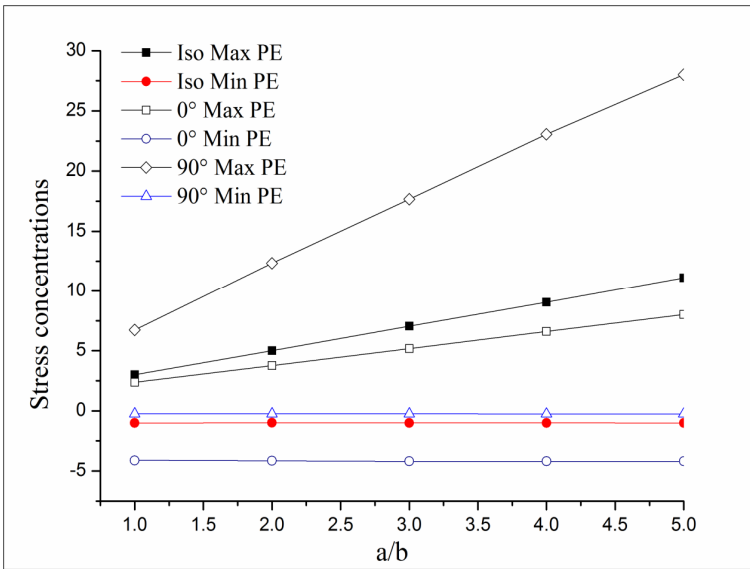
(b)

Fig. 4 Effect of *a/b* ratio on SCFs in (a) Glass-epoxy (b) Graphite-epoxy plates $\beta = 0°$ under *y*-axis tension

As presented in Figs. 4, the results demonstrated that the SCF is affected considerably by the ratio *a/b*. The obtained results showed that the SCF increased linearly with the increase of the ellipse major axis and minor axis ratio *a/b*. For the maximum compressive stress, we can see also that, for various aspect ratio *a/b*, the SCFs are not affected too much by the changes in *a/b*. From another hand, as observed in Fig.4, for $\theta=90°$, the maximum values for Glass-epoxy are found smaller in comparison to those obtained for Graphite-epoxy laminate.

4   Conclusion

In this paper, a recently developed quadrilateral plate element [13] is used to evaluate the stress distribution in perforated isotropic and laminated composite plates with circular or elliptical cutouts. Numerical and analytical studies are conducted to investigate the effects of variation in cutout shape (circular and elliptical holes), cutout sizes (*a/b*) and hole orientation on the values of SCF in flat plate under uniaxial tension load. The results presented herein indicated that the SCF of perforated plates can be significantly changed using proper cutout shape (circular or elliptical hole), cutout sizes and hole orientation. It is observed that, the SCFs increases with the increasing of the ratio *a/b* and the inclination angle. For laminated composite plates, the SCFs in Glass-epoxy laminate are less than the SCFs in Graphite-epoxy laminated. As a result of this investigation, we can see the all the obtained numerical results showed that the present element can effectively capture the dramatic variation of stress around elliptical hole. Hence, the present element can be employed to effectively evaluate the stress SCF associated with elliptical holes.

References

Wang, H., Qin, Q.-H.: A new special element for stress concentration analysis of a plate with elliptical holes. Acta Mechanica 223(6), 1323–1340 (2012)

Louhghalam, A., et al.: Analysis of stress concentrations in plates with rectangular openings by a combined conformal mapping–finite element approach. International Journal of Solids and Structures 48(13), 1991–2004 (2011)

Muskhelishvili, N.I.: Some basic problems of the mathematical theory of elasticity. Springer (1977)

Sharma, D.S.: Stress Concentration around Circular/Elliptical/Triangular Cutouts in Infinite Composite Plate. Engineering Letters 20(1) (2012)

Nishioka, T., Atluri, S.: Stress analysis of holes in angle-ply laminates: an efficient assumed stress "special-hole-element" approach and a simple estimation method. Computers & Structures 15(2), 135–147 (1982)

Piltner, R.: Special finite elements with holes and internal cracks. International Journal for Numerical Methods in Engineering 21(8), 1471–1485 (1985)

Chen, H.C.: Special finite elements including stress concentration effects of a hole. Finite Elements in Analysis and Design 13(4), 249–258 (1993)

Pan, E., et al.: Stress analyses around holes in composite laminates using boundary element method. Engineering Analysis with Boundary Elements 25(1), 31–40 (2001)

Khechai, A., Tati, A., Guettala, A.: Finite element analysis of stress concentrations and failure criteria in composite plates with circular holes. Frontiers of Mechanical Engineering 9(3), 281–294 (2014)

Tati, A., Abibsi, A.: Un element fini pour la flexion et le flambage des plaques minces stratifiees en materiaux composites. Revue Des Composites Et Des Materiaux Avances 17(3), 279 (2007)

Forest, S., et al.: Mécanique des milieux continus. Cours de l'Ecole des Mines de Paris (3121), p. 2005 (2004)

Rezaeepazhand, J., Jafari, M.: Stress concentration in metallic plates with special shaped cutout. International Journal of Mechanical Sciences 52(1), 96–102 (2010)

Water Absorption and Stress Relaxation Behavior of PP/Date Palm Fiber Composite Materials

Sonia Boukettaya[1], Fahad Almaskari[2], Ahmed Abdala[2],
Ahmad Alawar[3], Hachmi Ben Daly[1], and Adel Hammami[4]

[1] LMS-ENISo, B.P. 264, 4023 Sousse Erriadh, Tunisie
 boukettaya_sonia@yahoo.fr, hachmi.bdaly@gmail.com
[2] The Petroleum Institute, P.O. Box 2533, Abu Dhabi, UAE
 {aabdala,falmaskari}@pi.ac.ae
[3] Polytechnic Abu Dhabi, P.O. Box 111499, Abu Dhabi, UAE
 ahmad.alawar@iat.ac.ae
[4] Solutions composites, Zone Industrielle, Hammam Zriba, Tunisia
 contact@solutions-composites.com

Abstract. In this study, the effects of the fiber loading, the coupling agent content and the amount of the absorbed humidity on the stress relaxation behavior of the PP/date palm fibers composite material were characterized, using a dynamic mechanical analyzer (DMA). The obtained results have indicated that the rate of stress relaxation decreases as the date palm fiber content increases. It is therefore suggested that the presence of the natural fibers in composite materials do not help polymer molecules to recover their original configurations, generally present in the polymer matrix before any mechanical loading. The use of the coupling agent was found to also reduce such rate, due to the improvement of the quality of adhesion between the reinforcing phase and the polymer molecules. By increasing the amount of the absorbed humidity, a higher relaxation rate was obtained. This is an expected result since the presence of water molecules in composite materials encourages the relative movement (sliding) of polymer molecules, reducing therefore their recovering time and these can regain their initial configuration at a higher rate.

Keywords: stress relaxation, polypropylene, date palm fiber, composite, coupling agent.

1   Introduction

In the recent years, a great interest has been given for the development of natural fibers, as a reinforcing phase in composite materials. It has been well recognized that these fibers offer interesting characteristics such as biodegradability and low densities, which allow a reduction of the weight of the natural fiber composite

materials. However, the main disadvantage of these fibers is their hydrophilic character (Saheb 1999), which could greatly affect their compatibility with some hydrophobic thermoplastic matrix and, consequently, leads to a significant decrease in the mechanical properties of natural fibers composite materials (Espert et al. 2002, Ashori and Sheshmani. 2010). Creep and stress relaxation are the two widely accepted test methods for the prediction of the long-term mechanical performance of the composites. The stress relaxation behavior determines the dimensional stability of load-bearing structures and the retention of clamping force for bolts fastened to composites (Mackenzie and Scanlan. 1984).The measurement of the stress relaxation is a very important aspect, since it represents the basic time-dependent response of the material. The nature of the relaxation curves depends on many parameters and changes especially during the final stages. George et al. have studied the stress relaxation behavior of short pineapple-reinforced polyethylene and found that the rate of relaxation decreases with fiber content and its amount decreases with strain level (George et al. 1998). Geethamma et al. have studied the relaxation response of short-coir-fiber-reinforced natural rubber composite and concluded that the rate of stress relaxation can be influenced by the strain level, fiber loading, and fiber orientation influence in the composite materials. At a high strain rate, the rate of stress relaxation was found to be low because of the major contribution of elastic components in the system. The rate of relaxation was highest for the natural rubber compound, and it decreased with the coir fiber loading increase (Geethamma et al. 2004). Mirzaei et al. have analyzed the stress relaxation performance of HDPE based injection molded composites containing four types of natural fibers (i.e., wood flour, rice hulls, newsprint, and kenaf fiber) at 25 and 50 wt% contents. The results revealed that incorporating more filler results in less relaxation and also decreases relaxation rate. Based on the findings of this study, the composite containing 50% wood flour without compatibilizer exhibited the best stress-relaxation performance (Mirzaei et al. 2011). Pothan et al. have investigated the effect of the fiber loading and the chemical treatment on the stress relaxation behavior of banana fiber reinforced polyester composites. It was observed that the rate of stress relaxation was found to be at a maximum during the initial stages. The incorporation of the banana fibers in the polyester matrix reduces this rate and the highest reduction is reached with the highest fiber loading (Pothan et al. 2004). Similar results have been widely reported in the literature (Jacob et al. 2006). However, reverse effects of natural fibers on the stress relaxation behavior have been obtained in the studies of Bhattacharyya et al. The authors have noted that the increase of fiber volume fraction increases the rate of stress relaxation. Such effect can be attributed to the lower contribution of the fibers in stress transfer. In this case, instead of acting as reinforcements, the natural fibers act as flaws, reducing therefore the mechanical properties of the composite material (Bhattacharyya et al. 2006).

As reported by Pothan et al., the application of chemical treatment on natural fibers and/or the addition of coupling agents lead generally to a decrease of the rate of stress relaxation. Such results can be associated with the improved fiber–matrix adhesion due to better stress transfer and interlocking between the fiber and

the matrix after such modifications (Pothan et al. 2004). Wang et al. have investigated the effects of fiber loading and chemical modification on the tensile and compressive stress relation behavior of wood flour/Polypropylene composite materials (Wang et al. 2011). It was found that the optimal loading level of a coupling agent for stress relaxation varied with the type of coupling agents and wood content. For the considered experimental conditions in this study, the optimal loading level for silane was 1.5% at 50% wood content and 2% at 60% wood content. The optimal loading level for MAPP was 2% at both wood contents.

The effect of water ageing on stress relaxation of PP composite materials has not been vastly detailed in the literature Sreekala et al have noted that the water aging increased the relaxation of such materials. Such result may be due to the changes in the interface properties attained on ageing (Sreekala et al. 2001).

The objective of this study is to assess flexural stress relaxation behavior of polypropylene/ Date palm fiber composites, consisting of different fiber and coupling agent contents, before and after physical ageing under various water immersion conditions.

2 Materials and Experiments

2.1 Materials

Both a commercially available grade of isotactic polypropylene (PP) and natural date palm fibers were used in this study. The extraction procedure of these fibers is summarized in the reference (Alawar et al. 2009). Date palm fiber/PP granulates were processed by extrusion mixing, using a twin-screw extruder. The amount of the date palm fibers was 25 wt% and 50 wt%. Two amounts of maleic anhydride grafted polypropylene (MAPP) were considered is this study (i.e. 5 wt% and 10 wt%). The obtained granulates were then injected to obtain short fiber composite plate. For convenience, samples molded without the use of MAPP will be referred as PP-25DPF. The others will be referred as PP-25DPF-5MA, PP-50DPF-5MA and PP-25DPF-10MA.

2.2 Water Absorption

The hygrothermal tests were performed by the immersion of all composite materials in distilled water during one month. Two different immersion temperatures are considered, i.e. 25°C and 65° C. The immersed samples were periodically taken out from the water and then weighed using an electronic microbalance (with a precision of 0.0001 g).

2.3 Mechanical Behaviors

Stress relaxation tests were performed using a dynamic mechanical analyzer (DMA). The measurements were carried out in a three point flexural mode using

rectangular specimens of dimensions 60mm x 10mm x 1mm. A controlled strain of 0.5% of the maximum strain, determined from a static flexural test, was applied during 2 hours. Both dry and aged specimens were considered for such mechanical characterization.

3 Results

3.1 Effect of Fiber Loading

Figure 1 shows the variation of the relative stress during the relaxation process (σ_t/σ_0) as a function of the time (represented in a logarithmic scale), for different fiber contents (i.e. 0 wt% , 25 wt% and 50 wt%). In this figure, σ_t represents the stress at a particular time and σ_0 in the initial stress.

As can be seen, the plot for the neat PP is almost linear. Similar results have been reported in the literature (Flink and Stenberg, 1990). It was suggested that for the unfilled materials, only one relaxation stress mechanism can take place, due to the rearrangement of the polymer molecules to regain their original configurations. By introducing date palm fibers, Figure 1, the relaxation process becomes much more complicated and can be divided into two steps. Different interpretations have been proposed in the open literature to explain such mechanism. According to Kar et al. (Kar et al. 2008), the stress relaxation behavior can be controlled by two important mechanisms: physical and chemical. The physical stress relaxation effect consists in a molecular rearrangement, that is, the molecules return to their most stable conformation. Such mechanism happens due to the breakage of the weak secondary Van der Waal's forces, which constitute the intermolecular interactions. As a result, internal relaxation occurs, and so the force (and stress) needed to sustain the constant strain decreases with time (Geethamma et al. 2004). The chemical stress relaxation mechanism is produced by chain scission or cross link formation.

Accordingly, each plot shown in figure 1 for the composites materials has been represented by two straight lines. The slopes of these lines and their cross times are summarized in Table 1. These slopes are proportional to the rate of stress relaxation. As can be seen, and for all composite materials considered in this study, the rate of relaxation is more important at the second step of solicitation. This result confirms those reported in the literature since it is suspected that during the first step, we are in the presence of the damage of both the intermolecular interactions between the polymer molecules and the quality of the interface area between the fibers and the matrix. As the amount of such damage becomes significant, the polymer molecules will be free, resulting in an easier recovery and in an increase of the stress relaxation rate.
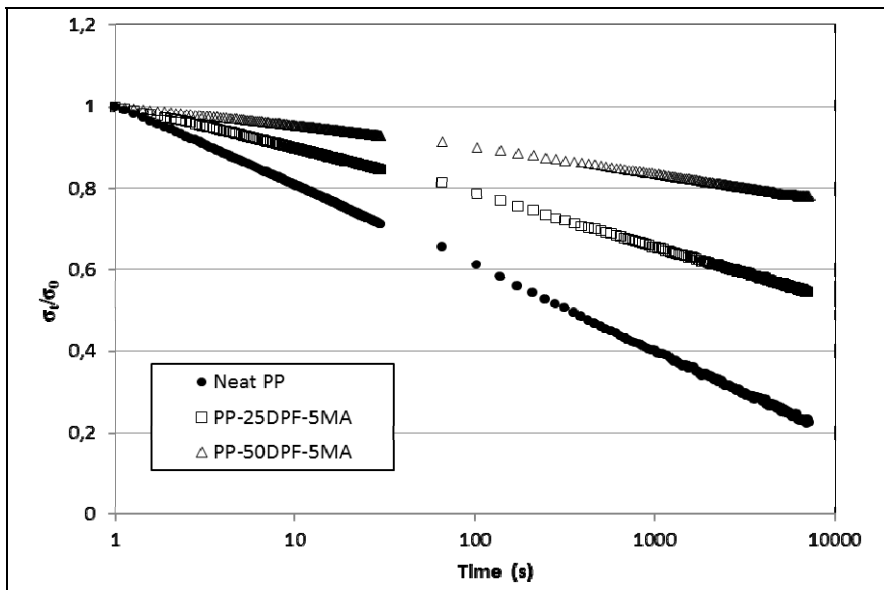
Fig. 1 Variation of σ_t/σ_0 with the time of the neat PP and PP/DPF composites

By comparing the results shown in table 1, it appears that the increase of the fiber content decreases the rate of the stress relaxation. This is due to the fact that as the fiber content increases, the relaxation process of the polymer molecules becomes more and more hindered, decreasing therefore their relaxation rate. Concerning the cross time, it tends to increase with the amount of natural fibers. This result supports our previous suggestions and clearly indicates that the introduction of the reinforcing phase in the composite materials delays the damage process (step 1), and this later should take much more time to be achieved. As a result, the cross time should increase.

Table 1 Characteristics of the stress relaxation curves of neat PP and its DPF composites

Material	Slope		Intercept		Cross time (s)
	I	II	I	II	
Neat PP	0.2047	-	1.0116	-	-
PP-25DPF-5MA	0.1127	0.1357	1.0047	1.0479	158.5
PP-50DPF-5MA	0.0506	0.0667	1.0024	1.0356	175.0

3.2 Effect of Coupling Agent Content

Figure 2 represents the effect of the coupling agent content on the stress relaxation behavior of PP reinforced with 25% by weight of date palm fibers. The main

characteristics (slopes and cross times) of the curves shown in this figure are re-
ported in the Table 2.
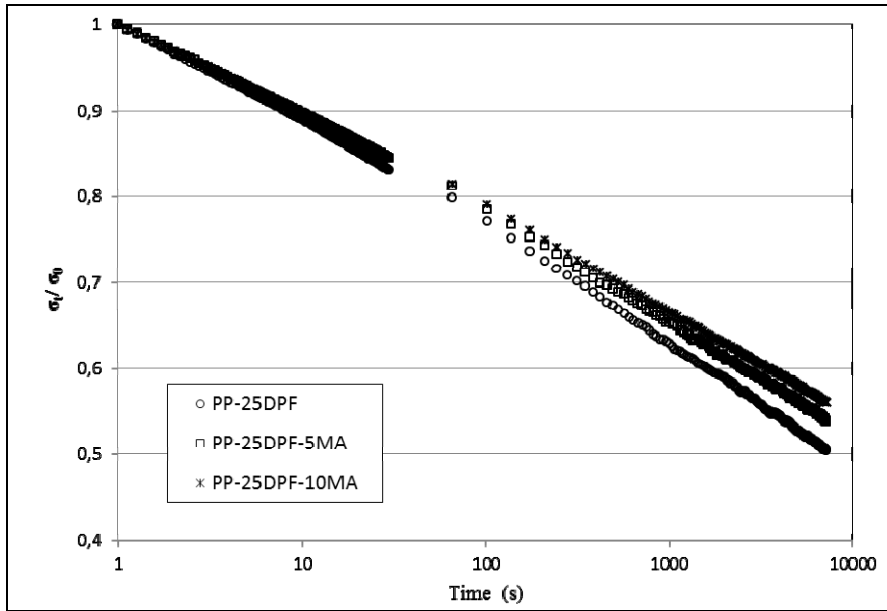
Fig. 2 Variation of σ_t/σ_0 with the time of untreated and treated PP reinforced with 25
wt% DPF composite materials

As can be seen, the increase of the amount of the coupling agent has increased
the cross time and decreased the stress relaxation rate. This is an expected result
since the increase of the amount of the coupling agent should improve the adhe-
sion between the fiber and the matrix at the interface area of the composite materi-
al. Hence, the damage in this area should be reduced during mechanical loadings.
This in turn should reduce the stress relaxation rate of the polymer molecules in
this area (Wang et al. 2011). As a result, the whole relaxation process (at the ma-
trix and at the interface zone) of the composite material should be reduced.

3.3   *Effect of Water Ageing*

It is well known that the presence of humidity in composite materials should affect
their mechanical properties. For dry composites, it is generally accepted that these
properties involve an ability for the chain molecules present in the matrix to slip
past each other and it is well recognized that the more difficult is the slippage of
the polymer molecules, the greater well be the mechanical performance. If the
humidity or water, a rather reactive agent, reaches the interior of the composite
matrix, it can react with the polymer chains, interfering with the intermolecular

interaction, dissecting the branches of these chains. This will result in a great free-
dom of polymer molecules to slide over each other, and the water molecules can
even lubricate the sliding motion of these molecules. Consequently, the mechani-
cal properties of the polymer composites should be reduced.

Figure 3 shows the effects of the immersion temperature in distilled water on
the stress relaxation behavior of the PP-25DPF-5MA composite material. The
main characteristics of the plots shown in this figure are summarized in Table 2.
Two main conclusions can be drawn from this table: (i) the cross time is reduced
and (ii) the rate of the stress relaxation is increased as the amount of the absorbed
humidity increases. Similar results have been reported by Sreekala et al (Sreekala
et al. 2011). In this study, it is believed that the stress relaxation becomes much
shorter and easier due to a combined effect of a damage at the interface area be-
tween the polymer and the natural fibers by the increase of the amount of the ab-
sorbed humidity, and the sliding process discussed above. Results shown in table 2
also indicate that relaxation process is longer as the coupling agent content in-
creases. This confirms the role of such agent in the composite material, improving
the adhesion of the matrix and the fibers and reducing its eventual damage during
a subsequent mechanical loading.
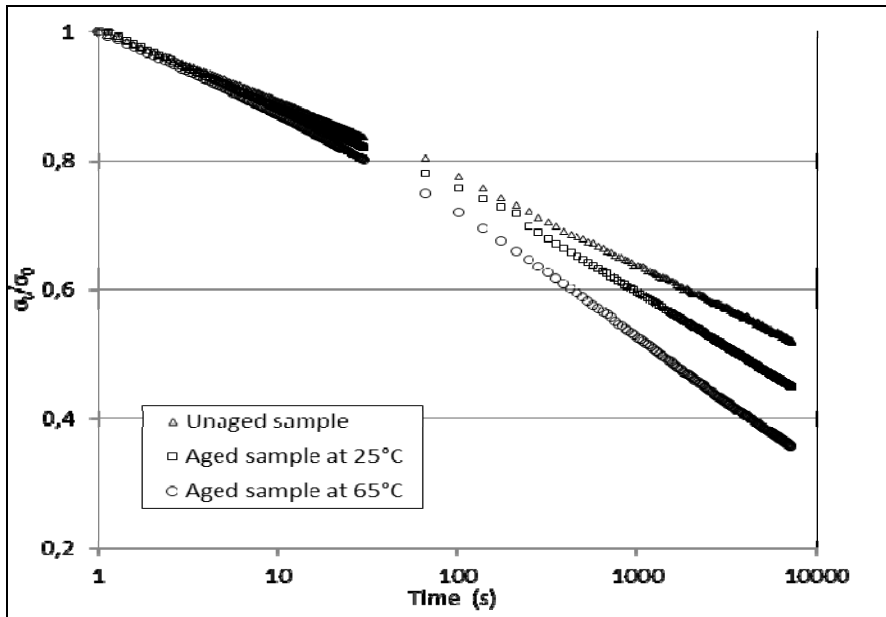
Fig. 3 Variation of σ_t/σ_0 with the time of unaged and aged PP-25 DPF-5MA composite
materials

A comparison of the effects of the coupling agent content before and after wa-
ter ageing is shown in Table 2. It is clear from these values that the stress relaxa-
tion behavior of the PP-25DPF-10MA composite is less affected by the water
absorption process, as compared to the one observed for the PP-25DPF material.

Such result clearly indicates that the increase of the amount of the coupling agent in the composite materials improves the quality of fiber/matrix adhesion, reducing therefore both the water absorption and the relaxation behaviors of these materials

Table 2 Characteristics of the stress relaxation curves of treated and untreated PP/ 25 DPF composite before and after water ageing at different temperatures

Material	Immersion temperature (°C)	Slope		Intercept		Cross time (s)
		I	II	I	II	
PP-25DPF	Dry	0.1173	0.1449	1.0049	1.0617	148.0
	25	0.1290	0.1785	1.0060	1.1120	138.5
	65	0.1520	0.2085	1.0112	1.1260	63.1
PP-25DPF-5MA	Dry	0.1127	0.1357	1.0047	1.0479	158.5
	25	0.1235	0.1700	1.0050	1.1060	142.0
	65	0.1403	0.1978	1.0101	1.1233	70.8
PP-25DPF-10 MA	Dry	0.1058	0.1242	1.0044	1.0355	195.0
	25	0.1127	0.1472	1.0060	1.0793	144.5
	65	0.1357	0.1863	1.0104	1.1072	81.8

4 Conclusion

The effects of the fiber loading, the coupling agent content and the amount of the absorbed humidity on the stress relaxation behavior of the PP reinforced date palm fiber composite materials have been investigated in this study. The main results can be summarized as follows:

- The rate of the stress relaxation decreases as the amount of the fiber increases. This was attributed to the fact that that the presence of the natural fibers in composite materials do not help polymer molecules to recover their original configurations.
- As the coupling agent content increases, the rate of stress relaxation decreases, due to the improvement of the interfacial adhesion between the PP matrix and the natural fibers.
- The water ageing leads to an increase of the rate of stress relaxation. Basically, the presence of water molecules in the composite materials increases the free volume between the polymer molecules, encouraging therefore their recover to their original configurations.

References

Alawar, A., Hamed, A.M., Al-Kaabi, K.: Characterization of treated date palm tree fiber as composite reinforcement. Composites Part B 40, 601–606 (2009)

Ashori, A., Sheshmani, S.: Hybrid composites made from recycled materials: Moisture absorption and thickness swelling behavior. Biores. Technol. 101, 4717–4720 (2010)

Bhattacharyya, D., Manikath, J., Jayaraman, K.: Stress relaxation of wood fiber–thermoplastic composites. J. Appl. Polym. Sci. 102, 401–407 (2006)

Espert, A., Vilaplana, F., Karlsson, S.: Comparison of water absorption in natural cellulosic fibres from wood and one-year crops in polypropylene composites and its influence on their mechanical properties. Compos. Part A 35, 1267–1276 (2002)

Flink, P., Stenberg, B.: An indirect method which ranks the adhesion in natural rubber filled with different types of cellulose fibres by plots of E (t)/Et= 0 versus log t. British Polymer J. 22, 193 (1990)

Geethamma, V.G., Pothen, L.A., Rhao, B., Neelakantan, N.R., Thomas, S.: Tensile stress relaxation of short-coir fiber-reinforced natural rubber composites. J. Appl. Polym. Sci. 94, 96–104 (2004)

George, J., Sreekala, M.S., Thomas, S., Bhagawan, S.S., Neelakantan, N.R.: Stress relaxation behavior of short pineapple fiber reinforced polyethylene composites. J. Reinf. Plast. Compos. 17, 651–772 (1998)

Jacob, M., Jose, S., Thomas, S., Varughese, K.T.: Stress Relaxation and Thermal Analysis of Hybrid Biofiber Reinforced Rubber biocomposites. J. Reinf. Plast. Compos. 25, 1903–1917 (2006)

Kar, K.K., Sharma, S.D., Kumar, P., Mohanty, A.: Stress Relaxation Behavior of Glass Fiber Reinforced Polyester Composites Prepared by the Newly Proposed Rubber Pressure Molding. Polym. Compos. 29, 1077–1097 (2008)

MacKenzie, C.I., Scanlan, J.: Stress relaxation in carbon-black-filled rubber vulcanizates at moderate strains. Polymer 25, 559–568 (1984)

Mirzaei, B., Tajvidi, M., Falk, R.H., Felton, C.: Stress-relaxation behavior of lignocellulosic high-density polyethlene composites. J. Reinf. Plast. Compos. 30, 875–881 (2011)

Pothan, L.A., Neelakantan, N.R., Rao, B., Thomas, S.: Stress Relaxation Behavior of Banana Fiber-Reinforced Polyester Composites. J. Reinf. Plast. Compos. 23, 152–165 (2004)

Saheb, D.N., Jog, J.P.: Natural Fiber Polymer Composites: A Review. Adv. Polym. Technol. 18, 351–363 (1999)

Sreekala, M.S., Kumaran, M.G., Joseph, R., Thomas, S.: Stress-relaxation behavior in composites based on short oil-palm fibres and phenol formaldehyde resin. Compos. Sci. Technol. 61, 1175–1188 (2011)

Wang, Y., Cao, J., Zhu, L.: Stress Relaxation of Wood Flour/Polypropylene Composites at Room Temperature. Wood and Fiber Science 43, 262–270 (2011)

Part III
Robotics and Mechatronics

Multi-axis Robotic Arm Control Using EC 40 Brushless DC Motor and Technosoft Motion Libraries (TML)

Jabli Tarek, Zaoui Chiheb, and Maalej Aref

Laboratory of Electromechanical Systems of University of Sfax, Tunisia
`jablitarek@hotmail.com, zaoui_chiheb@yahoo.fr,`
`aref_maalej@enis.rnu.tn`

Abstract. The aim of this paper is to present a method to control the Adam robot which is a platform provided by two arms designed to bring out the role of the arms and the trunk during the compensation of external disturbances. This method is based on using the brushless DC motor EC 40 and the IPOS4808 driver; a new member of the iPOS family of Technosoft intelligent drives. The programming of the drives is done with TML (Technosoft Motion Language); a high-level language that can program complex motion profiles for the intelligent drive/motor to execute independently. The required movements and accelerations of the arms parts necessary to maintain the stability of the robot are determined using the inverse dynamic modal .This paper shows also the way to implement a network between the drives to simplify the communication between then and the PC.

Keywords: Robotic, Control, Brushless, Driver, TML.

1   Introduction

There are several types of actuators in robotic arms which can be classified on two types: the synchronous Actuator (Brushless, DCmotor, Stepper and Brushed DC motor) and the asynchronous Actuator (Traction motor, AC servo motor, pneumatic and hydraulic) (Vinod 2013). Concerning the robot Adam, It is motorized with a brushless DC motor EC 40. This motor is used on different robots like the Hubo robot manufactured by the Korea Advanced Institute of Science and Technology, also we found this motor installed on the technology firm Xi'an Chaoren Robots. Many surgical manipulators are also equipped with this motor. The robot Adam contains two arms and each one had three motors EC 40 and each motor is controlled by an IPOS 4808. The TML CAN network is implemented to connect the drivers together and also to connect them with the host (the PC).

2   Presentation of ADAM Robot

The considered robot named Adam is a 9 degree of freedom. It was manufactured in the Electromechanical System Labotaory (LASEM). It weights 12 kg for a 48

cm height. It comprises a chest, two arms, two forearms and two pliers. The six motors EC 40 are mounted on the arms of the robot. The first step in our project was the creation of some typical simulation examples in different fields of robotics by using the VRML so that we create a virtual word showing the motion of the arms. The second step is to command this robot practically using the drives and TML libraries. This robot was designed to show the role of the arms in the compensation of an external force applied on the trunk.

Fig. 1 ADAM robot

3   Presentation of Adam Robot

The robot is initially stable and the external forces are applied to destabilize it. These perturbations are detected by means of a force sensor located at its recessed point. The goal is to maintain, at this point, the components of the effort torsor equal to zero and Fy equal to the weight of the robot. To maintain the stability of the biped robot submitted to external disturbances for a vertical posture, the approach was based on research of the motions to do, with instant compensation; the different parts of the trunk used for the stabilization and therefore deduce the needed compensation efforts for the stabilization of the robot (Zaoui et al. 2009).

   In what follows, the body Ci (i = 61, 71, 62, and 72) represents the pats of the two arms used to compensate the external disturbances. We start by writing the equations of the dynamics of each candidate's body mechanism in its clamping point.
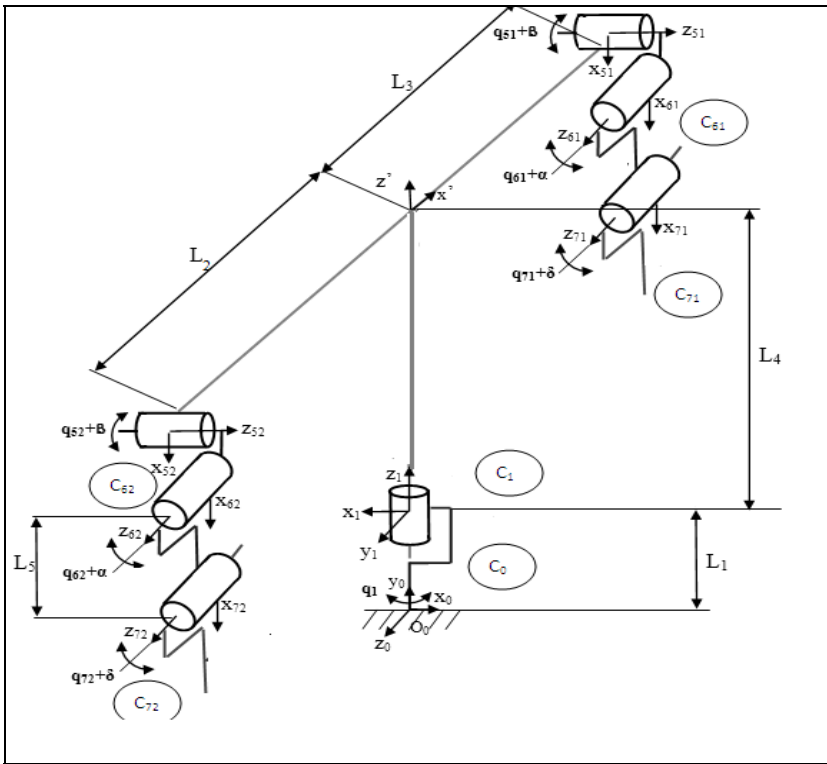
Fig. 2 Modelling of the robot ADAM

The dynamic equations of the upper part of the robot are developed using the Newton-Euler formulation. The efforts applied to the trunk located on point O0 are given by

$$\begin{cases} \vec{F}_0 = \sum_{i=0}^{1} m_i(\vec{\gamma}_i - \vec{g}) + \sum_{i=6}^{7}\sum_{j=1}^{2} m_{ij}(\vec{\gamma}_{Gij} - \vec{g}) - \sum_{i=0}^{5}\vec{P}_i \\ \vec{M}_0 = \sum_{i=0}^{1}(\vec{h}(i,O_0) - \vec{M}(m_i\,\vec{g},O_0)) - \sum_{i=0}^{5}\vec{M}(\vec{P}_i,O_0) + \sum_{i=6}^{7}\sum_{j=1}^{2}[(\vec{h}(ij,O_0) - \vec{M}(m_{ij}\,\vec{g},O_0)] \end{cases} \quad (1)$$

After the elimination effort in the connections using essentially the mutual actions principle, we can write the following system of equations:

The system of equations (1) can be put in the following form:

$$\begin{bmatrix} \ddot{q}_{51} \\ \ddot{q}_{61} \\ \ddot{q}_{71} \\ \ddot{q}_{52} \\ \ddot{q}_{62} \\ \ddot{q}_{72} \end{bmatrix} = \begin{bmatrix} g_1(q_1,...q_6,\dot{q}_1,...\dot{q}_6,L_{ge},L_{in},F_x,F_y,F_z,M_x,M_y,M_z,P_{0x},P_{0y},P_{0z},....,P_{5x},P_{5y},P_{5z}) \\ . \\ . \\ . \\ . \\ g_6(q_1,...q_6,\dot{q}_1,...\dot{q}_6,L_{ge},L_{in},F_x,F_y,F_z,M_x,M_y,M_z,P_{0x},P_{0y},P_{0z},....,P_{5x},P_{5y},P_{5z}) \end{bmatrix} \quad (2)$$

With:

• $\vec{h}(i, O_0)$: Derivation of element C_i angular momentum calculated at point O_0.

• $\vec{F_0} = [F_x, F_y, F_z]^T$ and $\vec{M_0} = [M_x, M_y, M_z]^T$: Efforts exerted by the frame on C_0 at point O_0.

• $\vec{P_i} = [P_{ix}, P_{iy}, P_{iz}]^T_{(i=0..5)}$: External forces applied respectively to C_0, C_1, C_{61}, C_{71}, C_{62}, et C_{72} (C_0 and C_1 are the elements in contact with the external environment of the robot).

• $\vec{\gamma_i}$: Acceleration of the C_i elements.

4   EC 40 Motor Description

The brushless DC motor provided in this paper is the EC 40   40 mm, 120 Watt from Maxon motors. The order number of the motor is 118896. The parameters used in the modeling are extracted from the datasheet of this motor with corresponding relevant parameters used. Find bellow in table 1 the major extracted parameters used for modeling task.

Table 1 EC 40 parameters

Parameters	Value
Nominal voltage	42 V
No load speed	10400 rpm
No load current	258 mA
Nominal speed	9290 rpm
Starting current	33.5 A
Max. efficiency	84 %
Terminal resistance phase to phase	1.25 Ω
Terminal inductance phase to phase	0.319 mH

The mathematical model of the EC 40 motor is modeled on the parameters from table 1. This is illustrated bellow:

$$G(s) = \frac{\frac{1}{K_e}}{\tau_e * \tau_m * s^2 + \tau_m * s + 1} \tag{3}$$

With: $\tau_m = \frac{3*J}{K_e^2}$

ke is the phase value of the EMF (voltage) constant; also there is a relationship between ke and kt ; using the electrical power (left hand side) and mechanical power (right hand side)equations; that is :

$$\tau_m = \frac{3RJ}{K_e K_t}$$

(4)

Therefore G(s) becomes:

$$G(s) = \frac{13.11}{1.45 \times 10^{-6} \times s^2 + 0.0171 \times s + 1}$$

(5)

5   Command of the EC 40 by the IPOS 4808 Driver

The iPOS4808 is part of a family of fully digital intelligent servo drives, based on the latest DSP technology and they offer unprecedented drive performance combined with an embedded motion controller. It is   suitable for control of brushless DC, brushless AC (vector control), DC brushed motors and step motors, the iPOS4808 drives accept as position feedback incremental encoders (quadrature or sine/cosine) and linear Halls signals (IPOS 4808 BX CAN, Technical reference, Technosoft 2013).

All drives perform position, speed or torque control and work in single, multi-axis or stand-alone configurations. Thanks to the embedded motion controller, the iPOS4808 drives combine controller, drive and PLC functionality in a single compact unit and are capable to execute complex motions without requiring intervention of an external motion controller. Using the high-level Technosoft Motion Language (TML) the following operations can be executed directly at drive level
 • Setting various motion modes (profiles, PVT, PT, electronic gearing1 or camming1, etc.).

 • Changing the motion modes and/or the motion parameters.
 • Executing homing sequences.
 • Controlling the program flow through TML interrupts generated on pre-defined or programmable conditions (protections triggered, transitions on limit switch or capture inputs, etc.).
• Waits for programmed events to occur.
• Performing data transfers between axes.
• Controlling motion of an axis from another one via motion commands sent between axes.

The brushless motor is controlled using Hall sensors for commutation. It works with rectangular currents and trapezoidal BEMF voltages. Scaling factors take into account the transmission ratio between motor and load.
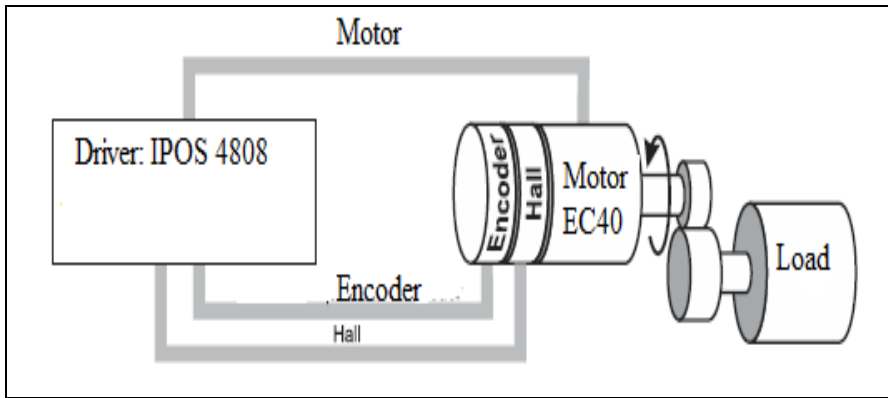
Fig. 3 Brushless motor commanded by IPOS4804

The driver IPOS 4808 works with parameters and variables represented in the drive internal units (IU). These correspond to various signal types: position, speed, current, voltage, etc. Each type of signal has its own internal representation in IU and a specific scaling factor.
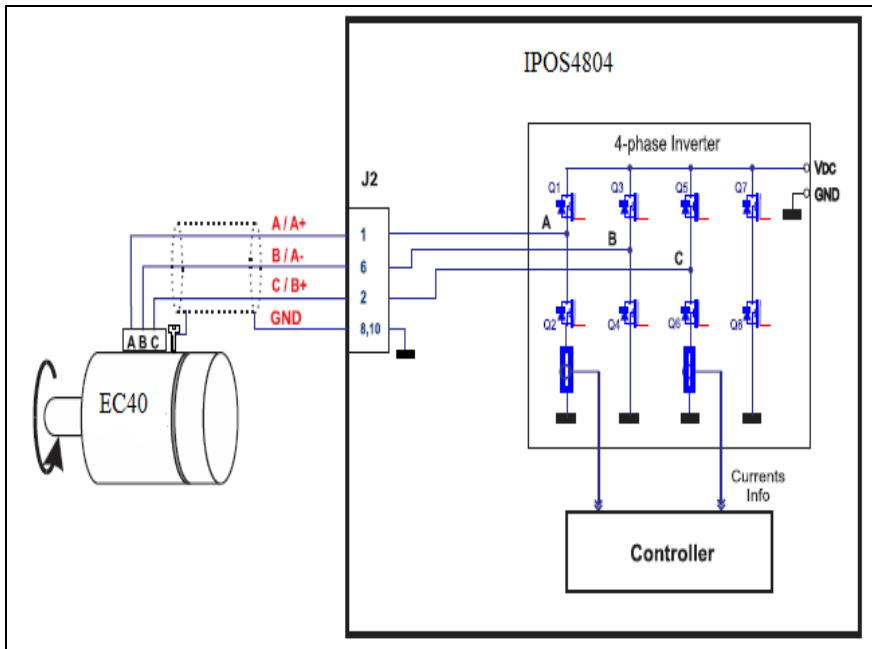
Fig. 4 EC40 connection

6   Programming the IPOS 4808 Driver by the Technosoft Motion Libraries (TML)

The Technosoft Motion Language (TML) is a high-level language allowing to:

 • Setup a drive built with Motion Chip II for a given application
 • Program and execute motion sequences
 •Describe the application configuration (as motor and sensors type)
 • Select specific operation settings (as motor start mode, PWM mode, sampling rates, etc.)
• Setup the controllers' parameters (current, speed, position), etc.
• Due to a powerful instruction set, the motion programming in TML is quick and easy even for complex motion applications.

6.1   CAN Connection

In multiple-axis configurations, each axis (drive) needs to be identified through a unique number the axis ID. This is a number between 1 and 255. The axis ID is initially set at power on by reading the Motion Chip II analogue input lines ADCIN10 to ADCIN14, as follows:

 •Axis ID = 255 if all the analogue inputs ADCIN10 to ADCIN14 are high;
 •Axis ID = 1 to 31, if at least one of the ADCIN10 to ADCIN14 inputs is low
   The CAN network requires a 120-Ohm terminator. Apart from the Axis ID, each drive has also a group ID. The group ID represents a way to identify a group of drives, for a multicast transmission. Each drive can be programmed to be member of one or several of the 8 possible groups. When a TML command is sent to a group, all the axes members of this group, will receive the command.
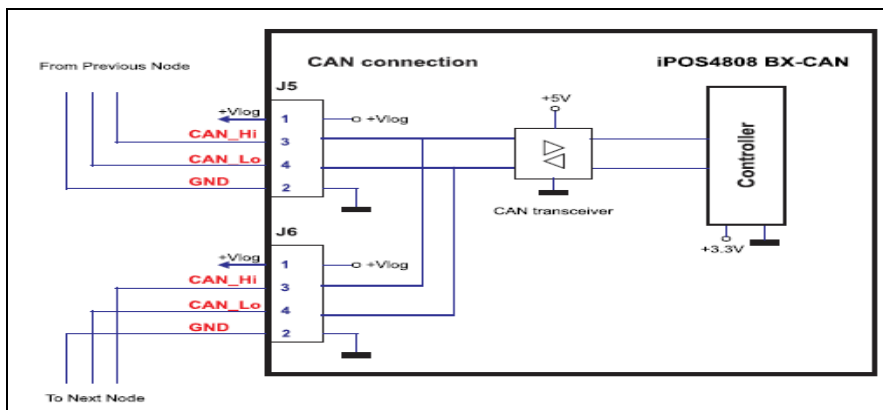
Fig. 5 CAN connection

6.2   Messages Types of CAN Bus Communication

The CAN-bus communication offers the possibility to work on a semi-duplex network like in a fullduplex one. The CAN controller automatically solves the conflicts that occur while two axes try to transmit messages in the same time. In an RS-485 network, such an event usually corrupts both messages, while in a CAN-bus the higher priority message always wins. The lower priority message is automatically sent after the transmission of the first message ends. Hence, in a CAN bus network, all the limitations mentioned for RS-485 are eliminated.

The CAN-bus communication protocol is based on two types of messages:

• Type A: Messages that don't require an answer (a return message). In this category enter for example the messages containing commands for parameter settings, commands that start or stop motion execution, etc.

• Type B: Messages that require an answer. In this category enter the messages containing commands that ask to return data, for example the value of TML parameters, registers, or variables
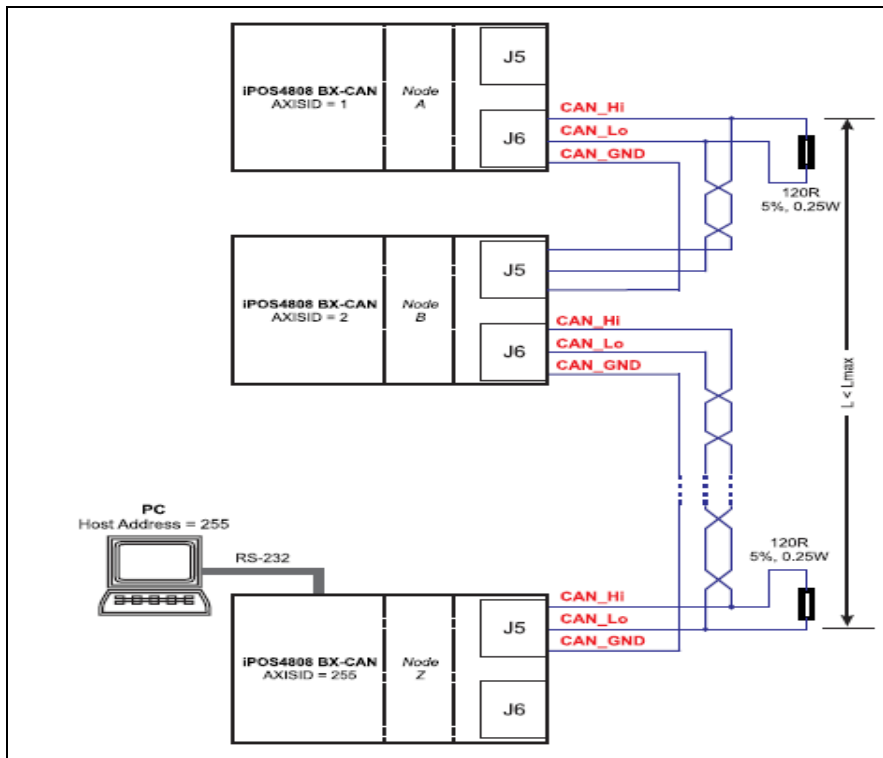
Fig. 6 Multiple axes CAN network

7   Conclusion

This paper showed the importance of the upper part in the stabilization of the robot in the presence of external disturbances. We used the TML and the driver IPOS4808 to set various motion applications, change the motion modes, execute homing sequences and also perform data transfers between axes. Due to a powerful instruction set, the motion programming in TML is quick and easy, even for complex motion applications. The result is a high-level motor-independent program which once conceived may be used in other applications, too.

References

Brown, W.: Brushless DC Motor Control Made Easy: Microchip Technology Inc. (2002)

Patel, V.K.S., Pandey, A.K.: Modeling and Simulation of Brushless DC Motor Using PWM Control Technique. International Journal of Engineering Research and Applications (IJERA) 3(3), 612–620 (2013)

Motion ship TML programming user manuel, Technosoft (2006)

IPOS 4808 BX CAN Intelligent Servo Drive for Step, DC, Brushless DC and AC Motors, Technical reference, Technosoft (2013)

John, O.: Oguntoyinbo pid control for brushless DC motor and robot trajectory planning and simulation with Matlab/Sumilink

Zaoui, C., Bruneau, O., Ouezdou, F., Maalej, A.: Simulation of the dynamic be-havior of a bipedal robot with trunk and arms subjected to 3D external distur-bances in a vertical posture, during walking and during object handling. Journal of Multibody-Dynamics (2009)

Sabourin, C., Bruneau, O., Buche, G.: Control strategy for the robust dynamic walk of a bi-ped robot. International Journal of Robotics Research 25, 843–860 (2006)

Ali, W., Zhang, Y., Akujuobi, C.M., Tolliver, C.L., Shieh, L.S.: DSP-based PID Controller Design for the PMDC Motor. International Journal of Modeling and Simulation 22(3) (2006) (in press)

Simulations of the Dynamic Behavior of the Robot ADAM with Trunk and Arms Subjected to 3D External Disturbances

Zaoui Chiheb, Jabli Tarek, and Maalej Aref

Laboratory of Electromechanical Systems of University of Sfax, Tunisia
zaoui_chiheb@yahoo.fr, jablitarek@hotmail.com,
aref_maalej@enis.rnu.tn

Abstract. This paper deals with an analytical approach based on the inverse dynamic model to maintain the stability of the ADAM robot in the presence of external disturbances. The stabilization is carried out with a trunk having 7 degrees of freedom. For a vertical posture of the robot, the arms of ADAM are used to compensate the external three-dimensional efforts applied to the robot. This study presents the simulation results of the dynamic behavior of the robot in the presence of external disturbances. During the simulation, this study enabled us to determine on-line the required movements and accelerations of the arms parts necessary to maintain the stability of the robot.

Keywords: Robot, Dynamic, Arms, Disturbances.

1   Introduction

When developing a useful humanoid robot, one of the main problems to be solved is the stability of bipedal robots. In more advanced robots: QRIO (Nagasaka et al. 2004), ASIMO (Sakagami et al. 2005), HRP-2 (Mike et al. 2006), KHR-3 (HUBO) (Woo et al. 2006), WABIAN-2 (Omer et al. 2005) and BHR-02 (Jie et al. 2006), stability control during walking is based on the well-known ZMP approach. In this context of biped stability, much research has focused on the importance of the upper part of the biped robots and on its utility during walking or during handling tasks. (Sabourin et al. 2006) developed the robustness of the dynamic walk of a biped robot subjected to disturbing external forces by using CMAC neural networks. The implementation of a neural network in the RABBIT robot made it possible for it to walk at a given speed and to compensate external disturbances applied to the robot. (Sentis and Khatib 2006) describe all the components of a behavior-oriented whole-body control framework, based on task prioritization. They establish three distinct control categories: constraints (contacts, joint limits, balancing), operational tasks, and postures. Based on this framework they have built a task-oriented behavior architecture which is now being implemented in the ASIMO robot. (Renner and Bhenke 2006) proposed a method to detect

instabilities that occur during omni-directional walking. The model takes the gait target vector into account. They estimate model parameters from a gait test sequence and detect deviations of the actual sensor readings from the model later on. (Zaoui et al. 2009) proposed a new approach based on the synergy between the dynamic motion of balancing masses and arms to reject large disturbances applied to the upper part of a bipedal robot. During simulation this study determined online, the required movements and accelerations of the robot's upper elements necessary to maintain the robot's stability. In this context, the objective of this work is to study the stability of the robot, subjected to an external disturbance. In this study, simulation tests are made on the trunk of ADAM.

This paper is broken down into sections as follows: in section 2, we introduce the modeling of the robot ADAM. The dynamics equations of the trunk are developed in the presence of external disturbing forces. Section 3 is dedicated to the simulation of the dynamic behavior of the ADAM's robot subjected to disturbing forces in a vertical posture of the robot. In section 4, to prepare the experimental validation of simulation results, the development of virtual interface for the robot ADAM is presented. Then, the simulations of the dynamic behaviour of the robot ADAM are presented using SimMechanic software. Finally conclusions and future developments of this work are presented.

2   Modeling of Adam's Robot

The robot is a simple original mechanism having 7 dofs: 7 rotational movements (Fig.1).

The element C_1 is connected by a rotational joint (R) to the body C_0. Each arm is connected to the body C_1 and has three degrees of freedom, 2 rotary joints on the shoulder and 1 rotary joint on the elbow.

The External forces $P_i = [P_{ix}, P_{iy}, P_{iz}]^T_{(i=0..5)}$ are applied respectively   to the bodies $C_0, C_1, C_{61}, C_{71}, C_{62}$, and C_{72}. The angles α, β and δ are variables $(0...30°)$ and allow us to choose an initial configuration for the two arms. The sagittal plane of trunk R3P is (O_0, X_0, Y_0) and the frontal plane is (O_0, Y_0, Z_0).

2.1   Method

The dynamic equations of the upper part of the robot are developed using the Newton-Euler formulation. The efforts applied to the trunk located on point O_0 are given by:

$$\begin{cases} \vec{F}_0 = \sum_{i=0}^{1} m_i (\vec{\gamma}_i - \vec{g}) + \sum_{i=6}^{7}\sum_{j=1}^{2} m_{ij} (\vec{\gamma}_{Gij} - \vec{g}) - \sum_{i=0}^{5} \vec{P}_i \\ \vec{M}_0 = \sum_{i=0}^{1} (\vec{h}(i,O_0) - \vec{M}(m_i\,\vec{g},O_0)) - \sum_{i=0}^{5} \vec{M}(\vec{P}_i,O_0) + \sum_{i=6}^{7}\sum_{j=1}^{2} \left[(\vec{h}(ij,O_0) - \vec{M}(m_{ij}\,\vec{g},O_0)\right] \end{cases} \qquad (1)$$

With:

• $\vec{h}(i, O_0)$: Derivation of element C_i angular momentum calculated at point O_0.

• $\vec{F}_0 = [F_x, F_y, F_z]^T$ and $\vec{M}_0 = [M_x, M_y, M_z]^T$: Efforts exerted by the frame on C_0 at point O_0.

• $\vec{P}_i = [P_{ix}, P_{iy}, P_{iz}]^T_{(i=0..5)}$: External forces applied respectively to C_0, C_1, C_{61}, C_{71}, C_{62}, et C_{72} (C_0 and C_1 are the elements in contact with the external environment of the robot).

• $\vec{\gamma}_i$: Acceleration of the C_i elements.

Direct and inverse kinematics are obtained using DH parameters modified by Khalil –Kleinfinger for arborescent open linkages.
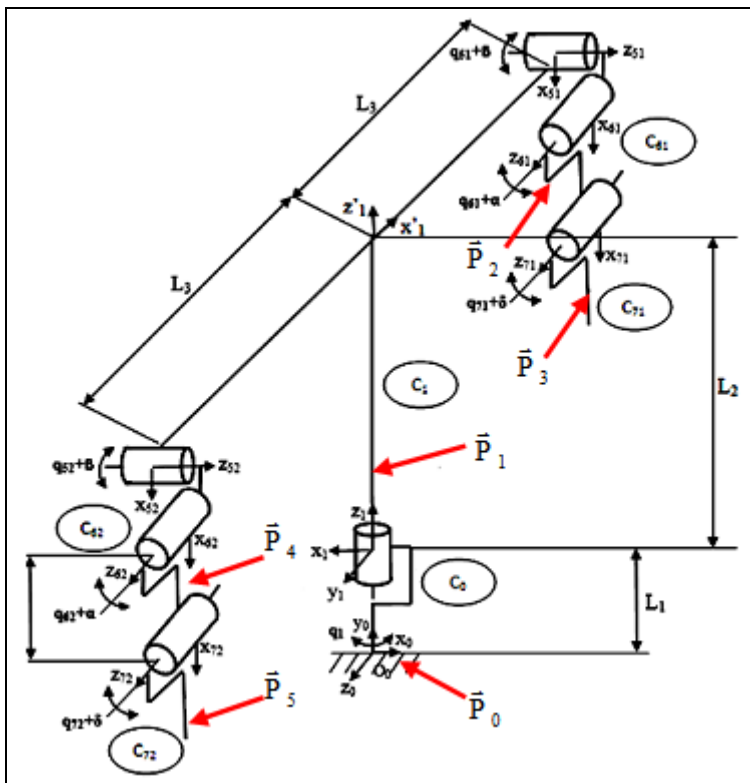
Fig. 1 Modeling of the robot ADAM subjected to the external forces $P_{i\,(i=1..5)}$

The motion equations based on the Newton-Euler formulation are calculated for each element C_i (i= 61, 71, 62 and 72) of the robot at the rigid support point O_0. They can be written in the following form:

$$
\begin{bmatrix}
\ddot{q}_{51} \\
\ddot{q}_{61} \\
\ddot{q}_{71} \\
\ddot{q}_{52} \\
\ddot{q}_{62} \\
\ddot{q}_{72}
\end{bmatrix}
=
\begin{bmatrix}
g_1(q_1,...q_6,\dot{q}_1,...\dot{q}_6,L_{ge},L_{in},F_x,F_y,F_z,M_x,M_y,M_z,P_{0x},P_{0y},P_{0z},...,P_{5x},P_{5y},P_{5z}) \\
. \\
. \\
. \\
. \\
g_6(q_1,...q_6,\dot{q}_1,...\dot{q}_6,L_{ge},L_{in},F_x,F_y,F_z,M_x,M_y,M_z,P_{0x},P_{0y},P_{0z},...,P_{5x},P_{5y},P_{5z})
\end{bmatrix}
\tag{2}
$$

With:

- $q,\dot{q},\ddot{q}$: Position, velocity and acceleration of the joint.
- L_{ge} and L_{in}: Geometrical and inertial parameters of R3P mechanism.

Elements C_i (i= 61, 71, 62 and 72) represent the mobile masses which are used to compensate the external disturbances.

2.2 Modeling of the Robot ADAM

Modeling and simulation of the dynamic behavior of the robot ADAM subjected to disturbing forces using the ADAMS software are given by Figure 2.
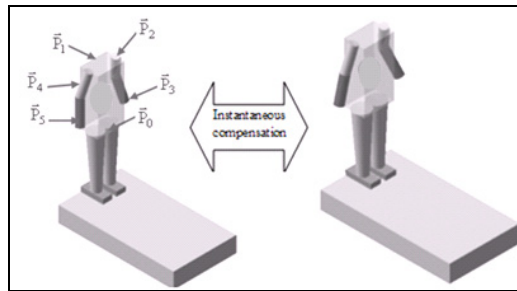
Fig. 2 Arms instantaneous compensation

The system (2) is solved to calculate the 6 accelerations to be generated to instantaneously compensate the external forces applied to the robot. The general state equation (GSE) used to compute the motion of the elements is built as follows:

- $\vec{X} = [x_1,....x_{12}]^T$: Vector of the system state:

$x_1 = q_{51}, x_2 = \dot{q}_{51}, x_3 = q_{61}, x_4 = \dot{q}_{61}, x_5 = q_{71}, x_6 = \dot{q}_{71}$

$x_7 = q_{52}, x_8 = \dot{q}_{52}, x_9 = q_{62}, x_{10} = \dot{q}_{62}, x_{11} = q_{72}, x_{12} = \dot{q}_{72}$

- $\vec{U} = [u_1,....u_{22}]^T$: Input vector of the system whose components are F_x, F_y, F_z, M_y, P_{ix}, P_{iy}, P_{iz} (i=0..5).

• $\vec{Y} = [q_{51}, q_{61}, q_{71}, q_{52}, q_{62}, q_{72}]^T$: Output vector of the system.

• $\vec{L} = [m_{i(i=0..4)}, a_{11}, a_{12}, a_{13}, a_{01}, a_{02}, a_{03}, a_1, a_2, a_3, a_4, L_1, L_2, L_3, L_4, g]^T$. parameter vector

3   Simulation of the Robot ADAM Subjected to Disturbing Forces with Adams Software

3.1   Method

During a simulation, the following operations are carried out:

• Extraction of the initial components (at t=0) of efforts from the rigid support point of the trunk: F_x= 0N, F_y = trunk weight, F_z = 0N, M_x = 0 Nm, M_y = 0 Nm. And M_z = 0 Nm.
And at each sample time:

• System (2) resolution and double integration using GSE formulation which yields the values of the components of the output vector: desired joints variables q_{51}, q_{61}, q_{71}, q_{52}, q_{62} and q_{72}.
• Application of the control law for the torque applied to each joint of the model. Components extraction of the generalized forces at rigid support point O_0 of mechanism R3P.

In a real application, a 6 axis DELTA F/T force sensor IF - 330 – 60 transducer located between the trunk and the robot waist is used to measure F_x, F_y, F_z, M_x, M_y, M_z. Thus the external forces can be calculated by the difference between the forces just before and during the disturbance.
During the simulation of the dynamic behavior of the robot, a PD controller is used to compute joint torque based on the current state and the desired motion. The PD controller determines the output torque according to the difference between the desired state $q_d, \dot{q}_d$ and the current state $q, \dot{q}$ (respectively positions and velocities vector) Where the design Kp_i and Kv_i are respectively called position and velocity gains, are symmetric positive definite and suitably selected.

$$\tau_i = K_{pi}(q_{di} - q_i) + K_{vi}(\dot{q}_{di} - \dot{q}_i) \tag{3}$$

Finally, based on the values of the external forces detected by the sensor, we apply for each joint of the model the corresponding torque in order to maintain stability e.g.   Keep Fx =0, Fy = trunk weight, Fz =0, Mx= My = Mz   = 0Nm.
The model of each external force is represented in Fig.3.
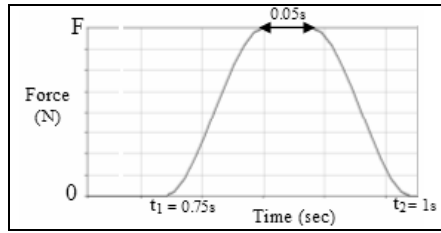
Fig. 3 External forces model

The external force is applied between t1=0.75s and t2=1s. It increases from 0 until the selected maximum amplitude F, then the force is maintained for 0.05s and finally it decreases from F to 0.

3.2   Three-Dimensional Disturbance Compensation Results in a Vertical Posture of the Robot

For this example the external forces is applied to the element C_1 during 0.25 second. The modeling of the robot and the external force are carried out. The first simulation is carried out without compensation: the robot rocks and falls down just after the application of the disturbance. The same simulation is carried out with compensation of the external forces using the 6 dofs of the arms to preserve balance. The movements of the arms solved by the GSE required to stabilize the robot are used in the control law. See (Fig. 4)
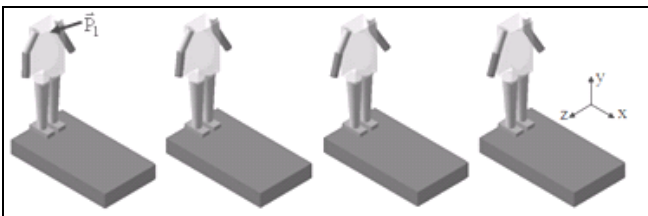
Fig. 4 Compensation of P1

4   Development of Virtual Interface for the Robot ADAM

4.1   Method

In this case, the software SimMechanic is used to simulate the stabilization of the robot in presence of external disturbances forces. SimMechanic's diagrams represent the physical interaction existing between two bodies. Geometrical and inertial proprieties of each body are introduced.

ADAM's arm is modeled by five blocks. The first joint bloc is between the ceilings and the rod, the second one is between the bodies arm. Bloc body actuator and bloc body sensor are added to respectively exercise torque and take position and speed measurements.

Solidworks's traductor export body's inertia to create the appropriate SimMechanics's element. To create SimMechanic model and VRML interface, every mechanism's body is described by declaring: (landmarks, inertial proprieties, type of links and initial values of the variable for every link). (Fig. 5 and 6)
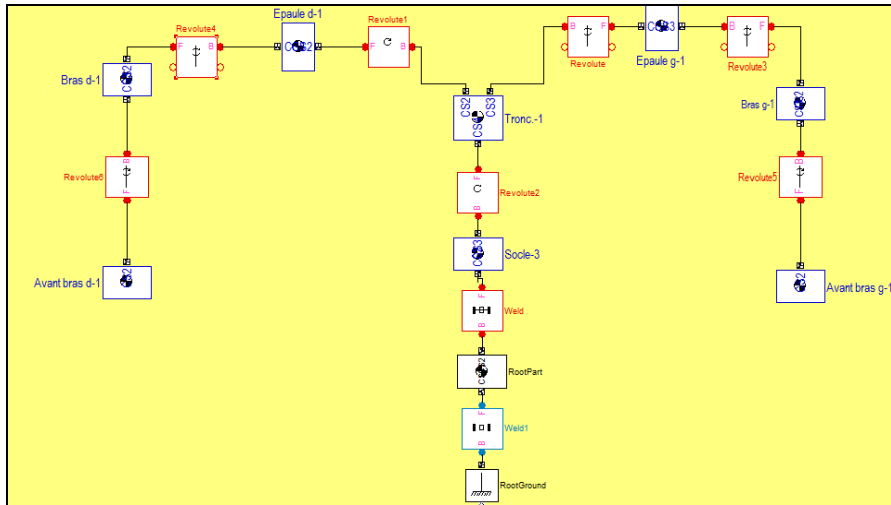
Fig. 5 SimMechanic model
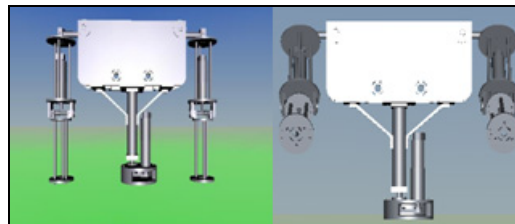
Fig. 6 VRML interface

4.2 Development of ADAM's Graphic

Reality Toolbox, another tool of Matlab is used to animate en 3D in a virtual environment SimMechanic's model. Figure 7 present the blocks used to simulate ADAM's behavior in presence of perturbations.

At each sample time, system (2) is solved and double integration using C++ program which yields the values of the components of the output vector: desired joints variables q_{51}, q_{61}, q_{71}, q_{52}, q_{62} and q_{72}.

During the simulation of the dynamic behavior of the robot, a PD controller is used to compute joint torque based on the current state and the desired motion. The diagram bellow present the blocks used to simulate output torque (Fig. 8).
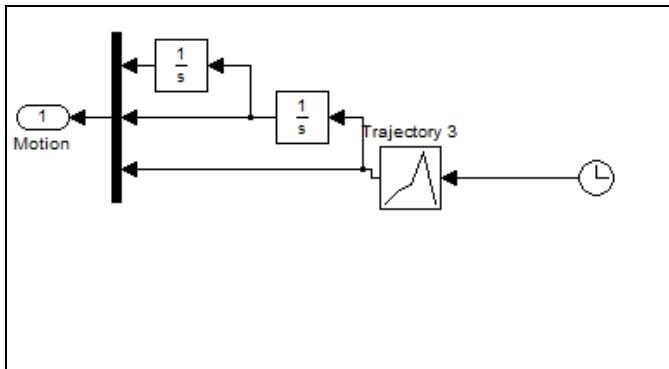
Fig. 7 Blocks motion
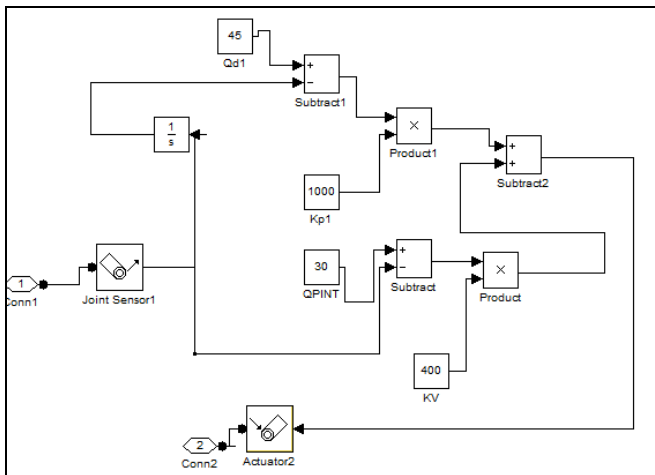
Fig. 8 Output torque blocks

Tow simulations are presented, the first one the robot is subjected to disturbance in the sagittal plane (OXY) (Fig. 9). The movements carried out by the two arms to compensate the external force. The second one the robot is subjected this time to frontal disturbance applied in the frontal plane (OYZ) this time only the movements carried out by the right arm compensate the external for (Fig. 10).
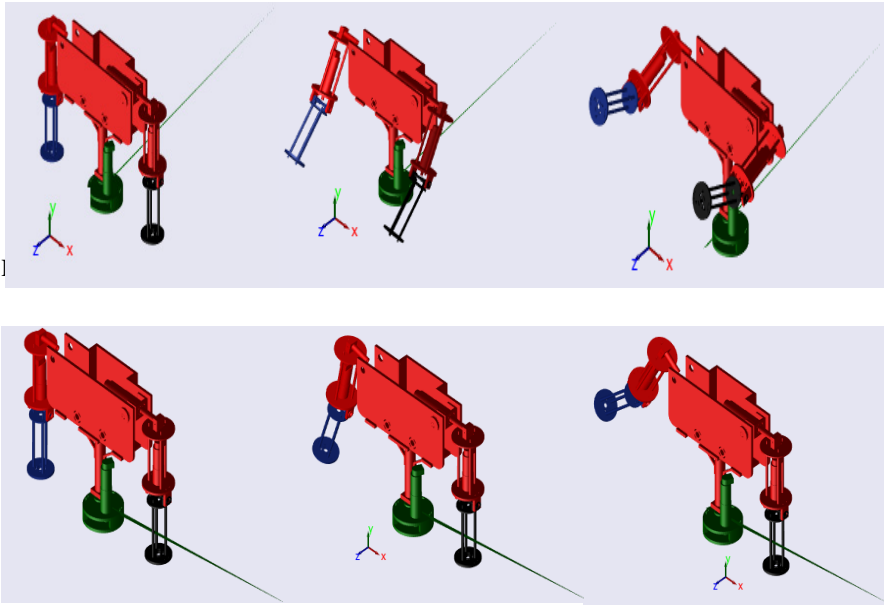
Fig. 10 Compensation of the frontal perturbation

5 Conclusion

The aim of our work, using the dynamic simulation of the virtual mockup of ADAM, was to show the importance of the upper part in the stabilization of the robot in the presence of external disturbances. The current arms of the ADAM robot are a 6R six rotational movements. A method was developed to calculate the movements and the accelerations of the parts of the trunk for the instantaneous compensation of the external forces. The study showed the importance of arms for stabilization in the case of large disturbances. Another important point developed in this paper was the interest of the global synergy between the arms to reject large disturbances applied to the upper part of a bipedal robot. Future work will consist in experimental validation of simulations results and their different limits to counteract external disturbances during various tasks and handling.

References

Nagasaka, K., Kuroki, Y., Suzuki, S., Itoh, Y., Yamaguchi, J.: Integrated motion control for walking, jumping and running on a small bipedal entertainment robot. In: Proceedings of the 2004 IEEE International Conference on Robotics and Automation, ICRA 2004, April 26-May 1, vol. 4, pp. 3189–3194 (2004)

Sakagami, Y., Watanabe, R., Aoyama, C., Matsunaga, S., Higaki, N., Fulimura, K.: The intelligent ASIMO, "system overview and integration". In: Proceeding IEEE - International Workshop on Intelligent Robots & Systems (IROS), p. 2478. EPFL Lausanne, Suisse

Park, W., Kim, J.-Y., Lee, J., Oh, J.-H.: Online Free Walking Trajectory Generation for Biped Humanoid Robot KHR-3(HUBO). In: Proceedings of the 2006 IEEE International Conference on Robotics and Automation, Orlando, Florida (May 2006)

Stilman, M., Nishiwaki, K., Kagami, S., Kuffner, J.J.: Planning and Executing Navigation Among Movable Obstacles. In: Proceedings of the 2006 IEEE/RSJ International Conference on Intelligent Robots and Systems, Beijing, China, October 9-15 (2006)

Omer, A.M.M., Ogura, Y., Kondo, H., Morishima, A., Carbone, G., Ceccarelli, M., Lim, H.-O., Takanishi, A.: Development of a humanoid robot having 2-DOF waist and 2-DOF trunk. In: Proceeding of 5th IEEE-RAS International Conference, pp. 333–338 (2005)

Yang, J., Huang, Q., Li, J., Li, C., Li, K.: Walking Pat-tern Generation for Humanoid Robot Considering Upper Body Motion. In: Proceedings of the 2006 IEEE/RSJ, International Conference on Intelligent Robots and Systems, Beijing, China (2006)

Sabourin, C., Bruneau, O., Buche, G.: Control strategy for the robust dynamic walk of a biped robot. International Journal of Robotics Research 25, 843–860 (2006)

Sentis, L., Khatib, O.: A Whole-Body Control Framework for Hu-manoids operating in Human Environments. In: Proceedings of the 2006 IEEE International Conference on Robotics and Automation, Orlando, Florida (2006)

Renner, R., Reimund, S.B.: Instability Detection and Fall Avoidance for a humanoid using Attitude Sensors and Reflexes. In: Proceedings of the 2006 IEEE/RSJ, International Conference on Intelligent Robots and Systems, Beijing, China (2006)

Zaoui, C., Bruneau, O., Ouezdou, F., Maalej, A.: Dynamic balance of a bipedal robot with trunk and arms subjected to 3D external. Journal of Multibody-Dynamics 21, 261–280 (2009), doi:10.1007/s11044-008-9143-1

Analytic Model for Orientation Errors of the Translational Parallel Manipulator RAF

Youssef Chouaibi[1], Ahmed Hachem Chebbi[1], Zouhair Affi[1], and Lotfi Romdhane[2]

[1] LGM, ENIM, University of Monastir, Tunisia
[2] Department of Mechanical Engineering, American University of Sharjah, UAE

Abstract. This paper deals with the analytical modeling and the analysis of the orientation error of the RAF translator due to the clearances in the joints. This model is presented in an analytical form, which allowed to the designer the influence of clearance in revolute and spherical joints on the orientation error in the whole workspace. Based on this model, we also developed an algorithm to map the pose error within the workspace of the manipulator.

Keywords: Translational parallel manipulator, Kinematics, statics, joint clearance, orientation error

1   Introduction

One of the main advantages of Parallel manipulators (PMs) is the high accuracy, high stiffness, and high load carrying capacity compared to serial manipulators. However, this accuracy can be altered by link dimension tolerances (Binaud et al. 2010; Al-Widyan et al. 2011), joints clearances (Innocenti 2002; Parenti-Castelli and Venanzi 2005; Chebbi et al. 2009) or a combination of both (Wu and Rao 2004; Chaker et al. 2013). These problems cannot be avoided unless all sources of errors have been identified and integrated in dedicated computational methods.

To identify and predict the effect of the clearance in the joints, several methods are used in the literature. The probabilistic methods used in (Chaker et al. 2013) to determine the pose error of the platform in the workspace due to the clearance in the joints. (Chebbi et al. 2009; Innocenti 2002; Parenti-Castelli and Venanzi 2005) use deterministic methods in order to determine the effect of the clearance on the accuracy of the end-effector.

In this work, we present an analytical model that expresses the orientation error as a function of the nominal pose, the external load applied to the platform, the structural parameters and the joints clearances. The advantage of having an analytical model is the ability to investigate the effect of each parameter of the robot in the overall orientation error of the platform. In particular, we showed analytically that the clearance in the joints of the parallelogram structure, of the passive legs, is the main source of the orientation error. A quantitative evaluation of the contribution of some of the parameters is also determined. This model can help the

designer allocate the functional joint clearance without affecting the manipulator cost and its accuracy.

The paper is organized as follows: in section 2, the architecture of the manipulator is presented. In section 3, the model that determines the orientation error of the translational parallel manipulator RAF, using a deterministic method, is presented in an analytical form. The distribution of the orientation error of the manipulator caused by the joints in the two passive kinematic legs (PKLs) is presented in section 4. Some concluding remarks are presented in section 5.

2 Architecture of the Translational Parallel Manipulator RAF

The translational parallel manipulator RAF proposed by (Romdhane et al. 2002), as shown in Fig.1, is composed of a platform connected to the base by three active legs of type SPS (S and P stand for spherical and active prismatic pairs, respectively) and two passive kinematic legs (PKLs), which are used to eliminate all possible rotations of the platform with respect to the base. Each PKL is composed of an arm (2) connected to the base by a revolute pair with axis Δ_i, $i = 1$ for the first PKL and $i = 2$ for the second PKL.
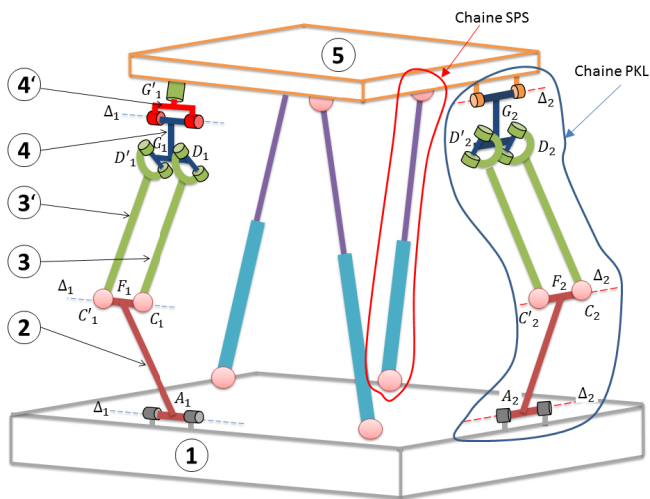
Fig. 1 The translational parallel manipulator RAF

Two forearms (3) and (3') are connected to the arm (2) by two spherical joints centered at C and C'. The line CC' is taken parallel to Δ_i. These two forearms (3) and (3') are also connected to the body (4) by two revolute joints with axes orthogonal to the line CC'. Thus, the points CC'DD' form a parallelogram, where the

points D and D' correspond to the intersection between the axes of the revolute joints and a perpendicular line going through C and C'. The body (4) is connected to the platform by a revolute joint with axis taken parallel to Δ_i, in order to eliminate all possible rotations of the platform with respect to the base. The axes of the first revolute joints connected to the base (for each PKL) cannot be parallel, for the system to work correctly. This architecture of the translational PM-RAF corresponds to an overconstrained mechanism. To remove the overconstraint, one can insert a link (4') in the first PKL between link (4) and the platform. Link (4') has two revolute joints with perpendicular axes, with the platform (5) and link (4), respectively.

3   Modeling of the Orientation Error of the Manipulator

In this section, an analytical model of pose error caused by the clearance in spherical joints and revolute joints are developed. The virtual work method is used in order to determine the relation between the local pose error in each joint due to the clearance and the corresponding pose error of the platform.

3.1   Local Pose Error of the Spherical Joint

The local pose error is the pose change caused by only one joint clearance. Let $\boldsymbol{\tau}_{s_{ij}}$ (determined by static analysis), be the wrench transmitted by the j-th spherical pair (Fig. 2) of the i-th PKL This wrench can be written as follows:

$$\boldsymbol{\tau}_{s_{ij}} = \begin{bmatrix} \mathbf{f}_{ij} \\ \mathbf{0} \end{bmatrix} = \mathbf{H}_{ij}.\boldsymbol{\tau}_{ext} \tag{1}$$
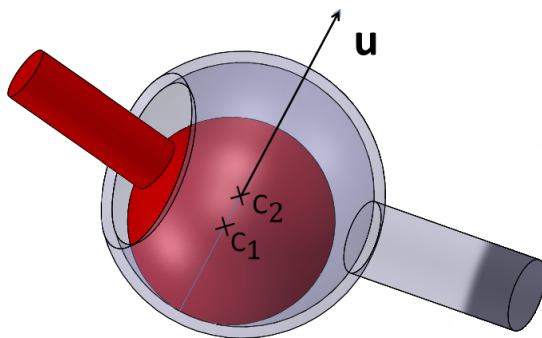
Fig. 2 Model of the spherical joint

where $\mathbf{f}_{ij}$ corresponds to the force transmitted by the j-th spherical pair of the i-th PKL and $\mathbf{H}_{ij}$ is a matrix that relates the reaction forces transmitted by the j-th joint of the i-th PKL to the external load $\boldsymbol{\tau}_{ext}$, applied to the platform.

Let $\mathbf{u}_{ij}$, be the unit vector of the force $\mathbf{f}_{ij}$, which can be written as:

$$\mathbf{u}_{ij} = \frac{\mathbf{f}_{ij}}{\|\mathbf{f}_{ij}\|} \tag{2}$$

Thus, the change of the pose caused by the clearance in the spherical joint is given by the following vector:

$$\Delta\boldsymbol{\delta}_{s_{ij}} = \mathbf{C_1 C_2} = \varepsilon.\,\mathbf{u}_{ij} \tag{3}$$

where ε corresponds to the magnitude of the vector $\Delta\boldsymbol{\delta}_{s_{ij}}$.

According to Eqs (2 and 3), the change of the pose caused by the clearance in the spherical joint can be written as:

$$\Delta\boldsymbol{\delta}_{s_{ij}} = \frac{\mathbf{H}_{ij}.\boldsymbol{\tau}_{ext}}{\|\mathbf{H}_{ij}.\boldsymbol{\tau}_{ext}\|}.\,\varepsilon \tag{4}$$

3.2   *Local Pose Error of the Revolute Joint*

The reaction forces and moments $\boldsymbol{\tau}_{r_{ij}}$ transmitted by the revolute joints (determined by static analysis) is equivalent to three contact forces $\mathbf{C}_{1,ij}$, $\mathbf{C}_{2,ij}$ and $\mathbf{C}_{3,ij}$.

• $\mathbf{C}_{1,ij}$ and $\mathbf{C}_{2,ij}$ are orthogonal to the joint axis and it is applied at points M_{1j} and M_{2j}, respectively (Fig. 3);

• $\mathbf{C}_{3,ij}$, has the same direction as the axis of the revolute joint (Fig. 3).

The expression of these contact forces are given as follows:

$$\begin{cases} \mathbf{C}_{1,ij} = -\frac{1}{2}\left[\mathbf{f}_{ij} \times \mathbf{q}_{ij} + \frac{1}{\lambda}\mathbf{m}_{ij}\right] \times \mathbf{q}_{ij} = \mathbf{W}_{1,ij}\boldsymbol{\tau}_{r_{ij}} \\ \mathbf{C}_{2,ij} = -\frac{1}{2}\left[\mathbf{f}_{ij} \times \mathbf{q}_{ij} - \frac{1}{\lambda}\mathbf{m}_{ij}\right] \times \mathbf{q}_{ij} = \mathbf{W}_{2,ij}\boldsymbol{\tau}_{r_{ij}} \\ \mathbf{C}_{3,ij} = \mathbf{f}_{ij}.\,\mathbf{q}_{ij} = \mathbf{W}_{3,ij}\boldsymbol{\tau}_{r_{ij}} \end{cases} \tag{5}$$

where $\mathbf{q}_{ij}$ is a unit vector along the axis of the revolute joint and $\mathbf{W}_{1,ij}$, $\mathbf{W}_{2,ij}$ are 3x6 matrices and $\mathbf{W}_{3,ij}$ is 1x6 matrix. These matrices allow the calculation of the three contact forces $\mathbf{C}_{1,ij}$, $\mathbf{C}_{2,ij}$ and $C_{3,ij}$ for a given wrench $\boldsymbol{\tau}_{r_{ij}}$, which is the one transmitted by the j-th revolute joint in the i-th PKL.
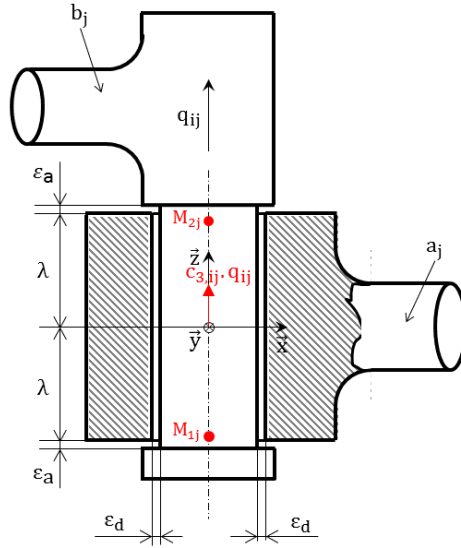
Fig. 3 Axial and radial clearances in a revolute joint

By applying the principle of virtual work, the local pose error caused by the clearance in the revolute joints can be determined as:

$$\Delta\boldsymbol{\delta}_{r_{ij}} = \left(\mathbf{W}_{1,ij}^{T}\frac{\mathbf{W}_{1,ij}\mathbf{H}_{ij}\boldsymbol{\tau}_{ext}}{\|\mathbf{W}_{1,ij}\mathbf{H}_{ij}\boldsymbol{\tau}_{ext}\|} + \mathbf{W}_{2,ij}^{T}\frac{\mathbf{W}_{2,ij}\mathbf{H}_{ij}\boldsymbol{\tau}_{ext}}{\|\mathbf{W}_{2,ij}\mathbf{H}_{ij}\boldsymbol{\tau}_{ext}\|}\right)\cdot\varepsilon_{d} + \mathbf{W}_{3,ij}^{T}\frac{\mathbf{W}_{3,ij}\mathbf{H}_{ij}\boldsymbol{\tau}_{ext}}{\|\mathbf{W}_{3,ij}\mathbf{H}_{ij}\boldsymbol{\tau}_{ext}\|}\cdot\varepsilon_{a} \qquad (6)$$

where ε_{a} and ε_{d} correspond to the axial and radial clearances in the revolute joint, respectively.

3.3   The Orientation Error Modeling

Let $\Delta\boldsymbol{\delta}_{ij}$ be the local pose error caused by the clearance in the j-th pair of the i-th PKL and $\boldsymbol{\tau}_{ij}$ the reaction forces and moments transmitted by this pair. We note by $\Delta\boldsymbol{\Gamma}_{ij}$, the corresponding pose error of the platform. By applying the virtual work principal:

$$\boldsymbol{\tau}_{ext}^{T}\cdot\Delta\boldsymbol{\Gamma}_{ij} + \boldsymbol{\tau}_{ij}^{T}\cdot\Delta\boldsymbol{\delta}_{ij} = 0 \qquad (7)$$

Substituting $\boldsymbol{\tau}_{ij}$ by its expression, we get the pose error:

$$\Delta\boldsymbol{\Gamma}_{ij} = -\mathbf{H}_{ij}^{T}\cdot\Delta\boldsymbol{\delta}_{ij} \qquad (8)$$

Thus, the platform pose error due to the clearance in all the joints is given by:

$$\Delta\mathbf{\Gamma} = -\sum_{i=1}^{2} \sum_{j=1}^{n_i} \mathbf{H}_{ij}^{T} . \Delta\mathbf{\delta}_{ij} \tag{9}$$

where n_i is the number of joints in the i-th PKL.

4   Distribution of the Orientation Error within the Workspace

In this section, the distribution of the orientation error of the manipulator, caused by the joints clearances, is presented. The orientation error around the $\mathbf{x_0}$ axis (θ_x) is caused by the joints clearances in the first PKL, while the orientation errors around $\mathbf{y_0}$ and $\mathbf{z_0}$(θ_y and θ_z) are caused by the joints clearances in the second PKL.

The desired workspace, where the pose error is presented, is a cube defined by:

$$-200 < x, y < 200 \text{ and } 200 < z < 600.$$

The architectural parameters of the manipulator and the characteristics of the spherical and revolute joints are given in Table 1 and Table 2.

4.1   Distribution of the Orientation Error Caused by the Clearance in the Joints of the First PKL

Figure 4 presents the distribution of the orientation error θ_x, caused by the clearances in the joints of the first PKL in two cross sections of the workspace ($z = 200 \ mm$). Table 3 presents the contribution of each joint clearance type to the total error θ_x. The external load applied to the platform is a unit torque around the x-axis.

One can conclude that the variation of θ_x in the desired workspace is mainly caused by the clearance in the joints forming the parallelogram. Table 3 presents the contribution of each joint clearance type to the total error θ_x.

Table 1 Architectural parameters of the RAF manipulator

l_2 [mm]	l_3 [mm]	$[\mathbf{a_1}]_{S_b}$	$[\mathbf{a_2}]_{S_b}$	$[\mathbf{g_1}]_{S_b}$	$[\mathbf{g_2}]_{S_b}$
400	400	$[\text{-}500\ 0\ 0]^T$	$[0\ \text{-}500\ 0]^T$	$[\text{-}300\ 0\ 0]^T$	$[0\ \text{-}300\ 0]^T$

Table 2 Characteristics of the revolute and spherical joints

Revolute joint	ε_a [mm]	0.01
	ε_d [mm]	0.01
	λ [mm]	30
Spherical joints	ε [mm]	0.01
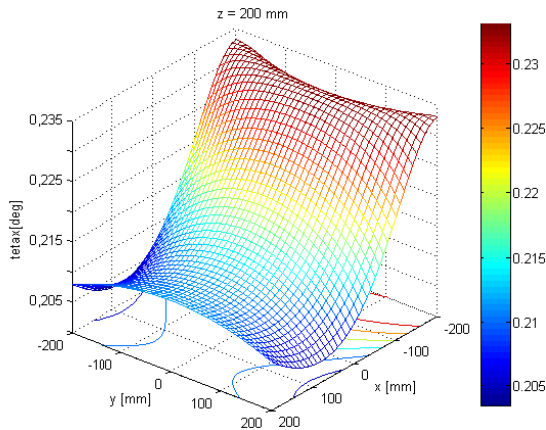
Fig. 4 Distribution of the orientation error θ_x in a section of the workspace

Table 3 Influence of each joint clearance on the orientation error θ_x

Sections	Error caused by the clearance in the revolute joints out of the parallelogram		Error caused by axial and radial clearance in the revolute joints in the parallelogram				Error caused by the clearance in the spherical joints		$\theta_{x_{Max}}$ [degré]
			Axial clearance		Radial clearance				
z=200	0.057	25%	0.012	5%	0.153	65%	0.012	5%	0.233
z=400	0.057	25%	0.012	5%	0.153	65%	0.012	5%	0.233
z=600	0.057	25%	0.01	5%	0.132	63%	0.012	6%	0.212

The clearances in the spherical joints, centered at C_1 and C'_1, participate by less than 6% of the total orientation error θ_x. However, the radial clearances in the revolute joints in the parallelogram structure have the greatest contribution to the value of θ_x (more than 68%).

4.2 Distribution of the Orientation Error Caused by the Clearance in the Joints of the Second PKL

The analysis of the orientation error, caused by the joints clearances in the second PKL, is relatively complex. Indeed, an external torque around y_0 or z_0, causes an orientation error around both directions, y_0 and z_0. This coupling is due to the motion around an axis parallel to the parallelogram plane. In the following, the different loading scenarios are discussed.

- Moment around y_0 and z_0 axes
Figure 5 presents the distribution of the orientation errors, θ_y and θ_z, in a section of the workspace (z = 200 mm). It can be noted that the maximum orientation error is less than 0.2 degree. The orientation errors are not sensitive to a displacement along the x−direction, but they are very sensitive to the one along the y−direction.
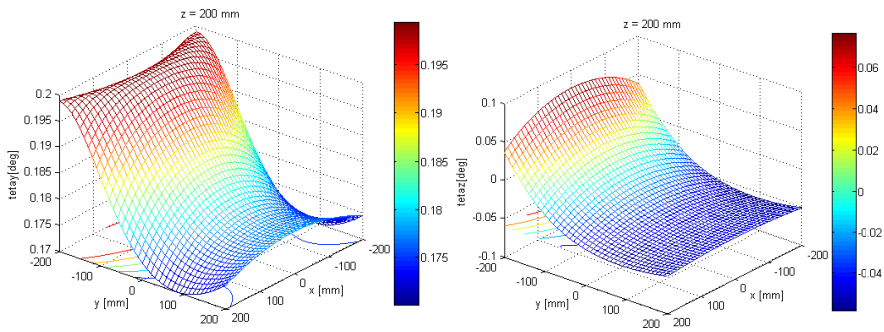
Fig. 5 Distribution of the orientation error θ_y and θ_z in a section of the workspace

- Moment around the y_0 axis
Figure 6 shows the distribution of the orientation errors, $_y$ and $_z$ in a section of the workspace (z = 200 mm).
It can be concluded that, similar to the first PKL, the variation of $_y$ and $_z$ in the desired workspace is mainly caused by the clearances in the joints forming the parallelogram.

- Moment is around z_0 axis
Figure 7, shows the distribution of the orientation errors, θ_y and θ_z in a sections of the workspace (z = 200mm). The remark is that we have a discontinuity in the variation of θ_y. This discontinuity is due to the change of contact mode in the revolute joints of the parallelogram structure. These contact modes of the revolute joint (Fig.8) depend on the value and the direction of the contact forces.
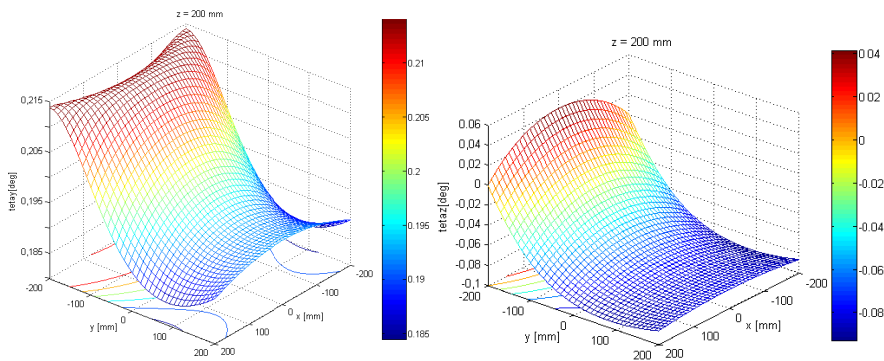
Fig. 6 Distribution of the orientation error θ_y and θ_z in a section of the workspace
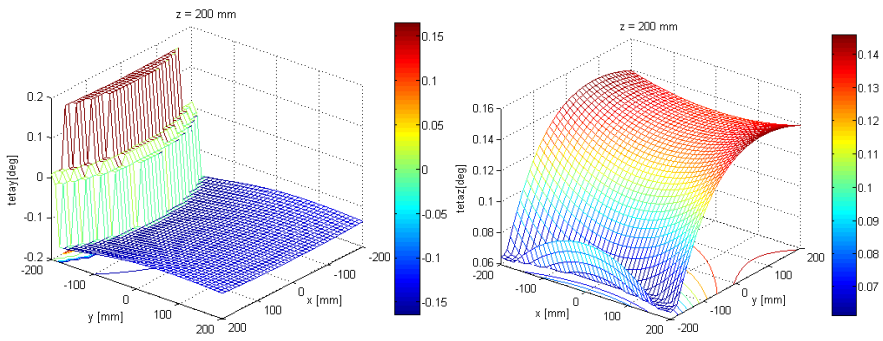
Fig. 7 Distribution of the orientation error θ_y and θ_z in a section of the workspace

(a)

(b)

(c)

(d)
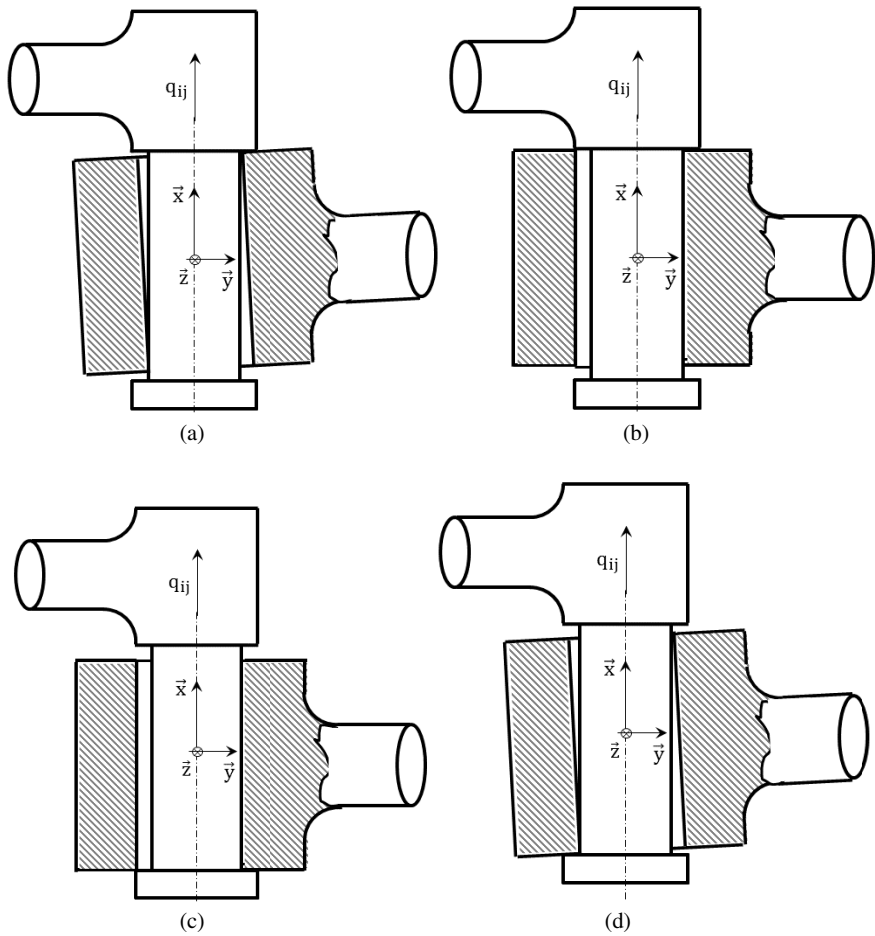
Fig. 8 The contact modes of the revolute joint

5   Conclusion

This work deals with the analytical modeling of the orientation error caused by the joints clearances in the passive legs of the translational PM-RAF. The orientation error of the manipulator was determined in an analytical form. We showed, in particular, that the orientation errors of the RAF were mainly caused by the radial clearances in the revolute joints forming the parallelogram structure of the passive legs. These results can help the designer allocate the functional joint clearance without affecting the manipulator cost and its accuracy. In particular, reducing the clearance in the joints forming the parallelogram is the most effective solution to improve the accuracy of this type of parallel manipulators with parallelogram structure.

References

Binaud, N., Caro, S., Wenger, P.: Sensitivity comparison of planar parallel manipulators. Mechanism and Machine theory 45, 1477–1490 (2010)

Al-Widyan, K., Ma, X.Q., Angeles, J.: The robust design of parallel spherical robots. Mechanism and Machine Theory 46, 335–343 (2011)

Innocenti, C.: Kinematic clearance sensitivity analysis of spatial structures with revolute joints. ASME Journal of Mechanical Design 124, 52–57 (2002)

Parenti-Castelli, V., Venanzi, S.: Clearance influence analysis on mechanisms. Mechanism and Machine Theory 40, 1316–1329 (2005)

Chebbi, A.H., Affi, Z., Romdhane, L.: Prediction of the pose errors produced by joints clearance for a 3-UPU parallel robot. Mechanism and Machine Theory 44, 1768–1783 (2009)

Wu, W., Rao, S.S.: Interval approach for the modeling of tolerances and clearances in mechanism analysis. Journal of Mechanical Design 126, 581–592 (2004)

Chaker, A., Mlika, A., Laribi, M.A., Romdhane, L., Zeghloul, S.: Clearance and manufacturing errors' effects on the accuracy of the 3-RCC Spherical Parallel Manipulator. European Journal of Mechanics A/Solids 37, 86–95 (2013)

Romdhane, L., Affi, Z., Fayet, M.: Design and singularity analysis of a 3-translational-DOF in-parallel manipulator. J. Mech. Des. 124, 419–426 (2002)

Reduced Inverse Dynamic Model of Parallel Manipulators Based on the Lagrangian Formalism

Safa El Hraiech[1], Ajmi Houidi[2], Zouhaier Affi[1], and Lotfi Romdhane[2,3]

[1] LGM, ENIM, University of Monastir, Tunisia
[2] LMS, ENISo, University of Sousse, Tunisia
[3] Department of Mechanical Engineering, American University of Sharjah, UAE
zouhaier.affi@gmail.com, safa_el_hraiech@hotmail.fr

Abstract. This paper deals with the dynamic modeling of the 3-UPU parallel robot based on the Lagrangian formalism. The reduced inverse dynamic model gives the actuators forces as function of only the active variables and the manipulator load. The closed loops equations are used in order to eliminate the passive coordinates from the equations of motion as well as the Lagrange multipliers. This type of model can be useful for the control of parallel robots.

Keywords: 3UPU manipulator, dynamics, Reduced model, Lagrangian formalism.

1   Introduction

Over the last decades, parallel manipulators have received increasing attention by researchers. Compared with the serial robots, the parallel ones have some special characteristics as greater rigidity, high stiffness, better accuracy and larger dynamic charge capacity (J. Cazalilla et al 2014). Serial manipulators have also many advantages as large workspace and simple mechanical structure (Stefan Staicu 2009). The dynamic formulation of manipulators can be established by Newton-Euler approach or Lagrange Formalism. In the Lagrangian formalism, the mechanical structure of the manipulator is incorporated, the coordinates and velocities are presented, and then the Lagrangian equations of motion are established (Leila Notash and Amin Kamalzadeh 2007). This method is suitable for the robot control because it provides only the actuator forces. The complexity of this approach is the closed loop chains nature of the parallel robot (Yunjiang Lou et al 2011).

In this paper, the reduced inverse dynamic model that gives the actuators forces as function of only the active variables and the manipulator load is developed in closed form. we present the structure of the robot 3-UPU in section1. In section2, we develop the Lagrangian method in order to find the robot motion equations. In section3, we will present the reduced inverse dynamic model that describes the actuator forces of robot based on the equations of closed loop chains. Finally, some concluding and remarks are presented.

2 Structure of the 3-UPU robot

The 3-UPU (universal–prismatic–universal) is a translational parallel robotic manipulator, where the moving platform is connected to the base by three legs. It has a closed-loop structure and it has a symmetrical mechanism composed of three kinematical chains of variable length, all connecting the base to the moving platform (S.M. Varedi et al 2009).The universal joints are passive and only the three prismatic joints are actuated (A.-H. Chebbi et al (2009). We can consider the passive universal joint as two revolute joints with concurrent axes. Since the platform motions are only translations, some geometrical conditions have to be imposed. The outer revolute joint axes of each leg are parallel and the two intermediate revolute joint axes are also parallel (Ping Ji and Hongtao Wu 2003). The centers of the universal joints connected the base, as well as the moving platform, can be arranged as an equilateral triangle placed at 120° each other (Fig.1).
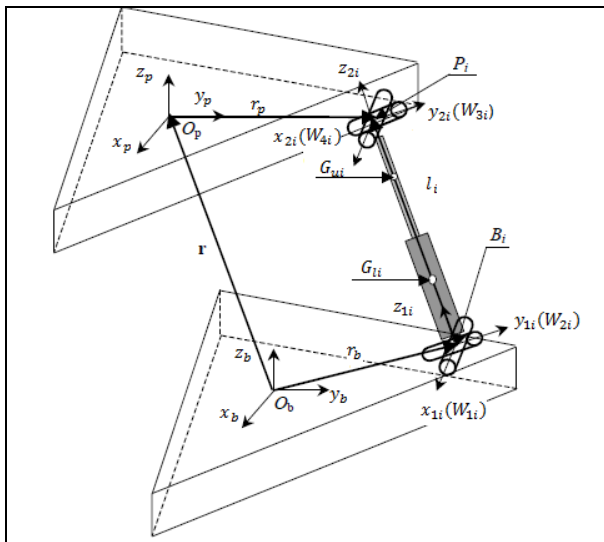
Fig. 1 The 3-UPU manipulator

The considered mechanism can be represented in Fig.1.

$R_b(O_b, x_b, y_b, z_b)$ is the reference frame attached to the base

$R_p(O_p, x_p, y_p, z_p)$ is the reference frame attached to the platform

r_b and r_p are the radius of the base and the radius of the platform respectively

l_i length of the ith leg

The centers of the universal joints connected to the fixed platform are denoted by B_i, also the centers of the moving platform are denoted by P_i. W_{1i} and W_{2i} are the two rotating axes of the bottom universal joint in the ith branch limb (i= 1, 2,

3), while $\mathbf{W}_{3i}$ and $\mathbf{W}_{4i}$ are the two rotating axes of the top universal joint of the limb. Consequently, θ_{1i}, θ_{2i}, θ_{3i} and θ_{4i} are the rotation angles around its corresponding axis.

Due to the special structure of the 3-UPU manipulator, there is a relation between these angles (L.W. Tsai 1996):

$$\theta_{1i} = -\theta_{4i}, (i = 1, 2, 3) \tag{1}$$

$$\theta_{2i} = -\theta_{3i}, (i = 1, 2, 3) \tag{2}$$

3   Inverse Dynamic Modeling of the 3UPU Robot

3.1   The Lagrangian

The Lagrangian is the difference between the kinematic energy and the potential energy of all the moving parts of the mechanism:

$$L = K - U \tag{3}$$

K is the total kinematic energy of the manipulator
U is the total potential energy of the manipulator

Since the robot has a symmetrical structure, the geometry of the three actuators is identical: m_u and m_l are the masses of the upper and the lower part of each actuator. l is the length of each part which are chosen to have the same length. I_{l0} and I_{u0} are the inertia matrix respectively of the lower and the upper part of the actuator $(i = 1, 2, 3)$. These matrices can be expressed as (k=u, l):

$$I_{k0} = \begin{pmatrix} \dfrac{m_k l^2}{12} & 0 & 0 \\ 0 & \dfrac{m_k l^2}{12} & 0 \\ 0 & 0 & 0 \end{pmatrix}_{/R_{ki}(G_{ki}, x_{1i}, y_{1i}, z_{1i})} \tag{4}$$

Since the friction force is ignored, the kinetic and potential energies can be expressed as follow:

$$K = K_p + \sum_{i=1}^{3} K_{aui} + \sum_{i=1}^{3} K_{ali} \tag{5}$$

K_p is the platform kinematic energy
K_{ali} is the kinematic energy of the actuator lower part of the ith leg
K_{aui} is the kinematic energy of the actuator upper part of the ith leg

$$K_p = \frac{1}{2}M(\dot{x}^2 + \dot{y}^2 + \dot{z}^2) \tag{6}$$

$$K_{ali} = \frac{1}{2}m_l V^2{}_{G_{li}} + 1/2w^T{}_{li/R_b} I_{l0} w_{li/R_b} \tag{7}$$

$$K_{aui} = \frac{1}{2}m_u V^2{}_{G_{ui}} + 1/2w^T{}_{ui/R_b} I_{u0} w_{ui/R_b} \tag{8}$$

x, y, z are the centre coordinates of the moving plateform in the global frame, M is the masse of the loaded moving platform, G_{li} is the center of gravity of the lower actuator part, G_{ui} is the center of gravity of the upper actuator part. w_{ij} is the angular velocity of the actuator corresponding part $(i = 1,2,3)$.

The potential energy of the whole system is:

$$U = U_p + \sum_{i=1}^{3} U_{ali} + \sum_{i=1}^{3} U_{aui} \tag{9}$$

U_p is the platform potential energy

U_{ali} is the potential energy of the actuator lower part of the ith leg (i=1,2,3)

U_{aui} is the potential energy of the actuator upper part of the ith leg (i=1,2,3)

The Lagrangian of the system can be expressed by:

$$L = \frac{1}{2}M(\dot{x}^2 + \dot{y}^2 + \dot{z}^2) + \sum_{i=1}^{3}\frac{1}{8}m_l l^2(\frac{d}{dt}\theta_{2i})^2(1 + \frac{1}{3}\cos^2\theta_{1i}) + \frac{1}{8}m_l l^2(\frac{d}{dt}\theta_{1i})^2(\cos^2\theta_{2i} + \frac{1}{3})$$

$$+ \sum_{i=1}^{3}(\frac{1}{2}m_u(\cos^2\theta_{2i}(\frac{d}{dt}\theta_{1i})^2(l_i^2 + \frac{1}{4}l^2 - l_i l) + (\frac{d}{dt}\theta_{2i})^2(l_i^2 + \frac{1}{4}l^2 - l_i l) + (\frac{d}{dt}l_i)^2$$

$$+ \frac{1}{24}m_u l^2(\frac{d}{dt}\theta_{1i})^2 + \frac{1}{24}m_u l^2(\frac{d}{dt}\theta_{2i})^2\cos^2\theta_{1i} - (Mgz + \sum_{i=1}^{3}m_l\,g\frac{l}{2}\cos\theta_{2i}\cos\theta_{1i}$$

$$+ \sum_{i=1}^{3}m_l\,g(l_i - \frac{l}{2})\cos\theta_{2i}\cos\theta_{1i} \tag{10}$$

g is the gravitational acceleration

3.2 Inverse Dynamic Modeling of the 3-UPU

The Lagrangian formulation allows us the equations of motion. For the 3-UPU robot, the dynamic equations can be written as follow [7]:

$$\frac{d}{dt}(\frac{\partial L}{\partial \dot{\theta}_{1i}}) - \frac{\partial L}{\partial \theta_{1i}} = \sum_{j=1}^{6}\lambda_j \frac{\partial \tau_j}{\partial \theta_{1i}} \tag{11}$$

$$\frac{d}{dt}(\frac{\partial L}{\partial \dot{\theta}_{2i}}) - \frac{\partial L}{\partial \theta_{2i}} = \sum_{j=1}^{6}\lambda_j \frac{\partial \tau_j}{\partial \theta_{2i}} \tag{12}$$

$$\frac{d}{dt}(\frac{\partial L}{\partial \dot{l}_i}) - \frac{\partial L}{\partial l_i} = F_i + \sum_{j=1}^{6}\lambda_j \frac{\partial \tau_j}{\partial l_i} \tag{13}$$

$$\frac{d}{dt}(\frac{\partial L}{\partial \dot{x}}) - \frac{\partial L}{\partial x} = F_{extX} + \sum_{j=1}^{6} \lambda_j \frac{\partial \tau_j}{\partial x} \tag{14}$$

$$\frac{d}{dt}(\frac{\partial L}{\partial \dot{y}}) - \frac{\partial L}{\partial y} = F_{extY} + \sum_{j=1}^{6} \lambda_j \frac{\partial \tau_j}{\partial y} \tag{15}$$

$$\frac{d}{dt}(\frac{\partial L}{\partial \dot{z}}) - \frac{\partial L}{\partial z} = F_{extZ} + \sum_{j=1}^{6} \lambda_j \frac{\partial \tau_j}{\partial z} \tag{16}$$

F_i and F_{ext} are respectively the actuator forces and a general external force applied to the platform.

τ_j are the independent closed loop equations which there number is given by:

$$\gamma = n_l - p + 1 = 2 \tag{17}$$

Where n_l and p are respectively the number of the mechanism joints and the number of the robot rigid bodies.

These equations are:

$$\overrightarrow{O_b B_1} + \overrightarrow{B_1 P_1} + \overrightarrow{P_1 O_p} + \overrightarrow{O_p P_2} + \overrightarrow{P_2 B_2} + \overrightarrow{B_2 O_b} = \vec{0} \tag{18}$$

$$\overrightarrow{O_b B_2} + \overrightarrow{B_2 P_2} + \overrightarrow{P_2 O_p} + \overrightarrow{O_p P_3} + \overrightarrow{P_3 B_3} + \overrightarrow{B_3 O_b} = \vec{0} \tag{19}$$

These two vectorial equations can be written as 6 scalar equations:

$$(r_b - r_p) + l_1 \sin\theta_{21} - l_2 \sin\theta_{22} - (r_b - r_p)\cos(\alpha_2) = 0 \tag{20}$$

$$-l_1 \sin\theta_{11} \cos\theta_{21} + l_2 \sin\theta_{12} \cos\theta_{22} - (r_b - r_p)\sin(\alpha_2) = 0 \tag{21}$$

$$l_1 \cos\theta_{11} \cos\theta_{21} + l_2 \cos\theta_{12} \cos\theta_{22} = 0 \tag{22}$$

$$(r_b - r_p)\cos(\alpha_2) + l_2 \sin\theta_{22} - l_3 \sin\theta_{23} - (r_b - r_p)\cos(\alpha_3) = 0 \tag{23}$$

$$(r_b - r_p)\sin(\alpha_2) - l_2 \cos\theta_{22} \sin\theta_{12} + l_3 \sin\theta_{13} \cos\theta_{23} - (r_b - rp)\sin(\alpha_3) = 0 \tag{24}$$

$$l_2 \cos\theta_{12} \cos\theta_{22} + l_3 \cos\theta_{13} \cos\theta_{23} = 0 \tag{25}$$

From these equations, the actuator forces can be expressed by:

$$F1 = mu(\frac{d^2}{dt}l_1) + \frac{1}{2}m_u(\frac{d^2}{dt}\theta_{21})(l - 2l_1) + \frac{1}{2}m_u(\frac{d^2}{dt}\theta_{11})\cos^2\theta_{21}(l - 2l_1)$$
$$+ g(M + m_u)\cos\theta_{21} \cos\theta_{11} - \lambda_1 \sin\theta_{21} + \lambda_2 \sin\theta_{11} \cos\theta_{21} - \lambda_3 \cos\theta_{21} \cos\theta_{11} \tag{26}$$

$$F2 = m_u(\frac{d^2}{dt}l_2) + \frac{1}{2}m_u(\frac{d^2}{dt}\theta_{22})(l - 2l_2) + \frac{1}{2}m_u(\frac{d^2}{dt}\theta_{12})\cos^2\theta_{22}(l - 2l_2)$$
$$+ g(M + m_u)\cos\theta_{22} \cos\theta_{12} - \lambda_1 \sin\theta_{22} - \lambda_2 \sin\theta_{12} \cos\theta_{22}$$
$$+ \lambda_3 \cos\theta_{22} \cos\theta_{12} - \lambda_4 \sin\theta_{22} + \lambda_5 \sin\theta_{12} \cos\theta_{22} - \lambda_6 \cos\theta_{12} \cos\theta_{22} \tag{27}$$

$$F3 = m_u(\frac{d^2}{dt}l_3) + \frac{1}{2}mu(\frac{d^2}{dt}\theta_{23})(l - 2l_3) + \frac{1}{2}m_u(\frac{d^2}{dt}\theta_{13})\cos^2\theta_{23}(l - 2l_3)$$
$$+ g(M + m_u)\cos\theta_{23} \cos\theta_{13} - \lambda_4 \sin\theta_{23} - \lambda_5 \sin\theta_{13} \cos\theta_{23} + \lambda_6 \cos\theta_{13} \cos\theta_{23} \tag{28}$$

3.3   Reduced Inverse Dynamic Model

To determine the actuator forces, we develop the reduced inverse dynamic model based on equations (27, 28, 29). Thanks to the closed loop equations, we can express the passive variables function of the active variables only as presented in the Appendix.

The proposed algorithm is implemented under Maple®.
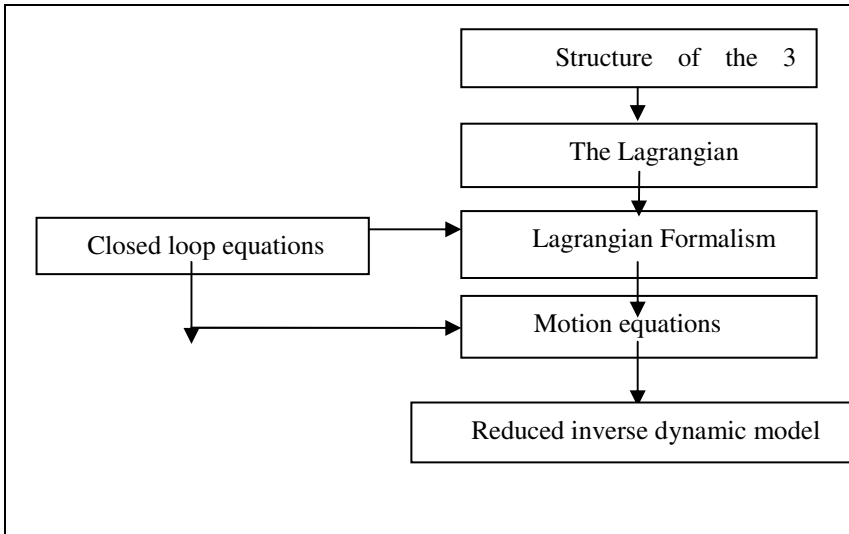
Fig. 2 Algorithm of reduced inverse dynamic model

4   Case Study

The considered geometric parameters of the robot are represented in Table1.

Table 1 Geometric parameters

Parameters	r_b (m)	r_p (m)	m_l (Kg)	m_u (Kg)	M(Kg)	l(m)	g(m/s²)
Value	0.02	0.01	2	1	10	0.04	9.8

For a trajectory of the platform given by $x = 0, y = 0, z = 5t$, due to the symmetrical structure of the 3-UPU robot, we get the same actuator force given by:

$$F_i = 42N, (i = 1, 2, 3) \tag{29}$$

For an arbitrary path of the moving platform given by $x = 5t, y = 5, z = 5$, we will have the following actuator forces:
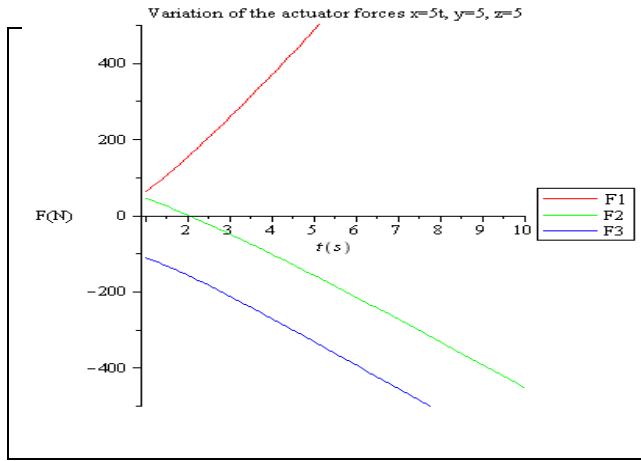
Fig. 3 The actuator forces (x=5t, y=5, z=5)

5   Conclusion

In this work, we have presented an inverse dynamic formulation for the 3-UPU parallel manipulator. This gives the actuators forces as function of only the active variables and the manipulator load. Using the closed loop equations, the passive coordinates are eliminated and the actuator forces are given only as function of active ones. Different paths are imposed to the platform and some simulation results are given.

References

Chebbi, A.-H., Affi, Z., Romdhane, L.: Prediction of the pose errors produced by joints clearance for a 3-UPU parallel robot. Mechanism and Machine Theory 44, 1768–1783 (2009)

Abdellatif, H., Heimann, B.: Computational efficient inverse dynamics of 6-DOF fully parallel manipulators by using the Lagrangian. Mechanism and Machine Theory 44, 192–207 (2009)

Cazalilla, J., Vallés, M., Mata, V., Díaz-Rodríguez, M., Valera, A.: Adaptive control of a 3-DOF parallel manipulator considering payload handling and relevant parameter models. Robotics and Computer-Integrated Manufactuing 30, 468–477 (2014)

Tsai, L.W.: Kinematics of a three-DOF platform with three extensible limbs. In: Recent Advances in Robot Kinematics, pp. 401–410. Kluwer Academic Publishers, Dordrecht (1996)

Notash, L., Kamalzadeh, A.: Inverse dynamics of wire-actuated parallel manipulators with a constraining linkage. Mechanism and Machine Theory 42, 1103–1118 (2007)

Ji, P., Wu, H.: Kinematics analysis of an offset 3-UPU translational parallel robotic manipulator. Robotics and Autonomous Systems 42, 117–123 (2003)

Varedi, S.M., Daniali, H.M., Ganji, D.D.: Kinematics of an offset 3-UPU translational parallel manipulator by the homotopy continuation method. Nonlinear Analysis: Real World Applications 10, 1767–1774 (2009)

Staicu, S.: Recursive modelling in dynamics of Agile Wrist spherical parallel robot. Robotics and Computer-Integrated Manufacturing 25, 409–416 (2009)

Lou, Y., Li, Z., Zhong, Y., Li, J., Li, Z.: Dynamics and contouring control of a 3-DoF parallel kinematics machine. Mechatronics 21, 215–226 (2011)

Appendix

$$L1 = \sqrt{(rb-rp)^2 - 2(rb-rp)x + x^2 + y^2 + z^2} \tag{30}$$

$$L2 = \sqrt{(rb-rp)^2 - \sqrt{3}(rb-rp)y + x^2 + y^2 + z^2 + (rb-rp)x} \tag{31}$$

$$L3 = \sqrt{(rb-rp)^2 + \sqrt{3}(rb-rp)y + x^2 + y^2 + z^2 + (rb-rp)x} \tag{32}$$

$$\theta_{11} = \arctan(\frac{y}{\sqrt{(y^2+z^2)}}), \frac{z}{\sqrt{(y^2+z^2)}}) \tag{33}$$

$$\theta_{12} = \arctan(\frac{(rb-rp)\sqrt{3} - 2y}{\sqrt{-(-4y^2 - 4z^2 - 3(rb-rp)^2 + 4(rp-rp)\sqrt{3}y)}},$$

$$-\frac{z}{\sqrt{-(-4y^2 - 4z^2 - 3(rb-rp)^2 + 4(rp-rp)\sqrt{3}y)}}) \tag{34}$$

$$\theta_{13} = \arctan(-\frac{(rb-rp)\sqrt{3} + 2y}{\sqrt{4y^2 + 4z^2 + 3(rb-rp)^2 + 4(rp-rp)\sqrt{3}y}},$$

$$\frac{z}{\sqrt{4y^2 + 4z^2 + 3(rb-rp)^2 + 4(rp-rp)\sqrt{3}y}}) \tag{35}$$

$$\theta_{21} = \arctan(-\frac{-(rb-rp)+x}{(rb-rp)^2 - 2(rb-rp)x + x^2 + y^2 + z^2},$$

$$\sqrt{-\frac{-y^2 - z^2}{(rb-rp)^2 - 2(rb-rp)x + x^2 + y^2 + z^2}}) \tag{36}$$

$$\theta_{22} = \arctan(\frac{(rb-rp)+2x}{\sqrt{(rb-rp)^2-\sqrt{3}(rb-rp)y+y^2+z^2+x^2+(rb-rp)x}},$$

$$-\frac{\sqrt{-3(rb-rp)^2+4(rb-rp)\sqrt{3}y-4y^2-4z^2}}{\sqrt{(rb-rp)^2-\sqrt{3}(rb-rp)y+y^2+z^2+x^2+(rb-rp)x}})$$

$$\tag{37}$$

$$\theta_{23} = \arctan(\frac{(rb-rp)+2x}{\sqrt{(rb-rp)^2+\sqrt{3}(rb-rp)y+y^2+z^2+x^2+(rb-rp)x}},$$

$$-\frac{\sqrt{-3(rb-rp)^2-4(rb-rp)\sqrt{3}y-4y^2-4z^2}}{\sqrt{(rb-rp)^2+\sqrt{3}(rb-rp)y+y^2+z^2+x^2+(rb-rp)x}})$$

$$\tag{38}$$

Advanced Parametric Analysis of Piezoelectric Actuators with Interdigitated Electrodes having Various Cross-Sections

Ajmi Jemai[1], Fehmi Najar[1], Moez Chafra[1,2], and Zoubeida Ounaies[3]

[1] Applied Mechanics and Systems Research Laboratory, Tunisia Polytechnic
   School, University of Carthage, B.P. 743, La Marsa 2078, Tunisia
   `jemaienit@yahoo.fr, fehmi.najar@gmail.com`
[2] Institut Préparatoire aux Etudes d'Ingénieurs d'El Manar, Université de Tunis
   El Manar, 1002 Tunis, Tunisia
[3] Department of Mechanical and Nuclear Engineering, The Pennsylvania State
   University, 157B Hammond Building, University Park, PA 16802, USA

Abstract. Finite Element (FE) analysis has been performed on the representative volume element of piezoelectric composite actuators with Interdigitated Electrodes (IDE). In these investigations, the effect of the IDE geometry on the deformation performances and the failure hazards, due to field concentrations, is modeled. These numerical models take into account local details such as complicated electrode patterns, local variations of the poling direction due to curved field lines and the existence of the electrodes. Numerical simulations show that the novel electrode designs can significantly ameliorate the micro-strain by selecting the appropriate geometrical parameters. Moreover, the developed results demonstrate that the electrical field concentrations, in case of newly electrode edge, can be highly decreased, allowing to reduce the risk of premature failure of the piezoelectric actuator. These proposed models are compared to previously classical models, which dont take into account local details.

Keywords: Actuation, Piezoelectric, Interdigitated Electrodes, Finite Element Analysis.

1 Introduction

During the past decade, many investigations have been conducted on application of smart materials to build effective and compact actuators. Several small, powerful, and reliable actuators using piezoelectric ceramic materials have been invented, e.g. Active Fiber Composite and Macro Fiber Composite (Bent et al. 1995; Wilkie et al. 2000).

Previously, Different mechanisms were utilized for the active components but approaches using piezoelectric actuators are very common. The conventional set-up of actuator, in which the piezoelectric sheet is poled in thickness direction, used the transverse piezoelectric effect. Unfortunately, the conventional piezoelectric films present several integration difficulties for applications requiring a complex geometry. In addition, due to the ceramic brittleness, this material has a limited stroke, which limits actuation capabilities to a small value when used as actuator. In this case, the use of a piezoelectric composite characterized by a polymer matrix in which piezoelectric material inclusions are embedded, generally in fiber form, is in many cases a good compromise between effective electromechanical coupling capabilities and mechanical flexibility. In 1992, Bent and Hagood (1995) developed a new piezoelectric composite known as Active-Fiber Composites (AFC), which consists of PZT fibers with circular cross-section embedded into an epoxy matrix and sandwiched between two sets of Interdigitated Electrodes. A similar composite, Macro Fiber Composite (MFC) was also developed at NASA Langley Research Center, where PZT fiber have a square cross section obtained by dicing a PZT wafers (Wilkie et al. 2000). These particular designs are characterized by their flexibility and large deformation capabilities, in addition to the use of the higher d_{33} coefficient particularly for bending motion.

Moreover, the multi-phase construction of these piezoelectric composites yields a more robust actuator easier to integrate into laminate composites. Also, the use of IDEs allows AFC and MFC to develop high forces and displacements. The majority of models treating piezoelectric actuator using IDE are based on FE analysis because of the complexity of modeling the electric field. Bowen et al. (2006) presented FE analysis and optimization of AFC actuator assuming that it is uniformly poled in the longitudinal direction. Beckert et al. (2003) developed FE analysis with an inhomogeneous poling state via a two-step processing in order to examine first the electric field distribution, which determines the local poling state in the AFC, and second the electric field distribution updated according to the new polarization. Paradies and Melnykowycz (2010) also developed FE analysis to study the influence of stress concentrations in the regions below the electrodes. The numerical developed model accounted for the electrode and fiber materials. Later, Jemai et al. (2013) proposed novel d_{33} mode active piezoelectric actuators by changing the section of the electrodes. Also, they gave parametric analysis in order to study the effect of the section of electrode on both micro-strain and electric field concentrations. These numerical models didnt take into account the presence of electrode, the local variation of polarization on the piezoelectric elements and the interaction of the fiber and the matrix phases. Although the influences of these local details have been found to be rather small in many studies, the models considering the local effects are highly useful for a better understanding of the behavior of piezoelectric actuators using Interdigitated Electrodes.

In this paper, we present advanced numerical models of the Interdigitated design for piezoelectric actuators with different cross-sections of electrode. These proposed models account for both electrode patterns and local polarizations and neglect the interaction between both fiber and matrix phases. Various Interdigitated Electrode maps (classical, triangular and cylindrical electrodes) were investigated and compared between them.

2 Finite Element Modeling

The d_{33}-mode piezoelectric composite cantilever beams using various cross-sections of Interdigitated Electrodes are studied to optimize the generating strain. By ignoring the influence of edge effects at the physical ends, the actuation cantilever beam can be decomposed into repeating unit cells of identical behavior. Finite Element models of the representative volume elements (RVE) with different cross-sections of electrode are highlighted, as shown in Fig. 1. A coupled field analysis was undertaken. The FE models are simplified as two-dimensional models. By ignoring the influence of interaction between fiber and matrix phases, these RVEs are modeled as monolithic material (PZT-5A). The electrodes material is considered. The electrode is made of 80% of Copper and Epoxy. The materials properties are represented in Table 1 and 2. The electrodes are modeled explicitly and the positive electrical potential was applied directly on nodes located at the surface of contact between electrode and piezoelectric materials. The appropriate mechanical and electrical boundary conditions are imposed, as shown in the Table 3. This element is set to plane strain conditions. The geometrical parameters of the considered RVEs are the half-electrode separation $d/2$ and the half-PZT thickness $h/2$. The geometrical parameters of classical and circular electrode patterns are respectively the half-width $L/2$ and the radius R. a and $b/2$ represent respectively the short-edges along y and x-axis of triangular electrode.
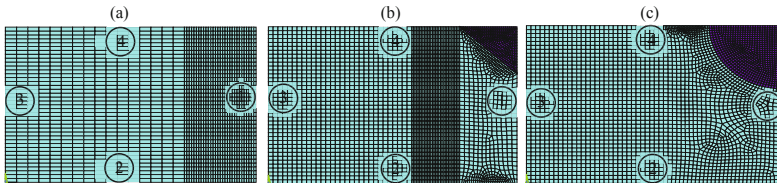
Fig. 1 RVEs of novel electrode designs with appropriate dimensions and Finite Element meshes

In this work, we consider two different FE models. The first represents the classical model (CFEM), in which the piezoelectric material is fully poled in the x-direction. This simplification is exclusively adequate for the case of large electrode separations (Bowen et al. 2006; Jemai et al. 2014). The second FE

model (AFEM) accounts for the local variations of the poling direction, due to curved electric field lines resulting from the complicated electrode pattern. The poling process simulation was realized by two steps (Beckert et al. 2003; Paradies and Melnykowycz 2010). In the first step, the electric field lines are computed with non-polarized and the poling vector aligned with the x-axis in all finite elements. In a second step, the poling direction in each element is aligned with the electric field lines. So, the updated piezoelectricity in each element is implemented by rotating the local coordinate system according to the polarizations direction within that element. Moreover, the material becomes partially (or fully) poled depending on the intensification of the electric field on that element.

Table 1 Material Property Data For Polarized and Non-Polarized PZT-5A used for the Finite Element Analysis

Material properties	Polarized PZT-5A	Non-Polarized PZT-5A
ρ (Kg/m^3)	7500	7500
C_{11} (GPa)	120	88
C_{12} (GPa)	75.2	37.7
C_{13} (GPa)	75.1	37.7
C_{33} (GPa)	111	88
C_{44} (GPa)	21	25.1
C_{66} (GPa)	22.4	25.1
e_{13} (GPa)	-5.2	–
e_{33} (GPa)	15.8	–
e_{15} (GPa)	12.3	–
$\epsilon_{11}^T/\varepsilon_0$	1730	1000
$\epsilon_{33}^T/\varepsilon_0$	1700	1000

Table 2 Material properties for electrodes Material used for the finite element analysis

Material property	Value
E (GPa)	90
ν	0.3
$\varepsilon/\varepsilon_0$	4.25

Therefore, we define the following poling strength factor X to determine the poling state in an element:

$$X = 0 \quad \text{if } |E| \leq E_C$$
$$X = \frac{E - E_C}{E_S - E_C} \quad \text{if } E_C \prec |E| \prec E_S \tag{1}$$
$$X = 1 \quad \text{if } |E| \geq E_S$$

which E_C and E_S are the coercive and saturation field values, respectively. The coercive field value is equal to $0.8kV/mm$. The saturated field value is approximately double the coercive field value.

Table 3 Boundary conditions of displacement, electrical potential and electrical displacement applied to the RVE

Surface number	Mechanical conditions	Electrical conditions
1	Symmetry	$D_x = 0$
2	Symmetry	$D_y = 0$
3	U_x coupled	$V = 0V$
4	Free	$V = +\frac{V}{2}$ on electrode and $D_y = 0$

The different local properties of the piezoelectric material are defined as:

$$C_{ij}^E = \left(C_{ij}^{E,P} - C_{ij}^{E,UP} \right) X + C_{ij}^{E,UP}$$
$$\varepsilon_{ij}^T = \left(\varepsilon_{ij}^{T,P} - \varepsilon_{ij}^{T,UP} \right) X + \varepsilon_{ij}^{T,UP} \tag{2}$$
$$e_{ij} = X \, e_{ij}^P$$

where $C_{ij}^{E,P}$, $\varepsilon_{ij}^{T,P}$ and e_{ij}^P are the fully poled stiffness, permittivity and piezo-electric constants, and are the unpoled stiffness and permittivity constants, respectively.

If the local electric field is lower than the coercive field value, the material remains the beginning state (non-polarized material). However, if the local electric field is higher than the coercive field value, the material becomes partially poled and when it reaches the saturation field value, it becomes fully poled. The developed poling process simulation was implemented in the ANSYS Parametric Design Language (APDL) in order to calculate the electric field in each element and the generating strain in the longitudinal axis of the whole substrate. The procedure is summarized in Fig.2.

2.1 Parametric Study and Finite Element Analysis

2.2 Finite Element Analysis

Now, we move to investigate the effect of the electrode width, electrode separation and substrate thickness on the strain developed in the x-direction per
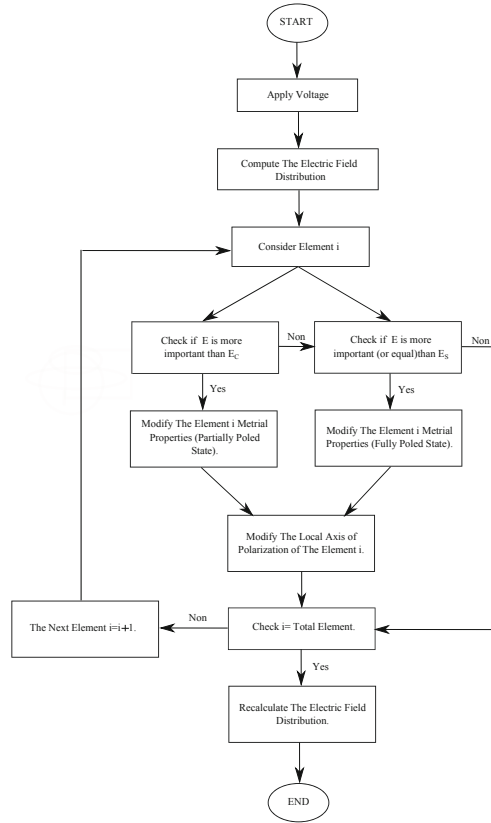
Fig. 2 Flow-chart for the electric field evaluation in piezoelectric elements with IDE

unit applied voltage. Finite Element results summarizing the distribution of the electric field and the x-strain within RVEs with different electrode patterns are presented in Fig.3 and Fig.4.
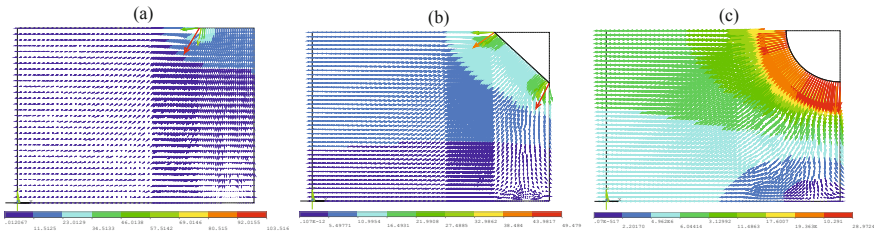
Fig. 3 Vector plots of electric field distribution within the modeled RVE of an IDE structures with three different electrode-configurations
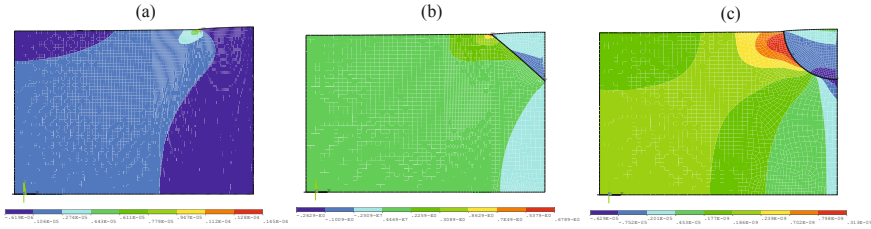
Fig. 4 contour plots of the x-strain distribution within the modeled RVE of an IDE structures with three different electrode-configurations.

These simulations confirm that the electric field distribution within each RVE is nonhomogeneous and anisotropic (Jemai et al., 2013; Jemai et al., 2014). In these last works, we demonstrated that the intensification of the electric field near the electrode is lower when the circular electrode pattern is used. Therefore, the risk of premature failure, due to the breakdown voltage, may be expected to decrease. Moreover, the electric field strength between two consecutive electrodes is higher when the circular electrode is used. Therefore, the actuation capabilities are greater and the x-strain may be expected to increase.

2.3 *Parametric Analysis*

In the next, we give a comparative study between the classical and advanced models in order to study the effect of the local variation of the polarization, due to the variation of the strength of the electric field, resulting from the different complicated electrode patterns (e.g. rectangular and circular electrodes). Although the local details have been found to be rather small in many studies, the Finite element analysis with considering these influences can be useful for a better under-standing of the behavior of piezoelectric actuators using Interdigitated Electrodes with novel shapes of electrode. More importantly, the stress concentrations which occur in the regions below the electrode fingers can be have an important influence on the actuation capabilities, as can be demonstrated by (Paradies and Melnykowycz, 2010). Therefore, the variation of the electrode finger shape can be have a great influence on the local stress concentration, as well as the generating strain of the whole piezoelectric beam.

2.4 *Effect of PZT Thickness*

Our results, showing the effect of PZT thickness on the developed x-strain of RVEs with different novel electrode patterns (triangular and circular electrodes), are presented in Fig. 5. In this analysis, the PZT thickness was

varied, while the electrode separation and electrode width remained constant ($R = b/2 = 2\mu m$ and $d/2 = 100\mu m$). As can be shown from Fig.5, as the PZT thickness is increased, the strain per unit applied voltage decreases. Secondly, the RVE with circular electrode generate more strain, for high values of PZT thickness. However, for its low values, the same x-strain is observed for different cases of electrode pattern. More importantly, by considering the local variation of polarization within RVEs, we can note that the x-strain is reduced, especially for high values of PZT thickness. In fact, when the PZT thickness is increased, the strength electric field between two consecutive electrodes is reduced, thus the low portion of piezoelectric becomes fully polled and the x-strain is expected to reduce.
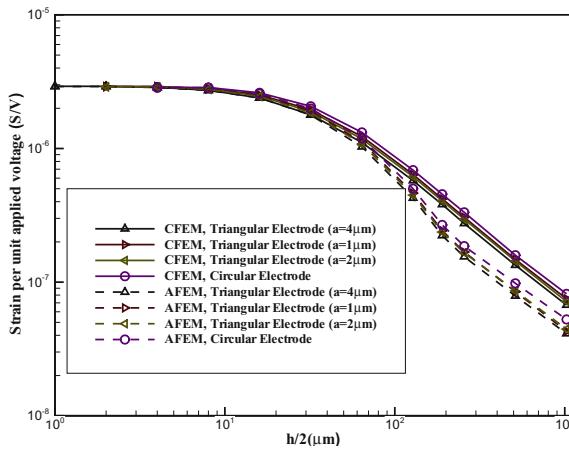
Fig. 5 The effect of PZT thickness h on the generating deformation for different electrode patterns, by using two FE models ($R = b/2 = 2\mu m$ and $d/2 = 100\mu m$).

2.5   Effect of Electrode Width

Now, we move to study the effect of the electrode width on the strain output of the devices with novel electrode patterns. Numerical results summarizing the effect of electrode width are presented in Fig. 6. In this analysis, the electrode width was varied, while the electrode separation and substrate thickness remained constant ($h/2 = 50\mu m$ and $d/2 = 10\mu m$).

From Fig.6, we can easily note that as the triangular electrodes width increases, the developed strain decreases. In addition, for high values of the electrode width, we can observe the same values of the strain output. However, when the circular electrode is used, non-monotonic behavior is observed. The strain output reaches approximately the maximum value at the half of the substrate thickness. More importantly, for relatively low values of electrode width for each device, discrepancy between the classical and advanced
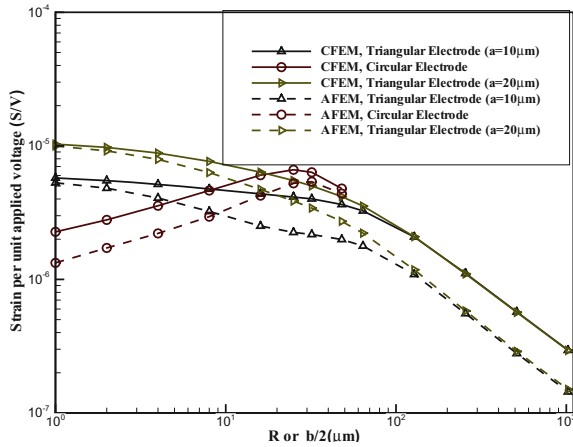
Fig. 6 The effect of electrodes width R or $b/2$ on the generating deformation for different electrode patterns, by using two FE models ($h/2 = 50\mu m$ and $d/2 = 10\mu m$)

model is observed. This is can be explain by the fact that as the electrode width is reduced, the strength electric field is decreased, thus the piezoelectric material becomes more unpoled.

2.6 Effect of Electrode Separation

The more important parameter to be examined for optimization is the electrode finger separation. Numerical results summarizing the effect of electrode separation are presented in Fig. 7. In this analysis, the electrode separation was varied, while both electrode width and substrate thickness remained constant ($R = b/2 = 50\mu m$ and $h/2 = 100\mu m$). By neglecting the local details, the behav-ior of the strain output with changing the electrode spacing is monotonic. However, when the local variation of the polarization, as well as the material properties are considered, the behavior of the strain becomes non-monotonic, especially for triangular electrode pattern.

In fact, by using the classical model, the generating strain decreases with the increasing of the electrode spacing, for each electrode pattern. When the advanced model is used in Finite Element analysis, the behavior of the strain is qualitatively the same, exclusively when the circular electrode is used. However, the behavior of the strain becomes qualitatively and quantitatively different, when the device uses triangular electrode. Indeed, as the electrode spacing increases, the strength electric field decreases and the high portion of piezoelectric material becomes non-polarized, thus the strain drastically drops for high values of electrode spacing. Furthermore, besides of the fact of the great majority of piezoelectric material underneath the electrode (the
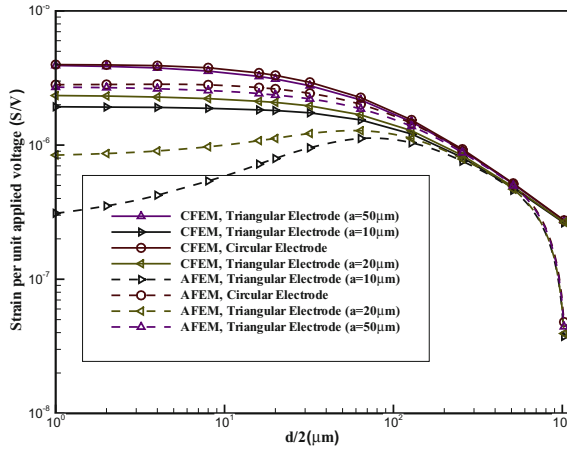
Fig. 7 The effect of electrode spacing d on the generating deformation for different electrode patterns, by using two FE models ($R = b/2 = 50\mu m$ and $h/2 = 100\mu m$).

death zone) is non-polarized, the poling direction of the whole device is approximately adjusted and aligned with the transversal axis. Therefore, the strain in the longitudinal direction is lower compared to the classical model (in which the poling direction is longitudinal), especially for low values of electrode spacing.

3   Conclusion

In this paper, we have developed a numerical parametric analysis of the interdigitated design for piezoelectric actuators by using Finite Element analysis. Modelling of the interdigitated electrode structure on a PZT-substrate for different shapes of electrode has given an insight into how the strain response is affected by electrode width, substrate thickness and electrode finger separation. Different numerical models, which have taken into account the existence of the electrode and local polarization due to the variation of the electric field, were developed. Classical numerical models, in which the polarization is aligned with the x-axis and the PZT material is fully poled, were also developed and used to give a comparative study.

References

Beckert, W., Kreher, W.S.: Modelling piezoelectric modules with interdigitated electrode structures. Computational Materials Science 26, 36–45 (2003)

Bent, A.A., Hagood, N.W., Rodgers, J.P.: Anisotropic actuation with piezoelectric fiber composites. J. of Int. Material Systems and Structures 6, 338–349 (1995)

Bowen, C.R., Nelson, L.J., Stevens, R., Cain, M.G., Stewart, M.: Optimisation of Interdigitated electrodes for piezoelectric actuators and Active Fiber Composites. J. of Electroceramics 16, 263–269 (2006)

Jemai, A., Najar, F., Chafra, M., Ounaies, Z.: Mathematical Modeling of an Active-Fiber Composite Energy Harvester with Interdigitated Electrodes. J. Shock Vib. (2014), doi:10.1155/2014/971597

Jemai, A., Najar, F., Chafra, M., Ounaies, Z.: Novel Electrode Design of a d33-Mode Active-Fiber Composite Piezoelectric Actuator. In: 5ième Congrès International Conception et Modélisation des Systèmes Mécaniques, Tunisia (2013)

Jemai, A., Najar, F., Chafra, M., Ounaies, Z.: Design and Performance of Vibration Energy Harvester with interdigitated Electrodes having Different Cross-Sections. In: 3ième Congrès Tunisien de Mécanique, Tunisia (2014)

Paradies, R., Melnykowycz, M.M.: State of stress in piezoelectric elements with interdigitated electrodes. J. Electroceram. 24, 137–144 (2010)

Wilkie, W., Bryant, R., High, J., Fox, R., Hellbaum, R., Jalink, A., Little, B., Mirick, P.: Low-cost piezocomposite actuator for structural control applications. In: Proceedings of SPIE Seventh Annual International Symposium on Smart Structures and Materials, Newport Beach, USA (2000)

A Model of Electrostatically Actuated MEMS and Carbon Nanotubes Resonators for Biological Mass Detection

Adam M. Bouchaala and Mohammed I. Younis

Physical Sciences and Engineering Division (PSE),
King Abdullah University of Science and Technology KAUST,
Thuwal 23955-6900, Saudi Arabia
adam.bouchaala@kaust.edu.sa

Abstract. We investigate the dynamics of electrically actuated Micro and Nano (Carbon nanotube (CNT)) cantilever beams implemented as resonant sensors for mass detection of biological elements. The beams are modeled using an Euler-Bernoulli beam theory including the nonlinear electrostatic forces and the added biological elements, which are modeled as a discrete point mass. A multi-mode Galerkin procedure is utilized to derive a reduced-order model, which is used for the dynamic simulations. The frequency shifts due to added mass of Escherichia coli (E. coli) and Prostate Specific Antigen (PSA) are calculated for the primary and higher order modes of vibrations. Also, analytical expressions of the natural frequency shift under dc voltage and added mass have been developed. We found that using higher-order modes of vibration of MEMS beams or miniaturizing the size of the beam to Nano scale leads to significant improved sensitivity.

Keywords: Mass detection, Resonator, MEMS, CNT, E. coli, PSA.

1   Introduction

Previously, several methods have been utilized in mass detection of chemical and biological elements, such as static deflection where the mass variation is detected by measuring the microstructure deflection due to the adsorbed mass(Wu et al. 2001). An alternative and more attractive approach, in terms of sensitivity is that the MEMS device can operate in dynamic mode in order to oscillate round its natural frequency (Park et al. 2010), (Dohn et al. 2005).

The resonance frequency of a MEMS device is very sensitive to the adsorbed mass onto the surface. For specific detection, MEMS have a functionalized surface with specific antibodies in order to attract the targeted pathogens. A change in mass of the MEMS biosensor is originally from the antigen antibody binding, which results in a change in the natural frequency. Several studies have been presented to study the frequency shift in micro cantilever beam formass detection (Souayeh and Kacem 2014), (Elishakoff et al. 2010), (Aboelkassem

et al. 2010), (Dohn et al2005). Increasing the sensitivity of detection through miniaturization also has been an active topic. Hence several researches have been conducted on the exploitation of CNTs for this purpose (Elishakoff et al. 2010).

The objective of this paper is to investigate the dynamics of an electrostatically cantilever MEMS and CNTs sensors using analytical and computational methods and to develop analytical expression to quantify the frequency shift as function of the number of biological elements and the position of the attached mass.

2   Microbeam

2.1   Problem Formulation

In this section, we formulate the problem governing the dynamics behavior of a MEMS cantilever beam with attached point mass. We consider a cantilever beam, actuated by nonlinear electrostatic force modeled as a parallel-plate electrode separated with a gap width d, V_{DC} is the dc voltage, V_{AC} is the harmonic voltage, Ω is the frequency and ε is the dielectric constant of air (Younis 2011). In the formulation, we consider the added mass as a discrete point mass at a position L_1 and of mass M_s, as shown in (Fig. 1).
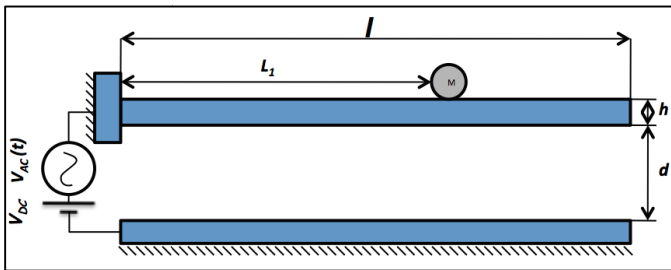
Fig. 1 Schematic of an electrically actuated microbeam with added mass

Assuming an Euler-Bernoulli beam model, the non-dimensional equation of motion governing the transverse deflection $w(x,t)$ of the cantilever beam is expressed as (Ouakad and Younis 2010)

$$\frac{\partial^4 w(x,t)}{\partial x^4} + c_{non}\frac{\partial w(x,t)}{\partial t} + \left(1 + \alpha_3 \times \delta(x - \alpha_{len})\right) \times \frac{\partial^2 w(x,t)}{\partial t^2} = \alpha_2 \frac{[V_{DC} + V_{AC}\cos(\Omega t)]^2}{\left(1 - w(x,t)\right)^2} \quad (1)$$

Where $\delta(x)$ is the delta function where $\delta(x - L_1) = \begin{Bmatrix} 1 & if\ x = L_1 \\ 0 & otherwise \end{Bmatrix}$.

The nondimensional variables in (1) are

$$\alpha_2 = \frac{6\varepsilon l^4}{Eh^3 d^3}, \qquad \alpha_3 = \frac{M_s}{\rho Al}, \qquad \alpha_{len} = \frac{L_1}{l}, \qquad c_{non} = \frac{12cl^4}{ETbh^3}, \qquad (2)$$

Where b the width, h the thickness, l the length, E the effective young's modulus, $A = b \times h$ the cross-sectional area, I the moment of inertia, ρ the material density and c the viscous damping coefficient.

The nondimensional boundary conditions for a cantilever structure are

$$w(0,t) = 0, \qquad \frac{\partial w(0,t)}{\partial x} = 0, \qquad \frac{\partial^2 w(1,t)}{\partial x^2} = 0, \qquad \frac{\partial^3 w(1,t)}{\partial x^3} = 0, \qquad (3)$$

2.2 Natural Frequency Shift under a DC Voltage

In this section, we develop an analytical expression of the natural frequency shift of a cantilever mass sensor actuated with a dc voltage. Toward this, we split the beam deflection into a static component $w_s(x)$ and a dynamic component $w_d(x,t)$

$$w(x,t) = w_s(x) + w_d(x,t) \qquad (4)$$

We substitute (4) into (1) and drop the damping and the higher order terms. We keep only linear terms in $w_d(x,t)$ to get the linearized equation:

$$\frac{\partial^4 w_d(x,t)}{\partial x^4} + (1 + \alpha_3 \times \delta(x - \alpha_{len})) \times \frac{\partial^2 w_d(x,t)}{\partial t^2} = \frac{2\,\alpha_2 V_{DC}{}^2}{(1 - w_s(x))^3} w_d(x,t) \quad (5)$$

Next, we rewrite $w_d(x,t)$ as:

$$w_d(x,t) = \phi_j(x) \times e^{i\omega_{nat,j}t} \qquad (6)$$

We substitute (6) into (5)

$$\frac{\partial^4 \phi_j(x)}{\partial x^4} - \omega_{nat,j}{}^2 \times (1 + \alpha_3 \times \delta(x - \alpha_{len})) \times \phi_j(x) = \frac{2\,\alpha_2 V_{DC}{}^2}{(1 - w_s(x))^3} \phi_j(x) \quad (7)$$

Next, we apply a one-mode Galerkin approximation to extract an analytical expression for the natural frequency in the presence of added mass and under the electrostatic force $\phi_j(x) = a_k \times \phi_k(x)$ where k is 1, 2, ... , n.

We replace $\phi_k'''' = \omega_{non,k}^2 \phi_k$, multiply the resulted equation by the mode shape ϕ_j, and integrate from 0 to 1. The outcome is as below:

$$-\omega_{nat,k}^2 \times (1 + \alpha_3 \times \phi_k(\alpha_{Len})^2) + \omega_{non,k}^2 = \int_0^1 \left(\frac{\alpha_2 V_{DC}{}^2}{(1 - w_s(x))^3} \phi_k^2(x) \right) dx \quad (8)$$

Where $\omega_{nat,k}$ is the natural frequency shifted by the dc voltage and the added mass, $\omega_{non,k}$ is the nondimensional natural frequency of a cantilever beam. $w_s(x)$ is the static deflection of the beam which is function of the applied voltage.

In (8) we can see the contribution of the dc voltage in the frequency shift δ_k

$$\delta_k = \int_0^1 \left(\frac{\alpha_2 V_{DC}{}^2}{(1 - w_s(x))^3} \phi_k^2(x) \right) dx \quad\quad (9)$$

The expression of the natural frequency of a cantilever beam under a dc voltage with added mass is represented in (10)

$$\omega_{nat,j} = \sqrt{\frac{\omega_{non,j}^2 - \int_0^1 \frac{2\alpha_2 V_{DC}{}^2}{(1 - w_s(x))^3} \phi_j^2(x) dx}{1 + \alpha_3 \times \phi_j(\alpha_{Len})^2}} \quad (10)$$

2.3   *The Reduced-Order Model*

To simulate the forced vibration response of the cantilever beam due to the ac and dc actuation, we discretize (1) and (3) using the Galerkin method to get a reduced-order model (ROM) (Ouakad and Younis 2010) and apply the beam's linear orthonormal modeshapes. The deflection of the cantilever beam is approximated as

$$w(x,t) = \sum_{i=1}^n u_i(t)\phi_i(x) \quad\quad (11)$$

Where $\phi_i(x)$ are the normalized linear undamped trial mode shapes of cantilever beam satisfying the boundary conditions, and $u_i(t)$ is the nondimensional modal coordinates.

2.4   *Dynamics Response to DC and AC Loads*

In this section we study the dynamic behavior of the cantilever beam due to combined dc and ac harmonic loads near the primary resonance of the first three natural frequencies of the beam. We usethree mode approximations and show results for different values of dc and ac voltages and for different masses from picogram to nanogram. In the dynamic analysis, we use long time integration of the reduced-order model equations of motion. Table 1 shows the geometrical and material properties of the beam under consideration.

Table 1 The geometrical properties of the studied micro-beam

Symbol	Quantity	Dimensions [μm]
L	Length	500
h	Thickness	3
b	Width	50
d	Gap	3
E	Young's modulus	166
ρ	Density	1400

2.5   *Results and Discussion*

The E. coli has been chosen as an attached mass M_s. The weight of a single *E*. coli is almost one picogram (10^{-15}Kg). In Table. 2, a significant improvement in frequency shift was achieved by operating the cantilever microbeam in the third bending mode.The simulated frequency response curves have been obtained using the Runge–Kutta methodof the reduced-order model.
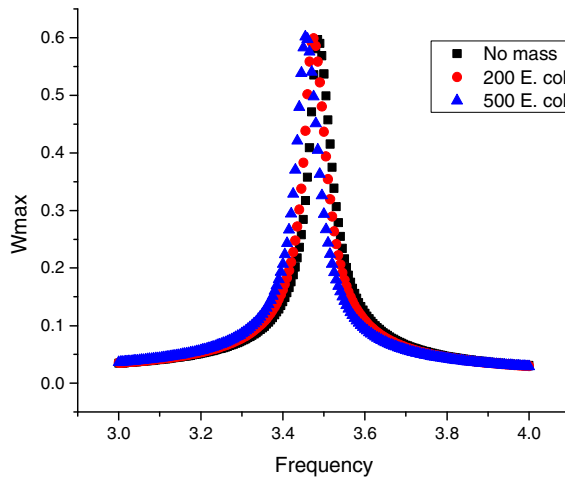
a)

Fig. 2 Frequency shift of a) the 1st mode, b) 2nd mode and c) 3rd mode as function of E. coli
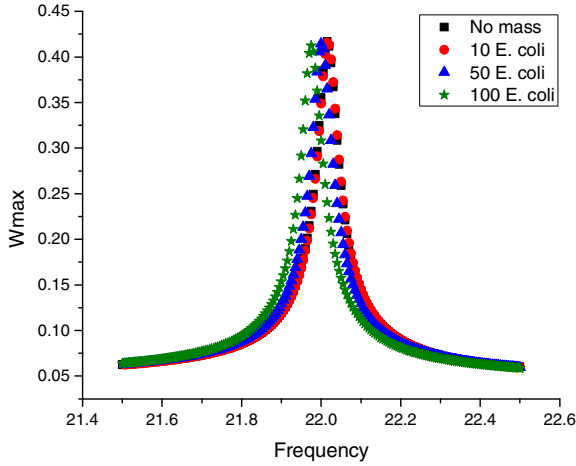
b)
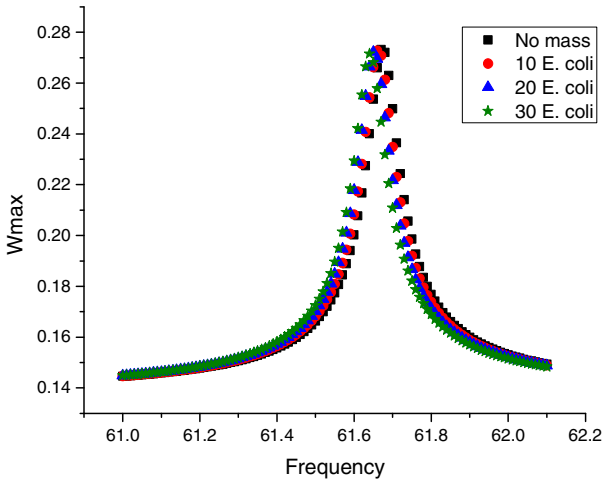
c)

Fig. 2 (*continued*)

In Fig. 3) a, we plot the frequency response of the micro-beam operating in the first mode, we found that at least 100 E. coli ($\alpha_3 = 0.1\%$) is needed to observe a frequency shift of 35 Hz. Then, to get a significant frequency shift of 180 Hz the number of E. coli should reach 500 ($\alpha_3 = 0.5\%$). A load of $V_{DC} = 2V$ and $V_{AC} = 0.5V$ hase been used to simulate the 1st mode. In Fig. 3) b, we operate the micro-beam in the second mode shape. We choose$V_{DC} = 4V$ and $V_{AC} = 2V$ for the simulation. We observe that 10 E. coli could be enough to reach 30 Hz of

frequency shift and 120 Hz for 50 E. coli. In Fig. 3) c, one can note that the 3rd mode is more sensitive than the 1st and the 2nd modes where we can reach 66 Hz of frequency shift with just 10 E. coli. In conclusion, operating the micro-beam in higher mode of vibration leads to an increase in the frequency shift and a reduction in the effective mass.

Table 2 Comparison of the frequency shift as function of E. coli for 3 modes

Number of E. coli	1st Mode [Hz]	2nd Mode [Hz]	3rd Mode [Hz]
0	0	0	0
1	0	12.0129811	24.0259623
10	0	30.0324528	66.07139622
20	0	36.0389434	132.1427924
30	0	60.0649057	204.2206792
50	0	120.129811	363.6243422
100	35.43829434	240.259623	725.1793566
200	72.07788679	482.235453	1440.113422
500	180.194717	1230.98108	3580.783553

To use (9), a static analysis has been done to calculate the value of the embedded integralδ_j, for each value of voltage V_{DC} we get a static deflection of the beam.

Table 3 Comparison of the numerical and analytical frequency shifts for a) 1st mode, b) 2nd mode and c) 3rd mode

a)

Number of E. coli	Numerical [Hz]	Analytical [Hz]	Difference [%]
0	0	0	0
1	0	0	0
50	18.0194717	20.0841428	15.66
100	35.43829434	40.1111037	13.18
200	72.07788679	79.9944414	11
500	180.194717	198.300081	10

b)

Number of E. coli	Numerical [Hz]	Analytical [Hz]	Difference [%]
0	0	0	0
10	30.03245283	25.248223	15.9
50	120.1298113	126.096659	4.9
100	249.2596226	251.833529	1

Table 3 (*continued*)

c)

Number of E. coli	Numerical [Hz]	Analytical [Hz]	Difference [%]
0	0	0	0
10	66.07139622	72.8106786	10.19
20	132.1427924	145.578111	10.16
30	204.2206792	218.302896	6.9

By comparing the numerical with the analytical solution, we found that the difference is from 1% to 16%. We considered the numerical values are the reference value to calculate the error. However, we used a step of 0.01 of Ω in the frequency sweep. To decrease the error values 0.001 step will be needed, even though it is time consuming.

3   Carbon Nanotube

3.1   *Problem Formulation*

In this section, we investigate the nonlinear dynamics of cantilevered CNT electrically actuated with ac and dc loads. An electrode underneath it with a gap width d actuates the CNT. The Euler-Bernoulli theory is used to model the CNT as a cylindrical beam of radius $\hat{R}$, length l, c the damping, a cross-sectional area $A = \pi\hat{R}^2$ and area of moment of inertia $I = \frac{\pi\hat{R}^4}{4}$.
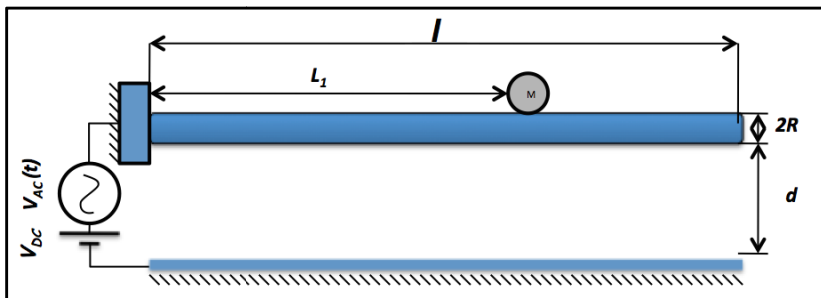
Fig. 3 Schematic of an electrically actuated CNT with added mass

The electrostatic force per unit length is approximated as a cylinder interacting with a lower electrode. Hence, non-dimensional equation of motion governing the

transverse deflection $w(x, t)$ of the CNT cantileveris written as (Ouakad and Younis 2010)

$$\frac{\partial^4 w}{\partial x^4} + c_{non}\frac{\partial w}{\partial t} + \left(1 + \alpha_3 \times \delta(x - \alpha_{Len})\right)\frac{\partial^2 w}{\partial t^2} = \frac{\alpha_2[V_{DC} + V_{AC}\cos(\Omega\hat{t})]^2}{\sqrt{(d-w)\times(d-w+2R)}\times\left(cosh^{-1}\left(1+\frac{d-w}{R}\right)\right)^2} \tag{12}$$

The nondimensional variables in (12) are defined as

$$\alpha_2 = \frac{\pi\varepsilon l^4}{EId^2}, \qquad \alpha_3 = \left(\frac{d}{l}\right)^2, \quad c_{non} = \frac{c\ l^4}{EI}, \quad R = \frac{\hat{R}}{d} \tag{13}$$

The nondimensional boundary conditions are given in (3)

3.2   *Analytical Expression*

The same method discussed previously has been used, in which we split the beam deflection into static and dynamic components, and then we linearize. Hence, the expression below is obtained

$$\omega_{nat,k} = \sqrt{\frac{\omega_{non,k}^2 - \int_0^1 \frac{2\alpha_2 V_{DC}^2 2\sqrt{(1-w_s)(1-w_s+2R)}+(1-w_s+R)(cosh^{-1}(1+\frac{1-w}{R}))}{(1-w_s)(1-w_s+2R)^{\frac{3}{2}}\times(cosh^{-1}(1+\frac{1-w}{R}))^3}\phi_k^2\ dx}{1 + \alpha_3 \times \phi_k(\alpha_{Len})^2}} \tag{14}$$

3.3   *Electrostatic Force Taylorexpansion*

One can note in (12) that the electrostatic force term can lead to complications while deriving a ROM (Ouakad 2010). One approach to deal with this is to expand
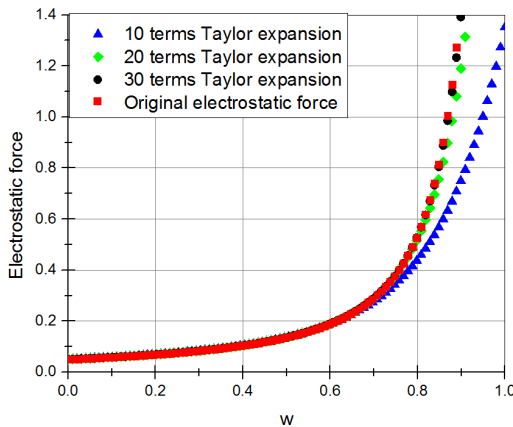
Fig. 4 Taylor series expansion of the nondimensional electrostatic force

the force into enough number of terms (Younis 2011), (Xu and Younis 2013). We need at least twenty terms of the expanded Taylor series form in order to reach a good convergence with the original electrostatic force.

3.4   Dynamics Analysis

Complex diseases like cancer require quantitative detection of proteins. We choose the prostate specific antigen (PSA) to be our mass reference. The mass of a single PSA is in the order of zeptogram (10^{-24} Kg).The properties of the carbon nanotube are in Table4.

Table 4 The geometrical properties of the studied carbon nanotube beam

Symbol		QUANTITY	Dimensions
L		Length	1000 [nm]
	$\widehat{R}$	Radius	5 [nm]
d		Gap	200 [nm]
E		Young's modulus	1 [TPa]
	ρ	Density	1350 [Kg/m^3]
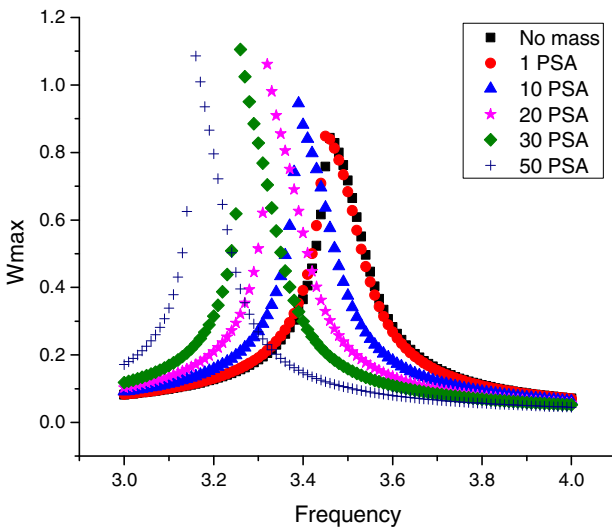
Fig. 5 Frequency shift 1st mode cantilever CNT as function of PSA

To simulate the dynamic response of the cantilever CNT, we integrate the differential equations with time.In Fig. 8, different masses have been used. The attached mass is placed at the tip of the CNT. We plot the results using a one-mode approximation, which is sufficient for convergence, for $V_{DC} = 1$ V, the amplitude of $V_{AC} = 1$ V.

For the CNT, the error between the numerical and the analytical expression is between 4% and 15%. This estimation is sufficient because we use more than single particle for sensing.

Table 5 Comparison Numerical and Analytical frequency shifts for 1 mode as function of PSA

Number of PSA	Numerical[KHz]	Analytical[KHz]	Error [%]
0	0	0	0
1	88.32808797	75.81829128	14.16
10	772.8707697	738.7728155	4.41
20	1545.741539	1436.910294	7.04

4   Conclusion

The dynamic analysis of a cantilever micro-beam with attached mass demonstrated a potential interest in biological applications such as bacteria and virus detection. The electrostatic actuation is considered as a simple and effective method for actuation of MEMS. Instead of functionalizing the entire cantilever surface we propose an alternative method based on the point mass model to reach optimum sensitivity. We demonstrated a significant increasing in sensitivity by operating the cantilever micro-beam in higher-order mode. We developed analytical expressions to measure the frequency shift as function of the added mass and the position that converge with the numerical results. The analytical expression is sufficient to predict efficiently the frequency shift in both MEMS and CNT.

References

Wu, G., Datar, R.H., Hansen, K.M., Thundat, T., Cote, R.J., Majumdar, A.: Bioassay of prostate-specific antigen (PSA) using microcantilevers. Nature Biotechnology (2001), doi:10.1038/nbt0901-85

Park, K., Kim, N., Morisette, D.T., Aluru, N.R., Bashir, R.: Resonant MEMS Mass Sensors for Measurement of Microdroplet Evaporation. Journal of Microelectromechanical Systems (2010), doi:10.1073/pnas.1011365107

Dohn, S., Sandberg, R., Svendsen, W., Boisen, A.: Enhanced functionality of cantilever based mass sensor using higher modes and functionalized particles. In: 2005 IEEE The 13th International Conference on Solid-State Sensors, Actuators and Microsystems (2005)

Souayeh, S., Kacem, N.: Computational models for large amplitude nonlinear vibrations of electrostatically actuated carbon nanotube-based mass sensors. Sensors and Actuators A (2014), doi:10.1016/j.sna.2013.12.015

Elishakoff, I., Versaci, C., Maugeri, N., Muscolino, G.: Clamped-free single-walled carbon nanotube-based mass sensor treated as Bernoulli-Euler beam. Journal of Nanotechnology in Engineering and Medicine (2011), doi:10.1115/1.4003734

Ouakad, H.: Nonlinear Structural Mechanics of Micro and Nano Systems (2010)

Aboelkassem, Y., Nayfeh, A.H., Ghommem, M.: Bio-mass sensor using an electrostatically actuated microcantilever in a vacuum microchannel. Microsyst. Technol. (2010), doi:10.1007/s00542-010-1087-8

Ouakad, H., Younis, M.: The dynamic behavior of MEMS arch resonators actuated electrically. International Journal of Non-Linear Mechanics 45, 704–713 (2010), doi:10.1016/j.ijnonlinmec.2010.04.005

Younis, M.I.: MEMS Linear and Nonlinear statics and dynamics. Springer (2011)

Ouakad, H., Younis, M.: Nonlinear Dynamics of Electrically actuated Carbon Nanotube Resonators. Journal of Computational and Nonlinear Dynamics 5, 011009-1 (2010)

Xu, T., Younis, M.I.: An Efficient Reduced-Order Model for the Nonlinear Dynamics of Carbon Nanotubes. In: IDETC 2014 (2013)

Ouakad, H.M., Younis, M.I.: The dynamic behavior of MEMS arch resonators actuated electrically. International Journal of Non-Linear Mechanics (2010), doi:10.1016/j.ijnonlinmec.2010.04.005

Novel Reduced Order Model for Electrically Actuated Microbeam-Based MEMS

Sarah Ben Sassi and Fehmi Najar

Applied Mechanics an Systems Research Laboratory, Tunisia Polytechnic School,
University of Carthage, B.P.743, La Marsa 2078, Tunisia
`fehmi.najar@ept.rnu.tn`

Abstract. We present a novel semi-analytical approach to solve nonlinear integral-partial-differential equation related to MEMS microactuators. The proposed approach is based on a reduced-order model of microbeams under the action of electrostatic force. Using Euler-Bernoulli beam theory, we derive the nonlinear equations governing the motion of a doubly clamped microbeam. The formulated model gives good account of nonlinearities such as midplane stretching effects and nonlinear electrostatic force. The dynamic response of the coupled electro-mechanical microsystem is simulated through an innovative approach based on a Galerkin procedure, which allows the use of only one mode in the ROM decomposition. Basis function of the Galerkin decomposition is obtained through the DQM decomposition. The obtained ROM is utilized in combination with the Finite Difference Method to simulate the limit cycle solutions of the microactuator. The novel ROM is applied to study cases provided in the literature and compared with classical Galerkin technique.

Keywords: MEMS, ROM, Nonlinear dynamics, Galerkin, DQM, FDM, Microbeam, Limit-cycle solution.

1   Introduction

Over the last years, micro devices had been largely utilized as a key component of micro-actuators, sensors, RF devices etc... The main features of microtechnology using electric actuation is the electro-mechanical coupling which is particularly dominant in small scale. Moreover, MEMS devices have many attractive advantages for instance small size and weight, good performance and low energy requirement. However, the design of these microsystems is particularly challenging because of their complex modeling and simulation. In fact, it has been proven that strong nonlinear phenomenon occur when electrostatic actuation is used (Nayfeh et al. 2007). For these reasons, a descent modeling strategy should be used to conserve the system's nonlinearity during the discretization step and at the same time allows a reduced-order representation of the MEMS device.

Nayfeh et al. (2005) reviewed several techniques to produce reduced-order models for MEMS application. They reported what they call node and domain methods. The node method uses space discretization while domain method rely on modal analysis. Younis et al. (2003) showed that using a Galerkin-based technique produces precise reduced-model for MEMS microactuators. The convergence was obtained with the first three symmetric linear mode shapes. Najar et al. (2005) demonstrated that using a node method, such as the Differential Quadrature Method (DQM), leads to accurate reduced-order system with only three ODEs. However, unlike the Galerkin approach, the DQM model showed interaction with high order modes at large orbits.

In this paper, we intend to combine the node and domain method by replacing the linear mode shape classically used in the Galerkin approach by the one calculated using the DQM and in which first order of the systems nonlinearity has been included. We start by formulate the problem of a doubly clamped beam using the Euler-Bernoulli beam theory. Next, we apply the DQM decomposition in order to discretize the space derivative. We solve the linear eigenvalue problem and obtain non-dimensional natural frequencies and mode shapes of the beam. We use the calculated mode shape as a basis functions in the Galerkin procedure. Then we apply the FDM to calculate limit-cycle solution. Our novel approach is shown to be accurate and fast converging compared with classical Galerkin decomposition used in the previous published literature.

2   Problem Formulation

We propose to study the dynamic response of electrically actuated double clamped microbeam as shown in Fig. 1. The system is composed by an upper movable electrode and a fixed substrate. It is connected to a voltage source than force the upper beam to deflect toward the substrate.
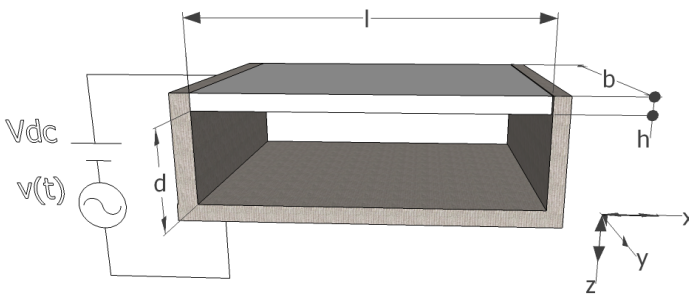
Fig. 1 Schematic view of electrically actuated microbeam

We use the Euler-Bernoulli beam theory in order to derive the governing equation of motion. We also use the von Karman strain to express the extension along with the cross section rotation, given by (Nayfeh and Pai 2008):

$$e = u' + \frac{1}{2} w'^2$$

$$\theta(x,t) = -w'$$

(1)

here prime (') denotes differentiation with respect to x. The transverse deflection is represented by w and the axial displacement is given by u. We express the virtual kinetic energy δK, the virtual potential energy δU and work done by external loads δV as:

$$\delta K = \int_0^L \left(m\dot{u}\delta\dot{u} + m\dot{w}\delta\dot{w} + J(\dot{w}' - \dot{u}'w')((1-u')\delta w' - w'\delta u') \right) dx$$

$$\delta U = \int_0^L \left(EA\left(u' + \frac{1}{2}w' - \frac{1}{2}u'w'^2 \right)\left((1-\frac{1}{2}w'^2)\delta u' + (1-u')w'\delta w' \right) \right.$$

$$+ EI\left(w'' - u'w'' - u''w' \right)\left(\delta w''(1-u') - \delta u'w'' - \delta u''w' - u''\delta w' \right) + c\frac{\partial w}{\partial t}\delta w) dx$$

$$\delta V_e = \int_0^L \frac{\xi b(V_{dc} + v(t))^2}{(d-w)^2} \delta w dx$$

(2)

here over dot denotes differentiation with respect to t. parameters m, b, d, E, I, A and c are the microbeam mass, width, air gap distance between the two electrodes, effective Young modulus, second moment of area, cross section area and viscous damping, respectively. Now applying the Hamilton principle, expanding the result for small displacement by keeping up to cubic terms, carrying out multiple integrations by parts and using boundary conditions of the doubly clamped microbeam yield the following governing equation of motion:

$$\ddot{w} + \bar{c}\dot{w} + w^{(4)} = w''\left(N_0 + \alpha_1 \int_0^L w'^2 dx \right) + \alpha_2 \frac{(V_{dc} + v(t))^2}{(1-w)^2}$$

(3)

with boundary conditions:

$$w(0,t) = w(1,t) = 0$$

$$w'(0,t) = w'(1,t) = 0$$

For convenience, Equation (3) is normalized using the following and parameters:

$$w = \frac{\tilde{w}}{d}, x = \frac{\tilde{x}}{L}, \tau = \sqrt{\frac{mL^4}{EI}}, \bar{c} = \frac{c\tau}{m}, \alpha_1 = \left(\frac{d_0}{l_0} \right)^2, \alpha_2 = \frac{6l_0^4}{d^3 Eh^3}$$

3   Linear Eigenvalue Problem

In order to calculate natural frequencies and mode shapes of the structure we first solve the static equation. It is obtained by letting all time derivatives equal to zero in Equation (3). We use then the DQM to discretize the space with $n= 9$ grid points using Chebychev-Gauss-Lobatto discretization. Then, we apply Newton-Raphson technique to solve the obtained set of algebraic equations. Next, we formulate the linear eigenvalue problem by linearizing the non-dimensional equation of motion around the equilibirium position and writing the transverse deflection as a combination of static component and a dynamic component written in the harmonic form as: $w_d(x,t) = \phi(x)e^{i\omega t}$. Applying the DQM and Newton-Cotes formula for the integral term, we obtain:

$$
\sum_{j=1}^{n} A_{i,j}^{(4)}\phi_j - \omega^2\phi_i = \sum_{j=1}^{n} A_{i,j}^{(2)}\phi_j \left[N_0 - \alpha_1 \sum_{p=1}^{n}\sum_{q=1}^{n} C_p w_p^s A_{p,q}^{(2)} w_q^s \right]
$$
$$
-\alpha_1 \sum_{j=1}^{n} A_{i,j}^{(2)}\phi_j \left[\sum_{p=1}^{n}\sum_{q=1}^{n}\sum_{r=1}^{n} C_p A_{p,q}^{(1)} A_{p,r}^{(1)} w_q^s \phi_r \right] + 2\alpha_2\phi_i \frac{V_{dc}^2}{(1-w_s)^3}
$$

(4)

With boundary conditions:

$$
\phi_1 = \phi_n = 0
$$
$$
\sum_{j=1}^{n} A_{1,j}^{(1)}\phi_j = \sum_{j=1}^{n} A_{n,j}^{(1)}\phi_j
$$

where ϕ represents the mode shape of the beam and ω its associated natural frequency. Following the work of (Najar et al. 2015), we apply DQM to the eigenvalue problem and solve the system for the n-4 first natural frequencies and associated mode shapes. For a high level of accuracy of the solution we choose n=25.

In Fig. 2 we compare the normalized fundamental natural frequency obtained using DQM with the results obtained by Galerkin decomposition using five symmetric modes (Nayfeh et al. 2005) and experimental results performed by Tilman and Legtenberg (1994). The microbeam parameters are given in Table 1. This superimposition shows a perfect agreement between our analytical approach and experimental results found in the literature. Besides, the proposed technique is computationally less costly than the classical Galerkin approach.

Table 1 Microbeam parameters

Parameters	Value
Young modulus of Silicon	166×10^9 N/m^2
Microbeam length	510 µm
Microbeam width	100 µm
Microbeam thichness	1.5 µm
Air permittivity	8.854×10^{-12}
Air gap	1.18 µm
Axial force	8.7 N
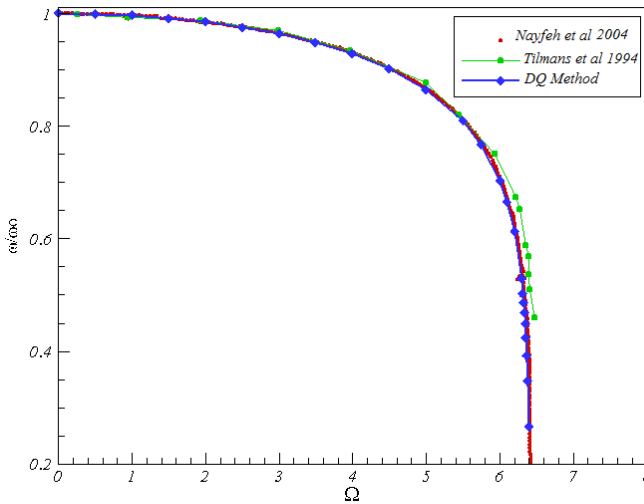
Fig. 2 Normalized fundamental natural frequency calculated using DQM and compared with results given by five symmetric modes with Galerkin procedure (Nayfeh et al 2005) and experimental data (Tilmans et al 1994)

4   Dynamic Behavior of the Electrically Actuated Beam

To simulate the dynamic response of the microstructure under the effect of a DC and AC voltages, we first apply DQM on Equation (3) then we use a ROM based on one mode Galerkin decomposition where the non-dimensional mode shape and natural frequency are solutions of the previous EVP. Then we multiply the resulting equations by $\phi_1(x)$ and integrate the outcome from $x=0$ to 1. Since we are manipulating a discretized system of ODEs and as long as the mode shape is discrete, we use the Newton-Cotes formula to approximate the integral term, that is,

$$\int_0^1 \phi_1(x)dx \approx \sum_{i=0}^{n} C_i\phi_{1i} \tag{6}$$

where:

$$C_i = \int_0^1 \prod_{v=1; v \neq i}^{n} \frac{x - x_v}{x_i - x_v} dx \tag{7}$$

and ϕ_{1i} is the function value of the first mode shape at point x_i. We note that the Newton-Cotes weights use the same number of grid points as the DQM. Then we apply an FDM technique to discretize the time derivative and use a Newton-Raphson technique to solve the set of ODEs given by

$$\left(\frac{q_{k+1} - 2q_k + q_{k-1}}{h^2} + \overline{c}\,\frac{q_{k+1} + q_{k-1}}{2h} \right) \sum_{j=1}^{n} C_j\phi_{1j}^2 + q_k \sum_{j=1}^{n} C_j\phi_{1j} \sum_{l=1}^{n} A_{jl}^{(4)}\phi_{1l}$$

$$= N_0 q_k \sum_{i=1}^{n} C_i\phi_{1i} \sum_{j=1}^{n} A_{ij}^{(2)}\phi_{1j} + \alpha_2 \sum_{j=1}^{n} C_j\phi_{1j} \frac{(V_{dc} + v(t))^2}{(1 - q_k\phi_{1j})^2} \tag{8}$$

$$- \alpha_1 \left(q_k^3 \sum_{j=1}^{n} C_j\phi_{1j} \left(\sum_{l=1}^{n} A_{jl}^{(2)}\phi_{1l} \right) \sum_{r=1}^{n} C_r\phi_{1r} \left(\sum_{i=1}^{n} A_{ri}^{(2)}\phi_{1i} \right) \right)$$

And the boundary conditions are:

$$\phi_{11} = \phi_{1n} = 0 \tag{9}$$

$$\sum_{j=1}^{n} A_{1,j}^{(1)}\phi_{1j} = \sum_{j=1}^{n} A_{n,j}^{(1)}\phi_{1j} = 0$$

here $h = \dfrac{2\pi}{N\Omega}$ is step size of the FMD scheme and N is the number of points that discretize the limit-cycle orbit and Ω is the excitation frequency. q_k represents the modal coordinate for $k = 1,.., N$.

Fig.3 shows a softening behavior governing the dynamic response of the electrically actuated microbeam. It shows also a superposition of results obtained by applying our ROM and results of Nayfeh et al (2007) where classical Galerkin decomposition is used with three symmetric modes to ensure convergence of solutions. However, in the proposed ROM only one mode is sufficient for the solution to converge.
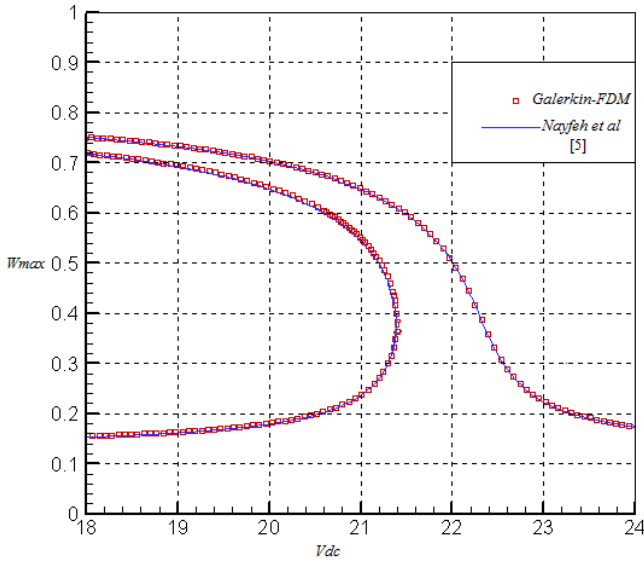
Fig. 3 Frequency response function of the microbeam when *Vdc=3.5V* and *Vac=0.1V*
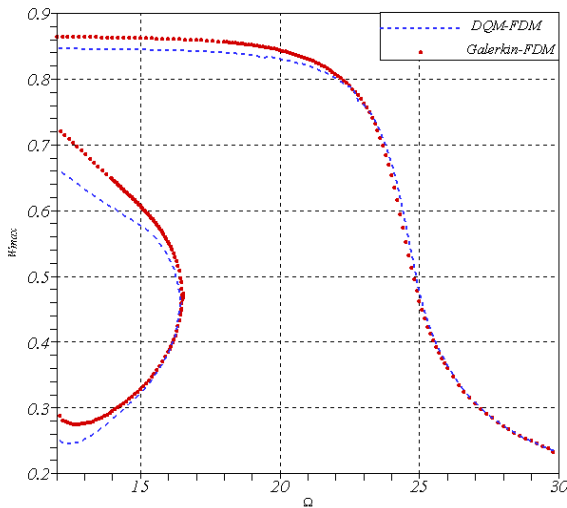
Fig. 4 Frequency response function of the microbeam when *Vdc=3.5V and Vac=1V*

Fig. 4 illustrates a softening behavior of the microbeam due to the highly applied voltage. The figure shows also an acceptable agreement between results using our approach and those using FDM-DQM given by Najar et al (2010). The observed difference is due to the fact that higher order interaction is captured by DQM method while the proposed method only consider first mode resonance.

5   Conclusion

We proposed a novel analytical approach the Galerkin procedure where the test function taken as the mode shapes are estimated using the DQM. The proposed approach can be utilized to study the dynamic behavior of MEMS devices. It uses only one mode in the Galerkin decomposition and thereby it reduces considerably the complexity of the problem and the computational time while in other cases convergence is obtained only by three to five modes. The proposed ROM was validated by results found in the literature, among them experimental findings.

References

Najar, F., Nayfeh, A.H., Abdel-Rahman, E.M., Choura, S., El-Borgi, S.: Nonlinear Analysis of MEMS Electrostatic Microactuators: Primary and Secondary Resonances of the First Mode*. Journal of Vibration and Control 16(9), 1321–1349 (2010)

Najar, F., El-Borgi, S., Reddy, J.N., Mrabet, K.: Nonlinear nonlocal analysis of electrostatic nanoactuators. Composite Structures 120, 117–128 (2015)

Nayfeh, A.H., Younis, M.I., Abdel-Rahman, E.M.: Reduced-order models for MEMS applications. Nonlinear Dynamics 41(1-3), 211–236 (2005)

Nayfeh, A.H., Younis, M.I., Abdel-Rahman, E.M.: Dynamic pull-in phenomenon in MEMS resonators. Nonlinear Dynamics 48(1-2), 153–163 (2007)

Nayfeh, A.H., Pai, P.F.: Linear and nonlinear structural mechanics. John Wiley & Sons (2008)

Tilmans, H.A., Legtenberg, R.: Electrostatically driven vacuum-encapsulated polysilicon resonators: Part II. Theory and performance. Sensors and Actuators A: Physical 45(1), 67–84 (1994)

Younis, M.I., Abdel-Rahman, E.M., Nayfeh, A.: A reduced-order model for electrically actuated microbeam-based MEMS. Journal of Microelectromechanical Systems 12(5), 672–680 (2003)

Part IV

**Dynamics and Vibration
of Mechanical Systems**

Dynamic Amplification of an Orthotropic, Multi Span Bridge Deck under Moving Truck with Tandem Axles

Youcef Fisli[1], Abdelouahab Rezaiguia[1], Salah Guenfoud[1],
Debra F. Laefer[2], and Mounia Kaddeche[1]

[1] Applied Mechanics of New Materials Laboratory, Guelma University,
 P.O.B 401, Guelma 24000, Algeria
 `a.rezaiguia@gmail.com`
[2] Urban Modeling Group, School of Civil, Structural and Environmental Engineering,
 University College Belfield, Dublin 4, Ireland
 `debra.laefer@ucd.ie`

Abstract. Vehicles crossing bridges at high speeds can cause significant dynamic effects and must be studied by accurately simulating the interactive, dynamic responses of the bridge deck and the load-applying vehicles. Specifically, a multi-span, orthotropic, bridge deck during truck loading is investigated to better understand the dynamic interaction between moving vehicles with tandem axles and highway bridge decks. The vehicle is modeled by a three-dimensional dynamic system with tandem axles with 9 degrees of freedom. The bridge deck is modeled by a thin, orthotropic, multi-span plate. The road surface irregularities are modeled by a random function characterized by a spectral roughness coefficient and power spectral density. The modal method is used to solve the equation of motion of the bridge deck. Equations of motion of the vehicle are obtained using a virtual work principle. The coupled equations of motion vehicle/bridge deck are integrated numerically by Newmark's method. A computational algorithm in FORTRAN is used to solve the integrated equations of motion in a decoupled, iterative process. A numerical example of an orthotropic, three-span bridge deck, excited in nine degrees of freedom truck is presented. The resulting distribution of the Dynamic Amplification Factor on the bridge deck does not reflect any particular trend, because high values of the DAF can be obtained at points where the vertical displacement is small. The DAF is significant only under the interaction force. Thus, the road surface roughness had a significant influence on the dynamic vehicle/bridge deck interaction forces.

Keywords: dynamic interaction, orthotropic bridge deck, vehicle, tandem axles.

523

1   Introduction

The difference in a structure's response under dynamic loading versus static loading is described as its Dynamic Amplification Factor (DAF) and is an especially important phenomenon in the design and analysis of bridges. The DAF caused by vehicles depends on several factors: pavement roughness and singular periodic irregularities of the surface, irregularities of the wheels directly, each vehicle's mass, and speed, as well as the stiffness and damping of the suspension system of the vehicle. The dynamic response of a bridge depends on span lengths, the natural frequencies of vibration, support types, soil-structure interaction, the physical condition of the bridge, and the viscous damping, etc, (Isabel 2001).

    To investigate these issues Zhu and Law (2002) modeled the deck of a multi-span highway bridge by a rectangular orthotropic plate with rigid, intermediate supports. Their vehicle was modeled with a three-dimensional dynamic system with seven degrees of freedom. They studied the influence of the position of the vehicle track on the dynamic response of the bridge and the influence of running speed and road surface irregularities on the dynamic amplification factor of the bridge. In related work Yang et al. (2004) studied the extraction of fundamental frequencies of a bridge from the dynamic response due to the passage of the vehicle; the objective was to comprehend the influence of the vehicle speed on the frequencies of the bridge. They showed in both analytical and finite-element studies that the bridge frequency can be extracted from the vehicle acceleration spectrum. Subsequently, Cai et al. (2007) developed a fully automatic coupled vehicle/bridge model. The methodology was validated with practical experiments on a typical bridge. The results of the experiments showed that this coupled model reliably predicted the dynamic response of bridges by taking into account the roadway irregularities and concluded that the initial conditions of the incoming vehicles on the bridge have a significant influence.

    Since then, Yin et al. (2010) presented a method to analyze the non-stationary random response of bridges using the equivalence of a covariance technique. In that, they employed a model of the vehicle with two axles and analyzed three typical bridge models. Numerical results indicated that the non-stationary, random response amplitude of wheels is proportional to the vehicle speed. They also showed that employing a stationary process to model the disturbance of the roadway profile at different speeds can both underestimate and overestimate the dynamic effects. In related work, Rezaiguia (2008) studied the vibro-acoustic behavior of a multi-span, highway bridge during the passage of vehicle. As part of this, the inclusion of the bridge-vehicle dynamic interaction and random irregularities of the track pavement were investigated.

    In this context, this paper investigates the dynamic behavior of a multi-span bridge deck during a passing truck and taking into account the dynamic interaction truck-bridge and random irregularities of the highway profile. The bridge deck is modeled as an orthotropic three-span plate. The truck is modeled dynamically with nine degrees of freedom and tandem axles at the rear. The road surface

roughness is modeled by a random function characterized by a power spectral density and spectral roughness coefficient. The modal approach coupled with a numerical integration by Newmark method is used to solve the coupled equations of bridge-truck motion because it is an unconditionally stable direct method of maximum precision. Solving these equations was achieved in an uncoupled manner using iterative calculations.

2   Modeling

2.1   Vehicle Model

The vehicle is modeled with a dynamic, lumped-mass system. The three-dimensional (3D), three-axle vehicle with a tandem axle has 9 degrees of freedom and consists of a rigid block supported by 6 wheels, as shown in Fig.1. The rigid body representing the truck chassis has three degrees of freedom (z_{v1}, z_{v2}, z_{v3}) to describe the displacements and rotations of the chassis. The masses of the axles and wheels are concentrated in lumped masses (m_1 to m_6) within the suspension system, leading to a further six degrees of freedom (z_1, z_2, z_3, z_4, z_5, z_6) to describe the vertical wheel displacements. The tire stiffness is modeled using linear springs and viscous dampers.
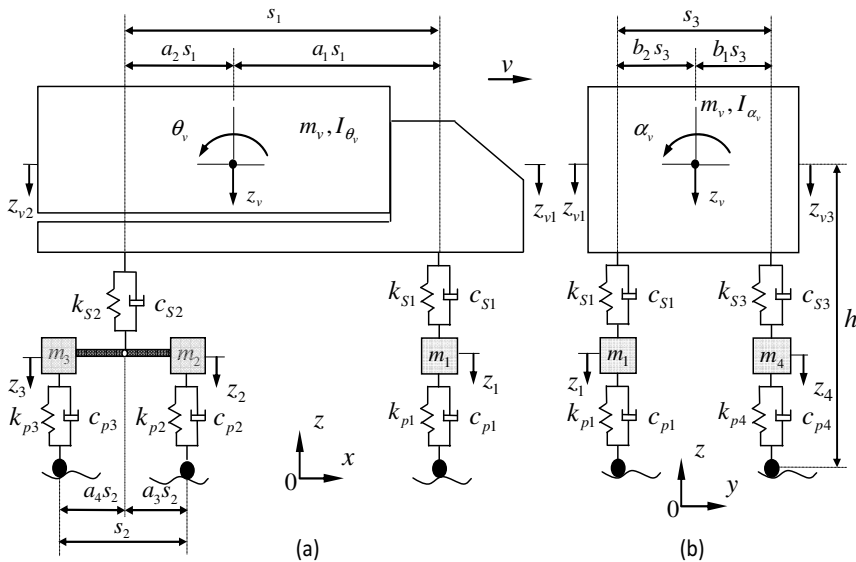
Fig. 1 Three-axle vehicle model with 9 degrees of freedom, (a): side view, (b): front view

In Fig.1, m_i, i = 1, 2, …, 6 are the masses of the wheels with axles of the front and rear axles, m_v, $I_{\theta v}$ and I_{av} are the mass and moments of inertia of rigid block of the truck, k_{pi}, i = 1, 2,…, 6 and c_{pi}, i = 1, 2, …, 6 are the tire rigidities and damping respectively, k_{si}, i = 1, 2, …, 4 and c_{si}, i = 1, 2, …, 4 are the suspension rigidities and damping, respectively.

The equations of motion of the vehicle model are obtained by applying the virtual work principle. The vertical displacements of the vehicle model are calculated from its static, equilibrium position. In Fig.2, the forces and moments acting on the vehicle are presented. The equation of virtual work for any virtual vehicle displacement can be expressed in matrix form as:

$$[M_v]\{\ddot{Z}_v\} + [C_v]\{\dot{Z}_v\} + [K_v]\{Z_v\} = \{F_g\} + \{F^{\text{int}}\} \tag{1}$$

Where $\{F^{\text{int}}\}$ is the interaction force vector applied to the vehicle, $\{F_g\}$ is the force vector caused by the effect of gravity; $[M_v]$, $[C_v]$ and $[K_v]$ are, respectively, the mass, damping, and stiffness matrices of the vehicle, and $\{Z_v\}$ is the vertical displacement vector of the vehicle's degrees of freedom.
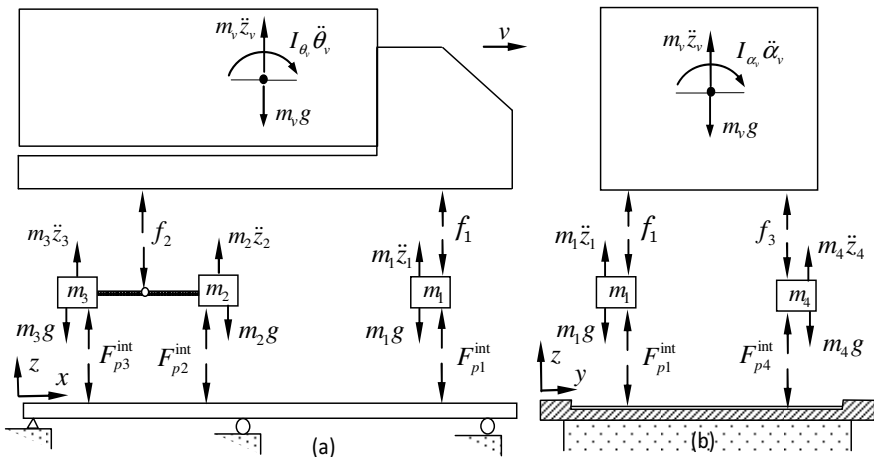
Fig. 2 Dynamic equilibrium of forces and moments, (a): side view, (b): front view

2.2 Bridge Deck Model

The bridge deck is modeled as a multi-span, orthotropic, rectangular plate. The bridge is continuous on the supports, simply supported in x = 0 and x = l and free in y = 0 and y = b (Fig. 3). The bridge has a linear elastic behavior, and the secondary effects (shearing and inertia of rotation) are neglected. The intermediate supports are linearly rigid and orthogonal at the free edges of the

bridge. As the dimensions (length and width) of the bridge deck are much larger compared to its thickness, the thin plate theory is used. The equation of motion of the bridge deck can be written as follows:

$$\overline{m}\frac{\partial^2 w}{\partial t^2} + c\frac{\partial w}{\partial t} + D_x\frac{\partial^4 w}{\partial x^4} + 2H\frac{\partial^4 w}{\partial x^2 \partial y^2} + D_y\frac{\partial^4 w}{\partial y^4} = -\sum_{k=1}^{nf} F_{pk}^{int}\delta(x - x_k(t), y - y_k) \qquad (2)$$

where $\overline{m} = \rho h$ is the mass density of the plate; c is the viscous damping coefficient of the bridge deck; $D_x = E_x h^3/12(1 - v_{xy}v_{yx})$ and $D_y = E_y h^3/12(1 - v_{xy}v_{yx})$ are flexural rigidities according to x- and y-directions, respectively; $H = v_{xy}D_y + 2D_{xy}$ is the equivalent flexural rigidity; v_{xy} and v_{yx} are the Poisson's ratios according to x- and y-directions respectively; $D_{xy} = G_{xy}h^3/12$ is the torsional rigidity of the bridge deck; G_{xy} is the shear modulus for the x-y plane, E_x and E_y are the Young's moduli according x-and y-directions respectively; F_{pk}^{int} is the interaction force between the kth wheel of the vehicle and the bridge, $(x_k(t), y_k(t))$ is the position of the kth interaction force on the bridge.
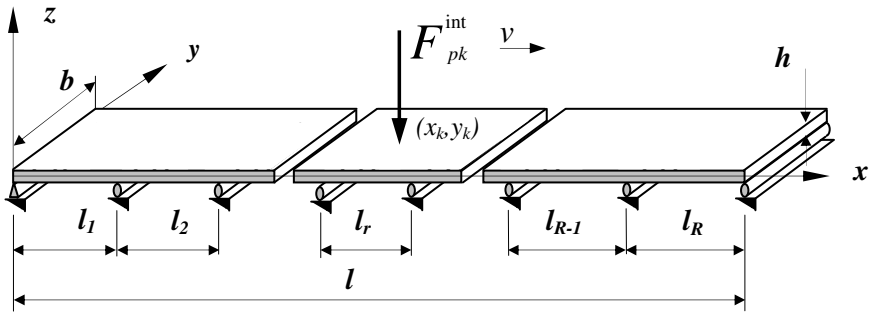
Fig. 3 Model of the continuous multi-span bridge deck

Appling the modal superposition method to the bridge deck, the vertical displacement of the orthotropic plate can be written as follows:

$$w(x, y, t) = \sum_{i=1}^{n} \sum_{j=1}^{m} \phi_{ij}(x, y) q_{ij}(t) \qquad (3)$$

where $\phi_{ij}(x, y)$ are the mode shapes of a multi-span, continuous, orthotropic plate (Rezaiguia and al 2012), and $q_{ij}(t)$ are the generalized coordinates.

Substituting equation (3) into equation (2), multiplying by $\phi_{kl}(x, y)$, integrating over the bridge deck surface, and applying the orthogonality conditions of mode shapes, the modal decoupled equations of the system are obtained, as shown in eq. (4).

$$M_{ij}\ddot{q}_{ij} + C_{ij}\dot{q}_{ij} + K_{ij}q_{ij} = F_{ij} \tag{4}$$

where M_{ij}, C_{ij} and K_{ij} are the modal mass, modal damping, and modal stiffness of the bridge deck, respectively, and F_{ij} are the modal interaction forces.

2.3   Road Surface Roughness

The road surface roughness is modeled by a random function as per equation 5.

$$r(x_k) = \sum_{i=1}^{N} \sqrt{4A_r \left(\frac{2\pi i}{L_c \omega_{s0}} \right)^{-2} \frac{2\pi}{L_c}} \cos(\omega_{si} x_k + \theta_i) \quad , k = 1, \ ..., 6 \tag{5}$$

where A_r is the spectral roughness coefficient (m^3/cycle) whose value is chosen depending on the road condition, ω_{s0} is the discontinuity pulsation ($\omega_{s0} = 1/2\pi$ cycle/m), ω_{si} is the wave number ($\omega_{si} = 2\pi i/L_c$ cycle/m). Generally L_c is equal to $2l$ (m), where l is the length of the bridge (m). N is the number of descritization points in wave number domain; and θ_i is a random variable that varies between 0 and 2π.

2.4   Vehicle-Bridge Deck Interaction Forces

The interaction force between the bridge and ith vehicle wheel is given by:

$$F_{pk}^{int} = k_{pk} \left[z_k - w(x_k, y_k, t) - r(x_k, y_k) \right]$$
$$+ c_{pk} \left[\dot{z}_k - \frac{\partial w}{\partial t}(x_k, y_k, t) - \left(\frac{\partial w}{\partial x} + \frac{\partial r}{\partial x} \right)_{x=x_k, y=y_k} \dot{x}_k \right] \quad k = 1, \ ..., 6 \tag{6}$$

where $w(x_i(t), y_i(t), t)$ is the vertical bridge displacement under the ith wheel, $r(x_i(t), y_i(t))$ is the road surface roughness under the ith wheel, and z_i is the vertical displacement of the ith wheel.

3   Solving Equations of Motion

To solve the coupled equations of motion of the bridge deck and the vehicle, Newmark's numerical integration method was applied. To achieve this, an

algorithm was developed for solving coupled equations of motion in a decoupled manner and an iterative calculation process.

4   Numerical Example

In this example, the dynamic behavior of a deck slab bridge is modeled by a three-span orthotropic rectangular plate was excited with a moving vehicle modeled by a dynamic model with nine degrees of freedom. The equivalent properties of the deck slab are as per Rezaiguia (2008): $l = 78\ m$, $l_1 = l_3 = 24\ m$ and $l_2 = 30\ m$, $b = 13.715\ m$, $h = 0.212\ m$, $\rho = 3265$ kgm^{-3}, $D_x = 2.41 \times 10^9\ Nm$, $D_y = 2.18 \times 10^7\ Nm$, $D_{xy} = 1.14 \times 10^8\ Nm$, $v_{xy} = 0.3$, $E_x = 3.06 \times 10^{12}\ N/m^2$, $E_y = 2.76 \times 10^{10}\ N/m^2$, $G_{xy} = 1.45 \times 10^{11}\ N/m^2$. The natural frequencies and mode shapes of three-span orthotropic bridge deck were calculated with recently developed approach based on the modal method taking into account the effect of intermodal coupling neglected in previous similar studies. The first ten natural frequencies of the deck slab were as reported in Rezaiguia and Laefer (2009): 4.13, 5.45, 6.30, 7.59, 7.75, 9.77, 9.08, 11.26, 11.97, and 15.07. The vehicle model parameters were assigned as per Broquet (1999): $m_v = 248000\ kg$, $m_1 = m_4 = 800\ kg$, $m_2 = m_5 = 1200\ kg$, $m_3 = m_6 = 1200\ kg$, $I_{\theta v} = 241359\ kgm^2$, $I_{av} = 34878.46\ kgm^2$, $h = 1.8\ m$, $S_1 = 5.55\ m$, $S_2 = 1.8\ m$, $a_1 = 0.71$, $a_2 = 0.29$, $a_3 = a_4 = 0.5$, $b_1 = b_2 = 0.5$, $k_{s1} = k_{s3} = 520000\ N/m$, $k_{s2} = k_{s4} = 2348000\ N/m$, , $k_{p1} = k_{p4} = 2000000\ N/m$, $k_{p2} = k_{p3} = k_{p5} = k_{p6} = 4000000\ N/m$, $c_{s1} = c_{s3} = 12194\ Ns/m$, $c_{s2} = c_{s4} = 40715\ Ns/m$, $c_{p1} = c_{p4} = 4000\ Ns/m$, $c_{p2} = c_{p3} = c_{p5} = c_{p6} = 6928\ Ns/m$.

4.1   Influence of the Loading Mode

Several numerical simulations were performed to identify the influence of the moving load on the dynamic responses of the deck slab bridge. The truck traversed the bridge at a speed of100 km/h along three different paths (Fig. 4).
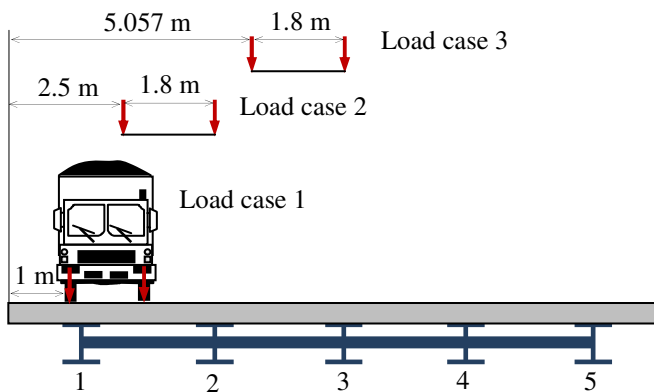
Fig. 4 Vehicle loading

Table 1 shows the influence of the loading mode on the DAF calculated in the middle of each span and in the middle of each girder. The maximum static response is obtained with the truck moving at the very slow speed of 0.01m/s. Based on those conditions, the following was observed

- The DAF is small near the vehicle and higher further away.
- The DAF of the middle of girders 4 and 5 were the highest for the first and second loading cases (DAF= 2.63 and 2.19). This may be due either to torsional modes excited by these loading cases or with the definition itself of the dynamic amplification factor as a response indicator.

Table 1 Distribution of the dynamic amplification factor on the bridge deck

Load case	Span	Dynamic Amplification Factor				
		Girder 1	Girder 2	Girder 3	Girder 4	Girder 5
	1	1.337	1.371	1.501	1.889	**2.630**
1	2	1.072	1.089	1.153	1.288	1.723
	3	1.133	1.157	1.194	1.291	1.778
	1	1.333	1.360	1.435	1.695	**2.191**
2	2	1.072	1.087	1.101	1.199	1.364
	3	1.137	1.135	1.171	1.224	1.402
	1	1.465	1.383	1.377	1.456	1.636
3	2	1.108	1.082	1.081	1.104	1.171
	3	1.154	1.138	1.128	1.168	1.184

Fig. 5 illustrates the influence of the loading mode on the vertical displacement at the middle point of a three-span bridge deck. This image shows the following

- High vertical displacement near the applied load, while the DAF is the opposite (see Table 1 and Fig.5).
- Positive vertical displacement when the load is eccentric (i.e. when the truck is located on either the first or the third span).
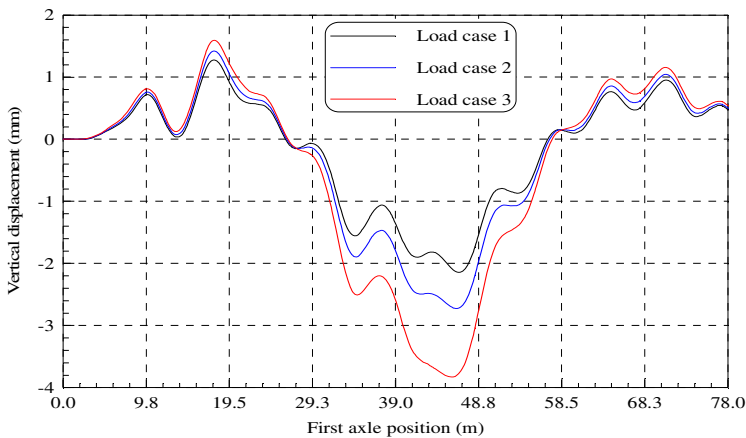
Fig. 5 Vertical displacement at middle of span 2 of girder 3 under different loading

4.2 Influence of Vehicle Speed

Figures 6 show the variation of the dynamic amplification factor of the bridge deck at the middle point girder 1 and 3 and in the middle of the span 2 under different loading cases as a function of the vehicle speed selected between 10 and 160 km/h. the DAF varies little up to vehicle speeds of around 110 km/h after which a rapid increase occurs to a critical speed of 133.2 km/h followed by a rapid decline.
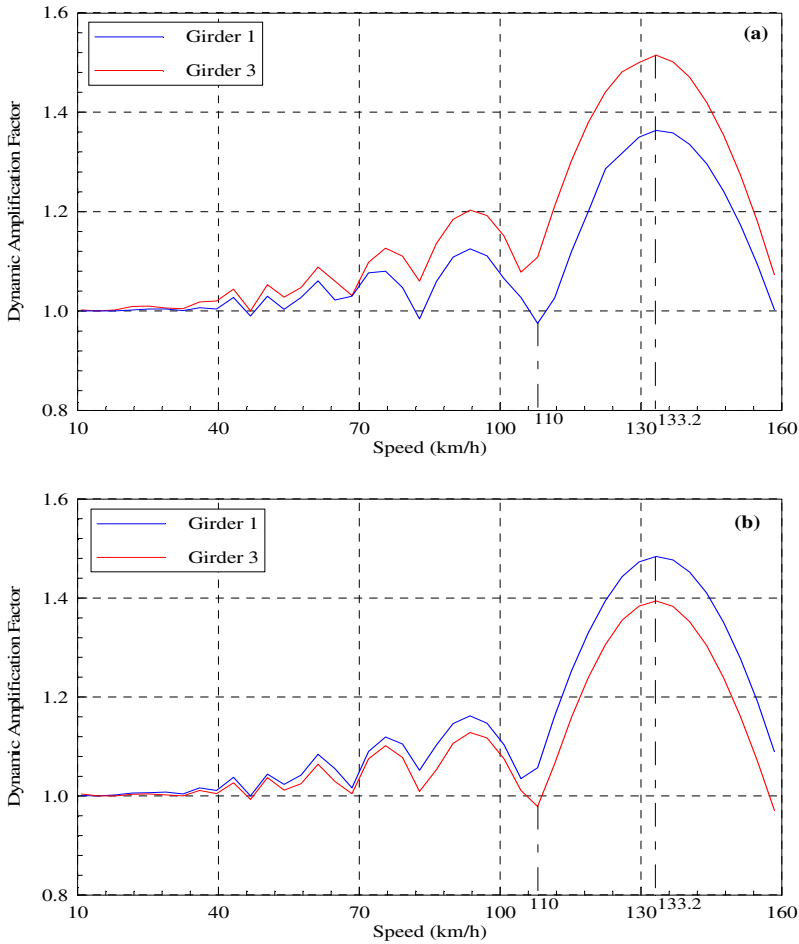
Fig. 6 Dynamic amplification factor at middle of span 2 of girder 1 and girder 3 as function of vehicle speed, (a): load case 1, (b): load case 3

4.3 Influence of Vehicle Mass

The mass difference between the loaded and unloaded truck can cause changes in the dynamic behavior of the bridge deck. To identify the influence of the truck mass on the dynamic response of the bridge deck, three load levels were simulated for the truck used: an unloaded truck (m_v = 8200 kg), a normally loaded truck (m_v= 24800 kg), and an overloaded truck (m_v= 31300 kg). Fig.7 shows the influence of the vehicle mass on the vertical displacement in the middle of the bridge deck. The truck through the bridge according to path of the load case 3 at a speed of 80 km/h. As expected, there is an increase of the vertical displacement in the middle of the bridge deck, especially when the truck is overloaded and located in the central span.
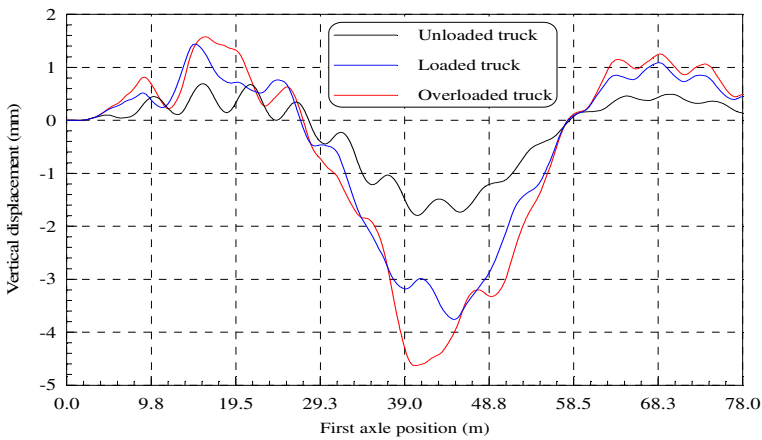
Fig. 7 Vertical displacement at middle of span 2 of girder 3 under different mass vehicle, v_x = 80 km/h, load case 3

Fig. 8 shows the influence of the truck mass on the dynamic amplification factor in the middle of girder 3 and the middle of span 2 with truck speeds from 10 to 160 km/h. Those results demonstrated the following:

- The critical speed corresponding to the maximum dynamic amplification factor decreases with the truck mass: for the unloaded truck, the critical speed was 144 km/h, for the normally loaded truck, the critical speed was 133.2 k/h, and for the overloaded truck, the critical speed was 126 km/h.
- For the critical speed, the DAF was higher in case of the normally loaded truck.
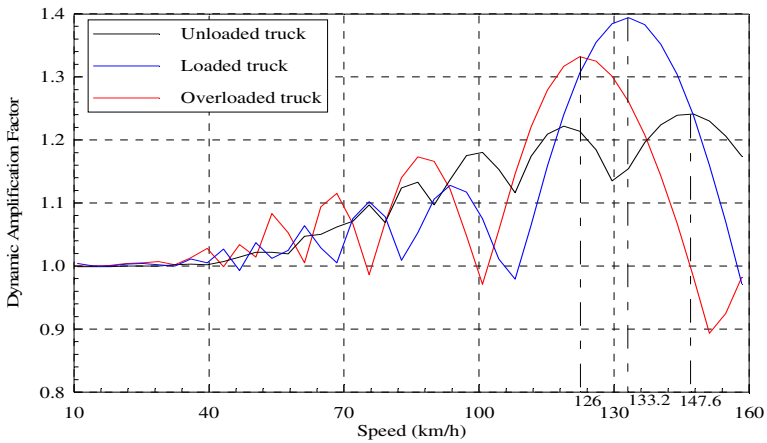
Fig. 8 Influence of vehicle mass on dynamic amplification factors in the middle of the bridge deck

4.4   Influence of Road Surface Roughness

Figure 9 shows the influence of the road surface roughness on the dynamic amplification factor in the middle of span 2, girder 3, for vehicle speeds varying from 10 to 160 km/h. The vehicle passes along the bridge deck under loading case 3. Notably, increased road surface roughness increases the DAF in the tread slab. Additionally at a speed of 133.2km/h and a bad road surface ($A_r = 150 \times 10^{-6}$m^3/cycle), an increase of about 25% of the maximum value of the DAF occurred.
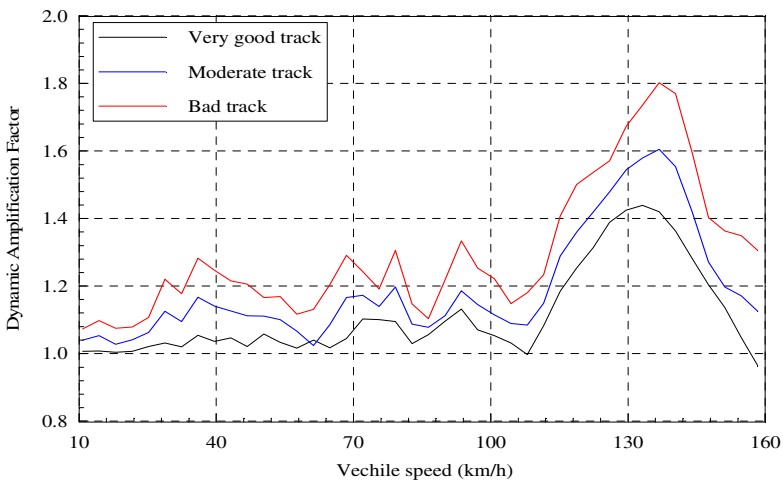
Fig. 9 Influence of the state of the track on the dynamic amplification factor in the middle of the deck slab for loading case3

Figure 10 shows the variation of the interaction forces exerted by a right rear wheel of the vehicle based on the track condition. The vehicle was moving at a speed of 100 km/h according to load case3.The results showed that changes in the amplitudes of the interaction forces increased significantly with greater track profile roughness. This means that the state of the track can significantly influence the vehicle vibrations than the rolling slab. Additionally, the interaction forces fluctuated around an average value, which corresponded to the static force.
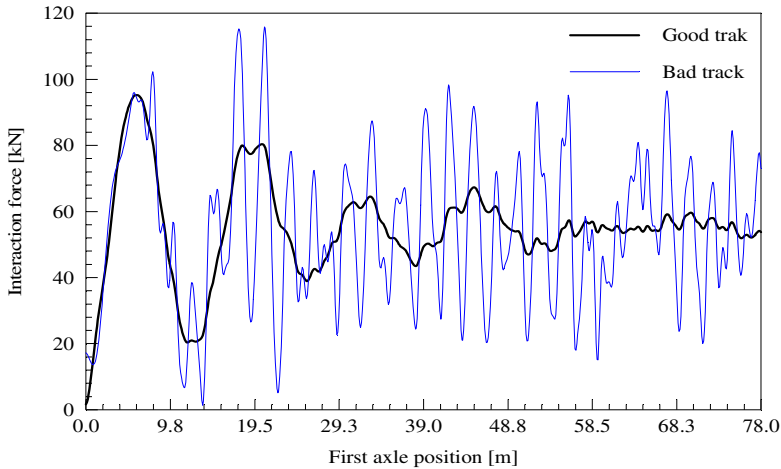
Fig. 10 Interaction force exerted by a right rear wheel of the vehicle, v_x=100 km/h, loading case 3

5   Conclusion

In this paper the dynamic interaction between a moving vehicle (modeled as a nine degree of freedom dynamic system with tandem axles) and a bridge (modeled as a three-span orthotropic plate) was studied taking into account road surface irregularities. The modal method and Newmark's numerical integration were used to solve the coupled equations of bridge-vehicle motion. For this an iterative algorithm is proposed for solving the coupled equations of bridge-vehicle motion in a decoupled manner. Numerical simulations have been performed to study the variation of dynamic amplification factor on the bridge deck. Two major observations were made:

1. The distribution of the dynamic amplification factor on the bridge deck does not reflect a particular tendency, because high dynamic amplification factors can occur in places where the vertical displacement is weak.
2. In the case studied, the critical speed corresponding to the maximum dynamic amplification factor was about 133.2 km/h. This value varies according to the vehicle mass.

References

Isabel, G.T.: Analyse par éléments finis de l'interaction dynamique entre les trains et les ponts ferroviaires. Mémoire de Maître ès en Art, Université Laval, Canada (2001)

Zhu, X.Q., Law, S.S.: Dynamic load on multi-lane bridge deck from moving vehicles. J. Sound Vib. 251, 697–716 (2002)

Yang, Y.B., Lin, C.W., Yau, J.D.: Extracting bridge frequencies from the dynamic response of a passing vehicle. J. Sound Vib. 272, 471–493 (2004)

Cai, C.S., Shi, X.M., Araujo, M., Chen, S.R.: Effect of approach span condition on vehicle-induced dynamic response of slab-on-girder road bridges. Eng. Struct. 29, 3210–3226 (2007)

Yin, X., Fang, Z., Cai, C.S., Deng, L.: Non-stationary random vibration ofbridges under vehicles with variable speed. Eng. Struct. 32, 2166–2174 (2010)

Rezaiguia, A.: Modélisation du comportement vibratoire et acoustique d'un pont de la chaussée lors du passage des véhicules. Thèse de doctorat, Université d'Annaba (2008)

Rezaiguia, A., Fisli, Y., Ellagoune, S., Laefer, D.F., Ouelaa, N.: Extension of semi- analytical approach to determine natural frequencies and mode shapes of a multi-span orthotropic bridge deck. Struct. Eng. and Mechanics 43, 71–87 (2012)

Rezaiguia, A., Laefer, D.F.: Semi-analytical determination of natural frequencies and mode shapes of multi-span bridge decks. J. Sound Vib. 328, 291–300 (2009)

Broquet, C.: Comportement des dalles de roulement des routes en béton sollicitées par le trafic routier. Thèse PhD, Ecole Politechnique Fidéral de Lausane (1999)

Uncertainties Propagation through Robust Reduced Model

Khaoula Chikhaoui[1,2], Noureddine Bouhaddi[1], Najib Kacem[1], Mohamed Guedri[2], and Mohamed Soula[2]

[1] FEMTO-ST Institute, UMR 6174, Applied Mechanics Department,
University of Franche-Comté, 24 Chemin de l'Epitaphe 25000 Besançon France
`{khaoula.chikhaoui,noureddine.bouhaddi,`
`najib.kacem}@femto-st.fr`
[2] National High School of Engineers of Tunis (ENSIT), University of Tunis,
5 Avenue Taha Hussein, BP 56, Bâb Manara, Tunis, Tunisia
`mohamed.guedri@isetn.rnu.tn, soulamed2003@yahoo.fr`

Abstract. Designing large-scale systems in which parametric uncertainties and localized nonlinearities are incorporated requires the implementation of both uncertainty propagation and robust model condensation methods. In this context, we propose to propagate uncertainties through a model, which combines the statistical Latin Hypercube Sampling (LHS) technique and a robust condensation method. The latter is based on the enrichment of a truncated eigenvectors bases using static residuals taking into account parametric uncertainty and localized nonlinearity effects. The efficiency, in terms of accuracy and time consuming, of the proposed method is evaluated on the nonlinear time response of a 2D frame structure.

Keywords: uncertainties, localized nonlinearities, robustness, model reduction.

1   Introduction

In a probabilistic framework, the well-known statistical LHS method (Helton and Davis 2003) allows propagating parametric uncertainties with high level of accuracy. It derives from the Monte Carlo Method (MC) (Rubinstein 1981) and converges faster than the latter since it distributes the sample points more evenly across intervals of equal probability. Nevertheless, the main issue of such method lies on the prohibitive cost of its implementation. The latter depends essentially on the great number of samples of random variables required for best accuracy. To overcome this issue, especially in the case of large-scale systems and iterative dynamic resolution procedures, it is inevitable to use reduced order models. In this context, the standard reduction methods are no longer efficient for designing

models, which incorporate both uncertainties and localized nonlinearities, since standard truncated eigenvectors bases of linear associated models do not contain any information about the latter aspects. Therefore, in order to form robust reduced models, we propose to enrich the standard bases by adding static residual vectors, which take into account the stochastic aspect and the localized nonlinearity effect.

In the literature, Balmès (Balmès 1996) and Masson (Masson et al. 2006) introduced the concepts of evaluating the static contribution of the neglected eigenvectors resulting in a set of additional vectors completing the original Ritz basis to evaluate frequency response of a modified structure. Segalman (Segalman 2007) added to the linear modes a set of basis functions to capture the nonlinearities to reduce the order of dynamical systems with localized nonlinearities. In (Bouazizi et al. 2006), a method based on the equivalent linearization method is applied to predict dynamic responses of structures affected by structural modifications and localized nonlinearities using a reduced basis enriched by static residual vectors.

Several works focus on coupling uncertainty propagation and model reduction methods. Guedri (Guedri et al. 2006) implemented the residuals enrichment technique to take into account uncertainties in the computation of the frequency responses of linear structures using stochastic spectral FE method (SSFEM). In (Maute et al. 2009), a reduced-order model (ROM) is integrated into SSFEM, using a basis spanned by displacements and derivatives of displacements, and implemented to optimize the shape of a linear shell structure.

In this work, the efficiency of the combination between the LHS method and the robust condensation technique, in terms of accuracy and computational time gain, is evaluated on the time response approximation of a frame structure, which contains localized nonlinearities and stochastic design parameters.

2   Robust Reduced Model Dedicated to the Propagation of Uncertainties

The nonlinear dynamic behavior of a mechanical system can generally be represented by the differential equation

$$[M]\{\ddot{y}\} + [B]\{\dot{y}\} + \{f_{\text{int}}\} = \{f_{ext}\} \tag{1}$$

Where $[K]$, $[M]$ and $[B]$ stand for the stiffness, mass and damping matrices of the system, $\{f_{int}\} = ([K]+\{f_{NL}\}(\{y\},\{y\Box\}))\{y\}$ for the internal forces vector and $\{f_{ext}\}$, and for the exciting forces vector.

Resolving the governing equation (1), in time domain, on the full finite element model (FEM) requires high numerical cost, especially when using nonlinear Newmark time integration scheme (Géradin and Rixen 1997). Hence, a reduced order model has to be implemented. Standard condensation techniques are based on the use of truncated eigenvectors bases $[T] = [\varphi_r]$ of the associated linear system, the index r is relative to the reduced term. Therefore, using such bases, in a stochastic case with localized nonlinearities, cannot satisfy the required accuracy.

To overcome this issue, the enrichment of $[\varphi_r]$ by adding a complementary subbasis $[\Delta T]$ is necessary in order to construct a robust basis $[T] = [\varphi_r \perp \Delta T]$.

$[\Delta T]$ is a set of static residual vectors calculated according to the type of enrichment. To take into account localized nonlinear effects, the static residuals must be computed (Bouazizi et al. 2006), according to the following form

$$\left[\Delta T_{NL}\right]_i = \left[K_0\right]^{-1}\{F_i\}, \quad i = 1,...,m \tag{2}$$

where $\{F_i\}$ is the residual force vectors containing unit values in nonlinear degrees of freedom and zeros otherwise, m is the total number of nonlinear degrees of freedom (dofs).

In addition, to take into account stochastic aspect (Guedri et al. 2006), another type of residual vectors

$$\left[\Delta T_S\right] = [R]\left[F_{S_z}\right] \tag{3}$$

must be computed, where $[R] = [K_0]^{-1}-[\varphi_r][\Lambda_r]^{-1}[\varphi_r]^t$ is the static residual flexibility matrix and $[F_{Sz}]$ is a set of force vectors representing the stochastic effects for each stochastic zone (z), $[K_0]$ is the deterministic stiffness matrix and $[\Lambda_r]$ is the spectral one (containing only retained eigenvalues).

Then, the singular value decomposition (SVD) and the normalization of the additional residuals similarly to the standard basis $[\varphi_r]$ are inevitable in order to ensure, respectively, the linear independence (the well-conditioning) and the orthogonality of the different vectors. Consequently, the enriched basis (EB) has the following form

$$[T] = \left[\varphi_r \;\vdots\; \Delta T_{NL} \;\vdots\; \Delta T_S\right] \tag{4}$$

Projecting the time response on this basis, such as $\{y\} = [T]\{q\}$ permits to express the equation of motion (1), at time step $n+1$, in the reduced following form

$$[M]_r\{\ddot{q}\}_{n+1} + [B]_r\{\dot{q}\}_{n+1} + \left(\{f_{\text{int}}\}_r\right)_{n+1} = \left(\{f_{ext}\}_r\right)_{n+1} \tag{5}$$

where $[M]_r = [T]^t [M] [T]$, $[B]_r = [T]^t [B] [T]$, $\{f_{ext}\}_r = [T]^t \{f_{ext}\}$, and $\{f_{int}\}_r = [T]^t([K]+\{f_{NL}\}([T]\{q\},[T]\{\dot{q}\}))[T]\{q\}$ are the reduced matrices and vectors.

Approximating the solution using the Newmark nonlinear time integration scheme and the iterative Newton-Raphson technique consists on minimizing the residual vector

$$R_{n+1} = [M]_r\{\ddot{q}\}_{n+1} + [B]_r\{\dot{q}\}_{n+1} + \left(\{f_{\text{int}}\}_r\right)_{n+1} - \left(\{f_{ext}\}_r\right)_{n+1} \tag{6}$$

The equation (6) can be approximated, for the iteration k, as:

$$\left(\left[K_{eff}\right]_r\right)^k_{n+1} \Delta\{q\}^k = -R^k_{n+1} \tag{7}$$

where $\left(\left[K_{eff}\right]_r\right)^k_{n+1} = \left[\dfrac{\partial R}{\partial\{q\}}\right]_{\{q\}^k_{n+1}}$ is the effective stiffness matrix function of the

tangent stiffness matrix, updated at each iteration,

$$\left(\left[K_T\right]_r\right)_{n+1} = [T]^t \left(\left[\dfrac{\partial\{f_{int}\}_{n+1}}{\partial\{y\}_{n+1}}\right]_{[T]\{q\}^k_{n+1}}\right)[T]. \tag{8}$$

The statistical LHS method (Helton and Davis 2003) of uncertainty propagation consists on computing N successive deterministic responses $\{Y^{(n)} = y(\xi^{(n)}),\ n=1,\ \ldots,\ N\}$ according to a set of N samples of random variables.

Statistical moments can then be computed, such as the mean and the variance (1st and 2nd moment).

The proposed method in this paper consists to combine the LHS uncertainty propagation approach and model reduction by projecting the responses on the robust enriched basis defined above.

3   Numerical Example

In order to valid the proposed method and to illustrate their numerical performances, a 2D frame model is proposed (Fig.1). The mechanical and geometrical properties of the structure are given by: the width $b=3.10^{-2}\ m$ and the thickness $h_0=5.10^{-2}\ m$ of the rectangular section, the length of the beams $L=1.5\ m$, the Young modulus $E_0=210$ GPa and the density $\rho_0=7800\ kg.m^{-3}$. We suppose that the damping is proportional so that the modal damping is $\eta=0.03$ and two localized nonlinear Duffing springs of stiffness $k_{NL} = 10^{20}\ N.m^{-3}$ are linked to the frame structure. Two localized forces with equal amplitude $F(N)=10^3\cos(2\pi f_2 t)$ excite the second eigenmode ($f_2=78.8\ rad.s^{-1}$) of the frame structure. Using two-dimensional beam finite elements (three dofs per node: u_x, v_y, θ_z) to discretize the 2D structure leads to 160 finite elements and a full model of 474 dofs.

Three zones (Fig.1) are supposed to be stochastic: the Young modulus and the density, in the vertical beams, and the thickness in the upper horizontal beam. Their randomness is modeled as

$$E = E_0\left(1+\sigma_E\xi_E\right); \rho = \rho_0\left(1+\sigma_\rho\xi_\rho\right); h = h_0\left(1+\sigma_h\xi_h\right) \tag{9}$$

where ξ_E, ξ_ρ and ξ_h are random variables of respectively lognormal, lognormal and exponential probability distributions and $\sigma_E = \sigma_\rho = \sigma_h = 0.2$ are the considered dispersions.
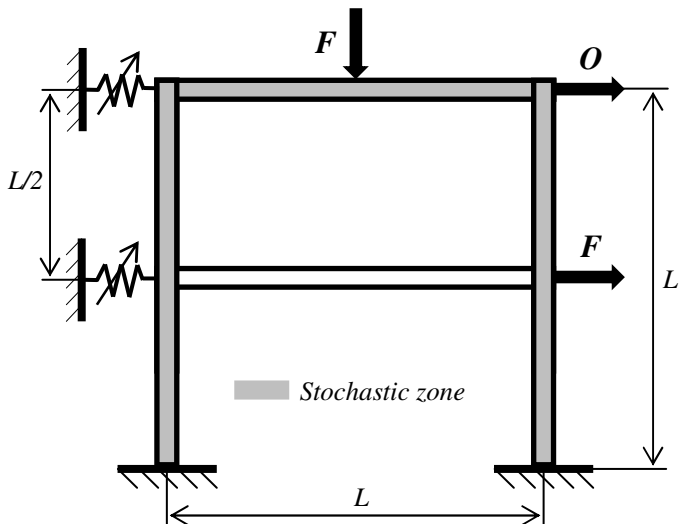
Fig. 1 Frame structure with stochastic parameters and localized nonlinearities

To evaluate the efficiency of the proposed method in nonlinear dynamic analysis, with uncertainties and localized nonlinearities, two different criteria have to be satisfied. The time indicators (Hemez and Doebling 2003)

$$\mathbf{M}_i = \int_{-\infty}^{+\infty} (t-t_s)^i \, y(t)^2 \, dt \,, \tag{10}$$

where i the order of the moment and t_s the temporal shift chosen in our case as $t_s = 0$ allow quantifying the accuracy of the response in terms of amplitude using the total energy $E = M_0$ and periodicity using the central time and the root mean square duration defined respectively by $T = M_1/M_0$ and $D^2 = (M_2/M_0) - (M_1/M_0)^2$.

To evaluate the time consuming, the Central Processing Unit (CPU) time is computed for each implemented method.

The obtained results combining the LHS method, for 1000 samples, and the robust reduced model (LHS-EB) are compared to the reference responses using LHS method, for 1000 sample on the full model (LHS-REF). Several observation dofs are considered; the results below correspond to a chosen dof (Fig. 1, dof O).

Note that high uncertainty and nonlinearity levels are chosen in order to evaluate the accuracy of the enriched basis with respect to the standard one.

The comparison between the deterministic modes and the mean of the stochastic ones through the MAC (Modal Assurance Criterion) matrix, Fig. 2, and the superposition of the deterministic response and the mean of the stochastic one, Fig. 3, illustrate the effect of the uncertainties. In fact, the randomness of the chosen uncertain input parameters affects both the stiffness and the mass matrices.
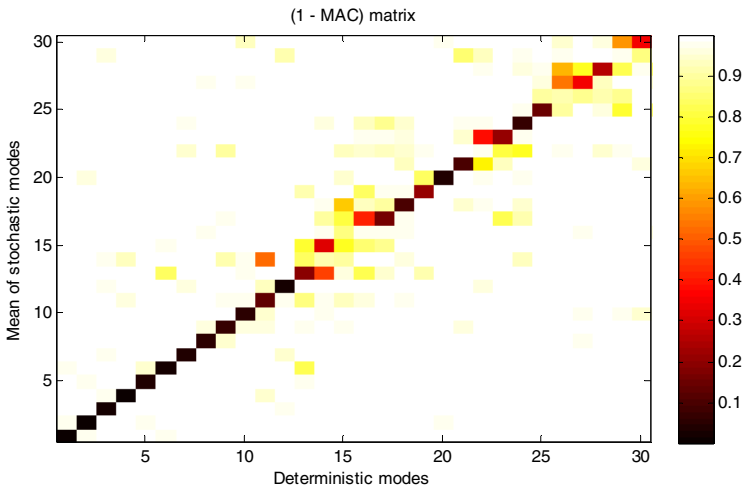
Fig. 2 MAC matrix comparing the deterministic modes and the mean of the stochastic modes
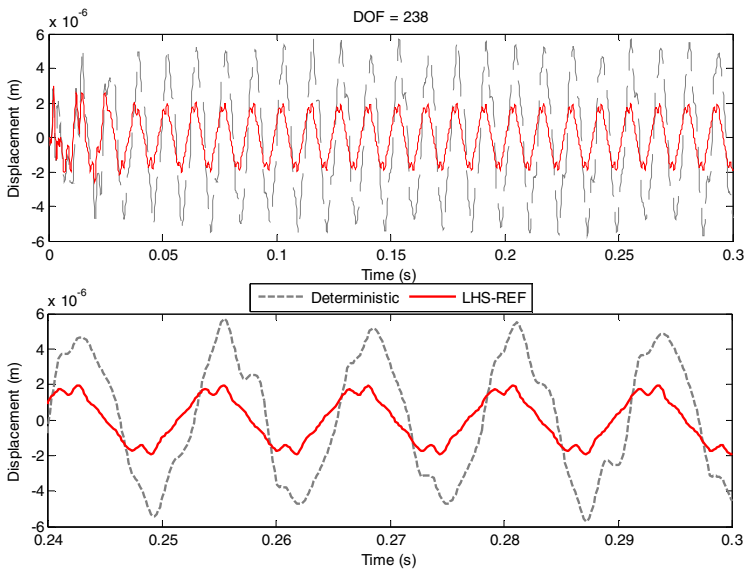
Fig. 3 Mean of the stochastic displacement computed with the full model (LHS-REF) compared to the deterministic model
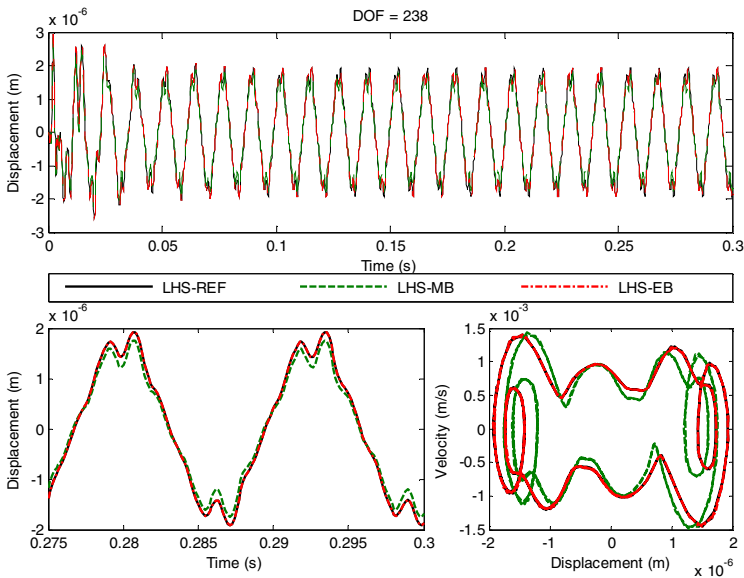
Fig. 4 Mean of the stochastic displacements and phase diagrams computed using the EB (LHS-EB), the standard truncated eigenvectors basis (LHS-MB) and the full model (LHS-REF)

Fig.4 shows the performance of the robust model (57 vectors in the enriched basis EB) by its comparison to the standard basis of same size, with respect to the reference responses obtained with the full model. The standard modal basis (MB) cannot represent the model behavior accurately while the enriched basis (EB) allows it.

The model size, the time indicators (mean values of all dof reponses) and the CPU time are listed in Table 1. The proposed method allows a reduction size ratio of 87.9 % and a computational time gain of 52.7 % with very small errors on accuracy.

Table 1 Model size and evaluation criteria

Method	Model size (dof)	Errors on Time indicators (%)			CPU time (%)
		E	T	D²	
LHS-REF	474	0.00	0.00	0.00	100
LHS-MB	57	0.70	0.10	0.05	39.9
LHS-EB	57	0.00	0.00	0.00	47.3

4   Conclusion

Combining uncertainties propagation and robust model reduction permits to approximate the dynamic behavior of mechanical structures containing stochastic design parameters and localized nonlinearities with a low computing time and without a significant loss of accuracy. The robustness of the model reduction method is achieved with the enrichment of the standard truncated modal basis using static residuals, which permits to take into account both the stochastic and the localized nonlinearity effects. Future work will include the extension of the proposed methodology to complex mechanical structures.

References

Helton, J.C., Davis, F.J.: Latin hypercube sampling and the propagation of uncertainty in analyses of complex systems. Reliability Engineering and System Safety 81, 23–69 (2003)

Rubinstein, R.-Y.: Simulation and the Monte Carlo methods. John Wiley & Sons (1981)

Balmès, E.: Parametric families of reduced finite element models. Theory and applications. Mechanical Systems and Signal Processing 10(4), 381–394 (1996)

Masson, G., Ait Brik, B., Cogan, S., Bouhaddi, N.: Component mode synthesis CMS based on an enriched Ritz approach for efficient structural optimization. Journal of Sound and Vibration 296(4-5), 845–860 (2006)

Segalman, D.J.: Model reduction of systems with localized nonlinearities. ASME Journal of Computational and Nonlinear Dynamics 2(3), 249–266 (2007)

Bouazizi, M.L., Guedri, M., Bouhaddi, N.: Robust component modal synthesis method adapted to the survey of the dynamic behavior of structures with localized nonlinearities. Mechanical Systems and Signal Processing 20, 131–157 (2006)

Guedri, M., Bouhaddi, N., Majed, R.: Reduction of the stochastic finite element models using a robust dynamic condensation method. Journal of Sound and Vibration 297, 123–145 (2006)

Maute, K., Weickum, G., Eldred, M.: A reduced-order stochastic finite element approach for design optimization under uncertainty. Structural Safety 31, 450–459 (2009)

Gérardin, M., Rixen, D.: Mechanical Vibrations: Theory and Application to Structural Dynamics, 2nd edn. John Wiley & Sons (1997)

Hemez, F.M., Doebling, S.W.: From shock response spectrum to temporal moments and vice-versa. In: International Modal Analysis Conference (IMAC-XXI), Kissirnmee, Florida, February 3-6 (2003)

Nonlinear Dynamic Response Analysis of Damaged Laminated Composite Structures

Saber Mahmoudi, Frédérique Trivaudey, and Noureddine Bouhaddi

Applied Mechanics Department, FEMTO-ST Institute - UMR 6174,
University of Franche-Comté-24, chemin de l'Épitaphe, 25000 Besançon, France
{saber.mahmoudi,noureddine.bouhaddi}@femto-st.fr,
frederique.trivaudey@univ-fcomte.fr

Abstract. In this work, a macro modeling is proposed to predict the dynamic response of damaged laminates made of unidirectional orthotropic layers of a polymer matrix reinforced with long fibers. The dynamic behavior of the composite structure is expressed through elasticity coupled with damage based on phenomenological approach for cracked structures. The structure is considered orthotropic but the damage is completely described by a single scalar variable whose evolution law is determined from the maximum dissipation principle. The incremental linear dynamic governing equations are obtained by using the classical Kirchhoff-Love theory of plates. Then, assuming that the damage induces nonlinearity, the obtained nonlinear dynamic equations are solved in time domain by Newmark method where an unconditionally stable scheme and iteration procedure are used. According to the numerical results, the mechanical behavior of the structure significantly change when the damage is taken into account. Under an impact load, damage increases and reaches its highest value with the maximum of the applied load and then remains unchanged. Besides, the eigenfrequencies of the damaged structure decrease comparing to the undamaged ones. This methodology can be used for monitoring strategies and life time estimations of hybrid complex structures because of the damage state is known in space and time.

Keywords: nonlinear dynamics, damage prediction, structural monitoring, laminated structures.

1 Introduction

Composite materials are defined as the combination of more than two different materials having different mechanical properties. This combination is performed so that the resulting material has a better mechanical behavior from that of the individual components. Comparing to metallic materials, composite structures are characterized by a high *resistance / weight* ratio (Reddy 1997) which explains their wide use in the industry. Over the last decades, composite materials are increas-

ingly used especially in high-tech products. As an example, the new project of aircraft such as Airbus A-380, where about 25% of the total weight of the aircraft is made of composite materials. They are characterized by sufficient strength with low density. In addition, they have other characteristics such as their resistance to corrosion and chemical attack. The composite structure is often subject to static or dynamic loads which can affect the mechanical properties and consequently which can change either the static or the dynamic responses (stress distribution and the deformation field or eigenfrequencies and mode shapes). These changes can induce a significant reduction in the structure lifetime. Various damage indicators are used to characterize the change in dynamic characteristics caused by the damage, such as natural frequencies (Vestroni and Capecchi 2000). In 1971, Kulkarni and Frederick (Kulkarni and Frederick 1971) have studied the presence and detection of delamination in a circular cylindrical composite shell through the decrease of eigenfrequencies. This idea was further investigated and deepened by Cawley and Adams (Cawley and Adams 1979). They have suggested that the shift of eigenfrequencies can be considered as a basis for a new nondestructive control technique. The change or the shift in the eigenfrequencies is then considered as an indicator able to report the damage evolution in composite structures. Thus, detection of the location and especially the degree of severity of the damage is of great importance in order to ensure the reliability and safety of service structures. Detecting damage using changes in the dynamic characteristics has been the subject of many research in the last years.

In this paper, a new investigation to predict the dynamic behavior and the damage evolution in composite structures, is proposed and developped. Based on a phenomenological model for cracked structures (Boubakar et al. 2002), the dynamic behavior is expressed through elasticity coupled with damage. The studied structures are made of unidirectional orthotropic layers of polymer matrix renforced with long fibers where the damage is expressed by a single scalar variable. The principal of maximum dissipation is used to determine the evolution of the damage which results in a material nonlinearity. Then, using the classical Kirchhoff-Love theory, the resulting nonlinear formulation is implemented in MATLAB$^{\circledR}$ software. Then, a numerical solution is obtained based on a Newmark unconditionally stable algorithm with a prediction-correction scheme. Several numerical simulations have been performed showing that, under an impact load, damage increases and reaches its highest value with the maximum of the applied load and then remains unchanged. Besides, the eigenfrequencies of the damaged structure decrease compared with those of an undamaged one. Indeed, the displacement of the damaged structure increases due to the decrease in rigidity parameters.

2   Problem Formulation

Initially used for modeling isotropic structures, the plate theories were later extended to model composite structures. A little reminder is provided, in this paragraph, around the formulations used to solve a dynamic problem in the case of

composite structures. These formulations are essentially divided into two categories; those which are based on the Equivalent Single Layer Theory and those that are based on the Layer-Wise theory. The first category includes mainly the Classical Laminate Theory, the First-order (FSDT) and High-order (HSDT) Shear Deformation Theories, while the second category includes the Independent and Dependent layers theories. According to Reddy (Reddy 1997), it is recommended to use a theory from the first category if the global response of the stucture is unknown such as the eigenfrequencies and mode shapes in dynamic analysis. In the present work, The *FSDT* is retained for its simplicity of implementation and also because of the small thikness of the studied structures. So, the displacement field of a plate is written as follow:

$$\{\underline{\mathbf{u}}(x, y, z, t)\} = \left\{ \begin{array}{c} u(x, y, z, t) \\ v(x, y, z, t) \\ w(x, y, z, t) \end{array} \right\} + z \left\{ \begin{array}{c} \varphi_y(x, y, t) \\ -\varphi_x(x, y, t) \\ 0 \end{array} \right\} \tag{1}$$

Where $\varphi_x(x, y, t)$ and $\varphi_y(x, y, t)$ are the rotation, respectively, with respect to the **x** and **y** axes. The mechanical behavior is considered elastic. Noting that E_p and E_c are respectively the total potential and the kinetic energies of the structure, and according to virtual work principle, then:

$$\delta \int_{t_1}^{t_2} (E_p + E_c) dt = 0 \tag{2}$$

The problem is discretized by finite elements method using a quadrangular element *Serendip Q8* with eight nodes. The choice of this type of element is justified by its excellent performance in finite element modeling of thin and thick composite stuctures (CHEE 2000). Using the Gaussian integration method with 4 integration points where the integration weight is assumed equal to 1, and a single point in the thickness direction located in the middle of each layer thickness, the global stiffness $[K]$ and mass $[M]$ matrices of the laminated structure consisting of "n" layers are obtained. In addition, the damping matrix is supposed proportional, and it is expressed by $[B] = \alpha_1[K] + \alpha_2[M]$. Finally, the dynamic equation of motion can be written as :

$$[M]\ddot{u} + [B]\dot{u} + [K(D)]u = F \tag{3}$$

The damage describes the creation of cavities and cracks within the structure (Lemaitre et al. 2001), that is in other words, the development of micro-discontinuities in the structure during the loading F. According to Boubakar *et al* (Boubakar et al. 2002), the effect of the damage on the elastic behavior depends on the micro-cracks opening mode as depicted in figue 1.

Then, a three parameters H_{22}, H_{44} and H_{66} are introduced to characterise those effects respectively on the transverse Young's modulus E_2, shear modules G_{12} and G_{23}. A self-consistent method (Perreux and Oytana 1993) permits to define a damage matrix $[H(D)]$ where the damage is fully expressed by a single scalar variable
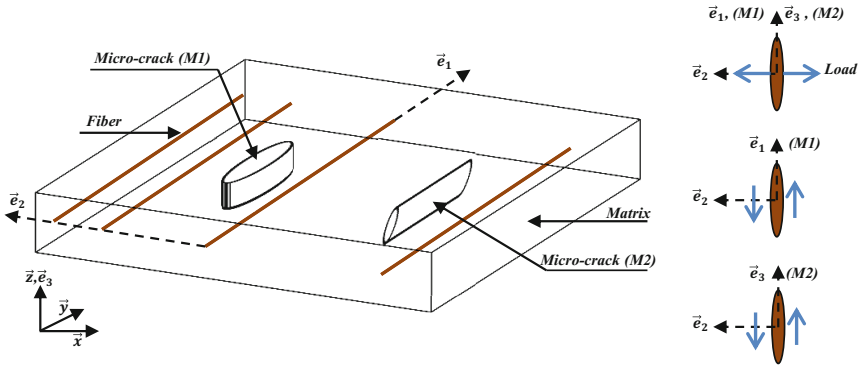
Fig. 1 *Micro-cracks orientation in the matrix (Boubakar et al. 2002)*

D which represents the relative reduction of the transverse Young's modulus:

$$[H(D)] = \begin{bmatrix} 0 & 0 & 0 & 0 & 0 & 0 \\ 0 & H_{22} & 0 & 0 & 0 & 0 \\ 0 & 0 & 0 & 0 & 0 & 0 \\ 0 & 0 & 0 & H_{44} & 0 & 0 \\ 0 & 0 & 0 & 0 & 0 & 0 \\ 0 & 0 & 0 & 0 & 0 & H_{66} \end{bmatrix} \quad ; \quad \begin{cases} H_{22} = \dfrac{D}{1-D} S_{22} \\ H_{44} = \dfrac{D}{\sqrt{1-D}} \sqrt{S_{11} S_{22}} \\ H_{66} = \dfrac{D}{\sqrt{1-D}} S_{22} \end{cases} \quad (4)$$

Where S_{ii} depict the flexibility components of $[S]$ of the undamaged material. The damaged flexibility matrix $[\tilde{S}]$ is expressed in function of $[S]$ and the damage matrix $[H(D)]$ as follows:

$$[\tilde{S}] = [S + H(D)] \tag{5}$$

For an undamaged case $D = 0$, $0 < D < 1$ for a damaged case, but there is a complete failure of the structure when $D = 1$. The damage evolution law is expressed by using the thermodynamics of irreversible processes. A thermodynamic force Y associated to the damage is obtained, $Y = \frac{1}{2}\sigma^T \left(\dfrac{\partial H}{\partial D}\right) \sigma$, where σ^T is the transpose of the stress tensor σ and $\left(\dfrac{\partial H}{\partial D}\right)$ is the derivative of $[H(D)]$ with respect to D . Indeed, a damage threshold function is defined as $\bar{Y} = Y_c + qD^p$ where Y_c, q and p are material constants. Thereby, the following charge function is established:

$$f_d = Y - \bar{Y} = \frac{1}{2}\sigma^T \frac{\partial H}{\partial D}\sigma - \bar{Y} \tag{6}$$

If $f_d < 0$, the damage thermodynamic force Y is less important than the damaged domain $\bar{Y}$, i.e. the damage does not yet appear. But, if the f_d function tends to

become positive, an increase of damage occurs so as to offset the increase of the function Y and make f_d and its derivative $\dot{f}_d$ null.

3 Solving

When the structure is subjected to a sufficient load able to trigger damage, this damaged state is kept in memory. So, it is recommended to use an incremental way in solving process. For each time iteration, a stress increment $\Delta\sigma$ is generated. This accumulation of stress continues until the function f_d becomes positive. This implies the creation of a damage increment ΔD which will be obtained by solving the consistence equation $\dot{f}_d$. As a results, the solution is reduced to seek the damage increment ΔD which cancels the function $f_{d,i+1}$ for the $(i+1)^{th}$ iteration, knowing the damage and stress states in $(i)^{th}$ iteration, and writing the stress σ_{i+1} us a function of ΔD. So, the equation with the unknown variable ΔD is:

$$f_{d,i+1} = \frac{1}{2}\left[\sigma_{i+1}\, H'(D_i + \Delta D)\, \sigma_{i+1}\right] - \left[Y_c + q(D_i + \Delta D)^p\right] \tag{7}$$
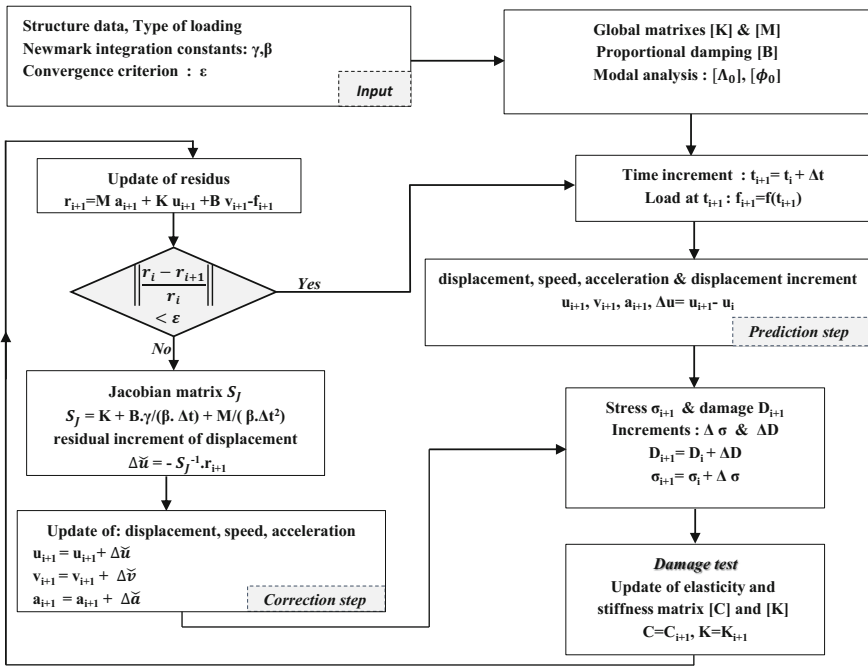
Fig. 2 Dynamic predictor-corrector scheme for predicting the damage evolution and the nonlinear response of laminated damaged structure

Where $H'(D_i + \Delta D)$ is the derivative of the damage tensor H with respect to D and expressed at $(D_i + \Delta D)$. The equation (7) is solved using the Newton-Raphson method. After getting the damage increment, the stiffness matrix must be updated to take into account for this change of material properties. With this new stiffness, displacement, strain and stress are also updated and a residue is calculated to ensure the dynamic equilibrium expressed by the convergence criterion $||\dfrac{r_{i+1} - r_i}{r_i}|| < \epsilon$. The computing steps are detailed in the predictor-corrector alghorithm shown in Figure 2. For the step of damage test, in each Gauss point, a damage criterion is introduced such that when the damage D_{i+1} exceeds 1 in a Gauss point, the stiffness in this point is assumed to be null.

4   Results and Discussion

Several numerical simulations have been performed in order to highlight the mutual influence between damage and dynamic response. The geometrical and mechanical properties of the considered laminated beam are given in table 1.

The beam is made of three layers oriented as $(90°/0°/90°)$, it is clamped at $x = 0$ and free at $x = L$. It is subjected to a distributed impact along its free side and in $\mathbf{x}$ direction with $F = 1971.5\,N$ as magnitude and $\tau = 1\,ms$ as a duration. In figure 3, the displacement amplitude is greater in the damaged case than in the undamaged one. Therefore, the damage has an important impact on the dynamic response since it affects the structure stiffness. This effect is visible in figure 4 and also when the eigenfrequencies of the undamaged and damaged beams are compared as in figure 5. So, when the damage is taken into account, the eigenfrequencies have a significant decrease which reaches up to 25% for the first mode. Moreover, comparing the damage evolution in curves (c) and (d) of the figure 3, the damage decreases from the clamped side towards the free end of the beam. This can be explained by the fact that the tensile stress has also the same monotony. Also, numerical simulations show that the damage has an exponential shape and its slope tends to be more

Table 1 Geometrical and mechanical properties of the laminated beam

Elastic modulus E_1 ($\mathbf{e}_1$)	$45680\,MPa$
Elastic modulus E_2 ($\mathbf{e}_2$)	$16470\,MPa$
Shear modulus G_{12}	$6760\,MPa$
Poisson ratio ν_{12}	0.34
Poisson ratio ν_{23}	0.34
Y_c	$0.0027\,MPa$
q	$1.246\,MPa$
p	0.816
Beam length ($\mathbf{x}$) : L	$0.3\,m$
Beam width ($\mathbf{y}$) : b	$0.03\,m$
Beam thickness ($\mathbf{z}$) :e	$0.001\,m$

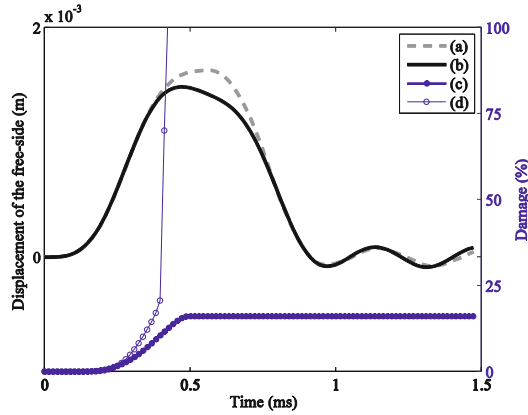**Fig. 3** Dynamic impulse response; (a) damaged beam, (b) undamaged beam & the damage evolution in time; (c) in a Gauss point located near the free side (d) in a Gauss point located near the clamped side
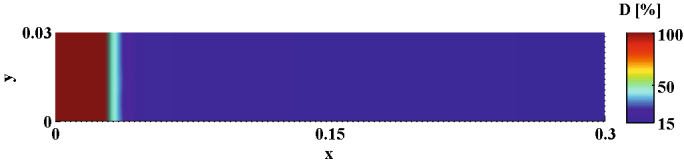

Fig. 4 Damage propagation in the first layer oriented as $90°$ of the laminated beam
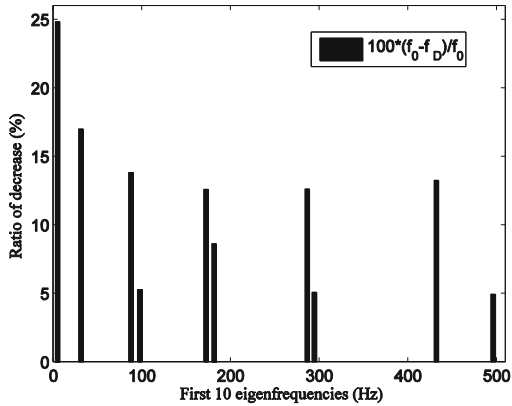
Fig. 5 Decrease ratio between the eigenfrequencies, f_D & f_0, respectively of damaged and undamaged laminated beam

vertical when the damage becomes increasingly important. From 30%, the scalar variable D increases considerably, and the function $f_{d,i+1}$ in equation (7) will no longer have solution in the real space, which means that the complete damage is reached in this area of the structure.

5 Conclusion

The non-linear dynamic response of laminated beam was investigated including the material nonlinearity generated by damage. Hence, a macro modeling was proposed and investigated to predict the damage in the structure and its dynamic reponse under an impact load. Several numerical simulations have been performed to highlight the effect of the damage on the dynamic behavior, particularly, the eigenfrequencies and mode shapes. Also, the proposed modeling permits to predict the damage evolution in the space-time reference during loading. Hence, the damage modifies significantly the dynamic reponse reflected in the increase of the displacement response and the decrease between the eigenfrequencies of damaged and undamaged structures. This decrease can be reach up to 25% for the first natural frequency in the case of an impact load. Hence, the damage should not be neglected. The benefit of this investigation is damage predicting and its localizing in time and space. The changing effect of material properties induced by damage is taken account and introduced into the dynamic analysis during loading. Therefore, this methodology can be used in monitoring strategies and life time estimations of the complex structures.

References

Boubakar, M.L., Trivaudey, F., Perreux, D., Vang, L.: A meso-macro finite element modelling of laminate structures: Part i: time-independent behaviour. Composite Structures 58, 271–286 (2002)

Cawley, P., Adams, R.D.: A vibration technique for non-destructive testing of fiber composite structures. Journal of Composite Materials 13, 161–175 (1979)

Chee, C.Y.K.: Static shape control of laminated composite plate smart structure using piezo-electric actuators. PhD thesis, University of Sydney, Aeronautical Engineering (2000)

Kulkarni, S.V., Frederick, D.: Frequency as a parameter in delamination problems-a preliminary investigation. Journal of Composite Materials 5, 112–119 (1971)

Lemaitre, J., Chaboche, J.L., Benallal, A., Desmorat, R.: Mécanique des matériaux solides. Dunod (2001)

Perreux, D., Oytana, C.: Continuum damage mechanics for microcracked composites. Composites Engineering 3, 115–122 (1993)

Reddy, J.N.: Mechanics of laminated composites plate: Theory and Analysis, 2nd edn. CRC Press, Florida (1997)

Vestroni, F., Capecchi, D.: Damage detection in beam structures based on frequency measurements. Journal of Engineering Mechanics 126, 761–768 (2000)

Non-linear Model Reduction Method Applied to Viscoelastically Damped Sandwich Structures

Souhir Zghal[1,2,3], Mohamed-Lamjed Bouazizi[2],
Noureddine Bouhaddi[3], and Rachid Nasri[1]

[1] National School of Engineers of Tunis, Applied Mechanics and Engineering Laboratory,
    University of Tunis El Manar, BP 37, 1002, Belvédère, Tunis, Tunisia
    `souhirzghal@yahoo.fr, rachid.nasri@enit.rnu.tn`
[2] Research Unit of Structural Dynamics, Modeling and Engineering of Muli-Physics
    Systems, 8000 M'rezga, IPEI Nabeul, Carthage University, Tunisia
    Mechanical Department, College of Engineering Salman Bin Abdulaziz University, KSA
    `lamjed.bouazizi@ipein.rnu.tn`
[3] FEMTO-ST Institute UMR 6174, Department of Applied Mechanics,
    University of Franche-Comté, 24 Chemin de L'Epitaphe, 25000 Besançon, France
    `noureddine.bouhaddi@univ-fcomte.fr`

Abstract. The aim of this paper is to present an efficient non-linear model reduction method intended to temporal dynamic analysis of viscoelastic sandwich structures. The proposed non-linear model reduction method is based on the combination of modal synthesis method, as well known, substructuring technique and Guyan reduction method. Each substructure is analyzed and reduced separately as a linear finite element model. The viscoelastic behavior of the core, which depends on frequency, is represented by Golla-Hughes-Mc Tavish (GHM) model. This model allows a correct representation of viscoelastic materials characteristics through the addition of dissipative coordinates. Once obtained, the reduced models of each substructure are assembled taking into account the local nonlinearities in the junctions leading to perform the capacity of the proposed method to reproduce the original model with accuracy and (CPU) time gain. Numerical examples are presented to illustrate the ability of the proposed non-linear model reduction method to handle both viscoelasticity and large finite elements models.

Keywords: Sandwich, Viscoelastic, GHM model, Nonlinearities, Reduction method.

1   Introduction

Sandwich Structures (Reddy, 1997) are commonly used in various fields of engineering such as: aerospace technology, marine and automotive industry. In fact, these structures allow a high way of vibration control due its light weight and high specific stiffness which make them a suitable choice of these manufactories. Since these structures are made of more than one layered materials, the dynamic analysis of their mechanical behavior requires a consistent model especially when they

---

incorporated viscoelastic materials which are frequency dependant. In addition, most modern control techniques require a time-domain model representation. This can be achieved through internal variables methods such as the Golla-Hughes-Mc Tavish (GHM) model (Golla and Hughes 1985; Hughes and Mc Tavish 1993) which allows an effective time-domain modeling of the frequency dependence of stiffness and damping properties of viscoelastically damped sandwich structures. Unfortunately, this is done at the price of increasing of finite elements models size due to the addition of dissipative degree of freedom to the system. Hence, model reduction methods should be applied. This was carried out in linear case in our previous work (Zghal et al. 2015). On other hand, the most of structures are assembled leading to nonlinear behavior which must be considered in the dynamic analysis of such structures. Therefore, to handle large finite elements models size, viscoelasticity and nonlinearities a non-linear model reduction method is proposed. This method is based on the combination of the substructuring procedure (Craig and Bampton, 1968; Kim 2002) with Guyan reduction method (Guyan 1965; Bouhaddi and Fillod 1992). In first step, the whole of structure is subdivided into substructures which are analyzed and reduced as linear system separately. In second step, the reduced models are assembled taking into account the local non-linearities in the junctions of these substructures. The performance of the proposed non-linear reduction model method is evaluated through the (CPU) time calculations for the full and reduced models leading to highlight the efficiency of this method for providing a faster computation in the reduction of nonlinear systems. Two numerical examples are presented in order to show the applicability and efficiency of the proposed method.

2   Golla-Hughes-Mc Tavish (GHM) Viscoelastic Model

Viscoelastic materials properties depend on many factors which the most significant parameter is the strain rate or frequency dependence. For that a consistent model should be considered to model correctly this dual character. One of the most attractive approaches is the Golla-Hughes Mc Tavish (GHM) model which describes the shear modulus, as a sum of mini-oscillators, accordingly to the following expression:

$$G(s) = G_0 \left(1 + \sum_{i=1}^{N_G} \alpha_i \frac{s^2 + 2\zeta_i \omega_i s}{s^2 + 2\zeta_i \omega_i s + \omega_i^2} \right) \tag{1}$$

G_0 represents the static modulus. Each mini-oscillator term is a second order rational function involving three positive constants (α_i, ζ_i, ω_i). These constants are determined experimentally by the curves fitting of the corresponding viscoelastic materials properties (Park et al, 1999). N_G is the number of used mini-oscillators.

Additional variables are introduced to the model as follows:

$$\{z_i(s)\} = \left\{ \frac{\omega_i^2}{s^2 + 2\zeta_i\omega_i s + \omega_i^2} \right\}\{q(s)\} \tag{2}$$

Where z_i represents the ith dissipative (generalized) coordinates and q are the structural (physical) coordinates.

Then, this model is incorporated into the finite element method to obtain the governing equations of a sandwich structure through mass, stiffness and damping elements matrices.

3   Governing Equations

Consider the finite element equation of motion of a sandwich structure composed by three layers and containing N degree of freedom (Dofs):

$$[M]\{\ddot{q}\} + [D]\{\dot{q}\} + [K]\{q\} = \{F\} \tag{3}$$

Taking into account the viscoelastic contribution of the core, the stiffness matrix can be decomposed into elastic $[K_e]$ and viscoelastic $[K_V(s)]$ parts as follows:

$$[K] = [K_e] + [K_V(s)] = [K_e] + G(s)[\overline{K}_V] \tag{4}$$

Substituting Eq. (4) into Eq. (3), the obtained equation of motion can be written in the Laplace domain as:

$$\left(s^2[M] + s[D] + [K_e] + [K_V^0]\right)\{q(s)\}$$
$$+ [K_V^0]\left(\sum_{i=1}^{N_G} \alpha_i \frac{s^2 + 2\xi_i\omega_i s}{s^2 + 2\xi_i\omega_i s + \omega_i^2}\right)\{q(s)\} = \{F(s)\} \tag{5}$$

Where $[K_V^0] = G_0[\overline{K}_V]$ is the static or low frequency stiffness matrix associated to the viscoelastic core.

After remplacing the dissipative coordinates by their expression (2) and doing some manipulations, the resulting (GHM) linear equations of motion in time domain is given as follows:

$$[M_G]\{\ddot{q}_G\} + [D_G]\{\dot{q}_G\} + [K_G]\{q_G\} = \{F_G\} \tag{6}$$

Where: $[M_G]; [D_G]$ and $[K_G] \in R^{n_G \times n_G}$, with $n_G = N(1 + N_G)$, are respectively the mass, damping and stiffness matrices of the global viscoelastic (GHM) model which are expressed as follows:

$$[M_G]=\begin{bmatrix} [M] & 0 & \cdots & 0 \\ 0 & \dfrac{\alpha_1}{\omega_1^2}\left[K_V^0\right] & 0 & \vdots \\ \vdots & 0 & \ddots & 0 \\ 0 & \cdots & 0 & \dfrac{\alpha_{N_G}}{\omega_{N_G}^2}\left[K_V^0\right] \end{bmatrix} \quad [D_G]=\begin{bmatrix} [D] & 0 & \cdots & 0 \\ 0 & \dfrac{2\alpha_1\zeta_1}{\omega_1}\left[K_V^0\right] & 0 & \vdots \\ \vdots & 0 & \ddots & 0 \\ 0 & \cdots & 0 & \dfrac{2\alpha_{N_G}\zeta_{N_G}}{\omega_{N_G}}\left[K_V^0\right] \end{bmatrix}$$

$$[K_G]=\begin{bmatrix} [K_e]+\left[K_V^{\infty}\right] & -\alpha_1\left[K_V^0\right] & \cdots & -\alpha_{N_G}\left[K_V^0\right] \\ -\alpha_1\left[K_V^0\right]^T & \alpha_1\left[K_V^0\right] & 0 & \vdots \\ \vdots & 0 & \ddots & 0 \\ -\alpha_{N_G}\left[K_V^0\right]^T & \cdots & 0 & \alpha_{N_G}\left[K_V^0\right] \end{bmatrix} \{F_G\}=\begin{Bmatrix} F \\ 0 \\ \vdots \\ 0 \end{Bmatrix} \{q_G\}=\begin{Bmatrix} q \\ z_1 \\ \vdots \\ z_{N_G} \end{Bmatrix}=\begin{Bmatrix} q \\ z \end{Bmatrix}$$

(7)

$$\left[K_V^{\infty}\right]=\left[K_V^0\right]\left(1+\sum_{i=1}^{N_G}\alpha_i\right)$$ represents the dynamic or high frequency stiffness

matrix associated to the viscoelastic layer.

However, the equation of motion (6) is unable to describe the really behavior of assembled structures. Hence, the inclusion of local nonlinearities in the junctions of these structures is required. Consequently, the localized nonlinearities can be added through the equation of motion (6) as follows:

$$[M_G]\{\ddot{q}_G\}+[D_G]\{\dot{q}_G\}+[K_G]\{q_G\}+\{f_{nl}(q_G)\}=\{F_G\} \tag{8}$$

Where $\{f_{nl}(q_G)\}$ indicates the added term of localized nonlinearities contribution. This term can be expressed by the Duffing oscillator as follows:

$$\{f_{nl}(q_G)\}=\sum_{j=1}^{m}\mu_j\left[(q_G)_i-(q_G)_j\right]^3=\left[K_{nl}(q_G)\right]\{q_G\} \tag{9}$$

As can be remarked, this non-linear load is a sum of the m attached non-linear springs relied to (i) dofs where μ_j represents the non-linear stiffness factor and $\left[K_{nl}(q_G)\right]$ is the non-linear stiffness matrix contribution.

Hence, as shown in these developments steps, the obtained non-linear equations of motion are in one hand of high order dimension due to the inclusion of the viscoelastic properties in the model and in other hand are complicated to resolve them due to the introduction of localized nonlinearities. Thereby, the development of a reduction method intended to non-linear viscoelastic sandwich structures becomes a double necessity. Motivated by the industrial viscoelastic sandwich structures nature and the fast calculations requirements in the finite elements codes, we propose a temporal model reduction method to the purpose of the study of the dynamic behavior of the non-linear viscoelastic sandwich structures.

4   Temporal Non-linear Model Reduction Method

The proposed non-linear reduction method consists to combine modal synthesis method and Guyan reduction method in order to handle both viscoelastic proper-ties and local nonlinearities in the junction of the assembled sandwich structures. Thereby, the non-linear reduced model of the order n<<n_G can be obtained as follows:

$$[M_c]\{\ddot{q}_c\}+[D_c]\{\dot{q}_c\}+[K_c]\{q_c\}+[K_{nlc}]\{q_c\}=\{F_c\} \tag{10}$$

Where $[M_c];[D_c];[K_c];[K_{nlc}]$ and $\{F_c\}$ represent respectively the reduced mass, damping, linear and non-linear (GHM) viscoelastic stiffness matrices and the reduced load vector which are expressed in the following forms:

$$\begin{cases} [M_c]=[T_{Gn}]^T[M_G][T_{Gn}] \\ [D_c]=[T_{Gn}]^T[D_G][T_{Gn}] \\ [K_c]=[T_{Gn}]^T[K_G][T_{Gn}] \\ [K_{nlc}]=[T_{Gn}]^T[K_{nl}][T_{Gn}] \\ \{F_c\}=[T_{Gn}]^T\{F_G\} \end{cases} \tag{11}$$

Hence, the passage from full to reduced non-linear (GHM) viscoelastic model is carried out by the proposed reduced basis $[T_{Gn}]$ which its form is given as fol-lows:

$$[T_{Gn}]=\begin{bmatrix} I_1 & 0 \\ t_1 & t_2 \\ 0 & I_2 \end{bmatrix} \tag{12}$$

Where:

$$[t_1]=-\left[K_q^{ii}\right]^{-1}\left[K_q^{ij}\right];[t_2]=-\left[K_q^{ii}\right]^{-1}\left[K_{qz}^{ij} \quad K_{qz}^{ii}\right] \tag{13}$$

$[I_1]$ and $[I_2]$ are the identity matrices with appropriate sizes.

The subscript i and j indicates respectively the interior (slave) and the junctions (master) dofs. In fact, in the reduction processus only master (or junctions) dofs are retained, the others unwanted dofs are removed. This basis allows a drastic re-duction of the full dofs of the viscoelastic sandwich structure with generation of a term $[t_2]$ which indicates the contribution of the viscoelastic materials properties through the (GHM) model. This term contains both purely structural and coupled

dissipative-structural effects. These effects are shown respectively through the stiffness matrices as follows:

$$\left[K_q \right] = \left[K_e \right] + \left[K_V^{\infty} \right] \tag{14.a}$$

$$\left[K_{qz} \right] = \left[-\alpha_1 \left[K_V^0 \right] \quad \cdots \quad -\alpha_{N_G} \left[K_V^0 \right] \right] \tag{14.b}$$

Therefore, this proposed method provides an efficient tool to reduce the large dimension systems at the presence of viscoelastic components and local nonlinearities with the minimum (CPU) time.

5   Numerical Examples

This section presents numerical examples, which were employed to illustrate the effect of inclusion of localized nonlinearities in the prediction of the dynamic behavior of viscoelastic sandwich structures and to test the efficiency and the accuracy of the proposed reduction method.

5.1   Non-linear Supported Viscoelastic Sandwich Beam

Firstly, a non-linear supported viscoelastic sandwich beam is examined.
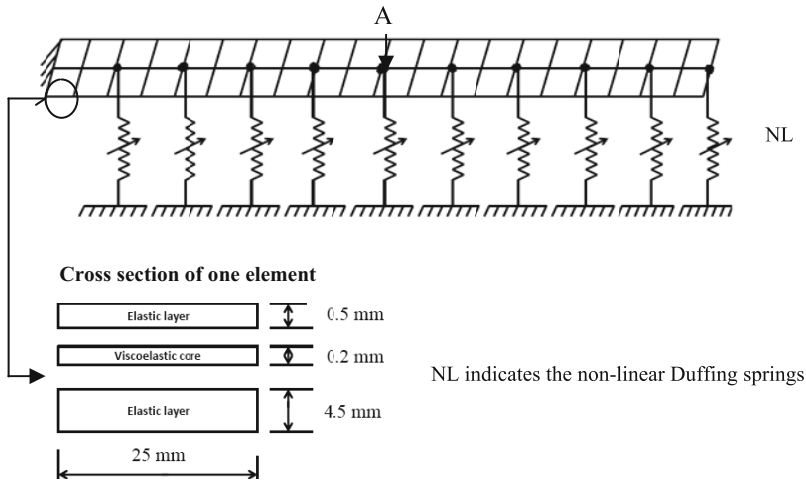
Fig. 1 Non-linear supported viscoelastic sandwich beam Al/242F01 3M[TM]/Al

It has L=500 mm of length and b=38mm of width. It is constituted by two faces made of Aluminum with Young modulus: $E_f=70\times 10^9$N/m^2; Poisson ratio: $\upsilon_f=0.3$; density: $\rho_f=2750$Kg/m^3; Thickness1:$h_{f1}=4.5$mm; Thickness3: $h_{f3}=0.5$mm and a viscoelastic core commercially available 242F01 3M^{TM} used at 25^0 C using the (GHM) shear modulus (Eq.1) with Poisson ratio: $\upsilon_c=0.5$; density: $\rho_c=1099.5$Kg/m^3 and Thickness: $h_c=0.2$mm. We use here one minioscillator with three constants: $\alpha_1=1.047$;$\zeta_1=3911.89$;$\omega_1=4943.06$rad/s and static modulus $G_0=0.079$ MPa. The mesh of the sandwich structure involves 20 elements through the length and 2 elements through the width as shown in Fig.1.

The viscoelastic sandwich beam is subjected to a harmonic load in the point A of amplitude 70N and frequency excitation f=18Hz (around its first vibration mode) to arise effectively the non-linear behavior. The value of the non-linear Duffing spring coefficient is $(\mu_j)_{j=1,...,10}=10^9$N.m^{-3}.The obtained temporal responses of full and reduced models in terms of relative displacements (w/h) and velocity are illustrated in Fig.2 (a) and (b).

(a)   (b)
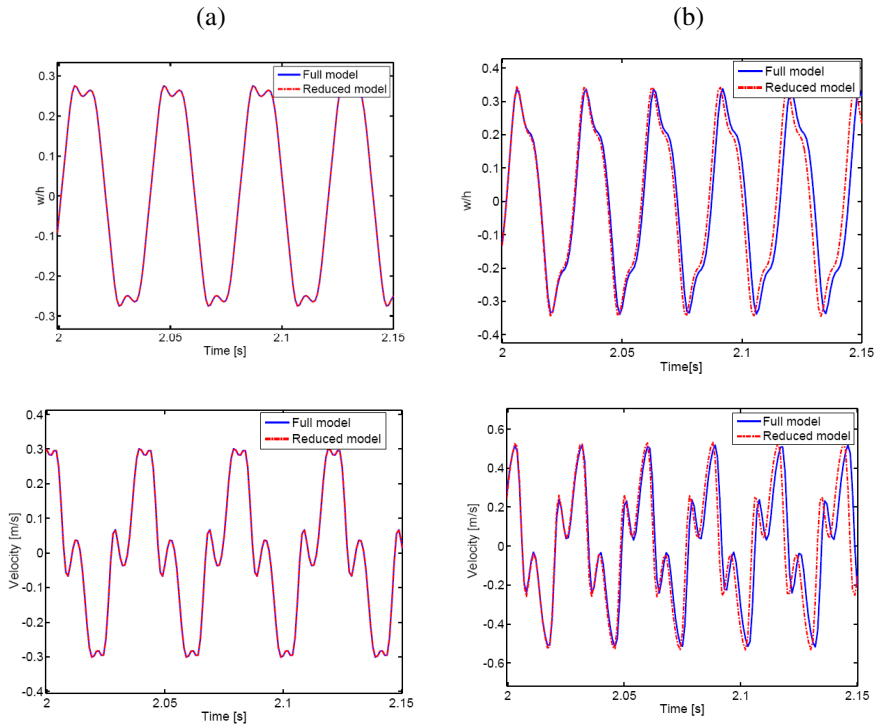
Fig. 2 Temporal responses of full and reduced models of the non-linear supported viscoe-lastic sandwich beam: (a) f<fc and (b): f>fc

Fig.2.(a) and (b) show the temporal responses of the non-linear supported vis-coelastic sandwich beam for two cases of harmonic excitation (f<fc and f>fc) with (fc=165Hz) is the cutoff frequency which is evaluated by the resolution of the

slave (or interior) eigenfrequencies problem associated to the conservative sandwich structure(Bouhaddi and Fillod, 1992). The dimension of reduced model is 810 compared to the full model which is equal to 1600 which leads to 50% of reduction in terms of size model. Furthermore, the full and reduced models are well correlated for an excitation frequency (f=18Hz) less than the cutoff frequency relative to those for excitation frequency (f=300Hz) high than the cutoff frequency which presents a shift between the two curves. On other hand, the relative error for the three temporal moments indicators (E, T, D) (Hemez and Doebling, 2003) does not exceeds 5% in E, 1% in T and 1% in D which leads to validate the accuracy of the proposed reduction method for such non-linear structures. As well as, the (CPU) time required for the calculation of the reduced model is about 15min compared to the full model which is about 2h which indicates a significant reduction ratio of 87%. Hence, the proposed non-linear reduction method improves its efficiency in terms of accuracy and time gain for such structures with localized nonlinearities.

5.2   Non-linear Assembled Viscoelastic Sandwich Beams

The second test consists of three viscoelastic sandwich substructures assembled through non-linear springs in their junctions as depicted in Fig.3. Each substructure has the same mechanical and geometrical propreties as described in section (5.1). Furthermore, the global viscoelastic sandwich structure is exihibited to a harmonic load of amplitude 70N in the point E.
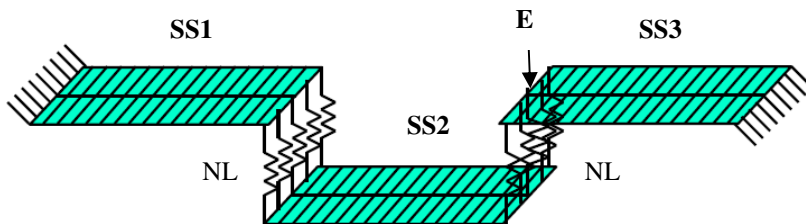
Fig. 3 Assembled viscoelastic sandwich beams

Firstly each substructure is reduced separately. The size of the obtained reduced model for the substructure (SS1) and (SS3) is 805 and for the substructure (SS2) is 810. The choice of junctions dofs (j=5 for SS1 and SS3) and (j=10 for SS2) is carried out on maximizing the cutoff frequency of each substructure which is equal to 165Hz.

After that, the reduced matrices are assembled taking into account the localized nonlinearities in the junctions between the three viscoelastic substructures (SS1) (SS2) and (SS3) leading to a global reduced system of order 2420. The obtained temporal results are presented in Fig.4 (a) and (b).

(a)   (b)
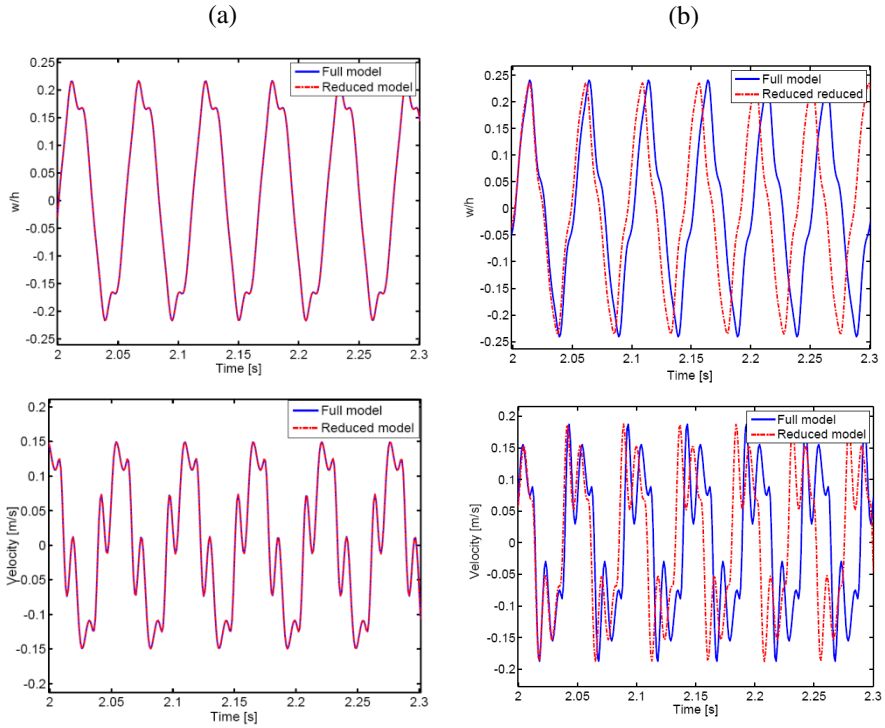
Fig. 4 Temporal responses of full and reduced model of the non-linear assembled viscoelastic sandwich beam (a): f<fc and (b): f>fc

Fig.4 (a) shows that the temporal reponses of full and reduced models are in good agreement for (f=25Hz<fc) in terms of relative displacement and velocity while those obtained for (f=400Hz>fc) (Fig.4 (b)) presents a shift in amplitude and time scales. This shift is about 4% in E, 0.1% in T and 0.2% in D for the displacement response and 6% in E, 0.3% in T and 0.1% in D for the velocity response. This leads to validate the applicability of the proposed method for non-linear viscoelastic structures in time domain. The reduction ratio of reduced model compared to full model in terms of (CPU) time is about 90% which indicates the passage from 10 h of calculations for full model to 1h for reduced model. This shows the performance of the proposed non-linear reduction method for such structures.

6   Conclusion

The present work has presented an alternative reduction method for non-linear sandwich structures. This method is based on the combination of Guyan reduction method and substructring method with viscoelastic components via (GHM) model.

In fact, (GHM) model used dissipative coordinates which added to finite elements models leads generally to high order system which needs to be reduced. Furthermore, the addition of localized nonlinearities in the junctions of these structures leads to complicated resolution scheme. Hence, a model reduction method for non-linear sandwich structures was proposed. This method has led to much faster computations on the reduction of full dofs of the global sandwich structure with satisfactory results. In particular, a reduction of 90% of full dofs in the case of three assembled substructures has shown the efficiency of the proposed method in terms of (CPU) time. Therefore, the proposed reduction method allows a soft handling of sandwich structures with large size and viscoelastic components at the presence of localized nonlinearities. This motivates to perform experiment investigations in our future work to more validate the numerical obtained results.

References

Reddy, J.N.: Mechanics of Laminated Composite Plates: Theory and Analysis, 2nd edn. CRC Press, Florida (1997)

Golla, D.F., Hughes, P.C.: Dynamics of viscoelastic structure-a time domain, finite element formulation. J. Appl. Mech. 52, 897–906 (1985)

Mc Tavish, D.J., Hughes, P.C.: Modeling of linear viscoelastic space structures. J. Vib. Acoust. 52, 103–115 (1993)

Craig Jr., R.R., Bampton, M.C.C.: Coupling of substructures for dynamic analysis. AIAA J. 6, 1913–1919 (1968)

Kim, T.: Component mode synthesis method based on optimal modal analysis. AIAA J. 2202-1226 (2002)

Guyan, R.J.: Reduction of Stiffness and Mass Matrices. AIAA J. 3, 380 (1965)

Bouhaddi, N., Fillod, R.: A method for selecting master dof in dynamic substructuring using the Guyan condensation method. Comput. Struct. 45, 941–946 (1992)

Park, C.H., Inman, D.J., Lam, M.J.: Model reduction of Viscoelastic finite element models. J. Sound. Vib. 219, 619–637 (1999)

Hemez, F.M., Doebling, S.M.: From shock response spectrum to temporal moments and Vice-versa. In: Proceedings of the 21st SEM International Modal Analysis Conference, Kissimmee (2003)

Zghal, S., Bouazizi, M.L., Bouhaddi, N., et al.: Model Reduction methods for viscoelastic sandwich structures in frequency and time domains. Finite Elem. Anal. Des. 93, 12–29 (2015)

A Critical Evaluation of the INOPMA Algorithm for In-Operation Modal Analysis

Maher Abdelghani[1], Shashank Chauhan[2], and Daniel J. Inman[3]

[1] ISSAT Sousse, Av. Ibn Khouldoun, Taffala, 4003 Sousse, Tunisia
 mahera@lycos.com
[2] Bruel & Kaer SV, Dannemark
 Shashank.chauhan@bksv.com
[3] University of Michigan, Ann Arbor, 48109 Michigan, USA
 daninman@umich.edu

Abstract. We propose in this paper a numerical modal appropriation method for use with in-operation modal analysis (INOPMA). The key idea is to realize that the correlation sequence of the system output is the sum of decaying sinusoids with a certain phase shift and therefore it may be considered as an impulse response. The method is based on performing a numerical convolution of a single sine wave force with the system output correlation sequence. The steps are then similar to the classical modal appropriation method, although the characteristic frequencies are different. This approach is validated and compared to a subspace method on simulated data as well as on experimental data and it is shown that INOPMA outperforms the subspace method.

1 Introduction

Classical modal parameter identification methods are usually based on frequency response functions or impulse response functions that require measurements of the input force and the resulting response. However, in some practical situations, modal parameters must be extracted from response measurements only. For example, for large structures (such as bridges, offshore platforms, and wind turbines), it is very difficult and sometimes impossible to measure actual excitation (such as wind, road noise, and wave excitation). The large amount of energy necessary to induce structural vibrations may cause local damage and excitation becomes very difficult to generate. Moreover, the actual operating conditions may differ significantly from the laboratory conditions. Therefore, in these applications, the system identification approach must be done on the basis of in-operation output-only data. The method of in-operation modal analysis has gained considerable attention in recent years. There have been several different approaches to estimate modal parameters from output-only data. They include peak-picking from power spectral density functions [3], Least Squares curve fitting technique [8], subspace methods [10,12] and the natural excitation

technique (NExT) [5] using cross correlation functions instead of impulse response functions.

On the other hand, one of the most powerful methods for modal identification is the modal (or force) appropriation method which uses one sine signal to generate forces at different points of the structure and adjusts the relative values of those forces so as to isolate a single mode. Such tests provide very accurate information on the modeshapes, which is then complemented by specific tests to determine the modal damping [2].

Inspired by this last method, we propose in this paper a modal appropriation based method for use with in-operation modal analysis (INOPMA). The key idea is the realization that the correlation sequence of the outputs of a vibrating structure may be considered as an impulse response but with a certain phase shift[5]. By taking the convolution of one sine wave with the correlation sequence we show that a mode is isolated at a characteristic frequency which depends on the damping ratio. By using a force that is in quadrature of phase with the first one, the damping ratio may be estimated which in turn leads to the estimation of the undamped natural frequency.

We investigate in this paper the performance of INOPMA, first on simulated data (SDOF, MDOF) and it is shown that this method provides estimates of the modal parameters with much less variance than subspace algorithm (the balanced realization algorithm (BR) [4]. Second, the method is validated on experimental data and comparable results with the subspace algorithm are obtained.

2   The Case of a Sdof System

Consider a SDOF system with undamped natural frequency ω_n and damping ratio ζ, excited with a random force with spectrum of amplitude S_0. The correlation sequence of the output $y(t)$ is given by [9]:

$$R(\tau) = \frac{S_0 \omega_n}{4\zeta} e^{-\zeta \omega_n \tau} \left[\cos(\omega_d \tau) + \frac{\zeta}{\sqrt{1-\zeta^2}} \sin(\omega_d \tau) \right] \tag{1}$$

Where $\omega_d = \omega_n \sqrt{1-\zeta^2}$

This correlation sequence is a decaying sinusoid but with a certain phase shift that depends on the damping ratio. Therefore it may be considered as an impulse response except that the phase shift needs to be taken into account.

Let's consider now the convolution of this correlation sequence with a pure sine wave with driving frequency ω, that is $f(t) = \sin(\omega t)$ and call the result $x(t)$ which is also a sine wave at the same frequency.

The transfer function $G(s) = \dfrac{x(s)}{f(s)}$ is given by [9]:

$$G(s) = \frac{S_0}{4\zeta} \frac{s + 2\zeta\omega_n}{s^2 + 2\zeta\omega_n s + \omega_n^2} \tag{2}$$

The tangent of the phase angle of this transfer function can be shown to be :

$$\tan(\phi) = -\frac{\omega}{2\zeta\omega_n^3}\left[\omega^2 - \omega_n^2(1 - 4\zeta^2)\right] \tag{3}$$

This phase angle is exactly zero at the following frequency:

$$\omega^* = \omega_n\sqrt{1 - 4\zeta^2} \tag{4}$$

By varying the driving frequency ω and computing the phase angle between the input and the output, this frequency can be identified exactly. We call this property the phase resonance. This is similar to the phase resonance property used in modal appropriation [2]. The convolution done between the force and the correlation sequence may be thought of as applying a harmonic force to a certain structure.

Notice however since the damping ratio is not known, it is not possible at this stage to identify ω_n. It is possible however to identify ω^* exactly as this is the frequency at which the phase becomes zero. Next the damping ratio needs to be estimated. With ζ known equation (4) yields an estimate of ω_n.

Once ω^* is identified, let us take the convolution of the correlation sequence with a harmonic signal that is in quadrature of phase (at pi/2) with respect to the first one and with amplitude α, that is $g(t) = (1 + j\alpha)f(t)$

We can show that the phase resonance now occurs at the frequency $\tilde{\omega}^*$ given by:

$$\tilde{\omega}^* = \omega^*\sqrt{1 + \alpha\zeta\beta(\zeta)} \tag{5}$$

Where $\beta(\zeta)$ is given by :

$$\beta(\zeta) = (1 - 4\zeta^2)^{-\frac{3}{2}} \tag{6}$$

By varying α and computing the new phase resonance frequencies, the damping ratio may estimated by solving the following equation:

$$\frac{1}{\omega^{*2}} \frac{\partial \tilde{\omega}^{*2}}{\partial \alpha} = \xi\beta(\zeta) \tag{7}$$

For exact estimation of ζ one can fit equation (7). However for a wide range of damping ratios, the function $\beta(\zeta)$ is almost 1. A very good estimate of ζ may be given by:

$$\zeta \approx \frac{1}{\omega^{*2}} \frac{\partial \tilde{\omega}^{*2}}{\partial \alpha} \tag{8}$$

Once the damping ratio is estimated, the natural frequency may be estimated from equation (4).

3   Simulation Study

In this section we consider a simulation study of the presented method. In particular we consider a Single Input Single Output system (SISO) and a Multi Input Single Output system (MISO). We show that the INOPMA method outperforms subspace methods (the BR algorithm) by providing modal parameters with much less bias and variance.

3.1   Siso Systems

We consider here a SDOF system excited with white noise. The mass, damping and stiffness values used are respectively m=100kg, c=80 Ns/m and k=100x10^3 N/m. 2000 data points were simulated and 2% noise was added to the output. A total of 60 experiments were performed where at each experiment a different realization of the excitation as well as the noise is used. The subspace algorithm was used for the extraction of the modal parameters with truncation of the Hankel matrix at the exact model order. Initially, at the first run, the empirical variances of the modal parameter estimates are set to zero. Then at each successive run the set of identified modal parameters increases and is used to compute the empirical variance of that set. As the runs increase the number of modal parameters increases and better estimates of the variances (variance of the set of the estimated modal parameters) are obtained which will eventually converge. The results are shown in Figures 1 and 2. It is obvious from the figures that INOPMA presents much less variance than the subspace algorithm. In order to study the bias on the modal parameters, the relative error (the exact value minus the estimated value over the exact value) on the frequency and damping is computed for 60 simulation runs. Inspection of Figure 3 and 4 shows that INOPMA outperforms the subspace algorithm.
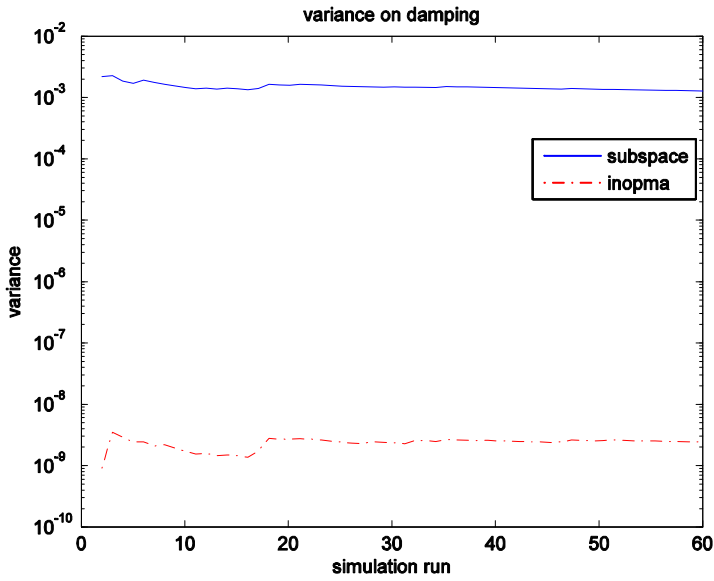
Fig. 1 Variance on damping, SDOF case

Fig. 2 Variance on frequency: SDOF case
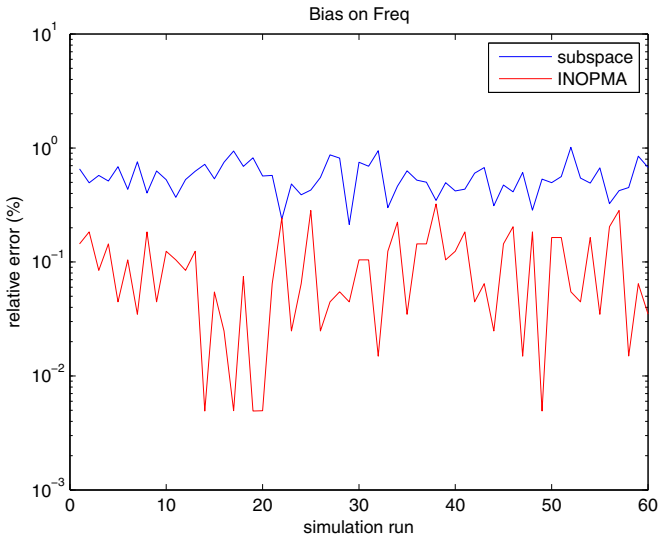
Fig. 3 Absolute value of the relative error on the frequency.
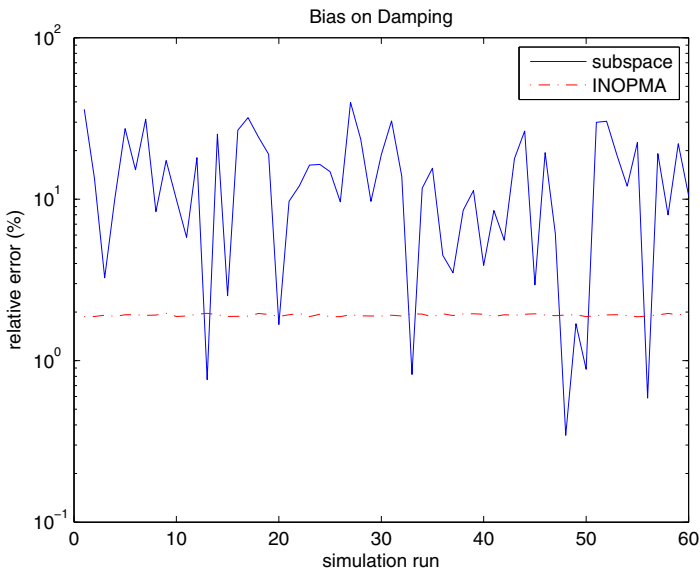
Fig. 4 Absolute value of the relative error on damping

3.2   Miso Systems

We consider here a simulation study of a MISO system. In particular, a 2DOF system is considered but only 1 output is chosen in the identification process. The mass, damping and stiffness matrices used are respectively:

$$M = \begin{bmatrix} 100 & 0 \\ 0 & 100 \end{bmatrix}, C = \begin{bmatrix} 200 & -100 \\ -100 & 300 \end{bmatrix}, K = \begin{bmatrix} 200 & -100 \\ -100 & 300 \end{bmatrix} \times 10^3$$

The same experiments as for the SDOF system are performed. The results are shown in Figures 5 and 6 where it is obvious that the INOPMA method again presents much less variance that the subspace algorithm. The bias on the first mode is illustrated in figures 7 and 8.

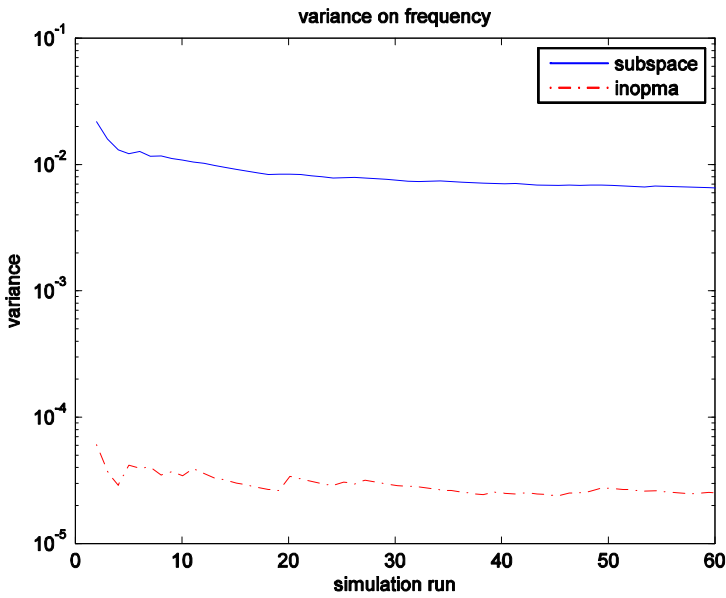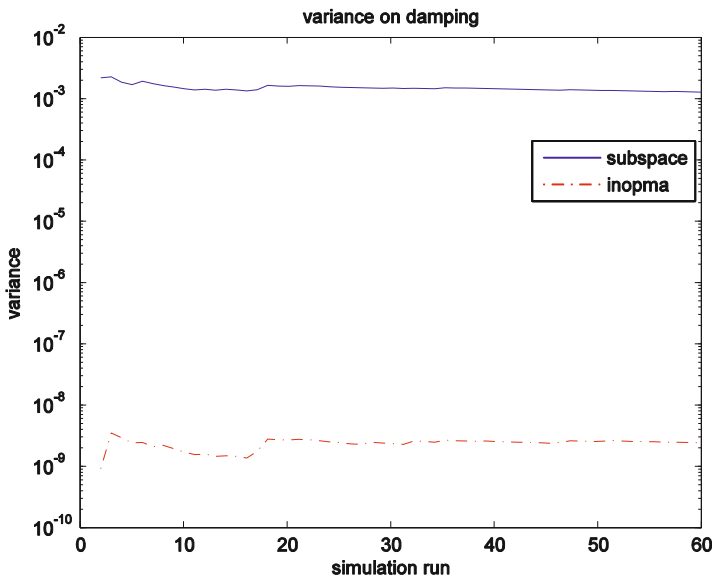**Fig. 5** Variance on damping: MISO system
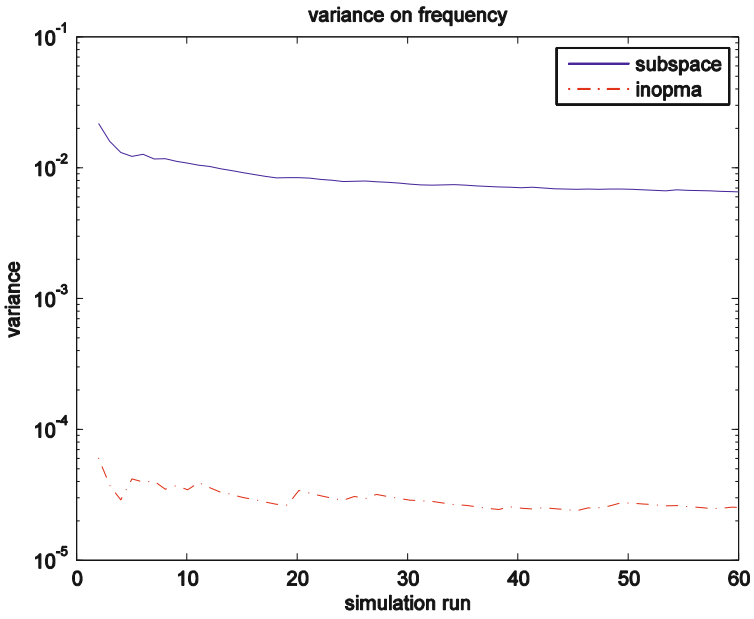
Fig. 6 Variance on frequency: MISO system
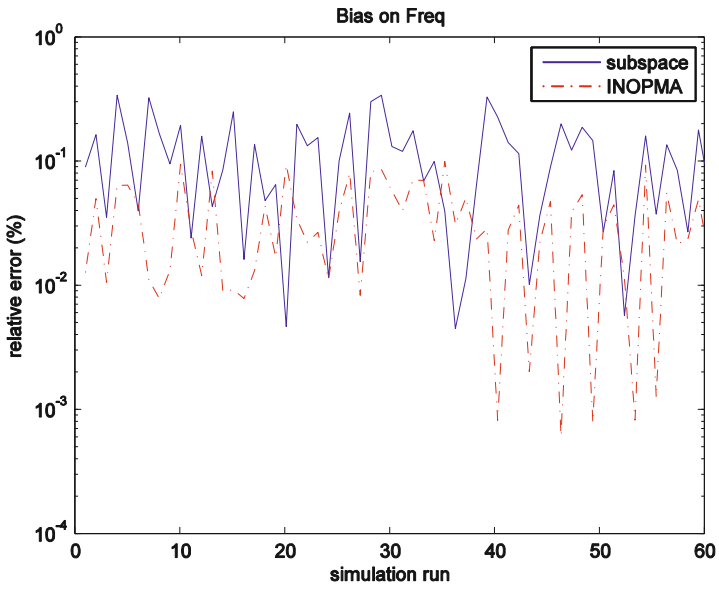
Fig. 7 Absolute value of the relative error on the frequency
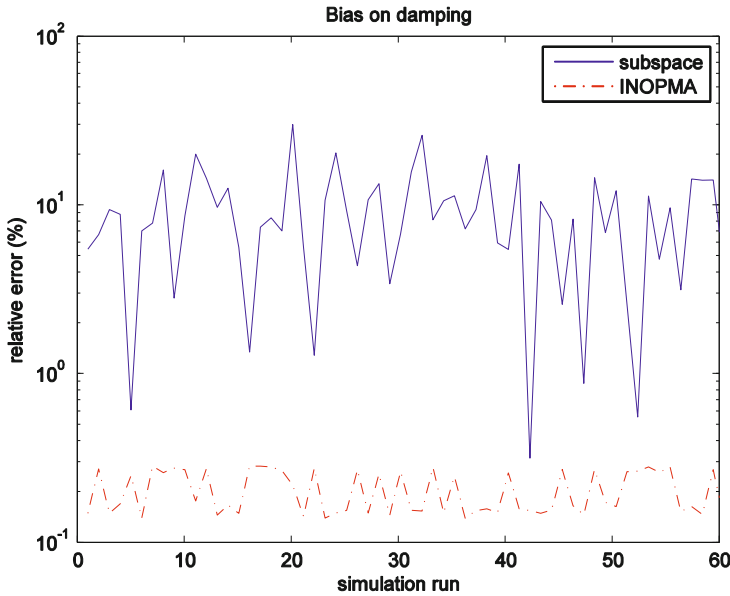
Fig. 8 Absolute value of the relative error on damping

4 Experimental Study

We compare in this section the INOPMA algorithm to the data-driven stochastic subspace algorithm (SSI). The tested structure used in this study consists of a suspended steel subframe structure. The structure is excited at two different locations using random noise inputs, and 28 accelerometers were used for measuring time responses. The analysis was performed on the 0-500 Hz frequency range and 32000 data points per channel were collected with a 1024 Hz sampling frequency. The LMS-Cadax system was used for data acquisition.

Conerning INOPMA, 256 lags were used to compute the convolution. The characteristic frequency was identified quite robustly however it is noticed that the damping ratio is more sensitive to the design parameter α. One of the advantages of INOPMA is that it does not require a stabilization diagram like subspace methods, moreover it isolates the modes mode by mode making the identification easy. Also, the problem of spurious modes encountered often with subspace methods is avoided with INOPMA.

Table 1 Identification results. INOPMA vs. Subspace

Mode	Frequency (Hz)		Damping (%)	
	INOPMA	SSI	INOPMA	SSI
1	119.27	118.99	0.28	0.25
2	155.02	154.59	0.31	0.29
3	192.68	192.05	0.29	0.30
4	215.21	214.87	0.32	0.30
5	227.85	228.96	0.22	0.21
6	239.58	238.88	0.45	0.42
7	284.36	285.29	0.23	0.21
8	320.47	320.16	0.92	1.1
9	333.24	332.95	0.28	0.25
10	352.05	351.28	0.48	0.52
11	397.29	398.01	0.24	0.21
12	416.87	416.63	0..23	0.21
	467.53	466.82	0.18	0.15

5   Conclusion

A new numerical modal appropriation based method for use with in-operation modal analysis (INOPMA) has been derived. The key concept is the realization that the output correlation sequence is a decaying sinusoid with a certain phase shift and therefore may be considered as an impulse response. The convolution of this correlation sequence with a pure sine wave allows the isolation of the mode at a characteristic frequency which depends on the damping ratio. By using a force in quadrature of phase with a sine it is possible to estimate the damping ratio which in turn allows the estimation of the undamped natural frequency. This approach is validated on simulated data and it is shown that the modal parameters determined in this way present much less variance and bias than subspace based identified methods. The proposed method is also validated on experimental data and it is shown that the results compare well with the subspace method. One of the advantages of this method is the fact that there is no need of a stabilization diagram as required in many modal identification methods (subspace). The extension of this approach to MIMO systems is on-going.

References

[1] Abdelghani, M., Inman, D.J.: Modal appropriation for use with in-operation modal analysis. Journal of Shock and Vibration (January 2015)
[2] Balmes, E., Chapelier, C., Lubrina, P., Fargette, P.: An evaluation of modal testing results based on the force appropriation method. In: International Modal Analysis Conference, Orlando (1996)

[3] Desforges, M.J., Cooper, J.E., Wright, J.R.: Spectral and modal parameter estimation from output-only measurements. Mechanical Systems and Signal Processing 9 (1995)

[4] Hermans, L., Auweraer, H.V.: Modal testing and analysis of structures under operational conditions: industriel application. Mechanical Systems and Signal Processing 13 (1999)

[5] James, G.H., Carne, T.G., Lauffer, J.P.: The natural excitation technique (NExT) for modal parameter extraction from operating structures. Modal Analysis 10 (1995)

[6] Lardies, J.: A stochastic realization algorithm with application to mocal parameter estimation. Mechanical Systems and Signal Processing 15 (2001)

[7] Lardies, J.: State space identification of vibrating systems from multi-output measurements. Mechanical Systems and Signal Processing 12 (1998)

[8] Luz, E., Wallaschek, J.: Experimental modal analysis using ambient vibration. The International Journal of Analytical and Experimental Modal Analysis 7 (1992)

[9] Meirovitch, L.: Elements of Vibration Analysis. McGraw-Hill (1986)

[10] Papakos, V., Fassois, S.D.: Multichannel Identification of Aircraft Skelton Structures Under Unobservable Excitation: A Vector AR/ARMA Framework. Mechanical Systems and Signal Processing 17 (2003)

Stochastic Optimal Design of Tuned Mass Damper Parameters Using Energetic Approaches

Elyes Mrabet[1], Mohamed Soula[2], Mohamed Guedri[1], Samir Ghanmi[1], and Mohamed Ichchou[3]

[1] Unité de Recherche en Dynamique des Structures, Modélisation et Ingénierie des Systèmes Multi-physiques, Preparatory Engineering Institute of Nabeul (IPEIN), 8000 M'rezgua, Nabeul, Tunisia

[2] Laboratory of applied mechanics and engineering, ENIT. Mechanical engineering department, École Nationale Supérieure des Ingénieurs de Tunis, University of Tunis, 5, Av. Taha Hussein Montfleury 1008 Bab Menara TUNIS Tunisia

[3] LTDS UMR5513 Ecole Centrale de Lyon, 36 Avenue Guy de Collongue, 69134 Ecully, France

Abstract. The present work is intended to introduce a new reliability based optimization strategy (RBO) of single-tuned mass damper (TMD) parameters. The strategy uses an energetic approach and consists to obtain the optimum TMD parameters so that a failure probability is minimized. The failure probability is related to the dissipated power process in the primary structure (DPP) and it's characterized by the out-crossing, for the first time, of the DPP across a certain threshold value during a time interval. The introduced RBO strategy is then compared with another related to the mean value of the DPP. The obtained results show a strong correlation between the presented strategies and equivalence can be made. The effectiveness of the TMD with the proposed optimum parameters is also investigated and compared with Bi-tuned mass dampers (Bi-TMDs). The results showed that the TMD optimized using the proposed strategy is more effective than the Bi-TMDs.

Keywords: Reliability based optimization of TMD parameters, Energy approach, Mean value dissipated power, Non-Gaussian processes, Rice's formula.

1 Introduction

Nowadays, the use of the TMD devices in order to mitigate vibrations in structures subject to stochastic loadings is a recognized practice in engineering field (Marano et al. 2010). To ensure the effectiveness of the TMD devices, designers have to carefully choose the optimum design parameters using appropriate criteria. Several optimization strategies, in both deterministic and uncertain context, can be found in the literature (Yu et al. 2013) and they all aims to get optimum TMD parameters so that a certain criteria is met. Through the existent optimization strategies, one can cite the stochastic structural optimization (SSO) (Marano et al. 2010),

in which the objective function is explicitly related to the root mean square displacement of the structure and the RBO, in which the objective function is a failure probability (Chakraborty and Roy 2011). In the context of the RBO strategy, the optimum parameters of the TMD are obtained so that a failure probability is minimized; the failure probability depends on the designer aim and it's strictly related to a certain failure mode. A failure mode can be for examples: (1) the exceedence, for the first time, of the Von Mises stress process into a given area of a structure, of a given threshold during a time interval (Gupta and Manohar 2005); or, (2) the exceedence of the displacement of a structure, on which the TMD device is attached (Chakraborty and Roy 2011), of a given threshold during a time interval.

The evaluation of the failure probabilities in the context of RBO constitutes a time depending problem of reliability analysis and one of the most common practice used when handling the RBO is the transformation of the problem into time invariant format (Gupta and Manohar 2005). Consequently and by making the Poisson assumptions (Crandall 1970), the classical Rice's formula (Li and Chen 2009) can be used and then the failure probability is easily expressed.

In the present work a new RBO strategy is introduced using the DPP which is strictly related to the damage in vibrating structures (Greco and Marano 2013). The strategy consists to get optimum TMD parameters so that the failure probability characterized by the exceedence of the DPP, for the first time, of a certain threshold during a time interval. The expression of the failure probability is presented in this work for a generic system of one degree of freedom subject to seismic motion.

In addition to the new RBO strategy, a second optimization strategy using an energetic criterion is also implemented; the strategy was recently introduced in (Greco and Marano 2013) and consists to find the TMD parameters so that the objective function, explicitly related to the mean values of the DPP, is minimized.

For sake of comparison, the effectiveness (vs. earthquake frequency) of the TMD device, for both strategies, is discussed and a correlation analysis is made.

The obtained results show, on one hand a strong correlation between these strategies and equivalence can be made, on the other hand, for frequencies close to the main structure natural frequency, both strategies are earthquake dependant. Besides, the frequency responses of the primary structure when it's equipped with a single-TMD and Bi-TMDs (Seug-Yong et al. 2009) are also examined. The results showed that a single-TMD optimized using the proposed approach is more effective than the Bi-TMDs optimized using the easy-to-use design formula proposed in (Seug-Yong et al. 2009).

2   Structural Model and Dissipated Power Expression

Figure 1 (a) shows an idealized mechanical model of a single-TMD attached to a primary structure. The natural frequencies and damping ratio of the TMD device

are $\omega_T = \sqrt{k_T/m_T}$ and $\xi_T = c_T/2\sqrt{k_T m_T}$, respectively. The primary structure is described by its natural frequency $\omega_s = \sqrt{k_s/m_s}$ and it damping ratio $\xi_s = c_s/2\sqrt{k_s m_s}$. The system is excited by a base acceleration $\ddot{y}_b$ due to seismic motion which is modeled by the well known Kanai-Tajimi stationary stochastic process (Marano et al. 2010).
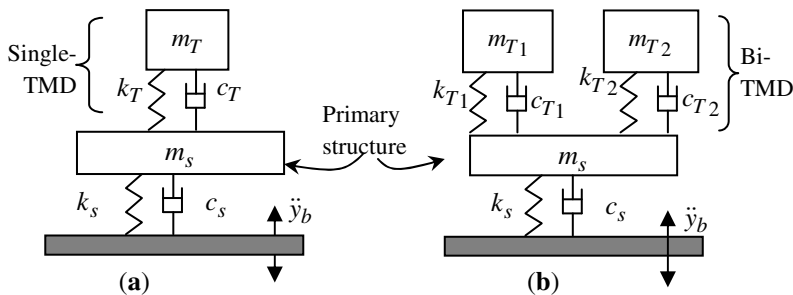
Fig. 1 The primary structure with: (a) single-TMD, (b) Bi-TMDs

2.1 Covariance Responses of the Primary Structure with Single-TMD and Mean Dissipated Power Expression

Let $\mu = m_T/m_s$ be the mass ratio, the system equations, for the single-TMD, written in the state space form is deduced from the characteristic system matrices:

$$
\mathbf{A} = \begin{pmatrix}
0 & 0 & 0 & 1 & 0 & 0 \\
0 & 0 & 0 & 0 & 1 & 0 \\
0 & 0 & 0 & 0 & 0 & 1 \\
-\omega_T^2 & \omega_T^2 & \omega_f^2 & -2\xi_T\omega_T & 2\xi_T\omega_T & 2\xi_f\omega_f \\
\mu\omega_T^2 & -(\mu\omega_T^2 + \omega_s^2) & \omega_f^2 & 2\mu\xi_T\omega_T & -2(\xi_s\omega_s + \mu\xi_T\omega_T) & 2\xi_f\omega_f \\
0 & 0 & -\omega_f^2 & 0 & 0 & -2\xi_f\omega_f
\end{pmatrix} \quad \text{and}
$$

$$
\mathbf{B} = 2\pi S_0 \begin{pmatrix} 0 & \cdots & 0 \\ \vdots & \ddots & \vdots \\ 0 & \cdots & 1 \end{pmatrix}
$$

where ξ_f, ω_f and y_f are the damping ratio, the natural frequency and the relative response (with respect to the ground) of the elastic filter (Marano et al. 2010). The global space state vector is then $\mathbf{Y} = \left(y_T, y_s, y_f, \dot{y}_T, \dot{y}_s, \dot{y}_f \right)^T$ and S_0 is the intensity of the stationary Gaussian zero mean white noise process applied at the bed

rock. The stochastic response of the system is completely known by the space state covariance matrix **R** which is the solution of the Lyapunov equation:

$$\mathbf{AR} + \mathbf{RA}^{\mathbf{T}} + \mathbf{B} = \mathbf{0} . \tag{1}$$

The root mean square displacement (rmsd) of the primary system can be obtained as $\sigma_{y_s} = \sqrt{\mathbf{R}(2,2)}$. The root mean square velocity (rmsv) is expressed as $\sigma_{\dot{y}_s} = \sqrt{\mathbf{R}(5,5)}$.

In stationary condition, the DPP in the primary structure and its time derivative can be written as follows (Greco and Marano 2013):

$$e(t) = c_s \dot{y}_s^2(t) = 2\xi_s \omega_s m_s \dot{y}_s^2(t) \quad \text{and} \quad \dot{e}(t) = de(t)/dt = 4\xi_s \omega_s m_s \dot{y}_s(t)\ddot{y}_s(t) \tag{2}$$

Let $\langle . \rangle$ denotes the expectation; the mean value of the DPP can be obtained as follows (Greco and Marano 2013):

$$\rho = \left\langle c_s \dot{y}_S^2(t) \right\rangle = 2\xi_s \omega_s m_s \left\langle \dot{y}_s^2(t) \right\rangle = 2\xi_s \omega_s m_s \sigma_{\dot{y}_S}^2 \tag{3}$$

The acceleration covariance matrix is related to the covariance matrix **R** and it is given by:

$$\mathbf{R_{\ddot{y}\ddot{y}}} = \left\langle \ddot{y}\ddot{y}^T \right\rangle = \begin{pmatrix} \mathbf{D}_1 & \mathbf{D}_2 \end{pmatrix} \mathbf{R} \begin{pmatrix} \mathbf{D}_1 & \mathbf{D}_2 \end{pmatrix}^T , \quad \mathbf{D}_1 = \begin{pmatrix} -\omega_T^{\ 2} & \omega_T^{\ 2} & \omega_f^{\ 2} \\ \mu\omega_T & -(\mu\omega_T^{\ 2} + \omega_s^{\ 2}) & \omega_f^{\ 2} \end{pmatrix}$$

and $\mathbf{D}_2 = \begin{pmatrix} -2\xi_T\omega_T & 2\xi_T\omega_T & 2\xi_f\omega_f \\ 2\mu\xi_T\omega_T & -2(\xi_s\omega_s + \mu\xi_T\omega_T) & 2\xi_f\omega_f \end{pmatrix}.$

Hence, the root mean square $\sigma_{\ddot{y}_s}$ of the relative acceleration $\ddot{y}_s$ can be immediately deduced and written as $\sigma_{\ddot{y}_s} = \sqrt{\mathbf{R_{\ddot{y}\ddot{y}}}(2,2)}$.

2.2 Frequency Response of the Primary Structure with Single-TMD

Let $\Phi(\omega) = S_0 \left(\omega_f^4 + 4\xi_f^2\omega_f^2\omega^2\right) \big/ \left((\omega_f^2 - \omega^2)^2 + 4\xi_f^2\omega_f^2\omega^2\right)$ be the Kanai-Tajimi PSD (Seug-Yong et al. 2009), the frequency response function of the primary structure is obtained using the state space representation as follows:

$$h_{y_s}(\omega) = \mathbf{Cy}(i\omega\mathbf{I} - \mathbf{A}_0)^{-1}\mathbf{G} \tag{4}$$

where $\mathbf{Cy} = (0 \ \ 1 \ \ 0 \ \ 0)$, $\mathbf{G} = (0 \ \ 0 \ \ -1 \ \ -1)^T$, $\mathbf{I}$ is the identity matrix, ω is the circular frequency argument; $\mathbf{A}_0$ is the state space matrix corresponding to the state vector $\mathbf{Y}_0 = (y_T, y_s, \dot{y}_T, \dot{y}_s)^T$ and it can be written as

$$\mathbf{A}_0 = \begin{pmatrix} 0 & 0 & 1 & 0 \\ 0 & 0 & 0 & 1 \\ -\omega_T^2 & \omega_T^2 & -2\xi_T\omega_T & 2\xi_T\omega_T \\ \mu\omega_T^2 & -(\mu\omega_T^2 + \omega_s^2) & 2\mu\xi_T\omega_T & -(2\mu\xi_T\omega_T + 2\xi_s\omega_s) \end{pmatrix}.$$

The displacement power spectral density (PSD) of the primary structure is immediately obtained as follows:

$$S_{yy}(\omega) = \left| h_{y_s}(\omega) \right|^2 \Phi(\omega) \tag{5}$$

3   The Proposed Optimization Strategies for the Single-TMD

In the present work, two optimization strategies are considered. The first one is a new RBO strategy involving the DPP $e(t)$ of the primary structure. The second is an optimization strategy recently introduced in (Greco and Marano 2013) involving not the DPP itself, but its mean value.

The new RBO strategy consists to find the optimum design parameters $\mathbf{d} = (\omega_T, \xi_T)^{\mathbf{T}}$, of the TMD device, that minimizes the failure probability P_f characterized by the exceedence, for the first time, of the DDP $e(t)$ of a certain threshold value β during a time interval $[0, T]$.

Considering the Poisson assumptions (Li and Chen 2009), the failure probability can be approximated by $P_f \approx 1 - \exp\left(-\upsilon_\beta(\beta)T\right)$ where $\upsilon_\beta(\beta)$ is the mean out-crossing rate of the DPP that can be obtained, using the classical Rice's formula, as follows:

$$\upsilon_\beta(\beta) = \int_0^\infty \dot{e}.p_{E\dot{E}}(\beta,\dot{e})d\dot{e} \tag{6}$$

where $p_{E\dot{E}}$ is the joint probability function (PDF) of the considered DPP and its time derivative. After manipulations, the mean out-crossing rate can be written as $\upsilon_\beta(\beta) = (\sigma_{\ddot{y}_s}/\pi\sigma_{\dot{y}_s})\exp\left\{-\beta/4\xi_s\omega_s m_s\sigma_{\dot{y}_s}^2\right\}$ and the failure probability can be deduced; therefore the RBO problem with DPP approach can be formulated as follows:

Find $\mathbf{d} = (\omega_T, \xi_T)$ To minimize

$$P_f = 1 - \exp\left\{-T(\sigma_{\ddot{y}_s}/\pi\sigma_{\dot{y}_s})\exp\left(-\beta/4\xi_s\omega_s m_s\sigma_{\dot{y}_s}^2\right)\right\} \tag{7}$$

The second optimization strategy is inspired by the work presented in (Greco and Marano 2013). The strategy is based on the mean value of the DPP expressed in Eq. (3) and can be formulated as follows:

Find $\mathbf{d} = (\omega_T, \xi_T)$ To minimize

$$\rho = 2\xi_s \omega_s m_s \sigma_{\dot{y}_s}^2 \tag{8}$$

4 Numerical Study

The purpose of the numerical study is to analysis the correlation between the proposed optimization strategies in one hand, and in the other, to investigate their effectiveness in absorb vibrations. To this end, the PSD displacement responses of the primary structure equipped with the proposed optimum TMD parameters are compared with a Bi-TMD. The Bi-TMDs, Fig.1 (b), is a device composed by two parallel TMDs and they have the following optimum parameters (Seug-Yong et al. 2009): $\omega_{T1} = \omega_s(1.0737 + 2.2593\mu)^{-1}$, $\xi_{T1} = 0.2623\mu^{0.3386}$ for the first Bi-TMDs, and $\omega_{T2} = \omega_s(0.9895 + 0.4418\mu)^{-1}$, $\xi_{T1} = 0.4054\mu^{0.4600}$ for the second Bi-TMDs.

The correlation analysis allows establishing relationships and possible equivalences between the proposed optimization approaches. To this end, a dimensionless quantity $\psi = \omega_f / \omega_s$ is introduced to make comparison between the obtained results of the proposed strategies. The structural parameters are assumed to be $m_s = 1$, $\omega_s = 8\pi$, $\xi_f = 0.4$, $\xi_s = 0.03$, $S_0 = 0.03$, $\mu = 2\%$, $\beta = 0.045$ and $T = 10s$. For the optimization, the genetic algorithm routine available in Matlab is used.

Figure 2 gives the optimum design parameters of the TMD when both approaches are applied. From Fig. 2(a) one can observe that, for both strategies, the optimum natural frequencies are earthquake dependant for $\psi < 2$. Indeed, the optimized natural frequencies are increasing functions until roughly $\psi \approx 1.5$ and then decreasing function until values neighboring $\psi \approx 2$. Besides, it seems that the natural frequencies become approximately constant for values $\psi > 2$, which means earthquake independence. Figure 2 (b) shows that the optimized damping ratios obtained using the proposed strategies are also earthquake dependent for $\psi < 2$ and they become independent for $\psi > 2$. In effect, the optimized damping ratios are roughly linear decreasing function until $\psi \approx 1$ where a minimum is reached, then increasing function until $\psi \approx 2$. In addition, the observed curve slope of the obtained results shown in Fig. 2(b) for $\psi < 1$, also prove that the TMD performances are strongly dependant on earthquake. The optimized failure probabilities P_f^* obtained using the RBO approach and the failure probabilities

P_f evaluated using the optimum values when the mean value of the DPP approach is applied as well as their corresponding relative error are shown in Fig.3.
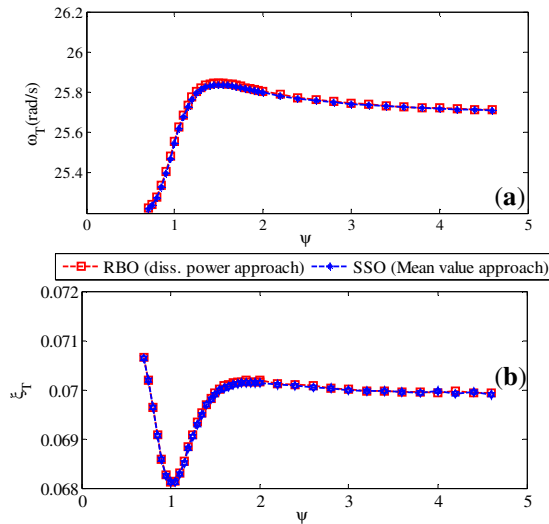

Fig. 2 Optimum natural frequencies (a) and damping ratios (b), obtained using the RBO and the mean value of the DPP approaches.

The obtained results shown in Fig. 3(a) confirm the remarks made previously in Fig.2. Indeed, the obtained values of P_f^* present large variability vs. ψ and the TMD performance is strongly earthquake dependant especially for the values neighboring $\psi \approx 1.15$ where a maximum is reached. It is also observed that the optimized failure probabilities are less sensitive, to earthquake, for $\psi > 2$. Besides, the examination of the curve corresponding to the optimized values showed that it is below the curve corresponding to the failure probability evaluated using the optimum parameters when the mean value approach is applied. Figure 3(b) shows the relative error between the optimized failure probabilities obtained when the RBO is applied and the failure probabilities evaluated using the optimum TMD parameters obtained when the mean value approach is applied. The examination of this figure demonstrates that a maximum is reached for $\psi \approx 1,05$ with an error $\varepsilon_1^{\max} = 6,610^{-3}\%$. Besides it has been also found that the error is smaller than $10^{-3}\%$ for $\psi > 3,8$.

Figure 4(a) shows the optimized mean values of the DPP ρ^* compared with the mean values ρ of the DPP evaluated using the optimum TMD parameters if the RBO approach is applied. The same observations made previously for Fig. 3(a) can be done for Fig. 4(a). Indeed the TMD performance is strongly

dependant on earthquake for values around $\psi \approx 1.15$ then it's less sensitive for $\psi > 2$. The curve corresponding to the optimized values are below the curve corresponding to the mean values of the DPP evaluated with the optimum parameters when the RBO approach is applied.
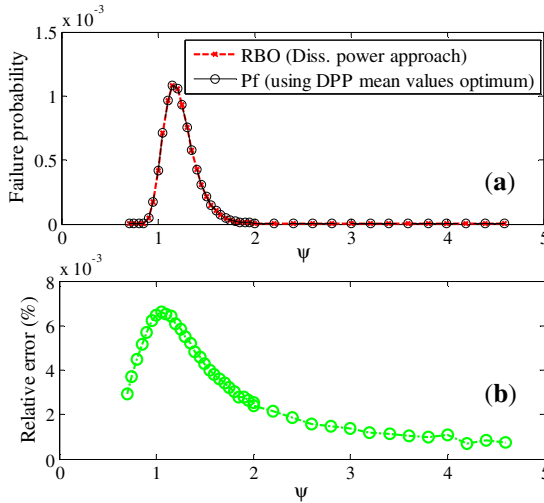
Fig. 3 (a) P_f^* obtained using the RBO approach compared with those evaluated using the optimum values obtained using the mean value DPP approach; (b) the relative error

The relative error between ρ^* and ρ is given in Fig.4 (b). The inspection of this figure shows that a maximum error $\varepsilon_2^{max} = 0,5.10^{-3}\%$ is reached for $\psi \approx 1.05$ and it is roughly zero for $\psi > 2$. The comparison of the obtained results in Fig.3 (b) and Fig.4 (b) demonstrate clearly that the RBO using the DPP approach is more robust than the approach using the mean value of the DPP. Herein, the robustness should be understood in sense that the RBO strategy can provide the results obtained with the mean value approach with an error less than $\varepsilon_2^{max} = 0,5.10^{-3}\%$, which is roughly twelve times less than the obtained error, $\varepsilon_1^{max} = 6,610^{-3}\%$, in the reciprocal case.

Figure 5 depicts the PSD displacement response of the primary structure when it's equipped with single and Bi-TMDs. The responses are compared with the PSD response without TMD. The examination of Fig.5 shows clearly that both optimization strategies have the same effectiveness and they are more effective than the Bi-TMDs. Indeed, for frequencies neighboring 26 rad/s, the PSD response with the proposed optimization strategies (i.e., the RBO and mean values) is less than the PSD response when the primary structure is equipped by Bi-TMDs. Nevertheless, it's also observed that the bandwidth frequency suppressed by the Bi-tuned

mass dampers is larger than those suppressed with the single-TMDs which is completely predictable.
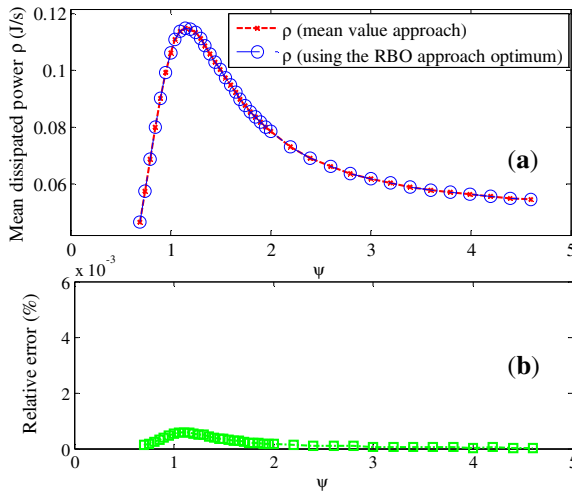
Fig. 4 (a) ρ^* obtained using the DPP mean values approach compared with those evaluated using the optimum values obtained with the RBO approach; (b) the relative error
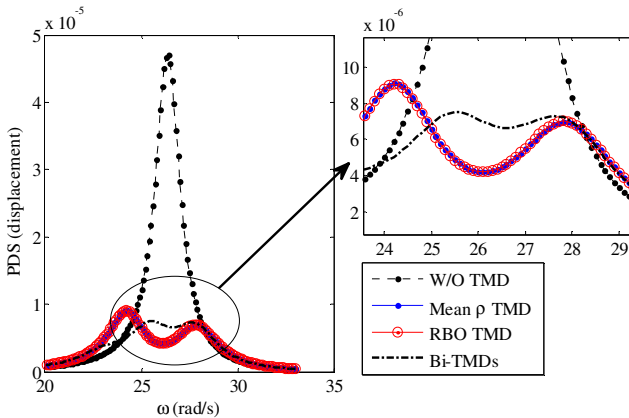
Fig. 5 Effectiveness of the proposed optimization approaches compared with Bi-TMDs $\psi = 1.10$

5   Conclusion

In this paper two optimization strategies of single-TMD parameters under stochastic loading are presented and compared. The selection of one of these strategies totally depends on the designer aim. The first one is a new RBO strategy and it uses

the DPP in the primary structure. The introduction of this strategy is motivated by the strictly relationship between the DPP in the primary structure and the damage level of the vibrating structure.

The second strategy is based on the mean value of the DPP and could refer to an SSO problem.

The expression of the failure probability, for the RBO approach, is presented and a comparison between the presented strategies is made. The obtained results show that both strategies are strongly earthquake dependent on values of earthquake frequencies close to main system frequency and they are less sensitive outside of this frequency.

The correlation analysis made between the presented strategies showed that the RBO approach is more robust in sense that it can provide the optimized TMD parameters if the mean value approach is applied; the maximum relative error raised is less than $0,5.10^{-3}\%$.

Besides, it has been found that the single-TMD device optimized with the new RBO strategy is more effective, to absorb vibration, than the Bi-TMDs.

References

Yu, H., Gillot, F., Ichchou, M.N.: Reliability based robust design optimization for tuned mass damper in passive vibration control of deterministic/uncertain structures. J. Sound Vib. 332, 2222–2238 (2013)

Marano, G.C., Greco, R., Sgobba, S.: A comparison between different robust optimum design approaches: Application to tuned mass dampers. Probab. Eng. Mech. 25, 108–118 (2010)

Chakraborty, S., Roy, B.K.: Reliability based optimum design of tuned mass damper in seismic vibration control of structures with bounded uncertain parameters. Probab. Eng. Mech. 26, 215–221 (2011)

Gupta, S., Manohar, C.S.: Probability Distribution of Extremes of Von Mises Stress in randomly vibrating structures. J. Vib. Acoust. 127, 547–555 (2005)

Crandall, S.H.: First crossing probabilities of the linear oscillator. J. Sound Vib. 12(3), 285–299 (1970)

Li, J., Chen, J.: Stochastic dynamics of structures. John Wiley, Asia (2009)

Greco, R., Marano, G.C.: Optimum design of Tuned Mass Dampers by displacement and energy perspectives. Soil Dyn. Earthq. Eng. 49, 243–253 (2013)

Ok, S.-Y., Song, J., Park, K.-S.: Development of optimal design formula for bi-tuned mass dampers using multi-objective optimization. J. Sound Vib. 322, 60–77 (2009)

An Analytical Solution for Vibration Reduction of a Thin Rectangular Plate Using Shunted Piezoelectric Patches

Enis Boukraa[1,2], Walid Larbi[1], Makram Chaabane[2],
Jean François Deü[1], and Mnaouar Chouchane[2]

[1] Conservatoire National des Arts et Métiers (Cnam), Structural Mechanics and Coupled
    Systems Laboratory, Chair of Mechanics, Case 353, 2 rue Conté, 75003 Paris, France
    `boukraa.enis@gmail.com,`
    `{walid.larbi,jean-francois.deu}@cnam.fr`
[2] Ecole Nationale d'Ingénieurs de Monastir (ENIM),
    Rue Ibn El Jazzar, 5000 Monastir, Tunisia
    `{mnaouar.chouchane,makram.chaabane}@enim.rnu.tn`

Abstract. In the context of vibration reduction using piezoelectric semi-passive techniques, this paper presents an analytical solution for the dynamic response of a thin plate with various boundary conditions fitted with a shunted piezoelectric patch. The proposed formulation is based on the classical plate theory and takes into account the effect of the mass and the stiffness of the piezoelectric patch. The Rayleigh-Ritz modal projection method is applied to convert the partial differential equations into ordinary differential equations. An example of a vibration attenuation application using an RL shunt circuit is presented.

Keywords: Vibration control, piezoelectric shunt, analytic solution, dynamic effect, plate structures.

1 Introduction

Piezoelectric patches have recently been the subject of numerous researches particularly in the field of vibration control and energy harvesting. These two research fields are closely related since they apply the conversion of the electromechanical energy of piezoelectric material systems. This has made these devices particulary atractive for researchers especially in the last two decades. Hence, numerous analytical and numerical models of piezoelectric structures such as piezoelectric plates have been devoloped.

In the analytical modeling, it is common to neglect the influence of the mass and stiffness of the patch in the coupled system. This assumption was proposed by Crawley and de Luis[1] who suggested that the induced bending of the actuator can be represented as an external load consisting of a pair of line moments of opposite signs located at the actuator edges. This assumption greatly simplifies calculations but it is reliable only when dealing with small size patches, precisely thin and lightweight

patches, compared to the dimensions of the plate. Several researchers have adopted this assumption. For exemple, a formulation assuming that these line moments are proportional to the applied voltage was proposed by Fuller, Elliott and Nelson[2]. The same formulation has been developed in the case of multiple patches attached to two plates forming a double wall by Pietrzko and Mao[3]. Aridogan, Basdogan and Erturk[4] applied the same modeling approach to a piezoelectric patch embedded in a resistive plate.

In general, the mass and the stiffness of the piezoelectric patch need to be considered for medium and large sized patches. Charette, Berry and Guigou[5], used the variational approach and Hamilton's principle to develop a model which is used to determine the dynamic effect of the piezoelectric elements on the mechanical response of the plate. They proved that the patch modifies the vibration modes and shifts the natural frequencies of the plate causing the emergence of unexpected resonance peaks that researchers previously attributed to experimental errors. Proulx and Cheng[6] have shown that patches, particulary those with large dimensions, affect the response of vibrating plates especially away from resonances. Maurini, Porfiri and Pouget[7] have found significant discrepancies between the experimental modes and those calculated without taking into account the dynamic effect of the patch. Liang and Batra[8] investigated the effect of thickness, mass, and stiffness of a piezoelectric patch on the natural frequencies of a plate. An analytical formulation of the equation of motion using the classical theory of plates was presented by Koshigoe and Murdock[9] ignoring the dynamic effect of the patch.

In this paper, we present a complete analytical formulation of a homogeneous thin rectangular plate fitted with a piezoelectric patch. We use the classical theory of plates and the Rayleigh-Ritz modal projection method taking into account the dynamic effect of the patch on the structure. This model is then applied in the case of a simply supported plate (SSSS) and clamped plate (CCCC). The response of the system is determined for a unit external harmonic pressure uniformly applied on the plate. Numerical and analytical frequency response functions (FRFs) are then compared to determine the accuracy of the developed model. The effect of dynamic parameters of the patch on the response of the structure is determined by comparison to the response of the unpatched plate. Furthermore, we consider the effect of piezoelectric coupling which is responsible for the electromechanical conversion of energy. Passive control technique using a resonant circuit is used. The motivation for choosing this technique is its simplicity and efficiency. Indeed, the resonant shunt method has proved to be very useful especially for local control of vibration. By adjusting the electrical parameters, the chosen vibration mode can then be controlled.

2 Equations of Motion

In this section, we present an analytical model for the frequency response of an elastic plate having a perfectly bound piezoelectric patch including the effect of mass and stiffness of the patch. Two types of conditions are considered: (i) simply supported plate on all four edges and (ii) clamped plate on all four edges.
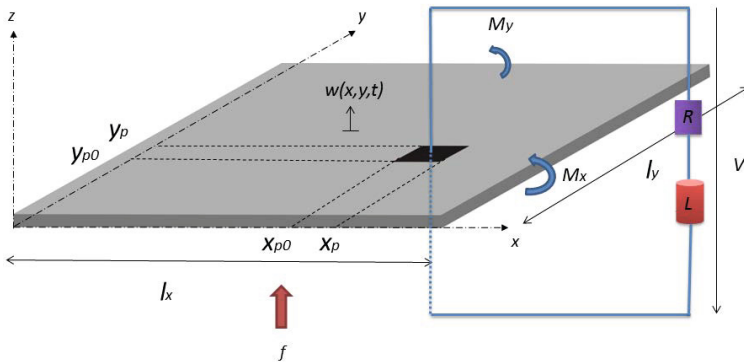
Fig. 1 A rectangular plate with a resonnant piezoelectric shunt

We consider in figure (1) a system composed of a homogeneous isotropic plate with dimensions l_x, l_y, h, Young's modulus E, mass density m and Poisson's ratio ν. This plate is partially covered with a rectangular piezoelectric patch with a dimensions l_{xp}, l_{yp}, h_p, Young's modulus E_p, mass density m_p and Poisson's ratio ν_p. The lower left corner of the patch is positioned at (x_{p0}, y_{p0}) on the top surface of the plate. We denote by w the transverse displacement of the plate. The linear piezoelectric constitutive equations of the system are:

$$\varepsilon_1 = \tfrac{1}{E}\sigma_1 - \tfrac{\nu}{E}\sigma_2 \qquad \varepsilon_1^p = \tfrac{1}{E_p}\sigma_1^p - \tfrac{\nu_p}{E_p}\sigma_2^p + d_{13}E_3$$

$$\varepsilon_2 = -\tfrac{\nu}{E}\sigma_1 + \tfrac{1}{E}\sigma_2 \qquad \varepsilon_2^p = -\tfrac{\nu_p}{E_p}\sigma_1^p + \tfrac{1}{E_p}\sigma_2^p + d_{23}E_3$$

$$\varepsilon_6 = \tfrac{E}{2(1-\nu)}\sigma_6 \qquad \varepsilon_6^p = \tfrac{E_p}{2(1-\nu_p)}\sigma_6^p + d_{63}E_3$$

$$D_3 = d_{13}\sigma_1^p + d_{23}\sigma_2^p + \epsilon_{33}E_3$$

(1)

where σ_i and ε_i are respectively the plate stresses and the plate strains. Similarly, σ_i^p and ε_i^p are stresses and strains of the piezoelectric element, d_{ij} are the piezoelectric coefficients, E_3 is the electric transverse field and D_3 is the electric displacement. It should be noted that d_{63} is generally neglected.

Consider now the case of a plate excited by a uniform external harmonic pressure f. The equation of motion, under Kirchhoff assumptions for thin plates, can be written as:

$$\frac{\partial^2(M_x + m_x + m_{ex})}{\partial x^2} + \frac{\partial^2(M_y + m_y + m_{ey})}{\partial y^2}$$
$$+ \frac{\partial^2(M_{xy} + m_{xy})}{\partial x \partial y} = (m + m_p \Gamma_{xy})\frac{\partial^2 w}{\partial t^2} + f$$

(2)

where:

• M_x, M_y and M_{xy} are the internal bending moments of the plate given by:

$$M_x = -D[\frac{\partial^2 w}{\partial x^2} + \nu \frac{\partial^2 w}{\partial y^2}] \quad M_y = -D[\frac{\partial^2 w}{\partial y^2} + \nu \frac{\partial^2 w}{\partial x^2}]$$

$$M_{xy} = -D(1-\nu)\frac{\partial^2 w}{\partial x \partial y} \tag{3}$$

• m_x, m_y, m_{xy} are the moments of the patch given by:

$$m_x = -D_p\Gamma_{xy}[\frac{\partial^2 w}{\partial x^2} + \nu_p \frac{\partial^2 w}{\partial y^2}] \quad m_y = -D_p\Gamma_{xy}[\frac{\partial^2 w}{\partial y^2} + \nu_p \frac{\partial^2 w}{\partial x^2}]$$

$$m_{xy} = -D_p\Gamma_{xy}(1-\nu_p)\frac{\partial^2 w}{\partial x \partial y} \tag{4}$$

D and D_p are respectively the bending stiffnesses of the plate and the patch:

$$D = \frac{E}{12(1-\nu^2)}h^3 \qquad D_p = \frac{E_p}{3(1-\nu_p^2)}(h_p^3 + \frac{3}{2}hh_p^2 + \frac{3}{4}h^2h_p) \tag{5}$$

and Γ_{xy} is a localisation function defined by:

$$\Gamma_{xy} = [H(x-x_{p0}) - H(x-x_p)][H(y-y_{p0}) - H(y-y_p)] \tag{6}$$

where H is the Heavyside function whose value is 1 on the surface of the patch A_p and 0 elsewhere.

• m_{ex} and m_{ey} are the electrical moments. Their expressions, under assumptions of an isotropic piezoelectric material ($d_{13} = d_{12}$) and a uniform electric field $E_3 = -\frac{V}{h_p}$ (V is the voltage across the patch), are given by:

$$m_{ex} = m_{ey} = -C_0\epsilon_0\Gamma_{xy} \tag{7}$$

where,

$$C_0 = \frac{E_p}{1-\nu_p}(\frac{hh_p+h_p^2}{2}) \qquad \epsilon_0 = \frac{d_{13}V}{h_p} \tag{8}$$

Substituting the expressions of moments (3), (4) and (7) in equation (2) yields:

$$(D + D_p\Gamma_{xy}) \left[(\frac{\partial^4 w}{\partial x^4}) + (\frac{\partial^4 w}{\partial y^4}) + 2(\frac{\partial^4 w}{\partial x^2 \partial y^2}) \right] +$$

$$D_p\frac{\partial^2 \Gamma_{xy}}{\partial x^2} \left[(\frac{\partial^2 w}{\partial x^2}) + \nu_p(\frac{\partial^2 w}{\partial y^2}) \right] + D_p\frac{\partial^2 \Gamma_{xy}}{\partial y^2} \left[(\frac{\partial^2 w}{\partial y^2}) + \nu_p(\frac{\partial^2 w}{\partial x^2}) \right] +$$

$$2D_p\frac{\partial \Gamma_{xy}}{\partial x} \left[(\frac{\partial^3 w}{\partial x^3}) + (\frac{\partial^3 w}{\partial x \partial y^2}) \right] + 2D_p\frac{\partial \Gamma_{xy}}{\partial y} \left[(\frac{\partial^3 w}{\partial y^3}) + (\frac{\partial^3 w}{\partial y \partial x^2}) \right] + \tag{9}$$

$$2(1-\nu_p)D_p\frac{\partial^2 \Gamma_{xy}}{\partial x \partial y}\frac{\partial^2 w}{\partial x \partial y} + (m + m_p\Gamma_{xy})\frac{\partial^2 w}{\partial t^2}$$

$$= C_0\epsilon_0\nabla^2\Gamma_{xy} - f$$

On the other hand, the expression of the electric charge for a thin plate is given by:

$$Q = \int_{A_p} -D_3(h/2 + h_p/2)dA_p \tag{10}$$

Using the expression of D_3 given in equation (1) and the stresses-moments relationships[15], we obtain:

$$Q = \frac{E_p d_{13}}{1 - \nu_p}[(h/2 + h_p/2)\int_{A_p}(\frac{\partial^2 w}{\partial x^2} + \frac{\partial^2 w}{\partial y^2})dA_p - \int_{A_p}\frac{2d_{13}V}{h_p}dA_p]+$$

$$\int_{A_p}\frac{\epsilon_{33}V}{h_p}dA_p \tag{11}$$

Thus, the exact equation of motion of a plate with a bound piezoelectric patch is obtained. Indeed, equations (9) and (11) define the electro-mechanical behavior of the coupled plate-patch system.

3   Solution Method by Rayleigh-Ritz Modal Projection

According to the Rayleigh-Ritz method, $w(x, y, t)$ may be expanded as follows:

$$w(x, y, t) = \sum_{p=1}^{k}\sum_{q=1}^{l}\phi_{pq}(x, y)q_{pq}e^{j\omega t} \tag{12}$$

where $\phi_{pq}(x, y)$ and q_{pq} are respectively the modal functions and the modal displacements and $j = \sqrt{-1}$. The numbers k and l must obviously tend towards infinity. In the following, we assume that the eigenfunctions of the unpatched plate are also valid for a plate with a patch system. This assumption is usually acceptable as long as the patch's structure is similar to that of the plate and its thickness is small compared to the thickness of the plate. Multiplying equation (9) by $\phi_{mn}(x, y)$, integrating over the surface of the plate A, and using the orthogonal property of the eigenmodes and the identity of the distribution:

$$< f(x), \frac{\partial \Gamma_{xy}}{\partial x} > = \int_A f(x)\frac{\partial \Gamma_{xy}}{\partial x}dA = < -\frac{\partial f(x)}{\partial x}, \Gamma_{xy} > \tag{13}$$

we obtain:

$$\left[-m\omega^2\int_A \phi_{mn}{}^2(x,y)dA\right]q_{mn} + \sum_{p=1}^{i}\sum_{q=1}^{j}\left[D\int_A \phi_{mn}(x,y)\nabla^4\phi_{pq}(x,y)dA+\right.$$

$$D_p\int_{A_p}\left\{2(1-\nu_p)\frac{\partial^2\phi_{pq}}{\partial x\partial y}\frac{\partial^2\phi_{mn}}{\partial x\partial y} + \nu_p(\frac{\partial^2\phi_{pq}}{\partial x^2}\frac{\partial^2\phi_{mn}}{\partial y^2} + \frac{\partial^2\phi_{pq}}{\partial y^2}\frac{\partial^2\phi_{mn}}{\partial x^2})+\right.$$

$$\left.\frac{\partial^2\phi_{pq}}{\partial x^2}\frac{\partial^2\phi_{mn}}{\partial x^2} + \frac{\partial^2\phi_{pq}}{\partial y^2}\frac{\partial^2\phi_{mn}}{\partial y^2}\right\}dA_p - m_p\omega^2\int_{A_p}\phi_{mn}\phi_{pq}dA_p\right]q_{pq}$$

$$= -\int_A f\phi_{mn}dA + \int_A C_0\frac{d_{13}V}{h_p}\nabla^2\Gamma_{xy}\phi_{mn}(x,y)dA$$

$$(14)$$

Note that the eigenfunctions for a simply supported plate are given by:

$$\phi_{pq}(x,y) = \sin(\frac{p\pi x}{l_x})\sin(\frac{q\pi y}{l_y}) \tag{15}$$

For a clamped plate, the eigenfunctions are:

$$\phi_{pq}(x,y) = [\cos(\gamma_p x) + \beta_p\sin(\gamma_p x) - \cosh(\gamma_p x) - \beta_p\sinh(\gamma_p x)]$$

$$[\cos(\gamma_q y) + \beta_q\sin(\gamma_q y) - \cosh(\gamma_q y) - \beta_q\sinh(\gamma_q y)] \tag{16}$$

where γ_p is the pth solution of the following frequency equation:

$$\cosh(\gamma l_x)\cos(\gamma l_x) = 1 \tag{17}$$

and:

$$\beta_p = \frac{\cos(\gamma_p l_x) - \cosh(\gamma_p l_x)}{\sinh(\gamma_p l_x) - \sin(\gamma_p l_x)} \tag{18}$$

Note that similar expressions are obtained for γ_q and β_q in the y axis direction.

4 Vibration Attenuation with a Resonant Shunt System

Semi-passive vibration control techniques are very useful because they require no external interventions. In this sense, piezoelectric shunts have recently been introduced including resistive shunts with a resistor R and resonant shunts combining a resistance R and an inductance L in series[10]. The resonant shunt is more interesting because it introduces the phenomenon of electric resonance which creates greater energy absorption. However, this technique has two major drawbacks: the difficulty associated with the selection of the value of the inductance L and the multimodal control. Indeed, the control of vibration via a resonant shunt requires usually a high inductance that can be of the order of thousands of Henries especially for the control of low frequencies or in the case of a small size patch. To overcome this problem,

electric capacitors are included in the circuit to create an RLC shunt which requires a much lower inductance[11]. The second obstacle lies in the fact that shunts can control only one vibration resonance mode. Some solutions include the introduction of other electrical circuit layouts but they are usually effective only for close frequencies[12]. Another solution consists in the introduction of a network of piezoelectric shunts[13]. In the following, we consider a patch connected to a resonant RL circuit in order to form a piezoelectric resonant shunt. Furthermore, we consider a harmonic solution for the voltage V:

$$V(t) = v e^{j\omega t} \tag{19}$$

Considering an RL circuit in series, we have:

$$V(\omega) = -R\dot{Q}(\omega) - L\ddot{Q}(\omega) \tag{20}$$

Combining equations (11) and (14) and using equation (20), we obtain the governing equation for a plate with a bound RL shunted piezoelectric patch:

$$\left[-m\omega_{mn}^2 \int_A \phi_{mn}^2(x,y)dA \right] q_{mn} + \sum_{p=1}^{i}\sum_{q=1}^{j}\left[D\int_A \phi_{mn}(x,y)\nabla^4\phi_{pq}(x,y)dA \right.$$

$$+ D_p \int_{A_p}\left\{ 2(1-\nu_p)\frac{\partial^2\phi_{pq}}{\partial x\partial y}\frac{\partial^2\phi_{mn}}{\partial x\partial y} + \nu_p(\frac{\partial^2\phi_{pq}}{\partial x^2}\frac{\partial^2\phi_{mn}}{\partial y^2} + \frac{\partial^2\phi_{pq}}{\partial y^2}\frac{\partial^2\phi_{mn}}{\partial x^2}) + \right.$$

$$\left. \frac{\partial^2\phi_{pq}}{\partial x^2}\frac{\partial^2\phi_{mn}}{\partial x^2} + \frac{\partial^2\phi_{pq}}{\partial y^2}\frac{\partial^2\phi_{mn}}{\partial y^2} \right\}dA_p - m_p\omega_{pq}^2 \int_{A_p}\phi_{mn}\phi_{pq}dA_p \right] q_{pq} +$$

$$\sum_{p=1}^{i}\sum_{q=1}^{j}[-\frac{C_0^2 d_{13}^2}{K_e h_p^2}\Delta\phi_{mn}\Delta\phi_{pq}G_{pq}]q_{pq} = -\int_A f\phi_{mn}dA \tag{21}$$

where,

$$K_e = \frac{l_{xp}l_{yp}}{h_p}(\epsilon_{33-2}\frac{d_{13}^2 E_p}{1-\nu_p})$$

$$\Delta\phi_{mn} = \int_{A_p}\left[\frac{\partial^2\phi_{mn}(x,y)}{\partial x^2} + \frac{\partial^2\phi_{mn}(x,y)}{\partial y^2} \right]dA_p \tag{22}$$

$$G_{pq} = \frac{jR\omega_{pq} - L\omega_{pq}^2}{K_e^{-1} + jR\omega_{pq} - L\omega_{pq}^2}$$

Thus, we obtain a complete model in which the electric coupling depends on the chosen values of R and L. These parameters can be used to modify the system's response in a restricted frequency range and therefore to control a single mode of vibration. The optimization of the electrical parameters for a single

mode has already been reported in reference [14] for the beam case. Indeed, an approximated coupling coefficient $\hat{k}_{mn}$, corresponding to a single mode problem ($q_{pq} = 0$ $\forall (p,q) \neq (m,n)$), can be calculated and maximized. For this case, we obtain:

$$\hat{k}_{mn} = \sqrt{-\frac{C_0{}^2 d_{13}^2}{\hat{K} K_e h_p^2} \Delta \phi_{mn}} \tag{23}$$

where $\hat{K}$ is the stiffness of a short circuit restricted to a single mode:

$$\hat{K} = D \int_A \phi_{mn}(x,y) \nabla^4 \phi_{mn}(x,y) dA + D_p \int_{A_p} \left\{ 2(1-\nu_p) \frac{\partial^2 \phi_{mn}}{\partial x \partial y} \frac{\partial^2 \phi_{mn}}{\partial x \partial y} + \right.$$
$$\left. \nu_p \left(\frac{\partial^2 \phi_{mn}}{\partial x^2} \frac{\partial^2 \phi_{mn}}{\partial y^2} + \frac{\partial^2 \phi_{mn}}{\partial y^2} \frac{\partial^2 \phi_{mn}}{\partial x^2} \right) + \frac{\partial^2 \phi_{mn}}{\partial x^2} \frac{\partial^2 \phi_{mn}}{\partial x^2} + \frac{\partial^2 \phi_{mn}}{\partial y^2} \frac{\partial^2 \phi_{mn}}{\partial y^2} \right\} dA_p \tag{24}$$

However, the vibration modes usually affect each other so these parameters should be adjusted depending on the considered problem.

5 Results and Discussion

We present in this section an example of a flexural vibration analysis of a rectangular simply supported thin plate equiped with a piezoelectric PIC151 patch under a harmonic uniformly distributed force of a unit amplitude. The patch is assumed to be perfectly bound to the plate on its top surface. All the material, geometric, dielectric and electroelastic parameters of the plate and the patch are given in Table (1).

Table 1 Material, geometric, dielectric and electroelastic parameters of plate-patch system

Property	Plate (Aluminium)	Patch (Pic151)
Length (m)	0.4	0.1
Width (m)	0.3	0.09
Thickness (mm)	3	1
Young's modulus (GPa)	66	44
Mass density (Kgm^{-3})	2700	7700
Poisson Ratio	0.3	0.34
Piezoelectric constant d_{13} (pmV^{-1})	-	-210
Permittivity constant ϵ_{33} (nFm^{-1})	-	21.24
X position x_{p0} (m)	-	0.14
Y position y_{p0} (m)	-	0.1

A complete model of the plate-patch system has been established including the effect of mass, stiffness and electromechanical coupling of the piezoelectric patch. The model is given in equation (21). Thus, we can determine the response of the structure under the effect of a uniform harmonic pressure. Consider at first the response of the structure without the piezoelectric coupling in order to investigate the
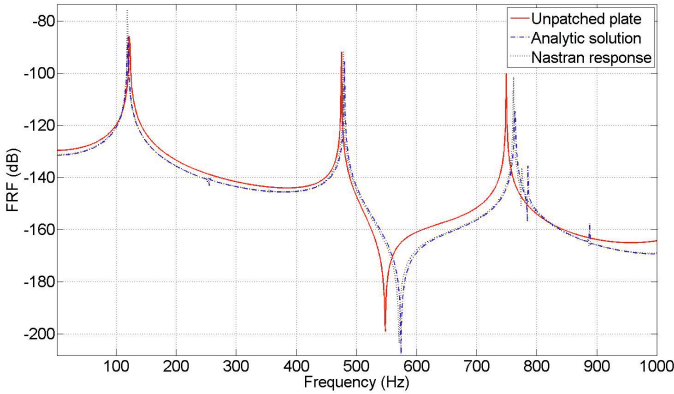
Fig. 2 Frequency response at the center of the simply supported plate without piezoelectric coupling effect
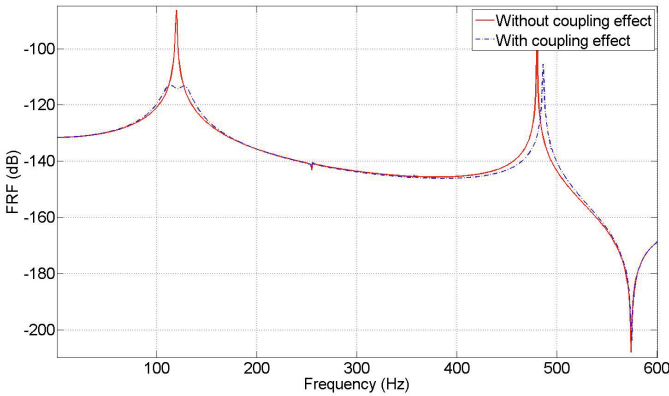
Fig. 3 Comparison of the responses with and without piezoelectric coupling effect for the simply supported plate

dynamic effect of the piezoelectric actuator. It is of interest to investigate these dynamic effects particularly in the case of heavy and large patches[5]. The FRF at the center of the plate under a unit pressure is plotted for the case of a simply supported boundary conditions in figure (2).

Figure (2) shows a good agreement between the analytical solution and the solution found using Nastan. Since the thikness of the patch is small compared to the thikness of the plate, using the eigenfunctions of the unpached plate gives valid results. We can also see that the patch affects slightly the response of the plate by shifting its natural frequencies and creating additionnal resonance peaks of small amplitudes. Although these effects are not of great significance on the overall behavior of the structure, they can nevertheless be taken into account in the

optimization of the mechanical and geometrical parameters of the patch. Notice that similar results are obtained for the clamped plate case.

We consider now the electromechanical coupling effect of the piezoelectric patch. In order to control the first vibration mode located at $122Hz$, the patch is tuned to an RL shunt circuit. The optimal values are $R = 1800\ \Omega$ and $L = 11\ H$. The frequency response is plotted in figure (3).

Figure (3) shows that the resonant magnitude for the first vibration mode is significantly reduced due to the shunt damping. Indeed, with appropriate resistance R and inductance L, a single mode of vibration can be controlled. Note that the response of the structure away from the controlled mode is very slightly altered. Since the optimum electrical values change from one vibration mode to another, the other vibration peaks are not attenuated as long as they are far from the first resonance. Thus, the electrical parameters make it possible to control a particular resonance amplitude. Here we obtain an attenuation of 25 dB for the first mode of the simply supported plate.

6 Conclusion

This paper describes the analytical modeling of the flexural vibration of a thin rectangular plate with piezoelectric shunt damping. This modeling takes into account the effects of the mass and the stiffness of the patch. A solution was developed using the Rayleigh-Ritz projection method. It has been shown that the patch, owing to its coupling effect, converts the mechanical vibration energy into an electrical load which can be dissipated in a resistive circuit through Joule effect. Thus, with suitable electrical parameters, a single vibration mode can be controlled. It has also been shown that the patch slightly affects, through its mass and stiffness, the response of the structure by shifting the natural frequencies of the plate and generating small resonance pics.

References

1. Crawley, E.F., De Luis, J.: Use of piezoelectric actuators as elements of intelligent structures. American Institute of Aeronautics and Astronautics Journal 25, 1373–1385 (1987)
2. Fuller, C.R., Nelson, P.A., Elliott, S.J.: Active Control of Vibration. Academic Press, London (1996)
3. Pietrzko, S.J., Mao, Q.: New results in active and passive control of sound transmission through double wall structures. Aerospace Science and Technology 12, 42–53 (2008)
4. Aridogan, U., Basdogan, I., Erturk, A.: Analytical modeling and experimental validation of a structurally-integrated piezoelectric energy harvester on a thin plate. Smart Materials and Structures 23 (2014) (in press)
5. Charette, F., Berry, A., Guigou, C.: Dynamic effects of piezoelectric actuators on the vibrational response of a plate. Journal of Intelligent Material Systems and Structures 8, 513–524 (1997)
6. Proulx, B., Cheng, L.: Dynamic analysis of piezoceramic actuation effects on plate vibration. Thin-Walled Structures 37, 147–162 (2000)

7. Maurini, C., Pouget, J., Porfiri, M.: Modal analysis of stepped piezoelectric beams with applications to electric vibration damping. In: Twelfth International Congress on Sound and Vibration, vol. 37 (2005)
8. Liang, X.Q., Batra, R.C.: Changes in frequencies of a laminated plate caused by embedded piezoelectric layers. AIAA Journal 35, 10 (1996)
9. Koshigoe, S., Murdock, J.W.: A unified analysis of both active and passive damping for a plate with piezoelectric transducers. AIAA Journal 93, 146 (1993)
10. Hagood, N.W., Von Flotow, A.: Damping of structural vibrations with piezoelectric materials and passive elctrical networks. Journal of Sound and Vibration 146, 243–268 (1991)
11. Behrens, S., Fleming, A.J., Moheimani, S.: Reducing the induction requirements of piezoelectric shunt damping systems. Smart Materials and Structures 12, 57 (2003)
12. Behrens, S., Fleming, A.J., Moheimani, S.: Multiple mode current flowing passive piezoelectric shunt controller. Journal of Sound and Vibration 266, 929–942 (2003)
13. Maurini, C.: Piezoelectric composites for distributed passive electric control: beam modelling, modal analysis, and experimental implementation. PhD thesis. Università Degli Studi di Roma, La Sapienza (2005)
14. Ducarne, J.: Modélisation et optimisation de dispositifs non-linéaires d'amortissement de structures par systèmes piézoélectriques commutés. PhD thesis. Conservatoire National des Arts et Métiers, Paris (2009)
15. Chakraverty, S.: Vibration of plates. CRC Press, New York (2009)

Nonlinear Resonance Phenomenon
in Cylindrical Helical Springs

Sami Ayadi and Ezzeddine Hadj Taïeb

Laboratory of Applied Fluid Mechanics and Modelling, University of Sfax,
National Engineering School of Sfax (ENIS), BP1173, 3038Sfax, Tunisia
samya@netcourrier.com, Ezed.Hadj@enis.rnu.tn

Abstract. In this paper, the non-linear resonance phenomenon of helical springs is studied. The mathematical formulation describing this phenomenon is constituted of a system of four non-linear partial differential equations of first order of hyperbolic type. The coefficients of this system are functions of the dependent variables of the problem. Those are the axial and rotational strains and velocities at any section of the spring. Since the governing equations are non-linear, the solution of the dynamic behavior of the spring can only be obtained by approximate numerical techniques. The non-linear characteristics method is applied to calculate the oscillating strains and velocities at equidistant sections of the spring. When the strains are small, the motion equations are rendered linear. In this case the impedance method is applied to calculate the natural frequency spectrum of the spring. The linear resonance of the spring may be produced by applying, at its extremity, a sinusoidal excitation of frequency coinciding with one of the natural frequencies. In these conditions, significant and amplified in time axial and rotational oscillations occur in the spring. A condition of resonance is then established. When the non linear system is excited with these frequencies the resonance phenomenon occurs at the beginning of the dynamic behavior. But, as the natural frequencies are function of strains, the results show that, the frequencies can deviate and after some time the variables starts to decrease and evolutes in a different manner of those in linear case.

Keywords: helical spring, method of characteristics, impedance method, natural frequency, resonance phenomenon.

1 Introduction

Helical springs are important mechanical components in many industrial applications (Wahl 1963) and (Wittrick 1966). The springs are elastic elements wide spread in all kinds of machinery and equipment. Their functions are very diverse. The main role of the springs is to absorb shock and reduce vibrations. Several accidents have been explained by different forms of resonance oscillations of springs. For this reason, the frequency study must be carefully done.

Waves in the spring are a time evolution phenomenon that we generally model mathematically using partial differential equations (PDEs). The actual form that the wave takes is strongly dependent upon the system initial conditions, the boundary conditions, the solution domain and any system disturbances. The spring can vibrate at a fundamental frequency and at integral multiples called harmonics. These waves are described by solutions to either linear or nonlinear PDEs.

Resonance is a phenomenon resulting from the propagation of linear waves that occur when the spring is excited by a sinusoidal signal which frequency is equal to the natural one. This phenomenon may be initiated very gradually, and that builds up a steady-oscillatory regime in real situations (unless failure occurs). Moreover, a beating of a transient nature develops when the period of the excitation is not fundamental or harmonic. Various numerical and analytical methods were applied to determine the natural frequencies of resonance of the spring. These include for example: the method of transfer matrix (Yildirim 1999), the formulation of the dynamic stiffness (Lee and Thompson 2001), the pseudo spectral method (Lee 2007) and the method of impedance (Ayadi and Hadj Taïeb 2009).

In this paper, we study the numerical propagation of elastic non linear waves in a cylindrical helical spring following a sinusoidal excitation of the axial velocity. The mathematical and numerical models describing wave propagation, in the case of gradual excitations in time, have been established by (Phillips and Costello 1971) and (Sinha and Costello 1978). The strain and velocity evolutions in different sections of the spring due to an excitation of the axial velocity are studied. The impedance method is applied to the literalized mathematical model consisting of four partial differential equations of order one to determine the natural frequencies. Then, the numerical solution is carried out by the method of characteristics for both linear and non linear model. The results were used to examine the evolution of angular and axial strains as a function of time at special points of the spring at different vibration frequencies. These results show the concepts related to the wave propagation phenomena such as resonance and beat. The non linear resonance is compared with the closed form solution of the governing equation in linear form.

2   Mathematical Model

The equations which describe nonlinear one-dimensional dynamic behaviour of helical springs can be adapted from the analytical model developed (Phillips and Costello 1971). Applying the theory of dimensional analysis, the general theory of bending and twisting of thin rods and the elementary strength of materials formulas to an element of the spring, between two sections x and $x + dx$, submitted to axial an force F and a torque T, yields the following equations of the spring motion (Ayadi, 2008):

$$\frac{\partial u_t}{\partial t} = a \frac{\partial u_x}{\partial x} + b \frac{\partial v_x}{\partial x} \tag{1}$$

$$\frac{\partial \upsilon_t}{\partial t} = b\frac{\partial u_x}{\partial x} + c\frac{\partial \upsilon_x}{\partial x} \tag{2}$$

$$\frac{\partial u_x}{\partial t} = \frac{\partial u_t}{\partial x} \tag{3}$$

$$\frac{\partial \upsilon_x}{\partial t} = \frac{\partial \upsilon_t}{\partial x} \tag{4}$$

where u is the axial displacement of the spring, $\upsilon = r\phi$ is the angular displacement, $u_x = \varepsilon = \partial u/\partial x$ is the axial deformation, $u_t = \partial u/\partial t$ is the axial velocity, $\upsilon_x = \beta = \partial \upsilon\,\partial x = r\,\partial\phi\,\partial x$ is the angular deformation and $\upsilon_t = \partial \upsilon/\partial t = r\,\partial\phi/\partial t$ is the angular velocity.

The coefficients a, b and c, occurring in equations (1) and (2), are given by the expressions:

$$a = \frac{h}{M}\frac{\partial F}{\partial \varepsilon} = \frac{EIh}{Mr^2}(\upsilon_x \sin\alpha + \cos\alpha)(\sin\alpha)\left\{\frac{-\nu}{1+\nu}(\upsilon_x \sin\alpha + \cos\alpha) + \frac{\cos^2\alpha}{\left[1-(1+u_x)^2 \sin^2\alpha\right]^{3/2}}\right\} \tag{5}$$

$$b = \frac{h}{M}\frac{\partial F}{\partial \beta} = \frac{h}{Mr}\frac{\partial T}{\partial \varepsilon} = \frac{EIh}{Mr^2}\sin^2\alpha\left\{\frac{(1+u_x)\cos^2\alpha}{\left[1-(1+u_x)^2 \sin^2\alpha\right]^{1/2}} - \frac{\cos\alpha}{1+\nu} - \frac{2\nu}{1+\nu}(1+u_x)(\upsilon_x \sin\alpha + \cos\alpha)\right\} \tag{6}$$

$$c = \frac{h}{Mr}\frac{\partial T}{\partial \beta} = \frac{EIh}{Mr^2}\sin\alpha\left[1 - \frac{\nu}{1+\nu}(1+u_x)^2 \sin^2\alpha\right] \tag{7}$$

where h is the length of the spring in the unstretched position, E is Young's modulus of the spring material, M is the total mass of the spring, I is the moment of inertia of the wire cross section, ν is Poisson's ratio of the spring material and α is the helix angle of the spring in the unstretched position. Thus, it can be seen that the coefficients a, b and c are functions of u_x and υ_x and hence, the governing equations of motion are non-linear. It can be deduced from equations (5), (6) and (7) that when the strains are small, i.e., $|u_x| \ll 1$ and $|\upsilon_x| \ll 1$ the coefficients will have the approximate constant values:

$$a = \frac{EIh}{Mr^2}\left(1 - \frac{\nu}{1+\nu}\cos^2\alpha\right)\sin\alpha$$

$$b = -\frac{EIh}{Mr^2}\frac{\nu}{1+\nu}\sin^2\alpha\cos\alpha \tag{9}$$

$$c = \frac{EIh}{Mr^2}\left(1 - \frac{\nu}{1+\nu}\sin^2\alpha\right)\sin\alpha$$

If these values are employed in place of the actual non-constant coefficients, the equations of motion are rendered linear.

3   Numerical Solution

The numerical solution of the initial boundary value problem governed by equations (1) to (4) may be obtained by the method of characteristics (Abbott 1966, Chou and Mortimer 1967, Sinha and Costello 1978, Hadj-Taïeb and Lili 1999...). This method, which is based on the concept of wave propagations, is applied to obtain ordinary differential equations that can be easily integrated alone the characteristic directions given by:

$$\left(\frac{dx}{dt}\right)_{1,2} = \sqrt{\frac{1}{2e}\left[(a+c)\pm\sqrt{(a-c)^2+4b^2}\right]} \text{ , and}$$

$$\left(\frac{dx}{dt}\right)_{3,4} = -\sqrt{\frac{1}{2e}\left[(a+c)\mp\sqrt{(a-c)^2+4b^2}\right]} \qquad (10)$$

When linear theory is used, we obtain (Ayadi et al. 2007) :

$$\left(\frac{dx}{dt}\right)_{1,4} = \pm c_f = \pm\sqrt{\frac{EIh}{Mr^2}\sin\alpha} = \pm\sqrt{\frac{\sin\alpha}{e}} \text{ , and}$$

$$\left(\frac{dx}{dt}\right)_{2,3} = \pm c_s = \pm\sqrt{\frac{EIh}{Mr^2}\frac{\sin\alpha}{1+\nu}} = \pm\sqrt{\frac{\sin\alpha}{e(1+\nu)}} \qquad (11)$$

where c_f is the fast speed of rotational waves (υ_x, υ_t) and c_s is the small speed of axial waves (u_x, u_t). The four roots defined equations (10) or (11) are real and, hence, the system is hyperbolic. The canonical form of a hyperbolic system along the characteristics (sometimes called either 'Compatibility equations') results:

$$\left\{1-c\left(\frac{dt}{dx}\right)^2\right\}du_x + \left\{b\left(\frac{dt}{dx}\right)^2\right\}d\upsilon_x - \left\{1-c\left(\frac{dt}{dx}\right)^2\right\}\left(\frac{dt}{dx}\right)du_t - \left\{b\left(\frac{dt}{dx}\right)^3\right\}d\upsilon_t = 0 \qquad (12)$$

Thus, the unknown values of (u_x, u_t, υ_x, υ_t), at any point L, as shown in Figure 1 (a), can be determined by knowing their values at the points P, Q, R and S, lying on the four characteristic lines passing through L, and then solving four simultaneous equations obtained by integrating equation (12) alone these lines: Although the characteristics are curved due to the non-linearity of equations (1) to (4), it will be assumed that *LP*, *LQ*, *LR* and *LS* are straight lines. Hence, equation (12) yields to:

$$\int_P^L \left\{ 1 - c\left(\frac{dt}{dx}\right)^2 \right\} du_x + \left\{ b\left(\frac{dt}{dx}\right)^2 \right\} dv_x - \left\{ 1 - c\left(\frac{dt}{dx}\right)^2 \right\} \left(\frac{dt}{dx}\right) du_t - \left\{ b\left(\frac{dt}{dx}\right)^3 \right\} dv_t = $$

$$\left[1 - c\left(\frac{dt}{dx}\right)_{1,P}^2 \right] \left(u_{x_L} - u_{x_P} \right) + \left\{ b\left(\frac{dt}{dx}\right)_{1,P}^2 \right\} \left(v_{x_L} - v_{x_P} \right) - \tag{13}$$

$$\left[1 - c\left(\frac{dt}{dx}\right)_{1,P}^2 \right] \left(\frac{dt}{dx} \right)_{1,P} \left(u_{t_L} - u_{t_P} \right) - \left\{ b\left(\frac{dt}{dx}\right)_{1,P}^3 \right\} \left(v_{t_L} - v_{t_P} \right) = 0$$

Three similar equations can be written for the points Q, R and S. By solving the four finite difference equations, the values of u_{xL}, v_{xL}, u_{tL} and v_{tL} can be obtained at any point L. It should be noted that the values at the points P, Q, R and S are computed by non-linear interpolation. Figure 1 (b) shows the characteristics lines in the case of linear theory where the wave speeds c_f and c_s are constant.

a. Non-linear theory   b. Linear theory

Fig. 1 Method of characteristics

4   Impedance Method

For the linear dynamic behavior, this method enables to determine the natural frequencies of the spring. Indeed, spring impedances vary with the frequency and are maximal for an infinite number of frequencies (Ayadi and Hadj Taieb 2010). They correspond to the zero of the expression (see fig. 2):

$$c_f c_s \, sin\left(\frac{\omega h}{c_f}\right) sin\left(\frac{\omega h}{c_s}\right) \tag{14}$$

That is:

$$\omega_{fk} = k \frac{\pi \cdot c_f}{h}, \quad \omega_{sk} = k \frac{\pi \cdot c_s}{h}, \quad k = 0,1,2,\cdots \tag{15}$$

So, frequencies vary with the wave speeds. The fundamentals correspond to the fast and slow instantaneous pulsation of resonance.

5   Applications and Results

5.1   System Description

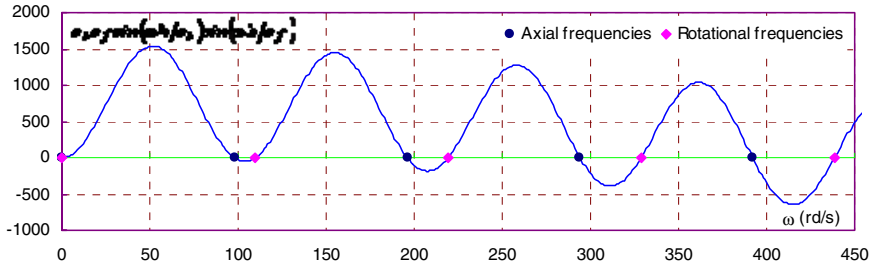Consider the spring system shown in figure 3. The characteristics of this steel helical spring are shown in Table 1.

Fig. 2 Natural frequencies of waves at the end of the spring x = h

Table 1 Mechanical and geometric of the considered springs

Height of the spring	h	119.38 cm
Helix angle	α	0.198281 rad
Number of turns	n	6
Poisson's ratio	ν	0.25
Young's modulus	E	206.85 GPa
Mass of the spring	M	2.12868 Kg
Radius of the spring	r	15.7607 cm
Wire radius	rf	0.7 cm
Initial compression	Δ	25.4 cm
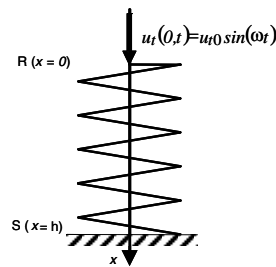
Fig. 3 Spring fitted at R $(x = 0)$ and loaded at S $(x = h)$

The natural frequencies are proportional to c_s and c_f respectively (Hamza et al. 2013) and they are the multiples of ω_s and ω_f (see Equations 15, Table 2 and Figure 2).

Table 2 Sample values of the natural frequencies

k	Slow axial frequency ω_s (rd/s)	Fast rotational frequency ω_f (rd/s)
1	98.035	109.607
2	195.264	218.745
3	291.249	327.912
4	388.881	434.607

For $x \in [0, h]$, the initial conditions are defined by:

$$u_x(x,0) = 0, \quad v_x(x,0) = 0, \quad u_t(x,0) = 0 \quad \text{and} \quad v_t(x,0) = 0 \qquad (16)$$

The boundary conditions are expressed by:

$$u_t(0,t) = u_{t0}\, sin(\omega t), \quad v_t(0,t) = 0, \quad u_t(h,t) = 0 \quad \text{and} \quad v_t(h,t) = 0 \qquad (17)$$

The dynamic response studied here is due to sinusoidal excitations of the axial velocity at the end of the spring $x = 0$. Figure 4 shows the excitation with the fundamentals frequencies.
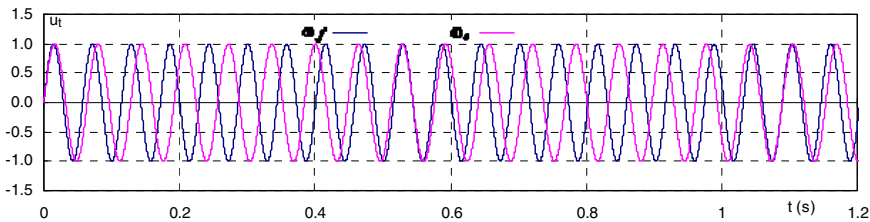
Fig. 4 Sinusoidal excitation of the axial velocity at the impacted end of the spring $x = 0$

5.2 *Excitation with Fast Frequency ω_{f1}*

The numerical results are shown in figures (5), (6), (7) and (8). These figures illustrate the dynamic response of the spring represented by the forced vibration of strains and velocities in the spring. This dynamic response plotted in different sections of the spring is due to a sinusoidal excitation of the axial velocity of amplitude $u_{t0} = 1 m\ s$ and of pulse corresponding to the linear fundamental frequency $\omega_f = \pi c\, f\, h = 109.607\, rd\ s$. As it can be seen on these figures, the resonance phenomenon occurs for the linear axial and rotational strains and velocities. The resonance corresponds to the fast fundamental frequency ω_f. We can clearly observe that for the linear model the resonance proceed in stages or by levels and builds up to an oscillatory regime of amplitude increasing infinitely until failure occurs. Similarly, it is confirmed that the beat phenomenon occurs for the non linear axial and

rotational strains and for the non linear axial and rotational velocities. The effects of the non linearity on the evolution of strains and velocities are very clear. The results show that there are systematic big differences between the linear and non linear behaviors. The frequency of the excitation is an instantaneous function of the strains. Referring to relations (10), we realize that, at each instant of time, a change in strains is accompanied by an instantaneous change of the wavespeed and therefore of the frequencies. The figures show that in the case of excitations produced initially with the linear frequenciy of resonance, fluctuations are amplified, and after some time it starts to decrease; unlike the case of the linear where the variables are always increasing. This is due to the fact that the instantaneous frequency, which varies with the strains, may deviate from its resonance value to an instantaneous of anti resonance one. To show this difference, the evolution of the variables is presented for important time period. For the non linear variables, strain and velocities, the resonance is damped and reduced to a beat. The effects of dynamical non-linearity, represented in the expressions (5), (6) and (7), are categorized by different configurations (shapes) in a chronological order.
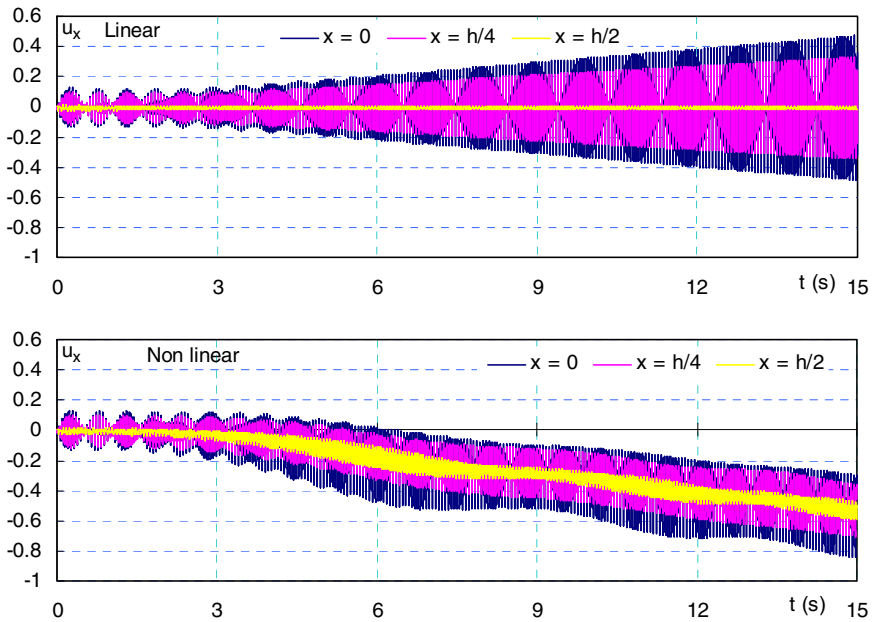
Fig. 5 Evolution of axial strains following an excitation at the fast frequency ω_f
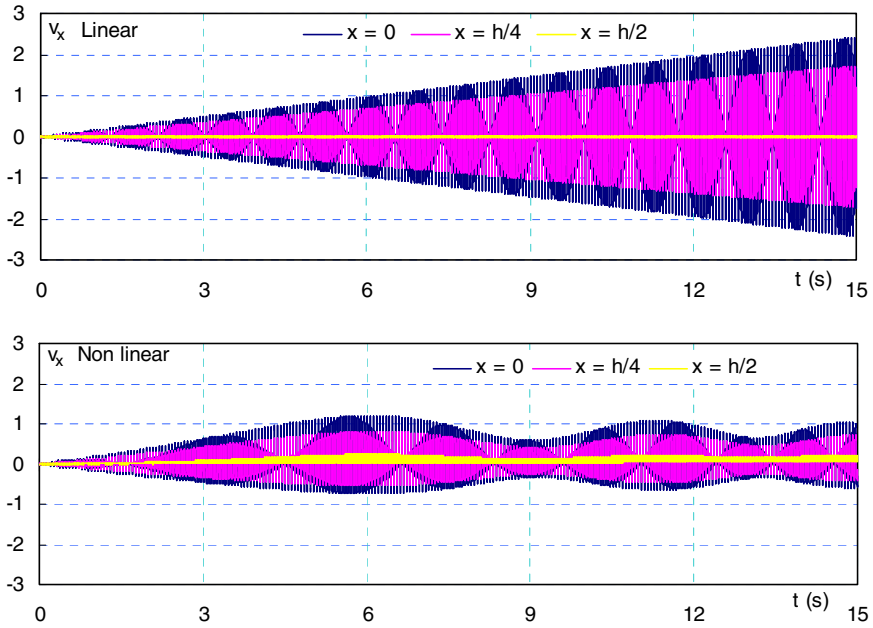
Fig. 6 Evolution of rotational strains following an excitation at the fast frequency ω_f
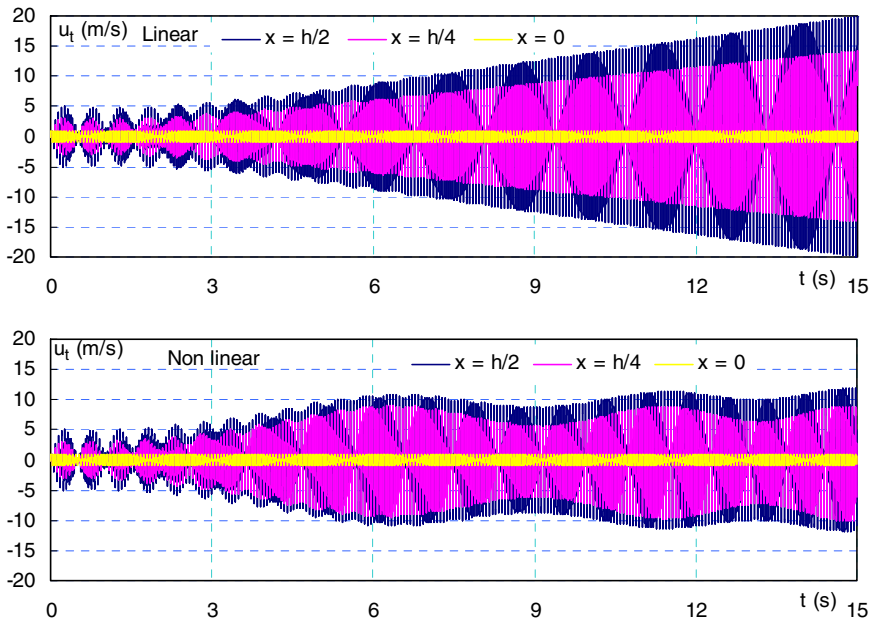

Fig. 7 Evolution of axial velocities following an excitation at the fast frequency ω_f
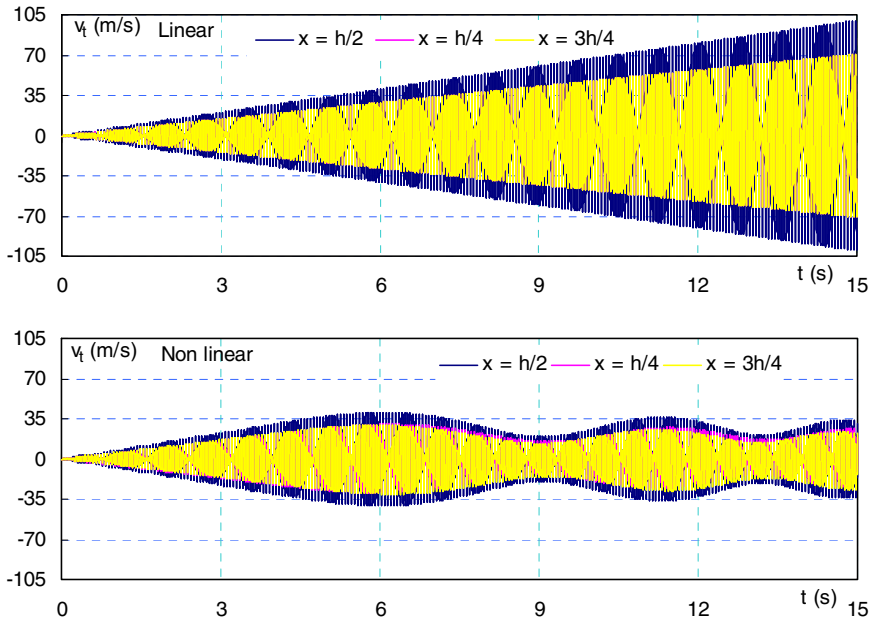
Fig. 8 Evolution of rotational velocities following an excitation at the fast frequency ω_f

6   Conclusion

To study the non linear resonance phenomenon in cylindrical springs, we presented a mathematical formulation describing this phenomenon constituted of a system of four non-linear partial differential equations of first order of hyperbolic type. Next, we proposed a numerical simulation based on the method of characteristics. The numerical results of the studied example were confronted with physical explanations for amplifying or damping strain and velocity waves. The evolutions of axial and rotational strains and velocities, as functions of time, are plotted at some sections of the spring. From these results, the variables are maximal at the extremities of the spring. Results show that, depending on the elastic parameters of the spring, the frequency can deviate from the resonance frequency and cause attenuation of strain and velocity fluctuations leading to a non resonance situation. Note that, the resonance occurs for all variables which are amplified continuously in the case of linear model and are attenuated in the non linear case.

References

1. Abott, M.B.: An introduction to the method of the characteristics, American. Elsevier, New York (1966)
2. Ayadi, S., Hadj-Taïeb, E., Pluvinage, G.: The numerical solution of strain waves propaga-tion in elastic helical springs. Materials and Technology MTAEC9 41(1), 47–52 (2007)

3. Ayadi, S.: Simulation numérique du comportement dynamique des ressorts hélicoïdaux, Thèse, ENIS, Tunisia (Februay 16, 2008)
4. Ayadi S., Hadj-Taieb E.: Evaluation of the natural frequencies of helical springs by the impedance method, ICSAAMM, Tarbes, France, September 7-10 (2009)
5. Ayadi, S., Hadj-Taïeb, E.: Vibrations de résonance dans les ressorts hélicoïdaux, XVI Colloque Vibrations Chocs et Bruit (VCB 2010), 16, 17 ,18 Juin 2010, Ecole Centrale de Lyon, France (2010)
6. Chou, P.C., Mortimer, R.W.: Solution of one dimensional elastic wave problems by the method of characteristics. J. Appl. Mech., Trans. ASME 34, 745–750 (1967)
7. Hadj-Taïeb, E., Lili, T.: The numerical solution of the transient two-phase flow in rigid pipelines. International Journal for Numerical Methods in Fluids 29, 501–514 (1999)
8. Hamza, A., Ayadi, S., Hadj Taieb, E.: The natural frequencies of waves in helical springs, C. R. Mecanique 341(2013), 672–686 (2013)
9. Lee, J., Thompson, D.J.: Dynamic stiffness formulation, free vibration and wave motion of helical springs. J. Sound Vib. 239(2), 279–320 (2001)
10. Lee, L.: Free vibration analysis of cylindrical helical springs by the pseudo spectral method. J. Sound Vib. 302, 185–196 (2007)
11. Phillips, J.W., Costello, G.A.: Large deflections of impacted helical springs, J. Acoust. Soc. Am. 51, 967–972 (1971)
12. Sinha, S.K., Costello, G.: The numerical solution of the dynamic response of helical springs. International Journal for Numerical Methods in Engineering 12, 949–961 (1978)
13. Wahl. Mechanical Springs, Penton Publishing Co., Cleveland, Ohio (1963)
14. Wittrick, W.H.: On elastic wave propagation in helical springs. Int. J. Mech. Sci. 8, 25–47 (1966)
15. Yildirim, V.: An efficient numerical method for predicting the natural frequencies of cy-lindrical helical springs. Int. J. Mech. Sci. 939, 41–919 (1999)

Damping Analysis of GFRP Bars

Abdelmonem Masmoudi, Fathi Djemal, Fakher Chaari, and Bassem Zouari

Mechanics Modelling and Production research Laboratory (La2MP),
National School of Engineers of Sfax (ENIS), B.P. 1173, 3038 Sfax, Tunisia
abdelmonem.masmoudi@enis.rnu.tn, fathidjemal@yahoo.fr,
{fakher.chaari,bassem.zouari}@gmail.com

Abstract. The main objective of this work is to contribute to a better understanding of the dynamic behavior of composite bars. In this work we propose an experimental modal analysis of Glass Fibers Reinforced Polymers (GFRP) bars. The objective is to characterize the damping properties of this material through vibration tests. It was found that these properties were acceptable especially for critical excitation such as earthquakes.

Keywords: Dynamic behavior, Damping, Modal analysis, GFRP bars

1   Introduction

The problem of steel bars corrosion reinforcements is one of the most important factors limiting the service life of structures. Moreover, the maintenance of concrete corroded reinforced elements is very expensive. A solution to this problem consists of the use of corrosion resistant materials such as Glass Fiber Reinforced Polymer (GFRP). Other attractive properties of GFRP materials include light weight and high strength. GFRP bars are gaining popularity as reinforcement for concrete bridge deck slabs and other concrete structures. Modal representation is relevant only in low-frequency ranges that extend to a few Hz in civil engineering, up to thousands of Hz for small mechanical structures. The vibration damping is a consequence of the dissipation of the mechanical energy during the oscillations. Lalanne (Lalanne 1999) compared with the mechanical behavior investigations on composite bars, few studies have been conducted on damping identification using test specimens, beam or plate, in flexural vibration or torsional vibration (Gibson1992) (Zhang and Hartwig 2002) or in longitudinal vibration (Ouis 2003). Studies show a frequency dependence of the elastic and damping characteristics of Glass Fibers Reinforced Polymers (GFRP) material (Gibson2000) (Berthelot and Sefrani 2000). The application of Virtual Work Principle allowed the determination of the mechanical properties in terms of rigidity and damping. It has been applied to identify the elastic properties of composite materials by measuring Kinematic filed (Berthelot and Sefrani 2004) (Wren and Kinra 1989) to the identification of plate rigidities in static and dynamic flexion (Botelho et al. 2006). The main objective of this work is to contribute to a better understanding of the dynamic behavior of composite bars. We propose an experimental investigation on the dynamic behavior GFRP bars with a special focus on dynamic properties.

2   Equipment and Materials

The GFRP bars used in this study are provided by the company Schok ComBAR®. The geometrical and mechanical characteristics of the studied bars are shown in Table 1.

Table 1 Geometric and mechanical characteristics of GFRP bars

GFRP bar	Value
Length (m)	1.5
Diameter (mm)	8 , 10 et 16
Modulus of Elasticity (GPa)	60
Density (Kg/m^3)	2200

In order to investigate the damping properties of GFRP bars, a clamped-free configuration is adopted. To excite the bar with harmonic force, an electrodynamic vibration shaker (LDS type V406a) is used (Figure 1). The shaker is excited by a frequency generator producing a sinusoidal signal. This signal is amplified by a power amplifier. Acceleration is measured at the free end of the bar by a piezoelectric sensor (Kistler) with a sensitivity of 200 mV/g. The measurements are acquired by a data acquisition card with 4 inputs for dynamic signal acquisition (National Instruments NI PXI-4462). An automatic frequency sweep in the frequency range 1 to 100 Hz is achieved during 200 seconds with acquisition of 10000 points/second.

Four different amplitudes of the power amplifier (500 mV, 1000 mV, 1500 mV and 2000 mV) were used to provide increasing values of forces.
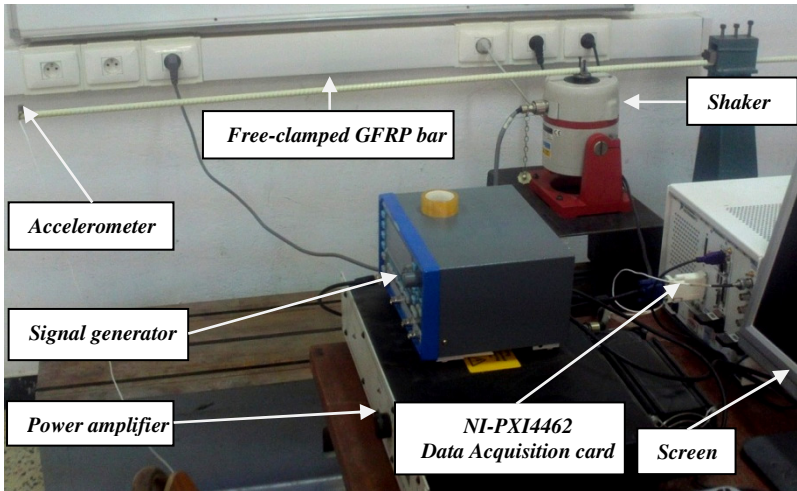

Fig. 1 Photo of the studied GFRP bar and data acquisition system

Lalanne (Lalanne 1999) showed that the power dissipated in vibration is proportional to the square of the FRF (Frequency Response Function). Dumping ξ can be deduced using the relationship: $\zeta = \dfrac{f_2 - f_1}{f_0}$

Where f_1 and f_2 are frequencies for which this power is half of the maximum dissipation. f_0 is the natural frequency response of the considered mode.

3   Results and Discussion

3.1   Frequency Analysis

Figure 2 shows an example of time evolution of the acceleration at the end of the free part of the GFRP bar with 16 mm diameter using the adopted frequency sweep. The FFT (Fast Fourier Transform) integrated in LabView software allows us to observe the natural frequencies. For each frequency excitation, we extract the RMS value of the corresponding time signal. Figure 3 shows the first three natural frequencies (5.2, 32.6 and 91.1 Hz respectively). The first natural frequency has the dominant amplitude.
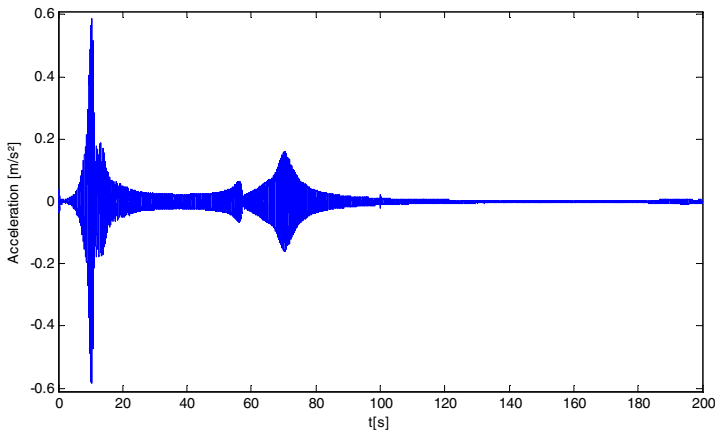
Fig. 2 Time signal of acceleration with frequency sweep

Figure 4 shows the evolution of natural frequency amplitude with respect to diameter of GFRP bar. It is well noticed that the increase of the diameter will lead to a decrease of the first mode vibration level when compared with those of mode 2 and 3.
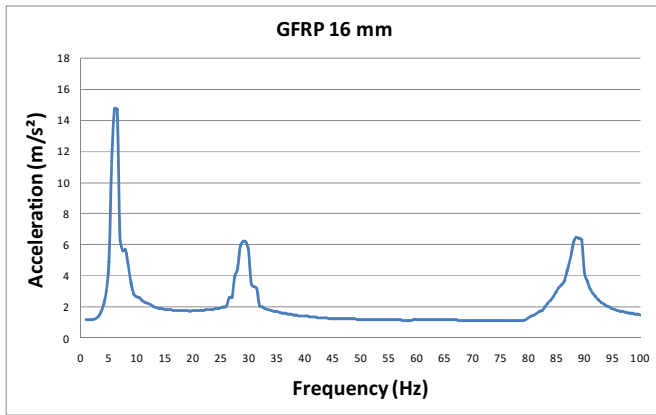
Fig. 3 First three modes associated to a GFRP bar (diameter 16 mm)
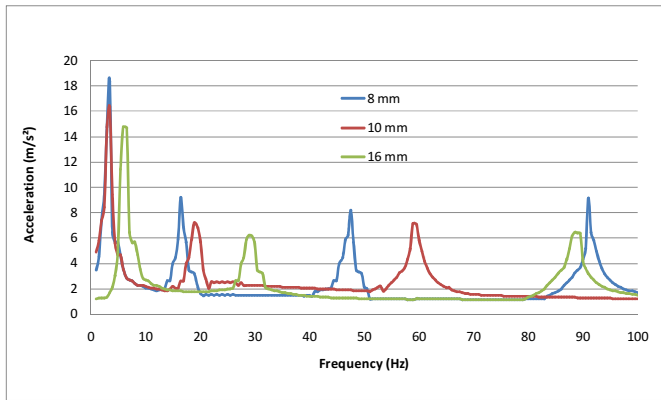

Fig. 4 Modes associated to a GFRP bar diameter 8 , 10 and 16 mm

3.2   *Identification of Bar Damping Properties*

Table 2 shows a comparison of modes and damping GFRP bars.

The damping ratio of GFRP bars ranges from 1.1% to 1.5% for all tested diameters as well as the first three modes. This quantitatively confirmed that the behavior of reinforced composite rods structures may have acceptable behavior for earthquake excitation for example. As the diameter increase the damping ratio reduces, this was noticed for the first mode.

Table 2 Damping ratio of different GFRP bars diameters

Diameter (mm)	Mode	Experimental frequency f0 500mv	1000mv	1500mv	2000mv	ξExp (%)
	1	2.4	2.5	2.5	2.6	1.1
	2	15.4	16.0	16.3	16.8	1.4
8	3	43.7	45.4	46.3	47.6	1.3
	4	87.5	88.13	89.4	91.7	1.2
	1	3.1	3.2	3.3	3.4	1.1
10	2	19.1	19.9	20.2	20.8	1.4
	3	54.1	56.3	57.3	59.0	1.3
	1	4.9	5.1	5.2	5.3	1.2
16	2	30.9	32.1	32.8	33.7	1.5
	3	86.5	90.0	91.7	94.3	1.4

4 Conclusion

The experimental modal analysis of GFRP has permitted to characterize the damping properties of this material through vibration tests. We can draw the following conclusions:

- The damping ratio ξ of GFRP bars ranges from 1.1% to 1.5% for all diameters tested with a sweeping of the first three modes.
- More than the diameter increases more than the damping increases this is noticed for the first mode. This quantitatively confirmed these properties were acceptable especially for critical excitation such as earthquakes. This result allows contributing to a better understanding of the dynamic behavior of composite bars GFRP.

References

Lalanne, C.: Vibrations et chocs mécaniques. Tome 2 Chocs mécaniques. Hermès, Paris (1999)

Ouis, D.: Effect of structural defects on the strength and damping properties of a solid material. European Journal of Mechanics A/Solids 22, 47–54 (2003)

Botelho, E.C., Campos, A.N., de Barros, E., Pardini, L.C., Rezende, M.C.: Damping behavior of continuous fiber/metal composite materials by the free vibration method. Composites: Part B 37, 255–263 (2006)

Wren, G.G., Kinra, V.K.: On the effect of an end-mass on a beam damping. Experimental Mechanics 9, 336–341 (1989)

Berthelot, J.M., Sefrani, Y.: Damping analysis of unidirectional glass and kevlar fibre composites. Composites Science and Technology 64, 1261–1278 (2004)

Gibson, R.F.: Damping characteristics of composites materials and structures. Journal of Materials Engineering and Performance 1, 11–20 (1992)

Gibson, R.F.: Modal vibration response measurements for characterization of composite materials and structures. Composites Science and Technology 60, 2769–2780 (2000)

Grédiac, M., Pierron, F.: A T-shaped specimen for the direct characterization of orthotropic materials. International Journal for Numerical Methods in Engineering 41, 293–309 (1998)

Grédiac, M., Fournier, N., Paris, P.A., Surrel, Y.: Direct determination of elastic constants of anisotropic plates by modal analysis: experimental results. Journal of Sound and Vibration 210(5), 643–659 (1998)

Grédiac, M., Pierron, F., Surrel, Y.: Novel procedure for complete in-plane composite characterization using a single T-shaped specimen. Experimental Mechanics 39(2) (1999)

Zhang, Z., Hartwig, G.: Relation of damping and fatigue damage of unidirectional fibre composite. International Journal of Fatigue 24, 713–718 (2002)ï

Dynamic Response of Cracked Shaft
in Rotor Bearing-Disk System

Mehdia Ghozlane

Applied Mechanics and Systems Research Laboratory, Tunisia Polytechnic School,
La Marsa 2078, Tunisia
mehdiaghozlane@yahoo.fr

Abstract. A simplified approach for modeling an open crack in a rotor based on the change of the flexibility is proposed in this paper. The crack model is incorporated in a two-node Timoshenko beam with 4 DOF at each node, which in turn represents one element of the finite element model of the rotor bearing system. The objectives of this work are twofold. The primary objective is to study the effect of the presence of crack on movement equation of rotor bearing system. Theoretically, it was shown that the crack generates external inertial, damping and elastic excitation forces which depend on the second harmonic of the rotational speed. The second objective is to calculate the dynamic response of the rotor bearing system with NEWMARK numerical integration method (average acceleration method) of non-linear equation. Results show that transverse crack produces peaks in the second harmonic of rotating speed modulated with natural frequency and the third harmonic of the rotation speed. The presence of a crack in a symmetric rotor causes asymmetry in the stiffness and consequently causes critical frequencies in backward whirl.

Keywords: Open crack, rotor modeling, dynamic response.

1   Introduction

Thanks to the progress made in engineering and materials science, rotating machinery has become faster and lighter as well as required to run for a longer period of time. All of these factors mean that the detection, location and analysis of faults play a vital role in the field of rotor dynamics.

One of the major areas of interest in modern day condition monitoring of rotating machinery is that of vibration. By measuring and analyzing the vibration of rotating machinery, it is possible to detect and locate important faults such as mass unbalance, shaft bow and misalignment [5]. Fatigue crack is an important rotor fault which can lead to catastrophic failure if undetected properly and in time. The study and investigation of dynamics of cracked shafts has increased since the last four decades and excellent reviews on this topic are available [1], [2].

When crack exists in a shaft, the stiffness is reduced and consequently the eigenfrequencies of the system are decreased [7], measuring these differences can help to identify a crack. Another approach of crack identification is based on the

modification of the dynamic response of the cracked rotor during steady-state operation[8].The knowledge of the dynamical behavior of cracked shafts has helped in predicting the presence of cracks in a rotor. Moreover, many studies in dynamic responses are carried out and more particularly on the tendency of the rotor to exhibit a harmonic component at twice shaft. The 2X component in the signature of cracked shaft is too sensitive to other factors such as misalignment to be a reliable indicator of shaft cracks. The inventors are of the opinion that continuous monitoring of the backward harmonics can reveal the presence of cracks.

The aim of this work is to find extensive simulation studies performed in order to develop feasible techniques for the identification of the crack based on the response of cracked rotor to unbalance, only by measuring vibration at bearing housings.

2 Open Crack Modeling

The presence of crack in shaft induces a reduction in the stiffness of the shaft. Christides and Barr considered the effect of a crack in a continuous beam and calculated the flexural stiffness EI for a rectangular beam to involve an exponential function [3].

$$EI(y) = \frac{EI_0}{1 + C \exp(-\dfrac{2\alpha \left| y - \dfrac{L}{2} \right|}{d})} \tag{1}$$

With: $C = \dfrac{I_0 - I_c}{I_c}$ $\alpha = 0.667$ $I_0 = \dfrac{w \times d^3}{12}$ $I_c = \dfrac{w \times (d - d_c)^3}{12}$

From the approach presented above, we will consider a shaft as a beam with circular cross-section, with R the radius, and which has the same second moment of area of a square section beam with side d .

$$I_{shaft} = I_{beam} \text{ With } I_{shaft} = \frac{\pi R^4}{4} \text{ and } I_{beam} = \frac{d^4}{12} \text{ then } d = (3\pi)^{\frac{1}{4}} R$$

The evaluable equation of Christides and Barr for a circular cross section will be described by the same equation (1) with replacing α by β which is equal to $\dfrac{\alpha}{(3\pi)^{\frac{1}{4}}}$ and I_0 by $I = I_x = I_z = \dfrac{\pi R^4}{4}$ in the expression of C .

I_c is equal to $\tilde{I}_x$ or $\tilde{I}_z$ [7] according to the plan of deflection, which is the second moment of area of cracked section.
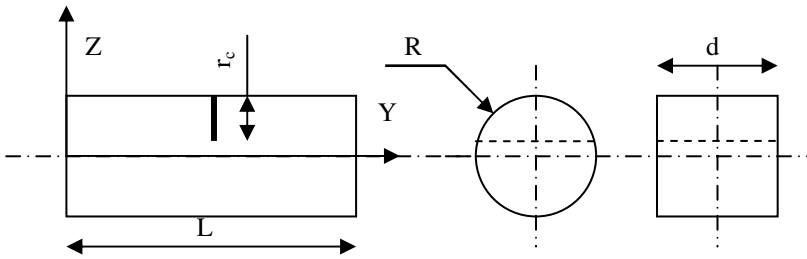
Fig. 1 Cracked cross section.

The variation of the stiffness using equation (1) is plotted in Fig.2. It is clear that most of the flexibility is local to the crack, although there are very small changes far away from the crack.

The stiffness reduction of Christides and Barr was approximated by a rectangular reduction shown in Fig. 2. Another simplification was used by Sinha and Friswell in [4] which does not reflect the depth of the crack.

As mentioned before, the stiffness reduction is local and flexural rigidity close to the crack is given by:

$$EI(y) = \begin{cases} EI_0 & 0 \le y \le \dfrac{L-L_c}{2} \\ EI_c & \dfrac{L-L_c}{2} \le y \le \dfrac{L+L_c}{2} \\ EI_0 & \dfrac{L+L_c}{2} \le y \le L \end{cases} \qquad (2)$$

L_c is the effective length where reduction is very important, which is calculated by integrating the stiffness reduction in equation (1) and making them equal. Ensuring that these integrals are equal would produce equal natural frequency changes.

$L_c = \dfrac{R}{\beta} \times \dfrac{1+C}{C} \times \ln(1+C)$, R and L are respectively the elementary radius and length of the shaft.
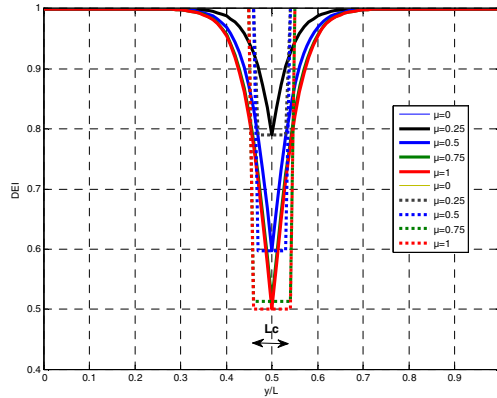
Fig. 2 Rectangular reduction approximation in XY plan

The effective length of the stiffness reduction near the crack in the two plans (XY) and (ZY) is exactly the same for very small crack depth and it is equal to $\dfrac{R}{\beta}$.

For larger value of the non-dimensional crack depth $\mu = \dfrac{r_c}{R}$ it increases a little until the value $\dfrac{2\ln(2) \times R}{\beta}$, and it will be different for both axes X and Z. The mean value is considered a linear function of the depth. In the next step, we will use the mean value $L_c = \dfrac{L_{cx} + L_{cz}}{2}$ in order to simplify the calculation.

3 Dynamics of a Cracked Rotor-Disk-Bearing System

The general formulation of the kinetic energy of an element of the shaft with a length dy is given in [9]. (I_x, I_y and I_z) are the area moment of inertia of the shaft cross-section about the neutral axes, which are dependent on y.

Kinetic energy is integrated along L, the length of the element shaft. The expression of kinetic energy gives two compounds: the first one represents kinetic energy of uncracked shaft while the second represents the reduction of kinetic energy caused by the presence of a crack in shaft element.

If we applied Lagrange's equation:

$$\frac{d}{dt}\left(\frac{\partial \Delta T_s}{\partial \dot{\delta}}\right) - \frac{\partial \Delta T_s}{\partial \delta} = \left[\Delta M^c\right]\ddot{\delta} + \Omega\left[\Delta G^c\right]\dot{\delta} + F^i\left(t, \ddot{\delta}, 2\Omega\right) + F^d\left(t, \dot{\delta}, 2\Omega\right) \quad (3)$$

The presence of crack reduces the rotatory mass as well as the gyroscopic effect by the first and the second term. In the other way there are two compounds: the third and fourth ones are considered as exciting forces caused by the fault. This can be represented as equivalent external forces. Fault excitation forces are considered as:

- Inertial exciting force:

$$F^i\left(t,\ddot{\delta},2\Omega\right)=\begin{bmatrix}\left[\Delta M^-\right]\cos(2\Omega t) & \left[\Delta M^-\right]\sin(2\Omega t) \\ \left[\Delta M^-\right]\sin(2\Omega t) & \left[\Delta M^-\right]\cos(2\Omega t)\end{bmatrix}\ddot{\delta} \quad (4)$$

- Damping exciting force:

$$F^d\left(t,\dot{\delta},2\Omega\right)=2\Omega\begin{bmatrix}-\left[\Delta M^-\right]\sin(2\Omega t) & \left[\Delta M^-\right]\cos(2\Omega t) \\ \left[\Delta M^-\right]\cos(2\Omega t) & \left[\Delta M^-\right]\sin(2\Omega t)\end{bmatrix}\dot{\delta} \quad (5)$$

$$\Delta M^{+/-}=\rho\frac{\Delta I^{+/-}}{30L}\begin{bmatrix}+t_1 & +t_2 & -t_1 & +t_2 \\ & +t_3 & -t_2 & +t_4 \\ & & +t_1 & -t_2 \\ sym & & & +t_3\end{bmatrix}\begin{cases}t_1=\dfrac{9}{2}\eta\left(3\eta^4-10\eta^2+15\right) \\ t_2=\dfrac{3}{4}L\eta\left(9\eta^4-20\eta^2+15\right) \\ t_3=\dfrac{L^2}{8}\eta\left(27\eta^4-10\eta^2+15\right) \\ t_4=\dfrac{L^2}{8}\eta\left(27\eta^4-50\eta^2+15\right)\end{cases}$$

With $\Delta I^-=\Delta I_z-\Delta I_x$, $\Delta I^+=\Delta I_z+\Delta I_x$, $\Delta I_x=\dfrac{I_0-\tilde{I}_x}{2}$, $\Delta I_z=\dfrac{I_0-\tilde{I}_z}{2}$,

$\eta=\dfrac{L_c}{L}$, ρ is the mass per unit volume.

The same step is applied to strain energy; the reduction of strain energy is calculated and gives the relation below:

$$\frac{\partial\Delta U_s}{\partial\delta}=\left[\Delta K^c\right]\delta-F^e\left(t,\delta,2\Omega\right) \quad (6)$$

In this situation, a fault (crack) reduces the stiffness of the shaft indicated by the first term; the second term depends on displacement and time which will be considered as elastic excitation forces.

$$F^e\left(t,\delta,2\Omega\right)=\begin{bmatrix}-\left[\Delta K^-\right]\cos 2\Omega t & \left[\Delta K^-\right]\sin 2\Omega t \\ \left[\Delta K^-\right]\sin 2\Omega t & \left[\Delta K^+\right]\cos 2\Omega t\end{bmatrix}\delta \qquad (7)$$

$$\Delta K^{+/-}=\frac{E\Delta I^{+/-}}{L^3(1+a)}\begin{bmatrix}+t_1 & +t_2 & -t_1 & +t_2 \\ & +t_3 & -t_2 & +t_4 \\ & & +t_1 & -t_2 \\ sym & & & +t_3\end{bmatrix} \qquad \begin{cases}t_1=12\eta^3 \\ t_2=6L\eta^3 \\ t_3=(4+a)L^2\dfrac{\left(\eta+3\eta^3\right)}{4} \\ t_4=(2-a)L^2\dfrac{\left(3\eta^3-\eta\right)}{2}\end{cases}$$

When Lagrange's equations are applied to global shaft, the equation of movement becomes:

$$\left(\left[M\right]-\left[\Delta M^c\right]\right)\ddot{\delta}+\left(\left[D\right]+\Omega\left(\left[G\right]-\left[\Delta G^c\right]\right)\right)\dot{\delta}+\left(\left[K\right]+\left[K_{st}\right]-\left[\Delta K^c\right]\right)\delta=$$
$$F^u(t,\Omega)+F^e(t,2\Omega,\delta)+F^d(t,2\Omega,\dot{\delta})+F^i(t,2\Omega,\ddot{\delta}) \qquad (8)$$

Where δ is the vector containing all the nodal displacement, $\left[M\right]$, $\left[G\right]$ and $\left[K\right]$ are respectively the mass, gyroscopic and stiffness matrix of the shaft and disks; $\left[D\right]$ and $\left[K_{st}\right]$ are respectively damping and stiffness of the bearings.

$\left[\Delta M^c\right]$ and $\left[\Delta G^c\right]$ represent a reduction in the effect of rotator inertia and gyroscopic effect induced by the presence of a crack. $\left[\Delta K^c\right]$ represents also a reduction of the stiffness of the shaft due to the cracked element.

The vector $F^u(t,\Omega)$ is the mass unbalance force. The system defined in equation (8) is as a non-linear equation:

4   Numerical Examples

In this study, the used rotor is 6 shaft finite elements with the same length as illustrated in Fig.3. All parameters are given in table 1. Three disks are mounted on the shaft. A mass unbalance of 200 g.mm is assumed to be on disk D2.

Disks in the system have the same thickness (0.05 mm), inner radius (0.025mm) and outer radius (0.125mm).
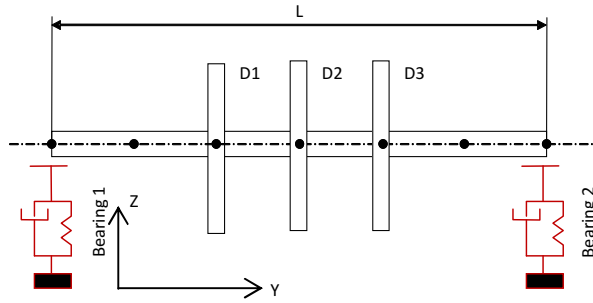
Fig. 3 Rotor Model

The common first step in the diagnosis of crack is the changes in natural frequencies. Table 2 gives the first six natural frequencies of the uncracked and cracked shaft at $\Omega = 0$, for different value of non-dimensional crack depth μ. We deduce that for the uncracked shaft, the 1st, 3rd and 5th natural frequencies are equal to the 2nd, 4th and 6th ones, either for the uncracked or cracked shaft.

In the other way, the reduction in natural frequencies increases with the depth of crack. This is due to the decrease of rigidity of the shaft due to the crack.

Table 1 Parameters of the rotor model

Parameters	$L(m)$	$D(m)$	$\rho(\frac{Kg}{m^3})$	$E(\frac{N}{m^2})$	v	$k_{xx} = k_{zz}(\frac{N}{m})$	$c_{xx} = c_{zz}(\frac{N}{\frac{m}{s}})$
Value	0.6	0.05	7800	2.10^{11}	0.3	5.10^7	2.10^2

The unbalance is defined by a mass m_u situated on the second disk (D2) at distance d from the geometric center. Centrifugal force is then applied to the rotor with synchronous excitation force.

Table 2 Six first natural frequencies $\Omega = 0$

	Uncracked	$\mu = 0.25$	$\mu = 0.5$	$\mu = 0.75$	$\mu = 1$
1st 2nd	75.89	75.65	74.60	72.62	67.97
3rd 4th	287.92	287.22	285.49	282.58	277.23
5th 6th	556.74	554.81	549.24	537.72	512.40

In the rotor dynamical system, eigenfrequencies depend on the rotation speed due to the gyroscopic effects. Campbell diagram (Fig. 4) is used to find the critical frequencies of rotor, which are the intersection of $f = \frac{N}{60}$ (N rotational speed of the rotor) with curves of backward BW and forward FW whirl.

With symmetric uncracked rotor the mass unbalance response indicates three peaks showed in Fig. 5: A & B represent the first BW and second FW critical speed, and D the forth FW one. We deduce that there is no critical speed in BW modes at the 3rd, 5th and 6th modes.
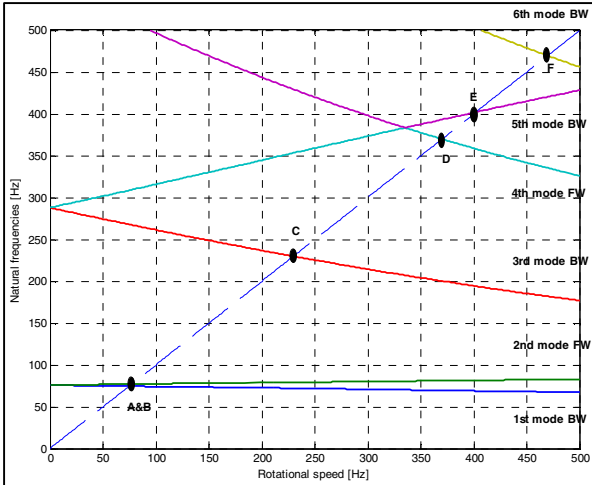

Fig. 4 Campbell Diagram of uncracked shaft

When a rotor presents crack at the third element, the mass unbalance response will present other peaks. In Fig. 5, peaks C, E and F represent BW critical speed caused by the presence of crack which has asymmetric effect.

We can also observe a split of FW peaks which indicates the decrease of critical speeds of cracked shaft.
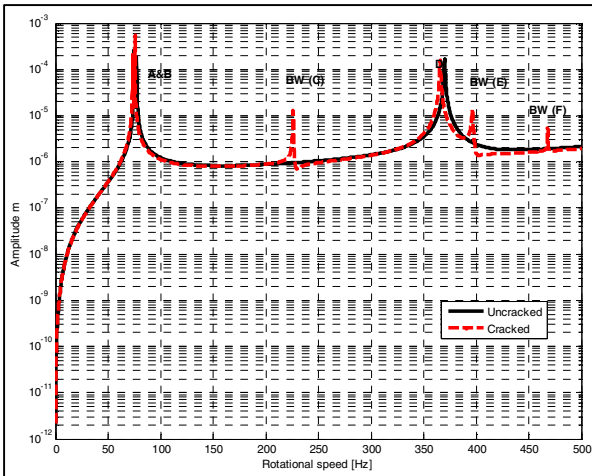
Fig. 5 Mass unbalance response of cracked shaft

The dynamic response is obtained by using the numerical integration method for non-linear system (NEWMARK method) when the rotor is excited by unbalance force only.

Fig. 6 shows the dynamic response at the bearing 1 in the Z direction and given in the frequency domain obtained by the Fast Fourier Transform (FFT). This chart indicates two peaks at 1X harmonic of rotating speed Ω and first natural frequency ω_1 of the shaft which is the signature of the unbalance fault in rotating machine.
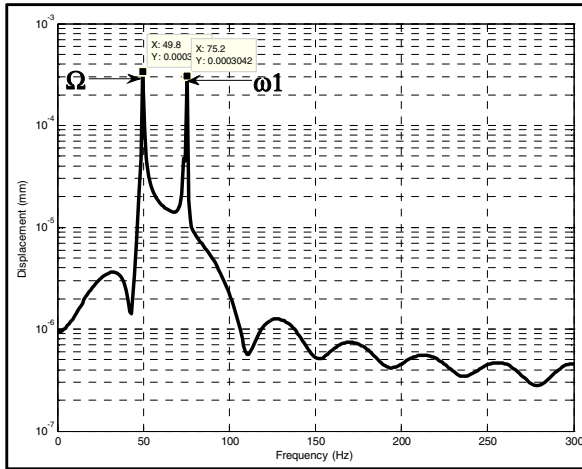
Fig. 6 Spectrum for uncracked shaft at $\Omega = 3000 RPM$

In the case of cracked shaft with non-dimensional crack depth $= 0.5$, other peaks appear in dynamic response in addition to the two peaks mentioned previously. Shown in Fig.7, we can observe one peak at 2X harmonic of rotating speed plus the first natural frequency ω_1, and another one at 3X harmonic of rotating speed.
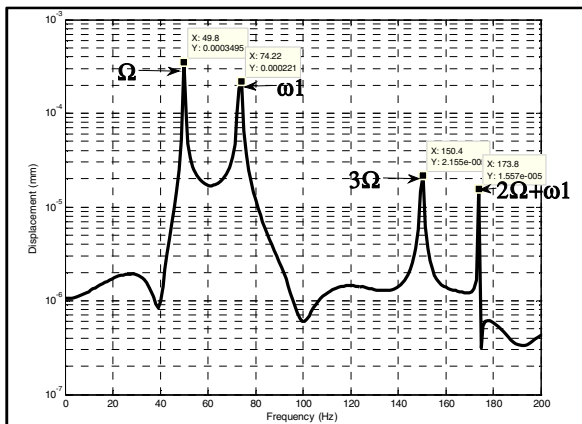
Fig. 7 Spectrum for cracked shaft $\mu = 0.5$ at $\Omega = 3000 RPM$

Experimental results are carried out by [10]. In this paper, auxiliary excitation of the shaft is added. The response of the uncracked rotor without excitation shows peaks which illustrate the first natural frequency and harmonics of rotating speed. With the presence of crack, the traces of combinational frequencies which are shown represent the modulation of harmonics and sub-harmonics of first natural frequency.

5   Conclusion

Based on the present study, the following general conclusions are given factors which help to identify the crack as follows. The first indication is the change in modal properties by the decrease of natural frequencies, and this is due to the looseness of stiffness.For symmetric rotor backward whirling appears du to the asymmetry caused by the crack. Second indication is in dynamic response. Cracks additionally produced 3X harmonic of rotational speed and 2X compound with modulation of first natural frequencie.

References

[1] Gasch, R.: A survey of the dynamic behavior of a simple rotating shaft with a transverse crack. Journal of Sound and Vibration 160(2), 313–332 (1993)

[2] Sabnavis, G., et al.: Cracked Shaft Detection and Diagnostics: A Literature Review. The Shock and Vibration Digest 36, 287 (2004)

[3] Christides, S., Barr, A.D.S.: One-dimensional theory of cracked Bernoulli-Euler beams. International Journal of Mechanical Sciences 26(11-12), 639–648 (1984)

[4] Sinha, J.K., et al.: Simplified models for the location of cracks in beam structures using measured vibration data. Journal of Sound and Vibration 251(1), 13–38 (2002)

[5] Edwards, S., et al.: Fault Diagnosis of Rotating Machinery; The Shock and Vibration Digest. 30(1), 4–13 (January 1998)

[6] AL-Shudeifat, M.A., et al.: General Harmonic Balance Solution of cracked rotor-bearing-disk system for harmonic and sub-harmonic analysis: Analytical and experimental approach. International Journal of Engineering Science 48, 921–935 (2010)

[7] Sinou, J.-J., Lees, A.W.: The influence of cracks in rotating Shafts. Journal of Sound and Vibration 285(4-5), 1015–1037 (2005)

[8] Sinou, J.-J.: Detection of cracks in rotor based on the 2x and 3x super-harmonic frequency components and the crack–unbalance interactions. Communications in Nonlinear Science and Numerical Simulation 13, 2024–2040 (2008)

[9] Lalanne, M., Ferraris, G.: Rotor dynamics Prediction in Engineering, 2nd edn. John Wiley (1998)

[10] Sawicki, J.T., et al.: Detecting cracked rotors using auxiliary harmonic excitation. Journal of Sound and Vibration 330, 1365–1381 (2011)

Modeling and Simulation for Lateral Rail Vehicle Dynamic Vibration with Comfort Evaluation

Mortadha Graa[1], Mohamed Nejlaoui[1], Ajmi Houidi[2],
Zouhaier Affi[1], and Lotfi Romdhane[2,3]

[1] Laboratoire de Génie Mécanique (LGM), Ecole Nationale d'Ingénieurs de Monastir,
   Université de Monastir, Tunisie
[2] Laboratoire de Mécanique de Sousse (LMS), Ecole Nationale d'Ingénieurs de Sousse,
   Université de Sousse, Tunisie
[3] On leave at the College of Engineering, the American University of Sharjah, UAE

Abstract. Investigation of vibration is an important topic for the purposes of ride comfort in railway engineering. The vibration of rail vehicles becomes very complex because it is affected by the condition of vehicles, including suspensions and wheel profile, condition of track sections, including rail profile, rail irregularities, cant and curvature. The present study deals with the effects of railway track imperfections on dynamic behavior, and investigates the effect of vehicle speed and the rail irregularity on ride comfort through numerical simulation. The numerical simulation of the vertical dynamic behavior of a typical railroad vehicle will be performed using Largrangian dynamics. The model consists of 17 degrees of freedom with 4 wheel-sets, 2 bogies and a car body. For the assessment of the ride comfort, the Sperling ride index (ISO2631) is calculated using filtered RMS accelerations. The ride characteristics of the vehicle provide an assessment of the dynamic behavior of the vehicle through the analysis of the accelerations at the vehicle body, whereas the ride comfort assesses the influence of the vehicle dynamic behavior on the human body. A parametric study was carried out to suggest design modifications in order to improve the level Sperling index.

Keywords: Sperling index, ride quality, rail vehicle, dynamic behavior, ride comfort, lateral dynamic vibration.

1   Introduction

Rail transport is one of the major modes of transportation, so it must offer a high comfort level for passengers and crew. In several research works, noise and vibration have been identified as the most important factors for high comfort. The main sources of vibration in a train are track defects in welding or rolling defects, rail joints, etc. The nature of vibration itself is random and covers a wide frequency range [1]. The improvement of the passenger comfort while travelling has been the subject of intense interest for many train manufacturers, researchers and companies

all over the world. The dynamic behavior of a train also depends on the load and its mechanical components, such as springs, dampers, etc., which interact with the wheels, the train body and bogies. The dynamic performance of a rail road vehicle as related to safety and comfort is evaluated in terms of specific performance indices. Sperling's ride index is a measure of the ride quality and ride comfort used by ISO 2631[2]. Measured track data are obtained by running a specialized railcar down the track. Analytic track data are created using mathematical shapes, such as cusps, bends, and harmonic functions, to represent the track geometry [3].

There have been several studies, which dealt with the dynamic analysis of rail vehicles in order to enhance the ride comfort while travelling. Nejlaoui et al [4] optimized the structural design of passive suspensions in order to ensure simultaneously passenger safety and comfort. Abood et al [5] investigated the Railway carriage simulation model to study the influence of vertical secondary suspension stiffness on ride comfort of railway car body. Kumar and Sujata [2] presented the numerical simulation of the vertical dynamic behavior of a railway vehicle and calculated Sperling ride index for comfort evaluation. Nielsen and Igeland [6] investigated the vertical dynamic behavior for a railway bogie moving on a rail which is discretely supported by sleepers resting on an elastic foundation. Effects of imperfections on the running surfaces of wheel and rail were studied by assigning irregularity functions to these surfaces.

2   Modeling of Rail Road Vehicle

To analyze the dynamic behavior of railway vehicles, usually the vehicle (and if necessary the environment) is represented as a multi body system. A multi body system consists of rigid bodies, interconnected via massless force elements and joints. Due to the relative motion of the system's bodies, the force elements generate applied forces and torques. Typical examples of such force elements are springs, dampers, and actuators combined in primary and secondary suspensions of railway vehicles.

2.1   Assumptions

The assumptions made in formulating the model are as follows:

- Bogie and car body component masses are rigid.
- The springs and dampers of the suspension system elements have linear characteristics.
- Friction does not exist between the axle and the bearing.
- The vehicle is moving with constant velocity on a rigid and constant gauge.
- All wheel profiles are identical from left to right on a given axle and from axle to axle and all wheel remain in contact with the rails.
- Straight track.
- An irregularity in the vertical direction with the same shape for left and right rails.

2.2 Rail Road Vehicle Model

Fig.1 illustrates the train vehicle model adopted in this study. It consists of a vehicle body, two bogies frames and four wheel-sets. Each bogie consists of the bogie frame, and two wheel sets. The car body is modeled as a rigid body having a mass M_c; and having moment of inertia J_{bx} and J_{cz} about the longitudinal and vertical axes, respectively. Similarly, each bogie frame is considered as a rigid body with a mass M_b (M_{b1} and M_{b2}) with moment of inertia J_{bx} and J_{bz} about the longitudinal and vertical axes, respectively. Each axle along with the wheel set has a mass M_w (for four axles M_{w1}; M_{w2}; M_{w3} and M_{w4}). The spring and the shock absorber in the primary suspension for each axle are characterized by a spring stiffness K_p and a damping coefficient C_p, respectively. Likewise, the secondary suspension is characterized by spring stiffness K_s and damping coefficient C_s, respectively. As the vehicle car body is assumed to be rigid, its motion may be described by the lateral displacement and rotations about the vertical axis (yaw or ψ_c) and about the longitudinal axis (roll or θ_c). Similarly, the movements of the two bogies units are described by three degrees of freedom Y_{bi}; ψ_{bi} and θ_{bi} (i=1, 2), each about their centers. Each axle set is described by two degrees of freedom Y_w; and ψ_w. about their centers. Totally, 17 degrees of freedom have been considered in this study for the vehicle model shown in Fig.1. The detailed parameters regarding the moment of inertia and mass of different component are given in Table 1.

Table 1 Detailed parameter of rigid bodies

Name of Rigid Bodies	Mass (Kg)	Moment of Inertia(Kg.m²)	
		I_{XX}	I_{ZZ}
Car Body	$6,7 \times 10^5$	10^5	10^6
Bogie-I and II	10^5	10^5	10^5
Wheel-set-I,II,III and IV	4000	4000	4000

Some parameters regarding the rigid bodies are already given in Table 1; however, the other parameters, which are essential for the simulation of the vehicle, are presented in Table 2. A typical rail road vehicle system is composed of various components such as car body, springs, dampers, Bogies, Wheel-set, and so forth. When such dynamic systems are put together from these components, one must interconnect rotating and translating inertial elements with axial and rotational springs and dampers, and also appropriately account for the kinematics of the system structure.

3 Track Inputs to Rail Road Vehicle

The dynamic wheel loads generated by a moving train are mainly due to various wheel/track imperfections. These imperfections are considered as the primary source of dynamic track input to the railroad vehicles. Normally, the imperfections that exist in the rail-track structure are associated with the vertical and lateral track profile, cross level, rail joint, wheel flatness, wheel/rail surface corrugations and sometimes uneven support of the sleepers.
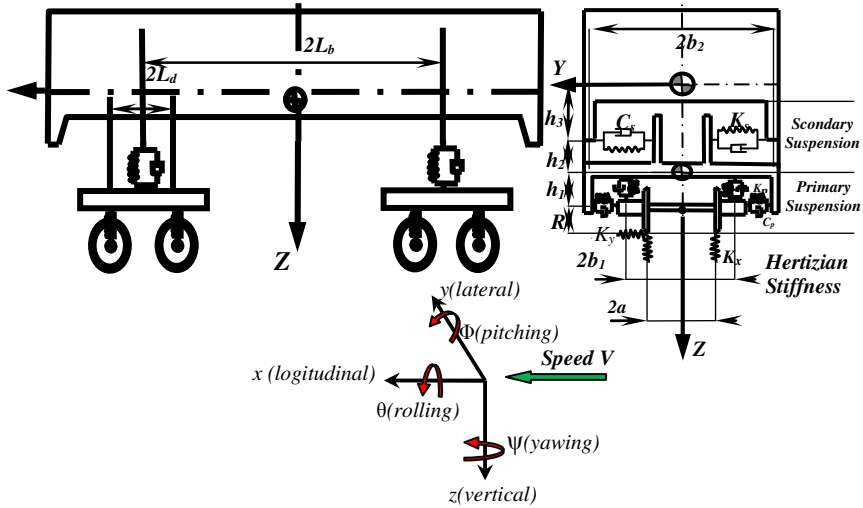
Fig. 1 Physical model of railway vehicle

In actual practice different types of periodic, a-periodic or random track irregularities may exist on the track, but in the present study a lateral local discontinuity type of irregularity is considered as shown in Fig.2. The shape of the irregularity is assumed to be similar on the left and the right rails.

Table 2 Vehicle parameters

Parameter	Nomenclature	Values
Primary spring stiffness	K_p	10^7 N/m
Secondary spring stiffness	K_s	$1,7 \times 10^{6}$ N/m
Primary damping coefficient	C_p	6×10^4 Ns/m
Secondary damping coefficient	C_s	10^5 Ns/m
Vertical hertz spring stiffness	K_{hz}	35×10^{9} N/m
Longitudinal distance between bogies I and II and car body mass center	L_b	6 m
Longitudinal distance between wheel-set and corresponding bogie origin	L_d	1,4 m
Lateral distance between a longitudinal primary suspension and corresponding wheel-set	d_p	1 m
Lateral distance between longitudinal secondary suspension and corresponding bogie origin	d_s	1 m
Lateral distance between contact point of wheel–rail and corresponding wheel-set origin	a	0,7163 m
Lateral distance between vertical primary suspension and corresponding wheel-set origin	b_1	1 m
Lateral distance between vertical secondary suspension and car body mass center	b_2	1 m
Nominal wheel radius	R_1	0,61 m
Vertical distance between wheel-set and bogie mass centers	h_1	0,3 m
Vertical distance between bogie mass center and lateral secondary suspension	h_2	0,2 m
Vertical distance between lateral secondary suspension and car body mass center	h_3	1,3 m

The excitations of the left wheels of leading bogies are as follows:

$$Y_{ri} = \begin{cases} H & for \quad t_{di} \leq t \\ 0 & otherwise \end{cases} \quad (i = 1..4) \tag{1}$$

Where

$$\left[t_{d1}, t_{d2}, t_{d3}, t_{d4} \right] = \left[0, \frac{2L_d}{V}, \frac{2L_b}{V}, \frac{2L_b + 2L_d}{V} \right] \tag{2}$$
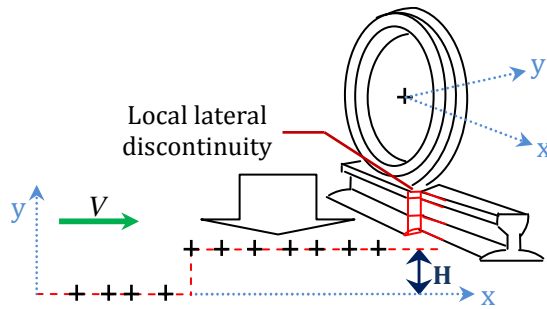
Fig. 2 Model of track irregularity

In the present study, *H* is taken as *0.03m*.

4   Simulation Study

The models were built in the MATLAB/ Simulink® environment. The fixed step solver ODE-45 (Dormand-Prince) was utilized, with the sampling time Ts=0.0001. Ts is smaller than the fastest half-car Active Vehicle Suspension Systems (AVSS) model dynamics, enabling observation of all model dynamics [7, 8]. Dynamic analysis was carried out for the vehicle at different speeds: 15m/s, 30m/s, 45m/s and 60m/s.

4.1   Dynamics Analysis

The following output parameters are evaluated:

- Lateral, yawing and rolling displacement and acceleration at the floor of the car body center of mass.
- Lateral displacement and acceleration at the front and the rear bogie center pivot.

The lateral and angular displacement and acceleration responses of the car body at speeds of 15m/s, 30m/s, 45m/s, 60m/s are shown, respectively, in Fig.3 and Fig.4.

(a)   (b)
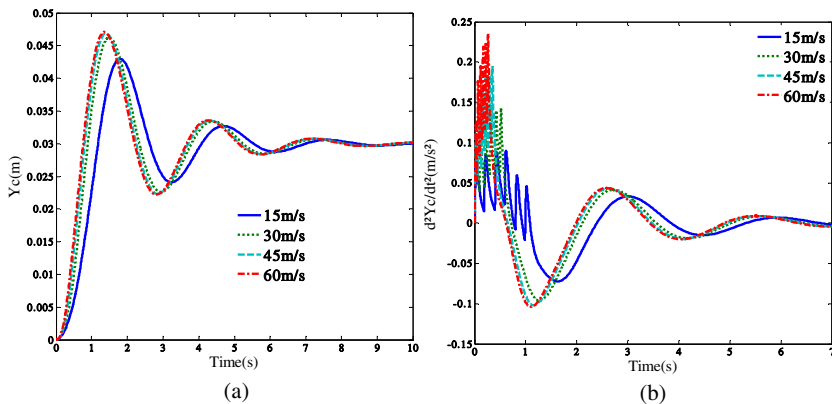
Fig. 3 The Lateral Car body displacement **(a)** and acceleration **(b)** for different vehicle speeds

Plots show that initially, the value of displacement and acceleration are nearly equal to zero, which is mainly the displacement and acceleration without track irregularity.
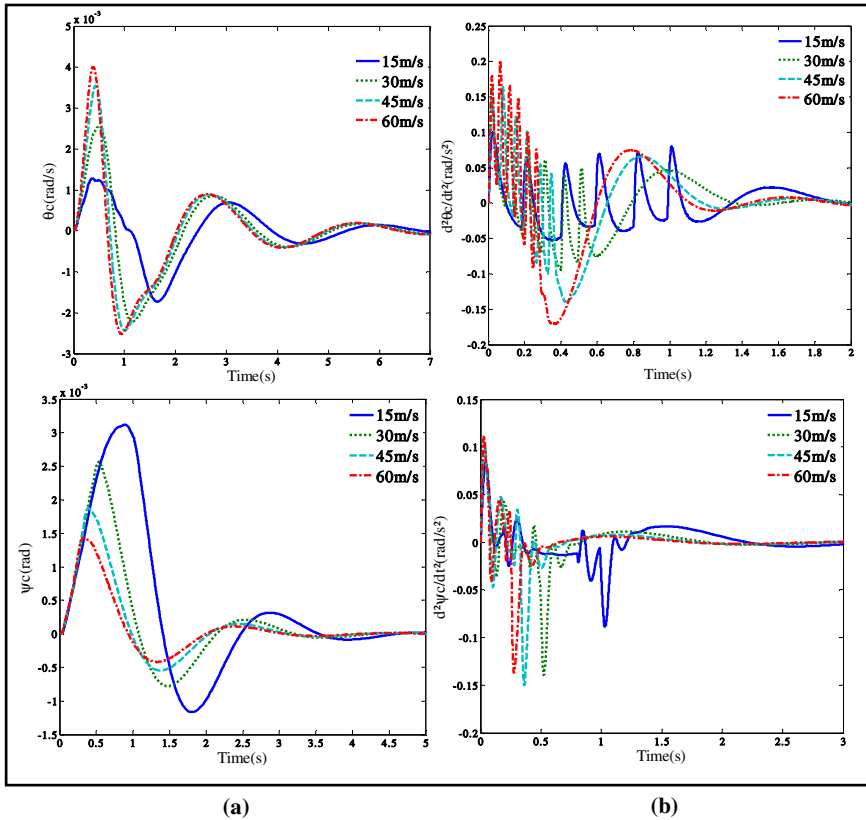
Fig. 4 The Rolling (θ_c) and Yawing (ψ_c) Car body displacement **(a)** and acceleration **(b)** for different vehicle speeds

Finally it goes to zero and 0.03m (case of Yc), when the vibration of the car body ceases and stabilizes. The displacement and acceleration are generally within an acceptable range and does not show any instability. The movement of the carboy is not very shifty with acceptable amplitudes and it stabilizes around 7 seconds. According to Fig.3 and Fig.4, this lateral local discontinuity default induced only swaying, rolling and yawing movements at the floor of the car body center of mass.

The displacement and acceleration response of front and the rear bogie with time are presented at different velocities of vehicle in Fig.5.a) and Fig.5.b), respectively. It is clear from the plots that initially the wheels of the front bogies

come in contact with the track irregularity and the vibration starts in the front bogie and later these vibrations are shifted to the rear bogies. The amplitude of the vehicle vibration also increased with the vehicle speed except for the case of yaw displacement movement (Fig.4).
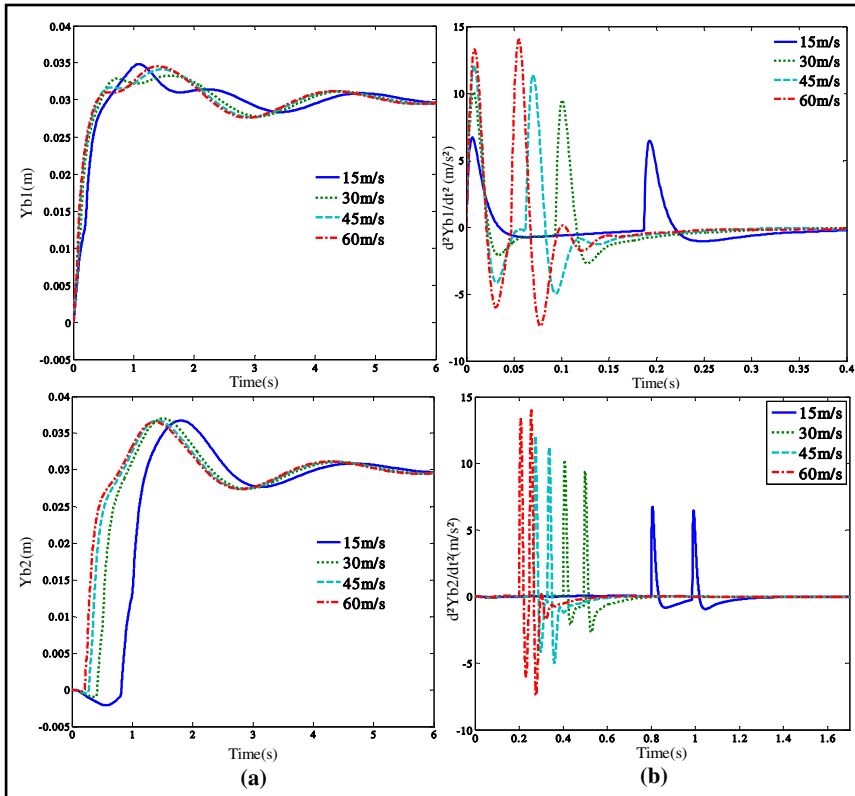
Fig. 5 The Lateral front (b1) and Rear (b2) Bogie displacement **(a)** and acceleration **(b)** for different vehicle speeds

4.2 Comfort Evaluation

Acceleration frequency response plots were generated for car body at vehicle speeds of 15m/s to 60 m/s and are shown in Figure.6 to calculate the Sperling ride comfort index [9, 10, 11]. The FFT plot is generated for a frequency range between 0 to 1000 Hz, as the human beings are most sensitive in the frequency range of 4 to 12.5 Hz. Ride comfort analysis has been performed for speeds ranging from 15m/s to 60m/s.

The analysis has been performed on the system model to calculate the vertical acceleration of the system. FFT output is taken to get the peak acceleration frequency component. Comfort index has been and presented in Table 3.
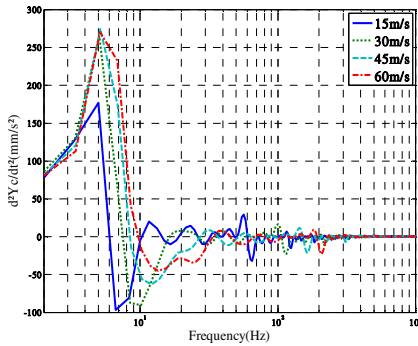
Fig. 6 The vertical Car body acceleration in frequency domain for different speeds
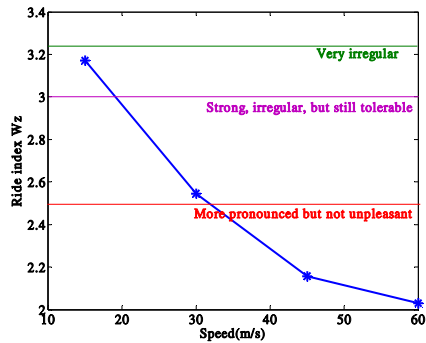
Fig. 7 The Sperling index comfort variation for different speeds

The maximum and minimum ISO Sperling Index values are respectively 3.17 and 2.03 for the rail vehicle speed respectively 15 m/s and 60 m/s. These values respectively indicate "Strong, irregular, but still tolerable" and "Clearly noticeable" zones. Fig.7 show that the comfort index decreases as the vehicle speed increases while maintaining an acceptable level of comfort. This means that the passengers are not much affected by the vibration as they are exposed to low level of vibrations for this type of irregularity.

Table 3 Sperling's ride comfort index an evaluation for different vehicle velocities

Vehicle Speed (m/s)	Sperling Index (W_z)	Ride comfort evaluation
15	3.17	Strong, irregular, but still tolerable
30	2.54	More pronounced but not unpleasant
45	2.15	Clearly noticeable
60	2.03	Clearly noticeable

The dynamic behavior of the rail vehicle is specific for the speed of 15 m/s relative to the other speeds. Indeed, this speed matches to the low excitation frequencies of the rail vehicle where different rigid bodies are critically solicited. While the others speeds matches to the medium and higher frequencies.

4.3   Parametric Study

A parametric study was undertaken to find the influence of different suspension parameters on the Sperling index (Wz). Fig.8 and Fig.9 show the variation of Wz index as a function of stiffness and damping respectively (primary and secondary). The increase in the primary suspension stiffness reduces the Wz index at the car

body marginally up to a speed of 60 m/s. The influence of secondary stiffness has been found to be just the opposite of the primary stiffness. A reduction of the secondary stiffness value from the present value reduces the Wz index at the car body at all the speeds. The variation of the primary damping is seen to have little influence on the Wz index at the car body. At speeds above 45 m/s, increase in the primary damping is shown to produce marginal reduction in the Wz index at the car body. The secondary damping has great influence at speeds higher than 30 m/s.
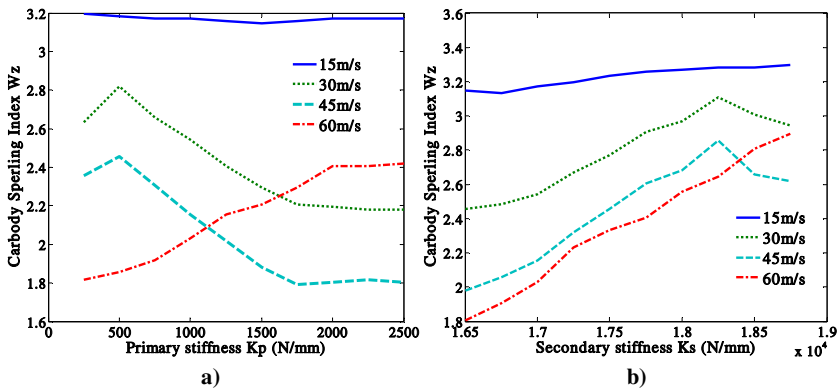
Fig. 8 The influence of Primary **a)** and secondary **b)** stiffness

An increase in the secondary damping reduces the Wz index at speeds greater than 30 m/s, whereas up to 30 m/s speed, the secondary damping has little influence. It has also been observed that all the primary damping have very limited influence at low speeds.
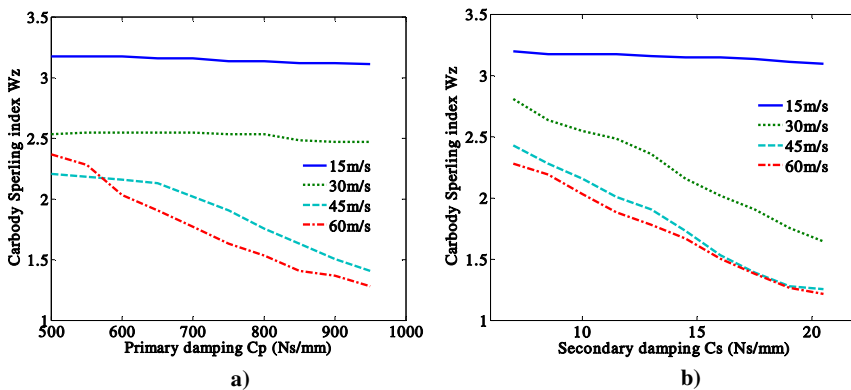
Fig. 9 The influence of Primary **a)** and secondary **b)** damping

5   Conclusion

Vertical dynamic analysis has been carried out for a Railway Vehicle. A 17 degree of freedom model is used for the analysis. Velocity input at all the wheel-set is given by considering similar lateral discontinuity at both right and left rail. A lateral acceleration response at the car body has been calculated in the frequency domain. The Sperling Ride index has been calculated and presented for the above vehicle at different speeds. The calculated values of the Sperling index are found well in the satisfactory limits defined by the ISO 2631 standard which means that the passengers are not much affected by the vibration as they are exposed to low level of vibrations. A parametric study has been carried out with emphasis on better ride index. The parametric study has brought out possible design changes required in different parameters to deliver better Sperling comfort index. It should be noticed that the parametric study was carried out to suggest design modifications to improve Wz index, but others dynamic and control behaviors like stability, control of secondary suspension were to be considered when implementing the design modifications.

References

1. Skarlatos, D., et al.: Railway fault diagnosis using a fuzzy logic method. Applied Acoustic 65(10), 951–966 (2004)
2. Kumar, H.: Sujata: Vertical dynamic analysis of a typical indian rail road vehicle. In: Proceedings on Computational Mechanics and Simulation, IIT, India, pp. 8–10 (2006)
3. Dukkipati, V., Amyot, J.: Computer Aided Simulation in Railway Dynamics. Marcel Dekker, New York (1988)
4. Nejlaoui, M., et al.: Multiobjective robust design optimization of rail vehicle moving in short radius curved tracks based on the safety and comfort criteria. Simulation Modelling Practice and Theory 30, 21–34 (2013)
5. Abood, K.H.A., Khan, R.A.: The Railway carriage simulation model to study the influence of vertical secondary suspension stiffness on ride comfort of railway carboy. Journal of Mechanical Engineering Science 225, 1349–1359 (2011)
6. Nielsen, J., Igeland, A.: Vertical dynamic interaction between train and track-influence of wheel and track imperfections. Journal of Sound and Vibration 187, 25–26 (1995)
7. Chen, H., et al.: Application of Constrained H∞ Control to Active Suspension Systems on Half-Car Models, Journal of Dynamic Systems, Measurement and Control. Transactions of the ASME 127(3), 345–354 (2005)
8. Pedro, J., Dahunsi, O.: Neural Network-based Feedback Linearization Control of a Servo-Hydraulic Vehicle Suspension System. International Journal of Applied Mathematics and Computer Science 21(1), 137–147 (2011)
9. Forstberg, J.: Ride comfort and motion sickness in tilting trains, - Human re-sponses to motion environments in train and simulator experiments. Master's Thesis, KTH/FKT/D-00/28-SE, Division of Railway Technology, KTH (2000)
10. Carg, V.K.: Dynamics of Railway Vehicle Systems. Academic Press (1984)
11. B153/RP21 Application of ISO Standard to Railway Vehicules,: Comfort Index Nmv Comparaison with the ISO/SNCF Comfort Note and with the Wz (European Rail Research Istitute) (1993)

Application of the Numerical Continuation Method in the Prediction of Nonlinear Behavior of Journal Bearings

Amira Amamou and Mnaouar Chouchane

Laboratory of Mechanical engineering, National Engineering School of Monastir,
University of Monastir, Tunisia
`amira.amamou@mailpost.tn, mnaouar.chouchane@enim.rnu.tn`

Abstract. Numerical continuation as a tool for analyzing nonlinear differential equations has proven to be very useful especially for the interactive numerical investigation. This paper examines the nonlinear behavior of a rigid rotor symmetrically supported by two identical short journal bearings. Within this contribution, bifurcation analyses and nonlinear phenomena of this rotor bearing system are investigated using MATCONT which is a numerical continuation package for the study of dynamical systems and their bifurcations.

Keywords: Rotor bearing system, Numerical continuation, Matcont, Bifurcations.

1   Introduction

The use of numerical continuation for the bifurcation analyses of the rotor-bearing system provides a basic understanding for the complex nonlinear rotordynamic behavior and the computation of limit cycles and their bifurcation points (Kuznetsov 1998) (Krauskopf 2007). Recent development in numerical continuation methods has provided the tools for the identification of periodic normal forms for codimension 1 bifurcations of limit cycles, normal forms for codimension 2, bifurcations of equilibria, detection of codimension 2 bifurcations of limit cycles (Dhooge et al 2008). The study of such dynamical systems requires a good and powerful software. Matlab is a powerful and widely used environment for scientific computing which can support flexible and extendible packages. MatCont is a Matlab continuation and bifurcation toolbox which is compatible with the standard Matlab Ordinary Differential Equations toolbox (Dhooge et al 2003).

In this paper, a brief introduction to the theory of numerical continuation will be given. An example of computation of the nonlinear behavior of a perfectly balanced rotor bearing system using Matcont will be carried out. Identification of

equilibrium points and their bifurcations, bifurcations of limit cycles, jump phenomena and coexistence of solutions will be presented.

2   Numerical Continuation Method

2.1   Equilibrium Point Continuation

Numerical continuation concerns itself with the following of the steady state solutions of systems of differential equations, as these solutions depend on parameters, using continuation software. For example, given a system of Ordinary Differential Equation (ODE) modeling a dynamical system of the form:

$$\dot{X} = \frac{d\vec{X}}{dt} = \vec{f}\left(\vec{X}, v\right) \tag{1}$$

where $\vec{X}(.) \in \mathbb{R}^n$ is the vector of the state coordinates of the system, $\vec{f}(.,.) \in \mathbb{R}^n$ is the continuously differentiable nonlinear function, $v \in \mathbb{R}$ is the parameter of the system that will be varied to follow a branch of steady state solutions, $t \in \mathbb{R}$ is time and an over dot denotes the total derivative with respect to t. An equilibrium solution of equation (1) $\vec{X}_s(t)$, for $v = v_c$, can be found by solving the following equation:

$$\vec{f}\left(\vec{X}_s, v_c\right) = 0 \tag{2}$$

Our goal is to compute a sequence of points which approximate a curve in $\left(\vec{X}, v\right)$ space that starts at a starting point $\left(\vec{X}_0, v_0\right)$ and describes how the equilibrium point varies. In more general terms, the continuation problem requires finding a solution curve to the problem (Kuehn 2011):

$$\vec{F}\left(\vec{y}\right) = 0 \tag{3}$$

where $\vec{y} = \left(\vec{X}, v\right)$ and $\vec{F}\left(\vec{y}\right) = \vec{f}\left(\vec{X}, v\right)$.

Starting from a known solution $\vec{y}_0$ such that $\vec{F}\left(\vec{y}_0\right) = 0$, the bifurcation parameter v is varied to calculate branches of fixed points or periodic solutions by following a branch of solution. The idea behind this method is to generate a sequence of points $y_i, i = 1, 2, \ldots$ along the curve, satisfying a chosen tolerance criterion: $\left\| \vec{F}\left(\vec{y}_i\right) \right\| \le \varepsilon_1$ for some $\varepsilon_1 > 0$ and an additional accuracy condition

$\left\| \delta \vec{y}_i \right\| \le \varepsilon_2$ where $\varepsilon_2 > 0$ and $\delta \vec{y}_i$ is the last Newton correction in the prediction-correction method discussed below .

To show how the points are generated, suppose we have found a point y_i on the curve and suppose we have a normalized tangent vector $\vec{v}_i$ at $\vec{y}_i$, i.e. $\vec{F}_y \left(\vec{y}_i \right) \vec{v}_i = 0 ; \left\langle \vec{v}_i , \vec{v}_i \right\rangle = 1$.

Most continuation algorithms implement a predictor-corrector method. The predictor generates an initial guess for the corrector part, in which the Newton method is used to find the next solution on the branch:

   • Prediction: Given $\vec{y}_0$, we want to find a point $\vec{y}_1$, Figure 1a. Suppose $h > 0$ which will represent a step size. A commonly used predictor is the tangent prediction: $\overline{y}_1 = \vec{y}_i + h \vec{v}_i$.

   • Correction: $\overline{y}_1$ will not be on the curve so we want to find $\vec{y}_1$ starting from $\overline{y}_1$ that satisfies $\vec{F} \left(\vec{y}_1 \right) \approx 0$, figure 1b.
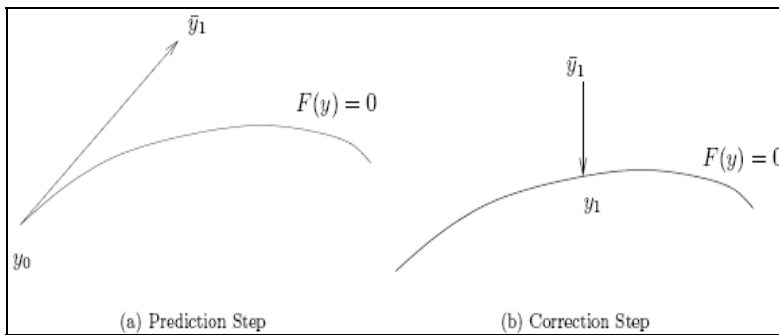
Fig. 1 The predictor-corrector method (Kuehn 2011)

2.2 *Bifurcation Detection*

The location of bifurcation points based on monitoring the eigenvalues λ_i of the Jacobian matrix $A = \dfrac{d\vec{f}}{d\vec{X}} \bigg|_{\vec{X}_s}$ is detected when one parameter of the system is varied

and a branch of steady-state solutions can be followed by means of the path-following method. The stability of a branch of steady-state solutions can change qualitatively at so-called codimension 1 bifurcations. Generally, these are the only bifurcations that can be encountered if one parameter is varied.

For a fixed point, there are two generic codimension 1 bifurcations that can be detected along the equilibrium curve: fold, also known as limit point (LP) and Hopf point (H).
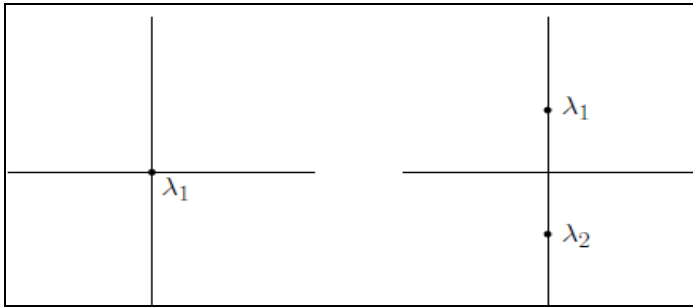

Fig. 2 The critical eigenvalues determining the bifurcations on the equilibrium curve

At the bifurcation point,

- Fold (LP): $\lambda_1 = 0$
- Andronov-Hopf (H): $\lambda_{1,2} = \pm i\psi_0$, $\psi_0 > 0$

2.3   Continuation of Limit Cycles

Assume the ODE system (1) has at v_0 an isolated periodic orbit (Limit cycle) C_0. Let $\vec{X}_0(t+T_0) = \vec{X}_0(t)$ denote the corresponding periodic solution with minimal period T_0. C_0 has Floquet multipliers $u_1, u_2, ..., u_{n-1}, u_n$, the eigenvalues of the monodromy matrix $M(T_0)$ which satisfies:

$$\dot{M}(t) - \vec{f}_x\left(\vec{X}_0(t), v_0\right)M(T_0) = 0 , \ M(0) = I_n \tag{4}$$

Similar to the fold bifurcation for branches of fixed-points, the predictor-direction parameter component is used as the cyclic fold test function. The number of unstable Floquet multipliers changes by one if a cyclic fold is passed (Kuznetsov 1998).

On a limit cycle curve the following bifurcations can occur:

- Fold also known as Limit Point Cycles (LPC): $u_1 = 1$;
- Flip also called Period Doubling (PD): $u_1 = -1$;
- Neimark-Sacker (NS): $u_{1,2} = e^{\pm i\theta_0}, 0 < \theta_0 < \pi$
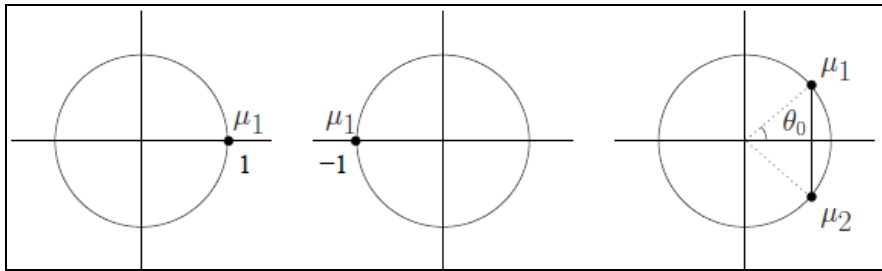
Fig. 3 Floquet multipliers determining the bifurcations of limit cycles (Kuznetsov 1998)

3 An Example of Application of Numerical Continuation Using Matcont

Consider the rotor-bearing system, whose specifications are listed in Table 1.

Table 1 Journal bearing geometry and operating parameters (Wang and Khonsari 2006)

Parameters	Value
Journal diameter (D=2R)	0.0254 m
Length of the bearing (L)	0.0127 m
Radial clearance (c)	50.8 10-6 m
Mass of the rotor (2M)	5.647 Kg
Oil viscosity (μ)	0.01 Pa.s
L/D ratio	0.5
Bearing parameter	$\Gamma = 0.8$

The rotor-bearing system consists of a rigid rotor symmetrically supported by two identical plain short journal bearings as shown in figure 4. Its corresponding bearing parameter $\Gamma = \dfrac{\mu R L^3}{2Mc^{2.5}g^{0.5}}$ depends only on the bearing geometry, the supported load and the oil viscosity.
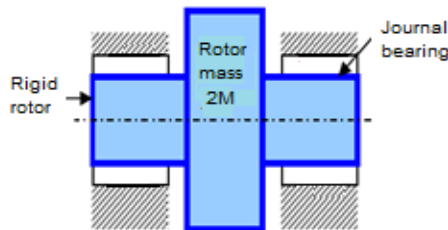
Fig. 4 A rigid rotor supported by two identical journal bearings

In order to depict the nonlinear behavior of the rotor-bearing system shown in figure 4, the method of numerical continuation is applied   using MATCONT.

First, we specify a new ODE system, say "*short bearing*", into Matcont (Chouchane and Amamou 2011) as shown in figure 5.
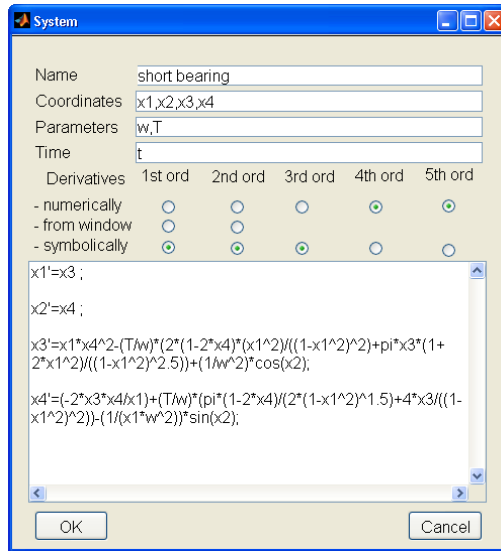
Fig. 5 The short bearing model in Matcont

Then, we locate the equilibrium point by starting from an arbitrary selected initial point to get an orbit converging to an equilibrium point, figure 6.
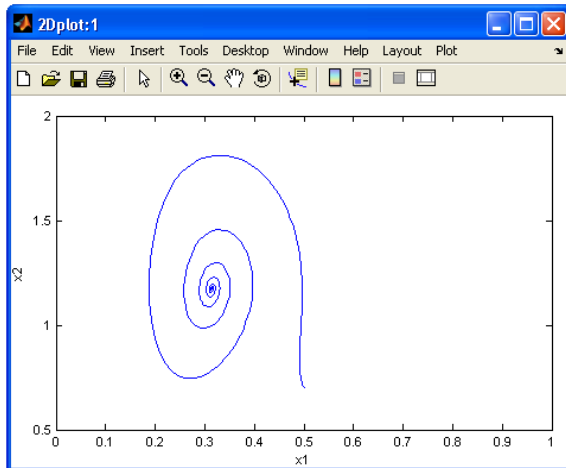

Fig. 6 Trajectory of rotor center carter approaching a stable equilibrium point for $\Gamma = 0.8$

In the following, the equilibrium point found by integration will be continued with respect to the dimensionless journal speed denoted as ϖ. The last point of the plotted orbit in figure 6 is selected and a continuation of an equilibrium curve is started. The equilibrium curve obtained by numerical continuation is shown in figure 7 in terms of   bearing eccentricity ε.
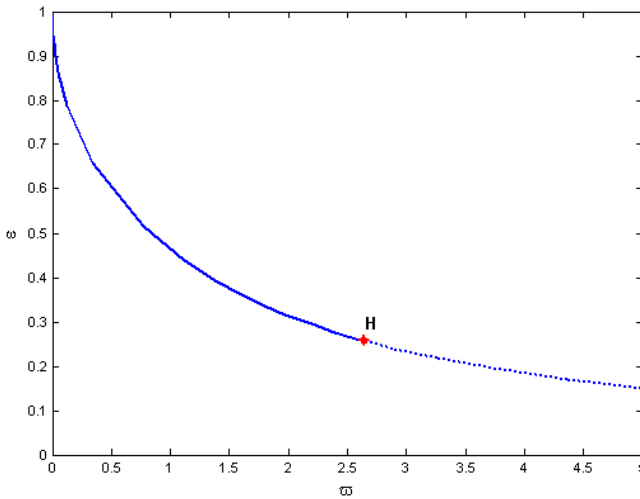
Fig. 7 Equilibrium curve, H denotes a Hopf point

Along the forward branch, Matcont stops at a Hopf point labeled H. Indeed, there are two eigenvalues of the equilibrium with $\mathrm{Re}\left(\lambda_{1,2}\right)\approx 0$ at this parameter value visible in the Matcont *Numeric* window in figure 8.
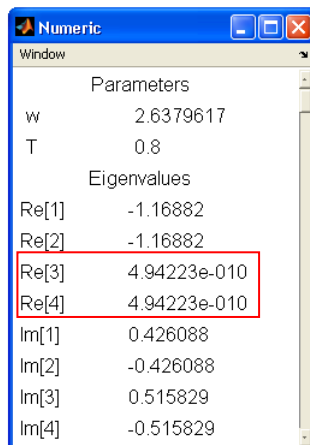
Fig. 8 Numeric window of Matcont at the Hopf point

The first Lyapunov coefficient for the Hopf bifurcation can be read in the MATLAB Command Window and it is equal to 1.86e-002." The critical frequency $\mathrm{Im}(\lambda_3) \neq 0$, ($\mathrm{Re}(\lambda_3) \approx 0$), while the first Lyapunov coefficient is positive. Thus, there should exist an unstable limit cycle bifurcating from the equilibrium point. Along the backward branch, no other specific points are detected. From the Hopf point H, Matcont may be used to continue the branch of the unstable limit cycles.
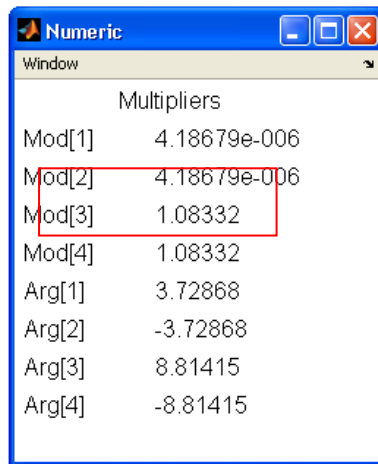
Fig. 9 The Numeric window at the LPC bifurcation point
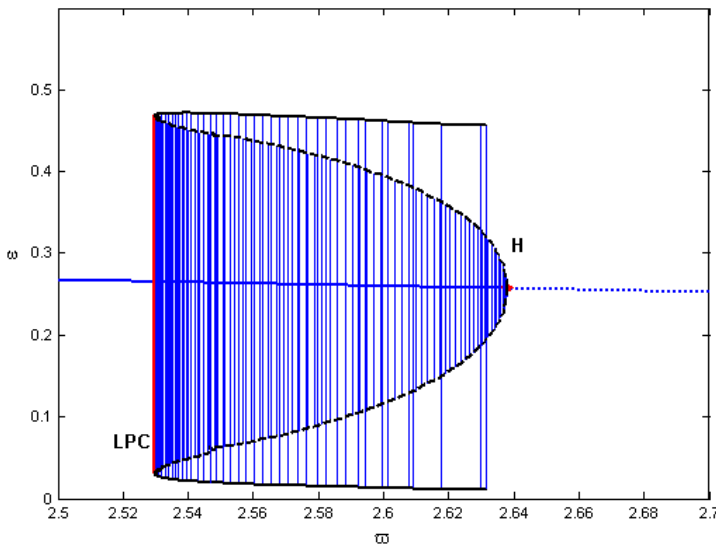
Fig. 10 The family of limit cycles bifurcating from the Hopf point H

   The Floquet multipliers are calculated during continuation. The absolute values and arguments in angular grades are displayed as shown in figure 9 corresponding to the Limit Point bifurcation LPC. An LPC point appears if the periodic solution have a pair of complex conjugated Floquet multipliers with a magnitude equal to one (Kuznetsov 1998).

   The critical cycle has approximately a double multiplier $\mu=1$. Thus, the limit cycle manifold has a fold here. When the computations are resumed, the continuation algorithm will automatically follow the second stable cycle branch after the LPC point. The computation produces the limit cycles manifold shown in figure 10.

   Figure 10 shows the branch of subcritical unstable limit cycles and its bifurcation. The contours of the stable limit cycles are represented by solid lines and those of unstable limit cycles are represented by dashed lines. The continuation process stops once a bifurcation point of limit cycles, "LPC", is encountered and another branch of limit cycles is continued from the LPC point.

   The unstable limit cycles, in the range $\varpi_{LPC} < \varpi < \varpi_H$, define the basin of attraction of the stable equilibrium point. If the journal centre undergoes a perturbation within the basin of attraction, it returns to the stable equilibrium point. For larger perturbations, it diverges away from the basin of attraction to another branch of other stable limit cycles as it is shown in figure 10. The size of the basin of attraction decreases significantly for higher bearing parameter Γ for which a perturbation of the journal position has more impact on the journal stability. Hence, if the journal speed is increased beyond ϖ_H , the journal jumps to a large size limit cycle at the Hopf point H. If the journal speed is decreased from a speed greater than ϖ_H , it would jump back to the equilibrium point at a rotor speed ϖ_{LPC} .

4   Conclusion

An example of application of numerical continuation method to identify the nonlinear journal bearing behavior using Matcont has been presented in this paper. The considered rotor bearing system has been shown to undergo a Hopf subcritical bifurcation with unstable limit cycles which disappear at a limit point of cycle bifurcation and fold into stable limit cycles.

References

Dhooge, A., Govaerts, W., Kuznetsov, Y.A., Meijerd, H.G.E., Sautois, B.: New features of the software MatCont for bifurcation analysis of dynamical systems. Mathematical and Computer Modelling of Dynamical Systems: Methods, Tools and Applications in Engineering and Related Sciences 14, 147–175 (2008), doi:10.1080/13873950701742754

Dhooge, A., Govaerts, W., Kuznetsov, Y.: Matcont: A matlab package for numerical bifur-
    cation analysis of odes. ACM TOMS 29, 141.1 (2003)
Chouchane, M., Amamou, A.: Bifurcation of limit cycles in fluid film bearings. Interna-
    tional Journal of Non-Linear Mechanics 46, 1258–1264 (2011)
Krauskopf, B.: Numerical continuation methods for dynamical systems: path following and
    boundary value problem. Springer, UK (2007)
Kuehn, C.: A mathematical framework for critical transitions: bifurcations, fast-slow sys-
    tems and stochastic dynamics. Physica D 240, 1020–103510 (2011), doi:10.1016/
    j.physd.2011.02
Kuznetsov, A.: Elements of Applied Bifurcation Theory. Springer, New York (1998)
Wang, J.K., Khonsari, M.M.: Application of Hopf bifurcation theory to rotor-bearing sys-
    tems with consideration of turbulent effects. ASME Journal of Tribology 39, 701–714
    (2006)

Stability Lobes for 1DOF and 2DOF Milling System

Cherifa Azoui[1] and Brahim Benmohammed[2]

[1] Université Hadj Lakhdar Batna, Faculté de Technologie, Département de Mécanique,
01 avenue Chahid Boukhlouf Mohamed El Hadi Batna (05000), Algérie
`az.cherifa@gmail.com`

[2] Laboratoire de Recherche en Productique (LRP), Université Hadj Lakhdar Batna,
Faculté de Technologie, Département de Mécanique,
01 avenue Chahid Boukhlouf Mohamed El Hadi Batna (05000), Algérie
`b.benmohammed@gmail.com`

Abstract. Recently, the investigation of periodic motion of the delay differential (DDEs) and the associated variation systems become into the focus of many studies. One of the most important motivations is the milling process analysis. In this work, the semi discretization method is briefly explained and have been applied for 1-DOF (degree of freedom) and 2-DOF milling system in order to build the stability lobes charts.

Keywords: milling, semi discretization method, stability lobes, hopf bifurcation, flip bifurcation.

1   Introduction

It has been known for a long time, that past effects need to be included in the modeling of certain dynamic problems.

The first delay models in engineering appeared for wheel shimmy and for ship stabilization. There are several other problems in engineering, where time delays arise, like in the modeling of machine tool vibrations in cutting processes, in robotics tele-manipulation with transport delay, or in neural network models, where the interactions of the neurons are delayed. Qualitative and quantitative analysis of delayed systems is therefore an important issue in many applications.

A numerical technique, the so called semi-discretization was used to obtain approximate solutions for retarded functional differential equations (RFDEs).

These all models use the so-called stability lobe diagrams, which make it possible to choose the maximum axial depth of cut for a given spindle speed associated with a chatter free machining. In many practical cases, however, the choice of the optimal speed is difficult because contradictory parameters interact with productivity, (Hartung et al 2006).

2   Semi Discretization Method

Semi discretization is a technique often used in computational fluid mechanics for solving partial differential equations (PDEs). The idea is to discretize the PDE along the spatial coordinates while leaving the time coordinate unchanged. This method was adapted to the analysis of delay differential (DDEs). The DDE is thereby approximated by a series of ordinary differential equations (ODEs), (Gradisek et al 2005).

The discretization is constructed over one period time interval T, such that: $T = k \Delta t$, where Δt is the length of the interval $\left[t_i, t_{i+1}\right]$, with: i=0,1,2… In our case the time period is chosen to be a time delay: $T = \tau$, (Salvat 2010-2011).

3   1 DOF and 2 DOF Milling Systems

The governing equation of motion of a 1 DOF milling model (Insperger and Stepan 2004)) is given as:

$$\ddot{x}(t) + 2\xi\omega_n \dot{x}(t) + \omega_n^2 x(t) = -\frac{wh(t)}{m_t}(x(t) - x(t - \tau)) \qquad (1)$$

Where ω_n is the angular natural frequency, ξ is the relative damping, w is the depth of cut, m_t is the modal mass of the tool. The delayed term $x(t - \tau)$ arise due to the regenerative effect.

The time delay τ is equal to the tooth passing period T. The specific cutting force coefficient $h(t)$ is determined by the technological parameters

$$h(t) = \sum_{j=1}^{Z} g\left(\phi_j(t)\right) \sin\left(\phi_j(t)\right)\left(K_t \cos\left(\phi_j(t)\right) + K_n \sin\left(\phi_j(t)\right)\right) \qquad (2)$$

where Z is the number of teeth, K_t and K_n are respectively the tangential and the normal linearized cutting force coefficients and $g_j(t)$ is the angular position of tooth j defined as:

$$\phi_j(t) = \left(2\pi\Omega / 60\right)t + j\,2\pi / Z \qquad (3)$$

where Ω is the spindle speed in (rpm). The function $g\left(\phi_j(t)\right)$ is a screen function, it is equal to 1, if the tooth j in the cutting material, and it is equal to 0, if tooth j is out of it. The terms ϕ_{st} and ϕ_{ex} are the start and the exit angles of the tooth j. Also $h(t)$ is in the time period with the tooth passing period τ.

For milling processes, the time delay is equal to the time period. For the spindle speed Ω (rpm), the time delay is $\tau = T = 60 / (Z\,\Omega)$, and the time step is given by:

$$\Delta t = T / k = 60 / (kZ\,\Omega) \qquad (4)$$

The discretized equation of motion has the form:

$$x\ddot{(t)}+2\xi\omega_n \dot{x}(t)+\left(\omega_n^2+\frac{wh_i}{m_t}\right)x(t)=\frac{wh_i}{m_t}x_{\tau,i} \qquad (5)$$

with: $t \in$ [ti, ti+1] and where:

$$h_i = \frac{1}{\Delta t}\int_{t_i}^{t_{i+1}} h(t)dt \qquad (6)$$

We find in Table 1 the used parameters for stability chart build for 1DOf milling system.

Table 1 Parameters used for stability chart build for 1-DOf milling system

Parameters	Value
Z	2 (number of teeth)
K_t	6.10^8 (N/m^2)
K_n	2.10^8 (N/m^2)
ω_0	922.2.л (rd/s)
ξ	0.011
m_t	0.03993 (kg)

We present in (Fig. 1) the chart of stability for 1 DOF system.
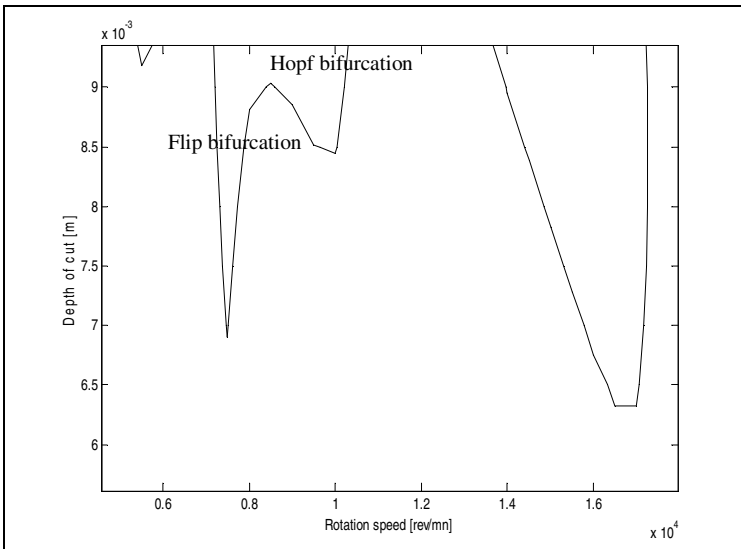
Fig. 1 Stability chart for 1 DOF system

The governing equation of motion of a 2DOF milling model with symmetric tool is given as:

$$
\begin{bmatrix} \ddot{x}(t) \\ \ddot{y}(t) \end{bmatrix} + \begin{pmatrix} 2\xi\omega_n & 0 \\ 0 & 2\xi\omega_n \end{pmatrix} \begin{bmatrix} \dot{x}(t) \\ \dot{y}(t) \end{bmatrix} + \begin{pmatrix} \omega_n^2 + \dfrac{wh_{xx}(t)}{m_t} & \dfrac{wh_{xy}(t)}{m_t} \\ \dfrac{wh_{yx}(t)}{mt} & \omega_n^2 + \dfrac{wh_{yy}(t)}{mt} \end{pmatrix} \begin{pmatrix} x(t) \\ y(t) \end{pmatrix}
\tag{7}
$$

$$
= \begin{pmatrix} \dfrac{wh_{xx}(t)}{m_t} & \dfrac{wh_{xy}(t)}{m_t} \\ \dfrac{wh_{yx}(t)}{m_t} & \dfrac{wh_{yy}(t)}{m_t} \end{pmatrix} \begin{pmatrix} x(t-\tau) \\ y(t-\tau) \end{pmatrix}
$$

$x(t)$ et $y(t)$ represent the tool displacement in x and y directions.

Where the angular natural frequency ω_n, the relative damping ξ and the modal mass m_t of the tool are considered to be equal in both x or y directions corresponding to the symmetric tool assumption.

All the parameters are the same as for equation (1) of the 1 DOF model.

In Equation (7), $h_{xx}(t)$, $h_{xy}(t)$, $h_{yx}(t)$ and $h_{yy}(t)$ are four projections of the specific cutting force coefficient and they are defined as:

$$
h_{xx}(t) = \sum_{j=1}^{Z} g\left(\phi_j(t)\right)\sin\left(\phi_j(t)\right)\left(k_t\cos\left(\phi_j(t)\right) + k_n\sin\left(\phi_j(t)\right)\right)
\tag{8}
$$

$$
h_{xy}(t) = \sum_{j=1}^{Z} g\left(\phi_j(t)\right)\cos\left(\phi_j(t)\right)\left(k_t\cos\left(\phi_j(t)\right) + k_n\sin\left(\phi_j(t)\right)\right)
\tag{9}
$$

$$
h_{yy}(t) = \sum_{j=1}^{Z} g\left(\phi_j(t)\right)\cos\left(\phi_j(t)\right)\left(-k_t\sin\left(\phi_j(t)\right) + k_n\cos\left(\phi_j(t)\right)\right)
\tag{10}
$$

$$
h_{yx}(t) = \sum_{j=1}^{Z} g\left(\phi_j(t)\right)\sin\left(\phi_j(t)\right)\left(-k_t\sin\left(\phi_j(t)\right) + k_n\cos\left(\phi_j(t)\right)\right)
\tag{11}
$$

We find in Table 2 the used parameters for stability chart build for 2DOf milling system.

Table 2 Parameters used for stability chart build for 2DOf milling system

Parameters	Value
Z	2 (number of teeth)
K_t	6.10^8 (N/m^2)
K_n	2.10^8 (N/m^2)
ω_{0x}	922.2.л (rd/s)
ω_{0y}	922.2.л (rd/s)
ξ_x	0.011
ξ_y	0.011
m_{tx}	0.03993 (kg)
m_{ty}	0.03993 (kg)

We present in (Fig. 2) the chart of stability for 2 DOF systems.
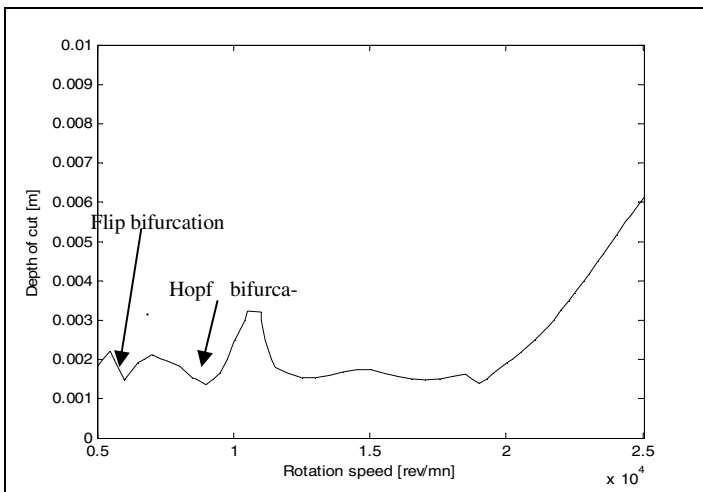
Fig. 2 Stability chart for 2 DOF system

In the figures 1and 2 w = function(Ω). we have used a Matlab code to obtain the stability chart (w=f(Ω)). The stability limit diagrams represents the limit of the system's stability, i.e., all combinations of parameters (rotational speed and depth of cut) leading to a stable cut are situated under the lobes, and on the contrary, chatter occurs for combinations situated over the lobes.

4 Conclusion

In this work we have presented briefly a semi discretization method and applied it to get the stability charts for a milling system (1DOF and 2 DOF). The stability charts have the same forms but there is a difference in the values of stability limits.

We could observe that the stability lobes have two forms, the U form present the so called hopf bifurcation, and a second form V shows the flip bifurcation.

Comparing the size and location of hopf and flip bifurcation lobes, it is important to note that the hopf lobes are much wider than the flip lobes.

References

Hartung, F., Insperger, T., Stépàn, G., Turi, J.: Approximate stability charts for milling processes using semi-discretization. Applied Mathematics and Computation 174, 51–73 (2006)

Gradisek, J., Kalveram, M., Insperger, T., Weinert, K., Stepan, G., Govedar, E., Grabec, I.: On stability prediction of milling. International Journal of Machine Tools & Manufacture 45(7-8), 769–781 (2005)

Salvat, N.: Abradable material removal in aircraft engines: a time delay approach, Master Sciences Technologies Santé, Mention Sciences de la Matière, Spécialité Mécanique, Matériaux, Structures et Procédés, Vibrations and Structural Laboratory, Faculty of Engineering-McGill University (2010-2011)

Insperger, T., Stepan, G.: Updated semi-discretization method for periodic delay-equations with discrete delay. International Journal for Numerical Methods in Engineering 61(1), 117–141 (2004)

Predictive Maintenance Program Based on Vibration Monitoring

Ramadan O. Saied[*], Mohammed S. Mostafa, and Hussein A. Hussein

Mechanical and Industrial Department, Faculty of Engineering,
University of Tripoli, Libiya
saied972004@gmail.com

Abstract. The early detection, identification and correction of machinery problems are paramount to anyone involved in the maintenance of industrial machinery to insure continued, safe and productive operation and to avoid any financial disaster, or personal injury and possible loss of life. Since the vibration analysis can help predict component failure, those parts identified as defective can be scheduled for repair or replacement during planned equipment shutdowns, rather than during costly emergency downtime due to equipment failure. This study presents the use of the machinery vibration as a tool for predicative maintenance program of the rotating machineries. The introduction to the predictive maintenance using vibration analysis in the literature is presented. Causes of vibration and techniques of vibration analysis are illustrated. Construction of the predicative maintenance program via vibration analysis is presented and a computer program named Vibrogram was built up using Visual Basic Language. The Vibrogram is implemented on three rotating machines as case studies at Al- Waha Oil Field, Libya. It was found that the vibration monitoring is a vital component of any good predictive maintenance program for any plant machinery.

Keywords: Vibration, condition monitoring, predictive maintenance, failure.

1   Introduction

The predictive maintenance or condition monitoring is among the planning maintenance part of other maintenances such as a preventive and production maintenances and it involves the trending and analysis of the machinery performance parameters to detect and identify developing problems before a catastrophic failure can occur. It indicates that when replacement of items that wear out should be done so preventing possible major failures. It can detect foreign matters (dirt, oil, moisture) in systems and an appropriate action can be taken [1, 2]. Several parameters can be served as starting point for a condition monitoring. Among these parameters the vibration monitoring for rotating

---

[*] Corresponding author.

machineries, especially for high speed machines such as turbines and compressors. Many industries have found that there are significant advantages of the vibration monitoring including cost saving, reduce the down time and increase the reliability of machines. In addition, the vibration in rotating machineries is not beneficial. It can cause excessive wear, cracking, loosening of fasteners, excessive noise and a host of other problems. In the case of aircraft, serious vibration can cause catastrophic failure leading to loss of life. The goal of vibration monitoring is to detect vibration patterns which will lead to failure.

The vibration monitoring and analysis have been studied by many researchers. The majority of these studies aimed to develop a self-adjusting and integrated monitoring system that is able to function under various working conditions with minimum cost. Hansen and Gao [3] studied the vibration behavior of a deep groove ball bearing with a structurally integrated force sensor. They conducted experimental studies on a ball bearing to validate the analytical and numerical solutions. A good agreement was found between the model-predicted sensor outputs and the experimental results. Mitchell [4], presented a technical article regarding the progress on the vibration measurements and condition based maintenance over the continuous seventy years. Alzadjali and Rameshkumar [5] presented an investigation on the effect of shaft misalignment on the vibration behavior of a centrifugal blower and they observed that the vibration amplitude component at 2X is predominant in all types of misalignment and the vibration increases with the machine speed. In field of wind energy, Sheng and Veers [6] found that the vibration analysis and oil monitoring are the most tools for condition monitoring of wind turbines. Zhun et al [7] developed on line a lubrication monitoring program for a wind mill using a particle filtering technique, in order to reduce the energy cost and improve the wind turbine availability and reliability. In this paper a predictive monitoring program based on the vibration analysis is presented and companion case studies are discussed.

2   Characteristics of Vibration

The vibration is simply a motion of machine or a part of machine back and forth from its equilibrium position. This vibratory motion can be modeled by a motion of mass suspended on end of a spring as explained in the elementary theory of simple harmonic motion [8]. The vibration can be characterized by several common terms. The frequency of the vibration is a number of cycles per second and usually measured in Hertz unit. The amplitude of vibration is a distance that the vibrating part travels back and forth. The increase in amplitude always accompanies an increase of mechanical troubles. The amplitude can be measured by a displacement, a velocity or acceleration. The displacement is a peak to peak displacement and measured in mils, mm or inch. The peak velocity is the rate of change of the displacement with respect to time, measured in mm/s or inch/ s. The peak acceleration is the rate of change of velocity with respect to time and measured in mm/s^2 or $inch/s^2$. Each of the vibration characteristic reveals something significant about the vibration.

3   Common Causes of Vibration

The vibration in rotating machineries occurs due to numerous causes. The unbalance of the rotating shafts is the major cause of vibration in the machines. The vibration may develop due to unequal distribution mass in rotating parts. The points of unbalance produce forces which cause vibration. The unbalance amplitude usually presents at a frequency equal to one time of the operation speed of the part (1x). Unbalance may be in single plane (static) or in multiple planes (dynamic unbalance). The second major cause of vibration is the misalignment between shafts of connected machines which generates vibrations that can be mistaken for unbalance. A distinguishing feature is that its principal frequency is at twice running speed (2x) and it contains a large axial component. Loose of mechanical parts of the machine generates 1x vibration but almost always contain higher harmonics. Worn gears, bent shafts, eccentricity of the bearing, aerodynamic and hydraulic forces, rubbing and resonance are also other sources of vibration in the rotating machineries. Figure 1 illustrates typical examples of the spectral characteristics for some causes of vibrations [9].
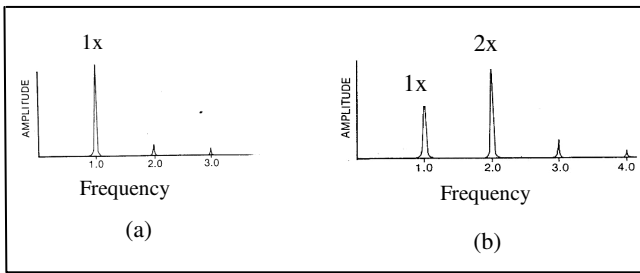
Fig. 1 Typical examples of spectral characteristics for (a): unbalance and (b): Misalignment

4   Analysis Techniques

The causes of vibration are usually identified by several techniques. The choice of the technique depends on the type of the machine and frequency levels. The frequency demand is the common practice to analyze the vibration, where the vibration signals are resolved and displayed as narrow band spectral components. In this technique, the frequency analyzer converts the complex vibration signal from the time domain to frequency domain producing a display of frequency versus amplitude. The other technique is the time domain waveform (orbit analysis). This technique became common practice several years ago when vibration signals displayed on an oscilloscope were utilized for analysis purposes [9]. By establishing the orbit of the rotating shaft on the oscilloscope screen, the picture of the shaft motion within the bearing clearance can be obtain and therefore, the cause of the vibration can be identified. Now days, modern analyzed equipments such as digital and computerized data collectors are used, instead of

the old equipments.   These, indeed provide accuracy with rapid analysis to produce an output which may be displayed on the screen of the analyzer immediately.

5   Vibration Monitoring Program

The construction of the vibration program for predictive maintenance of rotating machineries is based on the following factors:

5.1   Plant Survey

The first step in the monitoring program is to study the plant equipments layout, process flow, production patterns, reliability, cost production and maintenance resources. Selection of the machines in the program should be done through the priority of the machines or those are critical to/or in support of, production. When the machines are selected, it should be listed on scheduling sheets.

5.2   Machine Condition

The condition of machines should be studied through the machine maintenance file (if not available, should be constructed). If the mechanical condition of machines is unknown, a complete vibration analysis should be performed. This vibration analysis will detect if machines is trouble free and also will established the start point for monitoring program. Furthermore, vibration levels for machines should be established from the manufacturer, similar machines or expert maintenance persons in the plant. The first vibration checkout may appear machine defects. These defects should be corrected prior to the next measurement, in order to reduce the vibration levels.

5.3   Selection of Measuring Points

The selection of points for vibration measurements should take into account some factors such as machine type, method of mounting, normal direction in which internal forces can be generated, etc. In general, the vibration measurements are usually taken at houses of bearings, because these are locations where rotation parts (shafts) come in touch with the stationary parts (casing). The vibration reading are usually taken in the vertical (V), horizontal (H) and axial (A) directions to the bearing axis of the machine

5.4   Selection of Measuring Instruments

Different modern instruments are available for measuring, analysis and displaying the vibration data. Vibration meters usually hand-held and battery operated are used for measuring displacement, velocity, acceleration and spike energy levels in

a frequency ranges up to 500,000 cycle/min. Data collectors are the instruments which capable of measuring a phase angle, displacement, velocity, acceleration. The modern data collectors are equipped with microprocessor programming capability to measure and store large amounts of vibration data of various parameters. They can measure the displacement, velocity, and acceleration (RMS, pk and pk-pk). Furthermore, collect and store the vibration data on- route and off-route monitoring points and download data to PC for advanced analysis. They can carry out spectrum analysis (FFT) and provide monitoring of rotating parts and dynamic balancing with stroboscope.

Transducers are important instruments, which are used to pick up the vibration readings by converting the mechanical energy into electrical energy. They produce an electrical signal which is function of mechanical vibration. Three types of transducers are commonly used; displacement, velocity and acceleration pickups.

5.5   *Period of Vibration Measurements*

The length between the check points of the vibration measurements is essential for the monitoring program. The interval of the vibration measurements should be designed according to a number of factors for each check point of each machine. Some of critical machines must be monitored on continuous basis. Periodic, normally monthly, monitoring also can be carried out on the machines according to their speeds. For example, machines operate at low speed (< 500 rpm), the vibration monitoring should be performed every three months, whereas the machines operate between 500 and 3000 rpm, they should be monitoring every month. High speed machines must be monitoring every two weeks [10]. However, other factors may alter the monitoring period such as type of the machines, history of frequent failures, safety and the operation experience which will most likely dictate how often the analysis should be performed. When the vibration interval has been established, it should be fed to the computer as a periodic vibration check chart.

5.6   *Vibration Tolerance and Limits*

The vibration tolerance should be established for each machine and check point. There are several sources of vibration tolerances are available such as ISO, British and ASME standards. The ISO 10816 Vibration Severity Chart [11] is divided into three zones, the zone A (green)for vibration values from new machines , zone B (yellow) for machines without restriction and zone C (red)for machines in which the damage could occur any time. It also defines four groups of machines, according to their size, base and purpose. In the absent of tolerance information for a machine, the vibration tolerance can be formulated from the maintenance experience or historical data. It should be mentioned that as experience is gained, each machine's tolerance can be reviewed and changed as required. Once the tolerances are established, these are entered on the check round chart.

5.7   Report of a Vibration Analysis

Recording system for vibration data should be established in order to issue the vibration report to concerning decision team for planning and scheduling of repairs immediate action. The report is usually a summary of vibration reading of machine trough a certain time (every three months) and it shows the health of the machine in this period of time as the vibration trend is gradually or sudden increase. When repairs have been completed, immediate notification to predictive maintenance team is important. New vibration reading should be taken on the machine after repairing. These will be very helpful in that they will be used to re-evaluate the vibration limits or tolerance for the machine.

5.8   Training Vibration Staff

The vibration staff should be having a good knowledge of machinery, trouble shooting and the elementary theory of the mechanical vibration. The vibration analysis requires thoroughness and patience. Those performing the work should be acquainted with the overall objective of the program and what the maintenance department hopes to accomplish. A team effort with vibration engineers, technicians, foremen and operating department heads should be developed.

6   Case Studies

The Waha Oil Field is selected for the applicative part of the study; since the technology of predictive maintenance using vibration monitoring is not fully applied there. The Waha Oil Field is the largest field in the Libyan Waha Oil Company. Three different machines used in three different plants have been chosen for the vibration monitoring program. Table 1 illustrates the technical specifications of each machine. Vibration levels were measured continually with permanently installed on-line vibration measuring systems using velocity or displacement transducers fixed on control panel of the machines. The transducer converts the machine vibration into an equivalent electrical signal that is read on the meter as a vibration level.

Table 1 Technical Specifications of the three machines

Machine	Model	Manufacturer.	Location	Duty	Vib. Alarm	Vib. Trip
GE Gas Turbine	5001	General Electric Co.	Power Plant	Drive a generator	0.5 in /s	1 in /s
Solar Gas Turbine	T-4500	Solar Co.	Gas Plant	Drive a compressor	1.7 mils	2 mils
Centrifugal Pump	DVS-EX	United Co.	Oil Plant	Pump crude oil	1.2 mils	1.8 mils

7   Computer Vibration Program

A vibration program named "**VIBROGRAM**" has been developed using Visual Basic Language, in order to implement the vibration monitoring for the three rotating machineries. Figure 2 shows the flowchart of the program. Once the program has been set up in the computer, the next step is to collect the vibration readings for machines involved. After starting the program, a window will display on the screen for recording the vibration data. A dialogue box will show up asking the technician to follow a few simple instructors to get the task accomplished. As soon as the down load of vibration readings finished, two kinds of reports can be generated; a vibration recording report and /or a graphical report. The reports give an overview about the condition of the machine over a period of data collection. The **VIBROGRAM** records the collection vibration readings from the vibration control panels of the machines for one month period.
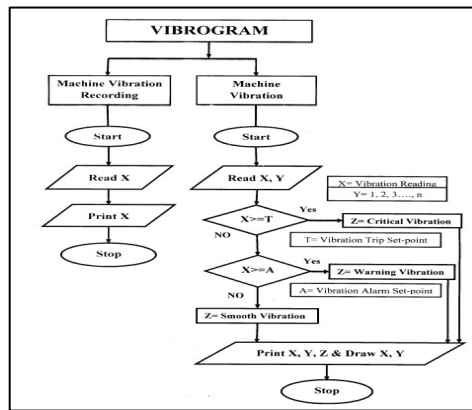
Fig. 2 Flowchart of the computer program "VIBROGRAM" for vibration monitoring

8   Results and Discussion

Table 2 shows the vibration readings of the three machines. The turbines readings were recorded for one month whereas the readings of the pump for fifteen days only, because it was shut down due to production requirements. As it can be seen that the vibration readings of the pump are acceptable and the pump runs in smooth condition.

Table 2 Machines vibration readings at axial direction

GT Turbine (m/s)			Solar Turbine (mils)		United Pump (mils)		
Pedestal Bearing	Comb. Bearing	Turb. Bearing	Comb. Bearing	Turb. Bearing	Pump	Motor Bearing	Pump Support
0.23	0.12	0.15	0.1	0.6	0.4	0.6	0.9
0.27	0.12	0.16	0.1	0.6	0.35	0.5	0.9
0.31	0.13	0.16	0.05	0.8	0.35	0.6	0.9
0.3	0.13	0.16	0.1	1	0.4	0.6	1
0.32	0.15	0.16	0.1	0.7	0.45	0.55	1.1
0.32	0.13	0.15	0.05	0.7	0.4	0.6	0.9
0.32	0.14	0.16	0.1	0.7	0.3	0.65	1
0.33	0.13	0.6	0.2	0.7	--	--	--
0.35	0.14	0.15	0.1	0.7	--	--	--
0.34	0.14	0.15	0.1	0.7	--	--	--
0.34	0.14	0.15	0.2	0.8	--	--	--
0.35	0.14	0.15	0.1	0.8	--	--	--
0.33	0.14	0.16	0.05	0.8	--	--	--
0.33	0.13	0.15	0.05	0.8	--	--	--
0.3	0.14	0.17	0.05	0.9	--	--	--

Figure 3 shows the trend of vibration readings of the GE turbine with time. There are three zones of colors according to the ISO standard [10]: the green zone for smooth region of vibration, the yellow zone for warning region and the red zone for critical region. It can be noted that all the readings are located in the green zone which means that they are within the acceptable range of vibrations. The curve is approximately steady with time. However, the vibration readings increase slightly up to .35 in/s near the warning board. This value is high for such turbo machineries. Therefore, it is recommended that this point should be monitored closely and checked again to analyze the cause of vibration.
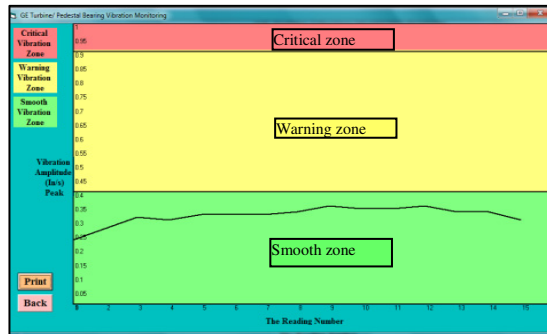
Fig. 3 vibration measurements of the GE turbine

Figure 4 illustrates a window of the Vibrogram monitoring for the bearing of the Solar turbine. Clearly it can be observed that the vibration readings are very low and within the acceptable (smooth) zone. This indicates that the bearing is in good condition.
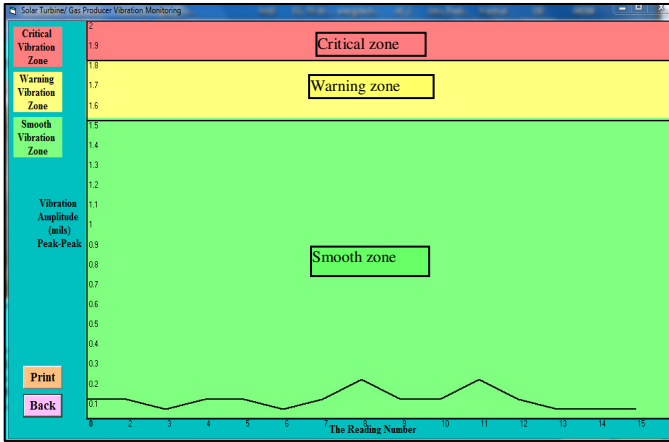
Fig. 4 Vibration measurements of the Solar turbine

9   Conclusions

Outlines of conclusions can be drawn from this study as:

- Vibration analysis provides a powerful tool to locate problems that cause abnormal machine vibration and to prevent catastrophic failure by correcting vibration-related problems.
- Vibration monitoring is a vital component of any good predictive maintenance program for any plant machinery.
- A predictive maintenance program that uses vibration monitoring allows repairs to be scheduled during regular maintenance rather than during costly unscheduled breakdowns, thus yielding significant annual savings in maintenance costs.
- Use of the modern digital instruments can provide an excellent and accurate analysis of vibration readings.

References

[1] Mobley, R.: Introduction to predictive maintenance, 2nd edn. Butterworth-Heinemann Inc. (2002)

[2] Thomson, W.: Theory of vibration with applications, 4th edn. Stanley Thorns Ltd., Butterworth-Heinemann (1993)

[3] Hansen, B., Gao, R.: Vibration analysis of a sensor-integrated ball bearing. Transaction of the ASME 222, 384–392 (2000)

[4] Mitchell, J.: From vibration measurements to condition based maintenance seventy years of continuous progress. Sound and Vibration, 62–75 (2007)

[5] Alzadjali, A., Rameshkumar, G.: Condition monitoring of centrifugal blower using vibration analysis. Int. J. of Multidisciplinary Science and Engineering 4, 50–59 (2013)

[6] Sheng, S., Veers, P.: Wind Turbine drive train condition monitoring- an over view. Presented at Applied System Health Management Conference, Virginia, USA, May 10-12 (2011)

[7] Zuhn, J., Yoon, M., He, D., Qu, Y., Bechhoefer: Lubrication oil condition monitoring and remaining useful life prediction with particle filtering. Int. J. of Prognostics and Health Management 20, 1–15 (2013)

[8] Inman, D.: Engineering vibration. Prentice Hall International edition, New Jersey (1994)

[9] Mitchell, J.: Machinery analysis and monitoring. Penn Well Publishing Co., USA (1981)

[10] Higgins, L.: Maintenance Engineering Handbook, 5th edn. McGraw-Hill, USA (1995)

[11] DIN ISO 10816-3 Evaluation standard for vibration monitoring, http://www.manteni-mientoplanificado.com (accessed December 19, 2014)

Prediction of Flaws in Pipes Using Wave Finite Element Method

Sonda Chaabene[1,2], Faker Bouchoucha[1], M. Kharrat[1,2], Mohamed Najib Ichchou[2], and Mohamed Haddar[1]

[1] Mechanics, Modeling and Manufacturing Research Laboratory,
  National Engineering School of Sfax, Tunisia
  `fakersbouchoucha@yahoo.fr`, `mohamed.haddar@enis.rnu.tn`,
  `sondachaabene@gmail.com`
[2] Tribology and System Dynamics Laboratory, Central School of Lyon,
  AV. Guy de Collongue, 69134 Ecully, France
  `mohamed.ichchou@ec-lyon.fr`

Abstract. A study of the reflection from defects can be predicted from cylindrical tube and its singularities using the wave finite element method (WFEM). Dealing with wave propagation and defect detection in straightforward specimens, there is great interest in extending the skills of the WFEM to include the characterization of defects. Numerical simulations have been carried out to ensure the performance of the WFEM. Thereby, a parametric study of the torsional-mode T(0,1) reflection from three dimensional (3D) defect is developed by varying axial and circumferential extent of defect in the first step then the position of the defect in the second step. The WFEM is seen to yield accurate results for defect detection in pipes.

Keywords: Guided Wave/Torsional mode /defect /Reflection Coefficient/pipes.

1   Introduction

A number of researchers have performed the analysis of defect detection in hollow cylinders and pipelines based on ultrasound and elastic guided wave in the oil, chemical, and other industries {(Bai et al. 2001), (Demma et al. 2004), (Alleyne et al. 1998) and (Zemanek 1972)}. Guided wave techniques have evolved considerably in the last two decades and revolve around the practical evaluation application. Some significant works can be considered revolutionaries in the Non-Destructive Testing (NDT) field {(Alleyne & Cawley 1996), (Li & Rose 2002), (Sun et al. 2003) and (Sun et al. 2005)}. Nevertheless, many critical subjects still remain largely unexplored, such as guided wave defect sizing competencies,

guided wave propagation characteristics and focusing possibility in pipes and its singularities. Hence, numerical developments are still needed to understand the scattering wave's phenomena.

A numerical finite element based approach named wave finite element method (WFEM) is previously developed in references {(Mead 1973), (Mead 1975)}. The dispersion curves and the mode shapes are among the primary properties to be given in Refs.{(Mencik and Ichchou 2005), (Duhamel 2006) and (Bouchoucha et al. 2012)}. Whereby, Ichchou (Ichchou et al. 2009) considered the wave propagation features for low and mid-frequency in cylindrical pipes with local inhomogeneities. For a pipe with non-axisymmetric geometries (such as defects and elbows), some numerical approaches have to be used instead of the analytical calculations to simulate the guided wave behaviors. Inspired by the work of Zhou (Zhou et al. 2008) and based on these previous works, the motivation for this paper is the need to accurately detect defect using wave finite element method. A parametric study allowing defect sizing and detection has been investigated in this work.

One of the major contributions of many researches resides in the mode choice since each mode is adapted for an application (i.e. defect detection) well targeted (crack, defect, fracture etc.). Torsional guided waves have been applied considerably to pipe inspection for their sensitivities to different kinds of defects {(Lovstard and Cawley 2011), (Bareille et al. 2012)}. The T(0,1) mode is non-dispersive and it is the lowest and fastest torsional mode and most suitable for defect detection in pipes {(Bareille et al. 2012), (Liu et al. 2006)} So, it will facilitate the time domain separation of the signals of interest from the rest of the received signal.

The remainder of this paper introduces the problem to be solved that means the scattering of guided waves by flaws in section 2. Section 3 is devoted to the modal description which involves post processing of Ansys FE specimen. Numerical simulations are developed and the main results are shown. Concluding remarks are made in section 4.

2   Problem Statement: Scattering of Guided Waves by Flaws

In this section, considering an infinite structural waveguide with local voids (flaws, etc.) which are basically due to lack of material or material variation, a monochromatic incident wave is assumed to be generated at x $-\infty$ and travel to x $+\infty$ direction. Scattering phenomenon occurs when there is interaction between the incident guided waves and flaws as shown in figure 1.
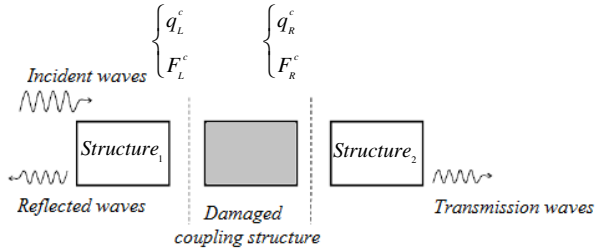
Fig. 1 Wave scattering in structure through local defect

The modeling of damaged cell is similar to that of typical one for modes extraction, except that additional interior dofs might be included. The coupling condition is governed by the dynamics equation of coupling structures:

$$\left[M^c\right]\left\{(\ddot{q}_L^c)^T \quad (\ddot{q}_I^c)^T \quad (\ddot{q}_R^c)^T\right\}+\left[K^c\right]\left\{(q_L^c)^T \quad (q_I^c)^T \quad (q_R^c)^T\right\}=\left\{(F_L^c)^T \quad 0 \quad (F_R^c)^T\right\} \tag{1}$$

Where $\left[M^c\right]$ and $\left[K^c\right]$ denote respectively the mass and stiffness matrices of the coupling structures. Eq. 1 can be condensed as:

$$\begin{bmatrix} S_{LL}^c & S_{LR}^c \\ S_{RL}^c & S_{RR}^c \end{bmatrix}\begin{Bmatrix} q_L^c \\ q_R^c \end{Bmatrix}=\begin{Bmatrix} F_L^c \\ F_R^c \end{Bmatrix} \tag{2}$$

To describe the scattered field, eigensolutions need to be decomposed to positive and negative going wave modes for the computational purpose. Then, the couple (q_i, F_i), where $i = 1, 2...2N$, can be divided into two sets with the same number: $(\left[^-q\right],\left[^-F\right])$ with $|\lambda|<1$ representing negative going waves, $(\left[^+q\right],\left[^+F\right])$ with $|\lambda|>1$ representing positive going waves, which are written as N by N base matrices. For undamped system, there exists the case $|\lambda|=1$ relating to the purely propagating waves, which can also be decomposed to positive going and negative going waves by observing the sign of the imaginary part of λ. The coupling conditions expressed as:

$$q_L^c =\left[^+q\right]\phi^{inc} +\left[^-q\right]\phi^{ref}, \quad q_R^c =\left[^+q\right]\phi^{tr} \tag{3}$$

and $$F_L^c =\left[^+F\right]\phi^{inc} +\left[^-F\right]\phi^{ref}, \quad F_R^c =-\left[^+F\right]\phi^{tr} \tag{4}$$

Considering the coupling conditions eq.2 can be written as:

$$
\begin{bmatrix}
S_{LL}^{c}\left[{}^{-}q\right]-\left[{}^{-}F\right] & S_{LR}^{c}\left[{}^{+}q\right] \\
S_{RL}^{c}\left[{}^{-}q\right] & S_{RR}^{c}\left[{}^{+}q\right]+\left[{}^{+}F\right]
\end{bmatrix}
\begin{Bmatrix}\phi^{ref} \\ \phi^{tr}\end{Bmatrix}
=
\begin{bmatrix}
\left[{}^{+}F\right]-S_{LL}^{c}\left[{}^{+}q\right] \\
-S_{RL}^{c}\left[{}^{+}q\right]
\end{bmatrix}
\left\{\phi^{inc}\right\}
\tag{5}
$$

Given a single or a set of incident modes as the input in Eq. 5, reflection and transmission modes acting as the output can be obtained. Numerically, the base number N_r is suggested to be frequency dependent. To simplify our calculation, the fixed-boundary CMS method is used here (Craig 1968) where a substructure is considered to be composed of interior and interface dofs. It condenses the system matrices by assuming the displacements of the interior dofs as a linear superposition of the constraint modes and the internal normal modes. Introduce the transformation matrix [T], the displacement vector of coupling substructure is represented in terms of generalized coordinates:

$$
\left\{(q_{L}^{c})^{T}\quad (q_{I}^{c})^{T}\quad (q_{R}^{c})^{T}\right\}^{T}=[T]\left\{(q_{L}^{c})^{T}\quad (q_{\delta}^{c})^{T}\quad (q_{R}^{c})^{T}\right\}^{T}
\tag{6}
$$

where q_{δ}^{c} is the modal displacement modal. The transformation matrix for the fixed boundary method can be written as:

$$
[T]=
\begin{bmatrix}
I & 0 & 0 \\
-\left[K_{II}^{c}\right]^{-1}\left[K_{IL}^{c}\right] & \Phi_{II} & -\left[K_{II}^{c}\right]^{-1}\left[K_{IR}^{c}\right] \\
0 & 0 & I
\end{bmatrix}
\tag{7}
$$

where Φ_{II} is the fixed interface normalized modal matrix, K_{II}^{c}, K_{IL}^{c} and K_{IR}^{c} are the interior dofs related components in the stiffness matrix. Thus equation 1 can be simplified as

$$
\left[M_{CB}^{c}\right]\left\{(\ddot{q}_{L}^{c})^{T}\quad (\ddot{q}_{\delta}^{c})^{T}\quad (\ddot{q}_{R}^{c})^{T}\right\}+\left[K_{CB}^{c}\right]\left\{(q_{L}^{c})^{T}\quad (q_{\delta}^{c})^{T}\quad (q_{R}^{c})^{T}\right\}=\left\{(F_{L}^{c})^{T}\quad 0\quad (F_{R}^{c})^{T}\right\}
\tag{8}
$$

Where the condensed mass matrix $\left[M_{CB}^{c}\right]=[T]^{T}\left[M^{c}\right][T]$, stiffness matrix $\left[K_{CB}^{c}\right]=[T]^{T}\left[K^{c}\right][T]$, q_{δ} is the truncated set of generalized modal displacement associated to the modal matrix Φ_{II}. Hence, Eq.5 can be modified as

$$
\begin{bmatrix}
\hat{S}_{LL}^{c}\left[{}^{-}q\right]-\left[{}^{-}F\right] & \hat{S}_{LR}^{c}\left[{}^{+}q\right] \\
\hat{S}_{RL}^{c}\left[{}^{-}q\right] & \hat{S}_{RR}^{c}\left[{}^{+}q\right]+\left[{}^{+}F\right]
\end{bmatrix}
\begin{Bmatrix}\phi^{ref} \\ \phi^{tr}\end{Bmatrix}
=
\begin{bmatrix}
\left[{}^{+}F\right]-\hat{S}_{LL}^{c}\left[{}^{+}q\right] \\
-\hat{S}_{RL}^{c}\left[{}^{+}q\right]
\end{bmatrix}
\left\{\phi^{inc}\right\}
\tag{9}
$$

where $\hat{S}_{LL}^{c}$, $\hat{S}_{LR}^{c}$, $\hat{S}_{RL}^{c}$ and $\hat{S}_{RR}^{c}$ are the matrices of the reduced system obtained by eliminating the modal shift q_{δ}:

$$\hat{S}_{LL}^c = D_{LL}^c - D_{L\delta}^c D_{\delta\delta}^{c\ -1} D_{\delta L}^c \ ; \ \hat{S}_{LR}^c = D_{LR}^c - D_{L\delta}^c D_{\delta\delta}^{c\ -1} D_{\delta R}^c$$
$$\hat{S}_{RL}^c = D_{RL}^c - D_{R\delta}^c D_{\delta\delta}^{c\ -1} D_{\delta R}^c \ ; \ \hat{S}_{RR}^c = D_{RR}^c - D_{R\delta}^c D_{\delta\delta}^{c\ -1} D_{\delta R}^c \tag{10}$$

After solving Eq. 9, the whole scattered wave fields can be obtained through equation 6 and Eq 8. Calculations were performed based on the connection between two homogeneous waveguides through inhomogeneous one including the defect as shown in figure 2. The waveguide 1 is a pipe section connected to a damaged coupling structure which is in turn connected to waveguide 2 similar to the first one. Hence, the reflection and transmission coefficients are defined as follow:

$$R_i = \frac{\phi_i^{re}}{\phi_i^{in}} \ , \ T_i = \frac{\phi_i^{tr}}{\phi_i^{in}} \tag{11}$$

Where $i = 1,..., N_r$.

3 Numerical Results and Discussion

This section provides numerical examples that illustrate some features of guided waves in the cylindrical steel isotropic tube in which we create a local crack (shown in Fig. 2). The study was led by using an Ansys FE calculation code to get the mass and stiffness matrices. The circumference of the pipe was divided into 22 elements. Hence, the above-described method was postprocessed in order to obtain the reflection and transmission coefficients using Matlab-code (its formulation is detailed in section 2). And we will focus only at the reflection coefficient (RC). The dimensions of the flaw such as axial (mm), depth and circumferential (%) extents are subscribed by a, b and c, respectively. The circumferential extent was varied by eliminating an element in every step that's why it's defined by percent of circumference.

Here, the torsional mode T(0,1) is selected thanks to its non-dispersive character based on many research in wave mode propagation in pipes [6, 12]. The material properties and geometry of the tube are listed in Table 1. RC-spectra in the 1–35 kHz range are obtained for different sizes and different flaws positions.

Table 1 Material and geometry data

Parameters	Value
Length (mm)	2
outside radium (mm)	70
inside radium (mm)	66
thickness (mm)	4
Density ρ (Kg/m^3)	7800
Young's modulus (Pa)	2.10^{11}
Poisson's ratio	0.3

Calculation was performed on the connection between two homogenous waveguides through inhomogeneous one including the defect as shown in Fig.2. The waveguide 1 is a pipe section connected to a damaged coupling structure which is consecutively connected to waveguide 2 similar to the first one.
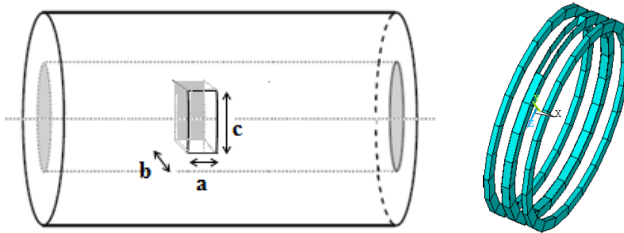
Fig. 2 Finite element coupling structures with flaw and its dimensions

3.1   Reflection Coefficient by Varying the Flaw Extents

- *Reflection coefficient by varying the flaw axial extents*

The flaw's axial extent was varied from 1 mm to 5 mm in steps of 1 mm whereas defect's circumferential extent is fixed at 9% (2 elements) from the circumference of the tube. The amplitude of the RC is not affected by varying the axial extent, as shown in Fig. 3 (it is about 1% for a 1 mm axial extent). Note that at higher frequencies, all the curves become straight lines, proving that torsional mode T(0,1) is non-dispersive at high frequencies.
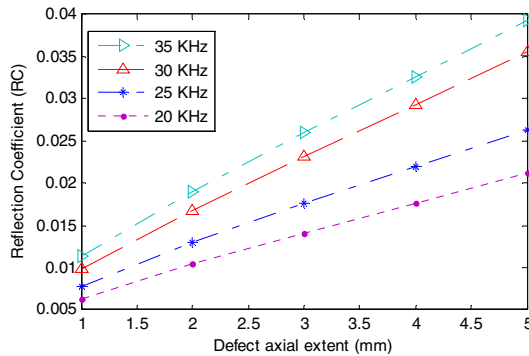
Fig. 3 Variation of RC by varying the axial extent defect for different excitation frequencies

- *Reflection coefficient by varying the flaw circumferential extents*

Fig. 4 shows the RC-curves for various defect's circumferential extent (9%, 14%, 23% and 27%) of the tube's circumference in the 1–35 kHz range. These curves show that the wave reflection is greater when the defect's circumferential

extent increases. Mainly, this illustration proves the dependency of RC with the frequency. To reveal the details of the solution at low and medium frequencies, the RC as a function of defect's circumferential extent for different excitation frequencies are plotted in Fig. 5 whereas defect's axial extent is fixed at 1 mm. Else from Fig. 5, it is seen that the RC from flaw become less important as it loses its straight character.
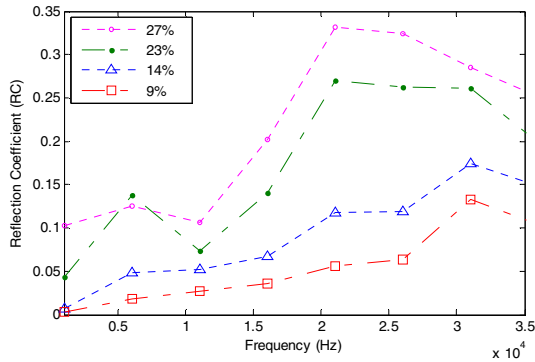
Fig. 4 Reflection Coefficient of varying defect's circumferential extent whereas fixed defect's axial extent (with a = 1mm)

The analysis of straightforward shaped defect using WFEM showed a linear dependency between the amplitude the RC and the ratio of circumferential extent, at a fixed depth of the defect (Fig.5).
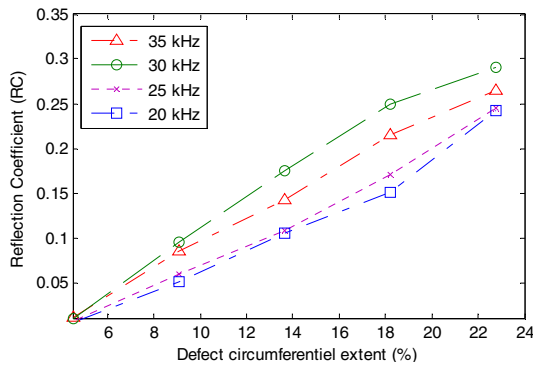
Fig. 5 Reflection coefficient by varying defect's circumferential extent for different excitation frequencies

- *Reflection maps for axisymmetric flaw*

The results presented below are 3 dimensions (3D) maps for axisymmetric flaws in the reference pipe. Figure 6 represents the 3D variation in of the RC for T(0,1) at different frequencies respectively 20 kHz, 25 kHz, 30 kHz and 35 kHz

incident on an axisymmetric rectangular flaw of varying axial and circumferential extent. These figures show that the reflection increases with the circumferential extent for a constant axial extent and increases slightly with axial length as circumferential constant.

3.2 Reflection Coefficient by Varying the Flaws' Position

In this section, different flaws are created in the coupling structure. Hence, the impact of the position of flaws to the WFE method is investigated. Different positions and defects are considered as shown in Fig.7 (more details about the flaws positions and severities in appendices 1&2). The sensitivity of RC to severity of defect is clear as the flaws' position: more than the defects are close to each other more their reflection will be (Fig.7 (i)). Fig.7 (j) shows that the RC rises clearly if the number of defect is important (3 defects). Hence, it is evident that variation in the position of the flaws in the circumferential direction has little effect on the amplitude of the RC.
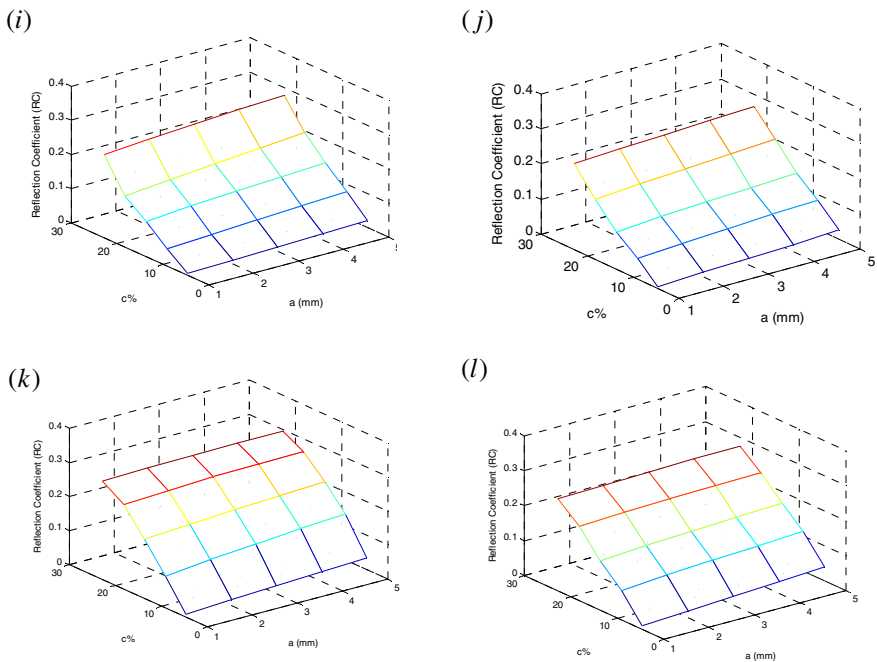
Fig. 6 Variation of RC with the circumferential extent and the axial extent of the defect for frequencies (*i*) 20 kHz, (*j*) 25 kHz, (*k*) 30 kHz and (*l*) 35 kHz
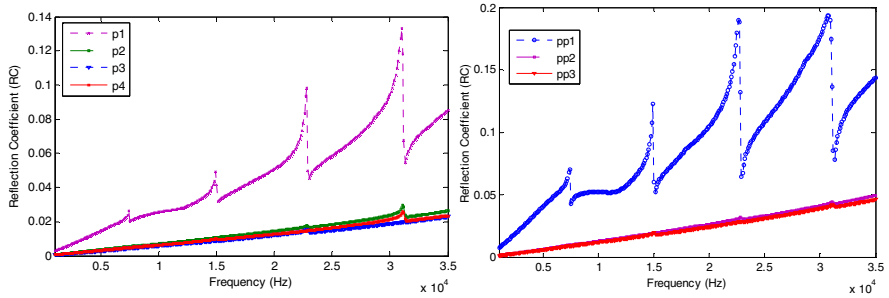
Fig. 7 Variation of Reflection Coefficient with flaws' positions (*i*) 2 elements (*j*) 3 elements (Appendices 1 and 2)

4   Conclusion

The investigation reported in this paper focused on scattering of guide waves by rectangular flaws in pipes. The emphasis of the investigation was on the evaluation of torsional modes excitation and propagation characteristics in pipes using WFE method based on the wave propagation characteristics. The main results can be summarized as follows:

1. The constructive interference phenomenon, which leads to a maximum of the reflection, was proven to appear in rectangular notch shapes.

2. These results clearly show that T(0,1) provides a convenient and effective way to characterize a straightforward defect in pipes for their defect's sensitivities. Both defect's circumferential and axial extent are studied.

3. Sensitivity of Wave finite element method (WFEM) to flaws' positions.

This work could be extended taking into account the impact of environmental factor change such as temperature.

References

Alleyne, D.N., Cawley, P.: The Excitation of Lamb Waves in Pipes Using Dry-Coupled Piezoelectric Transducers. J. NDT&E 15(1) (1996)

Alleyne, D., Lowe, M., Cawley, P.: The reflection of guided waves from circumferential notches in pipes. J. Appl Mech. 65, 635–641 (1998), PIf so041 624X(97)00038-3

Lovstard, A., Cawley, P.: The reflexion of fundamental torsional guided wave from multiple circular holes in pipes. J. NDT&E International 44, 553–562 (2011), doi:10.1016/j.ndteint.2011.05.010

Bai, H., Shah, A.H., Popplewell, N., Datta, S.K.: Scattering of Guided Waves by Circumferential Cracks in Steel Pipes. J. Appl. Mech. 68, 619–631 (2001), doi:10.1115/1.1364493

Bareille, O., Kharrat, M., Zhou, W., Ichchou, M.N.: Distributed piezoelectric guided-T-wave generator, design and analysis. Mechatronics 22, 544–551 (2012), doi:10.1016/j.mechatronics.2011.11.005

Bouchoucha, F., Akrout, M., Fakhfakh, T., Ichchou, M.N., Haddar, M.: Damage Detection in Cylindrical Pipe through Diffusion Matrix in Wave Finite Element Method. Advances in Structural Engineering 15(3) (2012)

Craig, R., Bampton, M.: Coupling of substructures for dynamic analysis. AIAA Journal 12, 1313–1319 (1968)

Demma, A., Cawley, P., Lowe, M., Roosenbran, A.G., Pavlakovic, B.: The reflection of guided waves from notches in pipes: a guide for interpreting corrosion measurements. NDT&E International 37, 167–180 (2004), doi:10.1016/j.ndteint.2003.09.004

Duhamel, D., Mace, B.R., Brennan, M.J.: Finite element analysis of the vibrations of waveguides and periodic structures. Journal of Sound and Vibration 294, 205–220 (2006), doi:10.1016/j.jsv.2005.11.014

Ichchou, M.N., Mencik, J.-M., Zhou, W.: Wave finite elements for low and mid-frequency description of coupled structures with damage. Comput. Methods Appl. Mech. Engrg. 198, 1311–1326 (2009)

Joseph Zemanek, J.R.: An Experimental and Theoretical Investigation of Elastic Wave Propagation in a Cylinder. The Journal of the Acoustical society of America 51(1, Pt. 2), 265–283 (1972)

Li, J., Rose, J.L.: Angular-profile tuning of guided waves in hollow cylinders using a circumferential phased array. IEEE Transactions on Ultrasonics, Ferroelectrics, and Frequency Control 49(12), 1720–1729 (2002)

Liu, Z., He, C., Wu, B., Wang, X., Yangwe, S.: Circumferential and longitudinal defect detection using T(0, 1) mode excited by thickness shear mode piezoelectric elements. Ultrasonics 44, 1135–1138 (2006), doi:10.1016/j.ultras.2006.05.154

Mead, D.J.: A general theory of harmonic wave propagation in linear periodic systems with multiple coupling. Journal of Sound and Vibration 27, 235–260 (1973)

Mead, D.J.: Wave propagation and natural modes in periodic systems: multi-coupled systems, with and without damping. J. Sound Vibration 40(1), 19–39 (1975)

Mencik, J.-M., Ichchou, M.N.: Multi-mode propagation and diffusion in structures through finite elements. European Journal of Mechanics A/Solids 24, 877–898 (2005), doi:10.1016/j.euromechsol.2005.05.004

Sun, Z., Rose, J.L., Song, W.-J., Hayashi, T.: Non-axisymmetric wave focusing in pipe inspection. Review of progress in quantitative NDT&E. American Institute of Physics (2003)

Sun, Z., Zhang, L., Rose, J.L.: Flexural torsional guided wave mechanics and focusing in pipe. Journal of Pressure Vessel Technology 127, 471–478 (2005)

Liu, Z., He, C., Wu, B., Wang, X., Yang, S.: Circumferential and longitudinal defect detection using T(0, 1) mode excited by thickness shear mode piezoelectric elements. Ultrasonics 44, e1135–e1138 (2006)

Zhou, W.J., Ichchou, M.N., Mencik, J.M.: Analysis of wave propagation in cylindrical pipes with local inhomogeneities. Journal of Sound and Vibration (2008), doi:10.1016/j.jsv.2008.05.039

Notation

$\boldsymbol{u}$	displacement vector
$\boldsymbol{q}_i$	nodal displacement vector

$(\begin{bmatrix} {}^-q \end{bmatrix}, \begin{bmatrix} {}^+q \end{bmatrix})$ denote the displacement vectors relating to the positive and negative going waves respectively

$\boldsymbol{F}_i$	nodal force vector

$(\begin{bmatrix} {}^-F \end{bmatrix}, \begin{bmatrix} {}^+F \end{bmatrix})$ denote the forces vectors relating to the positive and negative going waves respectively

f	frequency
D	pipe diameter (mm)
t	thickness' pipe (mm)
a	defect's axial extent (mm)
c%	defect's circumferential extent (non-dimensioned parameter such

c% such that $c\% = \dfrac{c}{2\pi D} \times 100$ with 2 **D is the pipe circumference (equals**

the elements' number in the circumference) and c is the defect's circumferential extent

b	defect's depth (it was considered constant in this study)

$\{\begin{bmatrix} M^c \end{bmatrix}, \begin{bmatrix} K^c \end{bmatrix}\}$ denote the mass and stiffness matrices of the coupling structure, respectively

$\bullet^{inc}, \bullet^{ref}, \bullet^{tr}$ denote respectively the incident, reflected and transmitted wave amplitude

λ denotes the propagation constant where $\lambda = e^{-jk\theta}$ (where $j^2 = -1$)

Appendices

Appendix 1

(p_1) (p_2) (p_3) (p_4)

Appendix 2

(pp1) (pp2) (pp3)
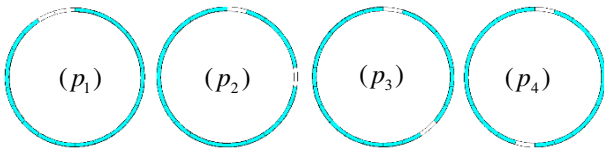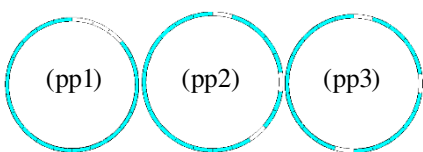
Structural Integrity of Laminated Composite with Embedded Piezoelectric Sensors

Sahir Masmoudi[1], Abderrahim El Mahi[1], Saïd Turki[2], and Rachid El Guerjouma[1]

[1] LUNAM University: Maine University, Acoustic Laboratory of Maine University
 (LAUM) CNRS UMR 6613, Avenue Olivier Messiaen, 72085 Le Mans CEDEX 9, France
 `{Sahir.Masmoudi.Etu,abderrahim.elmahi,`
 `Rachid.el_Guerjouma}@univ-lemans.fr`
[2] Sfax University, Sciences Faculty of Sfax, Physics Department BP1171,
 3000 Sfax, Tunisia
 `Said.Turki@fss.rnu.tn`

Abstract. Recent progress in sensor technologies, signal processing and electronics made it possible to fulfil the need for the development of in-service structural health monitoring (SHM) systems. An experimental study of local damage materials using acoustic emission (AE) has been conducted to characterize the mechanic behavior of E-glass/epoxy unidirectional composites instrumented by piezoelectric implant. A series of specimens of composite laminates with and without embedded piezoelectric were tested in static loading while constantly monitoring the response by AE technique. The acoustic signals were analyzed by the classification multi-parameters method available on NOESIS (k-means) in order to identify the different damage and to follow the evolution of these various mechanisms for both types of materials (simple and instrumented). The results show that integration of the sensors presents advantages of the detection of the acoustic events and also show the presence of three types of damage during tests. Comparing embedded sensor to sensor mounted on the surface, the embedded sensor showed a much higher sensitivity.

Keywords: Laminated Composite, Piezoelectric Implant, Tensile, Three Points Bending, Acoustic Emission, k-means.

1   Introduction

The increasing demands to improve the performance of aerospace and other engineering systems require a new class of materials/structures, such as smart, intelligent or adaptive materials/structures. These can be defined as the system that has built-in capability or with intrinsic sensors that perceive and process the operating environments, and take effective action to fulfill the intended mission. The future of smart structure/materials technology is very promising (Mall 2002).

It has been considerable interest in the use of piezoelectric materials in conjunction with the light-weight and high-strength/modulus polymeric laminated composites as one type of smart materials/structures. One class of piezoelectric materials is the lead zirconate-titanate (PZT) based ceramics. Its use in smart structures/materials has received a great deal of attention in the areas of vibration suppression/control, actuation and health/load monitoring (Mall 2002, Paget et al. 2002, Monnier et al. 2000). The aim of the present study is to follow experimentally the temporary evolution of damage in unidirectional composite materials, implanted by piezoelectric sensors using acoustic emission (AE).

1.1   Integrated Non Destructive Testing

The integrated systems of measurement result generally from the Non Destructive Testing (NDT) traditional: for example, dynamic methods of propagation of ultrasonic waves (echography or transmission) or acoustic listening (Bois 2003). These techniques generally use piezoelectric accelerometers or transducers coupled on the faces of materials with silicon grease, which poses problems: the wave can be attenuated before reaching the material surface. For this reason, the piezoelectric sensor must be attached to material with a minimum of loss of the interface sensor-material. In order to cure the problems caused by the fact of placing the sensor on surface, researches are directed with the follow-up in-situ and in real time of the health of materials, by integrating the sensors within the tested material. To adapt the methods of traditional NDT to in-situ measurement, it is necessary to reduce the size of the sensors. At this end, we have used piezoelectric sensors having a disc form with diameters and thickness of 5-10 mm and 0.5-1 mm respectively.

1.2   Acoustic Emission

Acoustic Emission (AE) represents the generation of transient ultrasonic waves in a material. When the material is deformed and fissured spontaneously under the external stress action (mechanical, thermal, chemical, etc), an elastic wave is created. AE is a useful tool for non-destructive testing. According to standard ASTM, the acoustic emission is a phenomenon of creation of transitory elastic waves resulting from micro internal displacements in the material (El Guerjouma et al. 2001, Berbaoui et al. 2009). The waves created at different nature and various frequencies, are propagated in material and undergo possible modifications before reaching studied surface. The vibrations of surface, collected by a piezoelectric sensor, are amplified and treated to provide the signal of sound emission (Fig. 1).
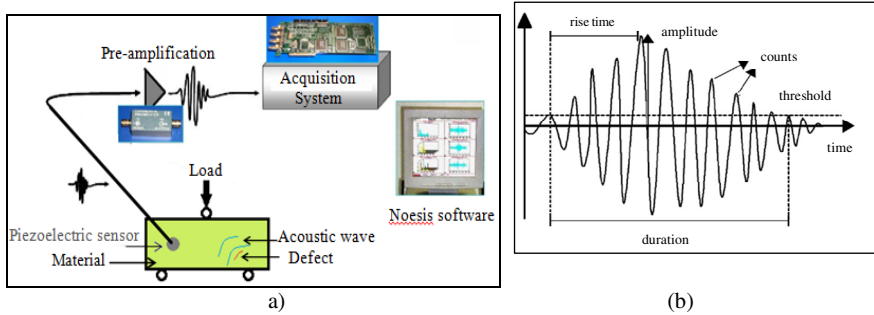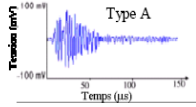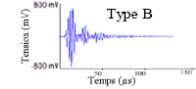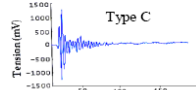
Fig. 1 a) Experimental setup of acoustic emission technique, b) Typical waveform and parameters calculated by the acquisition system for each acoustic emission event

1.3 Multi-parametric Analysis

The multi-parametric analysis of the characteristics extracted signals of AE is more used to separate and identify the various damage mechanisms. Many works (Nechad 2004, Marec 2008), undertaken on model of unidirectional composite material, made it possible to identify three types of signals A, B, and C which correspond respectively to the matrix cracking, debondings in the fiber-matrix interface and fibers breakage. Their principal characteristics are gathered in table 1.

Table 1 Characteristics of acoustic emission signals: A, B and C

Damage mechanism	Amplitude	Rise time	Duration of the signal	Decrease of the signal	Type of the signal	Form of the signal
Type A (matrix cracking)	~50-70	Means	Means	Slow	Resonant	
Type B (debonding in fiber-matrix interface)	~55-80	Short	Means	Short	Impulse	
Type C (fibers breakage)	~70-100	Short	Short	Short	Impulse	

2 Materials

The materials used in this work are unidirectional GFRP composed of long glass fibers (density 300 g/m^2) arranged in (0°) and resins epoxy of type SR1500/

SD2505. Composite panels were constructed using mixed preg/hand lay-up using vacuum bagging technique. The composite panels are elaborated with following proportion: fiber 50%, epoxy resin 50%. The various layers are laminated and impregnated at ambient temperature. The piezoelectric sensor was embedded during the manufacturing stage. It was placed within the plies on the neutral plane of the composite specimen. The specimens have been cut up with a diamond disk, from plates of 300x300 mm^2. Table 2 gives the geometrical characteristics of the test- specimens studied as well as the conditions of tests.

Table 2 Characteristics of laminate specimens and conditions of tests

Test	Tensile	Three points bending
Types of materials	$[0°]_{12}$	$[0°]_{24}$
Dimensions of specimens	250 x 30 x 3 mm^3	150 x 30 x 6 mm^3
Test conditions	length of the part enters the hydraulic bits of 150 Misters	distance between supports of 120 mm

3   Experimental Set-Up

The composite specimens are subjected to various mechanical tests at ambient temperature in tensile and three points bending in static.

(a)   (b)
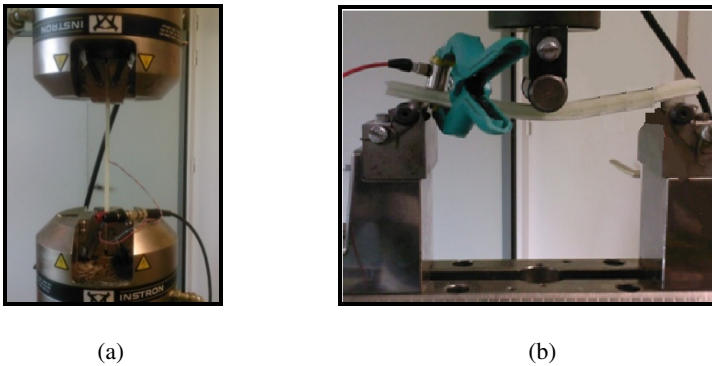
Fig. 2 Experimental set-up: a) tensile test (embedded sensor), b) three points bending test (sensor coupled to the surface of the specimen)

Experimental tests were carried out on a standard hydraulic machine INSTRON 8516 of ±100 kN capacity. The displacement can be measured using a linear displacement transducer (LVDT). Experimental set-up is shown in figure 2.Three specimens are tested for each material type in order to check the repeatability of the results.

3.1   Acquisition of AE Signals

The acquisition of the acoustic emission signals is carried out using software AE Win (Euro Physical Acoustics). This system is gauged before each test using a procedure to generate sources of propagation of elastic waves simulating the AE. The signals of AE are detected by piezoelectric sensors, and then amplified using the preamplifier of 40 dB of profit located between the sensors and the numerical chart of acquisition.

4   Experimental Results

4.1   Tensile Static Tests

Static tensile tests were performed under displacement control, in which laminates were loaded until failure, at a constant rate of 1 mm/min. Figure 3 gives the load-displacement curves for three types of laminate specimens : S2 (without sensor), SCP (integrated with small sensor) and SCG (integrated with large sensor).
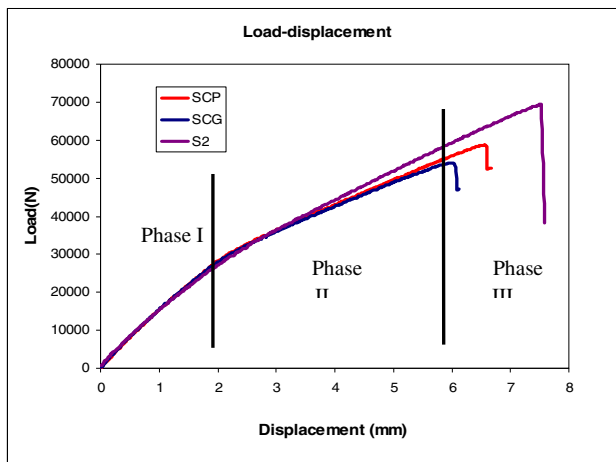
Fig. 3 Static tests: Load-displacement curves measured in tensile tests

As it can be shown, the mechanical behavior of materials can be divided on three phases:

- A first phase corresponding to the elastic part of material.
- A second phase characterized by the initiation of damage and development of microscopic cracks within material.
- A third phase corresponding to the propagation of cracks leading to the specimens rupture.

4.2   Three Points Bending Static Tests

Static tests were performed in three points bending under displacement control, in which laminate specimens were loaded until failure, at a constant rate of 2 mm/min.

The load variation vs displacement of the simple and instrumented laminate, with different sensors is presented on figure 4. As can be shown, the mechanical behavior is linear until the fragile rupture of material. In addition, the integration of sensor within materials influences especially the fracture stress and the corresponding displacement, which decrease when increasing dimensions of sensors. We have also observed that the influence of thickness of sensors is more significant than that of the diameter.
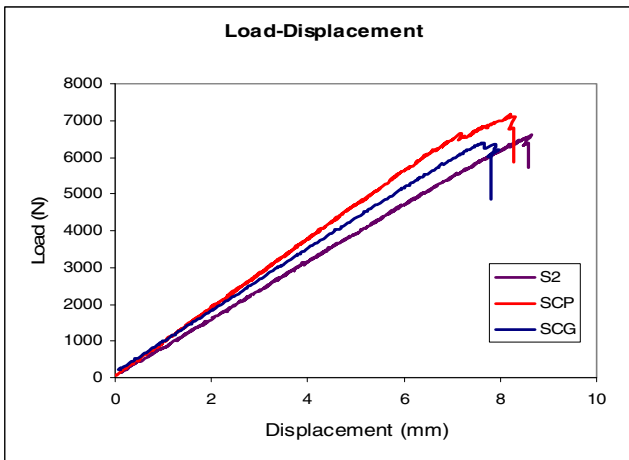
Fig. 4 Static tests: Load-displacement curves measured in three points bending tests

4.3   Identification of the Acoustic Signature for Damage

The acoustic signals collected during tests were analyzed by the *k*-means classification method available on NOESIS. This analysis is achieved in order to identify the acoustic signals emitted by different damage, and to follow the evolution of these various mechanisms in two materials (simple and instrumented) during tests.

Figure 5 shows the results of the classification of AE signals for two laminate specimens (S2) and (SCP) tested in tensile loading. We have observed only the presence of three types of damage: matrix cracking (signal A), fiber-matrix debonding (signal B) and fibers breaking (signal C).

However, the chronology of appearance of the different damage mechanisms is shown in figure 6. The results show that the instrumented composite (SCP) presents the initiation and the evolution of matrix cracking and fiber-matrix interface in parallel (Fig 6-b). These damages are propagated then along fibers. The fibers breaking appear at the end of the test, and cause the failure of the materials.

(a):S2   (b):SCG
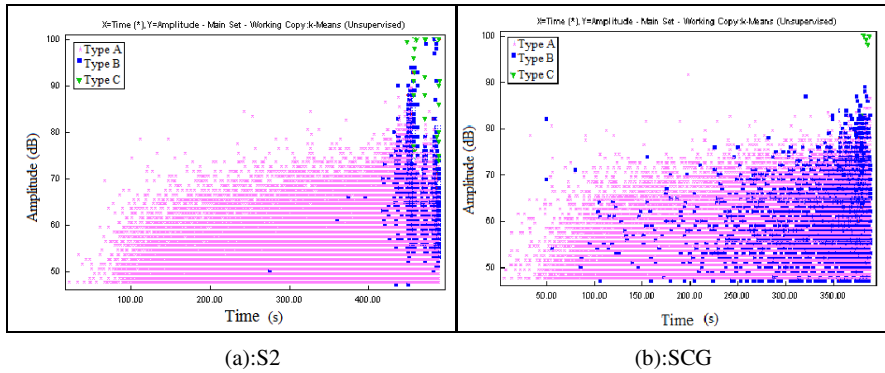
Fig. 5 Amplitude-time of: a) simple laminate: (S2), b) instrumented laminate: (SCG)

(a):S2   (b):SCG
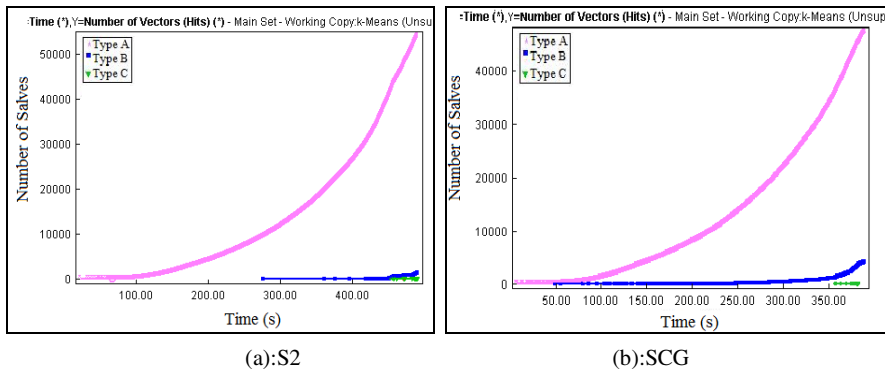
Fig. 6 Chronology of appearance of the different damage mechanisms of: a) simple laminate: (S2), b) instrumented laminate: (SCG)

5   Conclusion

The integrity of the E-glass/epoxy laminate as well as of the embedded active PZT sensor and others coupled to the surface of the specimen under monotonic loads were investigated experimentally. Acoustic emission (AE) is used in order to study the effect of the insert of piezoelectric sensors in the material on the mechanical behavior. The results obtained in this analysis can be summarized as follow:

- The mechanical behavior of simple and integrated materials shows no difference in the form but the integration of sensor influences the fracture stress of cracking and degrades the mechanical properties of material especially.
- The integration of sensors supports the detection of initiation, the propagation and the accumulation of the microscopic defects.
- The comparison of AE signals of both type of materials, shows that the shape of the signals remains identical for the similar phenomena.

References

Mall, S.: Integrity of graphite/epoxy laminate embedded with piezoelectric sen-sor/actuator under monotonic and fatigue loads, Wright-Patterson, USA Smart Materials and Structures, 527–533 (2002)

Paget, C., Levin, K., Delebarre, C.: Actuation performance of embedded piezoce-ramic transducer in mechanically loaded composites. Smart Mater. Struct. 11, 886–891 (2002), doi:s0964-1726(02)39935-X

Monnier, T., Jayet, Y., Guy, P., Baboux, J.C.: The piezoelectric implant method: implementation and practical applications," GEMPPM, UMR CNRS 5510, INSA, 69621 Villeurbanne Cedex, France, pp. 267–272 (2000)

Bois, C.: Mesure et prévision de l'évolution des endommagements dans les composites stratifiés", thèse Université de la Méditerranée Aix-Marseilles II (2003)

El Guerjouma, R., Baboux, J.C., Ducret, D., et al.: Non destructive evaluation of dam-age and failure of fiber reinforced polymer composites using ultrasonic waves and acoustic emission. Adv. Eng. Mat. 3, 601–608 (2001), doi:10.1002/1527-2648(200108)3:8

Berbaoui, R., Marec, A., Tomas, J.H., El Mahi, A., El Guerjouma, R.: Investigation of damage mechanisms of polymer concrete: Multivariable analysis extracted from acoustic emission signals. In: NDTCE Conference, Nantes, June 30-July 3 (2009)

Nechad, H.: Evaluation de l'endommagement et de la rupture de matériaux hétérogènes par ultrasons et émission acoustique: estimation de la durée de vie restante. PhD Thesis, INSA Lyon, Lyon, France (2004) (in French)

Marec, A.: Contrôle de santé des matériaux hétérogènes par émission acoustique et acoustique non linéaire Discrimination des mécanismes d'endommagement et estimation de la durée de vie restante, thèse de doctorat, Université du Maine (2008)

Part V

Fluid Structure Interaction

Numerical Simulation of Wave-Structure Interaction around an Obstacle

Sonia Ben Hamza[1], Sabra Habli[2], Nejla Mahjoub Saïd[2],
Hervé Bournot[3], and Georges Le Palec[3]

[1] LGM, National Engineering School of Monastir, University of Monastir, Tunisia
  soniabenhamza@yahoo.fr
[2] LGM, Preparatory Institute for Engineering Studies, University of Monastir, Tunisia
  sabra.habli@fsm.rnu.tn, nejla.mahjoub@fsm.rnu.tn
[3] IUSTI, UMR 7343, Faculty of Sciences, University of Aix-Marseille, France
  georges.lepalec@univ-amu.fr

Abstract. In this work, we study a turbulent two-phase free surface flow around an obstacle in unsteady regime. A dynamic study relating to the formation of coherent vortex structures enables us to determine the shape of the flow and to clarify its main characteristics (shear layer, recirculation and reattachment). We determine first the dynamic structure of the flow through a numerical approach using the computer code ANSYS Fluent (closure model is k-ε). In the second part we study the impact of these vortices on such configurations. A series of numerical simulations have been conducted to further verify the applicability of this model for wave simulations interaction with vortex structures of various shapes.

Keywords: Turbulence, obstacle, free surface, wave-structure interaction, VOF.

1 Introduction

The wave-structure interaction (WSI) is one of the most important coastal and ocean engineering applications of free surface flow hydrodynamics. The physical understandings and robust numerical computations of the wave-structure interactions are crucial to assess the wave impact on structures as well as the structural responses to these wave attacks. In many numerical models, the wave-structure interaction problems can be solved by employing either a simultaneous solution or a partitioned solution, and the solid structures are often discretized into a Lagrangian form (Lin 2007, Liu et al. 2013, Maruzewski et al. 2009, Shao 2009). Although it is anticipated that the vortices generated around the submerged obstacle have only minor effects on the wave energy transmission (without wave breaking) and stability of the submerged obstacle, this localized rotational and dissipative vortices have a definite impact on the mixing process, sediment transport and scouring process.

The 3D computation of wave-structure interaction based on Navier-Stokes equation (NSE) can be very expensive, considering the fact that the model needs

to resolve the free surface, the bottom topography, and the surface of a body. As a matter of fact, the simpler problem of 3D wave propagation over an uneven bottom sometimes is challenging enough to a modeler if the domain size is too large. This was the reason that in the earlier age of wave simulation, the 3D model was developed in which the hydrostatic pressure is assumed and the total water depth is mapped into a σ-coordinate. For example, Casulli and Cheng 1992 presented a three-dimensional model. The model was used to simulate the flooding and drying of tidal waves. Such an approach has been adopted in many other ocean circulation models. It is realized, however, that all the above approaches are only applicable for relatively long waves or ocean currents for which the assumption of hydrostatic pressure is valid.

Interactions between water waves and submerged marine structures are important in the solution of many coastal engineering problems. With rapid advances in computing technology, more researchers and engineers are using numerical simulations to better understand the fluid-structure interactions. However, it is difficult to study numerically complex free-surface evolutions and irregular boundaries. The challenge is even higher if the structure is in motion (Shen and chan 2008).

Lin and Li 2002 made use of a σ-coordinate transformation to map a irregular physical domain to a computational domain of rectangular shape. Lin 2006 developed a three-dimensional (3D) multiple-layer σ-coordinate model to simulate surface wave interaction with various types of structures, including submerged, immersed, and floating structures. In general, such methodologies are capable of producing accurate predictions of free-surface displacements. A limitation, however, is the modeling of free surface of arbitrary configuration, such as in the case of wave breaking. Compared to the application of the coordinate transformation technique, it is still more convenient to carry out numerical simulations of wave-structure interactions in a cartesian coordinate system. Due to the complexity in modeling a general irregular solid boundary, many studies were limited to simpler cases such as wave flows over a submerged rectangular obstacle (Chang et al. 2001, Huang et al. 2001, Tang et al. 1998).

Hur and Mizutani 2003 used a VOF-based model to simulate the interaction of waves and a permeable submerged breakwater and to estimate the wave force acting on it. Hus et al. 2002 included the volume averaged equations for porous flows derived by Van Gent 1995 into the VOF-based model proposed by Lin and Liu 1998, to study wave motions and turbulence flows in front of a composite breakwater. Comparisons of the numerical results and laboratory data showed a good agreement. Shen et al. 2004 used a VOF version of the SOLA-VOF code with a two-equation k-ε model to simulate the propagation of non-breaking waves over a submerged bar. Their simulated results showed a reasonable agreement with experimental data by Ohyama et al. 1995.

Other numerical studies based on the VOF-based two-phase flow model for the simulation of water wave motions have been reported. Hieu and Tanimoto 2002 developed a VOF-based two-phase flow model to study wave transmission over a submerged obstacle. Karim et al. 2003 developed a VOF-based two-phase flow

model for wave-interactions with porous structures and studied the hydraulic performance of a rectangle porous structure against non-breaking waves. Their numerical results surely showed good agreements with experimental data. Hieu et al. 2004 simulated breaking waves in a surf zone using a VOF-based two-phase flow model. Their numerical results were compared with experimental data provided by Ting and Kirby 1994 for the spilling breaker on a sloping bottom. Their results agreed well with the experimental data. However, the wave motion in porous media and the non-reflective wave source method were not included in the model by Hieu et al. 2004.

The objective of the present study is to develop a volume of fluid (VOF) based two-phase flow model and to discuss the applicability of this model to the simulation of wave-structure interactions. The numerical VOF based two-phase flow model has been developed and applied to the simulations of wave interactions with a submerged obstacle. Numerical results are then exploited to verify the applicability of the numerical model to the simulations of complex interactions of waves and permeable vortex structures, including the effects of wave breaking. It is concluded that the two-phase flow model with the aid of the advanced VOF technique can provide with acceptably numerical results.

2   Mathematical Formulation

2.1   Assumptions

We considered a two-phase free surface flows in the turbulent regime, the surface tension effect are also taken into account. The considered two fluids are air and water, which have been assumed Newtonian and immiscible.
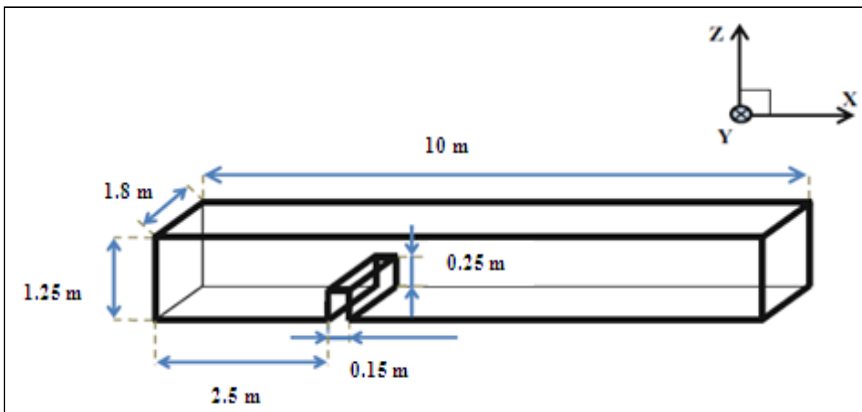
Fig. 1 Computational domain geometry

We select a portion of an urban sewerage network of Monastir in order to show the real condition of a water flow interaction. The domain was a rectangular 10 m long channel with a width of 1.8 m and maximum depth of 1.25 m. The water level was 0.35 m (Fig. 1). The rectangular obstacle has been placed at distance $x_{obst} = 2.5$ m from the channel inlet with a height of 0.25 m and a thickness of 0.15 m.

2.2 Governing Equations

The Reynolds-averaged Navier-Stokes equations are computationally solved, for an unsteady and incompressible turbulent fluid. The mass (1) and the momentum (2) conservation equations are presented in the Cartesian coordinates system as follow:

$$\frac{\partial U_i}{\partial x_i} = 0 \tag{1}$$

$$\frac{\partial U_i}{\partial t} + \frac{\partial}{\partial x_k}(U_k U_i) = -\frac{1}{\rho}\frac{\partial P}{\partial x_i} + \frac{\partial}{\partial x_k}\left[\nu\left(\frac{\partial U_i}{\partial x_k} + \frac{\partial U_k}{\partial x_i}\right) - \overline{u_i' u_k'}\right] + g_i \tag{2}$$

Where $\overline{u_i' u_k'}$ is the Reynolds stresses and i, k = 1, 2, 3 refer to x, y and z respectively. U_i is the mean velocity and x_i is the coordinate in the i direction.

The turbulence model that was used for the calculations is the k-ε model. It is considered one of the most efficient model, and this because it is essentially a model that assumes the existence of non-isotropic turbulence.

The multiphase model used in this work is the Volume Of Fluid model (VOF). It allows locating the interface between two different media fields. It is applicable to immiscible fluids (water, air) when there is no interpenetration between them.

2.3 Boundary Conditions

A water velocity of 5m/s and a superficial air velocity of 1m/s were chosen for the CFD calculations. The model inlet was divided into two parts: in the lower 50% of the inlet cross section, water was injected and in the upper 50% air (Fig. 2).

Both phases have been treated as isothermal and incompressible at 25°C and at a reference pressure of 1 bar. A hydrostatic pressure was assumed for the liquid phase.

At the inlet, the turbulence properties were equivalent to a turbulence intensity of 5% (Chang et al. 2001) in both phases. The inner surface of the channel walls has been defined as hydraulically smooth with a non-slip boundary condition applied to both gaseous and liquid phases. The channel outlet was modeled with a pressure outlet boundary condition.
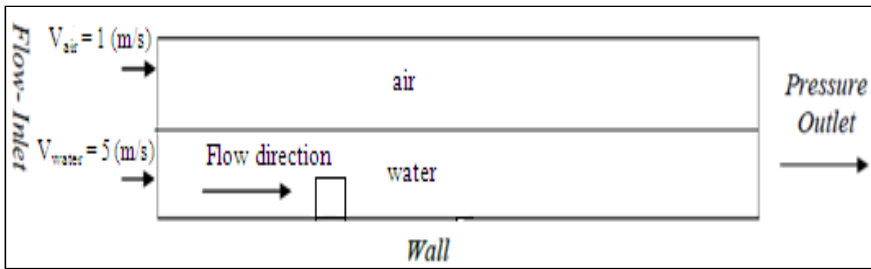
Fig. 2 Domain geometry with boundary conditions

3 Numerical Method

Numerical computations were carried out using ANSYS Fluent which is based on the finite volume approach.

The discretized equations, along with the initial and boundary conditions, were solved using the segregated solution method. Using the segregated solver, the governing equations were solved sequentially.

In order to improve accuracy, the second order upwind scheme was used. The SIMPLE method was used to calculate the pressure–velocity coupling. It uses a relationship between velocity and pressure corrections to enforce mass conservation and obtain the pressure field. The maximum residual of all variables was 10^{-3} in the converged solution.

The mesh was periodically refined and the computation was repeated until the variation in results was adequate. It was found, that the optimal number of grid points is approximately 150 000.

4 Results and Discussion

4.1 Dynamic Study of the Flow Structure around an Obstacle

To see how the wave height varies as a solitary wave passes over an obstacle, Figure 3 shows the maximum value of the water elevation at different times in the channel. In this figure, the rectangle indicates the location of the obstacle. The rise of the wave height near the leading edge of the obstacle can be explained as due to the shallow effect. Consequently, the wave height decreases slightly as part of the wave is positively reflected due to the energy dissipation caused by the wave and structure interaction and reaches a minimum value at the trailing edge. Afterwards, the wave height increases a little, as the negatively reflected wave is generated. The positively and negatively reflected waves can be seen in this figure with a longer distance between them. This result is proved by Huang et al. 2003.

Fig. 3 also shows that as the waves propagate over the obstacle, higher harmonics are generated due to the nonlinear effect. Hence, they are gradually detached from the main crest, as it can be seen. As the waves propagate into the deep water region, the wave non-linearity becomes so weak that the bound waves are
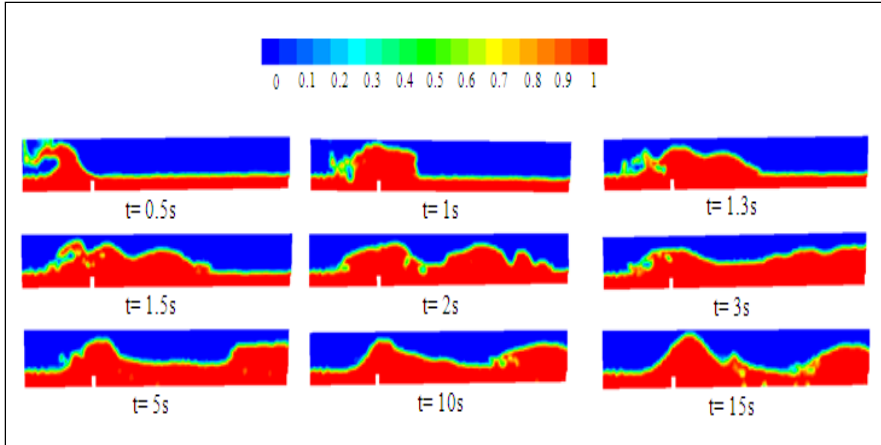
Fig. 3 Water volume fraction contours in presence of a rectangular obstacle at different times in the channel
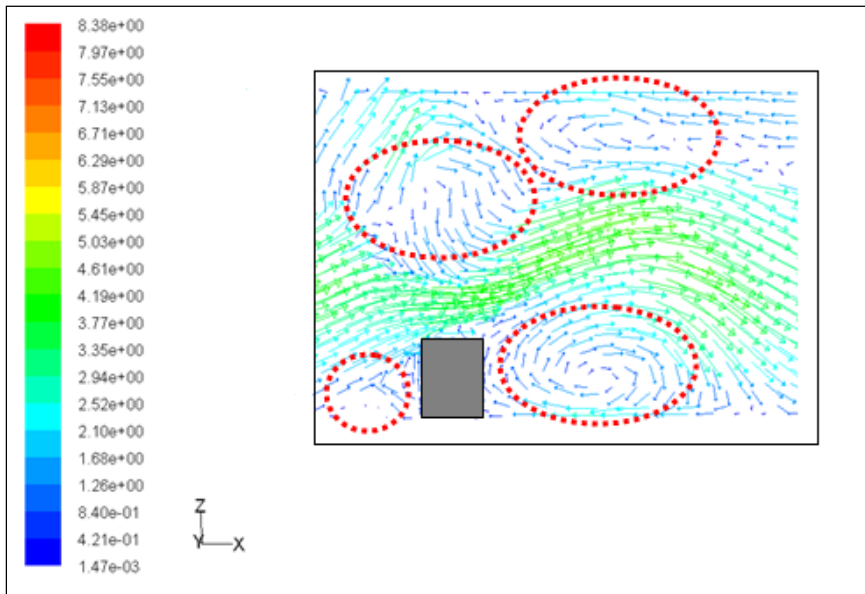
Fig. 4 Velocity vectors at t = 15s

substantially reduced and a large amount of energy is transformed from the bound waves into the free waves (Huang and Dong 2001).

By analyzing the flow through the Fig. 4, we can identify four vortex structure, the first one is upstream the obstacle characterized by low intensity, a second one is just above the obstacle with a small size but without reattachment as it was

confirmed by Bouteraa et al. 2002. The mixing layer formed downstream of the obstacle, shows the existence of two counter-rotating vortices type Kelvin-Helmotz, one small size trapped between the wall and the ground and other of larger size.

In the same figure which shows the velocity vectors, we observe that the detachment of the shear layer causing the appearance of a vortex. It is interesting to note the tendency to the organization into elongated structures. The wake structure downstream of the obstacle reveals a driveway swirling consisting of counter-rotating structures, in accordance with existing experimental and numerical results of Bouterra et al. 2002. These lines circumvent the obstacle and espouse its geometry by restricting three characteristic zones of the flow: stagnation, separation and recirculation.

The stagnation zone upstream of the obstacle is low intensity. The separation zone above the obstacle with a small thickness is dominated by strong shear present without gluing as was observed by Zhang 1991. The mixture layer formed downstream of the obstacle, is characterized by two counter rotating vortex structure. The first, small size is trapped between the wall and soil. The second structure, of elongated shape, and is larger behind the wall. These results confirm the experimental work of Eaton and Johnston 1980.

4.2   Flow Disturbed by the Presence of Two Obstacles

In the case of the presence of two obstacles, Fig. 5 shows the existence of four regimes based on the size of the obstacles and the distance between them. When the
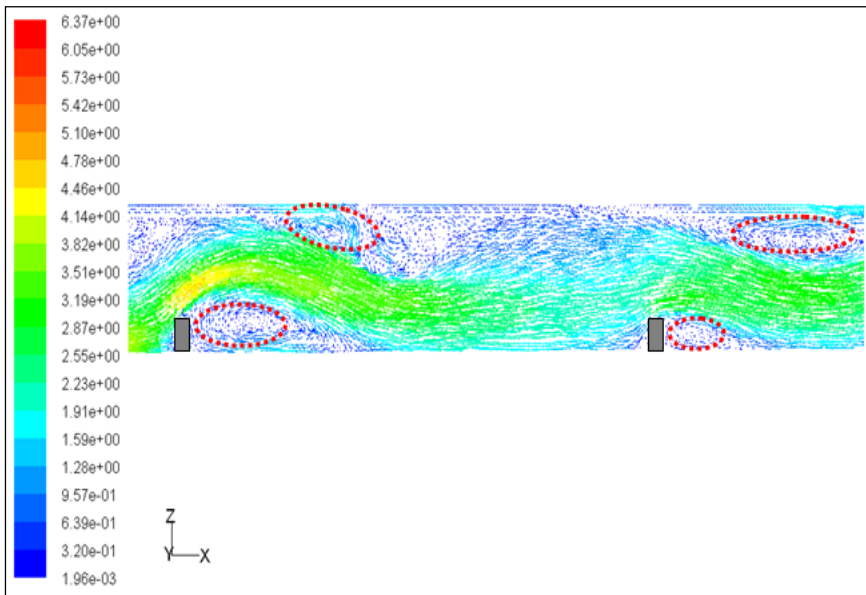
Fig. 5 Structure of the flow behind two obstacles at t= 15s

obstacles are well spaced from each other, the flow is like a succession of identical structures around obstacles isolated and the wakes are disturbed. The flow downstream of an obstacle is reinforced by a deflection at the upstream side of the obstacle adjacent, so the flow will close and a recirculation zone is established at spacing identical to the other. This result is confirmed by Abderrahmane 2012.

5   Conclusion

In this work, we study the dynamic of the flow field around an obstacle. We note that the formation of coherent structures provides information about the pace of the flow and specify its principal features (shear layer, recirculation and reattachment). The aim of this study is to understand the fundamental mechanisms which govern the flow.

Note also from this paper, due to the nonlinear effect, the wave height above the obstacle increases continually which may eventually result in wave breaking. The presence of these instabilities provides a new perspective in the description of turbulent flows.

References

Abderrahmane, N.: Etude des écoulements à surface libre en présence des obstacles dans le fond. PhD Thesis, University of Abou Bekr Belkaid Tlemcen (2012)

Bouterra, M., El Cafsi, A., Laatar, A.H., Belghith, A., Le Quéré, P.: Numerical simulation of a stratified two-dimensional turbulent flow around an obstacle. Int. J. Therm. Sci. 41, 281–293 (2002)

Casulli, V., Cheng, R.T.: Semi-implicit finite difference methods for three-dimensional shallow water flow. Int. J. Numer. Methods Fluids 15, 629–648 (1992)

Chang, K.A., Hsu, T.J.: Vortex generation and evolution in water waves propagating over a submerged rectangular obstacle: Part I. Solitary waves. Coast. Eng. 44, 13–36 (2001)

Eaton, J.K., Johnston, J.P.: Turbulent flow reattachment: an experimental study of the flow and structure behind a backward-facing step. Stanford University Rep. 39 (1980)

Huang, C.J., Dong, C.M.: On the interaction of a solitary wave and a submerged dike. Coastal Engineering 43, 265–286 (2001)

Hieu, P.D., Tanimoto, K.: A two-phase flow model for simulation of wave transformation in shallow water. In: Proceedings of the Fourth International Summer Symposium, Kyoto, JSCE, pp. 179–182 (2002)

Hus, T.J., Sakakiyama, T., Liu, P.L.F.: A numerical model for wave motions and turbulence flows in front of a composite breakwater. Coastal Engineering 46, 25–50 (2002)

Huang, C.-J., Chang, H.-H., Hwung, H.-H.: Structural permeability effects on the interaction of a solitary wave and a submerged breakwater. Coastal Engineering 49, 1–24 (2003)

Hur, D.S., Mizutani, N.: Numerical estimation of the wave forces acting on a three-dimensional body on submerged breakwater. Coastal Engineering 47, 329–345 (2003)

Hieu, P.D., Tanimoto, K., Ca, V.T.: Numerical simulation of breaking waves using a two-phase flow model. Applied Mathematical Modeling 28, 983–1005 (2004)

Karim, M.F., Tanimoto, K., Hieu, P.D.: Simulation of wave transformation in vertical permeable structure. In: Proceedings of the 13th International Offshore and Polar Engineering Conference, Hawaii, USA, pp. 727–733 (2003)

Lin, P., Liu, P.L.-F.: A numerical study of breaking waves in the surf zone. Journal of Fluid Mechanics 359, 239–264 (1998)

Lin, P., Li, C.W.: A σ-coordinate three-dimensional numerical model for surface wave propagation. International Journal for Numerical Methods in Fluids 38, 1045–1068 (2002)

Lin, P.: A multiple-layer σ-coordinate model for simulation of wave-structure interaction. Computers and Fluids 35, 147–167 (2006)

Lin, P.Z.: A fixed-grid model for simulation of a moving body in free surface flows. Comput. Fluids 36, 549–561 (2007)

Liu, X., Xu, H., Shao, S., Lin, P.: An improved incompressible SPH model for simulation of wave–structure interaction. Computers & Fluids 71, 113–123 (2013)

Maruzewski, P., Le Touze, D., Oger, G., Avellan, F.: SPH high-performance computing simulations of rigid solids impacting the free-surface of water. J. Hydraul. Res. 47, 126–134 (2009)

Ohyama, T., Kioka, W., Tada, A.: Applicability of numerical models to nonlinear dispersive waves. Coastal Engineering 24, 297–313 (1995)

Shen, Y.M., Ng, C.O., Zheng, Y.H.: Simulation of wave propagation over a submerged bar using the VOF method with a two-equation k–ε turbulence modeling. Ocean Engineering 31, 87–95 (2004)

Shen, L., Chan, E.-S.: Numerical simulation of fluid–structure interaction using a combined volume of fluid and immersed boundary method. Ocean Engineering 35, 939–952 (2008)

Shao, S.D.: Incompressible SPH simulation of water entry of a free-falling object. Int. J. Numer. Methods Fluids 59, 91–115 (2009)

Ting, F.C.K., Kirby, J.T.: Observation of undertow and turbulence in a laboratory surf zone. Coastal Engineering 24, 51–80 (1994)

Tang, C.J., Chang, J.H.: Flow separation during solitary wave passing over submerged obstacle. Journal of Hydraulic Engineering 124, 742–749 (1998)

Van Gent, M.R.A.: Wave interaction with permeable coastal structures. PhD Thesis, Technical University Delft (1995)

Zhang, C.X.: Simulation numérique d'écoulements turbulents autour d'un obstacle. PhD Thesis, University of Nante (1991)

Computational Study of Velocity Field of a Counterflowing Circular Jet

Amani Amamou[1], Sabra Habli[2], Nejla Mahjoub Saïd[2],
Philippe Bournot[3], and Georges Le Palec[3]

[1] LGM, National Engineering School of Monastir, University of Monastir, Tunisia
  `amani.amamou@yahoo.fr`
[2] LGM, Preparatory Institute for Engineering Studies, University of Monastir, Tunisia
`{sabra.habli,nejla.mahjoub}@fsm.rnu.tn`
[3] IUSTI, UMR 7343, Faculty of Sciences, University of Aix-Marseille, France
`{georges.lepalec,philippe.bournot}@univ-amu.fr`

Abstract. This paper treats the complex and very interesting "round jet in uniform counterflow stream" configuration which is known to enhance mixing and dispersion efficiency owing to flow reversal. The complexity of the problem originates from the interaction occurring between the jet and the counterflow. The interest of this configuration is essentially due to its presence in various applications (disposal of wastewater into seas or rivers, premixing fuel in aircraft engines, combustion, etc...) and in more than a field (industrial, environmental, chemical engineering, etc...). For the matter, a computational study of a turbulent circular jet discharging into a uniform counterflow is conducted in order to investigate the characteristics of the mean velocity field of the jet fluid. The investigation is carried out for three different cases of jet-to-current velocity ratios; low, median and high velocity ratios. The Reynolds Stress Model (RSM) is used in the comparison with available experimental measurements. The decay of the centerline velocity and the dynamic proprieties of the flow together with radial profiles of axial velocity are computationally analyzed in this paper.

Keywords: counterflow stream, jet, penetration, velocity.

1   Introduction

Round jets have been widely studied due to their important application in industry. Many configurations of round jet were encountered in literature as free jet, coflow jet, counterflowing jet and cross flow jet. Few investigations have been concerned in the counterflow configuration owing to the intense instability observed upon interaction between the mean jet flow and the secondary flow. In this paper, we are focusing on round turbulent jet in uniform counterflow stream which is known to enhance mixing and dispersion efficiency due to the reverse flow phenomenon (Lam and Chan 1995, Lam and Chan 1997 and Chan and Lam 1998). This type of flow configuration is a typical application in environmental engineering

such as the disposal of wastewater into seas or rivers (Lam and Chan 1995 and Lam and Chan 1997).

A jet flow discharging from the nozzle exit penetrates into a counterflow for a longitudinal distance, called penetration length L_p. This scale is the axial distance from the jet exit to the mean stagnation point (Yoda and Fiedler 1996). The jet spreads radially before it is entrained by the counterflow stream and convected backward, contributing to the creation of the stagnation stream surface which is the boundary between the forward flow and the backward flow passing through the stagnation point (Beltaos and Rajaratnam 1973, Yoda and Fiedler 1996 and Bernero 2000). Along the penetration distance, the velocity of the jet flow drops gradually up to the stagnation point. The rate of the centerline decay depends on the jet-to-counterflow velocity ratio $R = U_j / U_0$ (Chan 1999), where U_j is the exit velocity of the jet and U_0 is the velocity of the counter-current flow, and it is found that the normalized penetration length is proportional to the velocity ratio (Arendt et al.1956) through a constant value of 2.4 or 2.7, proposed by Rajaratnam 1976, and 2.8 as suggested by Yoda and Fiedler 1996.

As well as the downstream axial penetration, the centerline velocity and/or concentration decay were investigated in many researches. Beltaos and Rajaratnam 1973 showed that the centerline velocity presents an hyperbolic decay with a constant of 5.83, for $x/L_p \leq 0.7$. In the same issue, Yoda and Fiedler 1996 demonstrated, from their experiments, that the centerline concentration decreases linearly with the inverse of the downstream axial distance with a constant equals to 4. Comparing with constant values of 6.3 (Rajaratnam 1976) and 5.4 (Dahm and Dimotakis 1990) for centerline velocity and concentration decay respectively, determined for jets in stagnant ambient, it is found that jet issuing in a counterflow ambient decays more rapidly than a jet in quiescent fluid.

The structure, the concentration field and the dilution behavior of counterflowing jet were studied using planar laser induced fluorescence (PLIF) technique (Yoda and Fiedler 1996, Chan and Lam 1999, Tsunoda and Saruta 2003, Tsunoda and Takei 2006 and Torres et al. 2012) at various jet-to-counterflow velocity ratios. Whereas, the laser Doppler anemometry (LDA) technique (Yoda and Fiedler 1996, Lam and Chan 1995, 1997 and 2002, Chan et al. 1998) and the particle imaging velocimetry (PIV) technique (Bernero and Fiedler 1999 and 2000, Tsunoda and Saruta 2003, Tsunoda and Takei 2006) were used to investigate the characteristics of the velocity field.

Numerical study of a turbulent circular jet issuing into a uniform counterflow stream is conducted in this paper. Three different cases of jet-to-current velocity ratios; low (R=1.3), median (R=10) and high (R=20) velocity ratios are used to investigate the characteristics of the velocity field. The Reynolds Stress Model (RSM) is used for comparison with available experimental data. The centerline velocity decay and radial profiles of axial velocity together with penetration length and jet width, which are used as length scales, are computationally analyzed.

2   Numerical Simulation

2.1   Governing Equations

The Reynolds-averaged Navier-Stokes equations are computationally solved, for a steady and incompressible turbulent fluid. The mass (1) and the momentum (2) conservation equations are presented in the Cartesian coordinates system as follow:

$$\frac{\partial U_i}{\partial x_i} = 0 \tag{1}$$

$$\frac{\partial}{\partial x_k}(U_k U_i) = -\frac{1}{\rho}\frac{\partial P}{\partial x_i} + \frac{\partial}{\partial x_k}\left[\nu\left(\frac{\partial U_i}{\partial x_k} + \frac{\partial U_k}{\partial x_i}\right) - \overline{u_i' u_k'}\right] \tag{2}$$

where $\overline{u_i' u_k'}$ is the Reynolds stresses and i, k = 1, 2, 3 refer to x, y and z respectively. U_i is the mean velocity and x_i is the coordinate in the i direction.

For the closure of this system of equations the second order turbulence model; Reynolds Stress Model (RSM) (Wilcox 2006) is used for all computations.

2.2   Configuration and Boundary Conditions

The counterflowing situation consisted of a circular water jet with a diameter D, emerging in a uniform counterflow water stream and placed at mid-depth. The velocity of the jet exit was U_j and the velocity of the opposite current was U_0. The dimension of the flow configuration was about 75D × 30D × 40D as illustrated in Fig. 1.

Boundary conditions are imposed on the nozzle exit of the jet (x = 0) and on the counter-current inlet (x = 75D). Numerical simulations are performed with the CFD software ANSYS FLUENT, for three jet-to-counterflow velocity ratios; R = 1.3, 10 and 20.
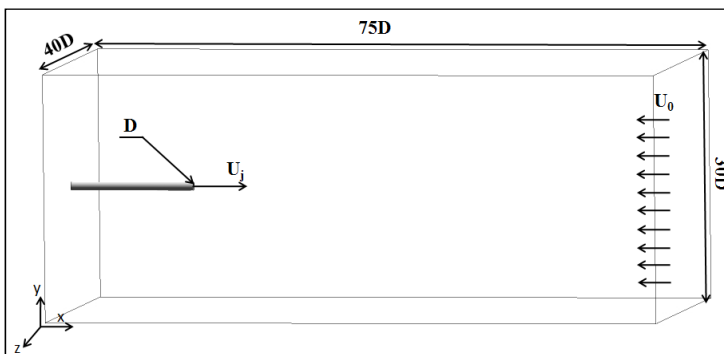
Fig. 1 Flow configuration

3   Results and Discussion

3.1   *Computational Validation*

The variation of the normalized centerline velocity of the jet (U_c/U_j) is presented, along the downstream axial distance, in Fig. 2. The results of numerical simulation are compared with experimental data of Chan et al. 1998 for three jet -to-current velocity ratios; low (R=1.3), median (R=10) and high (R=20) velocity ratios.
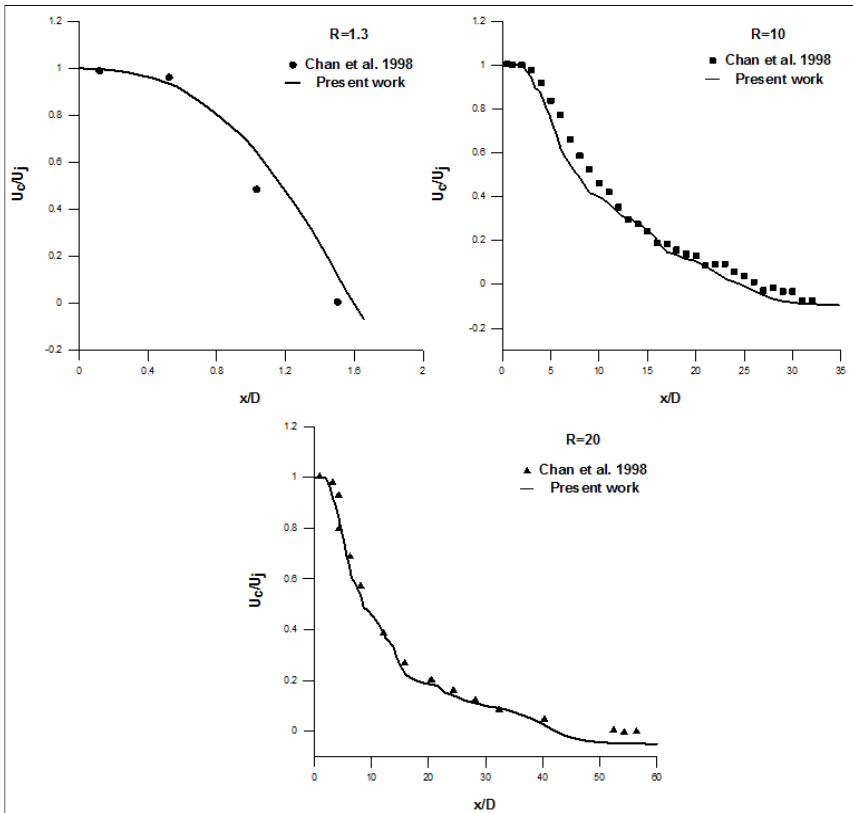
Fig. 2 Centerline velocity decay for low, median and high velocity ratios

This figure shows that the RSM turbulence model predicts quite well the physical velocity decay for the different velocity ratios. It is also shown that the velocity decay along the centerline axis increases as the velocity ratio decreases. The decay curves of the centerline velocity indicate the different flowfield regions. Indeed, the region immediately downstream of the jet exit, known as the potential core region, is characterized by a constant axial velocity and its length depends on the velocity ratio. The next region is the zone of established flow (Yoda and Fiedler 1996) outlined by a drop of jet centerline velocity while moving downstream.

3.2   Penetration Length

As previously defined, the penetration length (denoted L_p) can be determined from the centerline velocity decay as the axial distance corresponding to the zero velocity U_c. Fig. 3 presents values of the penetration length against velocity ratios, obtained by the present numerical simulation as well as Chan et al. (1998) and Morgan et al. (1976) experiments. Linear relationships suggested by Rajaratnam (1976) ($L_p / D = 2.4R$ and $L_p / D = 2.7R$) are also presented in Fig. 3.
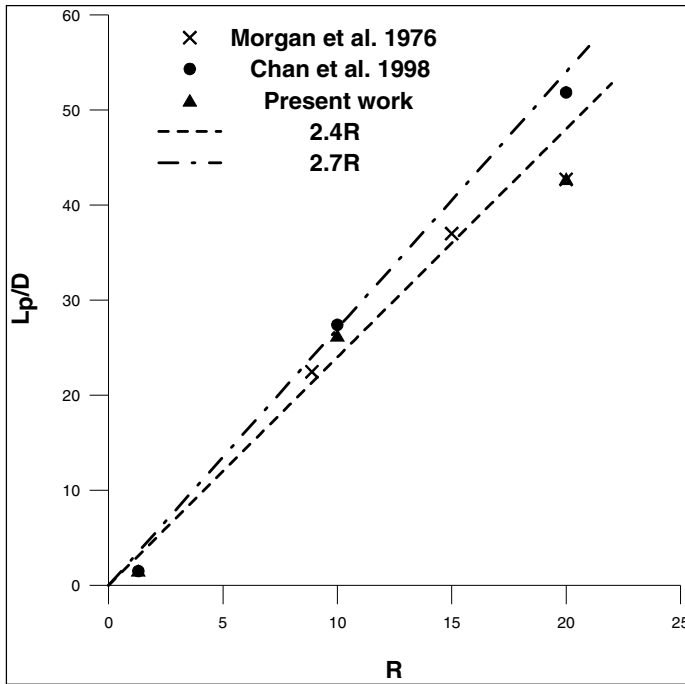
Fig. 3 Normalized penetration length against velocity ratios

It is clear that the penetration length increases with the velocity ratio (Yoda and Fiedler 1996). For the low and the median velocity ratios, the penetration distances numerically determined are in good agreement with experimental ones and it is found that the linearity between the penetration length and the jet-to-counterflow velocity ratio is verified. The constant of linearity is found to fall between 2.4 and 2.7 as suggested by Rajaratnam (1976). For low R, data is quite far from linearity due to the coexisting of the stable and unstable flow case, as reported by König and Fiedler (1991) and Yoda and Fiedler (1996). Large discrepancy appears for Chan et al. (1998) penetration length and both Morgan et al. (1976) and predicted values for the weaker counterflow (R=20). The departure from linearity can be explained by the confinement effect of walls as verified by Morgan et al. (1976).

3.3   *Velocity Field*

To analyze the behavior of counterflowing jets under different counter-current strength, axial velocity vectors are shown in Fig. 4 at low, median and high velocity ratios. The jet flow penetrates horizontally over some distances (L_p) into the counterflow stream and then is bent backwards. It is also seen in Fig. 4 the radial
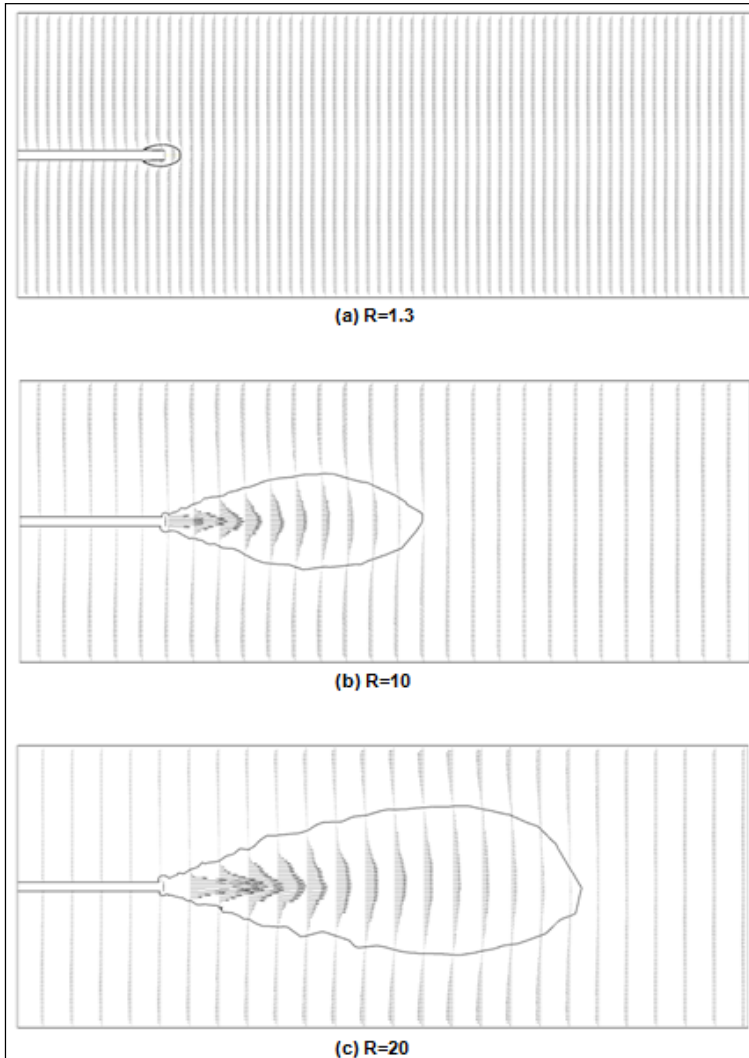
Fig. 4 Velocity vectors and dividing streamlines for low (a), median (b) and high (c) velocity ratios

spreading of the jet fluid to merge into the opposing flow and the counterflow de-
viation around the jet envelope, producing the dividing streamline. Downstream
closed curves illustrate dividing lines between the jet flow and the backward am-
bient flow, at the three velocity ratios. The dividing streamline extends gradually
from the jet edge up to a maximum width and then contracts more rapidly to con-
verge at the penetration length.

Comparing different ranges of velocity ratios, it is found that the radial extent
of the jet as well as the penetration length is larger when the velocity ratio is high-
er. This can indicate that more the main flow is weaker, the jet and the
counterflow mixing occurs further downstream.

3.4   Radial Distribution of the Velocity

Fig. 5 displayed the variation of the normalized axial velocity (U/U_j) along the ra-
dial direction at various x positions, for $R = 10$ and $R = 20$. These curves exhibit a
Gaussian aspect quasi symmetric relative to the jet axis. Radial velocity profiles
are characterized by a drop of the maximum value of longitudinal velocity U, go-
ing from $x/D = 6$ to $x/D = 21$ ($x/D = 24$ for $R = 20$). Besides, these profiles present
a continuous broadening while moving away from the jet exit, attaining the veloci-
ty of the counter-current (U_0) far from the jet axis, as it is observed at velocity
vectors and dividing lines in Fig. 4. More the streamwise position is deeper in the
couterflow, more the radial distribution is flat to join the counterflow velocity.
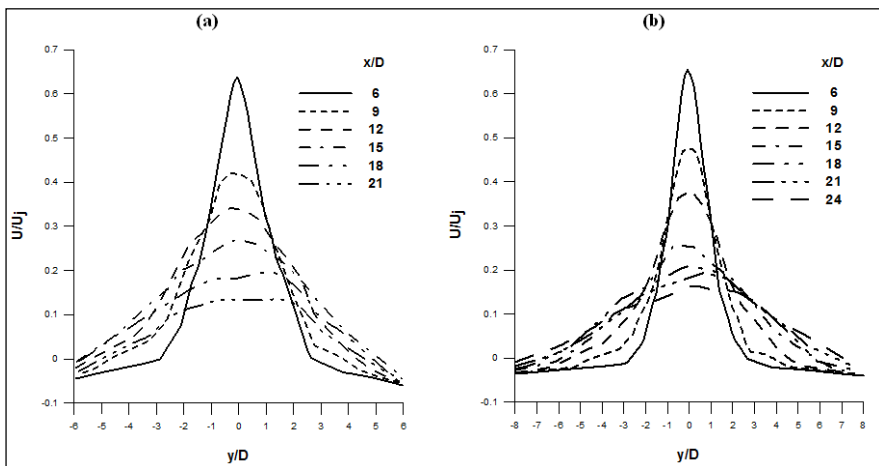
Fig. 5 Radial variation of the normalized longitudinal velocity at different axial positions;
(a) R=10 and (b) R=20

In order to verify self-similarity, radial velocity profiles normalized with centerline excess velocity and jet width are plotted in Fig. 6, at the median and the high velocity ratios. The jet width b is defined as the radial distance at which the local excess velocity $(U+U_0)$ equals to $1/e$ the centerline excess velocity (U_c+U_0) (Lam and Chan 1997). The Gaussian distribution is also plotted in this figure for comparison.

It is clear from Fig. 6 that the present computational data are well fallen onto the Gaussian curve at the $-1 < y/b < 1$ zone, as in the case of a free jet. While at the radial edges of the flow ($y/b < -1$ and $y/b > 1$), radial profiles do not collapse to a single curve and lie above the Gaussian distribution. This leads to conclude that in the external region the dimensionless velocity profiles are not self-similar and self-similarity is limited to the inner jet region ($-1 < y/b < 1$), as reported by Yoda and Fiedler (1996) and Chan (1999).
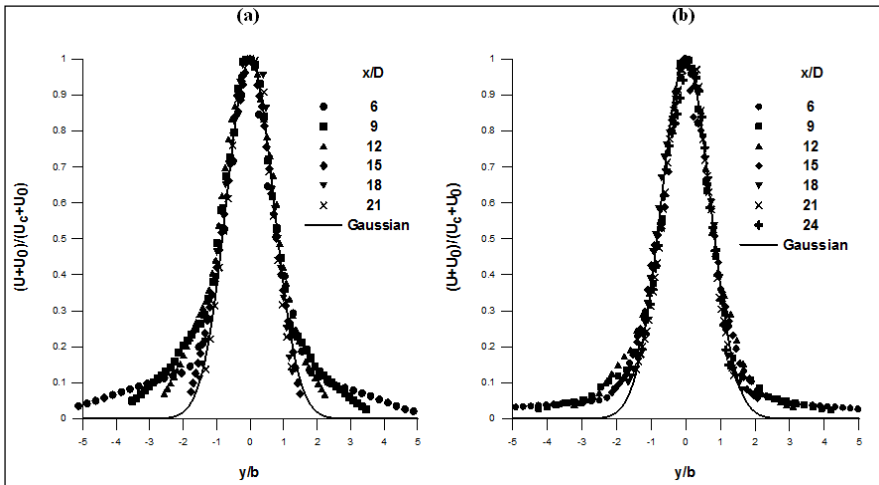
Fig. 6 Similarity of the radial profiles of the axial velocity; (a) R=10 and (b) R=20

4   Conclusion

A numerical simulation was performed to investigate the dynamical aspect of a turbulent round jet emerging in a uniform counterflow stream. These results are compared with experimental data deduced from the literature.

Axial and radial spreading of counterflowing jet are studied by means of numerical tools, at low, median and high ranges of jet-to-current velocity ratios and the locus of zero-axial velocity which marks the dividing streamline is presented for various velocity ratios.

The axial development of the jet can be described by the profile of the U-velocity along the centerline and it is found that the centerline velocity decreases

more rapidly as the main opposing flow is stronger. While the penetration length rises as the velocity ratio increases.

The continuous broadening of the radial distribution of axial velocity shows that the extent of the jet in counterflow is enhanced while moving in the forward jet direction. On the other hand, it is seen that a jet emerging in counterflow stream never reaches true self-similarity and normalized velocity profiles collapse into a single curve only in the inner region of the jet.

References

Arendt, J., Babcock, H.A., Schuster, J.C.: Penetration of a jet into counterflow. Journal of Hydraulic Division Proceeding of ASCE 82, 1038-8–1038-11 (1956)

Beltaos, S., Rajaratnam, N.: Circular turbulent jet in an opposing infinite stream. In: First Canadian Hydraulics Conference, Edmonton (1973)

Bernero, S., Fiedler, H.E.: Simultaneous PIV and LIF experiments on a round jet in counterflow. In: Proc.1st Int. Symp. on Turbulence and Shear Flow Phenomena, Santa Barbara, pp. 1053–1058 (1999)

Bernero, S.: A Turbulent Jet in Counterflow. PhD Thesis, Technical University of Berlin (2000)

Bernero, S., Fiedler, H.E.: Application of particle image velocimetry and proper orthogonal decomposition to the study of a jet in a counterflow. Exp. Fluids 29, S274–S281 (2000)

Chan, H.C.: Investigation of a round jet into a counterflow. PhD thesis, University of Hong Kong (1999)

Chan, H.C., Lam, K.M.: Centreline Velocity Decay of a Circular Jet in a Counterflowing Stream. Phys. Fluids 10, 637–644 (1998)

Chan, H.C., Lam, K.M.: The concentration field of a circular jet in a counterflow. In: Proceedings of the 28th IAHR Congress, Graz, Austria, vol. 342, pp. 22–27 (1999)

Chan, H.C., Lam, K.M., Bernero, S.: On the penetration of a round jet into a counterflow at different velocity ratios. In: Proceedings of the Second International Symposium on Environmental Hydraulics, pp. 229–234 (1998)

Dahm, W.J.A., Dimotakis, P.E.: Mixing at large Schmidt number in the self-similar far field of turbulent jets. J. Fluid Mech. 217, 299–330 (1990)

König, O., Fiedler, H.E.: The structure of round turbulent jets in counterflow: a flow visualization study. Advances in Turbulence 3, 61–66 (1991)

Lam, K.M., Chan, H.C.: Investigation of turbulent jets issuing into a counterflowing stream using digital image processing. Experiments in Fluids 18, 210–222 (1995)

Lam, K.M., Chan, H.C.: Round jet in ambient counterflowing stream. Journal of Hydraulic Engineering 123(10), 895–903 (1997)

Lam, K.M., Chan, H.C.: Time-averaged mixing behavior of circular jet in counterflow: Velocity and concentration measurements. Journal of Hydraulic Engineering 128(9), 861–865 (2002)

Morgan, W.D., Brinkworth, B.J., Evans, G.V.: Upstream penetration of an enclosed counterflowing jet. Industrial and Engineering Chemistry Fundamentals 15, 125–127 (1976)

Rajaratnam, N.: Turbulent Jets. Elsevier Scientific Publishing Company, Amsterdam (1976)

Torres, L.A., Mahmoudi, M., Fleck, B.A., Wilson, D.J., Nobes, D.: Mean Concentration
    Field of a Jet in a Uniform Counter-Flow. Journal of Fluids Engineering 134(1), 1–5
    (2012)
Tsunoda, H., Saruta, M.: Planar laser-induced fluorescence study on the diffusion field of a
    round jet in a uniform counter-flow. Journal of Turbulence 4, 1–12 (2003)
Tsunoda, H., Takei, J.: Statistical Characteristics of the Cross-Sectional Concentration Field
    in a Round Counter Jet. J. of Fluid Sci. and Tech. 1, 105–113 (2006)
Wilcox, D.C.: Turbulence Modeling for CFD, 3rd edn. DCW Industries, Inc. (2006)
Yoda, M., Fiedler, H.E.: The round jet in a uniform counterflow: flow visualization and
    mean concentration measurements. Experiments in Fluids 21(6), 427–436 (1996)

Numerical Study of a Turbulent Offset Jet Flow

Ali Assoudi[1], Sabra Habli[2], Nejla Mahjoub Saïd[2], Philippe Bournot[3],
and Georges Le Palec[3]

[1] LGM, National Engineering School of Monastir, University of Monastir, Tunisia
   ali.assoudi@yahoo.fr
[2] LGM, Preparatory Institute for Engineering Studies, University of Monastir, Tunisia
   {sabra.habli,nejla.mahjoub}@fsm.rnu.tn
[3] IUSTI, UMR 7343, Faculty of Sciences, University of Aix-Marseille, France
   {georges.lepalec,philippe.bournot}@univ-amu.fr

Abstract. A dynamic study of the mean flow behavior of a three-dimensional turbulent offset jet issuing into a quiescent ambient is presented. The flow is characterized by a longitudinal variation of curvature, skewed impingement onto a flat surface, a recirculating region, and the development of a wall jet region. A numerical simulation is used, by means of the finite volume method with the second order turbulent closure model: the Reynolds stress Model (RSM), to investigate the influence of certain parameters such as jet discharge height and the geometric nozzle. Flow structure is described in the preimpingement, recirculation and impingement regions. Interdependence is shown among the offset height (h) and the geometric nozzle (plane jet and circular jet). The obtained results are presented in terms of the jet dimensionless velocity distribution, maximum velocity decay and vectors velocity of the flow. The jet decay is presented. The recirculation region is fed by a relatively strong backflow for the reported high offset height and it is shown that the reattachment point depends strongly with the jet form and the offset height.

1   Introduction

A jet that is discharged into the quiescent surroundings or a moving stream (co-flowing) above a plane wall parallel to the jet axis with a certain distance is designated as an offset jet. There are many situation in which flows of an offset jets have attracted extensive research attention mainly due to their important and diverse practical and theoretical applications. Some of these applications include: flow separation control, where offset jets are mixed with the ambient flow to provide additional momentum to a boundary layer at the verge of separation; film-cooling technology in which this types of flow are used to improve the thermal performances of gas turbines; evaporation enhancement such as in automobile defrosters; air distribution in enclosed environments; thrust-augmenting ejectors for vertical/short takeoff and landing aircrafts (designated by V/STOL); effluent disposal into water bodies such as in marine tailings; and predicting the nature of aircraft exhausts and the loading effects of aircraft exhausts on ground structures.

The flow field of an offset jet is complex and is described in different regions. Indeed, during its evolution, entrainment of ambient fluid bounded by the jet, the offset wall and the horizontal wall creates a low pressure zone causing the jet to deflect towards the wall and eventually attaches to it at the impingement point. This is called the 'coanda effect'. After reattachment, part of the inner shear layer fluid is deflected upstream from the attachment point into the recirculation zone by an adverse pressure gradient. Downstream from the attachment point, in the attachment region, the flow is subjected to the effects of stabilizing curvature, adverse pressure gradient and the strong interaction with boundary layer at the offset wall. Far downstream from the nozzle plate, in the wall jet region, the flow remains attached to the wall and evolves downstream to resemble a wall jet flow.

A detailed literature study shows that most of the previous studies are concentrated on two dimensional (2D) offset jets such as Bourque and Newman [1], Sawyer [2], Hoch an Jiji [3], Pelfrey and Liburdy [4], Holland and Liburdy [5] and Nasr and Lai [6], etc. for instance, early investigations of Bourque and Newman [1] and Sawyer [2] had assumed the measurements of static pressure distributions within the recirculation zone, mean velocities and some turbulence characteristics using hotwires and Pitot tubes.

A turbulent plane offset jet with small offset ratio of 2.125 discharged into a quiescent medium has been experimentally studied by Nasr and Lai [6]. Mean velocities, turbulence intensities; static pressure and Reynolds shear stress have been investigated using a non-intrusive two-component laser Doppler anemometry.

Three-dimensional (3D) offset jets have not received the attention that their 2D counterparts. In the very few studies on 3D offset jets found in the open literature, the investigation of Davis and Winarto [7], Nozaki and al. [8] and the recent study of Agelin and Tachie [9]. This investigation discharges into a quiescent medium.

Recently, Agelin and Tachie [9] have studied the effects of offset height and Reynolds number on the structure of a turbulent offset jet using the particle image velocimetry (PIV) technique. The authors have reported that in the early region of flow development clearly show significant influences of Reynolds number and offset distances on the decay of maximum mean velocity and growth of the shear layer. On the contrary, downstream of the jet exit, the decay and spread rates were found to be nearly independent of offset height.

This work is devoted to the influence of the exit nozzle configuration on the evolution of dynamic characteristics of the jet flow: two nozzle configurations, rectangular and circular, are tested. The effects of the offset height on the structure of a turbulent 3D offset jet are also analyzed.

2   Numerical Simulation

The flow is assumed to be steady, incompressible, turbulent and three-dimensional. An air jet from a nozzle with an ejection velocity u_0 is subjected to quiescent medium. The jet is discharged from a vertical wall offset by a height h above the horizontal wall. To simulate the different flows and scale the different features, the geometry and the coordinate system used is shown on figure 1.
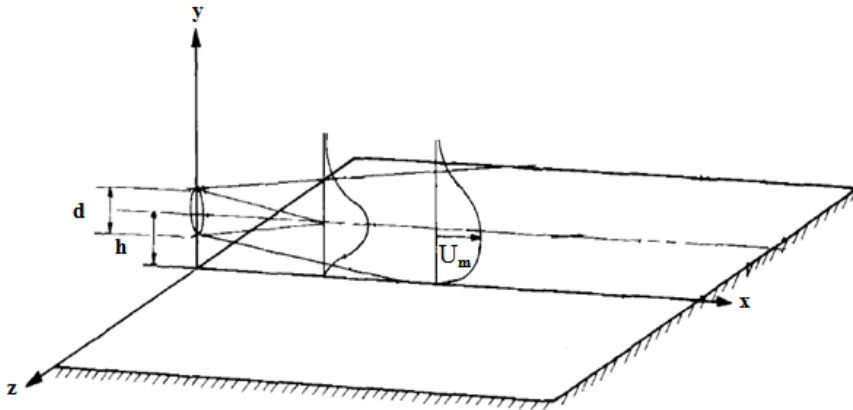
Fig. 1 geometry and coordinate system of the offset jet among the whole domain

Under the above assumptions, the averaged equations describing the behavior of the offset jet flow can be written as:

$$\frac{\partial U_i}{\partial x_i} = 0 \tag{1}$$

$$\frac{\partial}{\partial x_k}(U_k U_i) = -\frac{1}{\rho}\frac{\partial P}{\partial x_i} + \frac{\partial}{\partial x_k}\left[\nu\left(\frac{\partial U_i}{\partial x_k} + \frac{\partial U_k}{\partial x_i}\right) - \overline{u_i' u_k'}\right] \tag{2}$$

where $\overline{u_i' u_k'}$ is the Reynolds stresses and i, k = 1, 2, 3 refer to x, y and z respectively. U_i is the mean velocity and x_i is the coordinate in the i direction. The resolution of these equations requires a turbulent closure model able to well characterize the fluctuating functions. The RSM turbulence closure (Wilcox 2006) [10] model was chosen for the matter due to its ability to efficiently reproduce the slightest variation and compute the destruction of turbulence kinetic energy.

3   Results and Discussion

In order to reveal some of the qualitative features of the flow in the near field, the contours of the mean velocities in the symmetry plane for an offset height h=0.5m are shown in figure 2. The jet discharges into a quiescent medium from an exit. Two configurations are treated: a circular nozzle (d=0.03m) and a rectangular nozzle (L=0.12m and l=0.006m). The ejection velocity was 2m.s^{-1}. There are three regions in the flow field: the first region shown the reverse flow region, which extends from the jet exit to the reattachment point (x_r); the second region presented the attachment region, which stretches from x_r to the beginning of the wall jet region; and third region was the wall jet region, where the jet develops the

characteristics of a generic wall jet. This figure show that the dividing streamline in flow is slightly curved in the first half of the separated region but curves more sharply close to the reattachment point. At reattachment, some of the fluid in the shear layer is deflected upstream by strong adverse pressure gradient into the reverse flow. We mark that for circular nozzle, the mean velocities show a maximum values along the centerline of the jet exit extended to x=4d. However for a rectangular nozzle, the contours of the mean velocities indicated a maximum values until x=1.3d.

(a)   (b)
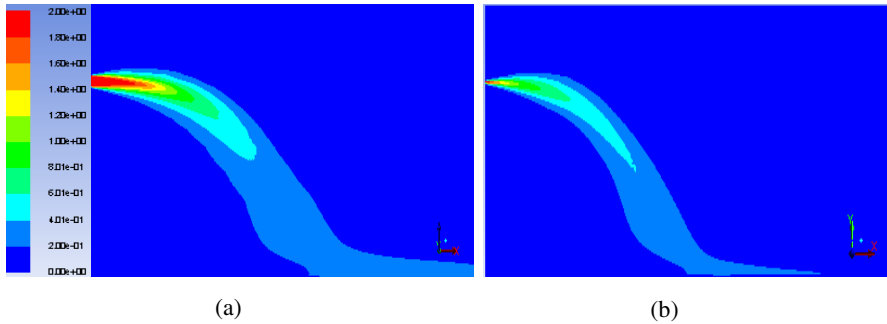
Fig. 2 Contours of the mean velocities U for an offset height h=0.5m (a) circular nozzle, (b) rectangular nozzle

Figures 3 and 4 presented the mean longitudinal velocity vectors for different configuration exit (circular and rectangular) and different offset height (h=0.2m and h=0.5m). An asymmetric pressure gradient takes place between the jet and the vertical wall thus deflecting the jet towards the horizontal wall. In both configurations, the jet is clearly moving towards the horizontal wall generating, upstream of the reattachment point, a large recirculation region between the jet and the walls (vertical and horizontal), whereas the flow reattaches to the horizontal wall downstream the impact point. The reduced pressure in the recirculation region is created by the big vortex and the air entrainment into the jet flow. One of the characteristics of the shear layer is the reattachment length, x_r. This was estimated as the distance from the exit to the location attachment point. Figure 3 shows the vectors of mean velocities u for circular and rectangular nozzle (the same rate $Q_v=1.4.10^{-3}$ m^3s^{-1}) for an offset height h=0.5m. It is observed that the reattachment length is nearly dependent of the diffuser (exit jet) geometry. The attachment points are $x_i=0.73m$ and $x_i=0.63m$ for a jet discharge from circular and rectangular nozzle respectively. In figure 4 we represent the overall average fields for two offset height h=0.2m and h=0.5m for a rectangular nozzle. This figure shows that the global mean flow configuration is governed mainly by the offset height, where extension defines the recirculation zone dimension. The reattachment lengths are $x_r=0.33m$ and 0.38m for h=0.2m and 0.5m, respectively, clearly indicating that the reattachment length is increased when the offset height is increased. Downstream the recirculation zone, the jet begins to become more like a wall jet flow.
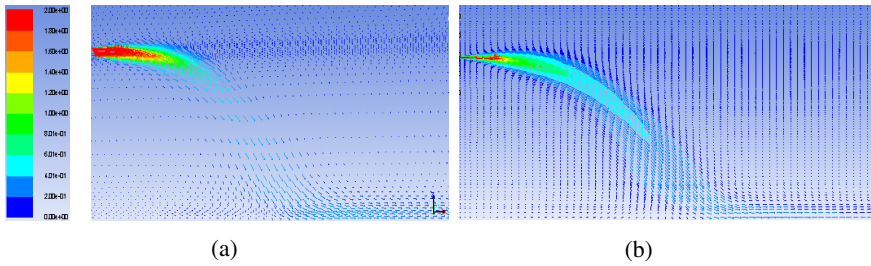
Fig. 3 Mean longitudinal velocities vectors U for an offset height h=0.5m (a) circular nozzle, **(b)** rectangular nozzle
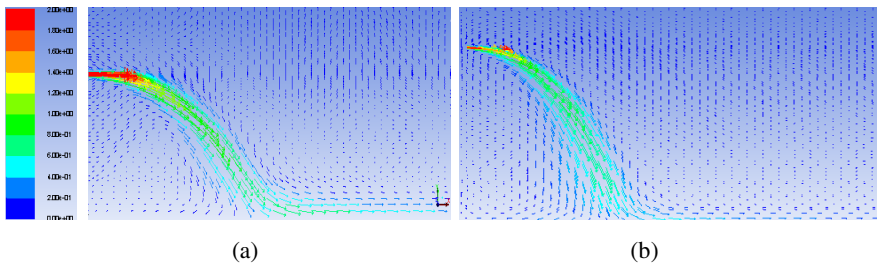
Fig. 4 Mean longitudinal velocities vectors U for a rectangular nozzle (a) offset height h=0.2m, (b) offset height h=0.5m

In order to focus on flow development in the impingement zone, the normalized velocity profiles (u/u_m) along the normalized vertical coordinate (x/d) for an offset height h=0.2m and 0.5m are plotted in figure 5. The results indicate that the wall jet location (beginning of the third region) depends linearly on the offset heights. This figure shows that the offset jet reattaches the horizontal wall at a distance x_r=0.33 for h = 0.2 m and x_r = 0.38 for h= 0.5 m, the reattachment point is defined as the location where the mean streamlines reattach to the wall. This is indicated that the maximum streamwise velocity of the reverse flow (Ur) was large for a higher offset height. The relatively large backward flow velocity would imply a large loss of jet momentum that is required to drive the recirculation region. The relatively lower reverse flow velocity is due to the retarding effect of the horizontal wall on the recirculation region. This figure also indicates that for small offset height, the size of recirculation region is decreased. Consequently the standing vortex was found to be very small compared to the higher offset height. The presence of the negative longitudinal velocity at x=0.3m for the offset height h=0.2m, show that this position was in the recirculation region. The same reasoning to the case of offset height h=0.5m, the presence of the important negative velocity peak at the position x=0.33m show that this position was defined in the recirculation region.

a.   h=0.2m

b.   h=0.5m
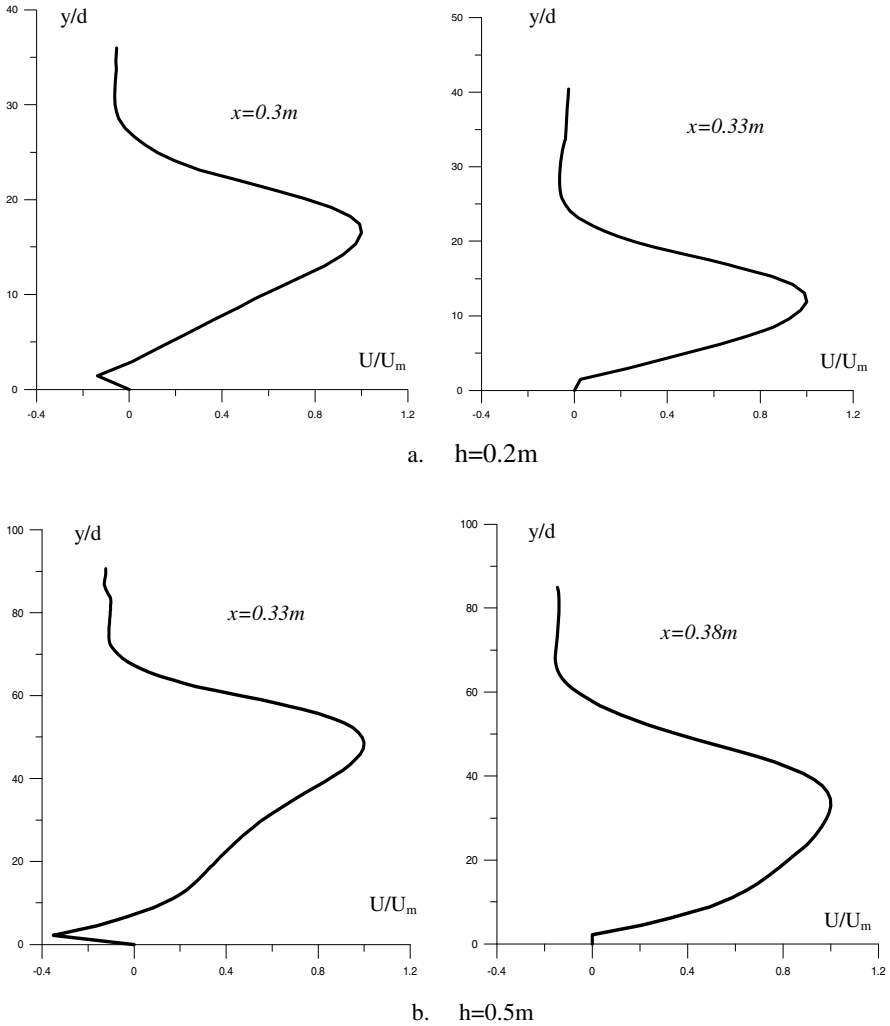
Fig. 5 The effect of the jet discharge height on velocity development along the symmetry plane for different offset height

Decay of the mean streamwise velocity u_m/u_j along the jet centerline of an offset jet is plotted in Figure 6. The results in the flow development clearly show significant effects of offset height on the decay of maximum mean velocity. The decay of the maximum velocity as function of the normalized distance x/d_h (d_h is the hydraulic diameter) is caused by the presence of the horizontal wall. The decay of u_m/u_j is more rapid for a larger offset height h. This result can be attributed to the upstream effects of the recirculation zone. As the jet impinges on the horizontal wall (the bottom wall), the pressure of the jet increases. Consequently, the

longitudinal velocity decays rapidly. After the reattachment, the high pressure causes the (attached) wall jet to accelerate. As the pressure relaxes to the ambient pressure, the maximum longitudinal velocity of the wall jet starts to decay.
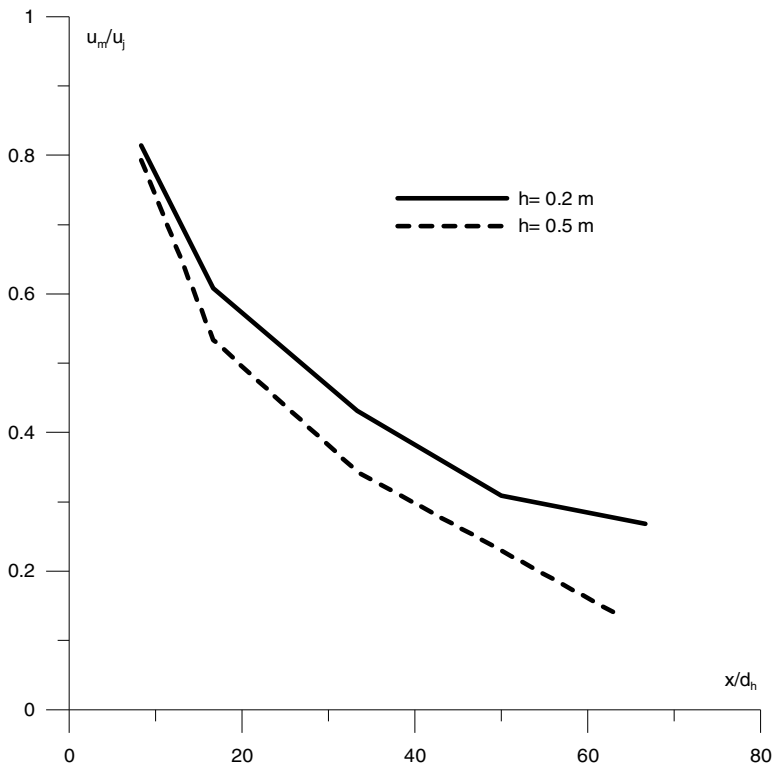
Fig. 6 The effect of the jet discharge height on maximum velocity decay

The velocity distributions of offset jet produced from different geometric nozzle (circular and rectangular) are presented in Figure 7. As shown, the velocity profiles for the circular and rectangular jet are relatively similar. They have a Gaussian shape. This figure also illustrate, that for both configuration the velocity profiles adopt a peak relative to the axis of the nozzle exit (y=0.5m) and this peak is very large for the circular nozzle. In the near field (x=0.05m), the velocity profiles show a maximum values. In this region, the jet behaves as a free jet. The profiles, at the level of jet exhaust, are symmetrical. When we advance in the streamwise direction, the values of longitudinal velocity decreased indicating the deviation of the jet towards the wall. Downstream the nozzle exit, the profiles indicate negative values in the vicinity of the horizontal wall for different longitudinal locations (x=0.1m, 0.2m and 0.3m). This latter indicates the presence of the recirculation region (this region characterized by the presence of vortices). For plane jet the recirculation zone appears at x=0.1m whereas for circular jet, the

recirculation zone begins at x=0.3m. For the longitudinal coordinate x =0.3m, the circular jet is not deflected yet while the jet plane presents a curvature and a dissymmetry in the profile.
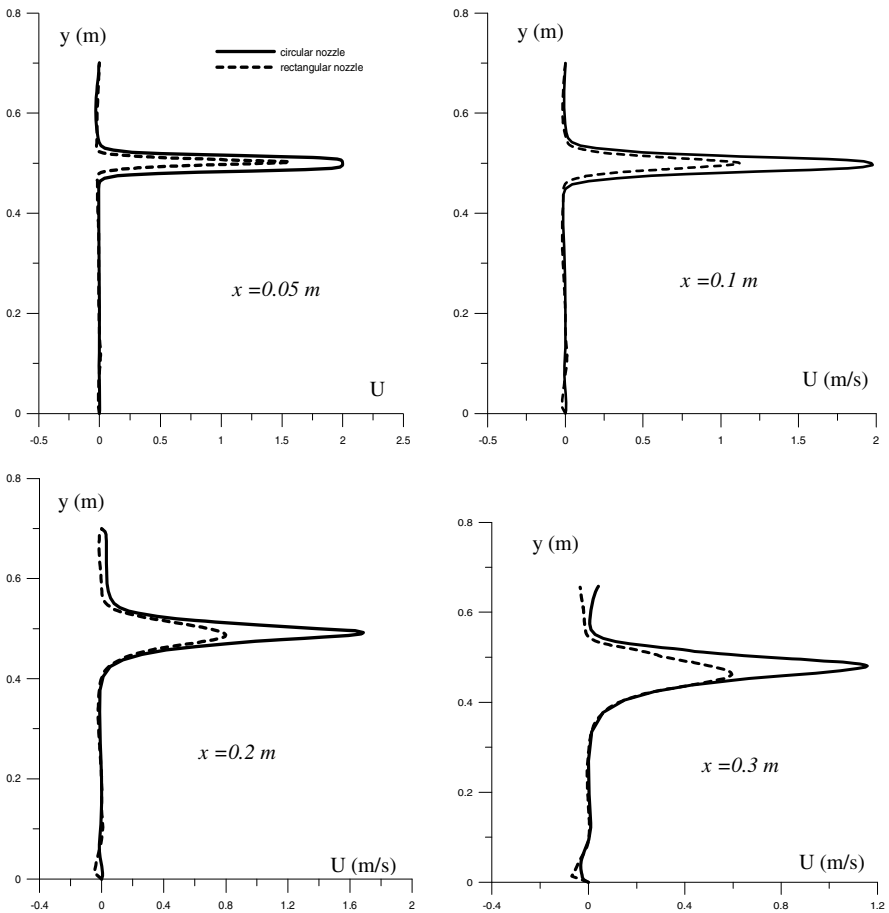
Fig. 7 The effect of nozzle geometry on the longitudinal velocity developments along the symmetry plane for an offset height h=0.5m

4 Conclusion

In the present study, a numerical simulation has been done to investigate the flow behavior of three-dimensional turbulent offset jet. The results of this work provide a detailed description of the mean flow characteristics primarily in the recirculating and impingement regions. Some discussion is provided on the effects of offset height and geometric nozzle on parameters such as the curvature strain rate, impingement point and the generated flow pattern. The results show that the flow development is strongly dependent on offset height and diffuser geometry.

The flow development is delayed with increasing offset heights. The decay rate increased with the offset heights. The results also noticed that the reattachment length increased linearly with offset height but is also dependent of geometric diffuser. The decay and spread rates were found to be nearly independent of offset height at larger downstream distances. For circular nozzle, the jet is transported into the recirculation region, resulting in a faster decay of the maximum velocity and a shorter reattachment length.

Nomenclature

h	*Offset* height (m)
d	Jet nozzle diameter (m)
w	Jet nozzle width (m)
d_h	hydraulic diameter (m)
P	Mean pressure (pa)
U_iU_j	Mean velocity components along the i and j directions
U, V, W	Mean velocity components along x, y, and z directions (m/s)
U_m	Maximum mean velocity (m/s)
x, y, z	Cartesian Coordinates (m)
0	Exit section of the jet
‾	Reynolds average
'	Fluctuation

References

[1] Bourque, C., Newman, B.G.: Reattachment of a two-dimensional in-compressible jet to an adjacent flat plate. Aero. Quart. 11, 201–232 (1960)
[2] Sawyer, R.A.: The flow due to a two dimensional jet issuing parallel to a flat plate. J. Fluid Mech. 9, 543–561 (1960)
[3] Hoch, J., Jiji, L.M.: Two-dimensional turbulent offset jet-boundary interaction. Trans. ASME J. Fluids Eng. 103, 154–161 (1981)
[4] Pelfrey, J.R.R.: Characteristics of a Turbulent Plane Offset Jet. PhD Thesis. Clemson University, New York, USA (1984)
[5] Holland, J.T., Liburdy, J.A.: Measurements of the thermal characteristics of heated offset jet. Int. J. Heat Mass Transfer 33, 69–78 (1990)
[6] Nasr, A., Lai, J.: A turbulent plane offset jet with small offset ratio. Exp. Fluids 24, 47–57 (1998)
[7] Davis, M.R., Winarto, H.: Jet diffusion from a circular nozzle above a solid plane. J. Fluid Mech. 101, 201–221 (1980)
[8] Nozaki, T., Hatta, K., Nakashima, M., Matsumura, H.: Reattachment flow issuing from a finite width nozzle (Report 2. Effects of Initial Turbulence Intensity). Bull. JSME 24(188), 363–369 (1981)
[9] Agelin-Chaab, M., Tachie, M.F.: Characteristics and Structure of Turbulent three-dimensionnal offset Jets and Wall jets. Int. J. of Heat and Fluid Flow 32(3), 608–620 (2010)
[10] Wilcox, D.C.: Turbulence Modeling for CFD, 3rd edn. DCW Industries, Inc. (2006)

Flow Structure of an Impinging Plane Jet

Rim Ben Kalifa[1], Sabra Habli[2], Nejla Mahjoub Saïd[2],
Philippe Bournot[3], and Georges Le Palec[3]

[1] LGM, National Engineering School of Monastir, University of Monastir, Tunisia
  rimbenkalifa@yahoo.fr
[2] LGM, Preparatory Institute for Engineering Studies, University of Monastir, Tunisia
  sabra.habli@fsm.rnu.tn, nejla.mahjoub@fsm.rnu.tn
[3] IUSTI, UMR 7343, Faculty of Sciences, University of Aix-Marseille, France
  georges.lepalec@univ-amu.fr, philippe.bournot@univ-amu.fr

Abstract. The current study attempt to examine and investigate the flow field of a plane air jet impinging normally on a flat surface. In order to understand the development of the flow generated from a rectangle turbulent jet impinging a flat plate, a detailed dynamic and turbulent simulation is presented. The plate is appropriately larger than the nozzle exit diameter. The ground plate can be moved vertically in order to simulate the height ratio h/e=28. Another aim of this study is to explore the effect of the Reynolds number (Re=1000, 2000, 3000) on the flow structure. A Computational Fluid Dynamics study is performed using the Reynolds-averaged Navier–Stokes equations by means of the RSM (Reynolds Stress Model) second order turbulent closure model. The results include mean and turbulent velocities and quantify the large effects of flow distortion on the turbulent structure of complex, three-dimensional impingement flow.

Keywords: Impinging jet, Reynolds number, velocity field, RSM model.

1   Introduction

Impinging jet flow is of great interest in a number of industrial applications because it is utilized more often to heat, cool or dry materials. Besides, the impact of the air system is used in other applications such as paper drying, cooling of electronics and shaping glass. This feature has led many researchers to explore the behavior of impinging jets. The aim of the research is to examine the heat and mass transfer (rather than the fluid dynamic), and they propose to examine the effect of Reynolds number, distance between the nozzle, the impinging plate. Impinging jets have been the subject of extensive experimental review summarized in many studies. In particular, Perry (1978) has shown that due to the shear layer instability of Kelvin–Helmholtz type present in plane impinging jets, a pair of spanwise rollers originates from the shear layers just downstream of the inlet plane. The identification of the physical mechanisms responsible for this phenomenon is extremely difficult, since measurement techniques cannot provide the evolution of the instantaneous fields in all space simultaneously. However, an understanding on heat

transfer in the impinging region is of considerable importance. According to the experiments of Sutera et al. (1963), the highest heat transfer rate in the impinging region is caused by counter-rotating vortex ribs along the impinging wall. Yokobori et al. (1983) describe clearly the evolvement of the flow structure including the forming, developing, moving, pairing and merging of the overall large-scaled eddies along the impinging wall and through the symmetry plane. Counter-rotating streamwise vortex pairs are also detected upstream of the stagnation point by some researchers (Sakakibara et al. 2001). Liu et al. (1996) examined the relationship between the vortical structures and local heat transfer by using flow visualization, heat transfer spectra and correlation between velocity and heat transfer. Experimental investigation of impinging jet can be resource demanding. In research facilities, the cost of running the installation and technical support is high. Computational Fluid Dynamics (CFD) simulations, appropriately validated, have the capability of producing meaningful data at reduced cost and time.

Numerical modeling of turbulent planar air jet impinging on a rectangular duct was performed by Huang et al. (1984). They have found that, when the plate velocity is higher, Nusselt numbers become smaller in the vicinity of the wall, when the wall velocity is opposed to the flow and is higher where the surface motion and the flow are in same direction. Sharif and Benerjee (2009), by using CFD Fluent code, investigated a numerical study based on the standard k-ε turbulence model combined to the enhanced wall treatment. Different parameters were considered: the jet exit Reynolds number (Re=5000, 20000) and the impinging distance (h/e=6 and 8).They show that the local Nusselt number along the moving plate reaches a maximum value near by the stagnation point for low velocity ratios, which can be explained by the thinning of dynamical and thermal boundary layers. At a given plate velocity, the average Nusselt number along the plate increases when the jet exit Reynolds number increases. Finally, unsteady numerical simulations of the impinging jet flow (LES/DNS) have been carried out (Cziesla et al. 2001). Further the major studies with LES model reported in the literature deal with the turbulent case (Uddin et al. 2013) but DNS results at moderate Reynolds number (Re < 2000) are also studied (Rohlfs et al. 2012).

The aim of this paper is to reach a thorough understanding of the impinging plane jet, by using computational fluid dynamics (CFD) simulations. For this purpose, RSM turbulent model is implemented to predict the mean flow field structure of an isothermal impinging jet on a flat surface. In the current investigation, the effect of the Reynold number on the flow development is examined.

2   Numerical Study

2.1   Description of the Computational Domain

The computational domain is summarized in Fig.1. The configuration includes the orifice and the target plate. The jet emitted from a nozzle of rectangular section ($l \times e$=42×3 mm^2). The jet exit velocity "v_j" is varied giving a Reynolds number

ranging from 1000 to 30000. The impinging distance H is fixed to 28×e in this study. As illustrated in Fig. 1, the size of the computational domain adopted in this study is according to: x (136×e), y (42×e) and z (42×e). The origin of the coordinate system is placed at the center of the flat surface. This choice is motivated by the symmetry of the resulting flow.

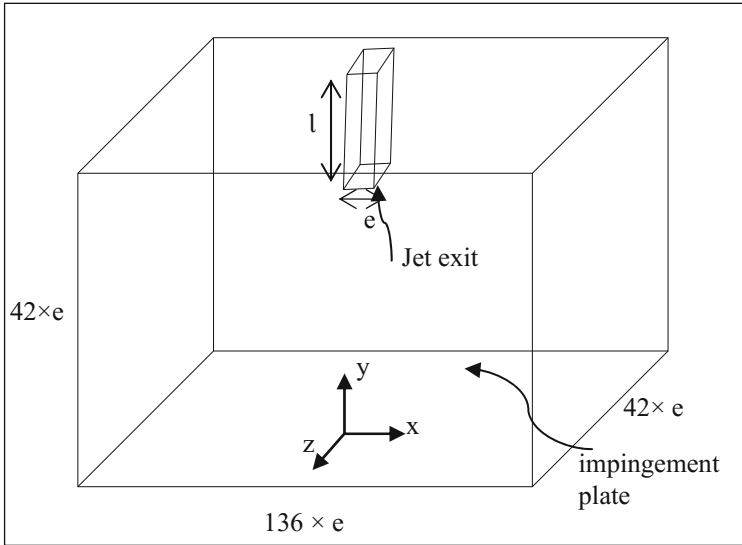A three dimensional, isothermal, steady, incompressible and turbulent flow is taken in consideration.

Fig. 1 Computational domain and coordinate system for impinging jet with h/e=28.

2.2 *Mathematical Formulation*

To simulate the flow of the impinging jet, the equations for conservation of mass, momentum with an appropriate turbulence model should be solved:

Continuity equation: $\dfrac{\partial (\overline{u_i})}{\partial x_i}=0$ (1)

Momentum equation: $\overline{u_j}\dfrac{\partial \overline{u_i}}{\partial x_j}=-\dfrac{1}{\rho}\dfrac{\partial}{\partial x_i}\left(\overline{p}\right)+\dfrac{\partial}{\partial x_j}\left(v\dfrac{\partial \overline{u_i}}{\partial x_j}-\overline{u'_i u'_j}\right)+g_i$ (2)

The introduction of the fluctuating sizes makes this system open. Its closing requires the use of a turbulence model that makes it possible to obtain a number of equations equal to the number of unknown parameters. In the present study, we used the second-order closure model (RSM). The computational grid was generated

using a hexahedral grid system. A sufficiently fine grid is managed near the jet and the wall, where prevails a very high gradient of different variables.

The conservation equations are solved with the following boundary conditions: a velocity inlet condition is imposed at the jet exit with uniform velocity. A wall condition is set for the impingement plate and a pressure-outlet condition is used for the other boundaries of the domain.

3   Results and Discussion

3.1   Mean Flow Properties

Fig.2 provides a global view of the mean velocity field for a turbulent air jet (Re=3000) impinging a flat surface. The jet is issuing from a plane nozzle with a large l/e ratio that ensured fully developed turbulent flow exit conditions. Fig. 2 shows three different regions. Firstly there is the free jet zone, which is the region that is largely unaffected by the presence of the impingement surface. This region extended from the nozzle up to a certain distance from the surface and can be divided, in turn, into the potential core region, the developing flow region, and impinging region. The potential core is the central portion of the flow in which the velocity remains constant and equal to the nozzle exit velocity.

Secondary, we can identify a stagnation zone that extends to a radial location defined by the spread of the jet. The stagnation zone includes the stagnation point where the mean velocity is zero and within this zone, the free jet is deflected into the wall jet flow. Finally, the wall jet zone extends beyond the radial limits of the stagnation zone.
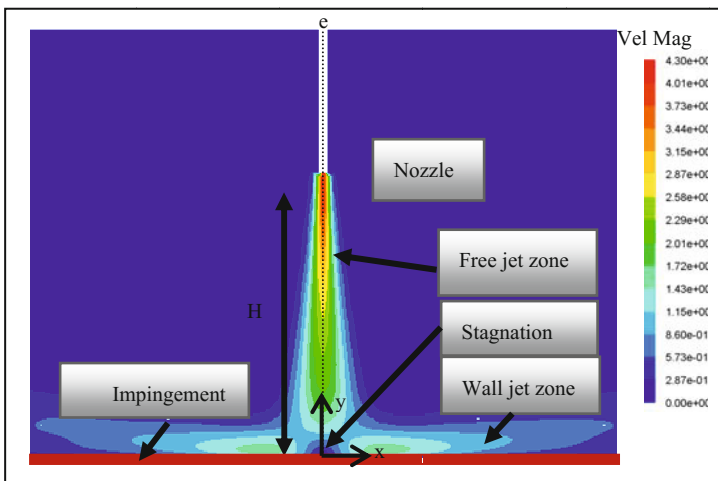
Fig. 2 Full jet development: Re=3000 and h/e=28

The impinging zone is not well known and it appears essential to thoroughly characterize the height of the impinging for various nozzles geometry. We propose to define the height of this zone by taking into account the velocity decrease in the developed zone and in the impinging zone. Figure 3 presents the evolution of the dimensionless vertical velocity (v/v_j) along the vertical coordinate (y/e) in the jet centerline ($x/e=0$). As shown in Fig.3, the distance to the wall is defined by the intersection of the lines AB and CD. A linear law represents the evolution of the axial velocity in the developed zone and close to the impingement. It is thus possible to determine the intersection from these two lines to obtain the height "L". It can be considered that the height of the impinging zone is close to a value equal to L=4,5×e. This result is in good agreement with the study of Mural et al. (2004).
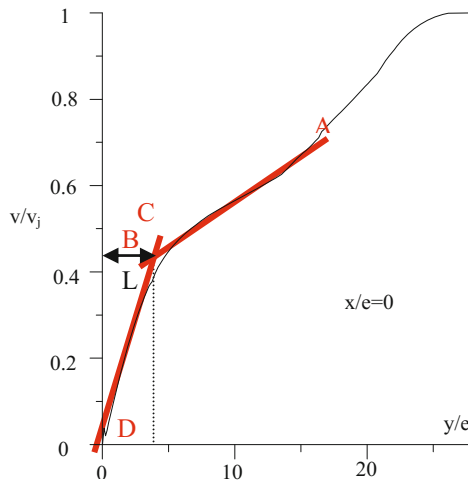
Fig. 3 Profile of the vertical velocity: Re=3000 and h/e=28

Fig. 4 presents the evolution of the turbulent kinetic energy obtained for Re=3000. Contours of the kinetic energy field reveals that its main production takes place in the high-shear regions, exactly in the jet-edge shear layer. The maximum value of the turbulent kinetic energy occurs in the shear layer roughly halfway downstream from the jet exit, then decays in the highly curved jet deflection region, and further downstream in the wall jet. In contrast, as seen from this figure, a high level of turbulence kinetic energy around the stagnation region. This behavior is observed with the experimental work of Uddin et al. (2009).
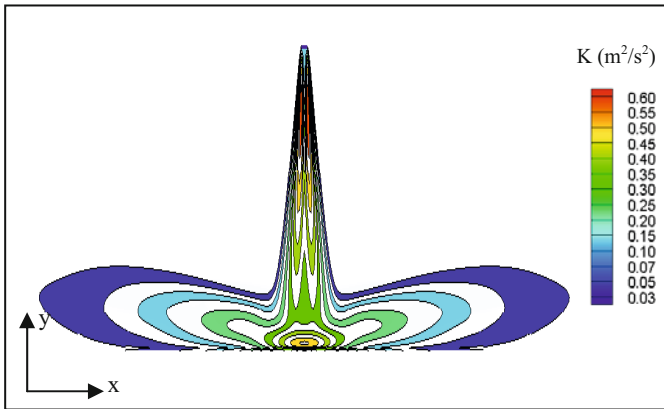
Fig. 4 Contours of the turbulent kinetic energy in the xy-plane for Re=3000 and h/e=28

3.2 Influence of the Reynolds Number on the Flow

Many authors reported interesting phenomena about the influence of Reynolds numbers on the development of the jet. Tailland et al. (1967) have shown that for a range between 8500 and 38000, Reynolds number does not affect the development of the jet. So, we propose to examine the influence of the Reynolds number for Re ≤3000.The Reynolds numbers investigated in this study are (Re=1000, 2000 and 3000).
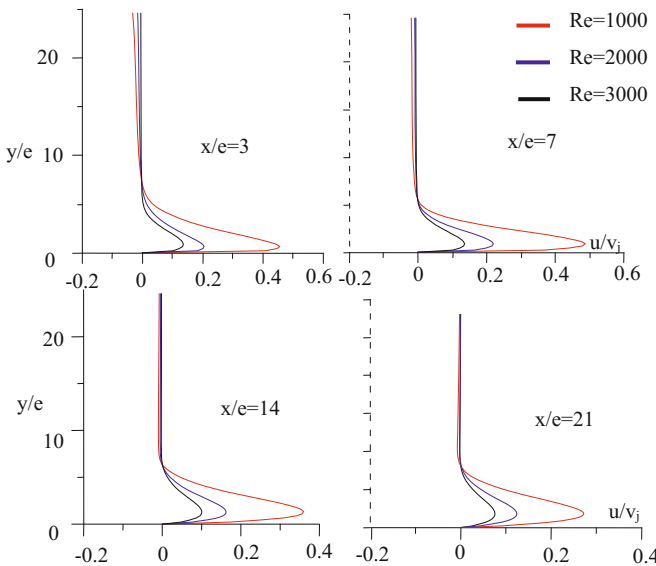
Fig. 5 Distributions of the horizontal velocity along the y-direction for different Reynolds number: h/e=28

Fig. 5 depicts the evolution of the longitudinal velocity normalized by the maximum jet exit velocity (u/v_j) according to the dimensionless vertical coordinate (y/e) and at four positions in the longitudinal direction (x/e =3, 7, 14 and 21). Profiles of the longitudinal velocity are similar for the different Reynolds number. We noticed that the velocity decays from a value close to the nozzle-exit velocity to a value that approaches zero in the stagnation zone. For $y/e=2.5$ and very close to the wall, we note that the velocity reaches a maximal value. However, this maximum value decreases with the jet Reynolds number. Furthermore, the longitudinal velocity decreases gradually along the wall from $x/e=14$ because the surface of the flow becomes larger, so the fluid will have more space to develop and extend.

The velocity decreases gradually when the longitudinal distance increases and when the Reynolds number increases.

In addition, we study the evolution of the Reynolds stresses with varying Reynolds numbers (Re=1000, 2000 and 3000). We propose to examine the evolution of longitudinal profiles of the Reynolds stress ($\overline{u'v'}/v_j^2$) near of the exit jet ($y/e=21$)

for different Reynolds numbers (Fig. 6). This figure shows the important turbulent activities near the boundary of the nozzle ($-2 \leq x/e \leq 2$) which shows the starting of the mixing layers near the shear zone of the jet. The maximum value of the turbulent stress reaches 0.014 for Re=3000 and 0.01 for Re=2000, however, the maximum value of ($\overline{u'v'}/v_j^2$) for Re=1000 didn't exceed 0.008.
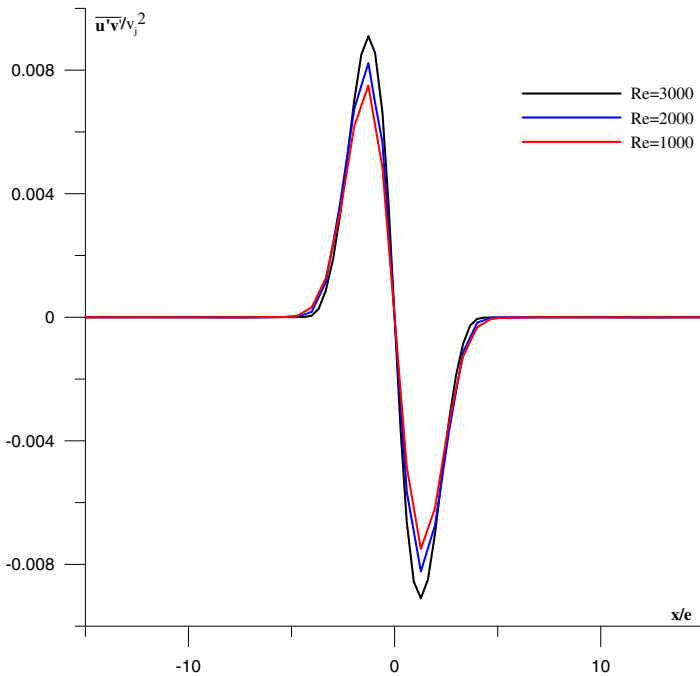
Fig. 6 Distribution of the Reynolds stress along the x-direction: Re=3000, y/e=21 and h/e=28

The distribution of the vertical stresses profiles along the y-direction for x/e=14 and for different Reynolds numbers (Re = 1000, 2000 and 3000) are illustrated in Fig. 7. The vertical stress for Re=1000 (Fig 7 a), is characterized by a maximum value of $\overline{v'v'}/v_j^2 = 0.06$ which appears near the position y/e=3.5, caused by the large shearing stress near the plate. In the development region of the jet in the wall jet, the vertical stress is weaker. This is due to the influence of the presence of recirculation region in the wall jet. Also, we note that the velocity fluctuations increase with increasing Reynolds numbers and reach a state independence on Reynolds number in the stagnation region. In contrast, the longitudinal Reynolds stress ($\overline{u'u'}/v_j^2$) represented in Fig.7 b, is characterized by high values of Reynolds stress seen at the position y/e=2.5, attributed to the turbulence production. This latter is caused by the high mean velocity gradient near the impingement region. Figure 7 b also shows that when the Reynolds number increases from 1000 to 3000, the value of the Reynolds stress increases, so the shear stress increases.
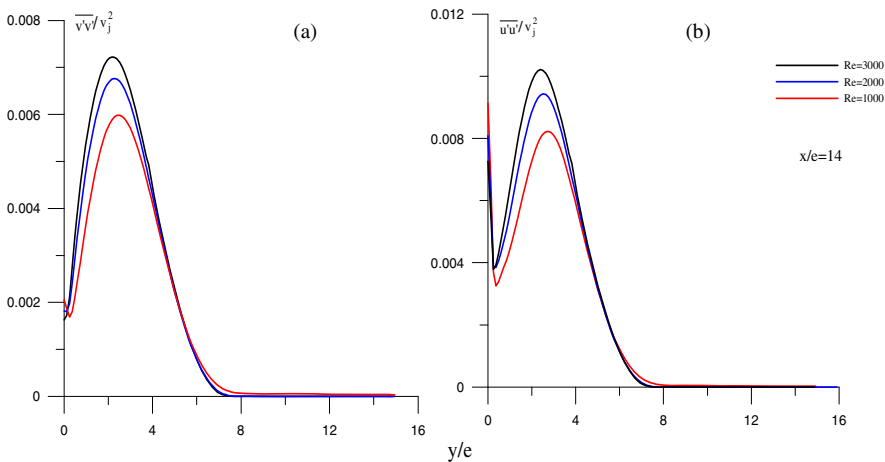
Fig. 7 Distribution of Reynolds stresses along the y-direction for Re=3000, x/e=14 and h/e=28. (a):vertical velocity fluctuation and (b) longitudinal velocity fluctuation

4   Conclusion

A numerical study is conducted to analyze the behavior of a slot air jet impinging on a flat plate, with nozzle to plate separation distances of h/e = 28. This study focuses on the dynamic and turbulent development of the flow. First, we introduce the RSM turbulence model. We noticed that the results indicate that the turbulence model is capable of capturing the main flow feature satisfactorily according to the previous studies findings. Besides, results allowed us to identify three regions: the shear layer of the free jet, the stagnation zone and the wall jet region. Finally, an

analysis of the plane jet was made to examine the influence of the Reynolds num-
ber (Re=1000, 2000 and 3000). According to the mean velocities and the turbu-
lence behavior, the flow field is affected by varying the Reynolds number.

References

Cziesla, T., Biswas, G., Chattopadhyay, H., Mitra, N.K.: Large-eddy simulation of flow and
    heat transfer in an impinging slot jet. Int. J. Heat Fluid Flow 22(5), 500–508 (2001)
Huang, P.G., Mujumdar, A.S., Douglas, W.J.M.: Numerical Prediction of Fluid Flow and
    Heat Transfer under a Turbulent Impinging Slot Jet with Surface Motion and Crossflow.
    Transactions of the ASME 33, 1–8 (1984)
Tianshu, L., Sullivan, J.P.: Heat Transfer and Flow structures in an excited circular imping-
    ing jet. Int. J. Heat Mass Transfer 39(17), 3695–3706 (1996)
Maurel, S., Rey, C., Solliec, C., Pavageau, M.: Caractéristiques cinématiques et
    structurelles d'un jet d'air plan turbulent frappant une plaque plane placée à distance
    variable. Mécaniques & Industries 5, 317–329 (2004)
Perry, A.E., Lim, T.T.: Coherent structures in coflowing jets and wakes. J. Fluid Mech. 88,
    451–463 (1978)
Rohlfs, W.: Haustein. H.D., Garbrecht O., Kneer R, Insights into the local heat transfer of a
    submerged impinging jet: influence of local flow acceleration and vortex-wall interac-
    tion. Int. J. Heat Mass Transfer (2012)
Sakakibara, J., Hishida, K., Phillips, R.C.: On the vortical structure in a plane imping-ing
    jet. J. Fluid Mech. 434, 273–300 (2001)
Sharif, M.A.R., Banerjee, A.: Numerical Analysis of Heat Transfer Due to Confined Slot-
    Jet Impingement on a Moving Plate. Applied Thermal Engineering 29(2-3), 532–540
    (2009)
Sutera, S.P., Maeder, P.F., Kestin, J.: On the sensitivity of heat transfer in the stagna-tion-
    point boundary layer to free-stream vorticity. J. Fluid Mech. 16, 497–520 (1963)
Taillan, A., Mathieu, J.: Jet parietal. J. Mecanique 6, 103–131 (1967)
Uddin, N., Neumann, S.O., Weigand, B.: LES simulations of an impinging jet: on the
    origin of the second peak in the Nusselt number distribution. Int. J. Heat Mass Trans-
    fer 57, 356–368 (2013)
Uddin, N., Neumann, S.O., Weigand, B.: Thermal & Flow Field Analysis of Turbulent
    Swirling Jet Impingement Using Large Eddy Simulation. In: High Performance Compu-
    ting in Science and Engineering, pp. 301–315 (2009)
Yokobori, S., Kasagi, N., Hirata, M.: Transport phenomena at the stagnation region of a
    two-dimensional impinging jet. Trans. Japan Soc. Mech. Engrs. B 49, 1029–1039 (1983)

Effect of Froude Number on the Turbulent Wall Jet in Coflow Stream

Syrine Ben Haj Ayech[1], Sabra Habli[2], Nejla Mahjoub Saïd[2],
Hervé Bournot[3], and George Le Palec[3]

[1] LGM, École Nationale d'Ingénieurs de Monastir, Université de Monastir, Tunisie
 ayechsyrine@hotmail.com
[2] LGM, Institut Préparatoire aux Etudes d'Ingénieurs de Monastir,
 Université de Monastir, Tunisie
 sabra.habli@fsm.rnu.tn, nejla.mahjoub@fsm.rnu.tn
[3] IUSTI, UMR 7343, Faculté des Sciences, Université de Aix-Marseille, France
 georges.lepalec@univ-amu.fr

Abstract. The influence of the coflow velocity ratio on the behavior of a non iso-thermal turbulent wall jet has been determined numerically. The numerical resolution of the governing equations is carried out using a finite difference method. Turbulence modeling is performed by a modified low-Reynolds number k–ε model. In this work, we are interested in the study of the effect of the coflow stream on the behavior of the dynamic and thermal properties of the wall jet subjected to a constant temperature. A comparison with a simple wall jet is carried out. Further, we will examine the influence of the Froude number on the wall jet emerging in a coflow stream.

Keywords: wall jet, turbulent, coflow stream, velocity ratio, natural convection, mixed convection, forced convection.

1   Introduction

Turbulent wall jet is formed when a fluid is discharged through a rectangular slot at a high velocity into a medium of the same fluid that is either stagnant or moving. This type of flow is widely used in many engineering processes such as inlet devices in ventilation, separation control in airfoils and film cooling of turbine blades. A wall jet has been the subject of several studies that combine both dynamic and thermal measurements in order to predict the flow behavior (Kechiche et al., (2004); Matthew 2010). An experimental study has been conducted by Tsuji and Nagano (1988) on the turbulent natural convection boundary layer in air along a vertical plate. The heat transfer rate and wall shear stress are determined by measuring mean temperature and mean velocity profiles near the wall. The concept of the viscous sublayer and the overall analogy between the velocity field and thermal field near the wall are discussed. Measurements are made by Abdulnour et al. (2002) on the local convection heat transfer coefficient for different boundary

conditions. These authors showed that the effect of the wall thermal conditions on the heat transfer coefficient by convection between the plate and the jet is significant, only very close to the ejection nozzle. Esmaeilzadeh et al. (2007) investigated the hydrodynamic and the heat transfer of the wall jet. A direct numerical simulation (DNS) is conducted by Ahlmen et al. (2007) to study a turbulent plane wall jet including the mixing of a passive scalar. The wall jet was discharged into a coflow stream with an inlet Reynolds numbers of Re=2000. Ben Haj Ayech et al. (2014) conducted a numerical study on the dynamic and thermal characteristics of an isothermal and non-isothermal laminar wall jet in coflowing stream. These authors found that results for low Grashof numbers (forced convection) are similar to the isothermal flow. For mixed convection, they noticed the absence of the influence of the coflow velocity on most parameters.

In this work a numerical study is investigated on the effect of the coflowing ambient stream on the dynamic and thermal behavior of a turbulent wall jet in comparison with a simple wall jet (jet evolving in an environment at rest). Further, we will examine the effect of the Froude number on the wall jet emerging in a coflow stream.

2   Problem Formulation

2.1   Assumptions

An incompressible flow jet issuing from a rectangular nozzle, with a slot width b, tangentially to an infinite flat plate is considered (Fig 1).The problem is valid for a two-dimensional boundary layer flow. The turbulent flow is steady and satisfies the Boussinesq approximation.
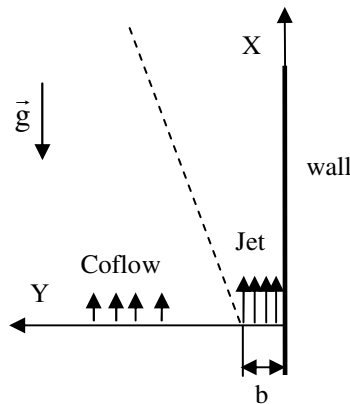
Fig. 1 Geometric configuration

2.2 Governing Equations

Using these following dimensionless variables:

$$X = \frac{x}{b}, \quad Y = \frac{y}{b}, \quad U = \frac{u}{u_0}, \quad V = \frac{v}{u_0}, \quad \theta = \frac{T - T_\infty}{T_p - T_\infty}, \quad K = \frac{k}{u_0^2} \quad \text{and} \quad E = \frac{\varepsilon\, b}{u_0^3} \tag{1}$$

The time averaging of the conservation equations can be expressed as follow:

$$\frac{\partial U}{\partial X} + \frac{\partial V}{\partial Y} = 0 \tag{2}$$

$$U\frac{\partial U}{\partial X} + V\frac{\partial U}{\partial Y} = \frac{\partial}{\partial Y}\left[\frac{1}{Re}\frac{\partial U}{\partial Y} - \overline{U'V'}\right] + \left(\frac{\theta}{Fr}\right) \tag{3}$$

$$U\frac{\partial \theta}{\partial X} + V\frac{\partial \theta}{\partial Y} = \frac{\partial}{\partial Y}\left[\frac{1}{Re\,Pr}\frac{\partial \theta}{\partial Y} - \overline{V'\theta'}\right] \tag{4}$$

The turbulence model adopted for the cloture of this problem is a modified version of the first order low Reynolds number turbulence model. This model is proposed by Herrero et al. (1991) and corrected by the empirical function C_μ proposed by Ljuboja and Rodi (1980). In this model, the equations of the kinetic energy of turbulence and its rate of dissipation can be written as:

$$U\frac{\partial K}{\partial X} + V\frac{\partial K}{\partial Y} = \left[\left(\frac{1}{Re} + \frac{\upsilon_T}{\sigma_k}\right)\frac{\partial K}{\partial Y}\right] + \upsilon_T\left(\frac{\partial U}{\partial Y}\right)^2 - E - \left(\frac{1}{Fr}\frac{\upsilon_T}{Pr_t}\frac{\partial \theta}{\partial X}\right) \tag{5}$$

$$U\frac{\partial E}{\partial X} + V\frac{\partial E}{\partial Y} = \frac{\partial}{\partial Y}\left[\left(\frac{1}{Re} + \frac{\upsilon_T}{\sigma_\varepsilon}\right)\frac{\partial E}{\partial Y}\right] + C_{\varepsilon 1}f_1\frac{E}{K}\upsilon_T\left(\frac{\partial U}{\partial Y}\right)^2 - C_{\varepsilon 2}f_2\frac{E^2}{K} - \left(\frac{C_{\varepsilon 1}}{Fr}\frac{E}{K}\frac{\upsilon_T}{Pr_t}\frac{\partial \theta}{\partial X}\right) \tag{6}$$

With

$$\upsilon_T = C_\mu f_\mu \frac{K^2}{E} \tag{7}$$

The Reynolds shear stress and the turbulent heat flux are given by the following relationships:

$$\overline{U'V'} = -\upsilon_T\frac{\partial U}{\partial Y} \quad \text{and} \quad \overline{V'\theta'} = -\frac{\upsilon_T}{Pr_t}\frac{\partial \theta}{\partial Y} \tag{8}$$

Functions as well as empirical constants used in the system of equations are those proposed by Herrero et al. (1991):

$$C_{\varepsilon 1} = 1.44, \quad C_{\varepsilon 2} = 1.92, \quad \sigma_k = 1.0 \quad \text{and} \quad \sigma_\varepsilon = 1.3 \tag{9}$$

The damping functions are written as:

$$f_\mu = \left[1 - exp(-0.066\, Re_k)\right]^2 \times \left[1 + 500\, exp\left(-0.0055\, Re_k \big/ Re_t\right)\right] \quad (10)$$

$$f_1 = 1 + \left(0.05\big/ f_\mu\right)^2 \quad (11)$$

$$f_2 = 1 - \left(0.3\big/ B\right) exp\left(- Re_t^2\right) \quad (12)$$

Avec $B = 1 - 0.7\, exp\left(- Re_k\right)$ $\qquad\qquad$ (13)

Where Re_k $\left(Re_k = y\sqrt{k}\big/v\right)$ and Re_t $\left(Re_t = k^2\big/v\varepsilon\right)$ represent the turbulence Reynolds numbers.

For the coefficient C_μ, we used the function given by Ljuboja and Rodi (1980):

$$C_\mu = 0.09 G_1 . G_2$$

$$\text{with } G_1 = \left(\frac{1 + \dfrac{3}{2}\dfrac{c_2 c_2'}{c_2}\, f}{1 + \dfrac{3}{2}\dfrac{c_1'}{c_1}}\right) , \quad G_2 = \left(\frac{1 - 2\dfrac{c_2 c_2' \dfrac{P}{\varepsilon}}{c_1 - 1 + c_2 \dfrac{P}{\varepsilon}}\, f}{1 + 2\dfrac{c_1'}{c_1 + \dfrac{P}{\varepsilon} - 1}}\right) \qquad (14)$$

$$f = \frac{k^{3/2}}{c_w\, y\varepsilon} \quad , \quad P = -\overline{u'v'}\frac{\partial u}{\partial y} \qquad (15)$$

The constants of C_μ used for the formulation are written as follow:

$$c_1 = 0.8 \, , \ c_2 = 0.6 \, , \ c_1' = 0.6 \, , \ c_2' = 0.3 \text{ and } c_w = 3.72$$

The boundary conditions for the wall jet written in dimensionless form are:

$$X = 0 : \begin{cases} 0 < Y < 1 : U = 1 ; V = 0 ; \theta = 0 ; K = 0.01 ; E = 0.0016 \\ Y \geq 1 : U = r ; V = 0 ; \theta = 0 ; K = 0 ; E = 0 \end{cases}$$

$$X > 0 : \begin{cases} Y = 0 : U = 0 ; V = 0 ; \theta = 1 ; K = 0 ; \dfrac{\partial E}{\partial Y} = 0 \\ Y \rightarrow \infty : U = r ; V = 0 ; \theta = 0 ; K = 0 ; E = 0 \end{cases} \qquad (16)$$

3   Numerical Resolution Method

The numerical solution of the equations governing the flow is provided by a finite difference method using an implicit scheme. The in-house code uses a parabolized marching algorithm in the flow direction. This method used an offsetted grid for the numerical stability: The transport equations of momentum, energy, turbulent kinetic energy and its dissipation rate are discretized at the nodes $(i, j+1/2)$, while the continuity equation is discredited at the node. In the longitudinal direction, a non-uniform grid is used. Indeed, the calculation step is taken very thin in the vicinity of the nozzle exit. Then, a little further, we increase its value gradually, in order to be able to go farther in the jet. In the transverse direction of the flow, the velocity and temperature gradients are very high close to the wall and therefore a non-uniform mesh is chosen. The convergence of the total solution is considered attained when the relative change in two successive iterations of the solution at each node of the field is lower than 10^{-7}.

4   Results and Discussion

4.1   Effect of the Coflow Stream on the Wall Jet in Natural Convection

In this section, we will study the effect of the coflow velocity on a non-isothermal wall jet in natural convection (Fr=2) and for a Reynolds number of Re=18000.

The effect of the coflow velocity on the longitudinal distribution of the excess maximum velocity ($U_{exm}=U_m-U_{co}$) is shown in Fig 2. In the vicinity of the nozzle, the profiles of the excess velocity remain constant and parallel with that of a simple jet (jet in a medium at rest). Downstream from the jet exit, in the plume zone, a quite good agreement appears between results obtained for a wall jet in coflow stream and that of a simple jet.
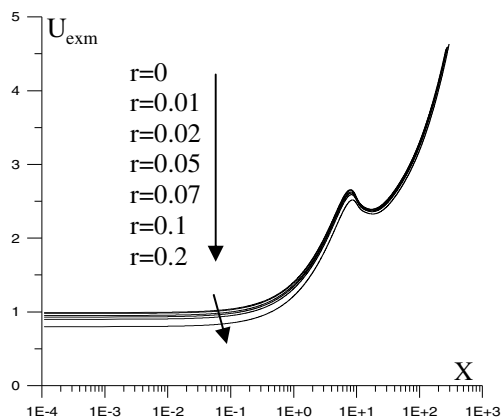
Fig. 2 Longitudinal evolution of the maximum velocity for different velocity ratios: Fr = 2 and Re=18000

In fig 3, we have analyzed the influence of the coflow stream on the longitudinal development of the local Nusselt number in natural convection (Fr=2).

This figure indicates a perfect agreement between the profiles of the local Nusselt number near the orifice for different velocity ratios. In the transition zone and the plume region, an increase of the velocity ratio generates a negligible decrease in the local Nusselt number. This means that, for low Froude numbers (a flow in natural convection) the effect of buoyancy forces is predominant over inertia forces, and the co-flow effect is negligible.
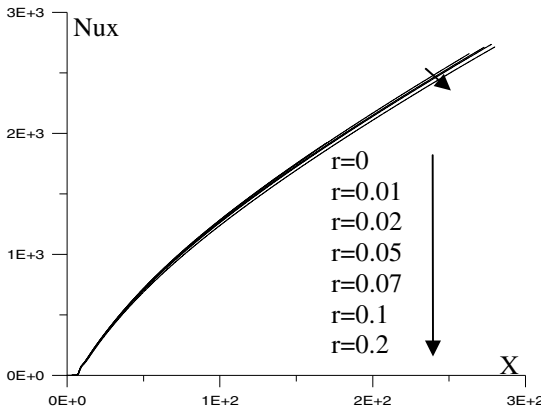
Fig. 3 Longitudinal evolution of the local Nusselt number for different velocity ratios: Fr=2 and Re=18000
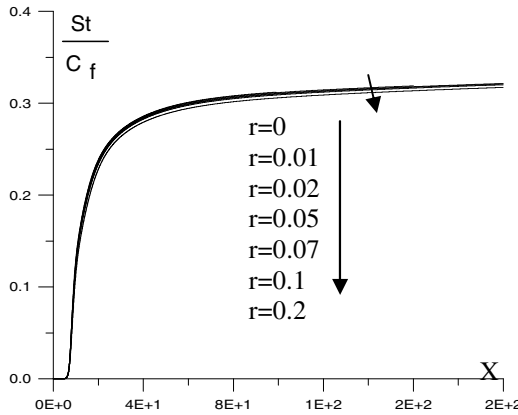
Fig. 4 Longitudinal evolution of the Reynolds analogy factor for different velocity ratios: Fr = 2 and Re=18000

The longitudinal distributions of the Reynolds analogy factor defined by the relationship $\dfrac{St}{Cf}$ in a coflow stream and in a medium at rest are plotted in Fig 4. Results show that the velocity ratio does not have any influence on the Reynolds analogy factor for r≤0.1 and the flow behaves as a simple wall jet (wall jet in a medium at rest).This is expected since the profiles of the ratio $\dfrac{St}{Cf}$ coincide for different velocity ratios. It is found that, for r ≥0.2 , the introduction of such perturbation leads to a slight reduction in the Reynolds analogy factor.

4.2   Effect of the Froude Number on the Wall Jet in Coflow Stream

The influence of Froude number on the wall jet emerging in a parallel coflow stream ($r = u_{co}/u_0$ =0.2) is shown in this part. The values of the Froude number are ranging from natural convection to forced convection passing by mixed convection (Fr=0.2, 2, 20, 100, ∞) and results of air flow (Pr=0.71) are presented in turbulent regime (Re=18000).

The axial evolution of the maximum longitudinal velocity of the jet is shown in the fig 5 for various Froude numbers. In a buoyant wall jet, three distinct regions exist. The first is an initial non-buoyant region called pure jet, where the buoyancy and coflow effects are not important and which occurs near the jet exit. In this region, the maximum velocity profiles remain constant and behave as a jet in a forced convection ($Fr=\infty$). This is followed by a second, transition region where the buoyancy and the inertia play equally important roles in determining the characteristics of the jet. In this region, the maximum velocity may go above or below the value at the output of the jet depending on the size of the buoyancy forces and inertia. Here, the coflow effect is no longer negligible. The third region, where the flow is away from the source, which is a plume, inertia effects are negligible and the buoyancy becomes the only important parameter. In this region, the maximum velocity increases with the distance X. Further, a decrease of Froude number leads to a shortening of the length of the pure jet region, and therefore the maximum velocity reaches faster the region of established flow.

The longitudinal distributions of the dynamic half-width are given in Fig 6 for different Froude numbers by maintaining the Reynolds number equal to Re=18000 and the velocity ratio (r=0.2). Near the jet exit, the half-width is constant for various Froude number and is independent of the coflow stream effect. As the Froude number increases, the length of the initial region increases. The influence of the heating wall on the dynamic half width begins at distances varying according to the importance of buoyancy and inertia forces. In the transition and plume regions, the half-width is higher for large values of the Froude number. Further, for low Froude numbers (a flow in natural convection) the effect of buoyancy forces, which become predominant over inertia forces, appear for low values of X and therefore the dynamic half-width reaches faster the region of established flow.
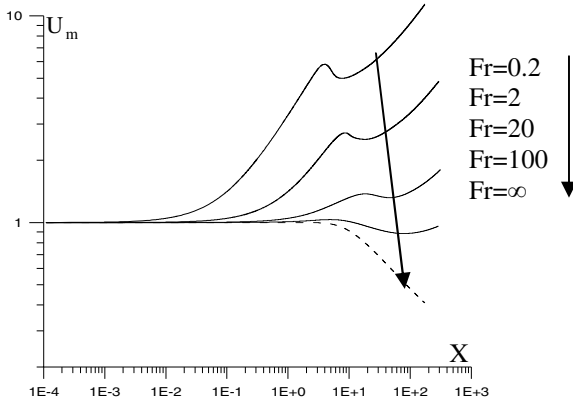
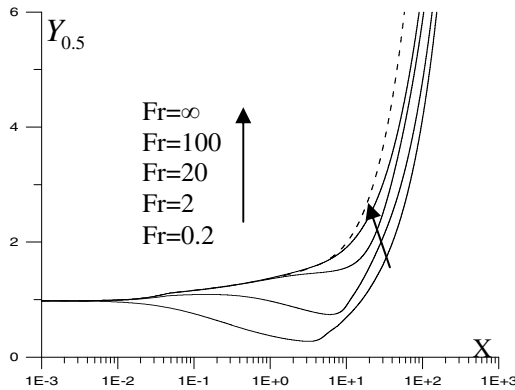**Fig. 5** Longitudinal evolution of the maximum velocity for different Froude numbers: r=0.2 and Re=18000

Fig. 6 Longitudinal evolution of the dynamic half-width for different Froude numbers: r=0.2 and Re=18000

The influence of the wall heating on the longitudinal distribution of the maximum turbulent kinetic is plotted in Fig 7 for r=0.2 and for different Froude numbers. Examination of this figure shows that, near the nozzle exit (in the pure jet region) and in the transition region, the maximum turbulent kinetic energy increase for low Froude numbers (natural convection), while decreases for large Froude numbers (in forced convection). Far from the nozzle exit (in the plume region), profiles of the maximum turbulent kinetic energy are constant and parallel. In this region, a decrease of Froude numbers leads to an increase in the maximum turbulent kinetic energy.
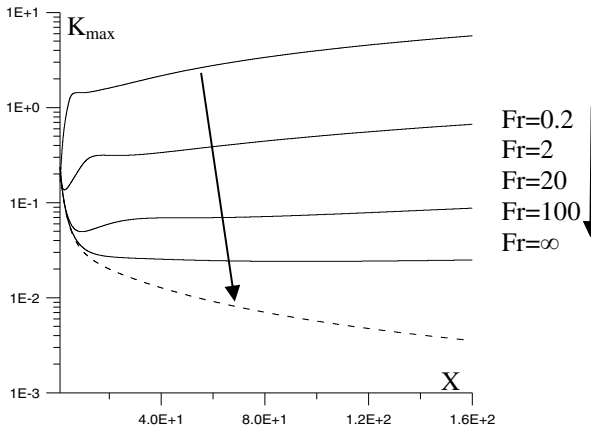
Fig. 7 Longitudinal evolution of the maximum turbulent kinetic energy for different Froude numbers: r=0.2 and Re=18000

5   Conclusion

This work investigates a numerical study of non-isothermal turbulent wall jet evolving in a coflow stream. The discussion focuses on the effect of the coflow velocity on the dynamic and thermal characteristics of the wall jet in comparison with a wall jet in a medium at rest. Further, we have examined the influence of Froude number on the wall jet in coflow stream.

It is found that, the velocity ratio does not have any influence on the dynamic and thermal parameters, near the nozzle exit (in the pure jet region) and profiles are found to be similar to that of a simple wall jet (wall jet emerging in a medium at rest). However, away from the jet exit in the transition zone and in the plume area, the coflow stream slightly influences the flow.

The influence of the Froude number on the wall jet emerging in a coflow stream (r=0.2) is discussed. We have shown that the influence of the heating wall on the different parameters begins at distances varying according to the importance of buoyancy and inertia forces.

Therefore, this study develops a new perspective to study the effect of a directed coflow stream on the flow in order to highlight the mixing of the two streams of fluid.

Nomenclature

Symbols

b   Ejection nozzle thickness, (m)

C_f Friction coefficient, $\left(Cf = 2\mu(\partial u/\partial y)_{y=0}\big/\rho u_m^2 \right)$

C_p Specific heat at constant pressure of the fluid, $(Jkg^{-1}k^{-1})$

Fr   Froude number ($Fr = Re^2/Gr$)

Gr   Grashof number ($Gr = g\beta b^3 (T_p - T_\infty)/v^2$)

h   Local convection coefficient, $(wm^{-2}k^{-1})$

K   Turbulent kinetic energy, (m^2s^{-2})

Nu   Local Nusselt number $(Nu = hx/\lambda)$

Pr   Prandtl number $(P_r = \mu C_p/\lambda)$

Pr_t Turbulent Prandtl number

r   Velocity ratio ($r = u_{co}/u_0$)

Re   Reynolds number $(Re = u_0 b/v)$

St   local Stanton number $\dfrac{h}{\rho C_p u_m}$

u, v   Longitudinal and transverse components of the velocity, respectively, (ms^{-1})

$u_{ex} = u - u_{co}$ Longitudinal excess velocity, (ms^{-1})

x,   Longitudinal and transversal coordinate, (m)

$Y_{0.5}$ Dynamic jet half-width, value of the lateral distance at which longitudinal velocity is half of the maximum value, (m)

Greek symbol

ε   Dissipation rate of k, $(m^2.s^{-3})$

ρ   Fluid density, $(kg\ m^{-3})$

μ   Dynamic viscosity of the fluid, $(kg\ m^{-1}\ s^{-1})$

λ   Thermal conductivity of the fluid, $(w\ m^{-1}k)$

υ   Fluid kinematic viscosity (μ/ρ), $(m^2\ s^{-1})$

α   Thermal diffusivity of the fluid (v/P_r), (m^2s^{-1})

Subscripts

P   Wall value

0   Value at the jet exit

∞   Ambient conditions value

M   Maximum value

Co   Coflow stream

ex   Excess

References

Abdulnour, R.S., Willenborg, K., McGrath, J.J., Foss, J.F., AbdulNour, B.S.: Measurements of the convection heat transfer coefficient for a planar wall jet: uniform temperature and uniform heat flux boundary. Experimental Thermal and Fluid Science 22, 123–131 (2000)

Ahlmen, D., Brethouwer, G., Johansson, A.V.: Direct numerical simulation of a plane turbulent wall jet including scalar mixing. Physics of Fluids 19, 65–102 (2007)

Ben Haj Ayech, S., Habli, S., Mahjoub Said, N., Bournot, H., Le Palec, G.: Effect of the coflow stream on a plane wall jet. Heat Mass Transfer 50, 1685–1697 (2014)

Esmaeilzadeh, E., Eslami, G., Beyghi, F.: In Investigation into the effect of injection parameter on hydrodynamic and heat transfer over a Flat plate in the presence of com-pound wall jet. In: 16th Australasian Fluid Mechanics, pp. 831–835 (2007)

Herrero, J., Grau, F.X., Grifoll, J., Frances, G.: A near wall k–e formulation for high Prandtl number heat transfer. Int. J. Heat Mass Trans. 34, 711–721 (1991)

Kechiche, J., Mhiri, H., Le Palec, G., Bournot, P.: Application of low Reynolds k-e turbulence models to the study of turbulent wall jet. Int. J. Thermal Sciences 43, 201–212 (2004)

Ljuboja, M., Rodi, W.: Calculation of turbulent wall jets with an algebraic Reynolds stress model. Journal of Fluids Engineering 102, 102–350 (1980)

Matthew, D.: An experimental study of a plane turbulent wall jet using particle image velocimetry, Master of Science in mechanical engineering, University of Saskatchewan, Canada (2010)

Nizou, P.Y., Tida, T.: Transferts de chaleur et de quantité de mouvement dans les jets pariétaux plans turbulents. Int. J. Heat Mass Transfer 38, 1187–1200 (1995)

Tsuji, T., Nagano, Y.: Characteristics of a turbulent natural convection boundary layer along a vertical flat plate. Int. J. Heat Mass Transfer 31, 1723–1734 (1987)

Effect of Water Hammer on Bent Pipes in the Absence or Presence of a Pre-crack

Manel Dalleli[1], Mohamed Ali Bouaziz[2], Mohamed Amine Guidara[2],
Ezzeddine Hadj-Taïeb[1], Christian Schmitt[2], and Zitouni Azari[2]

[1] Laboratoire de Mécanique des Fluides Appliqués, Génie des Procédés et Environnement,
Ecole Nationale d'Ingénieurs de Sfax, BP 1173, 3038, Sfax, Tunisie
`manel.dalleli@gmail.com`, `ezed.hadj@enis.rnu.tn`
[2] Laboratoire de Biomécanique, Polymères et Structures (LaBPS),
Ecole Nationale d'Ingénieurs de Metz, 57070 Metz, France
`schmitt@enim.fr`, `azari@enim.fr`,
`mohamedali.bouaziz@gmail.com`, `gem3_guidara@yahoo.fr`

Abstract. In this study, transient pressure in piped liquid due to waterhammer is a function of structural restraint at elbows. To study the effect of this phenomenon on polyethylene elbowed pipe networks, experimental tests were performed on polyethylene bent pipes, either in the absence or presence of a pre-crack by measuring the toughness and determining the mechanical behavior of HDPE. These characteristics were been used to perform simulations using ABAQUS software, the internal pressure increase, to investigate the safety of bent pipes using an angle of 90 ° bend with 11.4 mm thickness and a right portion of 150 mm as length.

We know that the crack size has a great influence on the fracture energy but we have also shown that the position of the pre-crack has effect on the safety of bent pipes, this is linked to the concentration of the stress.

Keywords: pipe, elbow, waterhammer, pre-crack, polyethylene HD.

1 Introduction

In conventional transient flow analysis pipe elasticity is incorporated in the propagation speed of the pressure waves [Streeter and Wylie (1967)]. Pipe inertia and pipe motion are not taken into account. This is acceptable for rigidly anchored pipe systems. For less restrained systems fluid-structure interaction may become of importance [Skalak (1956), Thorley (1969) and Williams (1977)]. In that case the dynamic behaviour of liquid and pipe system should be treated simultaneously.

Three liquid-pipe interaction mechanisms can be distinguished [Tijselling (1993)]: ftiction coupling, Poisson coupling and junction coupling. Friction coupling represents the mutual ftiction between liquid and pipe. The more important Poisson coupling relates the pressure in the liquid to the axial stresses in the pipe through the radial contraction or expansion of the pipe wall. It is named

after Poisson in connection with his contraction coefficient ν, and is associated with the breathing or hoop mode of the pipe. Poisson coupling leads to precursor waves [Stuckenbruck et al. (1985)]. These are stress-wave induced disturbances in the liquid which travel faster than, and hence in front of, the classical waterhammer waves. Where ftiction and Poisson coupling act along the entire pipe, junction coupling acts at specific points in a pipe system such as unrestrained valves, bends and tee [Hatfield et al. (1982) and Wiggert et al. (1987)].

The breaking of the elbowed pipes, quite common phenomenon in urban areas, starts by default under the effect of stresses caused by an unusual load (waterhammer). High density polyethylene has excellent resistance to chemical corrosion, an outstanding ductile property and also a viscoelastic behavior that gives it a good resistance to waterhammer.

We are interested in this paper in investigating the security of high density polyethylene elbowed pipes when it is exposed to the water hammer phenomenon.

We start by presenting some results in the case of metallic pipe networks. Then we performs experimental tests in order to determine mechanical behavior (stress-strain curve) and failure analysis (J_{Ic}) of high density polyethylene.

The finite element simulation was performed on ABAQUS to calculate the integral J around the crack type, placed in different positions of the bend pipe under internal pressure and accurate results, the mesh was created using HyperMesh in three dimensions.

The study of the evolution of damage measured on the elbowed pipes is based on the calculation of the integral J (Rice 1968).

2   Waterhammer in Elbowed Copper Pipe Networks

Figure 1 is a schematic of the experimental pipe setup studied by Wiggert et al. (1985). It includes 47.9 meters of 26 mm inside diameter copper pipe. The pipe
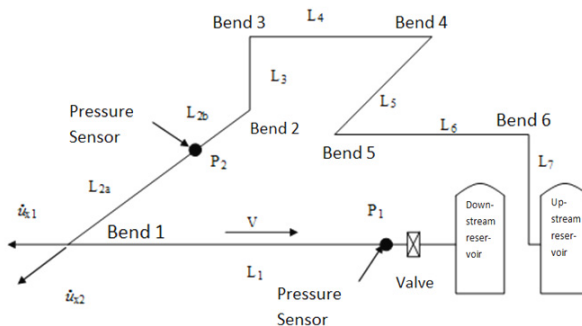
Fig. 1 Experimental setup [Wiggert et al. (1985)]

material constants are: the density ρ=8940 Kg m^3, Young's modulus E = 117GPa, Poisson's ratio n = 0.34 and thickness e = 1.27mm. The system has a total of six elbows with radius of 20.6 mm. The elbow to be studied is elbow 1 and connecting pipe reaches L1 and L2 are suspended by wires that contribu $\rho = 8940 kgm^3$ te negligible stiffness, inertia and damping for motion in the plane of the elbow.

Figure 2 shows numerical and experimental pressure responses at P1 and P2. The pressure response at P1 in Case B is significantly different from that of Case A. The pressure fluctuates due to the elbow motion and the precursor strass wave in the pipe wall. The elbow motions result in increase in pressures of 22%.
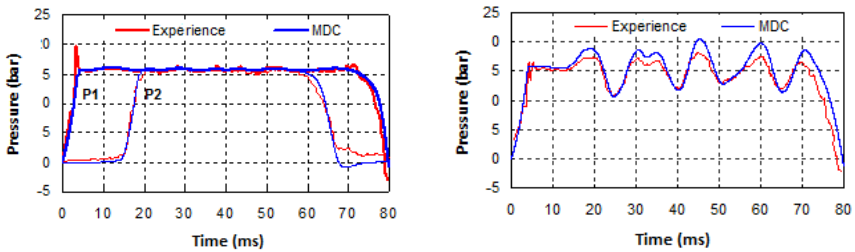
Case A: Immobile Elbows 1 and 2   Case B: No restrained Elbows 1 and 2

Fig. 2 Numerical and experimental pressures at P1 and P2

3   Mechanical behavior and Failure Analysis of High Density Polyethylene

3.1   Tensile Testing

Tensile test was conducted on a standard traction-compression machine piloted in displacement mode using an extensimeter to measure the deformation of the specimen were carried out at three different test strain rates ($\dot{\varepsilon}$) of 10^{-3}, 5.10^{-3} and 10^{-2} s-1. Stress- strain curves for each strain rate are represented in figure 3.

3.2   Determination of Fracture Toughness JIC

For materials with an elasto-plastic behavior, toughness is not defined by a single value but by curves (named R) describing the energy requirements of an additional advancement of the crack after priming. They indicate both when (energy / area), and how (stability of propagation) rupture will occur.

ASTM D 6068 standard describes the conditions for determining the JR curves elasto-plastic polymer materials with a spread of slow and steady mode I crack in a state of plane strain.

The general configuration of the test (specimen type, experimental, etc.) is identical to that performed in the linear-elastic fracture mechanics (ASTM D 5045). The proposed construction method of JR curves requires testing multiple specimens (7 minimum) up arrow or different levels of openness, and an optical measurement (visual) actual crack advances corresponding microscope from the fracture surface of the specimens.

Each sample leads to the determination of a pair of values (J, Δ_{ap}.) that is to say a point of the curve JR.

All tests were carried out at room temperature using partial unloading compliance method on a servo-hydraulic testing machine.
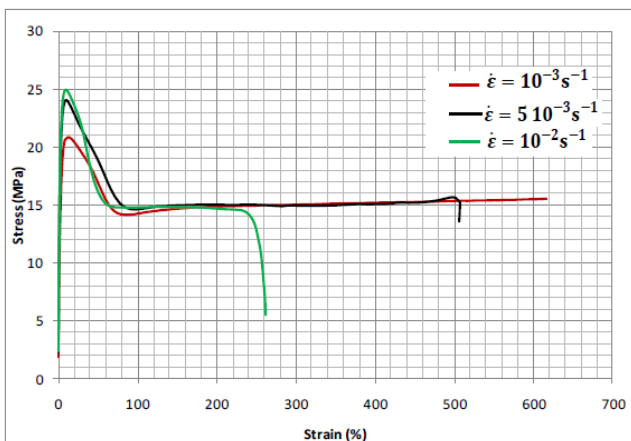
Fig. 3 Stress-strain curves for the HDPE

The crack growth was followed by an optical microscope on specimen cracked surfaces to calculate the average physical crack extension Δ_{ap}.

The energy required to extend the crack, U, is used to calculate J. The total energy, U_T, determined from the area under the load versus load-point displacement curve obtained for each specimen is the sum of U and U_i, the indentation energy. And J is calculated according to the following relation:

$$J = \frac{\eta U}{b(W - a_0)}$$

Figure 4 shows a representative J-Δa curve obtained from the 8 mm thick CT specimen.
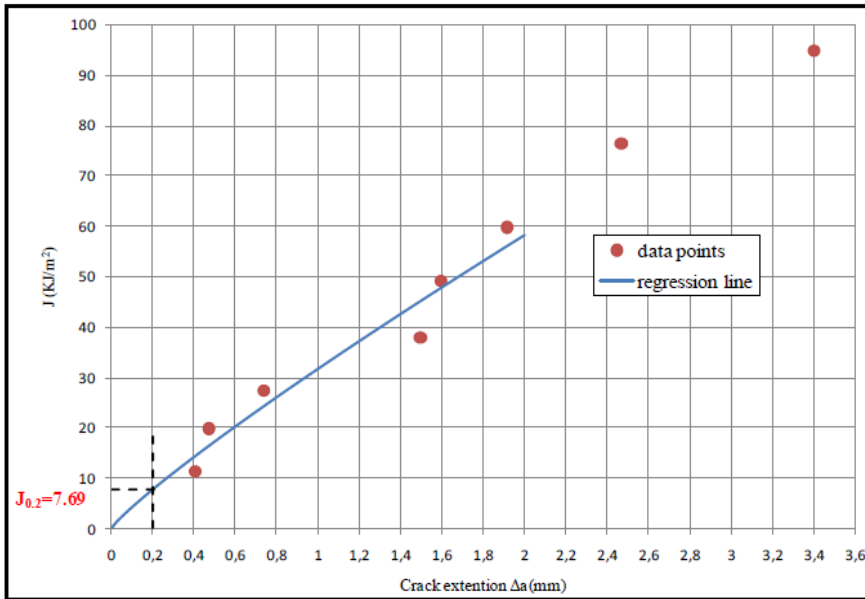
Fig. 4 Fracture Resistance vs Crack Growth

The intersection point between the regression line and 0.2 mm offset line gives a candidate value J_Q which becomes J_{IC} provided that the validity requirements are satisfied. In the case of HDPE PE100, $J_{IC} = 7.69 KJ / m^2$.

4   Properties of the Pipe Elbow Used

The bent pipes used are in high density polyethylene. It's stronger than standard polyethylene, acts as an effective barrier against moisture and remains solid at room temperature. It resists insects, rot and other chemicals. The properties of this material are given below in table 1.
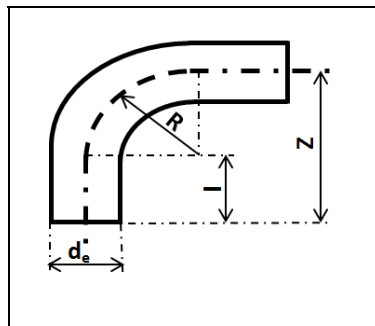
Fig. 5 Bent pipe used

The dimensions of the bent pipe, showed in Figure 5, external diameter de=125mm, length right part l=150 mm, radius of bend R=d$_e$=125mm and length Z=275 mm.

Table 1 Mecanical properties of PEHD material

Proportional limit (MPa)	Tensile strength(MPa)	Elongation at fracture (%)	Hardening exponent	strength coefficient K (MPa)
$\sigma_y = 15$	$\sigma_u = 21\text{-}25$	250-700	n = 0,23	42

5   Numerical Study

We started by a general study on the bent pipes in good condition to locate the stress concentration region. The material used is high-density polyethylene (elastoplastic materials).

The calculations are made with the geometrically nonlinear ABAQUS software (large displacements) by taking into account the variation of the strain rate. A pressure of about 60 bar were applied.

It is clear from Figure 6 that the intrados part presents a stress concentration
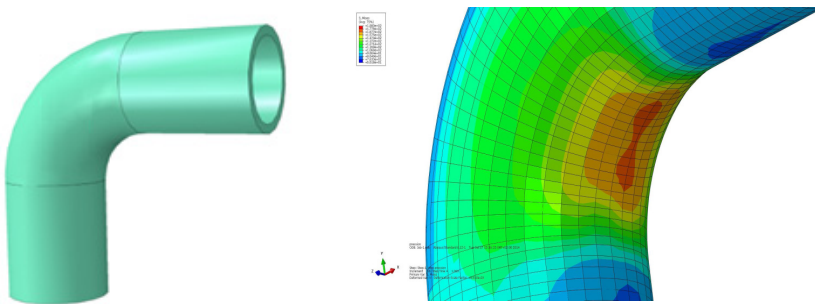
Fig. 6 Elbow without defect under interior pressure

The methods, originally developed to characterize the elastic-plastic fracture of ductile metallic materials, are most commonly used to characterize ductile polymers these methods are based on the concept of the J- integral to determine plane- strain fracture toughness values(Steve Lampman 2003).

The crack is initiated when J reaches a critical value J_{IC}, which is an intrinsic characteristic of the material. The value of J_{IC} is determined using the compact tension method CT. In the case of HDPE PE100, $J_{IC} = 7.69 KJ / m^2$.

5.1   Crack in the Middle

It will be assumed now that we have a fault of fissure type, with a depth nearly half the thickness, on the middle part of the elbow.

For reasons of simplification and to reduce the computation time, only a quarter of the model is studied. The mesh was created using HyperMesh in three dimensions with quadratic elements (figure 7).

With the same calculation software ABAQUS and applying the same pressure (60 bar), we determined the curve of variation of the fracture toughness J versus time.

The figure 8 shows the evolution of the fracture energy in different contours in the normal plane to the crack front. They converge at the same value.

The curve of the fracture energy versus pressure and the value of the critical failure energy ($J_{1c} = 7.69 KJ / m^2$) allow to determine the ultimate pressure ($P_u = 196*60/360 = 32.67 bar$) which lead to the crack initiation.
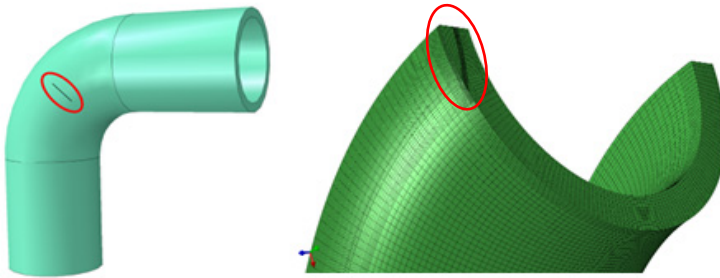
Fig. 7 Bent conduit with a crack to the middle
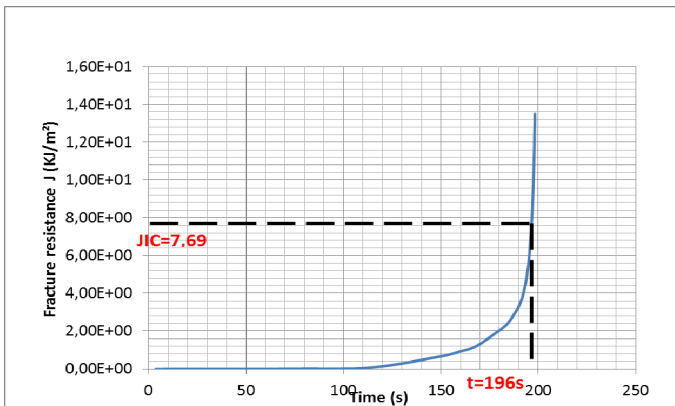
Fig. 8 Variation of the fracture toughness J versus time

5.2 *Intrados Crack*

We took the same simulation, but this time the crack is on the intrados surface of the elbow (fig.9).

We have already seen in Fig. 6 that we has a stress concentration in the intrados portion of the bent pipe but the curve of evolution of fracture resistance in the case where the pre-crack is located on the intrados surface shows that we cannot reach rupture even if the same internal pressure is applied .

This can be connected to the discharge phenomenon between stress concentration and crack, so the stress concentration is no longer at the intrados part of the bend and there is no rupture.

The experimental tests will be performed to verify the theoretical results that has already found.
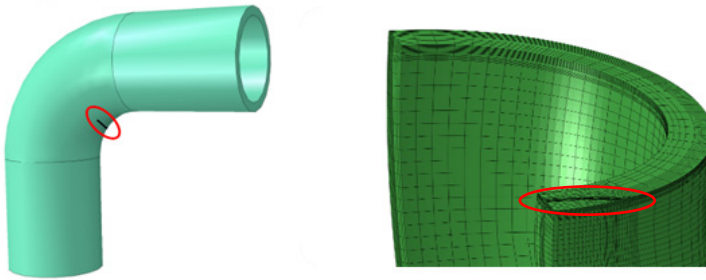
Fig. 9 Bent conduit with an intrados crack
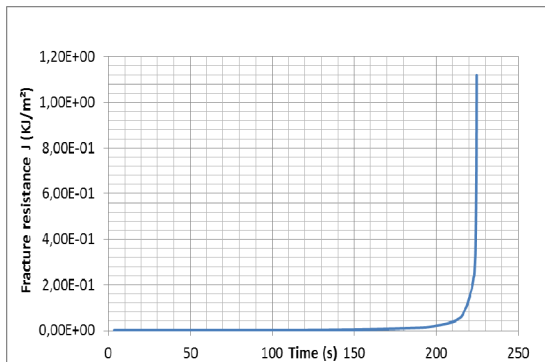
Fig. 10 Variation of the fracture toughness J versus time

5.3 *Extrados Crack*

We took the same simulation, but this time the crack is on the extrados surface of the elbow (fig.11).
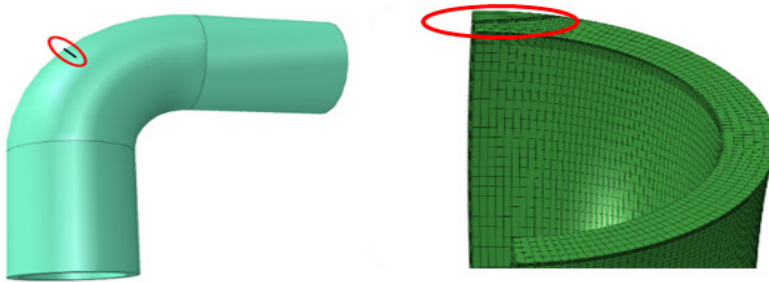
Fig. 11 Bent conduit with an extrados crack
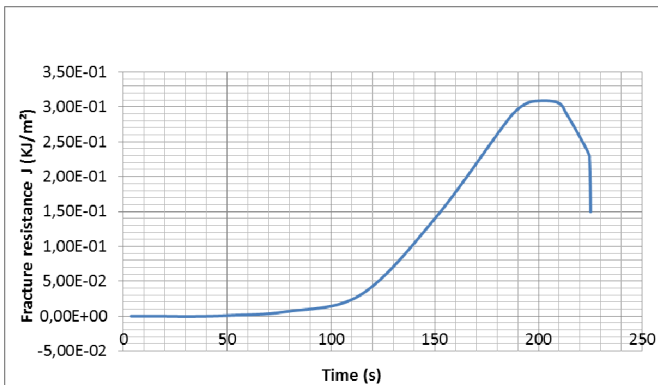
Fig. 12 Variation of the fracture toughness J versus time

We note that even, in the case of a pre-crack in the suction surface, J does not reach its critical value J_{IC}. These results are confused with the results of Fig.6.

6   Conclusion and Perspectives

First, the numerical solution of the transient flows in quasi-rigid pipelines has been presented in this paper. To examine the mechanisms of liquid-pipe interaction, Poisson coupling and structural restraint of an elbow have been considered. Numerical results accurately predicted the experimental data obtained by Wiggert et al. No pressure reflection from the immobile elbow was detected. However, when the elbow was not fully restrained, alterations of the transient where observed including 33 percent increase in maximum pressure. These alterations are related to the direction and amplitude of the motion of the elbow and are dependent on supports conditions

Next, thermoplastic materials such as PE 100 have been studied. This material has a viscoelastic behavior and a high degree of ductility. Normally, the fracture behavior (the initiation and propagation of cracks) must be analyzed using the concept of viscoelastic-plastic fracture mechanics (Brostow et al. 1991) and

(Favier et al. 2002). However, it has been shown (Benhamena et al. 2010, 2011) that the elastic–plastic approaches can approximate with acceptable accuracy the critical J integral of the polyethylene.

We studied in this work the effect of the crack's depth on the ultimate pressure of a PE100 pipe.

Results show that the crack is initiated in the radial direction. And the position of the crack has a great influence on the energy of rupture and consequently on the ultimate pressure.

The numerical results obtained should be verified by experimental testing

References

Benhamena, A., Bouiadjra, B., Amrouche, A., Mesmacque, G., Benseddiq, N., Benguediab, M.: Three finite element analysis of semi-elliptical crack in high density polyethylene pipe subjected to internal pressure. Materials and Design 31, 3038–3043 (2010)

Benhamena, A., Aminallah, L., Bouiadjra, B., Benguediab, M., Amrouche, A., Benseddiq, N.: J integral solution for semi-elliptical surface crack in high density poly-ethylene pipe under bending. Materials and Design 32, 2561–2569 (2011)

Bouaziz, M., Guidara, M., Schmitt, C., Hadj-Taïeb, E., Azari, Z.: Water hammer effects on a gray cast iron water network after adding pumps. Engineering Failure Analysis (2014), doi:10-1016/j.engfailanal,04.023

Brostow, W., Fleissner, M., Müller, W.: Slow crack propagation in polyethylene: etermination and prediction. Polymer 3, 419–425 (1999)

Favier, V., Giroud, T., Strijko, E., Hiver, J.M., G'Sell, C., Hellinckx, S., et al.: Slow crack propagation in polyethylene under fatigue at controlled stress intensity. Polymer 43, 1375–1382 (2002)

Guidara, M.A., Bouaziz, M.A., Schmitt, C., Capelle, J., Haj Taieb, E., Azari, Z., Hariri, S.: Burst test and J-integral crack growth criterion in high density poly-ethylene pipe subjected to internal pressure. In: Multiphysics Modelling and Simulation for Systems Design, MMSSD 2014, Sousse-Tunisia, Decembre 17-19, Paper ID 92 (2014)

Rice, J.R.: A Path Independent Integral and the Approximate Analysis of Strain Concentration by Notches and Cracks. Journal of Applied Mechanics 35, 379–386 (1968)

Hou, Q., Kruisbrink, A.C.H., Pearce, F.R., Tijsseling, A.S., Yue, T.: Smoothed particle hydrodynamics simulations of flow separation at bends. Computers & Fluids 90, 138–146 (2014)

Lampman, S.: Characterization and Failure Analysis of Plastics. ASM International, France (2003)

Theoretical Study and Measurement of the Characteristic Curves of a Centrifugal Pump

Noura Bettaieb and Ezzeddine Hadj Taïeb

Research Laboratory "Applied Fluid Mechanics, Process Engineering and Environment"
Engineering School of Sfax, BP'W'3038 Sfax, Tunisia
Noura_bettaib1@hotmail.fr, Ezed.Hadj@enis.rnu.tn

Abstract. In this study, experimental and analytical investigations are carried out in order to determine the steady state performance curves of a centrifugal pump. The pump rotor of the hydraulic facility (TE-83), available at the fluid laboratory of the National Engineering School of Sfax (ENIS), is used for the steady state calculations. The characteristic curves (flow-head) of the pump were determined by measuring the difference between the outlet and the inlet pressures for different steady flow rates. The curves were plotted for various values of the rotating speed. For each speed the head is recorded then plotted at different discharge openings. Results are further processed to determine the head and flow coefficients. These coefficients are obtained by applying the theory of dimensional analysis and similitude. The head coefficient is plotted versus the flow coefficient to form a curve of these two dimensionless numbers using only one machine. This curve can then be used to give information for any machines geometrically similar to the test machine.

Keywords: Centrifugal pump, characteristic curve, dimensional analysis, similitude.

1 Introduction

The centrifugal pump is the most used pump type in the world. The principle is simple, well-described and thoroughly tested. Numerous studies on centrifugal pumps have been investigated (Łazarkiewicz and Troskolański 1965, shames 1983, Sayers 1990, Shulhoff 1991, Srinivasan 2008, Dixon 2010,...). The studies included also the prediction of pump as turbine performance (PAT) (Yang SS et al 2010, Yang SS et al 2012...) The first type of a centrifugal pump was already built 1689 by the French physicist Denis Papin. Since then the centrifugal pump found entrance in many fields of the technology. In particular radial-flow pumps are used for liquid-delivering in a dominant number of constructions. Beside water every other liquid is applicable as delivery medium. In particular oil, but in addition, aggressive liquids or liquid solid mixtures. In this context numerical study on behavior of a centrifugal pump when delivering viscous oils were done (Li WG 2008, M.H. Shojaeefard a, M. Tahani 2012…). The performance of a turbomachine may be

defined with the characteristic curves (Head-Volume flow) plotted for different values of the rotating speed. In order to study the variations of all involved quantities, an excessive number of experiments is required but it is impossible to make a concise presentation of the results. The most of these complications can be eliminated using the dimensional analysis, which creates dimensionless groups of the variables involved in the study.

1.1   Generalities

A turbomachine is a machine whose essential part is an impeller with blades arranged symmetrically around an axis. The flow of the fluid throughout the blades causes the energy exchange between the fluid stream and the shaft of the machine.

In the limited context of this paper, it is not possible to expose all the theory of turbomachinery.

We limit ourselves to deliver the results we need to introduce the definition and the use of the characteristic curves of the pump (figure 1). The torque exerted from outside on the shaft of the pump, by neglecting the mechanical and hydraulic frictions, is given by the formula:
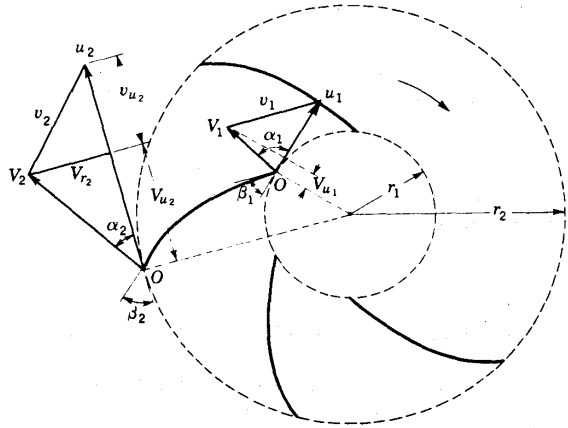
Fig. 1 Velocity diagrams for centrifugal pump

$$M = \varpi \frac{Q\left(r_2 V_{u2} - r_1 V_{u1}\right)}{g} \tag{1}$$

So the power is:

$$P = M\omega = \varpi Q \frac{\left(U_2 V_{u2} - U_1 V_{u1}\right)}{g} \tag{2}$$

In this formula, the following expression is homogeneous to a height:

$$H_{eff} = \frac{\left(U_2 V_{u2} - U_1 V_{u1}\right)}{g} \tag{3}$$

It is called the Euler head and represent the theoretical head developed by the pump impeller.

The only fluid pressure drops through the pump are those due to the friction between the liquid fillets, and between the liquid and the fixed and moving blades of the pumps. Denote ξ_d the set of these losses occurring in the fixed blades of the

diffuser, by ξ_r the losses occurring in the impeller and by ξ_c the loss which come from the mismatch of the directions of liquid threads with the blades of the impeller (at the entrance) and the blades of the diffuser (at the outlet). Therefore, providing the pump shaft with an energy represented by the head H_{eff}, we get the total head H developed by the pump:

$$H = H_{eff} - \xi_d - \xi_r - \xi_c \tag{4}$$

The efficiency of the pump is defined as:

$$\eta = \frac{H}{H_{eff}} \tag{5}$$

1.2 Characteristic Curves

A centrifugal pump rarely works at an optimal operating condition; it usually occurs the change in the state due to the needs of the exploitation.

It follows from the previously established formulas (3) and (4) that for the aforementioned operating system (Q and N are given), the head (H_{eff} or H) is perfectly determined.

Ultimately, the performance of a centrifugal pump in different possible regimes is characterized by a surface given as:

$$F = f(H, Q, N) \tag{6}$$

Each point on this surface corresponds to an operating point of the machine. If we connect, on the surface $F = f(H, Q, N)$, the points for which the machine has the same efficiency, curve networks are obtained with the same performance.

However, this three-dimensional representation system is quite complicated and it is preferred to adopt a simpler one, a two-dimensional system, which presents the process of characteristic curves.

In this mode of representation, we consider only one of the three variables H, Q or N constant, which leads to a function with two variables, in other words, a planar representation.

- The characteristic $H_{eff} = f(Q)$ at a constant speed;
- The characteristic $H = f(Q)$ at a constant speed;
- The characteristic $P = f(Q)$ of the power applied to the shaft of the pump according to the flow, at a constant speed;
- The characteristic $\eta = f(Q)$ at a constant speed.

We will not consider the characteristic of the Euler head which is of little practical interest and we will limit ourselves to examine the characteristic of the total head at a constant rotational speed.

Given the variation of these different pressure losses indicated in equation (4) according to the flow, H is expressed as a function of the flow rate Q and the rotational speed N:

$$H = \mu N^2 + \lambda NQ + \kappa Q^2. \tag{7}$$

The coefficients μ, λ and κ are functions of the pump's characteristics (dimensions and shapes of the blades).

2   Presentation of the Hydraulic Test Bench (TE-83)

The head-flow characteristic is determined experimentally, considering the hydraulic test bench (TE-83), available at ENIS, represented by the simplified diagram presented in figure 2. This bench has two identical centrifugal pumps that allows for the study of a single pump, two pumps in parallel and two pumps in series.

-L1=0.5 m, D1=0.04 m

-L2=1.5 m, D2=0.04 m
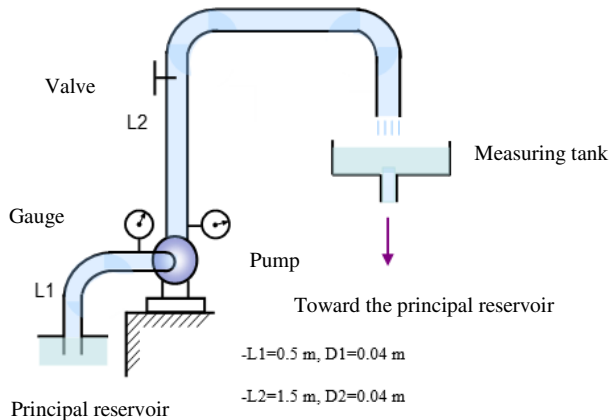
Fig. 2 Simplified diagram of the hydraulic test bench TE-83

In figure 2 only one pump is shown.

This bench also includes gauges that indicate the pressure on the suction and discharge side of the pump. The engine speed is adjusted by potentiometers. A mechanical device is used to determine the engine torque. An intermediate measuring tank is placed between the discharge circuit and the main reservoir to determine the volume flow of the pump.

2.1   Operating Procedure

In order to determine this characteristic, the pump is rotated at a constant speed, a vacuum gauge is placed in the suction (p_s) and a pressure gauge is placed in the discharge (p_d). A differential pressure gauge, connected to the two corresponding points (Figure 3), can also be used to determine the total head as given by equation (8). Water is drawn from the principal reservoir, mounted on castors forms the

base of the set, by way of a foot valve and a strainer. The pump delivery is taken to a swivel valve by a means of which the water may be either returned to the principal reservoir or delivered to the calibrated measuring tank. The flow quantity is equal to the recovered volume in the measuring tank by the recorded time in the stop watch. The flow can also be measured by the equation (9) of a Venturi meter (Figure 4) or a rotameter flowmeter.
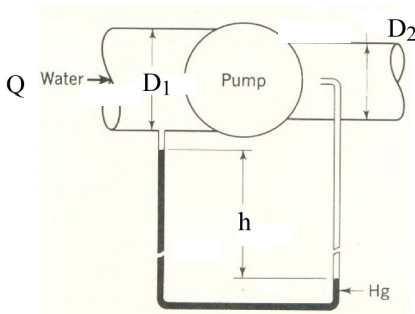
Fig. 3 Differential pressure gauge   **Fig. 4** Venturi meter
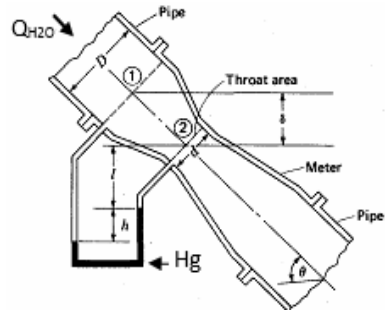
$$H = \frac{1}{12.1} Q^2 \left(\frac{1}{D_2^4} - \frac{1}{D_1^4} \right) + 12.6h \tag{8}$$

$$\frac{1}{12.1} Q^2 \left(\frac{1}{d^4} - \frac{1}{D^4} \right) = 12.6h \tag{9}$$

For each setting of the valve, H is noted from the differential pressure gauge as:

$$H = \frac{p_d - p_s}{\rho g} \tag{10}$$

Thus, the characteristic $H = f(Q)$ is plotted point by point.

2.2 Experimental Results

Repeating the operating procedure described previously for different rotational speeds, one gets the different curves plotted in figure 5.

This figure shows the dimensional presentation of the performance of the given pump for the range of speeds 1500<N<3000 rev/min.
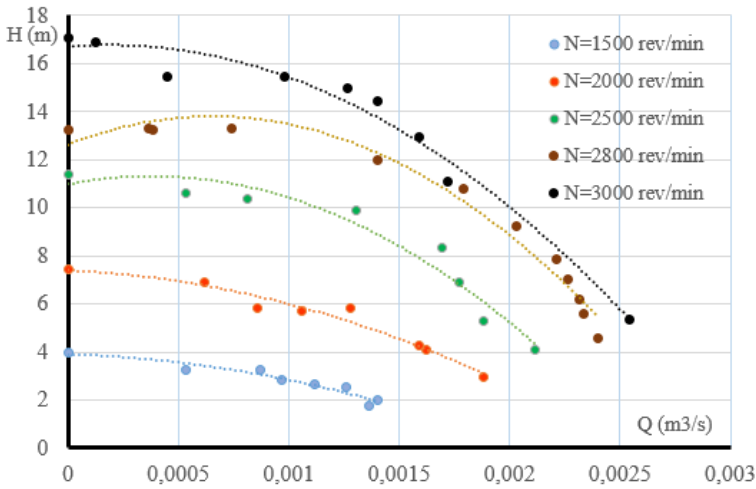
Fig. 5 Experimental Head-volume characteristic curve for diffrents rotational speed

3   Dimensional Analysis

3.1   Similarities Equations

The large number of variables used to describe the performance of a turbomachine requires the use of dimensional analysis to reduce the number of variables into dimensionless groups.

Dimensional analysis is used to express the power P in terms of dimensionless numbers (Sayers, 1991):

$$\overline{P} = f(\mathrm{Re}, \phi, \psi) \tag{11}$$

Where $\overline{P} = \dfrac{P}{\rho N^3 D^5}$ is the power coefficient, $\phi = \dfrac{Q}{ND^3}$ is the flow coefficient

and $\psi = \dfrac{g\Delta H}{N^2 D^2}$ is the load coefficient.

The term $\dfrac{\rho ND^2}{\mu}$ is equivalent to Reynolds number Re as the peripheral velocity is proportional to ND.

In the case of hydraulic machines, it was found that the Reynolds number is usually very large and the fluid viscosity has a very small effect on the power. So:

$$\overline{P} = f(\phi, \psi) \tag{12}$$

For two geometrically similar machines (equal ratios of all lengths) dynamic similarity (the ratio of the driving forces at corresponding points is constant)

implies the kinematic similarity (the ratio of the velocities of fluid particles at corresponding points is constant).

To achieve this similarity, the dimensionless groups in equation (12) must remain the same for both machines.

3.2   *Dimensionless Head-Flow Characteristic*

The operating condition of a turbomachine will be dynamically similar at two different rotational speeds if all fluid velocities at corresponding points within the machine are in the same direction and proportional to the blade speed. If two points, one on each of two different head-flow characteristics, represent dynamically similar operation of the machine, then the non-dimensional groups of the variables involved, ignoring Reynolds number effects, may be expected to have the same numerical value for both points. On this basis, non-dimensional presentation of performance data has the important practical advantage of collapsing into virtually a single curve, results that would otherwise require a multiplicity of curves if plotted dimensionally (Dixon 2010).

For similar pumps, experience shows that the head coefficient $gH/(ND)^2$ is a function of flow coefficient Q/ND^3 (Shames 1982).

$$\frac{gH}{(ND)^2} = f\left(\frac{Q}{ND^3}\right) \tag{13}$$

If Q/ND^3 is the same for two geometrically similar machines (for example model and prototype) then they are dynamically similar and have the same head coefficient. Therefore, certain information of the prototype can be determined, in particular, from the data N and D and those of the prototype model. Thus, dimensionless presentation of the performance of data has a significant practical advantage of the results presented in a single curve that requires a multiplicity of curves if plotted with dimension.

3.3   *Characteristic Equation of a Centrifugal Pump*

In order to establish the characteristic equation of the centrifugal pump of the hydraulic test bench (TE-83), the measurement points in figure 6 were approached with a second order polynomial function. One can observe deterioration in performance at high speeds due to the effect of cavitation.

The equation of the characteristic curve can be written in the form:

$$\frac{gH}{(ND)^2} = -2141.8\left(\frac{Q}{ND^3}\right)^2 + 0.81\left(\frac{Q}{ND^3}\right) + 0.1279 \tag{14}$$
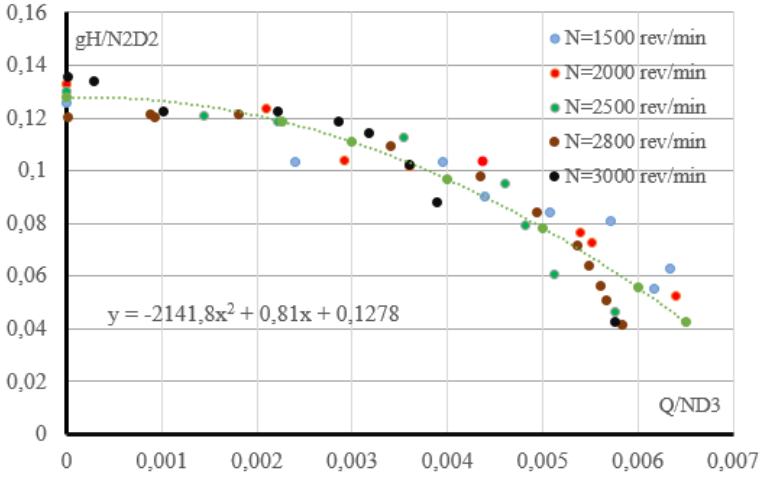
Fig. 6 Polynomial approximation of measurement points

3.4 Theoretical Head-Flow Characteristic Curve of a Centrifugal Pump

Quite often the performance data for a specific pump is presented as H versus Q. We can arrive at such a plot for a specific pump of impeller diameter D_0 and speed of operation N_0 by using the curves of dimensionless groups developed from tests of another geometrically similar pump operating at a different speed and over a range of flow Q (Shames 1982).

Multiplying equation (14) by $(ND)^2$:

$$H = \frac{0.1278 D^2}{g} N^2 + \frac{0.81}{gD} NQ + \frac{-2141.8}{gD^4} Q^2 \tag{15}$$

This equation has the same form as equation (7) where:

$$\mu = \frac{0.1279 D^2}{g}, \quad \lambda = \frac{0.81}{gD} \quad \text{and } \kappa = \frac{-2141.8}{gD^4}.$$

As the diameter of the impeller is equal to $D = 0{,}112$ m, the equation (15) would be:

$$H = 0.00016 N^2 + 0.737 NQ - 1387515 Q^2 \tag{16}$$
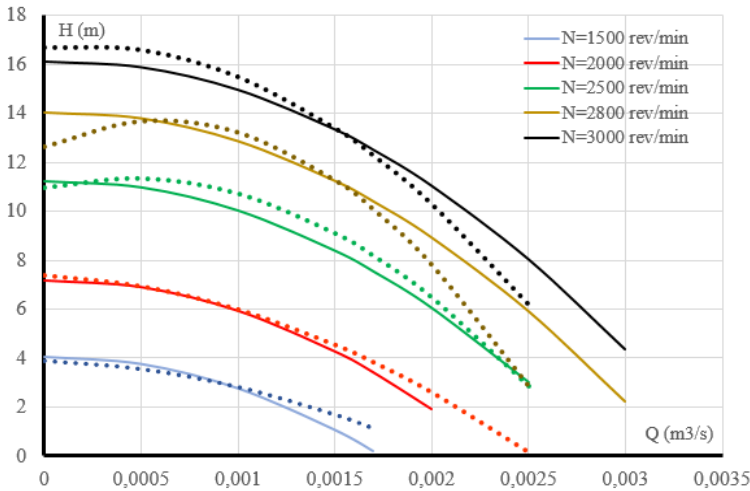
Fig. 7 Comparision between theoritical and exprimentel Head-volume characteristic curve for diffrents rotational speed

The dimensionless results shown in figure 6 have been obtained for a particular pump. They would also be approximately valid for a range of different pump sizes so long as all these pumps are geometrically similar and the cavitation is absent. Thus, neglecting any change in performance due to change in Reynolds number, the dynamically similar results in figure 6 can be applied to predict the dimensional performance of a given pump for required speeds. Figure 7 shows dimensional presentations of the pump presented as H versus Q. It will be clear from the above discussion that the locus of dynamically similar points in the H-Q field lies on a parabola since H varies as N^2 and Q varies as N (Dixon 2010).

As we can see, only the experimental characteristic curves corresponding to the rotational speeds $1500 < N < 2500$ show good concordance with the analytical results shown in figure 7. For $N > 2500$ rev/min, the inlet pressure head decreases and small vapor bubbles appear within the liquid and close to solid surfaces. The bubbles increase both in size and number, coalescing into pockets of vapor which affects the whole field of flow. This is called cavitation inception and commences in the regions of lowest pressure.

This growth of vapor cavities is usually accompanied by a sharp drop in pump performance as shown conclusively. It may seem surprising to learn that with this large change in bubble size, the solid surfaces are much less likely to be damaged than at inception of cavitation. The avoidance of cavitation inception in conventionally designed machines can be regarded as one of the essential tasks of both pump and turbine designers. However, in certain recent specialized applications pumps have been designed to operate under supercavitating conditions. Under these conditions large size vapor bubbles are formed but, bubble collapse

takes place downstream of the impeller blades. An example of the specialized application of a supercavitating pump is the fuel pumps of rocket engines for space vehicles where size and mass must be kept low at all costs.

4 Conclusion

In this paper, experimental and theoretical characteristic curves of a centrifugal pump have been determined in order to predict the performance of other geometrically similar prototype machine. Experimental measurement on the pump rotor of the hydraulic facility (TE-83) were made to obtain the experimental head-volume characteristic curves. Dimensional analysis and similarities equations were applied on these curves for different rotating speeds in order to determine its characteristic equation. Theoretical curves were plotted depending on the characteristic equation. This curves show concordance with the experimental ones only for rotating speeds $1500 < N < 2500$. For higher speeds the characteristic curves show a sharp drop in pump performance due to the cavitation phenomenon.

References

Li, W.: Numerical study on behavior of a centrifugal pump when delivering viscous oils – Part 1: Performance. Int. J. Turbo Jet Engines 25(2), 61–79 (2008)

Yang, S.S., Kong, F.Y., Shao, F.: Numerical simulation and comparison of pump and pump as turbine. In: ASME, Fluids Engineering Summer Meeting, Montreal, Canada, pp. 1–10 (2010)

Yang, S.-S., Kong, F.-Y., Jiang, W.-M., Qu, X.-Y.: Effects of impeller trimming influencing pump as turbine. Elsevier. J Comp Fluid 67, 72–78 (2012)

Shojaeefard, M.H., Tahani, M., Ehghaghi, M.B., Fallahian, M.A., Beglari, M.: Numerical study of the effects of some geometric characteristics of a centrifugal pump impeller that pumps a viscous fluid. Elsevier. J. Comp Fluid 60, 61–70 (2012)

Dixon, S.L.: Hall Fluid Mechanics and Thermodynamics of Turbomachinery, 6th edn. Butterworth-Heinemann, Elsevier, Burlington, MA 01803, USA (2010)

Sayers, A.T.: Hydraulic and compressible flow turbomachines. McGraw-Hill, New York (1990)

Schulhof, P.: Les stations de pompage d'eau, Lavoisier Tech & Doc, Paris (1991)

Shames, I. H.: Mechanics of fluids, 2nd edn. McGraw-Hill Book Company (1982)

Srinivasan, K.M.: Rotodynamic pumps (Centrifugal and Axial). New Age International (P) Ltd., Publishers, New Delhi (2008)

Łazarkiewicz, S., Troskolański, A.T.: Impeller pumps. Pergamum Press (1965)

Geometrical Analysis of a Scroll Compressor and Fluid Mechanical Modeling

Manel Wannassi and Manuel Buisson

Department Mechanics and Glasses, Institut de Physique de Rennes,
UMR 6251- CNRS/University of Rennes 1, France
`{manel.wannassi,manuel.buisson}@univ-rennes1.fr`

Abstract. The importance of the geometrical description of the scroll wraps for scroll compressor models was shown in Blunier et al. (2006). In fact, geometry is one of the main factors affecting the efficiency of the compressor so that the geometry of scroll wraps has to be known before establishing an accurate thermodynamic model. Via formal calculus, this paper uses the novel description of the geometry based on the parametric equations for the circle involutes of Blunier et al. (2006), existence conditions of the conjugacy points on the circle involutes are also considered. Finally, a new coupled model which is based on synchronized pistons is introduced in order to couple the proposed geometric model with the thermodynamic model.

Keywords: scroll, compressor, involutes, fluid mechanics, geometry, simulation.

1   Introduction

The scroll compressor for air or refrigerant was originally invented by Leon Creux (1905). The scroll compressor has been put into commercial use since the early 1980s. The machine consists of two nested identical scrolls; classically, these scrolls are represented by involutes of circle. We can see in Figure 2 how we can assemble these two scrolls so that they can touch themselves at different points and form a series of successive chambers. Well known advantages of the scroll compressor are a small number of moving parts, high efficiency and a low level of noise and vibrations.

However, the design of the scroll profile is difficult and this design plays a key role in their performances: thus analytical descriptions are useful and may investigate various shapes as done in a lot of papers. Modern analysis review of the geometries of the scroll compressor has been detailed in Bell et al. (2010) with references to Yanagisawa et al. (1990) for a complete analytical model of the compressor and the analysis of Halm (1997), Chen et al. (2002), Lee and Wu (1995) and Hirano et al. (1990) for the discharge process. Bell et al. (2010) cite also the major breakthrough in the scroll compressor geometry analysis of Gravensen et al. (1998); Gravensen and Henriksen (2001), with novel reference

frame. They announce the reference for the work of Blunier et al. (2006) and Blunier (2009) who introduced an original way to describe the geometry of the scroll wraps and used the symmetries to establish a thermodynamic model of the scroll compressor. We present in this paper the development of a comprehensive scroll model, based on the idea of Gravensen (Gravensen and Henriksen, 2001) and Blunier et al. (2006), using a set of function developed with Mathematica. This analytical approach and computing method is able to successfully manage the complicated geometries. A new concept is introduced in this research. The fully coupled thermodynamic process is modeled by a series of synchronized pistons which represent the three chambers of the scroll compressor (suction, compression, discharge) and the valve opening ending the discharge process is modeled using a spring model.

Let us note that we have to couple all these phenomena:

-the pistons are synchronized due to the driving movement of the moving scroll
-leakages between the chambers of these pistons come unavoidably from machining tolerance and wear.
-opening process of the valve.

In a first step and in order to achieve this coupling we assume that the mechanism of the valve is a single spring ((Chen et al. (2002)) with an opening yield-pressure. In future, others phenomena like stiction, acoustic of the flow may be considered.

2   Analytical Analysis of Scroll Compressor Geometry

We use in Figure 1 an involute of circle in a general frame. The fixed and orbiting scrolls are therefore defined as two involutes that develop around a common basic circle with radius r and are offset by a constant distance. Each involute is defined by introducing the orthonormal frame (t, n):

$$t(\varphi) = (\mathrm{Cos}\varphi, \mathrm{Sin}\varphi)$$

$$n(\varphi) = (-\mathrm{Sin}\varphi, \mathrm{Cos}\varphi)$$

(1)

Where (φ) is the unit tangent vector and (φ) the unit normal vector. The involute of a circle is given by Blunier et al. (2006):

$$S_{\mathrm{xy}}(\varphi) = r_b t(\varphi) - r_b\big(\varphi - \varphi_{\mathrm{y}0}\big) n(\varphi) + \xi$$

(2)

Where r_b is the involute basic circle radius, φ is the involute angle, $\varphi_{\mathrm{y}0}$ the internal or external involute initial angle with x∈{f, m} and y∈{i, e}.
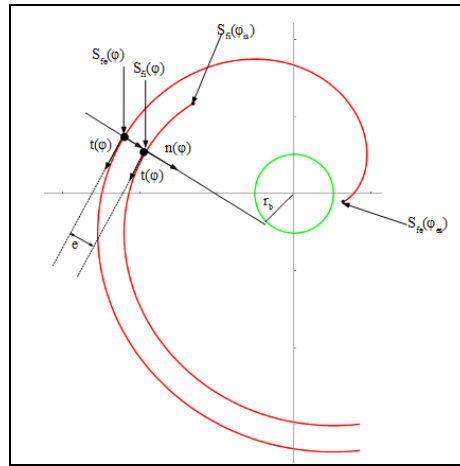
Fig. 1 Spiral geometry

2.1   Fixed Scroll

The representation of the fixed (f) scroll can be determined as follows:

$$S_{\text{fe}}(r_b, \varphi_{e0}, \varphi) = r_b * (t(\varphi) - (\varphi - \varphi_{e0}) * n(\varphi)) \tag{3}$$

$$S_{\text{fi}}(r_b, \varphi_{i0}, \varphi) = r_b * (t(\varphi) - (\varphi - \varphi_{i0}) * n(\varphi)) \tag{4}$$

Where S_{fe} and S_{fi} are, respectively, the external (e) and internal (i) involutes. The angles φ_{es} and φ_{is} are the external and internal starting angles, φ_{max} the involute ending angle, φ_{e0} and φ_{i0} the initial angles of the external and internal involutes. The domains of definition of the internal and external involutes are, respectively, $I_e = [\varphi_{es}, \varphi_{max}]$ and $I_i = [\varphi_{is}, \varphi_{max}]$.

2.2   Orbiting Scroll

The geometry of the orbiting scroll is deduced from the fixed one but with an offset of π so that the two scrolls are in conjugacy.

Defining θ as the orbiting angle, it follows:

$$S_{\text{me}}(r_b, \varphi_{e0}, \varphi, r_0, \theta) = -S_{\text{fe}}(r_b, \varphi_{e0}, \varphi) - r_0 * n(\theta) \tag{10}$$

$$S_{\text{mi}}(r_b, \varphi_{e0}, \varphi, r_0, \theta) = -S_{\text{fi}}(r_b, \varphi_{e0}, \varphi) - r_0 * n(\theta) \tag{11}$$

The domains of definition of the internal and external involutes are, respectively, $I_e = [\varphi_{es}, \varphi_{max}]$ and $I_i = [\varphi_{is}, \varphi_{max}]$.

Where $r_0 = r_b(\varphi_{e0} - \varphi_{i0} + \pi)$ is the orbiting radius.

The shape of the investigated scroll is shown in Figure 2, with the fixed scroll in red and the orbiting scroll in blue.
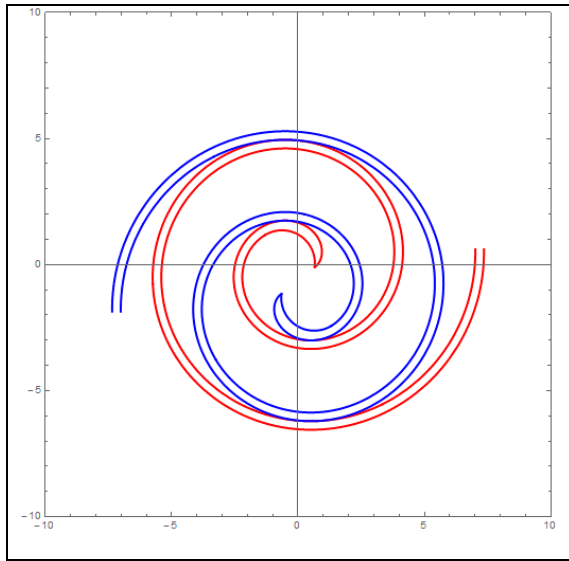
Fig. 2 General Scroll reference frames

2.3   *Novel Reference Frame*

In order to exploit the symmetry of the two scrolls, a novel reference frame is presented in Figure 3 (Blunier et al. (2006)). In this frame, the representation of the fixed scroll is given by:

$$\tilde{S}_{fe}(\varphi, \theta) = r_b(t(\varphi) - (\varphi - \varphi_{e0})n(\varphi)) + \frac{1}{2}r_0 n(\theta) \tag{12}$$

$$\tilde{S}_{fi}(\varphi, \theta) = r_b(t(\varphi) - (\varphi - \varphi_{i0})n(\varphi)) + \frac{1}{2}r_0 n(\theta) \tag{13}$$

The orbiting scroll is given by:

$$\tilde{S}_{me}(\varphi, \theta) = -\tilde{S}_{fe}(\varphi, \theta) \tag{14}$$

$$\tilde{S}_{mi}(\varphi, \theta) = -\tilde{S}_{fi}(\varphi, \theta) \tag{15}$$

(a) Real reference frame   (b) Novel reference frame
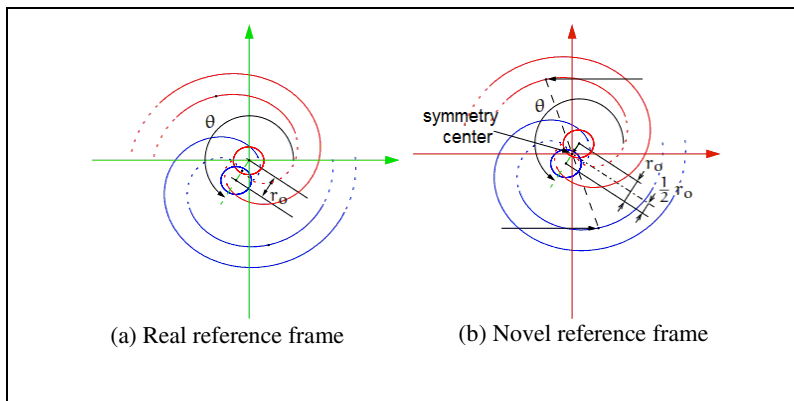
Fig. 3 Reference frames of the scroll compressor

2.4   *Points of Conjugacy*

The kth point of conjugacy φ_{cik} at the internal involute is determined by:

$$\varphi_{cik}(\theta, k) = \theta + 2(k - 1)\pi \quad \text{For k} \in \{1 .. 3\} \tag{16}$$

The kth point of conjugacy φ_{cek} at the external involute is determined by:

$$\varphi_{cek}(\theta, k) = \theta - \pi + 2(k - 1)\pi \quad \text{For k} \in \{1 .. 3\} \tag{17}$$

3   **Estimation of the Chamber Volumes**

3.1   *Suction Chamber*

The suction chamber volume computation is expressed as follow:

$$V_{suc}(\theta) = h(A_{suca}(\theta) + A_{sucb}(\theta)) \tag{18}$$

Where:

$$A_{suca}(\theta) = \frac{1}{2} \int_{\varphi_{cik}}^{\varphi_{max}} \left\| \tilde{S}_{fi}(\varphi, \theta) x \tilde{S}_{fi}{}'(\varphi, \theta) \right\| d\varphi$$
$$- \frac{1}{2} \int_{\varphi_{cek}}^{\varphi_{max} - \pi} \left\| \tilde{S}_{me}(\varphi, \theta) x \tilde{S}_{me}{}'(\varphi, \theta) \right\| d\varphi \tag{19}$$

With $k = \begin{cases} 3 \; if \; \exists \; \varphi_{ci3} \\ 2 \; elsewhere \end{cases}$

and h corresponds to the height of the scroll

The resulting volume needs to be corrected by the area $A_{sucb}(\theta)$.

3.2 Compression Chamber

In the same way, we define the area enclosed by the involutes of the orbiting and the fixed scrolls between two conjugate points, multiplied by the height of the scroll.

$$V_{com}(\theta) = \begin{cases} \frac{h}{2}\left(\int_{\varphi_{cik}}^{\varphi_{cik}+1}\left\|\tilde{S}_{fi}(\varphi,\theta)x\tilde{S}_{fi}{}'(\varphi,\theta)\right\|d\varphi - \int_{\varphi_{cek}}^{\varphi_{cek}+1}\left\|\tilde{S}_{me}(\varphi,\theta)x\tilde{S}_{me}{}'(\varphi,\theta)\right\|d\varphi\right) & if\ k = \begin{cases}1\ if\ \exists\ \varphi_{ci1}\\2\ if\ \exists\ \varphi_{ci3}\end{cases} \\ V_{01}(\theta) & elsewhere \end{cases} \tag{20}$$

V_{01} is the central volume expressed in details in Blunier et al. (2006).

3.3 Discharge Chamber

The discharge chamber volume computation vs. the orbiting angle is given as:

$$V_{dis}(\theta) = \begin{cases} \frac{1}{2}V_0(\theta)\ if\ \exists\ \varphi_{ci1}\ \vee\ \varphi_{ci3} \\ \frac{1}{2}V_{00}(\theta) \quad elsewhere \end{cases} \tag{21}$$

The volumes of the suction, compression and discharge chambers are shown in Figure 4. Although volumes are representing through discontinuous functions, the compression process is continuous. Indeed, there is good continuity between suction, compression and discharge volumes as shown in the Figure 4: for example, when the suction chamber opens to compression chamber, there is good continuity of volume, pressure and temperature ensuring a continuous process.
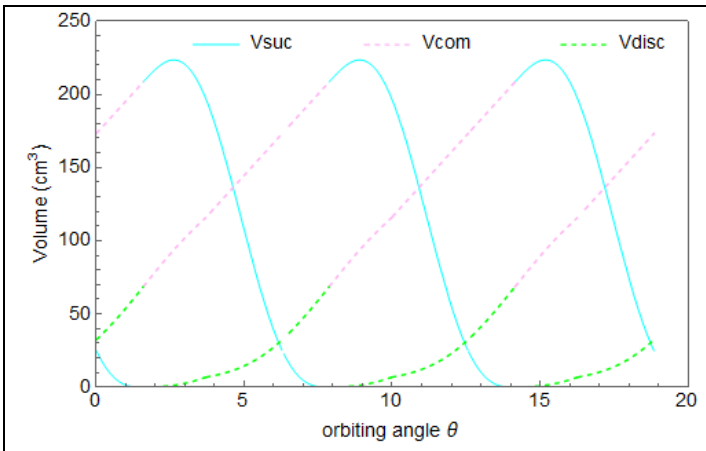
Fig. 4 Chambers volumes

4   Thermodynamic Model

4.1   Governing Equations

Following Howell (1999): "*The governing equations for the flow are the compressible Navier-Stokes equations*:

$$\frac{\partial \rho}{\partial t} + div(\rho u) = 0 \tag{22}$$

$$\rho \frac{Du}{Dt} = -grad\ p + (\lambda + \mu)grad\ div\ u + \mu \nabla^2 u \tag{23}$$

Where ρ, u and p are the density, velocity and pressure fields, λ and μ are the dilatational and shear viscosities, and D / Dt is the usual convective derivative. Equation (22) represents conservation of mass, while (23) is the generalization of the usual incompressible Navier Stokes equation.

We add the equation of state assuming a perfect gas:

$$p = \rho\ R\ T \tag{24}$$

Where the gas constant R: is $R = c_p - c_v$

With c_v is the specific heat at constant volume and c_p is the specific heat at constant pressure.

Using the lubrication approximation, we end with the Navier- Stokes equations in a dimensionless form (see (Howell (1999) for more details) :

Thus,

$$\begin{cases} \frac{\partial^2 u(\theta)}{\partial^2 y} = \frac{\partial p(\theta)}{\partial x} \\ \frac{\partial p(\theta)}{\partial y} = 0 \end{cases} \tag{25}$$

$$u(\theta) = \frac{1}{2}\frac{\partial p(\theta)}{\partial x}y^2 + A(\theta)y + B(\theta) \tag{26}$$

A and B are found using the dimensionless version of (26) with boundary conditions (Howell (1999)).

The conservation of mass equation (22) gives:

$$q(\theta) = \int_{h_1}^{h_2} \rho\ u(\theta)dy \tag{27}$$

Now we simply substitute the analytic form (27) into (26), we find:

$$q(\theta) = \frac{\Omega\rho h(\theta)(u_1(\theta)+u_2(\theta))}{2} - \frac{\rho h(\theta)^3}{12}\frac{\partial p(\theta)}{\partial x} \tag{28}$$

Where h is the gap thickness. $u_1(\theta)$ and $u_2(\theta)$ are the scroll velocities.

4.2   Solution in the Quasi-Steady Limit

Equation (28) can be further simplified by taking the quasi-steady limit $\Omega \to 0$ and if also we consider that the gas is isothermal. So, by setting $\Omega=0$ in (28) we find that the flux:

$$q(\theta) = -\frac{\rho(h(\theta)))^3}{12}\frac{\partial p(\theta)}{\partial x}$$

(29)

Now we simply divide by $h(\theta)^3$ and integrate with respect to x from $-\infty$ to $+\infty$, to obtain:

(30)

$$q(\theta) = \frac{\left(P_1^2(\theta)- P_2^2(\theta)\right)}{24\,T(\theta)(\gamma-1)}\left(\int_{-\infty}^{+\infty}\frac{1}{(h(\theta))^2}\,dx\right)^{-1}$$

This tells us how the leakage through the gap depends on the pressure:

The main driving of leakage is due to the difference of pressure between chamber and also due the geometry of the channel. Howell remarks that the minimum gap thickness is very small so that the integral in (30) is dominated by the behavior of h near its minimum: in the neighborhood of this point, Howell approximates the integral in (30) with:

$$\int_{-\infty}^{+\infty}\frac{1}{(h(\theta))^2}\,dx = \frac{3\pi}{4\,d^{5/2}\sqrt{2k(\theta)}}$$

(31)

Where k is key geometrical parameter corresponding to the difference between the curvatures of the two channel walls at their closest point. We obtain finally:

$$q(\theta)=\frac{\left(P_1^2(\theta)- P_2^2(\theta)\right)d^{5/2}\sqrt{k(\theta)}}{9\pi\sqrt{2T(\theta)(\gamma-1)}}$$

(32)

5   The Coupled Problem

The coupled thermodynamic process is modeled by a series of synchronized pistons. Figure 5 shows three instantaneous positions for the successive chambers and the discharge process is modeled using a spring model (Chen et al. (2002)) with a stiffness k. The chambers are interconnected by the leakage sections and we assure that the diameters of these sections depend on the θ parameter so that full synchronization is done.

We have a series of chambers, in the n_{th} of which the gas is at pressure $P_n(\theta)$ and temperature $T_n(\theta)$. The flux between the n_{th} and $(n+1)_{th}$ chamber is denoted by $q_n(\theta)$, with the sign convention that $q_n(\theta)>0$ if the gas flow from chamber n to n+1. We know (approximate model of Howell (1999)) that in each gap between the chambers, the temperature is constant, but the value of that constant is affected by the sign of $q(\theta)$.
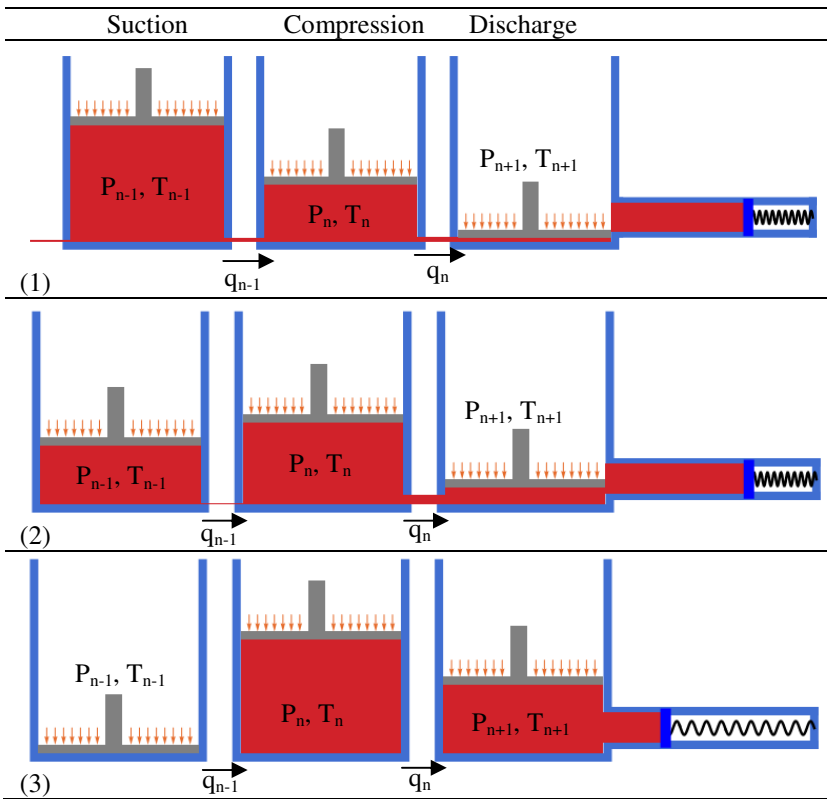
Fig. 5 Thermodynamic system modeled by successive pistons

if $q_n(\theta) > 0$ then the gas transported by $q_n(\theta)$ has temperature $T_n(\theta)$, while if $q_n(\theta) < 0$ it is at $T_{n+1}(\theta)$. Thus we obtain the following expression for $q_n(\theta)$

$$q_n(\theta) = \frac{\left(P_n^2(\theta) - P_{n+1}^2(\theta)\right) d^{5/2} \sqrt{k(\theta)}}{9\pi\sqrt{2}(\gamma - 1)} \begin{cases} \dfrac{1}{T_n} & if \quad P_n(\theta) > P_{n+1}(\theta) \\ \dfrac{1}{T_{n+1}} & if \quad P_n(\theta) < P_{n+1}(\theta) \end{cases} \tag{35}$$

6   Conclusion

This paper proposes an original way to describe the geometry of the scroll wraps via a mapping construction of synchronized «REPRESENTATIVES PISTONS" interrelated by leakage in order to establish a thermodynamic model of the scroll compressor. The object of the synchronization is to respect the chamber volumes because they are imposed by the spirals movement.

A complete geometrical description of the scroll is given using Mathematica. The novel reference frame of Blunier et al. (2006) is used and the points of conjugacy are expressed. The compression process is described in detail and the estimation of the chamber volumes is given. The compressible lubrication theory is used to obtain a theoretical prediction of the leakage between adjoining chambers in a scroll compressor.

References

Creux, L.: Rotary engine, U.S Patent 801182.A (1905)

Hirano, T., Hagimoto, K., Maada, M.: Scroll profiles for scroll fluid machines. MHI Technical Review 27(1), 35–41 (1990)

Yanagisawa, T., Cheng, M., Fukuta, M., Shimizu, T.: Optimum operating pressure ratio for scroll compressor. In: Proceeding of the International Compressor Engineering Conference at Purdue, pp. 425–433 (1990)

Lee, Y.-R., Wu, W.-F.: On the profile design of a scroll compressor. International Journal of Refrigeration 18(5), 308–317 (1995)

Halm, N.P.: Mathematical modeling of scroll compressor. Master's thesis, Herrick Lab., School of Mechanical Engineering, Purdue University (1997)

Gravensen, J., Henriksen, C., Howell, P.: Danfoss: Scroll Optimization, Final report. Department of Mathematics, Technical University of Denmark, Lyngby. 32nd European Study Group with Industry (1998)

Howell, P.: Fluid mechanical modelling of the scroll compressor. In: Fitt, A., Cum Berbatch, E. (eds.) Mathematical Modelling: Case Studies. Cambridge University Press, Cambridge (1999)

Gravensen, J., Henriksen, C.: The geometry of the scroll compressor. Society for Industrial and Applied Mathematics 43, 113–126 (2001)

Chen, Y., Halm, N.P., Groll, E.A., Braun, J.E.: Mathematical modeling of scroll compressor – part I: compression process modeling. International Journal of Refrigeration 25, 731–750 (2002)

Blunier, B., Cirrincione, G., Miraoui, A.: Novel geometrical model of scroll compressor for the analytical description of the chamber volumes. In: Proceedings of International Compressor Engineering Conference at Purdue, no. CO74 (2006)

Bell, I.H., Groll, E.A., Braun, J.E., King, G.B.: Update on Scroll Compressor Chamber Geometry, In: Proceedings of International Compressor Engineering Conference at Purdue, no. 2033 (2010)

Wolfram Research, Inc., Mathematica, Version 10.0, Champaign, IL (2014)

Determination of Natural Frequencies in Piping Systems Using Transfer Matrix Method

Mohamed Amine Guidara[1], Lamjed Hadj Taieb[1,2], and Ezzeddine Hadj Taïeb[1]

[1] Laboratory of Applied Fluids Mechanics, Process Engineering and Environmental,
 ENIS, P.B. 1173, 3038 Sfax, Tunisia
[2] College of Engineering, Salman Bin Abdulaziz University, AlKharj, KSA
 gem3_guidara@yahoo.fr, l.hadjtaieb@sau.edu.sa,
 Ezed.Hadj@enis.rnu.tn

Abstract. In this paper we propose to study the natural frequencies in pipe flows with consideration of fluid-structure interaction. More specifically, it is to assess system characteristics such as vibration response, the transfer function, the maximum pressure, etc., for a wide range of frequencies and show the influence of fluid-structure interaction in piping systems. The transfer matrix method and the Laplace transformation are used to calculate the natural frequencies of systems with various boundary conditions taking into account the fluid-structure interaction. Results of numerical analysis for some simple piping systems are presented to illustrate the application of the proposed method and to show the effect of fluid-structure interaction on the values of natural frequencies.

Keywords: natural frequency, fluid-structure interaction, impedance method, resonance, Laplace transformation.

1   Introduction

In a network of pipes, during rhythm manoeuvres, it establishes a certain distribution of speed and load variations due to the propagation of pressure waves.

For certain frequencies of these manoeuvres that coincide perfectly with the natural frequency of the installation, the amplitudes can become very large, so there is resonance.

Usually, the traditional studies of frequencies don't take into account the fluid-structure interaction. They are acceptable for decoupled systems where the pipes are rigidly anchored but they are dubious for the systems less rigid because the dynamic behavior of the pipe may significantly affect the frequency spectrum of the piping systems.

In this study, we present a method based on the transfer matrix and the Laplace transform. This method allows the analysis of natural frequencies of systems with various boundary conditions taking into account the fluid structure interaction.

The model with four equations, representing the flow in pipes with fluid-structure interaction, has been adopted in this paper.

2   Mathematical Formulation

A description of a transient flow in horizontal axisymmetric thin walled pipes can be developed in the next section; we use the four equation model (Tijsseling 2003, Skalak 1956) for that. This mathematical model describes the axial vibration of liquid-filled pipes. Two fluid equations have been coupled with two wall pipe equations through boundary conditions and terms proportional to Poisson's contraction ratio.

   The four equations, governing fluid pressure, p, fluid velocity, V, axial pipe stress, σ_x, and axial pipe velocity, $\dot{u}_x$, can be presented by a set of first order partial differential equations of hyperbolic type:

$$
\begin{aligned}
&\frac{\partial V}{\partial t} + \frac{1}{\rho_f}\frac{\partial P}{\partial x} + \frac{2}{\rho_f R}\tau_0 = 0 \\[2mm]
&\frac{1}{\rho_f c_f^2}\frac{\partial P}{\partial t} + \frac{\partial V}{\partial x} - 2\nu\frac{\partial \dot{u}_x}{\partial x} = 0 \\[2mm]
&\frac{\partial \dot{u}_x}{\partial t} - \frac{1}{\rho_f}\frac{\partial \sigma_x}{\partial x} - \frac{1}{e\rho_f}\tau_0 = 0 \\[2mm]
&\frac{\nu}{E}\frac{R}{e}\frac{\partial P}{\partial t} - \frac{1}{\rho_f c_p^2}\frac{\partial \sigma_x}{\partial t} + \frac{\partial \dot{u}_x}{\partial x} = 0
\end{aligned}
\tag{1}
$$

where τ_0 is shear stress, ν is Poisson ratio, R is the pipe radius, e is the pipe-wall thickness, ρ_f and ρ_p are mass densities of fluid and pipe-wall respectively, x is the axial coordinate along the pipe and t is the time.

   The uncoupled axial wave speeds in the two media satisfy

$$
c_f^2 = \left\{\rho_f\left(\frac{1}{K} + (1-\nu^2)\frac{2R}{Ee}\right)\right\}^{-1} \quad \text{and} \quad c_p^2 = \frac{E}{\rho_p}
\tag{2}
$$

where E is Young's modulus of pipe wall material and K is fluid bulk modulus.

3   Transfer Matrix

3.1   General Solution

The equations (1) that govern the flow into pipes can be expressed with matrices as follow

$$
\mathbf{A}\frac{\partial X(x,t)}{\partial t} + \mathbf{B}\frac{\partial X(x,t)}{\partial x} + \mathbf{C}X(x,t) = 0
\tag{3}
$$

where X is a vector of unknown physical (fluid velocity, pressure, etc.) and $\mathbf{A}$, $\mathbf{B}$ and $\mathbf{C}$ are matrices of constant coefficients.

$$
\mathbf{A} = \begin{pmatrix} 1 & 0 & 0 & 0 \\ 0 & \dfrac{1}{\rho_f c_f^{\,2}} & 0 & 0 \\ 0 & 0 & 1 & 0 \\ 0 & \left(\dfrac{v}{E}\right)\left(\dfrac{R}{E}\right) & 0 & \dfrac{-1}{\rho_p c_p^{\,2}} 0 \end{pmatrix}, \quad \mathbf{B} = \begin{pmatrix} 0 & \dfrac{1}{\rho_f} & 0 & 0 \\ 1 & 0 & -2v & 0 \\ 0 & 0 & 0 & \dfrac{-1}{\rho_p} \\ 0 & 0 & 1 & 0 \end{pmatrix} \tag{4}
$$

$$
\mathbf{C} = \begin{pmatrix} f_f & 0 & -f_f & 0 \\ 0 & 0 & 0 & 0 \\ -f_p & 0 & f_p + D_p & 0 \\ 0 & 0 & 0 & 0 \end{pmatrix}, \quad X = \begin{pmatrix} V \\ P \\ \dot{u}_x \\ \sigma_x \end{pmatrix} \quad et \quad N = 4 \tag{5}
$$

It is clear that the matrices $\mathbf{A}$ and $\mathbf{B}$ are regular. The matrix $\mathbf{C}$ that contains the terms resulting in the dispersion can be singular.

The friction coefficients (f_f, f_p) and the Damping coefficient D_p in matrix $\mathbf{C}$ are obtained from Zhang et al. (1999).

Assuming that the initial conditions are zero, the Laplace transform of equation (3) is written

$$
s\tilde{X}(x,s) + \mathbf{BB}(s)\frac{\partial \tilde{X}(x,s)}{\partial x} = 0 \tag{6}
$$

with $\mathbf{BB}(s) = \mathbf{AA}^{-1}(s)\mathbf{B}(s)$ and $\mathbf{AA}(s) = \mathbf{A}(s) + \dfrac{\mathbf{C}(s)}{s}$

The solution of the equation (6) is

$$
\tilde{X}(x,s) = e^{-sx\mathbf{BB}^{-1}}\tilde{X}(0,s) \tag{7}
$$

The eigenvalues of $\mathbf{BB}$ are the roots of the characteristic equation:

$$
\det(\mathbf{BB} - \lambda I) = 0 \tag{8}
$$

If the dispersion matrix $\mathbf{C}$ is zeros, this equation has four roots which are:

$$
\lambda_1^{\,2} = \lambda_2^{\,2} = \frac{1}{2}\left\{ q^2 - (q^4 - 4c_p^2 c_f^2)^{\frac{1}{2}} \right\} \tag{9}
$$

$$\lambda_3^2 = \lambda_4^2 = \frac{1}{2}\left\{ q^2 + (q^4 - 4c_p^2 c_f^2)^{\frac{1}{2}} \right\} \tag{10}$$

with q is defined by $q^2 = c_f^2 + c_p^2 + 2v^2 \dfrac{\rho_f}{\rho_p} \dfrac{R}{e} c_f^2$

λ_1 and λ_2 are the celerity of pressure waves in the fluid, λ_3 and λ_4 are the celerity of the stress waves in the pipe wall.

Since $\mathbf{BB}^{-1}$ is a four-by-four matrix, then, from algebraic theory, the equation (7) can be written (Fröberg 1979, Hadj Taieb et al. 2002):

$$\tilde{X}(x,s) = \left[A(x,s)\right]\tilde{X}(0,s)$$
$$\tilde{X}(x,s) = \left[a_0 I + a_1\left(-sx\mathbf{BB}^{-1}\right) + a_2\left(-sx\mathbf{BB}^{-1}\right)^2 + a_3\left(-sx\mathbf{BB}^{-1}\right)^3\right]\tilde{X}(0,s) \tag{11}$$

where a_r are defined by using the determinants:

$$a_r = \frac{D_r}{D} \text{ with } D = \begin{vmatrix} 1 & 1 & 1 & 1 \\ -\dfrac{sx}{\lambda_1} & -\dfrac{sx}{\lambda_2} & -\dfrac{sx}{\lambda_3} & -\dfrac{sx}{\lambda_4} \\ \left(-\dfrac{sx}{\lambda_1}\right)^2 & \left(-\dfrac{sx}{\lambda_2}\right)^2 & \left(-\dfrac{sx}{\lambda_3}\right)^2 & \left(-\dfrac{sx}{\lambda_4}\right)^2 \\ \left(-\dfrac{sx}{\lambda_1}\right)^3 & \left(-\dfrac{sx}{\lambda_2}\right)^3 & \left(-\dfrac{sx}{\lambda_3}\right)^3 & \left(-\dfrac{sx}{\lambda_4}\right)^3 \end{vmatrix} \tag{12}$$

D_r is obtained by replacing the elements $\left(-\dfrac{sx}{\lambda_i}\right)^r_{i=1,\dots,4}$ in D by $\left(e^{-\frac{sx}{\lambda_i}}\right)_{i=1,\dots,4}$.

In equation (11), let $x = 0$ and $x = L$, we get four relations

$$\tilde{X}(0,s) = \left[A(0,s)\right]\tilde{X}(0,s) \tag{13}$$

$$\tilde{X}(L,s) = \left[A(L,s)\right]\tilde{X}(0,s) \tag{14}$$

Suppose that the Laplace transformed boundary conditions are linear ($\tilde{X}_i$) in and are known at the locations $x = 0$ and $x = L$ of the domain $0 \leq x \leq L$.

Then, upon assuming a total of N equations in N unknowns, there will generally be $N/2$ relationships at each end.

The boundary conditions at upstream ($x = 0$) and downstream ($x = L$) end of the pipe can be expressed by

$$G(0,s)\tilde{X}(0,s) = F(0,s) \tag{15}$$

$$G(L,s)\tilde{X}(L,s) = F(L,s) \tag{16}$$

Combining equations (13)-(16) and substituting into equation (11), we get

$$\tilde{X}(x,s) = \left[A(x,s)\right]\mathbf{R}^{-1}(s)\mathbf{F}(s) \tag{17}$$

3.2   *Impedance Matrix and Frequency Equation*

Combining equations (11), (15) and (16) we get:

$$\begin{bmatrix} \left[A(L,s)\right] & \left[-I\right] \\ \left[G(0,s)\right] & \left[0\right] \\ \left[0\right] & \left[G(L,s)\right] \end{bmatrix} \begin{bmatrix} \tilde{X}(0,s) \\ \tilde{X}(L,s) \end{bmatrix} = \begin{bmatrix} \left[0\right] \\ \mathbf{F}(s) \end{bmatrix} \tag{18}$$

where $\left[I\right]$ is the identity matrix and $\left[0\right]$ is a zero matrix.

Equation (18) may be written in matrix form

$$ZX = F \tag{19}$$

Since F is the external excitation acting at the end of the pipe, Z is, therfore, the impedance matrix. Z^{-1} is the frequency response matrix of the pipe subject to the external excitation acting at the end of the pipe.

Setting the right-hand term in equation (19) equal to zero. Since X is not always equal to zero, there must be

$$\det Z = 0 \tag{20}$$

Equation (20) is the frequency equation (Li et al (2002)) desired with $s = j\omega$ as a variable, the natural frequencies can be obtained by setting the equation (20) equal to zero.

4   Applications and Results

Considering the example studied previously by Zhang et al. (1999) which consist of a simple reservoir-pipe-valve system as shown in figure 1. The pipe is fixed to a constant pressure reservoir at its upstream end and has an unrestrained valve at its downstream end. In the steady state situation fluid is flowing from reservoir to valve. The properties of the fluid and the pipe are given in Table 1.

At the time $t = 0$, the liquid and pipe wall at the valve are suddenly exited by an instantaneous closure of the valve.

At the valve, the boundary condition is

$$V(L) - \dot{u}_x(L) = -V_0 \text{ and } S_f P(L,t) - S_p \sigma_x(L,t) = m_L \frac{d\dot{u}_x(L,t)}{dt} \tag{21}$$

where V_0 is the initial fluid velocity ($V_0 = 1\,m/s$) and S_f and S_p are cross-sectional area of fluid and pipe respectively.

At the upstream end of the pipe, the constant pressure is equal to zero.
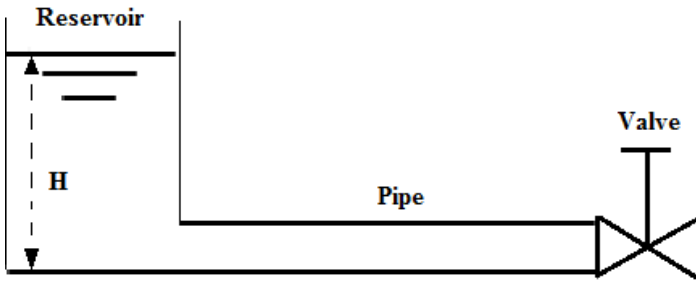
Fig. 1 Reservoir-pipe-valve system

The natural frequencies from decoupled and coupled models (for the pipe wall and the fluid) are given in Table 2. These results are determined by the frequency equation (20).

In this example the FSI has led to the decrease of pressure wave speed in the fluid and the increase of stress wave speed in the walls of the pipe ($\lambda_{1,2} = \pm 1025\,m/s$ and $\lambda_{3,4} = \pm 5281\,m/s$)

The celerity of pressure waves $\lambda_{1,2}$ in equation (9) is smaller than the classical value c_f, because the latter does not allow for the axial inertia of the pipe wall. The axial stress wave speed $\lambda_{3,4}$ in equation (10) is larger than the classical value c_p, because the latter does not account for pressure changes provoked by axial stresses.

When the natural frequencies of the fluid and the pipe wall are close to each other, there is a tendency that the coupled values of natural frequency to deviate from the uncoupled values.

Table 1 Properties of fluid and pipe

Pipe	Fluid
$L = 20\,\text{m}$	$K = 2.1\,\text{GPa}$
$\rho_p = 7900\,\text{Kg/m}^3$	$\rho_f = 1000\,\text{Kg/m}^3$
$f_p = 0.002$	$f_f = 0.0005\text{Hz}$
$D_p = 21\text{Hz}$	
$e = 8\,\text{mm}$	
$E = 210\,\text{GPa}$	
$R = 398.5\,\text{mm}$	
$v = 0.3$	
$m_L = 0$	

Table 2 Natural frequencies in reservoir-pipe-valve system (Hz)

Calculation with FSI	Fluid ($v = 0.3$)	Fluid ($v = 0$)	Pipe
12.4	13.12	12.82	
31.82	39.36	38.46	
55.69	65.59	64.1	
73.17	-	-	64.45
96.92	91.83	89.74	
116.19	118.07	115.39	
140.99	144.31	141.03	
160.53	170.54	166.67	
184.52	196.78	192.31	
202.04	-	-	193.34
225.68	223.02	217.95	
244.8	249.26	243.59	
269.58	275.49	269.23	
289.23		294.88	

This is the case for the frequencies of the fluid's third and eighth modes (simple model) which have very similar to those of the pipe's first and second modes, respectively. (See Table 2 and figure 2)

For this reason, as shown in figure 3, the frequency spectrum's pressure obtained by the coupled model completely changes its appearance compared with that without FSI near the natural frequencies of the pipe 64 Hz and 193 Hz.

In the same frequency range, the number of natural frequencies with FSI increases relative to him without FSI (Table 2).

Note that natural frequencies in Table 2 calculated by the proposed method are the same as those obtained from Zhang et al. (1999) using Laplace transformation.

The matrix **C**, including in the equation (3), contains terms of dispersion and damping. If the matrix **C** is not zero, the number of resonance frequencies and amplitudes of the parameters studied (stress, pressure, etc.) will decrease (figure 4). Subsequently the effects and risks of resonance are reduced.
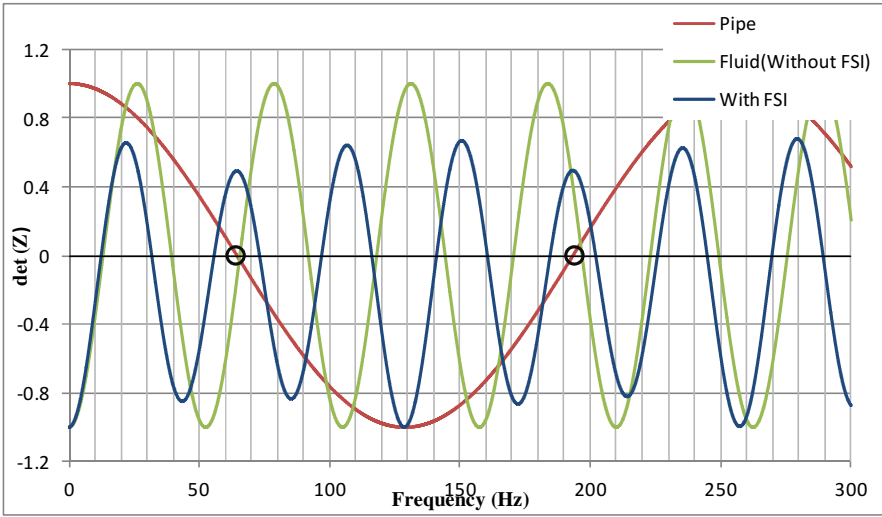
Fig. 2 Frequency spectrum of the determinant of the impedance matrix (Pipe wall and fluid)
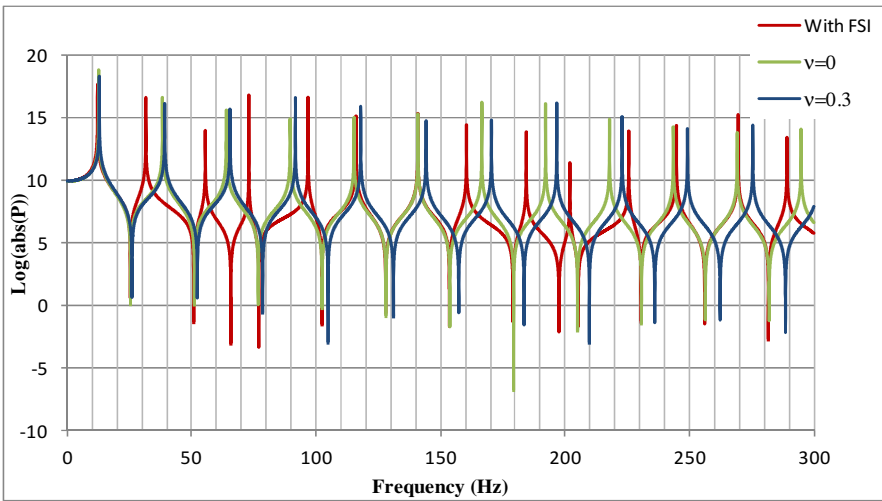
Fig. 3 Frequency spectrum of pressure at $x = L$ (With and without FSI)
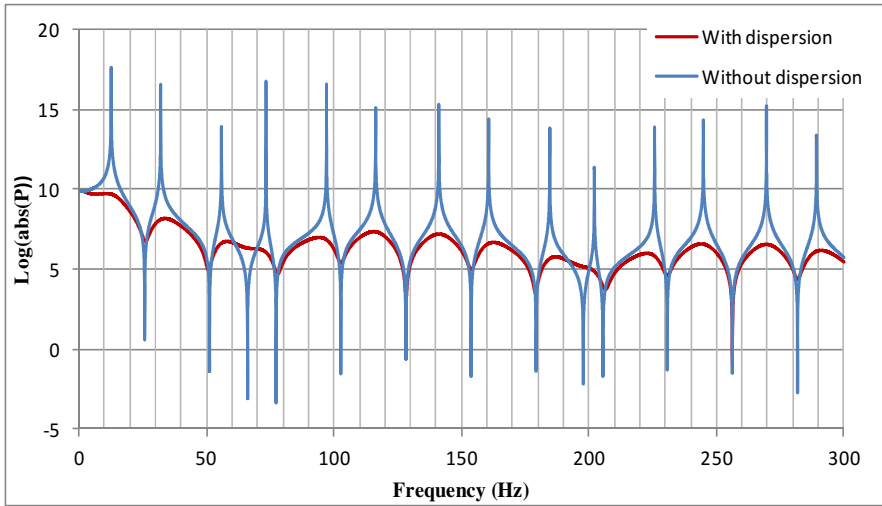
Fig. 4 Influence of dispersion on pressure frequency spectrum of at $x = L$

In the following, the piping system (figure 1) was excited with the natural frequency (65.59 Hz) of decoupled model. The pressure upstream of the pipe is:

$$P(t) = 9.81 + 0.3 \times \sin(2 \times \pi \times 65.95 \times t) \tag{22}$$

Downstream, the valve is kept closed.

After resolution by the characteristic method (Tijsseling A S (2003)), the pressure has been calculated at valve. The resonance phenomenon appeared (figure 5), but for the same frequency we get a beat phenomenon with FSI resolution.
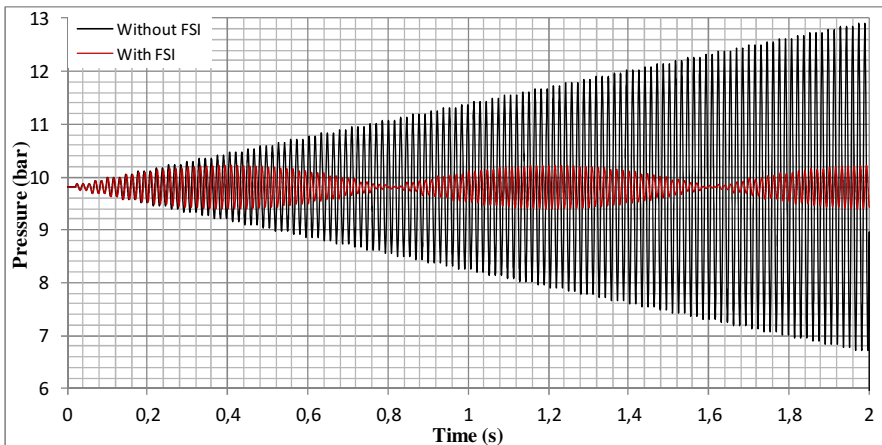
Fig. 5 Pressure at the valve with and without FSI

5   Conclusion

In this work we were able to study the dynamic behavior of a simple piping system using the transfer matrix method. The results obtained show that the FSI led to the decrease of the pressure waves and to the variation of the frequency response of system. If the end of the pipe has the ability to move, the calculations with FSI are required because it is necessary to consider the coupling junction.

References

Fröberg, C.E.: Introduction to numerical analysis. Addison-Wesley Publishing Company, USA (1979)

Hadj Taieb, L., Elaoud, S., Hadj Taieb, E.: Determination of natural frequen-cies of pipe flows by the impedance method with fluid-structure coupling. In: 16th Collogue Vibrations Chocs et Bruit (VCB), Lyon, France (2010)

Li, Q.S., Yang, K., Zhang, L., Zhang, N.: Frequency domain analysis of fluid structure interaction in liquid-filled pipe systems by transfer matrix method. International Journal of Mechanical Sciences 44, 2067–2087 (2002)

Skalak, R.: An extension of the theory of water hammer. Transactions of the ASME 78, 105–116 (1956)

Tijsseling, A.S.: Exact solution of linear hyperbolic four-equation system in axial liquid-pipe vibration. Journal of Fluids and Structures 18, 179–196 (2003)

Zhang, L., Tijsseling, A.S., Vardy, A.E.: FSI analysis of liquid-filled pipes. Journal of Sound and Vibration 224(1), 69–99 (1999)

Passive Control on the NACA 4412 Airfoil and Effects on the Lift

Hocine Tebbiche[1] and Mohammed S. Boutoudj[1,2]

[1] Département de Génie Mécanique, Université Mouloud Mammeri,
  15 000 Tizi-Ouzou, Algérie
  Hocinetebbiche@yahoo.fr
[2] Laboratoire d'Energétique, Mécanique et Matériaux –LEMM,
  Université Mouloud Mammeri, 15 000 Tizi-Ouzou, Algérie
  Boutoudj_ms@yahoo.fr

Abstract. The boundary layer separation on the upper surface of airfoils results in a decrease of the aerodynamic performances accompanied by vibrations and noise. Passive flow control with vortex generators (VGs) is a simple solution to delay or eliminate the flow separation. Lin's generators V-shaped are among the most efficient and allow a significant increase in lift associated with a drag reduction when their height is less than the boundary layer thickness. The present work concerns the effectiveness of a new VGs configuration, delta wing shape, placed on line on the suction surface of a curved profile (NACA 4412). The experimental study conducted in a wind tunnel at Reynolds number equals to $2.5 \ 10^5$ shows improved lift with an increase of 20% and one degree delay of the stall incidence. The study also highlights the VGs geometrical parameters influence such as their height, their position from the leading edge, their spacing and their apex angle.

Keywords: Airfoil, Boundary layer, Vortex Generators, Lift.

1   Introduction

The flow on the upper surface airfoil is subject to an adverse pressure gradient when the incidence increases. This leads to the boundary layer separation which causes looses in the aerodynamic performances (lift decrease and drag increase). It is well known that the lift around an airfoil is rather created by the suction on the upper surface than the overpressure on the lower one. The flow control (Gad-el Hak et al. 1998) aims to delay or eliminate the fluid separation and then to take away its undesirable effects like vibrations and aerodynamic noise.

Passive vortex generators (VGs) are simple use and known to bring momentum in the boundary layer which leads to the delay or suppression of the flow separation (Lin 1999, Bak et al. 2000, Godard and Stanislas 2006).

Vortex generators enhance the aerodynamic performances and the most efficiency are the Lin's ones V-shaped when their height is less than the boundary

layer thickness (Lin 1999). Their interest is all the greater as they also have the advantage to be retractable when they are not in use.

The present work focuses on the control of incipient separation on the upper NACA 4412 airfoil by means of VGs with delta shape to improve the aerodynamic performances. The choice of the delta wing configuration type to control the separated flow is linked to the formation of two strong vortices at its leading edges. These vortices are counter-rotating ones which are the most efficiency for the flow control. Furthermore, they break down only at high incidences. The obtained results are analyzed taking into account in several parameters such as spacing, the height, the apex angle, and the relative incidence angle of VGs as well as their position according to the chord length.

2   Experiments Description

2.1   *Experimental Conditions*

The studied model is the NACA 4412 profile; the chord length is L = 150 mm and the depth is equal to 200 mm. The lift force was measured by way of an aerodynamic balance connected to an acquisition chain. Each test realized was repeated three times and averaged. The time of acquisition was 60 s with 500 Hz frequency.

All the experiments were performed in a Deltalab™ type open circuit. Maximum speed is higher than 45 m/s. The turbulence rate is fixed by a grid at the entry of 5×5 mm^2. The length and the wind tunnel section are respectively 100 cm and 30×30 cm^2.

2.2   *Vortex Generators*

The vortex generators studied are small delta wings placed on the suction face of the airfoil. The choice for using the delta wing configuration type to control the separated flow resides in the fact that when a delta wing is subjected to a wind flow, starting from relatively weak incidences, it's observed the appearance of winding vortices at the leading edges which produces two swirls generated by the longitudinal flow. These two vortices are known to be very strong, bursting only at high incidences (Werlé 1971) and they may bring momentum in the boundary layer to delay its separation.

A line of the vortex generators is laid on the suction face of the NACA 4412 profile at x/L = 0.1 as shown in Fig.1. The delta wings are set relatively at weak incidences in order to avoid the unhooking of the wings. The influence of the VGs geometrical parameters (Fig. 1) such as spacing [λ], the height [H], the apex angle [β], the relative incidence angle of VGs [γ] as well as their position according to the chord length were considered and are presented in the following.

The boundary layer thickness δ around the airfoil without the VGs was first numerically determined using a CFD code (Fluent) in order to take this parameter into account in the design of the VGs. Its value is estimated to 3 mm at x/L = 0.16 for a Reynolds number equal to $2.5 \ 10^5$.
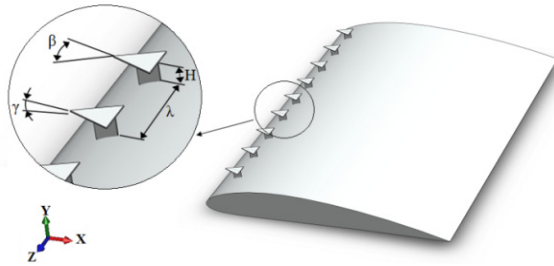
Fig. 1 Shape and disposition of the delta VGs

3   Results and Discussion

The effect of the passive flow control on the profile is presented in the following sections. NACA 4412 airfoil brand the unhooking around of 18 degrees and only the attack angles at post stall (19°) are described as part of this comparative study. The objective is focused on the aerodynamic lift increase and the contributions of the different geometrical parameters above enumerated.

The lift coefficient C_L is commonly defined as:

$$C_L = \frac{2F_y}{\rho U_\infty^2 S} \tag{1}$$

F_y is the lift measured with the aerodynamic balance, ρ is the volumic weight, S the surface airfoil and U_∞ the upstream velocity which was fixed to 25 m/s corresponding to $2.5 \ 10^5$ Reynolds number.

The results shown in Figs. 2-6 illustrate the aerodynamic load related to the variation of the vortex generators geometrical parameters. The lift is expressed as a percentage profit related to the baseline case.

The measurements of the data lift in Fig. 2 denote the variation effect of the H parameter; the curve shows a behavior which increases from $H/\delta = 1.1$ until $H/\delta = 1.8$, where a decreased performance is observed. It is noticed that the values of H/δ lower than 1.1 were not represented sake of loud noise production by the VGs. For this first configuration the other parameters were kept constant and relatively equal to $\beta = 45°$, $\gamma = 10°$, $\lambda = 19$ mm and $x/L = 0.1$.

Thereafter, H/δ is kept constant and equal to 1.8 whereas the remaining parameters are varied one after the other in order to determine the influence of each one on the lift enhancement. The same procedure is then repeated to each varied parameter in order to find its optimal value, and so on. However, the different geometric parameters may interact and the optimization scheme appears somehow in a simplified way.

The variation effect of the λ parameter (Fig. 3) is observed to spacing between $3.8 < \lambda/H < 4.6$, due the formation of a quasi-constant level on the highlighted range and then one can see a decrease of the generated lift. So, it's recommended to maintain the spacing $\lambda/H = 3.8$ for the remainder of the study which allows additional VGs for better performances.
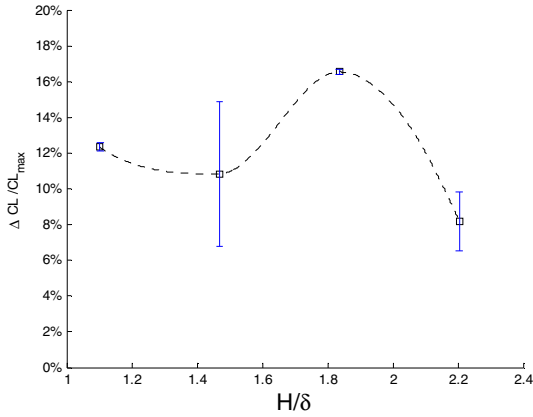
Fig. 2 Effect of the height H of the Δ-VGs, β=45°
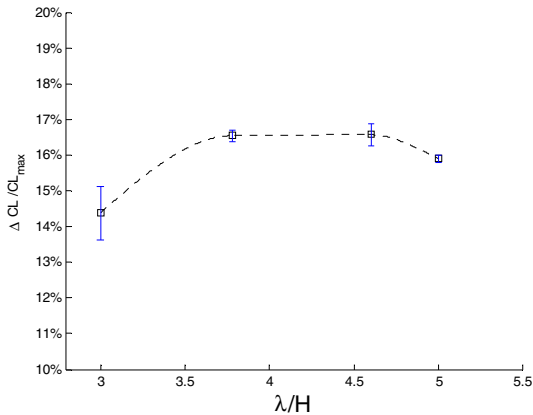
Fig. 3 Effect of the spacing λ between the Δ-VGs, β=45°

The evolution of the lift as a function of the relative incidence γ (Fig. 4) shows a linear increase up to γ = 10°. From this incidence, we see the beginning of the fall in overall performance; this is probably due to the stall of the delta wings VGs and the cessation on the production of organized vortices. The experiments were conducted in a range of angles from β = 30° until β = 74.6° but only the case corresponding to β = 45° is here presented.

It is well known than the leading edge vortices are formed at an incidence around seven or eight degrees. This can explain the inefficiency of the VGs at the lowest incidence tested (5 degrees) as shown in Fig. 4. One can also see in this last figure than the maximum lift generated by the VGs is obtained for 10 degrees of the relative incidence.

For the study of the apex angles effects (Fig. 5), all used angles are privileged ones that are known to be able to create high intensity vortices compared with the non-privileged ones (Le Ray et al. 1985). A peak value is distinguished for $\beta = 45°$ which produce a maximum lift profit that can reach approximately 16.5%.
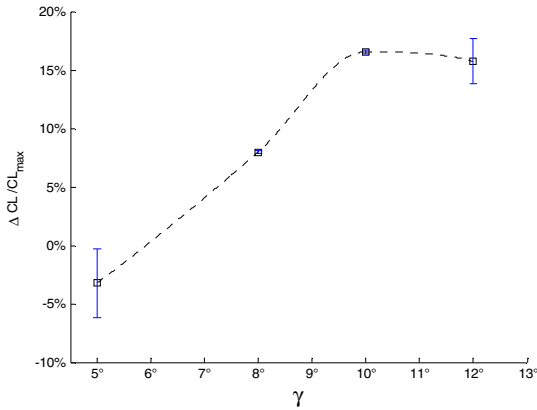
Fig. 4 Effect of the relative incidence angle γ of the Δ-VGs, $\beta=45°$
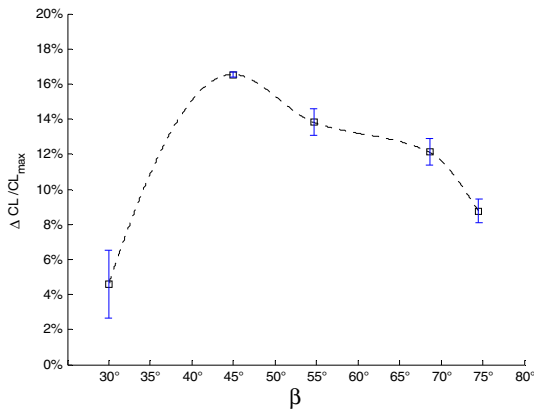
Fig. 5 Apex angle β effect of the Δ-VGs

The position effect along the chord length was also studied by moving the line of the vortex generators. The outlined curve shows that the VGs effectiveness decreases while displacing from the leading edge (Fig. 6). The best recorded position equals 10%.

The final configuration of the flow control on the NACA 4412 airfoil was composed by VGs having the obtained optimal parameters and was supplemented by two others VGs. The lift coefficient versus the angle of attack is represented in Fig. 7 for the controlled and the uncontrolled flows. One can see in this figure that the total profit lift can reach 19% with one degree stall angle delay.
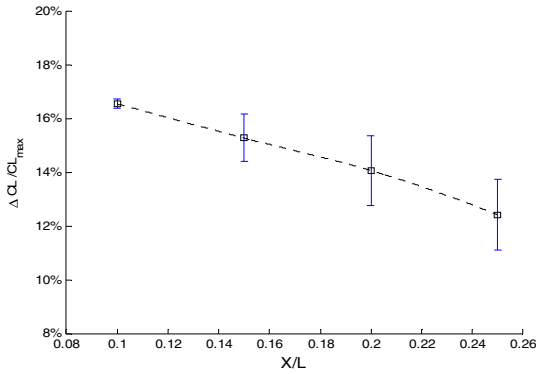
Fig. 6 VGs position effect on the lift coefficient along the chord length
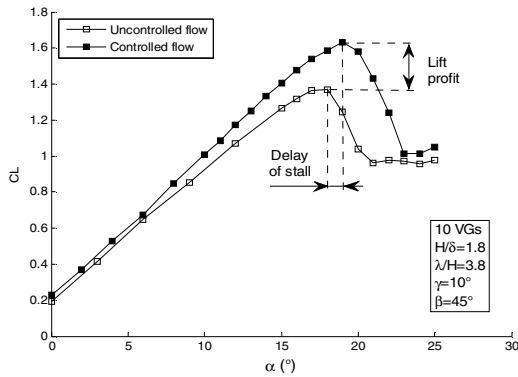
Fig. 7 Maximum lift profit of the final Δ-VGs configuration, Re=2.5 10^5

4   Conclusion

We have in the foregoing proposed a new configuration of vortex generators of
delta wing shape and determined some characteristics in order to improve the
aerodynamic performances of NACA profiles. The study has shown lift enhance-
ment and highlighted the several geometrical parameters importance.

The maximum profit is obtained when the geometrical parameters of VGs are
maintained to H/δ = 1.8, λ/H = 3.8, γ = 10° and β = 45°.

The flow control with the delta wings VGs reaches 20% in lift increase and a
delay of one degree of stall angle for the considered Reynolds number.

References

[1] Gad-el-Hak, M., Pollard, A., Bonnet, J.P.: Flow control: fundamentals and practices. Springer, Heidelberg (1998)

[2] Lin, J.C.: Control of turbulent boundary-layer separation using micro-vortex generators. AIAA paper, 3404 (1999)

[3] Bak, C., Fuglsang, P., Johansen, J., Antoniou, I.: Wind tunnel tests of the NACA 63-415 and a modified NACA 63-415 airfoil. Risø National Laboratory, Roskilde, Denmark (2000)

[4] Godard, G., Stanislas, M.: Control of a decelerating boundary layer. Part 1: Optimization of passive vortex generators. Aerospace Science and Technology 10(3), 181–191 (2006)

[5] Werlé, H.: Sur l'éclatement des tourbillons. Office National d'Études et de Recherches Aéronautiques (1971)

[6] Le Ray, M., Deroyon, J.P., Deroyon, M.J., Minair, C.: Critères angulaires de stabilité d'un tourbillon hélicoïdal ou d'un couple de tourbillons rectilignes, rôle des angles privilégiés dans l'optimisation des ailes, voiles, coques des avions et des navires. Bulletin de l'Association technique maritime et aéronautique, 511–529 (1985)

On the Existence of Wavy Plug-Zone for a Bingham Fluid in Mixed Convection between Two Horizontal Plates

Hakim Mkacher and Abdelhak Ayadi

Computational Fluid Dynamic and Transfer Phenomena ENIS, University of Sfax, Tunisia
{Hakim.mkacher,Abdelhak.ayadi}@gmail.com

Abstract. In this paper, we carried out a two dimensional simulation of a Bingham fluid or commonly named yield-stress fluid in Rayleigh-Bénard Poiseuille flow between two horizontal plates with the non-slip boundary condition. The pure laminar flow of such fluid is characterized by a central high-viscous zone. Raising the Rayleigh number in the aim to assist to convective instability passes through a primordial state where streamlines present wavy shape. This work investigates the existence of a central continuous high-viscous zone in such state for the combination of dimension-less numbers Bn=10, Pr=7 and Re=1. The bi-viscous model is used to describe the rheological behavior of the Bingham fluid. The simulations are carried on Fluent software. In reliance on the present results, the rigid zone described in a Bingham Poiseuille flow does not seem obvious that it remains fully continuous. Indeed, in a Bingham Poiseuille Rayleigh-Bénard flow, the high-viscous zones present boomerang shaped fragments even when the streamlines are slightly wavy and the Rayleigh number is below the threshold of the convective instability. To conclude, one can predict that the critical Rayleigh number is identified and is estimated between 7125 and 7135 for the considered dimension-less numbers.

Keywords: Poiseuille Rayleigh-Bénard flow, Bingham fluid, mixed convection, plug- zone, critical Rayleigh number.

Nomenclature		u_i	i^{th} velocity component (m/s)
		x_i	coordinate in the ith direction (m)
Bn	Bingham number (-)	α	thermal diffusivity (m^2/s)
C_p	specific heat at constant pressure (J/kg K)	β	thermal expansion coefficient (1/K)
e	half of the gap (m)	γ	ratio between the two viscosities ($=\mu/\mu_0$) (-)
g	gravitational acceleration (m/s^2)		
L	length of the domain (m)	δ_{ij}	Kronecker symbol
P	static pressure (N/m^2)	λ	thermal conductivity (W/mK)
Pe	Peclet number	μ_0	yield viscosity (Ns/m^2)
Pr	Prandtl number (-)	μ	plastic viscosity (Ns/m^2)
Ra	Rayleigh number (-)	ρ	density (m^3/kg)
Re	Reynolds number (-)	τ_y	yield stress (N/m^2)
T	temperature (K)		

1   Introduction

Bingham or commonly called yield-stress fluids represent a wide range of industrial and daily-use fluids (glue, toothpaste, gel, yogurt…). Their rheological behavior is characterized by the existence of a rigid-like zone or plug-zone if the shear stress is under a unique threshold property of the fluid.

To describe the behavior of these fluids, Bingham introduced his own model (Bingham 1922) considering the plug-zone as solid. This model is the simplest but includes the major ambiguity that the material is considered at the same time fluid and solid.

Several regularized models were introduced to define a viscosity in the plug-zone. Papanastasiou (Papanastasiou 1987) added an exponential term in the constitutive equation to represent the area below the threshold as high-viscous instead of rigid.

The bi-viscosity model defines a proper viscosity in the plug-zone and another elsewhere as shown by Ayadi (Ayadi 2011). By changing the ratio between the two viscosities γ, the bi-viscosity model can mimic at once Newtonian and yield-stress fluids. O'Donovan and Tanner (O'Donovan and Tanner 1984) showed that taking $\gamma=10^{-3}$ is sufficient to describe Bingham fluids correctly. It is worth to mention that the bi-viscosity model can be retrieved from the Herschel-Bulkley model (Herschel and Bulkley 1926) taking the fluidity index n=1.

In mixed convection or Rayleigh-Bénard Poiseuille flow, convective cells appear when the Rayleigh number reaches a critical value Ra_c. This value remains an elusive element in the literature because no criteria were fixed to precisely indicate the transition to convective instability.

The genesis of Bénard cells passes through primordial mode where streamlines present wavy shape. In this paper, we investigate whether the plug-zone of the yield-stress fluid will remain intact during this primordial mode.

2 Mathematical Background

The bi-viscosity model is used to represent a Bingham fluid.

2.1 Constitutive Equations for a Bi-viscous Fluid

$$\bar{\bar{\tau}} = \mu_0 \bar{\bar{\dot\gamma}} \qquad\qquad \text{for } \bar{\tau} \le \tau_y \tag{1}$$

$$\bar{\bar{\tau}} = \left(\frac{\tau_0}{\bar{\dot\gamma}} + \mu\right)\bar{\bar{\dot\gamma}} \qquad\qquad \text{for } \bar{\tau} > \tau_y \tag{2}$$

Where $\tau_0 = \tau_y\left(1 - \frac{\mu}{\mu_0}\right)$, $\bar{\tau} = (\text{tr}[\bar{\bar{\tau}}.\bar{\bar{\tau}}])^{\frac{1}{2}}$, $\bar{\dot\gamma} = \left(\text{tr}[\bar{\bar{\dot\gamma}}.\bar{\bar{\dot\gamma}}]\right)^{\frac{1}{2}}$

2.2 Dimension-Less Governing Equations

The governing equations can be written in two different ways depending on the region of interest:

• In the high-viscous region:

Mass conservation equation:

$$\frac{\partial u_i^*}{\partial x_i^*} = 0 \tag{3}$$

Momentum conservation equation:

$$\text{Re}\gamma\,\frac{\partial u_i^*}{\partial t^*} + \text{PeRe}\gamma\frac{\partial u_i^*}{\partial x_j^*}u_j^* = -\gamma\frac{\partial P^*}{\partial x_i^*} + \delta_{i2}\text{Ra}\gamma T^* + \text{Pe}\frac{\partial \dot\gamma_{ij}^*}{\partial x_j^*} \tag{4}$$

Energy conservation equation:

$$\frac{\partial T^*}{\partial t^*} + \text{Pe}\,u_j^*\frac{\partial T^*}{\partial x_j^*} = \frac{\partial}{\partial x_j^*}\left(\frac{\partial T^*}{\partial x_j^*}\right) \tag{5}$$

• In the fluid region:

Mass conservation equation:

$$\frac{\partial u_i^*}{\partial x_i^*} = 0 \tag{6}$$

Momentum conservation equation:

$$\text{Re}\frac{\partial u_i^*}{\partial t^*} + \text{PeRe}\frac{\partial u_i^*}{\partial x_j^*}u_j^* = -\frac{\partial P^*}{\partial x_i^*} + \delta_{i2}\text{Ra}T^* + \text{Pe}\frac{\partial \dot\gamma_{ij}^*}{\partial x_j^*} + \text{PeBn}(1-\gamma)\frac{\partial}{\partial x_j^*}\left(\frac{\dot\gamma_{ij}}{\bar{\dot\gamma}}\right) \tag{7}$$

Energy conservation equation:

$$\frac{\partial T^*}{\partial t^*} + \text{Pe}\,u_j^*\frac{\partial T^*}{\partial x_j^*} = \frac{\partial}{\partial x_j^*}\left(\frac{\partial T^*}{\partial x_j^*}\right) \tag{8}$$

The (*) sign is used to indicate non-dimensional terms. The dimension-less form is obtained by using U_0 the medium horizontal velocity as velocity scale, the

gap between the two plates 2e as length scale, $U_0/(2e)$ as velocity gradient scale, $(\mu\alpha)/(4e^2)$ as pressure scale and $(2e)^2/\alpha$ as time scale. The modified non-dimensional temperature T^* is $T^* = (T - T_C)/(T_H - T_C) = (T - T_C)/\Delta T_{ref}$.

Finally, the dimension-less numbers are defined as:

$Bn = (2e\tau_y)/(\mu U_0), Pe = (2eU_0)/\alpha, Pr = (\mu C_p)/\lambda, Ra = (8e^3\rho g\beta\Delta T_{ref})/(\mu\alpha)$ and $Re = (2e\rho U_0)/\mu$.

3   Numerical Implementation

3.1   Numerical Methods

FLUENT software is used to solve the conservation equations of mass, momentum and energy. The Boussinesq approximation is employed to simulate buoyancy forces while the properties of the fluid are considered independent of temperature.

A second order unsteady solver is used with the time step size $\Delta t = 0.1s$. Further, a second order upwind scheme is used to discretize the momentum and energy equations, as well a second order scheme for the pressure gradient. The convergence criterion is set to 10^{-6} for all the scaled residuals.

3.2   Computational Domain

The computational domain is shown in figure 1. The two horizontal walls are maintained at different temperatures where $T_H > T_C$. The non-slip boundary condition is employed.
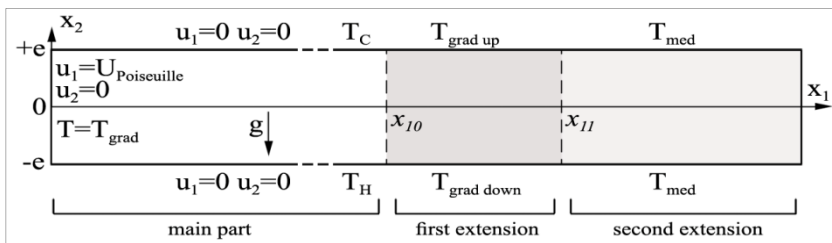
Fig. 1 Schematic of the computational domain

At the entry, Poiseuille flow and linear temperature profile are imposed. To avoid backflow at the exit, two extensions were added. In the first extension, the temperature difference between the horizontal walls is reduced gradually. For the second extension, the walls are maintained at the same medium temperature T_{med}.

Initial conditions are the Poiseuille flow for the velocity and T_C for the temperature. The aspect ratio of the main part is 1:10 with a structured and uniform mesh of 40x400. The horizontal mesh density of the rest of the domain is reduced to minimize numerical costs. For the rest of the paper only results concerning the main part will be shown.

3.3   *Validation*

Validation of our method is obtained by reproducing previous experimental works of Ouazzani (Ouazzani et al. 1990) and numerical works of Nicolas (Nicolas et al. 1997) using the water as a fluid of study. Table1 represents the maximum vertical velocity recorded in the medium horizontal plane for different Reynolds and Rayleigh numbers.

Table 1 The maximum vertical velocity obtained by the present work and previous works

Ra	Re	Vmax ($\mu m.s^{-1}$) Present study	Vmax ($\mu m.s^{-1}$) Ouazzani experimental study	Vmax ($\mu m.s^{-1}$) Nicolas numerical study
1804	0.21	79	106	71
2490		295	292	289
2420	0.19	280	273	274
	0.53	276	273	273
	0.65	276	273	273
2024	0.15	181	180	174
	0.42	179	180	173

Simulations were carried for Bn=10, Re=1 and Pr=7. Rayleigh number was varied in the aim to assist to the previously described primordial mode.

4   **Results and Discussion**

We have changed the Rayleigh number to get closer to the critical state without driving the flow to convective instability. For Ra=7125 (Fig. 2), the plug-zone is already destroyed even the streamlines are slightly wavy. The plug-zone is sawn in inflection areas (where the streamlines change direction) showing boomerang-shaped fragments. For simulation with Ra=7000, 7100 and 7125, fluctuations in the streamlines will vanish, leaving the Poiseuille flow take over the running.
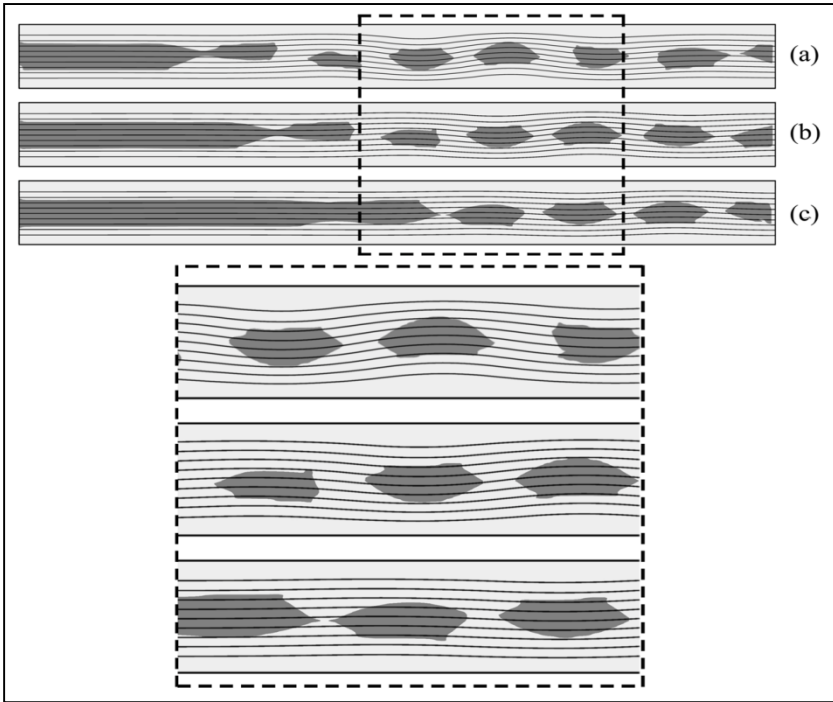
Fig. 2 Streamlines for Ra=7125 with high-viscous zones shaded in dark gray, (a) t=600s, (b) t=700s and (c) t=800s

In the case of Ra=7135 (Fig. 3), the fragmented areas materialize at the beginning, but the convective instability overcomes the laminar flow, giving birth to Bénard cells, while the rest of the plug-zone is almost disintegrated under the high shear stress.

The graphic shown in figure 4 (Fig.4) Represents the vertical velocity in function of time recorded at the horizontal mid-plane at x_1=10e (five times the gap). In other words, it shows the footprint of fluctuations in streamlines passing through the considered point.

For Ra=7100 and 7125 the decrease of the magnitude of the vertical velocity beyond 600s announces the transition from the primordial mode to a pure laminar flow. Although, for Ra=7135, the expansion of the fluctuations witnesses the convective instability switch, confirmed by the formation of convective rolls. Therefore, for Bn=10, Pr=7 and Re=1, the critical Rayleigh number is located between these two values (7125<Ra_c<7135).
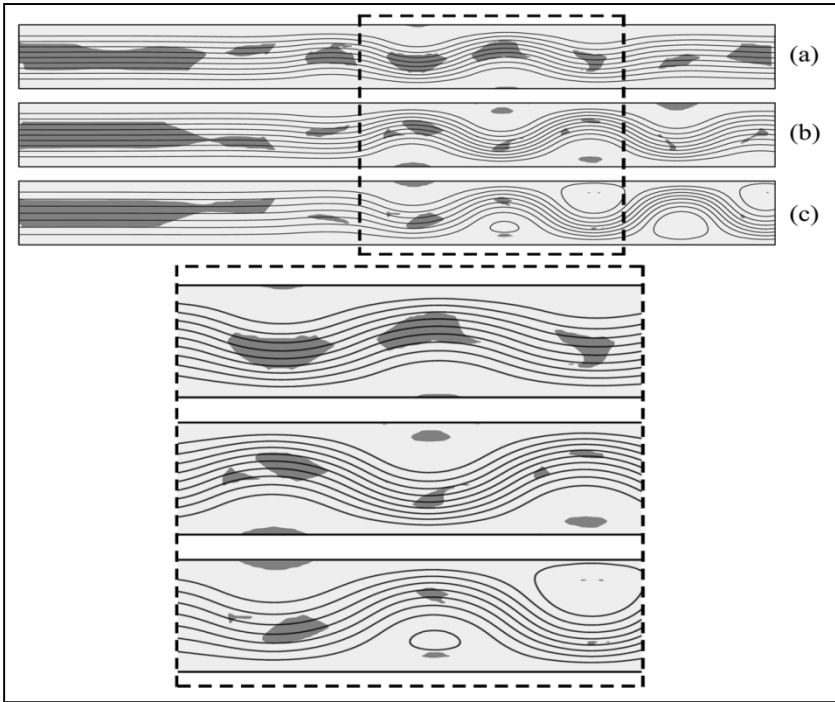
Fig. 3 Streamlines for Ra=7135 with high-viscous zones shaded in dark gray, (a) t=600s, (b) t=700s and (c) t=800s
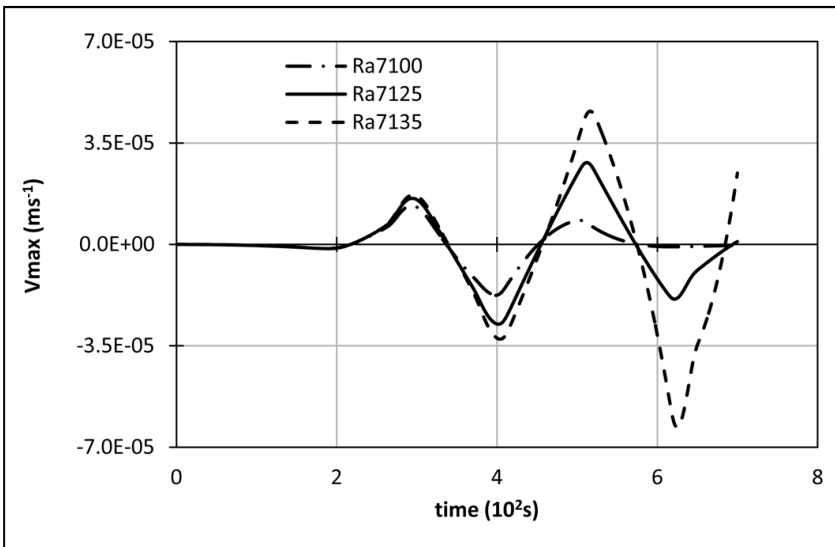
Fig. 4 Vertical velocity function of time recorded at the horizontal mid-plane for x_1=10e

5   Conclusion

Laminar mixed convection of yield-stress fluid between two horizontal plates has been processed numerically for specific Reynolds, Prandtl and Bingham numbers (Re=1, Pr=7, Bn=10) and a range of Rayleigh numbers around the critical value (7000≤Ra≤7135). For Ra=7125 which is below Ra_c, even the streamlines are slightly wavy, the shear stress is enough to destroy the plug-zone. Therefore, In our case, the combination of dimension-less numbers will not result in a wavy plug-zone.

The initial conditions considered in our case gave rise to a first traveling instability that will vanish if the flow become purely laminar or will grow giving birth to convective instability. We have characterized this switch upon the variation of the temporal vertical velocity values token in a specific point in the horizontal mid-plane.

The fragmented high-viscous regions are located where the shear stress is minimal, mainly in straight streamlines and around the epicenters of the convective rolls.

References

Ayadi, A.: Exact analytic solutions of the lubrication equations for squeeze-flow of a biviscous fluid between two parallel disks. Journal of Non-Newtonian Fluid Mechanics 166, 1253–1261 (2011), doi:10.1016/j.jnnfm.2011.08.003

Bingham, E.C.: Fluidity and Plasticity, vol. 2. McGraw-Hill Book Company, Incorporated (1922)

Herschel, W.H., Bulkley, R.: Konsistenzmessungen von gummi-benzollösungen. Kolloid-Zeitschrift 39(4), 291–300 (1926)

Nicolas, X., Mojtabi, A., Platten, J.K.: Two-dimensional numerical analysis of the Poiseuille–Bénard flow in a rectangular channel heated from below. Physics of Fluids (1994-present) 9(2), 337–348 (1997), doi:10.1063/1.869235

Ouazzani, M.T., Platten, J.K., Mojtabi, A.: Etude expérimentale de la convection mixte entre deux plans horizontaux à températures différentes—II. International Journal of Heat and Mass Transfer 33(7), 1417–1427 (1990), doi:10.1016/0017-9310(90)90039-W

O'Donovan, E.J., Tanner, R.I.: Numerical study of the Bingham squeeze film problem. Journal of Non-Newtonian Fluid Mechanics 15(1), 75–83 (1984), doi:10.1016/0377-0257(84)80029-4

Papanastasiou, T.C.: Flows of materials with yield. Journal of Rheology (1978-present) 31(5), 385–404 (1987), doi:10.1122/1.549926

New Correlation for Hydrogen-Natural Gas Mixture Compressibility Factor

Zahreddine Hafsi, Sami Elaoud, Mohsen Akrout, and Ezzeddine Hadj Taïeb

Laboratory of Applied Fluids Mechanics Process and Environment Engineering,
ENIS P.O. Box, W, Sfax, 3038, Tunisia
`hafsi.zahreddine@gmail.com, elaoudsa@yahoo.fr`

Abstract. In this paper, new correlation of hydrogen-natural gas mixture compressibility factor will be built. Based on Soave Redlich-Kwong (SRK) real gases equation of state (EOS) and under an isothermal condition, the evolution of gas compressibility factor will be followed up and compared to experimental data. The established correlation will be used to solve equation of motions in steady state and to evaluate the pressure drop through hydrogen natural-gas mixture pipeline.

Keywords: SRK equation of state, compressibility factor, hydrogen-natural gas mixture, linear regression.

1   Introduction

The pressure-volume-temperature (PVT) behavior of gases was the subject of numerous researches along the four previous centuries.

In 1845, Victor Regnault and by applying Avogadro's hypothesis on the volume occupied by one mole of an ideal gas, introduced the general equation of state on ideal gases $PV = nRT$, where n is the number of moles of gas and R is the universal gas constant. This relationship is the general equation that governs the PVT behavior of all substances that behave as ideal gases. In 1873, Johannes Diderik Van der Waals proposed correction terms to the Regnault ideal gas equation ($PV = nRT$). He added additional terms to both the P (pressure) and V (volume) variables in the ideal gas equation. these new correction terms introduced the effect of molecular attraction forces on the pressure term and took into account the size of real molecules on the volume term, in that way, Van der Waals replaced the pressure P in ideal gas equation with $(P + a^2/V)$ and the volume V with $(V - b$), so that his equation of state was written under the form:

$$(P + a^2/V)(V - b) = RT \tag{1}$$

where the terms a and b described, respectively, the molecular interaction forces and the actual volume occupied by the gas molecule.

Inspired from Van der Waals efforts, a large number of equations of state was constructed and several modifications were made to the original VDW equation, one can cite Pitzer EOS (1955), Beattie-Bridgeman EOS (1927), Benedict-Webb-Rubin (BWR) EOS (1940) and Redlich-Kwong EOS (1949). In 1955, Pitzer introduced the concept of acentric factor. This presents a measure of the configuration and sphericity of the molecule. In 1972, Giorgio Soave modified the Redlich-Kwong equation and introduced what known as SRK EOS.

In this paper, the SRK EOS will be the basis to establish a linear correlation of the compressibility factor evolution in binary gas mixture. The established Z factor expression will be used to integrate motions equation and to develop an expression of the pressure drop through pipeline of gas mixture.

2   SRK Equation of State

For computing purposes, a correction factor is introduced into the ideal gas EOS of state so, for real gases, the equation of state in its general form is written:

$$PV = ZRT \tag{2}$$

Where P is the pressure, V is the molar volume of the gas, Z is the compressibility factor R is the universal gas constant and T is the temperature

The major limitation of the above equation is that the gas compressibility factor Z is not a constant but it's a function of the pressure and the temperature of the considered gas, it was usually determined experimentally. However many correlations were established to evaluate Z with direct relations (Papp Correlation, 1995; Beggs and Brill correlation, 2005) or iterative relations (Hall-Yarborough Correlation, 1973; Dranchuk-Abu-Kassem Correlation, 1975) or even by considering a pseudo-constant Z factor in isothermal condition (Tabkhi, 2011).

Added to that, the SRK equation of state is written as follows (Tester and Modell, 1996; Prausnitz et al., 1998; Sandler, 1999):

$$P = \frac{RT}{V-b} - \frac{a}{V(V+b)} \tag{3}$$

where

$$b = 0.08664 \, \frac{RT_c}{P_c} \tag{4}$$

$$a = 0.42748 \frac{(RT_c)^2}{P_c} \left[1 + k\left(1 - \sqrt{T_r}\right)\right]^2 \tag{5}$$

T_c and P_c are respectively the critical temperature and the critical pressure of the considered gas, T_r is the reduced temperature defined by:

$$T_r = \frac{T}{T_c} \tag{6}$$

and

$$k = 0.480 + 1.574\omega - 0.176\omega^2 \tag{7}$$

where ω is Pitzer's acentric factor defined as follows

$$\omega = log_{10}\left(\frac{P_c}{P_{vp}}\right) - 1 \tag{8}$$

P_{vp} is the saturated vapor pressure of the gas at $T = 0.7T_c$

Equation (2) can be written as follows

$$V = \frac{ZRT}{P} \tag{9}$$

Equation (9) combined with equation (3) (the SRK EOS) gives:

$$\frac{RT}{ZRT-bP} - \frac{aP}{(RT)^2Z^2+bPRTZ} = 1 \tag{10}$$

Equation (10) is a 3rd order equation in term of Z, its development leads to:

$$(RT)^3Z^3 - (RT)^3Z^2 + [aPRT - bP(RT)^2 - (bP)^2RT]Z - abP^2 = 0 \tag{11}$$

The cubic equation (11) was numerically solved and the evolution of the compressibility factor Z versus pressure P for different temperature values was compared to curves issued from experimental data. Figure 1 shows a good concordance between numerical and experimental results for methane compressibility factors mainly for medium and high pressure range.
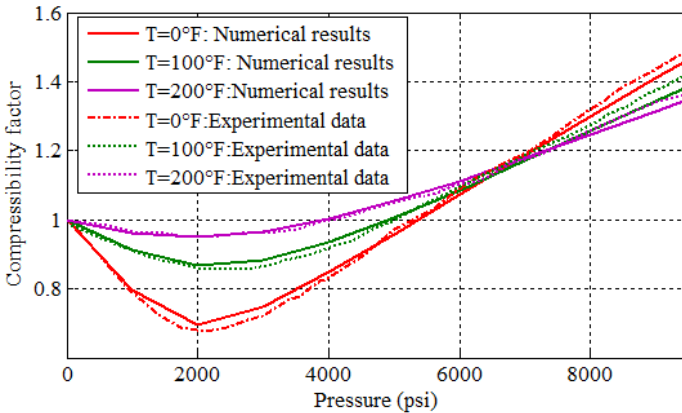
Fig. 1 Methane compressibility factor evolution (Experimental data source: Jeffrey L. Savidge, 2000)

In the following section, and using Matlab software for solving equation (11), a new correlation of Z factor expression for binary gas mixture will be established.

3   Compressibility Factor of Hydrogen Gas Mixture in Isothermal Condition

For pure substances, SRK EOS parameters a and b are determined by using the critical properties and the acentric factor. For mixtures, the parameters a and b are expressed through defined mixing rules. Most of the applications of EOS to mixtures used the classical Van der Waals mixing rules which give accurate results [Adachi and Sugie, 1985; Trebble, 1988; Shibata and Sandler, 1989].

The classical VDW mixing rules are given by the following expressions:

$$a_m = \sum_{i=1}^{n} \sum_{j=1}^{n} y_i y_j a_{ij} \tag{12}$$

$$b_m = \sum_{i=1}^{n} \sum_{j=1}^{n} y_i y_j b_{ij} \tag{13}$$

where y_i is the mole fraction of the component i, a_{ij} and b_{ij} $(i = j)$ are parameters corresponding to pure component (i) while a_{ij} and b_{ij} $(i \neq j)$ are called the unlike-interaction parameters.

Customarily, the geometric mean is used for the force parameter a_{ij} while the arithmetic mean is used for the volume parameter b_{ij}:

$$a_{ij} = \left(a_i a_j\right)^{\frac{1}{2}} \tag{14}$$

$$b_{ij} = \frac{b_i + b_j}{2} \tag{15}$$

Taking into consideration equation (15), the expression of b will be reduced to the following one-summation simple form:

$$b_m = \sum_{i=1}^{n} x_i b_i \tag{16}$$

For a binary mixture, using equations (12) and (16), one obtains:

$$a_m = x_1^2 a_1 + 2x_1 x_2 \sqrt{a_1 a_2} + x_2^2 a_2 \tag{17}$$

$$b_m = x_1 b_1 + x_2 b_2 \tag{18}$$

Considering a binary mixture of hydrogen and natural gas and, Table 1 shows the physical properties and the SRK EOS parameters a and b of hydrogen and natural gas calculated using equations (4) and (5) in a temperature $T = 288K$.

Table 1 Physical properties and SRK EOS parameters of hydrogen and natural gas

	Hydrogen (H2)	Methane(CH4)	Unit
Molecular weight (M)	2.02	16.04	g/mol
Critical temperature (Tc)	33.2	190.65	K
Critical pressure (Pc)	13.5	45.5	bar
Acentric factor (ω)	-0.215	0.008	
a	$1.3362.10^{-7}$	$1.8864.10^{-6}$	$bar.m^6.mol^-$
b	$1.8072.10^{-5}$	$3.0251.10^{-5}$	$m^3.mol^{-1}$

Let y be the mole fraction of hydrogen in the mixture, applying the simple mixing rules given by equations (17) and (18) for different mole fractions, the values of the SRK EOS parameters a_m and b_m of the binary mixture are reported in table 2.

Table 2 SRK EOS coefficients values for the mixture (T=288K)

y	0	0.25	0.5	0.75	1
a_m	$1.8864.10^{-6}$	$1.2577.10^{-6}$	$7.5604.10^{-7}$	$3.8134.10^{-7}$	$1.3362.10^{-7}$
b_m	$3.0251.10^{-5}$	$2.7206.10^{-5}$	$2.4161.10^{-5}$	$2.1117.10^{-5}$	$1.8072.10^{-5}$
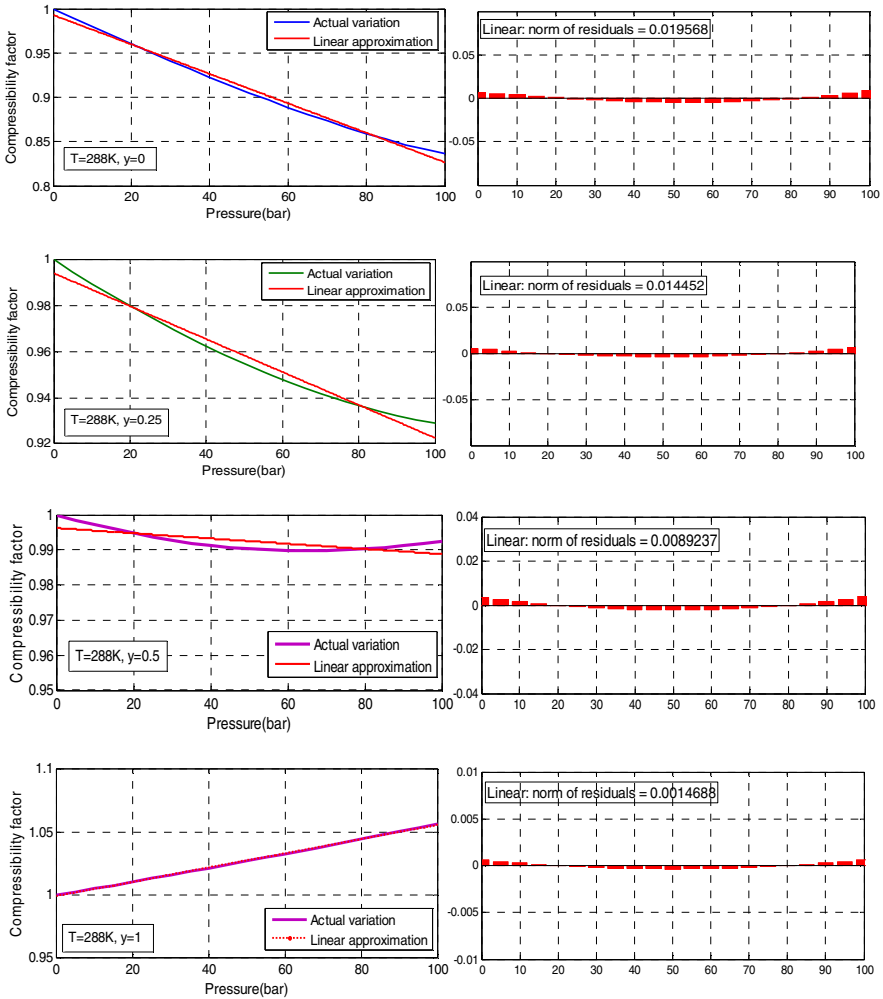
Fig. 2 Linear regression of the compressibility factor evolution

Considering the calculated SRK EOS parameters of the mixture in an isothermal condition ($T = 288K$) and in a range of pressure $0 < P(bar) < 100$, equation (11) was numerically solved and the evolution of the compressibility factor Z versus pressure for different y values is shown in figure 2.

The above curves show that, in the considered range of pressure, a linear approximation of Z factor's isothermal evolution is acceptable, then:

$$Z = \alpha P + \beta \tag{19}$$

where $\alpha = \alpha(y,T)$ and $\beta = \beta(y,T)$ depend on the temperature and the mole proportions of the gas mixture components.

Table 3 shows the calculated coefficients of equation (19) at $T = 288\ K$ and for different mole fractions of hydrogen in the mixture.

Table 3 Coefficients of the linear approximation

y	0	0.25	0.5	1
$\alpha(bar^{-1})$	$-166.26.10^{-5}$	$-71.636.10^{-5}$	$-7.4351.10^{-5}$	$56.396.10^{-5}$
β	0.99299	0.99421	0.99624	0.99936

4   Steady State Analysis

The mass conservation and momentum laws, applied to an element of fluid between two sections of abscissa x and $x + dx$ of an horizontal pipe, lead to the following equations that describe one-dimensional adiabatic compressible gas flow (Wylie et al, 1993):

$$\frac{\partial \rho V}{\partial x} + \frac{\partial \rho}{\partial t} = 0 \tag{20}$$

$$\frac{\partial \rho V}{\partial t} + \frac{\partial P}{\partial x} + \frac{\partial \rho V^2}{\partial x} + \frac{\lambda \rho V|V|}{2D} = 0 \tag{21}$$

where λ is the coefficient of friction, V is the velocity of the gas, ρ is its density, P is its pressure and D is the pipe internal diameter.

Mass flow rate m, also called pipe throughput, is expressed as function of the density, the gas velocity and the cross section area of the pipe A:

$$m = \rho V A \tag{22}$$

Using equation (9), the gas density ρ can be expressed, by introducing the compressibility factor Z and the average molecular mass of the gas M, as follows:

$$\rho = \frac{PM}{ZRT} \tag{23}$$

For gas mixture, M can be calculated using the simple mixing rule (Kay's rule):

$$M = \sum_{i=1}^{n} x_i M_i \tag{24}$$

Where M_i's are the molecular masses of species.

Considering equation (23), equations (21) and (22) can be, rearranged in the basis of mass flow rate and pressure, expressed as follows:

$$\frac{1}{A}\frac{\partial m}{\partial x} + \frac{M}{R}\frac{\partial}{\partial t}\left(\frac{P}{ZT}\right) = 0 \tag{25}$$

$$\frac{1}{A}\frac{\partial m}{\partial t} + \frac{\partial P}{\partial x} + \frac{R}{MA^2}\frac{\partial}{\partial x}\left(\frac{m^2 ZT}{P}\right) + \frac{\lambda m|m|ZRT}{2DA^2 PM} = 0 \tag{26}$$

In the case of the steady state ($\frac{\partial}{\partial t} = 0$), equations (25) and (26) become:

$$\frac{dm}{dx} = 0 \tag{27}$$

$$\frac{dP}{dx} + \frac{2RmZT}{PMA^2}\frac{dm}{dx} + \frac{m^2 R}{MA^2}\frac{d}{dx}\left(\frac{ZT}{P}\right) + \frac{\lambda m|m|ZRT}{2DA^2 PM} = 0 \tag{28}$$

Considering equation (27), equation (28) is written:

$$\frac{dP}{dx} + \frac{\lambda}{2D}\frac{ZRT}{PMA^2}m|m| + \frac{m^2 R}{MA^2}\frac{d}{dx}\left(\frac{ZT}{P}\right) = 0 \tag{29}$$

Taking into account equation (19), in isothermal condition it comes:

$$\frac{dP}{dx} + \frac{\lambda RT}{2DMA^2}\left(\alpha + \frac{\beta}{P}\right)m|m| + \frac{RT}{MA^2}m^2\frac{d}{dx}\left(\alpha + \frac{\beta}{P}\right) = 0 \tag{30}$$

Which leads to:

$$\frac{dP}{dx} = \frac{\lambda RT}{2DMA^2}m|m|\frac{\beta P + \alpha P^2}{\beta\frac{RT}{MA^2}m^2 - P^2} \tag{31}$$

Denoting,

$$\begin{cases} c_1 = \alpha\frac{\lambda RT}{2DMA^2}m|m| \\ c_2 = \beta\frac{\lambda RT}{2DMA^2}m|m| \\ c_3 = \beta\frac{RT}{MA^2}m^2 \end{cases} \tag{32}$$

It can be written then:

$$dx = \frac{c_3 - P^2}{P(c_1 P + c_2)}dP \tag{33}$$

Integrating equation (33) between $x = 0$ ($P = P_1$) and $x = L$ ($P = P_2$), one obtains

$$P_2 - P_1 = \alpha\frac{RT}{MA^2}m^2\ln\frac{P_2}{P_1} + \left(\frac{\beta}{\alpha} - \alpha\frac{RT}{MA^2}m^2\right)\ln\left(\frac{\alpha P_2 + \beta}{\alpha P_1 + \beta}\right) - \alpha\frac{\lambda RT}{2DMA^2}m|m|L \tag{34}$$

The friction factor λ is given by Colebrook-White equation (Giles 1962; Fox 1992; Shames 1989; White 1994):

$$\frac{1}{\sqrt{\lambda}} = -2\log_{10}\left(\frac{e}{3.7D} + \frac{2.51}{Re\sqrt{\lambda}}\right) \tag{35}$$

where e is the internal roughness of the pipe and R_e is the Reynolds number.

For fully turbulent flow or a rough turbulent flow ($R_e \gg 0$), the second term of equation (35) can be neglected and it can be, simply, written:

$$\frac{1}{\sqrt{\lambda}} = -2log_{10}(\frac{e}{3.7D}) \tag{36}$$

5   Case Study

The studied case is an installation composed of a compressor pumping the hydrogen-natural gas mixture through a steel Sch80 pipeline ($L = 900\ m$).as shown in figure 3. The pipe characteristics and the friction factor calculated using equation (36) are reported in table 4.
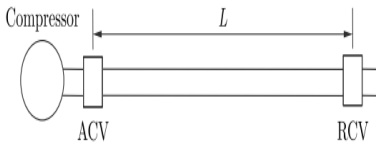
Fig. 3 Gas mixture installation

Table 4 Tubular pipes material properties: steel Sch 80 pipe (ANSI standards)

Designation	Value	Unit
Internal roughness (e)	0.0459	mm
Nominal Pipe Size (NPS)	500	mm
Internal diameter (D)	455.625	mm
Friction factor (λ)	1.012	–

An entry pressure $P_1 = 70\ bar$ is applied in the upstream side with a mass flow rate $m = 60\ Kg/s$ of the gas mixture. Figure 4 shows a comparison of the pressure drop along the pipeline between the developed model and the model that considers the compressibility factor as a constant (Tabkhi, 2011). The comparison between these two models is considered for natural gas ($y = 0$). In the model of (Tabkhi, 2011), the compressibility factor is a function of the critical properties of the gas mixture, average pressure of the pipe segment and the temperature that has been considered as constant (Mohring et al., 2004):

$$Z = 1 + (0.257 - 0.533\frac{T_c}{T})\frac{P_{ij}}{P_c} \tag{37}$$

$$P_{ij} = \frac{2}{3}\left(P_i + P_j - \frac{P_iP_j}{P_i+P_j}\right) \tag{38}$$

According to figure 4, it can be noted that assuming a constant compressibility factor may be sufficient in short pipes but in long and relatively long ducts, the Z factor variations have to be taken into account. In fact, the latter influence the pressure drop value in steady state which will affect the transient regime behavior.

Figure 5 illustrates the evolution of pressure through the pipe for different values of hydrogen mole fractions. It shows that the injection of hydrogen in the natural gas duct increases the pressure drop value.
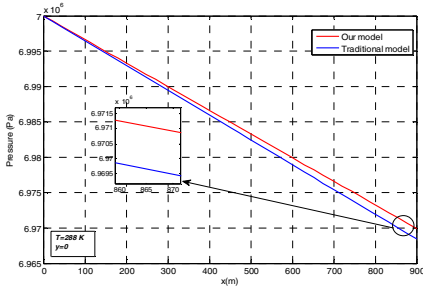
Fig. 4 Comparison between models   **Fig. 5** Pressure drop through the duct
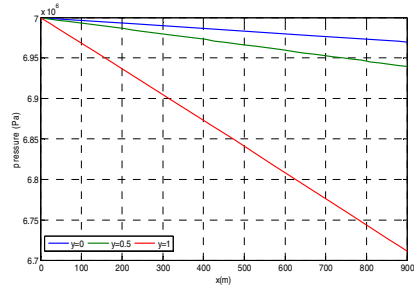
6   Conclusion

In this study, a linear approximation of hydrogen-natural gas mixture compressibility factor evolution was carried out and validated. Thus, a new expression of pressure drop through gas duct was established and used to evaluate the pressure evolution in a gas mixture installation for different mole fractions.

The compressibility factor approximation was based on resolution of cubic equation derived from SRK EOS in isothermal condition using Matlab software. A linear regression using Matlab fitting curves was adopted and validated.

References

Guo, B., Ghalambor, A.: Natural Gas Engineering Handbook. Gulf Publishing Company (2005)

Yarborough, L., Hall, K.R.: Oil and Gas (1973)

Dranchuk, P.M., Abou-Kassem, J.H.: J. Can. Petrol. Tech. (1975)

Sandler, S.I.: Chemical and Engineering Thermodynamics. Wiley, USA (1999)

Savidge, J.L.: The first requirement of gas measurement is accuracy. D.A.Tefankjian ISHM. Lawrence Reid Award Recipient (2000)

Tester, J.W., Modell, M.: Thermodynamics and Its Applications, 3rd edn. Prentice Hall, Englewood Cliffs (1996)

Fox, R.W., McDonald, A.T.: Introduction to Fluid Mechanics. Wiley, USA (1992)

Shames, I.H.: Mechanics of Fluids, p. 692. McGraw-Hill Book Co., New York (1989)

Three-Dimensional Numerical Flow Simulation in a Centrifugal Pump

Issa Chalghoum, Sami Elaoud, Mohsen Akrout, and Ezzeddine Hadj Taïeb

Research Laboratory
"Applied Fluid Mechanics, Process Engineering and Environment"
Engineering School of Sfax, BP'W'3038 Sfax, Tunisia
{chalghoumissa,elaoudsa}@yahoo.fr

Abstract. This paper shows numerical simulations of the three-dimensional fluid flow through centrifugal pump. The standard turbulence model $k - \varepsilon$ is adopted to describe the turbulent flow process. These simulations have been made with a steady calculation using the multiple reference frames (MRF) technique to take into account the impeller volute interaction. The computational domain composed by a single stator and rotor blade passages is discretized by a structured multi-block meshes .The transport equations associated with the appropriate boundaries conditions are solved by the ANSYS CFX finite-volume code. In addition, the steady state simulation are made to construct the performance for centrifugal impeller. This work is aimed to analyze the pressure and velocity distribution inside the pump impeller using the ANSYS-CFX computational fluid dynamics simulation tool.

Keywords: Centrifugal pump, CFD, pressure distribution, velocity distribution.

1   Introduction

Centrifugal pumps are widely used for hydraulic transportation of liquids over short to medium distance through pipelines mainly where the requirements of head and discharge are moderate. Few efforts were made to study the off-design performance of pumps. Computational fluid dynamics (CFD) has successfully contributed to the prediction of the flow through pumps and the enhancement of their design. Various researchers have considerably contributed to reveal the flow mechanisms inside centrifugal pump impellers with spiral volute aiming to design high performance centrifugal turbomachines. On the other hand, it was found that few researchers had compared flow and pressure fields among different types of pumps. Therefore, there is still a lot of work to be done in these fields.

Computational analysis of a centrifugal pump presented by Bcharoudis et al., 2008 reveals the flow mechanisms through centrifugal impellers and performance by varying outlet blade angle.

Nursen.et.al 2003 have developed a computer program for selection of centrifugal pumps by assuming that the head developed, the input power and NPSH of the pump could be represented in the form of polynomial of the flow rate. (Liu et al.1994) have made the measurement on centrifugal pumps and reported that impeller flow separation was observed on blade surface at off-design flow rate as compared to smooth flow within the impeller passage at design point. (Zhou, W. et al, 2003) have used a CFD code to study three-dimensional turbulent flow through water-pump impellers during design and off-design conditions.

(Baun, D. O. et al 2003) have observed the comparison between the characteristics of the lateral impeller forces and the hydraulic performances of four and five vane impeller operating in the spiral volute, concentric volute and double volute.

In this study, a numerical model was used to calculate steady hydrodynamics in centrifugal impeller. A structured grid was used in the impeller. To evaluate the effect of turbulence model on the flow field, the $k - \varepsilon$ turbulence model was tested. The numerical simulation has permitted study the distribution of the pressure and the velocity inside centrifugal impeller.

2   Mathematical Formulations

2.1   Governing Equations

The steady, conservative forms of Navier-Stokes equations in three-dimensional forms for an incompressible flow in the pumps can be described with the conservations laws of movement and mass of a constant viscosity fluid as follows:

Continuity:

$$\frac{\partial \rho}{\partial t} + \nabla.(\rho U) = 0 \tag{1}$$

Momentum:

$$\frac{\partial \rho U}{\partial t} + \nabla.(\rho U \otimes U) = \nabla.(-P\delta + \mu_{eff}(\nabla U + (\nabla U)^T)) + S_M \tag{2}$$

where vector notation has been used, $\otimes$ is a vector cross product; U is the velocity; ρ is the fluid's density, μ_{eff} is the fluid effective viscosity, P is the pressure; δ is the identity matrix and S_M is the additional sources of momentum.

For flows in a rotating frame of reference that are rotating at the constant rotation speed Ω, the effects of the Coriolis are modeled in the code.

$$S_M = -\rho\left[2\vec{\Omega}\otimes U + \vec{\Omega}\otimes(\vec{\Omega}\otimes\vec{r})\right] \tag{3}$$

where $\vec{r}$ is the locator vector and U is the velocity

2.2   Turbulence Model

The simplest and most widely used two-equations turbulence model is the standard k- model that solves two separate transport equations to allow the turbulent kinetic energy and its dissipation rate to be independently determined. The transport equations for k and in the standard k- model are:

$$\frac{\partial\rho k}{\partial t} + \nabla.(\rho Uk) - \nabla.(\Gamma_k\nabla k) = p_k - \rho_\varepsilon \tag{4}$$

$$\frac{\partial\rho\varepsilon}{\partial t} + \nabla.(\rho U\varepsilon) - \nabla.(\Gamma_\varepsilon\nabla\varepsilon) = \frac{\varepsilon}{k}(C_{\varepsilon 1}p_k - C_{\varepsilon 2}\rho_\varepsilon) \tag{5}$$

where the diffusion coefficients are given by

$$\Gamma_K = \mu + \frac{\mu_t}{\sigma_k} \quad \text{and} \quad \Gamma_\varepsilon = \mu + \frac{\mu_t}{\sigma_\varepsilon}$$

where turbulent viscosity

$$\mu_t = C_\mu\rho\frac{k^2}{\varepsilon}$$

and $C_{\varepsilon 1} = 1.44$; $C_{\varepsilon 2} = 1.92$; $C_\mu = 0.09$; $\sigma_k = 1.0$; and $\sigma_\varepsilon = 1.3$ are constants. The p_k in Equations (4) and (5) is the turbulent kinetic energy production term, which is for incompressible flow.

$$p_k = \mu_t\nabla U.(\nabla U + \nabla U^T) - \frac{2}{3}\nabla.U(\mu_t\nabla.U + \rho k) \tag{6}$$

Equations (1), (2), (4), and (5) form a closed set of nonlinear partial differential equations governing the fluid motion.

3   Numerical Simulation and Performance Prediction

3.1   Simulation Parameters and Boundary Conditions

With the three-dimensional model, there is a useful approach for investigation of flow behavior in impeller. Figure.1 shows the structured grid generation. There are 224160 cells in the impeller. The simulation is steady and moving reference frame is applied. The original impeller has a specific speed of 32 .The main parameters of the impeller presented in Table 1.

The specifications of the centrifugal pump selected for this analysis are indicated below.

Table 1 Specification of the impeller

Parameters	Value	Description
Ri	115 mm	Inlet flange radius
R1	75 mm	Mean impeller inlet radius
B1	85.9 mm	Inlet impeller width
β_1	$70°$	Inlet blade angle
θ_1	$37°$	Blade LE inclination angle
R_2	204.2 mm	Mean impeller outlet radius
B_2	42 mm	Outlet impeller width
β_1	$63°$	Outlet blade angle
θ_2	$90°$	Blade TE inclination angle
Na	5	Blade number
e	8 mm	Blade thickness
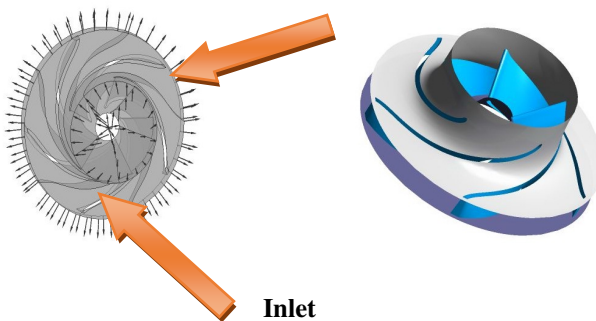
Inlet

Fig. 1 Computational domain of pump impeller

At the inlet of the computational domain, an imposed pressure is specified (Table 2 and Figure 1). At the outlet, a mass flow Q is imposed following the operating condition (Table 3). A no-slip flow condition is applied on the walls (on the blade, hub and shroud).

Table 2 Boundary conditions of impeller in the pump NS32

Flow simulation domain	Impeller
Grid	Impeller structured
Fluid	Water at standard condition
Outlet	Total pressure=1atm
Turbulence model	$k - \varepsilon$
Convection scheme	Second order
RMS (Rout Mean Square)	4-Oct

Table 3 Value of different mass flow Q/Qv

Value	0.5	0.8	1	1.2

3.2 *Numerical Investigation*

The transport equations associated with the given boundaries conditions describing the internal flow in centrifugal pump are solved by the CFX code. This code is based on the finite-volume method to discretize the transport equations.

In CFX, the pressure and velocity coupling is solved using the Rhie-Chow algorithm. Second order high-resolution scheme have been adopted for convection terms.

4   Results

4.1 *Meridian Velocity for Different Mass Flow*

Figure 2 shown the meridional velocity profile uniform output impeller promotes the functioning of the downstream of the impeller.

In the study of a pump, an analysis of its behavior, nominal outside is very important; especially in partial flow. Figure 2 shows the distribution of meridional velocity at 50%, 80%, 100% and 120 % of rated flow. We note the appearance of a small perturbation to the leading edge at the front flange, reflecting a less stable velocity distribution for the machine.

The perfect fluid flows are not able to make realistic forecasts in this area. Nevertheless, the main structures of the flow as the high accelerations at the origin of the recirculation are highlighted in all flow of operation of the pump.

Q/Qv=0.5   Q/Qv=0.8

Q/Qv=1   Q/Qv=1.2
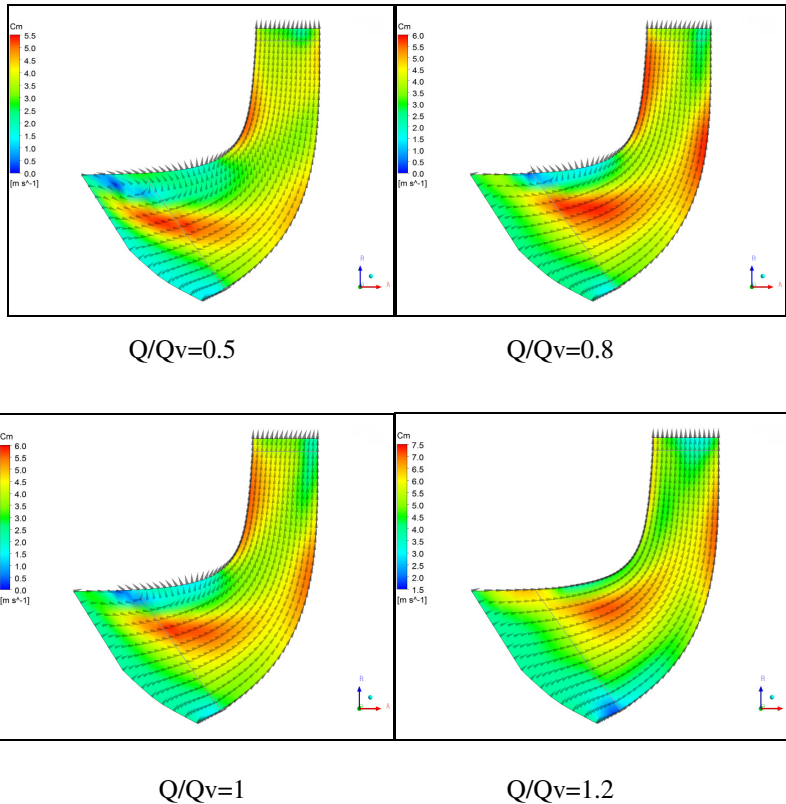
Fig. 2 Meridian velocity Cm for different mass flow

4.2 *Blade Loading at Pressure and Suction Side*

The blade loading of pressure and suction side are drawn at three different locations on the blade at the span of 20%, 50% and 80% from hub towards the shroud. Figure 3 gives the pressure loading on the impeller blade and plot along the streamwise direction. It is observed that the pressure evolution inside the impeller blades is asymmetry distributed. The minimum pressure area appears at the back of the pump impeller blade suction side, at the inlet.
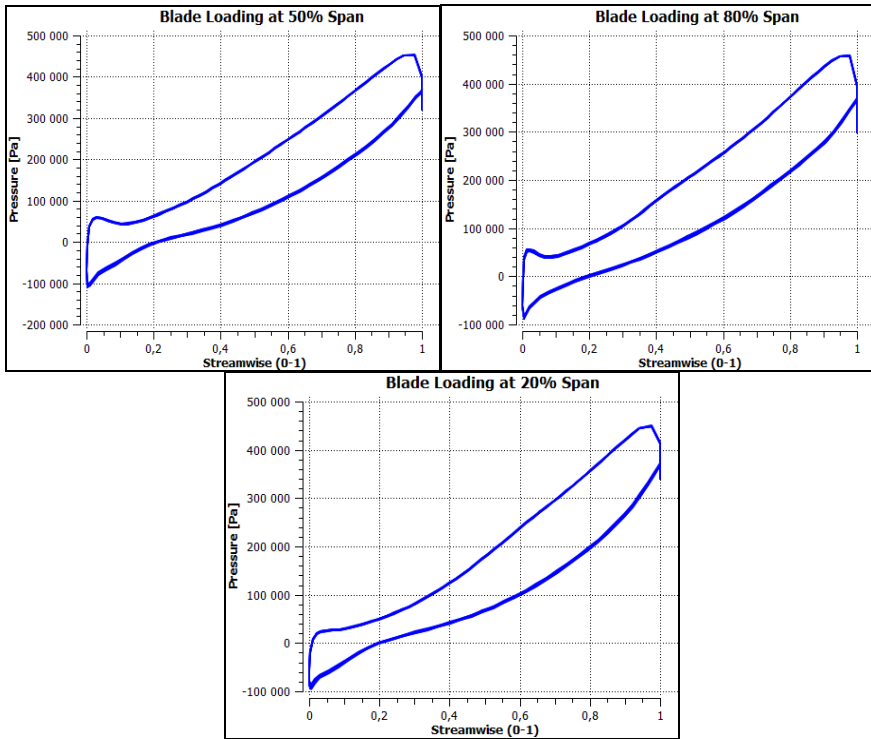
Fig. 3 Blade loading at 20, 50 and 80 span nominal mass flow (Q/Qv=1)

4.3 Distribution of Pressure for Different Mass Flow in the Impeller

Figure 4 shown the distribution of total pressure of the impeller for different mass flow (Q/Qv=0.5; Q/Qv=0.8; Q/Qv=1 and Q/Qv=1.2). The lower pressure appears at the inlet of the impeller suction side. This is the position where cavitation often appears in the centrifugal pump. This figure gives that the total pressure is inversely proportional to the mass flow rate .The lowest total pressure occurs at the outlet of impeller, where the mass flow rate reaches its maximum. It is observed that the static pressure inside the impeller blades is asymmetry distributed. The minimum contour pressure area appears at the back of the impeller blade suction side at the inlet.

Q/Qv=0.5   Q/Qv=0.8

Q/Qv=1   Q/Qv=1.2
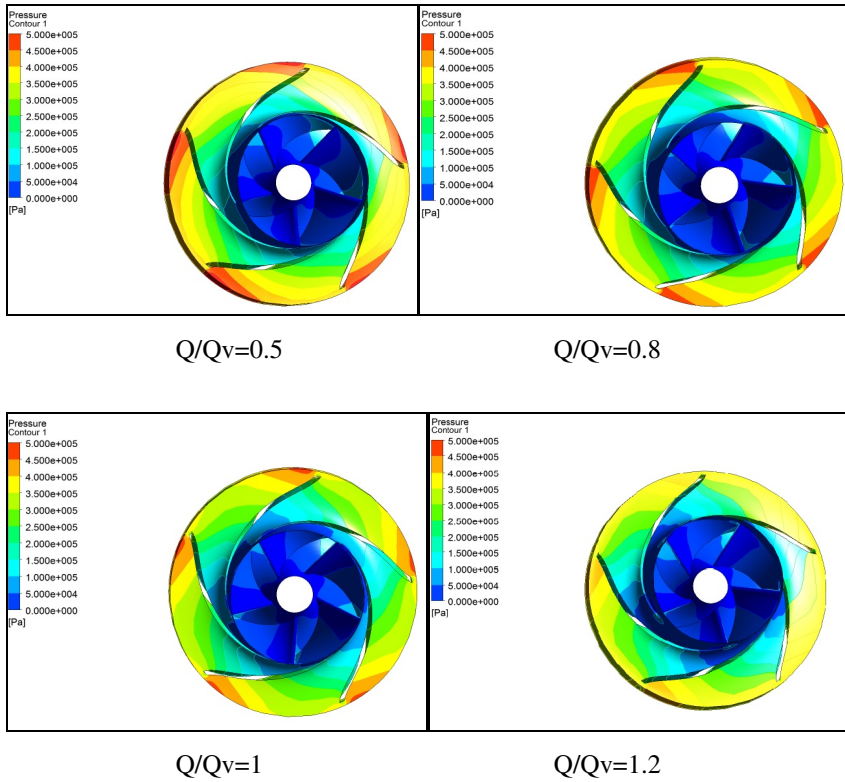
Fig. 4 Distribution of pressure for different mass flow

5   Conclusion

A numerical model of an impeller has been generated and the complex internal flow fields are investigated by using the Ansys-CFX computational code. A turbulence model $k - \varepsilon$ was chosen to simulate the internal flow of a centrifugal pump impeller. The centrifugal pump including impeller side gaps has modeled and meshed with a structured grid .The internal flow is not quite smooth in the suction and pressure side of the blade due to non-tangential inflow conditions which results in the flow separation at the leading edge. However, the Pressure and velocity distribution inside the impeller of the centrifugal pump have been directly influenced due to change of flow rate. Similar computational simulation models can also be used for analyzing the pressure and velocity of the turbines, compressor and fan.

References

Younsi, M., Kergourlay, G., Bakir, F., Rey, R.: Influence of splitter blades on the flow field of a centrifugal pump: test-analysis comparison. International Journal of Rotating Machinery 7, 1–13 (2007), doi:10.1155/2007/85024 ID 85024

Baun, D.O., Flack, R.D.: Effects of volute design and number of impeller blades on lateral impeller forces and hydraulic performance. International Journal of Rotating Machinery 9(2), 145–152 (2003), doi:10.1080/10236210390147461

Nursen, E.C., Ayder, E.: Numerical calculation of the three-dimensional swirling flow inside the centrifugal pump volutes. International Journal of Rotating Machinery 9, 247–253 (2003), doi:10.1080/10236210390202856

Zhou, W., Zhao, Z., Lee, T.S., Winoto, S.H.: Investigation of flow through centrifugal pump impellers using computational fluid dynamics. International Journal of Rotating Machinery 9(1), 49–61 (2003),
doi:10.1080/10236210390147380.

Bacharoudis, E.C., Filoios, A.E., Mentzos, M.D., Margaris, D.P.: Parametric study of a centrifugal pump impeller by varying the outlet blade angle. Open Mechanical Engineering Journal 2, 75–83 (2008), doi:1874-155X/08

Cezmi Nursen, E., Ayder, E.: Numerical calculation of the three-dimensional swirling flow inside the centrifugal Pump volutes. International Journal of Rotating Machinery 9, 247–253 (2003), doi:10.1080/10236210390202856

Thermal Study of a Parabolic Trough Collector

Asma Messadi and Youssef Timoumi

LGM, National Engineering School of Monastir, University of Monastir,
Monastir, Tunisia
asmamessadi@hotmail.com, Youssef.Timoumi@enim.rnu.tn

Abstract. Against the background of an increasing energy demand and growing environmental problems due to the use of fossil fuels reserves, the renewable energy resources offer interesting opportunities especially the solar thermal energy used for powering industrial applications and power generation. In the present work, we are interested to the simulation of outlet temperature of the Heat Transfer Fluid (HTF) in a parabolic trough solar collector. The study of the solar collector involves two essential sections: the first section is related to modeling the Direct Normal Irradiation (DNI) corresponding to the latitude of considered place. The second section is dedicated to studying the heat transfer in the absorber tube and the glass envelope for determining the output temperature of HTF. A mathematical model is developed to determine the outlet temperature of HTF. The results show clearly that the outputs temperatures are very depending to the incident solar radiation and surrounding environmental conditions. They are compared with measured data of the collector outlet temperature at SEGS VI power plant.

Keywords: Solar thermal energy, Parabolic trough collector, Direct Normal Radiation, Heat transfer Fluid, Outlet Temperature of HTF.

1   Introduction

Concentrated Solar Power (CSP) generation is a promising technology. It plays an important role in fossil fuel saving and CO2 emission mitigation.

Electricity production requires high temperatures of 400 ° C to 1200 ° C. These temperatures can be provided by concentration of the solar radiation with the aid of various types of collector systems which can achieve temperatures of 1000 °C (Heide, 2010).

Solar Concentration Systems have been widely developed and they are considered to be an effective tool for conversion of solar energy. They are used in many regions of the world (Hang et al. 2008). The first power plant with Parabolic Trough Collector (PTC) technology was built since 1984 in the United States (California Majove desert: SEGS VI) (Franchin et al, 2013).These systems can

provide about 7% of the total electricity production capacity of the world required in 2030 and 25% in 2050 (Izquierdo et al. 2010, Ziuku et al 2014).

The technology of parabolic trough solar thermal power plant is considered as one of the most successful, attractive and proven solar technologies which are used to produce electricity from thermal solar energy. Currently, several power plants under construction and many others under operation. At the end of 2010, approximately 1220 MW of installed capacity of CSP uses parabolic trough technology (IRENA, 2012).

Given its design and operating conditions to assess the power and to evaluate the outlet temperature of HTF, the study of a parabolic trough collector requires a detailed analysis of the energy conversion process of solar thermal energy. The process of energy conversion by PTC consists of two main sections:

- Optical capture system and concentration of direct solar radiation on a focal line (Solar collector field).
- Conversion system of concentrated solar radiation into heat or electricity (power bloc).

2   Parabolic Trough Solar Power Plant Technology

Parabolic trough collector (PTC) is a long parallel row that consists of curved glass mirrors (reflector), an absorber tube and a metal structure. The reflector is used to focus and to concentrate direct solar radiation into an absorber tube (receiver) located along the focal line of collector. The metal structure (support) ensures the attachment system as shown in Fig.1.The receiver consists of a special tube through that can heat a flowing fluid up about 400°C. The absorber tube role is to absorb the maximum of solar energy sent by the collector to heat the fluid. The collector must be equipped with a solar tracking system to address climate change that affects the solar radiation. The reflector must be continuously placed in front of the sun. Then, PTC converts solar energy into heat that can run a standard steam turbine generator.

The heat transfer between the different elements of the heat collection element (HCE) is shown in fig.2. The solar energy, reflected by the mirrors, passes through the glass envelope and it will full on the absorber tube. The absorber tube mounted in a glass envelope to minimize energy losses to the outside by using the effect of greenhouse. The envelope has high transparent to incoming solar radiation and high opaque to outgoing thermal radiation emitted from wall of the tube. The good reflector can reach a reflection coefficient up to 97% of the incident radiation. The absorber tube is coated with an optically selective coating that allows absorbing much of the solar energy while emitting only a small amount of thermal radiation. The receiver tube is surrounded by a glass envelope to reduce heat losses from the receiver tube. The annulus between absorber tube and the glass envelope is evacuated to eliminate convective heat transfer between the tube and the envelope.

1- Reflector

2- Absorber tube

3- Metal construction

4- Pipe installation
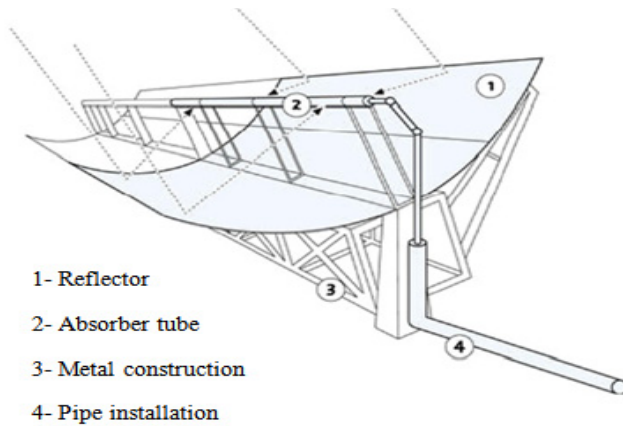
Fig. 1 Parts of a parabolic trough collector assembly

The heat transfer analysis in the PTC system is very important. It assesses the impact of the deterioration of the collector, and HTF flow control strategies on the PTC (Quoilin et al, 2011). Many models have been proposed since the 1970s. Forristall (2003) developed a heat transfer model with one and two dimensional detail of the solar receiver. This model was used to determine the thermal performance of parabolic trough with different operating conditions. Stuetzle et al (2002) proposed a heat transfer analysis of the heat collector element of parabolic trough solar receiver for calculating the outlet of the temperature of the solar field. The results obtained with the model showed good agreement with measured outlet temperatures. Clark (1982) conducted an analysis of the effects of design parameters and factors influencing the thermal and economic performance of parabolic trough receivers. Padilla (2011) presented a detailed analysis of a heat transfer model of a parabolic trough collector. Radiating a complete analysis was implemented in this study for the heat losses in the absorber and the glass envelope. To validate the proposed numerical model, he compared with experimental data obtained from SNL (Sandia National Laboratories), and Dudley et al (1994).

2.1 *Modeling of the Heat Collection Element*

The heat transfer model is based on an energy balance between the heat transfer fluid (HTF), and the different components of the heat collection element (fig.3). The absorber receives solar energy reflected by the mirrors through the glass. The absorbed solar energy is not fully transmitted to the heat transfer fluid. There are heat losses at the absorber and the glass.

In fact, the direct normal irradiation sunlight DNI fall on the collector by an incident angle θ. Then the absorbed solar energy will be directed to the absorber tube named $q_{absorbed}$.The heat transfer between the glass and the envelope is a medium of heat exchange by convection and radiation $q_{external}$, then the heat

transfer between the glass and the absorber tube is a heat exchange by convection and radiation $q_{internal}$ (the glass envelope is always colder than the absorber tube $T_{ABS} > T_{ENV}$). Finally, the heat transfer between the absorber tube and the HTF is exchanged by convection q_{gained}.
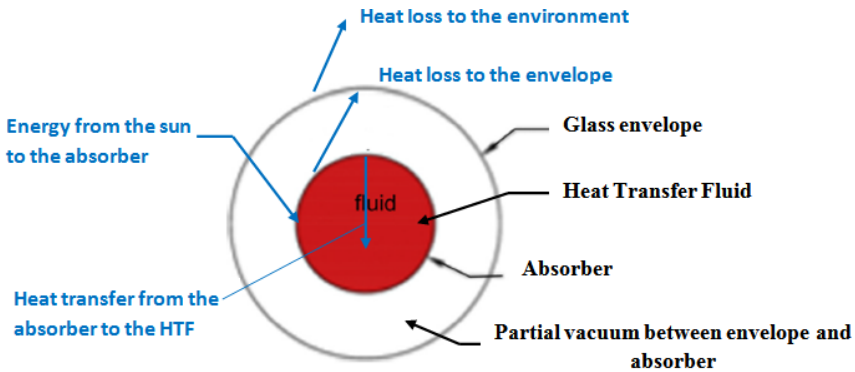
Fig. 2 A cross section of the heat collection element

The exchange in the HCE is studied with the following assumptions:

- The collector follows perfectly the sun.
- The flow of fluid in the receiver tube is one-dimensional.
- Uniform distribution of the temperature of coolant of the absorber tube and the glass envelope.
- The exchange by conduction in the absorber and the glass is negligible.
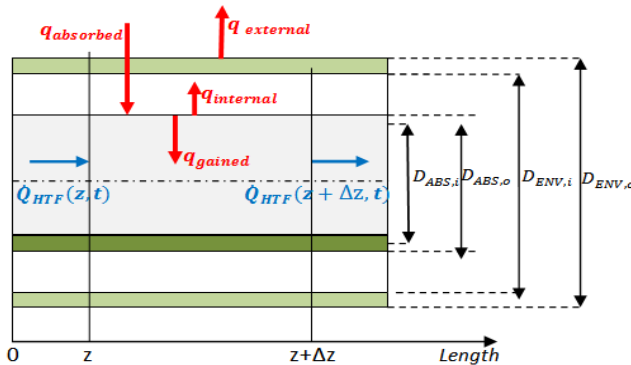
Fig. 3 Schema of the heat transfer

2.2   Partial Differential Equation for Temperatures

A detailed physical model for the collector is presented in figure 3. The energy balance for the HCE results in potential differential equations temperatures of the HTF, the absorber and the glass envelope. Heat transfer between the absorber and the HTF, between the absorber and the glass envelope, and between the envelope and the environment is established. The absorbed solar energy from the direct normal solar radiation is estimated.

The energy balance between the HTF and the absorber tube results in a partial differential for the HTF temperature (stuetzle, 2002):

$$\rho_{HTF} \; c_{HTF} \; A_{ABS,i} \; \frac{\partial T_{HTF}(z,t)}{\partial t} = -\rho_{HTF} \; c_{HTF} \; \frac{\dot{V}_{HTF}}{n_{collecteurs}} \; \frac{\partial T_{HTF}(z,t)}{\partial z} + q_{gained}(z,t) \quad (1)$$

$c_{HTF}, \rho_{HTF}, T_{HTF}$ as the specific heat of HTF, the HTF density and temperature. $A_{ABS;i}$ is the cross-sectional area of the inside tube of the absorber, $\dot{V}_{HTF}$ is the HTF volume flow rate that depends on the time since the fluid is considered to be incompressible and $n_{collectors}$ is the numbers of collectors. The time is t and the distance along the collector is z.

To solve the equation (1) we need an initial condition (2) and a boundary condition (3).

$$T_{HTF}(z,0) = T_{HTF,int}(z) \tag{2}$$

$$T_{HTF}(0,t) = T_{HTF,inlet}(t) \tag{3}$$

$T_{HTF,inlet}$ as the inlet temperature of the HTF of the collector field.

The temperature of the absorber tube T_{ABS} is given by (Stuetzle, 2002):

$$\rho_{ABS} \; c_{ABS} \; A_{ABS} \; \frac{\partial T_{ABS}(z,t)}{\partial t} = q_{absorbed}(t) - q_{internal}(z,t) - q_{gained}(z,t) \tag{4}$$

$c_{ABS}, \rho_{ABS}, T_{ABS}$ as the specific heat of absorber tube, the density and temperature. A_{ABS} is the cross-sectional area of the absorber. The initial condition for Eq. (4) is:

$$T_{ABS}(z,0) = T_{ABS,int}(z) \tag{5}$$

The heat balance between the envelope glass and the environment leads to the differential equation for the temperature of the glass envelope is given through (Stuetzle, 2002):

$$\rho_{ENV} \; c_{ENV} \; A_{ENV} \; \frac{\partial T_{ENV}(z,t)}{\partial t} = q_{internal}(z,t) - q_{external}(z,t) \tag{6}$$

$c_{ENV}, \rho_{ENV}, T_{ENV}$ as the specific heat of the glass envelope, the density and temperature. A_{ENV} is the cross-sectional area of the glass envelope.

The initial condition for solving the equation (6) is:

$$T_{ENV}(z,0) = T_{ENV,\text{int}}(z) \tag{7}$$

The structure of the absorbed solar heat input model by the collector is explained and summarized by several researchers (Clark, 1982, Edenburn 1976 and Manzolini et al. 2011, Padilla 2011). The energy absorbed in the solar receiver is affected by the optical properties and imperfections of the solar collector system (Padilla, 2011).The solar radiation absorbed by the receiver tube [W/m^2] is given by (Esmail et al, 2014):

$$q_{absorbed} = \eta_{opt} \quad \text{ANI} \tag{8}$$

Where η_{opt} is the optical efficiency and ANI [W/m^2] is the aperture normal irradiance that can be calculated by (Esmail et al, 2014):

$$\text{ANI} = \text{DNI}\cos(\theta) \tag{9}$$

DNI [W/m^2]   is the direct normal radiation and θ is the angle of incidence in degree.

The solar normal radiation is the solar energy that would be gained from the solar beam radiation without any optical losses. Due to the optical losses, ANI is not totally absorbed by the tube. The optical efficiency of the mirrors, the glass envelope and the receiver that depends on the materials, coating, and alignment accounts for losses at these surfaces. It was calculated in (Padilla, 2011). The nominal design point of the collector optical efficiency characterizes the collector's ability to focus incoming direct normal radiation on the receiver tube.

2.3   *Direct Solar Normal Radiation*

The solar radiation absorbed by the receiver is a fraction of the direct normal insolation because CSP systems focus and concentrate only the direct normal irradiance (DNI). Extraterrestrial solar radiation is divided into several parts: one part is absorbed by the air and water vapor, the other part is reflected back into space and the remaining part is scattered. The direct beam reaches the surface of the earth and the scattered radiation reaches the surface from the sky (Padilla, 2011).

There are many empirircal and physical models that can be found in literature (Kasten 1980, Iqbal 1983, Geymard 1989, Rigollier 2000, Janjai 2011). The direct normal solar radiation in this work is estimated by the Solis model to clear sky (Ineichen, 2008). The Solis model (Mueller et all, 2004) was established within the frame of the European project Heliostat-3. It is a spectrally resolved physical model that needs as main input parameters atmospheric water vapor column (w) and aerosol optical depth (AOD). These two parameters are the constituents of the atmosphere that have the greatest influence on solar radiation. They can be retrieved from the site of Nasa Earth Observations (http://neo.sci.gsfc.nasa.gov/).

3   Simulation Results

To implement all collected equations and to simulate the desired results, we have developed an algorithm using the mathematical computing software Matlab. Direct solar radiation is modeled with the Solis model estimation of clear sky as shown in fig.4.
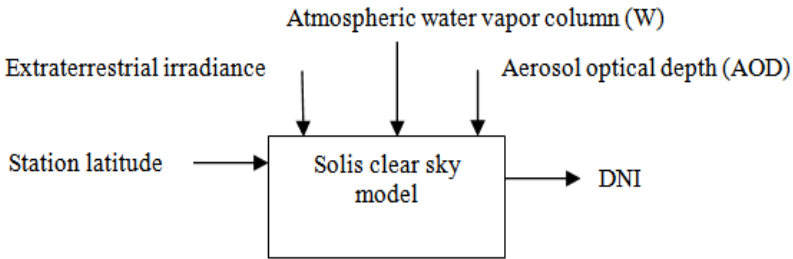
Fig. 4 Modeling of the DNI with the Solis model

In the present work, direct normal radiation is calculated under southern desert of California weather condition on June, 20 (Fig.5). In order to validate the model, the calculated results of DNI are compared with the results of Nrel Solar Radiation Research Laboratory (BMS, http://www.nrel.gov/) and with the measured results by using a Normal Incidence Pyrheliometer (NIP) (Stuetsle 2002). The direct normal radiation is variable between sunrise and sunset.

The solar collector field is modeled with Matlab code to solve nonlinear first order partial differential equations (PDE), (1),(4) and (6) listed in section 2.2 above. An information flow diagram for the solar field model is shown in Fig.5.
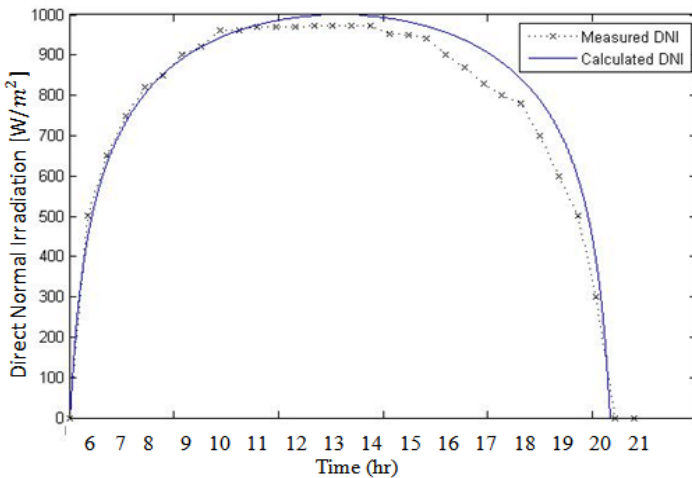
Fig. 5 Calculated DNI on June, 20 and measured Collector Outlet Temperature vs. Time on June 20, 1998
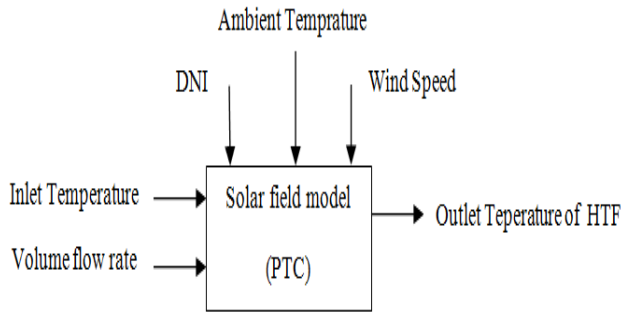
Fig. 6 Power Plant Model with inputs and outputs

The model allows to predict the outlet temperature of the HTF by introducing geographic coordinates, climate data (wind speed, ambient temperature, DNI), characteristics of parabolic trough collector (table1), volume flow rate, and the inlet temperature of the collector field.

The heat collector element is divided into several segments, and the energy balance was carried out for each control volume. The partial differential equations are discretized using the method of finite difference. The simulation process is carried out every hour from sunrise to sunset and for specific days during the year: September 19, December 16, for a parabolic trough concentrator whose geometrical characteristics are shown in Table 1.

The results of the evolution of the outlet HTF temperature obtained by the presently developed code with the synthetic oil (Syltherm 800) as a heat transfer fluid show that this temperature depends on the incident solar radiation and the surrounding weather conditions.

They have been firstly validated against results from the literature and against those obtained by SEGS VI power plant under Mojave desert, California (Stuetsle 2002). The overall match between measured and calculated results is good. It confirms that the model is validated as a model for the real SEGS VI power plant and the assumption made at the beginning of this work can be considered.

Table 1 Geometrical data of collectors of SEGS VI

Parameters	Value
Length of a tidy collectors	L=753.6m
Collector width	a=4.823
Number of tubes	N_{tubes}=50
Inner diameter of the absorber tube	$D_{ABS,i}$=0.066m
Outer diameter of the absorber tube	$D_{ABS,o}$=0.07m
Inner diameter of the glass envelope	$D_{ENV,i}$=0.112m
Outer diameter of the glass envelope	$D_{ENV,o}$=0.115m
Distance between two rows of collectors	Lsp=13m
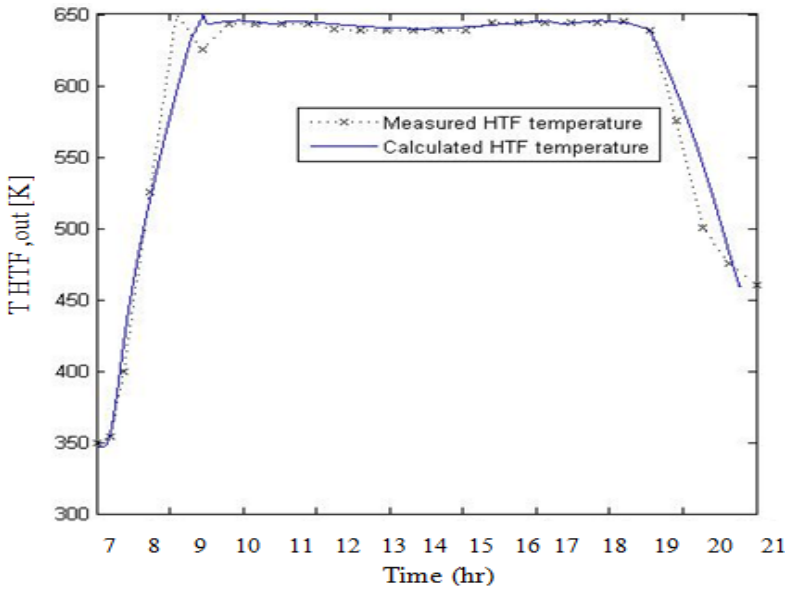
Fig. 7 Calculated outlet temperature of HTF on September, 16 and measured Collector Outlet Temperature vs. Time on September 19, 1998
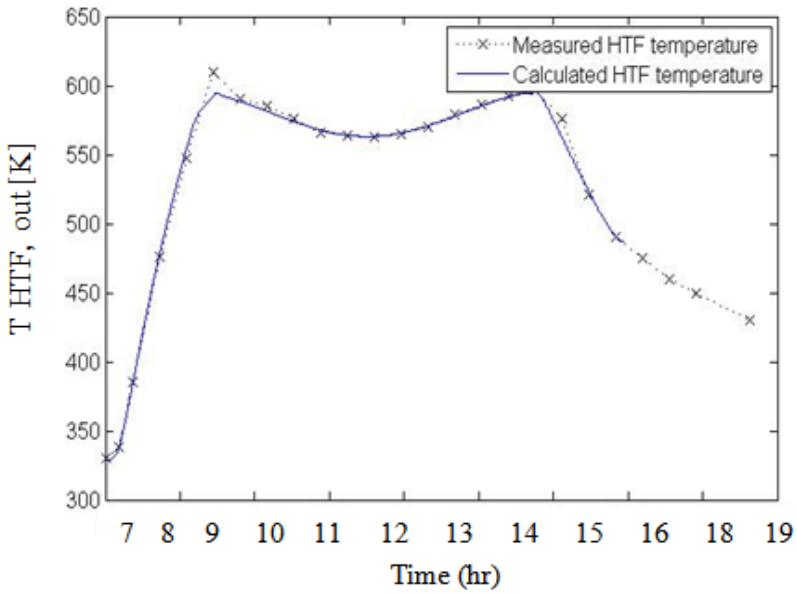
Fig. 8 Calculated outlet temperature of HTF on December, 16 and measured Collector Outlet Temperature vs. Time on December 19, 1998

4   Conclusion

This work proposes a digital simulation of the HTF heating of the absorber tube temperature with a parabolic trough solar collector.

From the heat exchanges in the heat collection element, a mathematical model is established to control the outlet temperature of the HTF. The obtained results show that this temperature depends on incident solar radiation and the surrounding weather conditions. The difference in temperature from the inlet of collector to the outlet for the days of the tests considered is important. In the other hand, the overall match between the measured outlet temperature of HTF and the calculated outlet temperature is good and confirms that the model presented in this work is validated as a model for the real SEGS VI trough collector field.

References

Dudley, V.E., Kolb, G.J., Mahoney, A.R., Mancini, T.R., Matthews, C.W., Sloan, M., et al.: Test results: SEGS LS-2 solar collector. NASA STI/Recon Technical Report N, 96,11437 (1994)

Clark, J.A.: An analysis of the technical and economic performance of a parabolic trough concentrator for solar industrial process heat application. Int. J. Heat Mass Transf. 25(9), 1427–1438 (1982)

Mokheimer, E.M.A., Dabwan, Y.N., Habib, M.A., Said, S.A.M., Al-Sulaiman, F.A.: Techno-economic performance analysis of parabolic trough collector in Dhahran. Saudi Arabia. Energy Conversion and Management (2014)

Forristall, R.: Heat transfer analysis and modeling of a parabolic trough solar re-ceiver implemented in Engineering Equation Solver. National Renewable Energy Laboratory, Golden (2003)

Franchini, G., Perdichizzi, A., Ravelli, S., Barigozzi, G.: A comparative study be-tween parabolic trough and solar tower technologies in Solar Rankine Cycle and Integrated Solar Combined Cycle plants. Solar Energy (2013)

Izquierdo, S., Montanes, C., Dopazo, C., Fueyo, N.: Analysis of CSP plants for the definition of energy policies: the influence on electricity cost of solar multiples, capacity factors and energy storage. Energy Policy 38, 6215–6221 (2010)

IRENA, Renewable energy technologies: cost analysis series. concentrating solar power. vol. 1. Power Sector Issue 2/5 (2012)

Ineichen, P.: A broadband simplified version of the Solis clear sky model. Solar Energy 758–762 (2008)

Quoilin, S., Orosz, M., Hemond, H., Lemort, V.: Performance and design optimization of a low-cost solar organic Rankine cycle for remote power generation. Solar Energy (2011)

Padilla, R.V.: Simplified Methodology for Designing Parabolic Trough Solar Power Plants, Department of Chemical and Biomedical Engineering College of Engineering University of South Florida (2011)

Heide, S., Freimark, M., Langnickel, U., Beukenberg, M., Pitz-Paal, R., Buck, R., Giuliano, S.: Design and operational aspects of gas and steam turbines for the novel solar hybrid combined cycle SHCC. In: Proceedings of the ASME Turbo Expo: Power for Land Sea and Air (2010)

Stuetzle, T., Blair, N., Mitchell, J.W., Beckman, W.A.: Automatic control of a 30 MWe SEGS VI parabolic trough plant. Solar Energy (2004)

Stuetsle, T.A.: Automatic control of the 30MWe SEGS VI parabolic trough plant, Dissertation, University of Wisconsin, Madison (2002)

Ziuku, S., Seyitini, L., Mapurisa, B., Chikodzi, D., van Kuijk, K.: Potential of Concentrated Solar Power (CSP) in Zimbabwe. Energy for Sustainable Development (2014)

Nomenclature		**Subscripts and superscripts**	
A	Area, m^2	ABS	Absorber tube
AOD	Aerosol optical depth	ENV	Glass envelope
ANI	Aperture normal irradiance, w/m^2	HTF	Heat transfer fluid
C	Specific heat, J/(Kg K)	I	Inside
DNI	Direct normal radiation w/m^2	Int	Initial
D	DIAMETER, m	opt	optical
q	Heat transfer per length w/m		
T	Temperature, °C		
t	Time		
$\dot{V}$	Volume flow rate m^3/s		
W	Atmospheric water vapor column		
z	Distance along the collector		
θ	Angle of incidence in degree		
η	Efficiency		
ρ	Density, Kg/m^3		

Effect of Obstacle Presence for Heat Transfer in Porous Channel

Saida Chatti[*], Chekib Ghabi[*], and Abdallah Mhimid[*]

Energetic department, National Engineering School of Monastir, Tunisia
Chatti_saida@yahoo.com, {ghabichekib,abdmhimid}@yahoo.fr

Abstract. In this study, heat transfer enhancement in porous medium was inspected. For this aims the lattice Boltzmann method was adopted to simulate mixed convection in porous domain. The Brinkman Forchheimer model was implemented to simulate porous channel including obstacles maintained at constant temperature. The velocity and the temperature are plotted at various parameters. The simulation was carried out for different porosity, Darcy and Reynolds. The Results show that by decreasing porosity, the heat transfer enhances. Also the result points that the obstacle position has effect on heat transfer.

Keywords: incompressible flow, lattice Boltzmann method, heat transfe, obstacle, porous media.

1   Introduction

During the past several decades, convective heat transfer in porous media has attracted many scientific researchers because of its various applications. The porous medium are usually used for improving heat transfer in industry such as nuclear Reactors cooling, heat pipes, packed bed reactors, fuel cells and heat exchangers. Huang and Vafai [1] simulated forced convection in a channel containing blocks arranged on the bottom wall. Kaviany [2] studied fluid flow and heat transfer in porous media with two isothermal parallel plates. Based on forced convection in a porous channel containing discrete heated blocks Rizk and Kleinstreuer [3] showed that an increase in heat transfer can be obtained by using porous channel. The lattice Boltzmann method (LBM) is an efficient and powerful numerical tool founded on kinetic theory for simulation of fluid flows and modeling the physics proprieties. The incompressible flows through porous media by using lattice Boltzmann method was studied by many researchers such as Seta and al. and Zhao and Guo [4]. In this study LBM is used to simulate flow behaviors and heat transfer in a channel with solid block located inside a porous media.

---

[*] Corresponding authors.

2   Lattice Boltzmann Method for Incompressible Flow in Porous Media

The LBM is defined as one of the computational fluid dynamics (CFD) methods. Counter to the others a macroscopic Navier Stokes (NS) method; the Lattice Boltzmann Method (LBM) is based on a mesoscopic approach to simulate fluid flows [5] [6]. The general form of Lattice Boltzmann equation with external force can be written as [7]:

$$f\left(\mathbf{x}+\delta t\mathbf{c}_i, t+dt\right)_i - f\left(\mathbf{x},t\right)_i = \frac{f\left(\mathbf{x},t\right)_i - f\left(\mathbf{x},t\right)^{eq}}{\Gamma_\nu} + \delta t\, \mathbf{F}_i. \tag{1}$$

Where δt denotes lattice time step, $\mathbf{c}_i$ is the discrete lattice velocity in direction, $\mathbf{F}_i$ is the external force in direction of lattice velocity $\mathbf{c}_i$, Γ_ν denotes the lattice relaxation time, $f^{eq}{}_i$ is the equilibrium distribution function. The local equilibrium distribution function determines the type of problem that needs to be solved. Equation (1) can be interpreted as two successive processes collision and streaming steps. The collision expresses various fluid particle interactions such as collisions and calculates new distribution functions [8]. Many models are advanced for the simulation of the fluid flow in the porous medium. The Brinkman-Forchheimer approach has been used successfully in simulation porous media in large values of porosities, Darcy, Rayleigh and Reynolds numbers [9]. This model includes the viscous and inertial terms by the local volume averaging technique. The Brinkman-Forchheimer equation is written as:

$$\frac{\partial \mathbf{u}}{\partial t} + \left(\mathbf{u}\cdot\nabla\right)\left(\frac{\mathbf{u}}{\varepsilon}\right) = -\frac{1}{\rho}\nabla\left(\varepsilon p\right) + \upsilon_e \nabla^2 \mathbf{u} + \mathbf{F}. \tag{2}$$

ε is the porosity, υ_e the effective viscosity, $\mathbf{F}$ is the total body force which contains the viscous diffusion, the inertia due to the porous medium, and an external force given by the Ergun's relation. The forcing term model is written as [10] [11]:

$$\mathbf{F}_i = \omega_i \rho \left(1 - \frac{1}{2\Gamma_\nu}\right)\left[\frac{3\mathbf{c}_i\,\mathbf{F}}{\mathbf{c}^2} + \frac{9\left(\mathbf{u}\,\mathbf{F}:\mathbf{c}_i\,\mathbf{c}_i\right)}{\varepsilon\,\mathbf{c}^4} - \frac{3\mathbf{u}\cdot\mathbf{F}}{\varepsilon\,\mathbf{c}^2}\right]. \tag{3}$$

The equilibrium distribution functions are calculated by [12]:

$$f_i^{eq} = \omega_i \rho \left[1 + \frac{3\mathbf{c}_i\,\mathbf{u}}{\mathbf{c}^2} + \frac{9\left(\mathbf{c}_i\,\mathbf{u}\right)^2}{2\varepsilon\,\mathbf{c}^4} - \frac{3\mathbf{u}^2}{2\varepsilon\,\mathbf{c}^2}\right]. \tag{4}$$

For D2Q9 model, the discrete velocities c_i are given by:

$$\begin{cases} c_0 = 0. \\ c_i = c\cos\left((i-1)\dfrac{\pi}{2}\right); \sin\left((i-1)\dfrac{\pi}{2}\right) i = 1,4 \\ c_i = c\sqrt{2}\cos\left((i-5)\dfrac{\pi}{2}+\dfrac{\pi}{4}\right); \sin\left((i-5)\dfrac{\pi}{2}+\dfrac{\pi}{4}\right) i = 5,8 \end{cases} \qquad .$$

(5)
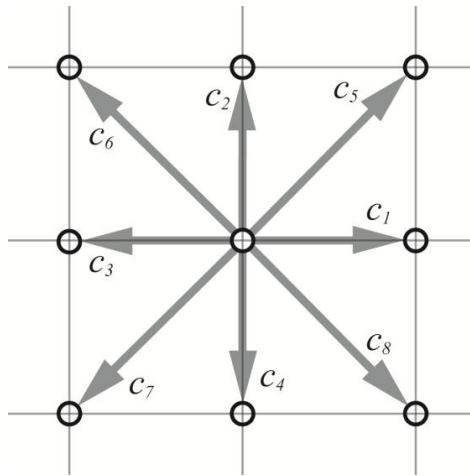
Fig. 1 The velocity distribution in the D2Q9 models

The weights are expressed as follows:

$$\omega_0 = \frac{4}{9}, \omega_i = \frac{1}{9}i = 1,4, \omega_i = \frac{1}{36}i = 5,8$$

(6)

The macroscopic quantities are accessed through the distribution functions. Indeed the density and the fluid velocity:

$$\rho(\mathbf{x,t}) = \sum_{i=0}^{8} f(\mathbf{x,t})_i \cdot$$

(7)

$$\mathbf{u}(\mathbf{x,t}) = \sum_{i=0}^{8} \frac{\mathbf{c}_i\, f(\mathbf{x,t})_i}{\rho} + \frac{\mathbf{F}\,\delta\mathbf{t}}{2} \cdot$$

(8)

In LBM the fluid viscosity is determined using the following relation:

$$v = \frac{\delta t c^2}{3}\left(\Gamma_v - \frac{1}{2}\right).$$

(9)

The temperature is carried out by a second distribution function denoted $g(x,c,t)$. It is governed in i direction by the following equation:

$$g\left(x+c_i\,\delta t, t+\delta t\right)_i - g\left(x,t\right)_i = -\frac{g\left(x,t\right)_i - g\left(x,t\right)_i^{eq}}{\Gamma_c}.$$

(10)

The equilibrium distribution functions are given by the following expressions:

$$\begin{cases} g_0^{eq} = -\frac{2\rho\varepsilon u^2}{3c^2} \\[2mm] g_i^{eq} = \frac{\rho\varepsilon}{9}\left[\frac{3}{2} + \frac{3}{2}\frac{c_i\,u}{c^2} + \frac{9}{2}\frac{\left(c_i\,u\right)^2}{c^4} - \frac{3u^2}{2c^2}\right] i = 1,4. \\[2mm] g_i^{eq} = \frac{\rho\varepsilon}{9}\left[\frac{3}{2} + \frac{3}{2}\frac{c_i\,u}{c^2} + \frac{9}{2}\frac{\left(c_i\,u\right)^2}{c^4} - \frac{3u^2}{2c^2}\right] i = 5,8 \end{cases}$$

(11)

The fluid temperature is obtained from the distribution function by:

$$T\left(x,t\right) = \frac{1}{\rho}\sum_{i=0}^{8} c_i\,g\left(x,t\right)_i .$$

(12)

The thermal diffusivity is:

$$\alpha = \sigma c_s^2\left(\Gamma_c - 0.5\right).$$

(13)

3 Problem Description

In the present study we consider a fluid flow in porous channel of width H. The walls are fixe. The upper plate is hot and the bottom one is cold. The computational domain contains hot solid blocks at different positions as shown in figure 2.

In simulation we adopt that the laminar and incompressible flow is viscous Newtonian, and the buoyancy effects are assumed negligible. All physical properties of the fluid and solid are constant.
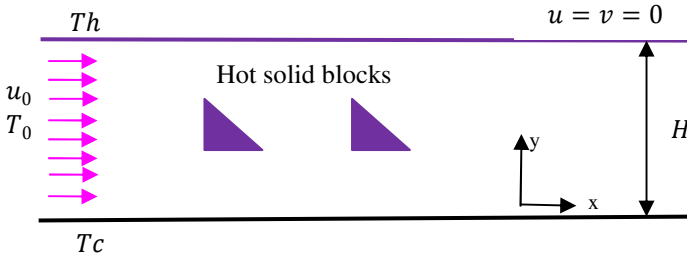
Fig. 2 Schematic of flow in the channel

For this flow in porous media the fluid behavior can be described by the following equations:

The continuity equation:

$$\nabla \cdot \mathbf{u} = 0 \cdot \tag{14}$$

The momentum equation:

$$\frac{\partial \mathbf{u}}{\partial \mathbf{t}} + (\mathbf{u} \cdot \nabla)\left(\frac{\mathbf{u}}{\varepsilon}\right) = -\frac{1}{\rho} \nabla(\varepsilon p) + \varepsilon \mathbf{G} - \frac{\varepsilon v}{K} \mathbf{u} + v_e \nabla^2 \mathbf{u} \cdot \tag{15}$$

Energy equation:

$$\sigma \frac{\partial T}{\partial \mathbf{t}} + \nabla \cdot (\mathbf{u} T) = \alpha \nabla^2 T \cdot \tag{16}$$

From physical limits (the velocity in the inlet of the flow is defined) to numerical ones we occur to the distribution functions. The distribution functions out of the domain are known from the streaming process. The unknown distribution functions are those toward the domain. The solid walls are assumed to be no slip, for this reason the bounce-back scheme is applied. For example in the north boundary the following conditions are used [13].

$$f_i = f_{-i} \cdot \tag{17}$$

$$i = 4, 7, 8$$

For the inlet the Zou and He boundary conditions are applied and an extrapolation in the outlet boundary is used [10] [11]. For the thermal boundary the Direchlet boundary are necessary.

4   Resultats and Discussion

In this simulation the Reynolds number changes from 150 to 50, the porosity is equal to 0.7 and the Darcy number set to be 0.1.
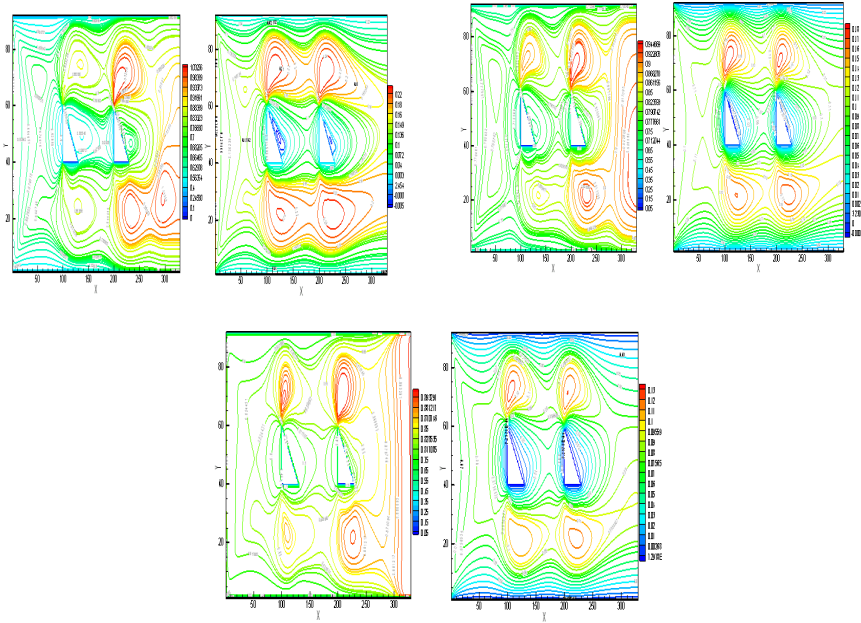
Fig. 3 Temperature (left) and velocity (right) profile at different Reynolds number (respectively 150, 80 and 50)
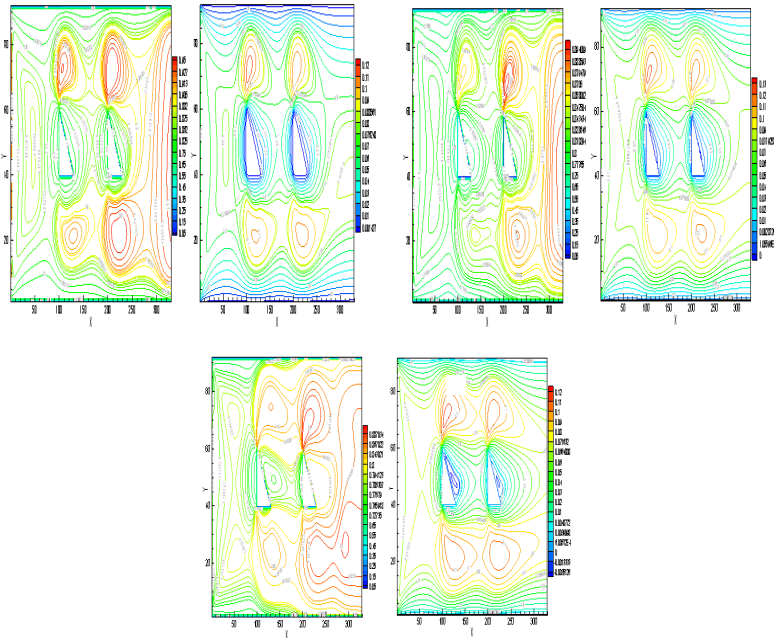
Fig. 4 temperature (left) and velocity (right) profile at different porosity (respectively 0.99, 0.5 and 0.3)

The figure shows that by increasing the Reynolds number the heat transfer in the channel raises. At high value of Reynolds the fluid velocity increases.

Then the porosity change from 0.99 to 0.3, the Reynolds number is equals to 50 and the Darcy one is 0.1.

The figure shows that for low value of porosity the heat transfer and the velocity of the flow are more important. Indeed With increasing the porosity the fluid temperature reduces due to lower values of effective thermal conductivity in blocks which can causes the heat transfer decreases. An Increase in the porosity value, the velocity rises. With increasing the porosity, it easier for fluid to change its path.

In this study the Darcy number changes from 10^{-3} to 1, porosity is 0.7 and the Reynolds number is taken 50.
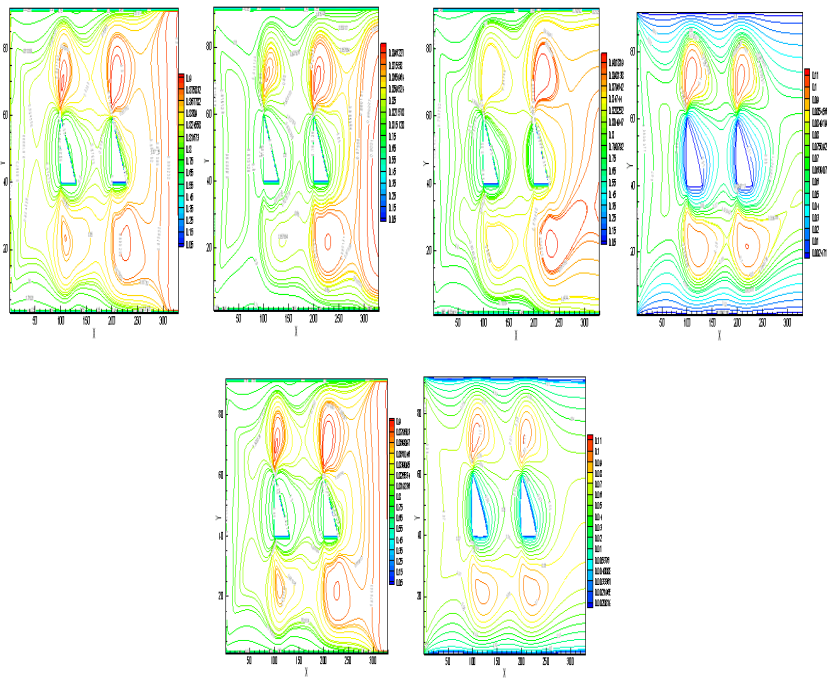
Fig. 5 temperature (left) and velocity (right) profile at different Darcy number (respectively 10^{-3}, 10^{-2} and 1)

The heat transfer is more important at high value of Darcy number.

Finally the porosity is equal to 0.7, the Reynolds number is 50 and the Darcy one is 0.1. The thermal conductivity ratio R_k changes from 29 to 69.
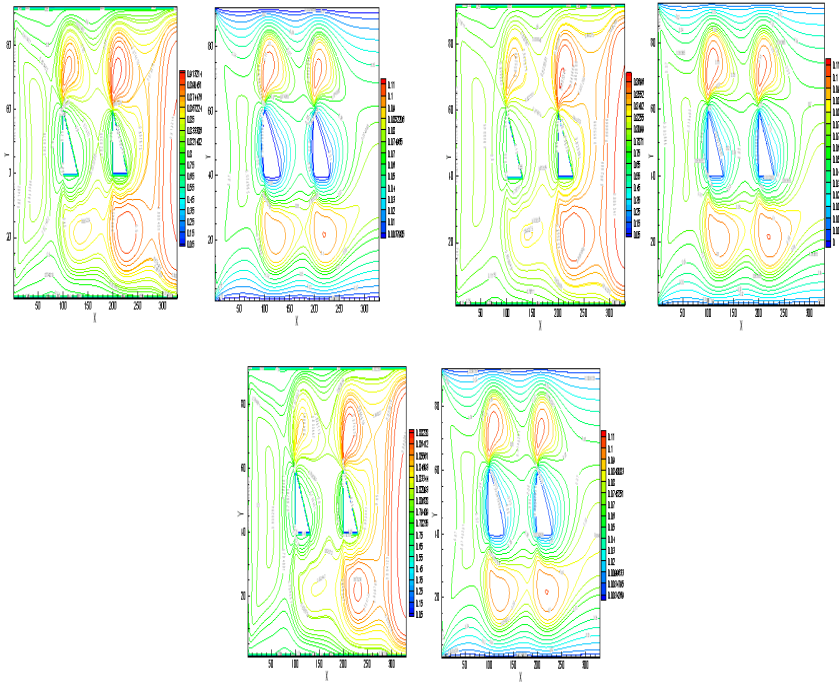
Fig. 6 temperature (left) and velocity (right) profile at different thermal conductivity ratio (respectively 29, ⌐⌐ and 69)

The heat transfer and the fluid velocity increase by decreasing the thermal conductivity ratio.

5   Conclusion

The heat transfer phenomena is abundant in many scientifique and engeeniring field. In this study a numerical simulation was carried out for Fluid flow and heat transfer in a porous channel containing hot solid blocks. This paper interested on the effect of parameters such as Reynolds number, thermal conductivity ratio and porosity on the flow field and thermal behavior is simulated by using thermal lattice Boltzmann method. Indeed the Brinkman-Forchheimer approach was adopted for simulation. The temperature of fluid reduces by increasing the porosity due to lower values of thermal conductivity. So that the heat transfer decreases with blocks. Increasing the thermal conductivity ratio the fluid temperature will be reduced. The results indicate that increasing the Reynolds and the Darcy number raises the heat transfer. The lattice Boltzmann method is a powerful tool for simulation of fluid flow and heat transfer in porous media and many phenomena.

Nomenclature

c	Lattice spacing	U	Fluid velocity
c_i	Discrete velocity for D2Q9 model	**Greek letters**	
Da	Darcy number	α	Thermal diffusivity
f	Density distribution function	Γ_c	Thermal time relaxation
f^{eq}	Density equilibrium distribution function	Γ_ν	Dynamic time relaxation
F	Total body force	δt	Time step
F_ε	Geometric factor	ε	Porosity
g	Thermal distribution function	υ	Viscosity
g^{eq}	Thermal equilibrium distribution function	υ_e	Effective viscosity
H	Channel width	ρ	Density
i	Lattice index in the x direction	Ω	Collision operator
j	Lattice index in the y direction	ω_i	The weights coefficient i in the direction
K	Permeability	**Subscripts**	
k	Thermal conductivity	e	effective
p	Pression	f	Fluid
Ra	Rayleigh number	i	Discrete velocity direction
Re	Reynolds number	**Superscript**	
T	Fluid temperature	eq	equilibrium
T_c	Cold temperature		
T_h	Hot temperature		

References

[1] Huang, P.C., Vafai, K.: Analysis of forced convection enhancement in a channel using porous blocks, AIAA J. Thermophys. Heat Transfer 18, 563–573 (1994)
[2] Kaviany, M.: Laminar flow through a porous channel bounded by isothermal parallel plate, Int. J. Heat MassTransfer 28, 851–858 (1985)
[3] Rizk, T., Kleinstreuer, C.: Forced convective cooling of a linear array of blocks in open and porous matrix channels, Heat. Transfer Eng. 12, 4–47 (1991)
[4] Zhang, J.M., Sutton, W.H., Lai, F.C.: Enhancement of heat transfer using porous convection-to-radiation converter for laminar flow in a circular duct, Int. J. Heat Mass Transfer 40, 39–48 (1996)
[5] Zhaoli, G., Zhao, T.S.: Lattice Boltzmann model for incompressible flows through porous media. Physical Review E 66 (2002)

[6] Azmi, M.: Numerical study of convective heat transfer and fluid flow through porous media, Thèse de doctorat, Université de Technologies de Malaysia (2010)

[7] Seta, T., Takegoshi, E., Kitano, K., Okui, K.: Thermal lattice Boltzmann model for incompressible flows through porous media. Jounal of Thermal Science and Technology, 90–100 (2006)

[8] Arab, M.: Reconstruction stochastique 3D d'un matériau céramique poreux à partir d'images expérimentales et évaluation de sa conductivité thermique et de sa perméabilité, Thèse de doctorat, Université de Limoges (2010)

[9] Jie, X.: A generalized Lattice-Boltzmann Model of fluid flow and heat transfer with porous media, National University of Singapore, Master of engineering (2007)

[10] Mohamad, A.A.: lattice Boltzmann method fundamentals and engineering applications with computer codes, Springer Verlag, London, 195 (2011)

[11] Janzadeh, N., Delavar, M.A.: Using Lattice Boltzmann Method to Investigate the Effects of Porous Media on Heat Transfer from Solid Block inside a Channel. Transport Phenomena in Nano and Micro Scales 1, 117–123 (2013)

[12] Farhadi, M., Mehrizi, A.A., Sedighi, K., Afrouzi, H.H.: Effect of Obstacle Position and Porous Medium for Heat Transfer in an Obstructed Ventilated Cavit, Jurnal Teknologi, pp. 59–64 (2012)

[13] Che Sidik, N.A., Khakbaz, M., Jahanshaloo, L., Samion, S., Darus, A.N.: Simulation of forced convection in a channel with nanofluid by the lattice Boltzmann method. Nanoscale Research Letters, 1–8 (2013)

Author Index